



PACIFIC EARTHQUAKE ENGINEERING RESEARCH CENTER

Experimental and Analytical Studies on the Seismic Behavior of Conventional and Hybrid Braced Frames

Jiun-Wei Lai

Stephen A. Mahin

Department of Civil and Environmental Engineering
University of California, Berkeley

Disclaimer

The opinions, findings, and conclusions or recommendations expressed in this publication are those of the author(s) and do not necessarily reflect the views of the study sponsor(s) or the Pacific Earthquake Engineering Research Center.

Experimental and Analytical Studies on the Seismic Behavior of Conventional and Hybrid Braced Frames

Jiun-Wei Lai

Stephen A. Mahin

Department of Civil and Environmental Engineering
University of California, Berkeley

PEER Report 2013/20
Pacific Earthquake Engineering Research Center
Headquarters, University of California, Berkeley

September 2013

ABSTRACT

This report summarizes both experimental and analytical studies on the seismic response of conventional steel concentrically braced frame systems of the type widely used in North America, and preliminary studies of an innovative hybrid braced frame system: the Strong-Back System. The research work is part of NEES small group project entitled “International Hybrid Simulation of Tomorrow’s Braced Frames.”

In the experimental phase, a total of four full-scale, one-bay, two-story conventional braced frame specimens with different bracing member section shapes and gusset plate-to-beam connection details were designed and tested at the NEES@Berkeley Laboratory. Three braced frame specimens were tested quasi-statically using the same predefined loading protocol to investigate the inelastic cyclic behavior of code-compliant braced frames at both the global and local level. The last braced frame specimen was nearly identical to one of those tested quasi-statically. However, it was tested using hybrid simulation techniques to examine the sensitivity of inelastic behavior on loading sequence and to relate the behavior observed to different levels of seismic hazard.

Computer models of the test specimens were developed using two different computer software programs. In the software framework OpenSees fiber-based line elements were used to simulate global buckling of members and yielding and low-cycle fatigue failure at sections. The LS-DYNA analysis program was also used to model individual struts and the test specimens using shell elements with adaptive meshing and element erosion features. This program provided enhanced ability to simulate section local buckling, strain concentrations, and crack development. The numerical results were compared with test results to assess and refine the ability of the models to predict braced frame behavior. A series of OpenSees numerical cyclic component simulations were then conducted using the validated modeling approach. Two hundred and forty pin-ended struts with square hollow structural section shape were simulated under cyclic loading to examine the effect of width-to-thickness ratios and member slenderness ratios on the deformation capacity and energy dissipation characteristics of brace members.

The concept of a hybrid system, consisting of a vertical elastic truss or strong-back, and a braced frame that responds inelastically is proposed herein to mitigate the tendency of weak-story mechanisms to form in conventional steel braced frames. A simple design strategy about member sizing of the proposed Strong-Back System is provided in this study. To assess the ability of the new Strong-Back System to perform well under seismic loading, a series of inelastic analyses were performed considering three six-story hybrid braced frames having different bracing elements, and three six-story conventional brace frames having different brace configurations. Monotonic and cyclic quasi-static inelastic analyses and inelastic time-history analyses were carried out. The braced frame system behavior, bracing member force-displacement hysteresis loops, and system residual drifts were the primary response quantities examined. These tests indicated that the new hybrid system achieved its design goals.

Experimental results show for the same loading history that the braced frame specimen using round hollow structural sections as brace members has the largest deformation capacity among the three types of bracing elements studied. Beams connected to gusset plates at the column formed plastic hinges adjacent to the gusset plate. The gusset plates tend to amplify the rotation demands at these locations and stress concentrations tended to result in early fractures of the plastic hinges that form. To remedy this problem, pinned connection details were used in the last two specimens; these proved to prevent failures at these locations under both quasi-static and pseudo-dynamic tests. Failure modes observed near the column-to-base plate connections in all of the specimens suggest the need for further study. Both OpenSees and LS-DYNA models developed in this study predict the global braced frame behavior with acceptable accuracy. In both models, low-cycle fatigue damage models were needed to achieve an acceptable level of fidelity. Shell element models were able to predict local behavior and the mode of failures with greater but not perfect confidence. OpenSees analysis results show that the proposed hybrid braced frames would perform better than conventional braced frames and that the story deformations are more uniform. Finally, future research targets are briefly discussed at the end of this report.

ACKNOWLEDGMENTS

This report would not have been written without the support of many individuals, and the authors want to express their deepest appreciation to them. Only some of them are particularly mentioned here.

Financial support of this research was provided in part by the National Science Foundation under grant number NSF-0619161, NEESR-SG: “International Hybrid Simulation of Tomorrow's Braced Frame Systems.” This support is greatly appreciated.

Laboratory assistance provided by NEES@Berkeley Laboratory and the Department of Civil and Environmental Engineering is appreciated. In particular, the assistance by managers of NEES@Berkeley Laboratory, Don Clyde and Dr. Shakhzod Takhirov, is greatly acknowledged. The authors would also like to thank the engineers and technicians at both the NEES@Berkeley Laboratory and Davis Hall Structural Laboratory, including Wesley Neighbour, Donald Patterson, David MacLam, Nathaniel Knight, Jose Robles, Robert Cerney, Bill MacCracken, and Jeff Higginbotham. Full-scale specimen preparation assistance by a number of students, including Yuichi Maeda, Carl Misra and Charbel Moubarak is greatly appreciated. Special thanks are also directed to Dr. Andreas Schellenberg, Dr. Selim Gunay, and Kung-Juin Wang for their help on the hybrid simulation tests. Library assistance provided by Charles James and NISEE staff is gratefully appreciated. The assistance of Claire Johnson in proofreading this report is also appreciated.

The authors would like to show their gratitude to the Herrick Steel Corporation for donating four full-scale specimens, providing lab fabrication manpower, and shop drawing supports; California Erectors for providing the second specimen lab fabrication manpower; Schuff Steel Company for providing test specimens; and Iron Workers Union Local 378 for donating manpower for specimen fabrication. Without their generous help, the full-scale testing program would not have been possible. Finite element analysis software supported by ARUP Engineers is gratefully acknowledged.

Many researchers and engineers around the world including Professor Charles Roeder, Professor Keh-Chyuan Tsai, Rafael Sabelli, Walterio A. López, Dr. Patxi Uriz, Frances Yang, Ronald O. Hamburger, and Brett R. Manning provided valuable suggestions and comments along this research project. Although not all of these suggestions were incorporated into this study, the authors would like to thank for their time on reviewing and providing professional advice.

While this report is due to the contributions of many, the findings, conclusions, and recommendations are those of the authors alone.

TABLE OF CONTENTS

ABSTRACT.....	iii
ACKNOWLEDGMENTS	v
TABLE OF CONTENTS	vii
LIST OF FIGURES	xi
LIST OF TABLES	xlix
LIST OF APPENDICES	liii
1 INTRODUCTION.....	1
1.1 Background and Research Motivation	1
1.2 Research Objectives and Scope	3
1.3 Overview and Organization of Report.....	4
2 LITERATURE REVIEW	7
2.1 Bracing Component.....	7
2.1.1 Issues Related to Net Reduced Section.....	7
2.1.2 Limitations on Slenderness Ratio and Width-to-Thickness Ratio	10
2.1.3 Experimental Studies on Brace Components.....	15
2.1.4 Analytical Modeling of Bracing Component.....	18
2.2 Gusset Plate Connection.....	20
2.2.1 The 30° Design Concept	20
2.2.2 Stability Issue.....	25
2.2.3 Connection Shape and Seismic Detail	27
2.3 Braced Frame System.....	28
2.3.1 Experimental Work on Braced Frame Systems	28
2.3.2 Frame Action in Braced Frame System	30
2.4 Steel Braced Frame Behavior during Past Earthquakes	30
2.4.1 Past Earthquakes in the United States.....	31
2.4.2 Past Earthquakes in Japan.....	33
2.5 Concluding Remarks	36
3 EXPERIMENTAL PROGRAM AND SPECIMEN DESIGN.....	37
3.1 Background	37

3.2	Experimental Program at University of California, Berkeley.....	38
3.3	Selection and Design of Test Set Up	44
3.4	Test Set Up at NEES@Berkeley Facility	46
3.5	Description of Test Specimens	50
3.6	Loading Sequence for Quasi-Static Tests	60
3.7	Instrumentation.....	61
3.8	Specimen Construction Sequence.....	66
3.8.1	Specimen TCBF-B-1	66
3.8.2	Specimen TCBF-B-2	72
3.8.3	Specimen TCBF-B-3	82
3.8.4	Specimen TCBF-B-4	86
3.9	Relation of Specimen Design to Prototype Design	92
3.9.1	Model (Prototype) Building.....	92
3.9.2	Seismic Forces	93
3.10	Experimental Controls	103
3.10.1	Quasi-Static Tests	103
3.10.2	Hybrid Simulation.....	103
3.11	Material Properties.....	105
4	EXPERIMENTAL RESULTS OF FOUR SPECIMENS	109
4.1	Quasi-Static Test Results of First Three Specimens.....	109
4.1.1	Specimen TCBF-B-1 (Square HSS Braces)	109
4.1.2	Specimen TCBF-B-2 (Round HSS Braces).....	179
4.1.3	Specimen TCBF-B-3 (Wide Flange Braces)	262
4.2	Hybrid Simulation Test Results of Specimen TCBF-B-4 (Square HSS Braces).....	334
4.2.1	Main Observations	336
4.2.2	Key Response Quantities	347
5	DISCUSSION OF EXPERIMENTAL RESULTS.....	405
5.1	Quasi-Static Test Results.....	405
5.1.1	Specimen Global Behavior	406
5.1.2	Brace Behavior.....	424
5.1.3	Column Behavior	437
5.1.4	Beam Behavior.....	439

5.1.5	Panel Zone Behavior	441
5.1.6	Gusset Plate Behavior	442
5.1.7	Test Set Up Behavior	442
5.2	Hybrid Simulation Results	442
5.2.1	Specimen Global Behavior	444
5.2.2	Brace Behavior	453
5.2.3	Column Behavior	456
5.2.4	Beam Behavior	457
5.2.5	Panel Zone Behavior	458
5.2.6	Gusset Plate Behavior	458
5.2.7	Test Set Up Behavior	459
5.2.8	Performance of Servo-Hydraulic Control System	459
5.3	Concluding Remarks	461
6	ANALYTICAL MODELING USING OPENSEES AND LS-DYNA	463
6.1	Calibration using Data Derived from Previous Strut Tests	463
6.2	Prediction of Quasi-Static Test Results	469
6.3	Predicting the Hybrid Simulation Results	475
6.4	Comparison of Square HSS Brace Cyclic Behaviors using OpenSees	488
6.5	Prediction of Strut and Braced Frame Specimen Behaviors using LS-DYNA	497
6.5.1	LS-DYNA Analysis of Individual Struts	498
6.5.2	LS-DYNA Analysis of Quasi-Static TCBF Test Specimens	505
6.6	Comparison between OpenSees and LS-DYNA Results	513
6.7	Concluding Remarks	523
7	HYBRID BRACED FRAMES: THE STRONG-BACK SYSTEM	525
7.1	Introduction	525
7.2	Previous Study	526
7.3	The Proposed Hybrid Braced Frame System	529
7.4	Analytical Study of the Strong-Back System	533
7.4.1	Example Building	533
7.4.2	Seismic Force-Resisting Systems and Design Strategies	534
7.4.3	Modeling	543
7.4.4	Ground Motions	543
7.5	Response of Hybrid Strong-Back System	545

7.5.1	Monotonic Pushover Results	545
7.5.2	Quasi-Static Cyclic Results.....	545
7.5.3	Nonlinear Response History Analysis Results	548
7.6	Discussion.....	553
7.6.1	Pushover Analysis.....	553
7.6.2	Dynamic Analysis.....	554
7.7	Cost Comparison.....	600
7.8	Effect of Gravity Leaning Columns	601
7.9	Concluding Remarks	615
8	CONCLUSIONS AND RECOMMENDATIONS.....	617
8.1	Experimental Phase	618
8.2	Analytical Phase.....	621
8.3	Recommendations for Future Research	623
	REFERENCES.....	625

LIST OF FIGURES

Figure 2.1	Net section failure mode in a brace without reinforcing plates.	8
Figure 2.2	Other possible net section reinforcing schemes.	9
Figure 2.3	Illustration of Whitmore effective width for bolted and welded connections.	21
Figure 2.4	Dimension of gusset plate specimens in the preliminary tension tests.	22
Figure 2.5	The Warren truss specimen tested by Wyss in 1923.	23
Figure 2.6	Illustration of rigid core in a gusset plate.	24
Figure 2.7	The stress trajectories of preliminary test specimens.	25
Figure 2.8	Illustration of stress distribution in a gusset plate.	25
Figure 2.9	Illustration of characteristic length of equivalent unit strips within the Whitmore effective width for bolted and welded connections.	26
Figure 2.10	Illustration of typical and elliptical yield line patterns to accommodate brace out-of-plane buckling (where t_g is thickness of gusset plate).	27
Figure 2.11	Connection details of beam end moment release.	30
Figure 2.12	Brace failures observed in the 1971 San Fernando earthquake.	32
Figure 2.13	Brace failures observed in the 1994 Northridge earthquake.	32
Figure 2.14	Global buckling of braces during 1995 Hyogoken-Nanbu (Kobe) Earthquake.	34
Figure 2.15	Connection failures in 1995 Hyogoken-Nanbu (Kobe) earthquake	34
Figure 2.16	Bolt failures in 1995 Hyogoken-Nanbu (Kobe) Earthquake.	35
Figure 2.17	Brace connection failures observed in the 2011 Great Eastern Japan Earthquake.	35
Figure 3.1	Different specimen types for each testing facility in the experimental phase of the NEES research project.	38
Figure 3.2	Test matrix of the 2D braced frame specimens in the research project.	39
Figure 3.3	Overview of Specimen TCBF-1 before test.	40
Figure 3.4	Overview of Specimen TCBF-1 during the test	40
Figure 3.5	Application of stacked chevron braced frame in a building structure.	41
Figure 3.6	Application of two-story split-X braced frame in a building structure.	42
Figure 3.7	Application of two-story diamond-shape braced frame in a building structure.	43

Figure 3.8	Possible testing configurations at the University of California, Berkeley, during the specimen design phase.	45
Figure 3.9	Overview of the final test set up.	47
Figure 3.10	Construction of reconfigurable reaction wall before pre-stressing.	47
Figure 3.11	Atlas 1.5 M-lb actuators at both floor levels.	48
Figure 3.12	The built-up floor beam after painting.	48
Figure 3.13	Load transfer beams below strong floor before erection.	49
Figure 3.15	Lateral stability frame (the orange cantilever beam and three blue HSS columns) in the test set up view from south-east side of laboratory.	49
Figure 3.16	Dimension of test specimen.	51
Figure 3.17	Specimen TCBF-B-1: member sizes.	52
Figure 3.18	Specimen TCBF-B-2: member sizes.	52
Figure 3.19	Specimen TCBF-B-3: member sizes.	53
Figure 3.20	Specimen TCBF-B-4: member sizes.	53
Figure 3.21	Specimen TCBF-B-1 before test.	55
Figure 3.22	Specimen TCBF-B-2 before first trial.	55
Figure 3.23	Specimen TCBF-B-3 before test.	56
Figure 3.24	Specimen TCBF-B-4 before hybrid simulation.	56
Figure 3.25(a)	Specimens TCBF-B-1 and TCBF-B-2: sub-assemblages.	57
Figure 3.25(b)	Specimens TCBF-B-3 and TCBF-B-4: sub-assemblages.	57
Figure 3.25(c)	Specimens TCBF-B-2 and TCBF-B-3: sub-assemblages.	58
Figure 3.25(d)	Specimens TCBF-B-3 and TCBF-B-4: sub-assemblages.	58
Figure 3.26	The 3/4-in.-one-piece gusset plate after tack welding to column flange.	59
Figure 3.27	Specimen TCBF-B-2: detail view of reinforcing plate.	59
Figure 3.28	Specimens TCBF-B-1, TCBF-B-2, and TCBF-B-3: cyclic loading protocol.	60
Figure 3.29	The 1.5-million-pound load cell.	63
Figure 3.30	Baldwin 4-million-pound universal test machine.	63
Figure 3.31	Steel jacket for rotating the 1.5 M-lb actuator during the load cell calibration.	64
Figure 3.32	Overview of the calibration set up during the load cell calibration.	64
Figure 3.33	Specimens TCBF-B: reusable magnetic labels.	65
Figure 3.34	Specimens TCBF-B: distribution of reusable magnetic labels.	65
Figure 3.35	The 1-1/8-in.-diameter all-thread anchor bolt.	67

Figure 3.36	The lateral supporting tee section.	67
Figure 3.37	Tee section sitting on the lateral supporting saddles.	68
Figure 3.38	Steel angle kickers below the tee section.	68
Figure 3.39(a)	Filler material used in the welding process.	69
Figure 3.39(b)	Standard shim plates for the column base adjustment.	69
Figure 3.40(a)	Specimen TCBF-B-1: lower beam-to-gusset plate connection details.	70
Figure 3.40(b)	Specimen TCBF-B-1: lower beam-to-gusset plate connection weld details.	70
Figure 3.41	Specimen TCBF-B-1: key construction steps.	71
Figure 3.42	Specimen TCBF-B-1: key welding processes.	72
Figure 3.43	Damaged specimen after cutting off the square HSS braces.	74
Figure 3.44	Specimen TCBF-B-2: splicing the lower beam to one-piece gusset plates.	74
Figure 3.45	Specimen TCBF-B-2: key construction steps.	75
Figure 3.46	Specimen TCBF-B-2: key welding processes.	76
Figure 3.47(a)	Specimen TCBF-B-2: lower beam-to-gusset plate connection details.	77
Figure 3.47(b)	Specimen TCBF-B-2: lower beam-to-gusset plate connection weld details.	77
Figure 3.48(a)	Crack in the CJP weld at west column base (north-west corner).	78
Figure 3.48(b)	Crack in the CJP weld at east column base (south-east corner).	78
Figure 3.49	Three-step crack detecting spray.	79
Figure 3.50	Crack detecting spray applied in the CJP weld at east column base (south-east corner).	79
Figure 3.51	The east column base (south-east corner) after gouging the cracked welds.	80
Figure 3.52	The west column base after weld repairs.	80
Figure 3.53	The east column base after weld repairs.	81
Figure 3.54	Specimen TCBF-B-2: entire after whitewash painting.	81
Figure 3.55	Lower beam to one-piece gusset plate connection detail.	83
Figure 3.56	Specimen TCBF-B-3: roof beam, gusset plate, and brace sub-assembly.	83
Figure 3.57	Specimen TCBF-B-3: key construction steps.	84
Figure 3.58	Specimen TCBF-B-3: key welding processes.	85
Figure 3.59	Damaged specimen after cutting off the wide flange braces.	87

Figure 3.60	Specimen TCBF-B-4: connection detail of the lower beam to one-piece gusset plates.	87
Figure 3.61	Grove prepared in the east side column flange near column base.	88
Figure 3.62	A 0.55-in. thick cover plate welded to the south face of column web with fillet welds at east-side W12 × 96 column base.	88
Figure 3.63	Two 0.55-in. thick vertical stiffener plates welded to the north face of column web with fillet welds at east-side W12 × 96 column base.	89
Figure 3.64	The east-side column base detail after repair and whitewash painting.	89
Figure 3.65	Specimen TCBF-B-4: key construction steps.	90
Figure 3.66	Specimen TCBF-B-4: key welding processes.	91
Figure 3.67	Typical floor plan of the model building.	92
Figure 3.68	Perspective view of the model building.	92
Figure 3.69	Elevation of the model building (<i>Y</i> -direction).	93
Figure 3.70	The snapshot of USGS Earthquake Ground Motion Parameters Java applet window.	93
Figure 3.71	Typical member sizes distribution in <i>Y</i> -direction.	97
Figure 3.72	Member stress ratios distribution in <i>Y</i> -direction.	98
Figure 3.73	Target spectrum screenshot from the online ground motion selection tool on PEER website.	98
Figure 3.74	Screenshot of ground motion search interface.	99
Figure 3.75	Snapshot of ground motion search results.	99
Figure 3.76	The elastic response spectrum of scaled ground motions mapping on design spectrum and MCE spectrum.	100
Figure 3.77	Original ground motion record and the scaled ground motions (NGA-960).	101
Figure 3.78	Specimen TCBF-B-4: hybrid modeling concept.	102
Figure 3.79	Experimental control of hybrid simulation.	104
Figure 3.80	Torch cutting the steel coupon from wide flange section.	105
Figure 3.81	Torch cutting the steel coupon from HSS section.	106
Figure 3.82	Specimen TCBF-B-1: steel coupons.	106
Figure 3.83	Specimens TCBF-B-2, TCBF-B-3, and TCBF-B-4: steel coupons.	107
Figure 4.1	Specimen TCBF-B-1: side view.	110
Figure 4.2	Specimen TCBF-B-1: western side of the first-story upper gusset plate.	114
Figure 4.3	Specimen TCBF-B-1: western side of the first-story upper gusset plate.	114

Figure 4.4	Specimen TCBF-B-1: bottom flange of east-side lower beam.	115
Figure 4.5(a)	Specimen TCBF-B-1: flaking of whitewash at second-story gusset plate.	115
Figure 4.5(b)	Specimen TCBF-B-1: flaking of whitewash at the middle length of braces.	116
Figure 4.6	Specimen TCBF-B-1: eastern-side, one-piece gusset plate.	117
Figure 4.7	Specimen TCBF-B-1: western-side, column base.	117
Figure 4.8	Specimen TCBF-B-1: western-side lower beam-to-gusset plate splice.	118
Figure 4.9	Specimen TCBF-B-1: middle portion of first-story western-side HSS brace.	118
Figure 4.10	Specimen TCBF-B-1: eastern-side lower beam-to-gusset plate splice.	119
Figure 4.11	Specimen TCBF-B-1: eastern-side gusset plate-to-column connection.	119
Figure 4.12	Specimen TCBF-B-1: first-story eastern-side square HSS brace.	120
Figure 4.13	Specimen TCBF-B-1: first-story western-side square HSS brace.	120
Figure 4.14	Specimen TCBF-B-1: crack propagation in the first-story western-side square HSS brace.	121
Figure 4.15	Specimen TCBF-B-1: flaking of whitewash on eastern-side column web.	121
Figure 4.16	Specimen TCBF-B-1: first-story square HSS braces.	122
Figure 4.17	Specimen TCBF-B-1: eastern-side gusset-to-beam splice.	122
Figure 4.18	Specimen TCBF-B-1: complete fracture of first-story eastern-side square HSS brace.	123
Figure 4.19	Specimen TCBF-B-1: crack propagation in the second-story eastern side square HSS brace.	123
Figure 4.20	Specimen TCBF-B-1 after test (view from north side fisheye lens).	124
Figure 4.21	Specimen TCBF-B-1: actuator displacement histories.	125
Figure 4.22	Specimen TCBF-B-1: actuator force histories.	125
Figure 4.23	Specimen TCBF-B-1: base shear versus roof displacement relationship.	126
Figure 4.24	Specimen TCBF-B-1: story shear versus story deformation relationship.	126
Figure 4.25	Specimen TCBF-B-1: time history of first-story column axial forces (location: 3 ft above column base plate).	127
Figure 4.26	Specimen TCBF-B-1: roof displacement versus first-story column axial forces.	128

Figure 4.27	Specimen TCBF-B-1: time history of first-story column bending moments (3 ft above column base plate and 3 ft below lower beam centerline).	128
Figure 4.28	Specimen TCBF-B-1: time history of the second-story column bending moments (3 ft above lower beam centerline and 3 ft below roof beam centerline).	129
Figure 4.29	Specimen TCBF-B-1: time history of the first-story column shear forces.	129
Figure 4.30	Specimen TCBF-B-1: time history of the second-story column shear forces.	130
Figure 4.31	Specimen TCBF-B-1: time history of the sum of east and west column shear forces in both stories.	130
Figure 4.32	Specimen TCBF-B-1: column shear stress versus shear strain relationships (locations: EC1-B-N, EC2-B-N, WC1-B-N, and WC2-B-N).	131
Figure 4.33	Specimen TCBF-B-1: story shear component from columns versus total story shear forces.	131
Figure 4.34	Specimen TCBF-B-1: time history of rosette-type strain gauge readings in the first-story column web (location: R1, EC1-B-N).	132
Figure 4.35	Specimen TCBF-B-1: time history of rosette-type strain gauge readings in the first-story column web (location: R5, WC1-B-N).	133
Figure 4.36	Specimen TCBF-B-1: time history of rosette-type strain gauge readings in the second-story column web (location: R3, EC2-B-N).	134
Figure 4.37	Specimen TCBF-B-1: time history of rosette-type strain gauge readings in the second-story column web (location: R7, WC2-B-N).	135
Figure 4.38	Specimen TCBF-B-1, first-story column: normalized maximum principal stress versus normalized minimum principal stress (location: R1).	136
Figure 4.39	Specimen TCBF-B-1, first-story column: normalized maximum principal stress versus normalized minimum principal stress (location: R5).	136
Figure 4.40	Specimen TCBF-B-1, second-story column: normalized maximum principal stress versus normalized minimum principal stress (location: R3).	137
Figure 4.41	Specimen TCBF-B-1, second-story column: normalized minimum principal stress (location: R7).	137
Figure 4.42	Specimen TCBF-B-1, first-story columns: normalized P-M interaction diagrams.	138
Figure 4.43	Specimen TCBF-B-1, first-story columns: normalized P-V interaction diagrams.	138

Figure 4.44	Specimen TCBF-B-1, second-story columns: normalized P-M interaction diagrams.....	139
Figure 4.45	Specimen TCBF-B-1, second-story columns: normalized P-V interaction diagrams.....	139
Figure 4.46	Specimen TCBF-B-1: deflection time history at the center of beam span (roof beam: W24 \times 117, lower beam: W24 \times 68).	140
Figure 4.47	Specimen TCBF-B-1: time history of strain readings at both exterior ends of W24 \times 68 lower beam.	141
Figure 4.48	Specimen TCBF-B-1: time history of strain readings at both exterior ends of W24 \times 117 roof beam.....	141
Figure 4.49	Specimen TCBF-B-1: time history of lower beam axial forces.	142
Figure 4.50	Specimen TCBF-B-1: time history of roof beam axial forces.....	142
Figure 4.51	Specimen TCBF-B-1: time history of lower beam end bending moment.	143
Figure 4.52	Specimen TCBF-B-1: time history of roof beam end bending moment.....	143
Figure 4.53	Specimen TCBF-B-1: lower beam estimated shear force time history.	144
Figure 4.54	Specimen TCBF-B-1: roof beam estimated shear force time history.....	144
Figure 4.55	Specimen TCBF-B-1: estimated unbalanced force time history of roof beam.....	145
Figure 4.56	Specimen TCBF-B-1: estimated brace axial forces versus brace axial deformations.	146
Figure 4.57	Specimen TCBF-B-1: estimated brace axial forces versus measured brace out-of-plane displacements.	146
Figure 4.58	Specimen TCBF-B-1: estimated brace axial force, brace axial deformation, and measured brace out-of-plane displacement relationships.	147
Figure 4.59	Specimen TCBF-B-1: time history of the decomposed strain components of first-story eastern-side HSS brace.	148
Figure 4.60	Specimen TCBF-B-1: time history of the decomposed strain components of first-story western-side HSS brace.....	148
Figure 4.61	Specimen TCBF-B-1: time history of the decomposed strain components of second-story eastern-side HSS brace.	149
Figure 4.62(a)	Specimen TCBF-B-1: time history of the decomposed strain components of second-story western-side HSS brace.	149
Figure 4.62(b)	Definition of the decomposed strain components.....	150
Figure 4.63	Specimen TCBF-B-1: estimated panel zone shear stress versus shear strain relationships.	151

Figure 4.64	Specimen TCBF-B-1, lower panel zone: time history of rosette-type strain gauge readings (location: R2).	152
Figure 4.65	Specimen TCBF-B-1, lower panel zone: time history of rosette-type strain gauge readings (location: R6).	153
Figure 4.66	Specimen TCBF-B-1, roof panel zone: time history of rosette-type strain gauge readings (location: R4).	154
Figure 4.67	Specimen TCBF-B-1, roof panel zone: time history of rosette-type strain gauge readings (location: R8).	155
Figure 4.68	Specimen TCBF-B-1, lower panel zone: normalized maximum principal stress versus normalized minimum principal stress (location: R2).....	156
Figure 4.69	Specimen TCBF-B-1, lower panel zone: normalized maximum principal stress versus normalized minimum principal stress (location: R6).....	156
Figure 4.70	Specimen TCBF-B-1, roof panel zone: normalized maximum principal stress versus normalized minimum principal stress (location: R4).	157
Figure 4.71	Specimen TCBF-B-1, roof panel zone: normalized maximum principal stress versus normalized minimum principal stress (location: R8).	157
Figure 4.72	Specimen TCBF-B-1: time history of rosette-type strain gauge readings in the one-piece gusset plate (location: R9).	158
Figure 4.73	Specimen TCBF-B-1: time history of rosette-type strain gauge readings in the one-piece gusset plate (location: R10).	159
Figure 4.74	Specimen TCBF-B-1: time history of rosette-type strain gauge readings in the one-piece gusset (location: R11).	160
Figure 4.75	Specimen TCBF-B-1: time history of rosette-type strain gauge readings in the one-piece gusset plate (location: R12).	161
Figure 4.76	Specimen TCBF-B-1: time history of rosette-type strain gauge readings in the one-piece gusset plate (location: R13).	162
Figure 4.77	Specimen TCBF-B-1: time history of rosette-type strain gauge readings in the one-piece gusset plate (location: R14).	163
Figure 4.78	Specimen TCBF-B-1: time history of rosette-type strain gauge readings in the one-piece gusset plate (location: R15).	164
Figure 4.79	Specimen TCBF-B-1: time history of rosette-type strain gauge readings in the one-piece gusset plate (location: R16).	165
Figure 4.80	Specimen TCBF-B-1: time history of rosette-type strain gauge readings in the one-piece gusset plate (location: R17).	166
Figure 4.81	Specimen TCBF-B-1: time history of rosette-type strain gauge readings in the one-piece gusset plate (location: R18).	167

Figure 4.82	Specimen TCBF-B-1: time history of rosette-type strain gauge readings in the one-piece gusset plate (location: R19).	168
Figure 4.83	Specimen TCBF-B-1: time history of rosette-type strain gauge readings in the one-piece gusset plate (location: R20).	169
Figure 4.84	Specimen TCBF-B-1: normalized maximum principal stress versus normalized minimum principal stress in one-piece gusset plate (location: R9).	170
Figure 4.85	Specimen TCBF-B-1: normalized maximum principal stress versus normalized minimum principal stress in one-piece gusset plate (location: R10).	170
Figure 4.86	Specimen TCBF-B-1: normalized maximum principal stress versus normalized minimum principal stress in one-piece gusset plate (location: R11).	171
Figure 4.87	Specimen TCBF-B-1: normalized maximum principal stress versus normalized minimum principal stress in one-piece gusset plate (location: R12).	171
Figure 4.88	Specimen TCBF-B-1: normalized maximum principal stress versus normalized minimum principal stress in one-piece gusset plate (location: R13).	172
Figure 4.89	Specimen TCBF-B-1: normalized maximum principal stress versus normalized minimum principal stress in one-piece gusset plate (location: R14).	172
Figure 4.90	Specimen TCBF-B-1: normalized maximum principal stress versus normalized minimum principal stress in one-piece gusset plate (location: R15).	173
Figure 4.91	Specimen TCBF-B-1: normalized maximum principal stress versus normalized minimum principal stress in one-piece gusset plate (location: R16).	173
Figure 4.92	Specimen TCBF-B-1: normalized maximum principal stress versus normalized minimum principal stress in one-piece gusset plate (location: R17).	174
Figure 4.93	Specimen TCBF-B-1: normalized maximum principal stress versus normalized minimum principal stress in one-piece gusset plate (location: R18).	174
Figure 4.94	Specimen TCBF-B-1: normalized maximum principal stress versus normalized minimum principal stress in one-piece gusset plate (location: R19).	175
Figure 4.95	Specimen TCBF-B-1: normalized maximum principal stress versus normalized minimum principal stress in one-piece gusset plate (location: R20).	175

Figure 4.96	Specimen TCBF-B-1: the actuator force versus bracket deformation relationship at both floor levels.....	176
Figure 4.97	Specimen TCBF-B-1: slippage time history between specimen and test set up boundaries.....	177
Figure 4.98	Specimen TCBF-B-1: out-of-plane deformation time history of lateral supporting frame at different monitoring points.....	178
Figure 4.99	Specimen TCBF-B-2: fracture of west-side column base flange CJP welds.	180
Figure 4.100	Specimen TCBF-B-2 after first trial.	180
Figure 4.101	Specimen TCBF-B-2: west-side column base after repair with 1-in. thick stiffener plates and a 2-in. thick flange cover plate.	181
Figure 4.102	Specimen TCBF-B-2 before second trial.....	181
Figure 4.103	Specimen TCBF-B-2 before test and after test.	182
Figure 4.104	Specimen TCBF-B-2: flaking of whitewash at the middle of west-side round HSS brace.	187
Figure 4.105	Specimen TCBF-B-2: flaking of whitewash near CJP welds at bottom flange of lower beam.	187
Figure 4.106	Specimen TCBF-B-2: yield pattern of the east column flange.....	188
Figure 4.107	Specimen TCBF-B-2: yield pattern of the west column flange.....	188
Figure 4.108	Specimen TCBF-B-2: global buckling of round HSS braces at both stories.	189
Figure 4.109	Specimen TCBF-B-2: additional flaking of whitewash flaking in braces.	189
Figure 4.110	Specimen TCBF-B-2: flaking of whitewash near gusset plate-to-column flange region.	190
Figure 4.111	Specimen TCBF-B-2: flaking of whitewash at the corner of gusset plate-to-roof beam connection.	190
Figure 4.112	Specimen TCBF-B-2: local buckling of east-side lower beam bottom flange.....	191
Figure 4.113	Specimen TCBF-B-2: local buckling of west-side lower beam top flange.....	191
Figure 4.114	Specimen TCBF-B-2: column web yielding at the east-side column at ground floor.	192
Figure 4.115	Specimen TCBF-B-2: crack near the flange CJP welds at west-side column base.	192
Figure 4.116	Specimen TCBF-B-2: complete fracture near the flange CJP welds at west-side column base.	193

Figure 4.117	Specimen TCBF-B-2: crack near the web CJP welds at west-side column base.	193
Figure 4.118	Specimen TCBF-B-2: west- side column base after repair.	194
Figure 4.119	Specimen TCBF-B-2: east side column base after repair.	194
Figure 4.120	Specimen TCBF-B-2: yielding in the column flange near 2-in.-thick cover plate.	195
Figure 4.121	Specimen TCBF-B-2: yield pattern between column base stiffener plates.	195
Figure 4.122	Specimen TCBF-B-2: fracture of west-side lower beam top flange.....	196
Figure 4.123	Specimen TCBF-B-2: partial fracture of east-side lower beam bottom flange finger plate.	196
Figure 4.124	Specimen TCBF-B-2: complete fracture of east-side lower beam bottom flange finger plate.....	197
Figure 4.125	Specimen TCBF-B-2: local buckling of column flange near 2-in.-thick cover plate.	197
Figure 4.126	Specimen TCBF-B-2: local buckling of west-side lower beam web.....	198
Figure 4.127	Specimen TCBF-B-2: local buckling of first-story west-side round HSS brace.....	198
Figure 4.128	Specimen TCBF-B-2: tearing of the vertical fillet welds at west-side column base.	199
Figure 4.129	Specimen TCBF-B-2: additional local buckling of first-story west-side round HSS brace.	199
Figure 4.130	Specimen TCBF-B-2: crack propagation into web at east-side lower beam.....	200
Figure 4.131	Specimen TCBF-B-2: crack initiation in first-story west-side round HSS brace.....	200
Figure 4.132	Specimen TCBF-B-2: additional tearing of fillet welds between cover plate and column flange.	201
Figure 4.133	Specimen TCBF-B-2: partial fracture of first-story west-side brace.....	201
Figure 4.134	Specimen TCBF-B-2: complete fracture of first-story west-side brace.	202
Figure 4.135	Specimen TCBF-B-2: crack in lower beam web at west-side near top flange.....	202
Figure 4.136	Specimen TCBF-B-2: crack initiation in first-story east-side round HSS brace.....	203
Figure 4.137	Specimen TCBF-B-2: tearing of vertical fillet welds at west column base.	203

Figure 4.138	Specimen TCBF-B-2: necking of first-story east-side round HSS brace before fracture.	204
Figure 4.139	Specimen TCBF-B-2: complete fracture of first-story east-side brace.	204
Figure 4.140	Specimen TCBF-B-2: entire side view of specimen after the second trial.	205
Figure 4.141	Specimen TCBF-B-2: Actuator displacement time histories.....	206
Figure 4.142	Specimen TCBF-B-2: actuator force time histories.....	206
Figure 4.143	Specimen TCBF-B-2: base shear versus roof displacement relationship.....	207
Figure 4.144	Specimen TCBF-B-2: story shear versus story deformation relationship.....	207
Figure 4.145	Specimen TCBF-B-2: time history of first-story column axial forces (location: 6 ft above column base plate).	209
Figure 4.146	Specimen TCBF-B-2: roof displacement versus first-story column axial forces (note that the vertical axis limit is from -600 kips to 800 kips; the horizontal axis limit is from -8 in. to 8 in.).	209
Figure 4.147	Specimen TCBF-B-2: time history of first-story column bending moments (3 ft above column base plate and 3 ft below lower beam centerline).	210
Figure 4.148	Specimen TCBF-B-2: time history of the second-story column bending moments (3 ft above lower beam centerline and 3 ft below roof beam centerline).	210
Figure 4.149	Specimen TCBF-B-2: time history of the first-story column shear forces.....	211
Figure 4.150	Specimen TCBF-B-2: time history of second-story column shear forces.....	211
Figure 4.151	Specimen TCBF-B-2: time history of sum of east and west column shear forces for both stories.	212
Figure 4.152	Specimen TCBF-B-2: estimated column shear stress versus shear strain relationships (locations: EC1-B-N, EC2-B-N, WC1-B-N and WC2-B-N).....	212
Figure 4.153	Specimen TCBF-B-2: story shear component from columns versus total story shear forces.	213
Figure 4.154	Specimen TCBF-B-2: time history of rosette-type strain gauge readings in first-story column web (location: R1).	214
Figure 4.155	Specimen TCBF-B-2: time history of rosette-type strain gauge readings in first-story column web (location: R5).	215
Figure 4.156	Specimen TCBF-B-2: time history of rosette-type strain gauge readings in the second-story column web (location: R3).	216

Figure 4.157	Specimen TCBF-B-2: time history of rosette-type strain gauge readings in the second-story column web (location: R7).....	217
Figure 4.158	Specimen TCBF-B-2: maximum principal stress versus minimum principal stress in first-story column (location: R1).	218
Figure 4.159	Specimen TCBF-B-2: maximum principal stress versus minimum principal stress in first-story column (location: R5).	218
Figure 4.160	Specimen TCBF-B-2: maximum principal stress versus minimum principal stress in second-story column (location: R3).....	219
Figure 4.161	Specimen TCBF-B-2: maximum principal stress versus minimum principal stress in second-story column (location: R7).....	219
Figure 4.162	Specimen TCBF-B-2: normalized P-M interaction diagrams of first-story columns.	220
Figure 4.163	Specimen TCBF-B-2: normalized P-V interaction diagrams of first-story columns.	220
Figure 4.164	Specimen TCBF-B-2: normalized P-M interaction diagrams of second-story columns.	221
Figure 4.165	Specimen TCBF-B-2: normalized P-V interaction diagrams of second-story columns.	221
Figure 4.166	Specimen TCBF-B-2: deflection time history at center of beam span (roof beam: $W24 \times 117$, lower beam: $W24 \times 68$).....	222
Figure 4.167	Specimen TCBF-B-2: time history of strain readings at both exterior ends of $W24 \times 68$ lower beam.	223
Figure 4.168	Specimen TCBF-B-2: time history of strain readings at both exterior ends of $W24 \times 117$ roof beam.....	223
Figure 4.169	Specimen TCBF-B-2: time history of lower beam axial forces.	224
Figure 4.170	Specimen TCBF-B-2: time history of roof beam axial forces.	224
Figure 4.171	Specimen TCBF-B-2: time history of lower beam end bending moment.	225
Figure 4.172	Specimen TCBF-B-2: time history of roof beam end bending moment.....	225
Figure 4.173	Specimen TCBF-B-2: lower beam estimated shear force time history.	226
Figure 4.174	Specimen TCBF-B-2: roof beam estimated shear force time history.....	226
Figure 4.175	Specimen TCBF-B-2: estimated unbalanced force time history of roof beam.	227
Figure 4.176	Specimen TCBF-B-2: estimated brace axial forces versus brace axial deformations.	228
Figure 4.177	Specimen TCBF-B-2: estimated brace axial forces versus measured brace out-of-plane displacements.	228

Figure 4.178	Specimen TCBF-B-2: estimated brace axial force, brace axial deformation and measured brace out-of-plane displacement relationships.	229
Figure 4.179	Specimen TCBF-B-2: time history of the decomposed strain components of first-story eastern-side HSS brace.	230
Figure 4.180	Specimen TCBF-B-2: time history of the decomposed strain components of first-story western-side HSS brace.	230
Figure 4.181	Specimen TCBF-B-2: time history of decomposed strain components of second-story eastern-side HSS brace.	231
Figure 4.182	Specimen TCBF-B-2: time history of decomposed strain components of second-story western-side HSS brace.	231
Figure 4.183	Specimen TCBF-B-2: estimated panel zone shear stress versus shear strain relationships.	232
Figure 4.184	Specimen TCBF-B-2, lower panel zone: time history of rosette-type strain gauge readings (location: R2).	233
Figure 4.185	Specimen TCBF-B-2, lower panel zone: time history of rosette-type strain gauge readings (location: R6).	234
Figure 4.186	Specimen TCBF-B-2, roof panel zone: time history of rosette-type strain gauge readings (location: R4).	235
Figure 4.187	Specimen TCBF-B-2, roof panel zone: time history of rosette-type strain gauge readings (location: R8).	236
Figure 4.188	Specimen TCBF-B-2, lower panel zone: normalized maximum principal stress versus normalized minimum principal stress (location: R2).	237
Figure 4.189	Specimen TCBF-B-2, lower panel zone: normalized maximum principal stress versus normalized minimum principal stress (location: R6).	237
Figure 4.190	Specimen TCBF-B-2, roof panel zone: normalized maximum principal stress versus normalized minimum principal stress (location: R4).	238
Figure 4.191	Specimen TCBF-B-2, roof panel zone: normalized maximum principal stress versus normalized minimum principal stress (location: R8).	238
Figure 4.192	Specimen TCBF-B-2: time history of rosette-type strain gauge readings in one-piece gusset plate (location: R9).	240
Figure 4.193	Specimen TCBF-B-2: time history of rosette-type strain gauge readings in one-piece gusset plat (location: R10).	241
Figure 4.194	Specimen TCBF-B-2: time history of rosette-type strain gauge readings in one-piece gusset plate (location: R11).	242
Figure 4.195	Specimen TCBF-B-2: time history of rosette-type strain gauge readings in one-piece gusset plate (location: R12).	243

Figure 4.196	Specimen TCBF-B-2: time history of rosette-type strain gauge readings in one-piece gusset plate (location: R13).	244
Figure 4.197	Specimen TCBF-B-2: time history of rosette-type strain gauge readings in one-piece gusset plate (location: R14).	245
Figure 4.198	Specimen TCBF-B-2: time history of rosette-type strain gauge readings in one-piece gusset plate (location: R15).	246
Figure 4.199	Specimen TCBF-B-2: time history of rosette-type strain gauge readings in one-piece gusset plate (location: R16).	247
Figure 4.200	Specimen TCBF-B-2: time history of rosette-type strain gauge readings in one-piece gusset plate (location: R17).	248
Figure 4.201	Specimen TCBF-B-2: time history of rosette-type strain gauge readings in one-piece gusset plate (location: R18).	249
Figure 4.202	Specimen TCBF-B-2: time history of rosette-type strain gauge readings in one-piece gusset plate (location: R19).	250
Figure 4.203	Specimen TCBF-B-2: time history of rosette-type strain gauge readings in one-piece gusset plate (location: R20).	251
Figure 4.204	Specimen TCBF-B-2: normalized maximum principal stress versus normalized minimum principal stress in one-piece gusset plate (location: R9).	252
Figure 4.205	Specimen TCBF-B-2: normalized maximum principal stress versus normalized minimum principal stress in one-piece gusset plate (location: R10).	252
Figure 4.206	Specimen TCBF-B-2: normalized maximum principal stress versus normalized minimum principal stress in one-piece gusset plate (location: R11).	253
Figure 4.207	Specimen TCBF-B-2: normalized maximum principal stress versus normalized minimum principal stress in one-piece gusset plate (location: R12).	253
Figure 4.208	Specimen TCBF-B-2: normalized maximum principal stress versus normalized minimum principal stress in one-piece gusset plate (location: R13).	254
Figure 4.209	Specimen TCBF-B-2: normalized maximum principal stress versus normalized minimum principal stress in one-piece gusset plate (location: R14).	254
Figure 4.210	Specimen TCBF-B-2: normalized maximum principal stress versus normalized minimum principal stress in one-piece gusset plate (location: R15).	255
Figure 4.211	Specimen TCBF-B-2: normalized maximum principal stress versus normalized minimum principal stress in one-piece gusset plate (location: R16).	255

Figure 4.212	Specimen TCBF-B-2: normalized maximum principal stress versus normalized minimum principal stress in one-piece gusset plate location: R17).....	256
Figure 4.213	Specimen TCBF-B-2: normalized maximum principal stress versus normalized minimum principal stress in one-piece gusset plate (location: R18).	256
Figure 4.214	Specimen TCBF-B-2: normalized maximum principal stress versus normalized minimum principal stress in one-piece gusset plate (location: R19).	257
Figure 4.215	Specimen TCBF-B-2: normalized maximum principal stress versus normalized minimum principal stress in one-piece gusset plate (location: R20).	257
Figure 4.216	Specimen TCBF-B-2: averaged axial strain time history in tapered eastern-side gusset plate.....	258
Figure 4.217	Specimen TCBF-B-2: bending strain time history in eastern-side tapered gusset plate.	258
Figure 4.218	Specimen TCBF-B-2: actuator force versus bracket deformation relationship at both floor levels.....	259
Figure 4.219	Specimen TCBF-B-2: slippage time history between specimen and test set up boundaries.....	260
Figure 4.220	Specimen TCBF-B-2: out-of-plane deformation time history of lateral supporting frame at different monitoring points.	261
Figure 4.221	Specimen TCBF-B-2: reconfigurable reaction wall tip deformation time histories.	262
Figure 4.222	Specimen TCBF-B-3: column base connection detail (four 7/8-in. gussets welded to the column flange and base plate).	263
Figure 4.223	Specimen TCBF-B-3: lower beam to one-piece gusset plate pin connection detail (eastern side of W24 × 68 beam).....	263
Figure 4.224	Specimen TCBF-B-3 before test and after test.	264
Figure 4.225	Specimen TCBF-B-3: flaking of whitewash on brace-to-gusset cover plates.	268
Figure 4.226	Specimen TCBF-B-3: flaking of whitewash on global buckled braces (west brace at the first story and east brace at the second story).	269
Figure 4.227	Specimen TCBF-B-3: flaking of whitewash at west-side roof beam-to-column connection.	269
Figure 4.228	Specimen TCBF-B-3: local flaking of whitewash in lower beam web near beam-to-gusset splice plate.	270

Figure 4.229	Specimen TCBF-B-3: buckling shapes of all four wide flange braces: three of them buckled to the north side while only the east-side brace at the first story buckled to the south side.....	270
Figure 4.230	Specimen TCBF-B-3: flaking of whitewash at the $2t$ gap region in gusset plate.....	271
Figure 4.231	Specimen TCBF-B-3: whitewash flaking patterns shown on column flanges near the west-side column base plate.	271
Figure 4.232	Specimen TCBF-B-3: whitewash flaking patterns shown on column flanges near column base plate.	272
Figure 4.233	Specimen TCBF-B-3: close view of local buckling at first-story west-side wide flange brace.....	272
Figure 4.234	Specimen TCBF-B-3: local yielding in the beam-to-gusset plate splices near the short-slotted holes.	273
Figure 4.235	Specimen TCBF-B-3: evidence of slippage between splice plate and one-piece gusset plate.	273
Figure 4.236	Specimen TCBF-B-3: east column flange fractured near base plate stiffeners (view from north-west side).....	274
Figure 4.237	Specimen TCBF-B-3: east column flange fractured near base plate stiffeners (view from east side).....	274
Figure 4.238	Specimen TCBF-B-3: west wide flange brace partially fractured near middle of the brace (view from north-west side).....	275
Figure 4.239	Specimen TCBF-B-3: west wide flange brace partially fractured near middle of the brace (view from east side).....	275
Figure 4.240	Specimen TCBF-B-3: top flange of the west wide flange brace completely fractured near the middle of brace (view from north-west side).....	276
Figure 4.241	West wide flange brace completely fractured near the middle of the brace (view from north side) of Specimen TCBF-B-3.	276
Figure 4.242	Specimen TCBF-B-3: crack tip in the web of east column near column base.	277
Figure 4.243	Specimen TCBF-B-3 after test.....	277
Figure 4.244	Specimen TCBF-B-3: actuator displacement time history.	278
Figure 4.245	Specimen TCBF-B-3: actuator force histories.....	279
Figure 4.246	Specimen TCBF-B-3: base shear versus roof displacement relationship.....	279
Figure 4.247	Specimen TCBF-B-3: story shear versus story deformation relationship.....	280

Figure 4.248	Specimen TCBF-B-3: time history of first-story column axial forces (location: 3 ft above column base plate).	281
Figure 4.249	Specimen TCBF-B-3: roof displacement versus first-story column axial forces.	281
Figure 4.250	Specimen TCBF-B-3: time history of first-story column bending moments (3 ft above column base plate and 3 ft below lower beam centerline).	282
Figure 4.251	Specimen TCBF-B-3: time history of second-story column bending moment (3 ft above lower beam centerline and 3 ft below roof beam centerline).	282
Figure 4.252	Specimen TCBF-B-3: time history of first-story column shear forces.	283
Figure 4.253	Specimen TCBF-B-3: time history of second-story column shear forces.	283
Figure 4.254	Specimen TCBF-B-3: time history of sum of east and west column shear forces for both stories.	284
Figure 4.255	Specimen TCBF-B-3: column shear stress versus shear strain relationships (locations: EC1-B-N, EC2-B-N, WC1-B-N, and WC2-B-N).	284
Figure 4.256	Specimen TCBF-B-3: story shear component from columns versus total story shear forces.	285
Figure 4.257	Specimen TCBF-B-3: time history of rosette-type strain gauge readings in first-story column web (location: R1).	286
Figure 4.258	Specimen TCBF-B-3: time history of rosette-type strain gauge readings in first-story column web (location: R5).	287
Figure 4.259	Specimen TCBF-B-3: time history of rosette-type strain gauge readings in first-story column web (location: R3).	288
Figure 4.260	Specimen TCBF-B-3: time history of rosette-type strain gauge readings in first-story column web (location: R7).	289
Figure 4.261	Specimen TCBF-B-3: maximum principal stress versus minimum principal stress in first-story column (location: R1).	290
Figure 4.262	Specimen TCBF-B-3: maximum principal stress versus minimum principal stress in first-story column (location: R5).	290
Figure 4.263	Specimen TCBF-B-3: maximum principal stress versus minimum principal stress in first-story column (location: R3).	291
Figure 4.264	Specimen TCBF-B-3: maximum principal stress versus minimum principal stress in first-story column (location: R7).	291
Figure 4.265	Specimen TCBF-B-3: normalized P-M interaction diagrams of first-story columns.	292

Figure 4.266	Specimen TCBF-B-3: normalized P-V interaction diagrams of first-story columns.	292
Figure 4.267	Specimen TCBF-B-3: normalized P-M interaction diagrams of second-story columns.	293
Figure 4.268	Specimen TCBF-B-3: normalized P-V interaction diagrams of second-story columns.	293
Figure 4.269	Specimen TCBF-B-3: deflection time history at center of beam span (roof beam: W24 × 117, lower beam: W24 × 68).....	294
Figure. 4.270	Specimen TCBF-B-3: time history of strain readings at both exterior ends of W24 × 117 roof beam.....	295
Figure. 4.271	Specimen TCBF-B-3: time history of strain readings at both exterior ends of W24 × 68 lower beam.	295
Figure 4.272	Specimen TCBF-B-3: time history of lower beam axial forces.	296
Figure 4.273	Specimen TCBF-B-3: time history of roof beam axial forces.....	296
Figure 4.274	Specimen TCBF-B-3: time history of the lower beam end bending moment.	297
Figure 4.275	Specimen TCBF-B-3: time history of roof beam end bending moment.....	297
Figure 4.276	Specimen TCBF-B-3: lower beam estimated shear force time history.	298
Figure 4.277	Specimen TCBF-B-3: roof beam estimated shear force time history.....	298
Figure 4.278	Specimen TCBF-B-3: estimated unbalanced force time history of roof beam.	299
Figure 4.279	Specimen TCBF-B-3: estimated brace axial forces versus brace axial deformations.	300
Figure 4.280	Specimen TCBF-B-3: estimated brace axial forces versus measured brace out-of-plane displacements at brace center point of each WF brace.....	300
Figure 4.281	Specimen TCBF-B-3: estimated brace axial force, brace axial deformation, and measured brace out-of-plane displacement relationships.	301
Figure 4.282	Specimen TCBF-B-3: time history of the decomposed strain components of first-story eastern-side wide flange brace.....	302
Figure 4.283	Specimen TCBF-B-3: time history of the decomposed strain components of first-story western-side wide flange brace.	302
Figure 4.284	Specimen TCBF-B-3: time history of the decomposed strain components of second-story eastern-side wide flange brace.....	303
Figure 4.285	Specimen TCBF-B-3: time history of the decomposed strain components of second-story western-side wide flange brace.....	303

Figure 4.286	Specimen TCBF-B-3: estimated panel zone shear stress versus shear strain relationships.	304
Figure 4.287	Specimen TCBF-B-3, lower panel zone: time history of rosette-type strain gauge readings (location: R2).	305
Figure 4.288	Specimen TCBF-B-3, lower panel zone: time history of rosette-type strain gauge readings (location: R6).	306
Figure 4.289	Specimen TCBF-B-3, roof panel zone: time history of rosette-type strain gauge readings (location: R4).	307
Figure 4.290	Specimen TCBF-B-3, roof panel zone: time history of rosette-type strain gauge readings (location: R8).	308
Figure 4.291	Specimen TCBF-B-3, lower panel zone: normalized maximum principal stress versus normalized minimum principal stress (location: R2).....	309
Figure 4.292	Specimen TCBF-B-3, lower panel zone: normalized maximum principal stress versus normalized minimum principal stress (location: R6).....	309
Figure 4.293	Specimen TCBF-B-3, roof panel zone: normalized maximum principal stress versus normalized minimum principal stress (location: R4).	310
Figure 4.294	Specimen TCBF-B-3, roof panel zone: normalized maximum principal stress versus normalized minimum principal stress (location: R8).	310
Figure 4.295	Specimen TCBF-B-3: time history of rosette-type strain gauge readings in one-piece gusset plate (location: R9).	312
Figure 4.296	Specimen TCBF-B-3: time history of rosette-type strain gauge readings in one-piece gusset plate (location: R10).	313
Figure 4.297	Specimen TCBF-B-3: time history of rosette-type strain gauge readings in one-piece gusset plate (location: R11).	314
Figure 4.298	Specimen TCBF-B-3: time history of rosette-type strain gauge readings in one-piece gusset plate (location: R12).	315
Figure 4.299	Specimen TCBF-B-3: time history of rosette-type strain gauge readings in one-piece gusset plate (location: R13).	316
Figure 4.300	Specimen TCBF-B-3: time history of rosette-type strain gauge readings in one-piece gusset plate of (location: R14).	317
Figure 4.301	Specimen TCBF-B-3: time history of rosette-type strain gauge readings in one-piece gusset plate (location: R15).	318
Figure 4.302	Specimen TCBF-B-3: time history of rosette-type strain gauge readings in one-piece gusset plate (location: R16).	319
Figure 4.303	Specimen TCBF-B-3: time history of rosette-type strain gauge readings in one-piece gusset plate (location: R17).	320

Figure 4.304	Specimen TCBF-B-3: time history of rosette-type strain gauge readings in one-piece gusset plate (location: R18).	321
Figure 4.305	Specimen TCBF-B-3: time history of rosette-type strain gauge readings in one-piece gusset plate (location: R19).	322
Figure 4.306	Specimen TCBF-B-3: time history of rosette-type strain gauge readings in one-piece gusset plate (location: R20).	323
Figure 4.307	Specimen TCBF-B-3: normalized maximum principal stress versus normalized minimum principal stress in one-piece gusset plate (location: R9).	324
Figure 4.308	Specimen TCBF-B-3: normalized maximum principal stress versus normalized minimum principal stress in one-piece gusset plate (location: R10).	324
Figure 4.309	Specimen TCBF-B-3: normalized maximum principal stress versus normalized minimum principal stress in one-piece gusset plate (location: R11).	325
Figure 4.310	Specimen TCBF-B-3: normalized maximum principal stress versus normalized minimum principal stress in one-piece gusset plate (location: R12).	325
Figure 4.311	Specimen TCBF-B-3: normalized maximum principal stress versus normalized minimum principal stress in one-piece gusset plate (location: R13).	326
Figure 4.312	Specimen TCBF-B-3: normalized maximum principal stress versus normalized minimum principal stress in one-piece gusset plate (location: R14).	326
Figure 4.313	Specimen TCBF-B-3: normalized maximum principal stress versus normalized minimum principal stress in one-piece gusset plate (location: R15).	327
Figure 4.314	Specimen TCBF-B-3: normalized maximum principal stress versus normalized minimum principal stress in one-piece gusset plate (location: R16).	327
Figure 4.315	Specimen TCBF-B-3: normalized maximum principal stress versus normalized minimum principal stress in one-piece gusset plate (location: R17).	328
Figure 4.316	Specimen TCBF-B-3: normalized maximum principal stress versus normalized minimum principal stress in one-piece gusset plate (location: R18).	328
Figure 4.317	Specimen TCBF-B-3: normalized maximum principal stress versus normalized minimum principal stress in one-piece gusset plate (location: R19).	329

Figure 4.318	Specimen TCBF-B-3: normalized maximum principal stress versus normalized minimum principal stress in one-piece gusset plate (location: R20).	329
Figure 4.319	Specimen TCBF-B-3: averaged axial strain time history in tapered eastern-side gusset plate.	330
Figure 4.320	Specimen TCBF-B-3: bending strain time history in tapered eastern-side gusset plate.	330
Figure 4.321	Specimen TCBF-B-3: actuator force versus bracket deformation relationship at both floor levels.	331
Figure 4.322	Specimen TCBF-B-3: slippage time history between specimen and test set up boundaries.	332
Figure 4.323	Specimen TCBF-B-3: out-of-plane deformation time history of lateral supporting frame at different monitoring points.	333
Figure 4.324	Specimen TCBF-B-3: reconfigurable reaction wall tip deformation time histories.	334
Figure 4.325	Specimen TCBF-B-4 before and after hybrid simulation.	335
Figure 4.326	Flaking of whitewash near repaired column base.	338
Figure 4.327	Global buckling of eastern-side brace in the first story.	339
Figure 4.328	Global buckling of western-side brace in the second story.	339
Figure 4.329	Local buckling of eastern-side brace in the first story.	340
Figure 4.330	Local buckling of western-side brace in the second story.	340
Figure 4.331	Local yielding in beam-to-gusset plate splice.	341
Figure 4.332	Additional flaking of whitewash near lower beam splice plate.	341
Figure 4.333	Panel zone yielding in the roof beam to column connection region.	342
Figure 4.334	Cracks in the first-story eastern-side brace.	342
Figure 4.335	Cracks in the second-story western-side brace.	343
Figure 4.336	Crack propagation in the second-story western-side brace.	343
Figure 4.337	Cracks in the first-story western-side brace.	344
Figure 4.338	Cracks opening in the second-story eastern-side brace.	344
Figure 4.339	Complete fracture of the second-story eastern-side brace.	345
Figure 4.340	Complete fracture of the second-story western-side brace.	345
Figure 4.341	Complete fracture of the first-story eastern-side brace.	346
Figure 4.342	Complete fracture of the first-story western-side brace.	346
Figure 4.343	Local buckling of column flanges in first-story columns.	347
Figure 4.344	Specimen TCBF-B-4: actuator displacement time history.	348

Figure 4.345	Specimen TCBF-B-4: actuator force histories.....	348
Figure 4.346	Specimen TCBF-B-4: base shear versus roof displacement relationship.....	349
Figure 4.347	Specimen TCBF-B-4: story shear versus story deformation relationship.....	349
Figure 4.348	Specimen TCBF-B-4: upper actuator force versus lower actuator force relationship.....	350
Figure 4.349	Specimen TCBF-B-4: actuator displacement versus lower actuator displacement relationship.....	350
Figure 4.350	Specimen TCBF-B-4: time history of first-story column axial forces (location: 3 ft above column base plate).	351
Figure 4.351	Specimen TCBF-B-4: roof displacement versus first-story column axial forces.	352
Figure 4.352	Specimen TCBF-B-4: time history of first-story column bending moments (3 ft above column base plate and 3 ft below lower beam centerline).	352
Figure 4.353	Specimen TCBF-B-4: time history of second-story column bending moments (3 ft above lower beam centerline and 3 ft below roof beam centerline).	353
Figure 4.354	Specimen TCBF-B-4: time history of the first-story column shear forces.....	353
Figure 4.355	Specimen TCBF-B-4: time history of second-story column shear forces.....	354
Figure 4.356	Specimen TCBF-B-4: time history of sum of east and west column shear forces for both stories.	354
Figure 4.357	Specimen TCBF-B-4: column shear stress versus shear strain relationships (locations: EC1-B-N, EC2-B-N, WC1-B-N and WC2-B-N).	355
Figure 4.358	Specimen TCBF-B-4: story shear component from columns versus total story shear forces.	355
Figure 4.359	Specimen TCBF-B-4: time history of rosette-type strain gauge readings in the first-story column web (location: R1).	356
Figure 4.360	Specimen TCBF-B-4: time history of rosette-type strain gauge readings in first-story column web (location: R5).	357
Figure 4.361	Specimen TCBF-B-4: time history of rosette-type strain gauge readings in first-story column web (location: R3).	358
Figure 4.362	Specimen TCBF-B-4: time history of rosette-type strain gauge readings in first-story column web (location: R7).	359

Figure 4.363	Specimen TCBF-B-4: maximum principal stress versus minimum principal stress in the first-story column (location: R1).	360
Figure 4.364	Specimen TCBF-B-4: maximum principal stress versus minimum principal stress in the first-story column (location: R5).	360
Figure 4.365	Specimen TCBF-B-4: maximum principal stress versus minimum principal stress in first-story column (location: R3).	361
Figure 4.366	Specimen TCBF-B-4: maximum principal stress versus minimum principal stress in first-story column (location: R7).	361
Figure 4.367	Specimen TCBF-B-4: normalized P-M interaction diagrams of first-story columns.	362
Figure 4.368	Specimen TCBF-B-4: normalized P-V interaction diagrams of first-story columns.	362
Figure 4.369	Specimen TCBF-B-4: normalized P-M interaction diagrams of second-story columns.	363
Figure 4.370	Specimen TCBF-B-4: normalized P-V interaction diagrams of second-story columns.	363
Figure 4.371	Specimen TCBF-B-4: deflection time history at center of beam span (roof beam: $W24 \times 117$, lower beam: $W24 \times 68$).	364
Figure 4.372	Specimen TCBF-B-4: time history of strain readings at both exterior ends of $W24 \times 117$ roof beam.	365
Figure 4.373	Specimen TCBF-B-4: time history of strain readings at both exterior ends of $W24 \times 68$ lower beam.	365
Figure 4.374	Specimen TCBF-B-4: time history of lower beam axial forces.	366
Figure 4.375	Specimen TCBF-B-4: time history of roof beam axial forces.	366
Figure 4.376	Specimen TCBF-B-4: time history of lower beam end bending moment.	367
Figure 4.377	Specimen TCBF-B-4: time history of roof beam end bending moment.	367
Figure 4.378	Specimen TCBF-B-4: lower beam estimated shear force time history.	368
Figure 4.379	Specimen TCBF-B-4: roof beam estimated shear force time history.	368
Figure 4.380	Specimen TCBF-B-4: estimated unbalanced force time history of roof beam.	369
Figure 4.381	Specimen TCBF-B-4: estimated brace axial forces versus brace axial deformations.	370
Figure 4.382	Specimen TCBF-B-4: estimated brace axial forces versus measured brace out-of-plane displacements at brace center point of each HSS brace.	370

Figure 4.383	Specimen TCBF-B-4: estimated brace axial force, brace axial deformation and measured brace out-of-plane displacement relationships.	371
Figure 4.384	Specimen TCBF-B-4: time history of decomposed strain components of first-story eastern-side HSS brace.	372
Figure 4.385	Specimen TCBF-B-4: time history of decomposed strain components of first-story western-side HSS brace.	372
Figure 4.386	Specimen TCBF-B-4: time history of decomposed strain components of second-story eastern-side HSS brace.	373
Figure 4.387	Specimen TCBF-B-4: time history of decomposed strain components of second-story western-side HSS brace.	373
Figure 4.388	Specimen TCBF-B-4: estimated panel zone shear stress versus shear strain relationships.	374
Figure 4.389	Specimen TCBF-B-4, lower panel zone: time history of rosette-type strain gauge readings (location: R2).	375
Figure 4.390	Specimen TCBF-B-4, lower panel zone: time history of rosette-type strain gauge readings (location: R6).	376
Figure 4.391	Specimen TCBF-B-4, lower panel zone: time history of rosette-type strain gauge readings (location: R4).	377
Figure 4.392	Specimen TCBF-B-4, lower panel zone: time history of rosette-type strain gauge readings (location: R8).	378
Figure 4.393	Specimen TCBF-B-4, lower panel zone: normalized maximum principal stress versus normalized minimum principal stress (location: R2).	379
Figure 4.394	Specimen TCBF-B-4, lower panel zone: normalized maximum principal stress versus normalized minimum principal stress (location: R6).	379
Figure 4.395	Specimen TCBF-B-4, lower panel zone: normalized maximum principal stress versus normalized minimum principal stress (location: R4).	380
Figure 4.396	Specimen TCBF-B-4, lower panel zone: normalized maximum principal stress versus normalized minimum principal stress (location: R8).	380
Figure 4.397	Specimen TCBF-B-4: time history of rosette-type strain gauge readings in one-piece gusset plate (location: R9).	382
Figure 4.398	Specimen TCBF-B-4: time history of rosette-type strain gauge readings in one-piece gusset plate (location: R10).	383
Figure 4.399	Specimen TCBF-B-4: time history of rosette-type strain gauge readings in one-piece gusset plate (location: R11).	384

Figure 4.400	Specimen TCBF-B-4: time history of rosette-type strain gauge readings in one-piece gusset plate (location: R12).	385
Figure 4.401	Specimen TCBF-B-4: time history of rosette-type strain gauge readings in one-piece gusset plate (location: R13).	386
Figure 4.402	Specimen TCBF-B-4: time history of rosette-type strain gauge readings in one-piece gusset plate (location: R14).	387
Figure 4.403	Specimen TCBF-B-4: time history of rosette-type strain gauge readings in one-piece gusset plate (location: R15).	388
Figure 4.404	Specimen TCBF-B-4: time history of rosette-type strain gauge readings in one-piece gusset plate (location: R16).	389
Figure 4.405	Specimen TCBF-B-4: time history of rosette-type strain gauge readings in one-piece gusset plate (location: R17).	390
Figure 4.406	Specimen TCBF-B-4: time history of rosette-type strain gauge readings in one-piece gusset plate (location: R18).	391
Figure 4.407	Specimen TCBF-B-4: time history of rosette-type strain gauge readings in one-piece gusset plate (location: R19).	392
Figure 4.408	Specimen TCBF-B-4: time history of rosette-type strain gauge readings in one-piece gusset plate (location: R20).	393
Figure 4.409	Specimen TCBF-B-4: normalized maximum principal stress versus normalized minimum principal stress in one-piece gusset plate (location: R9).	394
Figure 4.410	Specimen TCBF-B-4: normalized maximum principal stress versus normalized minimum principal stress in one-piece gusset plate (location: R10).	394
Figure 4.411	Specimen TCBF-B-4: normalized maximum principal stress versus normalized minimum principal stress in one-piece gusset plate (location: R11).	395
Figure 4.412	Specimen TCBF-B-4: normalized maximum principal stress versus normalized minimum principal stress in one-piece gusset plate (location: R12).	395
Figure 4.413	Specimen TCBF-B-4: normalized maximum principal stress versus normalized minimum principal stress in one-piece gusset plate (location: R13).	396
Figure 4.414	Specimen TCBF-B-4: normalized maximum principal stress versus normalized minimum principal stress in one-piece gusset plate (location: R14).	396
Figure 4.415	Specimen TCBF-B-4: normalized maximum principal stress versus normalized minimum principal stress in one-piece gusset plate (location: R15).	397

Figure 4.416	Specimen TCBF-B-4: normalized maximum principal stress versus normalized minimum principal stress in one-piece gusset plate (location: R16).	397
Figure 4.417	Specimen TCBF-B-4: normalized maximum principal stress versus normalized minimum principal stress in one-piece gusset plate (location: R17).	398
Figure 4.418	Specimen TCBF-B-4: normalized maximum principal stress versus normalized minimum principal stress in one-piece gusset plate (location: R18).	398
Figure 4.419	Specimen TCBF-B-4: normalized maximum principal stress versus normalized minimum principal stress in one-piece gusset plate (location: R19).	399
Figure 4.420	Specimen TCBF-B-4: normalized maximum principal stress versus normalized minimum principal stress in one-piece gusset plate (location: R20).	399
Figure 4.421	Specimen TCBF-B-4: actuator force versus bracket deformation relationship at both floor levels during hybrid simulation.	400
Figure 4.422	Specimen TCBF-B-4: slippage time history between specimen and test set up boundaries during hybrid simulation.	401
Figure 4.423	Specimen TCBF-B-4: out-of-plane deformation time history of lateral supporting frame at different monitoring points during hybrid simulation.	402
Figure 4.424	Specimen TCBF-B-4: reconfigurable reaction wall tip deformation time histories during hybrid simulation.	403
Figure 5.1	Backbone curves of each specimen (both cycle one and cycle two in each load stage).	416
Figure 5.2	Total cumulative energy dissipation of each specimen (GB: global buckling, LB: local buckling, CF: first brace completely fracture).	416
Figure 5.3	Specimen TCBF-B-1: total energy dissipation in each excursion and total cumulative energy dissipation.	417
Figure 5.4	Specimen TCBF-B-2: total energy dissipation in each excursion and total cumulative energy dissipation.	417
Figure 5.5	Specimen TCBF-B-3: total energy dissipation in each excursion and total cumulative energy dissipation.	418
Figure 5.6	Total roof plastic displacement in each excursion and total cumulative roof plastic displacement of three specimens.	419
Figure 5.7	Normalized energy dissipation in each excursion and cumulative normalized energy dissipation of three specimens.	420

Figure 5.8	Specimen TCBF-B-1: story deformation ratio.	421
Figure 5.9	Specimen TCBF-B-2: story deformation ratio.	421
Figure 5.10	Specimen TCBF-B-3: story deformation ratio.	422
Figure 5.11	Specimen TCBF-B-1: story energy dissipation ratio.....	422
Figure 5.12	Specimen TCBF-B-2: story energy dissipation ratio.....	423
Figure 5.13	Specimen TCBF-B-3: story energy dissipation ratio.....	423
Figure 5.14	Specimen TCBF-B-1: buckling shape of the first-story eastern-side brace in compression excursions.	427
Figure 5.15	Specimen TCBF-B-1: buckling shape of the first-story western-side brace in compression excursions.	427
Figure 5.16	Specimen TCBF-B-1: buckling shape of the second-story eastern-side brace in compression excursions.	428
Figure 5.17	Specimen TCBF-B-1: buckling shape of the second-story western-side brace in compression excursions.	428
Figure 5.18	Specimen TCBF-B-2: buckling shape of the first-story eastern-side brace in compression excursions.	429
Figure 5.19	Specimen TCBF-B-2: buckling shape of the first-story western-side brace in compression excursions.	429
Figure 5.20	Specimen TCBF-B-2: buckling shape of the second-story eastern-side brace in compression excursions.	430
Figure 5.21	Specimen TCBF-B-2: buckling shape of the second-story western-side brace in compression excursions.	430
Figure 5.22	Specimen TCBF-B-2: buckling shape of the first-story eastern-side brace in compression excursions.	431
Figure 5.23	Specimen TCBF-B-2: buckling shape of the first-story western-side brace in compression excursions.	431
Figure 5.24	Specimen TCBF-B-2: buckling shape of the second-story eastern-side brace in compression excursions.	432
Figure 5.25	Specimen TCBF-B-2: buckling shape of the second-story western-side brace in compression excursions.	432
Figure 5.26	Specimen TCBF-B-1: brace cumulative normalized energy dissipation and normalized energy dissipation in each excursion.....	433
Figure 5.27	Specimen TCBF-B-1: brace cumulative plastic deformations and plastic deformations in each excursion.	433
Figure 5.28	Specimen TCBF-B-2: brace cumulative normalized energy dissipation and normalized energy dissipation in each excursion.....	434

Figure 5.29	Specimen TCBF-B-2: brace cumulative plastic deformations and plastic deformations in each excursion.	434
Figure 5.30	Specimen TCBF-B-3: brace cumulative normalized energy dissipation and normalized energy dissipation in each excursion.....	435
Figure 5.31	Specimen TCBF-B-3: brace cumulative plastic deformations and plastic deformations in each excursion.	435
Figure 5.32	Specimen TCBF-B-1: source of total energy dissipation in each excursion and total cumulative energy dissipation.	436
Figure 5.33	Specimen TCBF-B-2: source of total energy dissipation in each excursion and total cumulative energy dissipation.	436
Figure 5.34	Specimen TCBF-B-3: source of total energy dissipation in each excursion and total cumulative energy dissipation.	437
Figure 5.35	Demonstration of geometry amplification effect at the lower beam to gusset plate connections.....	440
Figure 5.36	The lower beam end rotation versus first-story drift ratio relationships of each specimen.....	441
Figure 5.37	Ground motion time history for the hybrid simulation.....	444
Figure 5.38	Specimen TCBF-B-4: floor level displacement time histories.....	449
Figure 5.39	Specimen TCBF-B-4: story force time histories.....	449
Figure 5.40	Specimen TCBF-B-4: total energy dissipation in each time segment and total cumulative energy dissipation.....	450
Figure 5.41	Specimen TCBF-B-4: total roof plastic displacement in each time segment and total cumulative roof plastic displacement.....	450
Figure 5.42	Specimen TCBF-B-4: normalized energy dissipation in each time segment and cumulative normalized energy dissipation.....	451
Figure 5.43	Specimen TCBF-B-4: story deformation ratio.....	452
Figure 5.44	Specimen TCBF-B-4: story energy dissipation ratio.....	452
Figure 5.45	Specimen TCBF-B-4: brace cumulative normalized energy dissipation and normalized energy dissipation in each time segment.....	455
Figure 5.46	Specimen TCBF-B-4: brace cumulative plastic deformations and plastic deformations in each time segment.....	455
Figure 5.47	Specimen TCBF-B-4: source of energy dissipation in each time segment and total cumulative energy dissipation.....	456
Figure 5.48	Specimen TCBF-B-4: lower beam end rotation versus first-story drift ratio relationships.....	458
Figure 5.49	Synchronization subspace plot of top actuator during hybrid test.....	460
Figure 5.50	Synchronization subspace plot of bottom actuator during hybrid test.....	460

Figure 6.1	Simple strut tests at University of California, Berkeley.	465
Figure 6.2	Loading protocols of simple strut tests.	466
Figure 6.3	Demonstration of the fiber sections and element numbers used in OpenSees strut models.	466
Figure 6.4	Axial force versus axial deformation relationship of Specimen #4 from experiment and OpenSees simulation.	467
Figure 6.5	Axial force versus out-of-plane displacement relationship of Specimen #4 from experiment and OpenSees simulation.	467
Figure 6.6	Axial force versus axial deformation relationship of Specimen #5 from experiment and OpenSees simulation.	468
Figure 6.7	Axial force versus out-of-plane displacement relationship of Specimen #5 from experiment and OpenSees simulation.	468
Figure 6.8	Demonstration of a braced frame model in OpenSees.	471
Figure 6.9	Base shear versus roof displacement relationship of Specimen TCBF- B-1 from experimental results and OpenSees simulation (Trial 1).	471
Figure 6.10	Specimen TCBF-B-1: base shear versus roof displacement relationship from experimental results and OpenSees simulation (Trial 2).	472
Figure 6.11	Specimen TCBF-B-1: brace axial force versus axial deformation relationships from experiment and OpenSees simulation (Trial 2).	472
Figure 6.12	Specimen TCBF-B-2: base shear versus roof displacement relationship from experiment and OpenSees simulation.	473
Figure 6.13	Specimen TCBF-B-2: brace axial force versus axial deformation relationships from experimental results and OpenSees simulation.	473
Figure 6.14	Specimen TCBF-B-3: base shear versus roof displacement relationship from experimental results and OpenSees simulation.	474
Figure 6.15	Specimen TCBF-B-3: brace axial force versus axial deformation relationships from experimental results and OpenSees simulation.	474
Figure 6.16	Specimen TCBF-B-4: displacement time histories from elastic hybrid test and OpenSees simulation (pinned lower beam ends).	478
Figure 6.17	Specimen TCBF-B-4: displacement time histories from elastic hybrid test and OpenSees simulation (semi-rigid lower beam ends).	479
Figure 6.18	Specimen TCBF-B-4: demonstration of semi-rigid lower beam ends.	479
Figure 6.19	Specimen TCBF-B-4: free vibration test results.	480
Figure 6.20	Specimen TCBF-B-4: displacement time histories of from DE and MCE hybrid test and OpenSees simulation (semi-rigid lower beam ends).	480

Figure 6.21(a)	Specimen TCBF-B-4: base shear versus roof displacement relationships from DE hybrid test and OpenSees simulation (semi-rigid lower beam ends).	481
Figure 6.21(b)	Specimen TCBF-B-4: base shear versus roof displacement relationships from MCE hybrid test and OpenSees simulation (semi-rigid lower beam ends).	481
Figure 6.21(c)	Specimen TCBF-B-4: base shear versus roof displacement relationships from DE and MCE hybrid test and OpenSees simulation (semi-rigid lower beam ends).	482
Figure 6.22	Specimen TCBF-B-4: brace axial force versus axial deformation relationships from DE and MCE hybrid test and OpenSees simulation (semi-rigid lower beam ends).	482
Figure 6.23	Simulated Specimen TCBF-B-4: displacement time histories subjected to MCE ground motion and then DE ground motion (semi-rigid lower beam ends).	483
Figure 6.24	Simulated Specimen TCBF-B-4: base shear versus roof displacement relationships subjected to MCE ground motion and then DE ground motion (semi-rigid lower beam ends).	483
Figure 6.25	Simulated Specimen TCBF-B-4: brace axial force versus axial deformation relationships subjected to MCE ground motion and then DE ground motion (semi-rigid lower beam ends).	484
Figure 6.26	Specimen TCBF-B-4: story shear force and story displacement histories subjected to DE ground motion and then MCE ground motion (with versus without leaning columns in the OpenSees models).	485
Figure 6.27	Specimen TCBF-B-4: story shear force histories under the DE ground motion (with versus without leaning columns in the OpenSees models).	486
Figure 6.28	Simulated Specimen TCBF-B-4: brace axial force versus axial deformation relationships subjected to DE and MCE ground motions.	487
Figure 6.29	Assumed braced bay for the square HSS struts and the relationship between brace axial deformation and story drift.	490
Figure 6.30	Normalized axial force versus normalized axial deformation and normalized out-of-plane deformation relationships of square HSS $6 \times 6 \times 3/8$ with $kL/r = 60$	491
Figure 6.31	Normalized axial force versus normalized axial deformation and normalized out-of-plane deformation relationships of square HSS $16 \times 16 \times 5/8$ with $kL/r = 100$	491
Figure 6.32	Normalized energy dissipation of selected square hollow structural sections until brace failure ($kL/r = 40$).	493

Figure 6.33	Normalized energy dissipation of selected square hollow structural sections until brace failure ($kL/r = 60$).....	494
Figure 6.34	Normalized energy dissipation of selected square hollow structural sections until brace failure ($kL/r = 80$).....	494
Figure 6.35	Normalized energy dissipation of selected square hollow structural sections until brace failure ($kL/r = 100$).....	495
Figure 6.36	Normalized energy dissipation of selected square hollow structural sections until brace failure ($kL/r = 150$).....	495
Figure 6.37	Normalized energy dissipation of selected square hollow structural sections until brace failure ($kL/r = 200$).....	496
Figure 6.38	Normalized energy dissipation until brace failure of selected square hollow structural sections with different kL/r ratios.	496
Figure 6.39	Group comparisons of normalized energy dissipation of selected square hollow structural sections with different kL/r ratios.....	497
Figure 6.40	Mesh pattern for the simple strut modeling in LS-DYNA.	499
Figure 6.41	Illustration of simplified models for the simple strut modeling in LS-DYNA.....	499
Figure 6.42	Axial force versus axial deformation relationship of Specimen #5 from experiment and LS-DYNA simulation.	500
Figure 6.43	Axial force versus out-of-plane displacement relationship of Specimen #5 from experiment and LS-DYNA simulation.	500
Figure 6.44	Comparison between actual test and LS-DYNA simulation results at the final cycle.....	501
Figure 6.45	Crack initiation in HSS brace section wall simulated by LS-DYNA model.....	502
Figure 6.46	Complete fracture in LS-DYNA strut model.....	502
Figure 6.47	Axial force versus axial deformation relationship of Specimen #4 from experiment and LS-DYNA simulation.	503
Figure 6.48	Axial force versus out-of-plane displacement relationship of Specimen #4 from experiment and LS-DYNA simulation.	503
Figure 6.49	Comparison between actual test and FE model under near-fault loading protocol.	504
Figure 6.50	Comparison between actual test and finite element model at the final stage of testing.	504
Figure 6.51	Specimen TCBF-B-1: mesh layout in the LS-DYNA simulation.	506
Figure 6.52	Specimen TCBF-B-1: base shear versus roof displacement from LS-DYNA simulation.	506

Figure 6.53	Specimen TCBF-B-1: Von Mises stress distribution at the end of LS-DYNA simulation.	507
Figure 6.54	Specimen TCBF-B-1: plastic strain distribution at the end of LS-DYNA simulation.	508
Figure 6.55	Specimen TCBF-B-1: estimated brace axial force versus axial deformation relationships from experimental results and LS-DYNA simulation.	509
Figure 6.56	Specimen TCBF-B-2: base shear versus roof displacement from LS-DYNA simulation.	509
Figure 6.57	Specimen TCBF-B-2: Von Mises stress distribution at the end of LS-DYNA simulation.	510
Figure 6.58	Specimen TCBF-B-2: plastic strain distribution at the end of LS-DYNA simulation.	510
Figure 6.59	Specimen TCBF-B-2: estimated brace axial force versus axial deformation relationships from experimental results and LS-DYNA simulation.	511
Figure 6.60	Specimen TCBF-B-3: base shear versus roof displacement from LS-DYNA simulation.	511
Figure 6.61	Specimen TCBF-B-3: Von Mises stress distribution at the end of LS-DYNA simulation.	512
Figure 6.62	Specimen TCBF-B-3: plastic strain distribution at the end of LS-DYNA simulation.	512
Figure 6.63	Specimen TCBF-B-3: estimated brace axial force versus axial deformation relationships from experimental results and LS-DYNA simulation.	513
Figure 6.64	SpecimenTCBF-B-1 model: base shear versus roof displacement from OpenSees.	514
Figure 6.65	SpecimenTCBF-B-2 model: base shear versus roof displacement from OpenSees.	515
Figure 6.66	SpecimenTCBF-B-3 model: base shear versus roof displacement from OpenSees.	515
Figure 6.67	SpecimenTCBF-B-1 model: estimated brace axial force versus axial deformation relationships.	516
Figure 6.68	SpecimenTCBF-B-1 LS-DYNA model: estimated brace axial force versus axial deformation relationships.	517
Figure 6.69	SpecimenTCBF-B-2 OpenSees model: estimated brace axial force versus axial deformation relationships.	518
Figure 6.70	SpecimenTCBF-B-2 LS-DYNA model: estimated brace axial force versus axial deformation relationships.	519

Figure 6.71	Specimen TCBF-B-3 OpenSees model: estimated brace axial force versus axial deformation relationships.....	520
Figure 6.72	Specimen TCBF-B-3 LS-DYNA model: estimated brace axial force versus axial deformation relationships.....	521
Figure 6.73	SpecimenTCBF-B-1 model from LS-DYNA output: time history of simulated strain at the roof panel zone region (corresponding to location R08).....	522
Figure 6.74	SpecimenTCBF-B-1 model from LS-DYNA output: normalized maximum principal stress versus normalized minimum principal stress at the roof panel zone region (corresponding to location R08).	523
Figure 7.1	Illustration of different braced frame systems [Khatib et al. 1988].	529
Figure 7.2	Comparison of concentrically braced frame drifts with and without strong-back concept.	531
Figure 7.3	Possible strong-back configuration details with buckling-restrained braces along the entire or partial height of the building.	531
Figure 7.4	More possible strong-back configurations with different spine systems.	532
Figure 7.5	Plan view of the example building and the two-dimensional model elevation.	534
Figure 7.6	Elevation views of six different bracing configurations.	536
Figure 7.7	Averaged spectrum of selected ground motion records.	544
Figure 7.8	Base shear versus roof displacement relationships of six models.	545
Figure 7.9	Base shear versus roof displacement relationships of each model under cyclic pushover.	547
Figure 7.10	Maximum story drift ratios for each model under different hazard level ground motions.	556
Figure 7.11	Residual story drift ratios for each model after different hazard level ground excitations.	557
Figure 7.12	Maximum floor level accelerations for each model under different hazard level ground motions.	557
Figure 7.13	Base shear versus roof displacement relationship of Model V6 under NGA 1119 fault-normal component ground motion.	558
Figure 7.14	Story drift ratio histories of Model V6 under NGA 1119 fault-normal component ground motion.	558
Figure 7.15	Fourth-story to sixth-story brace axial force versus axial deformation relationships of Model V6 under NGA 1119 fault-normal component ground motion.	559

Figure 7.16	First-story to third-story brace axial force versus axial deformation relationships of Model V6 under NGA 1119 fault-normal component ground motion.....	560
Figure 7.17	Base shear versus roof displacement relationship of Model V6 under NGA 1602 fault-parallel component ground motion.....	561
Figure 7.18	Story drift ratio histories of Model V6 under NGA 1602 fault-parallel component ground motion.....	561
Figure 7.19	Fourth-story to sixth-story brace axial force versus axial deformation relationships of Model V6 under NGA 1602 fault-parallel component ground motion.....	562
Figure 7.20	First-story to third-story brace axial force versus axial deformation relationships of Model V6 under NGA 1602 fault-parallel component ground motion.....	563
Figure 7.21	Base shear versus roof displacement relationship of Model X6 under NGA 1119 fault-normal component ground motion.	564
Figure 7.22	Story drift ratio histories of Model X6 under NGA 1119 fault-normal component ground motion.....	564
Figure 7.23	Fourth-story to sixth-story brace axial force versus axial deformation relationships of Model X6 under NGA 1119 fault-normal component ground motion.....	565
Figure 7.24	First-story to third-story brace axial force versus axial deformation relationships of Model X6 under NGA 1119 fault-normal component ground motion.....	566
Figure 7.25	Base shear versus roof displacement relationship of Model X6 under NGA 1602 fault-parallel component ground motion.....	567
Figure 7.26	Story drift ratio histories of Model X6 under NGA 1602 fault-parallel component ground motion.....	567
Figure 7.27	Fourth-story to sixth-story brace axial force versus axial deformation relationships of Model X6 under NGA 1602 fault-parallel component ground motion.....	568
Figure 7.28	First story to third story brace axial force versus axial deformation relationships of Model X6 under NGA 1602 fault-parallel component ground motion.....	569
Figure 7.29	Base shear versus roof displacement relationship of Model X6-3 under NGA 1119 fault-normal component ground motion.	570
Figure 7.30	Story drift ratio histories of Model X6-3 under NGA 1119 fault-normal component ground motion.....	570
Figure 7.31	Fourth-story to sixth-story brace axial force versus axial deformation relationships of Model X6-3 under NGA 1119 fault-normal component ground motion.....	571

Figure 7.32	First-story to third-story brace axial force versus axial deformation relationships of Model X6-3 under NGA 1119 fault-normal component ground motion.....	572
Figure 7.33	Base shear versus roof displacement relationship of Model X6-3 under NGA 1602 fault-parallel component ground motion.....	573
Figure 7.34	Story drift ratio histories of Model X6-3 under NGA 1602 fault-parallel component ground motion.....	573
Figure 7.35	Fourth-story to sixth-story brace axial force versus axial deformation relationships of Model X6-3 under NGA 1602 fault-parallel component ground motion.....	574
Figure 7.36	First-story to third-story brace axial force versus axial deformation relationships of Model X6-3 under NGA 1602 fault-parallel component ground motion.....	575
Figure 7.37	Base shear versus roof displacement relationship of Model SB6-3 under NGA 1119 fault-normal component ground motion.....	576
Figure 7.38	Story drift ratio histories of Model SB6-3 under NGA 1119 fault-normal component ground motion.....	576
Figure 7.39	Fourth-story to sixth-story brace axial force versus axial deformation relationships of Model SB6-3 under NGA 1119 fault-normal component ground motion.....	577
Figure 7.40	First-story to third-story brace axial force versus axial deformation relationships of Model SB6-3 under NGA 1119 fault-normal component ground motion.....	578
Figure 7.41	Base shear versus roof displacement relationship of Model SB6-3 under NGA 1602 fault-parallel component ground motion.....	579
Figure 7.42	Story drift ratio histories of Model SB6-3 under NGA 1602 fault-parallel component ground motion.....	579
Figure 7.43	Fourth-story to sixth-story brace axial force versus axial deformation relationships of Model SB6-3 under NGA 1602 fault-parallel component ground motion.....	580
Figure 7.44	First-story to third-story brace axial force versus axial deformation relationships of Model SB6-3 under NGA 1602 fault-parallel component ground motion.....	581
Figure 7.45	Base shear versus roof displacement relationship of Model SB6-3B under NGA 1119 fault-normal component ground motion.....	582
Figure 7.46	Story drift ratio histories of Model SB6-3B under NGA 1119 fault-normal component ground motion.....	582
Figure 7.47	Fourth-story to sixth-story brace axial force versus axial deformation relationships of Model SB6-3B under NGA 1119 fault-normal component ground motion.....	583

Figure 7.48	First-story to third-story brace axial force versus axial deformation relationships of Model SB6-3B under NGA 1119 fault-normal component ground motion.	584
Figure 7.49	Base shear versus roof displacement relationship of Model SB6-3B under NGA 1602 fault-parallel component ground motion.	585
Figure 7.50	Story drift ratio histories of Model SB6-3B under NGA 1602 fault-parallel component ground motion.	585
Figure 7.51	Fourth-story to sixth-story brace axial force versus axial deformation relationships of Model SB6-3B under NGA 1602 fault-parallel component ground motion.	586
Figure 7.52	First-story to third-story brace axial force versus axial deformation relationships of Model SB6-3B under NGA 1602 fault-parallel component ground motion.	587
Figure 7.53	Base shear versus roof displacement relationship of Model SB6-3L under NGA 1119 fault-normal component ground motion.	588
Figure 7.54	Story drift ratio histories of Model SB6-3L under NGA 1119 fault-normal component ground motion.	588
Figure 7.55	Fourth-story to sixth-story brace axial force versus axial deformation relationships of Model SB6-3L under NGA 1119 fault-normal component ground motion.	589
Figure 7.56	First-story to third-story brace axial force versus axial deformation relationships of Model SB6-3L under NGA 1119 fault-normal component ground motion.	590
Figure 7.57	Base shear versus roof displacement relationship of Model SB6-3L under NGA 1602 fault-parallel component ground motion.	591
Figure 7.58	Story drift ratio histories of Model SB6-3L under NGA 1602 fault-parallel component ground motion.	591
Figure 7.59	Fourth-story to sixth-story brace axial force versus axial deformation relationships of Model SB6-3L under NGA 1602 fault-parallel component ground motion.	592
Figure 7.60	First-story to third story brace axial force versus axial deformation relationships of Model SB6-3L under NGA 1602 fault-parallel component ground motion.	593
Figure 7.61	Sixth-story brace axial force versus axial deformation relationships of Model SB6-3 under ground motion numbers 11, 14, and 18.	594
Figure 7.62	Sixth-story brace axial force versus axial deformation relationships of Model SB6-3B under ground motion numbers 11, 14, and 18.	595
Figure 7.63	Sixth-story brace axial force versus axial deformation relationships of Model SB6-3L under ground motion numbers 11, 14, and 18.	596

Figure 7.64	Fourth-story to sixth-story brace axial force versus axial deformation relationships of Model SB6-3 under ground motion number 13.	597
Figure 7.65	Fourth-story to sixth-story brace axial force versus axial deformation relationships of Model SB6-3 under ground motion number 18.	598
Figure 7.66	First-story brace axial force versus axial deformation relationships of Model SB6-3 under ground motion number 18.	599
Figure 7.67	Fourth-story and fifth-story tie-column axial force versus axial deformation relationships of Model SB6-3B under ground motion number 14.	599
Figure 7.68	Fourth-story and fifth-story tie-column axial force versus axial deformation relationships of Model SB6-3 under ground motion number 19.	600
Figure 7.69	Maximum story drift ratios for each model under different hazard level ground motions (without leaning columns).	607
Figure 7.70	Residual story drift ratios for each model after different hazard level ground excitations (without leaning columns).	607
Figure 7.71	Maximum floor level accelerations for each model under different hazard level ground motions (without leaning columns).	608
Figure 7.72	Fifty-story brace axial force versus axial deformation relationships of Model V6 under NGA 1602 fault-parallel component ground motion (top: with leaning columns; bottom without leaning columns).	609
Figure 7.73	Fifty-story brace axial force versus axial deformation relationships of Model X6 under NGA 1602 fault-parallel component ground motion (top: with leaning columns; bottom without leaning columns).	610
Figure 7.74	Fifty-story brace axial force versus axial deformation relationships of Model X6-3 under NGA 1602 fault-parallel component ground motion (top: with leaning columns; bottom without leaning columns).	611
Figure 7.75	Fifty-story brace axial force versus axial deformation relationships of Model SB6-3 under NGA 1602 fault-parallel component ground motion (top: with leaning columns; bottom without leaning columns).	612
Figure 7.76	Fifty-story brace axial force versus axial deformation relationships of Model SB6-3B under NGA 1602 fault-parallel component ground motion (top: with leaning columns; bottom without leaning columns).	613
Figure 7.77	Fifty-story brace axial force versus axial deformation relationships of Model SB6-3L under NGA 1602 fault-parallel component ground motion (top: with leaning columns; bottom without leaning columns).	614

LIST OF TABLES

Table 2.1	Slenderness ratio and width-to-thickness ratio limitations.	14
Table 3.1	Name, member size, material type, and test method of the specimens.	54
Table 3.2	Section properties of beams and columns.	54
Table 3.3	Section properties of HSS braces (square and round).	54
Table 3.4	Section properties of wide flange braces.	54
Table 3.5	Vertical distribution of seismic forces.	96
Table 3.6	The site information of selected ground motion.	100
Table 3.7	Material mechanical properties from mill certificates.	108
Table 4.1	Specimen TCBF-B-1: major observations noted during test.	113
Table 4.2	Specimen TCBF-B-2: major observations noted during test.	186
Table 4.3	Specimen TCBF-B-3: major observations noted during test.	267
Table 5.1	Specimens TCBF-B: loading protocol details.	406
Table 5.2	Specimen TCBF-B-1: base shear and roof displacement data ($P_y = 556.4$ kips from experiment, corresponding to $D_{by} = 0.6$ in. at roof).	410
Table 5.3	Specimen TCBF-B-2: base shear and roof displacement data ($P_y = 589.0$ kips from experiment, corresponding to $D_{by} = 0.6$ in. at roof).	412
Table 5.4	Specimen TCBF-B-3: base shear and roof displacement data ($P_y = 584.8$ kips from experiment, corresponding to $D_{by} = 0.6$ in. at roof).	414
Table 5.5	Measured eccentricities of brace before test and buckling direction during test.	426
Table 5.6	Specimen failure characteristics (brace completely fractures).	426
Table 5.7	Input ground motion parameters.	443
Table 5.8	Specimen TCBF-B-4: story shear and floor level displacement data ($P_y =$ 589.3 kips from hybrid simulation, corresponding to $D_{by} = 0.6$ in. at roof).	447
Table 5.9	Specimen TCBF-B-4 brace failure characteristics (brace completely fractured).	454

Table 6.1	Input parameter details in OpenSees 2D model.....	465
Table 6.2	The dimensions of selected square hollow structural sections.	490
Table 6.3	Normalized cumulative energy dissipation of selected square hollow structural sections under different kL/r ratios.	492
Table 6.4	Normalized cumulative energy dissipation of selected group of square hollow structural sections under different kL/r ratios.	493
Table 6.5	Comparison between OpenSees and LS-DYNA simulation.	514
Table 7.1	Six-story model building with different seismic force-resisting systems.	536
Table 7.2	Model V6 member size information.	537
Table 7.3	Model X6 member size information.	538
Table 7.4	Model X6-3 member size information.	539
Table 7.5	Model SB6-3 member size information.	540
Table 7.6	Model SB6-3B member size information.	541
Table 7.7	Model SB6-3L member size information.	542
Table 7.8	Predefined ground motion search criteria.	544
Table 7.9	Selected ground motion pairs for nonlinear dynamic response history analysis.	544
Table 7.10	Prescribed roof displacements for cyclic pushover analyses.	546
Table 7.11	Identification number list for all ground motions.	549
Table 7.12	Fundamental and second mode periods of each mode.	549
Table 7.13	Mean responses of each model under selected ground motions (10% probability of exceedance in 50-years events, fault-normal component).	550
Table 7.14	Mean responses of each model under selected ground motions (10% probability of exceedance in 50-years events, fault-parallel component).	551
Table 7.15	Mean responses of each model under selected ground motions (2% probability of exceedance in 50 years, fault-normal component).	552
Table 7.16	Mean responses of each model under selected ground motions (2% probability of exceedance in 50 years, fault-parallel component).	553
Table 7.17	Steel weight contributions and estimated initial construction costs for each model (only includes the seismic force resisting system).	601
Table 7.18	Fundamental and second mode periods of each model (without leaning columns).	602

Table 7.19	Mean responses of each model under selected ground motions (10% probability of exceedance in 50-years events, fault-normal, without leaning columns).....	603
Table 7.20	Mean responses of each model under selected ground motions (10% probability of exceedance in 50-years events, fault-parallel, without leaning columns).....	604
Table 7.21	Mean responses of each model under selected ground motions (2% probability of exceedance in 50-year events, fault-normal, without leaning columns).....	605
Table 7.22	Mean responses of each model under selected ground motions (2% probability of exceedance in 50-year events, fault-parallel, without leaning columns).....	606

LIST OF APPENDICES

Appendix A: Test Set Up Design Calculations

http://peer.berkeley.edu/publications/peer_reports/reports_2013/AppendixA-PEER-2013-20.pdf

Appendix B: Test Set Up Shop Drawings

http://peer.berkeley.edu/publications/peer_reports/reports_2013/AppendixB-PEER-2013-20.pdf

Appendix C: Shop Drawings for Specimens TCBF-B-1 to TCBF-B-4

http://peer.berkeley.edu/publications/peer_reports/reports_2013/AppendixC-PEER-2013-20.pdf

Appendix D: Channel Locations and Lists for Specimen TCBF-B-1

http://peer.berkeley.edu/publications/peer_reports/reports_2013/AppendixD-PEER-2013-20.pdf

Appendix E: Channel Locations and Lists for Specimen TCBF-B-2

http://peer.berkeley.edu/publications/peer_reports/reports_2013/AppendixE-PEER-2013-20.pdf

Appendix F: Channel Locations and Lists for Specimen TCBF-B-3

http://peer.berkeley.edu/publications/peer_reports/reports_2013/AppendixF-PEER-2013-20.pdf

Appendix G: Channel Locations and Lists for Specimen TCBF-B-4

http://peer.berkeley.edu/publications/peer_reports/reports_2013/AppendixG-PEER-2013-20.pdf

Appendix H: Specimens TCBF-B-1 to TCBF-B-4 Design Calculation Sheets

http://peer.berkeley.edu/publications/peer_reports/reports_2013/AppendixH-PEER-2013-20.pdf

Appendix I: Specimens TCBF-B-1 to TCBF-B-4 Mill Certificate Report

http://peer.berkeley.edu/publications/peer_reports/reports_2013/AppendixI-PEER-2013-20.pdf

Appendix J: Response Plots of Square Hollow Structural Sections

http://peer.berkeley.edu/publications/peer_reports/reports_2013/AppendixJ-PEER-2013-20.pdf

1 Introduction

1.1 BACKGROUND AND RESEARCH MOTIVATION

Over the past few decades, steel concentrically braced frame systems are considered an efficient and economical lateral force-resisting systems to control the lateral deformation in building structures under wind loading or earthquake ground shaking. Already widely used in the United States, this kind of structural system has been increasingly employed in the Pacific west coast given that another design strategy—steel moment-resisting frames—have proved susceptible to large deformations during strong ground shaking. In addition to the larger displacements, significant damage observed in the 1994 Northridge earthquakes necessitated giving special attention to the beam-to-column connections in moment-resisting frames to avoid problems associated with brittle failures in these regions. However, a review of structural damage to the concentrically steel braced frame systems after several major earthquakes has identified some anticipated and unanticipated damages [Steinbrugge et. al. 1971; EERI 1978; Tanaka et al. 1980; Kato et al. 1980; SEAOC 1991; Phipps et. al. 1992; AIJ 1995; Bonneville and Bartoletti 1996; EERI 1998; Kelly et al. 2000]. This damage has prompted many engineers and researchers in highly seismic zones to consider new approaches to improve the behavior of steel concentrically braced frame systems.

One of the key components that controls the system behavior of steel concentrically braced frame is the bracing member. Typically, this member will buckle under compression loads and yield under tension forces, which inherently make the behavior complex. The asymmetric hysteretic behavior under cyclic loadings with compression capacity degradation further limits the cyclic deformation capacity of individual braces. Given that such a complex cyclic behavior accompanies a wide range of different structural configurations, it is often difficult to proportion the braces within a braced frame system to achieve uniform brace demand-to-capacity ratios along the height of the braced bay. This variation has been shown to be one of critical factors causing the concentration of deformation on certain floor levels.

Another key component that affects the braced frame behavior is the connection. A significant number of failure modes associated with connections have been observed in both the laboratory and the field. Although these failure modes are often localized near the region of the connection, these failures have substantial effects on the braced frame global behavior. For instance, premature or brittle failures in the brace-to-gusset plate connections near the net section regions usually occurs before inelastic demands develop in the braces, meaning that the entire braced frame is essentially elastic when the connection fails.

Many strategies exist to improve the concentric steel braced frame behaviors; they vary from component level to system level. For example, one way to make changes at the component level is to use devices such as buckling-restrained braces [Watanabe et al. 1988; Kalyanamaran et al. 1998, 2003; Chen et al. 2001; Mahin et al. 2004; Lai et al. 2004] or self-centering braces [Christopoulos et al. 2008; Tremblay et al. 2008]. These kinds of braces have excellent and stable hysteresis behaviors but have drawbacks: they are usually more expensive than the conventional buckling braces and typically require paying proprietary fees. The more recently developed re-centering braces exhibit a flag-shaped pattern of hysteresis loops that almost re-centered to the un-deformed condition of structure. But most of this research has been conducted on small-scale models, and much more research needs to be conducted before field applications are viable.

Another way to improve the seismic behavior of steel concentric braced frame is to prevent local concentration of overall system deformation at one or a few stories by improving the distribution of inelastic demand along the entire height of the structure [Khatib et al. 1988]. Although this concept was proposed several decades ago, the analytical and experimental state-of-the-art weren't adequate at that time. Recently this concept has been revived by several researchers [Sabelli 2001; Tremblay 2003; Tremblay and Merzouq 2004; Tirca and Tremblay 2004; Mahin and Lai 2008; Yang et al. 2008, 2010] and adopted in seismic retrofit projects and new steel constructions [Mar 2010]. Note that there are many other ways to improve the behavior of braced frame behaviors that will not be discussed herein.

Although many experimental studies of conventional buckling brace components and several braced frame specimens have been investigated over the past forty years (e.g., Black et al. [1980]; Ballio and Perotti [1987]; Lee and Goel [1987]; Bertero et al. [1989]; Tremblay [2002]; Yang and Mahin [2005]; Fell [2008]; Uriz and Mahin [2008]; Clark et al. [2008]; Yang et al. [2008]; and Lumpkin et al. [2010]; for a more detailed list see Chapter 2), the number of studies on the full-scale concentric braced frames is still limited. Many of these existing research efforts focused on investigating individual brace behavior by using reduced-scale brace specimens, and some of the specimens tested initially used structural details rarely used in current practice. As for the braced frames, they were often single-story, one-bay small-scale specimens loaded at the top of one-story structures that focused on the brace-to-gusset plate connection behaviors. Through the improvement of test equipment and laboratory techniques, the cyclic behaviors of several large-scale multi-story braced frame specimens have been tested and studied. However, even with the improved testing set ups, these braced frame specimens have been typically loaded at roof level only, which does not represent real conditions. Moreover, quasi-static cyclic loading sequences were often used in these tests, and only a few of them were tested pseudo-dynamically to simulate the braced frame behaviors under actual ground motion records.

Most existing analytical investigations focused on the study of nonlinear cyclic behavior of structural components in braced frames; few of them tackled the inelastic behavior of large-scale specimens. Analytical studies of system level performances are comparatively rarer and often limited to conventional brace configurations, such as chevron bracing (inverted-V), V-shaped bracing, or split-X bracing configuration.

These observations have stimulated the experimental and analytical study of the nonlinear behavior of concentrically steel braced frame systems designed to current codes and structural details. The opportunity to improve and validate the design concepts for tomorrow's concentrically steel braced frame structures through developing innovative braced frame systems and validating practical computer models exists, with the added benefit of using these improved models under the framework of modern performance-based earthquake engineering to evaluate braced frame systems.

Conducted at the NEES Berkeley site, the experimental part of this research consisted of four full-scale one-bay two-story steel concentrically braced frames that were constructed and tested under a series of incremental cyclic loadings increasing in amplitude up to a maximum roof drift ratio of about 4%. Hybrid simulations were also conducted to examine the braced frame system behavior under two selected hazard level ground motions, with maximum expected roof drift ratio up to 5% or more. Note that in a companion study [Chen and Mahin 2010; Lai et al. 2010], nonlinear dynamic analyses showed that under the most severe hazard level (i.e., 2% probability of exceedance in 50 years), the median expected maximum story drift ratio was about 3.3%. In a previous analytical study with a 10% probability of exceedance in 50-year ground motions [Sabelli 2001], the mean maximum story drift ratio in the concentrically steel braced frame could be as large as 3.9%, and the mean residual story drift ratio could be as large as 2.5%.

For the analytical portion, testing data obtained from previous individual brace components were first used to validate the analytical models at the component level. Next, the new data obtained from the full-scale braced frame specimens were used to confirm the validation of analytical model at the system level. With the calibrated and validated models in hand, forty compact square hollow structural sections were selected from the steel design manual. These sections were numerically tested under prescribed cyclic loadings with various slenderness ratios to investigate the sensitivity of inelastic behaviors of brace components to actual width-to-thickness ratios and member slenderness ratios. Finally, a series of nonlinear dynamic response history analyses were performed to examine the dynamic behaviors of six braced frame systems, including the proposed Strong-Back System and hybrid braced frame system.

1.2 RESEARCH OBJECTIVES AND SCOPE

The fundamental goal of this research was to investigate the system performance of steel concentrically braced frame structures subjected to both quasi-static cyclic loadings and severe ground motions. Through experimental studies on full-scale specimens, the structural characteristics that control the system global behaviors can be identified and better understood. As mentioned previously, in the last forty years only a few large-scale steel braced frame specimens have been performed, and some of them had unrealistic lateral force distributions or loading boundary conditions in the test set up. Accordingly, reported herein is a new test program and test set up that imposes a lateral force pattern on the braced frame specimen that better represents the lateral force distribution that occurs in a real seismic event. The hybrid simulation or pseudo-dynamic testing techniques introduced into the experimental program

document the steel braced frame specimen cyclic behaviors under different hazard level input ground motions. The main objectives and scope of the test program are as follows:

- To obtain the experimental data on the behavior of key components such as bracing components, gusset plates, connections and braced frame systems.
- To provide full-scale braced frame testing data for developing and validating the improved analytical models in both OpenSees and LS-DYNA analysis tools.
- To devise improved design and analysis methods, proposing modifications where appropriate.
- To identify the improved design concepts and structural details.
- To confirm the improvements by both quasi-static cyclic loading tests and hybrid simulations of full-scale steel concentrically braced frame specimens.

In view of the observations from existing studies and past earthquakes, the analytical part of this research aims at scrutinizing the nonlinear behavior of braced frame systems specifically on several topics such as:

- The sensitivity of bracing component cyclic behaviors to slenderness ratios and sectional width-to-thickness ratios.
- Performance evaluation of different design configurations of steel concentrically braced frames.
- Proposal of a hybrid braced frame system—the Strong-Back System—and investigating the inelastic behavior of this system. A series of nonlinear dynamic response history analyses will be performed to examine the dynamic behaviors of the proposed Strong-Back System and hybrid braced frame systems.
- Initiating feasible design recommendations on the proposed system so that it can be incorporated into future design provisions.

1.3 OVERVIEW AND ORGANIZATION OF REPORT

To achieve the above-mentioned research objectives, a series of experimental and analytical studies were carried out on various steel concentrically braced frame systems. To support this research, a review of relevant literature is presented in Chapter 2 that examines steel concentric braced frames related to analytical simulations of cyclic and dynamic response and the evolution of applicable building code provisions. This review identifies and discusses several key parameters, such as brace slenderness ratios and width-to-thickness ratios. Experimental studies from previous tests of components, connections, sub-assemblages, and complete braced frames are reviewed. Finally, observations based on reported damage to steel braced frame systems from past earthquakes, including the recent 2011 Great Eastern Japan Earthquake Disaster, are presented.

Chapter 3 describes the overall experimental aspects of the research. Beginning with an overview of the entire test program with an emphasis on the experimental program at Berkeley site, a newly developed full-scale test rig is introduced in detail, followed by detailed design descriptions of four full-scale braced frame specimens. Next the quasi-static loading sequences,

specimen instrumentation plans, and construction sequences are presented for each specimen, concluding with a discussion of the design philosophy of hybrid simulation specimen.

Both quasi-static and hybrid simulation test results are present in Chapter 4. The first specimen considered was the braced frame Specimen TCBF-B-1, which used square hollow structural sections (HSS) as bracing members. The second specimen considered, TCBF-B-2, used round HSS braces, and the third specimen, TCBF-B-3, used wide-flange bracing members. Finally, to investigate on the braced frame behavior under different hazard level ground shakings, the results of hybrid simulations of Specimen TCBF-B-4 are presented where the same square HSS braces are those used as those used in Specimen TCBF-B-1. Response quantities measured during the experiments were either plotted or tabulated in common formats. Selected still photos taken during the test are also shown at the end of each section.

Further test results are discussed in Chapter 5. Systematic comparisons between quasi-static test results are presented from global responses to local responses. Discussion on the hybrid simulation results are then conducted similarly.

Before conducting the analytical study on the proposed braced frame systems, a series of numerical modeling validations and calibrations were performed in OpenSees and LS-DYNA using the test data obtained from previous experimental works and current studies. All these analytical modeling details and discussions are included in Chapter 6. Based on calibrated models, results of a simple parametric study on the square HSS bracing members are presented and discussed at the end of this chapter.

Based on current experimental study and extensive literature reviews, a new hybrid braced frame system was developed—the Strong-Back System—and is described in Chapter 7. Static pushover analyses and nonlinear dynamic response history analyses were conducted on six different predefined six-story models including the Strong-Back System to investigate system behaviors and to validate system performance analytically.

Chapter 8 contains the conclusions and summary of the current experimental and analytical study. Several topics not covered herein and investigated in current research are discussed and areas for future study are presented.

Detailed full-scale specimens and test rig design calculations, shop drawings, material mill certificate copies, instrumentation sensor lists, and experimental data reductions are presented in the Appendices, followed by a detailed reference list. Extra plots from the parametric study are also attached in this section.

2 Literature Review

This chapter briefly summarizes literature related to the current study. Relevant literature related to component-level studies is examined first, followed by information on connections and systems. Finally, some observations on the behavior of steel concentric braced frames during past earthquakes are presented. Because of the extensive literature that exists on these topics, only major references used to guide the overall scope of this study are discussed in this chapter. Additional references are presented throughout the report.

2.1 BRACING COMPONENT

2.1.1 Issues Related to Net Reduced Section

Bracing members are critical components in braced frame systems. They often contribute 75% or more of the total system lateral stiffness and strength. The behavior of braces under tension forces is well understood. Special issues related to the tension behavior at the brace-to-gusset plate connection are reviewed below.

The hollow structural sections frequently used as braces are usually slotted at the end so that they can be welded to the gusset plate. This is a simple and economic approach, but the tip of the slot and the gap between slot tip and gusset plate edge typically form a reduced net section, which may cause premature brittle failure. In the very first “Steel Tips” about the seismic design of special concentrically steel braced frames, Becker [1995] noted that the reduced net section resulting from holes in bolted brace-to-gusset plate connections were identified as a potential problem. It was pointed out that the effective net areas at the connection needed to be checked in the design process and reinforced if necessary. Brittle failures at these locations were observed in past earthquakes [EERI 1978; AIJ 1995; EERI 1998; Astanek-Asl 1998] and were generally attributed to poor detailing. Later, possible net reduced section issues in slotted HSS braces were identified, and the use of net section reinforcement side plates was demonstrated as an example [Cochran 2000, 2003].

The net reduced section failure mode (see Figure 2.1) was studied in a series of simple strut tests [Yang and Mahin 2005]. A total of six specimens having end connections mimicking brace-to-gusset plate detailing were tested quasi-statically under different uniaxial loading protocols. In addition to conventional protocols having symmetrically incremented cycles of

displacement, tension-dominated cyclic near-fault type excursions and compression-dominated near-fault type protocols were used to examine the cyclic behavior of braces with and without reinforcing cover plates at the net reduced section regions. Five square hollow structural section braces (HSS $6 \times 6 \times 3/8$) and one extra strong pipe section brace (Pipe 6 XS) were employed in the experimental program. The results showed that net reduced section failures occurred when the braces were not reinforced at the net reduced section regions. The type of loading history and cross-sectional shape also had significant effects on the net section failures. For example, the tension-dominated loading histories typically triggered the net reduced section failure of an unreinforced brace earlier than the symmetrical histories, while the compression-dominated histories might not trigger this failure mode at all. The net section failure in the square HSS brace typically happened earlier than the net section failure in the pipe section brace under the same loading history. While considerable yielding was noted in the unreinforced sections in the vicinity of the reduced net section, the small length of member yielding compared to the total length of the member resulted in a small (nearly brittle) ductility capacity for the braces in tension.



(a) square HSS



(b) pipe section

Figure 2.1 Net section failure mode in a brace without reinforcing plates (extracted from Figures 9 and 16 of Yang and Mahin [2005]).

Similar net reduced section failures were found in monotonic static loading tests [Korol 1996; Cheng et al. 1998; Willibard et al. 2006; Packer 2006], and the tear-out failure mode (block shear) along the weld lines also reported. Similar failures were noted under static and dynamic cyclic loading protocols [Fell 2008; Fell and Kanvinde 2010].

The first edition of AISC Seismic Provisions for Structural Steel Buildings [AISC 1992] listed a minimum ratio of effective net section area to gross section area for bolted brace connections to account for the net section problem. To prevent connection local failures, five years later the second edition of AISC seismic provisions [AISC 1997] extended the net section provisions from bolted connections to any types of bracing connections under tension forces. Later, the 2002 and 2005 editions [AISC 2002; AISC 2005b] explicitly stated that the strength of the net section should be greater than the smaller of expected tensile strength of the brace and the

maximum force that will develop in the brace. Reinforcing cover plates were mentioned as one scheme to overcome strength deficiencies at the net reduced section. In some instances, welds were wrapped around the gusset plate edges as reinforcement. These were not recommended by many in the United States because of possible poor fit up of the leading edge of the gusset plate and the end of the slot on the brace (making the weld effectiveness difficult to judge), and the potential for high stresses in this area (due to applied loads or weld shrinkage) that could lead to ductility reduction [Cheng et al. 1998] or crack initiation. Other possible reinforcing schemes (Figure 2.2), while not prohibited by AISC, were not mentioned, including extended gusset plate details [Mitsui and Kurobane 1981], pad attachments [Mitsui and Maeda 1986], and modified hidden gap detailing [Packer 2006; Martinez-Saucedo et al. 2008a, 2008b]. The most recent version of the AISC Seismic Provisions [AISC 2010a] retains the basic requirements from the 2005 edition. As the specific issues of the behavior of the net reduced section region and detailing to mitigate the effects of strength deficiencies are not the subject of this work, simple approaches (i.e., cover plates) will be used herein to avoid premature brittle failures in these regions.

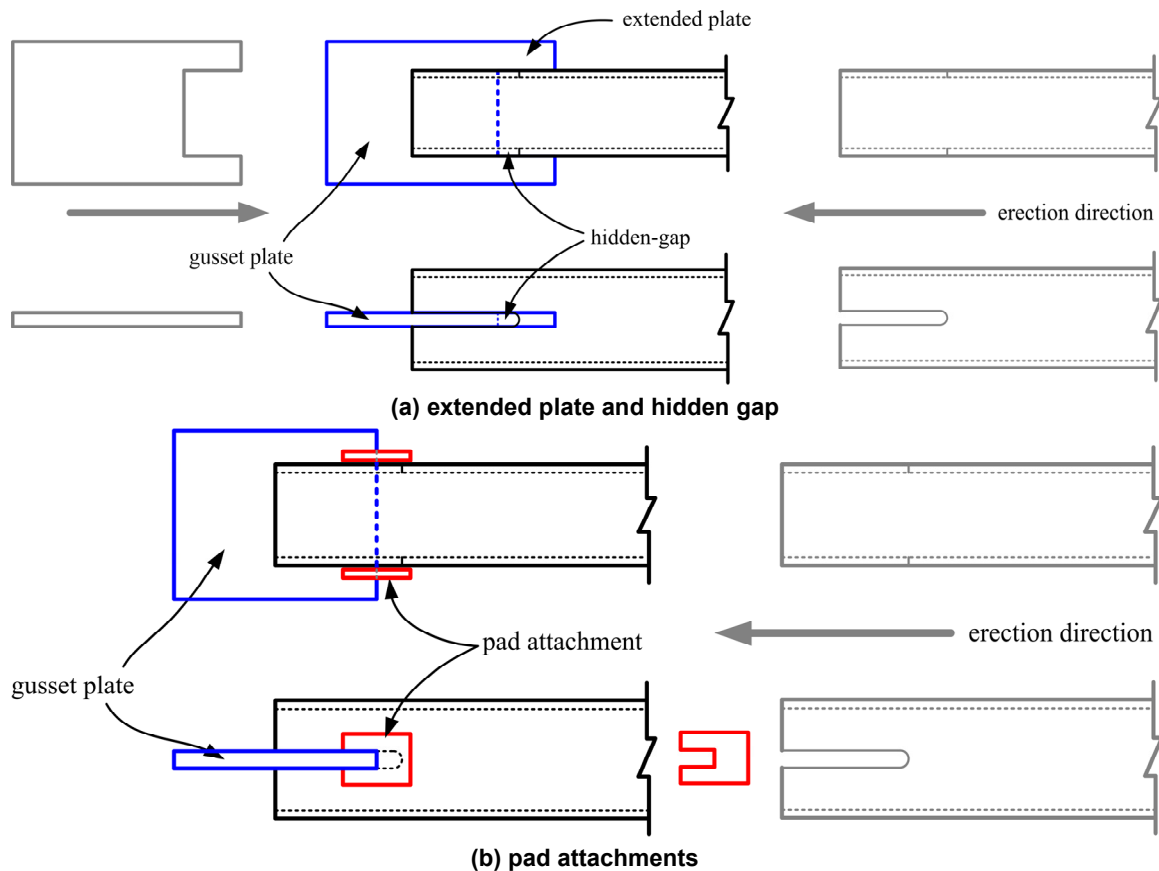


Figure 2.2 Other possible net section reinforcing schemes.

2.1.2 Limitations on Slenderness Ratio and Width-to-Thickness Ratio

The behavior of braces under compression or cyclic loadings is typically governed by global stability (brace end boundary conditions and slenderness ratio) and local stability (width-to-thickness ratios and brace sectional shapes) issues. Various test results suggest that the slenderness ratio and width-to-thickness ratios should be limited to achieve adequate ductile behavior. For example, observations from shaking table tests of a 0.3-scale model of a six-story concentrically braced frame suggested that the P_{cr}/P_y and b/t ratios should be limited [Uang and Bertero 1986]. To prevent undesirable behavior, it was suggested that the P_{cr}/P_y ratio should be greater than 0.8, and b/t ratio should be less than 18 for square HSS braces. Based on those suggestions—along with an assumption that the limitation of b/t ratio is inverse proportional to $\sqrt{F_y}$ and applying the allowable stress design (ASD) column design formula at that time for intermediate and stocky members—the kL/r and b/t ratio limitations could be derived. That is,

$$\frac{P_{cr}}{P_y} = \frac{F_a}{F_y} = \frac{1}{FS} \left[1 - \frac{\left(\frac{kL}{r}\right)^2}{2 C_c^2} \right] \geq 0.8 \quad (2.1)$$

$$C_c = \sqrt{\frac{2 \pi^2 E}{F_y}} \quad (2.2)$$

$$FS = \frac{3}{5} + \frac{3}{8} \frac{\frac{kL}{r}}{C_c} - \frac{1}{8} \frac{\left(\frac{kL}{r}\right)^3}{C_c^3} \quad (2.3)$$

where P_{cr} and P_y are allowable compression force and yield force of brace, respectively, F_a and F_y are allowable compression stress and yield strength of brace, respectively, FS is the safety factor, L is the brace length, r is the radius of gyration of the brace section, k is the effective length factor, and C_c is the slenderness ratio that separates the long and short columns for ASD column design.

The slenderness ratio limitation can then be found by solving the above equations; getting

$$\frac{kL}{r} \leq 0.8123 \cdot C_c = 0.8123 \cdot \sqrt{\frac{2 \pi^2 E}{F_y}} = \frac{615}{\sqrt{F_y}} \quad (2.4)$$

where E is the elastic modulus of elasticity of the steel. For the b/t ratio limitation,

$$\frac{b}{t} \leq 18 = \frac{x}{\sqrt{F_y}} \quad (2.5)$$

where the coefficient x remains to be determined. Assuming ASTM A500 grade B steel for the square HSS braces,

$$F_y = 46 \text{ ksi} \quad (2.6)$$

and x can be solved, resulting in the following b/t ratio limitation formula for square HSS braces:

$$\frac{b}{t} \leq \frac{122}{\sqrt{F_y}} \quad (2.7)$$

Note that b is the width of compression element as defined in AISC specification for structural steel buildings (Section B4.1 of AISC 360-10) and t is the wall thickness of compression element.

In the first edition of AISC seismic provisions [AISC 1992], bracing members used in the concentrically steel braced frames could be compact or non-compact sections, but the overall L/r ratio had a limit.

$$\frac{L}{r} \leq \frac{720}{\sqrt{F_y}} \quad (2.8)$$

If $k = 1.0$ in this case, this corresponds to $P_{cr}/P_y = 0.65$ using the ASD column formula. The width-to-thickness ratio limits for round HSS and rectangular HSS sections were

$$\frac{OD}{t} \leq \frac{1300}{F_y} \quad (\text{Round HSS}) \quad (2.9)$$

$$\frac{b}{t} \leq \frac{110}{\sqrt{F_y}} \quad (\text{Rectangular HSS}) \quad (2.10)$$

where OD is outer diameter of round HSS sections. A 0.9 reduction factor applied was to the b/t ratio limit, as suggested by the shaking table test results [Uang and Bertero 1986]. However, this limitation was 16% higher than the b/t limit ($b/t \leq 95/\sqrt{F_y}$) proposed by other researchers [Tang and Goel 1987], which was chosen simply to be half the limitation used in the plastic design ($b/t \leq 190/\sqrt{F_y}$ from AISC [1978]).

In the 1997 version of the AISC Seismic Provisions [AISC 1997], the slenderness ratio was limited as

$$\frac{kL}{r} \leq \frac{1000}{\sqrt{F_y}} \quad (2.11)$$

This further relaxed the P_{cr}/P_y ratio limitation to 0.46 (derived from the ASD column formula). The width-to-thickness ratio limits for round HSS and rectangular HSS sections were taken as the same as used in the 1992 Seismic Provisions.

In the 2002 version of Seismic Provisions [AISC 2002], the slenderness ratio was limited as

$$\frac{kL}{r} \leq 5.87 \sqrt{\frac{E}{F_y}} = \frac{1000}{\sqrt{F_y}} \quad (2.12)$$

which is the same as the limit in 1997 Seismic Provisions, provided F_y is 50ksi. The width-to-thickness ratio limits for round HSS and rectangular HSS sections were changed to

$$\frac{D}{t} \leq 0.044 \frac{E}{F_y} = \frac{1276}{F_y} \quad (\text{Round HSS}) \quad (2.13)$$

$$\frac{b}{t} \leq 0.64 \sqrt{\frac{E}{F_y}} = \frac{109}{\sqrt{F_y}} \quad (\text{Rectangular HSS}) \quad (2.14)$$

where D is outer diameter of round HSS sections; these were essentially the same as 1997 seismic provisions. However, the limitation of slenderness ratio was reduced in the 2005 seismic provisions

$$\frac{kL}{r} \leq 4 \sqrt{\frac{E}{F_y}} = 4 \sqrt{\frac{29000}{F_y}} = \frac{681}{\sqrt{F_y}} \quad (2.15)$$

The resulting corresponding P_{cr}/P_y ratio limitation was 0.70, returning close to the limitation in 1992 Seismic Provisions. The width-to-thickness ratio limits for round HSS and rectangular HSS sections were the same as 2002 Seismic Provisions.

In the 2010 Seismic Provisions, the limitation of slenderness ratio of bracing members in SCBF changed to 200, but the previous limitation was retained for bracing member in ordinary concentric braced frames (OCBF). That is:

$$\frac{kL}{r} \leq 200 \quad (\text{SCBF}) \quad (2.16)$$

$$\frac{kL}{r} \leq 4 \sqrt{\frac{E}{F_y}} = \frac{681}{\sqrt{F_y}} \quad (OCBF) \quad (2.17)$$

Note that the noted slenderness limit is for V and inverted-V brace configurations in OCBF system. The 2010 AISC Seismic Provisions further stipulated the width-to-thickness limitations for round HSS and rectangular HSS sections are based on the ductility factor of the bracing members. The width-to-thickness limitations for highly ductile and moderately ductile members were different. For moderately ductile members, the same limitations as in the 2005 seismic provisions applied.

$$\frac{D}{t} \leq 0.044 \frac{E}{F_y} = \frac{1276}{F_y} \quad (Round \ HSS) \quad (2.18)$$

$$\frac{b}{t} \leq 0.64 \sqrt{\frac{E}{F_y}} = \frac{109}{\sqrt{F_y}} \quad (Rectangular \ HSS) \quad (2.19)$$

For highly ductile members, the width-thickness ratio limits were 14% smaller than the limits for moderately ductile members.

$$\frac{D}{t} \leq 0.038 \frac{E}{F_y} = \frac{1102}{F_y} \quad (Round \ HSS) \quad (2.20)$$

$$\frac{b}{t} \leq 0.55 \sqrt{\frac{E}{F_y}} = \frac{94}{\sqrt{F_y}} \quad (Rectangular \ HSS) \quad (2.21)$$

Note that the b/t ratio limitation for highly ductile rectangular HSS braces is very close to the proposed limitation from the study by Tang and Goel [1987]. Table 2.1 summarizes the slenderness ratio and width-to-thickness ratio limitations for square HSS, round HSS and also the wide flange braces listed in the seismic provisions from the first version to the current version.

Table 2.1 Slenderness ratio and width-to-thickness ratio limitations.

Version of Seismic Provisions	kL/r		Section Shape			
	OCBF	SCBF	Square HSS	Round HSS	Wide Flange	
			b/t	D/t	Flange	Web
					b/t	h/t
1992	$\frac{720 k}{\sqrt{F_y}}$	N.A.*	$\frac{110}{\sqrt{F_y}}$	$\frac{1300}{F_y}$	N.A.	$\frac{P_u}{\phi_b P_y} \leq 0.125$ $\frac{520}{\sqrt{F_y}} [1 - 1.54 \frac{P_u}{\phi_b P_y}]$ $\frac{P_u}{\phi_b P_y} > 0.125$ $\frac{191}{\sqrt{F_y}} [2.33 - \frac{P_u}{\phi_b P_y}] \geq \frac{253}{\sqrt{F_y}}$
1997	$\frac{720}{\sqrt{F_y}}$ **	$\frac{1000}{\sqrt{F_y}}$	$\frac{110}{\sqrt{F_y}}$	$\frac{1300}{F_y}$	N.A.	(the same as 1992 version)
2002	$4.23 \sqrt{\frac{E}{F_y}}$ **	$5.87 \sqrt{\frac{E}{F_y}}$	$0.64 \sqrt{\frac{E}{F_y}}$	$0.044 \frac{E}{F_y}$	$0.30 \sqrt{\frac{E}{F_y}}$	$\frac{P_u}{\phi_b P_y} \leq 0.125$ $3.14 \sqrt{\frac{E}{F_y}} [1 - 1.54 \frac{P_u}{\phi_b P_y}]$ $\frac{P_u}{\phi_b P_y} > 0.125$ $1.12 \sqrt{\frac{E}{F_y}} [2.33 - \frac{P_u}{\phi_b P_y}]$
2005	$4 \sqrt{\frac{E}{F_y}}$ **	$4 \sqrt{\frac{E}{F_y}}$	$0.64 \sqrt{\frac{E}{F_y}}$	$0.044 \frac{E}{F_y}$	$0.30 \sqrt{\frac{E}{F_y}}$	$\frac{P_u}{\phi_b P_y} \leq 0.125$ $3.14 \sqrt{\frac{E}{F_y}} [1 - 1.54 \frac{P_u}{\phi_b P_y}]$ $\frac{P_u}{\phi_b P_y} > 0.125$ $1.12 \sqrt{\frac{E}{F_y}} [2.33 - \frac{P_u}{\phi_b P_y}] \geq$ $1.49 \sqrt{\frac{E}{F_y}}$
2010 (moderately ductile members)	$4 \sqrt{\frac{E}{F_y}}$ **	200	$0.64 \sqrt{\frac{E}{F_y}}$	$0.044 \frac{E}{F_y}$	$0.38 \sqrt{\frac{E}{F_y}}$	$1.49 \sqrt{\frac{E}{F_y}}$
2010 (highly ductile members)	$4 \sqrt{\frac{E}{F_y}}$ **	200	$0.55 \sqrt{\frac{E}{F_y}}$	$0.038 \frac{E}{F_y}$	$0.30 \sqrt{\frac{E}{F_y}}$	$1.49 \sqrt{\frac{E}{F_y}}$

(*Note: in the 1992 seismic provisions, there was no specific terminologies for ordinary concentrically braced frames or special concentrically braced frames)

(** Limitations for V or inverted-V brace configurations)

2.1.3 Experimental Studies on Brace Components

One of early experimental study on the effect of slenderness ratio and b/t ratio upon the inelastic local buckling of single-angle and double-angle braces was done by Mangat [1969] at the University of Windsor. The experiments were conducted under monotonic compression load on twenty-four pin-ended single-angle braces (sections varied from $L3 \times 3 \times 3/16$ to $L4 \times 4 \times 5/16$), thirty-two fix-ended single-angle braces (sections varied from $L1-3/4 \times 1-3/4 \times 1/8$ to $L3-1/2 \times 3-1/2 \times 5/16$), twenty-four pin-ended double-angle braces (sections varied from $L1-3/4 \times 1-3/4 \times 1/8$ to $L3-1/2 \times 3-1/2 \times 3/16$), and twenty-four fix-ended double-angle braces (sections varied from $L1-3/4 \times 1-3/4 \times 1/8$ to $L3-1/2 \times 3-1/2 \times 3/16$) with 4-ft and 1-ft in length. The b/t ratios of angles varied from 10.67 to 18.67, and the slenderness ratios were between 20 and 96. Based on these experiments several conclusions were drawn:

- The boundary conditions at single-angle brace ends did not affect to any degree the compression capacity. For $16 < b/t \leq 18.67$ single-angle braces, local buckling will occur when the braces fail.
- Similar to single-angle braces, for $16 < b/t \leq 18.67$ double-angle braces, local buckling will occur when the braces fail.
- The compression capacities of fix-ended double-angle braces with $16 < b/t \leq 18.67$ were greater than that of pin-ended double-angles braces at about 14%.
- The number of bolts used at the connections did not have significant effects on the compression capacity of angle braces.

Although design recommendations were also provided for angle brace design, these were only for angle brace compression capacities with slenderness ratios between 20 and 96.

An early literature survey of existing research findings on the cyclic behavior of structural steel bracing systems was performed at University of California, Berkeley (UCB) [Popov et al. 1976]. About thirty publications, mostly from the United States and Japan, were reviewed and discussed extensively in this report; some alternative concepts of braced frame design were also proposed. The investigation suggested that more accurate and efficient analytical models, testing on braces of larger sizes, and improved design concepts were needed.

In Japan, cyclic behavior of conventional buckling braces was extensively investigated during the 1970s at Kyoto University [Wakabayashi et al. 1972; Shibata et al. 1973; Wakabayashi 1973; Wakabayashi et al. 1973; Wakabayashi et al. 1974; Wakabayashi et al. 1976; Wakabayashi et al. 1977]. Square and H-shaped sections were used in the relatively small-scale brace specimens (specimen length ranged from 7.6 in. to 36.5 in.) with different slenderness ratios varied from 40 to 160. Incremental cyclic displacement amplitudes were selected as loading protocol during the tests. The effect of brace-end fixities (restraints) was studied and represented through an amplification factor. Axial force versus axial deformation and axial force versus out-of-plane displacement hysteresis loops were examined and compared with empirical formula proposed in the studies. Comparisons between test results and the empirical theory were found to be satisfactory.

During this period, several studies were underway in the U.S. at the University of Michigan, Ann Arbor. Sixteen hot-rolled steel bars of various lengths (specimen length ranged from 24 in. to 59 in.) were tested under static and quasi-dynamic cyclic loadings [Khan and Hanson 1976] to verify the findings of theoretical studies of braces [Higginbotham 1973]. The slenderness ratios (kL/r) of the brace specimens investigated in the experiments varied from 85 to 210; all specimens had a nominal cross section of 1 in. \times 0.5 in. It was found that the experimental results generally agreed with existing theory. Net elongation phenomenon was observed under cyclic loading, and cyclic degradation of compressive strength was also noted. Quasi-dynamic loading effect on brace hysteretic response was found to be small but made the tension region response stiffer. Full-size bracing component tests were suggested to further develop design provisions.

Within a year after Khan and Hanson presented their work, Jain, Goel, and Hanson [1977] published a cyclic test report of twenty-four 1-in. \times 1-in. cold-rolled steel tubes with a b/t ratio equaled to 7.52. The tubular specimens covered a wide range of slenderness ratio from 30 to 140 and were tested statically and dynamically. Three loading frequencies, 1/60 Hz (static), 1/16 Hz (slow dynamic) and 1 Hz (fast dynamic), were applied in eighteen static tests and six dynamic tests on tubular specimens. It was found that the rate of loading did not have significant influences upon the test results (as shown in previous studies by Hanson). Brace residual elongations were found to be larger for smaller slenderness ratio specimens, and the slenderness ratio seemed to be the most important factor governing brace hysteretic behavior.

Based on the detailed literature survey on the braced frame systems [Popov et al. 1976)], researchers at UCB conducted a series of cyclic axial loading tests on steel struts [Black et al. 1980]. There were twenty-four commercially available steel struts selected to represent the common bracing members in braced frames. Larger and heavier sections were selected but within the capacity of test equipment. Eighteen out of twenty-four specimens were pinned at both ends with slenderness ratios of 40, 80, and 120. The remaining six specimens were fixed at one end and pinned at the other with slenderness ratios of 40 and 80. A total of eight different cross sectional shapes, including double-angles, double-channels, wide flanges, tees, thin-walled pipes, thick-walled pipes, thin-walled square tubes and thick-walled square tubes, were tested in the experimental program. The primary goals were to examine the effects of cross-sectional shapes, slenderness ratios, brace-end conditions, and load patterns on the hysteresis characteristic of the struts. The slenderness ratio was identified again as the most influential parameter influencing brace hysteretic behavior. Normalized hysteretic envelopes were proposed to compare specimen responses with different loading histories, and several design suggestions were made.

Behavior of tubular braces in the offshore platforms was also studied at UCB [Zayas et al. 1980a]. Six tubular brace specimens representing one-sixth scale brace models for an offshore platform were subjected to inelastic cyclic loading. Different brace-end fixities (pinned and fixed), diameter-to-thickness ratios ($D/t = 33$ and 48), and heat treatment procedures (annealed and un-annealed) were examined. Test results showed that the struts with lower diameter-to-thickness ratio performed better than the struts with higher diameter-to-thickness ratio, and brace-end conditions had significant effects on the responses. Since the manufacturing process of

tubes at that time caused the steel to be highly work-hardened, the brittle failure occurred in the heat-affected zones of the welds at the ends of the un-annealed specimens. It was suggested the annealing process should be done for the tubes subjected to severe cyclic loading. Developing analytical models that could simulate local buckling of tube walls and experiments on large size specimens were mentioned for future study.

A series of quasi-static cyclic loading tests on seventeen double-angle braces with unequal legs were conducted at University of Michigan [Astaneh-Asl 1982; Astaneh-Asl et al. 1985]. The slenderness ratios of specimens ranging from 81 to 189 and the b/t ratios of angles varied from 4 to 20. Nine out of seventeen double-angle braces were designed to buckle out-of-plane, while the remaining eight were designed to buckle in plane. Modified design procedures for double-angle braces under cyclic loading were proposed to improve the ductility performance. An improved design procedure for stitches in the out-of-plane buckled double-angle braces was presented to increase the ductility. One major conclusion suggested that a minimum free length equaled to twice the gusset plate thickness will improve the ductility of gusset plate under cyclic loading. It was noted that the longer free length may cause a stability problem in the gusset plate. Two plastic hinges instead of one may form in the same gusset plate, potentially reducing the ductility significantly. Several examples of this type of damage to steel buildings after earthquakes can be found [AIJ 1995; Okazaki et al. 2013] and also observed in the laboratory after pseudo-dynamic tests [Tsai et al. 2008] of a full-scale buckling-restrained braced frame.

Because local buckling of bracing member typically has a significant effect on the hysteresis behavior, experimental tests on concrete filled-in-tube braces were performed [Goel and Liu 1987; Liu and Goel 1988]. It was found that the filled concrete can successfully delay the crack initiation from local buckling of braces and improve the cyclic behavior. However, the filled concrete did not effectively delay initiation of local buckling in the brace members. In addition, the strength of concrete did not have any significant effect on the brace behavior. The improvement from concrete fill was not significant except for smaller b/t ratio braces [Lee and Goel 1987].

It is interesting to note that the number of experimental studies in the United States on bracing members during the 1990s was relatively low, with most of research works focused on the analytical modeling of braces or braced frame behaviors. Meanwhile, the 1994 Northridge earthquake and 1995 Kobe earthquake brought out several issues for urgent study. Compared to other systems, braced frames performed about as expected.

However, researchers in at University of Toronto, Canada, performed five cyclic tests on square hollow structural section (HSS $4 \times 4 \times 1/4$) braces with slenderness ratio 83 and b/t ratio 13.9 [Pons 1997]. The objective was to investigate on the brace-to-gusset plate connection details that were feasible for use in braced frames under severe cyclic loading. Several design comments were provided based on the experimental findings.

Another group of Canadian researchers conducted a series of experiments on nine square HSS braces [Shaback 2001; Shaback and Brown 2003] with different effective slenderness ratios (from 52 to 66) and width-to-thickness ratios (from 8.93 to 15.1). The selection of specimens

was based on the Canadian code provisions. Similar to previous works done by many researchers, the effective slenderness ratio (kL/r) was found to be the most important parameter that affected the behavior of brace. A statistically better equation to predict the fatigue life of braces was proposed based on their experimental results, accompanied by the suggestion that a more reliable fracture prediction model was required.

As the testing set ups have improved, so has the size of the specimens. Eleven square HSS braces with slenderness ratios varied from 69 to 90 and b/t ratios ranging from 8.1 to 28.3 were tested cyclically in a 45° single diagonal layout [Han et al. 2007]. The net reduced section failure mode was found in the smallest b/t ratio specimen at the earlier loading stage without any local buckling observed in the section walls. This failure mode was noted in earlier laboratory tests [Yang and Mahin 2005]. Another interesting finding was that the energy dissipation capacity of braces increased with decreased b/t ratio, and a b/t ratio of 14 seemed to achieve the maximum energy dissipation capacity based on test results.

More recent experimental work on the brace components was done by researchers at University of California, Davis [Fell 2008; Fell and Kanvinde 2010]. A total of nineteen braces at two-third scale were tested statically and dynamically. The specimen sections included square HSS, standard pipe, and wide flange sections. Slenderness ratios of specimens varied from 63 to 153, two b/t ratios were selected (14.2 and 8.5) for square HSS specimens, two D/t ratios were used for the pipes, and b/t ratio equaled to 7.5 for wide flange braces. Two square HSS specimens were filled with grout and subjected to two different loading protocols (standard and near-fault compression dominated). One of major findings was that the fracture ductility of a brace is more related to the section compactness and less related to the brace slenderness or loading histories. Another finding was that the width-to-thickness ratio limitations of bracing members in the 2005 AISC seismic provisions needed to be reduced to insure adequate member deformation capacity. Similar to past studies, the loading rate and the effect of mortar fill did not have significant effects on the brace cyclic behavior.

Canadian researchers recently conducted thirty-four large-scale brace specimen tests (between 17 ft to 26 ft in length of working points) with a variety range of b/t ratios, two different kL/r ratios (40 and 60), and three different sectional shapes (nineteen square HSS, nine round HSS and six wide flange sections) that are commonly used in the field [Tremblay et al. 2008a]. All specimens were reinforced at the net section connection regions. Both out-of-plane and in-plane buckling braces were tested quasi-statically. It was found that the square HSS and round HSS with similar slenderness ratios and approaching to code-limited b/t (and D/t) ratios had comparable cyclic behaviors until fracturing. The slenderness ratio seemed to affect the fracture performance of square HSS compared to round HSS braces. Also, the wide flange braces had better cyclic deformation capacities based on test observations.

2.1.4 Analytical Modeling of Bracing Component

There are many existing numerical models that simulate the behavior of brace components. Early models modified elastic truss elements to very simple representations of brace buckling, e.g., tension-only behavior, nonlinear elastic buckling, and ideal bilinear hysteretic behavior. Because

these models did not represent observed brace cyclic behavior very well, more advanced modeling techniques were developed. Basically, these models can be categorized into three types: physical theory models, phenomenological models, and finite element models. The following paragraphs briefly review the relevant work, especially the computer simulations based models; more detailed literature reviews can be found elsewhere [Zayas et al. 1981; Uriz and Mahin 2008].

2.1.4.1 Physical Theory Models

These models were very simple: only cross section properties and effective length of braces needed to be defined. Several early brace models of this type include the Point Hinge Model [Singh 1977; Jain et al. 1978a], Elasto-Plastic Hinge Model [Wakabayashi et al. 1972], Higginbotham Model [Higginbotham 1973], Refined Model [Ikeda and Mahin 1984; Ikeda and Mahin 1986], and Inelastic Beam-Column Element Model [Uriz et al. 2008]. Some of these models were implemented into DRAIN-2D [Powell 1973; Kannan and Powell 1973] and OpenSees [McKenna 1997] to simulate the cyclic buckling behavior of braces [Jain and Goel 1978b; Ikeda and Mahin 1984; Uriz et al. 2008]. These preliminary models were only accurate in cases with braces with higher slenderness ratios and could not simulate the strength deterioration. Refined models were developed but still did not account for Bauschinger effects, progressive cyclic degradation of strength, and local buckling of braces. Although more recent developed models—such as Inelastic Beam-Column Model—can simulate the Bauschinger effect including strength cyclic degradation within acceptable accuracy, they still cannot account for the effect of local buckling.

2.1.4.2 Phenomenological Models

The most common type of model, at least nine different models were proposed and developed in the past [Higginbotham 1973; Nilforoushan 1973; Singh 1977; Roeder and Popov 1977; Jain and Goel 1978b; Marshall 1978; Maison and Popov 1980; Gugerli and Goel 1982; Ikeda et al. 1984]. Here, the shape of brace hysteresis loop segments based on the mathematical equations or empirical results were pre-defined. Although such models are computationally efficient, the rules can become very complicated and calibration against experimental results is required [Ikeda et al. 1984; Zayas et al. 1981; Uriz et al. 2008].

2.1.4.3 Finite Element Models

The most general among the three categories, in this model the entire brace is subdivided into numerous finite elements to define the three-dimensional (3D) geometry of the brace. The finite elements can be shell or solid elements. The material properties are defined for each element. The program and elements need to be able to represent the inelastic behavior of the steel and the large displacements associated with yielding, local buckling, and lateral (global) buckling. However, this type of models is often computationally expensive and may not be suitable for

simulating the response of large structures. Past studies typically applied the 3D finite element models to component level models [Huang and Mahin, 2007, 2010; Ding et al. 2008; Fell 2008], sub-assembly structure [Field 2003; Mahin et al. 2004; Yoo et al. 2008, 2009; Huang and Mahin 2010], and infrequently to simulate a complete structure.

2.2 GUSSET PLATE CONNECTION

Connections are always critical components in any structural system. In concentrically braced frames, gusset-plate behavior plays an important role. Several papers and reports describe and summarize previous gusset plate research in detail (e.g., Birkemoe [1966]; Rabinovitch [1993]; Astaneh-Asl [1998]; Chambers and Ernst [2005]; and Dowswell [2006]). This section highlights a few of the findings.

2.2.1 The 30° Design Concept

Currently, gusset plates are designed based on a rule of thumb called the Whitmore section [Whitmore 1952]. As can be seen in Figure 2.3, the Whitmore effective section is determined by extending two lines at about 30° with respect to the longitudinal axis of the brace and beginning at the first row of bolts or gusset-to-brace weld at the tip of the gusset plate. The intersection of these two lines with a line perpendicular to the brace through the last row of bolts (or end of the welds) defines the width of Whitmore section. The original definition of Whitmore effective width was initially applied to bolted connections and extended to welded connections by Astaneh-Asl [1982].

In Whitmore's experimental study, a prototype bottom chord connection of a Warren truss model was tested to examine the stress distribution in the gusset plates. Strain gauges were used to measure the local strain distributions in the gusset plate. Tests were conducted under service load and did not continue to failure. The bending stresses in the gusset plate were not linearly distributed, and the neutral axis did not coincide with the centerline of the connecting members. Maximum bending stress did not occur at the extreme edges of the gusset but at an interior location. Shear-stress distributions did not follow the classic parabolic distribution. Whitmore concluded that standard beam theory could not be applied to gusset-plate design. The most rational method to determine the maximum normal stresses in the gusset plate was to use a spread out angle of 30° to define an effective section for estimating the maximum stress.

However, the concept of the 30° spread to determine an effective critical area was suggested about thirty years earlier. As noted by Dowswell [2006], stress analysis of iron truss gusset plates by Theophil Wyss [1923] in his doctoral dissertation at Swiss Federal Institute of Technology, Zurich incorporated a similar idea. In the preliminary tension tests of two gusset plates, as shown in Figure 2.4, Wyss tried to determine the stress distributions in the gusset plate specimens and investigated ideal shapes of gusset plates. Almost uniformly distributed stresses were found in the section cuts perpendicular to the loading direction for both 20° and 12° tapered specimens (gusset plate A and B in Figure 2.4). Stress concentrations at the edges of the rivet holes—about 2.2 times the averaged stress—were also found in the tension tests. He concluded

that the shape of gusset plate whereby the edges converge symmetrically to the direction of force is an optimum configuration for the gusset plate. It also provides smooth and gradual force transition in the connection region.

In the main experimental study performed by Wyss, a 6-m-span, 1.5-m-high, statically determinate Pratt truss (Figure 2.5) was tested under simple loading and unloading at the node of top chord. In the study, he noted that the rigid core (rigid zone) in a gusset plate (see Figure 2.6) affects the bending stiffness and moment capacity of the gusset plate. He also pointed out that the connection size also affects the deformations in the gusset plate. Elastic behavior of the gusset plate was studied based on the beam theory at the time and secondary stress effects were included.

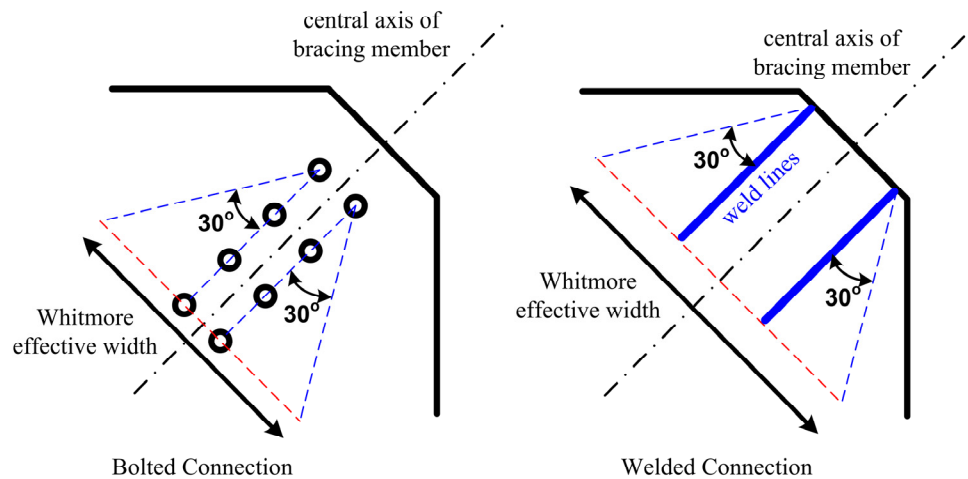


Figure 2.3 Illustration of Whitmore effective width for bolted [Whitmore 1952] and welded connections [Astaneh-Asl 1982].

↑ 20.0 t.



Figure 2.4

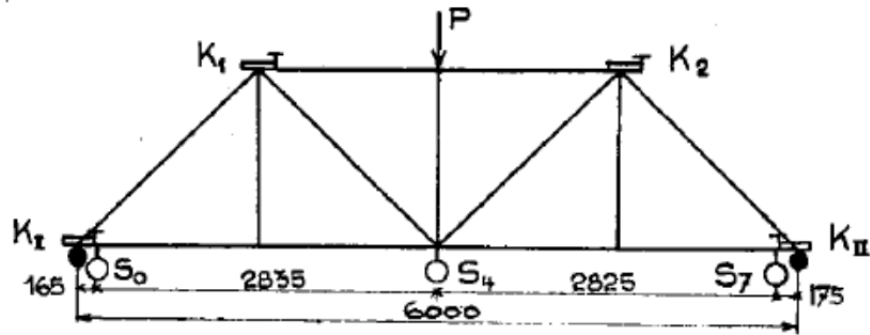
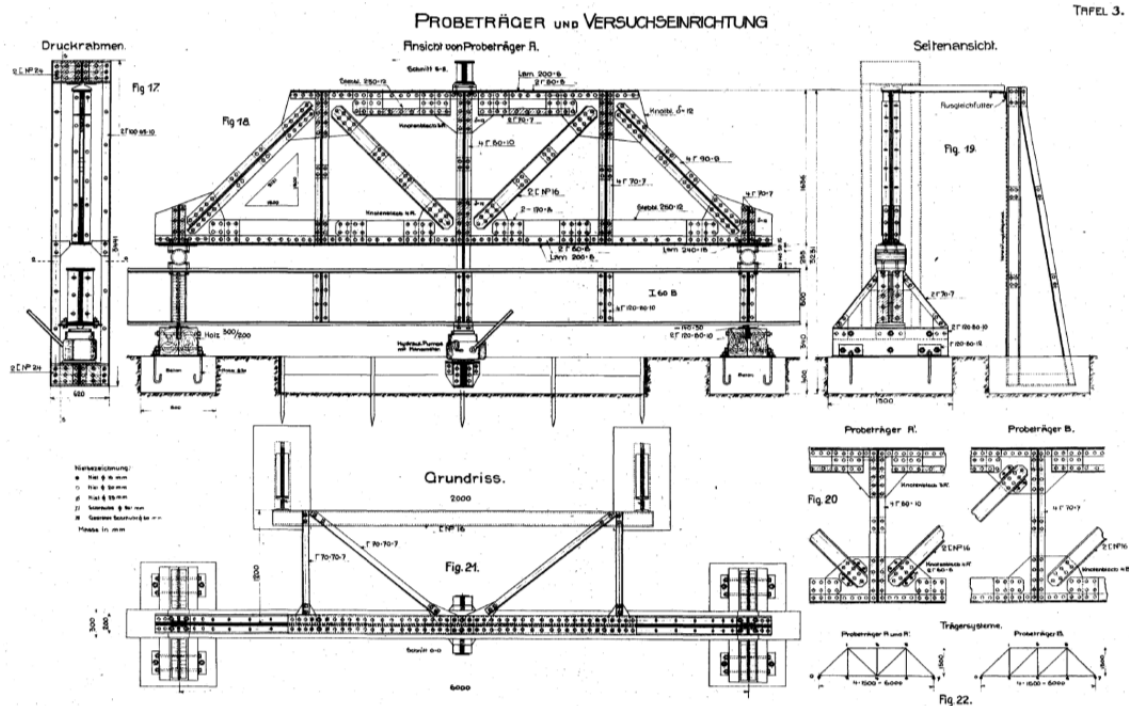


Abb. 17.

(a) Instrumentation points and loading point



(b) Shop drawings of test specimen and test frame

Figure 2.5 The Warren truss specimen tested by Wyss in 1923 (extracted from Figures 17 and 22 of Wyss [1923]).

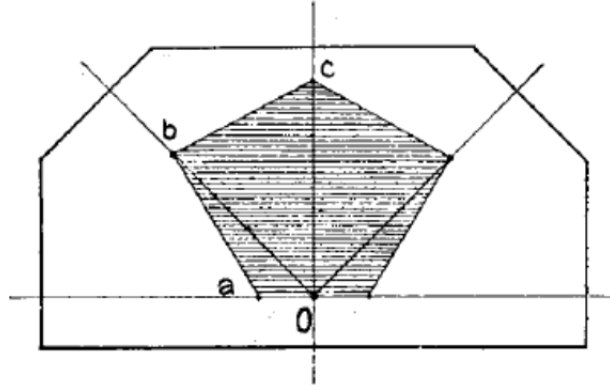


Abb. 22. Knotenblech mit starrem Kern.

Figure 2.6 Illustration of rigid core in a gusset plate (extracted from Figure 22 of Wyss [1923]).

Based on the preliminary experimental results, Wyss drew the gusset plate stress trajectories under tension and shear forces as illustrated in Figure 2.7. Normal stress, shear stress, and bending stress distributions along a section cut were also shown in Figure 2.7. The relationship between stress along the course of stress trajectory σ_o and the normal stress σ_α at the section cut was derived thus:

$$\sigma_o = \frac{\sigma_\alpha}{\cos^2 \alpha} = \frac{P}{F_{net}} \frac{1}{\cos^2 \alpha} \quad (2.22)$$

where α is the angle between stress trajectory and the direction of applied force P , and F_{net} is the cross-section area along the section cut that perpendicular to the symmetric axis. He proposed a method to determine the width of the gusset plate given that allowable stress in the gusset plate is known as $\sigma_{allowable}$.

$$b' = \frac{P}{d \sigma_{allowable} \cos^2 \gamma} ; \gamma < 30^\circ \quad (2.23)$$

where γ is gusset plate tapered angle, b' is gusset plate width, d is thickness of gusset plate and P is the applied force. The $\gamma = 30^\circ$ is assumed to be the critical tapered angle and $\sigma_o = 1.33 \sigma_\alpha$ when this angle applied. Secondary stresses based on beam formulas were also derived and combined with primary stresses to determine the critical stresses in the gusset plate.

$$\sigma_o = \left(\frac{P}{F_{net}} \pm \frac{M}{W} \right) \frac{1}{\cos^2 \gamma} = \sigma_{max} ; \gamma < 30^\circ \quad (2.24)$$

where γ is gusset plate tapered angle, P is the applied force, F_{net} is the cross section area along the section cut that perpendicular to the symmetric axis, M is the bending moment applied to the

gusset plate, and W is the elastic section modulus. For asymmetric gusset plates, he noted that the formulas can also apply to the situation only the 30° critical angle is introduced as shown in Figure 2.8. This also came from his observations during the main experiments. The method Wyss proposed in 1923 is similar to the concept of Whitmore's section as done in current practice, except the 30° extension lines did not start at the first row of rivet holes, but at the edge of the channel sections, as illustrated in Figure 2.8.

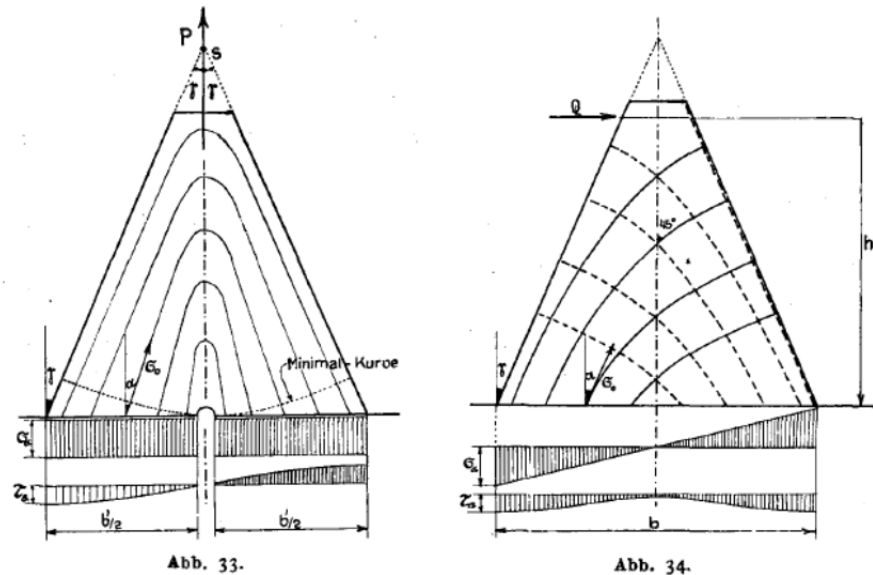


Figure 2.7 The stress trajectories of preliminary test specimens (extracted from Figures 33 and 34 of Wyss [1923]).

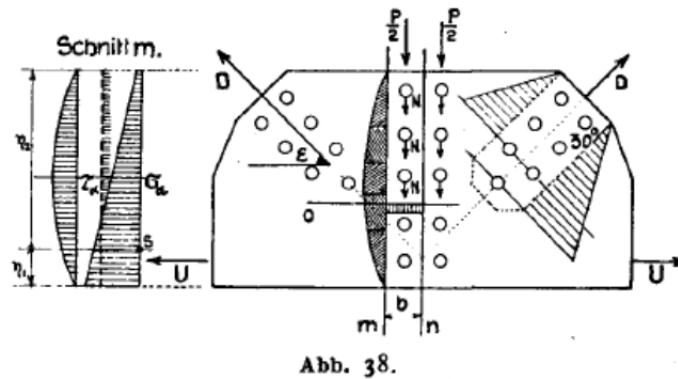


Figure 2.8 Illustration of stress distribution in a gusset plate (extracted from Figure 38 of Wyss [1923]).

2.2.2 Stability Issue

For the gusset plate stability under compression, Thornton [1984] proposed a simple method to calculate the elastic buckling capacity of gusset plate using equivalent unit strips within the Whitmore effective section. The definition of the characteristic length of the strips is illustrated in Figure 2.9, and the critical length to determine the buckling capacity is selected from the

maximum among these characteristic lengths: L_t , L_c , and L_b . Typical column buckling formula were used with effective length factor $k = 0.65$ to determine the buckling stress of the critical strip within the effective width. Several modified or generalized methods have also been proposed and investigated in later studies [Yam 1994; Yam and Cheng 2002; Lehman et al. 2004; Yoo 2006; Dowsell 2006].

A free-edge buckling equation was proposed [Brown 1988] as a design check equation to ensure the gusset plates yield before edge buckling. The general form of the edge buckling equation

$$\frac{a}{t} \leq \sqrt{\frac{\pi^2 E}{12 (1 - \nu^2) F_y k^2}} = 0.79 \sqrt{\frac{E}{F_y}} \quad (2.25)$$

where a is the gusset plate free edge length, t is the thickness of gusset plate, k is the effective length factor, and ν is Poisson's ratio of steel. The 24 gusset plate monotonic compression tests conducted by Brown indicated that $k = 1.2$ was the most appropriate value. Later, Astaneh-Asl [1989] proposed an equation for checking cyclic free-edge buckling based on experimental results; the length-thickness limit was reduced about 5% for cyclic loading.

$$\left(\frac{a}{t}\right)_{cyclic} \leq 0.75 \sqrt{\frac{E}{F_y}} \quad (2.26)$$

Other methods were also proposed and investigated [Walbridge et al. 1998; Nast 1999].

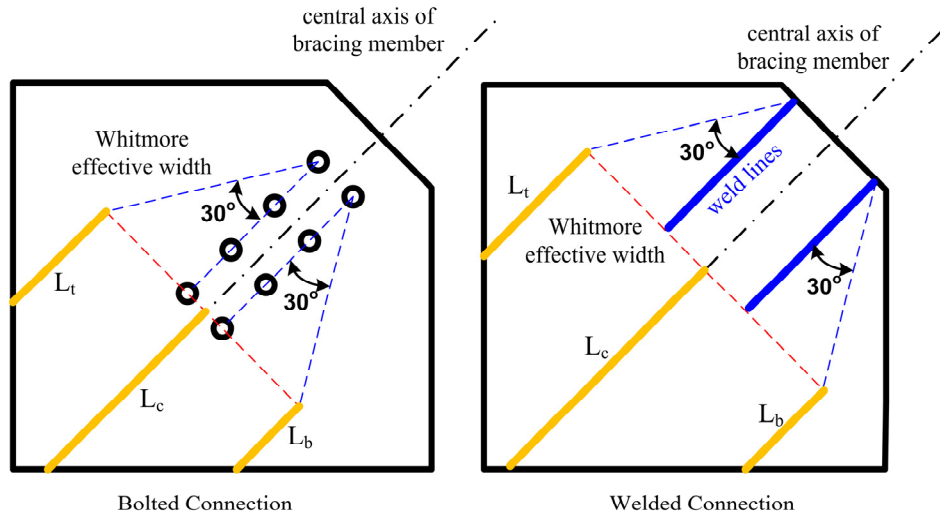


Figure 2.9 Illustration of characteristic length of equivalent unit strips within the Whitmore effective width for bolted and welded connections.

2.2.3 Connection Shape and Seismic Detail

The shape and dimension of gusset plates are usually determined by the force demands in the gusset plate-to-beam and gusset plate-to-column connection interfaces. Several methods are available to estimate the force demands in the connection interfaces, such as the KISS method (keep it simple and stupid) [Thornton 1992], the parallel force method (developed by David Ricker) [Thornton 1991], the truss analogy method [Astaneh-Asl 1989], and the uniform force method [Thornton 1991], etc. Current AISC includes the uniform force method in the Manual of Steel Construction [AISC 2005a] as the preferred method. However, the constraints on this method sometimes result in awkward looking and excessively large gusset plates. Recently, a modified uniform force method was proposed [Muir 2008] that provides a way to design gusset plates more economically and also retain the basic concept underlying the uniform force method. Geometric formulas for the gusset-plate design were also developed recently [Chambers and Bartley 2007].

Detailing of gusset plates in special concentrically braced frames allowing out-of-plane buckling of braces typically follows a straight yield line pattern with $2t_g$ in width [Astaneh-Asl 1982; Astaneh-Asl et al. 1986], where t_g is the thickness of gusset plate as shown in Figure 2.10. The clearance at both ends of brace allows the plastic hinges formed in the gusset plates without any restraints and reduces deformation concentrations in the gusset plate through spreading out the inelastic regions. Other yield patterns, such as elliptical yield line pattern, were also proposed [Roeder and Lehman 2007; Roeder et al. 2011a] as an alternative design scheme (Figure 2.10).

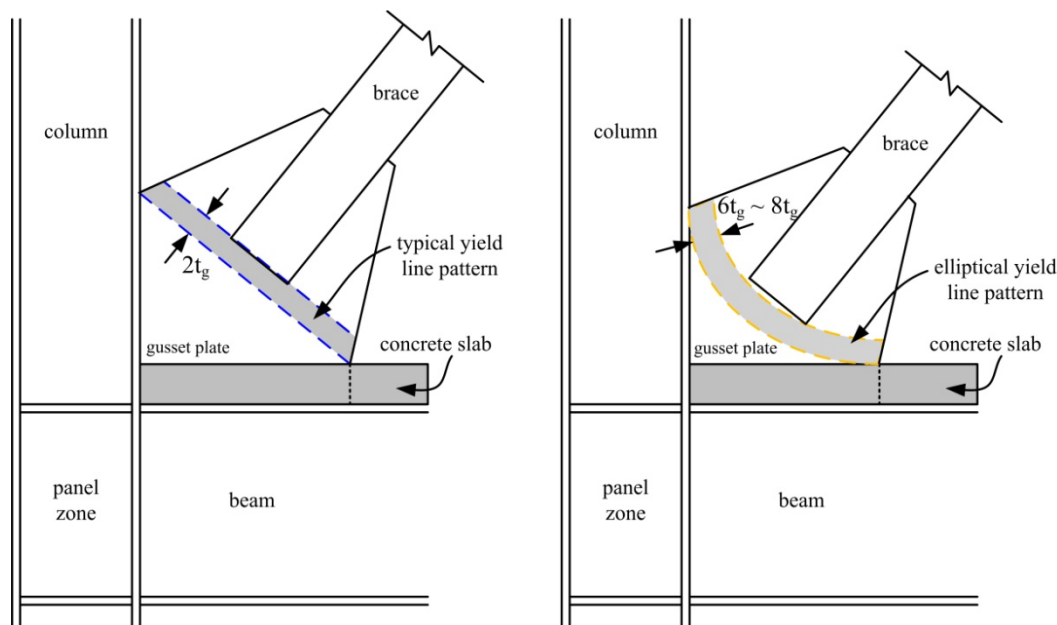


Figure 2.10 Illustration of typical and elliptical yield line patterns to accommodate brace out-of-plane buckling (where t_g is thickness of gusset plate).

2.3 BRACED FRAME SYSTEM

2.3.1 Experimental Work on Braced Frame Systems

Early braced frame tests were conducted at Takenaka Technical Research Laboratory in Japan [Fujimoto et al. 1972; Tanabashi et al. 1973]. The braced frame specimens were one-bay, two-story reduced-scale (about 1/2-scale) braced frame models. Those specimens were tested cyclically in a two-million-pound universal test machine. Both concentrically and eccentrically braced frames were studied in this project to compare the system's cyclic performance. Although the maximum story drift ratio imposed in the concentric braced frame specimen was only about 0.6% and the peak story shear was less than 150 kips, it provided valuable information about braced frame behaviors under cyclic loading.

Later on, four one-story one-bay, X-braced frame tests under monotonic and cyclic loadings were conducted at Kyoto University [Wakabayashi et al. 1974]. Pinched hysteresis loops were found in two cyclic loading tests. The base shear versus lateral displacement relationships were also found to be relatively unaffected by the gravity forces applied in the experiments.

One of the earliest shake table tests on steel braced frames were performed at UCB [Ghanaat 1980]. An existing three-story moment-resisting frame model was used as a base structure, and three different types of bracing members were used (rods, pipes, and double-angles) in a single-story X-configuration. The 0.6-scale model braced frame was then subjected to a series of ground shakings to investigate on the dynamic behavior of braced frames. Test results showed that the model structures with pipe braces and double-angle braces performed better than the structure with rod braces. Recommendations on the slenderness ratio limitations for braced frame systems were also made.

About the same time, two carefully prepared 1/6-scale X-braced frame specimens were tested at UCB as part of a research program on offshore platforms [Zayas et al. 1980b]. All members were made from round tubular sections. Cyclic prescribed displacements were imposed at the tip of an X-braced frame to simulate earthquake effects. Results found that using compact sections as bracing members actually did not prevent the occurrence of local buckling under larger cyclic displacements. However, using members with lower D/t ratio helped delay local buckling and improved cyclic response of entire structure, suggesting that performing pseudo-dynamic tests on the X-braced frames would be desirable. Subsequently, these hybrid tests were performed [Mahin and Shing 1985].

To examine the dynamic effect on the tubular braced frames used in offshore platforms and the failure mechanism, a two-dimensional 5/48-scale model was built and tested on the shake table at UCB [Ghanaat and Clough 1982]. The frame model results demonstrated that a moderate amount of energy dissipation was achieved under severe ground shakings. One major observation was that the damage of tubular braces was concentrated at the upper panel region, which was not observed in the cyclic testing conducted previously [Zayas et al. 1980b]. Significant table-specimen interaction from pitching motion of the shaking table was reported.

Beginning in the early 1980s, the U.S.-Japan cooperative earthquake research program initiated a series of studies to improve seismic safety. One of the core research topics was the testing of a six-story full-scale steel structure. The entire test program consisted of four testing phases. The first phase tested a concentrically steel braced frame [Foutch et al. 1986, 1987; Roeder 1989; Yamanouchi et al. 1989]. This was the first time that a six-story full-scale braced frame was tested using the pseudo-dynamic testing technique. For these experiments, each floor level was attached by at least one servo-controlled actuator to apply the required story displacements. Test results not only demonstrated the importance of the energy-dissipation mechanism and redundancy within the structure, it also showed how important were design details and ductility. Square HSS braces with b/t ratios varied from 9.9 to 22.8 and kL/r ratios ranging from 51.2 to 78.6 (assuming $k = 0.7$) were installed in the Chevron brace configuration specimen. The brace connection details—different than current practices—were directly welded as fixed connections to the beams. Both in-plane and out-of-plane buckling of square HSS braces were observed in the tests. Maximum story drift of 1.9% occurred in the second story of the building, and the maximum base shear was about 720 kips. It was noticed that the HSS braces with higher b/t ratio (22.8) in the second and third story either completely fractured or partially tore during the final test.

Under the same research program, a reduced-scale six-story Chevron braced frame specimen was tested on the shake table at UCB and subjected to twenty earthquake ground motions [Uang and Bertero 1986; Bertero et al. 1989]. It represented a 0.3-scale model of the full-scale building tested in Japan. Slightly different b/t ratios of HSS braces were used in the model but similar observations were found. The stories with higher b/t ratio braces had larger column shear demand, and the braces ruptured at either the lower end or at mid-length of the brace, suggesting that limitations on both slenderness ratio and b/t ratio should be included in seismic design provisions.

Before testing on the full-scale six-story braced frame specimen mentioned above, six three-story 0.5-scale concentrically braced frame tests were conducted to understand the possible behavior of the lower story of a full-scale building [Fukuta et al. 1989]. Gravity forces were applied on the top of each column line and lateral force applied at the roof level only. Both in-plane and out-of-plane buckling behavior of braces were studied. A Chevron brace configuration with braces of slenderness (L/r) between 70 and 120 was selected. It was concluded that the specimens had stable hysteresis loops and were comparable to moment resisting frames, and that the hysteresis model proposed predicted the system behavior quite well.

Recently, a two-story one-bay Chevron configuration special concentrically braced frame test was performed at UCB [Uriz and Mahin 2008]. Relatively larger beam, column and brace member sizes were used in the braced frame specimen. No gravity forces were applied in the columns and only one actuator installed to apply lateral force at roof level. Both stories used HSS $6 \times 6 \times 3/8$ braces, and reinforcing plates were welded at both sides of net section connection regions. Beam to column connections were designed as pin connections. From the cyclic loading test results, it was clear that the individual brace behaved as expected from the component tests [Yang and Mahin 2005]. Formation of a soft story mechanism at the lower story was observed. Significant cracks were initiated between shear tab and column flange and

propagated through the column web, suggesting that further tests on different brace configurations (such as split-X and single-story diagonal) should be conducted to investigate the effect of brace configuration on the system behavior. Since the loading protocol affects the cyclic behavior of braces, frame tests with different loading protocols were recommended.

2.3.2 Frame Action in Braced Frame System

Frame action typically exists in a steel braced frame system. This framing action is an important factor in determining the behavior of braced frames following the deterioration and fracture of one or more braces.

Previous experiments have shown [Mahin et al. 2004] that the frame action in buckling restrained braced frames can induce distortional pinching forces in the gusset plate itself and can buckle the gusset plate when the brace is in tension. The pinching force can be reduced through using smaller and compact shaped gusset plates or by releasing the moment at the edge of gusset-to-beam interfaces [Thornton and Muir 2009]. Existing connection details often can help to achieve this goal. Figure 2.11 illustrates two examples that were designed to release the moment at the edge of gusset-to-beam interfaces.

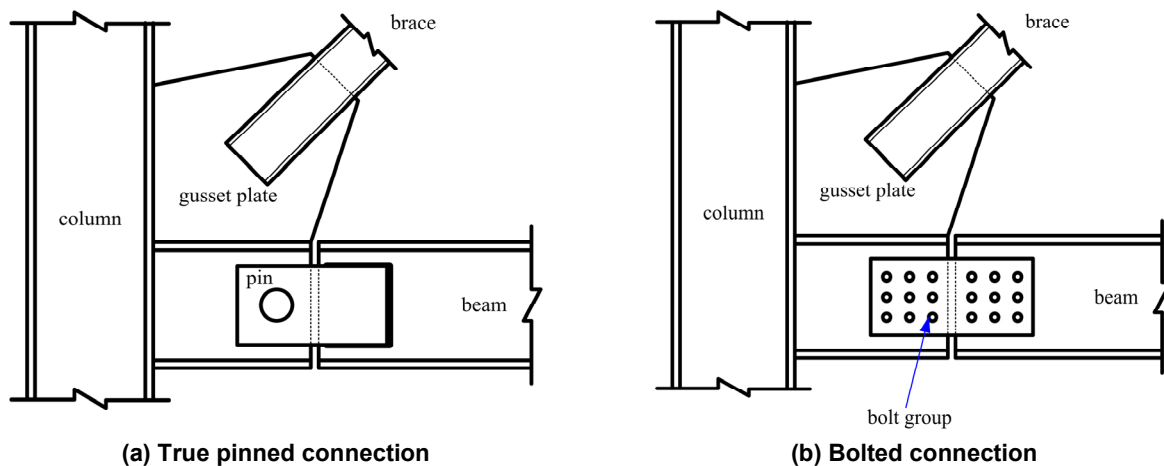


Figure 2.11 Connection details of beam end moment release.

2.4 STEEL BRACED FRAME BEHAVIOR DURING PAST EARTHQUAKES

Past earthquakes usually provide opportunities to judge the adequacy of the building codes or design guidelines. Damage observations provide valuable information and stimulus for engineers and researchers to develop better structures to resist earthquakes. Several major seismic events are briefly discussed in the following sections.

2.4.1 Past Earthquakes in the United States

Damage to a light steel braced frame was reported in the magnitude 6.6 San Fernando earthquake on February 9, 1971 [Steinbrugge et. al. 1971], where the out-of-plane buckling of steel flat-bars in the single story x-braced frame was observed. Figure 2.12 shows the braced bays after the earthquake. In another three-story chemical storage building, in-plane buckling of double-angle braces was observed after this earthquake (Figure 2.12 right).

Significant damage of a two-story steel braced frame in Palo Alto was reported after the magnitude 6.9 1989 Loma Prieta earthquake that struck the San Francisco Bay Area [SEAOC 1991] on October 17. The building was built in 1985. The downtime after the earthquake needed for repair was about five months. Three failure modes were identified within fourteen braced frames on the perimeter of the building: (1) twisting of W12 steel beams at brace-to-beam intersections where the beams were not properly supported; (2) buckling of bracing members; and (3) weld failures at brace connections. It was believed that the twisting of the interstitial beam contributed to the loss of brace compression capacity in some braced bays and consequently increased the force demands in the other braced bays, which resulted in the brace buckling and weld failures. Another report listed the damages of four nearly identical two-story braced frames in Silicon Valley [Phipps et al. 1992]. These buildings were constructed in 1973 and were used for administration and development purposes. Buckling of braces was reported after the earthquake, and the downtime of these four buildings was nine months. It was also noted that the slenderness of the buckled bracing members ranged from 110 to 160 in these cases.

Another major event occurred in Northridge, California, on January 17, 1994, where a magnitude 6.9 earthquake caused significant amount of damages to the steel structures. One of damaged steel concentrically braced frame was extensively examined and studied after the earthquake [Bonneville and Bartoletti 1996]. The building was a four-story stacked Chevron braced frame constructed in 1986 based on the 1980 Los Angeles Building Code (LABC). The foundation of this office building was sitting on medium dense to very dense soil, and the site was about 10.5 miles from the epicenter. The width-to-thickness ratios of square hollow structural section braces used in the braced frames varied from 27.1 to 31.4, and the slenderness ratio varied from about 54 to 66. No $2t$ straight yield line details were introduced into the original design of brace-to-gusset plate connections. Several brace failure pictures after earthquake are shown in Figure 2.13. Typical brace failure modes were local buckling of brace section walls, brace gross section fracture, and weld failures at brace-to-gusset plate connections. During the post-earthquake repairs, the square HSS braces were replaced by wide-flange braces, and the $2t$ straight yield line details were applied. The brace configuration changed to zipper system configuration [Khatib et. al. 1988], but the ground-story braces were designed to remain elastic.



(a) out-of-plane buckling of steel flat-bars (source: NISEE e-Library by K.V. Steinbrugge)



(b) in-plane buckling of double-angle braces (source: NISEE e-Library by K.V. Steinbrugge)

Figure 2.12 Brace failures observed in the 1971 San Fernando earthquake.



(a) local buckling of square HSS brace section wall (source: NISEE e-Library)



(b) weld failures at brace-to-gusset plate connection (source: EERI, 1998)

Figure 2.13 Brace failures observed in the 1994 Northridge earthquake.

2.4.2 Past Earthquakes in Japan

The 1978 Miyagiken-Oki earthquake ($M_s = 7.7$) was a major seismic event that severely damaged twenty-eight steel building structures in Sendai City [Tanaka et. al. 1980; Kato et. al. 1980] and a number of steel buildings were slightly damaged. Among those buildings, eight of them collapsed, and twenty had more than 3.33% residual drift angles. Structural failure modes such as brace connection failures, column base failures, interior wall failures, and exterior wall failures were observed [EERI 1978]. It was noted that most of severely damaged steel structures were limited to one or two-story braced frames. Post-earthquake investigations indicated that insufficient strength of brace connections, poor detailing of brace connection regions, and the over-estimation of post-elastic strength were critical factors. The EERI report pointed out that inadequate connection strength typically came from insufficient effective areas (i.e., net section areas), insufficient bolt shear strengths, poor workmanship, and poorly done welds. This insufficient connection strength caused the premature failure of braces and had significant effects on the nonlinear behavior of the braced frame systems and the ultimate capacity of the systems, suggesting the urgent research needed in designing of brace connections and nonlinear behavior of the braced frames.

The 1995 Hyogoken-Nanbu (Kobe) magnitude 6.8 earthquake resulted in a significant amount of damages to steel buildings. A post-earthquake reconnaissance team surveyed 988 damaged steel buildings around the effective earthquake area [AIJ 1995] and then categorized the survey results into four types based on the lateral force resistant system of the buildings:

- Moment frame in both directions (type R-R)
- Moment frame in one direction and braced frame in another direction (type R-B)
- Braced frame in both directions (type B-B)
- Other types not listed above

Among the surveyed steel buildings, about 17% (168 out of 988) were steel braced frames and more than 50% (89 out of 168) of those braced frames were classified as severely damaged or totally collapsed. The severely damaged buildings typically had residual drifts of more than 1%, and significant fractures were noticed in the main structural components that proved difficult to repair. All collapsed steel braced frame buildings used single-story X-bracing configuration. For the severely damaged steel braced frame buildings, only 4% used the Chevron brace configuration, and 96% of them used the single-story X-bracing configuration. Section shapes used for the brace components were also included in the survey. Many total collapsed or severely damaged buildings used light-gauge steel braces such as round-bars, flat-bars, or angles. Photographs of failure modes are shown in Figures 2.14, 2.15, and 2.16. Note that similar damages occurred in both 1978 Miyagiken-Oki earthquake and earthquakes in United States.

This was neither the first time nor the last time that brace connection failures occurred after the major earthquakes in Japan. In the 1922 Uruga Channel earthquake [Naito 1926], brace connection in a five-story knee-braced frame in Tokyo City failed due to the shear rupture of fasteners. Recently, in the 2011 Great Eastern Japan Earthquake, brace connection failures were

again observed in low-rise industrial buildings and a two-story parking structure in Sendai City. Several connection failure photos are shown in Figure 2.17.



(a) wide flange brace



(b) double-tee single-story X

Figure 2.14 Global buckling of braces during 1995 Hyogoken-Nanbu (Kobe) Earthquake (extracted from AIJ [1995]).



(a) connection failure in a single-story X braced frame using round HSS braces



(b) buckling of gusset plate

Figure 2.15 Connection failures in 1995 Hyogoken-Nanbu (Kobe) Earthquake (extracted from AIJ [1995]).



(a) bolt failures in a double channel brace-to-gusset plate connection



(b) bolt failures in a gusset plate-to-column connection

Figure 2.16 Bolt failures in 1995 Hyogoken-Nanbu (Kobe) Earthquake (extracted from AIJ [1995]).



(a) brace connection fractures in a two-story parking structure



(b) detail view of a brace connection fracture in a two-story parking structure



(c) gusset plate buckling in a two-story parking structure



(d) gusset plate net section failure in a low-rise industrial building

Figure 2.17 Brace connection failures observed in the 2011 Great Eastern Japan Earthquake (extracted from Midorikawa [2011]).

2.5 CONCLUDING REMARKS

Steel concentrically braced frame systems are considered to be efficient and economical lateral load resisting systems to control the lateral deformation in civil structures under wind loading or earthquake ground shaking. A review of structural damages to the braced frame systems after several major earthquakes—including recent earthquakes—has identified some anticipated and unanticipated damage. This damage has prompted many engineers and researchers around the world to consider new approaches to improve the behavior of braced frame systems. Extensive experimental studies over the last forty years of conventional buckling brace components and several braced frame specimens have been briefly reviewed above, highlighting that the number of studies on the full-scale concentric braced frames is still limited.

3 Experimental Program and Specimen Design

3.1 BACKGROUND

The NEES research project entitled, “International Hybrid Simulation of Tomorrow's Braced Frame Systems,” involved coordinated research at the University of Washington, Seattle (UW), the National Center for Research in Earthquake Engineering (NCREE), Taipei, Taiwan, the University of Minnesota, Minneapolis (UM), and UCB. Researchers at each locale provided valuable experimental data and analytical results. A schematic drawing of the different types of specimens tested as part of the overall research program is shown in Figure 3.1.

At the UW, more than thirty single-bay one-story conventional concentric braced frame specimens and five single-bay one-story buckling restrained braced frame specimens were tested under unidirectional quasi-static cyclic loading. Three single-bay two-story conventional concentric braced frame specimens with a double-story-X bracing configuration and three single-bay three-story concentric braced frame specimens with stacked double-story-X bracing configurations were similarly tested at NCREE [Powell et al. 2008; Roeder et al. 2011b]. To account for the 3D and floor slab effects in the braced frame system, two-story, one-bay \times one-bay, concentric braced frame specimens with conventional braces (in a single story-X braced configuration) and buckling restrained braces were tested under bi-directional cyclic loading in the MAST laboratory at UM [Palmer et al. 2011]. At UCB, four single-bay two-story conventional concentric braced frame specimens having a V and inverted-V bracing configuration in the first and second story, respectively (i.e., an overall diamond-shaped configuration), were tested under unidirectional loading. In three specimens, unidirectional loading was applied quasi-statically at each floor level, and in one of the specimens hybrid simulation techniques were used to determine the deformation histories applied at each floor level. The tests conducted at the NEES shared-use experimental laboratory at UCB (NEES@Berkeley) are the subject of this report.

In this chapter, the design and construction of the specimens and test set up are described in detail, as is the instrumentation used to monitor the response of the specimens during testing. This chapter also discusses the selection of the quasi-static loading protocol used for three of the specimens and the assumptions utilized to develop and carry out the hybrid test of one specimen.

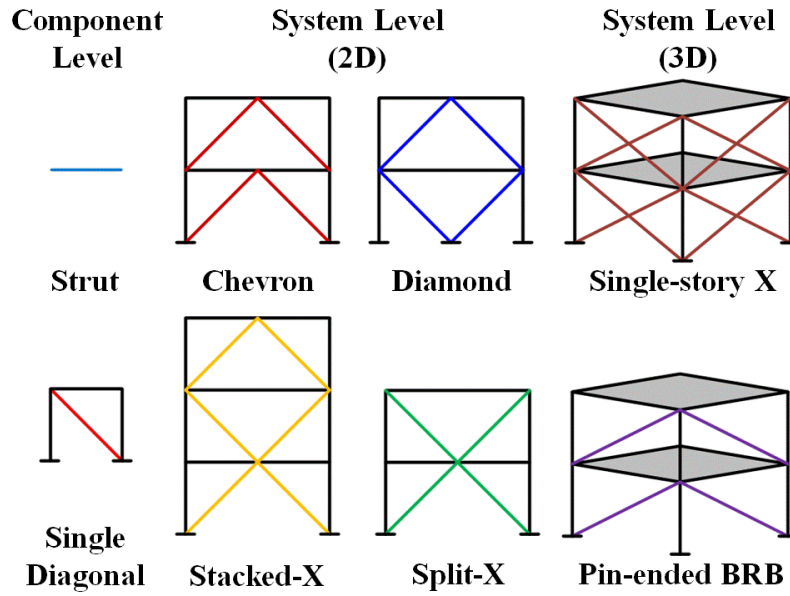


Figure 3.1 Different specimen types for each testing facility in the experimental phase of the NEES research project.

3.2 EXPERIMENTAL PROGRAM AT UNIVERSITY OF CALIFORNIA, BERKELEY

As part of the overall NEES small group research project, testing of two-story tall specimens considered the test matrix graphically represented in Figure 3.2. The two-story chevron brace configuration [Figure 3.2(a)] with square HSS braces was tested previously at UCB in 2004 [Uriz 2005]. An overview of the test set up for this test is shown in Figure 3.3. As noted previously, modern construction practices are moving away from the stacked Chevron configuration, towards the Split-X configuration. Thus, the double story split-X brace configuration with square HSS braces and wide flange braces in Figures 3.2(b) and 3.2(h), respectively, were tested at NCREE in 2007 and 2008 [Powell et al. 2008]. Figure 3.4 illustrates the test set up for three two-story tall specimens tested at NCREE. For these specimens, testing was stopped before significant damage occurred in the beams and columns, and these members were reused for all tests; only the braces (and gusset plates) were replaced to enable subsequent tests. In these NCREE experiments, loads were only imposed at the roof level so that shears in both stories were identical.

In keeping with the test matrix, tests at UCB examined specimens with a two-story diamond-shape bracing configuration, as illustrated schematically in Figure 3.2 (c, f, and i). In comparison with other specimens, these tests focus attention on the behavior of the floor levels where two braces intersect at a column line. To better represent the actual force distribution in the structure when different sized braces occur in adjacent stories, servo-controlled actuators were installed for these tests at both floor levels.

Figures 3.5, 3.6, and 3.7 show some typical steel concentric braced frame buildings located in California that use the common brace configurations shown in the testing matrix.

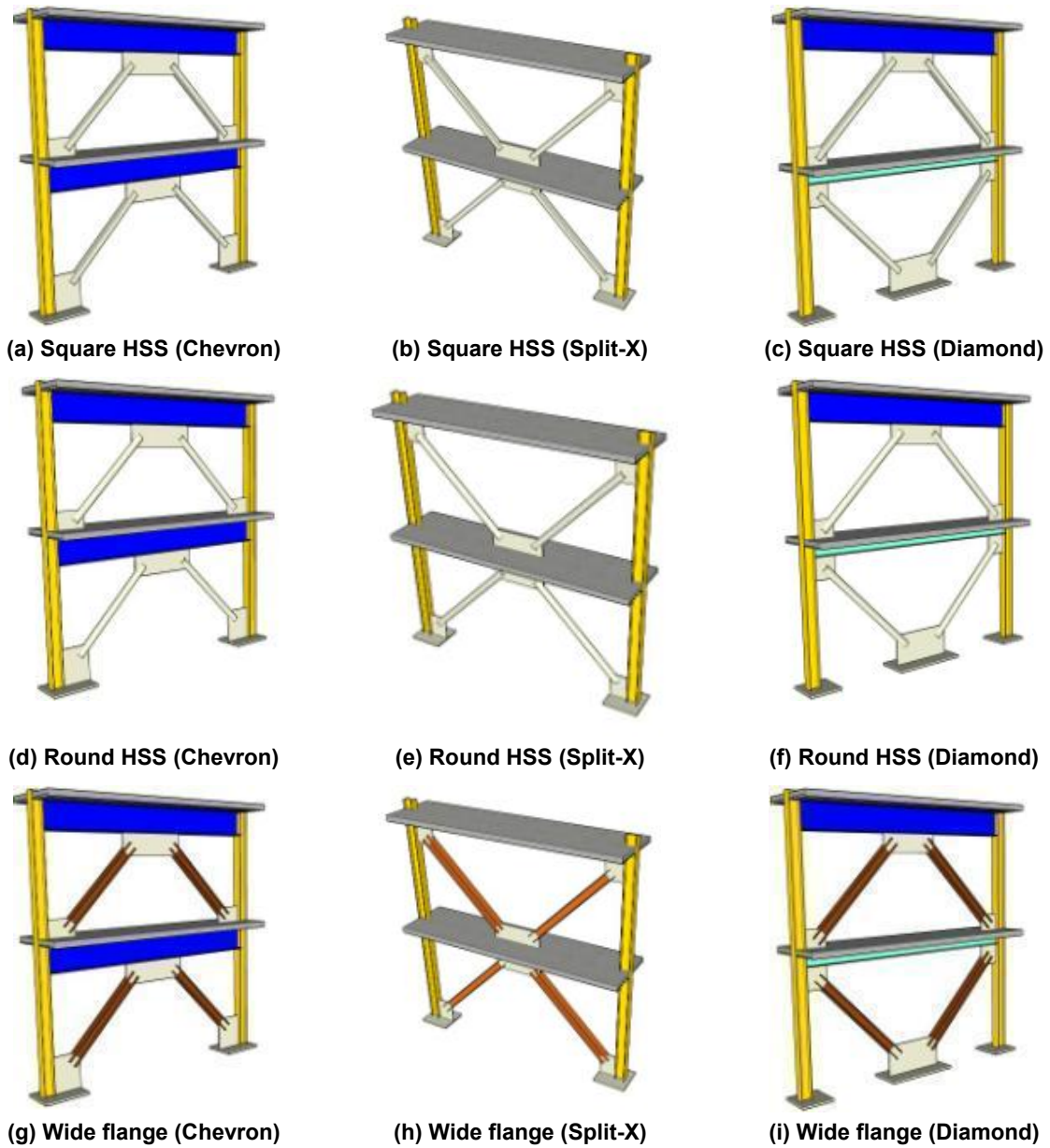


Figure 3.2 Test matrix of the 2D braced frame specimens in the research project.



Figure 3.3 Overview of Specimen TCBF-1 before test [Uriz 2005)].



**(a) Square HSS
(TCBF1-HSS)**



**(b) Wide flange
(TCBF1-WF)**



**(c) Square HSS
(TCBF1-HSS-2t)**

Figure 3.4 Overview of Specimen TCBF-1 during the test (source: <http://exp.ncree.org/cbf/>).



(a) (photo courtesy of Professor Stephen A. Mahin)



(b)

Figure 3.5 Application of stacked chevron braced frame in a building structure.



(a) Ferry Landing, Oakland, California



(b) Skyline College, South San Francisco, California

Figure 3.6 Application of two-story split-X braced frame in a building structure.



(a) West Elm, Emeryville, California



(b) A two-story auditorium at Vista Grande Elementary School, Danville, California (photo courtesy of Professor Stephen A. Mahin)

Figure 3.7 Application of two-story diamond-shape braced frame in a building structure.

3.3 SELECTION AND DESIGN OF TEST SET UP

At the beginning of the specimen design process, several testing configurations were carefully considered and evaluated. Some of the design criteria, constraints, desirable conditions, prescribed loading capacities, and deformation capabilities considered are listed below:

1. The testing condition should be as close to the actual field conditions as possible.
2. The test set up should permit as large (in terms of base shear capacity and size) of framed specimen as possible.
 - a. As to the dimension range of framed specimen, a beam span between 20 ft and 30 ft in length and a story height between 9 ft and 12 ft were considered.
 - b. Previous tests had considered braced frames with capacities of approximately 1000 kips.
4. Based on previous dynamic analyses for maximum considered events in near-fault regions of California [Uriz and Mahin 2004], a minimum target roof drift of about 5% maximum target was selected.
5. Use of as small of lab footprint as possible to enable the reaction wall in the NEES@Berkeley lab to be shared with other research projects.
6. Limit loads on specimen to the capacity of the reaction wall and strong floor in the NEES@Berkeley lab.
 - a. Limit the maximum overturning moment and total web shear force that will develop in the two-cell box girder strong floor to less than 20,000 kip-ft and 1500 kip, respectively [Aktan and Bertero 1981].
 - b. The maximum concentrated uplift force per anchorage hole in the strong floor should be 100 kips or less [Skidmore et al. 1963, 1964].
5. The weight of each member or component of the test set up should be less than the capacity of the overhead crane (24 kip) in the laboratory.
6. Use existing actuators, instrumentation, other equipment, and material to the extent possible.
7. Design specimen and set up considering simplicity, economy and ease of fabrication, erection and repair.
8. Design test set up considering:
 - a. Strength and stability in the in-plane and out-of-plane directions, including effects of possible specimen over-strength.
 - b. Reliability and accuracy of instrumentation and visual/photographic observation during tests.

Three-dimensional sketches illustrating the evolution of the test set up during the design process are shown in Figure 3.8. The final set up used is described in the next section.

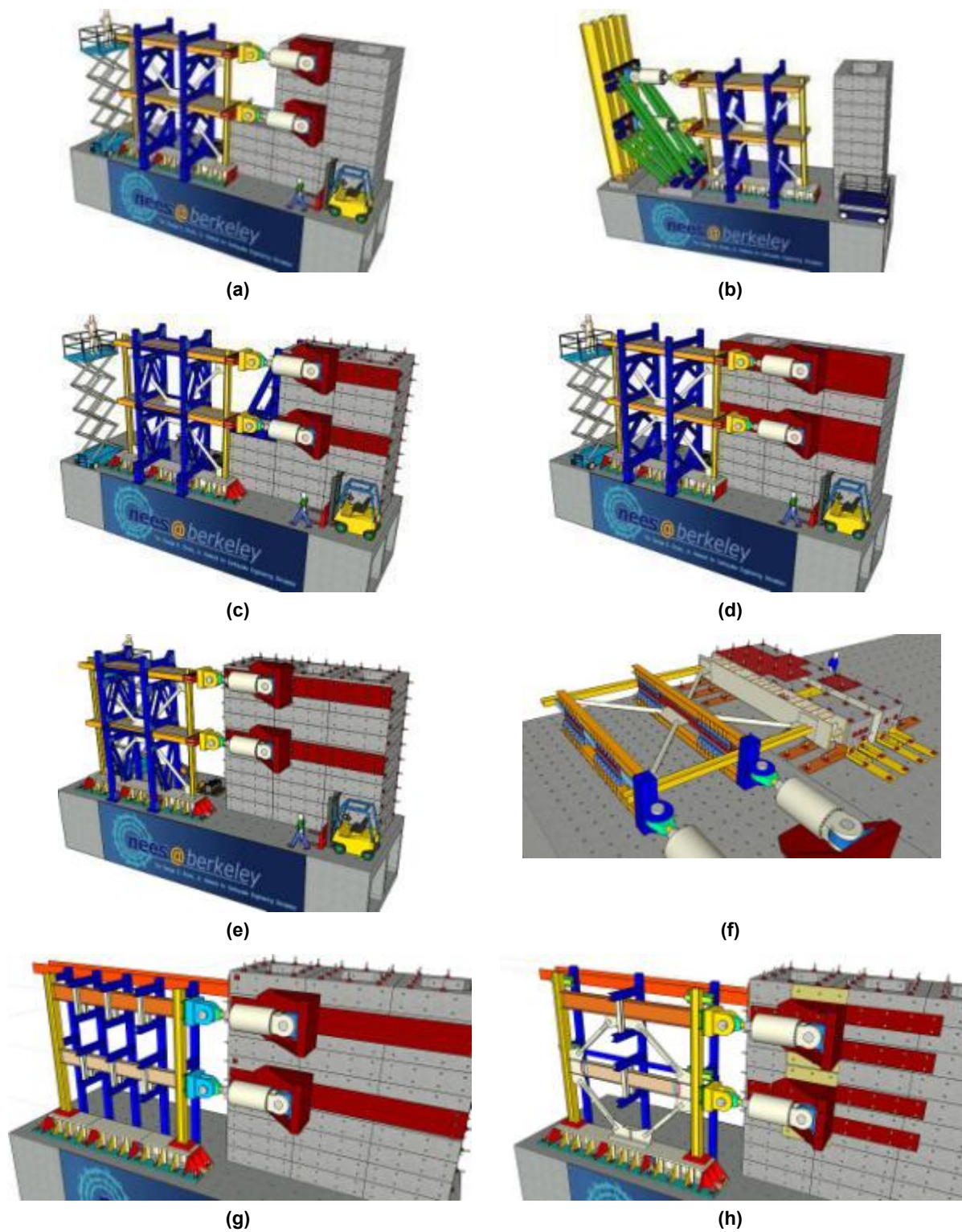


Figure 3.8 Possible testing configurations at the University of California, Berkeley, during the specimen design phase.

3.4 TEST SET UP AT NEES@BERKELEY FACILITY

The overview of the final configuration of the test set up is shown in Figure 3.9. For the specimen to fit in the laboratory, and satisfy the other criteria outlined in Section 3.3, the specimen was designed to have a 20-ft spacing between columns and a distance of 9 ft between the mid-depth of beams. This geometry limited the base shear that could be imposed on the specimen to 900 kips, with 600 kips being applied at the top level and 300 kips at the lower level (i.e., considering an inverted triangular force distribution).

To develop the lateral reactions that could be imposed on the specimens during tests, a total of 30 reconfigurable reaction blocks (ten blocks per stack and each block weighs about 20 kips) were grouted and post-tensioned horizontally and vertically together to create an integrated reaction wall. Figure 3.10 shows a photo taken during the construction of the NEES@Berkeley reconfigurable reaction wall. Detailed calculations related to the reaction wall and adequacy of the floor system are presented in Appendix A.

Actuators for the tests were selected from among those available in the laboratory, considering the loads and displacement targets. While the specimen's design criteria limits the peak actuator force to about 600 kips, for accuracy in control during hybrid simulations an actuator with a capacity 50% larger ($1.5 \times 600 \text{ kips} = 900 \text{ kips}$) [Schellenberg et al. 2009]. Thus, two Atlas 1500-kip actuators with ± 12 -in. stroke length were used, with one installed at each floor level, as shown in Figure 3.11. With these actuators, a roof level displacement equal to about 5% of the specimen height can be imposed. Large brackets were installed on the reaction wall to attach the actuators. Due to the weight and size of the actuators, brackets were also installed on walls to help support the actuators during construction and testing. Detailed calculations and shop drawings for these brackets are presented in Appendices A and B, respectively.

To distribute the concentrated shear and axial loads applied at the base of a specimen to the strong floor, a heavy built-up floor beam (Figure 3.12) was provided at the top of the strong floor top slab, and a series of relatively stiff load transfer beams (Figures 3.13 and 3.14) were provided on the bottom side of the top slab. The floor beam and load transfer beams were connected by post-tensioned anchor rods. Detailed calculations and shop drawings for these details at the base of the specimen are presented in Appendices A and B, respectively.

Several different systems were considered to provide lateral restraint for the test specimen (Figure 3.8). To improve access to the specimen during erection and repair, and to facilitate observation during testing, the lateral stability system shown in Figures 3.9 and 3.15 was used. Detail design calculations for the lateral support frame are described in Appendix A. Shop drawings of the frame are provided in Appendix B.

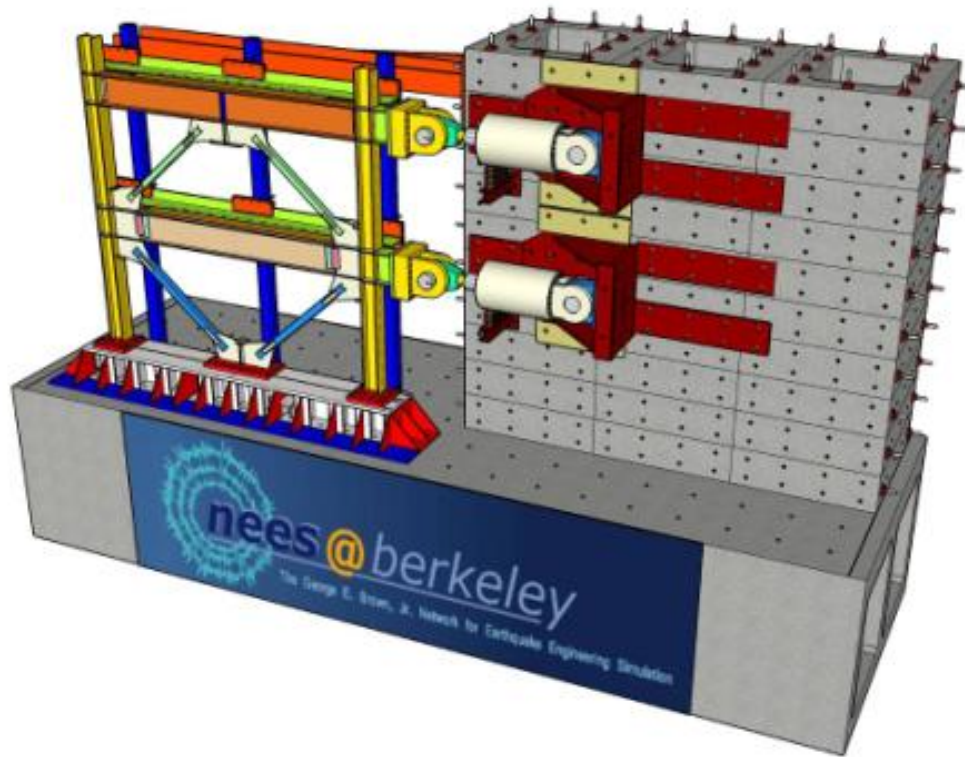


Figure 3.9 Overview of the final test set up.



Figure 3.10 Construction of reconfigurable reaction wall before pre-stressing.



Figure 3.11 Atlas 1.5 M-lb actuators at both floor levels.



Figure 3.12 The built-up floor beam after painting.



Figure 3.13 Load transfer beams below strong floor before erection.



Figure 3.15 Lateral stability frame (the orange cantilever beam and three blue HSS columns) in the test set up view from south-east side of laboratory.

3.5 DESCRIPTION OF TEST SPECIMENS

Four nearly identical braced frame specimens were designed, constructed, and tested as part of this test program. Each test specimen consists of a two-story single-bay concentric braced frame. As shown in Figure 3.16, the story height is 9 ft measured from beam center line to center line of the top two beams (or from base to the centerline of the lower beam), and the bay width is 20 ft measured from column center line to center line. All specimens were detailed in compliance with the AISC Seismic Provisions for Structural Steel Buildings [AISC 2005b]. Detailing provided was consistent with out-of-plane buckling of the braces. Specifics of the design process related to a prototype structure are described in Section 3.9. However, the basic design was arrived at by iteratively designing a structure, consistent with AISC Seismic Provisions and ASCE-7 [2005] requirements such that the ultimate base shear of the specimen did not exceed the 900 kips limit of the test set up considering an inverted triangular distribution of lateral forces.

To explore construction details that might speed field construction, special one-piece gusset plates were used at the ends of the lower floor beam where the beam intersects with two braces and the column (Figure 3.9). The single piece gusset was shop welded to the column (Figure 3.26), and attached by field welding to the braces and beam. Slotted stiffener (finger) plates were used to replicate the appearance and function of beam flanges that would have been present if the gusset was welded to a continuous beam extending from column to column.

The first three specimens were tested quasi-statically under cyclic loading excursions. These specimens were provided with square HSS, round HSS, and WF bracing elements. The fourth specimen was the same as the first specimen with square HSS bracing, but it was tested using hybrid simulation techniques. Based on experience with the first two specimens, some of the details of the second two specimens were modified to improve behavior.

The specimen naming convention is TCBF-B- \times , where TCBF stands for “Tomorrow’s Concentric Braced Frame”, B stands for “Berkeley” specimen, and the “ \times ” stands for the specimen sequential number in the test program. The specimen name, member size, steel material type, and test method of each specimen are listed in Table 3.1. Details of the specimens are shown in Figures 3.17, 3.18, 3.19, and 3.20. Shop drawings for each specimen are summarized in Appendix C. Basic dimensional and engineering properties of sections used for beams, columns, and braces are listed in Tables 3.2, 3.3, and 3.4. Photographs in Figures 3.21 to 3.24 show the entire side view of the completed specimens TCBF-B-1, TCBF-B-2, TCBF-B-3, and TCBF-B-4 before testing.

Photographs of the fabricated sub-assemblages used to erect all four specimens are shown in Figure 3.25. The gusset plates were all tapered and constructed from 3/4-in.-thick plate. The $2t_g$ separation from the end of the brace to the end of the taper on the gusset plate recommended in the AISC Seismic Provisions for out-of-plane brace buckling was used. One-piece gusset plates with two finger plates (see Figure 3.26, flush the beam top and bottom flanges) welded on them and spliced to the W24 \times 68 lower beam. The one-piece gusset plates were welded to columns with double-side fillet welds (details are shown in Appendix C).

All of the braces were slotted and welded to the gusset plates per AISC requirements. Based on these requirements, reinforcing plates were welded to the braces at the net reduced section of the braces where the slot continued for a short distance past the end of the gusset plate (Figure 3.27). This type of reinforcement was found to prevent premature failure of bracing components connected to gusset plates in this manner when loaded under loading histories with significant cycles of tensile deformation.

Note that after testing of Specimens TCBF-B-1 and TCBF-B-3, the W24 \times 117 roof beam, two W12 \times 96 columns and 2-in.-thick base plates were re-used to reduce costs of constructing Specimens TCBF-B-2 and TCBF-B-4.

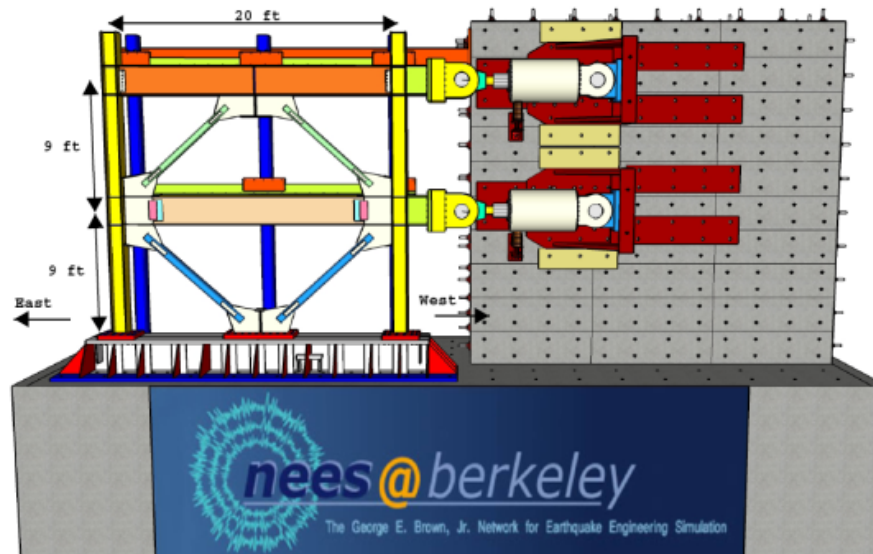


Figure 3.16 **Dimension of test specimen.**

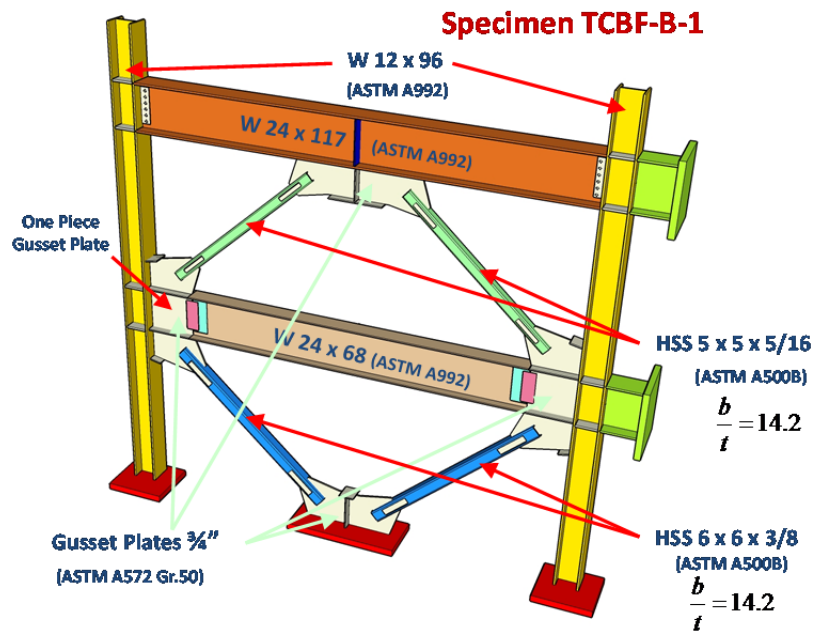


Figure 3.17 Specimen TCBF-B-1: member sizes.

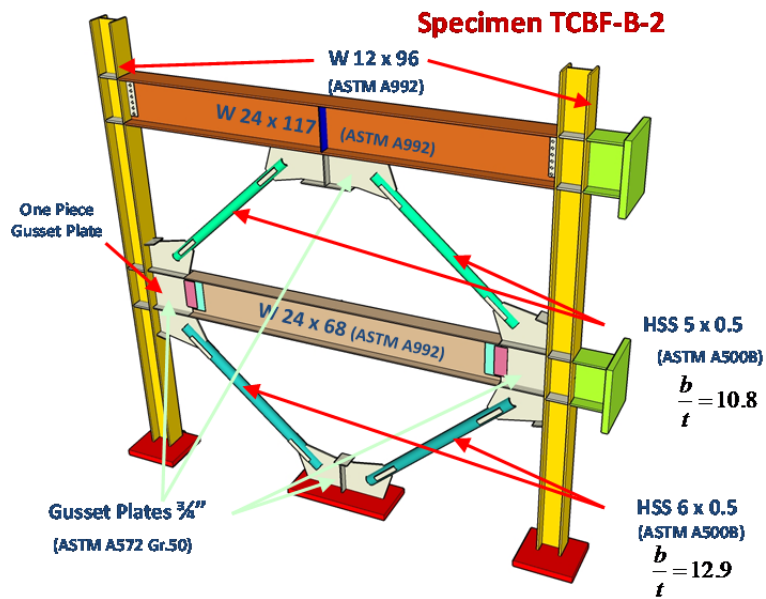


Figure 3.18 Specimen TCBF-B-2: member sizes.

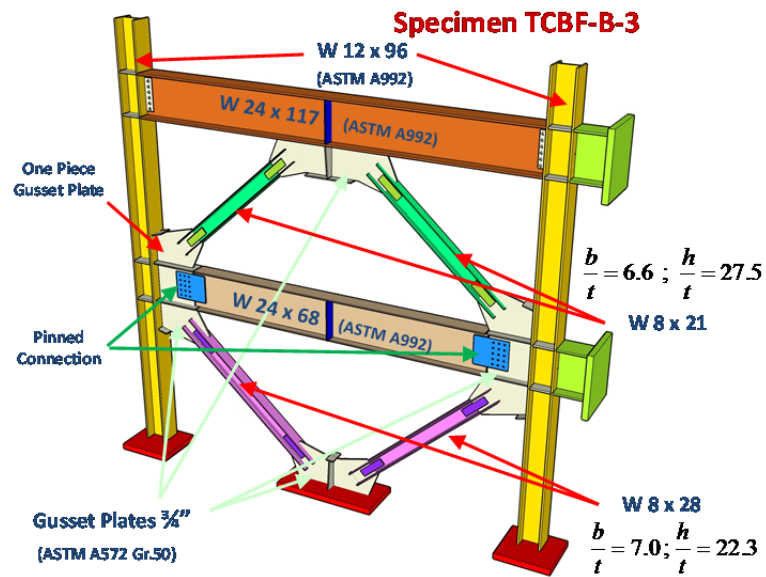


Figure 3.19 Specimen TCBF-B-3: member sizes.

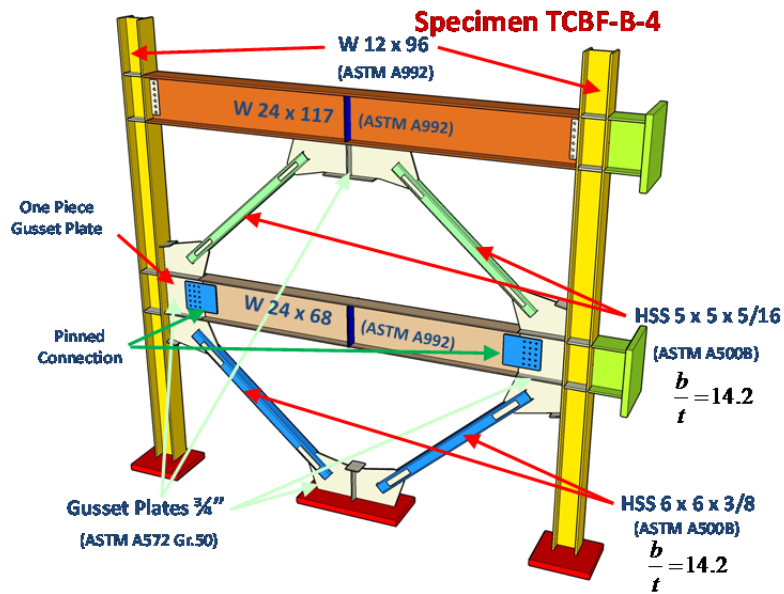


Figure 3.20 Specimen TCBF-B-4: member sizes.

Table 3.1 Name, member size, material type, and test method of the specimens.

Name	Column & Beam	Brace		Test Method
TCBF-B-1	W12 × 96 (Column) (ASTM A992)	HSS 5 × 5 × 5/16 HSS 6 × 6 × 3/8	ASTM A500B	Cyclic Loading
TCBF-B-2		HSS 5 × 0.5 HSS 6 × 0.5	ASTM A500B	Cyclic Loading
TCBF-B-3	W24 × 117 (Roof Beam) W24 × 68 (Lower Beam) (ASTM A992)	W 8 × 21 W 8 × 28	ASTM A992	Cyclic Loading
TCBF-B-4		HSS 5 × 5 × 5/16 HSS 6 × 6 × 3/8	ASTM A500B	Hybrid Simulation

Table 3.2 Section properties of beams and columns.

Section	d (in)	t _f (in)	b (in)	t _w (in)	A _s (in ²)	I _x (in ⁴)	S _x (in ³)	Z _x (in ³)
W24 × 117	24.3	0.85	12.8	0.55	34.4	3540	291	327
W24 × 68	23.7	0.59	8.97	0.42	20.1	1830	154	177
W12 × 96	12.7	0.9	12.2	0.55	28.2	833	131	147

Table 3.3 Section properties of HSS braces (square and round).

Section	A _s (in ²)	B (in)	t (in)	I _y (in ⁴)	r _y (in)	S _x (in ³)	Z _x (in ³)
HSS 6 × 6 × 3/8	7.58	6	0.375	39.5	2.28	13.2	15.8
HSS 5 × 5 × 5/16	5.26	5	0.3125	19	1.9	7.62	9.16
HSS 6 × 0.5	8.09	6	0.5	31.2	1.96	10.4	14.3
HSS 5 × 0.5	6.62	5	0.5	17.2	1.61	6.88	9.6

Table 3.4 Section properties of wide flange braces.

Section	d (in)	t _f (in)	b (in)	t _w (in)	A _s (in ²)	I _x (in ⁴)	r _x (in)	I _y (in ⁴)	r _y (in)	S _x (S _y) (in ³)	Z _x (Z _y) (in ³)
W8 × 28	8.06	0.47	6.54	0.29	8.24	98	3.45	21.7	1.62	24.3 (6.63)	27.2 (10.1)
W8 × 21	8.28	0.4	6.27	0.25	6.16	75.3	3.49	9.77	1.26	18.2 (3.71)	20.4 (5.69)

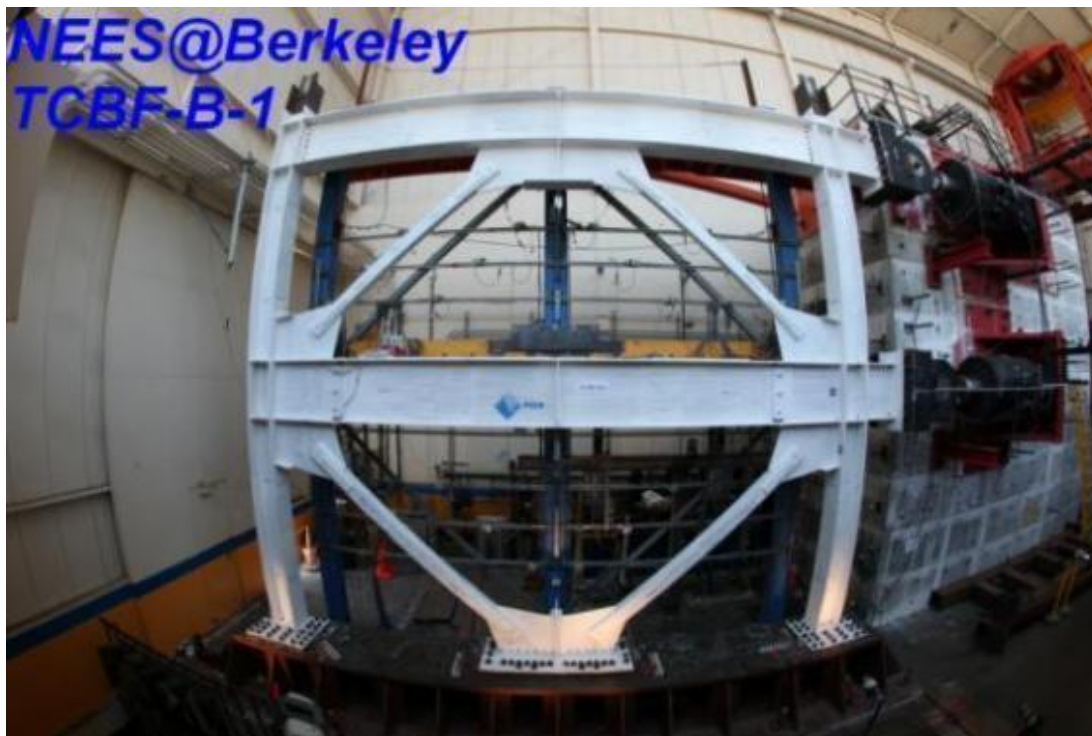


Figure 3.21 Specimen TCBF-B-1 before test.



Figure 3.22 Specimen TCBF-B-2 before first trial.



Figure 3.23 Specimen TCBF-B-3 before test.



Figure 3.24 Specimen TCBF-B-4 before hybrid simulation.



Figure 3.25(a) Specimens TCBF-B-1 and TCBF-B-2: sub-assemblages.



Figure 3.25(b) Specimens TCBF-B-3 and TCBF-B-4: sub-assemblages.



Figure 3.25(c) Specimens TCBF-B-2 and TCBF-B-3: sub-assemblages.



Figure 3.25(d) Specimens TCBF-B-3 and TCBF-B-4: sub-assemblages.



Figure 3.26 The 3/4-in.-one-piece gusset plate after tack welding to column flange.



Figure 3.27 Specimen TCBF-B-2: detail view of reinforcing plate.

3.6 LOADING SEQUENCE FOR QUASI-STATIC TESTS

Specimens TCBF-B-1 through TCBF-B-3 were tested quasi-statically, with a prescribed history of roof displacement imposed. The displacement of the roof beam was monitored and controlled during the entire test process; however, the lower level actuator was force controlled. Throughout the tests, the force applied at the lower level was one-half of the instantaneous force measured in the load cell of the upper level actuator. This makes the lateral force pattern imposed on the specimen an inverted triangular distribution throughout the entire experiment. In this way, drifts in each story would evolve during the tests according to the damage occurring in each story.

The displacement protocol imposed at the roof was modified from the Appendix T of the AISC Seismic Provisions [AISC 2005b]. This was used in order to compare the results with previous tests and tests conducted by others. However, because the specimens were special concentric braced frames and were likely to buckle prior to the deformations at first yield of a buckling restrained braced frame for which Appendix T applies, an additional eight cycles corresponding to one half of the elastic design drift ($6@0.5D_{be}$) and two cycles at the elastic design drift ($2@D_{be}$) were added to the test protocol.

Figure 3.28 shows the cyclic loading protocol for the first three specimens in terms of roof displacement and roof drift ratio. The sign convention for imposed displacements and forces are that positive displacements and forces correspond to the actuator pushing the specimen to the east side of laboratory (Figure 3.16), while negative values correspond to the actuator pulling the specimen to the west side of laboratory.

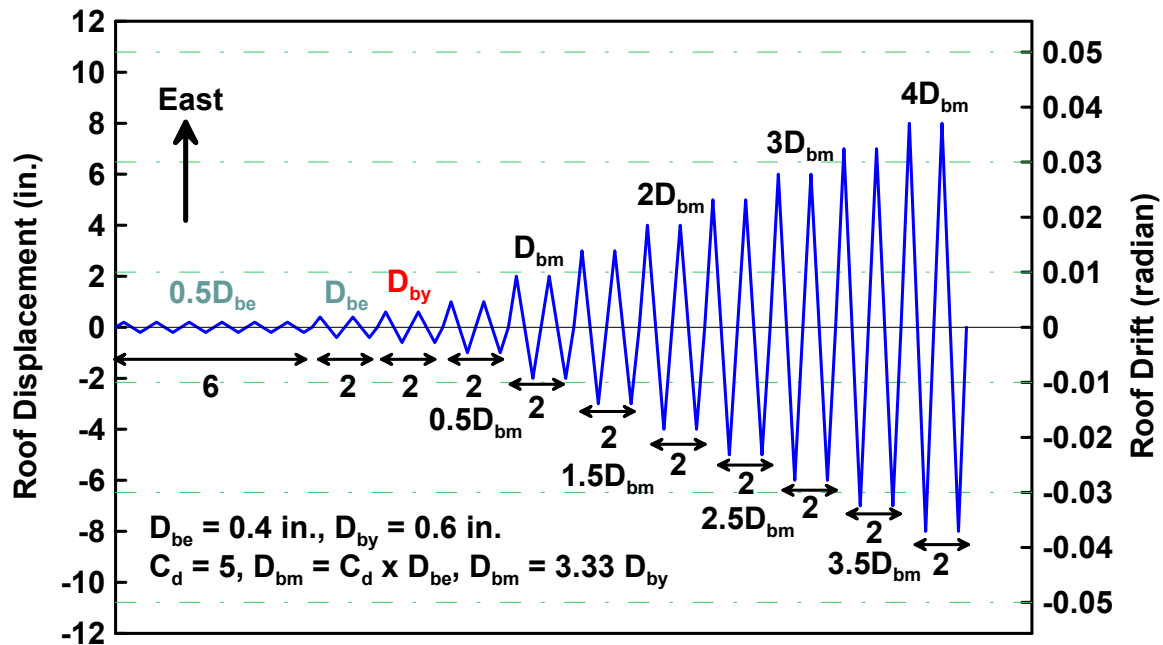


Figure 3.28 Specimens TCBF-B-1, TCBF-B-2, and TCBF-B-3: cyclic loading protocol.

During the entire test process the motion of the actuators was paused for a short time whenever major events such as fracture of braces, weld cracking, or unanticipated flaking of whitewash were observed. The overall test was terminated following the cycle whenever both braces at the same story (typically the first story) completely fractured.

3.7 INSTRUMENTATION

Each specimen was extensively instrumented with displacement transducers, tilt meters, strain gauges, and load cells. The detailed location of instrumentation points, corresponding channel numbers, extension cable numbers, device serial numbers, device types, instrumentation ranges, and detail descriptions for all four specimens are listed in Appendixes D, E, F, and G.

Displacement transducers consisted of more than 75 digital encoders, linear variable differential transducers (LVDTs), Direct Current Displacement Transducers (DCDT), and wire pots. These were used to measure the floor level displacements, actuator displacements, longitudinal and lateral displacements of braces, local deformations of plastic hinge regions, and movement of the test set up (in-plane and out-of-plane). A set of brackets was installed on the out-of-plane displacement restraining system to provide support for displacement transducers measuring out-of-plane motion of the braces. Displacement transducers installed at the east end (with measuring target located at intersection of the center line of roof beam and the center line of east column exterior flange) of the first three specimens were used for external displacement control during the quasi-static tests. This was done to ensure the specimens were actually pushed and pulled to the displacements specified in the MTS-STC control software. For the last specimen (hybrid simulation specimen), the displacement transducer measuring targets were located at the west end of the specimen (i.e., at the actuator side) for safety reasons.

Two tilt meters were installed on the specimen. These were used to measure the rotation relative to an absolute vertical axis of the lower level beam-to-gusset plate connections.

Depending on the specimen, nearly 140 linear-type strain gauges and rosette strain gauges were utilized. Many of the strain gauges were attached to portions of beams and columns where elastic behavior was expected. Engineering principles were then used to estimate curvatures, average axial strains, bending moments, shears, and axial loads in these members. Strain gages were also attached to braces, gusset plates, panel zone regions, and in plastic hinge regions to measure strains for subsequent comparison with numerical predictions.

The force acting in the 1500 kip actuators were monitored by calibrated load cells (Figure 3.29) between the rod head clevis and the actuator rod. Both load cells were calibrated before the experiment. The Baldwin 4000-kip universal test machine (Figure 3.30) was used to calibrate the load cell. This machine is calibrated to NIST standards on a regular basis. Figure 3.31 shows the steel jacket used for rotating the actuator to an upright position for calibration without the need to unscrew the load cell unit. Figure 3.32 shows a photo of overall set up during the calibration process.

The instruments and load cells were connected to three switch boxes using extension. These switch boxes are integrated into a high-speed data acquisition system programmed to scan every channel and record the data into a desktop computer under specified sampling rate defined before testing.

Reusable magnetic labels (Figures 3.33 and 3.34) were used at column ends, beam ends, and brace ends to easily identify the locations and orientations of specific photos during post processing. All of the specimens were painted with whitewash prior to testing to facilitate detection of yield patterns (see Figures 3.21 to 3.24).

Thousands of digital photos in different views and angles were taken and stored in a desktop computer as a secondary observation tool; a hand-held digital single-lens reflex camera was the primary observation tool. During the entire experimental process, high-quality videos captured the global response of the specimen and captured locally the incipient fracture of bracing components. Four Canon EOS 5D Mark-II digital single-lens reflex (DSLR) cameras were connected to data acquisition system and triggered to take still photos every 0.2-in. roof displacement (measured at the east end of specimen). Three Canon EOS D1 digital single-lens reflex cameras were connected to desktop computers and shot the still photos every 10 (or 15) sec continuously throughout the entire test. The resolution of these DSLR cameras was very high, allowing for detailed post-test examination of behavior.

A 3D Leica high definition laser scanner was also used to capture the specimen deformed shape throughout the cyclic loading tests. The resulting point clouds permit examination of the 3D deformed shape of the specimen to within about 0.04 in.



Figure 3.29 The 1.5-million-pound load cell.



Figure 3.30 Baldwin 4-million-pound universal test machine.



Figure 3.31 Steel jacket for rotating the 1.5 M-lb actuator during the load cell calibration.



Figure 3.32 Overview of the calibration set up during the load cell calibration.



Figure 3.33 Specimens TCBF-B: reusable magnetic labels.



Figure 3.34 Specimens TCBF-B: distribution of reusable magnetic labels.

3.8 SPECIMEN CONSTRUCTION SEQUENCE

3.8.1 Specimen TCBF-B-1

The first specimen (TCBF-B-1) was erected within a six-hour period in the laboratory (this time does not including the welding process). First, the gusset plate assemblage at ground level was placed on the floor beam. Then, two columns were lifted and moved into position on the floor beam and temporarily secured by several 1-1/8 in.-diameter all-thread anchor bolts (Figure 3.35) at base. The HSS $6 \times 6 \times 3/8$ braces were then inserted and bolted to the gusset plates at both ends with ASTM A307 erection bolts. The W24 \times 68 lower beam was then lifted up and spliced to the one-piece gusset plate using bolts. After the lower beam was fully bolted to the shear tabs at both ends, the yellow painted tee section (Figure 3.36)—which is part of the out-of-plane bracing system—was then lifted up and positioned in three saddles (Figure 3.37) connected at the elevation of the top flange of the lower beam to three vertical (blue) HSS columns. The tee section was bolted to a 14-ft-long, 3/4-in.-thick splice plate (made of ASTM A36 mild steel). This plate was in turn fillet welded along the center line of the lower beam's top flange. Three steel angle kickers were provided below the tee section and braced to the bottom flange at the middle span of the W24 \times 68 beam, which were also braced to the bottom continuity plates at the beam column joint panel zones, as shown in Figure 3.38.

In the next step, the W24 \times 117 roof beam was lifted and bolted to the shear tabs on the interior side of column flange at both ends. The HSS $5 \times 5 \times 5/16$ braces for second story were then installed and bolted to the gusset plates. Finally, the lateral supporting tee section at roof level was placed on adjustable saddles and connected to the top flange of roof beam (similar to the lower beam).

Welding of beam-to-column connections, gusset plate-to-beam splices and gusset plate-to-brace connections were continued after the whole specimen was aligned to insure that it was plumb and fit up. Self-shielded, flux-cored wires for self-shielded arc welding were used in this specimen. All welding consumables were AWS E71T-8-H16 low hydrogen electrodes or equivalent filler metal (Figure 3.39a). Ultrasonic inspection of welds was performed in the shop. Only visual inspection of welds was performed in the field (laboratory).

Complete joint penetration weld details were specified at the lower beam-to-gusset plate connections. The beam top and bottom flanges were 45° grooved, and welded to gusset plate finger stiffeners. Backing bars were used on the flange welds. Note that the backing bars on top flange and bottom flange welds were not removed after welding. The beam web was also 45° grooved and welded on one side. Beam-to-gusset plate shear tab with shim plate and bolt holes at beam side were used for fabrication and served as a backing plate. Figure 3.40 shows the lower beam-to-gusset plate connection and welding details.

All high-strength fasteners and anchor bolts were tightened to the minimum required pretension forces specified in AISC manual using impact gun based on the torque table provided by the tool manufacturer. Standard shim plates (Figure 3.39b) were used between base plates and top flange of floor beam to ensure that the columns remained plumb in the specimen to within

1/16 in. between column tip and column base. A laser level and a traditional level were used to monitor that the columns remained plumb. Figures 3.41 and 3.42 show the key construction steps and welding processes of this specimen.



Figure 3.35 The 1-1/8-in.-diameter all-thread anchor bolt.



Figure 3.36 The lateral supporting tee section.



Figure 3.37 Tee section sitting on the lateral supporting saddles.



Figure 3.38 Steel angle kickers below the tee section.



Figure 3.39(a) Filler material used in the welding process.



Figure 3.39(b) Standard shim plates for the column base adjustment.



Figure 3.40(a) Specimen TCBF-B-1: lower beam-to-gusset plate connection details.

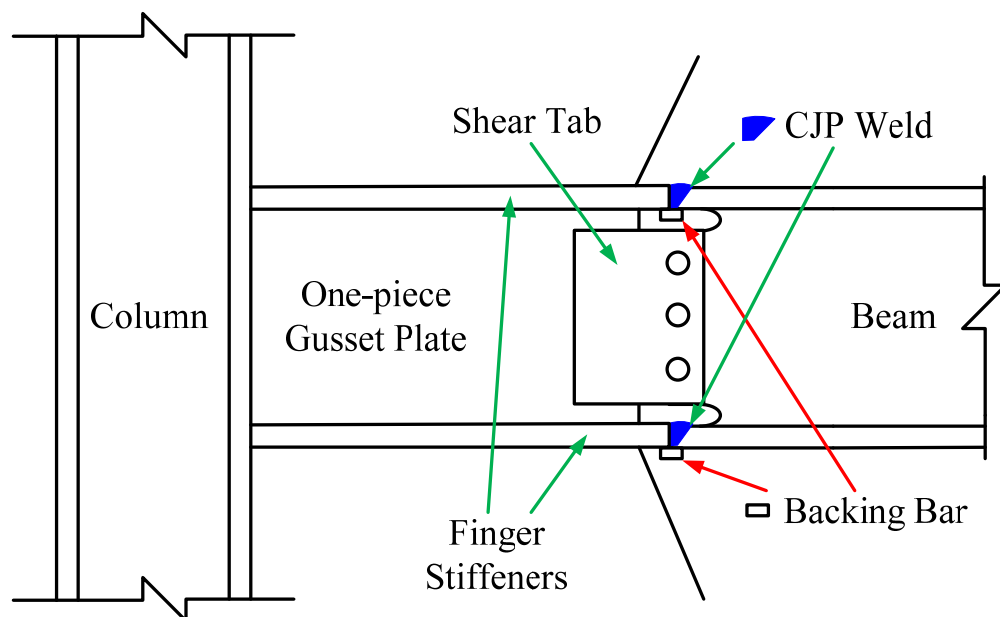


Figure 3.40(b) Specimen TCBF-B-1: lower beam-to-gusset plate connection weld details.

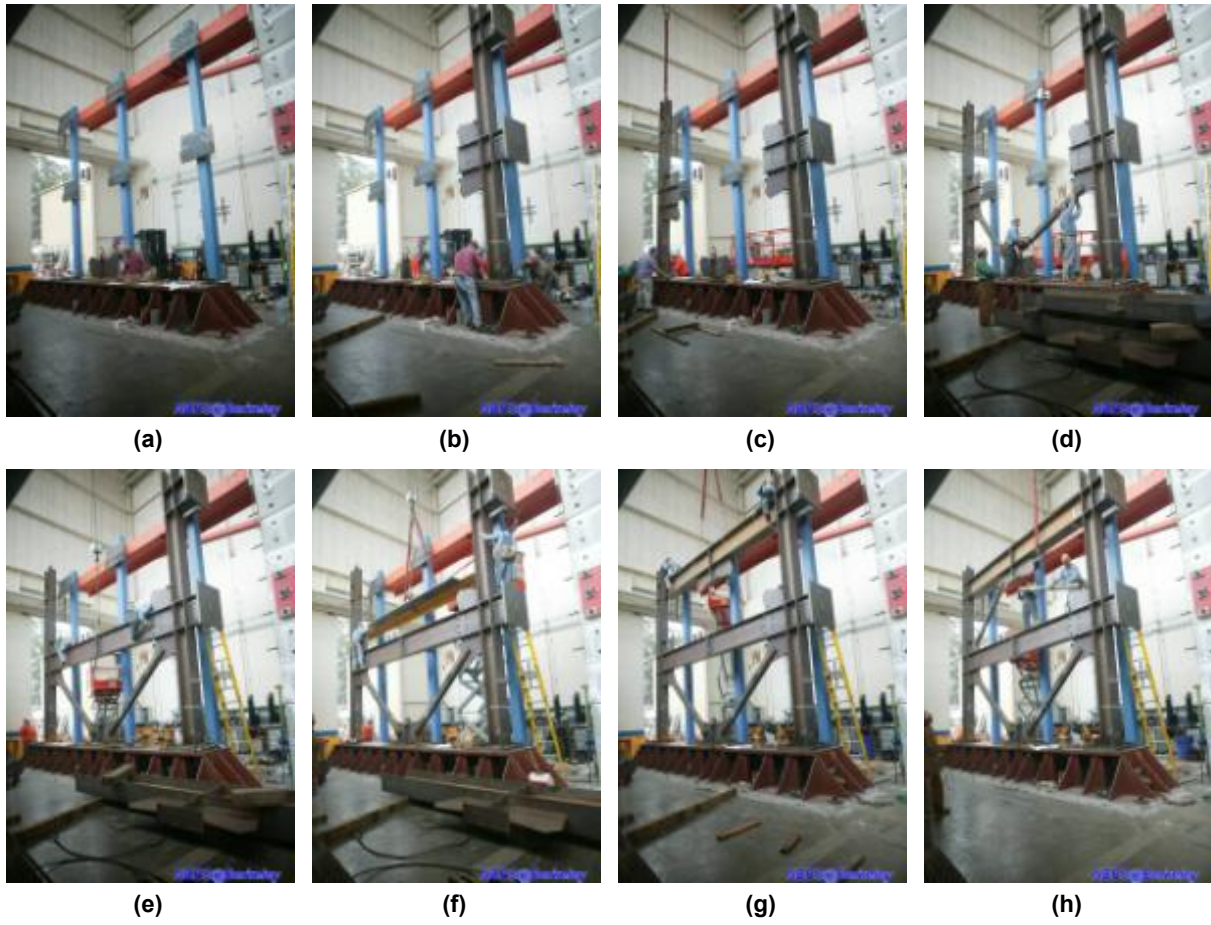


Figure 3.41 Specimen TCBF-B-1: key construction steps.

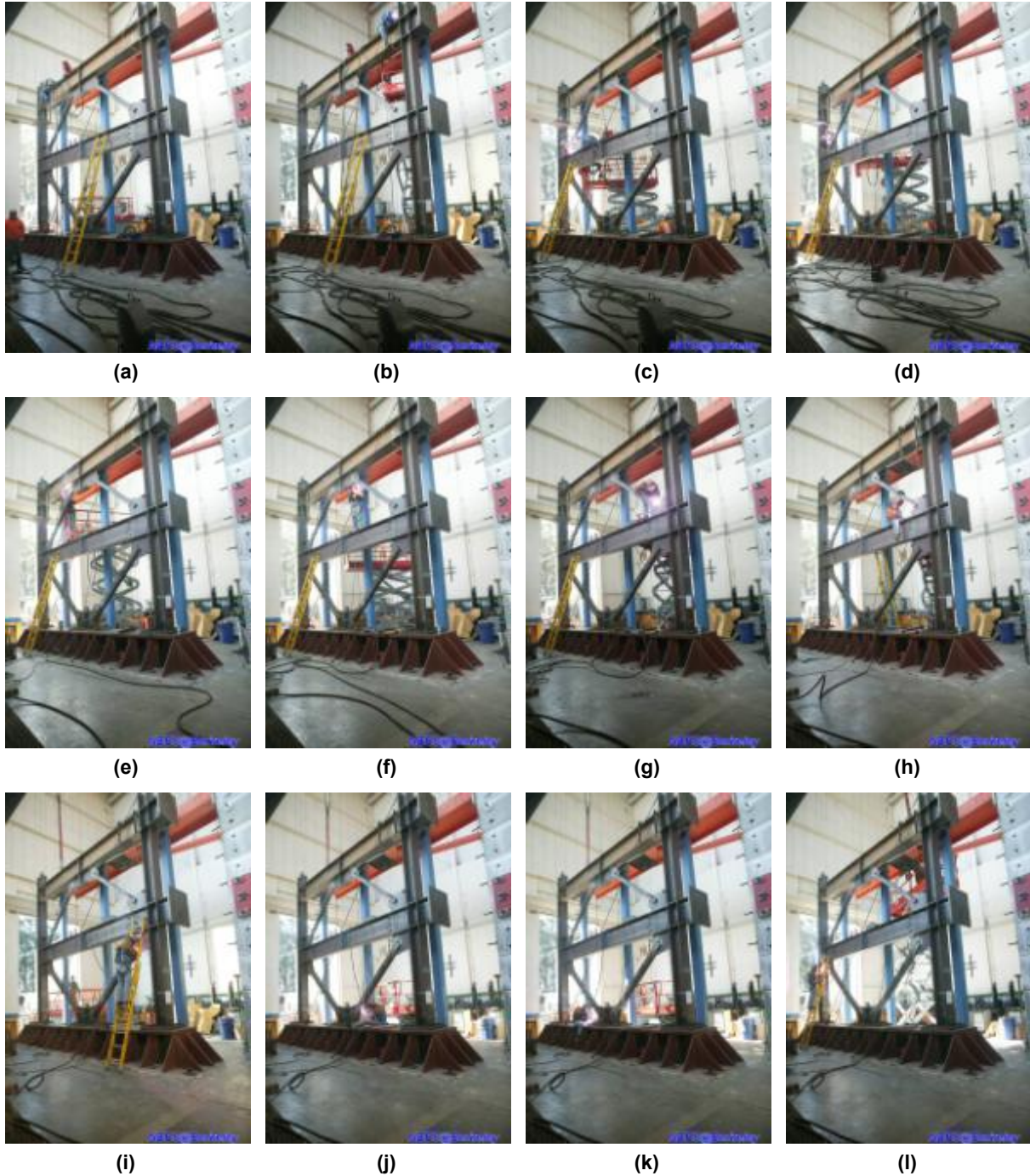


Figure 3.42 Specimen TCBF-B-1: key welding processes.

3.8.2 Specimen TCBF-B-2

The second specimen (TCBF-B-2) reused the same $W24 \times 117$ roof beam, $W12 \times 96$ columns, and the 2-in. thick base plates from Specimen TCBF-B-1. Only the $W24 \times 68$ lower beam and 3/4-in.-thick gusset plates were replaced. Round HSS braces were used instead of square HSS braces in this specimen.

After testing of the first specimen, the damaged square HSS braces were cut off from the frame specimen using the torch cutting tool. The specimen with the braces removed is shown in Figure 3.43. The specimen without braces was straightened to a vertical position using two hydraulic actuators. The residual deformation at roof level was monitored from the position transducer installed during the first test. The manual control of the actuator was used to move and straighten the specimen back to its original position. When the residual deformation was within an acceptable tolerance (about 1/8 in. out-of-plumb between column tip and column base in the in-plane direction), the actuators were locked and then the W24 × 68 lower beam and gusset plates were cut off using a torch cutting device. Air-carbon arc equipment was used to remove the old welds and any base metal that was still sticking out. A hand grinder was then used to grind the surface to an acceptable surface condition for welding new materials to it. Some surface weld repairs were performed during this process.

After surface preparation was done, the gusset plate assemblages were then tack welded to the 2-in.-thick base plate, roof beam, and two columns. Next, the round HSS braces in both stories were connected to the gusset plates by erection bolts. Then, the new lower beam was bolted to the one-piece gusset plate at both ends (Figure 3.44). The ends of W24 × 68 beam were slightly trimmed to fit the space between gusset plate assemblages. A simple alignment check was performed before welding process. Similar field welding procedures were used as those performed on Specimen TCBF-B-1. Figures 3.45 and 3.46 show some key construction steps and welding processes of the specimen. The one-piece gusset plates were welded to column using double-side fillet welds.

Similar to Specimen TCBF-B-1, the complete joint penetration weld details were also specified at the lower beam-to-gusset plate connections. The beam top and bottom flanges were 45° grooved, and welded to gusset plate finger stiffeners. Backing bars were used on the flange welds. Note that the backing bars on top flange welds were not removed after welding. Single-pass fillet welds were applied to bottom flange welds after removal of backing bar. The beam web was also 45° grooved and welded on one side. Beam-to-gusset plate shear tab with shim plate and bolt holes at beam side were used for fabrication and served as a backing plate. Figure 3.47 shows the lower beam-to-gusset plate connection and welding details.

Several small weld fractures were found at both column bases during the final surface inspection (Figure 3.48) before whitewash painting. The three-step dye penetrant (cleaner/remover, penetrant and developer; see Figure 3.49) crack-detecting method was used to help determine the length of cracks (Figures 3.50). Inferior welds and cracks were gouged using air-carbon arc equipment. Two additional inches of gouging measured from the crack tips was done along the course of cracks or welds, as illustrated in Figure 3.51. Preheating before repair welding was also included in the repair weld procedure. The two column bases after weld repairs are shown in Figures 3.52 and 3.53. The side view of entire Specimen TCBF-B-2 after whitewash painting is shown in Figure 3.54.



Figure 3.43 Damaged specimen after cutting off the square HSS braces.



Figure 3.44 Specimen TCBF-B-2: splicing the lower beam to one-piece gusset plates.

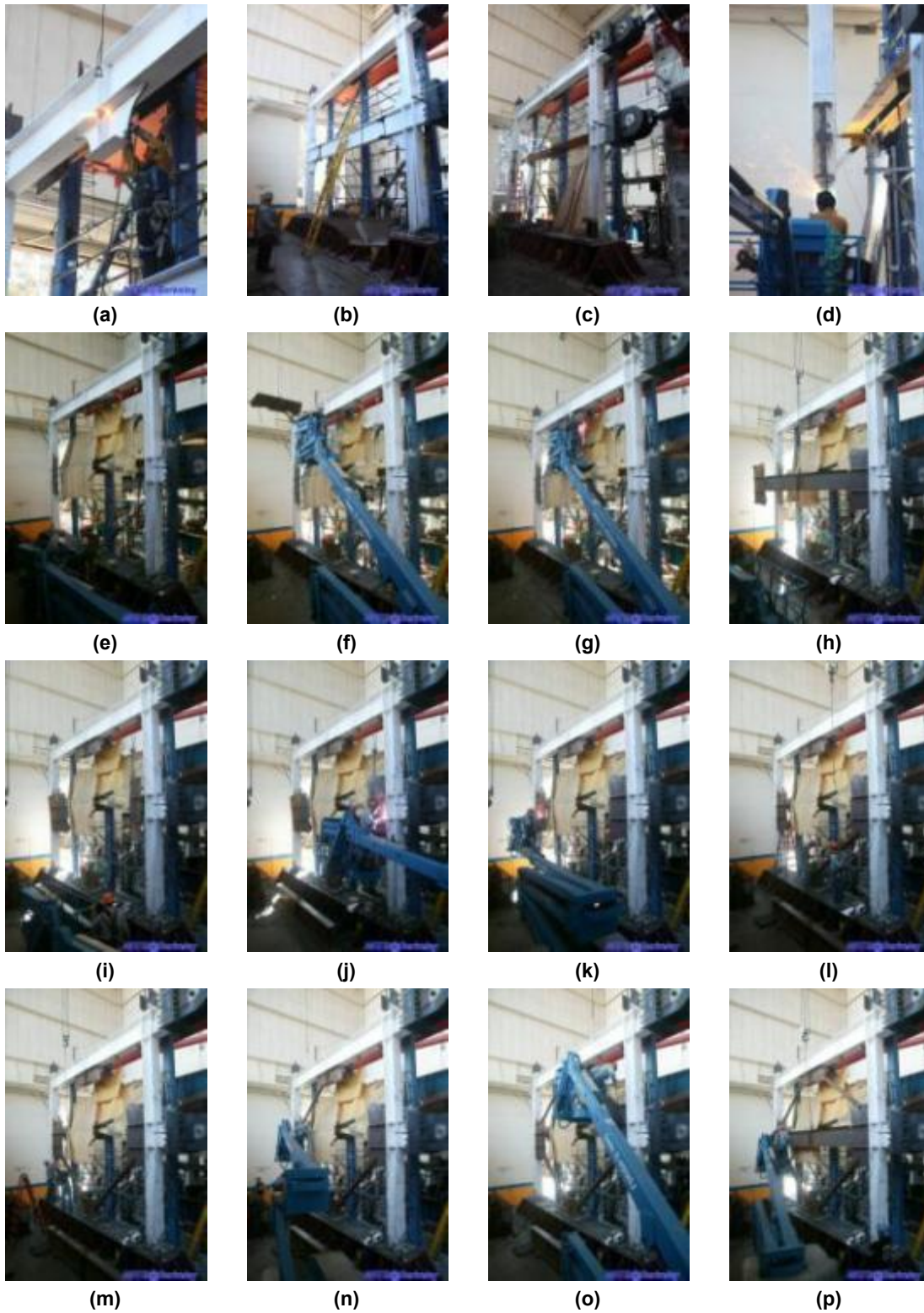


Figure 3.45 Specimen TCBF-B-2: key construction steps.

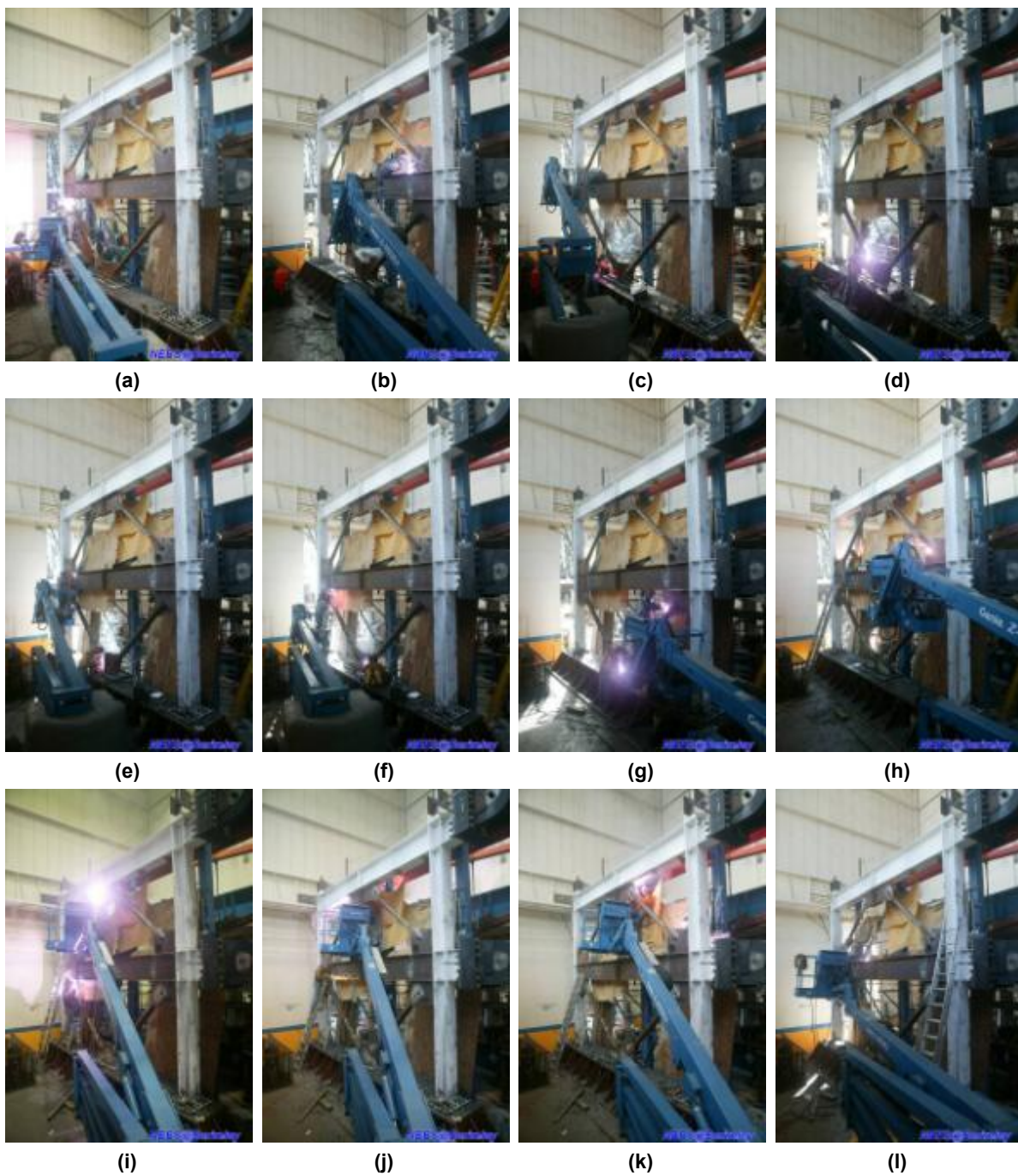


Figure 3.46 Specimen TCBF-B-2: key welding processes.



Figure 3.47(a) Specimen TCBF-B-2: lower beam-to-gusset plate connection details.

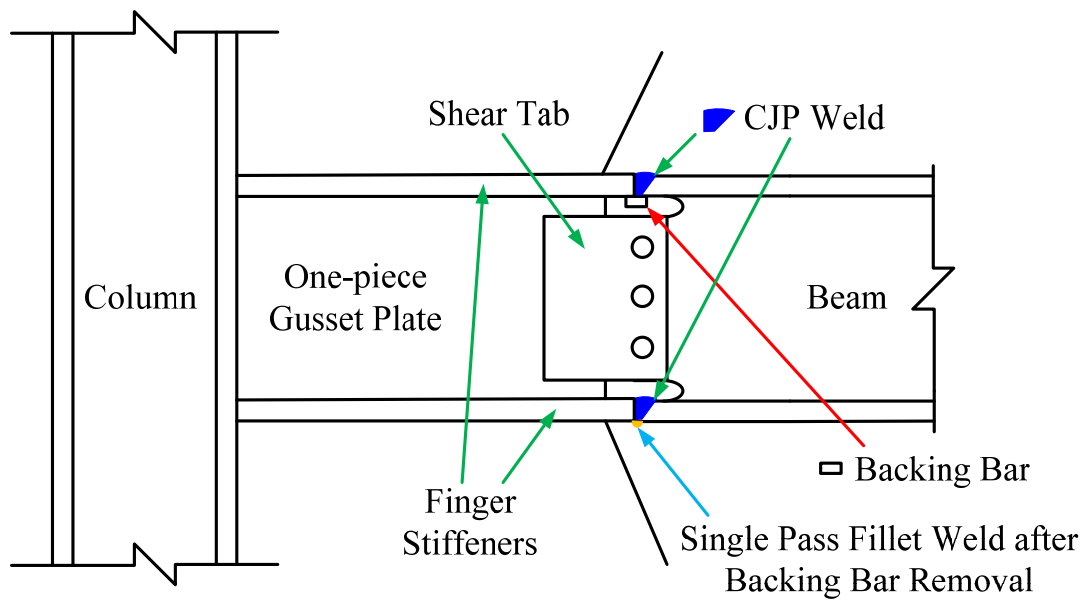


Figure 3.47(b) Specimen TCBF-B-2: lower beam-to-gusset plate connection weld details.



Figure 3.48(a) Crack in the CJP weld at west column base (north-west corner).



Figure 3.48(b) Crack in the CJP weld at east column base (south-east corner).



Figure 3.49 Three-step crack detecting spray.



Figure 3.50 Crack detecting spray applied in the CJP weld at east column base (south-east corner).



Figure 3.51 The east column base (south-east corner) after gouging the cracked welds.

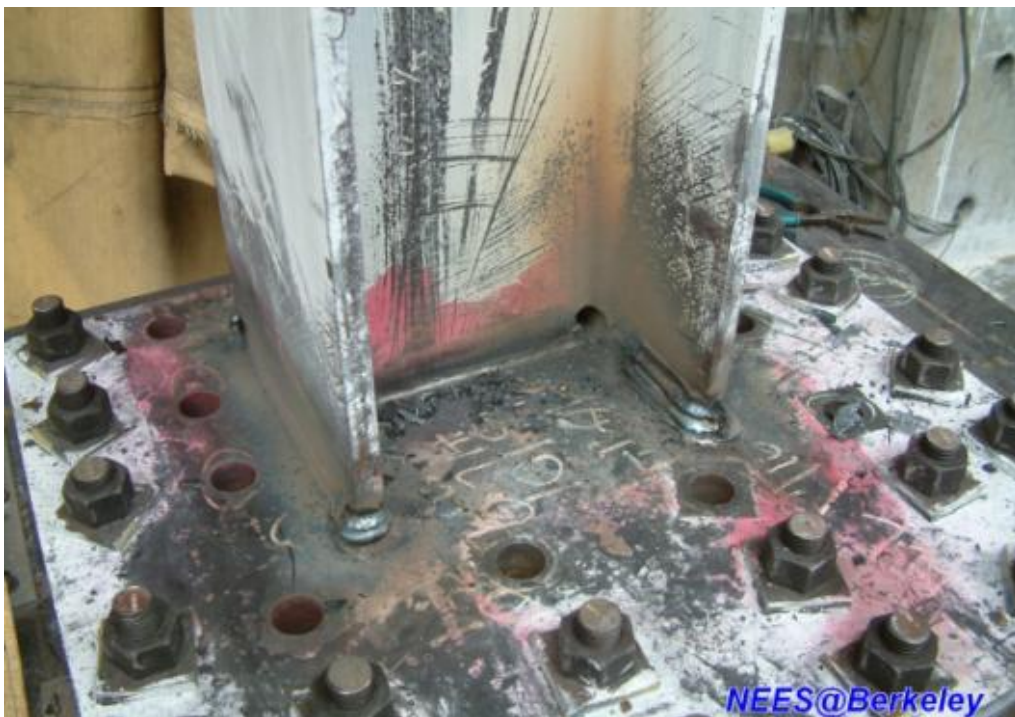


Figure 3.52 The west column base after weld repairs.



Figure 3.53 The east column base after weld repairs.

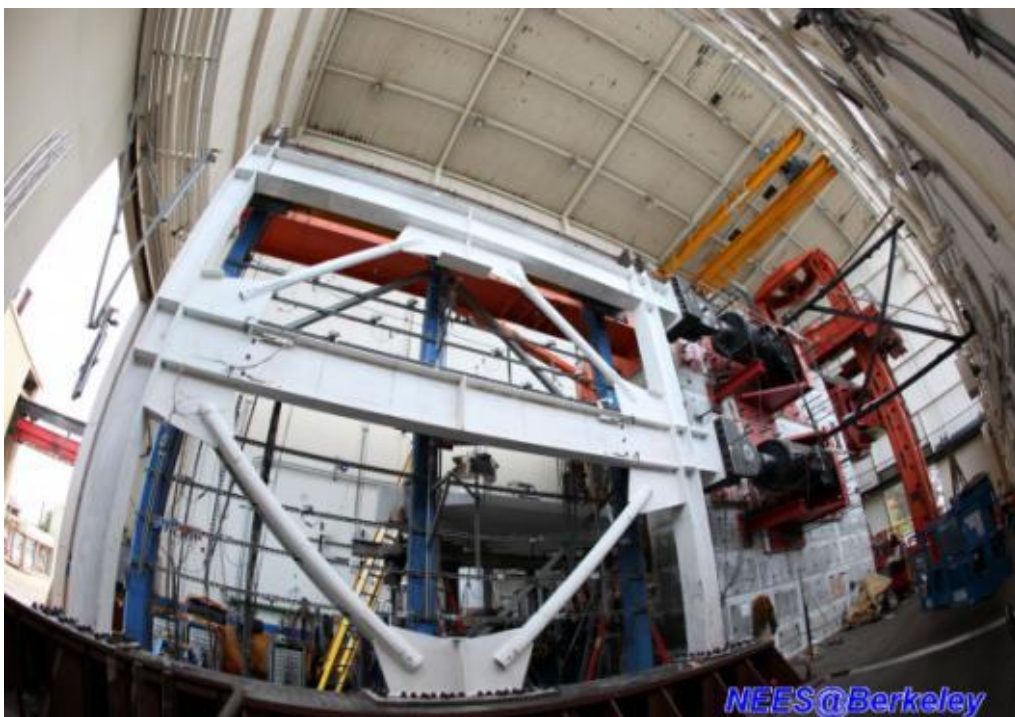


Figure 3.54 Specimen TCBF-B-2: entire after whitewash painting.

3.8.3 Specimen TCBF-B-3

The third specimen (TCBF-B-3) with wide-flange braces was an entirely new specimen. It did not reuse the roof beam or columns from previous test. The specimen erection, not including the welding process, took about eight hours in the laboratory.

As before, two columns were initially lifted and moved to the position on the floor beam and temporarily secured by several 1-1/8-in.-diameter all-thread anchor bolts at their base. Note that four gusset stiffeners were welded at base of each column for this specimen. The gusset plate assemblage at ground level was then placed on the floor beam. The first story $W8 \times 28$ braces were then inserted and bolted to the gusset plates at both ends with ASTM A307 erection bolts.

The $W24 \times 68$ lower beam was then lifted up and spliced to the one-piece gusset plate with fifteen tension control bolts at both ends (Figure 3.55). Following the first two tests, it was decided (as discussed in Chapter 4 and 5) to change the detail at the end of the beams where they attached to the gusset plates. Rather than fully welding the beam to the gusset plate, to simulate a continuous member only the beam web was bolted to the gusset plate, providing a more pin connection. After the lower beam was temporary connected to the gusset plates, the existing lateral supporting tee section (sitting on the saddles connected to vertical blue HSS columns at lower level that hold the entire tee section during the test) was then adjusted to bolt to a 14-ft-long, 3/4-in.-thick splice plate and fillet welded to the top flange center line of lower beam. Three steel angle kickers were provided below the tee section and braced to the bottom flange at the middle span of the $W24 \times 68$ beam, and also braced to the bottom continuity plates at the beam column joint panel zones.

Next, a sub-assemblage consisting of a $W24 \times 117$ roof beam, top gusset plate, and two $W8 \times 21$ braces (see Figure 3.56) were lifted and bolted to the shear tabs on the interior side of column flange at both ends. The $W8 \times 21$ braces for second story were then bolted to the gusset plates. Finally, the lateral supporting tee section at roof level was connected to the top flange of roof beam.

The welding of beam-column connections, gusset plate-to-beam splices, and gusset plate-to-brace connections were completed after aligning the specimen. Self-shielded, flux-cored wires for self-shielded arc welding were used in this specimen. All welding was accomplished using AWS E71T-8-H16 low hydrogen electrodes or equivalent filler metal. All high-strength fasteners and anchor bolts were tightened to the minimum required pretension forces specified in AISC manual using tension control wrench and impact gun based on the torque table provided by the tool manufacturer. Standard shim plates were used between base plates and top flange of floor beam to control the plumb of the columns in the specimen within 1/16 in. out of plumb between column tip and column base. A laser level and traditional level were used to check for ensure that the columns were plumb. Figures 3.57 and 3.58 show the key construction steps and welding processes of this specimen.



Figure 3.55 Lower beam to one-piece gusset plate connection detail.



Figure 3.56 Specimen TCBF-B-3: roof beam, gusset plate, and brace sub-assembly.

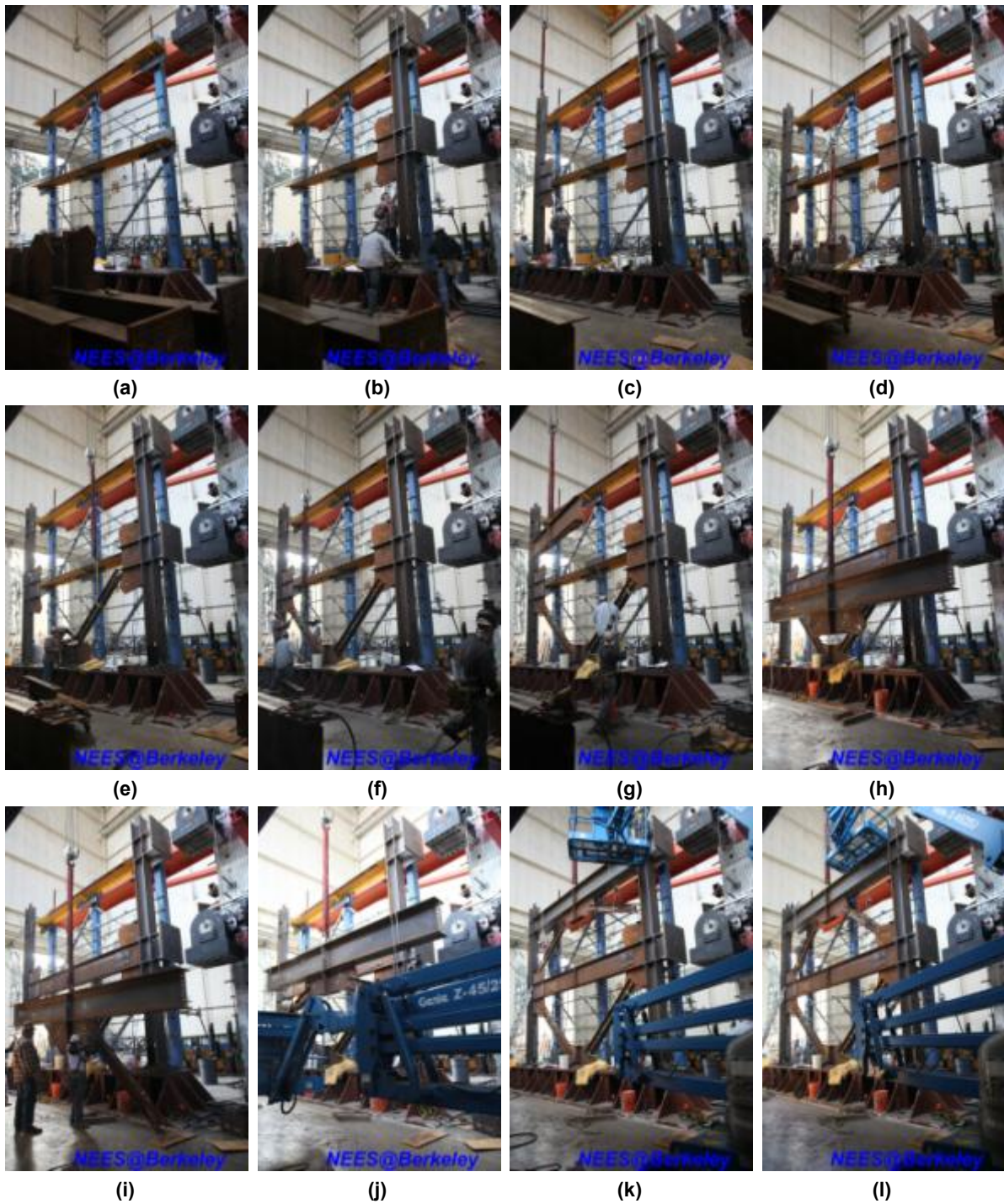


Figure 3.57 Specimen TCBF-B-3: key construction steps.

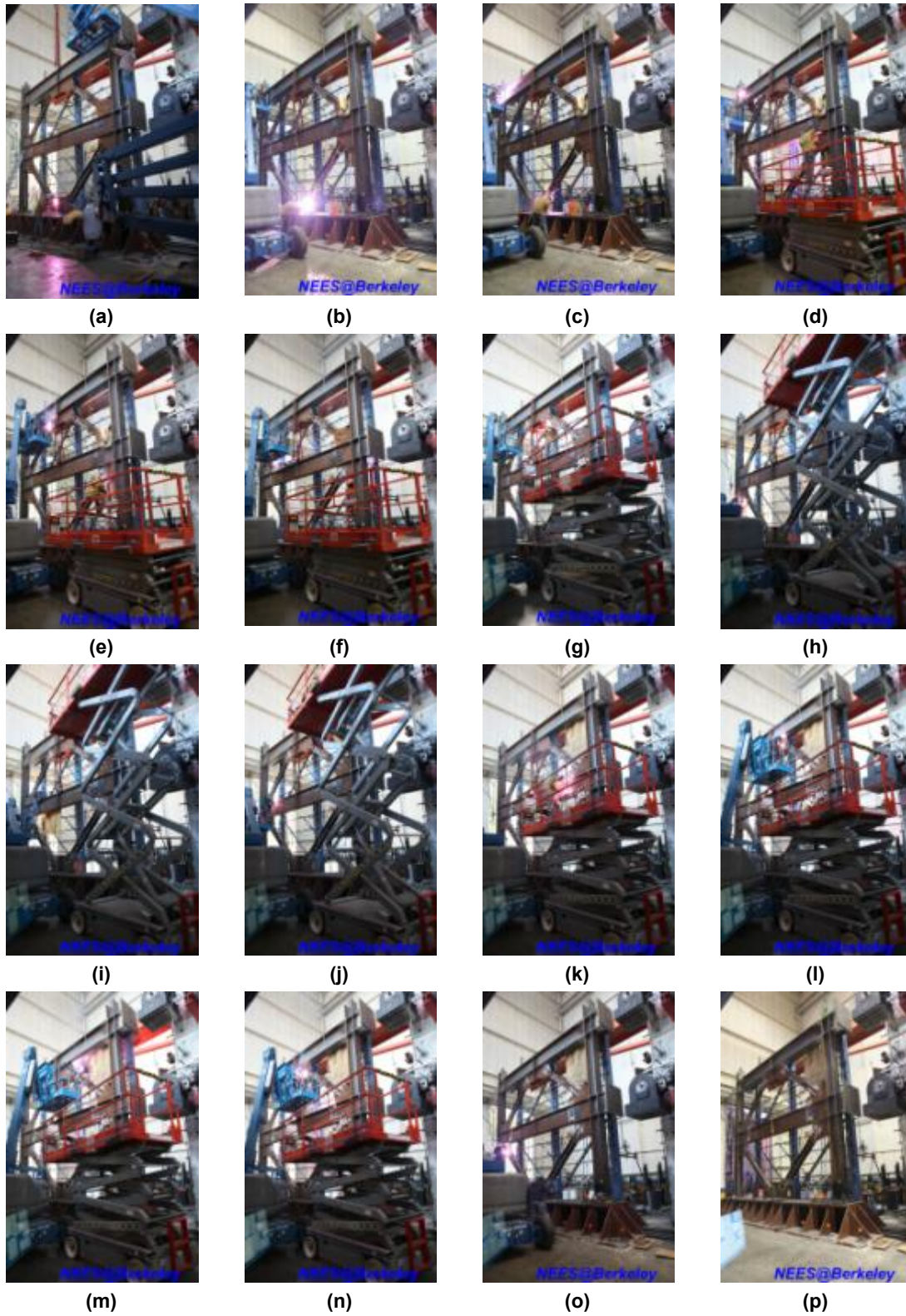


Figure 3.58 Specimen TCBF-B-3: key welding processes.

3.8.4 Specimen TCBF-B-4

The fourth specimen (TCBF-B-4) reused the $W24 \times 117$ roof beam, $W12 \times 96$ columns, and the 2-in.-thick base plates from Specimen TCBF-B-3. Only the $W24 \times 68$ lower beam and 3/4-in.-thick gusset plates were replaced. Square HSS braces identical to those used in TCBF-B-1 were used in this specimen.

After testing of the Specimen TCBF-B-3, the damaged wide flange braces were cut off from the frame specimen (Figure 3.59) using a torch-cutting tool, and then the specimen without braces was straightened by the actuator at roof level. The residual deformation at roof level was monitored from the position transducer installed during the previous test. The manual control of the actuator was used to move and straighten the specimen back to its original position. When the residual deformation was within an acceptable tolerance, the actuator position was locked.

Before welding the new sub-assemblages, air-carbon arc equipment was used to remove the old welds and sticking out base metal. A hand grinder was used to grind the surface to an acceptable surface condition for welding. Some surface weld repairs were performed during this process. After the surface preparation was done, the gusset plate assemblages were then tack welded to the 2-in.-thick base plate, roof beam, and two columns. Next, the square HSS braces in both stories were connected to the gusset plates by erection bolts. Then, the new lower beam was spliced to the one-piece gusset plate at both ends (Figure 3.60). This detail was the primary difference between Specimens TCBF-B-1 and TCBF-B-4. Slightly trimming of the ends of $W24 \times 68$ beam were done to fit the space between gusset plate assemblages. A simple alignment check was performed before welding process. The remainder of the erection process and field welding used were similar to that used for the Specimen TCBF-B-1.

The east side column flange near the column base had fractured completely during the previous test and was repaired with complete joint penetration welds. The groove in the column flange prepared for complete joint penetration welds is shown in Figure 3.61. The fracture that extended into the column web near the base of the same column was also repaired. Here, a cover plate and pair of vertical stiffener plates were attached to the column web to bridge over the fracture (Figures 3.62 and 3.63). A weld access hole remained in the column web (see Figure 3.62). The repaired column base after whitewash painting is shown in Figures 3.64.

Figures 3.65 and 3.66 show some key construction steps and welding processes of the specimen.



Figure 3.59 Damaged specimen after cutting off the wide flange braces.



Figure 3.60 Specimen TCBF-B-4: connection detail of the lower beam to one-piece gusset plates.



Figure 3.61 Grove prepared in the east side column flange near column base.



Figure 3.62 A 0.55-in. thick cover plate welded to the south face of column web with fillet welds at east-side W12 × 96 column base.



Figure 3.63 Two 0.55-in. thick vertical stiffener plates welded to the north face of column web with fillet welds at east-side W12 × 96 column base.

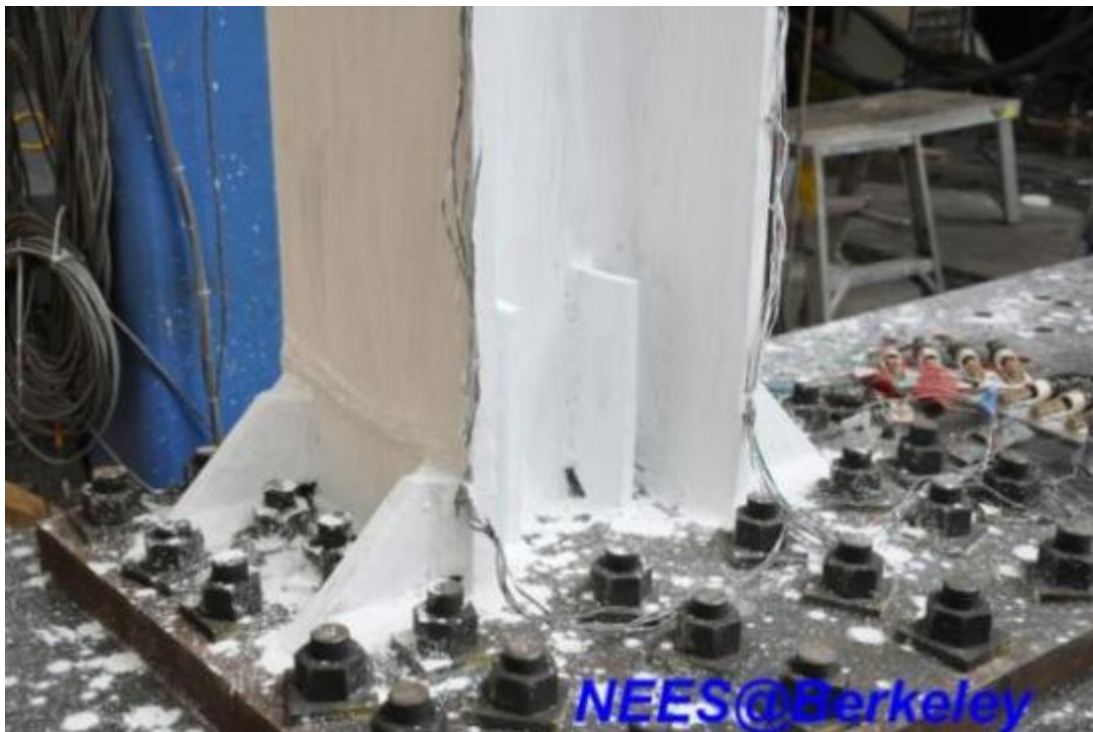


Figure 3.64 The east-side column base detail after repair and whitewash painting.

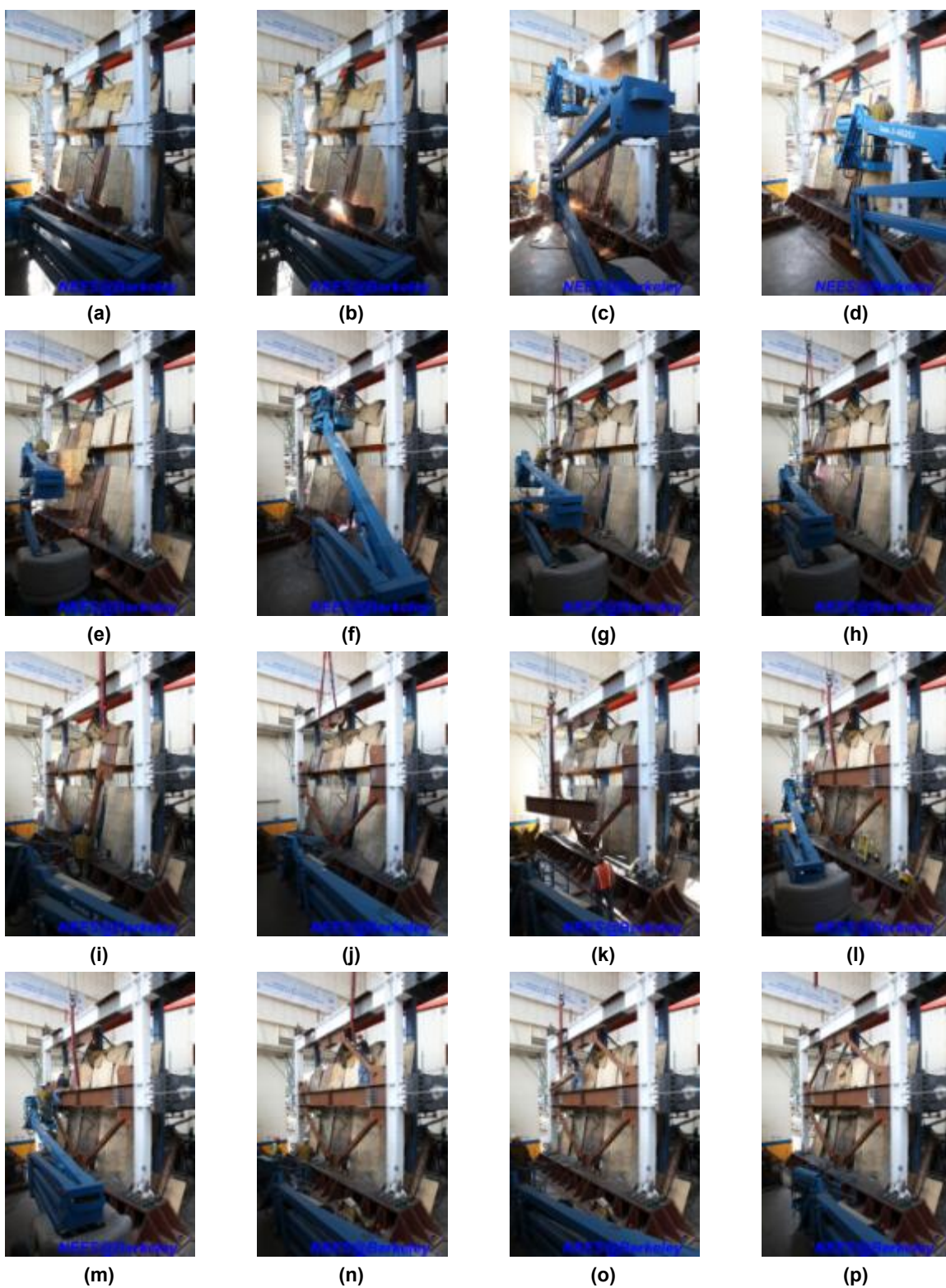


Figure 3.65 Specimen TCBF-B-4: key construction steps.

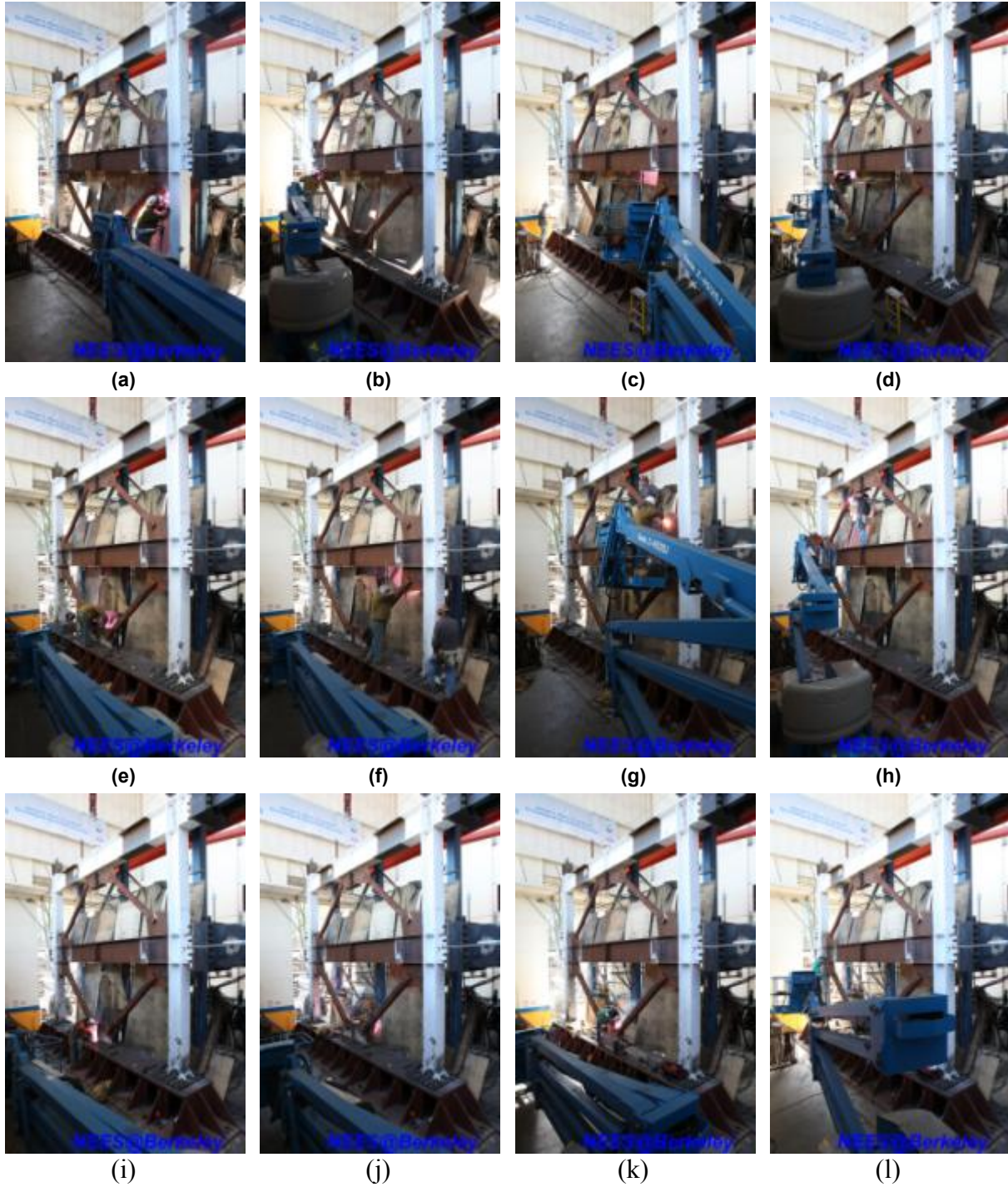


Figure 3.66 Specimen TCBF-B-4: key welding processes.

3.9 RELATION OF SPECIMEN DESIGN TO PROTOTYPE DESIGN

The test specimen designs were based on the constraints imposed by the laboratory test set up, and detailed according to AISC's *Seismic Provisions for Special Concentric Braced Frames* [AISC 2005b]. However, it is interesting to assess how these specimens might relate to an actual structure designed for a seismic region like California. Moreover, to implement the hybrid tests, a prototype structure is needed to identify the inertial and damping characteristics of the structure, as well as the properties associated with the gravity load resisting system. In this subsection, the 2005 edition of the ASCE-7 building code is used along with the mechanical properties of the test specimens to identify characteristics of a prototype structure for which the specimen could be used to provide lateral load resistance.

3.9.1 Model (Prototype) Building

The model or prototype building was selected as a two-story building with special concentric braced frames in both directions. The typical beam span and story height were 20 ft and 9 ft in both *X*- and *Y*-direction. Although these values are small compared to usual dimensions, they are close enough that a larger scale factor need not be used. Typical floor plan, perspective view, and the elevation considered in identifying the model building design are shown in Figures 3.67, 3.68, and 3.69. The LRFD design method was used to select member sizes and the loading followed the ASCE-7-05 LRFD load combinations. The detailing and design basically followed the 2005 AISC Seismic Provisions. The braced bays in the *Y*-direction (Figure 3.69) were intentionally moved to the corner of the building to represent the actual testing configuration in the laboratory.

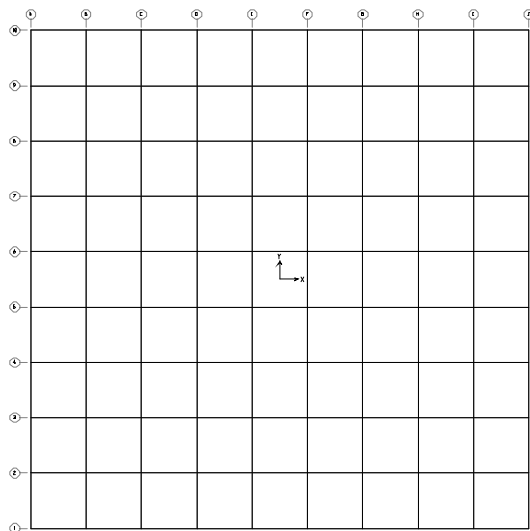


Figure 3.67 Typical floor plan of the model building.

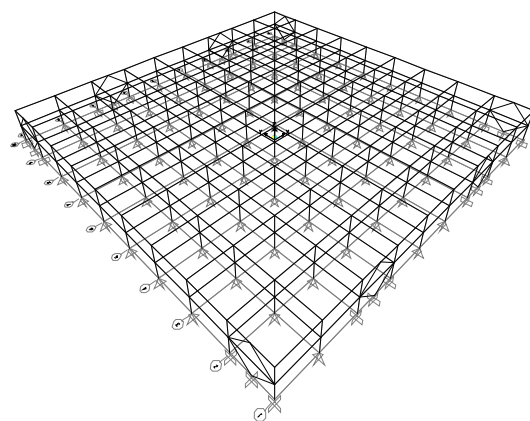


Figure 3.68 Perspective view of the model building.

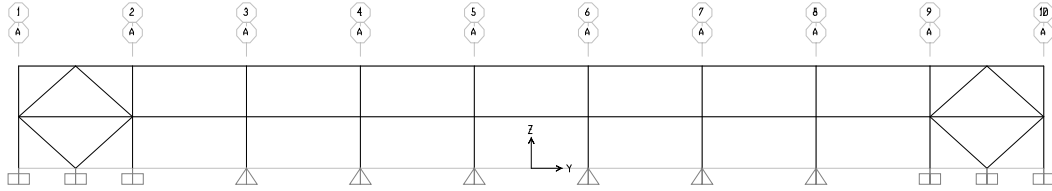


Figure 3.69 Elevation of the model building (Y-direction).

3.9.2 Seismic Forces

The model building was assumed to be located in Berkeley, California. According to the USGS Java software tool, Earthquake Ground Motion Parameters, Ver. 5.1.0 (see Figure 3.70), the mapped MCE, 5% damped, spectral response acceleration parameter at 1 sec and short periods can be determined:

$$S_1 = 0.787 \quad S_S = 2.014 \quad (3.1)$$

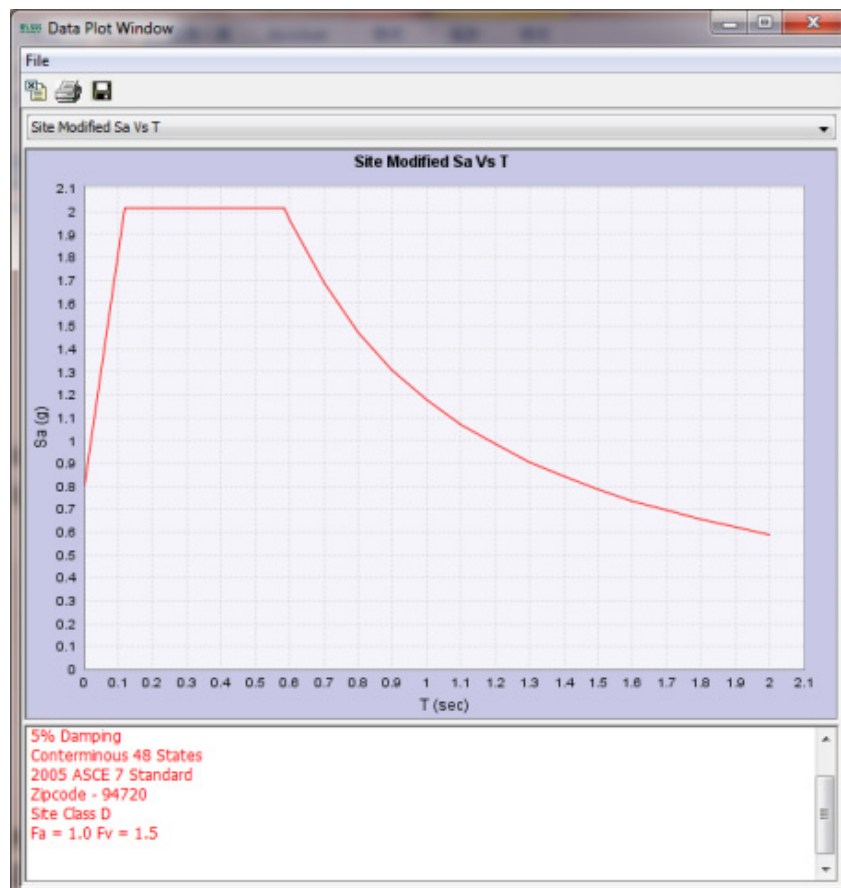


Figure 3.70 The snapshot of USGS Earthquake Ground Motion Parameters Java applet window.

Then the default site class D was selected per ASCE-7-05, Section 11.4.2, the site coefficients and acceleration parameters can be calculated as:

$$\begin{aligned} F_a &= 1.0 \\ F_v &= 1.5 \end{aligned} \quad (3.2)$$

$$\begin{aligned} S_{M1} &= F_v \cdot S_1 = 1.181 \\ S_{MS} &= F_a \cdot S_s = 2.014 \end{aligned} \quad (3.3)$$

$$\begin{aligned} S_{D1} &= \frac{2}{3} \cdot S_{M1} = 0.787 \\ S_{DS} &= \frac{2}{3} \cdot S_{MS} = 1.343 \end{aligned} \quad (3.4)$$

The selected occupancy category is taken as II, the importance factor is taken as 1.0 and the seismic design category is set as E. Per ASCE-7-05, Section 11.6 and ASCE-7-05, Figure 22-15, characteristic periods in defining the design response spectrum can be calculated as:

$$T_0 = 0.2 \cdot \frac{S_{D1}}{S_{DS}} = 0.117 \quad (3.5)$$

$$T_s = \frac{S_{D1}}{S_{DS}} = 0.586 \quad (3.6)$$

$$T_L = 8 \quad (3.7)$$

Also from ASCE-7-05, Table 12.2-1, the design coefficients and factors for special steel concentrically braced frame were extracted:

$$R = 6; \Omega_o = 2; C_d = 5 \quad (3.8)$$

With the above information, the seismic base shear for the model building can be calculated using the following equations:

$$V = C_s \cdot W \quad (3.9)$$

$$C_s = \frac{S_{DS}}{(R/I)} = \frac{1.343}{6} = 0.224 \quad (3.10)$$

$$T_a = C_t \cdot h_n^x = 0.02 \cdot 18^{0.75} = 0.175 \quad (3.11)$$

$$T_a < T_L = 8 \text{ (second)}$$

The derived seismic response coefficient also needs to be within the limitations calculated from the following equations:

$$C_{s \text{ (limit 1)}} = \frac{S_{D1}}{T (R/I)} = \frac{0.787}{0.175 \cdot 6} = 0.75 > C_s \quad (3.12)$$

$$C_{s \text{ (limit 2)}} = 0.01 < C_s \quad (3.13)$$

$$C_{s \text{ (limit 3)}} = \frac{0.5 \cdot S_{S1}}{(R/I)} = \frac{0.5 \cdot 0.787}{6} = 0.066 < C_s \quad (3.14)$$

$$C_u = 1.4 \quad (3.15)$$

It is clear that the derived seismic response coefficient 0.224 passed the limitation checks.

For the building weight calculation, it was assumed that the tributary floor dead load was 100 psf for both floor levels. Tributary live load for the roof level is 100 psf (roof garden) and 50 psf for the typical floor level (typical office building) based on the ASCE-7-05, Table 4-1. From the calculations shown below, the total weight of the model building shown in Figure 3.67 is 6480 kips, and the seismic base shear is 1451.5 kips. It will be shown below that the test specimen is adequate for these loads. Table 3.5 lists the vertical distribution of seismic forces in both *X*- and *Y*-direction.

$$\begin{aligned}
W_1 &= 100 \text{ psf} \times 180 \text{ ft} \times 180 \text{ ft} = 3240 \text{ kip} \\
W_2 &= 100 \text{ psf} \times 180 \text{ ft} \times 180 \text{ ft} = 3240 \text{ kip} \\
W &= W_1 + W_2 = 6480 \text{ kip} \\
V &= C_s \cdot W = 0.224 W = 1451.5 \text{ kip}
\end{aligned}
\tag{3.16}$$

Table 3.5 Vertical distribution of seismic forces.

Floor Level	W_x (kip)	h_i (ft)	h_x (ft)	$W_x h_x^k$ ($k=1$)	C_{vx}	F_x (kip)
2F	3240	9	9	29,160	1/3	483.8
Roof	3240	9	18	58,320	2/3	967.7
Σ	6480	-	-	87,480	1.0	1451.5

The seismic masses for each floor level for dynamic analysis are calculated using the following equations:

$$\begin{aligned}
m_1 &= \frac{3240 \text{ kip}}{386 \frac{\text{in}}{\text{sec}^2}} = 8.39 \frac{\text{kip} - \text{sec}^2}{\text{in}} \\
m_2 &= \frac{3240 \text{ kip}}{386 \frac{\text{in}}{\text{sec}^2}} = 8.39 \frac{\text{kip} - \text{sec}^2}{\text{in}}
\end{aligned}
\tag{3.17}$$

For the load combination, four basic combinations were used according to ASCE-7-05:

- ①. $1.4 D$
- ②. $1.2 D + 1.6 L$
- ③. $1.2 D \pm 1.0 E + L$; where $E = E_h + E_v$
- ④. $0.9 D \pm 1.0 E$; where $E = E_h - E_v$

where $E_h = \rho$, $Q_E = 1.3 Q_E$; $E_v = 0.2$, and $S_{DS} D = 0.2686 D$. If this is plugged into the original combinations, the load combinations then become:

- ①. $1.4 D$
- ②. $1.2 D + 1.6 L$
- ③. $1.4686 D + 1.3 Q_E + L$
- ④. $0.6314 D + 1.3 Q_E$

$$\textcircled{5}. 0.9314 D - 1.3 Q_E + L$$

$$\textcircled{6}. 1.1686 D - 1.3 Q_E$$

The load combinations (amplified) used to check column design are listed below:

$$(1.2 + 0.2 S_{DS})D \pm \Omega_o E + L$$

$$(0.9 - 0.2 S_{DS})D \pm \Omega_o E$$

Applying S_{DS} and Ω_o values to the equations, we obtain:

$$\textcircled{1}. 1.4686 D + 2.0 Q_E + L$$

$$\textcircled{2}. 0.6314 D + 2.0 Q_E$$

$$\textcircled{3}. 0.9314 D - 2.0 Q_E + L$$

$$\textcircled{4}. 1.1686 D - 2.0 Q_E$$

The integrated structural analysis and design software, SAP2000 [Computers and Structures 2009] was used in static analysis to check the stress state of the members and the deformation under the load combinations given above. Final member sizes in the exterior frame (Frame A) and interior frame (Frame B) in Y -direction are identified in Figure 3.71. The members are the same size as used for the test specimen. Note that square HSS braces were used in this analytical model. Under the given load combinations, the maximum member stress ratio occurred in the square HSS brace in the first story and was equal to 0.935. The maximum column stress ratio was 0.590 in the $W12 \times 96$ column in the same braced bay, as shown in Figure 3.72. The stress ratio in the $W12 \times 96$ columns were also checked using the amplified load combinations to make sure they essentially remained elastic. The maximum stress ratio under these amplified load combinations was 0.864. The amplified story drift at first story (1.54%) and second story (1.25%) were less than the 2% code limit.

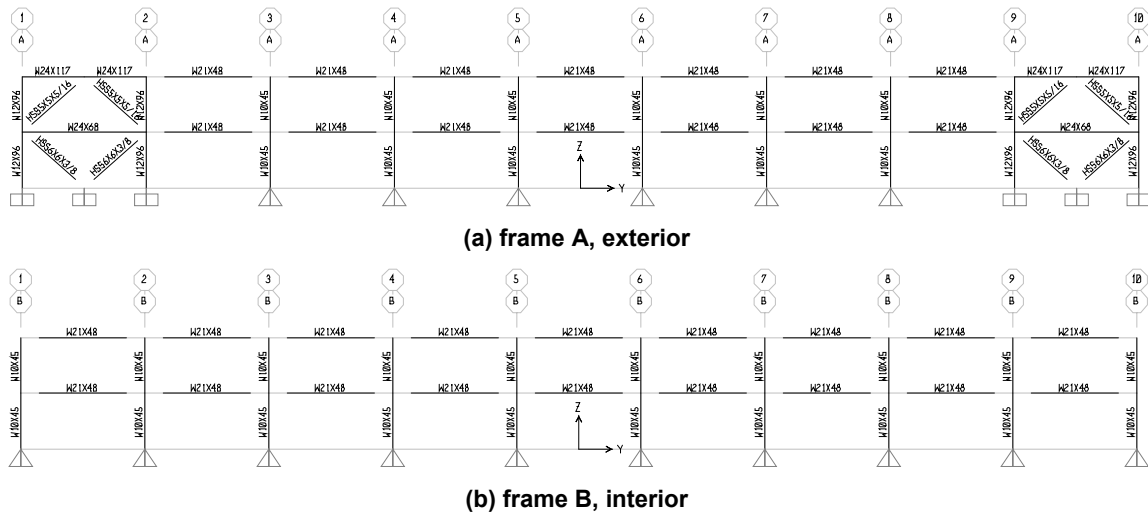


Figure 3.71 Typical member sizes distribution in Y -direction.

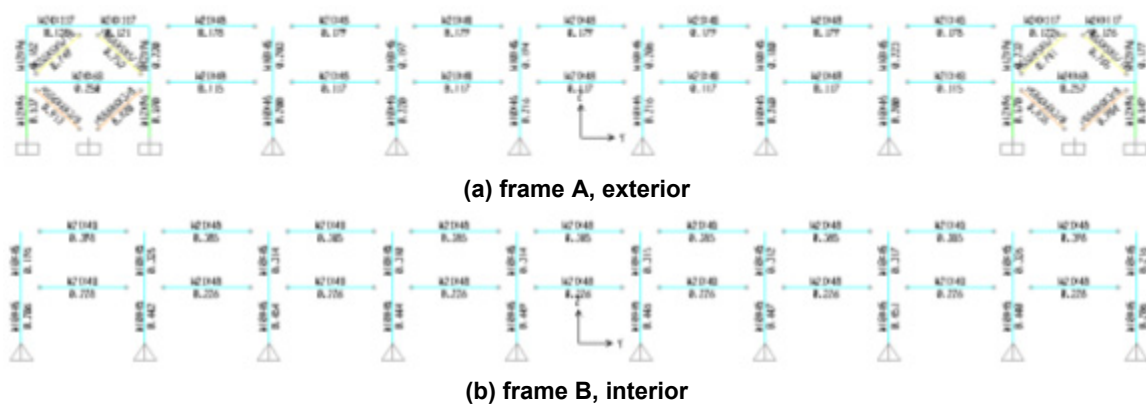


Figure 3.72 Member stress ratios distribution in Y-direction.

The computer model built in SAP2000 directly represents both Specimens TCBF-B-1 and TCBF-B-4 because diagonal braces were the same sizes and the same section shapes (square HSS). For Specimens TCBF-B-2 and TCBF-B-3, only brace section shapes and bracing member sizes changed while the beam and column sizes remained the same. The selections of bracing member size for these two specimens were performed in a customized Excel calculation spreadsheet. All required weld sizes and bolt sizes for connections in three specimens were calculated in the same Excel spreadsheet. Detail calculations are listed in Appendix H.

For the hybrid simulation, an input ground motion record is required. The ground motion selecting and scaling tool in the PEER Ground Motion Database was used (http://peer.berkeley.edu/peer_ground_motion_database/). To do this, values of S_{ds} , S_{d1} , and T_L were input to get the target spectrum, as shown in Figure 3.73. Next, the search criteria was entered, as shown in Figure 3.74, to find representative ground motions in the database.

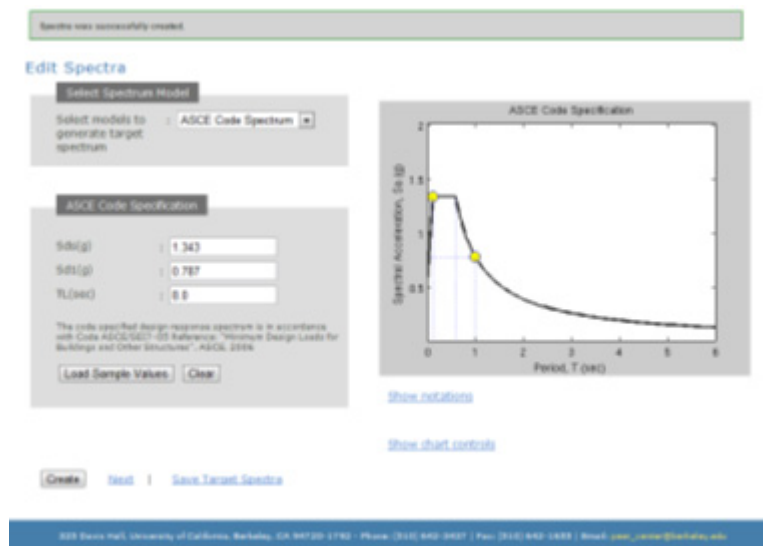


Figure 3.73 Target spectrum screenshot from the online ground motion selection tool on PEER website.

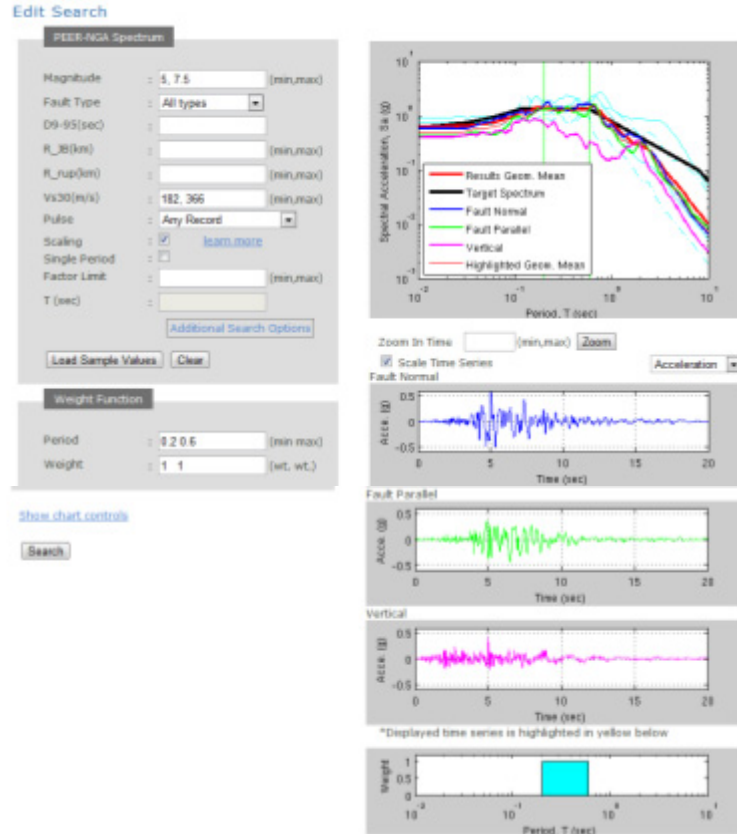


Figure 3.74 Screenshot of ground motion search interface.

Results

*Click on the record below to display Spectra and Time series

☒ Plot Selected

Result#	Comp.	NGA#	MSE	Scale#	Pulse	Tp(s)	DS-0.00	Event	Year	Station	Mag	Mechanism	Rb(km)
<input type="checkbox"/> 24	GM	1602	0.0052	0.9762	0.1	0.91	8.5	Duzce, Turkey	1999	Bolu	7.14	Strike-Slip	12.0
<input type="checkbox"/> 9	GM	558	0.0034	1.2348	0.0	---	7.0	Chalfant Valley-02	1986	Brothers Ranch	6.19	Strike-Slip	6.4
<input checked="" type="checkbox"/> 17	GM	960	0.0043	1.2545	0.0	---	6.1	Northridge-01	1994	Country - W. Lost Cañon	6.69	Reverse	13.4
<input checked="" type="checkbox"/> 29	GM	182	0.0054	2.0173	1.1	4.2	4.8	Imperial Valley-06	1979	Array #7	6.53	Strike-Slip	0.6
<input checked="" type="checkbox"/> 8	GM	614	0.0033	2.3551	0.0	---	4.1	Whittier Narrows-01	1987	Downey - Birchdale	5.99	Reverse-Oblique	14.9
<input type="checkbox"/> 3	GM	1736	0.0025	2.6564	0.0	---	2.7	Northridge-06	1994	Converter Sta	5.28	Reverse	[6.5]
<input type="checkbox"/> 12	GM	326	0.0037	4.7687	0.0	---	15.3	Coolinga-14.6	1983	Parkfield - Cholame ZWA	6.36	Reverse	43.8
<input type="checkbox"/> 30	GM	710	0.0055	6.0961	0.0	---	9.7	Whittier Narrows-02	1987	Inglewood - Union Oil	5.27	Reverse-Oblique	[22.0]
<input type="checkbox"/> 16	GM	3272	0.0042	8.2715	0.0	---	45.8	Chi-Chi, Taiwan-06	1999	Chi033	6.30	Reverse	72.9
<input type="checkbox"/> 19	GM	1782	0.0049	8.5936	0.0	---	15.9	Hector Mine	1999	Forest Falls Post Office	7.13	Strike-Slip	74.9

Figure 3.75 Snapshot of ground motion search results.

The search results are shown in Figure 3.75. Note that the records are ordered from smaller scale factors to larger scale factors. The scale factor of the ground motion was limited to be below 3.0. Finally, the NGA #960 (Northridge-01, 1994) ground motion record was selected as the input ground motion in hybrid simulation. Note that the V_{s30} value of the site where the ground motion was recorded also falls into the V_{s30} range listed in ASCE-7 for the site condition D. The scale factor for the selected ground motion to match the target spectrum is 1.3. Detail site information of the selected ground motion is listed in Table 3.6. The response spectrum of scaled

ground motions are shown in Figure 3.76 to compare with the design spectrum and the MCE spectrum. The original ground motion record and the scaled ground motions are plotted in Figure 3.77 for reference. Figure 3.78 illustrates the hybrid modeling concept used on Specimen TCBF-B-4. Only one-fourth of entire structure was modeled during the hybrid simulation.

Table 3.6 The site information of selected ground motion.

Earthquake Record Name	NGA #	PGA (g)	Magnitude	D_R (km)	Mechanism	V_{s30} (m/s)	Δt (sec)	Duration (sec)	Scale Factor
Northridge-01, 1994	960	0.396	6.69	12.4	Reverse	308.6	0.01	19.99	1.3

(Note that the PGA is from original unscaled ground motion)

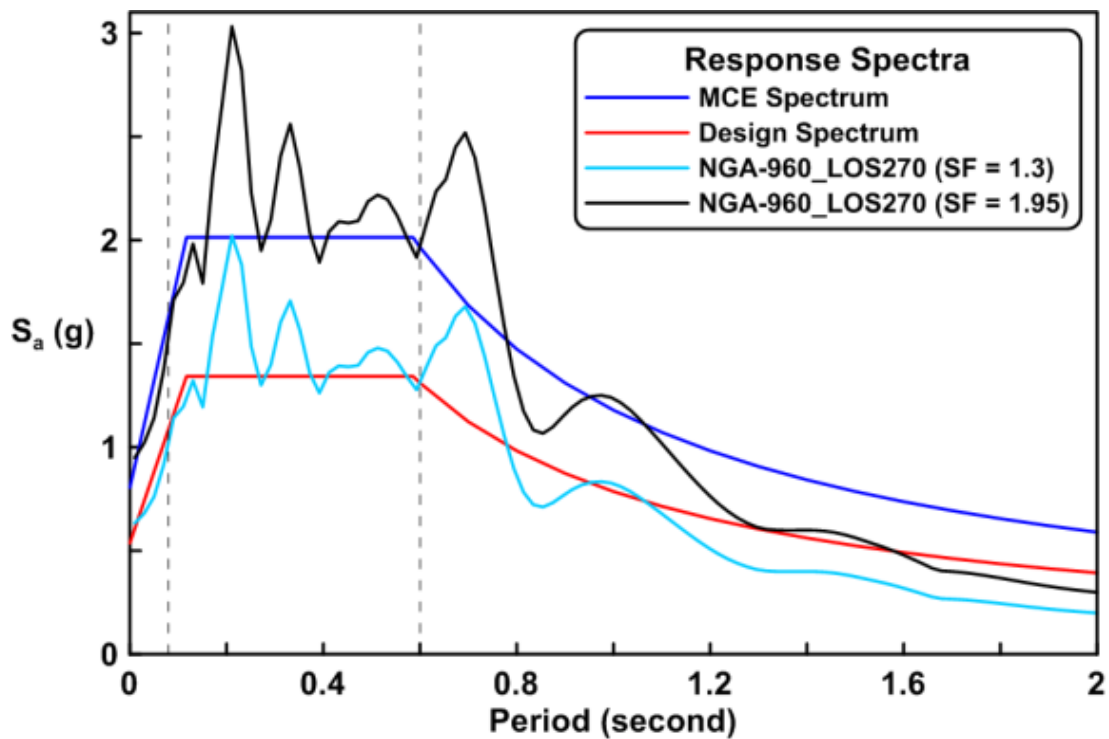


Figure 3.76 The elastic response spectrum of scaled ground motions mapping on design spectrum and MCE spectrum.

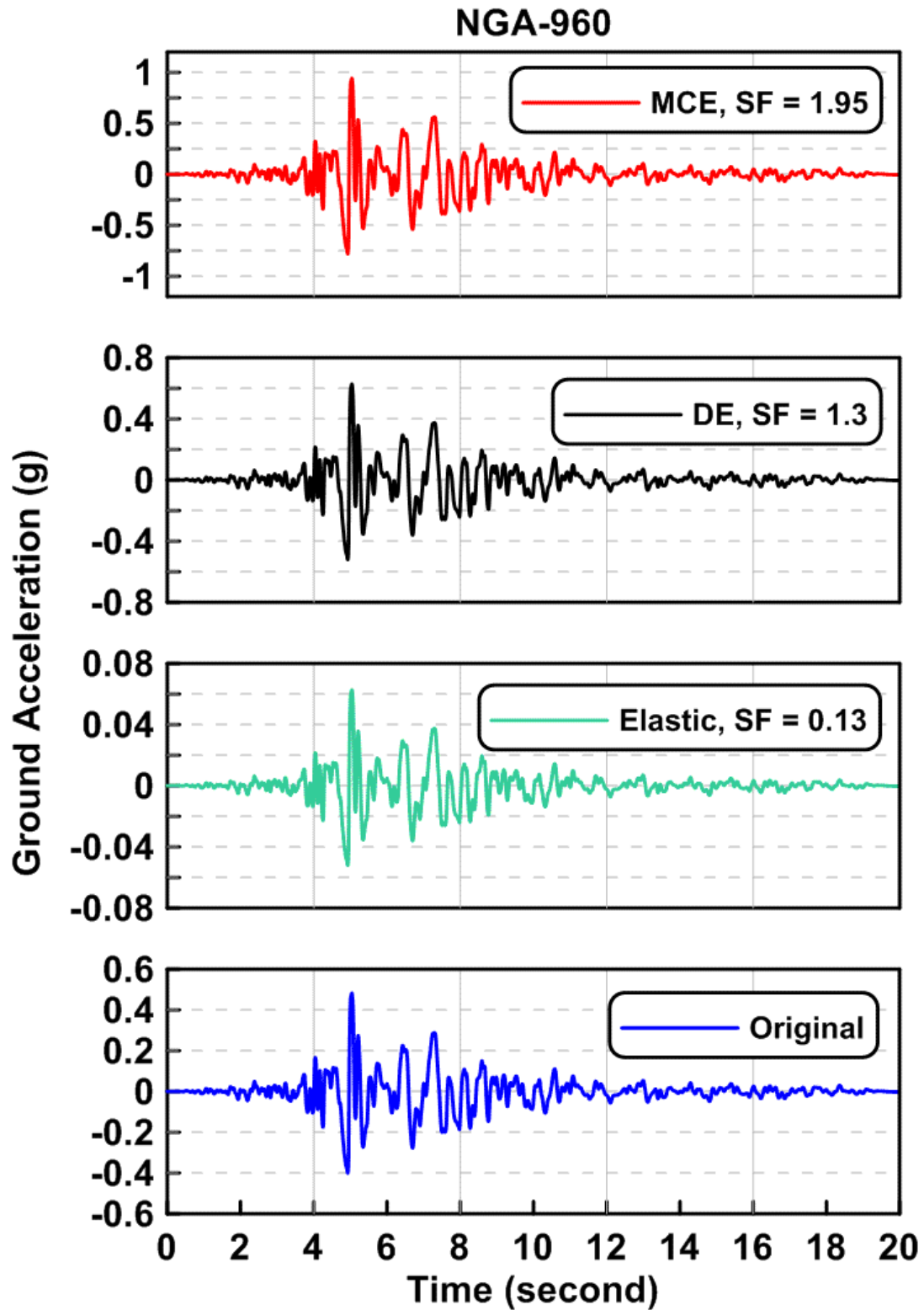


Figure 3.77 Original ground motion record and the scaled ground motions (NGA-960).

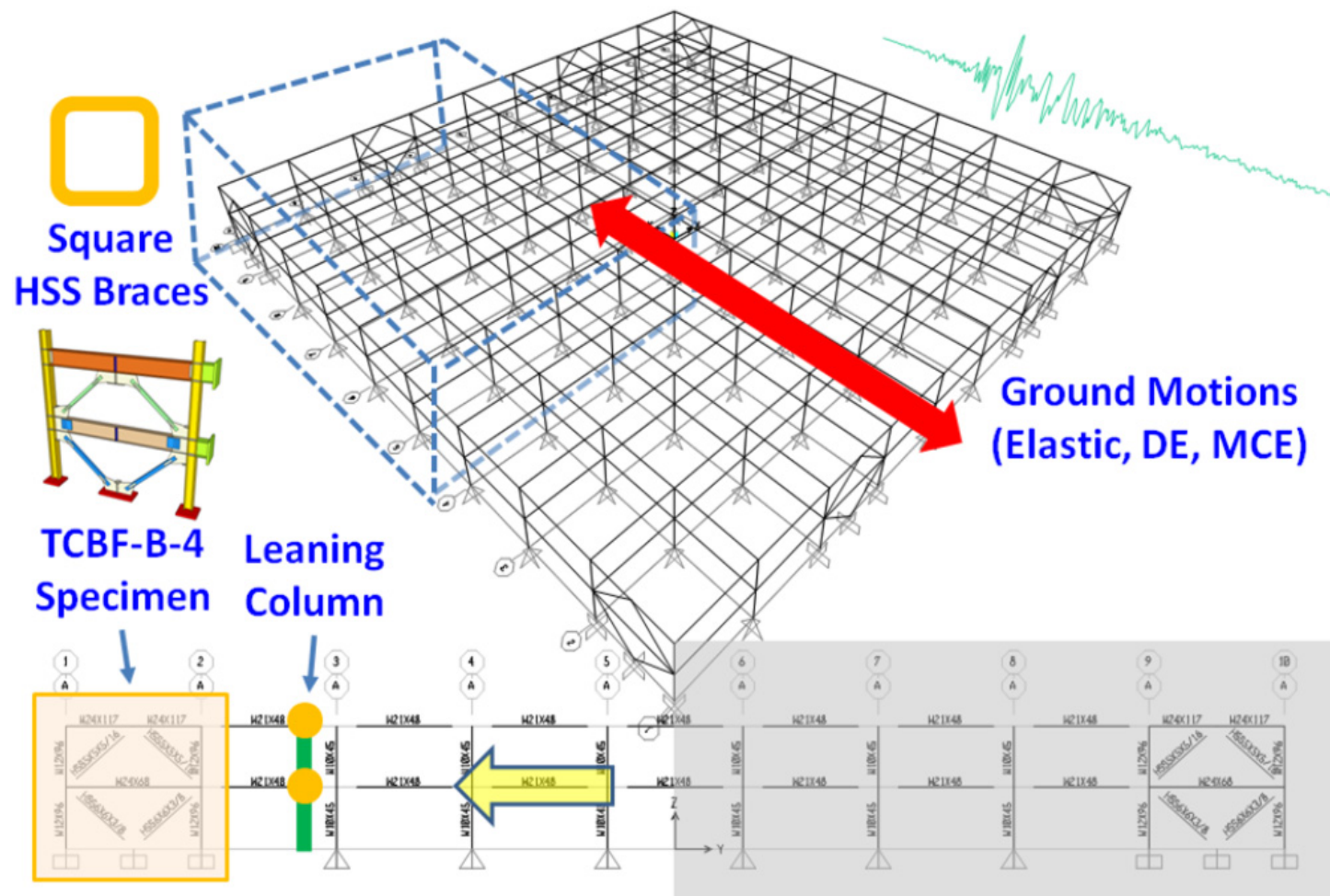


Figure 3.78 Specimen TCBF-B-4: hybrid modeling concept.

3.10 EXPERIMENTAL CONTROLS

3.10.1 Quasi-Static Tests

The displacement controlled actuator (roof level) was programmed to move with a constant velocity of 0.01 in./sec through the entire test. The Δt in the input binary file for MTS Structural Test System (STS) controller software was set equal to 1/64 sec. The sampling rate for the proportional–integral–derivative (PID) control loop in the STS controller was set to 1024 Hz. The persistence value was set to be equal to 0.0078 sec. The lower level actuator was force controlled and set to impose one half the load cell force feedback of the roof level actuator through settings for the “master-slave matrix” in the STS controller software. Actuator displacement and force interlocks were also specified in the software to prevent any damage to the actuators and the test set up in the event of larger than anticipated responses. Real-time XY plots showing selected instrument channel readings were displayed on four Panasonic plasma display screens in the control room through the Real-time Data Viewer (RDV) software provided by NEES [Daugherty et al. 2011].

3.10.2 Hybrid Simulation

The Open-Source Framework for Experimental Set up and Control, OpenFresco [Schellenberg et al. 2009], was used for hybrid control and OpenSees was used for structural analysis during the hybrid simulation. Figure 3.79 illustrates experimental control concepts and the corresponding abstract components of the OpenFresco software architecture. Detailed OpenFresco software architecture discussions can be found in the report by Schellenberg et al. [2009].

One Simulink model (HybridControllerD3D3_Vconst_rec100Hz.mdl) and two tcl files (server.tcl and client.tcl) were prepared for the hybrid simulation. The Simulink model was built and uploaded to xPC target and the model utilized displacements for prediction and correction. Integration time step was set to 0.005 sec in the Simulink model. In the server.tcl file, the xPCtarget experimental control was specified through OpenFresco expControl command. No transformation was defined in this hybrid test. Actor experimental site was defined in this tcl file.

As mentioned before, only one-fourth of entire prototype building was modeled during the hybrid test. A two-story physical specimen was built in the laboratory and a substructure was defined in OpenSees tcl file. In this client.tcl file, two generic experimental elements (1-DOF), two rigid-link trusses, and a leaning column were defined (Figure 3.79). P- Δ effects were considered through introducing a leaning column in the OpenSees model. The section properties of the leaning column were derived from the gravity columns using the following equations.

$$A_{\text{leaning column}} = \sum_i A_{\text{gravity columns}} \quad (3.18)$$

$$I_{leaning\ column} = \sum_j I_{gravity\ columns} \quad (3.19)$$

Lump floor mass and concentrated point loads from gravity forces were assigned at the nodes of leaning column at each floor level as illustrated in Figures 3.78 and 3.79. Pinned boundary condition was assigned at the base of leaning column in OpenSees model. Rayleigh damping parameters were set be equal to 0.01 for mode one and 0.02 for mode two in the OpenSees model. Newmark method for hybrid simulation with fixed number of iteration was used. The γ factor and β factor in the Newmark integrator object were set to 0.5 and 0.25 (average acceleration method), respectively. The number of iterations was set to 10, and the analysis time step was set to 0.01 sec. Shadow experimental site was defined in the client.tcl file.

Both actuators were displacement controlled and the actuator speed (displacement rate) was selected as 0.002 in./sec during the hybrid simulation. Similar to the settings used in the quasi-static tests, the sampling rate for the PID control loop in STS controller was set to 1024 Hz. The persistence value was set to be equal to 0.0078 sec, the same as previous specimens. Actuator displacement and force interlocks were also specified in the STS software to prevent any possible damage to the actuators and the test set up. Real-time *XY* plots, selected instrument channel readings, and specimen overview were displayed on four Panasonic plasma display screens in the control room. The RDV software was not used in the hybrid test.

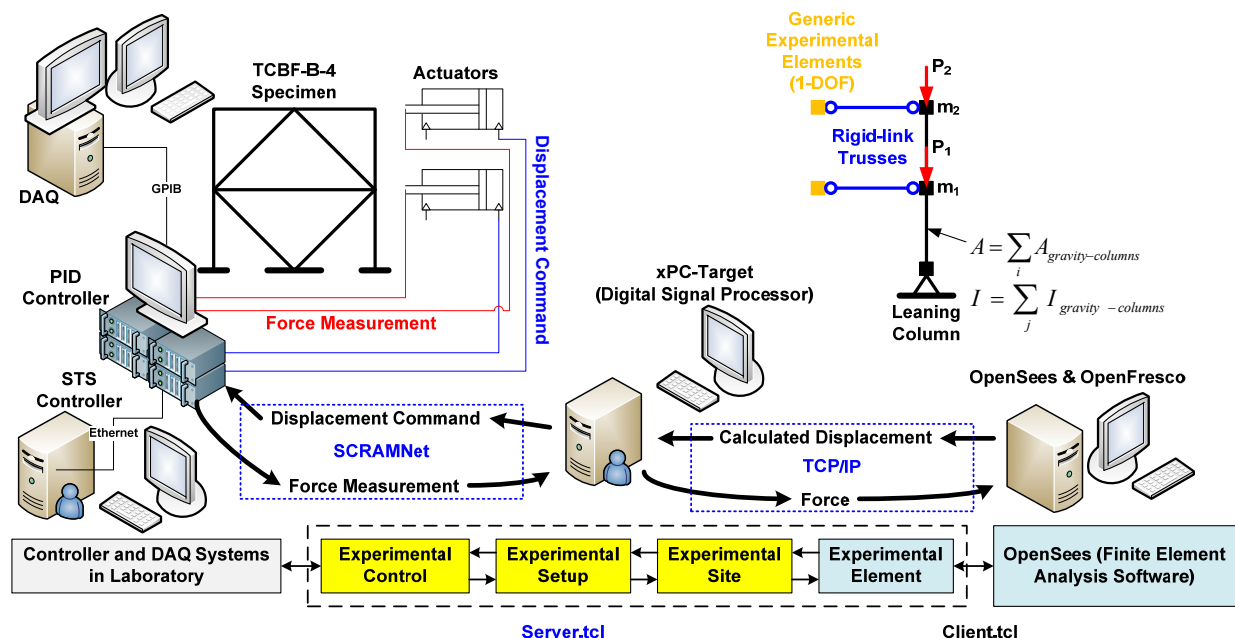


Figure 3.79 Experimental control of hybrid simulation.

3.11 MATERIAL PROPERTIES

All wide flange beams, wide flange columns and wide flange braces in the specimens were ASTM A992 steel sections. All braces using hollow structural sections (HSS) were ASTM A500 Grade B steel tubes for both square and round sections. The 3/4-in.-thick gusset plates, 2-in.-thick base plates, 2-in. stub beam end plates, 1/2-in. shear tabs, 5/8-in. finger plates, 5/8-in. continuity plates, 3/8-in. washer plates for all-thread anchor rods, and brace reinforcing cover plates were made of ASTM A572 Grade 50 steel plates. The beam web stiffener plates, lifting lugs, shim plates, and miscellaneous parts were made of ASTM A36 steel plates. High strength structural fasteners that satisfy the ASTM A490 standard were used at beam-column connections and one-piece gusset plate-to-beam splices. All-thread high-strength anchor bolts (ASTM A193 Grade B7) were used at column base plates and a gusset-to-floor-beam base plate.

Steel tensile test coupons were sampled during the shop fabrication process, as shown from Figures 3.80 to 3.83. The material tensile test results extracted from the mill certificates are summarized in Table 3.7. The original mill certificates from steel fabricators are reproduced in Appendix I.



Figure 3.80 Torch cutting the steel coupon from wide flange section.



Figure 3.81 Torch cutting the steel coupon from HSS section.



Figure 3.82 Specimen TCBF-B-1: steel coupons.



Figure 3.83 Specimens TCBF-B-2, TCBF-B-3, and TCBF-B-4: steel coupons.

Table 3.7 Material mechanical properties from mill certificates.

Description	Heating Number	Yield Strength F_y (psi)	Tensile Strength F_u (psi)	Yield to Tensile Ratio	Elongation (%)
W24 \times 117 ^(1, 2)	30406710	52,400	68,500	0.76	25.3
W24 \times 117 ^(3, 4)	30424590	51,850	71,350	0.73	24.6
W24 \times 68 ⁽¹⁾	22477490	53,100	71,750	0.74	25.6
W24 \times 68 ^(2, 3, 4)	316424	57,000	74,000	0.77	25
W12 \times 96 ^(1, 2)	313889	57,500	74,500	0.77	26.5
W12 \times 96 ^(3, 4)	338703	55,500	72,500	0.77	25.5
3/4 in. plate ⁽¹⁾	M8G153	58,000	71,000	0.82	26
3/4 in. plate ^(2, 3, 4)	284241	65,049	78,683	0.83	18
HSS 6 \times 6 \times 3/8 ⁽¹⁾	H080304	46,397	66,986	0.69	28
HSS 5 \times 5 \times 5/16 ⁽¹⁾	F3979	56,000	68,100	0.82	37
HSS 6 \times 0.5 ⁽²⁾	53786048	68,100	77,600	0.88	33
HSS 5 \times 0.5 ⁽²⁾	T82669	65,881	72,580	0.91	33.1
W8 \times 28 ⁽³⁾	291731	54,000	73,000	0.74	25
W8 \times 21 ⁽³⁾	207071031	54,027	78,320	0.69	33
HSS 6 \times 6 \times 3/8 ⁽⁴⁾	L1084	58,710	69,163	0.85	37
HSS 5 \times 5 \times 5/16 ⁽⁴⁾	23021M08	61,970	72,264	0.86	35
1/2 in. splice plate ^(3, 4)	B7J635	59,000	76,000	0.78	36
2 in. base plate ^(3, 4)	0500464	58,450	84,350	0.69	17.5
5/8 in. plate ^(3, 4)	M13742	56,500	70,500	0.80	24.5
7/8 in. plate ^(3, 4)	1W380	67,000	95,000	0.71	23
1-1/8-7 \times 9 in. rod	225082	133,000	146,000	0.91	22
3/8 in. washer plate	254334	56,700	76,600	0.74	32
7/8-9 \times 3 in. bolt	NU844781	-	161,508	-	-
7/8-9 \times 2-1/2 in. bolt	NU844781	-	164,351	-	-
7/8-9 \times 2-3/4 in. bolt	IN391612	-	165,138	-	-

(Note: the numbers in the small bracket indicate the specimen number, for example, 1 indicates the Specimen TCBF-B-1, etc.)

4 Experimental Results of Four Specimens

4.1 QUASI-STATIC TEST RESULTS OF FIRST THREE SPECIMENS

For first three experiments, more than two hundred instrumentation points were monitored and recorded through the entire test process. Numerous photos and videos were also taken. The measured time history and hysteretic loops provided valuable data to compare the behavior of the specimens. The following subsections discuss the test results and describe the main observations for each cyclically tested specimen.

4.1.1 Specimen TCBF-B-1 (Square HSS Braces)

The test started at around 1:06 PM on Sunday, August 9, 2009. Before initiating the pre-defined loading, two complete cycles of 0.15 in. (about 25% yield roof displacement) peak roof displacement were imposed to check all instrument readings and the actuator control algorithms in the MTS Structural Test System. The side views of the entire specimen from the north-west side of the lab before and after test are shown in Figure 4.1.



(a) before test



(b) after test

Figure 4.1 Specimen TCBF-B-1: side view.

4.1.1.1 Main Observations

As illustrated in the pre-defined loading protocol (see Figure 3.28), the experiment process was divided into several sets of loading steps (amplitudes or phases). Every loading step contained two complete cycles except that the first loading step ($0.5D_{be}$) contained six complete cycles. Detailed information about each of these cycles is described sequentially below. Some key observations are illustrated on the testing protocol and listed with brief descriptions in Table 4.1.

$\Delta = 0.5 D_{be} = 0.2$ in. (Roof Drift $\delta = 0.1$ %), from 1:06 PM to 1:14 PM

The test began at 1:06 PM after two small cycles were completed, and all instrument readings were carefully checked. During this loading amplitude, the entire frame remained elastic. No special findings were found anywhere through this loading step.

$\Delta = 1.0 D_{be} = 0.4$ in. (Roof Drift $\delta = 0.2$ %), from 1:14 PM to 1:19 PM

Very minor yielding (determined from visible flaking of whitewash) was noted near the tip of fillet welds at the brace-to-gusset plate connection at first-story gusset plate, as illustrated in Figure 4.2.

$\Delta = 1.0$ D_{by} = 0.6 in. (Roof Drift $\delta = 0.3\%$), from 1:19 PM to 1:27 PM

Some local flaking of whitewash developed near the beginning of 30° tapered region of gusset plate at first story (Figure 4.3).

$\Delta = 0.5$ D_{bm} = 1.0 in. (Roof Drift $\delta = 0.5\%$), from 1:27 PM to 1:40 PM

At the beginning of the first half-cycle of the loading step, some local flaking of the whitewash developed near the backing bar on the bottom flange of middle beam at eastern side (Figure 4.4). Additional flaking of the whitewash in the top and bottom flanges was found near the backing bar at both sides of lower beam. Some local flaking of whitewash developed near the 30° tapered region of eastern gusset plate at the second story [Figure 4.5(a)]. The braces at both stories started global buckling (all out-of-plane to the north), and the whitewash on braces began flaking [Figure 4.5(b)]. Additional flaking developed on the gusset plates.

$\Delta = 1.0$ D_{bm} = 2.0 in. (Roof Drift $\delta = 0.9\%$), from 1:40 PM to 2:07 PM

At the beginning of the first half-cycle of this loading step, some flaking of whitewash developed on the one-piece gusset plate near gusset-to-column flange welds at eastern side and the lower beam web closed to the shear tab (Figure 4.6). Additional flaking developed in panel zone area and the $2t$ gap region on the gusset plates. Minor yielding was noted in the column flanges near the base plates (Figure 4.7).

$\Delta = 1.5$ D_{bm} = 3.0 in. (Roof Drift $\delta = 1.4\%$), from 2:07 PM to 2:47 PM

Near the end of the first half-cycle of this loading step, the top flange and web of lower beam at western side began localized buckling (Figure 4.8). Local buckling of section walls was also found at the middle portion of the brace (Figure 4.9). Additional flaking of whitewash developed on the gusset plate $2t$ gap fold region. The bottom flange and web of lower beam at eastern side began localized buckling (Figure 4.10). The lower beam formed plastic hinges at both ends. Additional flaking of whitewash developed on the column flanges near the base plate. At the beginning of the third half-cycle of the loading step, lots of flaking of whitewash occurred on lower story column flanges near gusset plate stiffener plates, as shown in Figure 4.11.

$\Delta = 2.0$ D_{bm} = 4.0 in. (Roof Drift $\delta = 1.9\%$), from 2:47 PM to 3:40 PM

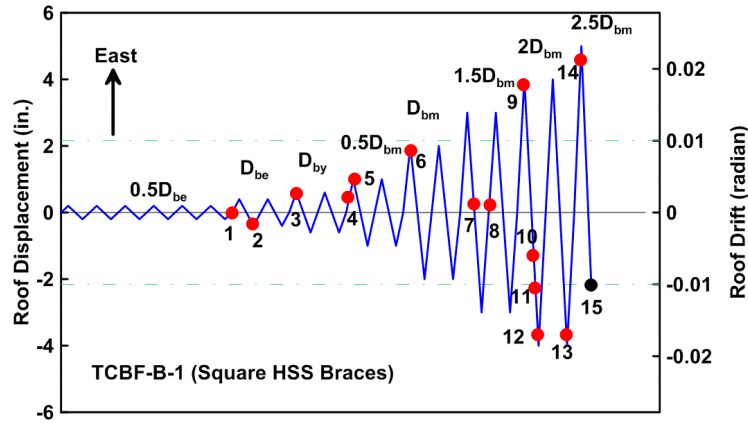
Near the peak displacement of the loading step in the first half-cycle, cracks initiated in the outside corners of HSS brace section at first story for both braces (see Figures 4.12 and 4.13). When the specimen moved across zero roof displacement and continued moving to the west, the cracks in the first-story western brace propagated from the outside corners to the center of the HSS brace section during the second half-cycle of the load step as shown in Figure 4.14. At around negative 2-in. roof displacement, a lot of flaking of whitewash occurred on the web of western and eastern columns at the first story (Figure 4.15). The western brace at ground story completely fractured during the first half-cycle of loading to a roof displacement of 3.8 in. to the west (Figure 4.16). The eastern brace at the ground story had cracks on the outside corner of the HSS section around the middle portion of the brace but did not completely fracture. Crack initiated at the outside corner of HSS brace section at second story for both braces. The bottom

flange at eastern side of lower beam fractured at the CJP weld line during the second cycle of this load step at roof displacement about 3.8 in. to the west (Figure 4.17).

$\Delta = 2.5 D_{bm} = 5.0$ in. (Roof Drift $\delta = 2.3\%$), from 3:40 PM to 4:02 PM

The eastern brace at first story completely fractured during the first cycle of $2.5D_{bm}$ load step at a roof displacement corresponding to 4.7 in. to the east (Figure 4.18). The cracks in the second-story eastern brace propagated from outside corners to the center of the HSS brace section during the first cycle of $2.5D_{bm}$ load step (Figure 4.19) but did not completely fracture. The test was manually stopped (the yellow button of controller was pressed) at about 2.2 in. of roof displacement to the west (so that the specimen could be unloaded to about zero lateral displacement) after unloading the entire specimen. The entire side view of the specimen after test is shown in Figure 4.20.

Table 4.1 Specimen TCBF-B-1: major observations noted during test.



1	No special findings through this loading step.
2	Very minor yielding (via. flaking of whitewash) was noted near the tip of fillet welds at brace-to-gusset connection at first-story gusset plate.
3	Some local flaking of whitewash developed near the beginning of the 30° tapered region of gusset plates at first story.
4	Some local flaking of whitewash developed near the backing bar on the bottom flange of middle beam at eastern side.
5	Some local flaking of whitewash developed near the 30° tapered region of eastern gusset plate at second story. The braces at both story start global buckling and the whitewash on braces start flaking (all out-of-plane to the north side). Additional flaking develops on the gusset plates.
6	Some flaking of whitewash developed on the one-piece gusset plate near gusset-to-column flange welds at eastern side and the lower beam web closed to the shear tab. Additional flaking developed in panel zone area, and the $2t$ gap region on the gusset plates. Minor yielding was noted in the column flanges near the base plates.
7	The top flange and web of lower beam at western side start local buckling (Figure 4.8). The braces start local buckling at the middle portion of the brace. Additional flaking of whitewash developed on the gusset plate $2t$ gap fold region. The bottom flange and web of lower beam at eastern side start local buckling. The lower beam formed plastic hinges at both ends. Additional flaking of whitewash developed on the column flanges near base plate.
8	Lots of flaking of whitewash occurred on lower story column flanges near gusset plate stiffener plates.
9	Crack initiated in the outside corner of HSS brace section at first story for both braces.
10	The cracks in the first-story western brace propagated from outside corners to the center of the HSS brace section during the first cycle of the load step (Figure 4.14).
11	Lots of flaking of whitewash occurred on the web of western and eastern columns at the first story.
12	The western brace at ground story completely fractured during the first half-cycle of loading to a roof displacement of 3.8 in. to the west. The eastern brace at the ground story has cracks on the outside corner of the HSS section around the middle portion of the brace but did not completely fracture. Crack initiated at the outside corner of HSS brace section at second story for both braces.
13	The bottom flange at eastern side of lower beam fractured at the CJP weld line during the second cycle of $2.0 D_{bm}$ load step at roof displacement about 3.8 in. to the west (Figure 4.17).
14	The eastern brace at first story completely fractured during the first cycle of $2.5 D_{bm}$ load step at roof displacement corresponded to 4.7 in. to the east (Figure 4.18).
15	The cracks in the second-story eastern brace propagated from outside corners to the center of the HSS brace section during the first cycle of $2.5 D_{bm}$ load step. Test stopped at about 2.2 in. of roof displacement to the west (to have specimen unload to about zero lateral displacement).

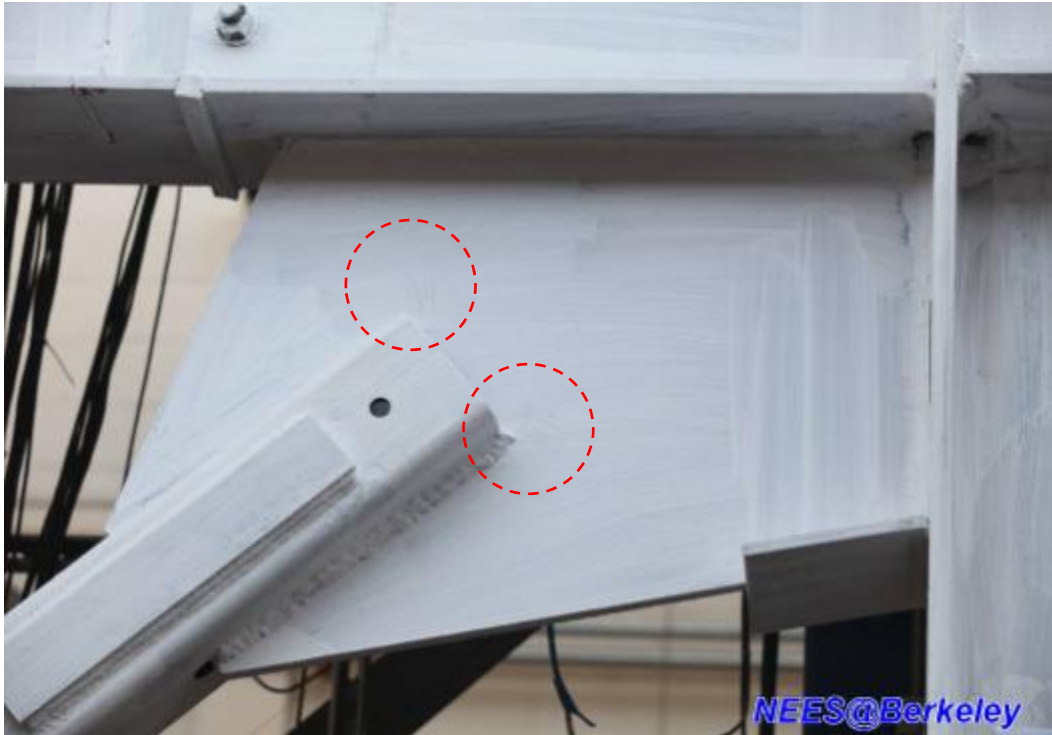


Figure 4.2 Specimen TCBF-B-1: western side of the first-story upper gusset plate.

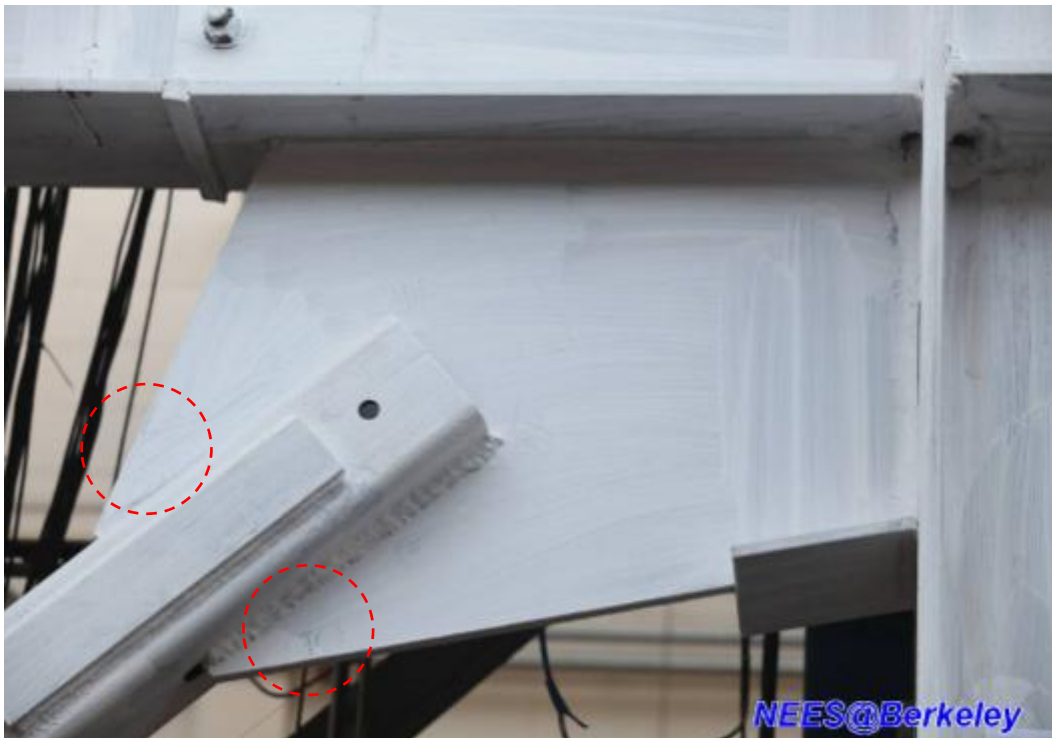


Figure 4.3 Specimen TCBF-B-1: western side of the first-story upper gusset plate.



Figure 4.4 Specimen TCBF-B-1: bottom flange of east-side lower beam.



Figure 4.5(a) Specimen TCBF-B-1: flaking of whitewash at second-story gusset plate.



Figure 4.5(b) Specimen TCBF-B-1: flaking of whitewash at the middle length of braces.

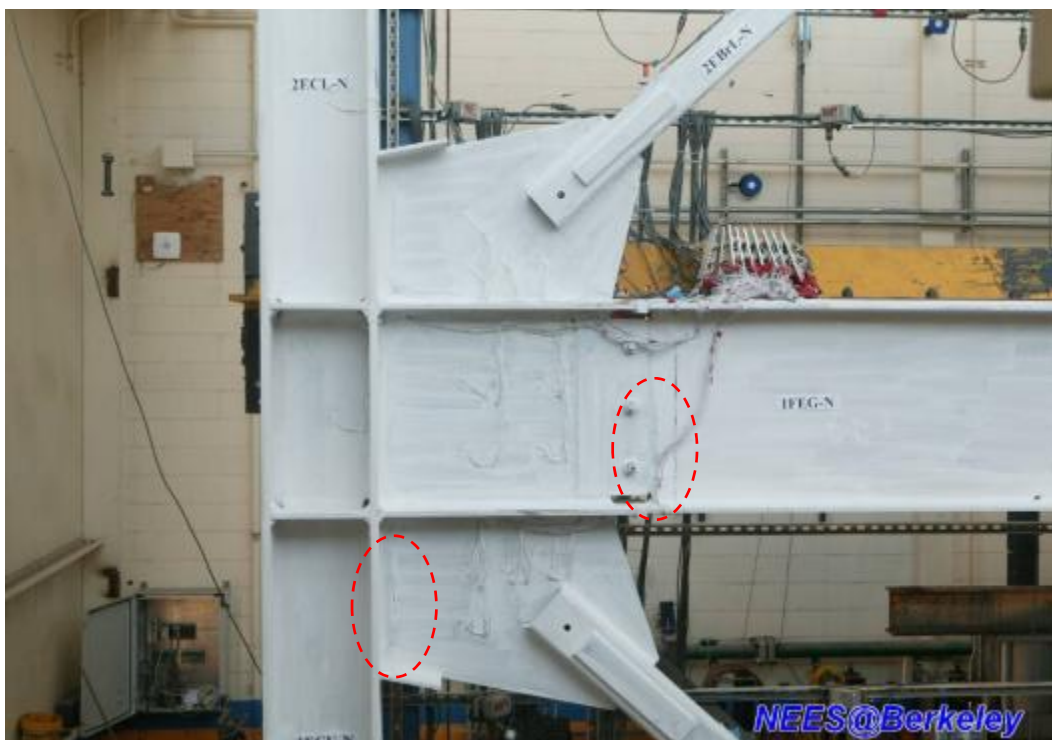


Figure 4.6 Specimen TCBF-B-1: eastern-side, one-piece gusset plate.



Figure 4.7 Specimen TCBF-B-1: western-side, column base.



Figure 4.8 Specimen TCBF-B-1: western-side lower beam-to-gusset plate splice.

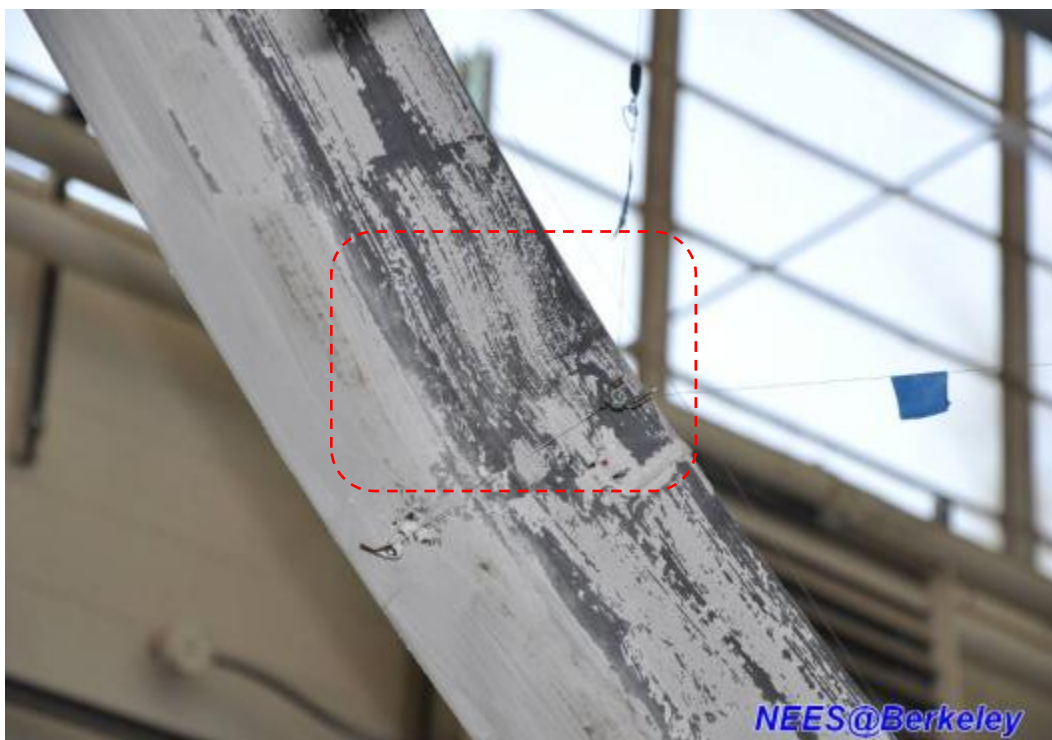


Figure 4.9 Specimen TCBF-B-1: middle portion of first-story western-side HSS brace.



Figure 4.10 Specimen TCBF-B-1: eastern-side lower beam-to-gusset plate splice.



Figure 4.11 Specimen TCBF-B-1: eastern-side gusset plate-to-column connection.

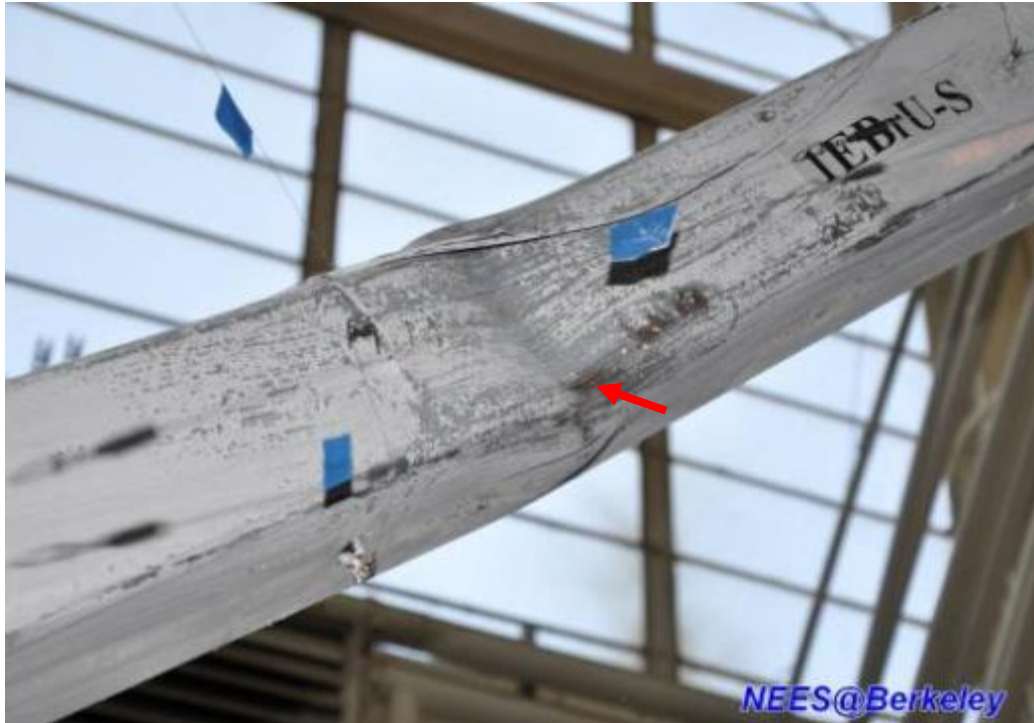


Figure 4.12 Specimen TCBF-B-1: first-story eastern-side square HSS brace.



Figure 4.13 Specimen TCBF-B-1: first-story western-side square HSS brace.

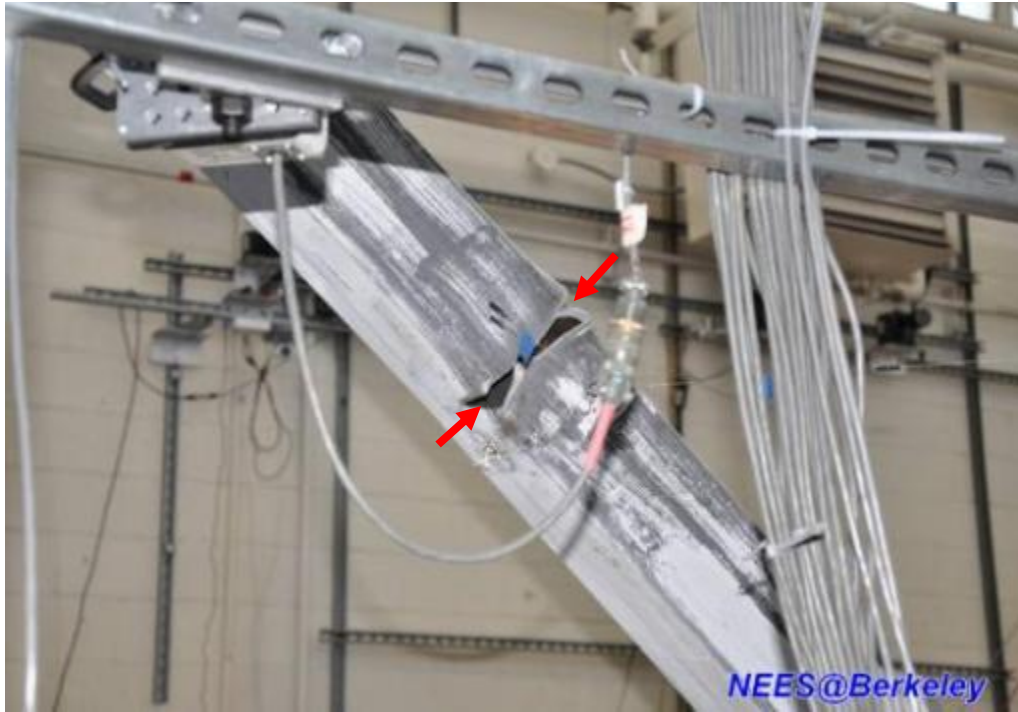


Figure 4.14 Specimen TCBF-B-1: crack propagation in the first-story western-side square HSS brace.



Figure 4.15 Specimen TCBF-B-1: flaking of whitewash on eastern-side column web.



Figure 4.16 Specimen TCBF-B-1: first-story square HSS braces.

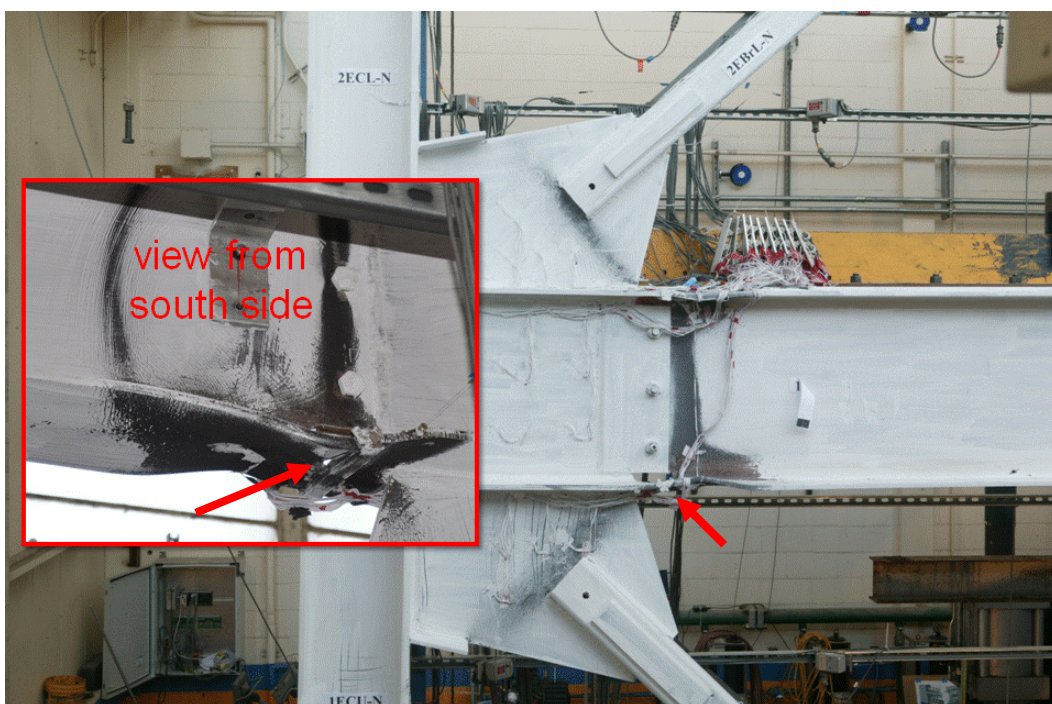


Figure 4.17 Specimen TCBF-B-1: eastern-side gusset-to-beam splice.



Figure 4.18 Specimen TCBF-B-1: complete fracture of first-story eastern-side square HSS brace.

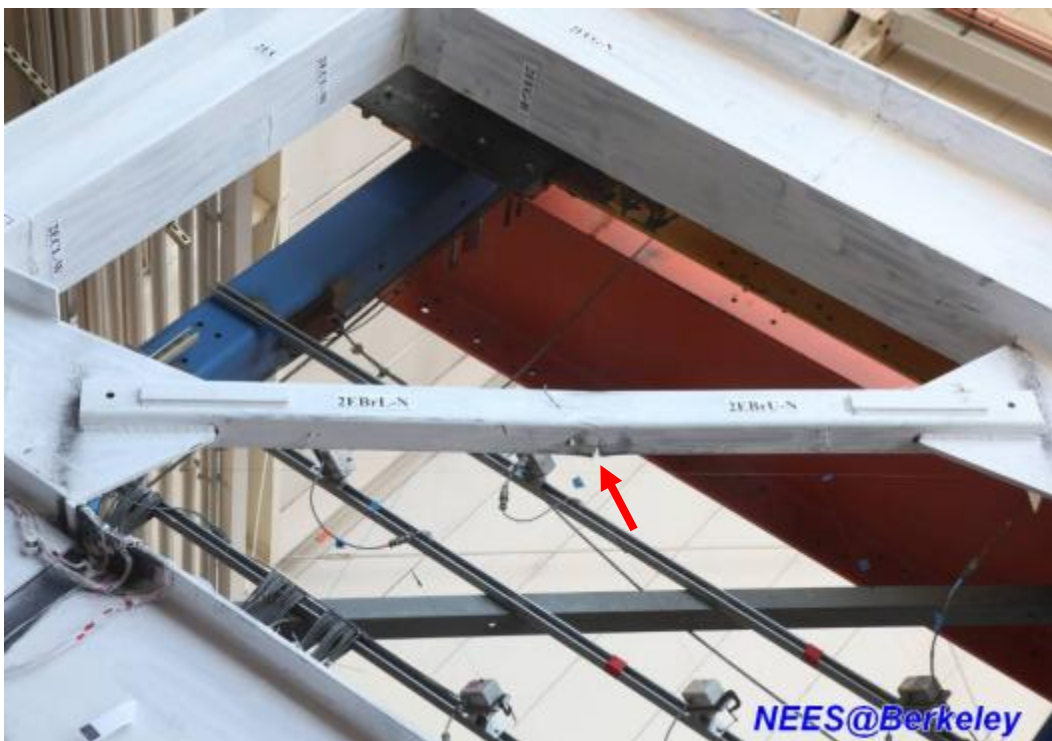


Figure 4.19 Specimen TCBF-B-1: crack propagation in the second-story eastern side square HSS brace.



Figure 4.20 Specimen TCBF-B-1 after test (view from north side fisheye lens).

4.1.1.2 Key Response Quantities

Following paragraphs briefly describe the response quantities recorded during the experiments and the post-processed response quantities derived from the raw data. Detailed interpretations of individual response quantities are described in Chapter 5. Locations of strain gauges can be found in Appendix D.

4.1.1.2.1 System Global Response

Figures 4.21 and 4.22 show two actuators displacement histories and two actuators load cell force feedback histories for Specimen TCBF-B-1. A hysteresis plot of the base shear versus controlled roof displacement is shown in Figure 4.23. The corresponding relationships between story shear and story drift for the specimen are shown in Figure 4.24.

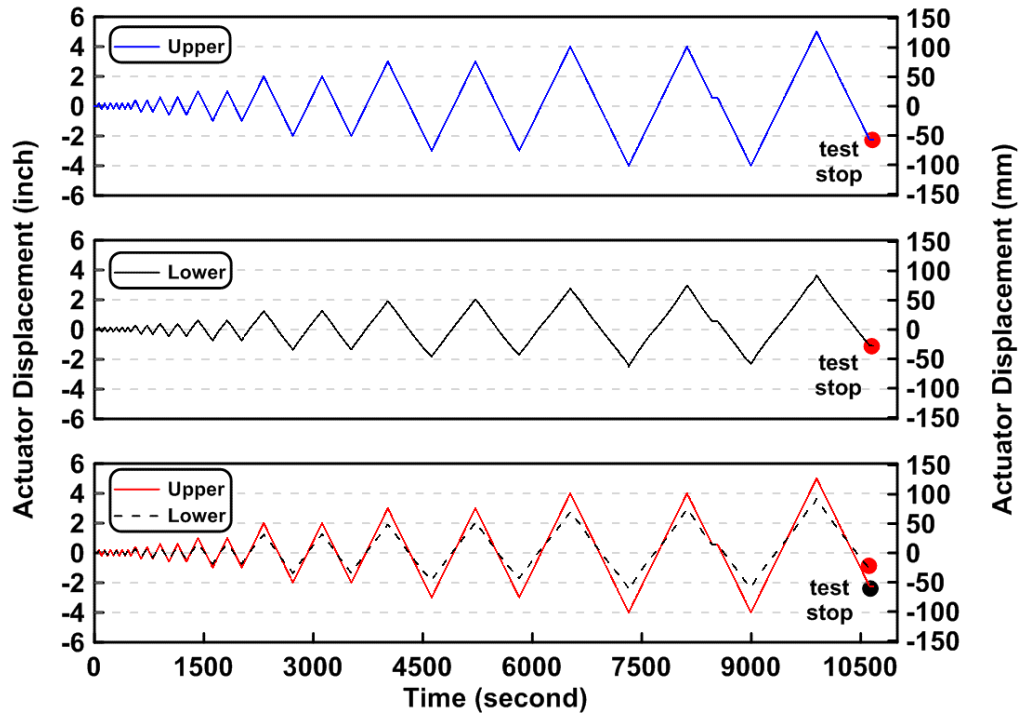


Figure 4.21 Specimen TCBF-B-1: actuator displacement histories.

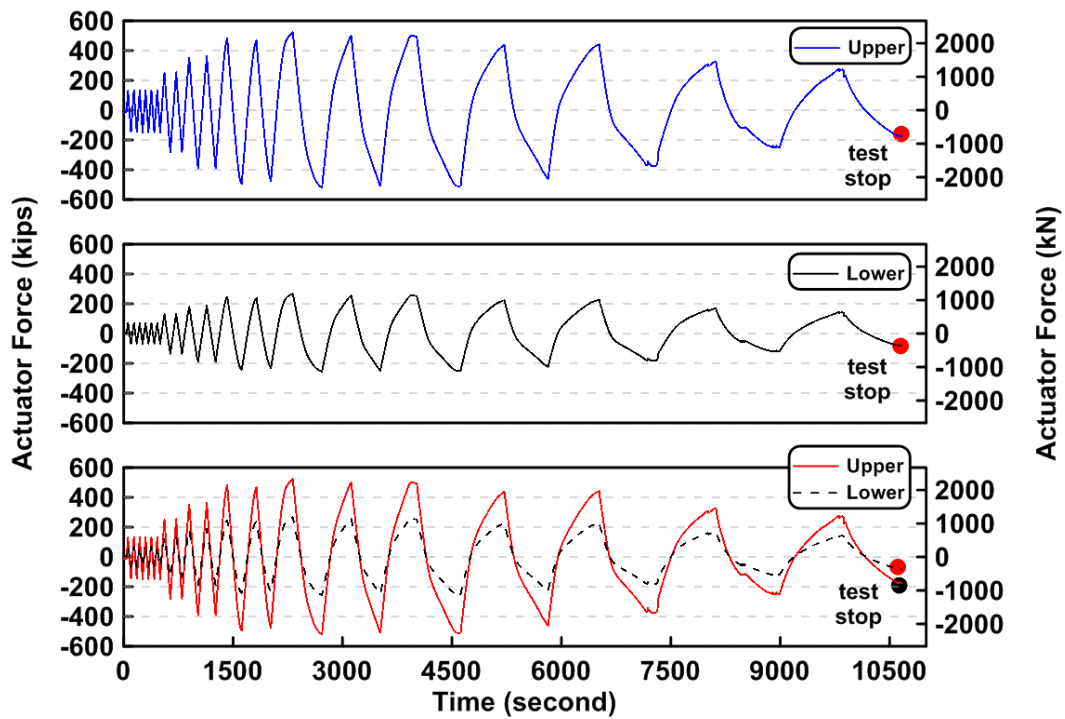


Figure 4.22 Specimen TCBF-B-1: actuator force histories.

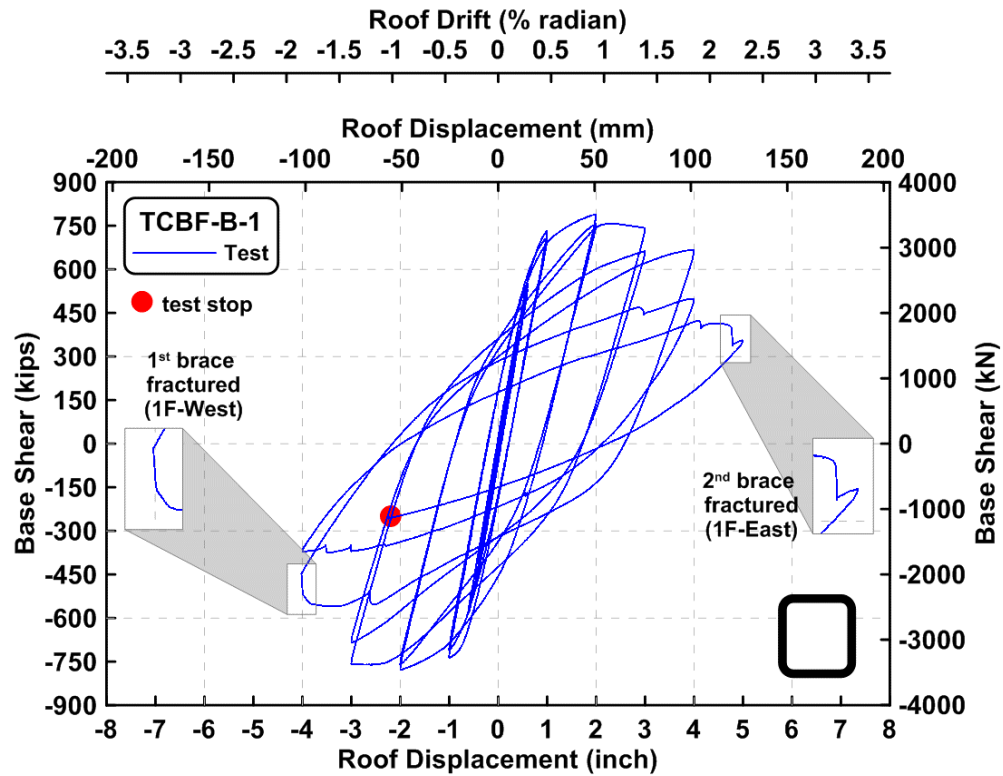


Figure 4.23 Specimen TCBF-B-1: base shear versus roof displacement relationship.

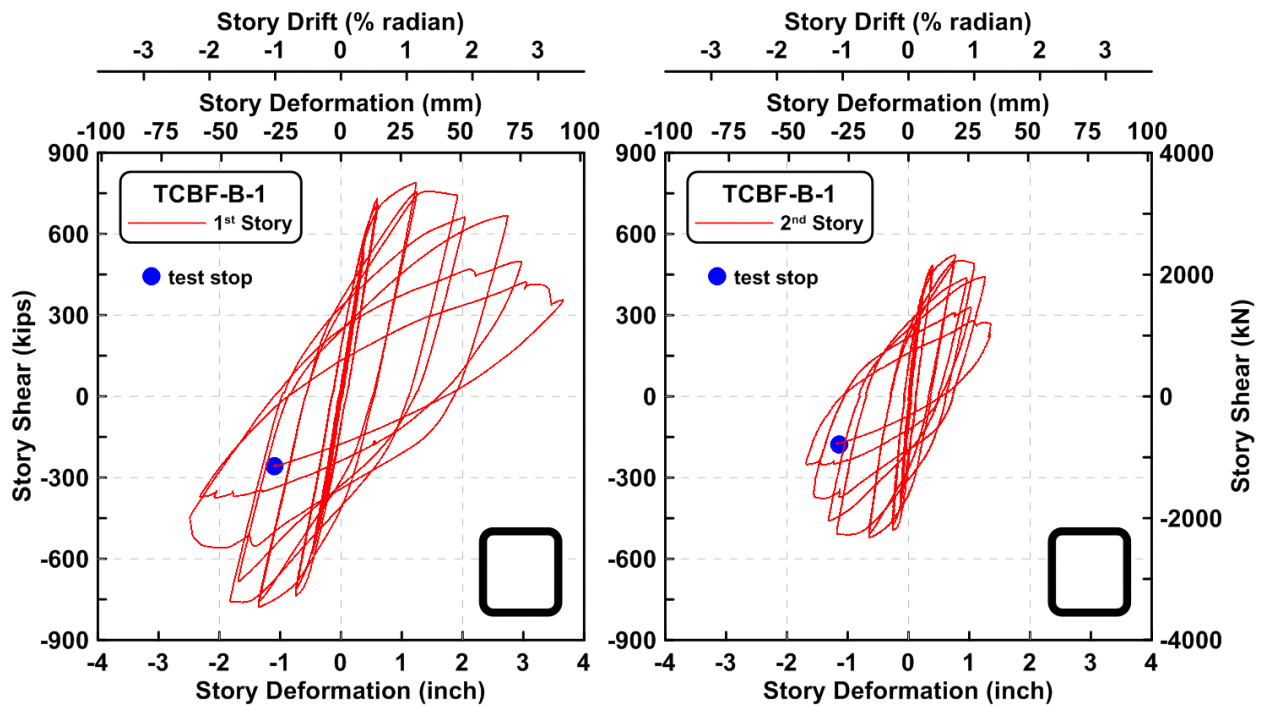


Figure 4.24 Specimen TCBF-B-1: story shear versus story deformation relationship.

4.1.1.2.2 Column Response

The time history of the axial forces in the first story W12 \times 96 columns at the western and eastern sides of the specimen is plotted in Figure 4.25. These are derived from strain gauge readings on the columns. Figure 4.26 shows the relationship between roof displacements and axial forces at both columns. The bending moment time history at the top and bottom ends of the column in each story are presented in Figures 4.27 and 4.28. The moments drift with time as a result of the unequal distribution of drifts in the upper and lower stories. Derived column shear force time history in both stories are plotted in the Figures 4.29 and 4.30, respectively. Two column shear forces in each floor were added together as shown in Figure 4.31. These are nearly identical during the first half of the test. The column web shear stress versus shear strain readings from strain rosettes are plotted in Figure 4.32. It appears that web of the east column in the bottom story yields. Figure 4.33 shows the sum of the column shear force components versus the total story shear forces for each story. This slope of the graphs on these plots indicates that the braces take a much larger portion of the total base shear during early cycles with relatively small displacement amplitudes and a smaller portion during subsequent cycles where the braces have suffered various forms of damage. The derived rosette-type strain gauge readings in the column web at each story are shown in Figures 4.34 to 4.37. Normalized maximum and minimum principal stress relationships along with different yield criteria are plotted in Figures 4.38 to 4.41. The normalized P-M and P-V interaction diagrams at column bases and column top ends are shown in Figures 4.42 to 4.45. The P-M diagrams indicate the presence of yielding during later cycles.

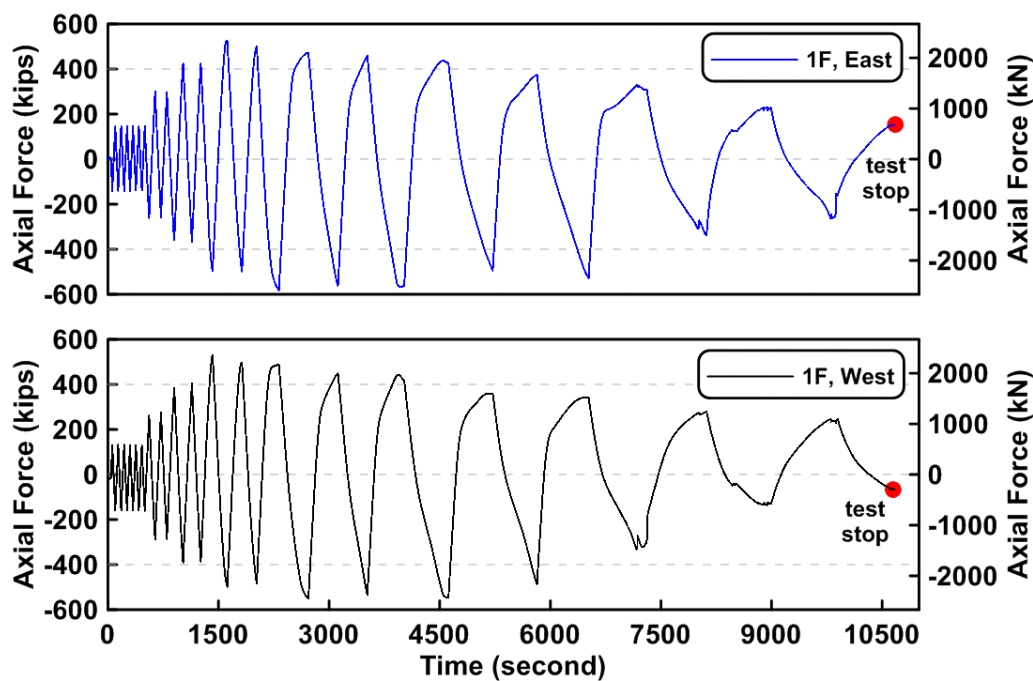


Figure 4.25 Specimen TCBF-B-1: time history of first-story column axial forces (location: 3 ft above column base plate).

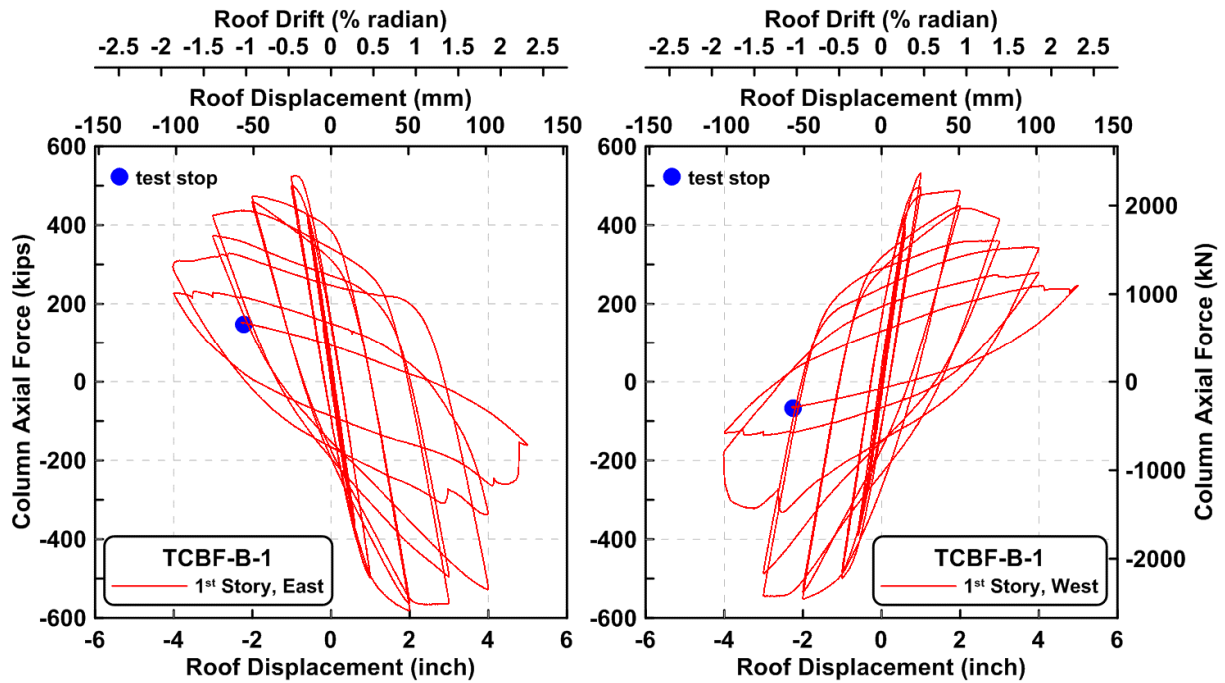


Figure 4.26 Specimen TCBF-B-1: roof displacement versus first-story column axial forces.

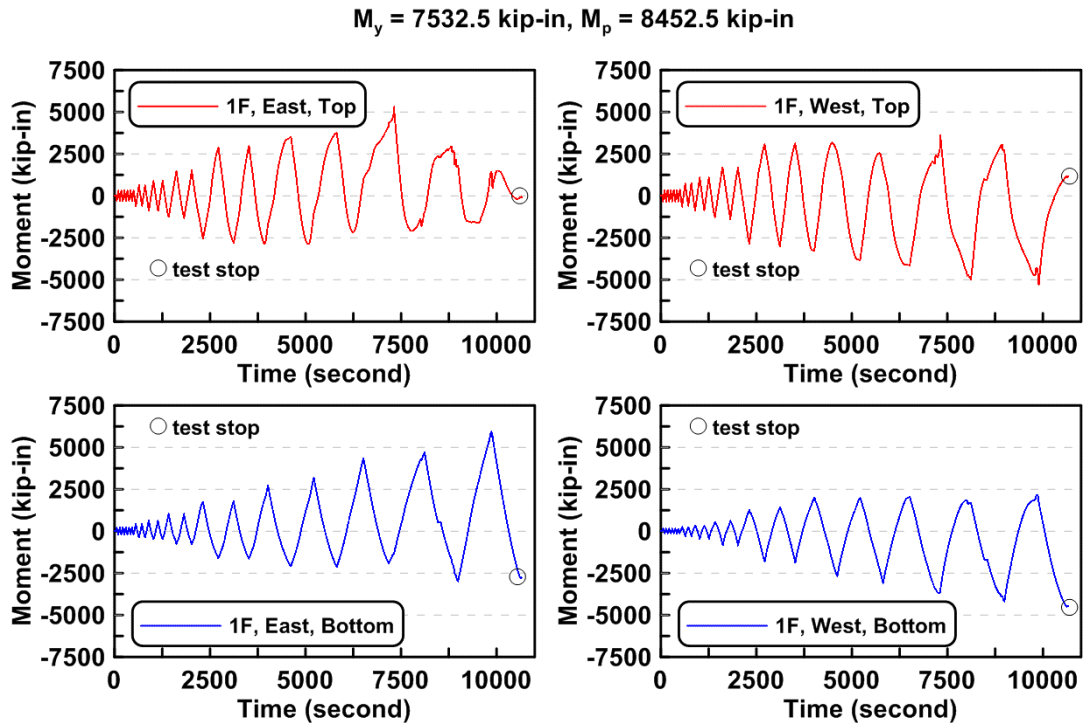


Figure 4.27 Specimen TCBF-B-1: time history of first-story column bending moments (3 ft above column base plate and 3 ft below lower beam centerline).

$$M_y = 7532.5 \text{ kip-in}, M_p = 8452.5 \text{ kip-in}$$

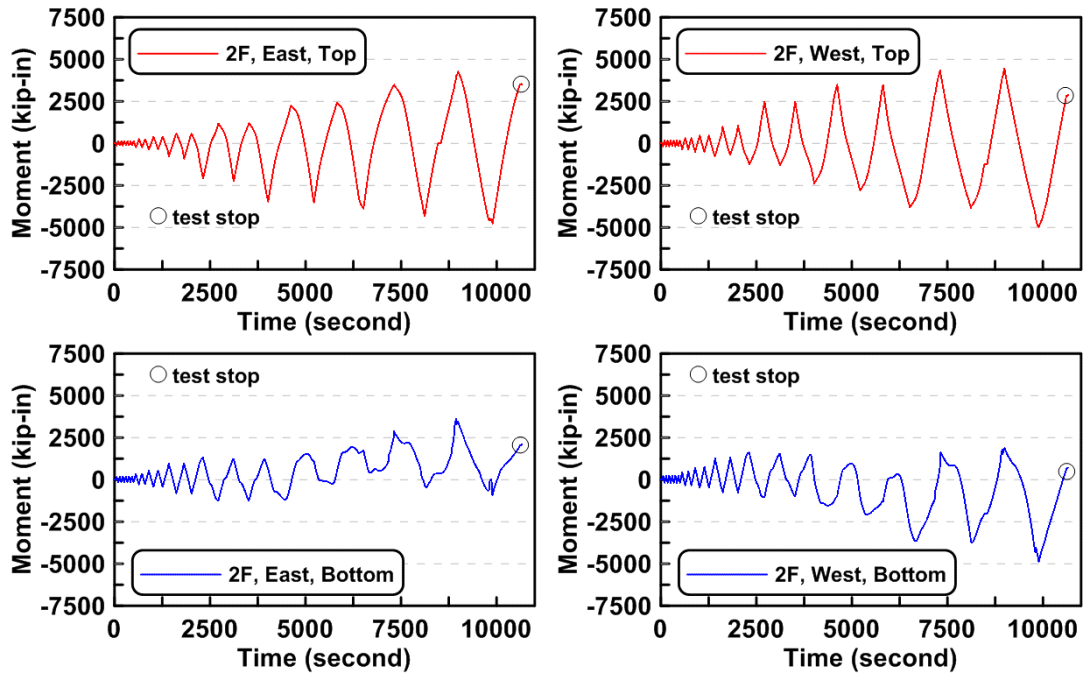


Figure 4.28 Specimen TCBF-B-1: time history of the second-story column bending moments (3 ft above lower beam centerline and 3 ft below roof beam centerline).

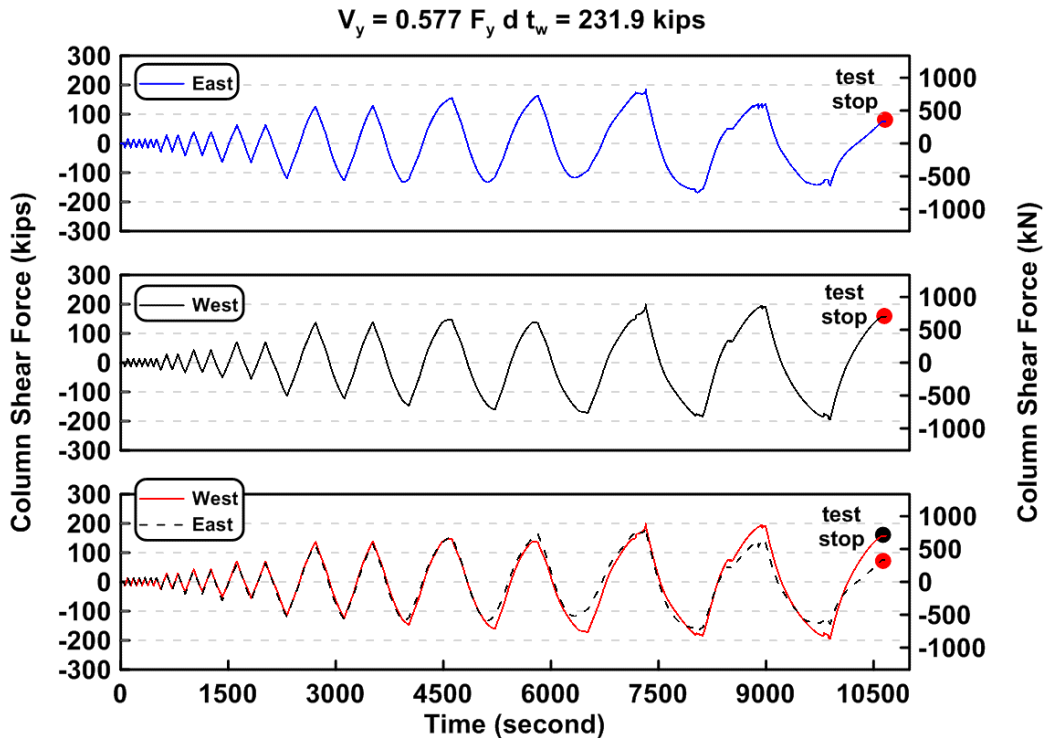


Figure 4.29 Specimen TCBF-B-1: time history of the first-story column shear forces.

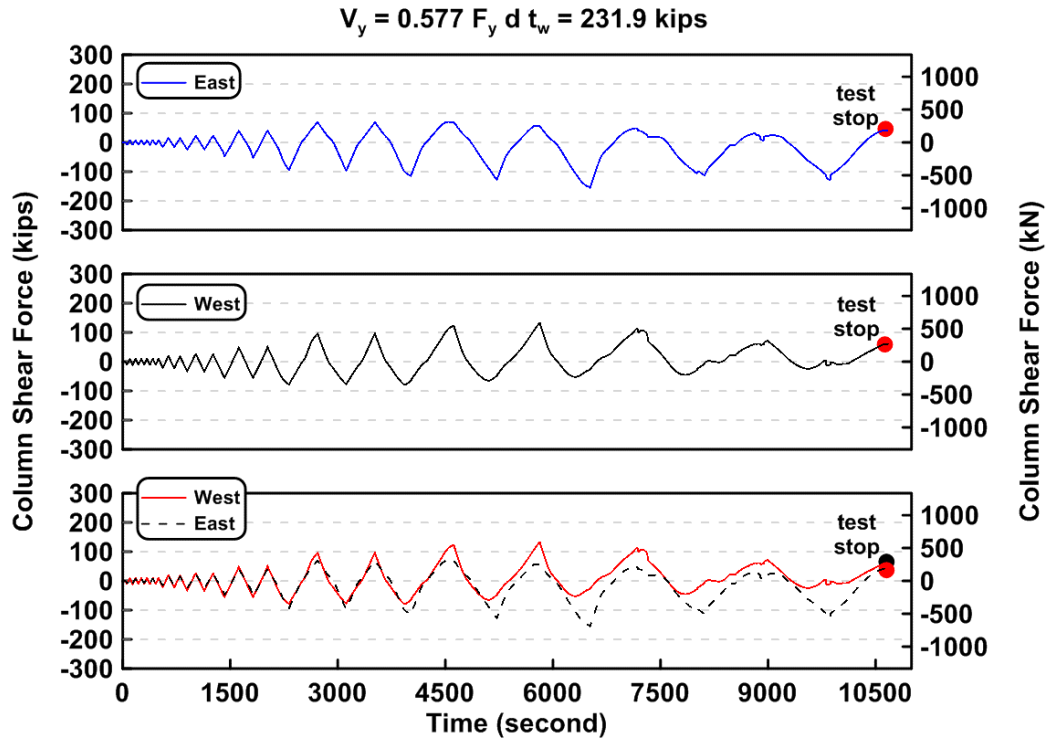


Figure 4.30 Specimen TCBF-B-1: time history of the second-story column shear forces.

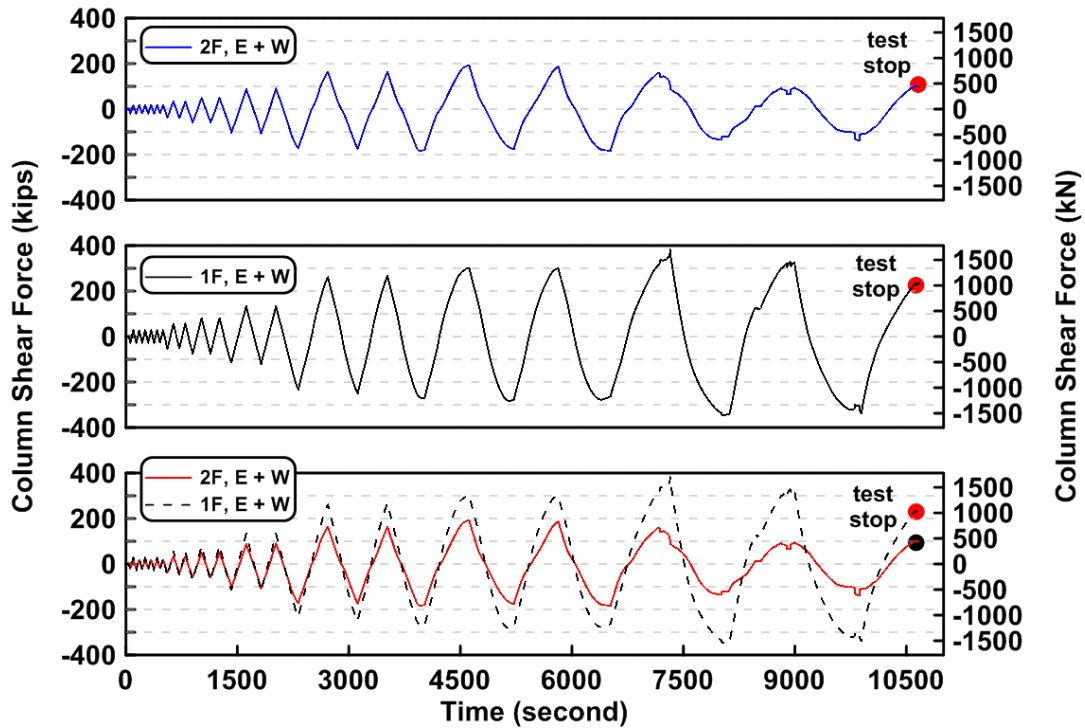


Figure 4.31 Specimen TCBF-B-1: time history of the sum of east and west column shear forces in both stories.

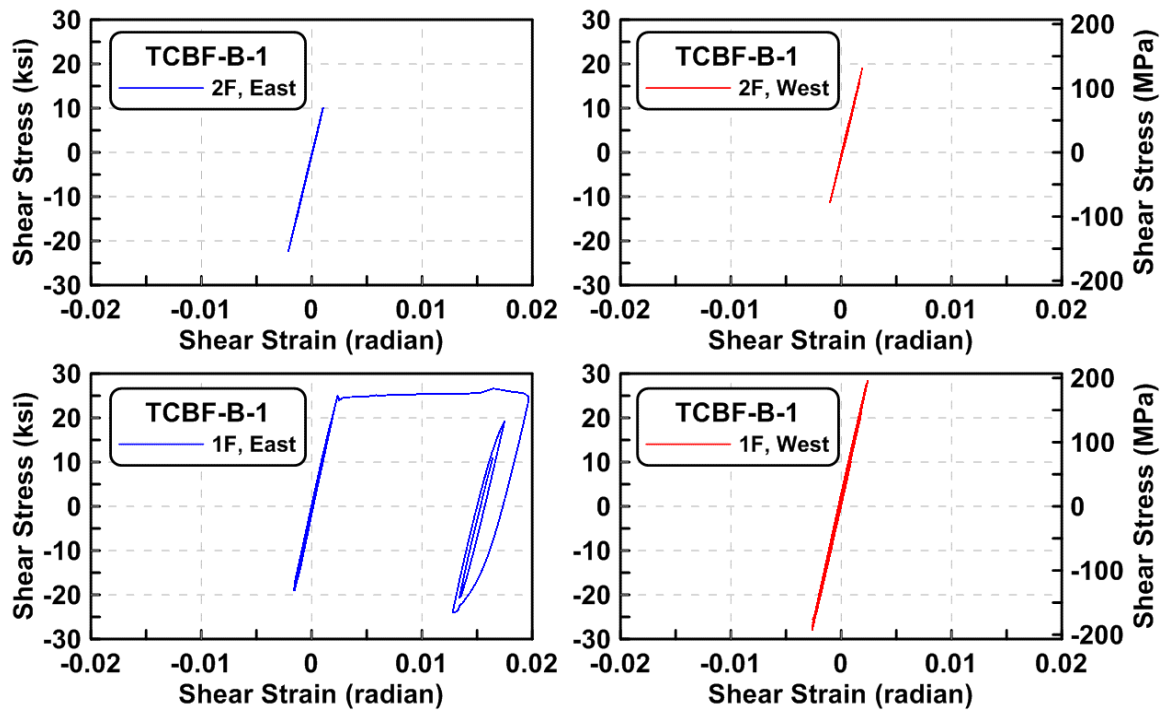


Figure 4.32 Specimen TCBF-B-1: column shear stress versus shear strain relationships (locations: EC1-B-N, EC2-B-N, WC1-B-N, and WC2-B-N).

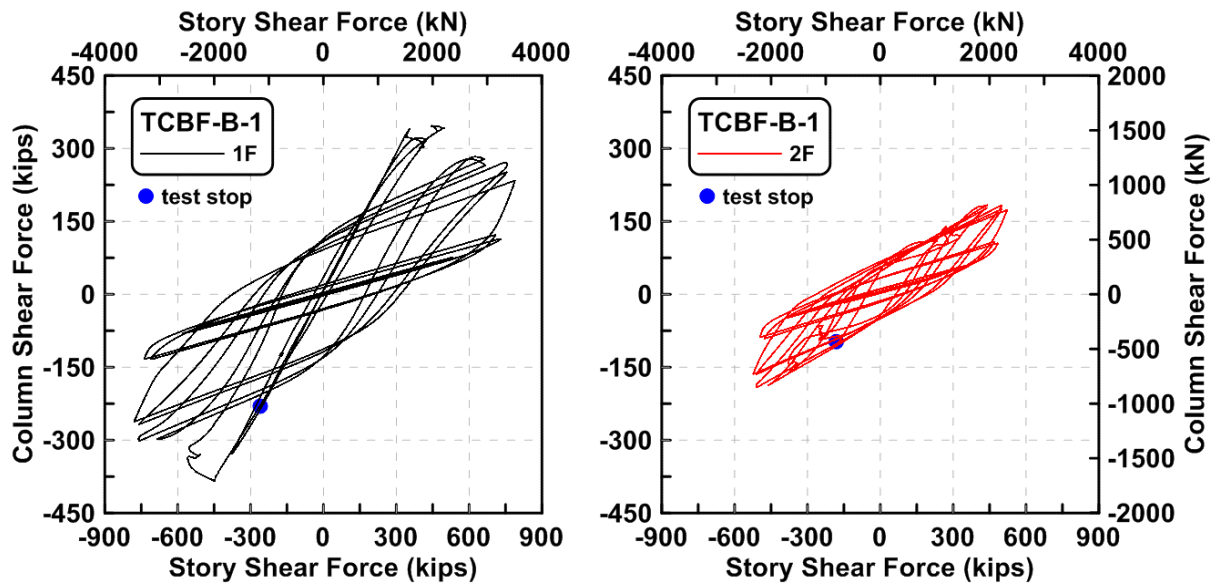


Figure 4.33 Specimen TCBF-B-1: story shear component from columns versus total story shear forces.

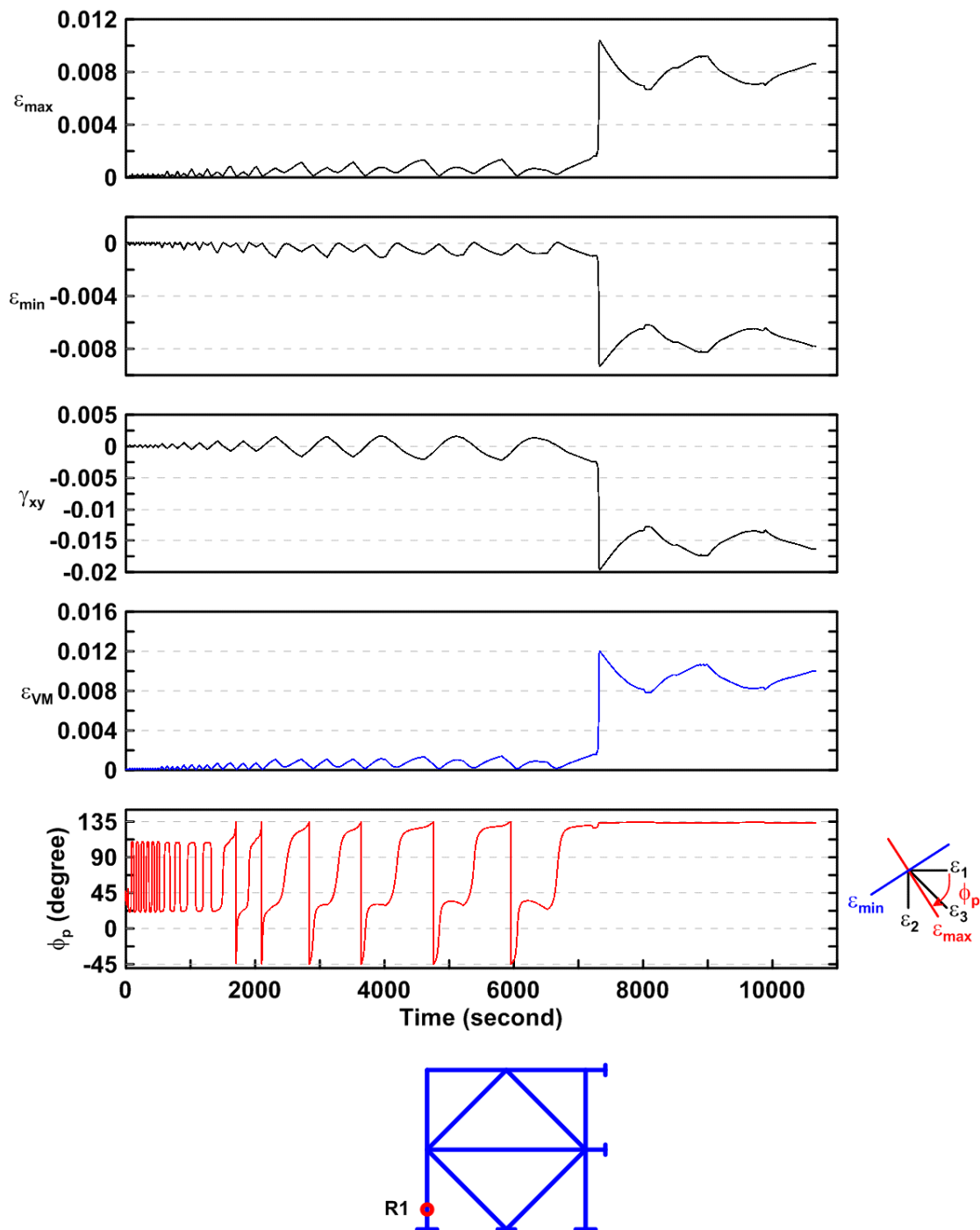


Figure 4.34 Specimen TCBF-B-1: time history of rosette-type strain gauge readings in the first-story column web (location: R1, EC1-B-N).

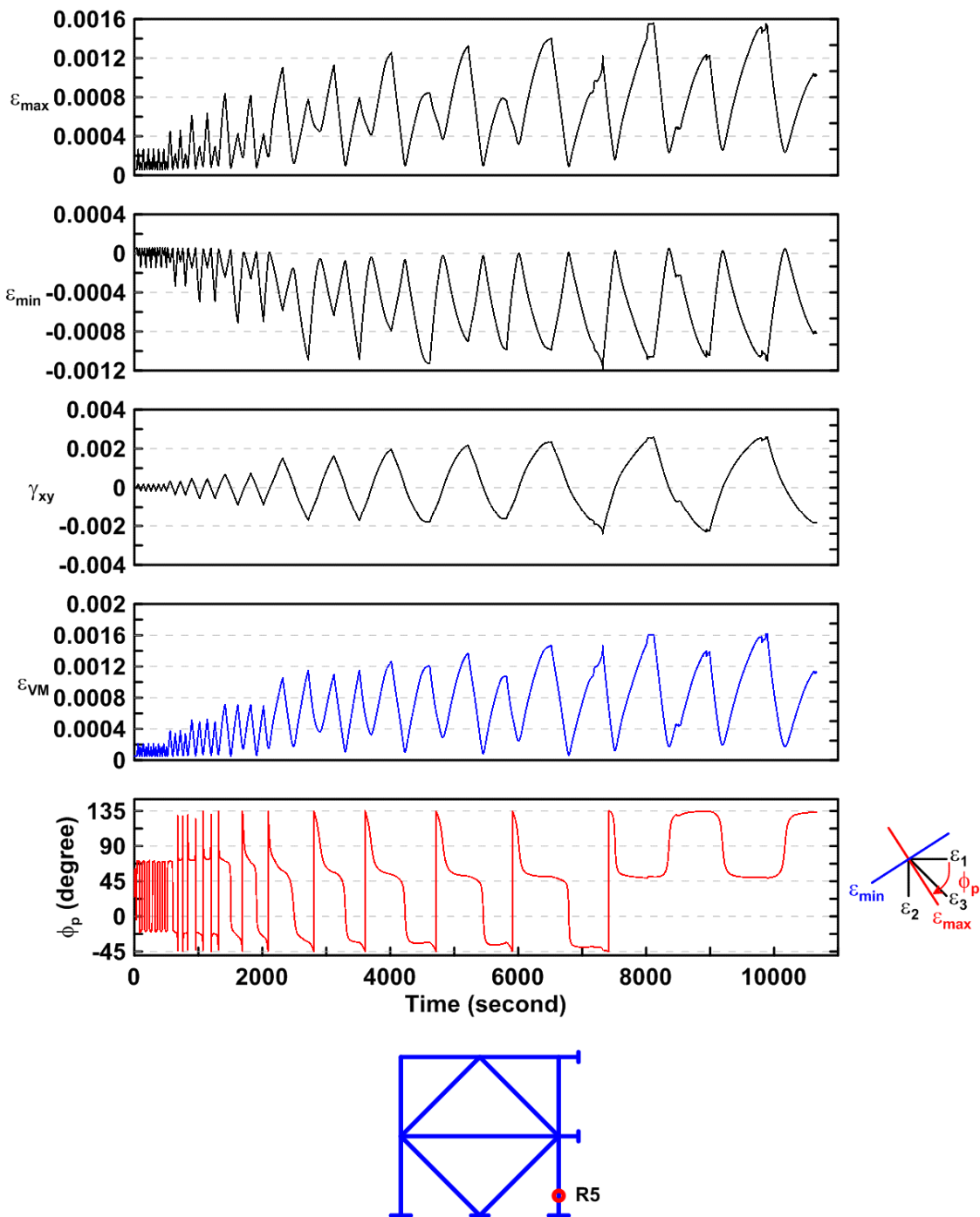


Figure 4.35 Specimen TCBF-B-1: time history of rosette-type strain gauge readings in the first-story column web (location: R5, WC1-B-N).

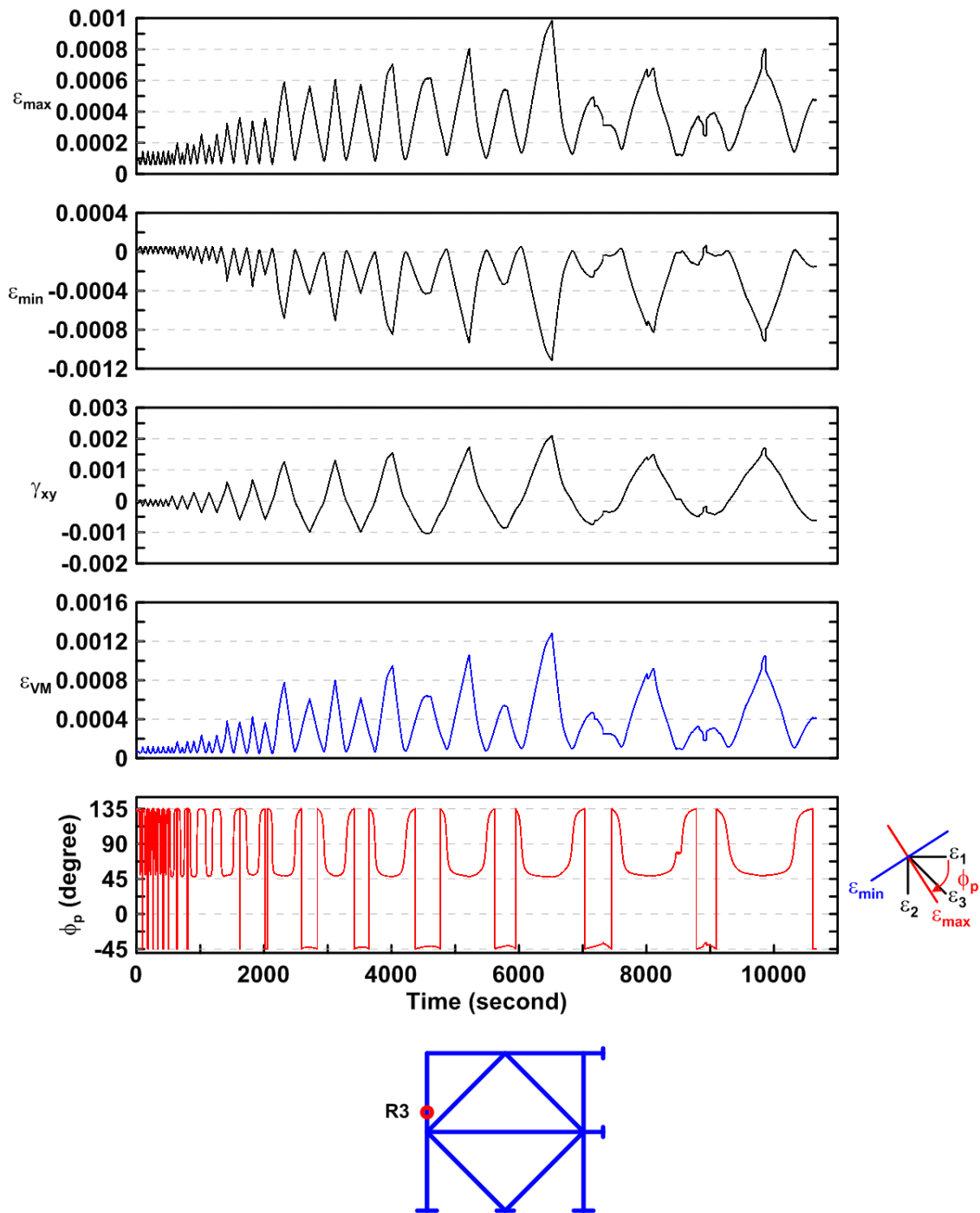


Figure 4.36 Specimen TCBF-B-1: time history of rosette-type strain gauge readings in the second-story column web (location: R3, EC2-B-N).

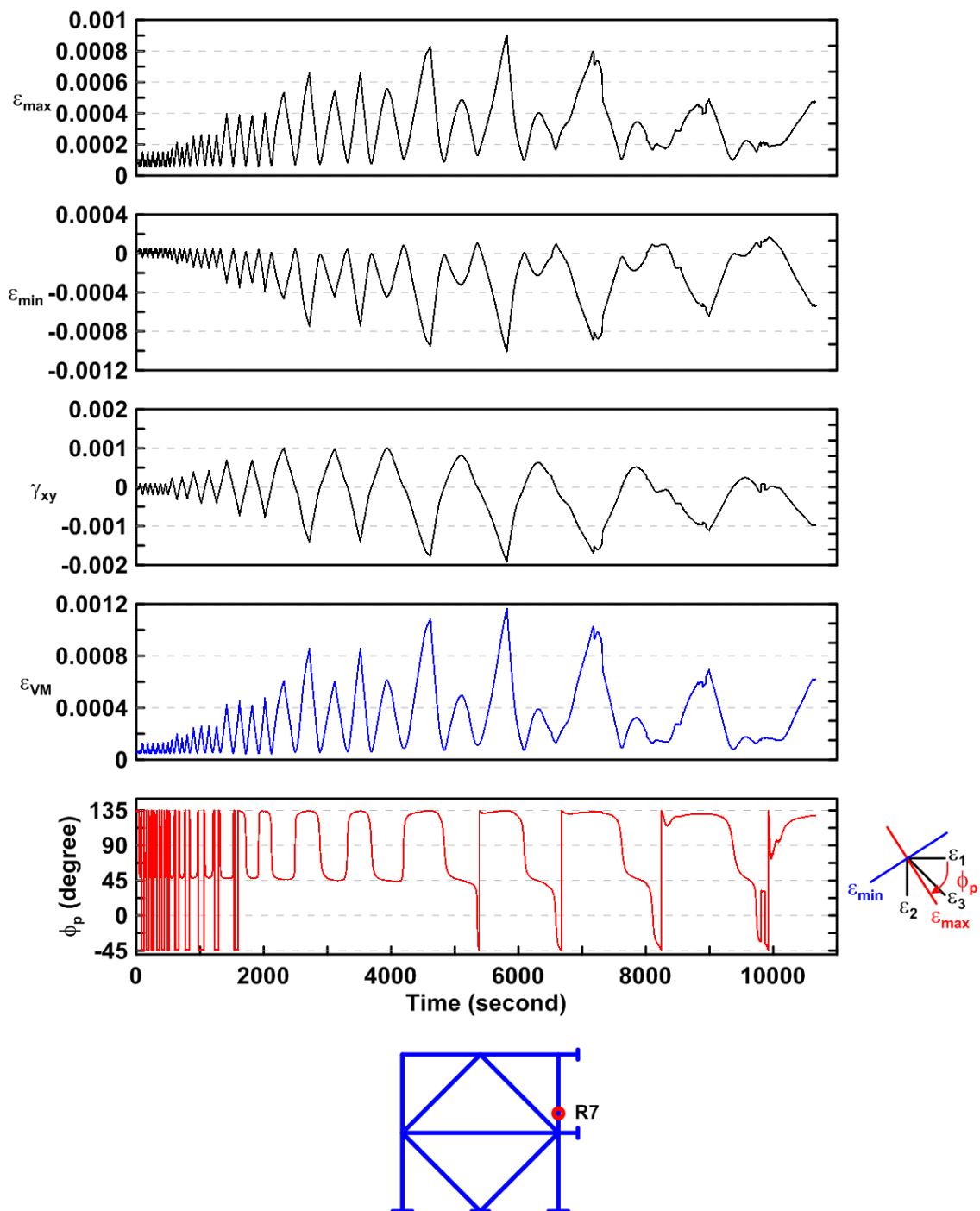


Figure 4.37 Specimen TCBF-B-1: time history of rosette-type strain gauge readings in the second-story column web (location: R7, WC2-B-N).

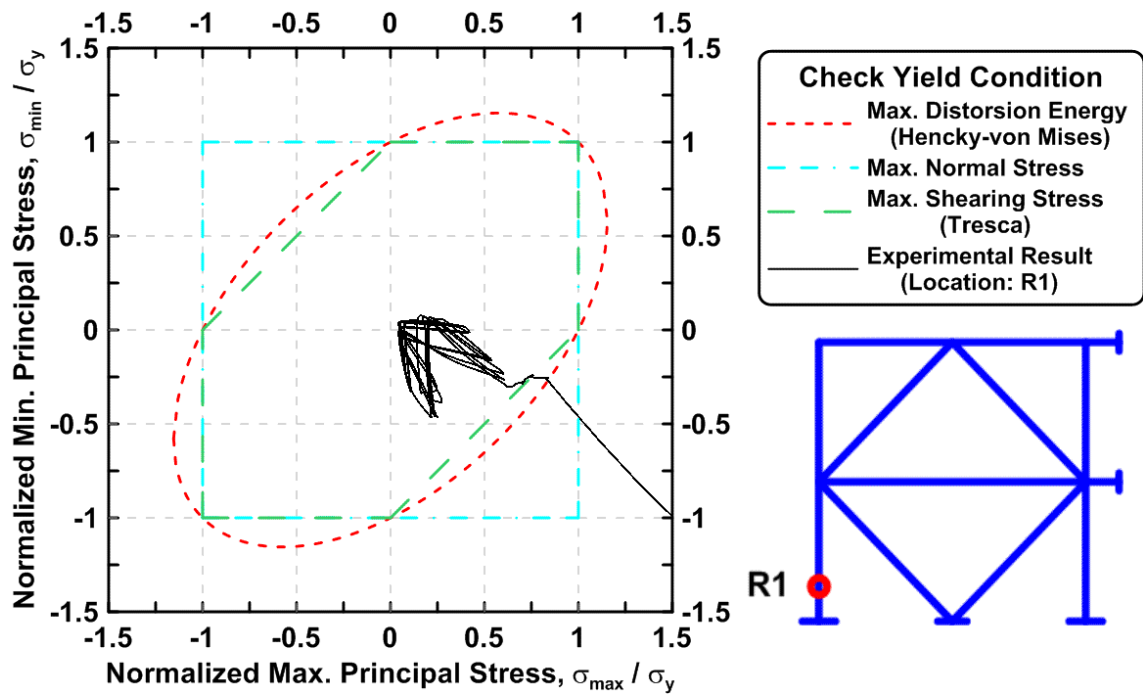


Figure 4.38 Specimen TCBF-B-1, first-story column: normalized maximum principal stress versus normalized minimum principal stress (location: R1).

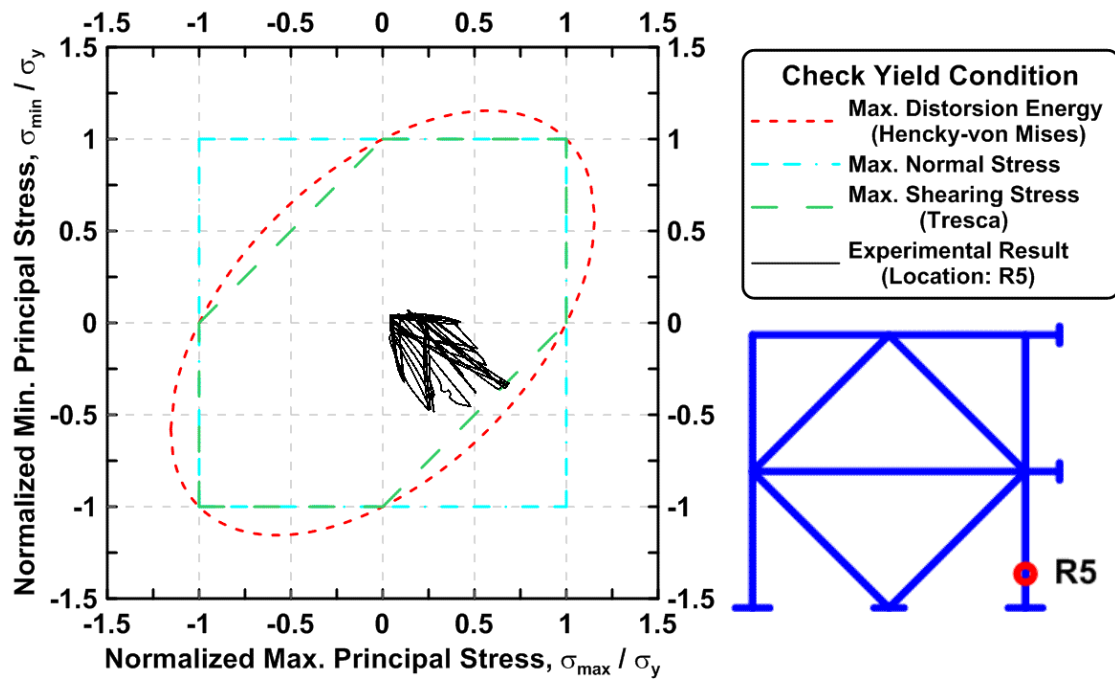


Figure 4.39 Specimen TCBF-B-1, first-story column: normalized maximum principal stress versus normalized minimum principal stress (location: R5).

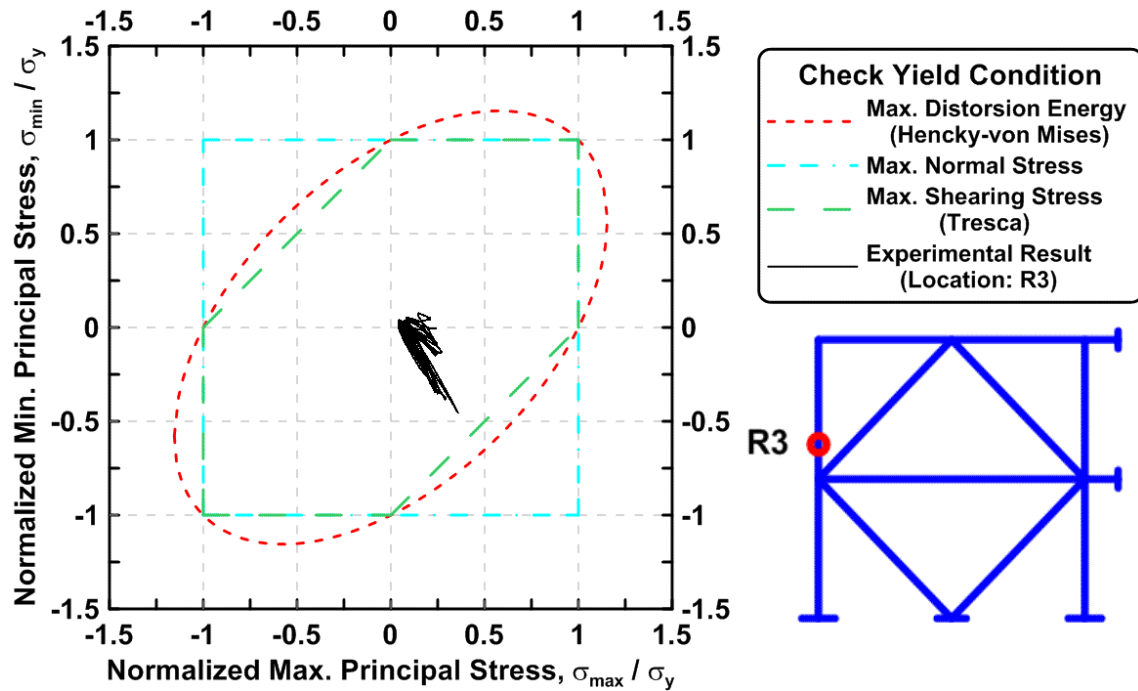


Figure 4.40 Specimen TCBF-B-1, second-story column: normalized maximum principal stress versus normalized minimum principal stress (location: R3).

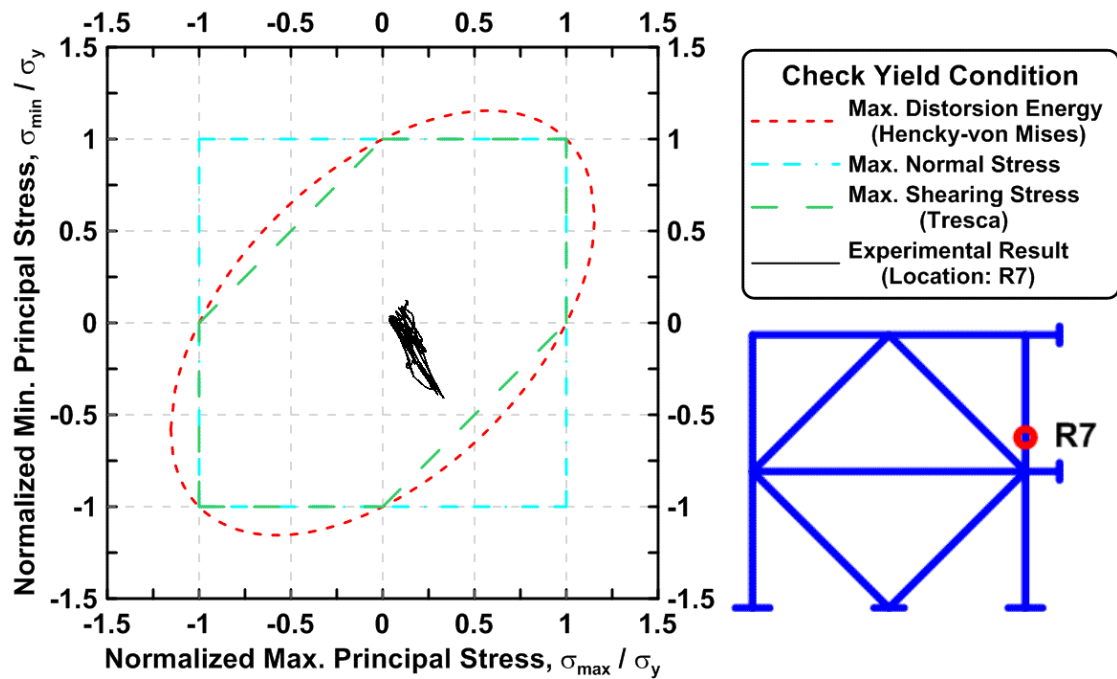


Figure 4.41 Specimen TCBF-B-1, second-story column: normalized minimum principal stress (location: R7).

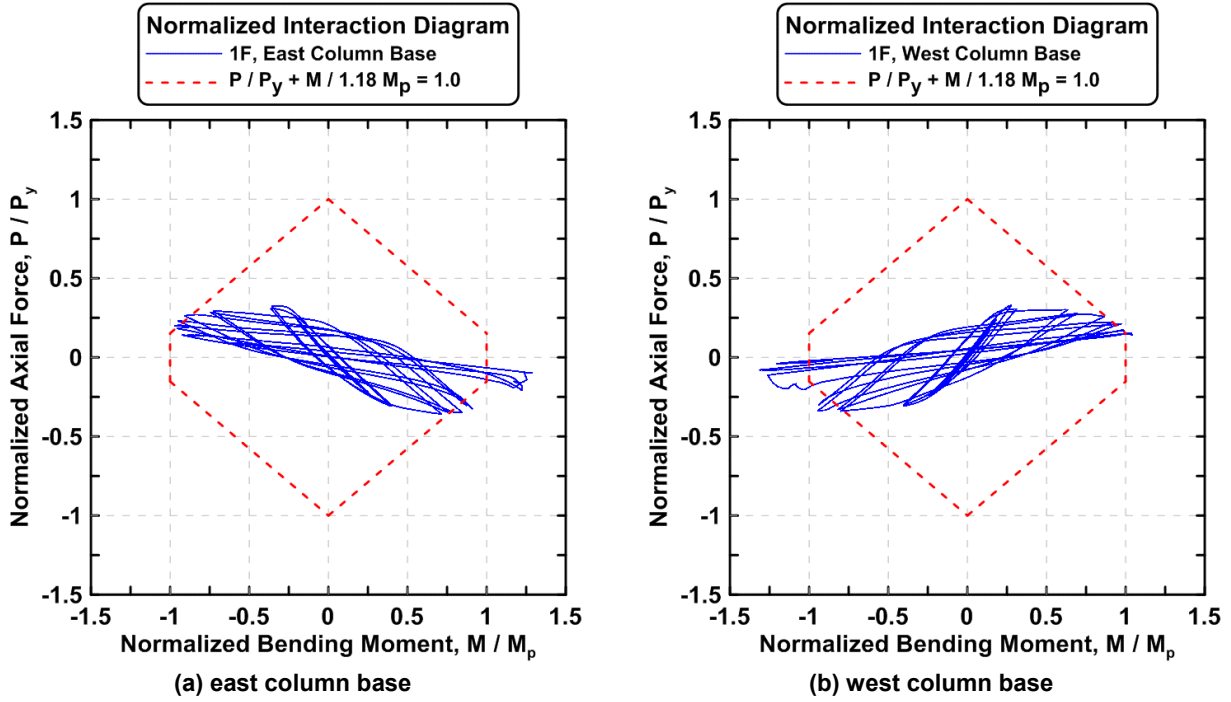


Figure 4.42 Specimen TCBF-B-1, first-story columns: normalized P-M interaction diagrams.

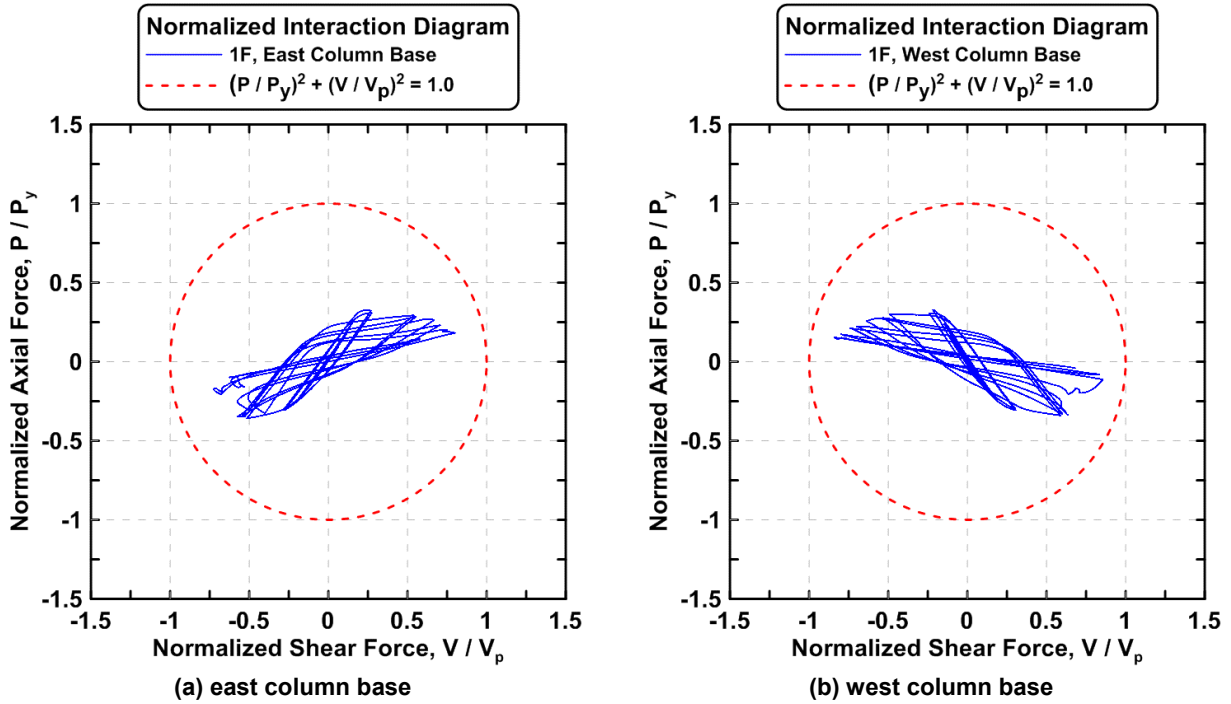


Figure 4.43 Specimen TCBF-B-1, first-story columns: normalized P-V interaction diagrams.

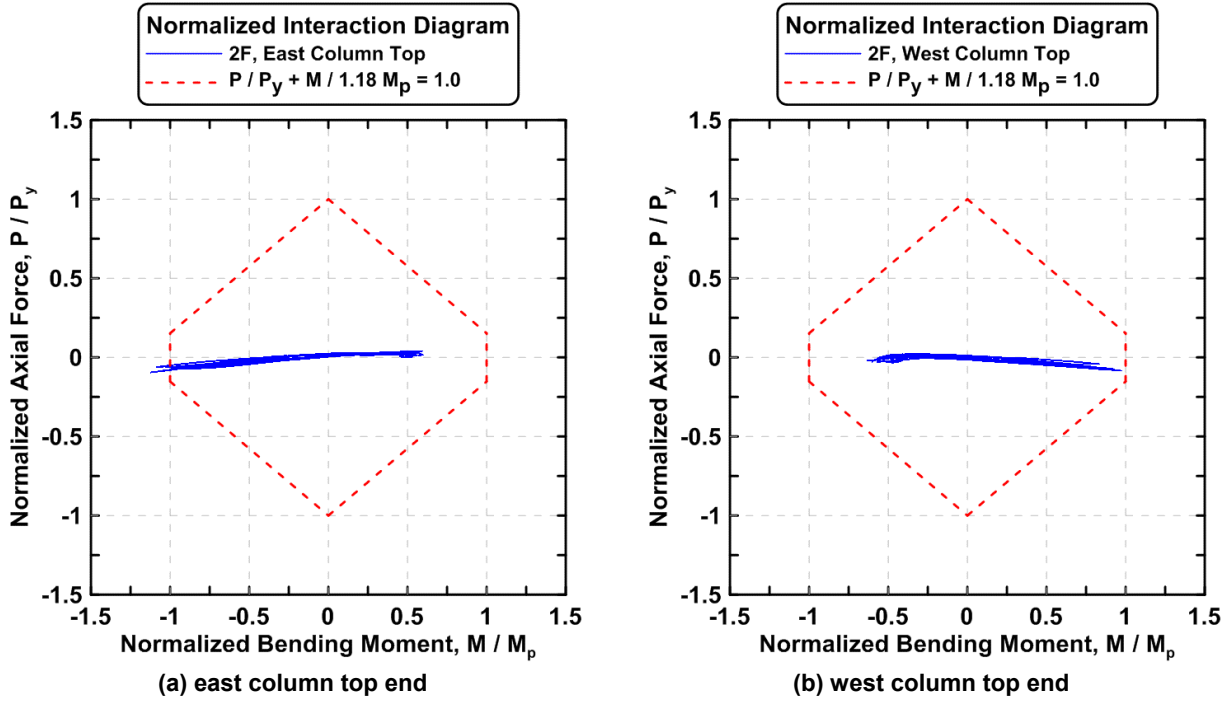


Figure 4.44 Specimen TCBF-B-1, second-story columns: normalized P-M interaction diagrams.

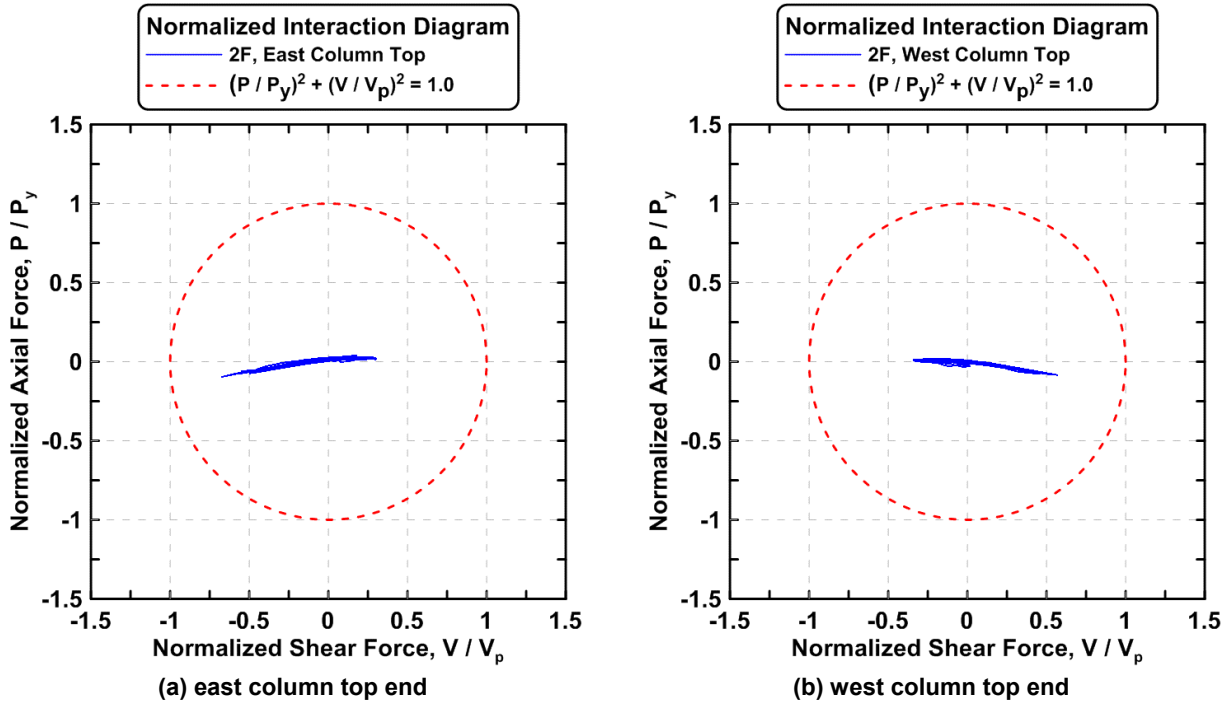


Figure 4.45 Specimen TCBF-B-1, second-story columns: normalized P-V interaction diagrams.

4.1.1.2.3 Beam Response

The vertical deflection time history at the center of W24 \times 117 roof beam and W24 \times 68 lower beam are plotted in Figure 4.46. The time history of strain readings at both ends of roof beam and lower beam are shown in Figures 4.47 and 4.48, respectively. Both beam axial force time histories derived from linear type strain gauge at different locations of the beams are plotted in Figures 4.49 and 4.50. The bending moment time histories of both beams are shown in Figures 4.51 and 4.52. Estimated beam shear force time histories are illustrated in Figures 4.53 and 4.54. Unbalanced force in the roof beam center is plotted in Figure 4.55.

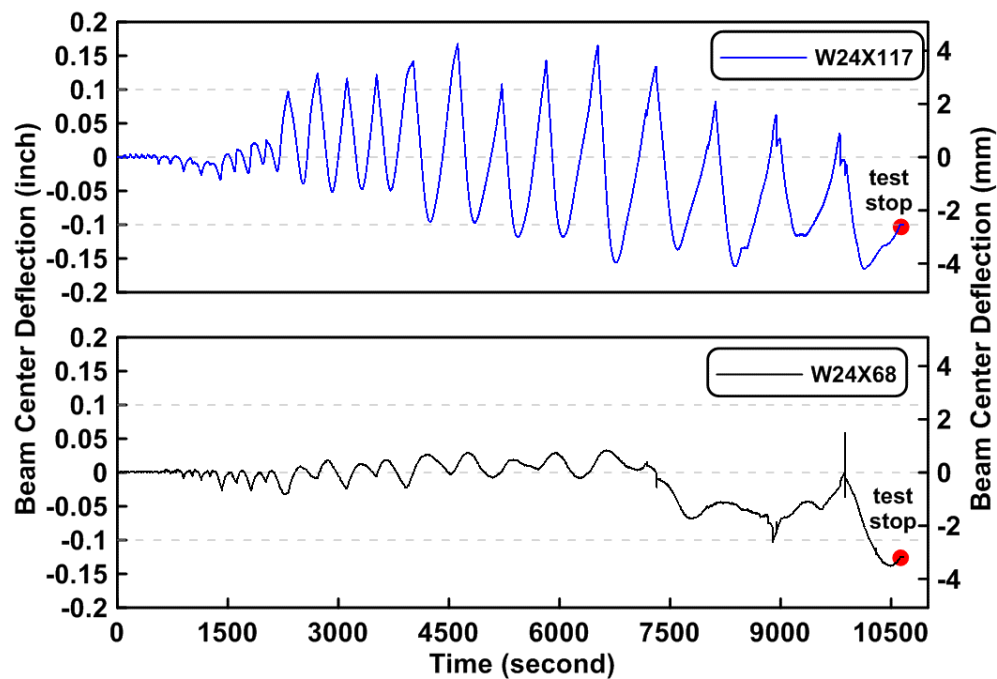


Figure 4.46 Specimen TCBF-B-1: deflection time history at the center of beam span (roof beam: W24 \times 117, lower beam: W24 \times 68).

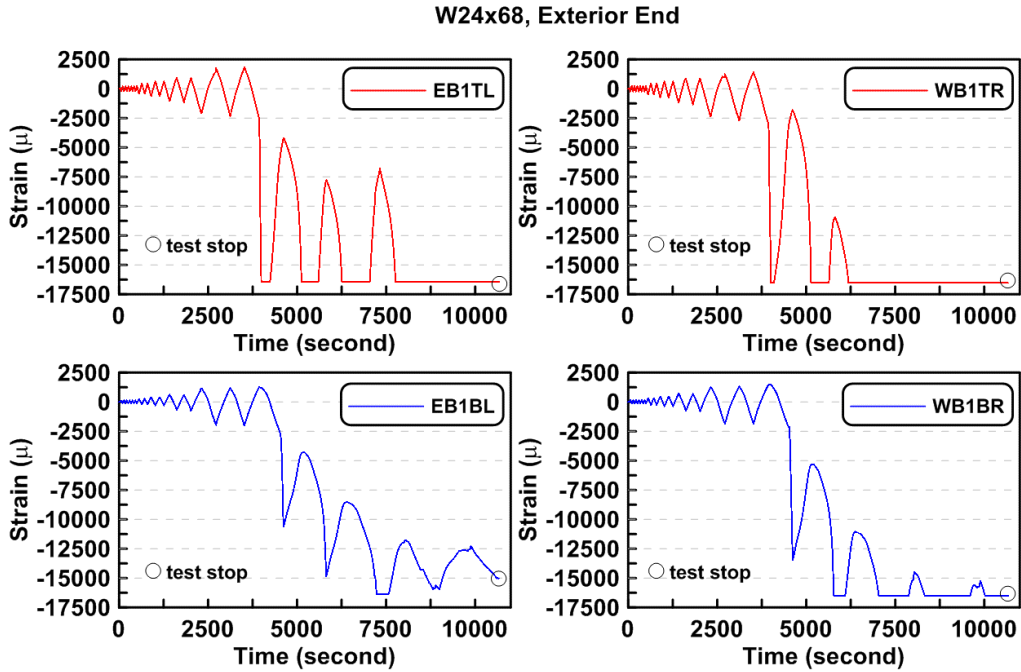


Figure 4.47 Specimen TCBF-B-1: time history of strain readings at both exterior ends of W24 × 68 lower beam.

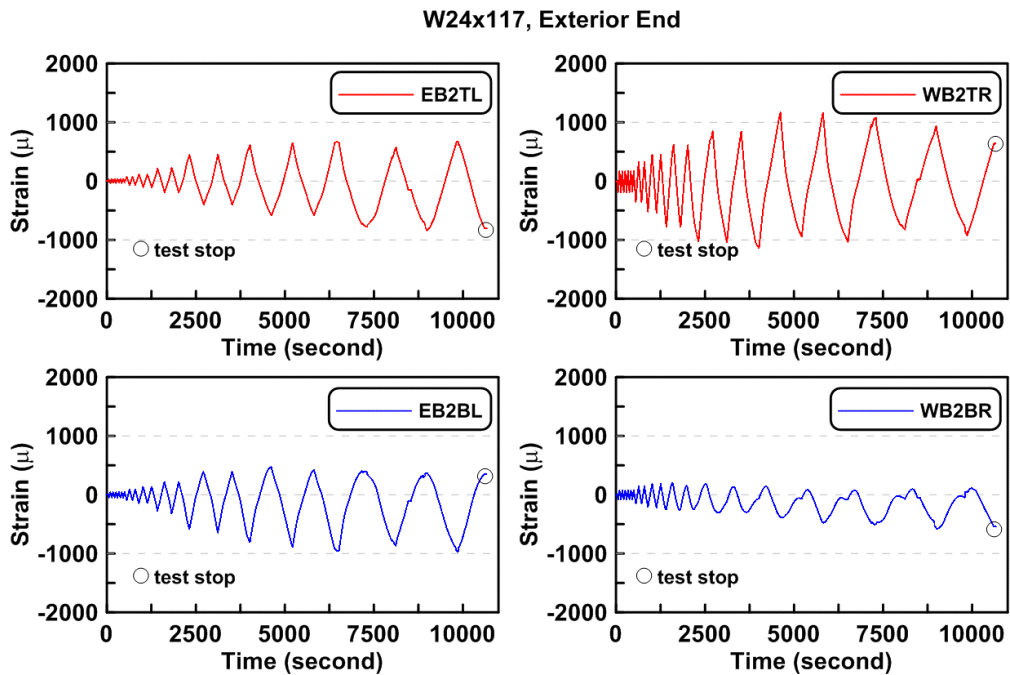


Figure 4.48 Specimen TCBF-B-1: time history of strain readings at both exterior ends of W24 × 117 roof beam.

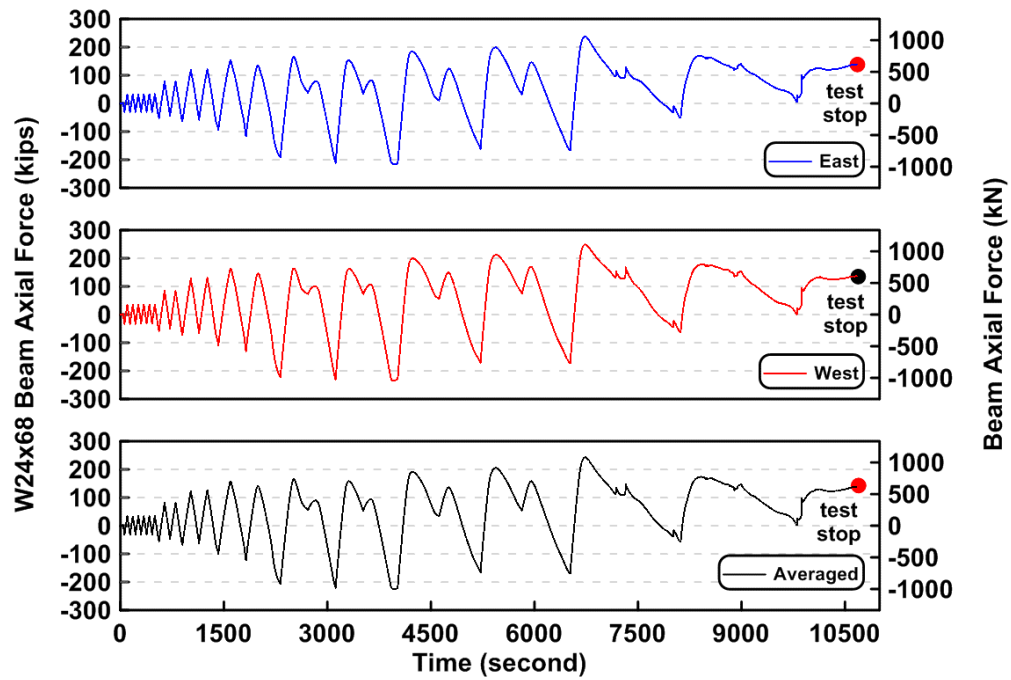


Figure 4.49 Specimen TCBF-B-1: time history of lower beam axial forces.

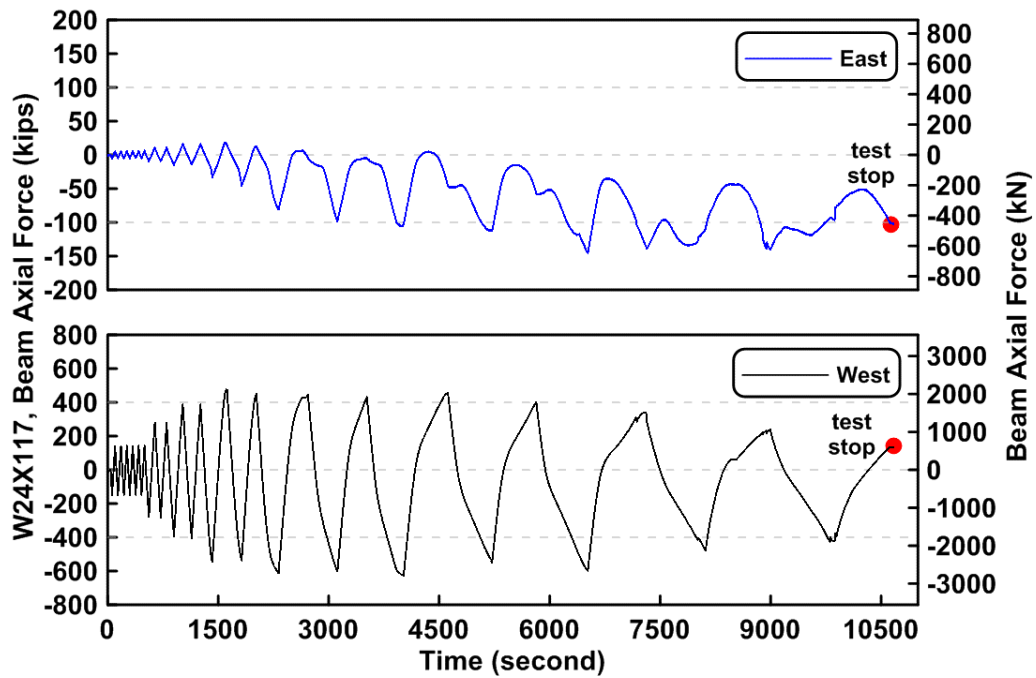


Figure 4.50 Specimen TCBF-B-1: time history of roof beam axial forces.

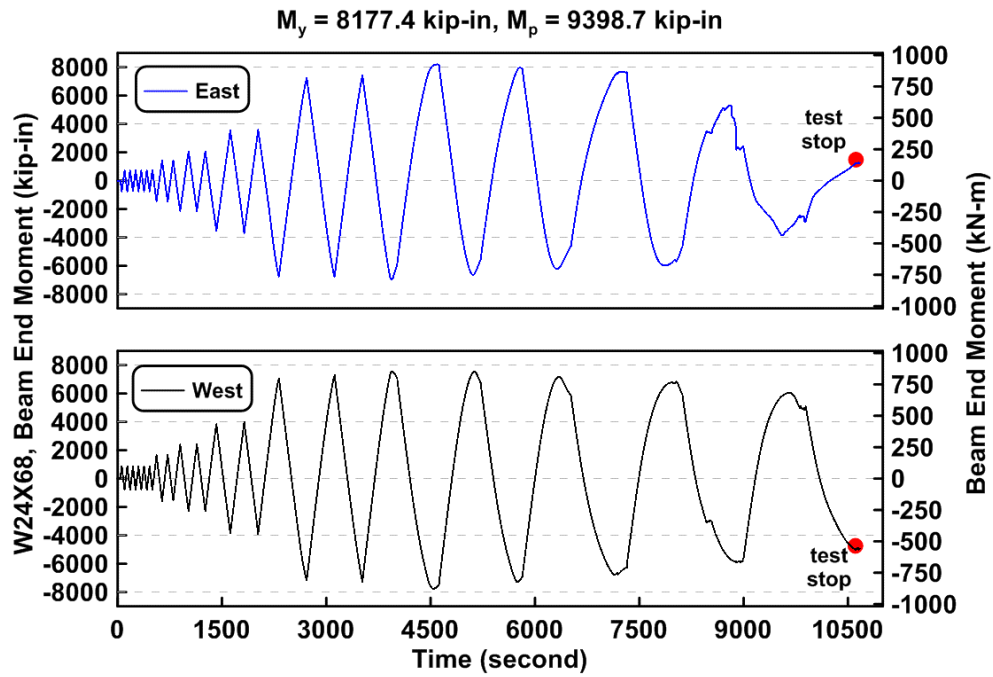


Figure 4.51 Specimen TCBF-B-1: time history of lower beam end bending moment.

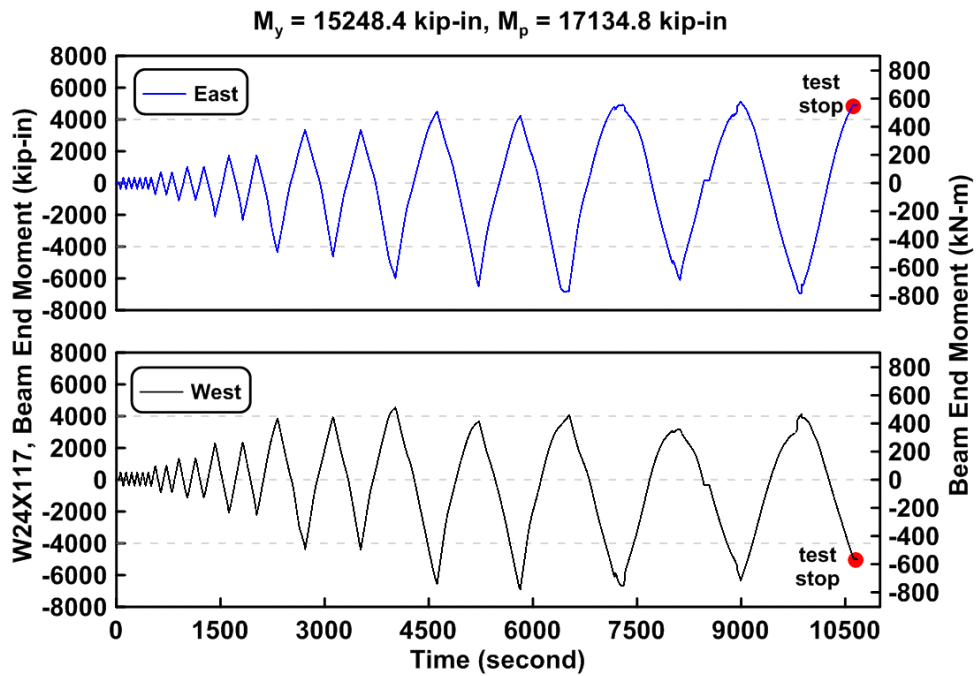


Figure 4.52 Specimen TCBF-B-1: time history of roof beam end bending moment.

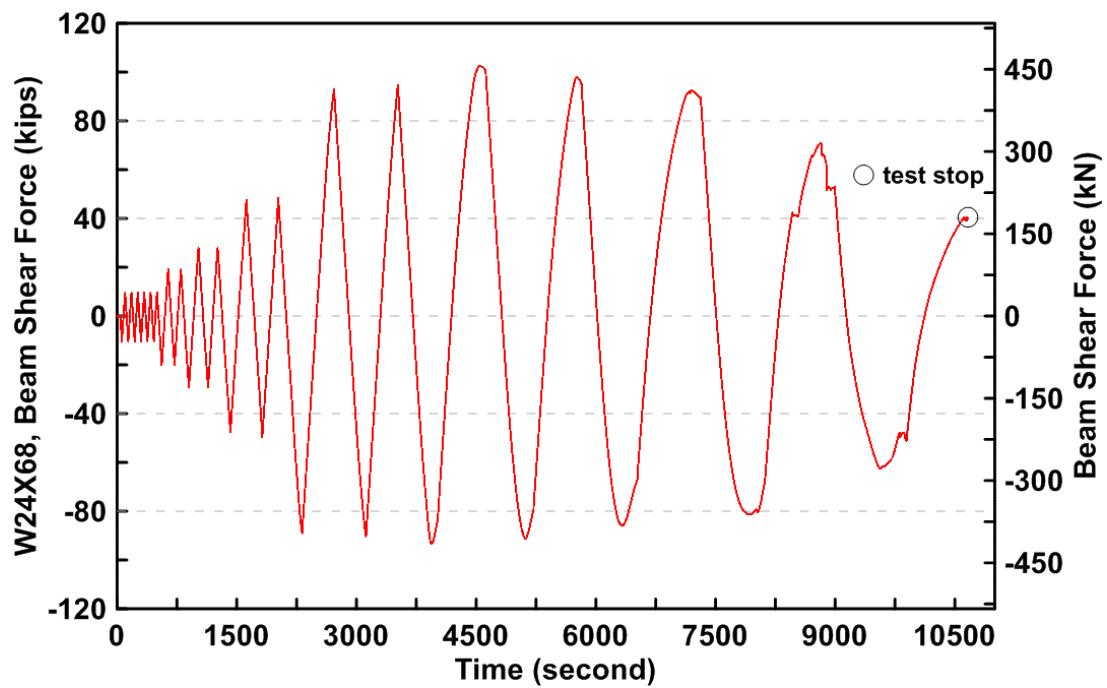


Figure 4.53 Specimen TCBF-B-1: lower beam estimated shear force time history.

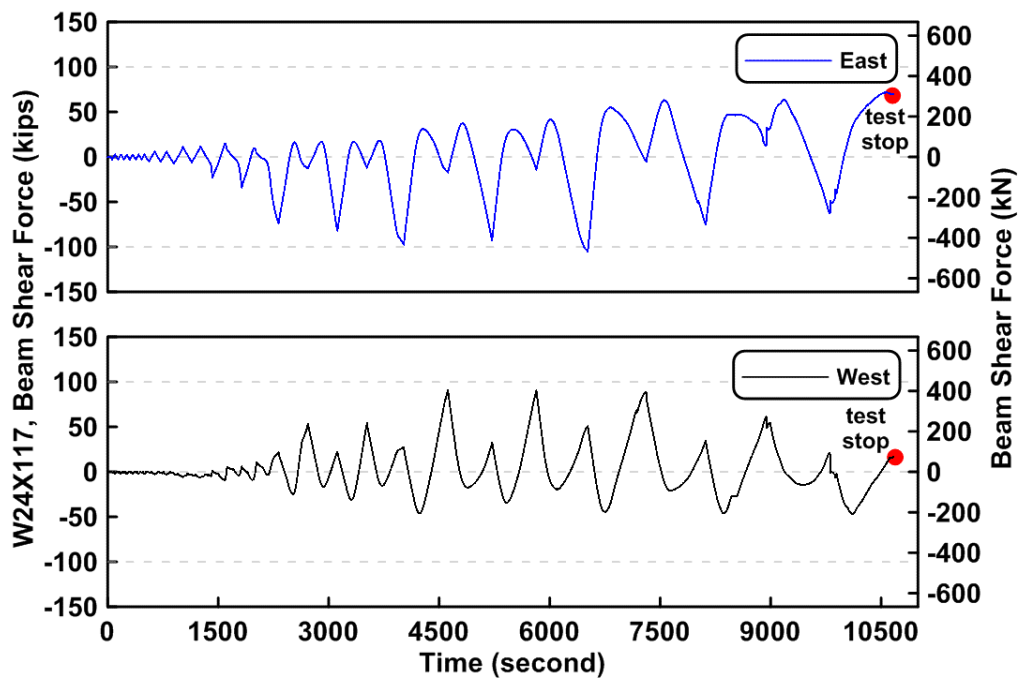


Figure 4.54 Specimen TCBF-B-1: roof beam estimated shear force time history.

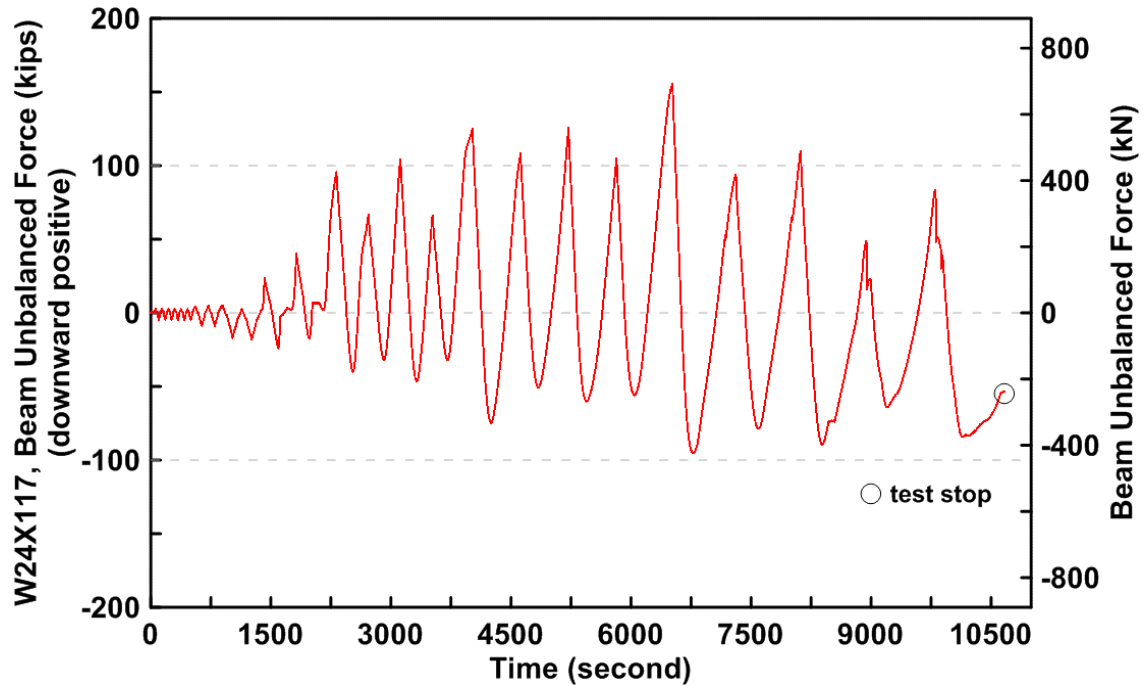


Figure 4.55 Specimen TCBF-B-1: estimated unbalanced force time history of roof beam.

4.1.1.2.4 Brace Response

The estimated brace axial forces versus brace axial deformations for each square HSS braces are shown in Figure 4.56. The estimated brace axial forces versus measured brace out-of-plane displacements at the brace center point for each square HSS braces are shown in Figure 4.57. Combined brace axial force, axial deformation, and out-of-plane displacement relationships are shown in Figure 4.58. The decomposed strain (axial strain, in-plane bending strain, out-of-plane bending strain, and warping strain) time histories of each brace are plotted in Figures 4.59 to 4.62(a). Figure 4.62(b) illustrates the definition of the decomposed strain components for the square HSS braces.

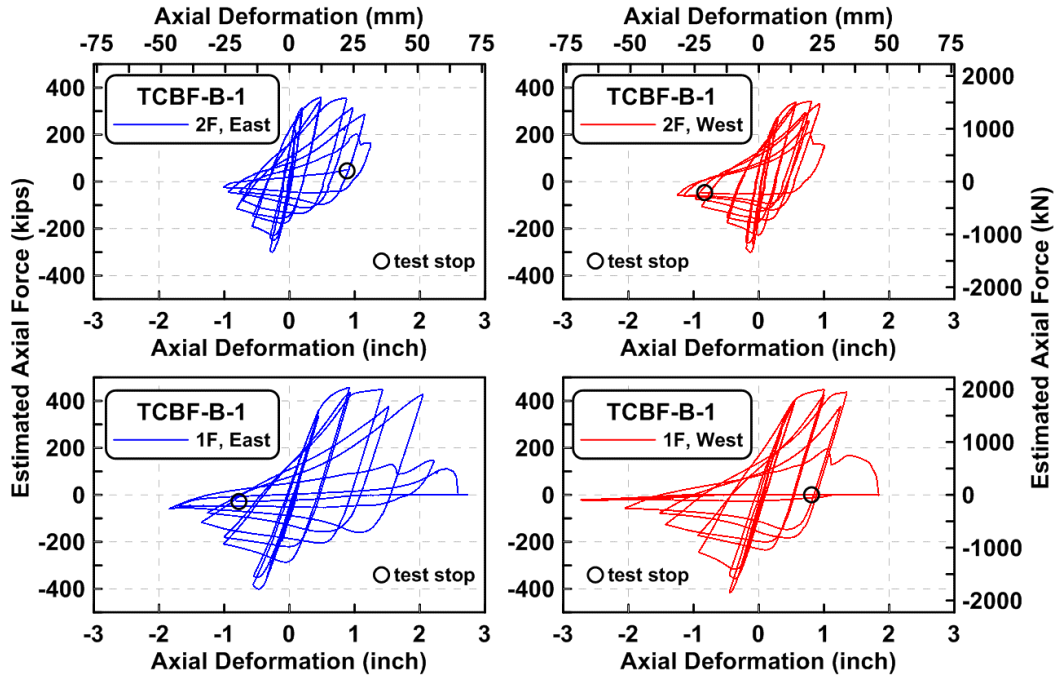


Figure 4.56 Specimen TCBF-B-1: estimated brace axial forces versus brace axial deformations.

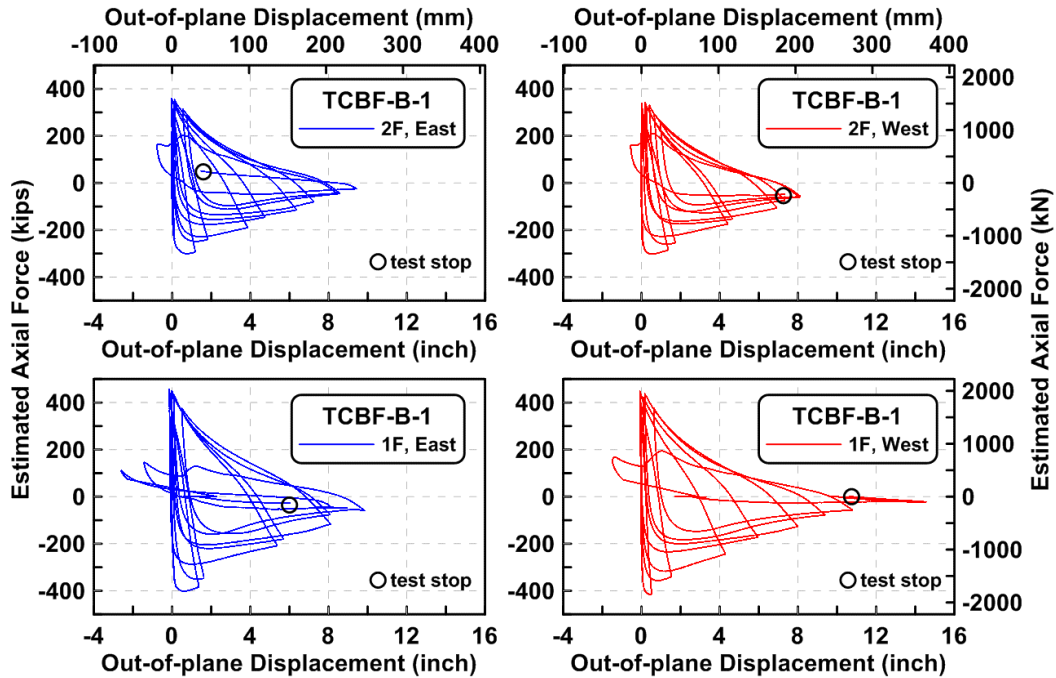


Figure 4.57 Specimen TCBF-B-1: estimated brace axial forces versus measured brace out-of-plane displacements.

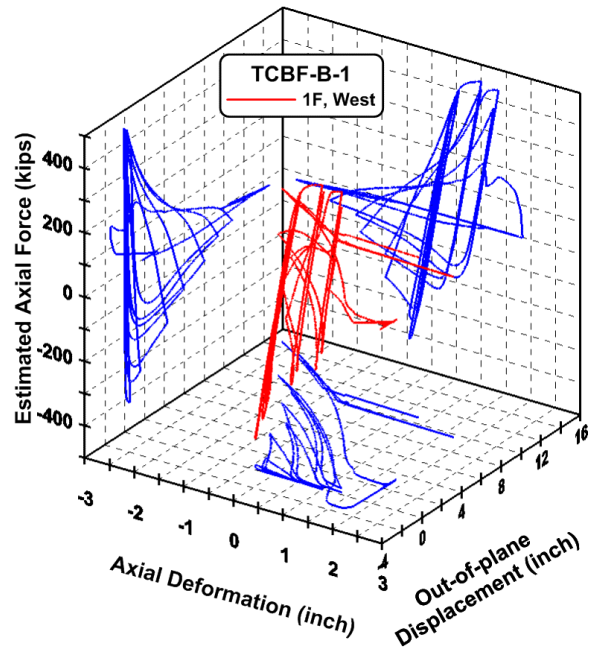
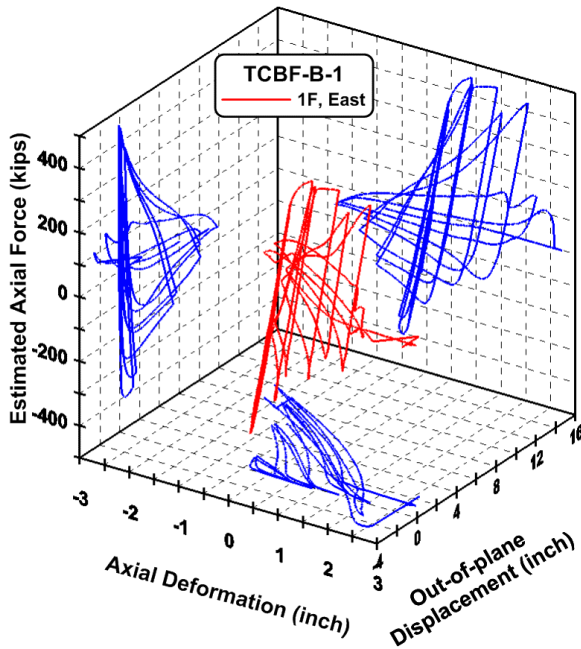
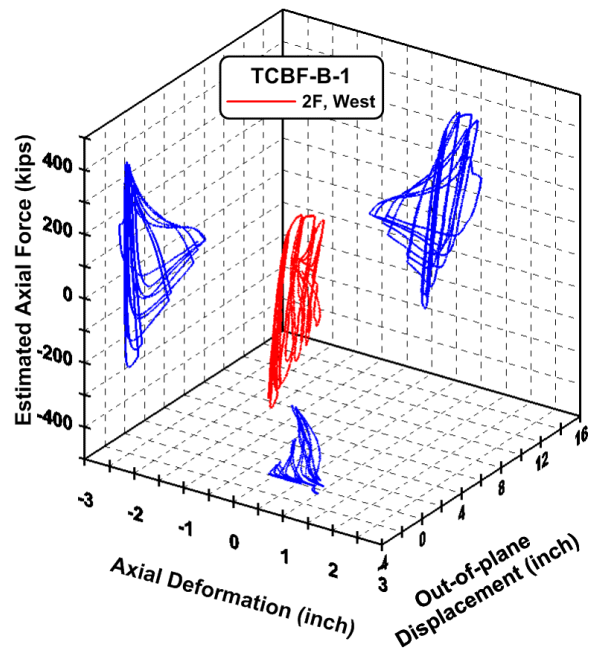
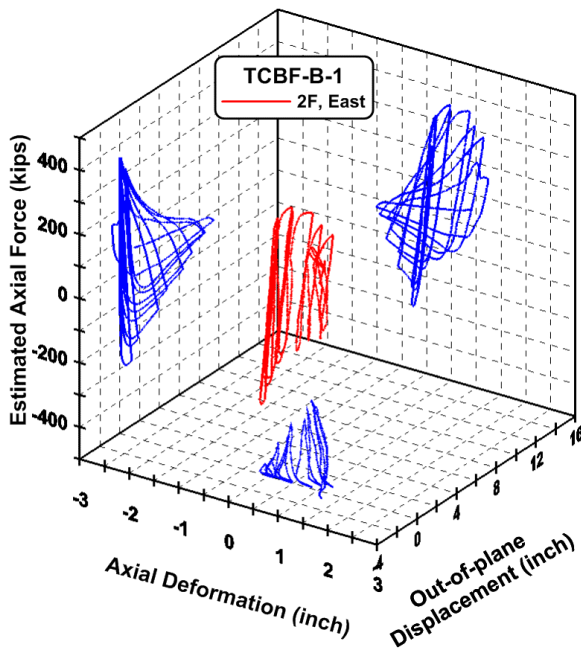


Figure 4.58 Specimen TCBF-B-1: estimated brace axial force, brace axial deformation, and measured brace out-of-plane displacement relationships.

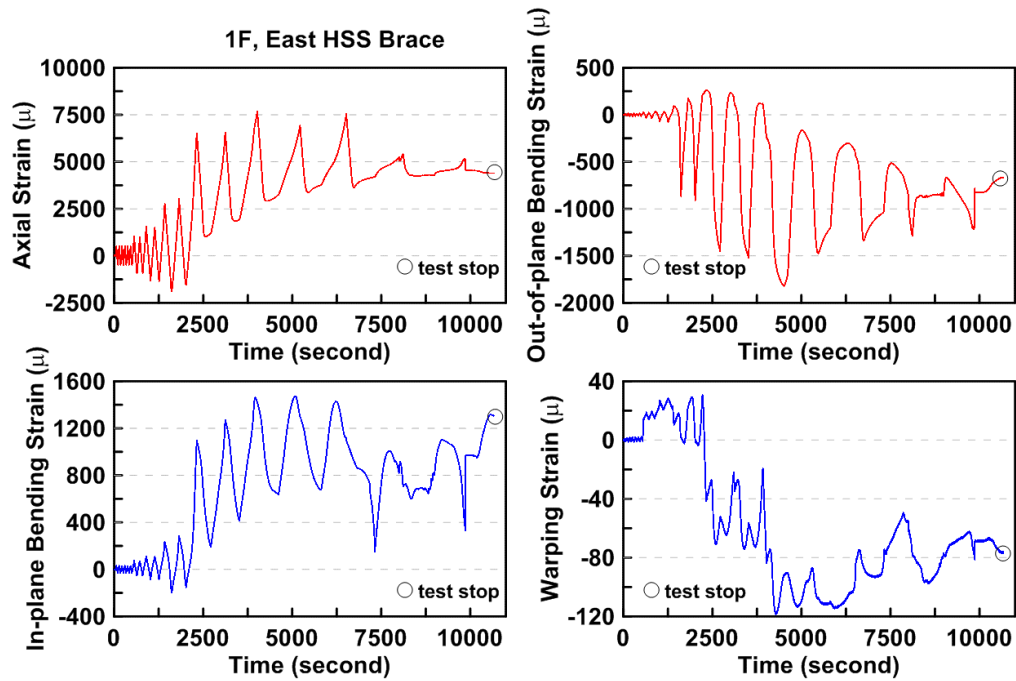


Figure 4.59 Specimen TCBF-B-1: time history of the decomposed strain components of first-story eastern-side HSS brace.

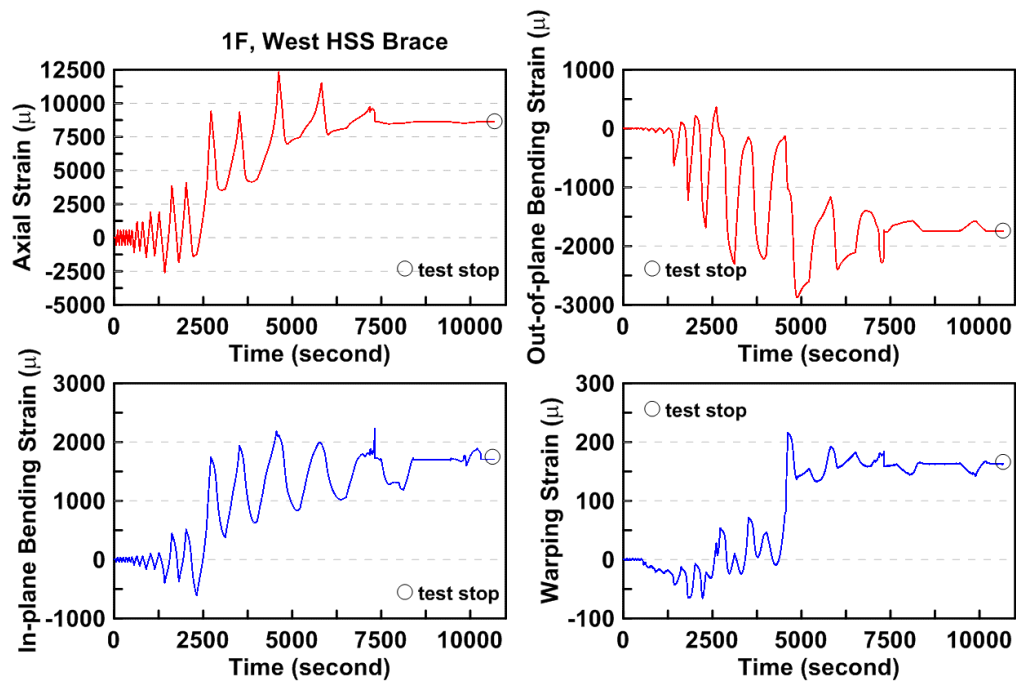


Figure 4.60 Specimen TCBF-B-1: time history of the decomposed strain components of first-story western-side HSS brace.

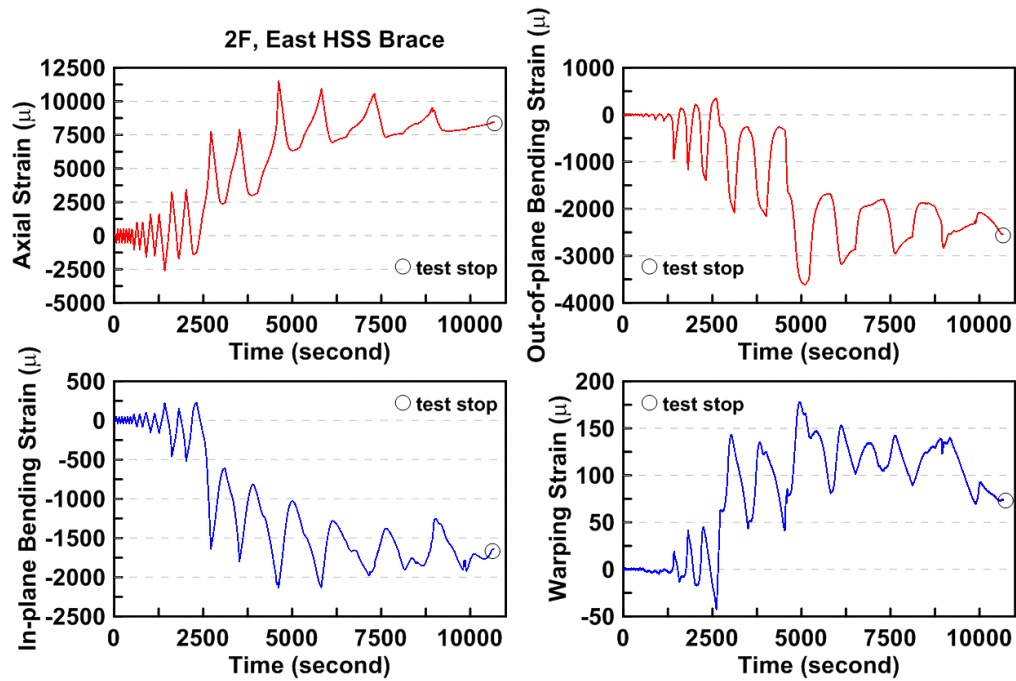


Figure 4.61 Specimen TCBF-B-1: time history of the decomposed strain components of second-story eastern-side HSS brace.

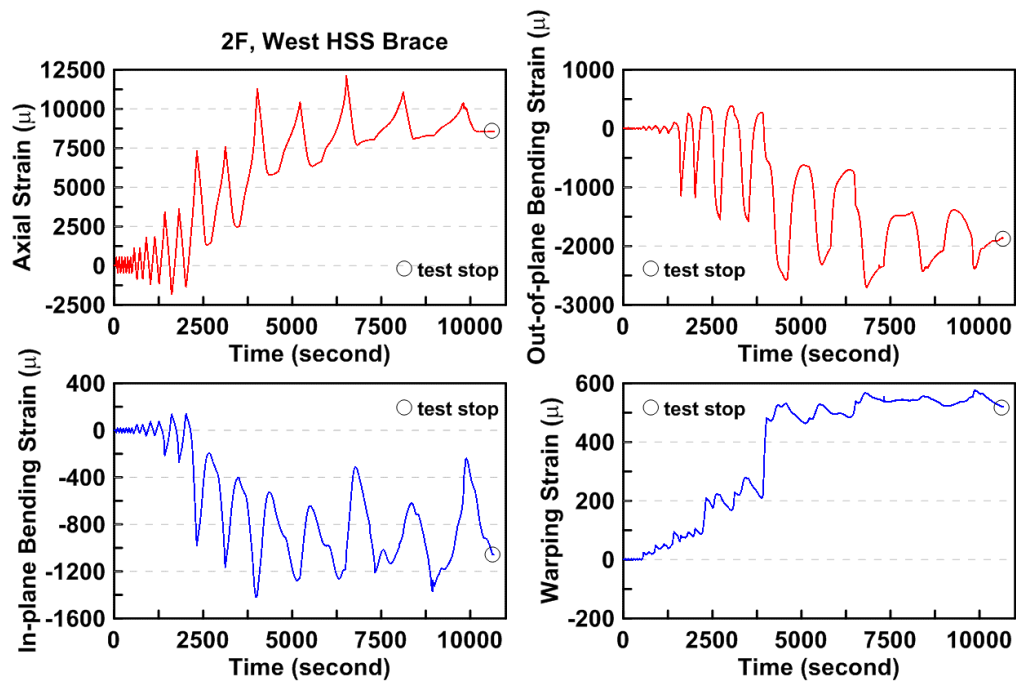


Figure 4.62(a) Specimen TCBF-B-1: time history of the decomposed strain components of second-story western-side HSS brace.

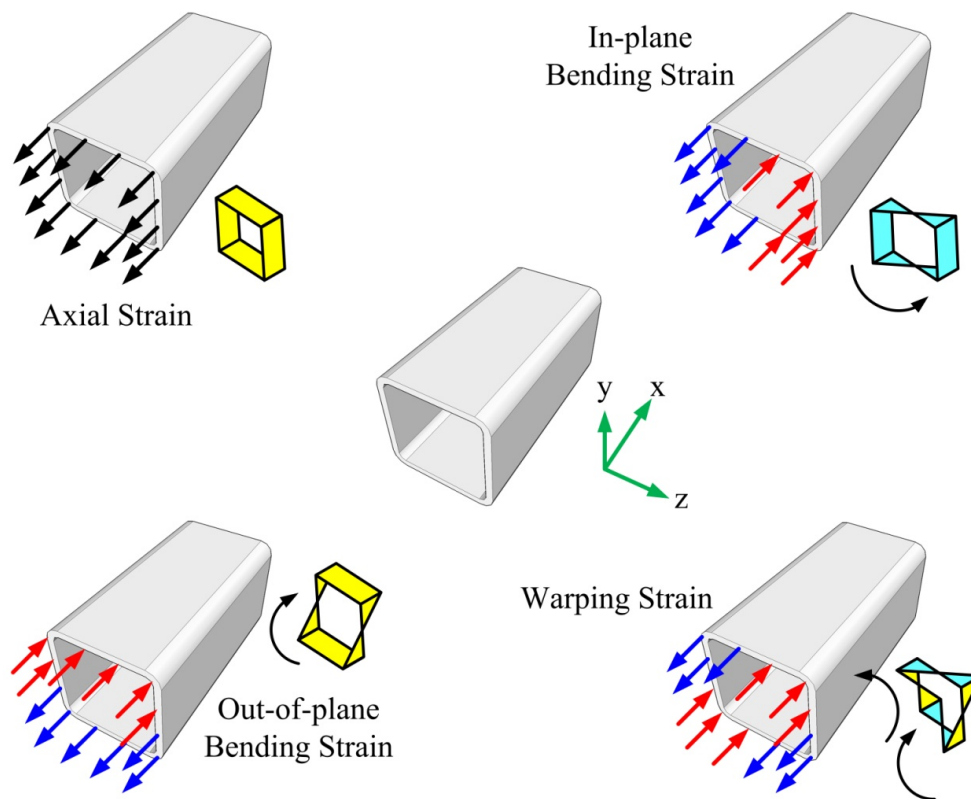


Figure 4.62(b) Definition of the decomposed strain components.

4.1.1.2.5 Panel Zone Response

Estimated panel zone shear stress versus measured panel zone shear strain relationship for four locations are plotted in Figure 4.63. This suggests that yielding occurs in the upper-floor, east-side panel zone. Time history of derived rosette-type strain gauge readings in the panel zone area at each story are shown in Figures 4.64 to 4.67. Normalized maximum and minimum principal stress relationships along with different yield criteria for the panel zone regions are plotted in Figures 4.68 to 4.71.

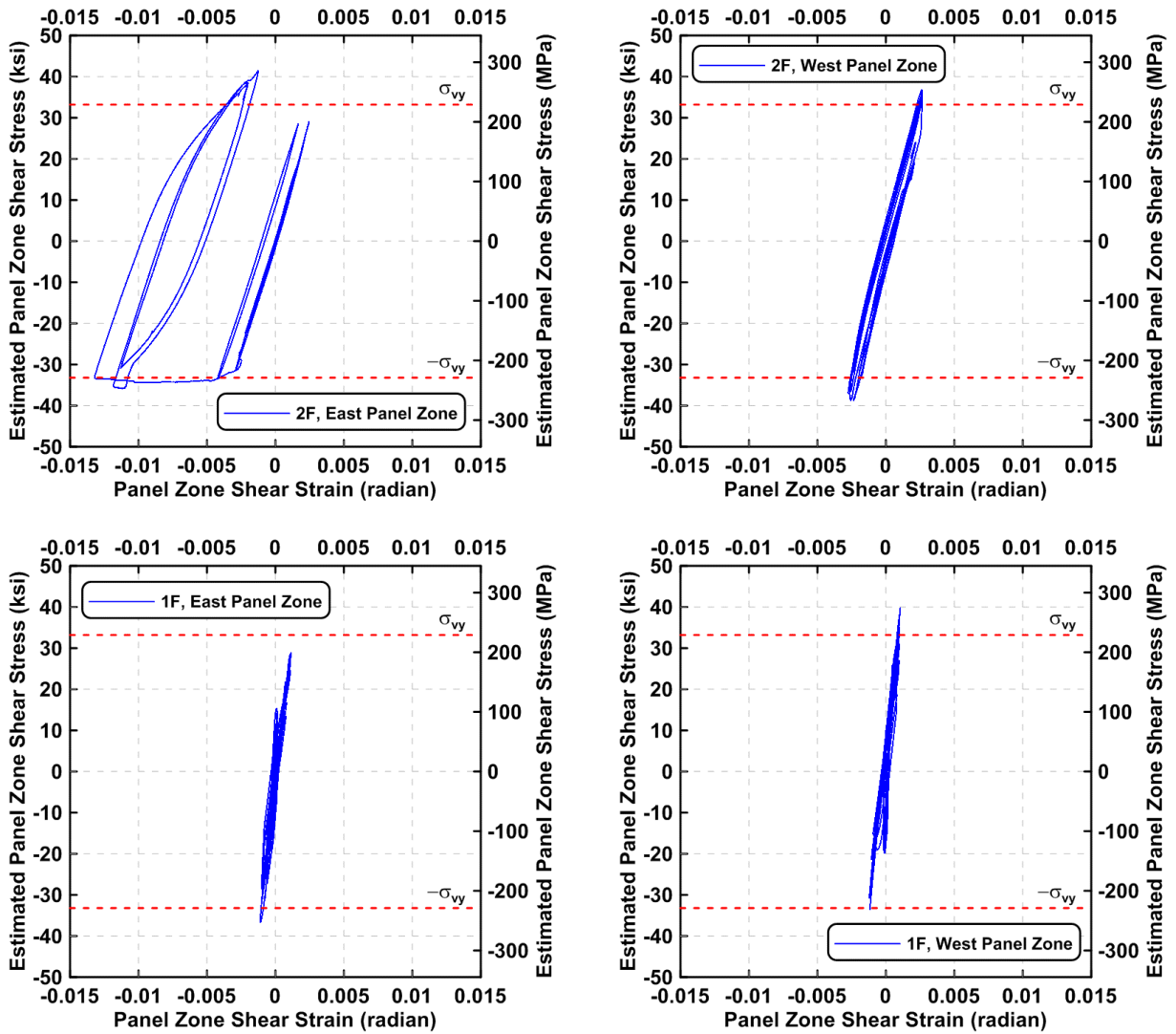


Figure 4.63 Specimen TCBF-B-1: estimated panel zone shear stress versus shear strain relationships.

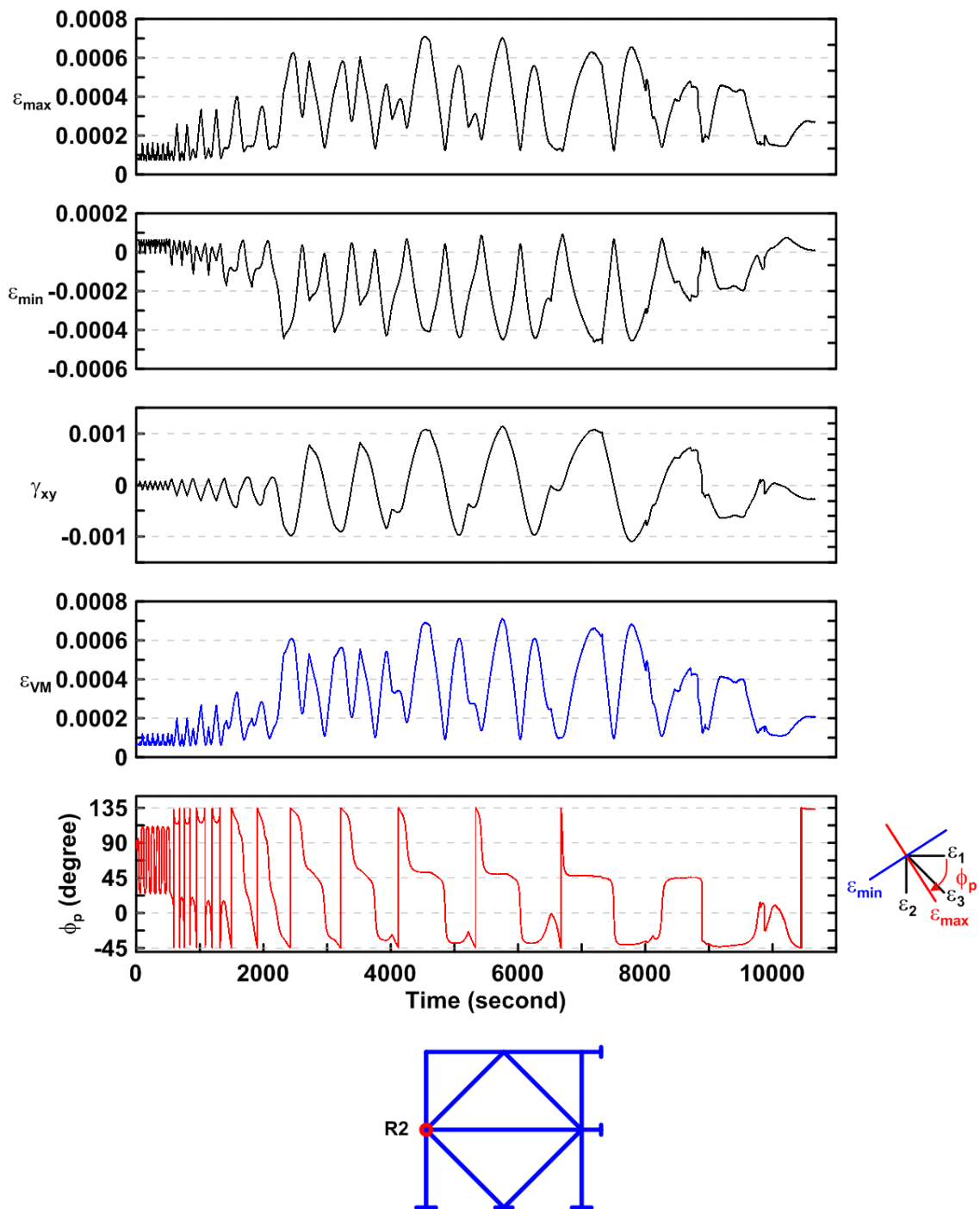


Figure 4.64 Specimen TCBF-B-1, lower panel zone: time history of rosette-type strain gauge readings (location: R2).

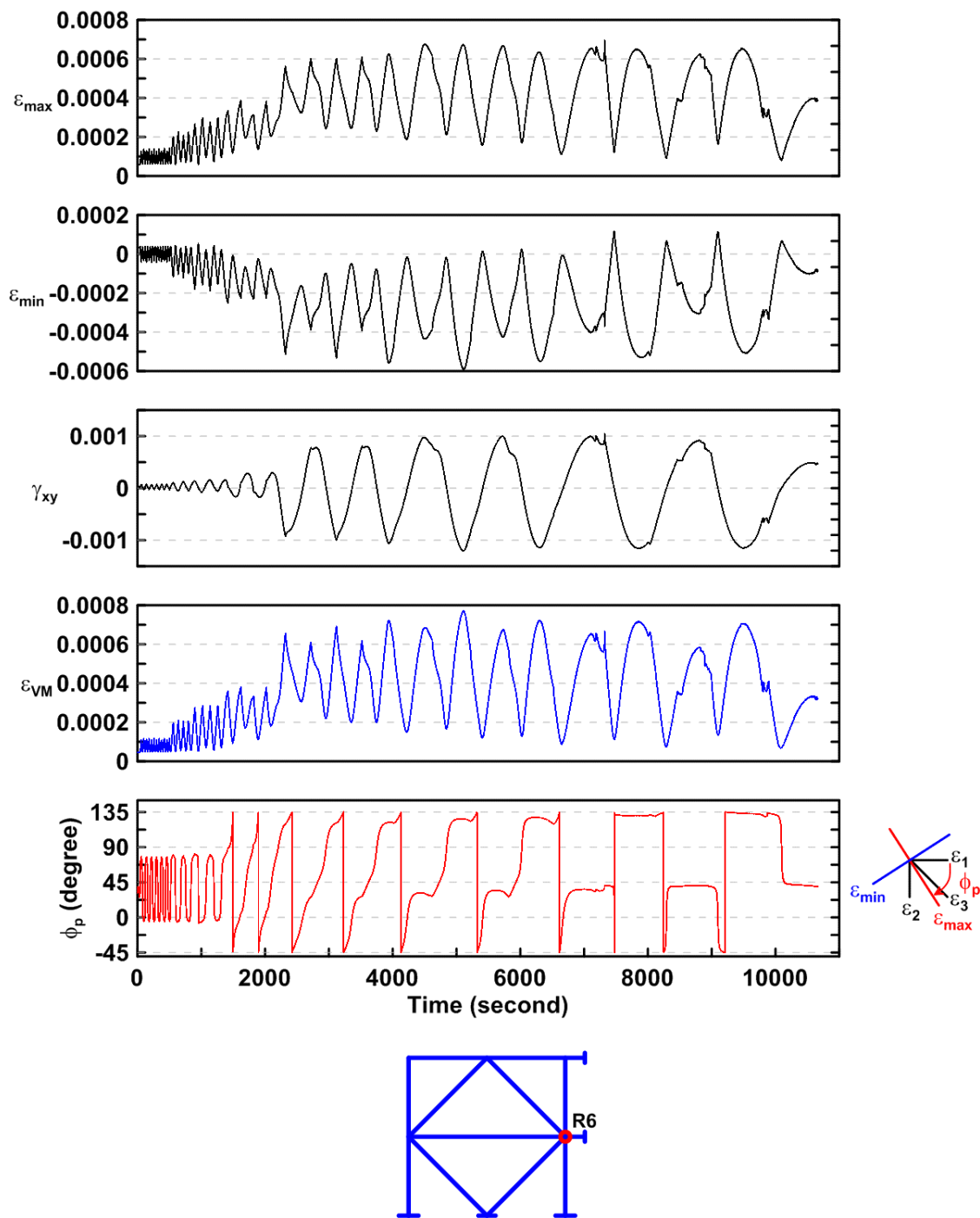


Figure 4.65 Specimen TCBF-B-1, lower panel zone: time history of rosette-type strain gauge readings (location: R6).

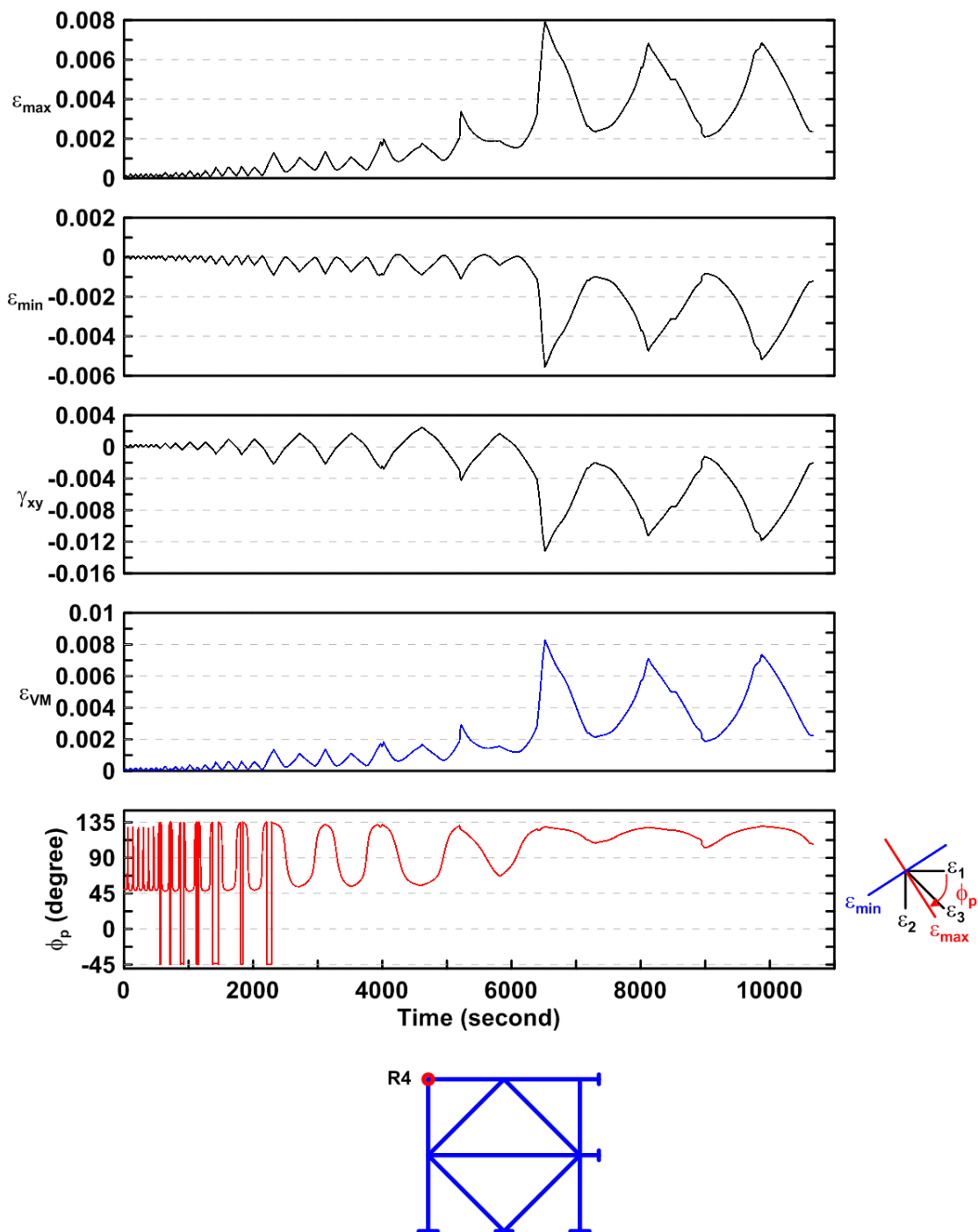


Figure 4.66 Specimen TCBF-B-1, roof panel zone: time history of rosette-type strain gauge readings (location: R4).

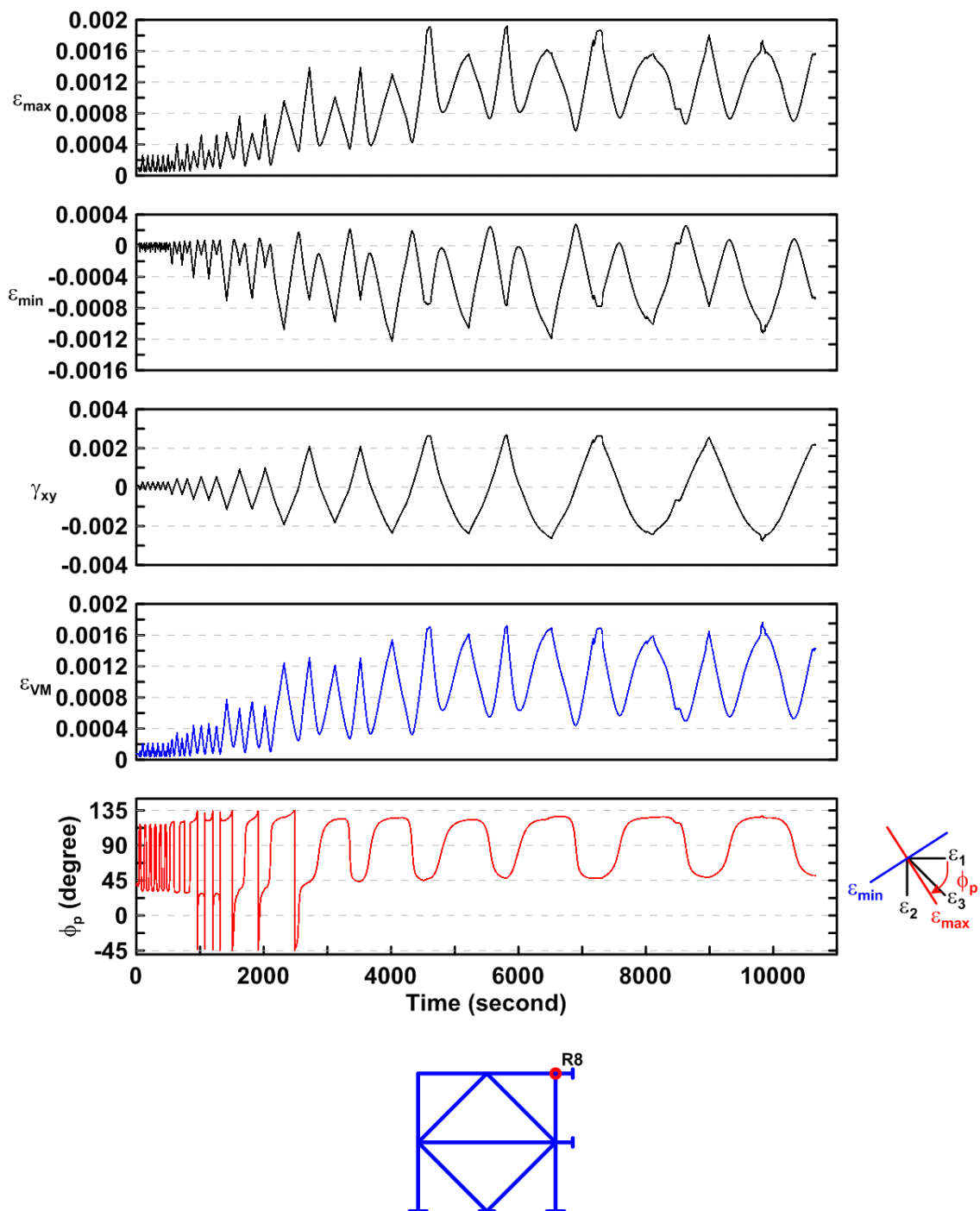


Figure 4.67 Specimen TCBF-B-1, roof panel zone: time history of rosette-type strain gauge readings (location: R8).

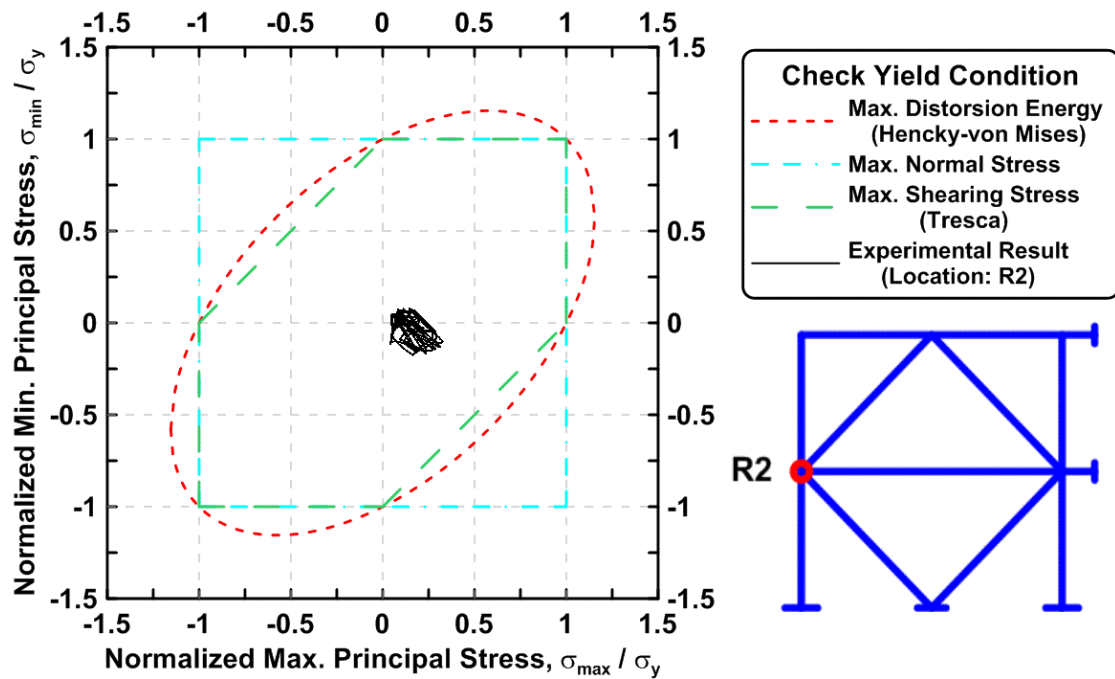


Figure 4.68 Specimen TCBF-B-1, lower panel zone: normalized maximum principal stress versus normalized minimum principal stress (location: R2).

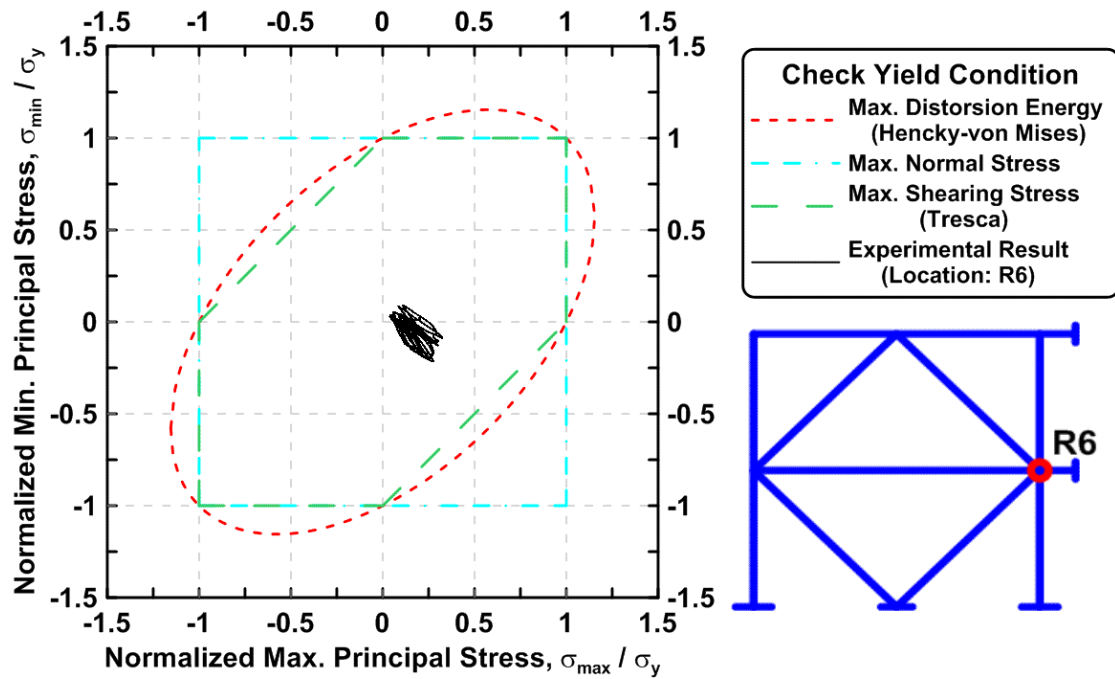


Figure 4.69 Specimen TCBF-B-1, lower panel zone: normalized maximum principal stress versus normalized minimum principal stress (location: R6).

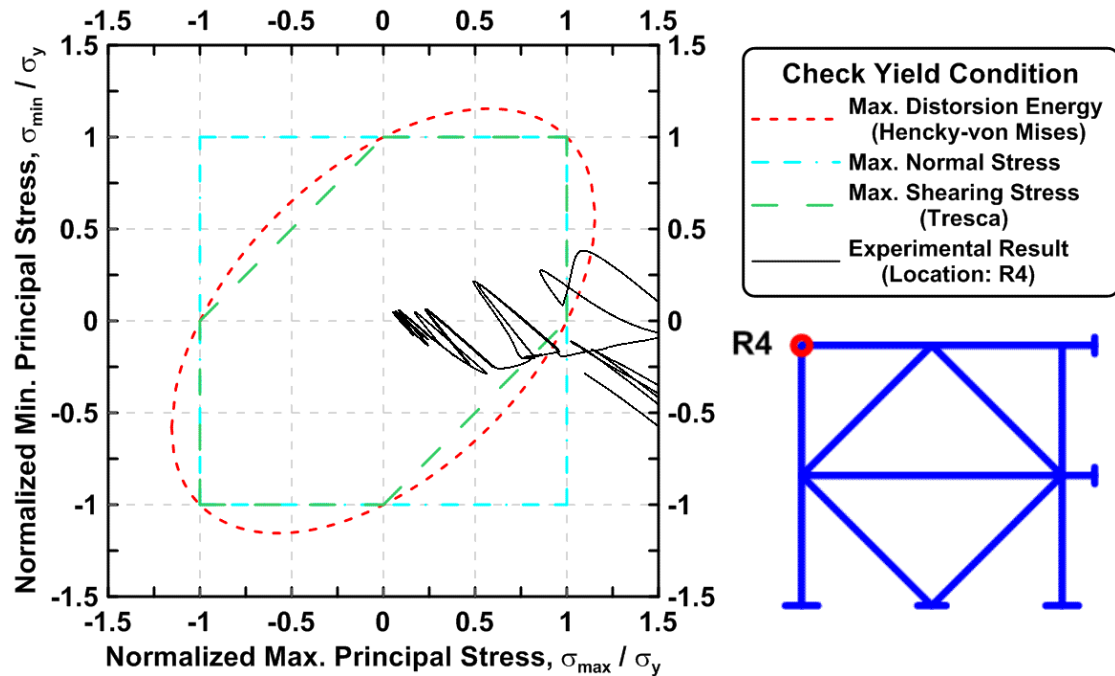


Figure 4.70 Specimen TCBF-B-1, roof panel zone: normalized maximum principal stress versus normalized minimum principal stress (location: R4).

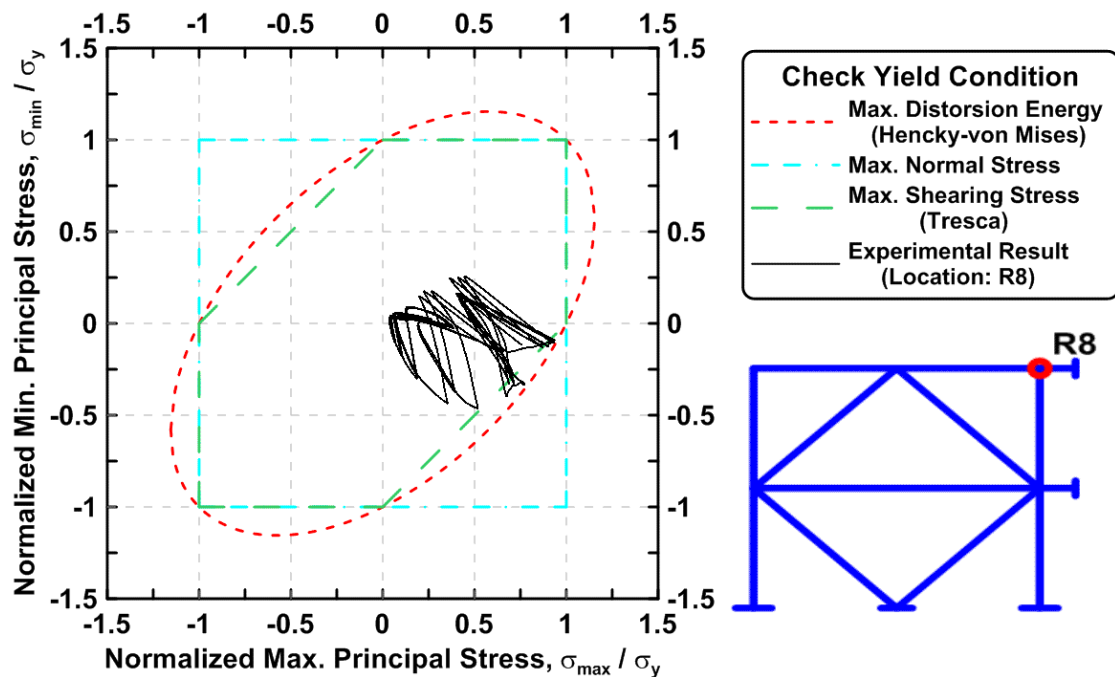


Figure 4.71 Specimen TCBF-B-1, roof panel zone: normalized maximum principal stress versus normalized minimum principal stress (location: R8).

4.1.1.2.6 Gusset Plate Response

The time history of derived rosette-type strain gauge readings in the 3/4-in.-thick one-piece gusset plate are shown in Figures 4.72 to 4.83. Normalized maximum and minimum principal stress relationships along with different yield criteria for the rosettes on the gusset plate are plotted in Figures 4.84 to 4.95.

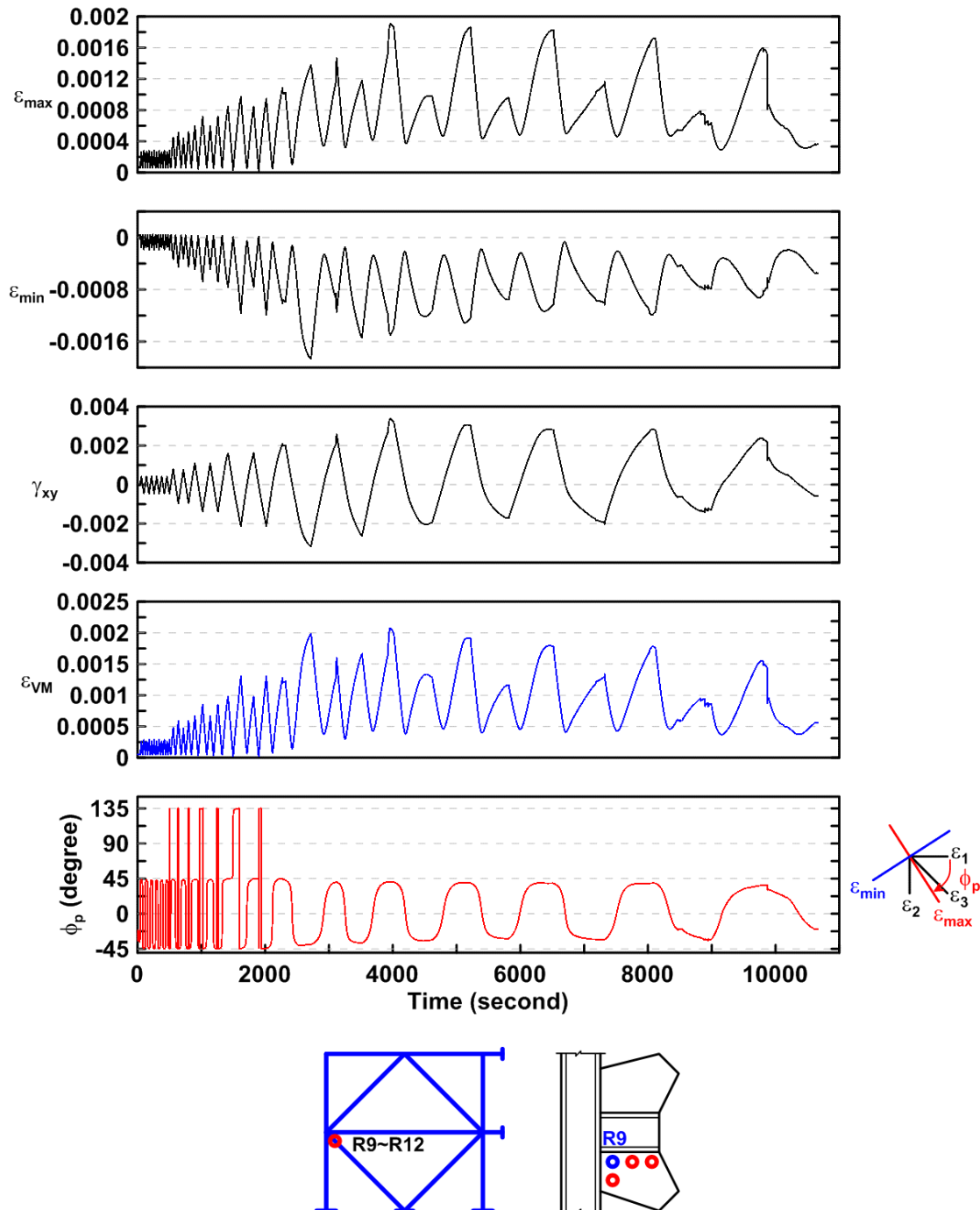


Figure 4.72 Specimen TCBF-B-1: time history of rosette-type strain gauge readings in the one-piece gusset plate (location: R9).

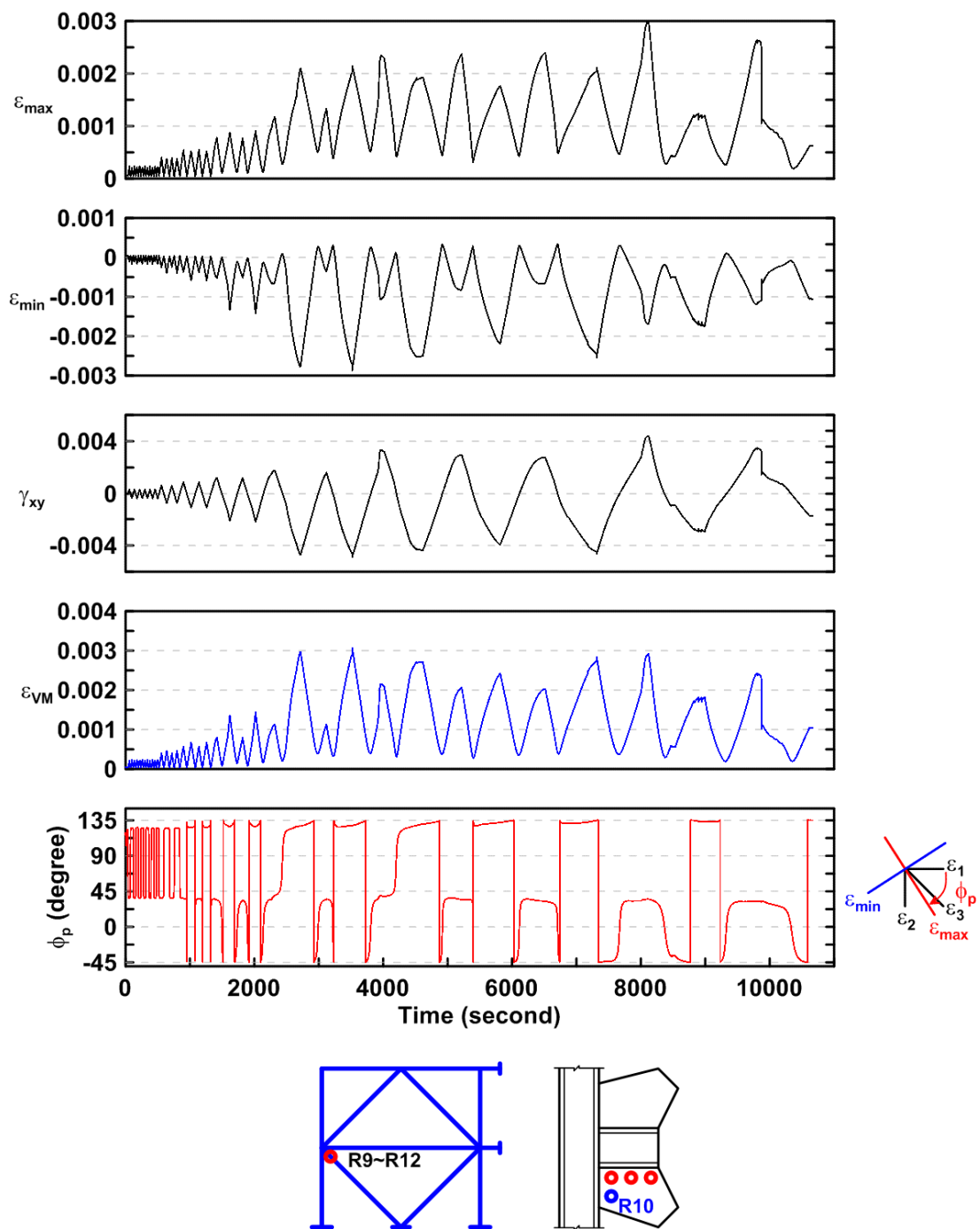


Figure 4.73 Specimen TCBF-B-1: time history of rosette-type strain gauge readings in the one-piece gusset plate (location: R10).

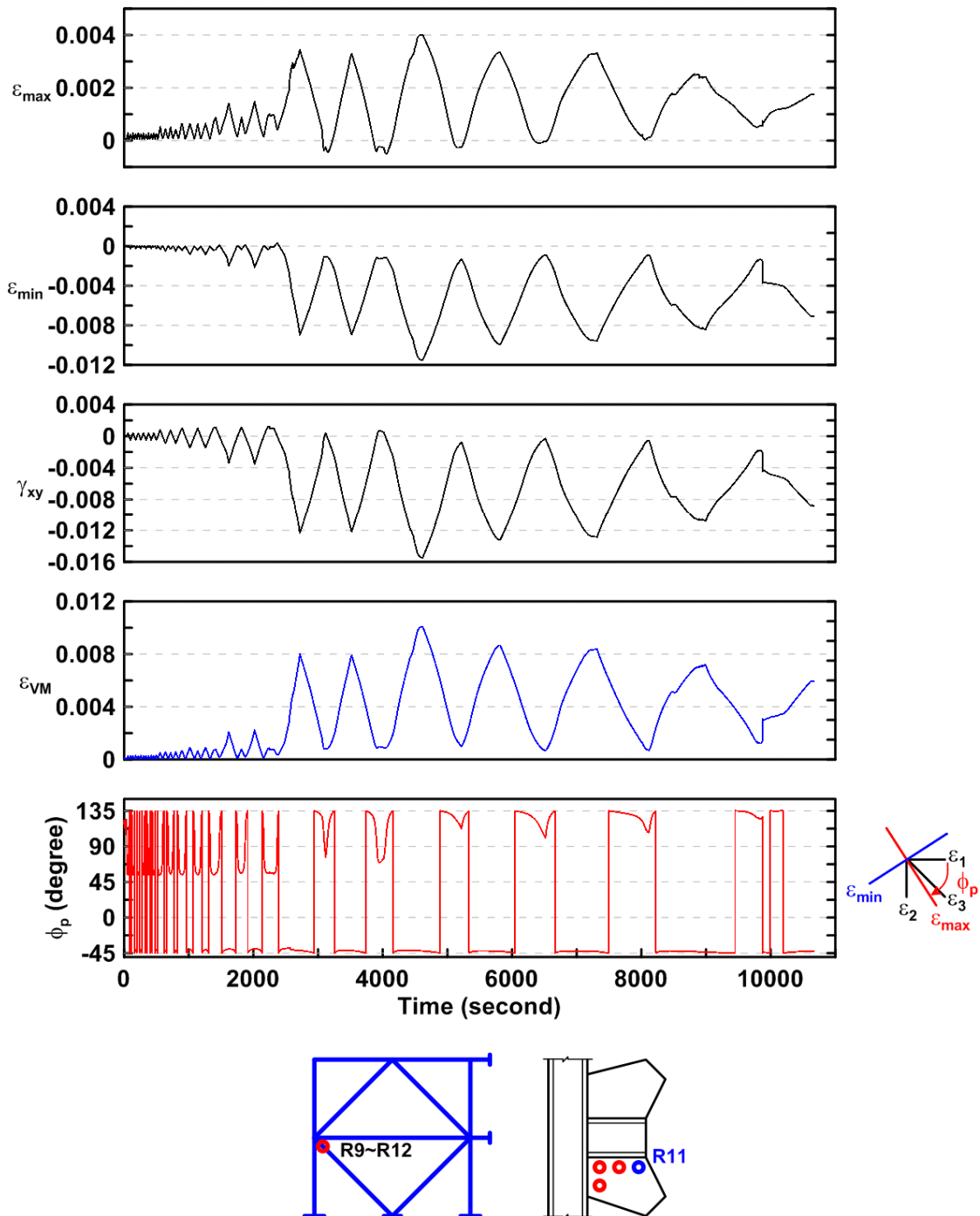


Figure 4.74 Specimen TCBF-B-1: time history of rosette-type strain gauge readings in the one-piece gusset (location: R11).

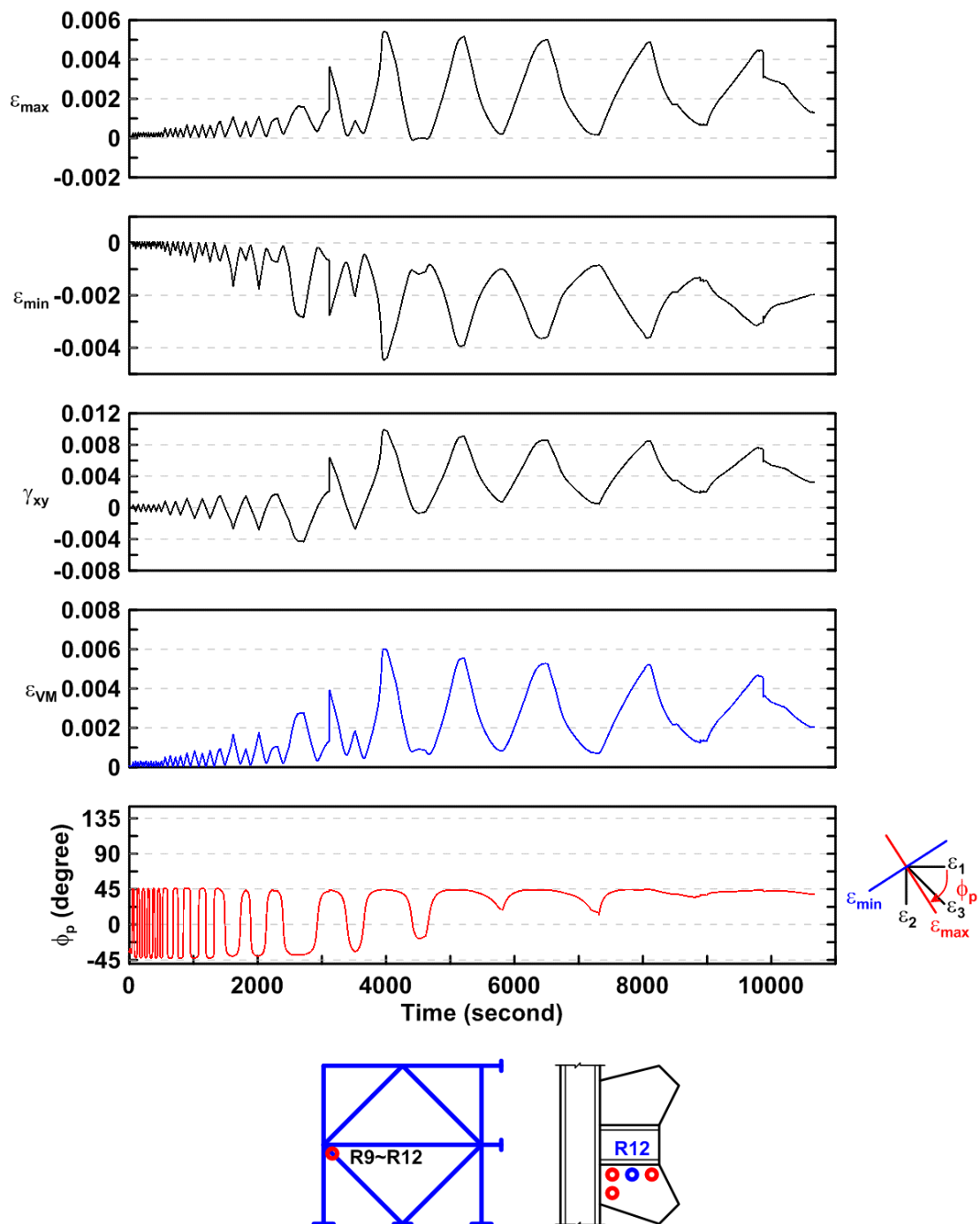


Figure 4.75 Specimen TCBF-B-1: time history of rosette-type strain gauge readings in the one-piece gusset plate (location: R12).

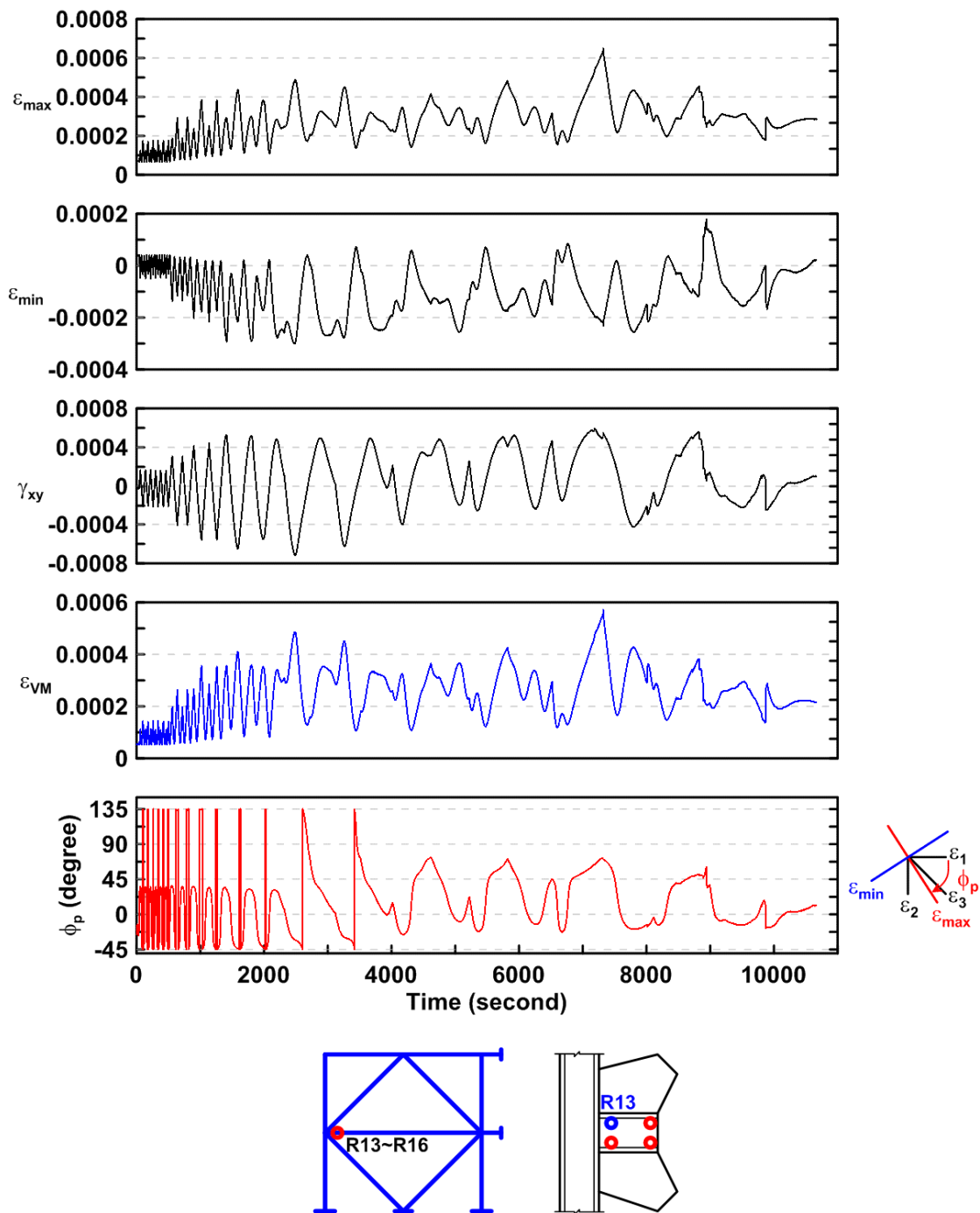


Figure 4.76 Specimen TCBF-B-1: time history of rosette-type strain gauge readings in the one-piece gusset plate (location: R13).

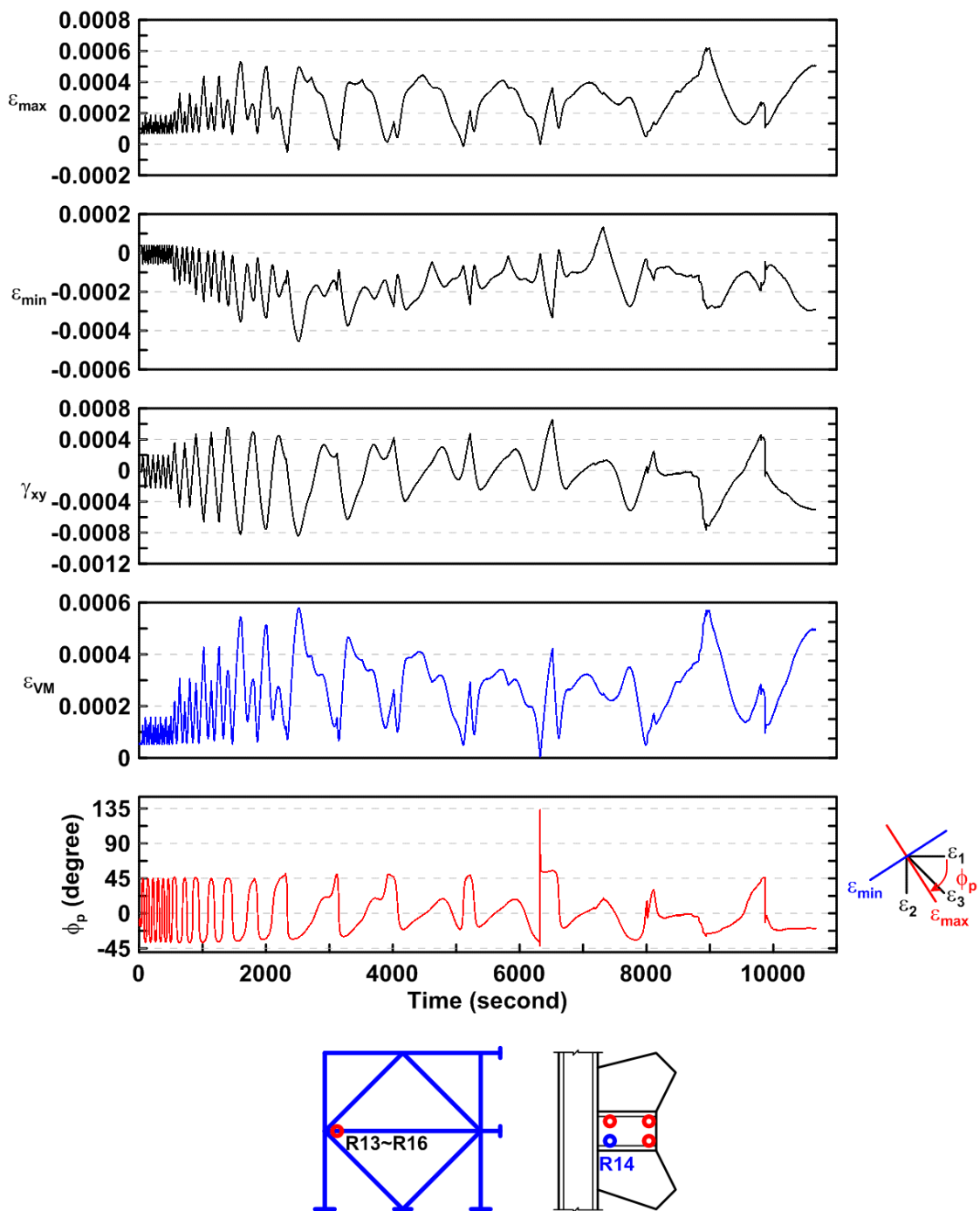


Figure 4.77 Specimen TCBF-B-1: time history of rosette-type strain gauge readings in the one-piece gusset plate (location: R14).

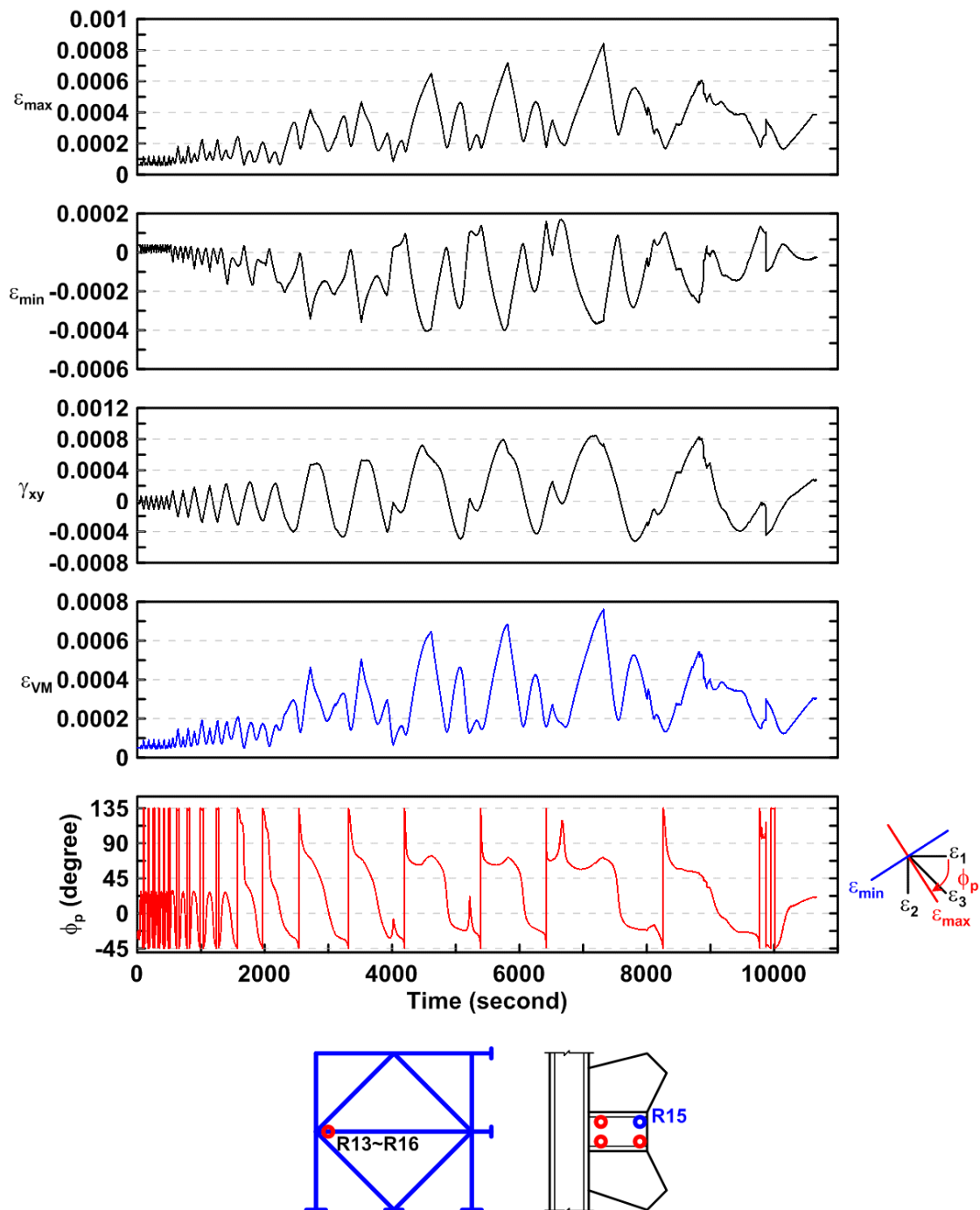


Figure 4.78 Specimen TCBF-B-1: time history of rosette-type strain gauge readings in the one-piece gusset plate (location: R15).

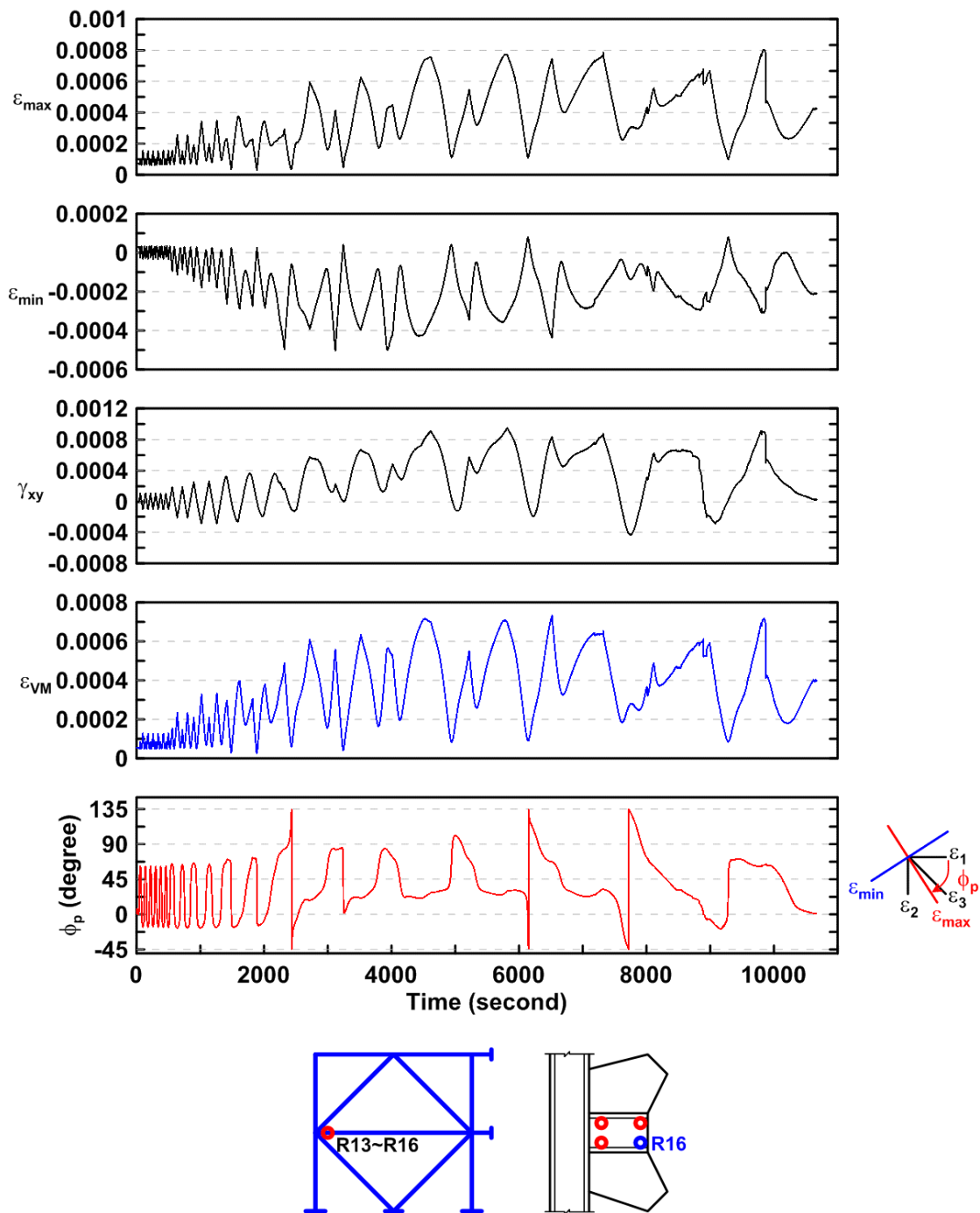


Figure 4.79 Specimen TCBF-B-1: time history of rosette-type strain gauge readings in the one-piece gusset plate (location: R16).

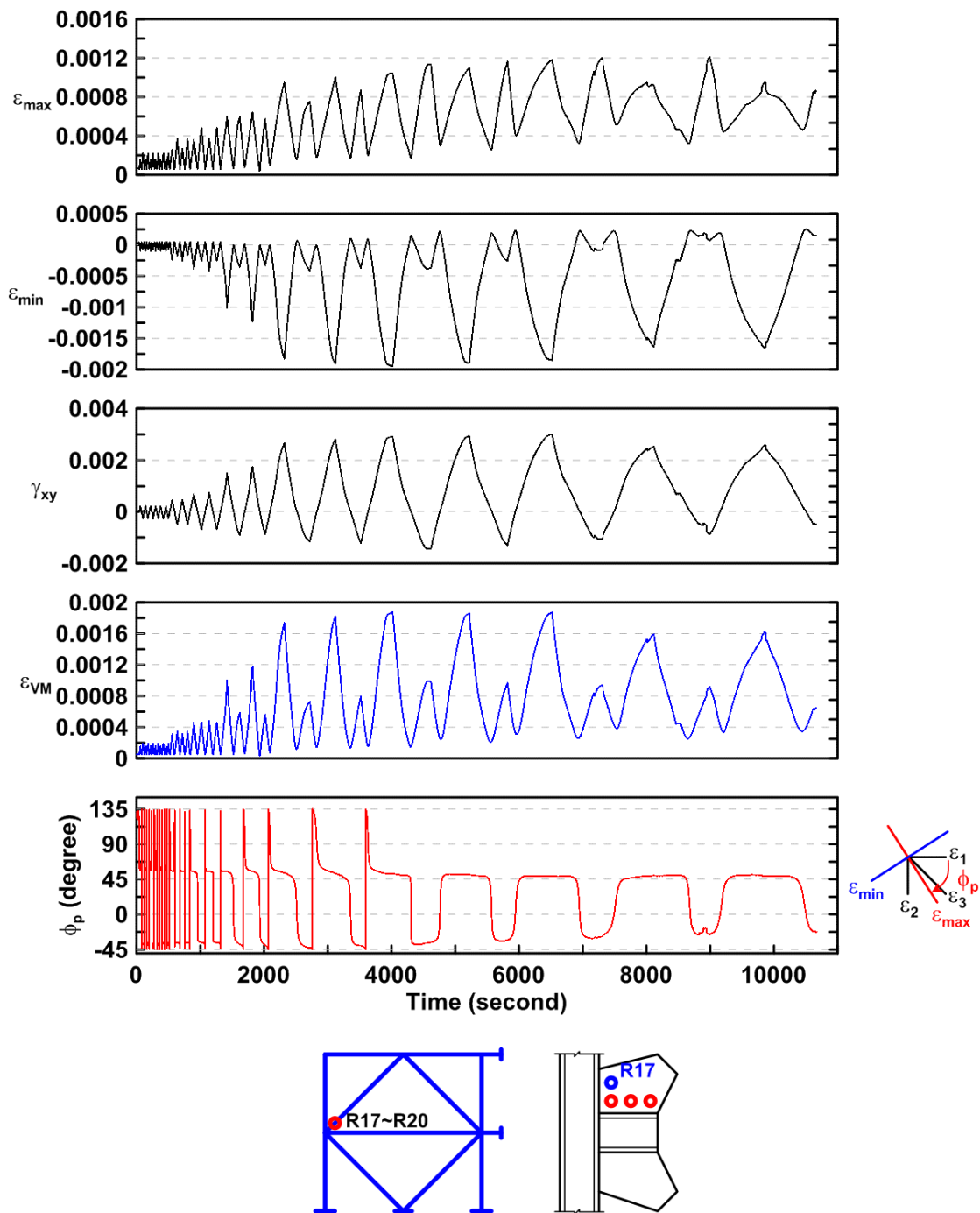


Figure 4.80 Specimen TCBF-B-1: time history of rosette-type strain gauge readings in the one-piece gusset plate (location: R17).

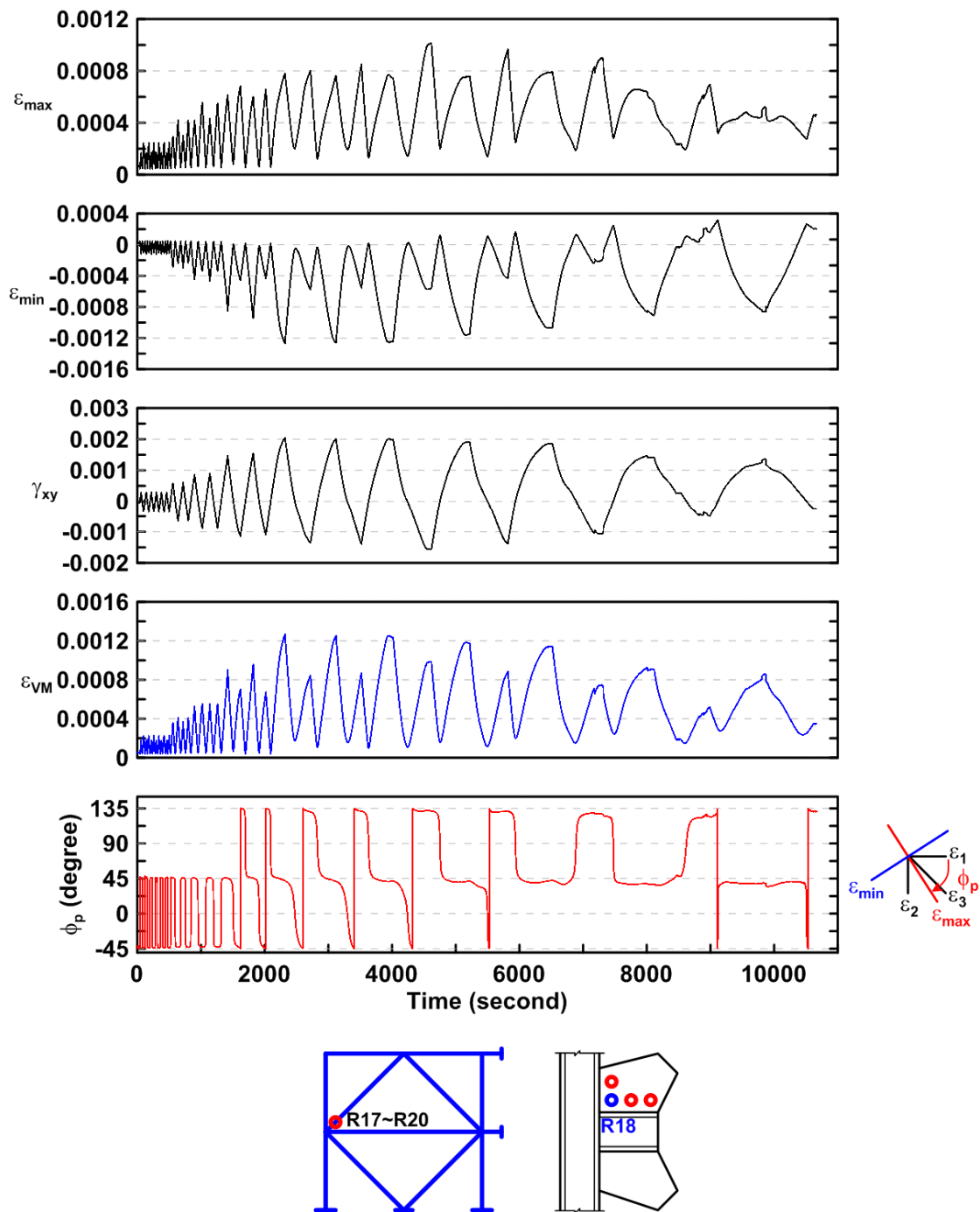


Figure 4.81 Specimen TCBF-B-1: time history of rosette-type strain gauge readings in the one-piece gusset plate (location: R18).

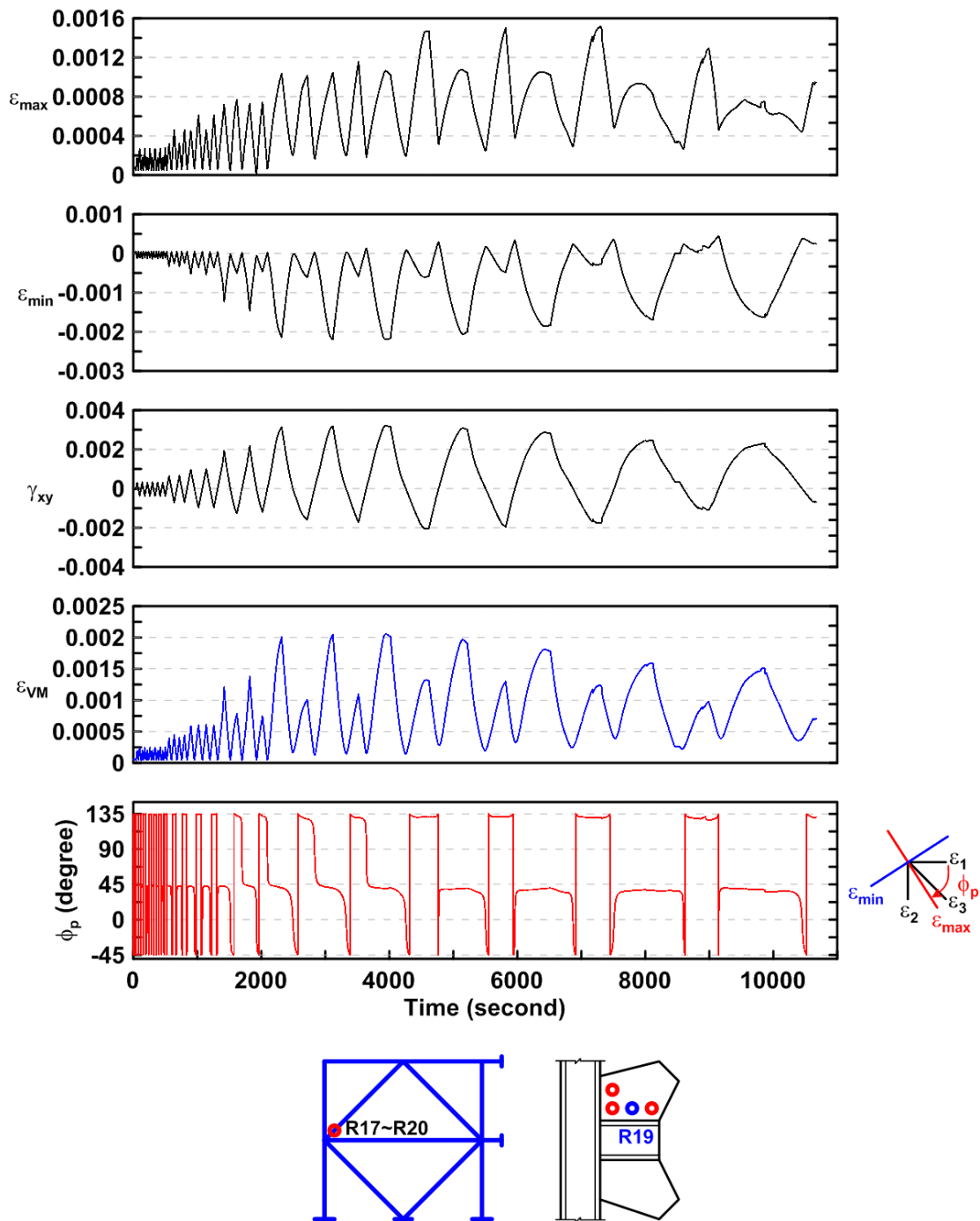


Figure 4.82 Specimen TCBF-B-1: time history of rosette-type strain gauge readings in the one-piece gusset plate (location: R19).

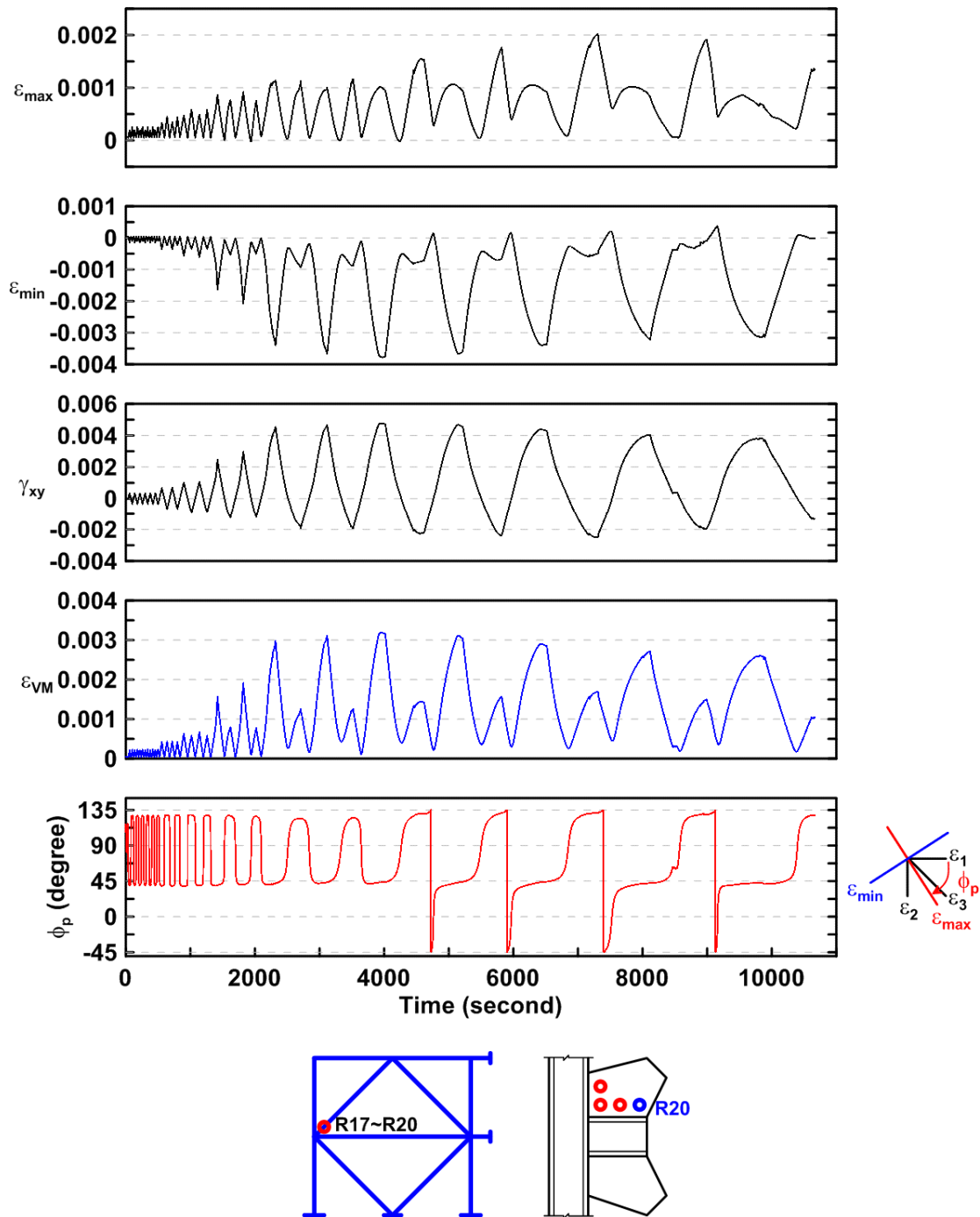


Figure 4.83 Specimen TCBF-B-1: time history of rosette-type strain gauge readings in the one-piece gusset plate (location: R20).

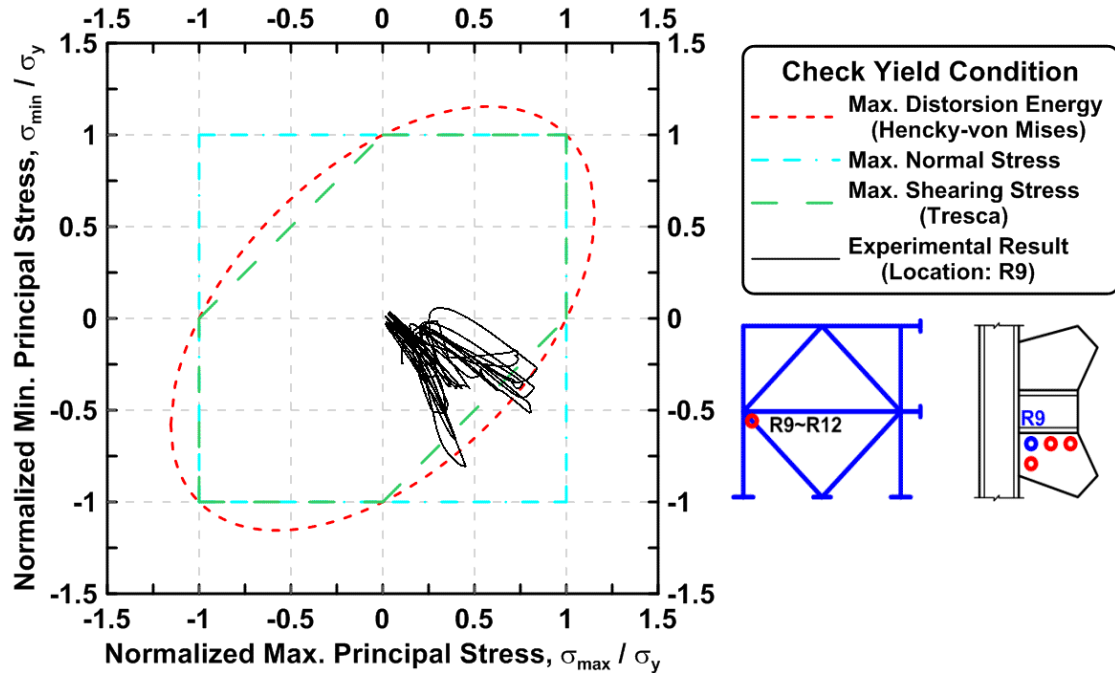


Figure 4.84 Specimen TCBF-B-1: normalized maximum principal stress versus normalized minimum principal stress in one-piece gusset plate (location: R9).

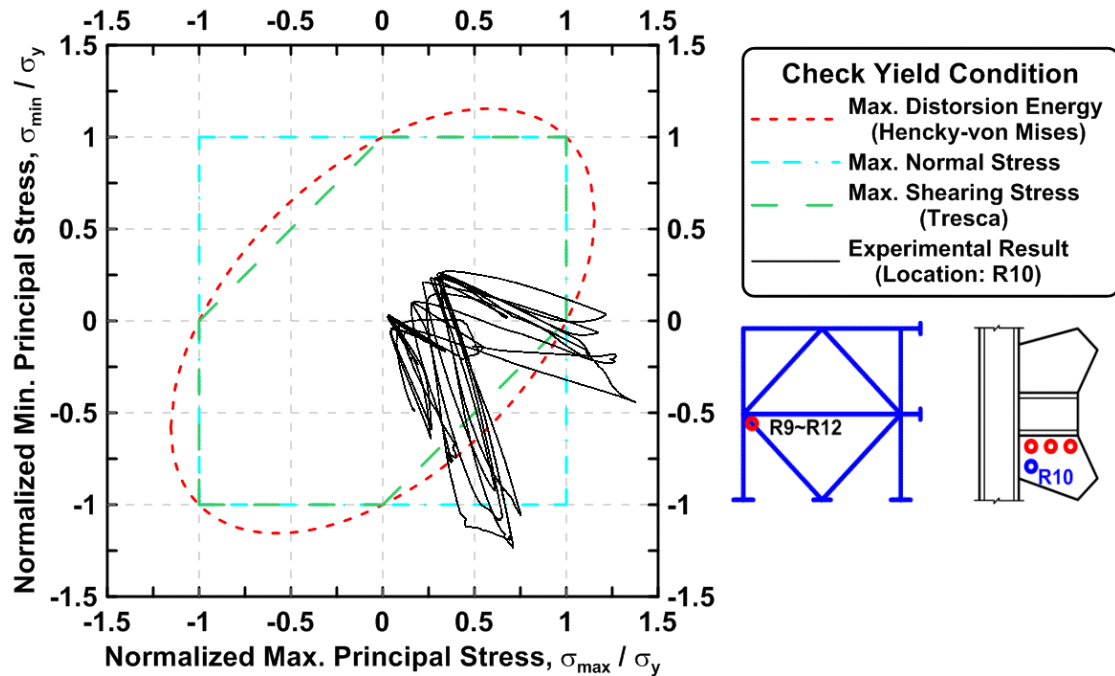


Figure 4.85 Specimen TCBF-B-1: normalized maximum principal stress versus normalized minimum principal stress in one-piece gusset plate (location: R10).

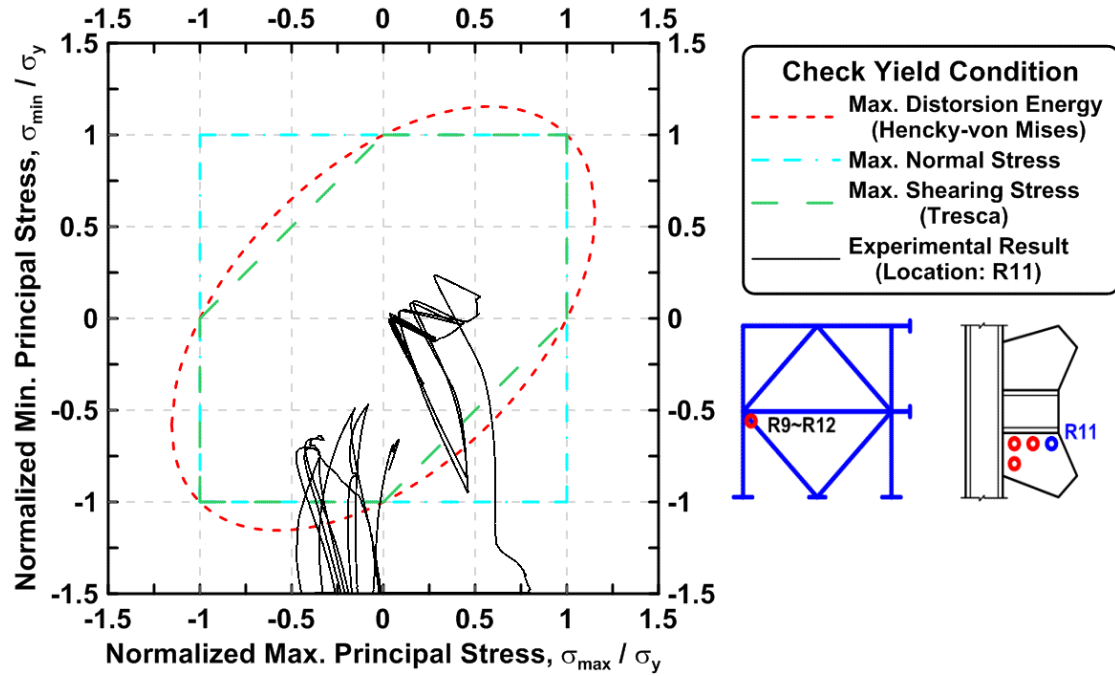


Figure 4.86 Specimen TCBF-B-1: normalized maximum principal stress versus normalized minimum principal stress in one-piece gusset plate (location: R11).

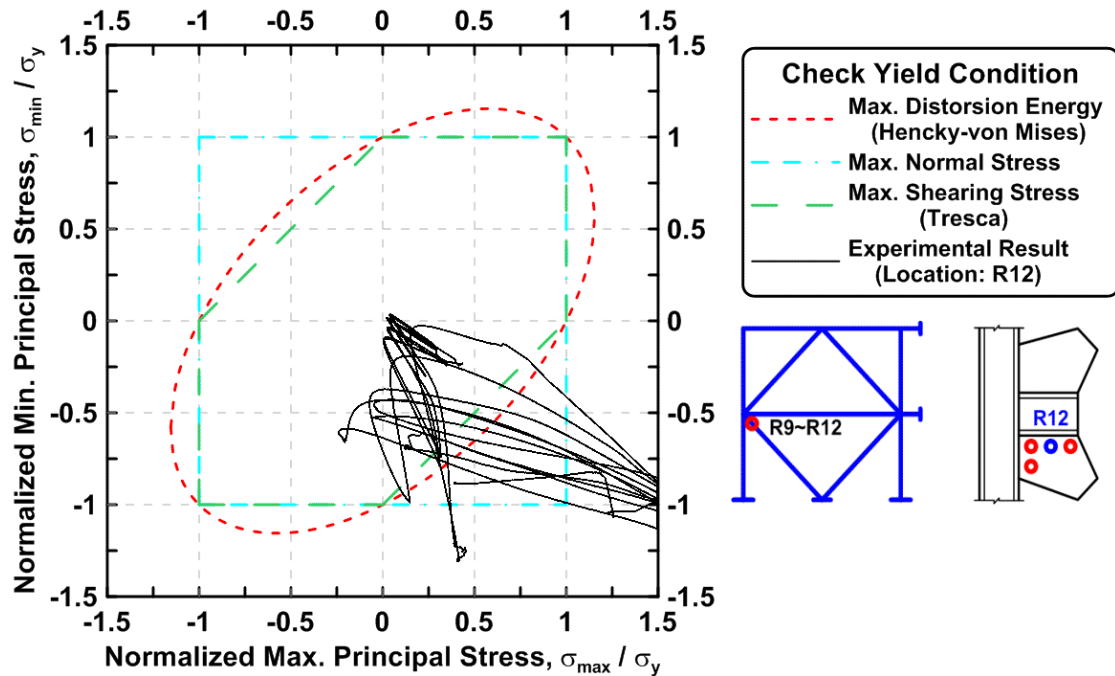


Figure 4.87 Specimen TCBF-B-1: normalized maximum principal stress versus normalized minimum principal stress in one-piece gusset plate (location: R12).

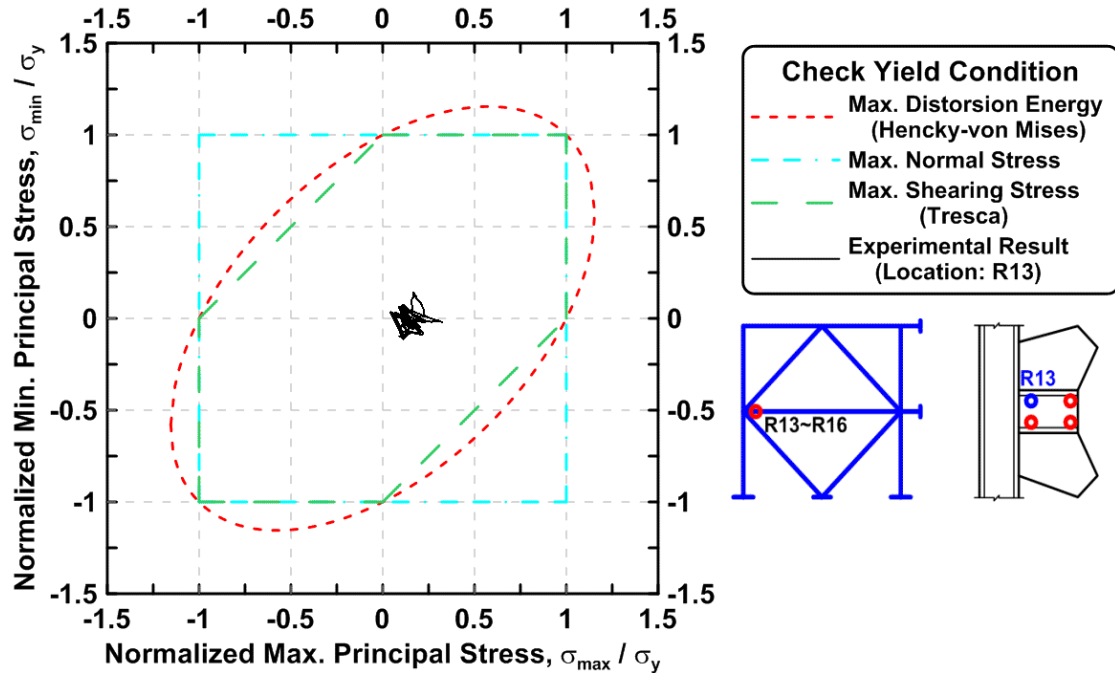


Figure 4.88 Specimen TCBF-B-1: normalized maximum principal stress versus normalized minimum principal stress in one-piece gusset plate (location: R13).

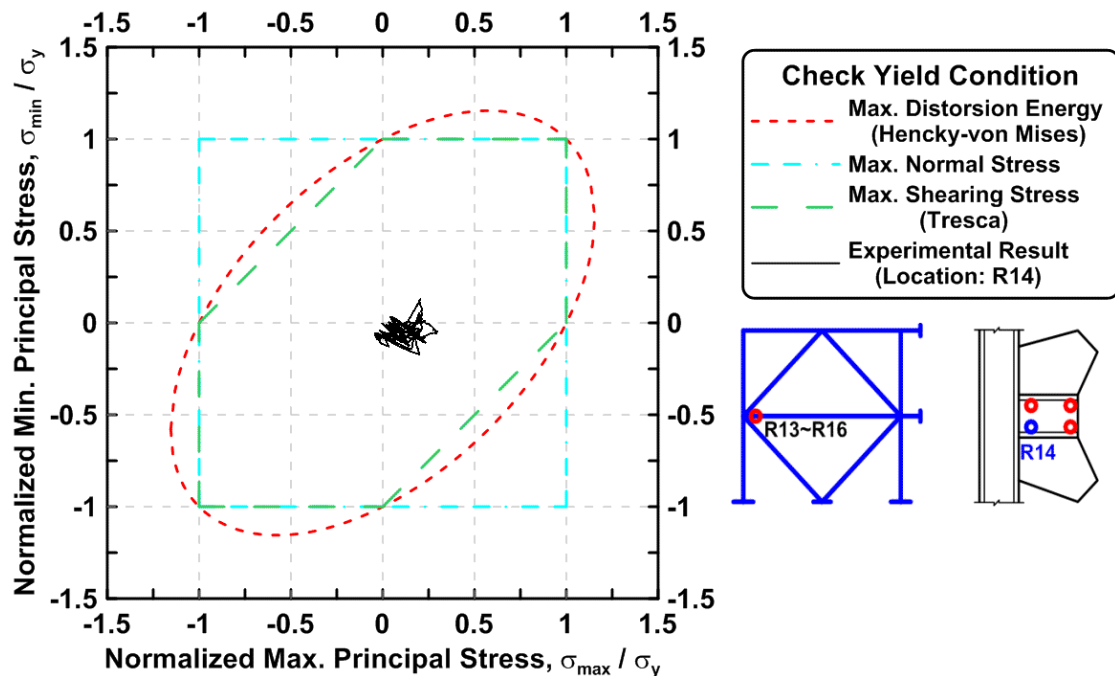


Figure 4.89 Specimen TCBF-B-1: normalized maximum principal stress versus normalized minimum principal stress in one-piece gusset plate (location: R14).

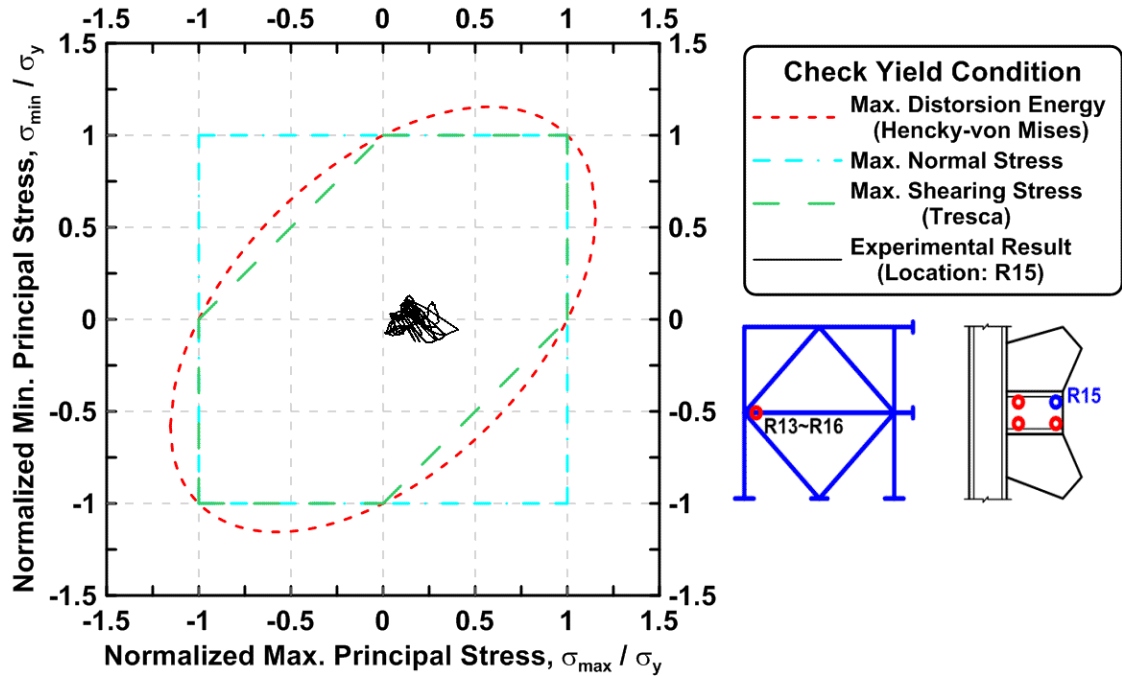


Figure 4.90 Specimen TCBF-B-1: normalized maximum principal stress versus normalized minimum principal stress in one-piece gusset plate (location: R15).

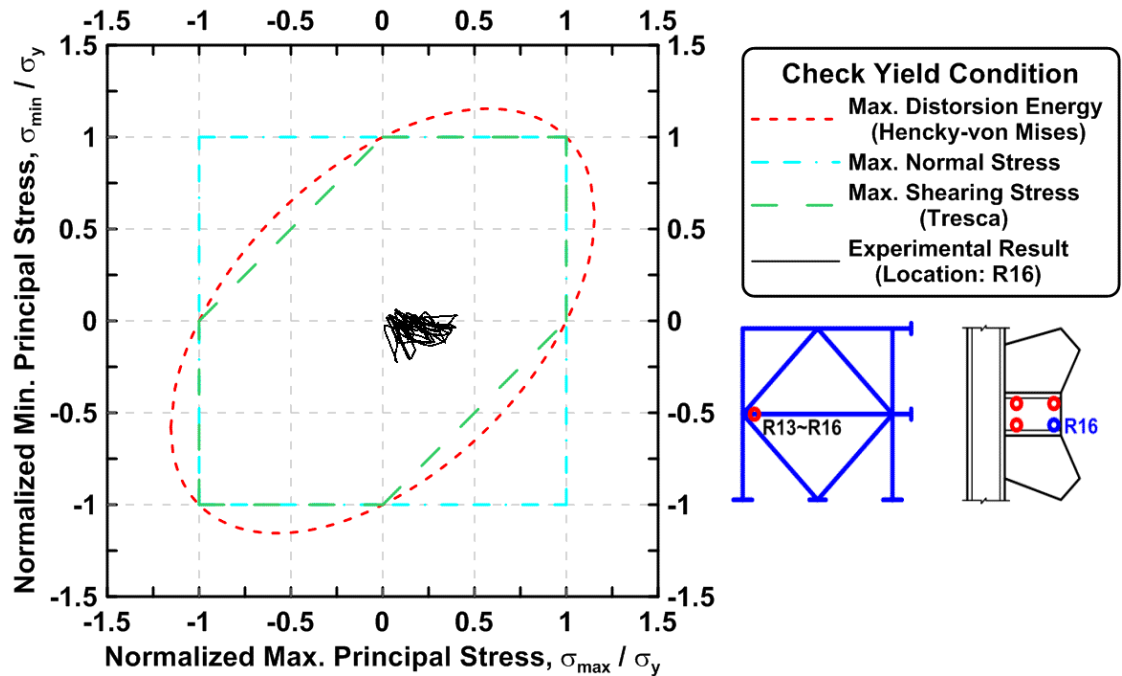


Figure 4.91 Specimen TCBF-B-1: normalized maximum principal stress versus normalized minimum principal stress in one-piece gusset plate (location: R16).

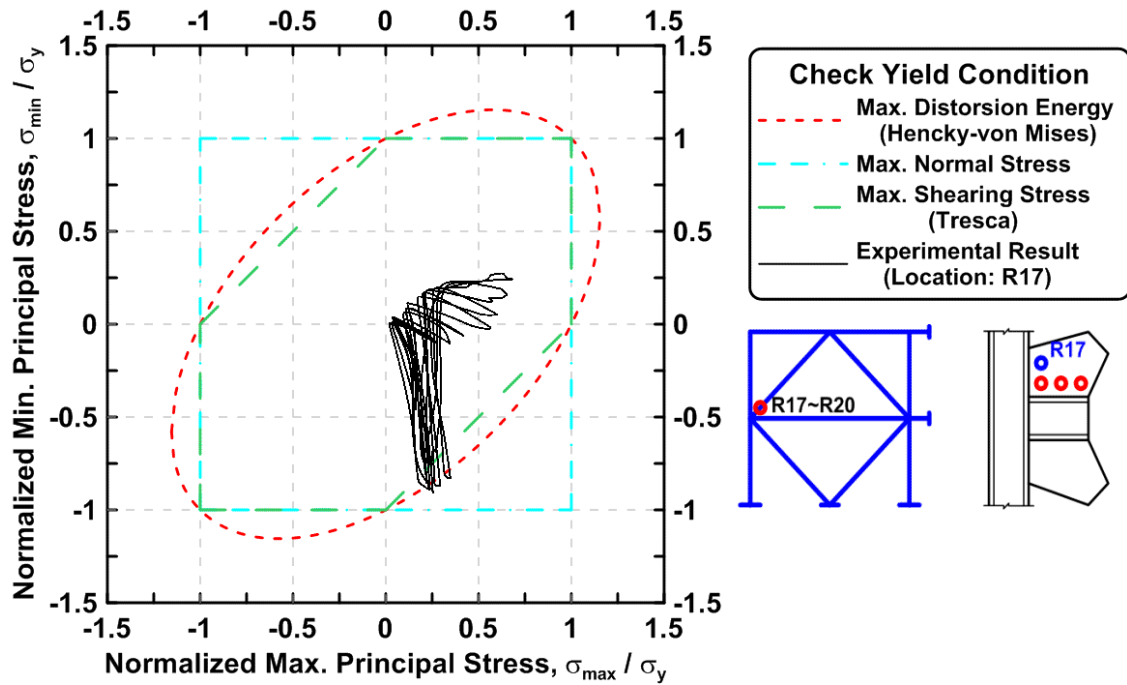


Figure 4.92 Specimen TCBF-B-1: normalized maximum principal stress versus normalized minimum principal stress in one-piece gusset plate (location: R17).

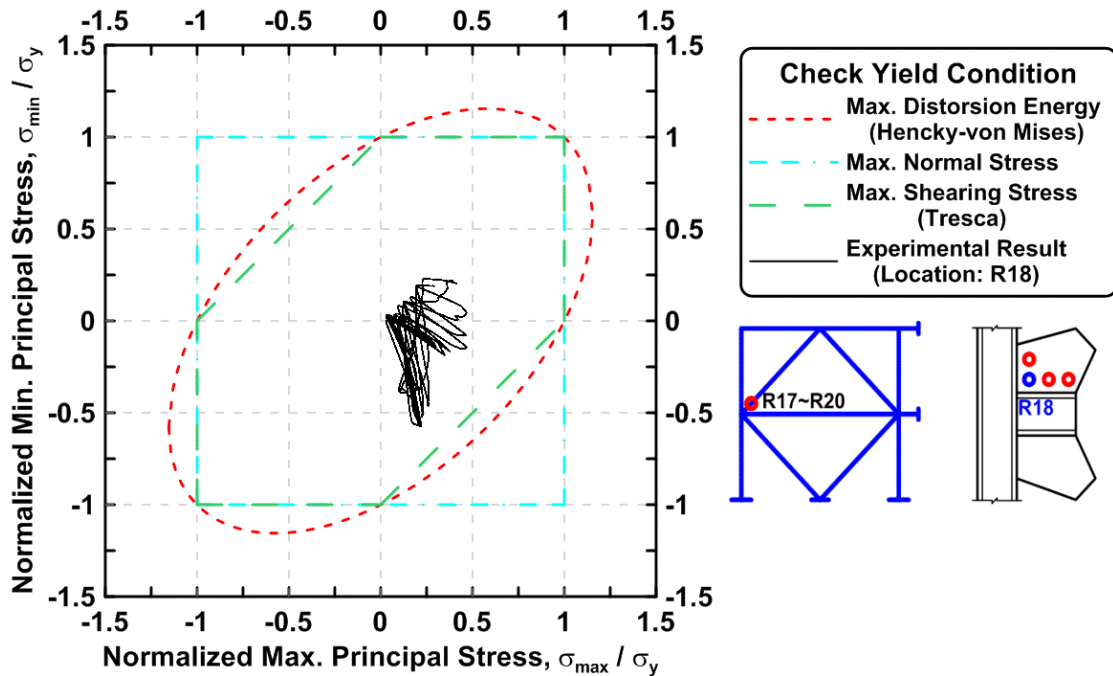


Figure 4.93 Specimen TCBF-B-1: normalized maximum principal stress versus normalized minimum principal stress in one-piece gusset plate (location: R18).

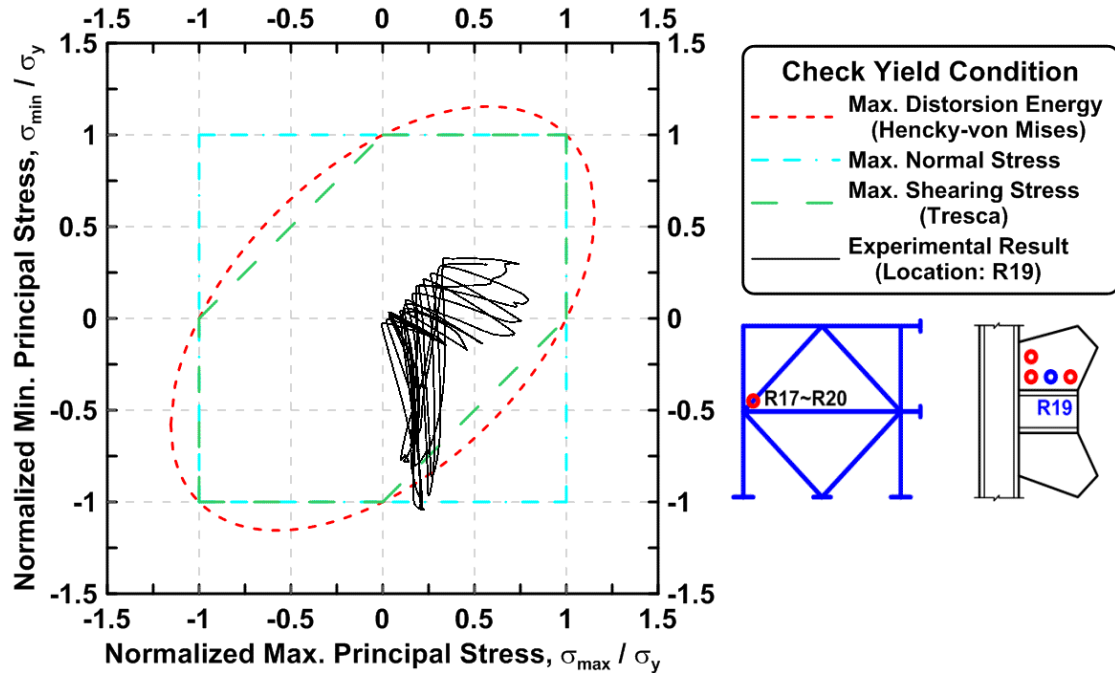


Figure 4.94 Specimen TCBF-B-1: normalized maximum principal stress versus normalized minimum principal stress in one-piece gusset plate (location: R19).

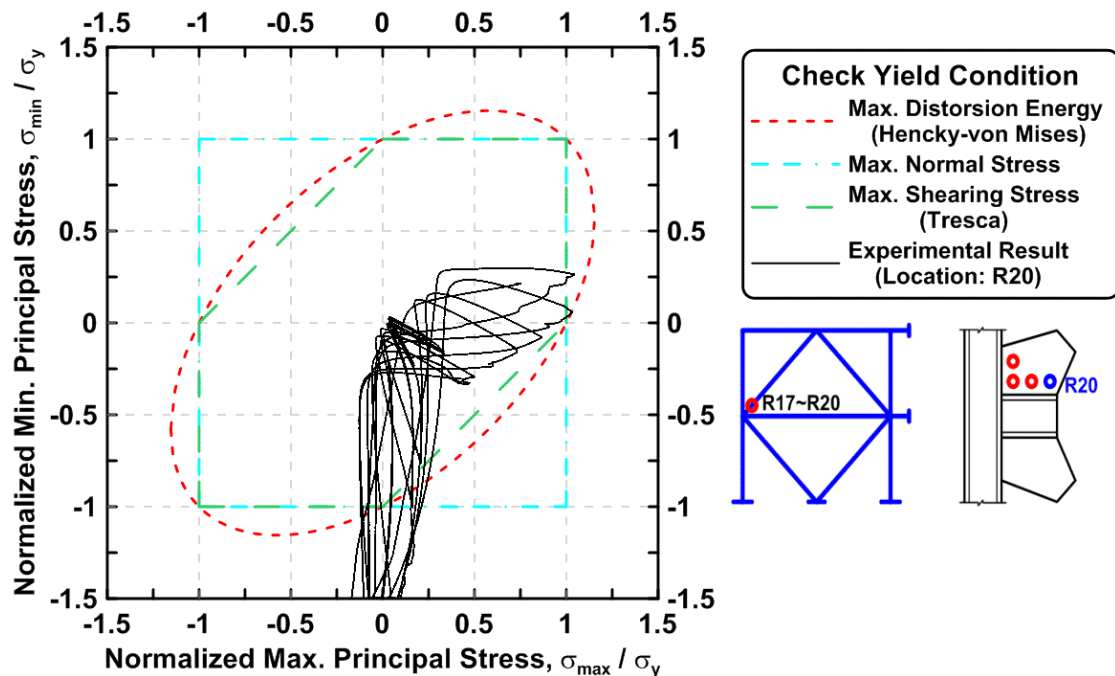


Figure 4.95 Specimen TCBF-B-1: normalized maximum principal stress versus normalized minimum principal stress in one-piece gusset plate (location: R20).

4.1.1.2.7 Test Set Up Response

While the strong floor and reaction wall are relatively stiff, they did deform during the tests. To assess this deformation, displacement transducers were attached to the laboratory building away from the reaction wall and used to measure the displacement of the brackets that supported the actuators in the direction of their applied load. The actuator bracket deformations versus actuator forces are plotted in Figure 4.96. It can be seen that the reaction wall and strong floor are distorting relative to the building; of course the building is likely deforming as well. The relative displacement time history between base plates of the specimen and the floor beam, relative displacement time history between floor beam and strong floor, and relative displacement time history between integrated reconfigurable reaction wall and strong floor at northern and southern sides are shown in Figure 4.97. The out-of-plane deformation time history of the lateral supporting frame with respect to the wall of the building at different locations are plotted in Figure 4.98.

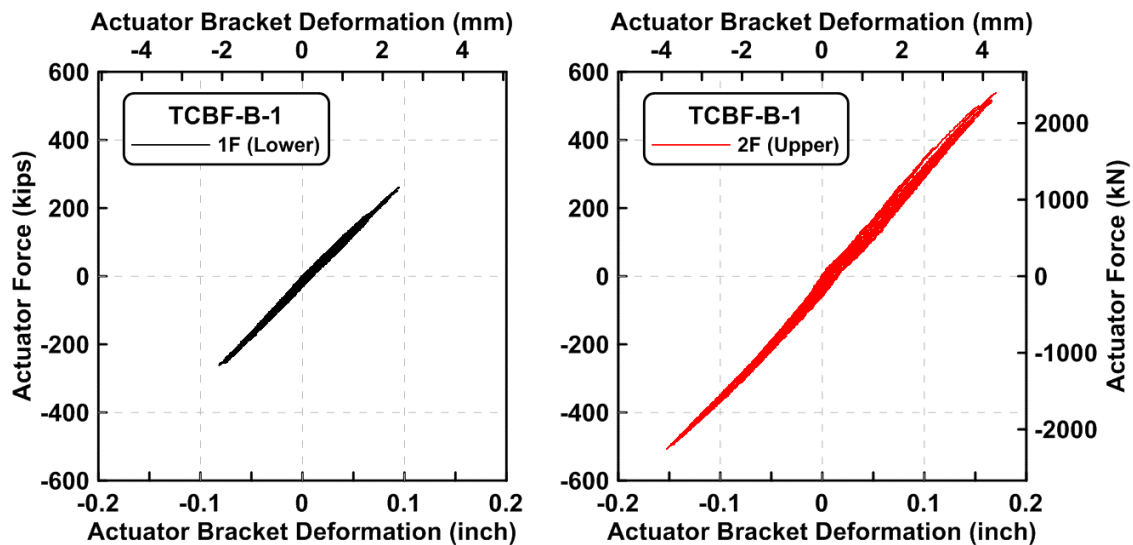


Figure 4.96 Specimen TCBF-B-1: the actuator force versus bracket deformation relationship at both floor levels.

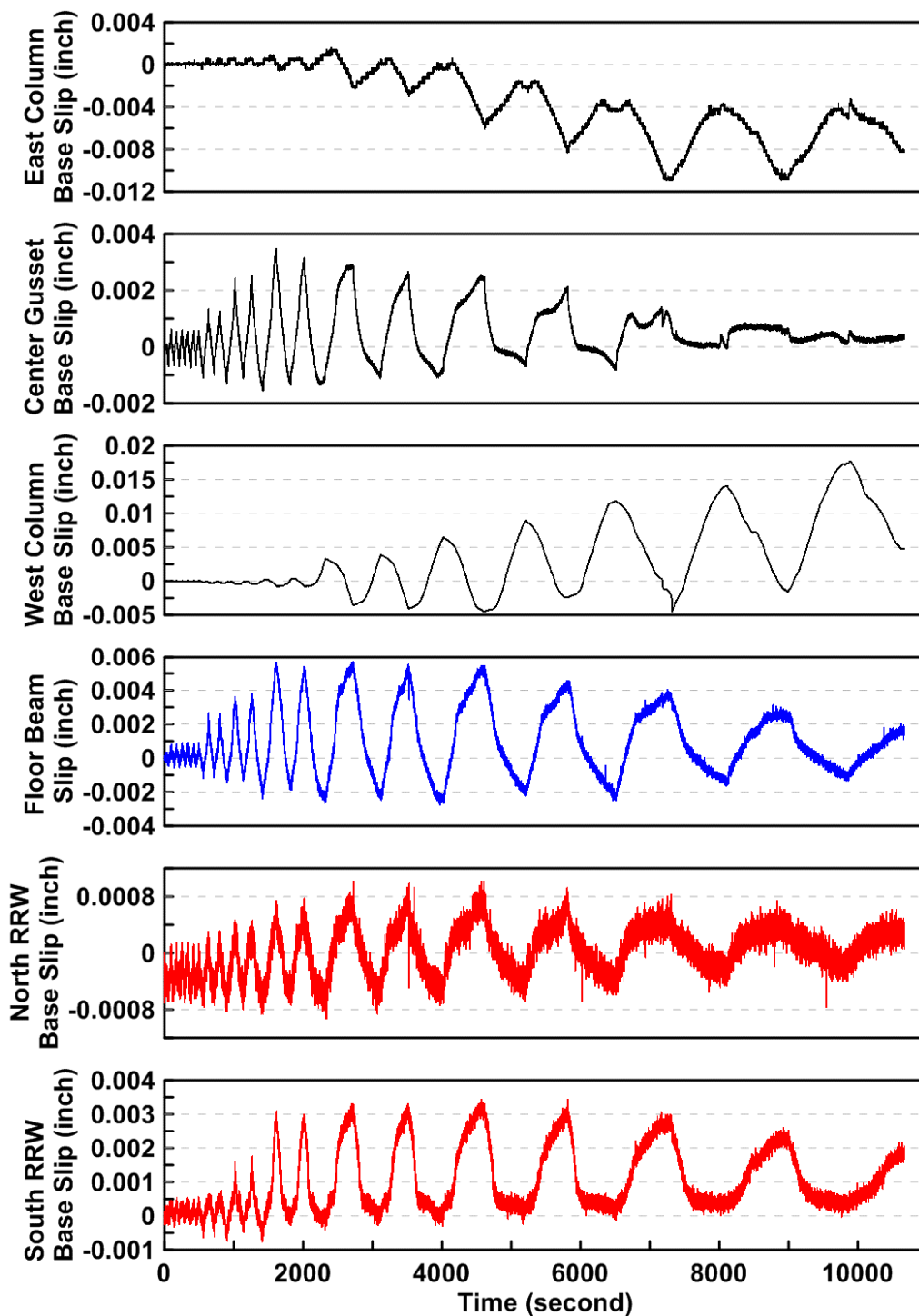


Figure 4.97 Specimen TCBF-B-1: slippage time history between specimen and test set up boundaries.

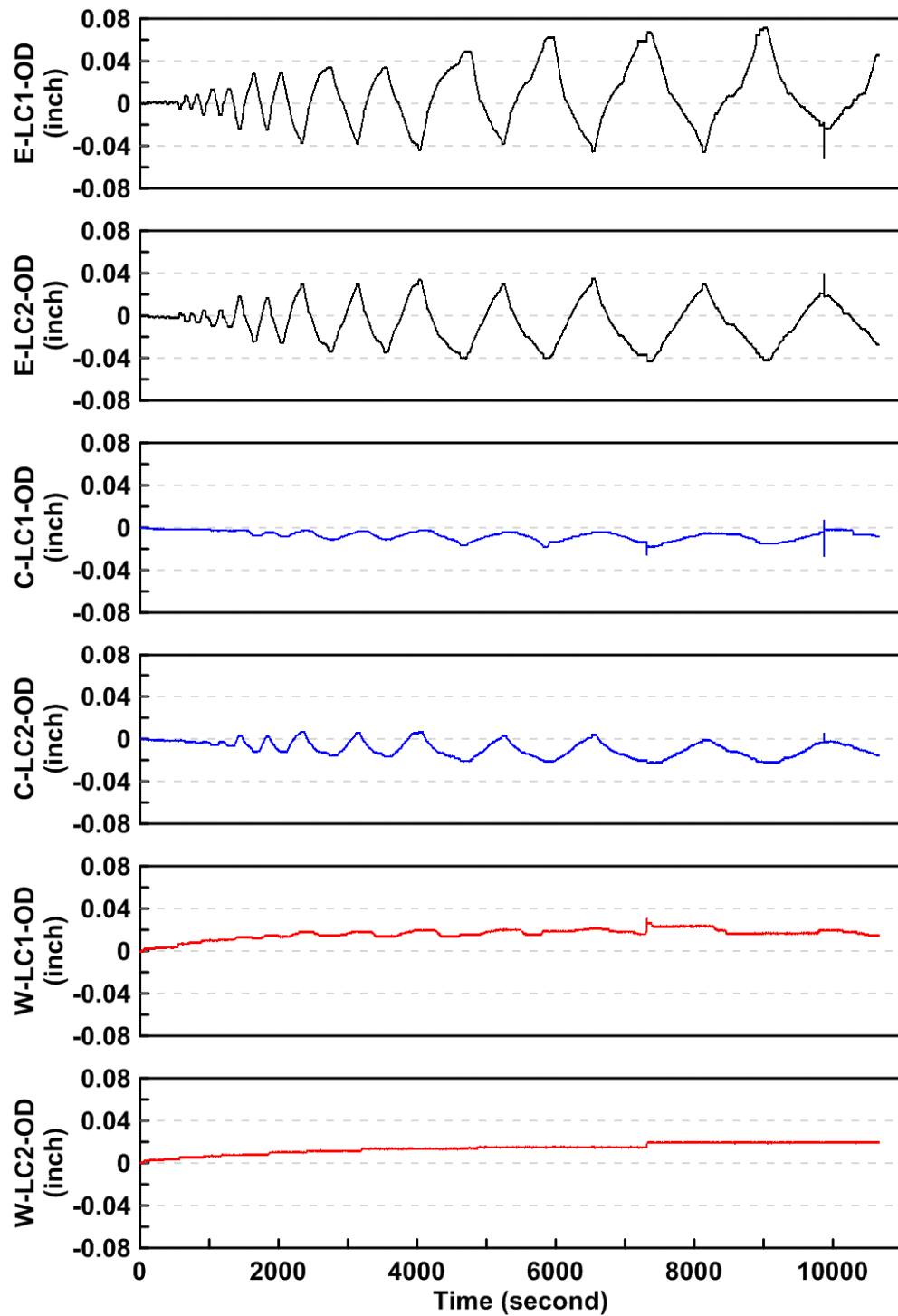


Figure 4.98 Specimen TCBF-B-1: out-of-plane deformation time history of lateral supporting frame at different monitoring points.

4.1.2 Specimen TCBF-B-2 (Round HSS Braces)

Specimen TCBF-B-2 re-used the $W24 \times 117$ roof beam, the $W12 \times 96$ columns, and 2-in.-thick base plates from the previous test. Before the first trial, some welding repairs were conducted at the column bases (see Figures 3.51, 3.52, and 3.53). Before conducting the actual test, two complete cycles of 0.15-in. peak roof displacement was performed to check all instrument readings and the actuator control algorithms.

The first trial of the braced frame with round HSS braces began at around 2:26 PM on Sunday, October 18, 2009. This test was similar to that carried out for TCBF-B-1. Because some of the channels recording the linear strain gauge readings saturated in the earlier test, the gain value was reduced from 200 to 50 for those channels where high local strain developed as recorded by the data acquisition system. The entire side view of the specimen before first trial is shown in Figures 3.22 and 3.54.

During the first trial at about 2-in. roof displacement (the second cycle of $1.5 D_{bm}$ load step), the west side column base fractured (see Figure 4.99). The test was paused for emergency repairs of the column base before continuing with the subsequent loading cycles. The entire side view of the specimen after first trial is shown in Figure 4.100.

Column bases at both sides of the specimen were stiffened with four 1-in.-thick stiffeners at both sides of column flanges. The column base at the western side that had fractured was stiffened with two additional 1-in.-thick stiffeners at both sides of column web. In addition, a 2-in.-thick flange cover plate was fillet welded to attach the fractured column flange to the base plate (Figure 4.101).

The second trial began at 4:36 PM on Thursday, October 22, 2009. The entire side view of the specimen before the second trial is shown in Figure 4.102. Figure 4.103 shows the specimen before the test and after the second trial.



Figure 4.99 Specimen TCBF-B-2: fracture of west-side column base flange CJP welds.



Figure 4.100 Specimen TCBF-B-2 after first trial.

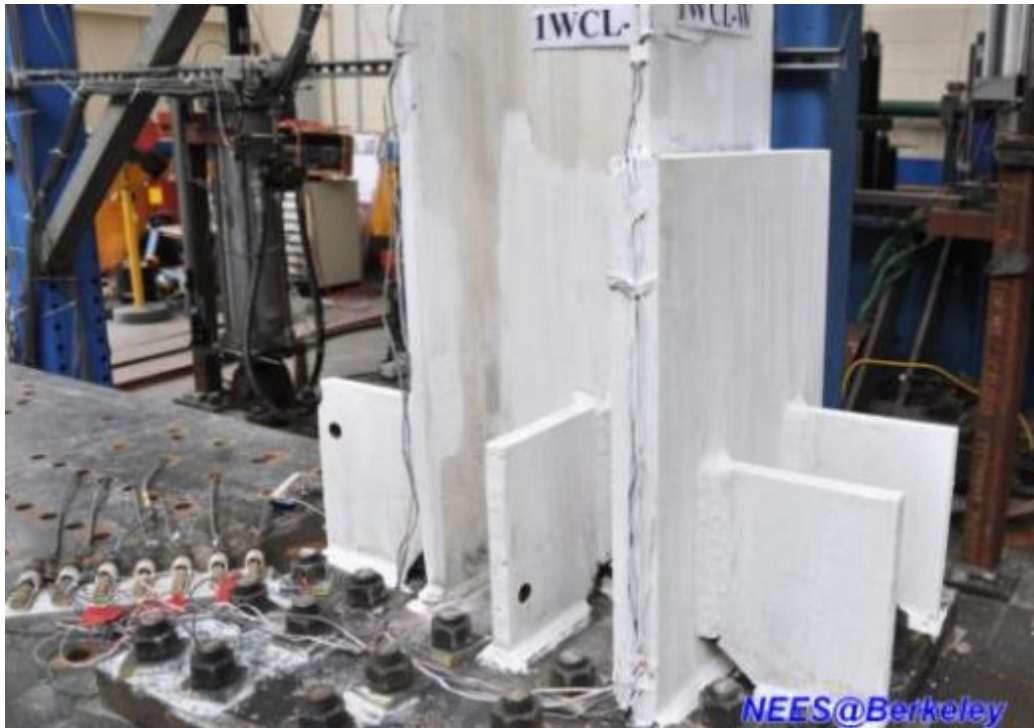


Figure 4.101 Specimen TCBF-B-2: west-side column base after repair with 1-in. thick stiffener plates and a 2-in. thick flange cover plate.



Figure 4.102 Specimen TCBF-B-2 before second trial.



(a) before test



(b) after second trial

Figure 4.103 Specimen TCBF-B-2 before test and after test.

4.1.2.1 Main Observations

As illustrated in the pre-defined loading protocol in Figure 3.28, the experiment process was divided into several stages of loading (amplitudes or phases). Every loading stage contained two complete cycles, except the first loading stage contained six complete cycles. Detailed information about each of these cycles is described sequentially below. Table 4.2 lists the major observations on the testing protocol along with brief descriptions.

$\Delta = 0.5$ D_{be} = 0.2 in. (Roof Drift $\delta = 0.1\%$), from 2:26 PM to 2:34 PM

After two small cycles were completed and all instrument readings were carefully checked, the formal loading protocol was started at 2:26 PM. During the first six low-amplitude cycles, the entire frame remained elastic. No special observations were made anywhere through during this loading stage.

$\Delta = 1.0$ D_{be} = 0.4 in. (Roof Drift $\delta = 0.2\%$), from 2:34 PM to 2:39 PM

The entire frame essentially remained elastic; no special observations were made during this loading stage.

$\Delta = 1.0$ D_{by} = 0.6 in. (Roof Drift $\delta = 0.3\%$), from 2:39 PM to 2:47 PM

Some local flaking of whitewash developed near the beginning of 30° tapered region of gusset plate at the first story (the eastern side gusset plate on the north face) and also the tips of brace-to-gusset plate fillet welds.

$\Delta = 0.5$ D_{bm} = 1.0 in. (Roof Drift $\delta = 0.5\%$), from 2:47 PM to 3:00 PM

At the beginning of the first half-cycle of the loading cycle, the first-story brace on the west side began global buckling out-of-plane to the south side of the specimen, and the whitewash on the round HSS brace began flaking at the middle of the brace (Figure 4.104). Some local flaking of whitewash developed near the beam splice welds in the bottom flange of the lower beam on the western side (Figure 4.105). Similar whitewash flaking was found near the backing bar in the top flange of the lower beam on the western end. Some minor local flaking of whitewash developed near the 30° tapered region of the eastern gusset plate at the second story (near the lower beam).

$\Delta = 1.0$ D_{bm} = 2.0 in. (Roof Drift $\delta = 0.9\%$), from 3:00 PM to 3:27 PM

At the beginning of the first half-cycle of the load step, some loud popping noises (probably from the base of the specimen) were heard at around 1-in. roof displacement while pushing the specimen to the east. Some yielding of the column flange was found at both east-side and west-side column base (Figures 4.106 and 4.107). Note that the yield lines were not parallel to the base plate, which were typical Lüder's bands (Lüder's lines) that had formed in the steel plates. The brace at top-story east side began global buckling out-of-plane towards the north side of the specimen when the roof displacement approached to 2 in. to the east. The brace at upper-story west side started out-of-plane global buckling (Figure 4.108) towards the south side of the specimen as the roof displacement approached to 1 in. to the west in the second half-cycle. Popping noises were heard again at the beginning of second load cycle at about 1-in. roof displacement towards the east. Additional flaking developed in the braces (Figure 4.109) and in the $2t$ gap region on the gusset plates. Some flaking of whitewash developed on the one-piece gusset plate near the gusset-to-column flange welds at eastern and western sides of the specimen (see Figure 4.110). The lower beam web at both ends close to the shear tab also had some whitewash flaking. Local yielding was found at gusset plate tip between roof beam and the gusset below the bottom flange (Figure 4.111).

$\Delta = 1.5$ D_{bm} = 3.0 in. (Roof Drift $\delta = 1.4\%$), from 3:27 PM to 4:03 PM on October 18, 2009 and 4:36 PM to 4:56 PM on October 22, 2009

Additional flaking of whitewash in both columns (near the bases), gusset plates, braces and beam-to-gusset plate splices were found in this load stage. Loud popping noises were heard at the beginning of first load cycle at about 2-in. roof displacement towards the east. No load drop occurred at this time. As the specimen continued to move to the east, at about 2.8-in. roof displacement, the bottom flange of the lower beam at east side and the top flange of the lower beam at west side began local buckling near the beam-to-gusset plate splices (Figures 4.112 and 4.113). As the first cycle of this stage was about to finish, vertical yield line patterns were observed in the east column web, as shown in Figure 4.114. The test was continued to the second load cycle. At around 1-in. roof displacement towards the east, cracks were detected near the CJP

weld at western side of the column base as shown in Figure 4.115. As the roof displacement continued to increase (moving to the east) up to about 2-in. roof displacement, a fracture near the outermost west side flange-to-base plate CJP weld was found (Figure 4.116). A significant load drop occurred at this time. A crack was also found between the column web and the base plate at south side of the western column (Figure 4.117). No significant cracks were found at the base of the eastern column. The test was paused to repair the column bases.

After a quick column base repair of both flanges of both column bases (see Figures 4.118 and 4.119), the second trial continued to finish the remainder of the loading protocol. At the second half of the second cycle of the $1.5D_{bm}$ load stage, about 2.8 in. to the west, a loud pop sound was heard from the top of the specimen. It remains uncertain where the sound came from (perhaps a crack initiating in one of the lower beam-to-gusset plate splices). No significant load drop was observed this time. Yielding was found (via flaking of whitewash) in the west $W12 \times 96$ column flange where it connected to the 2-in.-thick cover plate used for the repair at the column base, as shown in Figure 4.120. Whitewash flaking between the two welded 1-in.-thick stiffener plates was found at the eastern side of column base (Figure 4.121). Additional flaking of whitewash developed on the gusset plate $2t$ gap fold regions, beam-to-gusset plate splice regions, braces, and column web at both sides in the ground story.

$\Delta = 2.0 D_{bm} = 4.0$ in. (Roof Drift $\delta = 1.9\%$), from 4:56 PM to 5:49 PM

Additional local buckling of the lower beam flanges (top flange at west side and bottom flange at east side) was observed at the beginning of this load stage. At the end of the first half-cycle, corresponding to about 0.66-in. (negative side) roof displacement to the west, the top flange of beam-to-gusset plate splice at west side of the lower beam completely fractured (Figure 4.122) and followed almost immediately by the partial fracture of the bottom finger plate (northern side of the net section) on the eastern end of the lower beam splice, as shown in Figure 4.123. When the actuator continued pulling the specimen to the west at around 0.96-in. (negative side) roof displacement, the bottom finger plate on the east end of the lower beam splice completely fractured as illustrated in Figure 4.124. The west side column flange near the 2-in. thick cover plate then began to buckle locally and the vertical fillet welds on both sides of the column flange tore (Figure 4.125). Note that the round HSS braces at both stories had not buckled locally at this time. Local buckling of the lower beam web was also observed during this load step (Figure 4.126).

$\Delta = 2.5 D_{bm} = 5.0$ in. (Roof Drift $\delta = 2.3\%$), from 5:49 PM to 6:56 PM

When the roof displacement passed the peak roof displacement in the previous load step (which is 4 in.) at about 4.5-in. displacement, the brace at the western side of the first story (Figure 4.127) and the eastern side brace at the top story buckled locally. The vertical fillet welds between the 2-in. cover plate and the $W12 \times 96$ column flange at north-west corner of column base in the ground story continued to tear apart (Figure 4.128). Additional local buckling of the western brace in the ground story was observed during the second load cycle at this stage (Figure 4.129). Tearing crack (initiates at the tip of welding access hole) between beam flange and web was observed (Figure 4.130) at the east end of the lower beam to gusset plate connection. After passing the negative peak roof displacement in the second load cycle, cracks initiated in the first

story west side round HSS brace at the local buckled region (Figure 4.131). Additional local buckling occurred in the lower story east side brace as the entire specimen passed the zero roof displacement at the end of this load step.

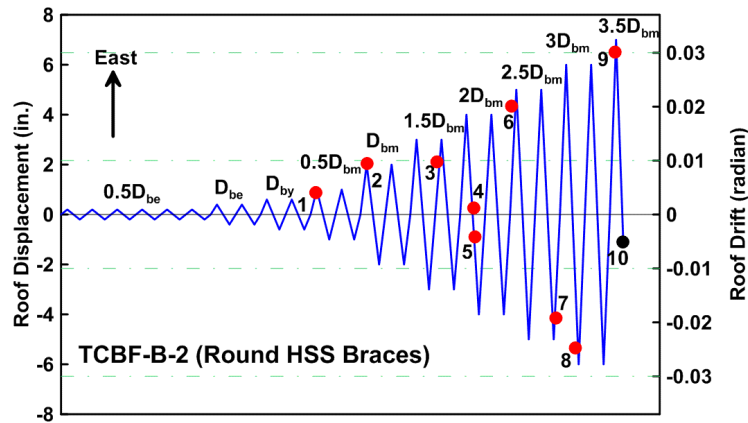
$\Delta = 3.0$ D_{bm} = 6.0 in. (Roof Drift $\delta = 2.8\%$), from 6:56 PM to 8:16 PM

After passing the first positive peak roof displacement at this stage, additional cracking and tearing of the vertical fillet welds between 2-in. flange cover plate and column flange at the west side of the column base were observed on both sides of the exterior flange (Figure 4.132). At about negative 2.71-in. roof displacement, the ground story brace on the west side partially fractured (Figure 4.133). The round HSS brace completely fractured at a negative 5.29-in. roof displacement, as shown in Figure 4.134. The western end of the lower beam web fractured from top the top flange and partially across the web towards the bottom of the beam (Figure 4.135). After passing the first negative peak displacements in this load stage, cracks initiated in the ground story east side brace at the center part of the brace (Figure 4.136). The vertical fillet welds between the 2-in. flange cover plate and column flange at the west side column base torn all the way down from top to bottom of the weld lines (Figure 4.137). After passing the second negative peak displacement, the test was paused to take detailed pictures.

$\Delta = 3.5$ D_{bm} = 7.0 in. (Roof Drift $\delta = 3.2\%$), from 8:16 PM to 9:02 PM

Before the specimen reached the peak roof displacement (about 6.9 in.) in this load stage, the east side round HSS brace at the ground story yielded significantly (via the necking of the round section) before the entire cross section fractured (Figure 4.138). At about 7-in. roof displacement in the first half-cycle at this stage, the eastern brace in the first story completely fractured (Figure 4.139). The test was manually stopped at about negative 1 in. to have a small residual roof deformation when unloaded based on the trend of unloading slope shown on the display screen. The entire side view of the specimen after test is shown in Figure 4.140.

Table 4.2 Specimen TCBF-B-2: major observations noted during test.



1	The brace at first story west side began global buckling (out-of-plane to the south side).
2	The brace at second story east side began global buckling (out-of-plane to the north side).
3	The brace at second story west side began global buckling (out-of-plane to the south side).
4	A very loud noise heard this time but no load drop observed.
5	The flange-to-base plate weld at the west side of column base completely fractured. Test paused to repair column base (Figures 4.116 and 4.118).
6	The top flange at western side of lower beam splices completely fractured at the CJP weld line (Figure 4.122). The bottom flange at eastern side of lower beam splices partially fractured at net section of finger plate (Figure 4.123).
7	The bottom flange at eastern side of lower beam splices completely fractured at net section of finger plate (Figure 4.124). No local buckling of braces observed at this time.
8	The braces began local buckling at the middle portion of the brace (1F-West and 2F-East). The northern side vertical fillet weld between cover plate and column flange was torn.
9	Cracks initiated in the middle of round HSS brace at first story western brace at the local buckling region (Figure 4.131).
10	Both northern and southern side vertical fillet welds between cover plate and column flange were torn and cracked.
11	The western brace at first story partially fractured.
12	The western brace at ground story completely fractured during the first cycle of $3.0 D_{bm}$ load step at roof displacement of 5.3 in. to the west. (Figure 4.134)
13	Cracks developed in the middle of round HSS brace at first story eastern brace at the local buckling region. The vertical fillet welds between cover plate and column flange cracked all the way down to cover-plate-to-base-plate connection.
14	The eastern brace at first story completely fractured during the first cycle of $3.5 D_{bm}$ load step at roof displacement corresponded to about 7 in. to the east. (Figure 4.139)
15	No local buckling or cracks in the second story braces were found. Test stopped at about 1.0 in. of roof displacement to the west.



Figure 4.104 Specimen TCBF-B-2: flaking of whitewash at the middle of west-side round HSS brace.



Figure 4.105 Specimen TCBF-B-2: flaking of whitewash near CJP welds at bottom flange of lower beam.



Figure 4.106 Specimen TCBF-B-2: yield pattern of the east column flange.

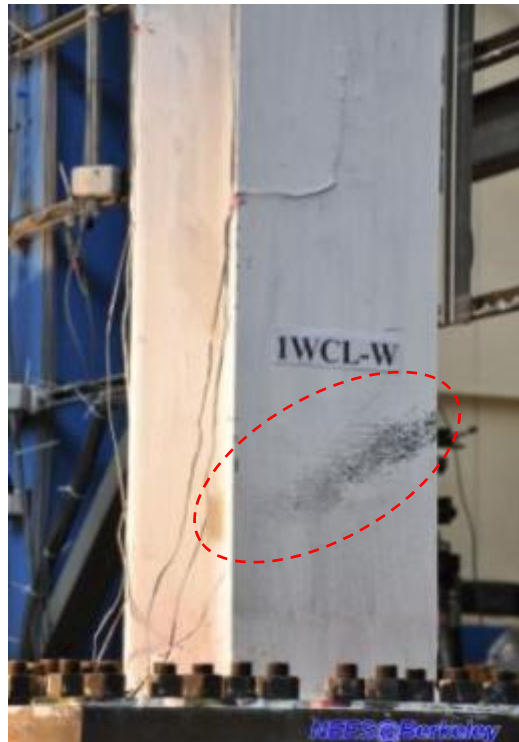


Figure 4.107 Specimen TCBF-B-2: yield pattern of the west column flange.



Figure 4.108 Specimen TCBF-B-2: global buckling of round HSS braces at both stories.



Figure 4.109 Specimen TCBF-B-2: additional flaking of whitewash flaking in braces.



Figure 4.110 Specimen TCBF-B-2: flaking of whitewash near gusset plate-to-column flange region.



Figure 4.111 Specimen TCBF-B-2: flaking of whitewash at the corner of gusset plate-to-roof beam connection.



Figure 4.112 Specimen TCBF-B-2: local buckling of east-side lower beam bottom flange.



Figure 4.113 Specimen TCBF-B-2: local buckling of west-side lower beam top flange.

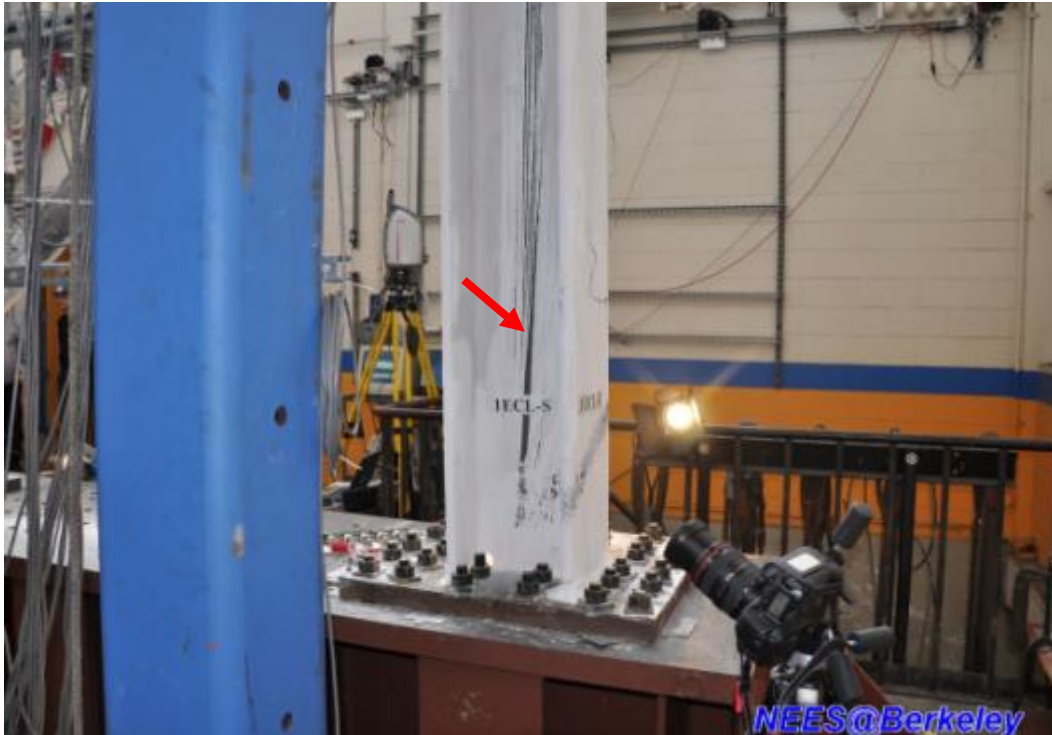


Figure 4.114 Specimen TCBF-B-2: column web yielding at the east-side column at ground floor.

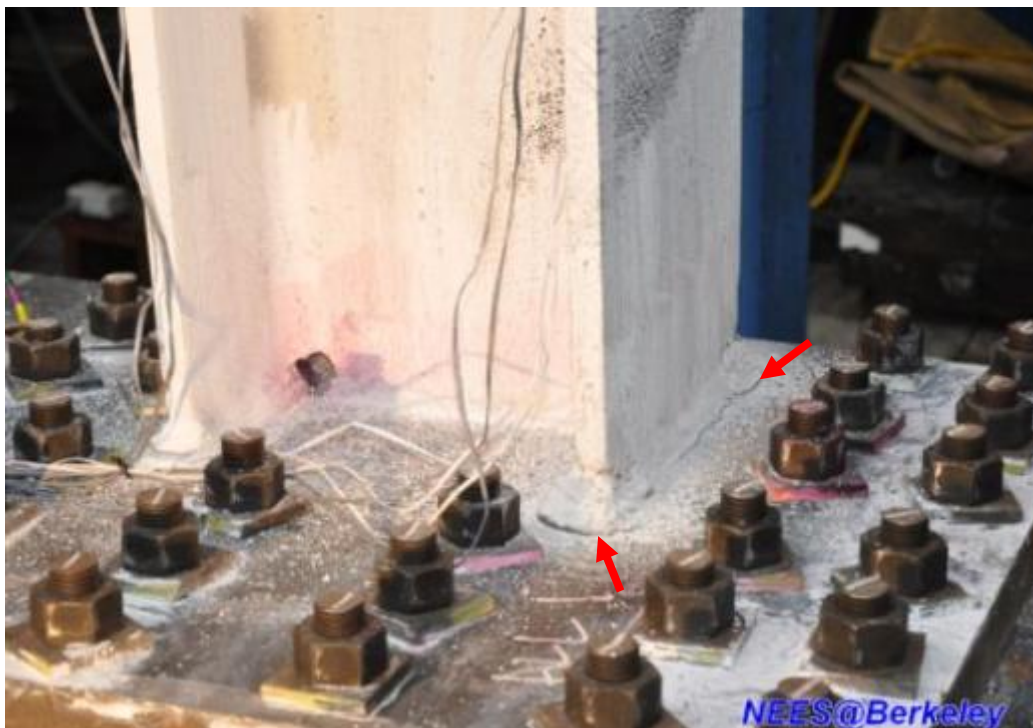


Figure 4.115 Specimen TCBF-B-2: crack near the flange CJP welds at west-side column base.



Figure 4.116 Specimen TCBF-B-2: complete fracture near the flange CJP welds at west-side column base.



Figure 4.117 Specimen TCBF-B-2: crack near the web CJP welds at west-side column base.

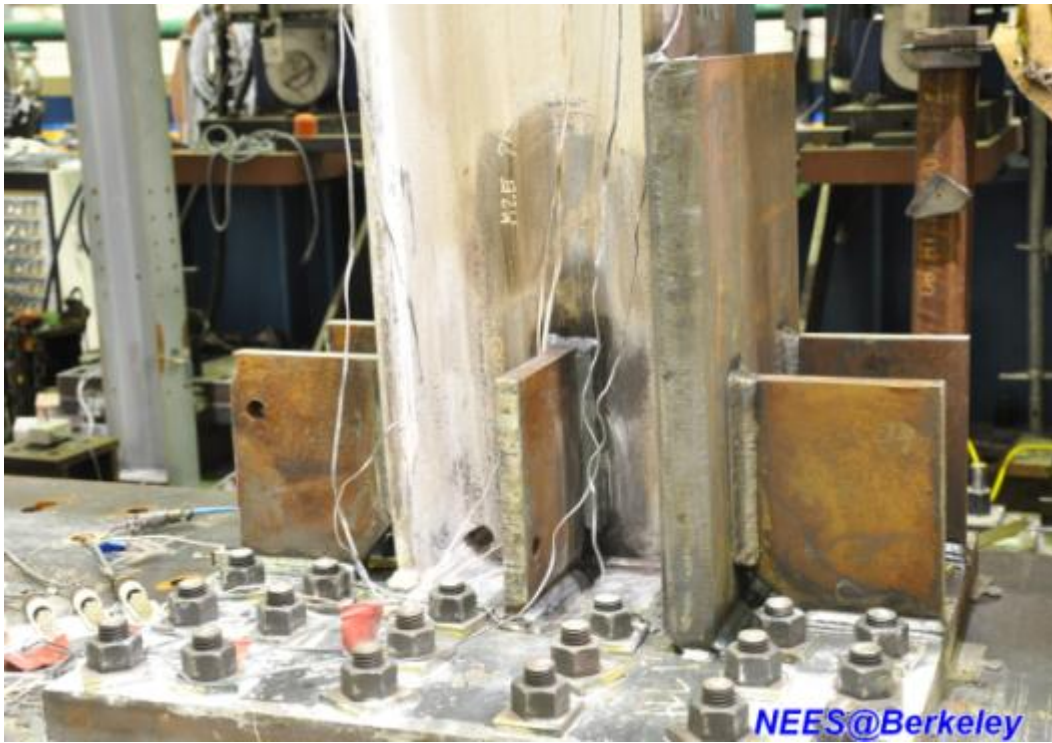


Figure 4.118 Specimen TCBF-B-2: west- side column base after repair.



Figure 4.119 Specimen TCBF-B-2: east side column base after repair.



Figure 4.120 Specimen TCBF-B-2: yielding in the column flange near 2-in.-thick cover plate.



Figure 4.121 Specimen TCBF-B-2: yield pattern between column base stiffener plates.



Figure 4.122 Specimen TCBF-B-2: fracture of west-side lower beam top flange.



Figure 4.123 Specimen TCBF-B-2: partial fracture of east-side lower beam bottom flange finger plate.

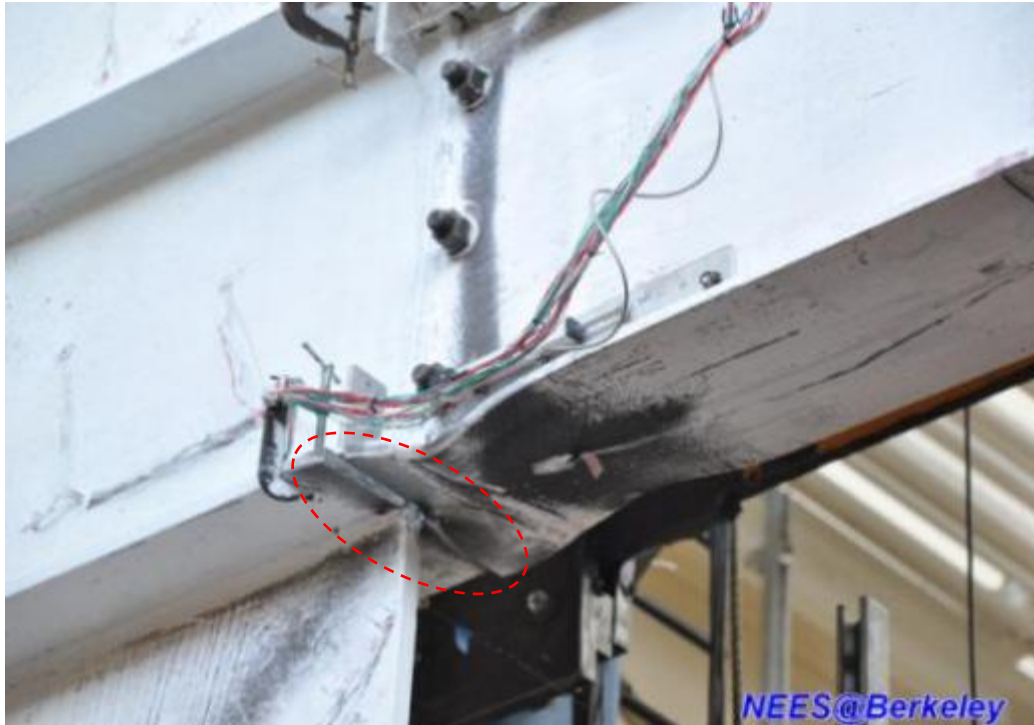


Figure 4.124 Specimen TCBF-B-2: complete fracture of east-side lower beam bottom flange finger plate.



Figure 4.125 Specimen TCBF-B-2: local buckling of column flange near 2-in.-thick cover plate.



Figure 4.126 Specimen TCBF-B-2: local buckling of west-side lower beam web.



Figure 4.127 Specimen TCBF-B-2: local buckling of first-story west-side round HSS brace.



Figure 4.128 Specimen TCBF-B-2: tearing of the vertical fillet welds at west-side column base.



Figure 4.129 Specimen TCBF-B-2: additional local buckling of first-story west-side round HSS brace.

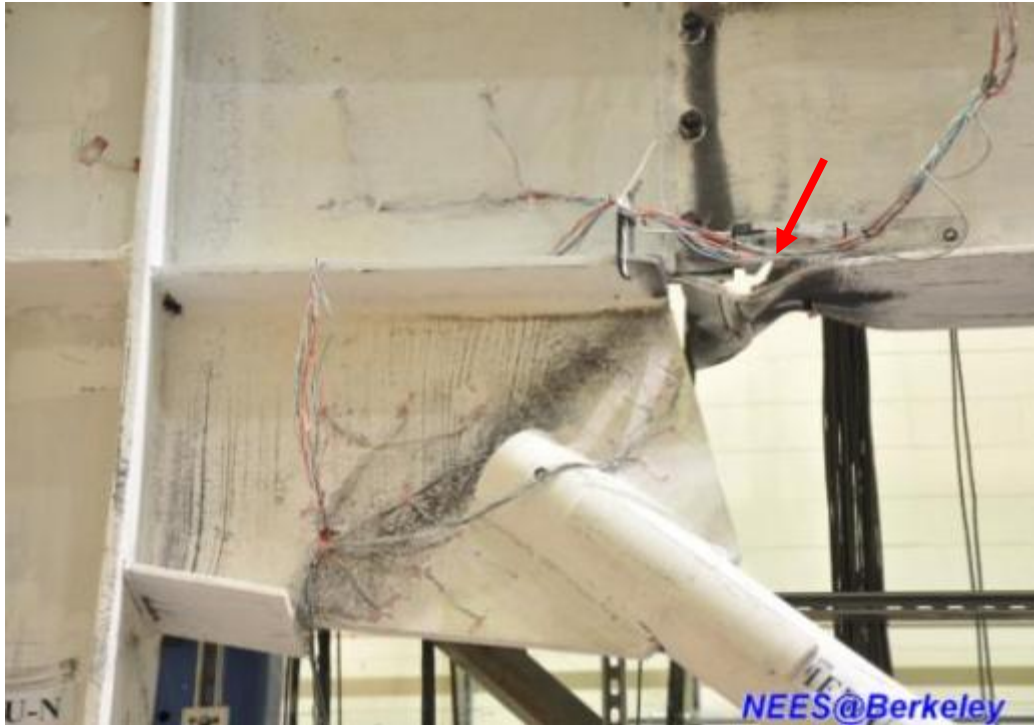


Figure 4.130 Specimen TCBF-B-2: crack propagation into web at east-side lower beam.

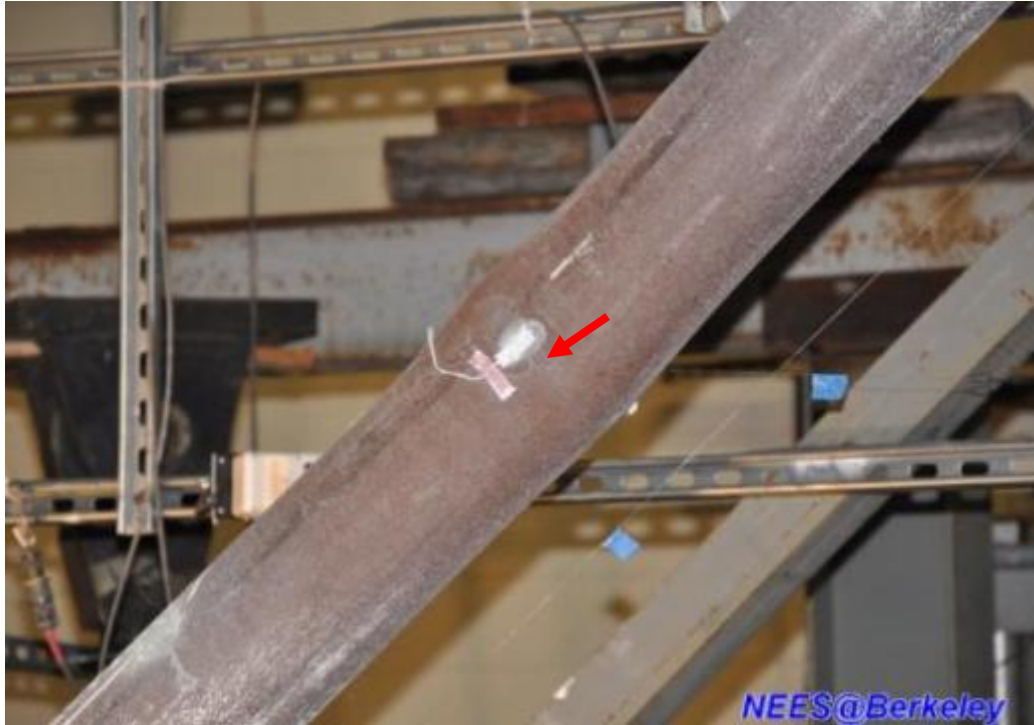


Figure 4.131 Specimen TCBF-B-2: crack initiation in first-story west-side round HSS brace.



Figure 4.132 Specimen TCBF-B-2: additional tearing of fillet welds between cover plate and column flange.

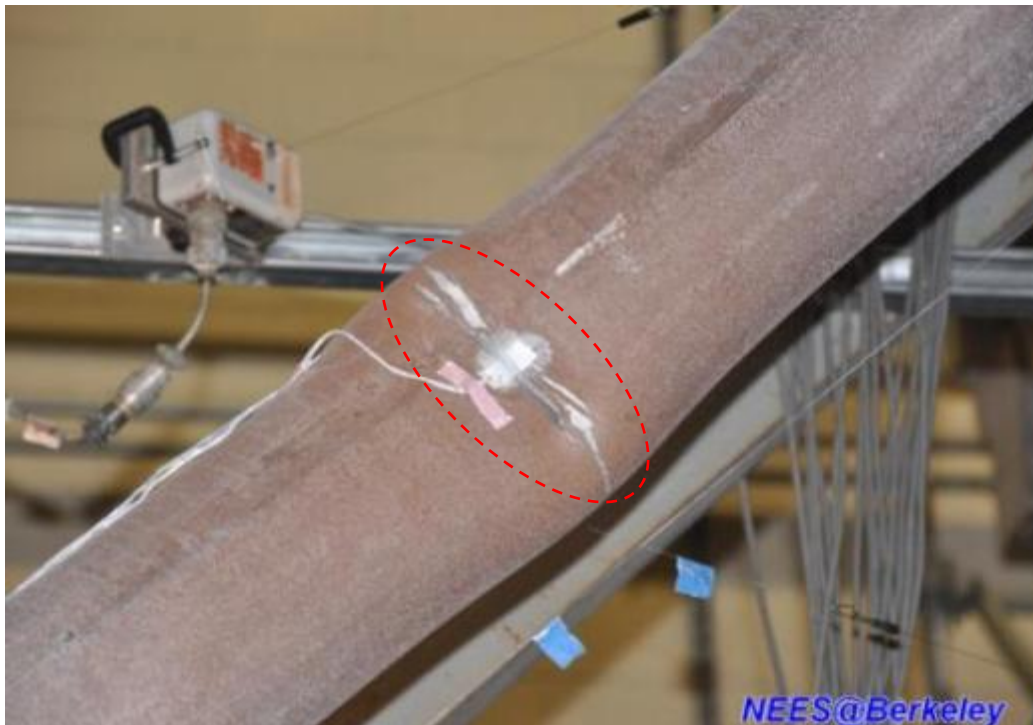


Figure 4.133 Specimen TCBF-B-2: partial fracture of first-story west-side brace.

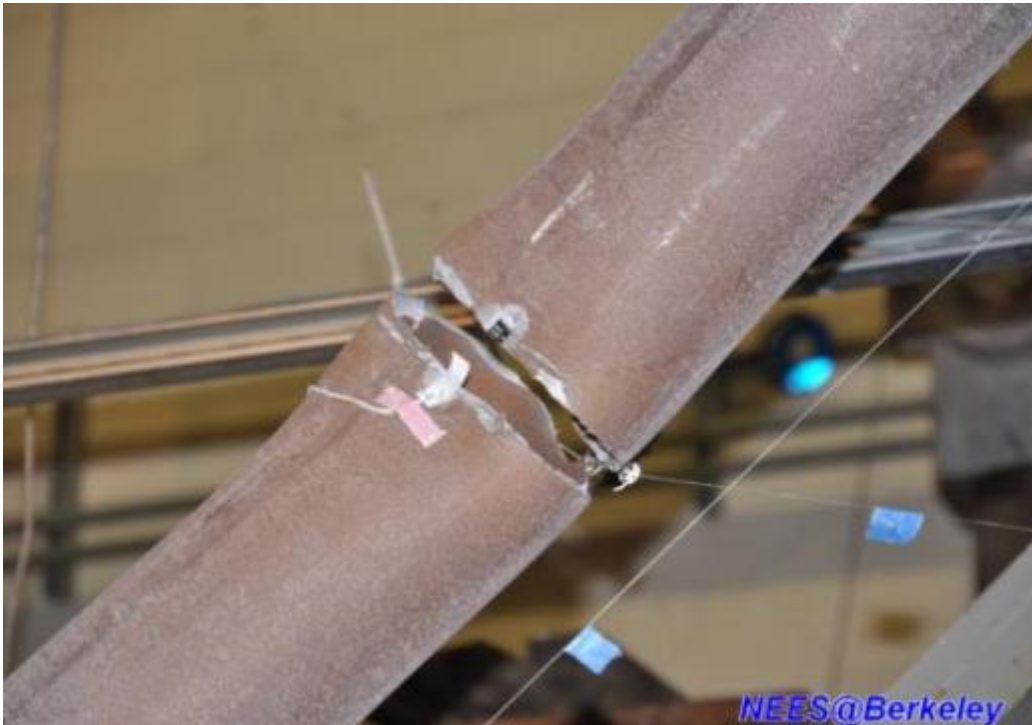


Figure 4.134 Specimen TCBF-B-2: complete fracture of first-story west-side brace.



Figure 4.135 Specimen TCBF-B-2: crack in lower beam web at west-side near top flange.

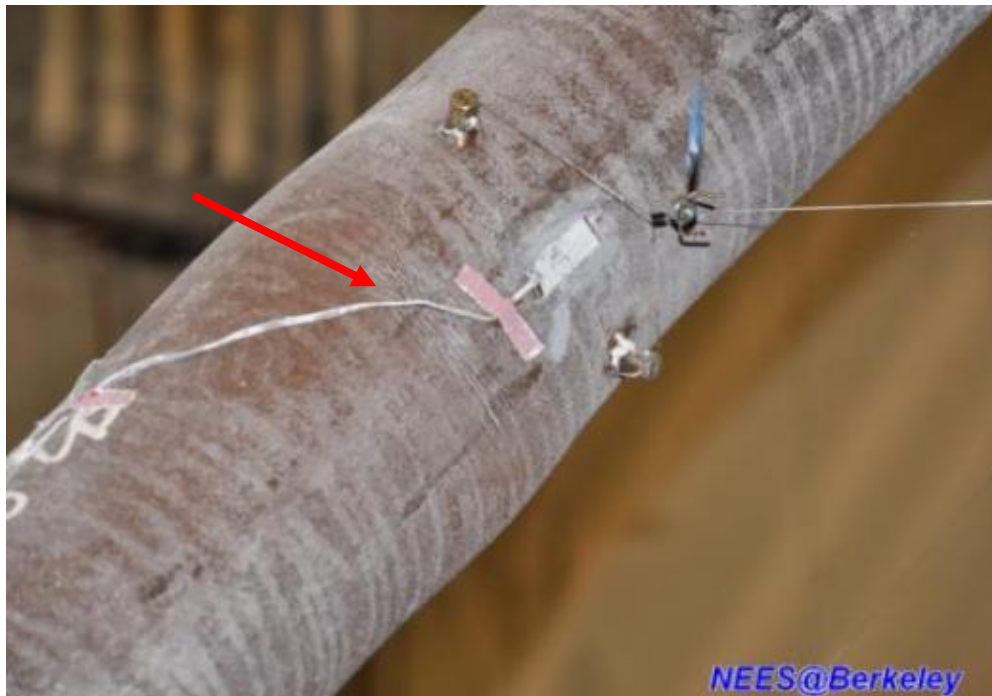


Figure 4.136 Specimen TCBF-B-2: crack initiation in first-story east-side round HSS brace.

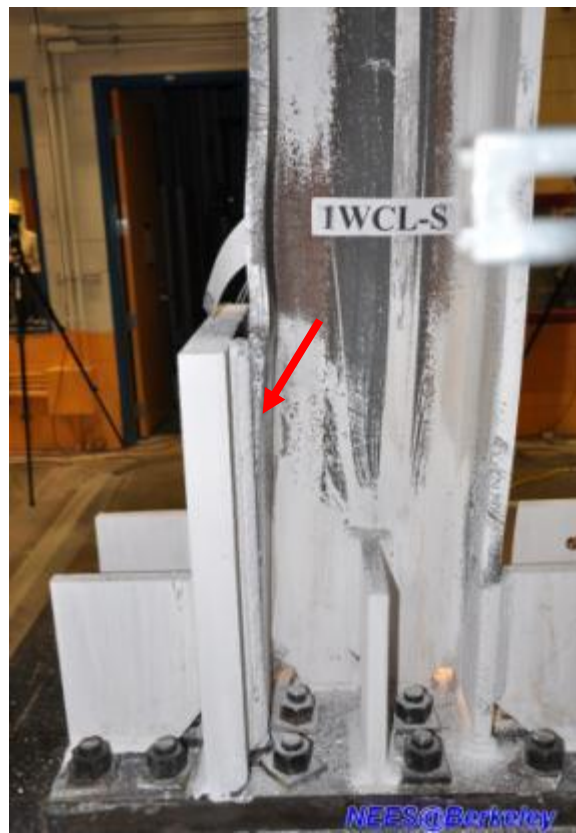


Figure 4.137 Specimen TCBF-B-2: tearing of vertical fillet welds at west column base.



Figure 4.138 Specimen TCBF-B-2: necking of first-story east-side round HSS brace before fracture.



Figure 4.139 Specimen TCBF-B-2: complete fracture of first-story east-side brace.



Figure 4.140 Specimen TCBF-B-2: entire side view of specimen after the second trial.

4.1.2.2 Key Response Quantities

The paragraphs below briefly describe the response quantities record in two test trials, and the post-processed response quantities derived from the raw data. Detailed discussion of the individual response quantities are described in Chapter 5.

4.1.2.2.1 System Response

Figures 4.141 and 4.142 show the time history of the actuator displacements and actuator load cell force feedbacks for Specimen TCBF-B-2. The base shear versus controlled roof displacement of the specimen is shown in Figure 4.143. The relationship between the story shear and story drift ratio for the specimen is shown in Figure 4.144.

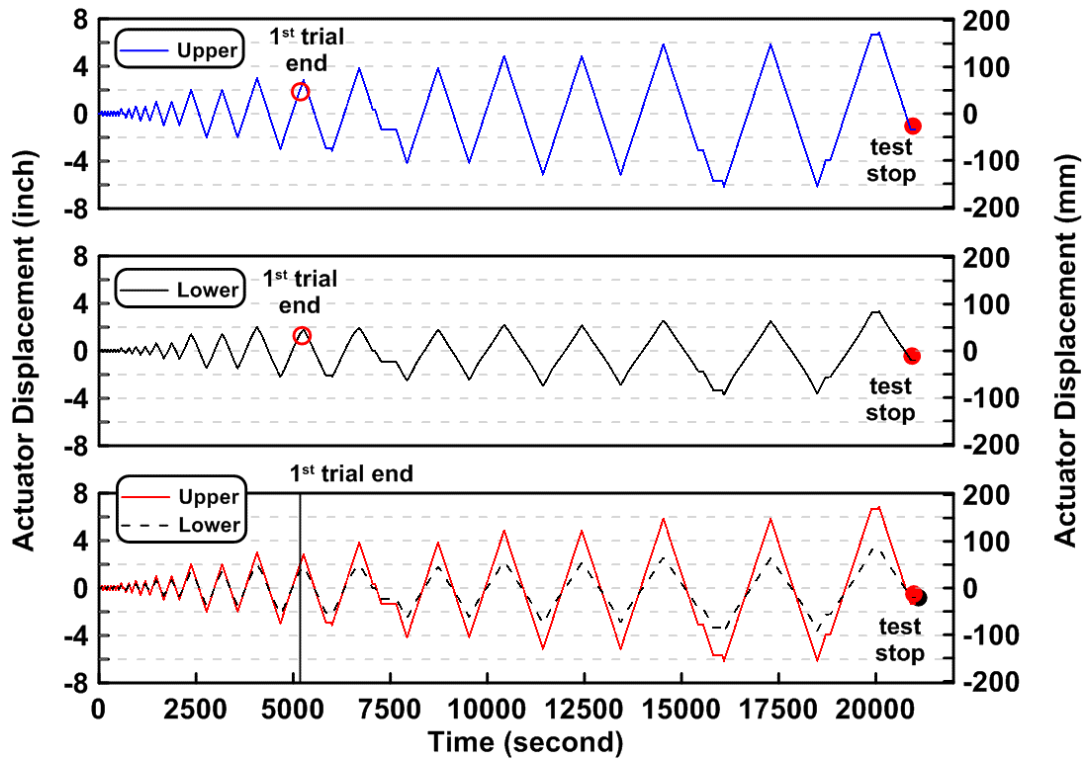


Figure 4.141 Specimen TCBF-B-2: Actuator displacement time histories.

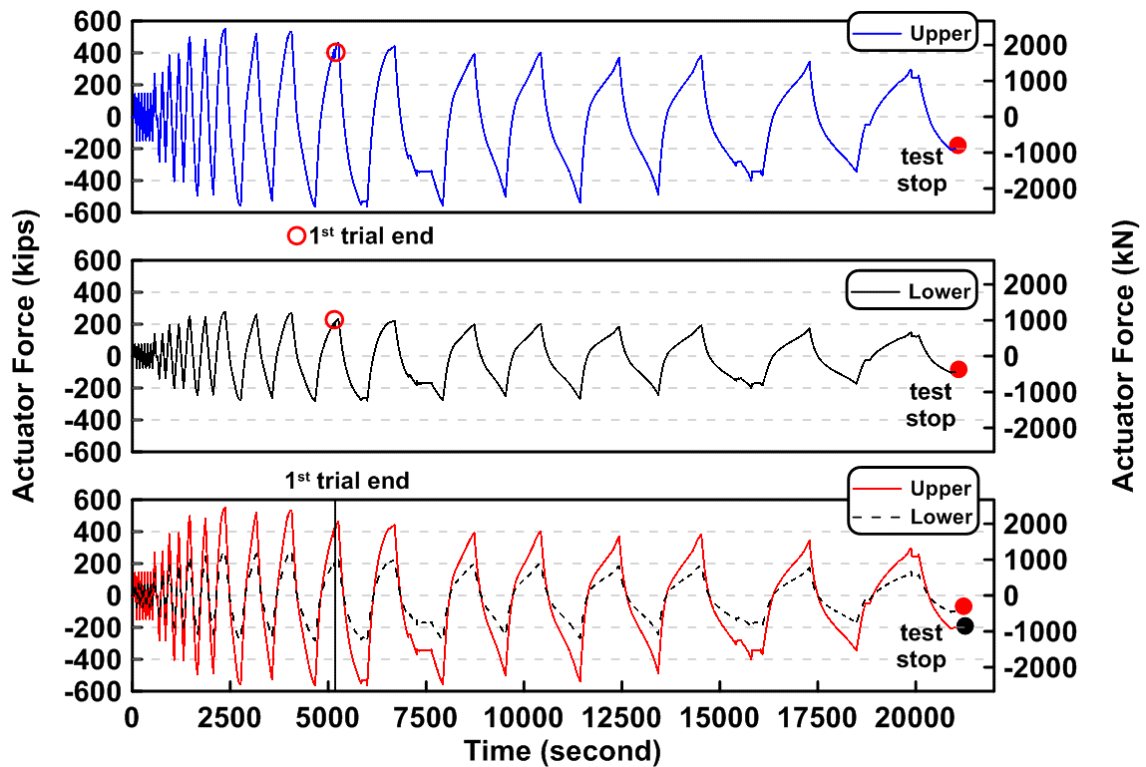


Figure 4.142 Specimen TCBF-B-2: actuator force time histories.

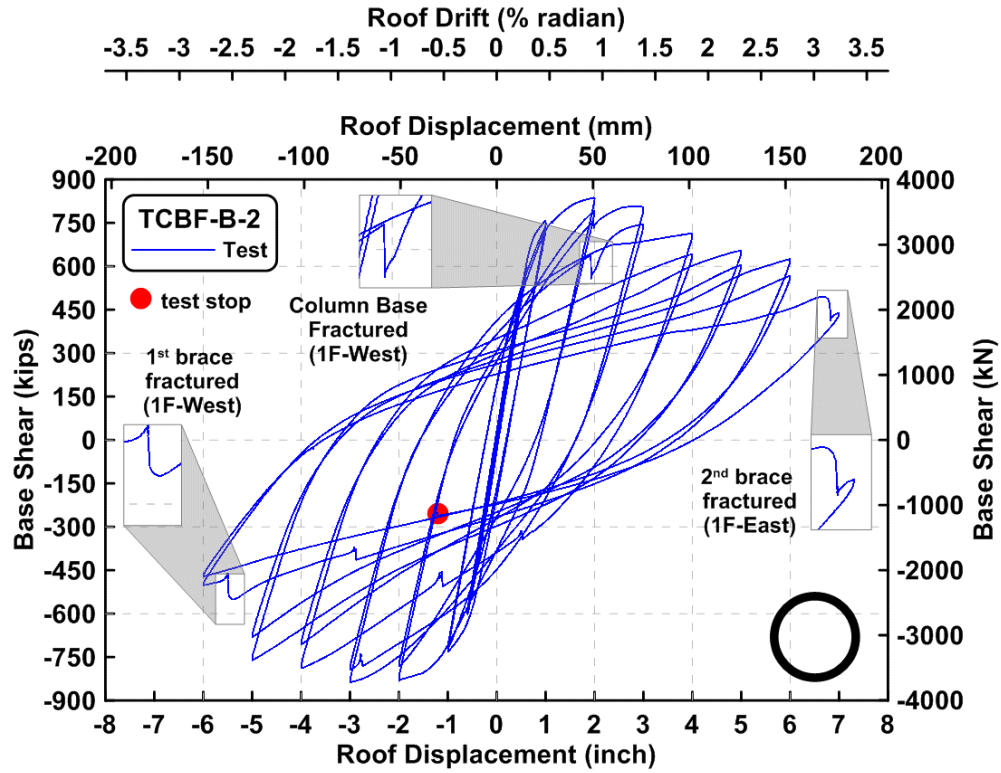


Figure 4.143 Specimen TCBF-B-2: base shear versus roof displacement relationship.

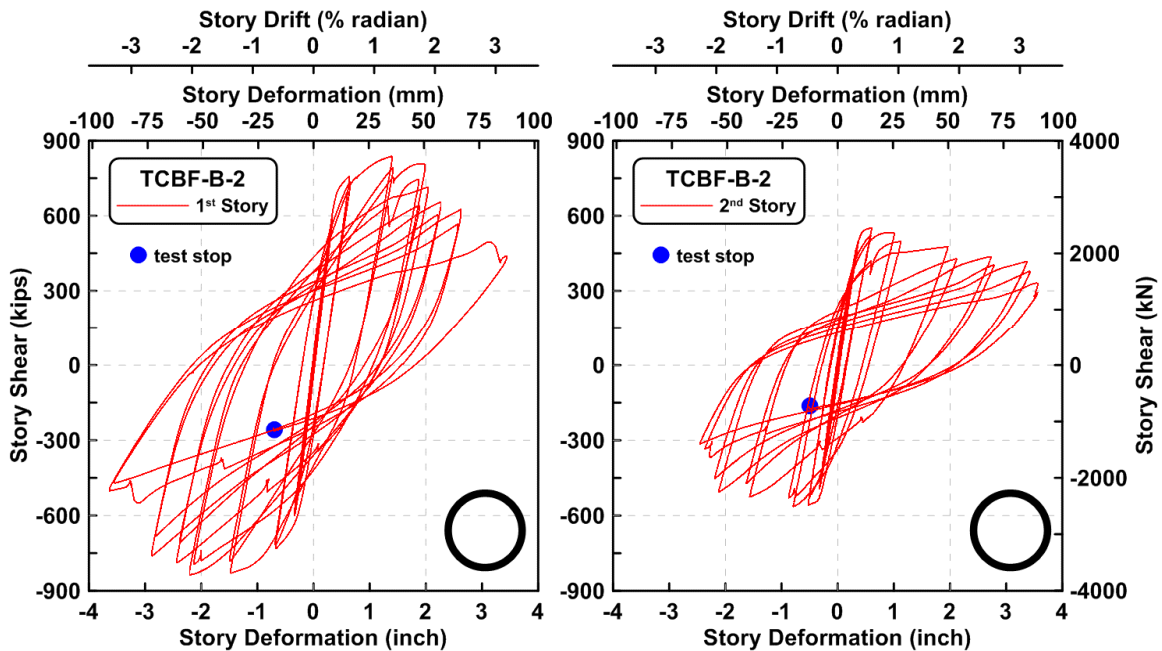


Figure 4.144 Specimen TCBF-B-2: story shear versus story deformation relationship.

4.1.2.2.2 Column Response

The time histories of the axial forces in the $W12 \times 96$ columns at the western and eastern sides of the specimen are plotted in Figure 4.145. Note that because significant yielding occurred in the column where the lower set of strain gauges were installed (around 3ft above the column base plate), only the strain gauge readings at 6ft above the base plate were used in estimating the column axial forces in this case. The relationships between roof displacements and axial forces at both columns are shown in Figure 4.146. The bending moment time history at the top and bottom ends of the column in each story are shown in Figures 4.147 and 4.148. Estimated column shear force time histories in the upper and lower stories are plotted in Figures 4.149 and 4.150, respectively. Estimated column shear forces in each floor were added together and the sum is plotted in Figure 4.151. The estimated column web shear stress versus shear strain readings from strain rosettes are plotted in Figure 4.152. The sum of the estimated column shear force components versus the total story shear forces for each story is shown in Figure 4.153. The derived rosette-type strain gauge readings in the column web at each story are shown from Figures 4.154 to 4.157. Normalized maximum and minimum principal stress relationships along with different yield criteria are plotted in Figures 4.158 to 4.161. The normalized P-M and P-V interaction diagrams at column bases and column top ends are shown in Figures 4.162 to 4.165.

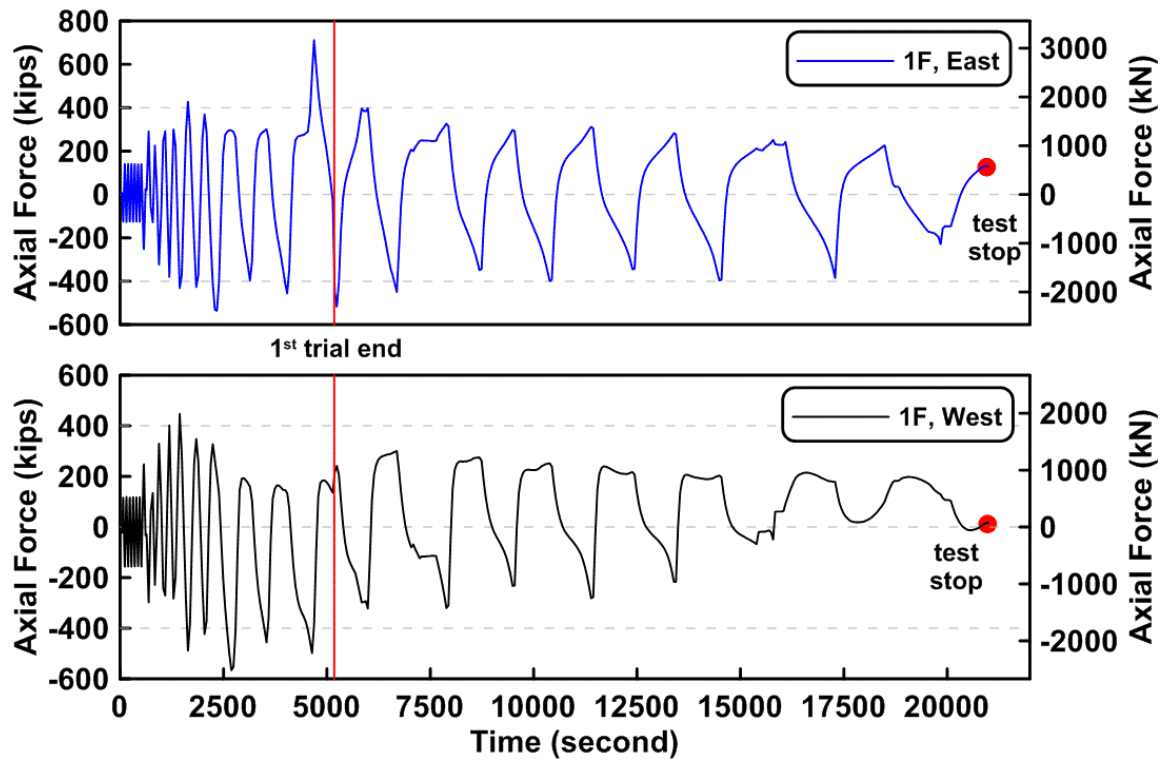


Figure 4.145 Specimen TCBF-B-2: time history of first-story column axial forces (location: 6 ft above column base plate).

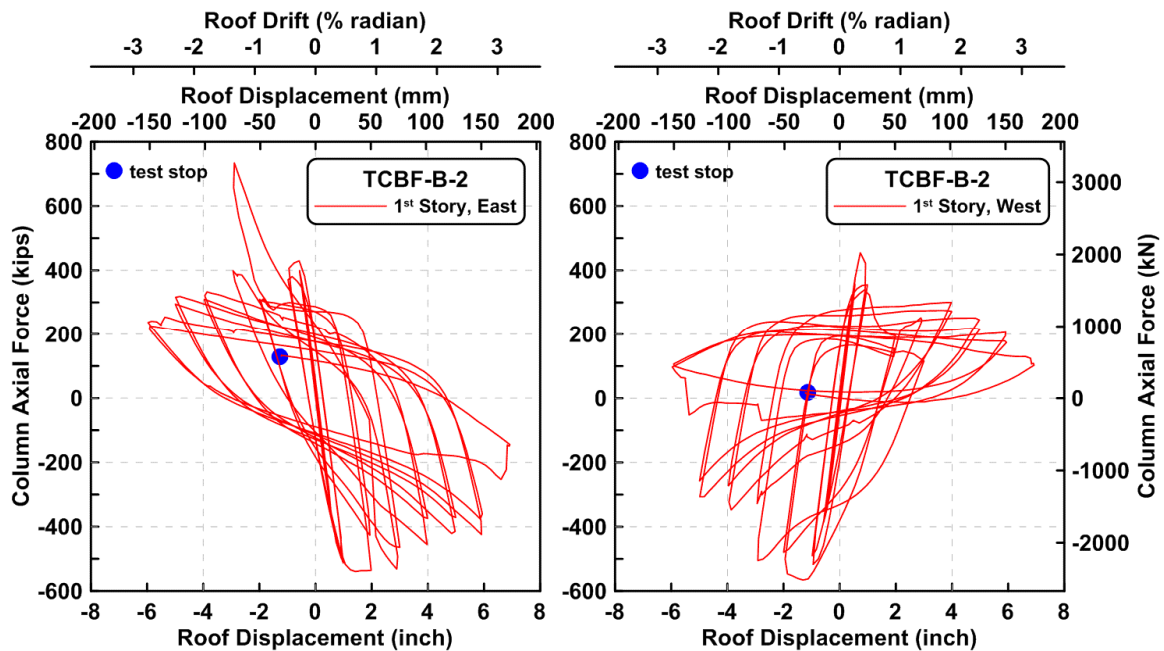


Figure 4.146 Specimen TCBF-B-2: roof displacement versus first-story column axial forces (note that the vertical axis limit is from -600 kips to 800 kips; the horizontal axis limit is from -8 in. to 8 in.).

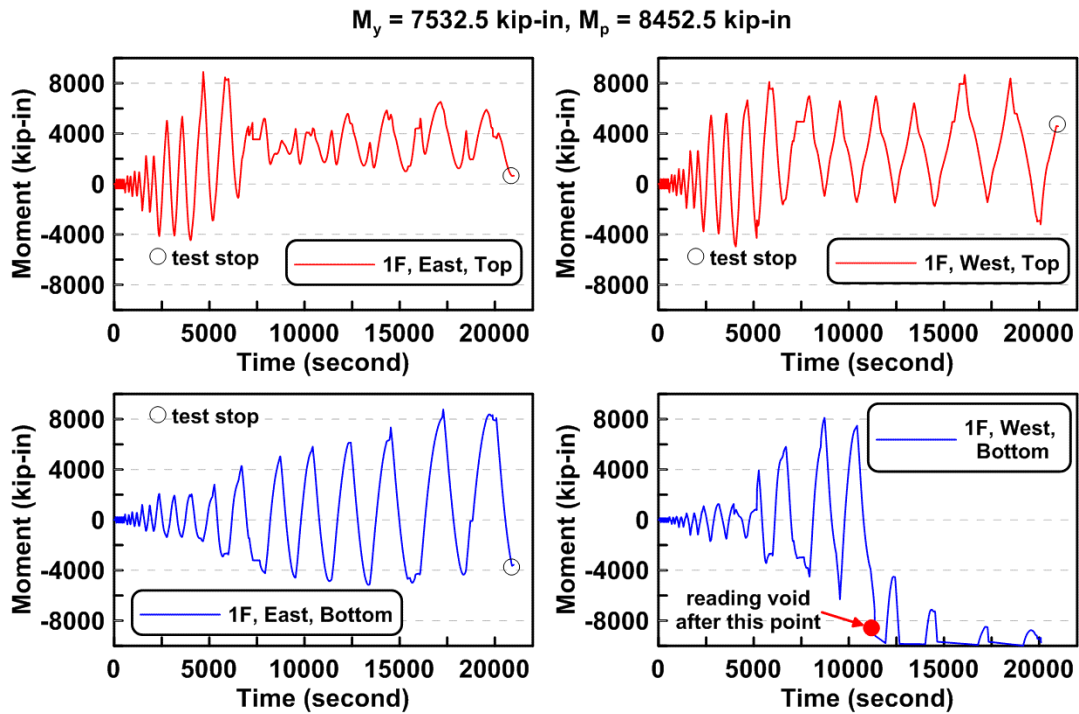


Figure 4.147 Specimen TCBF-B-2: time history of first-story column bending moments (3 ft above column base plate and 3 ft below lower beam centerline).

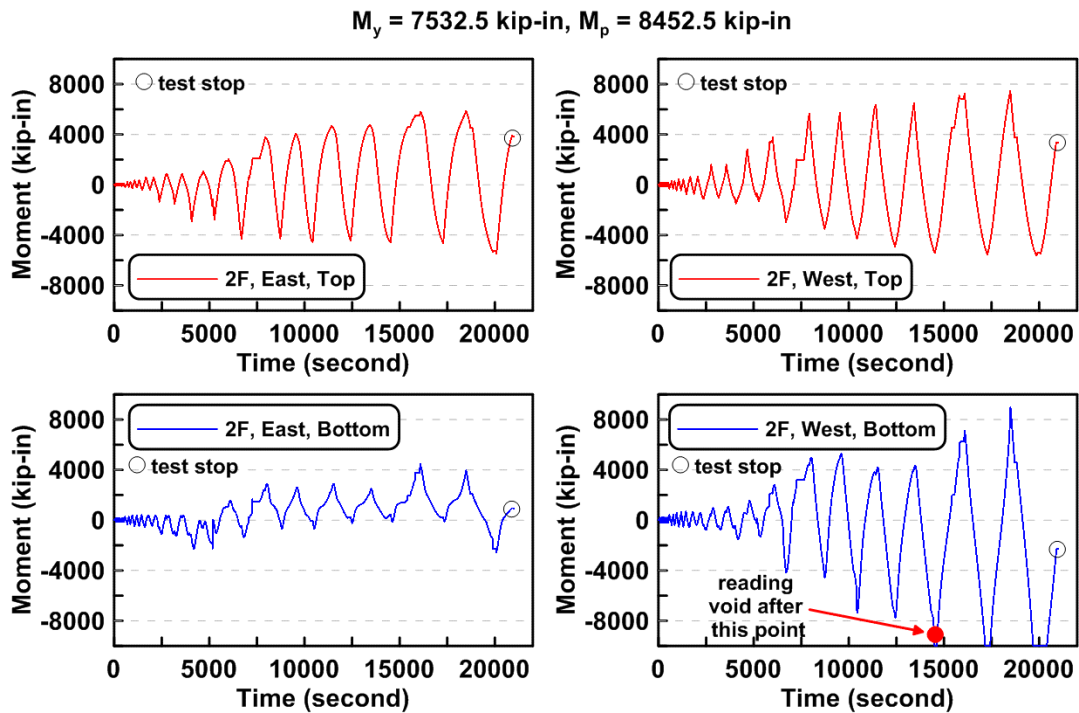


Figure 4.148 Specimen TCBF-B-2: time history of the second-story column bending moments (3 ft above lower beam centerline and 3 ft below roof beam centerline).

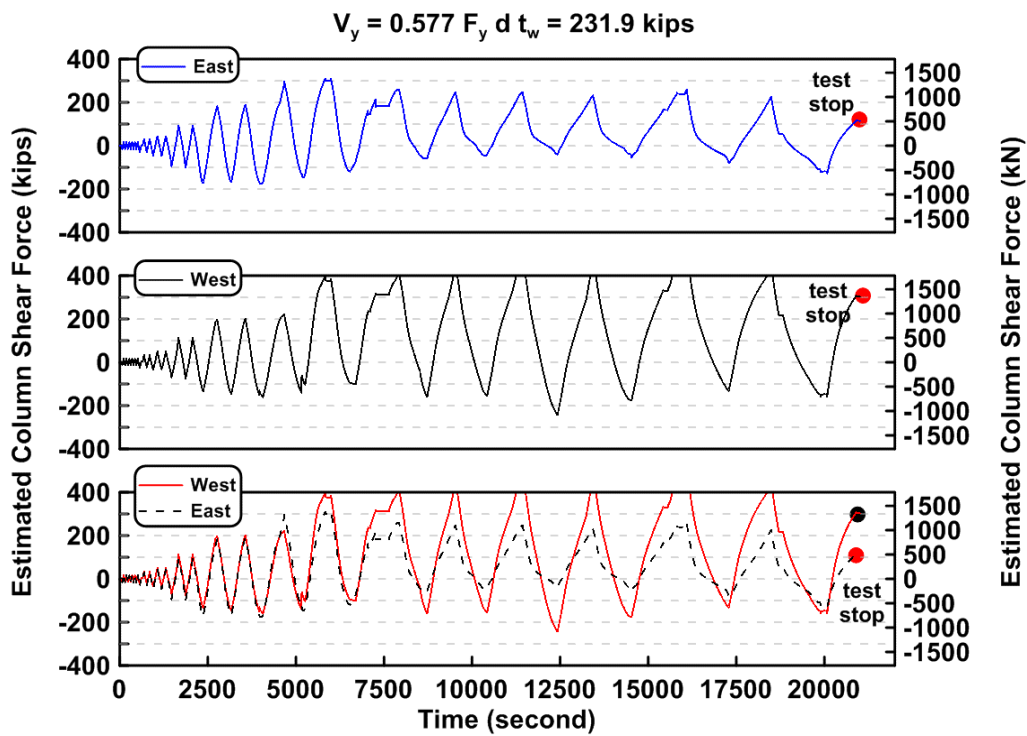


Figure 4.149 Specimen TCBF-B-2: time history of the first-story column shear forces.

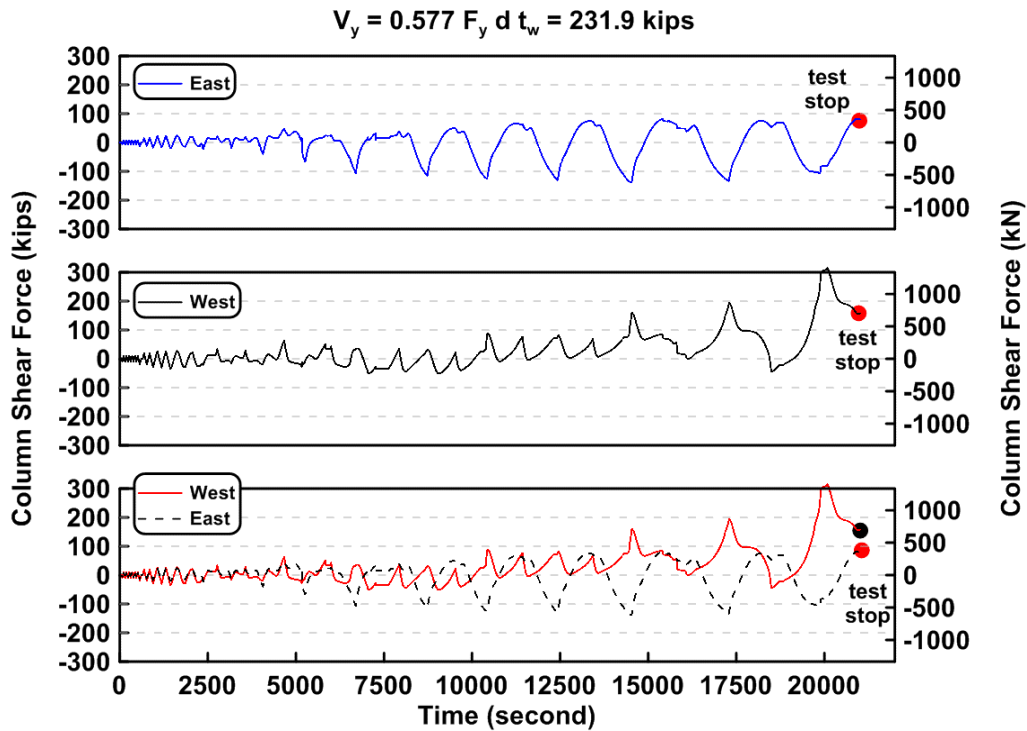


Figure 4.150 Specimen TCBF-B-2: time history of second-story column shear forces.

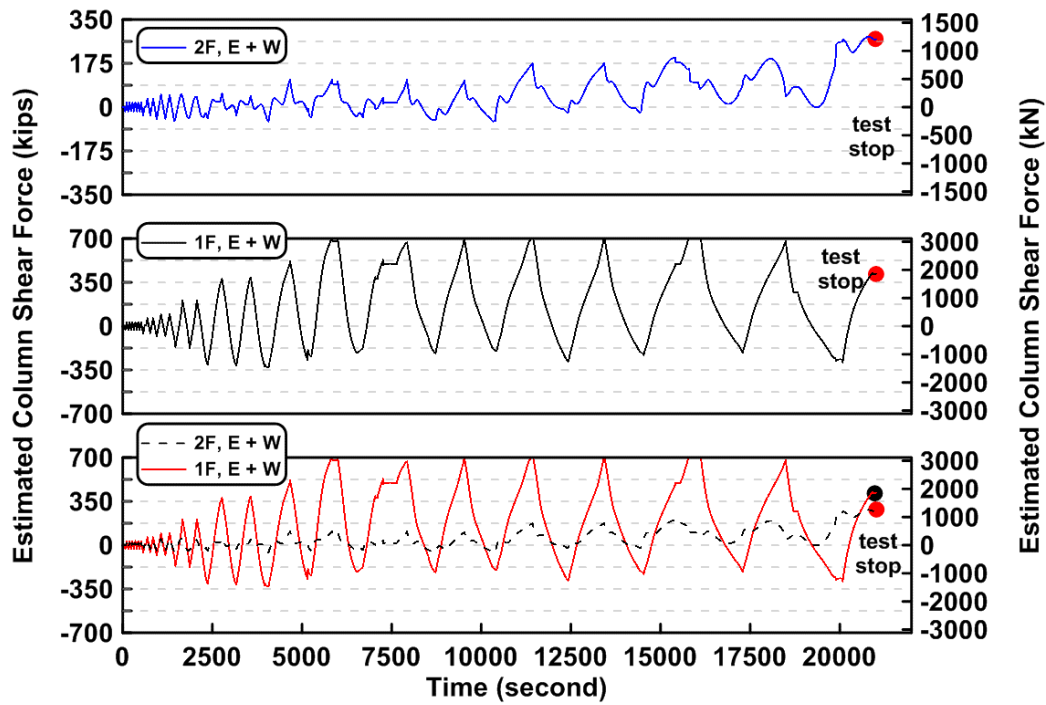


Figure 4.151 Specimen TCBF-B-2: time history of sum of east and west column shear forces for both stories.

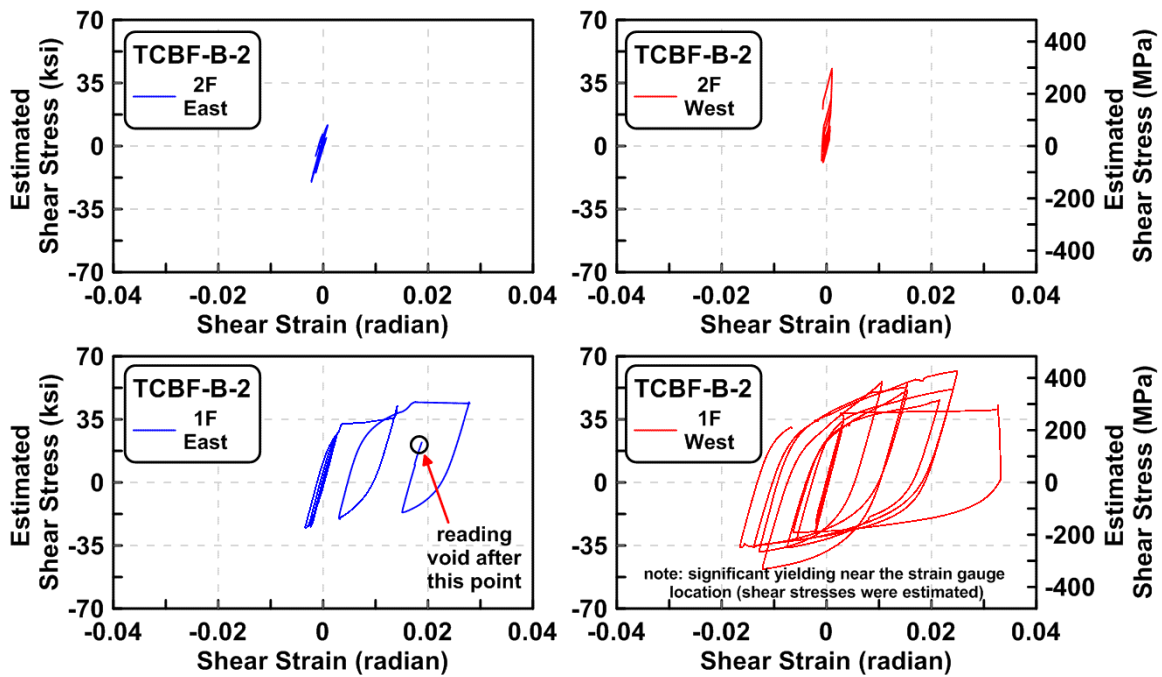


Figure 4.152 Specimen TCBF-B-2: estimated column shear stress versus shear strain relationships (locations: EC1-B-N, EC2-B-N, WC1-B-N and WC2-B-N).

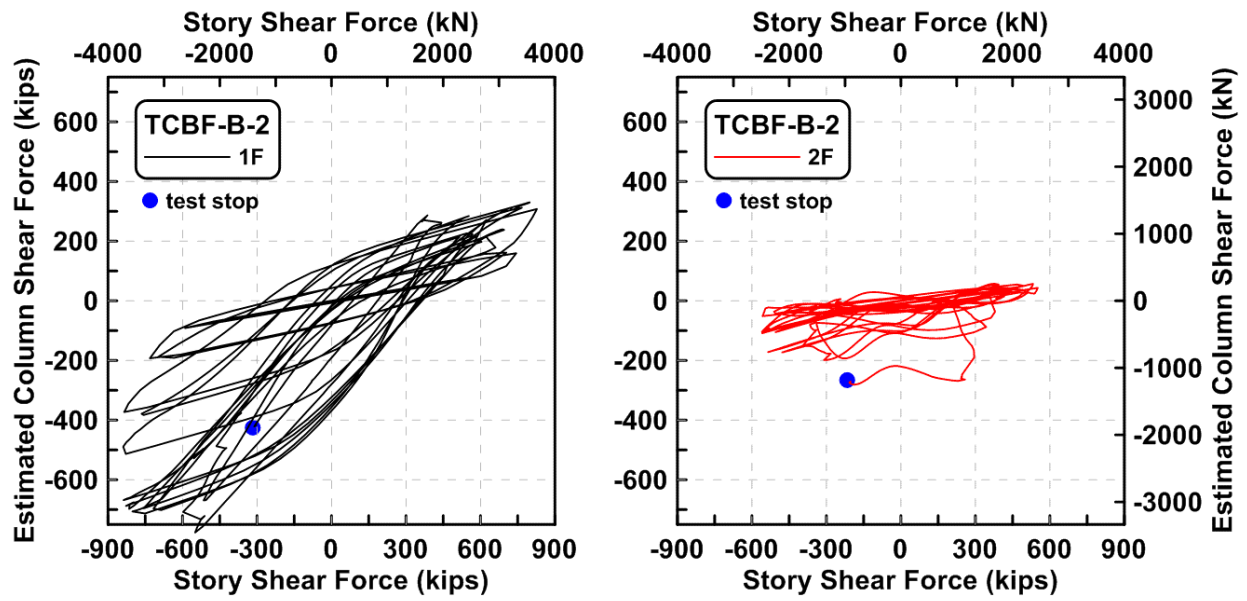


Figure 4.153 Specimen TCBF-B-2: story shear component from columns versus total story shear forces.

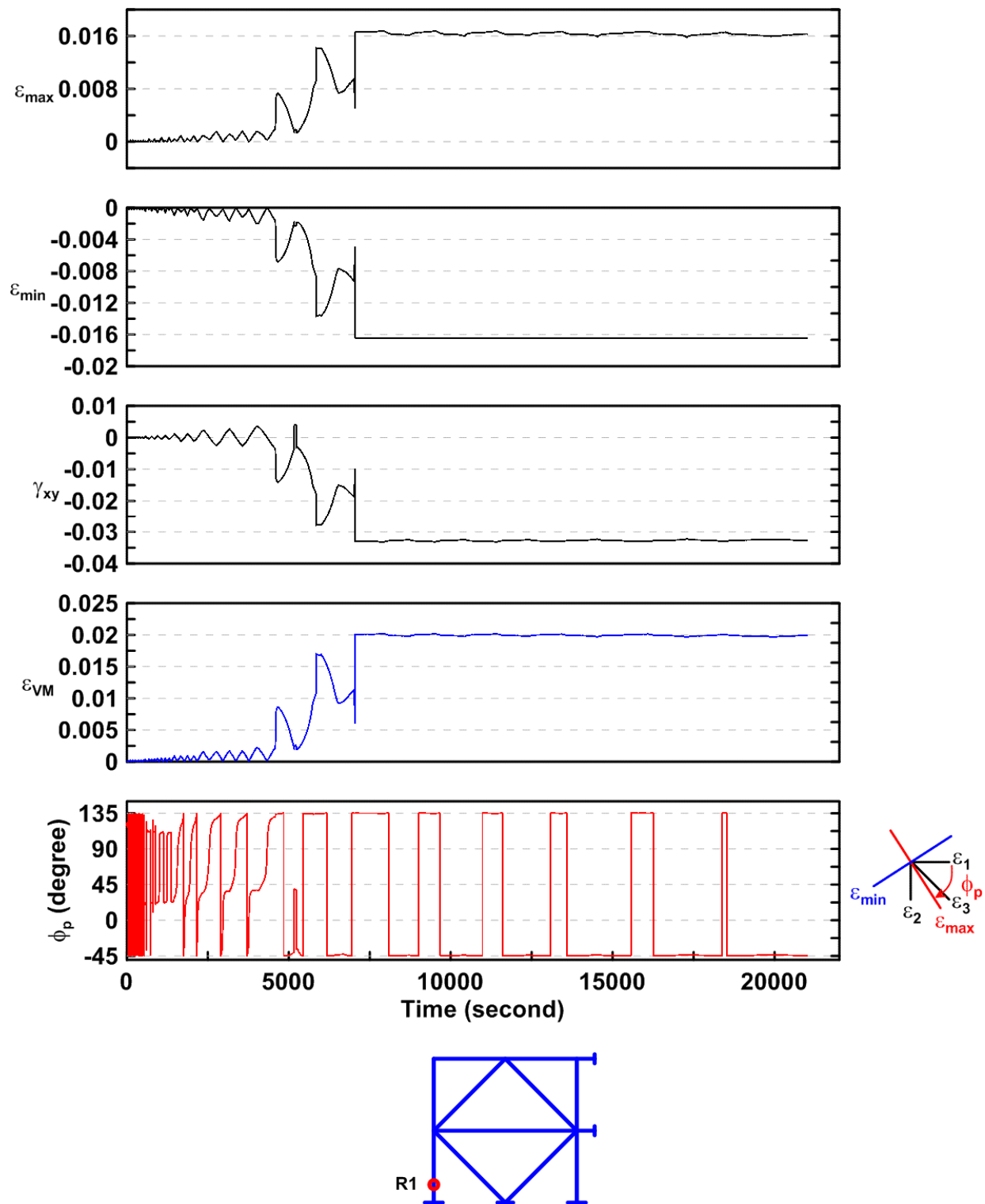


Figure 4.154 Specimen TCBF-B-2: time history of rosette-type strain gauge readings in first-story column web (location: R1).

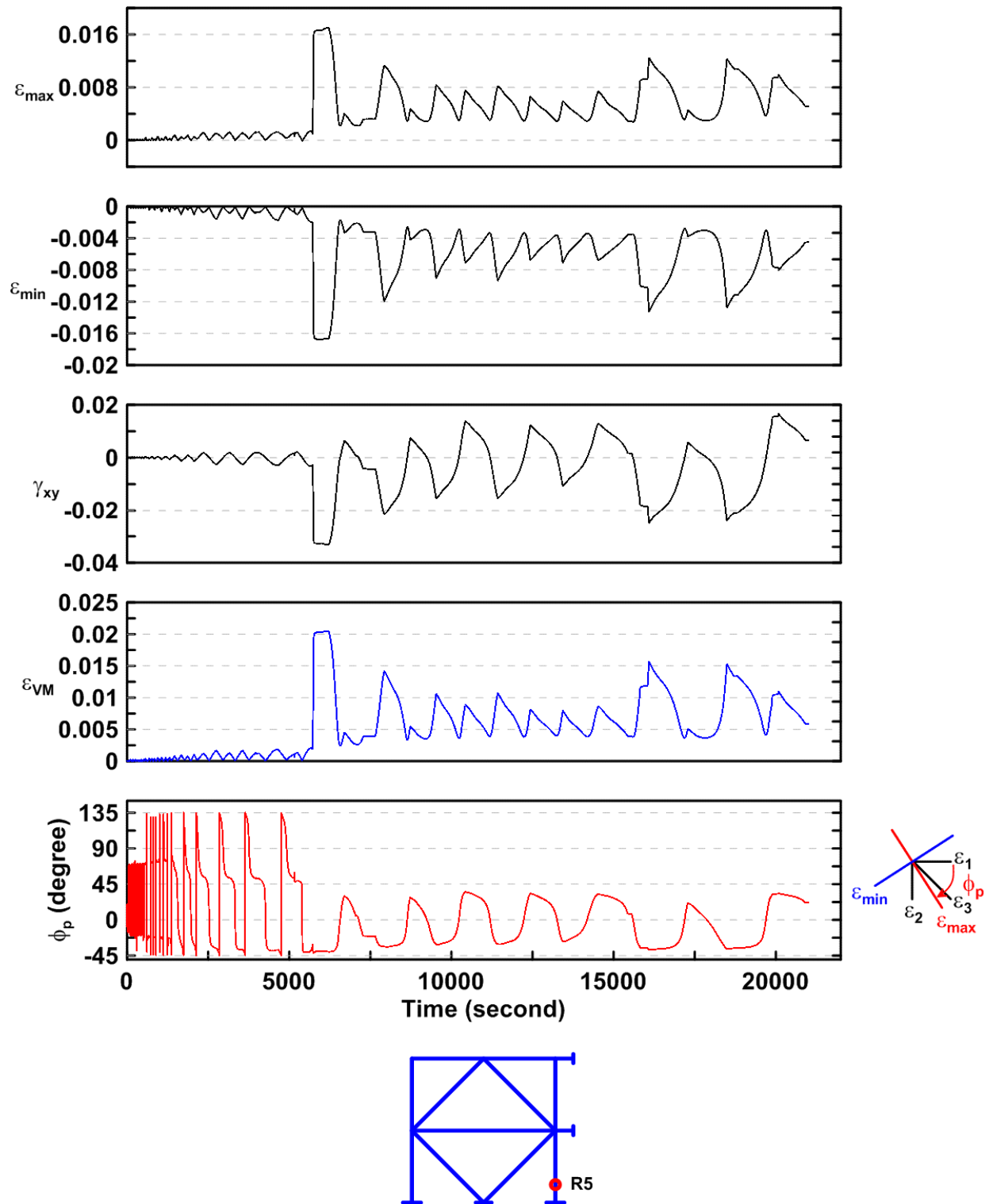


Figure 4.155 Specimen TCBF-B-2: time history of rosette-type strain gauge readings in first-story column web (location: R5).

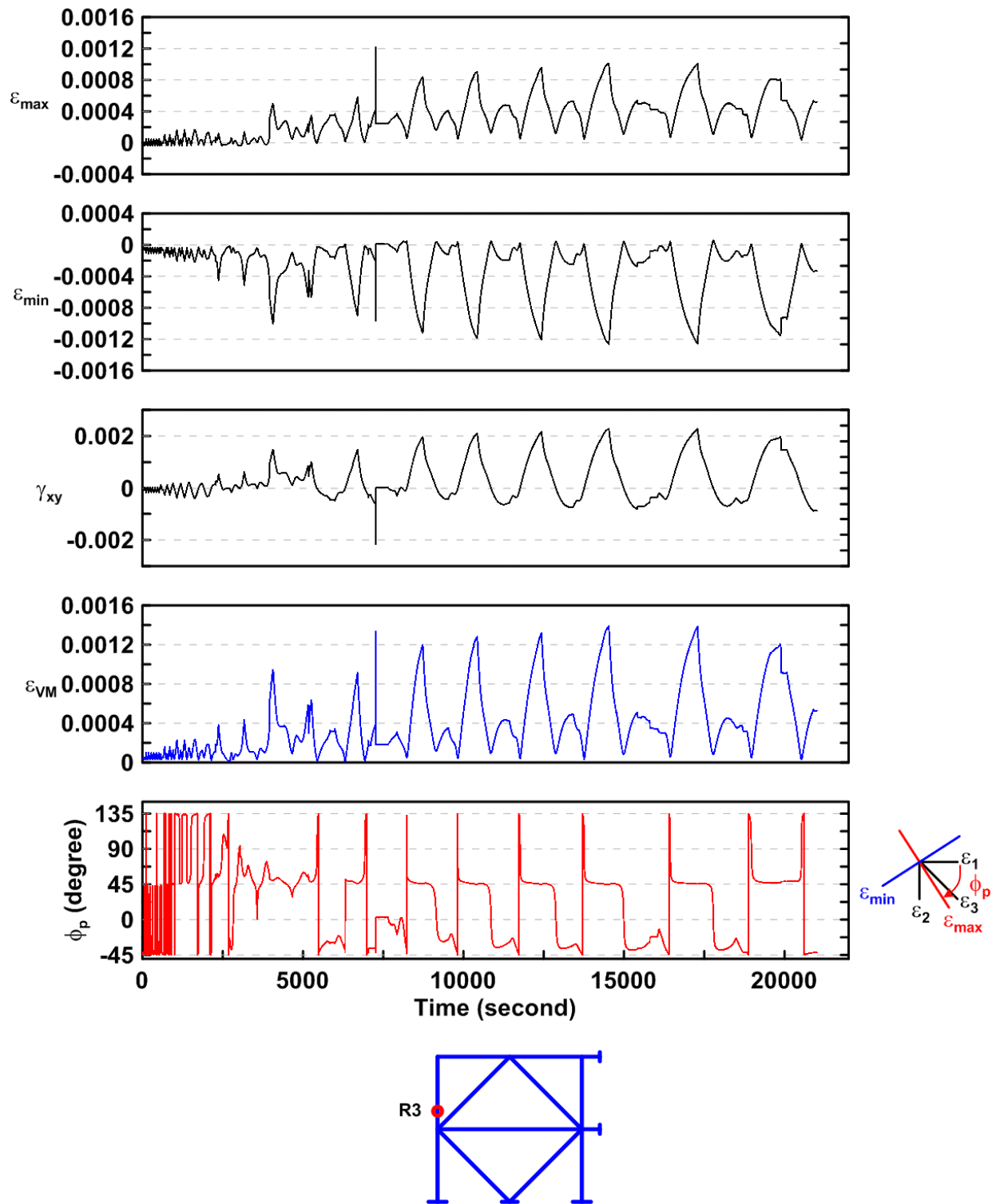


Figure 4.156 Specimen TCBF-B-2: time history of rosette-type strain gauge readings in the second-story column web (location: R3).

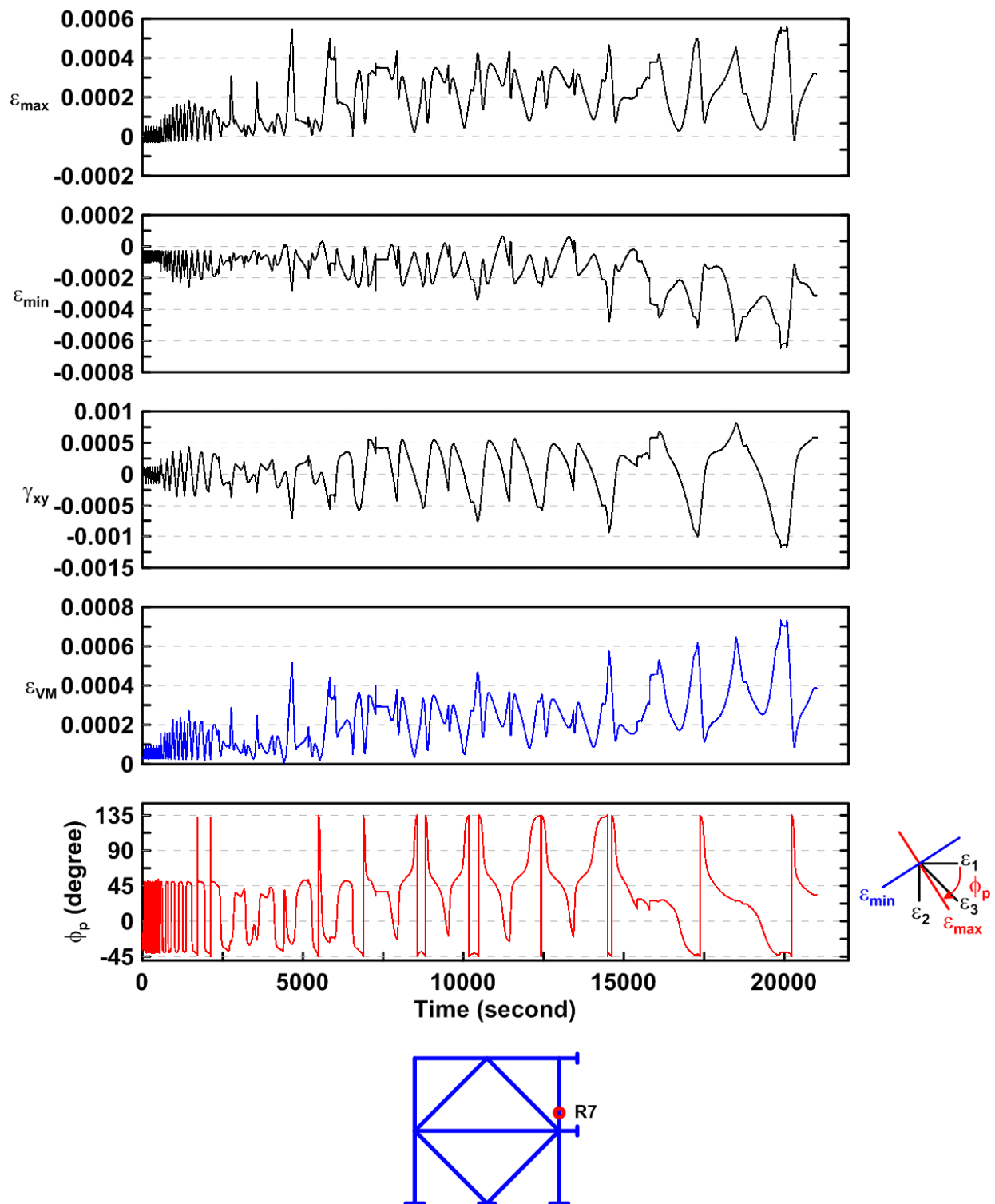


Figure 4.157 Specimen TCBF-B-2: time history of rosette-type strain gauge readings in the second-story column web (location: R7).

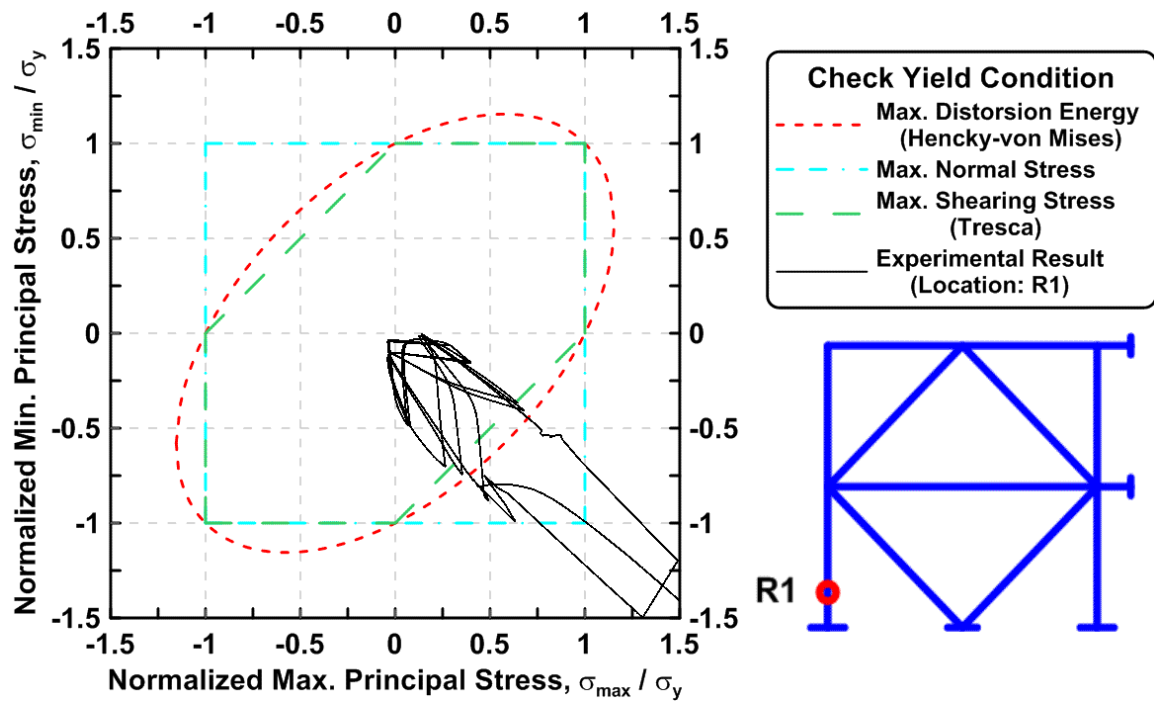


Figure 4.158 Specimen TCBF-B-2: maximum principal stress versus minimum principal stress in first-story column (location: R1).

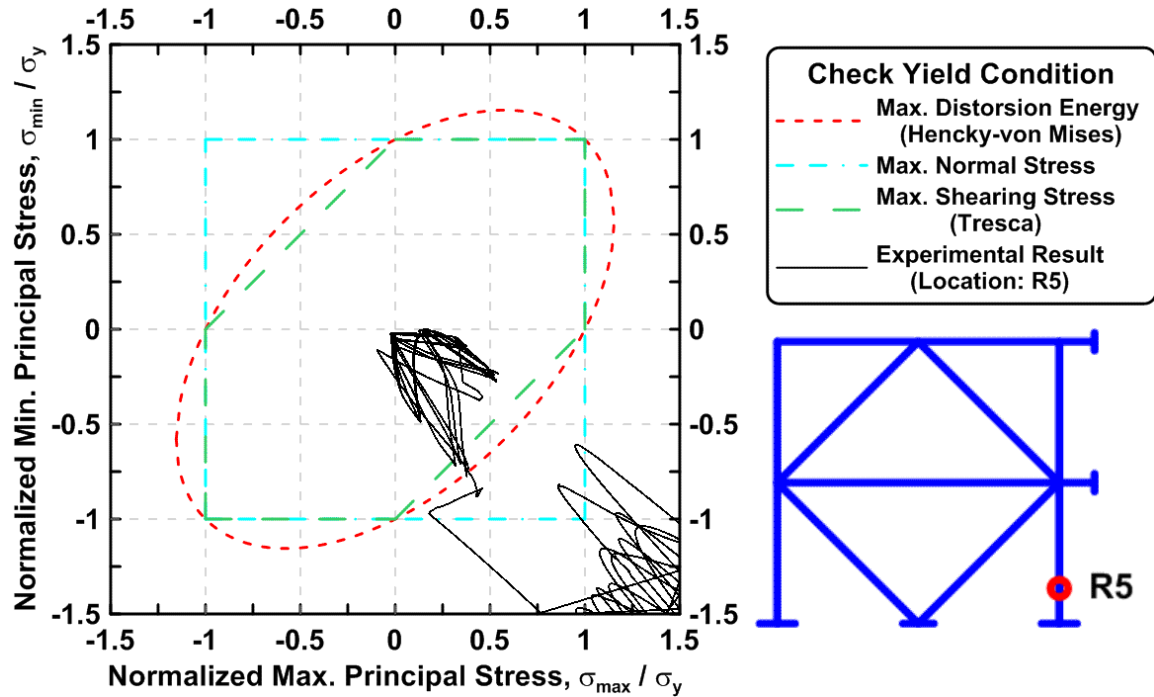


Figure 4.159 Specimen TCBF-B-2: maximum principal stress versus minimum principal stress in first-story column (location: R5).

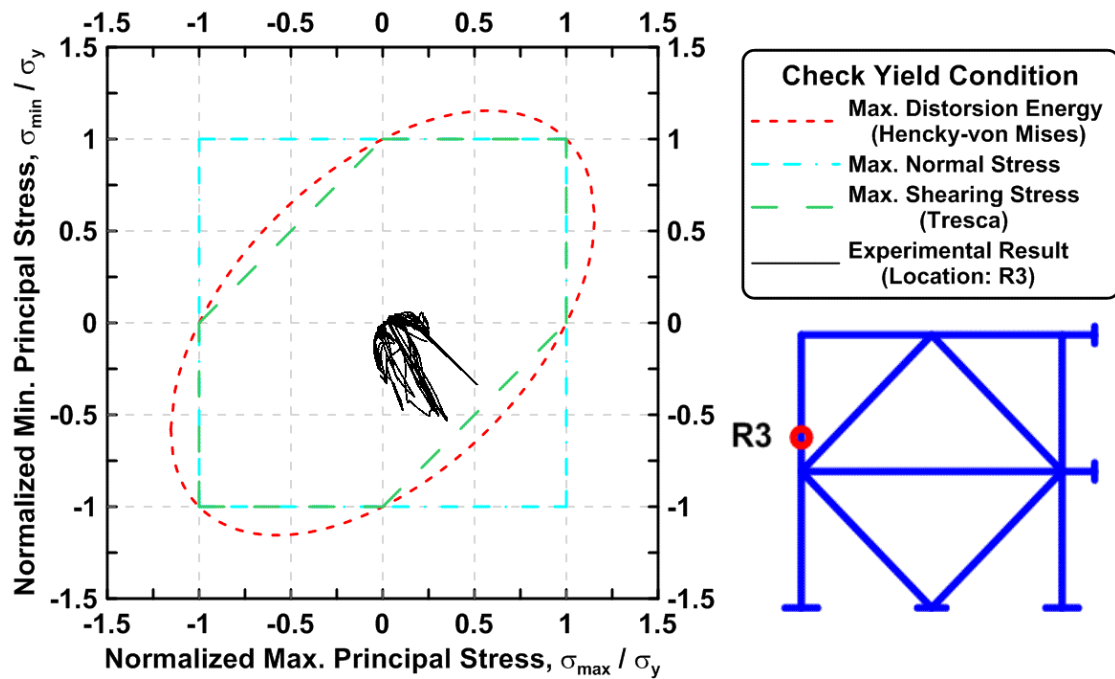


Figure 4.160 Specimen TCBF-B-2: maximum principal stress versus minimum principal stress in second-story column (location: R3).

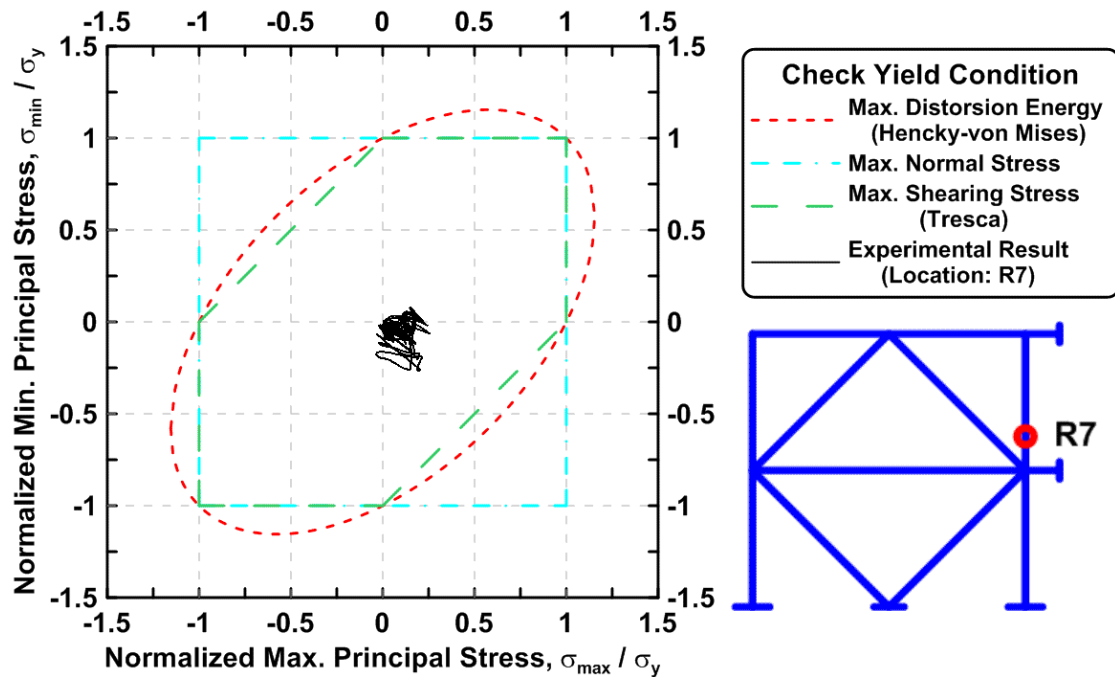


Figure 4.161 Specimen TCBF-B-2: maximum principal stress versus minimum principal stress in second-story column (location: R7).

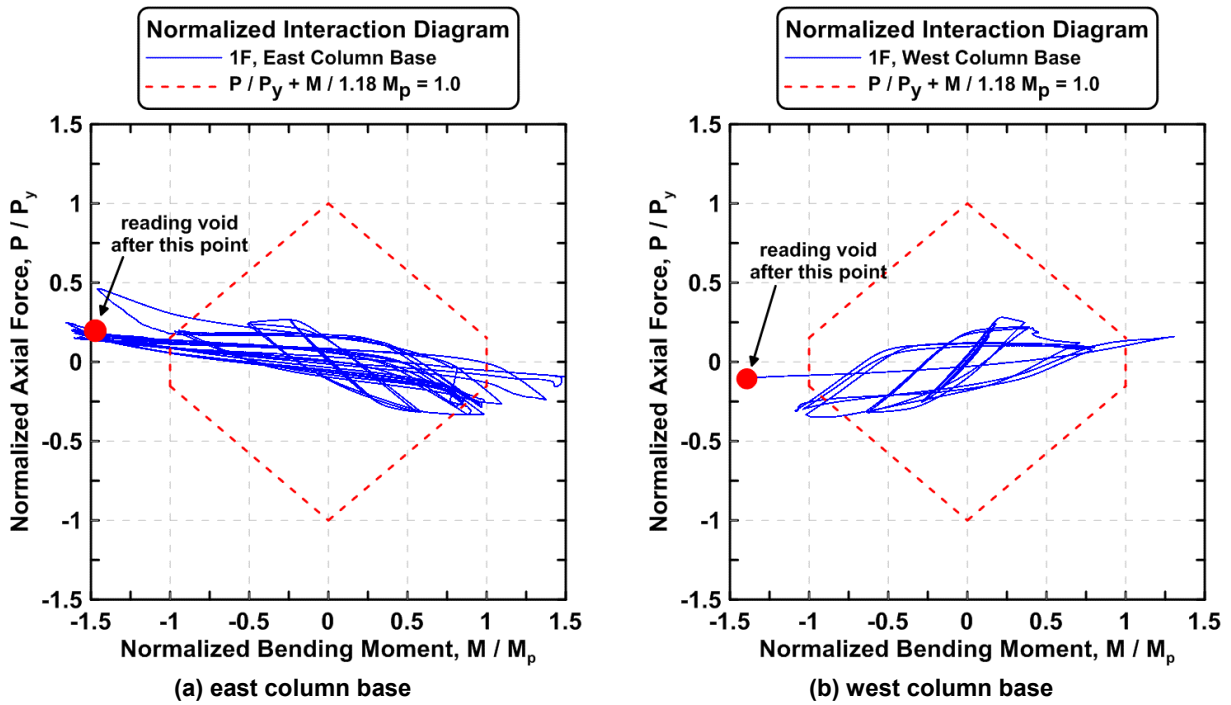


Figure 4.162 Specimen TCBF-B-2: normalized P-M interaction diagrams of first-story columns.

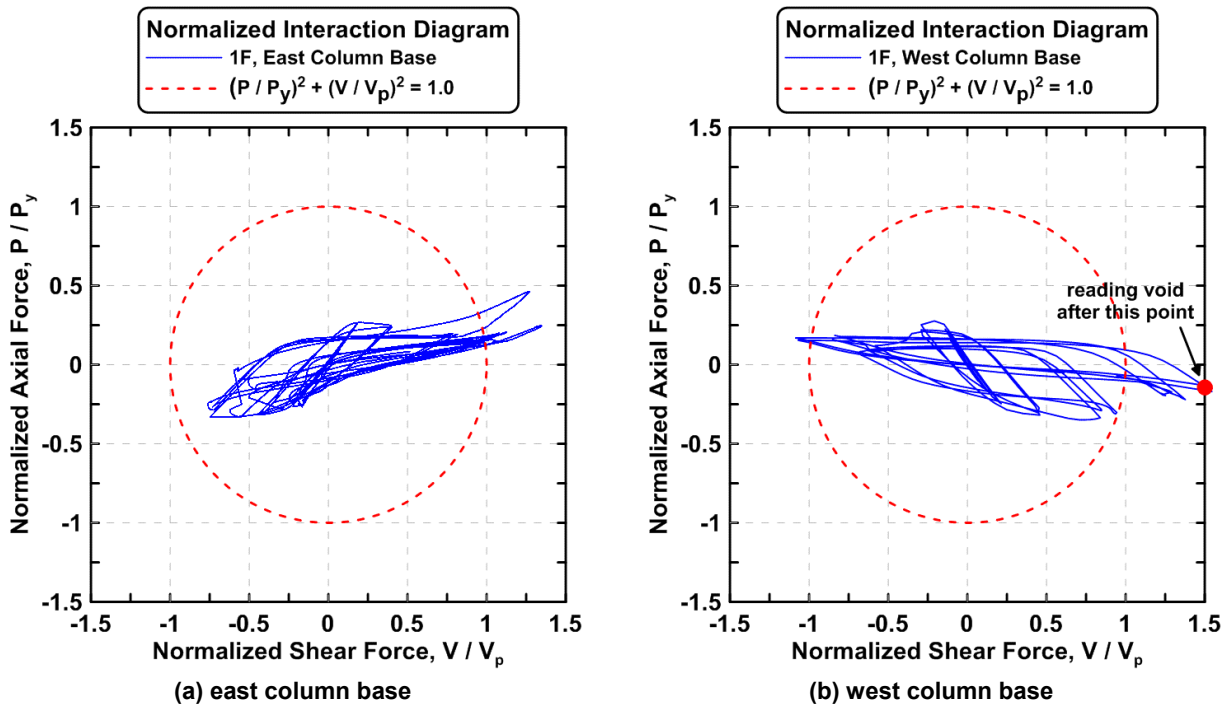


Figure 4.163 Specimen TCBF-B-2: normalized P-V interaction diagrams of first-story columns.

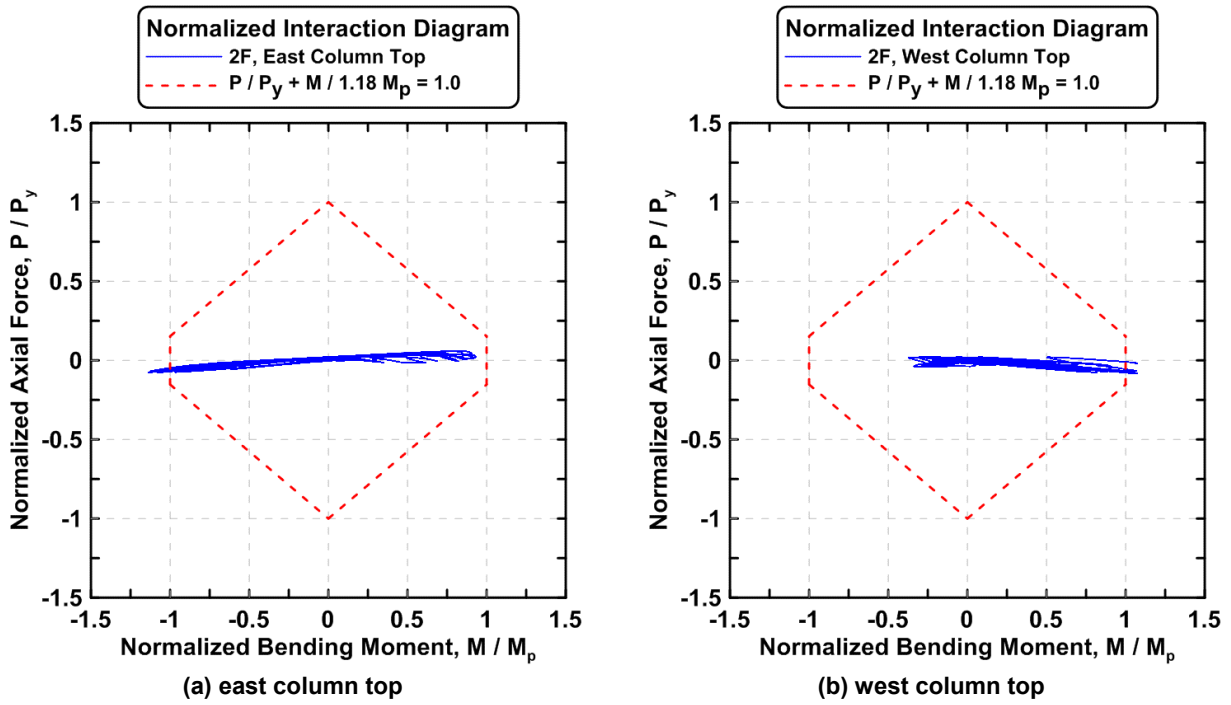


Figure 4.164 Specimen TCBF-B-2: normalized P-M interaction diagrams of second-story columns.

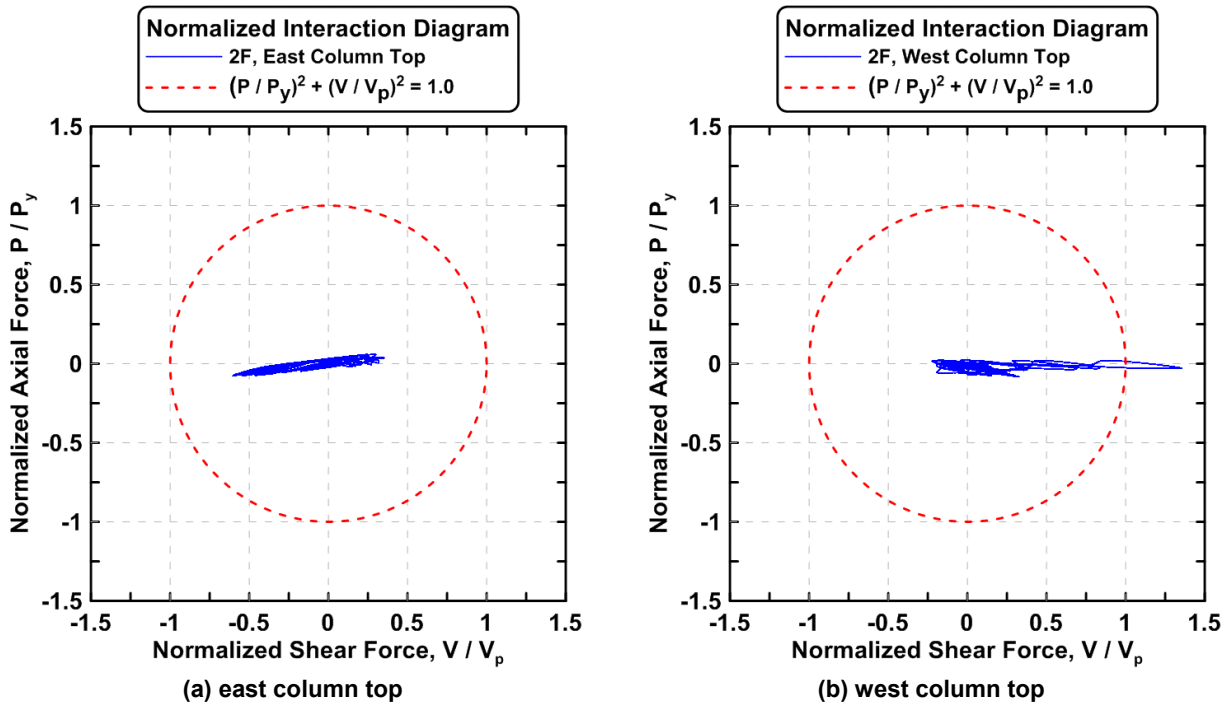


Figure 4.165 Specimen TCBF-B-2: normalized P-V interaction diagrams of second-story columns.

4.1.2.2.3 Beam Response

The vertical deflection time history at the center of the W24 \times 117 roof beam and the W24 \times 68 lower beam are plotted in Figure 4.166. The time history of strain readings at both ends of the roof beam and lower beam, respectively, are shown in Figures 4.167 and 4.168. Both beam axial force time histories derived from linear strain gauges at different locations along the beams are plotted in Figures 4.169 and 4.170. The bending moment time histories of both beams are shown in Figures 4.171 and 4.172. Estimated beam shear force time histories are illustrated in Figures 4.173 and 4.174. The estimated vertical unbalanced force at the center of the roof beam is plotted in Figure 4.175.

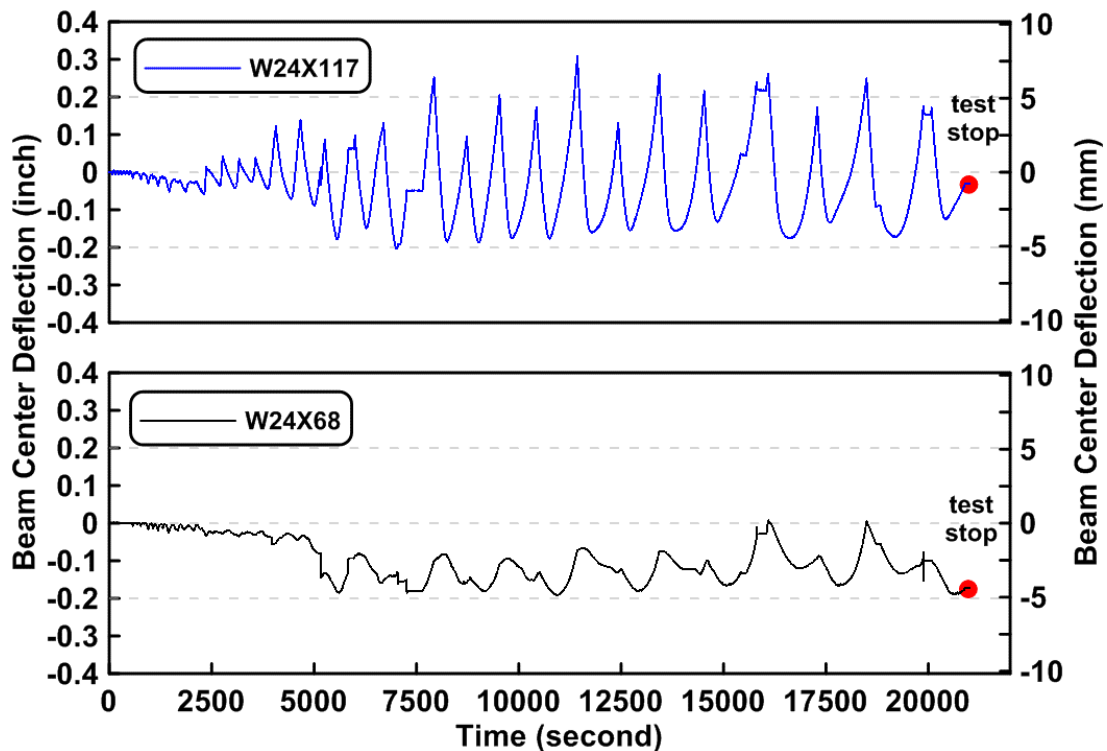


Figure 4.166 Specimen TCBF-B-2: deflection time history at center of beam span (roof beam: W24 \times 117, lower beam: W24 \times 68).

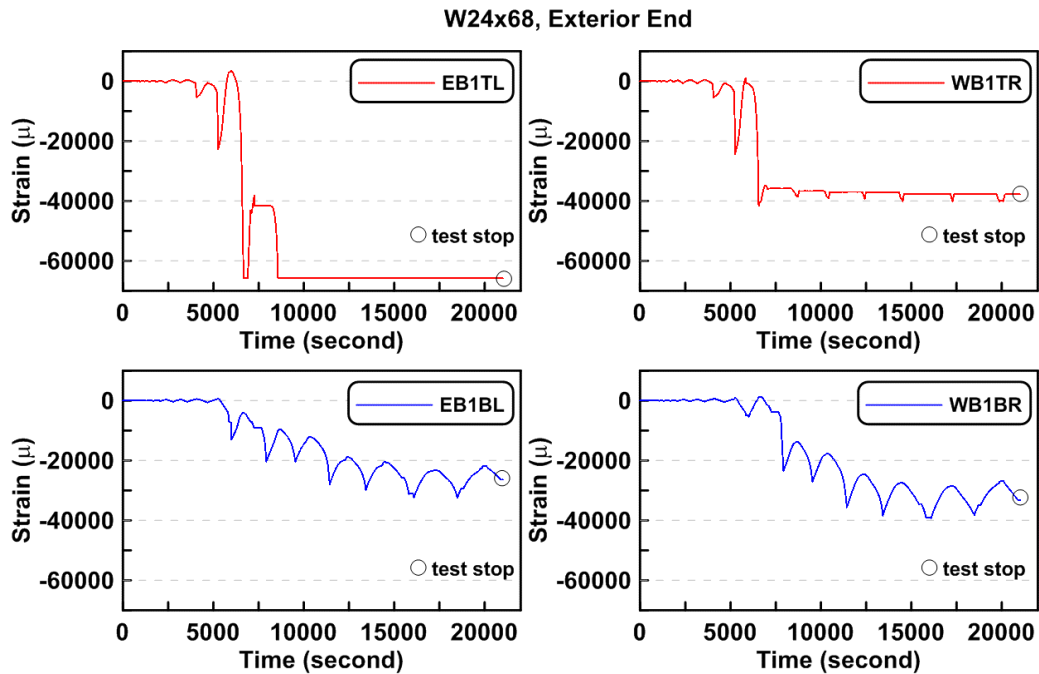


Figure 4.167 Specimen TCBF-B-2: time history of strain readings at both exterior ends of W24 \times 68 lower beam.

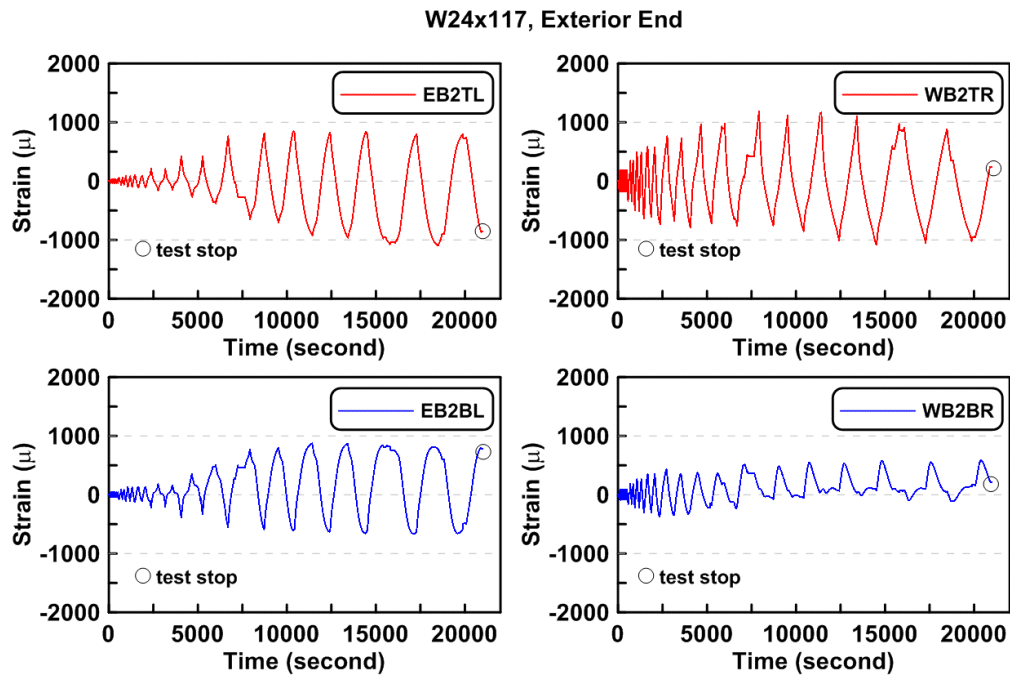


Figure 4.168 Specimen TCBF-B-2: time history of strain readings at both exterior ends of W24 \times 117 roof beam.

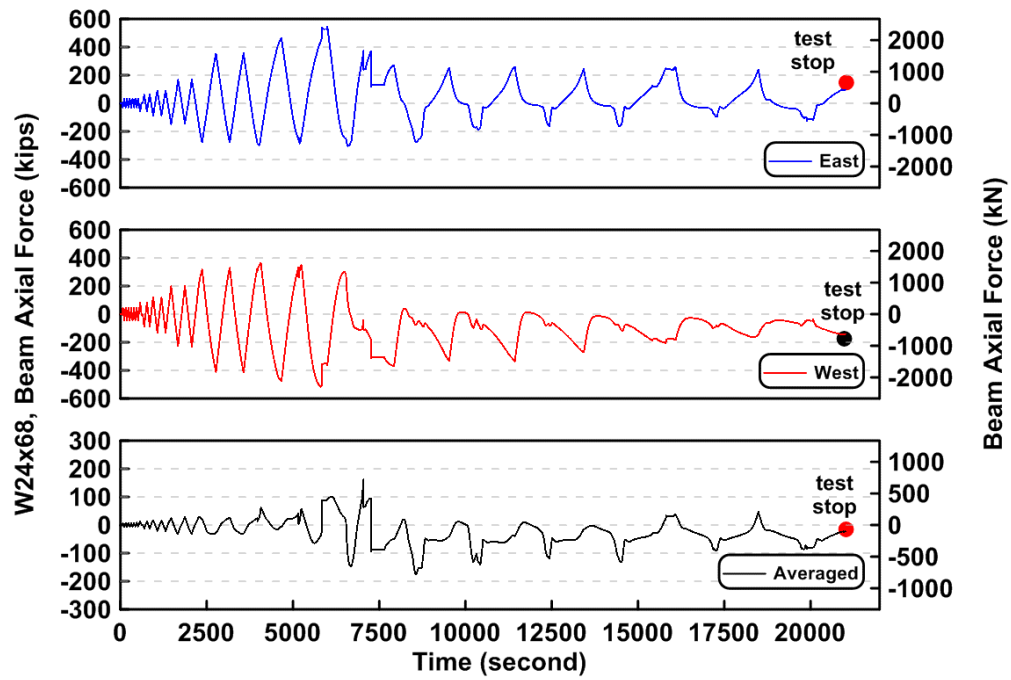


Figure 4.169 Specimen TCBF-B-2: time history of lower beam axial forces.

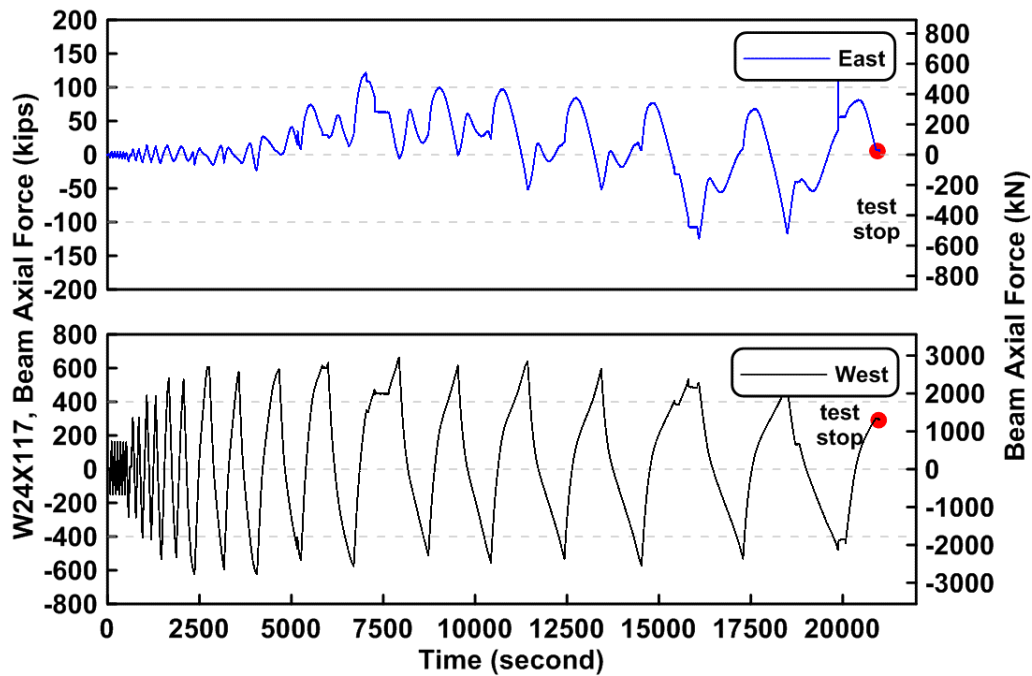


Figure 4.170 Specimen TCBF-B-2: time history of roof beam axial forces.

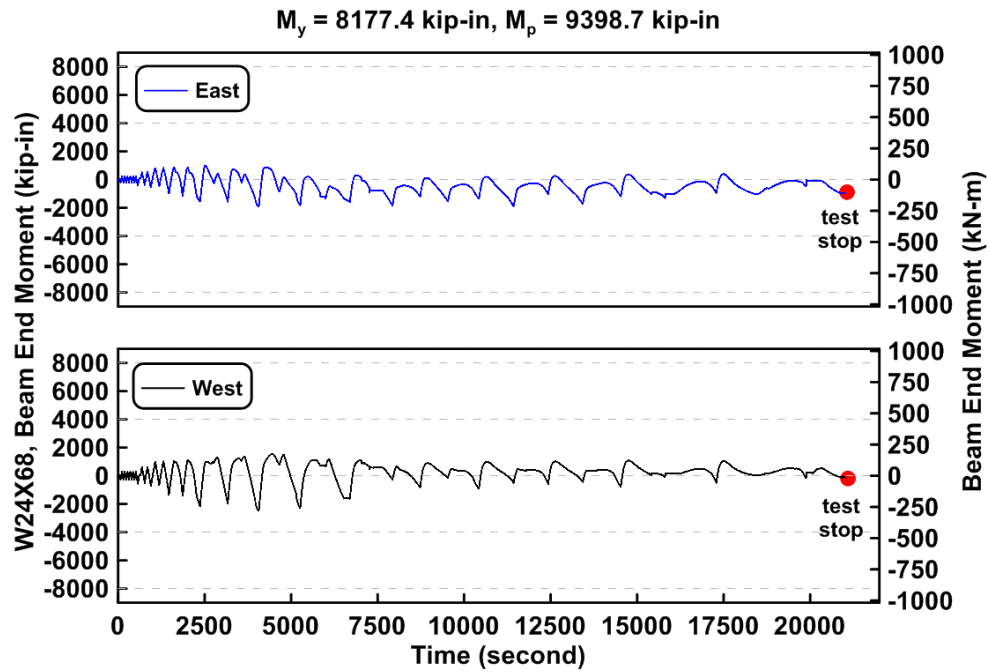


Figure 4.171 Specimen TCBF-B-2: time history of lower beam end bending moment.

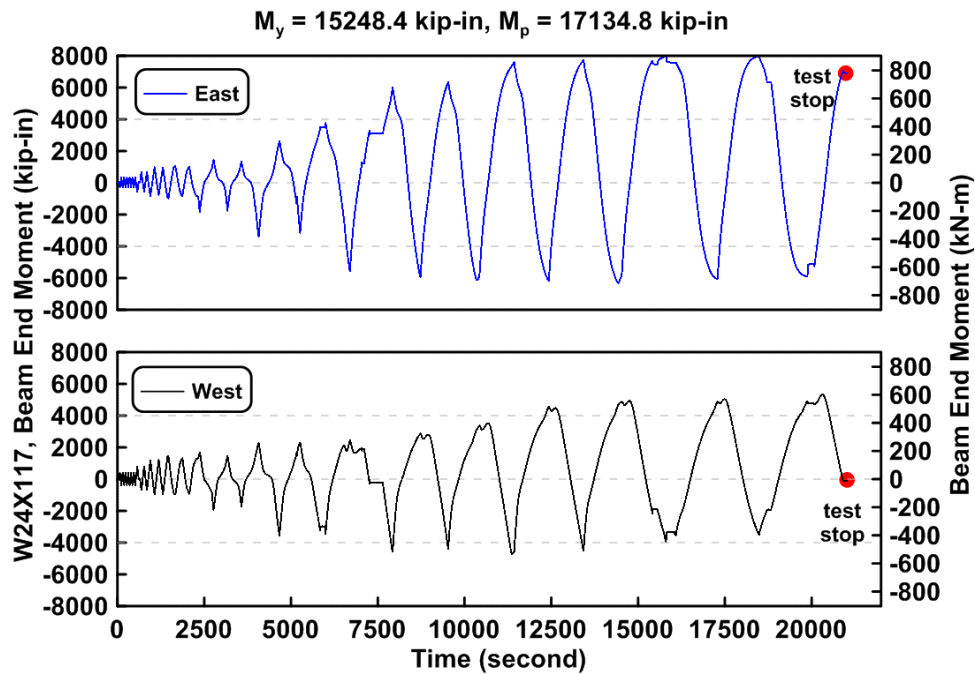


Figure 4.172 Specimen TCBF-B-2: time history of roof beam end bending moment.

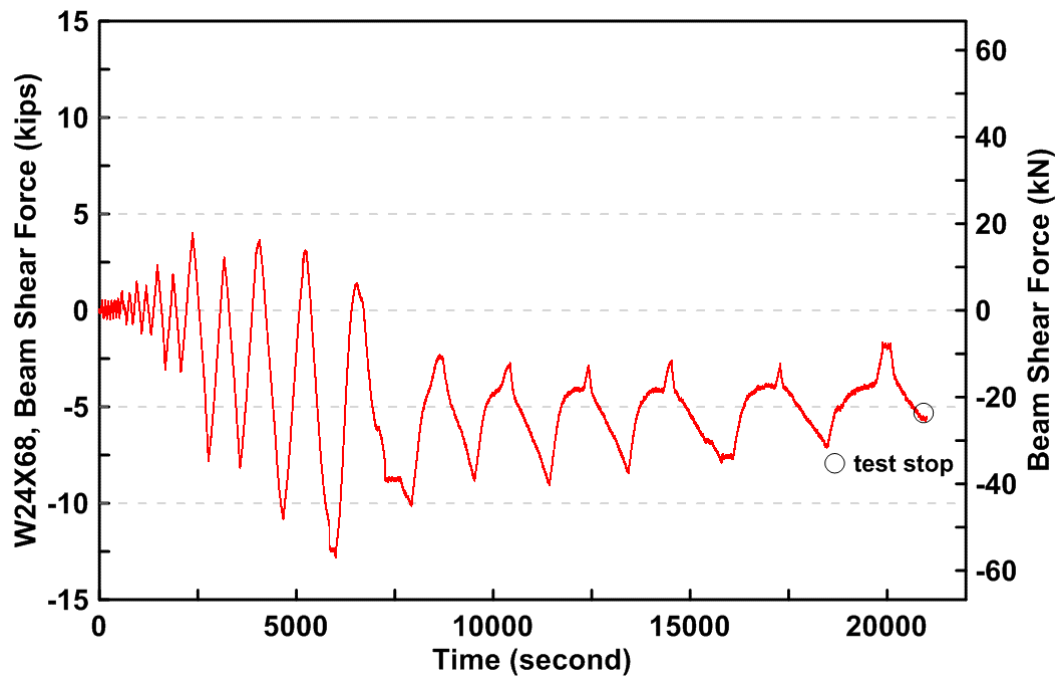


Figure 4.173 Specimen TCBF-B-2: lower beam estimated shear force time history.

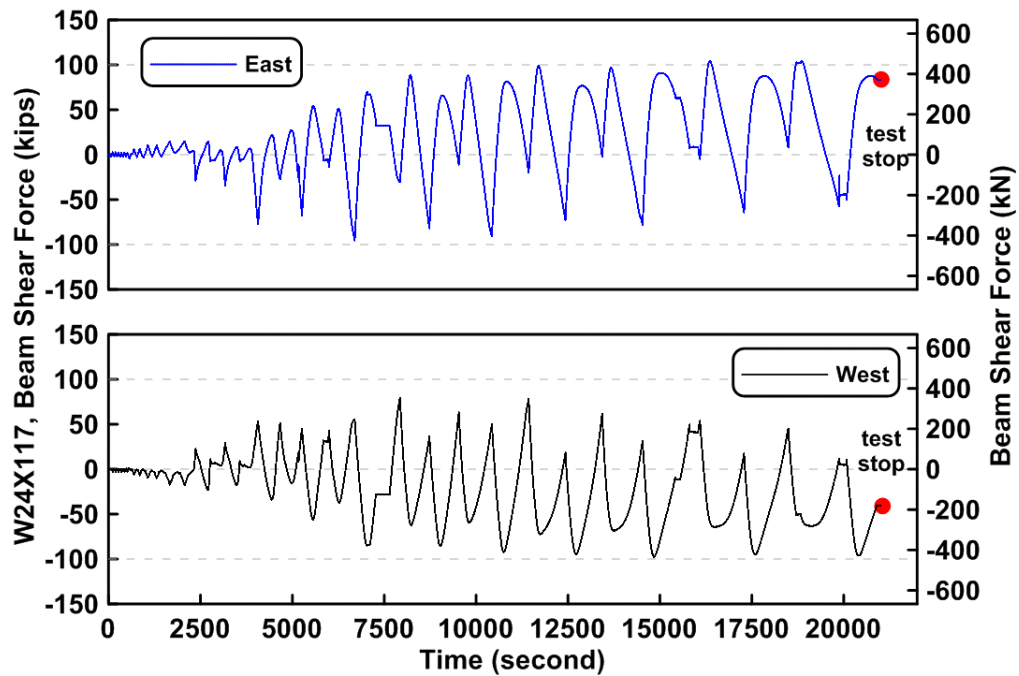


Figure 4.174 Specimen TCBF-B-2: roof beam estimated shear force time history.

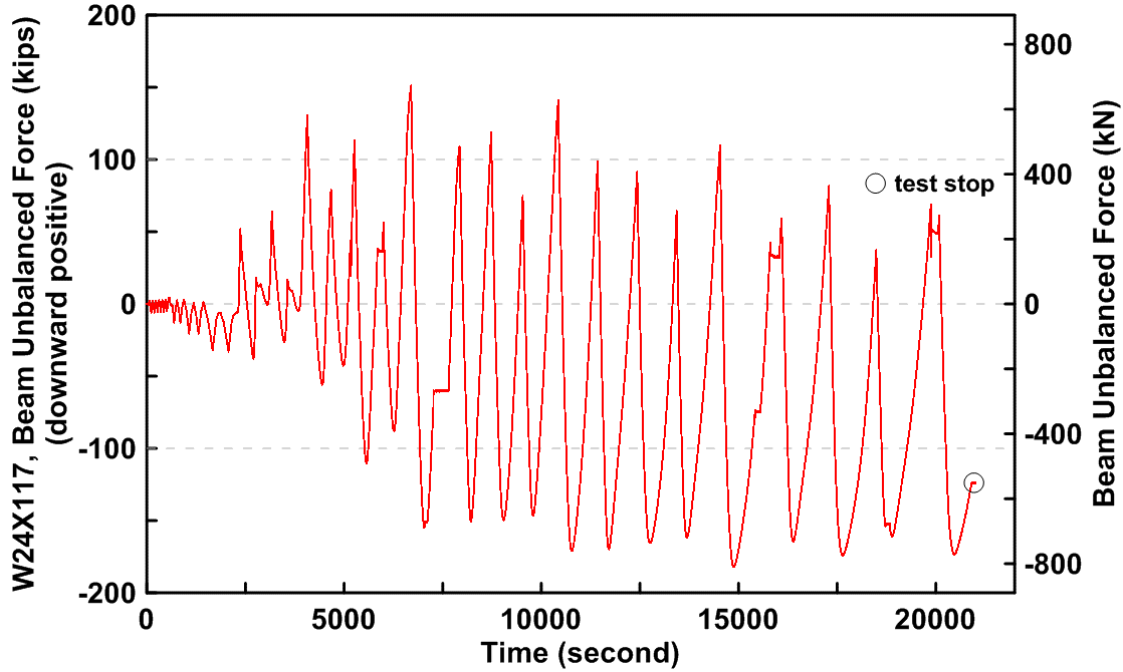


Figure 4.175 Specimen TCBF-B-2: estimated unbalanced force time history of roof beam.

4.1.2.2.4 Brace Response

The estimated brace axial forces versus brace axial deformations for each round HSS brace are shown in Figure 4.176. The estimated brace axial forces versus measured brace out-of-plane displacements at the brace center point for each round HSS braces are shown in Figure 4.177. Combined brace axial force, axial deformation, and out-of-plane displacement relationships are shown in Figure 4.178. The decomposed strain [axial strain, in-plane bending strain, out-of-plane bending strain, and warping strain; definition of strain components are similar to that shown in Figure 4.62(b) but assuming no warping strain for round HSS braces] time histories of each brace are plotted in Figures 4.179 to 4.182.

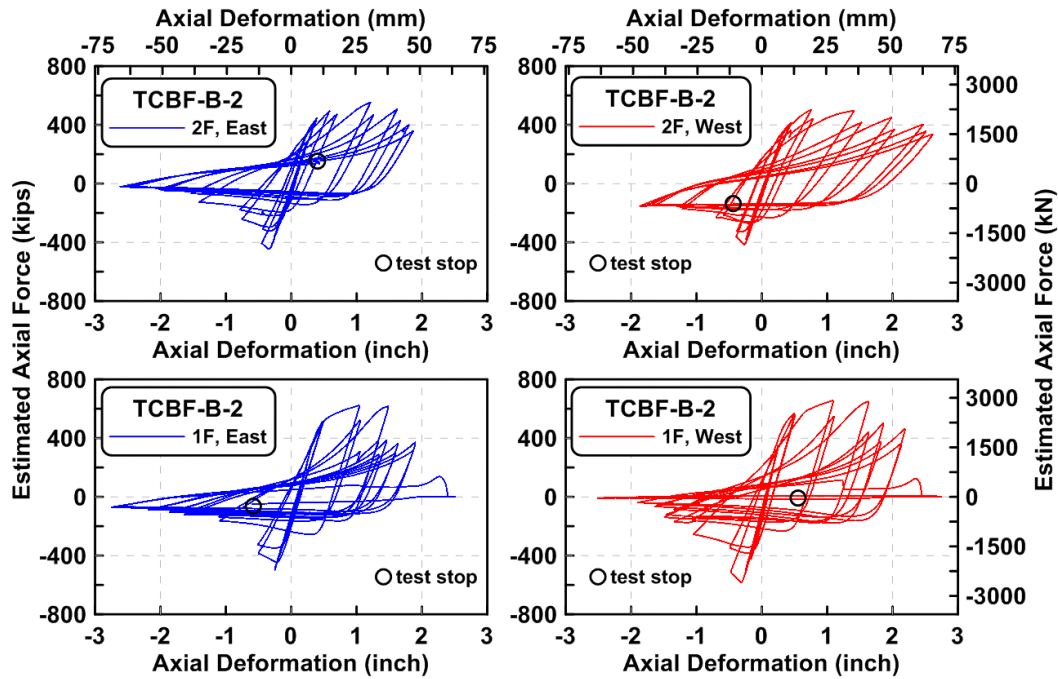


Figure 4.176 Specimen TCBF-B-2: estimated brace axial forces versus brace axial deformations.

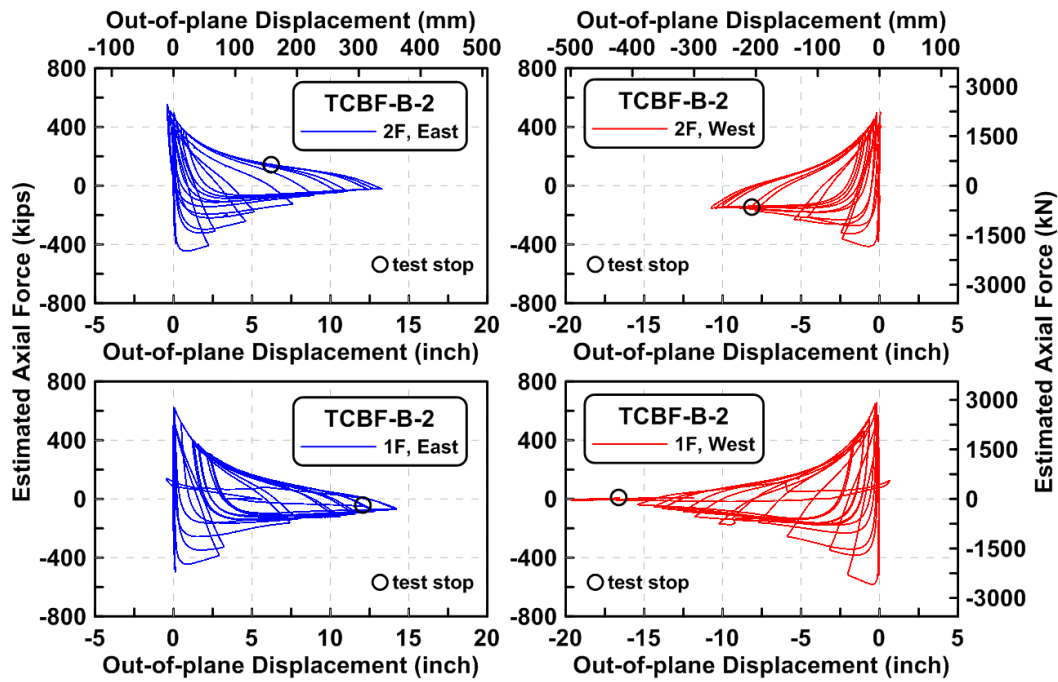


Figure 4.177 Specimen TCBF-B-2: estimated brace axial forces versus measured brace out-of-plane displacements.

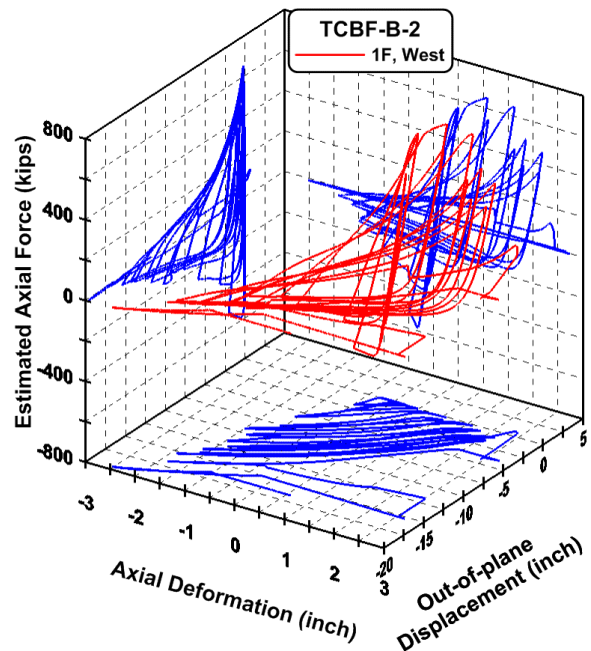
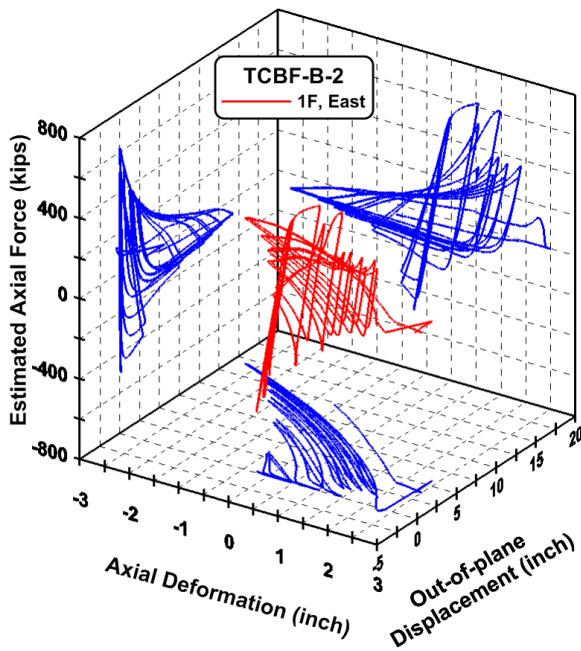
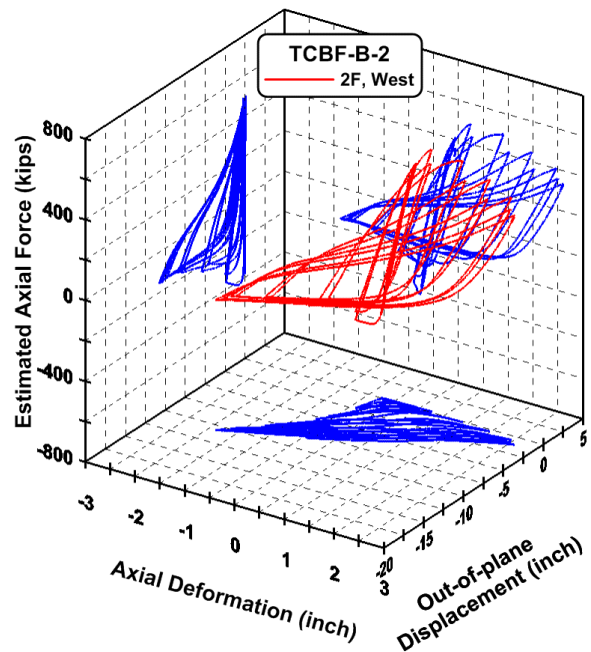
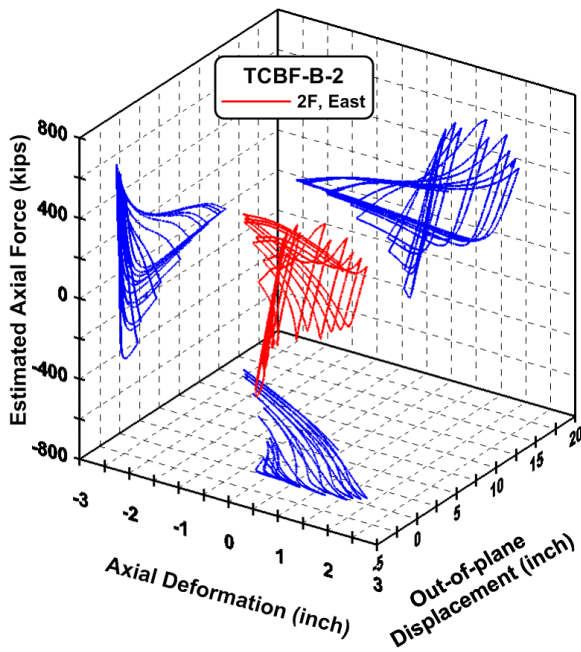


Figure 4.178 Specimen TCBF-B-2: estimated brace axial force, brace axial deformation and measured brace out-of-plane displacement relationships.

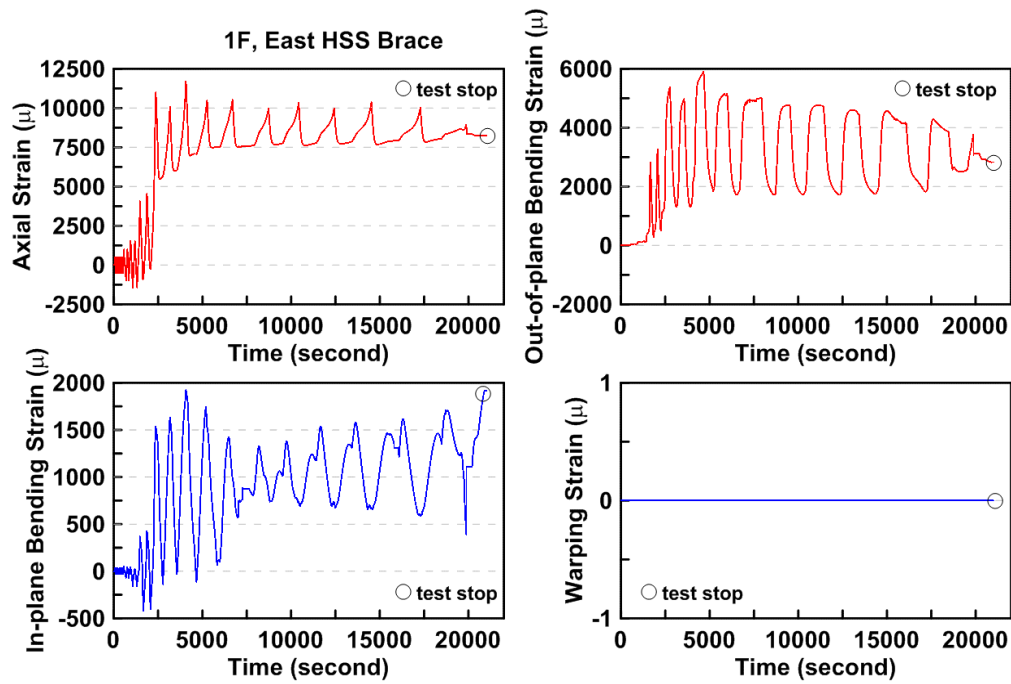


Figure 4.179 Specimen TCBF-B-2: time history of the decomposed strain components of first-story eastern-side HSS brace.

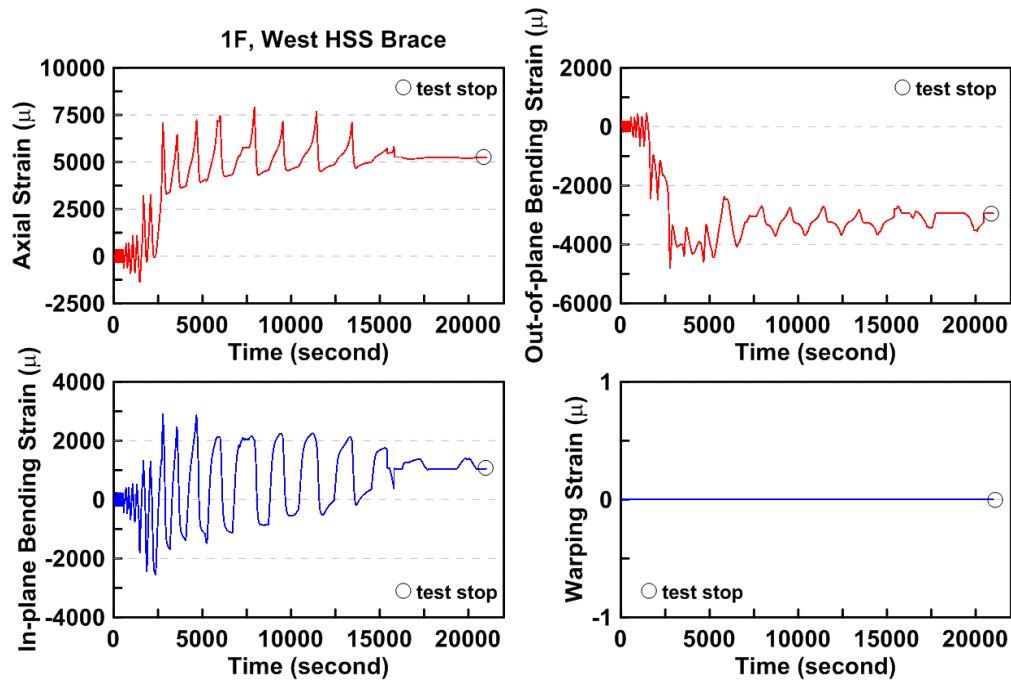


Figure 4.180 Specimen TCBF-B-2: time history of the decomposed strain components of first-story western-side HSS brace.

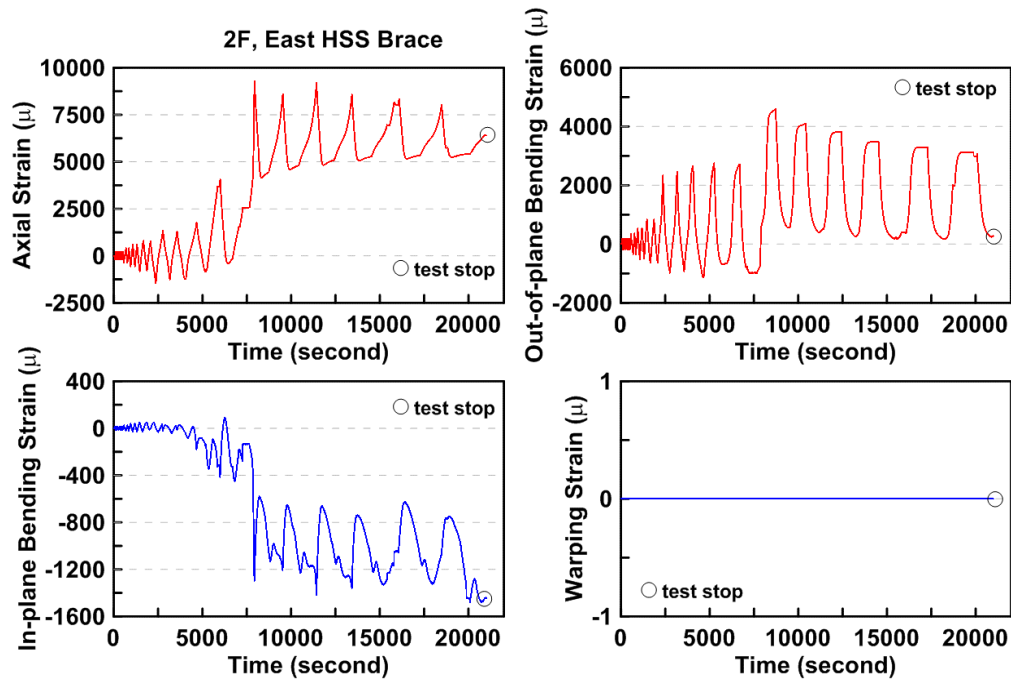


Figure 4.181 Specimen TCBF-B-2: time history of decomposed strain components of second-story eastern-side HSS brace.

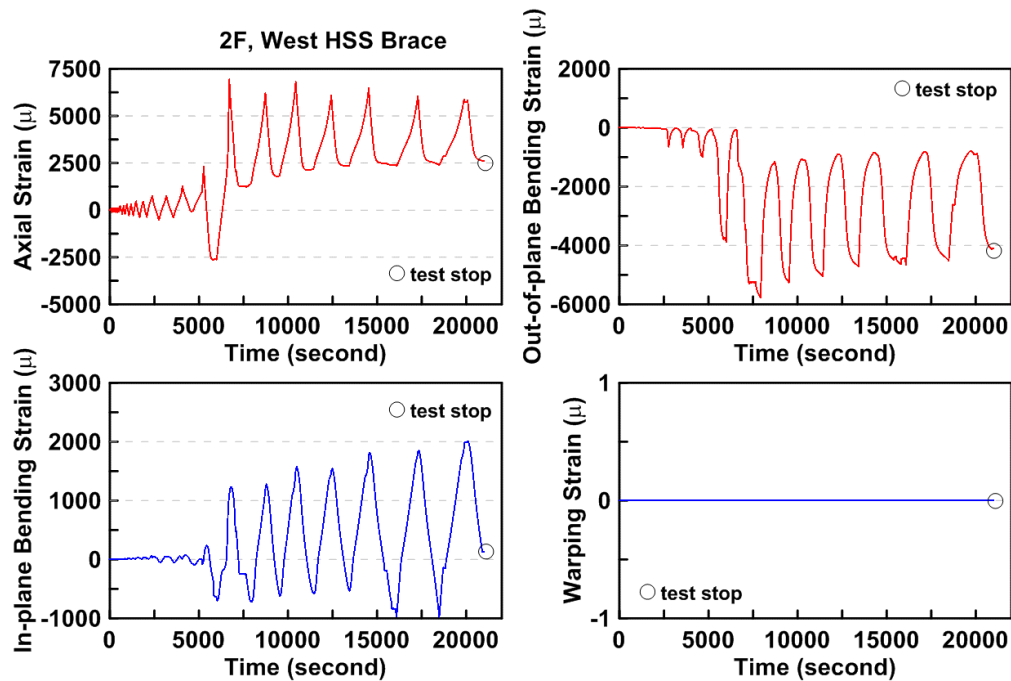


Figure 4.182 Specimen TCBF-B-2: time history of decomposed strain components of second-story western-side HSS brace.

4.1.2.2.5 Panel Zone Response

Estimated panel zone shear stress versus measured panel zone shear strain relationships for four locations is plotted in Figure 4.183. Time histories of derived rosette-type strain gauge readings in the panel zone area at each story are shown in Figures 4.184 to 4.187. Normalized maximum and minimum principal stress relationships along with different yield criteria for the panel zone regions are plotted in Figures 4.188 to 4.191.

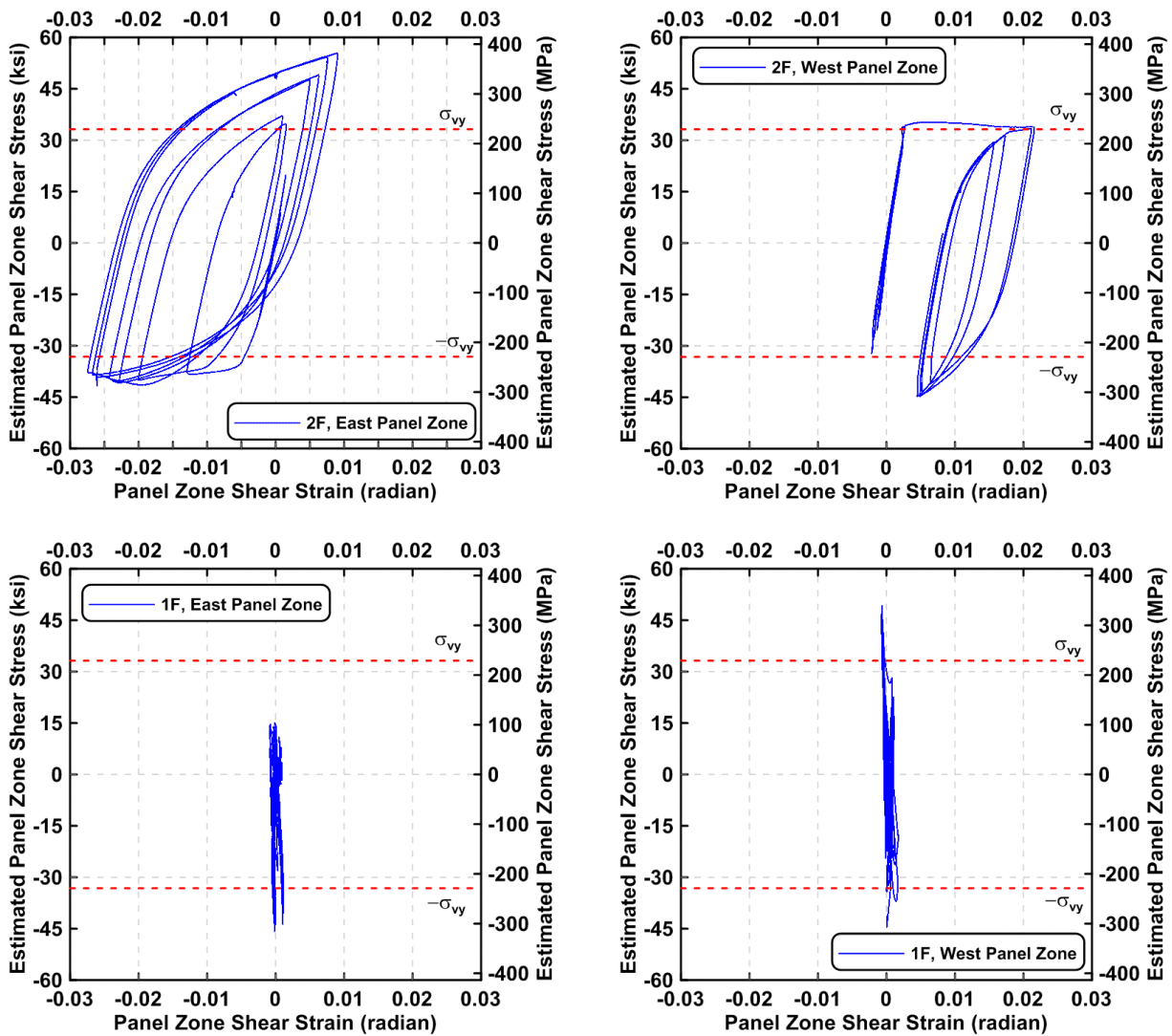


Figure 4.183 Specimen TCBF-B-2: estimated panel zone shear stress versus shear strain relationships.

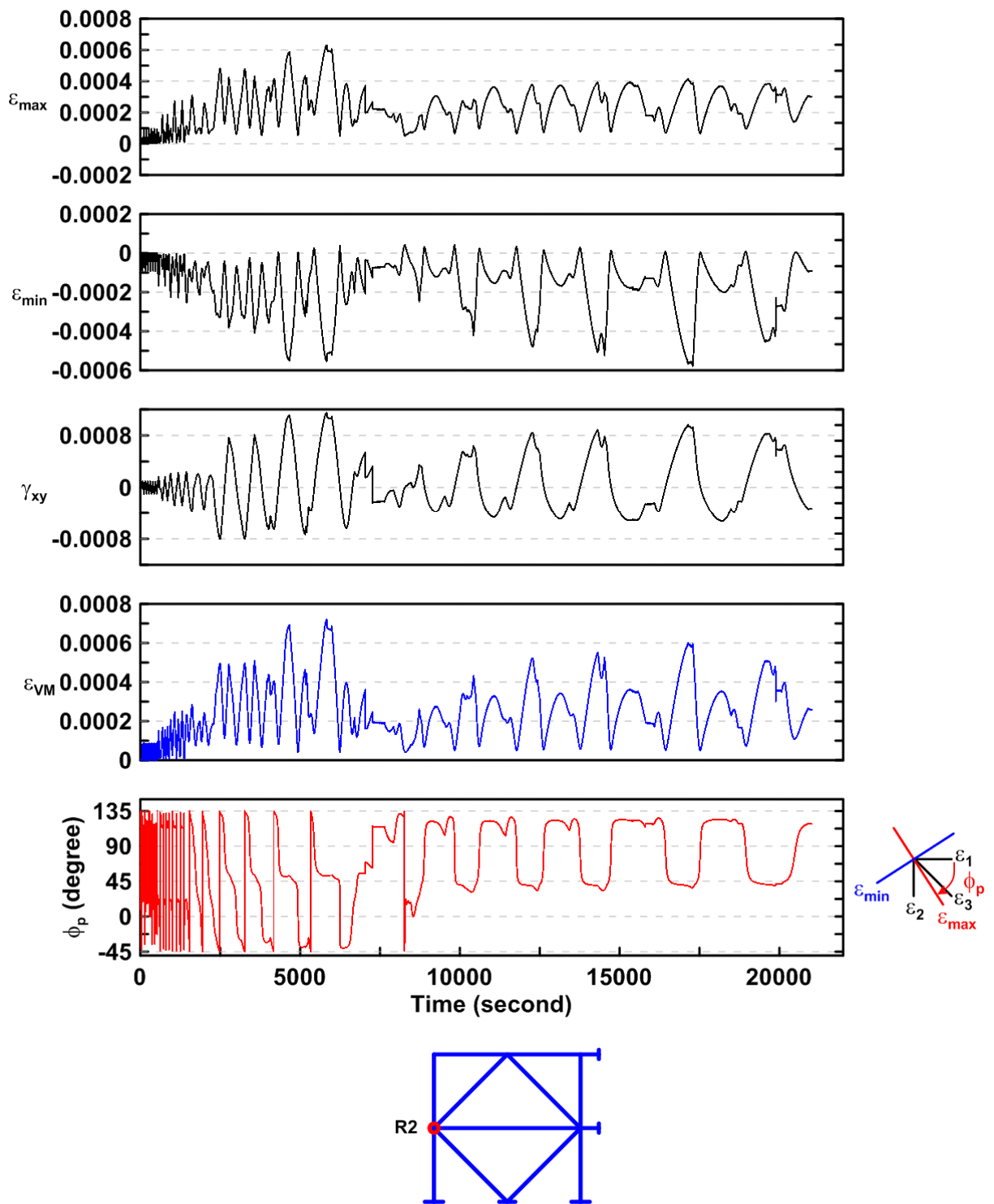


Figure 4.184 Specimen TCBF-B-2, lower panel zone: time history of rosette-type strain gauge readings (location: R2).

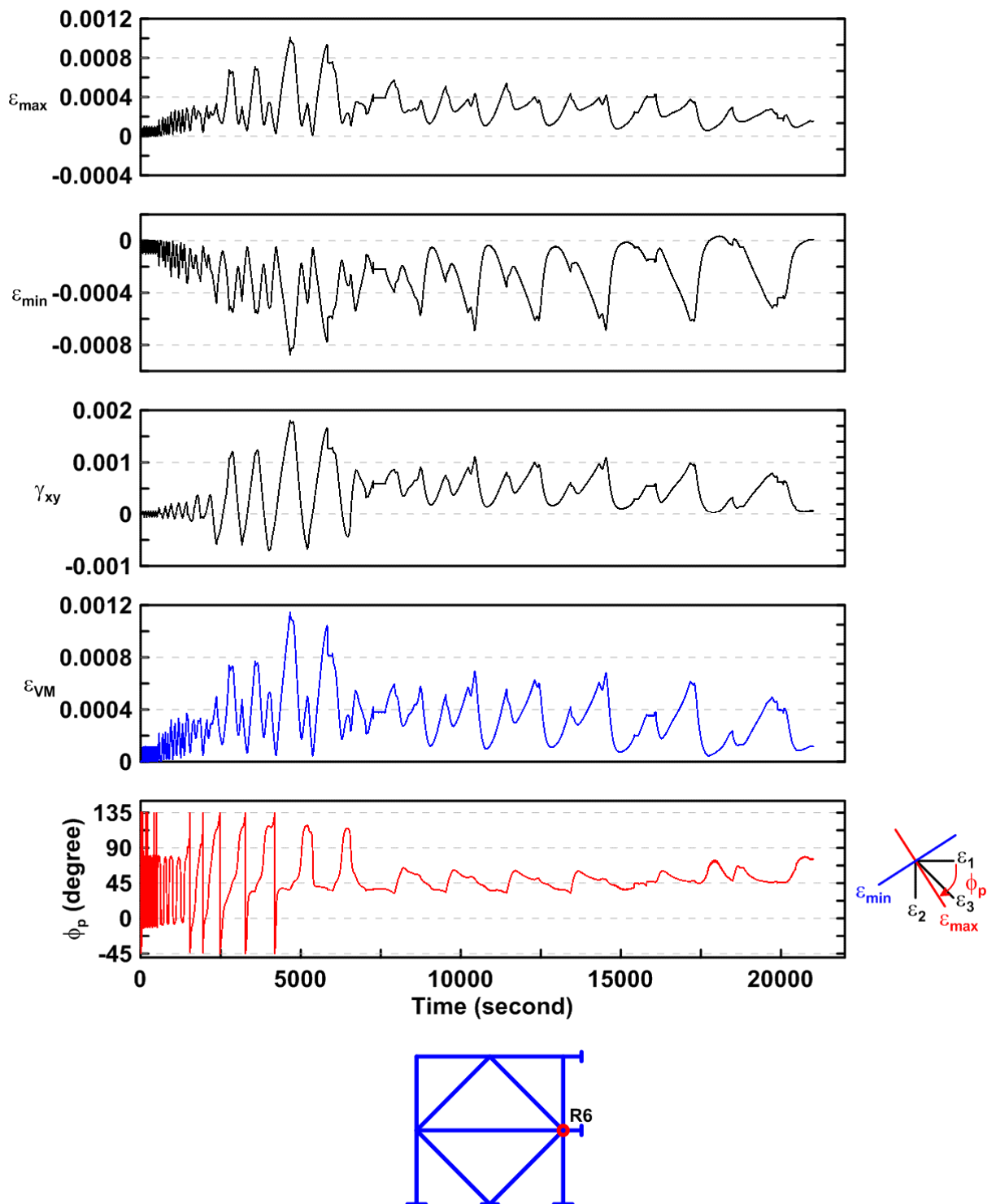


Figure 4.185 Specimen TCBF-B-2, lower panel zone: time history of rosette-type strain gauge readings (location: R6).

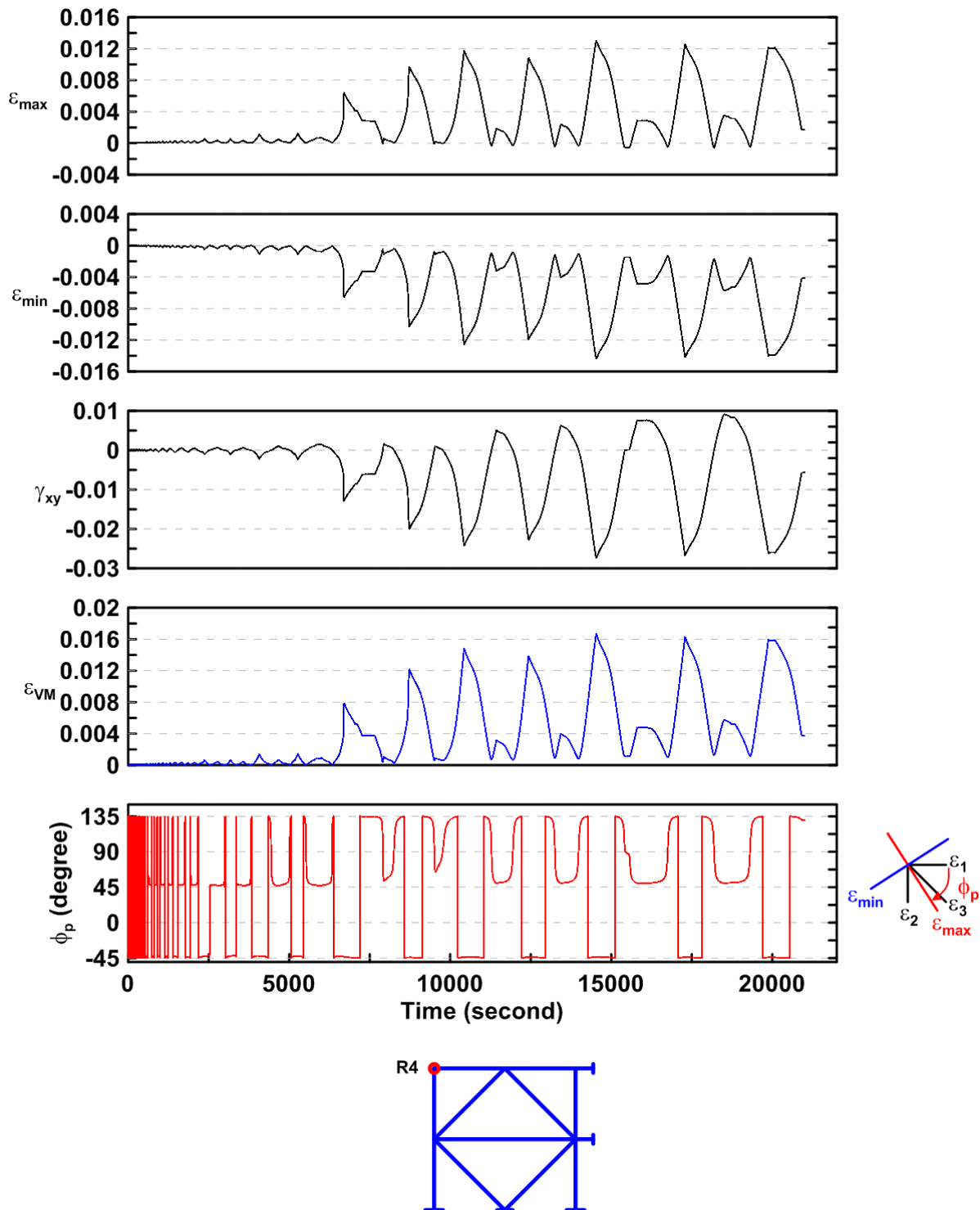


Figure 4.186 Specimen TCBF-B-2, roof panel zone: time history of rosette-type strain gauge readings (location: R4).

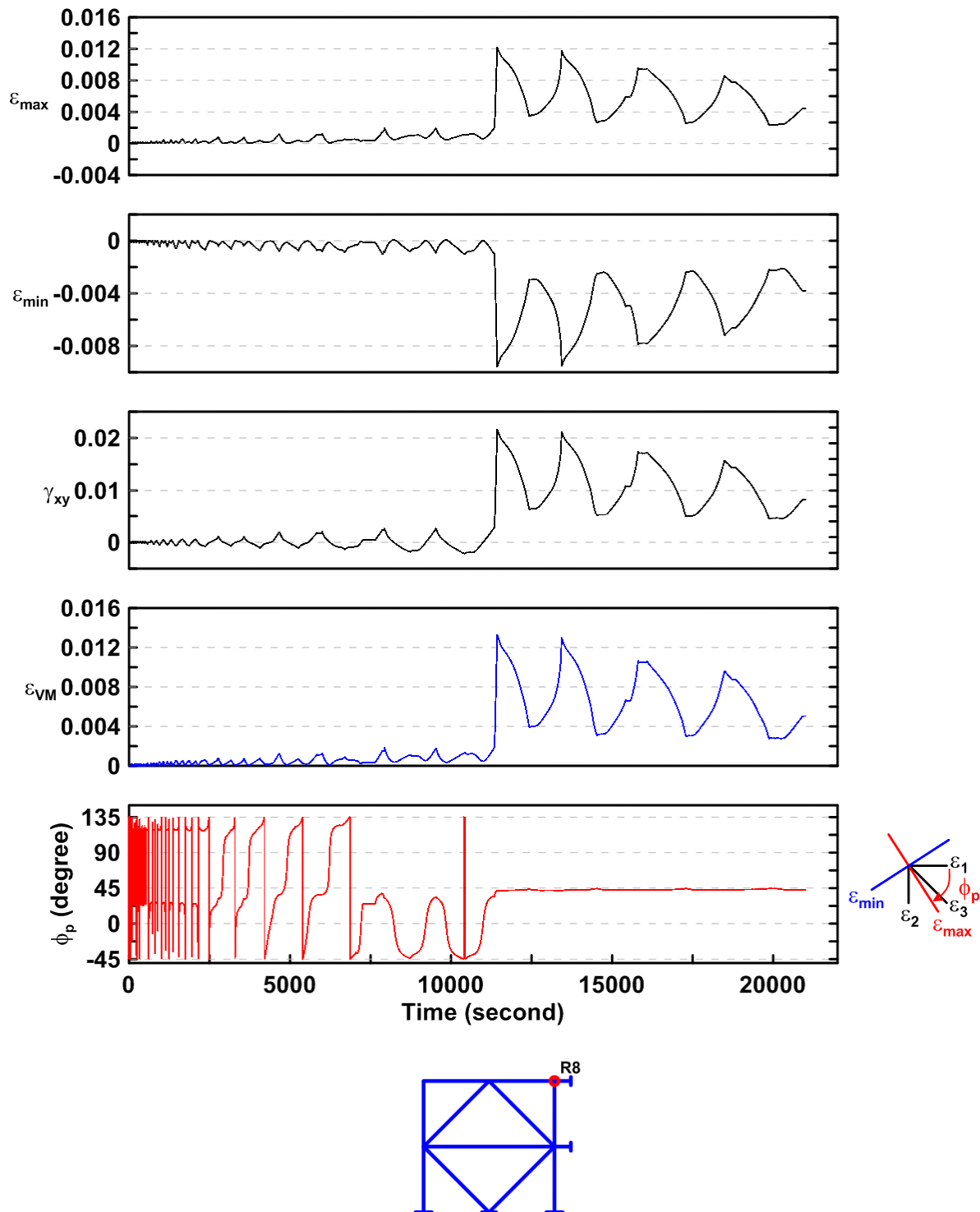


Figure 4.187 Specimen TCBF-B-2, roof panel zone: time history of rosette-type strain gauge readings (location: R8).

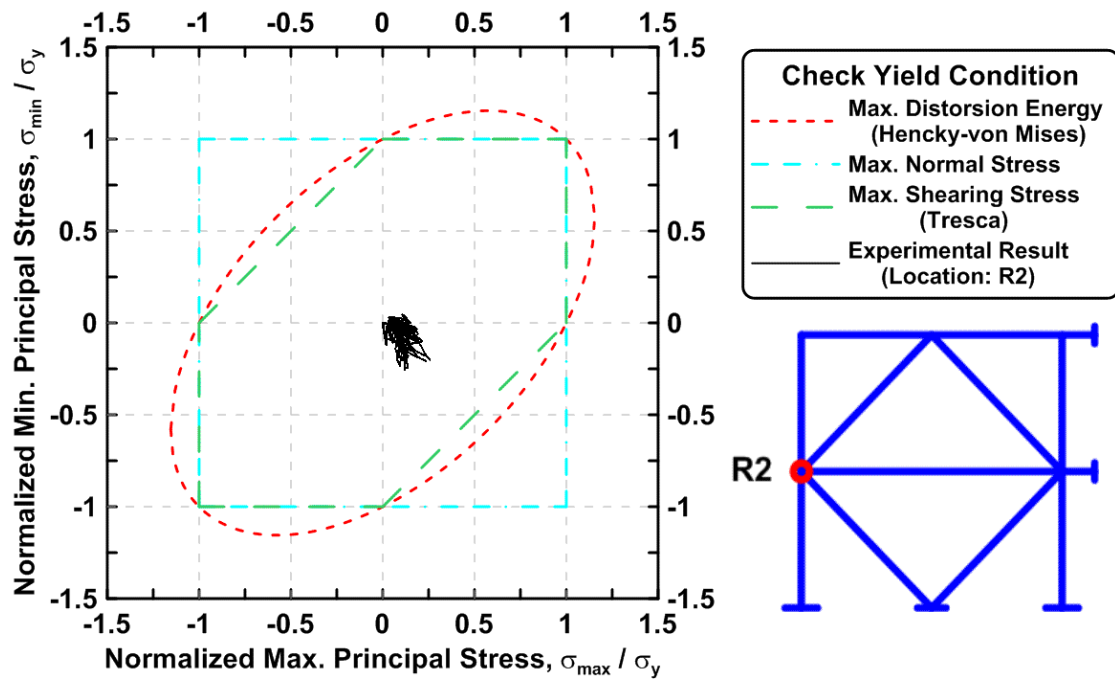


Figure 4.188 Specimen TCBF-B-2, lower panel zone: normalized maximum principal stress versus normalized minimum principal stress (location: R2).

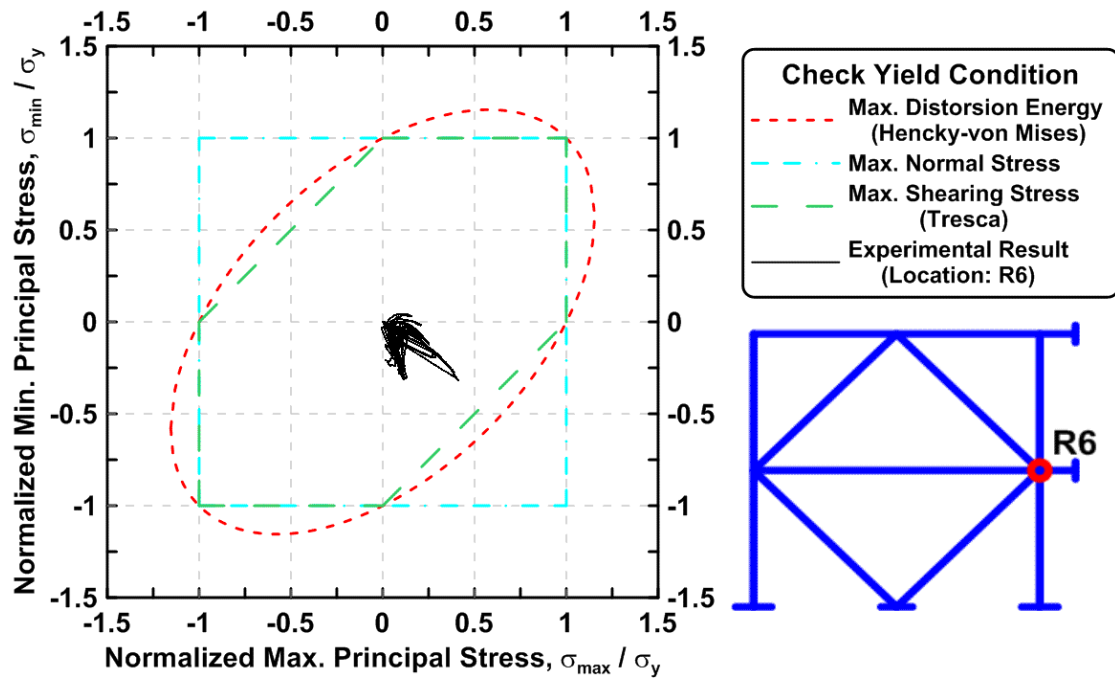


Figure 4.189 Specimen TCBF-B-2, lower panel zone: normalized maximum principal stress versus normalized minimum principal stress (location: R6).

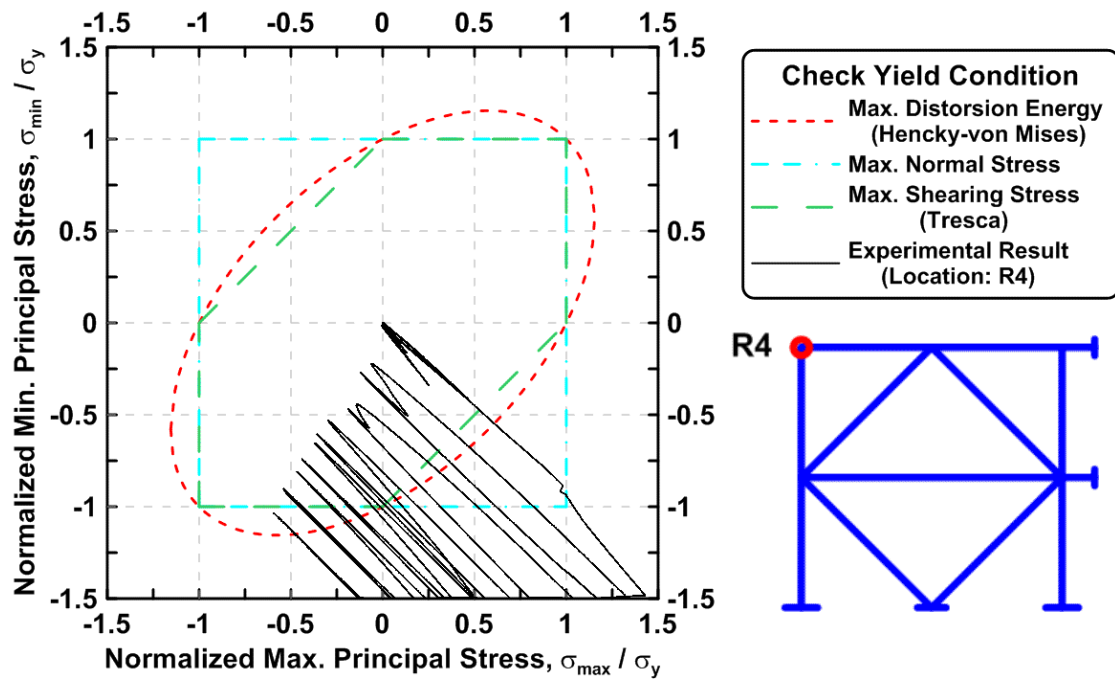


Figure 4.190 Specimen TCBF-B-2, roof panel zone: normalized maximum principal stress versus normalized minimum principal stress (location: R4).

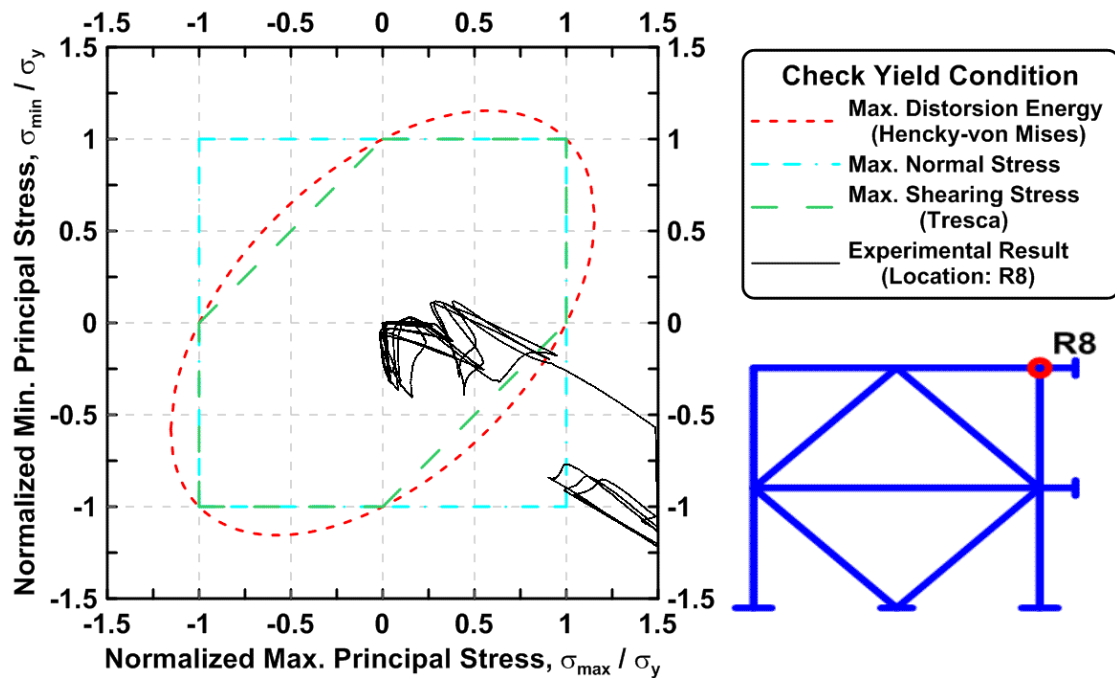


Figure 4.191 Specimen TCBF-B-2, roof panel zone: normalized maximum principal stress versus normalized minimum principal stress (location: R8).

4.1.2.2.6 Gusset Plate Response

The time history of derived rosette-type strain gauge readings in the 3/4-in.-thick one-piece gusset plate are shown in Figures 4.192 to 4.203. Normalized maximum and minimum principal stress relationships along with different yield criteria for the rosettes on the gusset plate are plotted in Figures 4.204 to 4.215. The averaged axial strain and bending strain time history in the tapered gusset plate at eastern side of the specimen are shown in Figures 4.216 and 4.217, respectively.

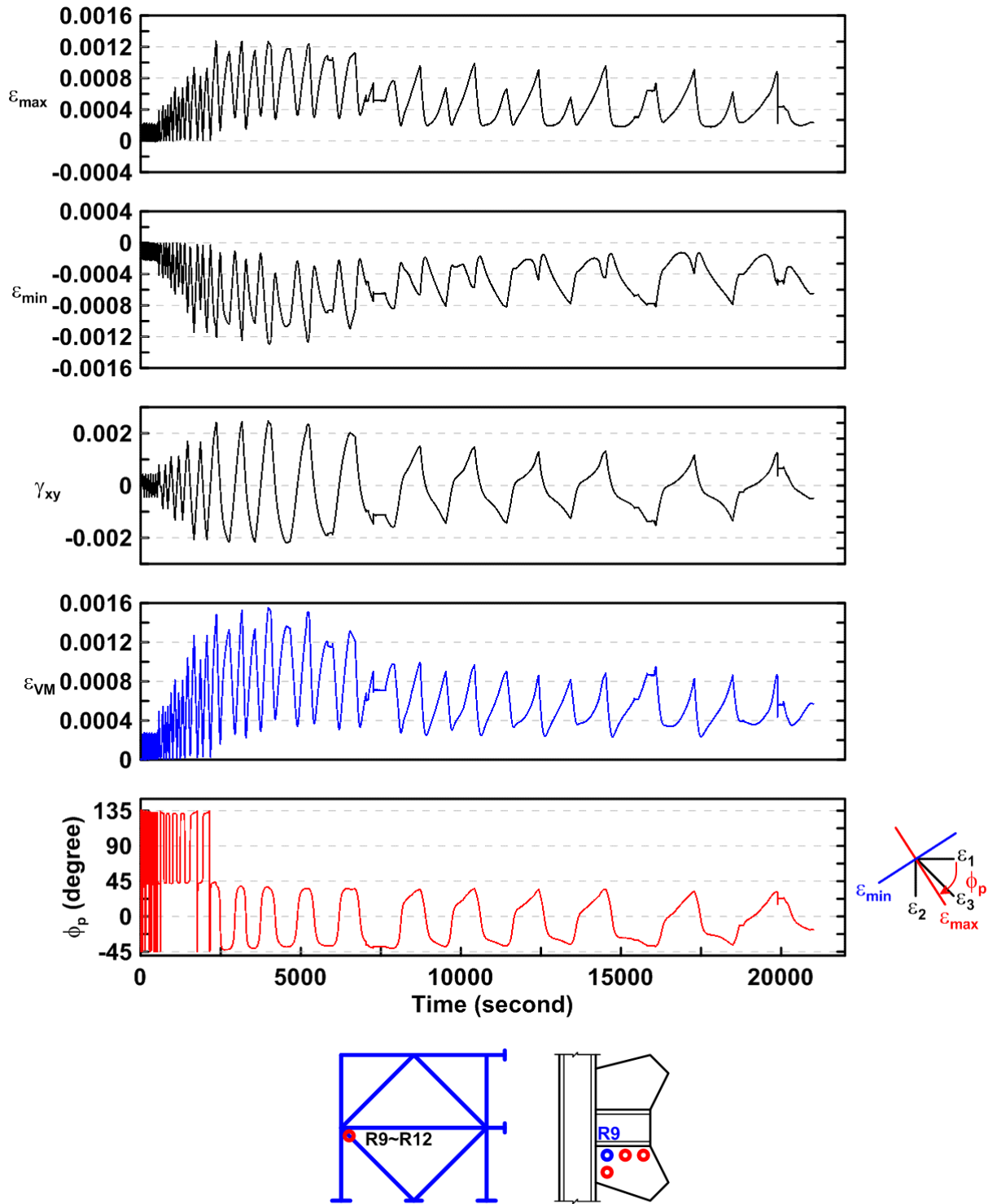


Figure 4.192 Specimen TCBF-B-2: time history of rosette-type strain gauge readings in one-piece gusset plate (location: R9).

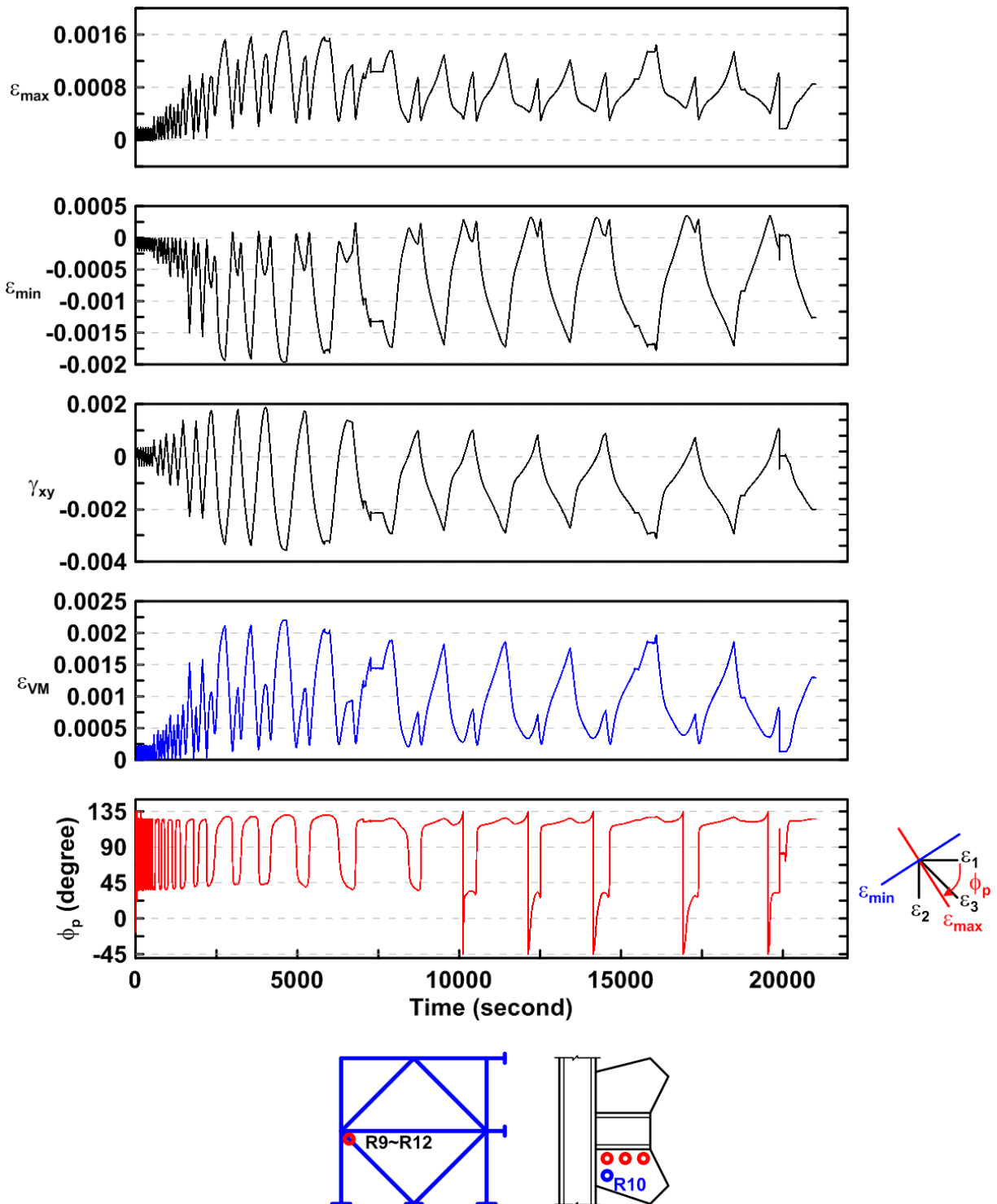


Figure 4.193 Specimen TCBF-B-2: time history of rosette-type strain gauge readings in one-piece gusset plat (location: R10).

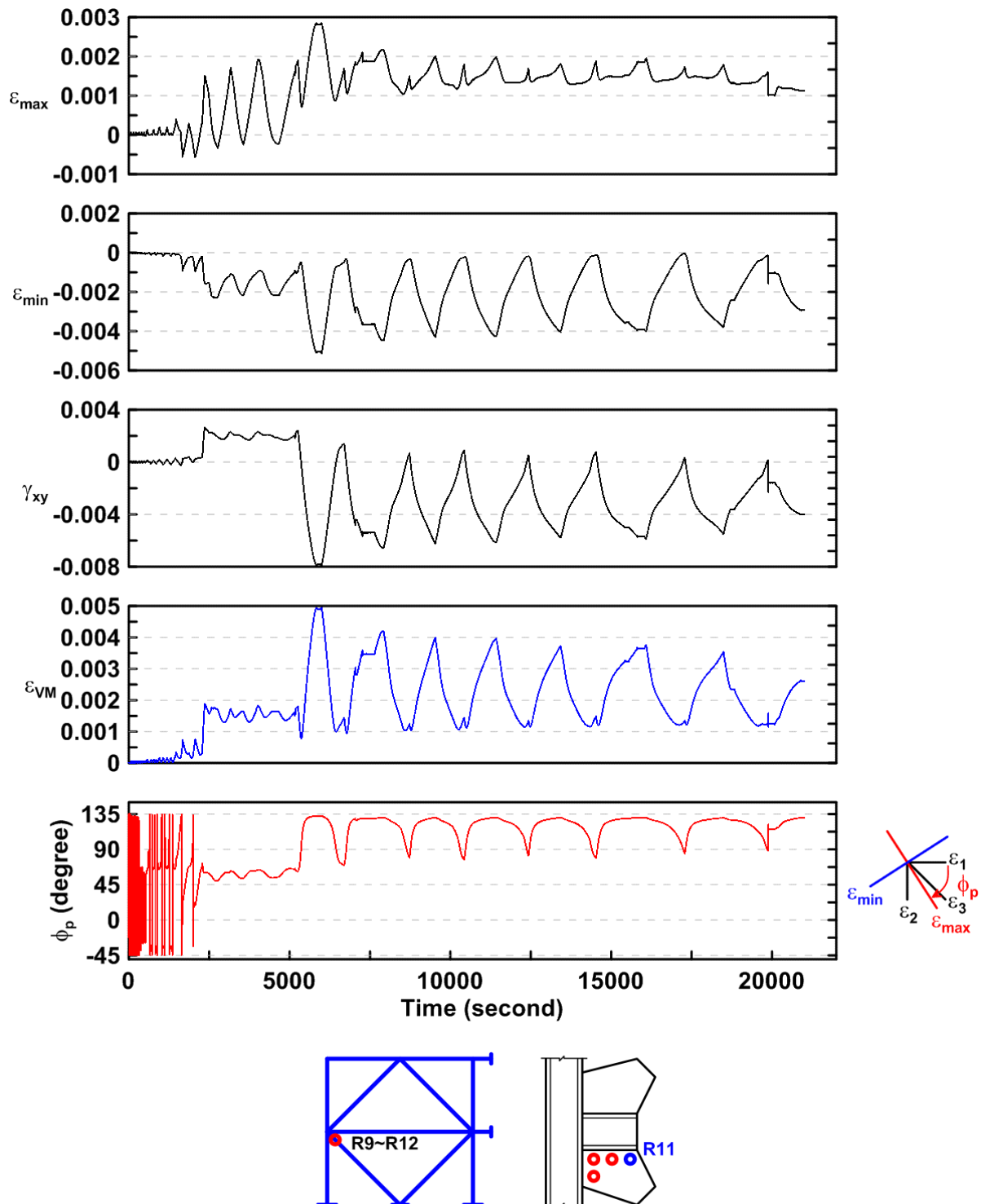


Figure 4.194 Specimen TCBF-B-2: time history of rosette-type strain gauge readings in one-piece gusset plate (location: R11).

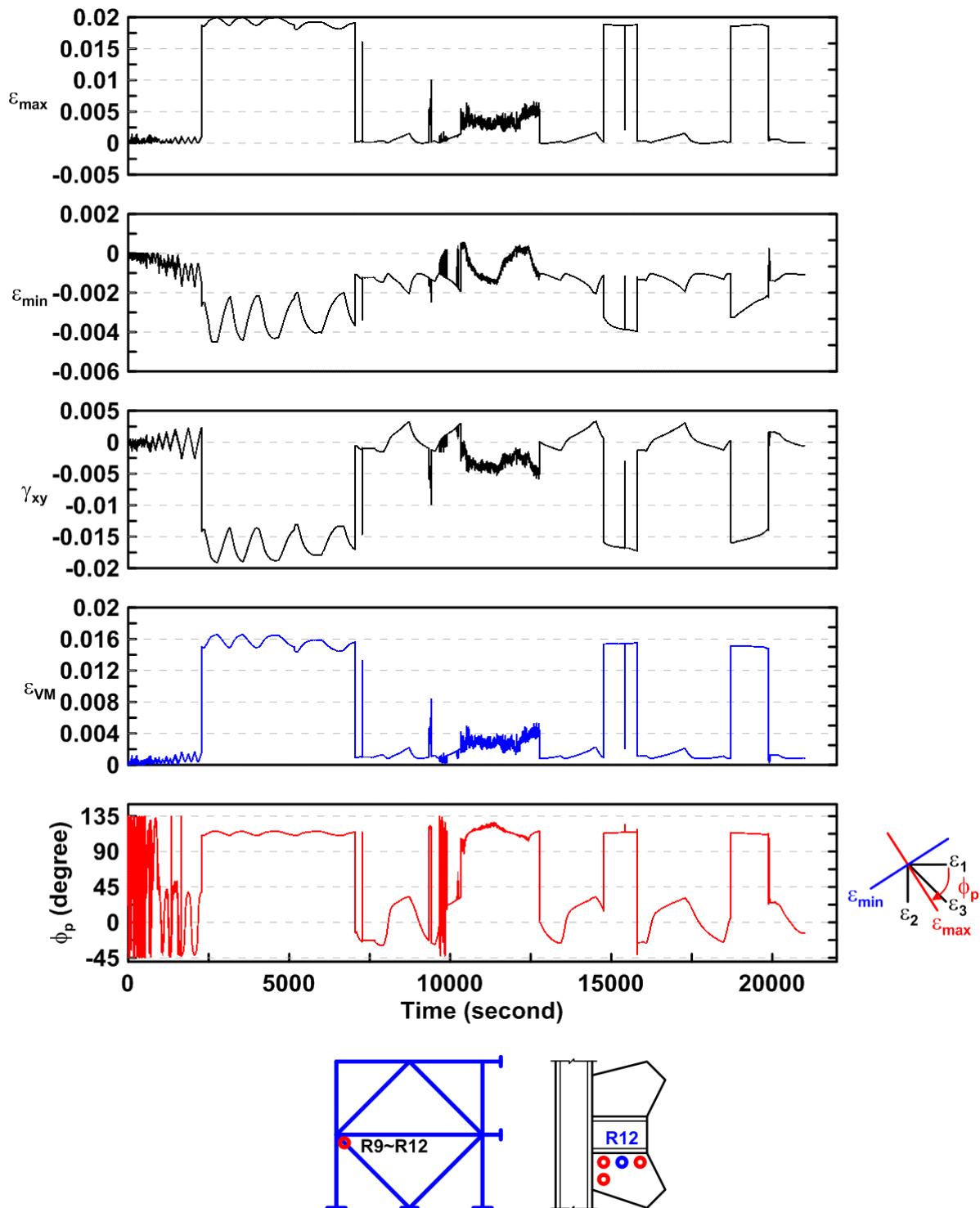


Figure 4.195 Specimen TCBF-B-2: time history of rosette-type strain gauge readings in one-piece gusset plate (location: R12).

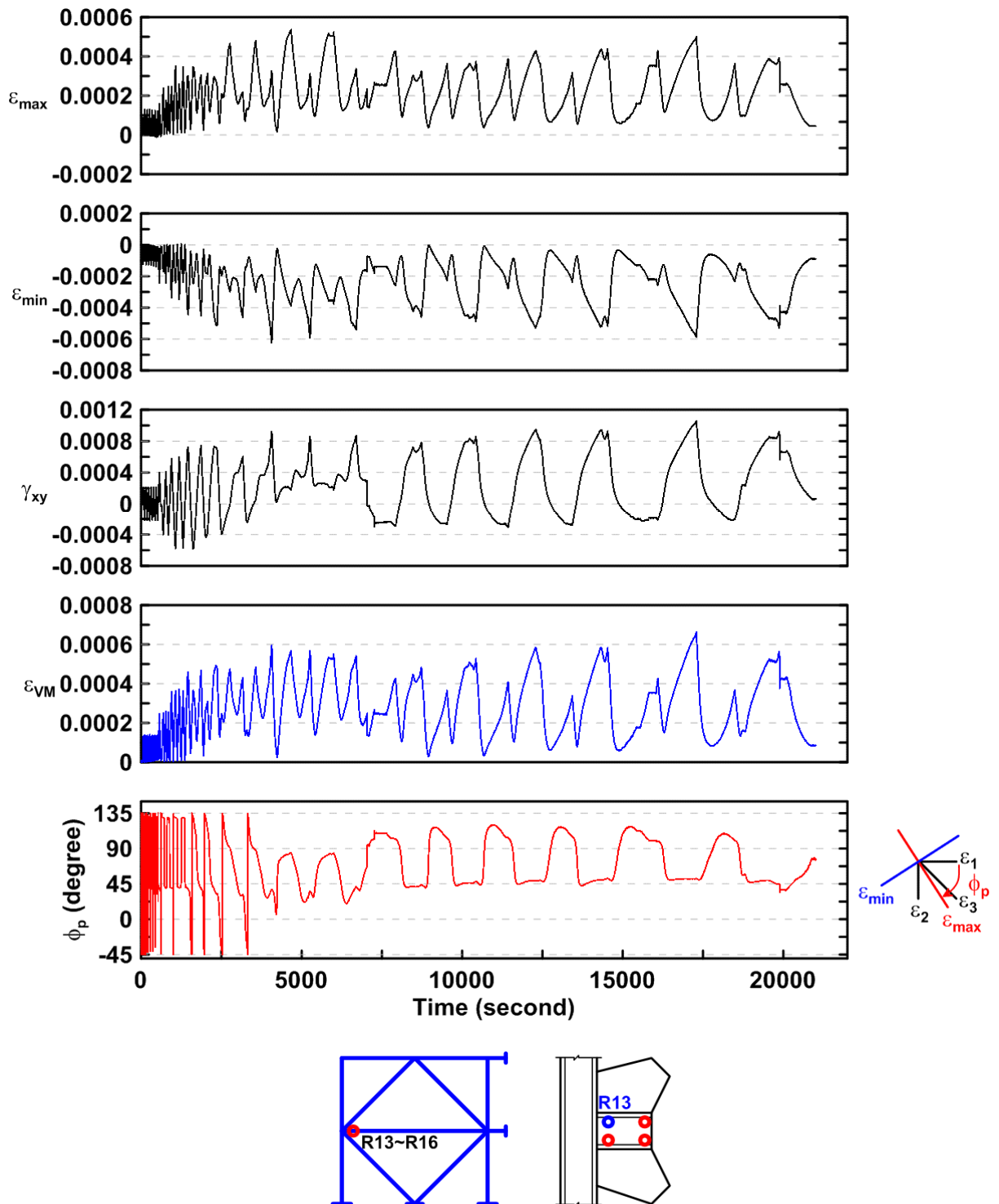


Figure 4.196 Specimen TCBF-B-2: time history of rosette-type strain gauge readings in one-piece gusset plate (location: R13).

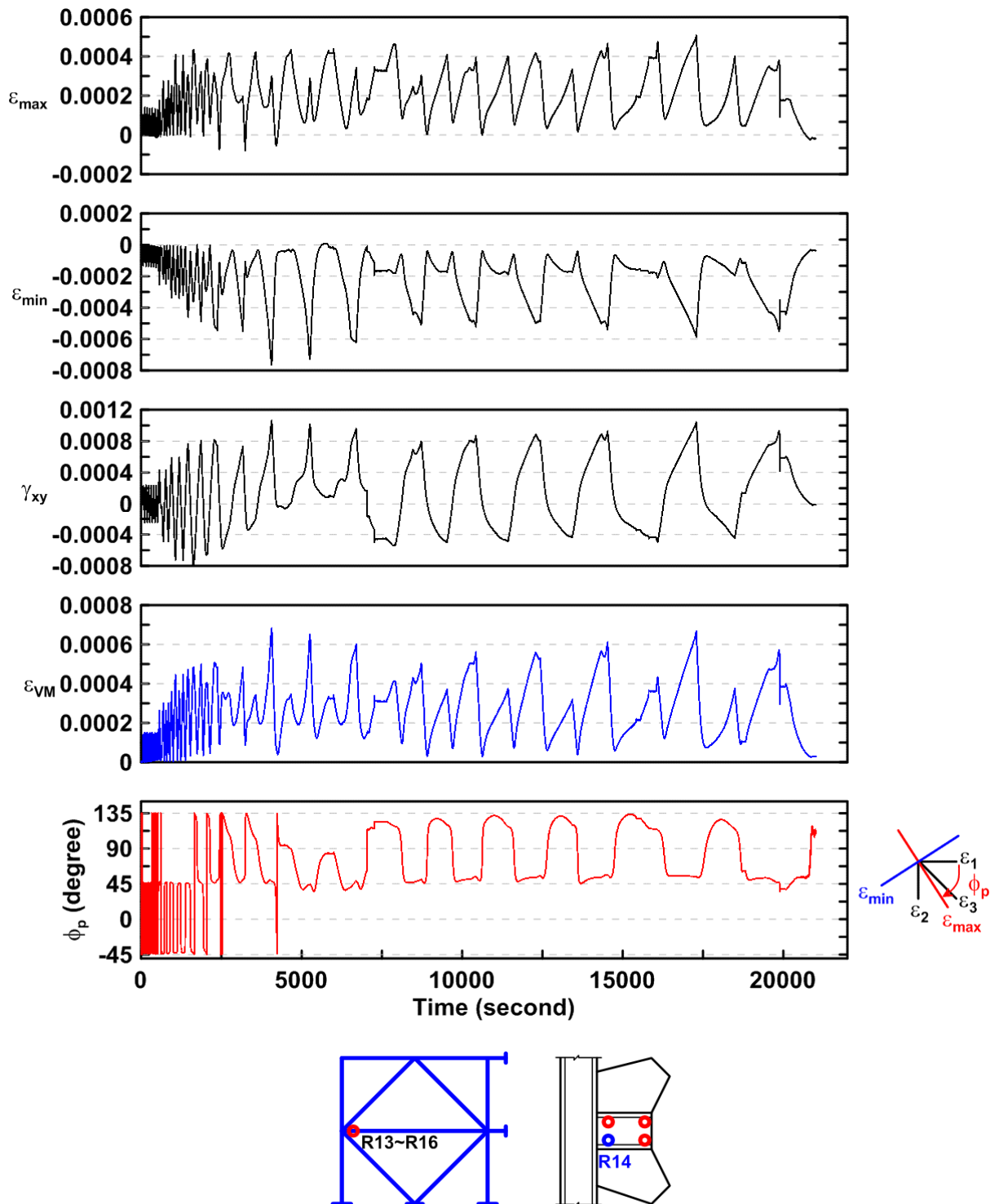


Figure 4.197 Specimen TCBF-B-2: time history of rosette-type strain gauge readings in one-piece gusset plate (location: R14).

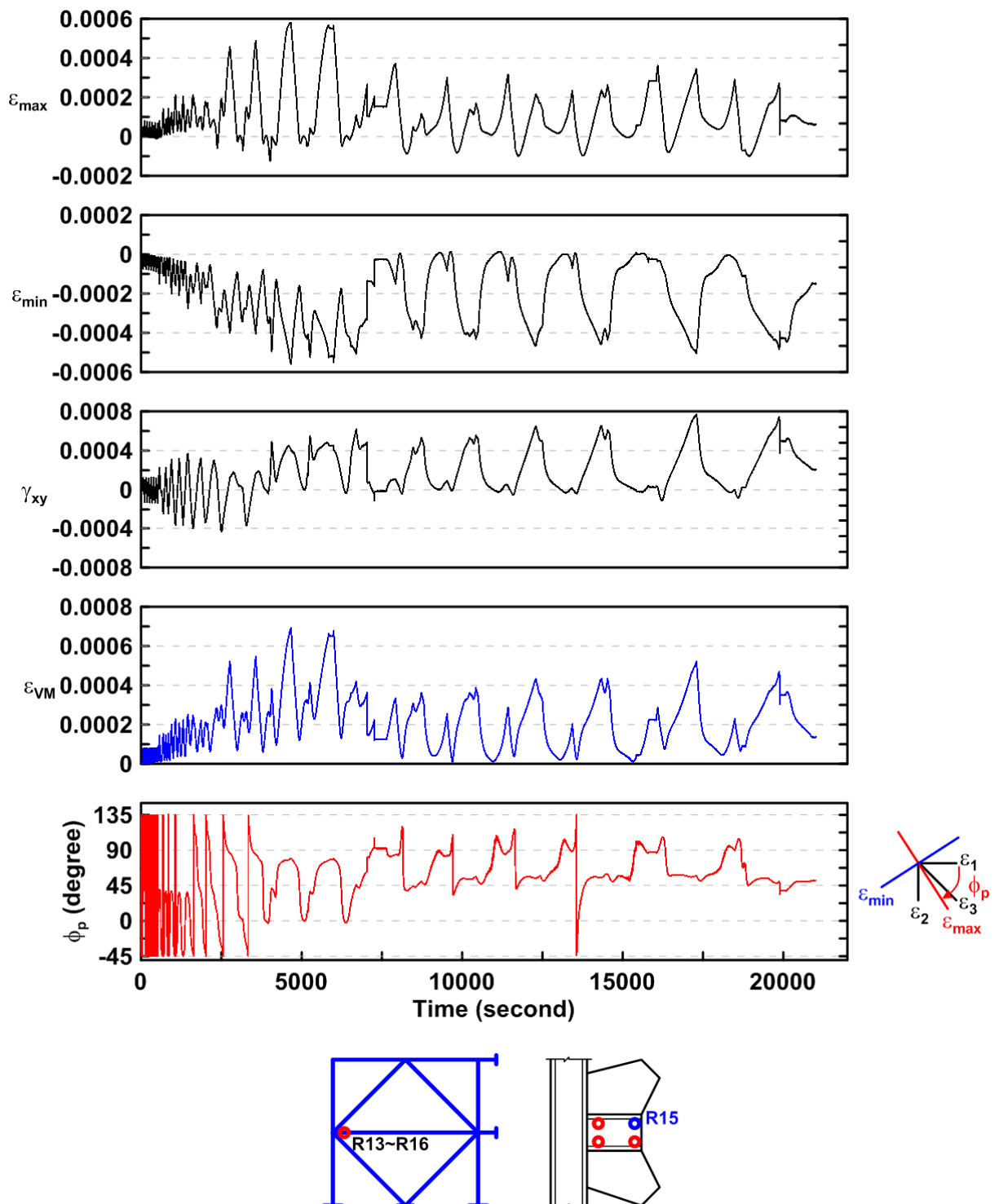


Figure 4.198 Specimen TCBF-B-2: time history of rosette-type strain gauge readings in one-piece gusset plate (location: R15).

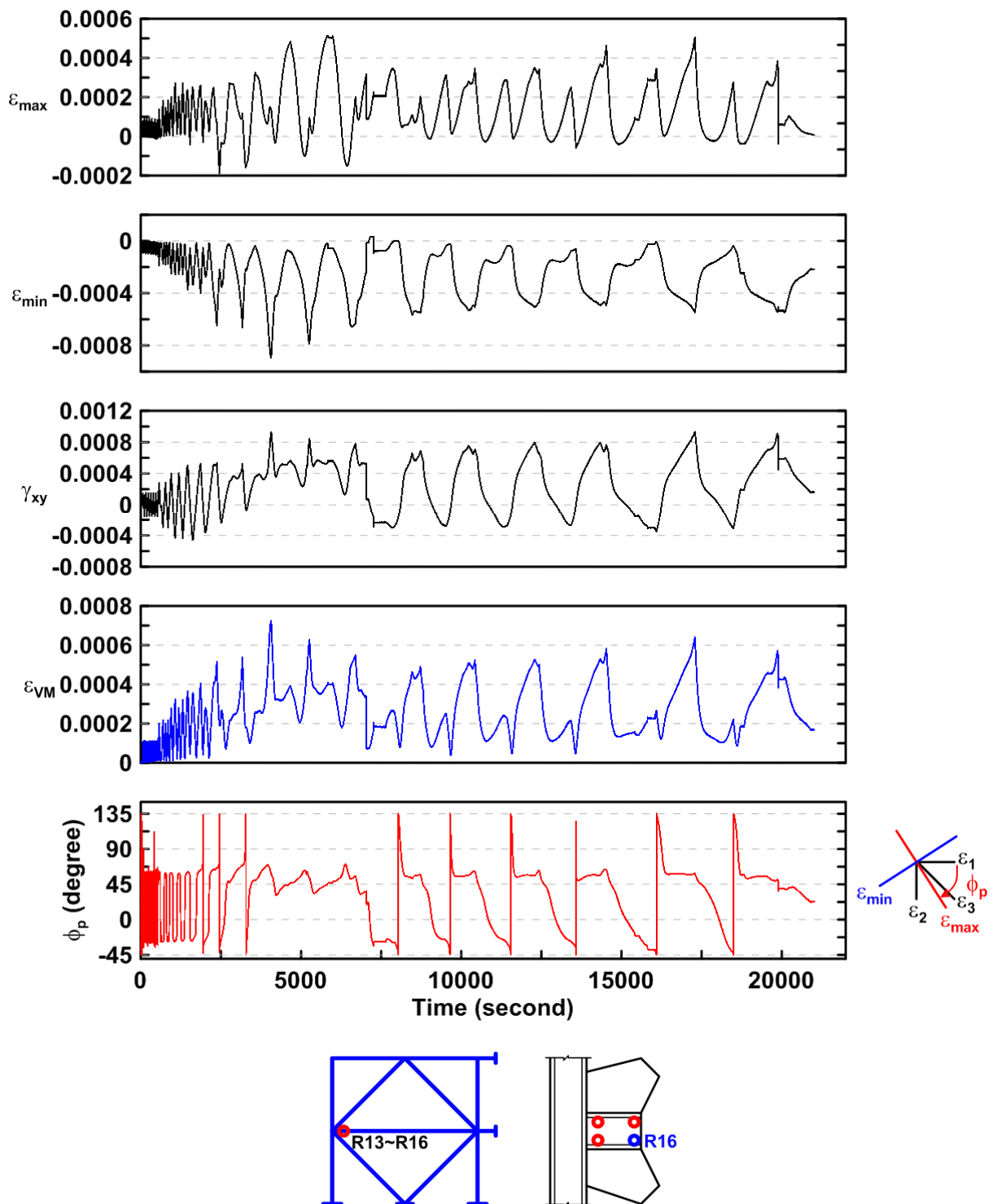


Figure 4.199 Specimen TCBF-B-2: time history of rosette-type strain gauge readings in one-piece gusset plate (location: R16).

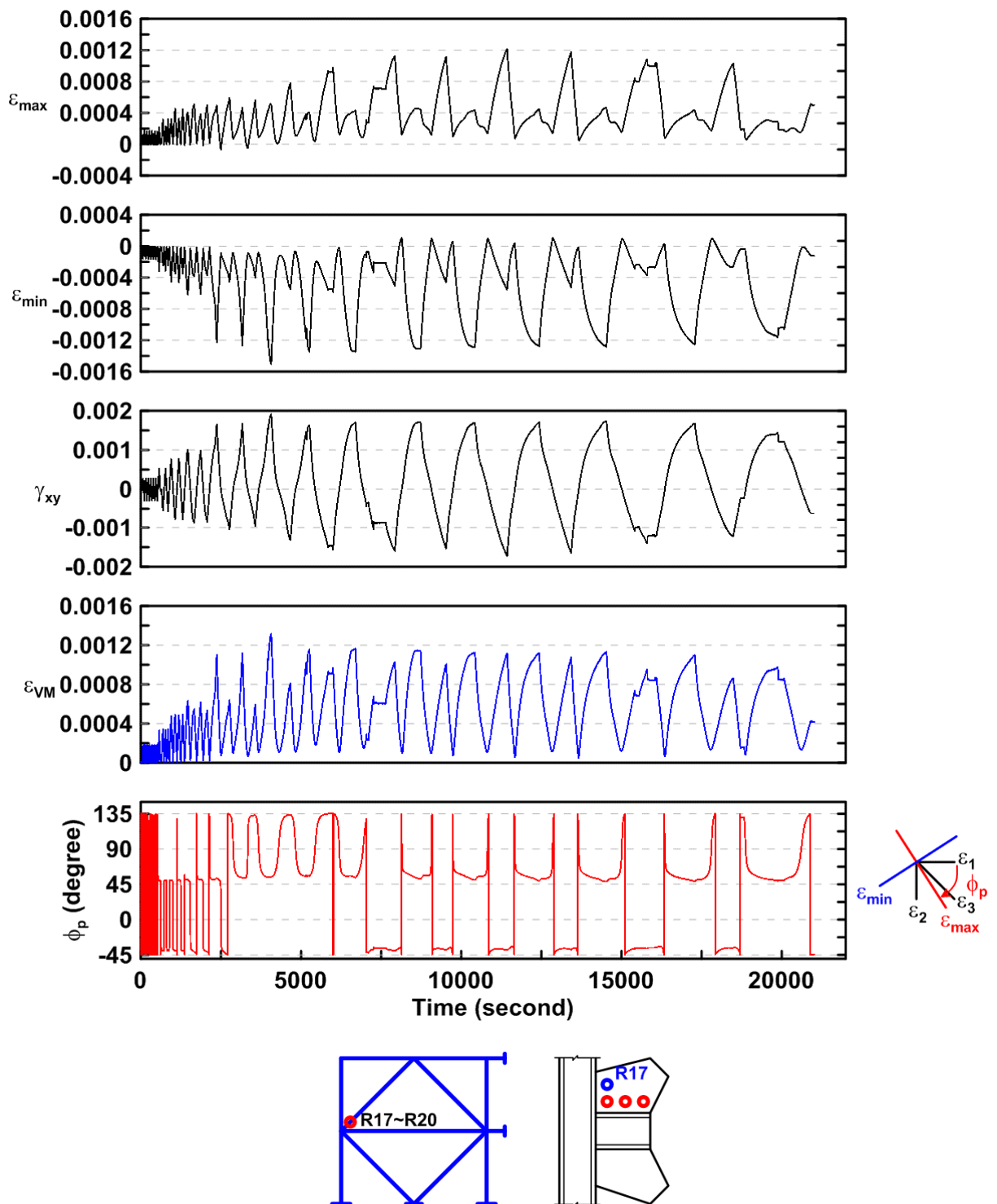


Figure 4.200 Specimen TCBF-B-2: time history of rosette-type strain gauge readings in one-piece gusset plate (location: R17).

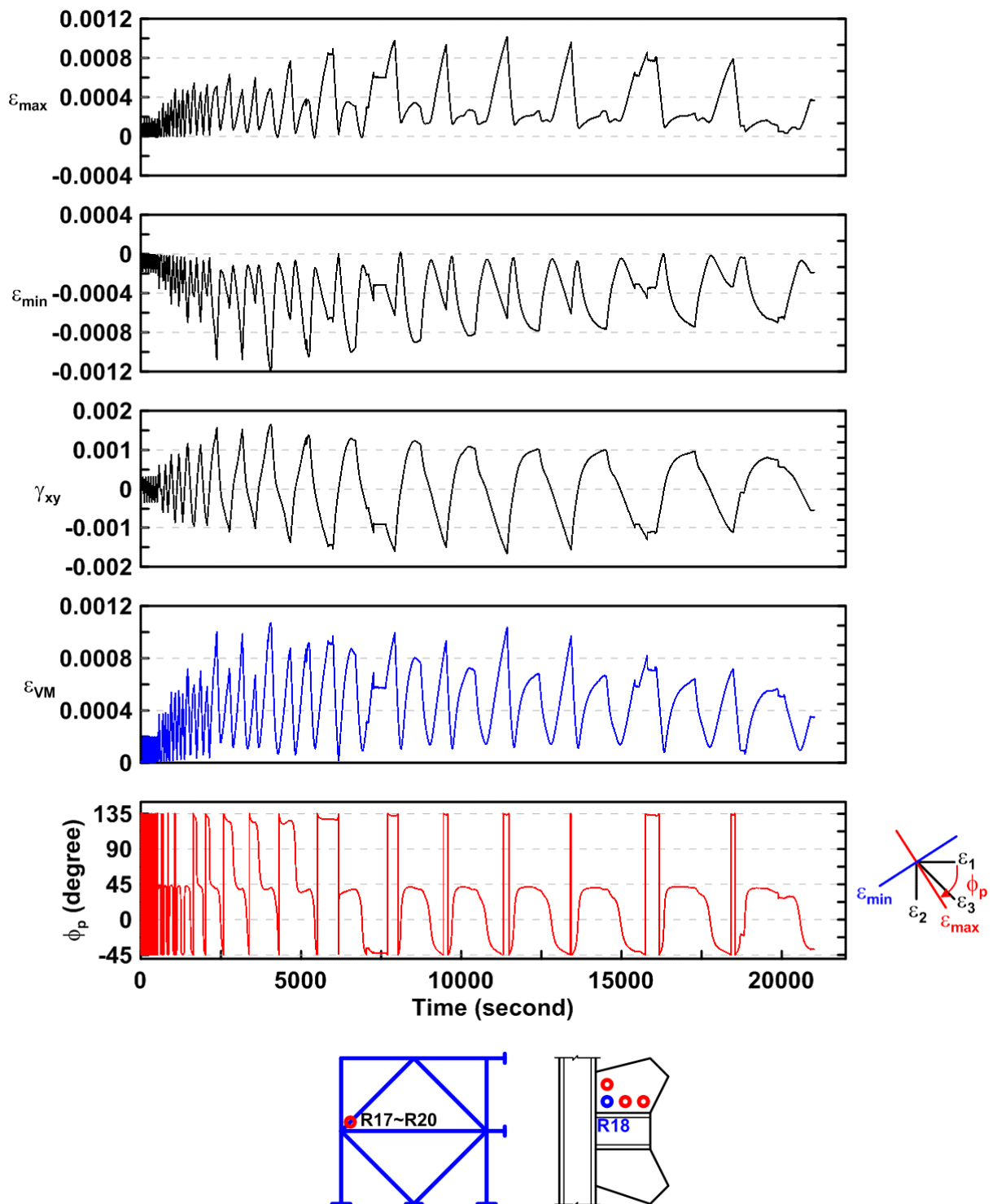


Figure 4.201 Specimen TCBF-B-2: time history of rosette-type strain gauge readings in one-piece gusset plate (location: R18).

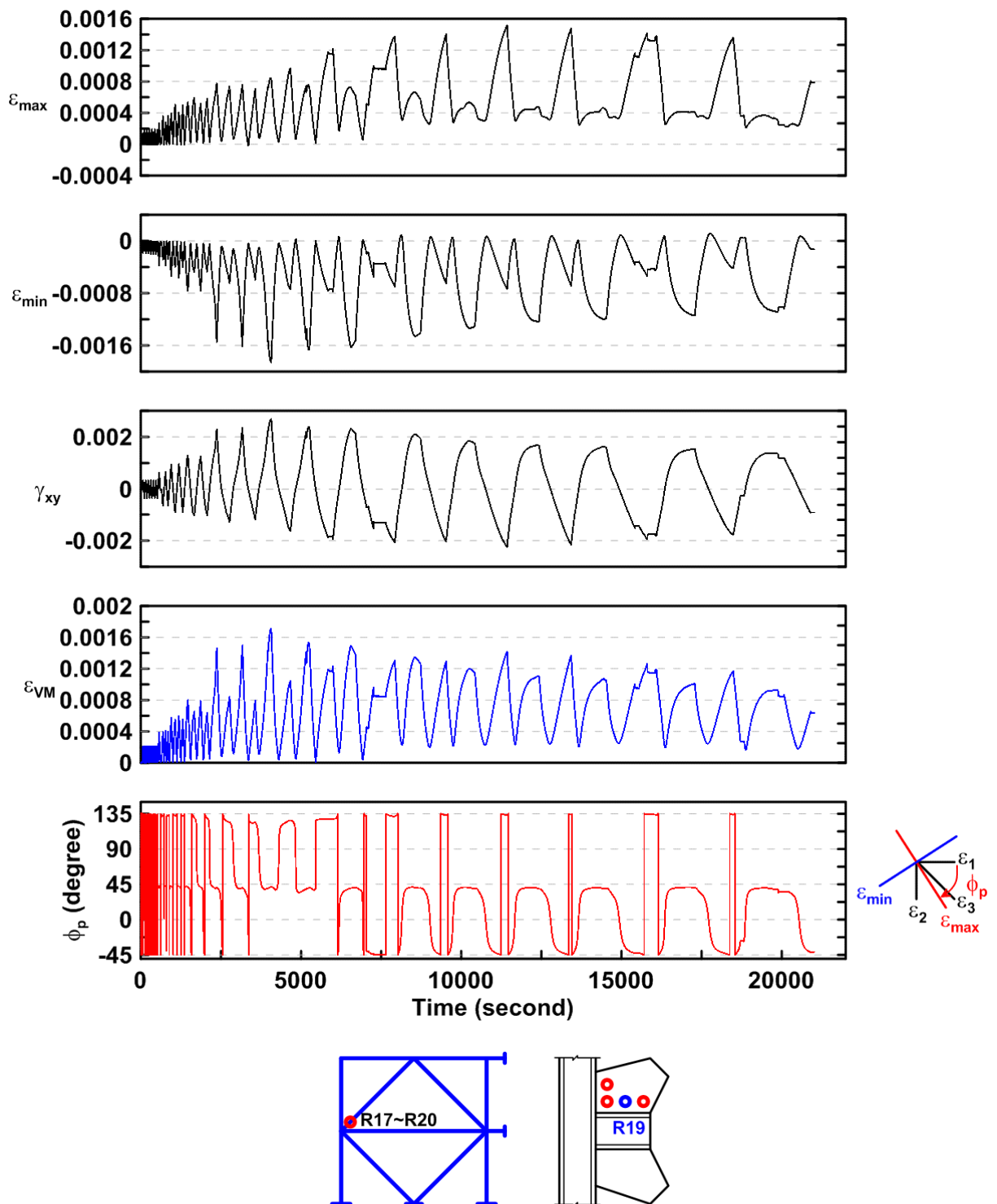


Figure 4.202 Specimen TCBF-B-2: time history of rosette-type strain gauge readings in one-piece gusset plate (location: R19).

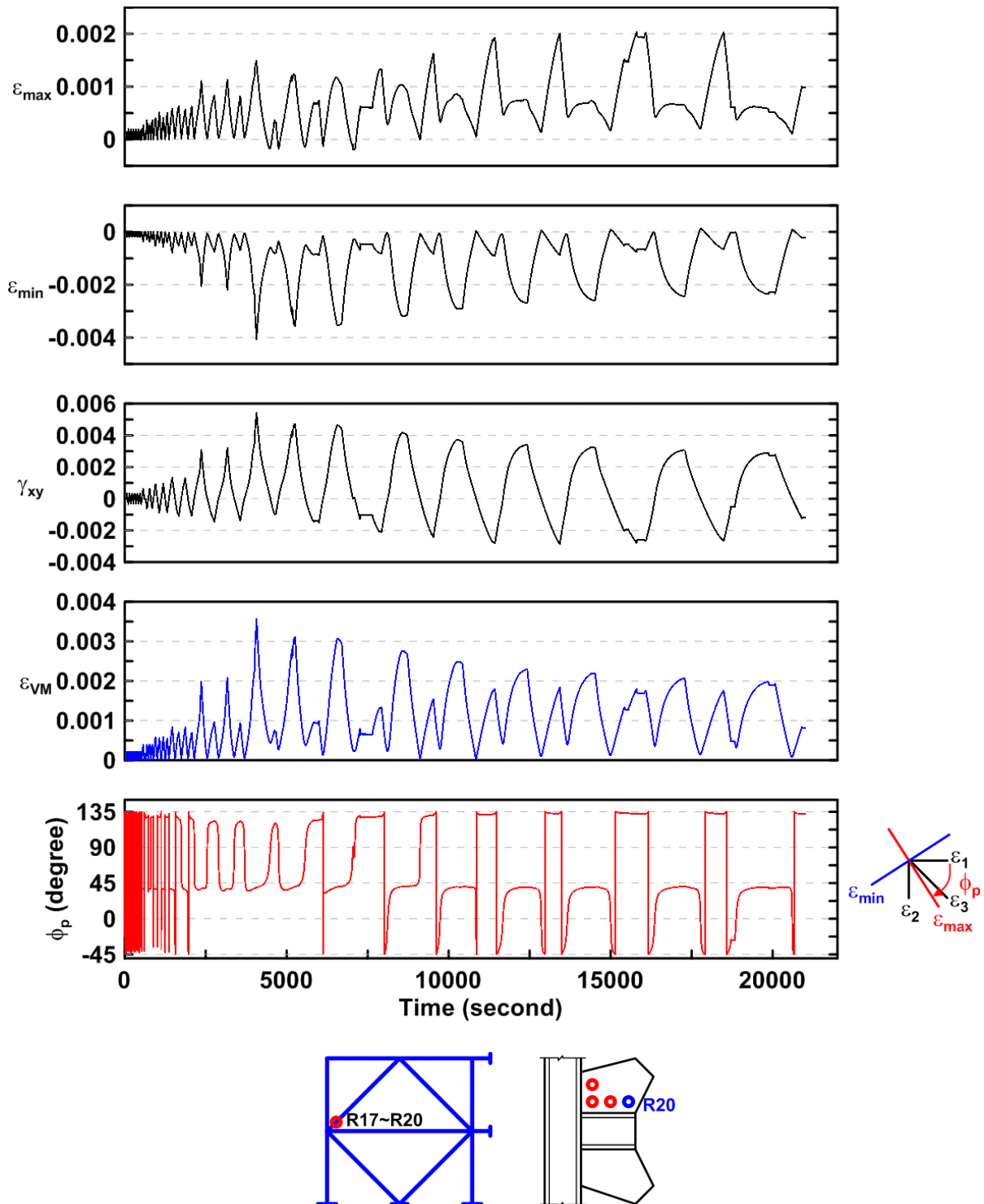


Figure 4.203 Specimen TCBF-B-2: time history of rosette-type strain gauge readings in one-piece gusset plate (location: R20).

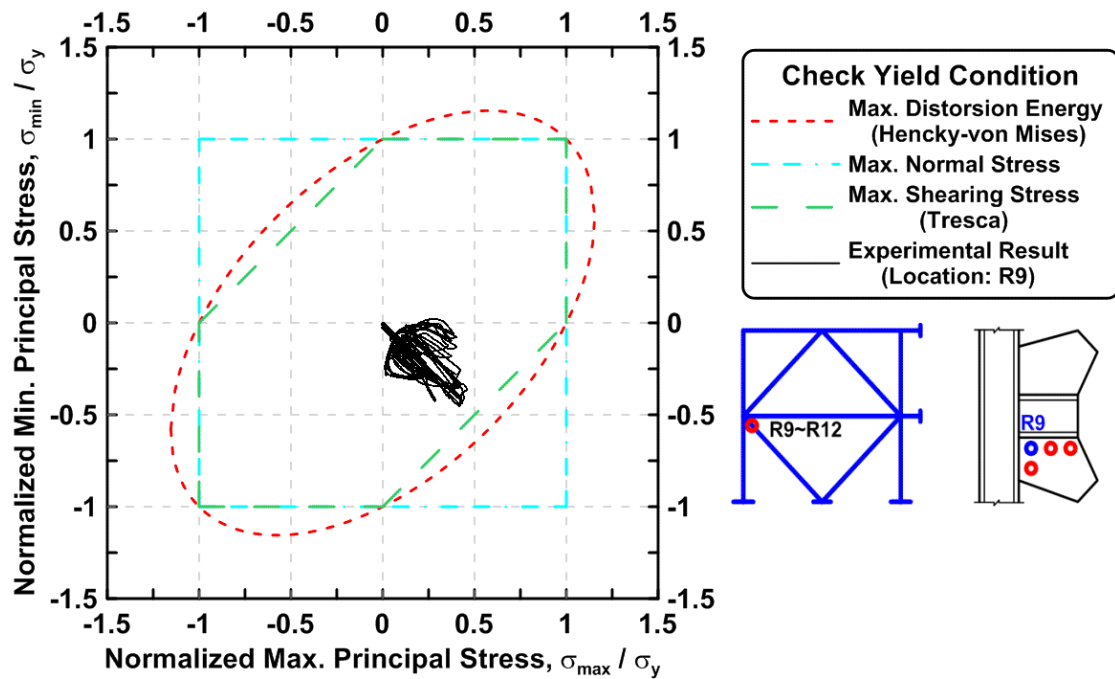


Figure 4.204 Specimen TCBF-B-2: normalized maximum principal stress versus normalized minimum principal stress in one-piece gusset plate (location: R9).

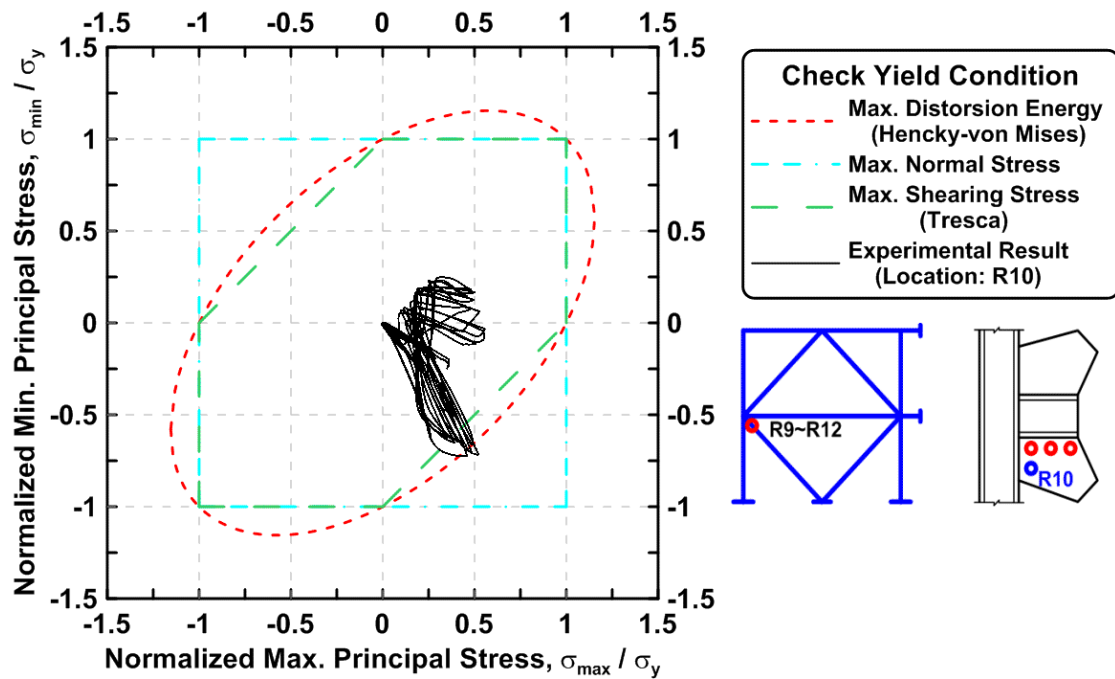


Figure 4.205 Specimen TCBF-B-2: normalized maximum principal stress versus normalized minimum principal stress in one-piece gusset plate (location: R10).

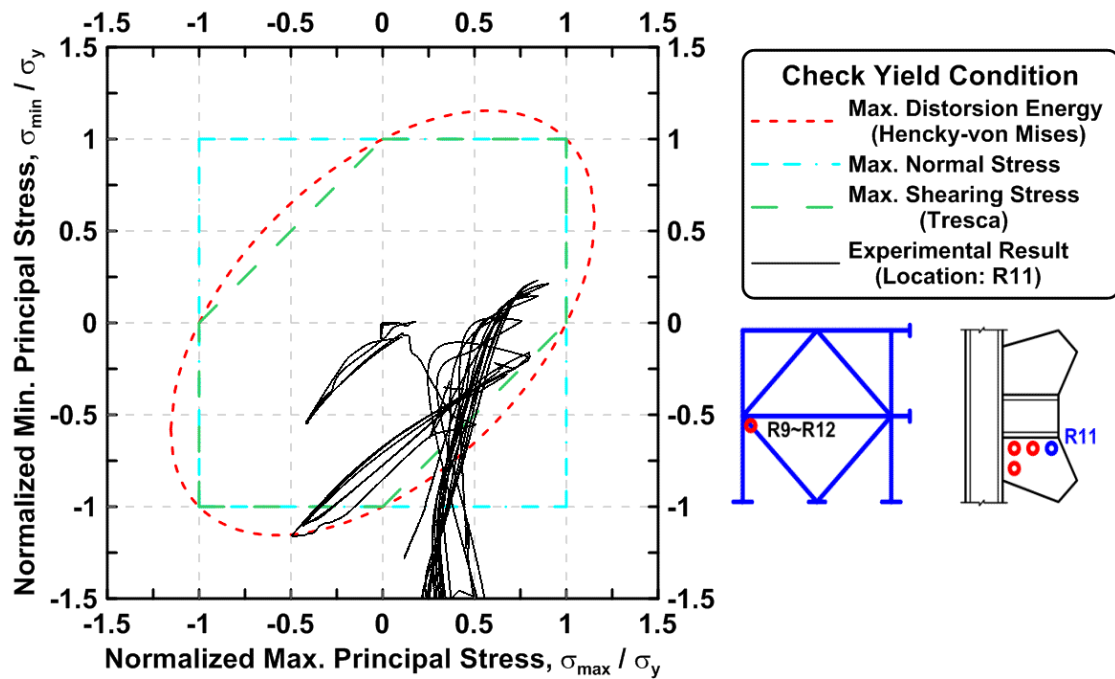


Figure 4.206 Specimen TCBF-B-2: normalized maximum principal stress versus normalized minimum principal stress in one-piece gusset plate (location: R11).

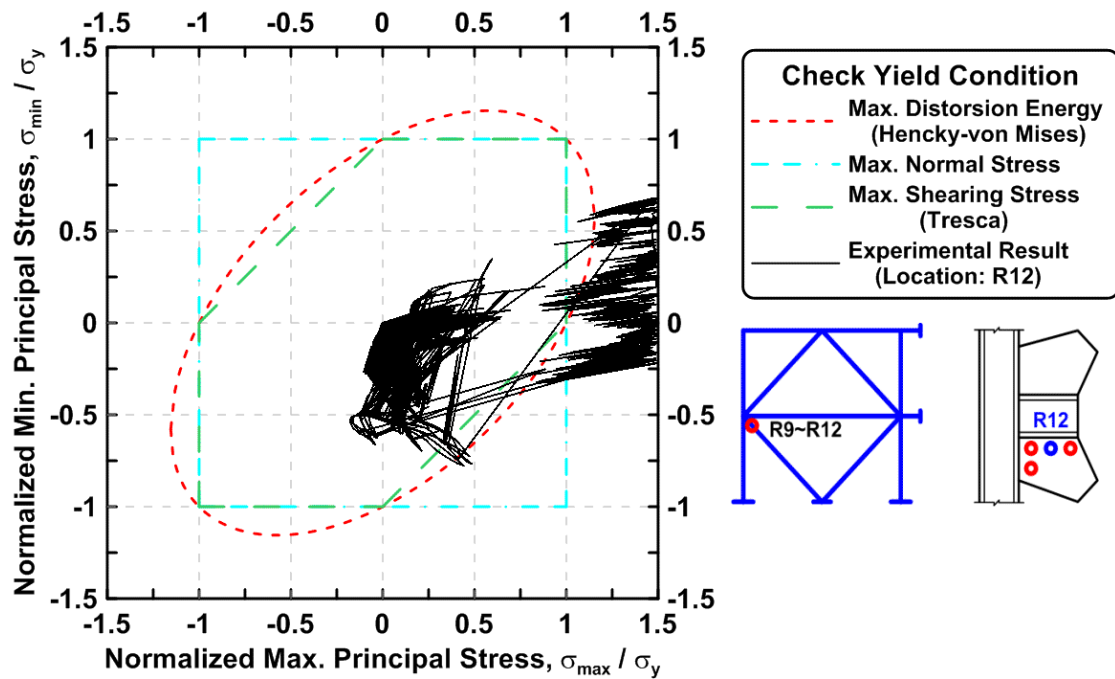


Figure 4.207 Specimen TCBF-B-2: normalized maximum principal stress versus normalized minimum principal stress in one-piece gusset plate (location: R12).

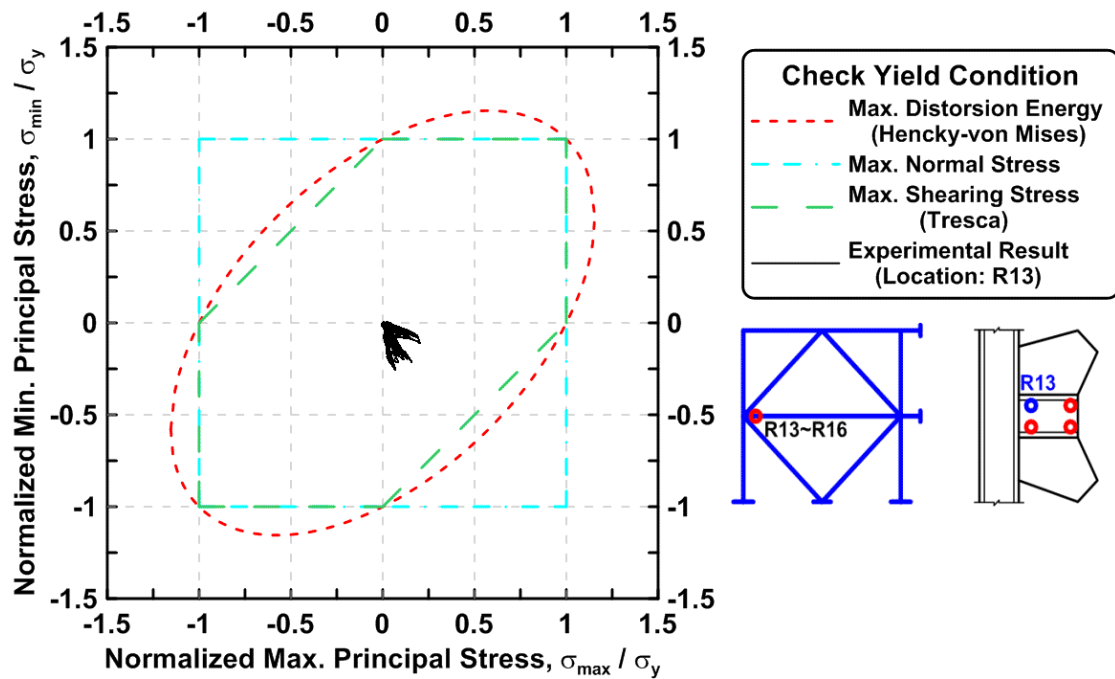


Figure 4.208 Specimen TCBF-B-2: normalized maximum principal stress versus normalized minimum principal stress in one-piece gusset plate (location: R13).

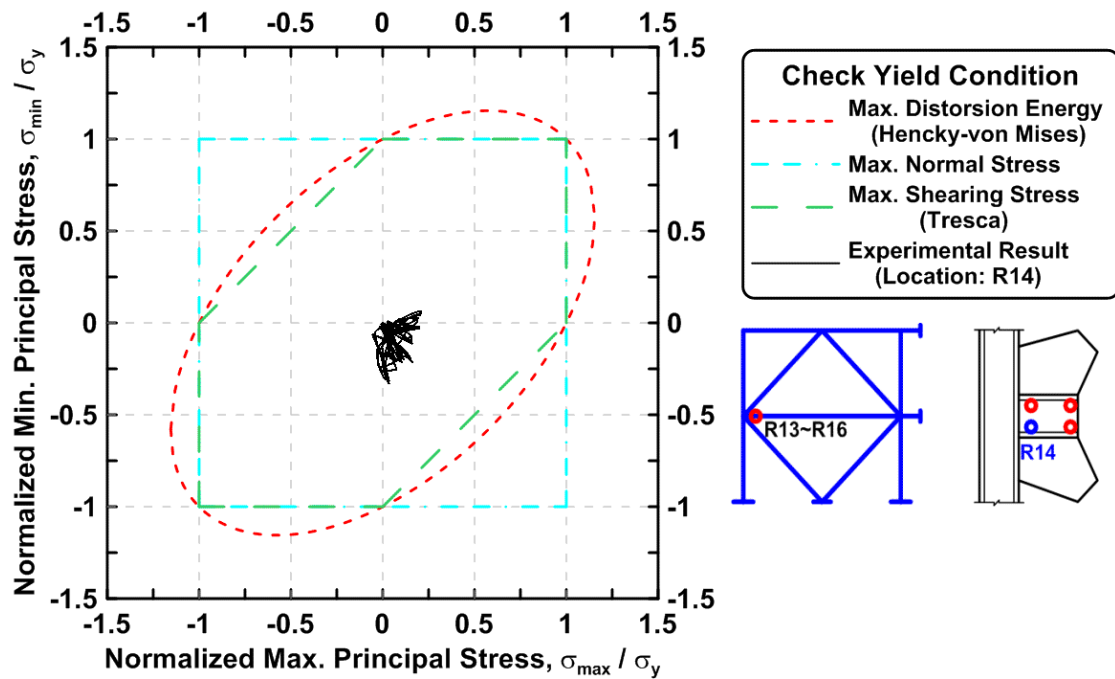


Figure 4.209 Specimen TCBF-B-2: normalized maximum principal stress versus normalized minimum principal stress in one-piece gusset plate (location: R14).

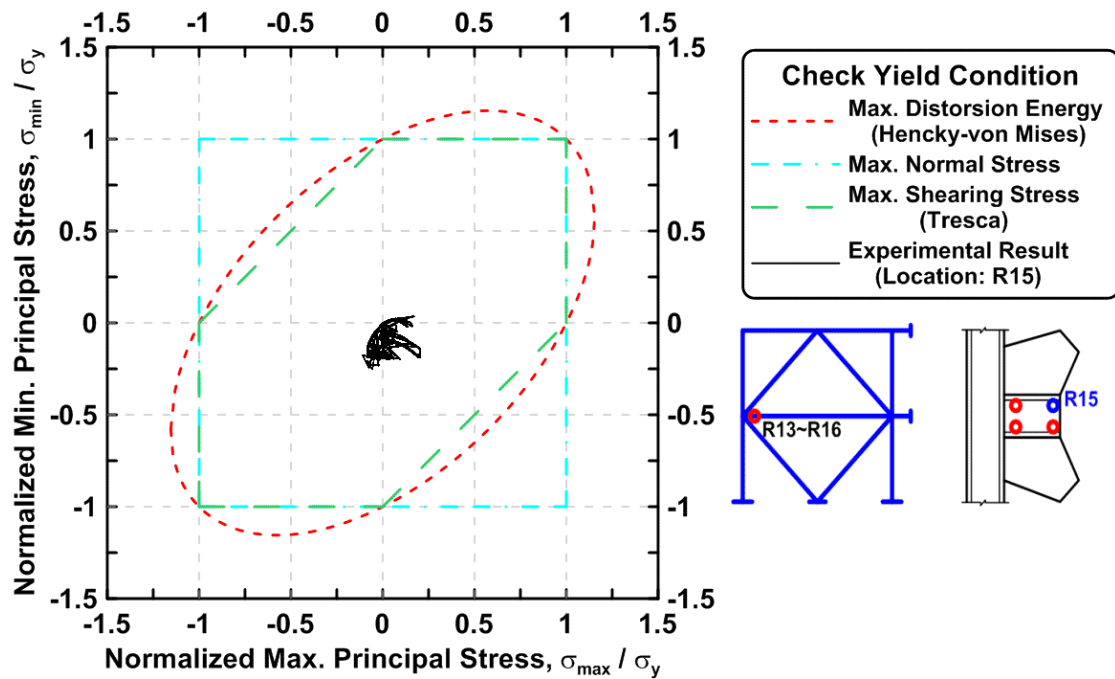


Figure 4.210 Specimen TCBF-B-2: normalized maximum principal stress versus normalized minimum principal stress in one-piece gusset plate (location: R15).

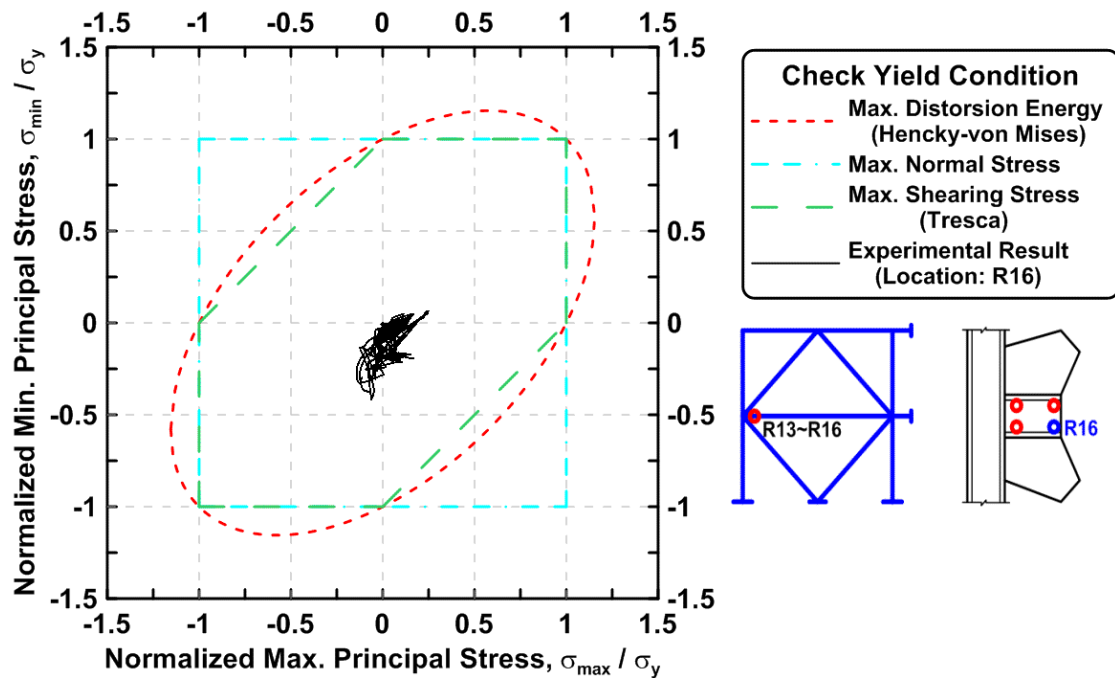


Figure 4.211 Specimen TCBF-B-2: normalized maximum principal stress versus normalized minimum principal stress in one-piece gusset plate (location: R16).

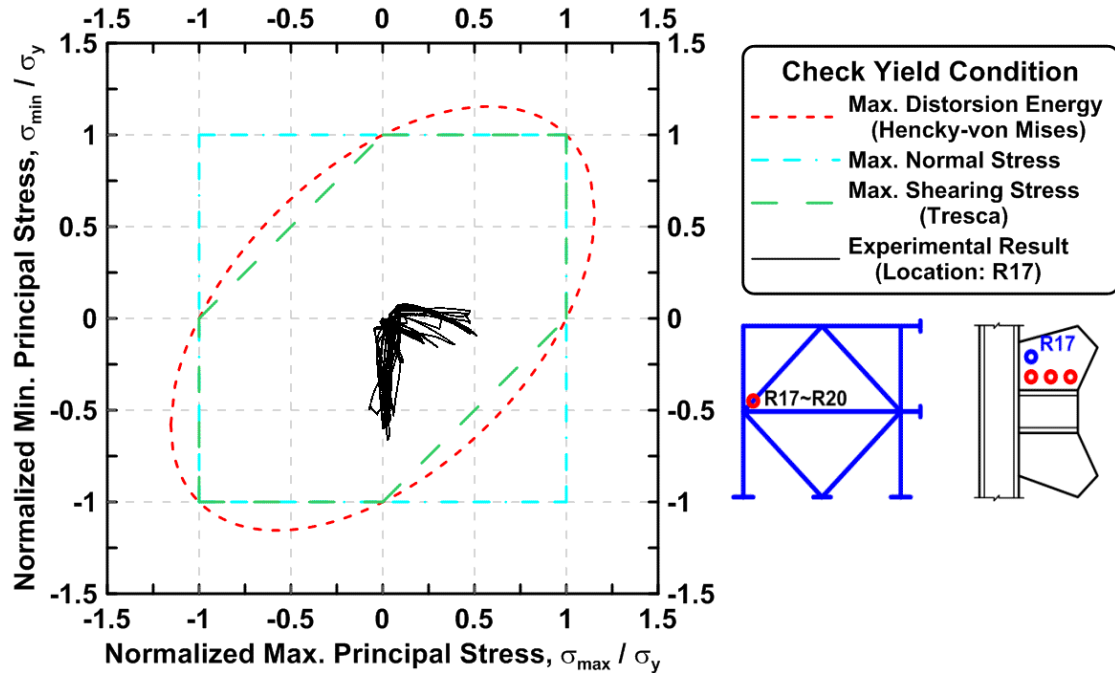


Figure 4.212 Specimen TCBF-B-2: normalized maximum principal stress versus normalized minimum principal stress in one-piece gusset plate location: R17).

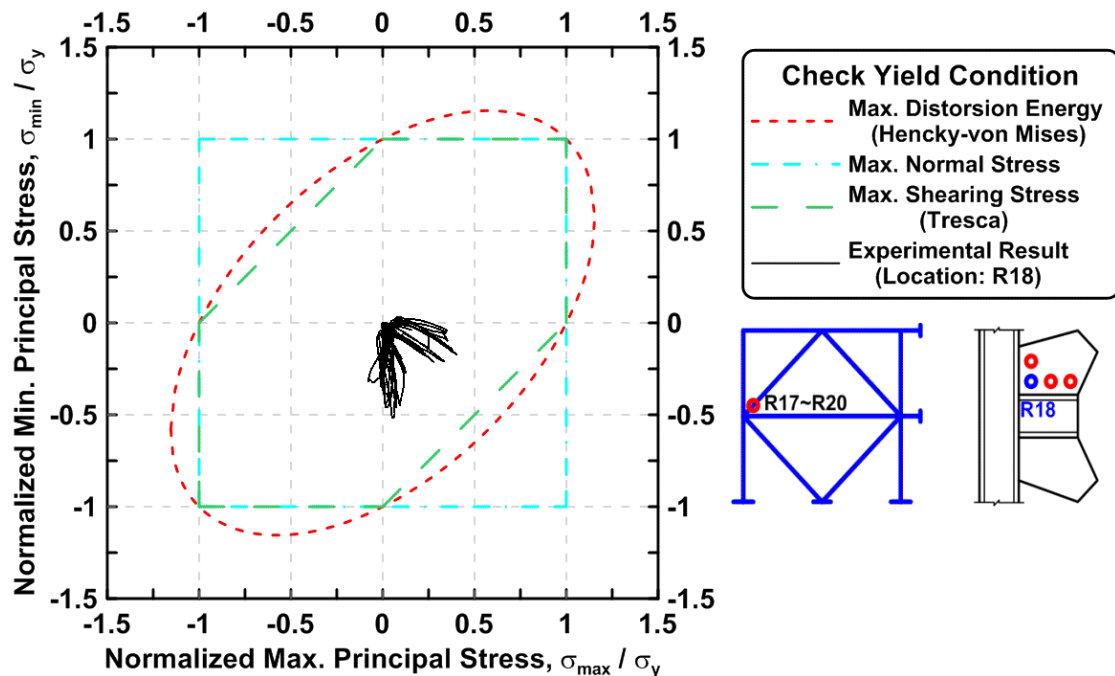


Figure 4.213 Specimen TCBF-B-2: normalized maximum principal stress versus normalized minimum principal stress in one-piece gusset plate (location: R18).

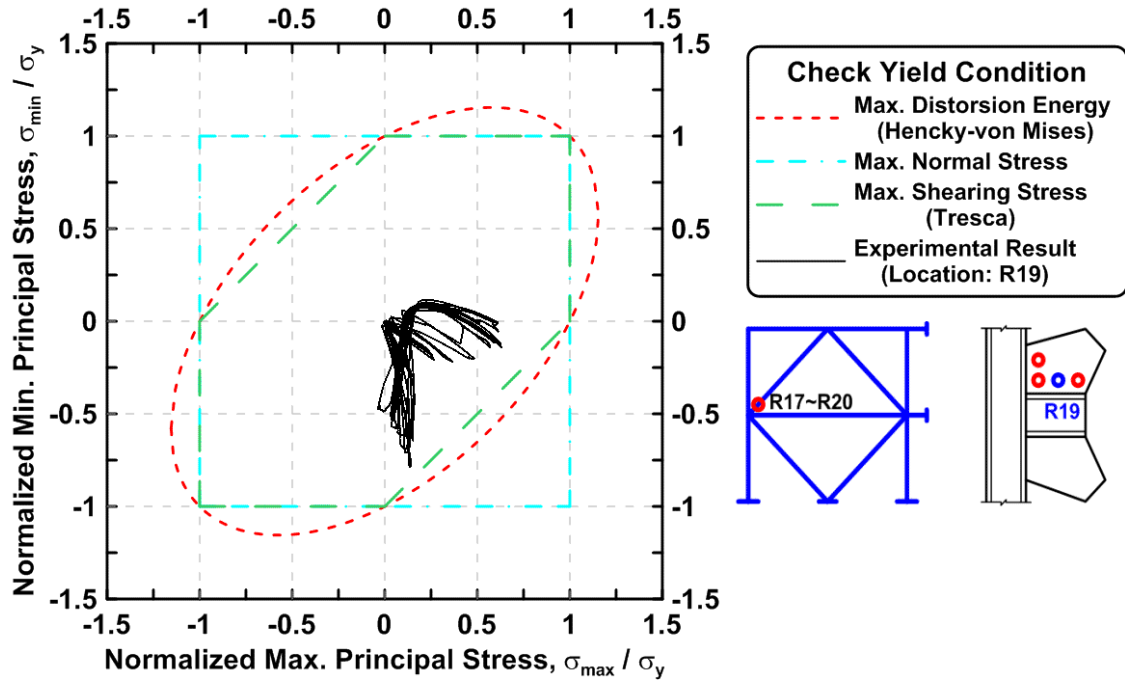


Figure 4.214 Specimen TCBF-B-2: normalized maximum principal stress versus normalized minimum principal stress in one-piece gusset plate (location: R19).

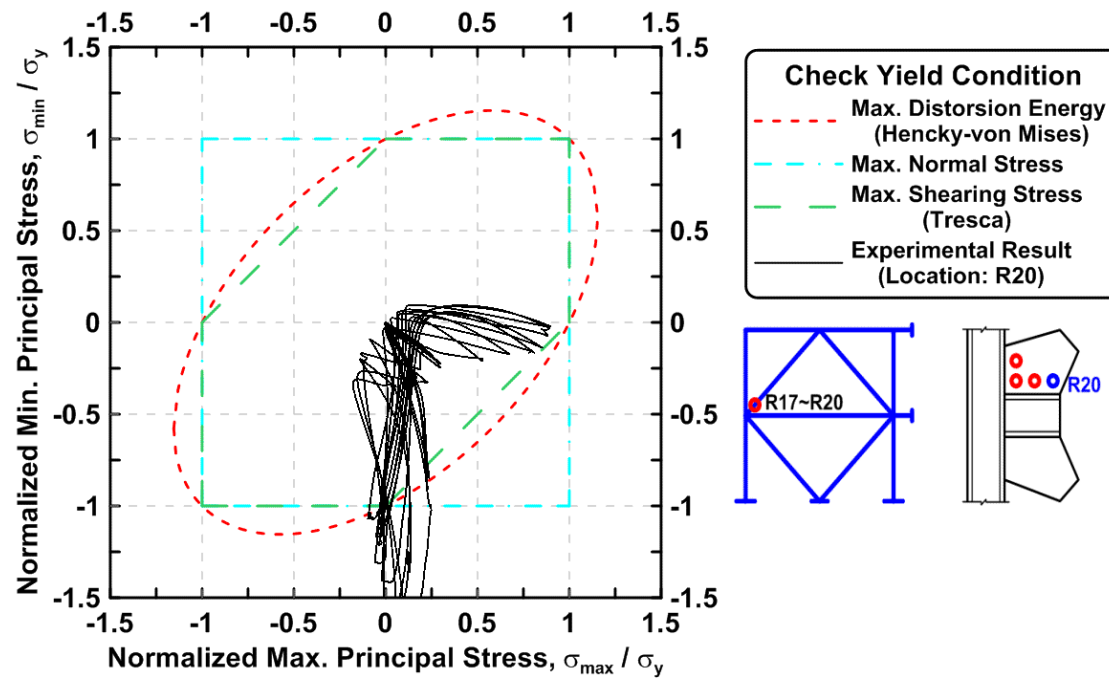


Figure 4.215 Specimen TCBF-B-2: normalized maximum principal stress versus normalized minimum principal stress in one-piece gusset plate (location: R20).

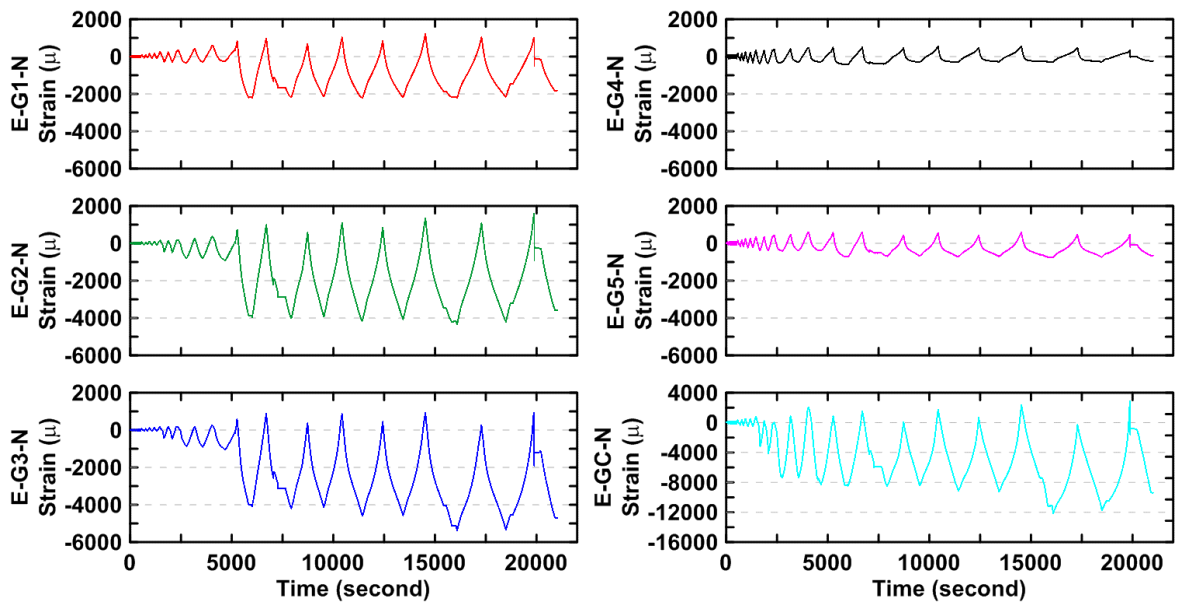


Figure 4.216 Specimen TCBF-B-2: averaged axial strain time history in tapered eastern-side gusset plate.

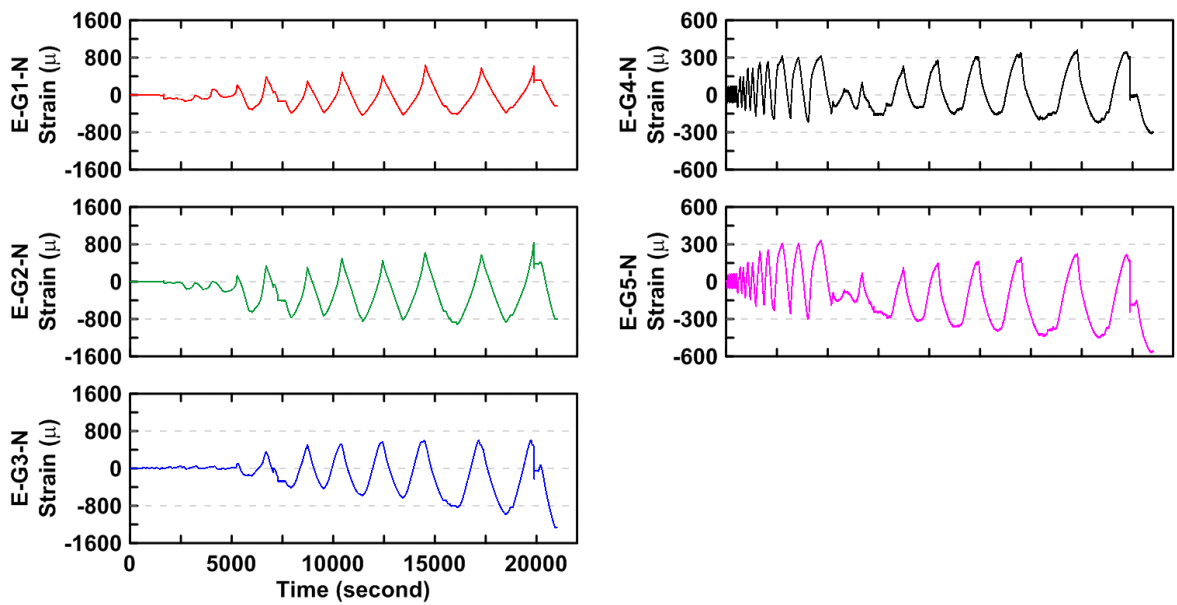


Figure 4.217 Specimen TCBF-B-2: bending strain time history in eastern-side tapered gusset plate.

4.1.2.2.7 Test Set Up Response

The actuator bracket deformations versus actuator forces are plotted in Figure 4.218. The relative displacement time history between base plates of the specimen and the floor beam, relative displacement time history between floor beam and strong floor, and relative displacement time history between integrated reconfigurable reaction wall and strong floor at northern and southern sides are shown in Figure 4.219. The out-of-plane deformation time history of the lateral supporting frame with respect to the wall of the building at different locations are plotted in Figure 4.220. The reconfigurable reaction wall (RRW) tip deformation time histories during the test are shown in Figure 4.221.

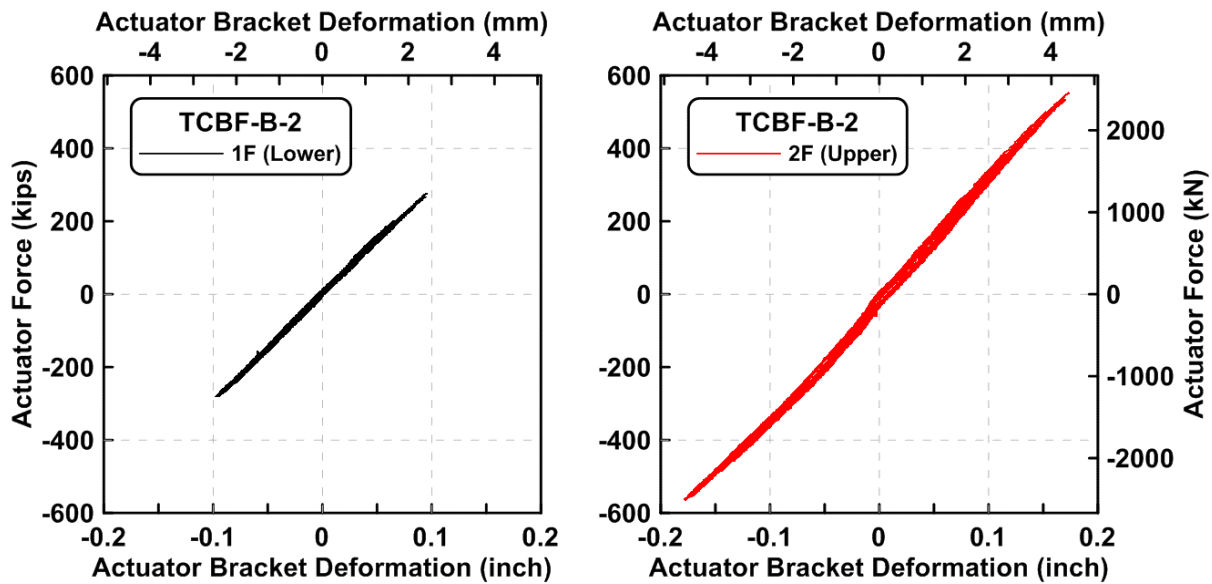


Figure 4.218 Specimen TCBF-B-2: actuator force versus bracket deformation relationship at both floor levels.

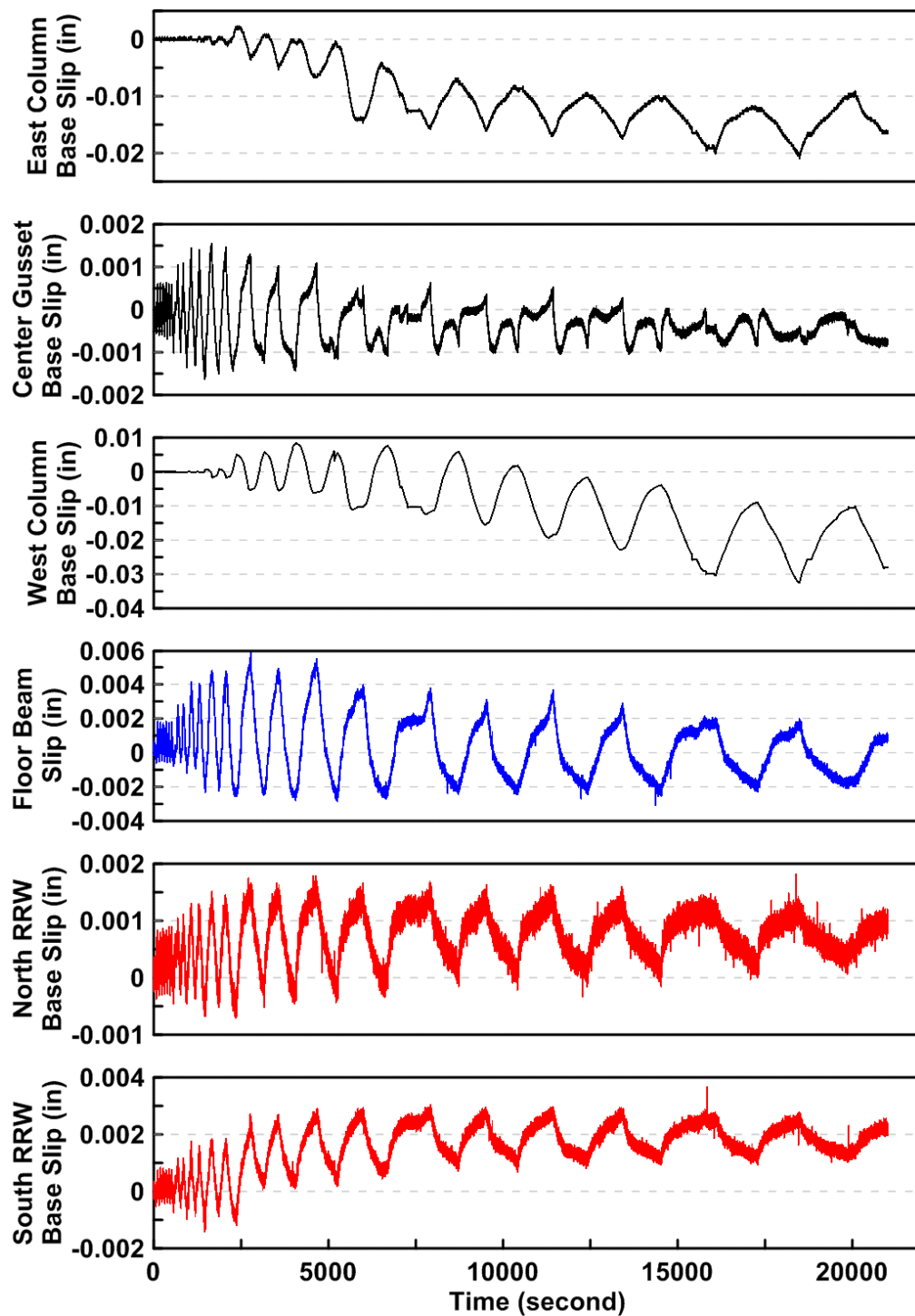


Figure 4.219 Specimen TCBF-B-2: slippage time history between specimen and test set up boundaries.

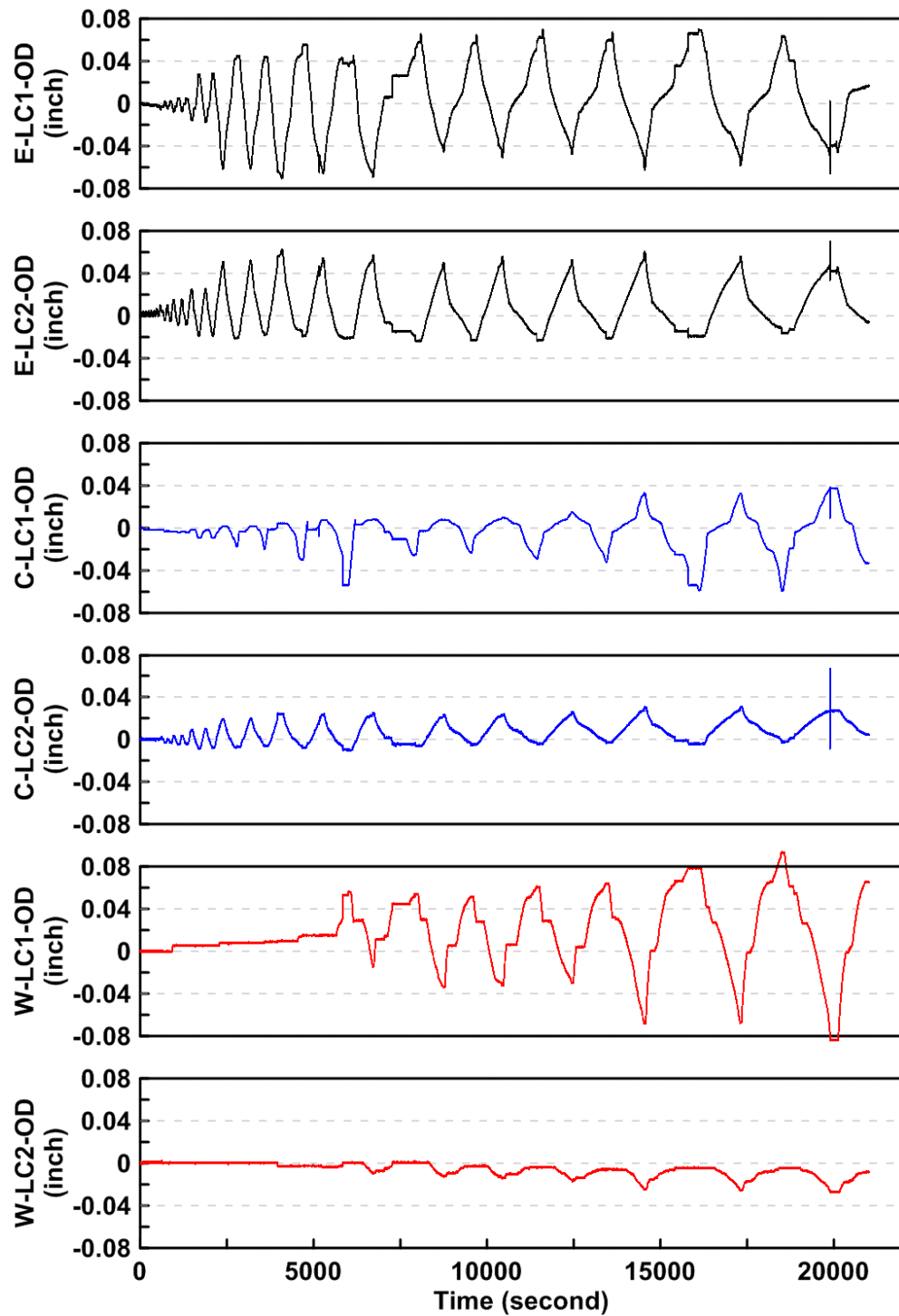


Figure 4.220 Specimen TCBF-B-2: out-of-plane deformation time history of lateral supporting frame at different monitoring points.

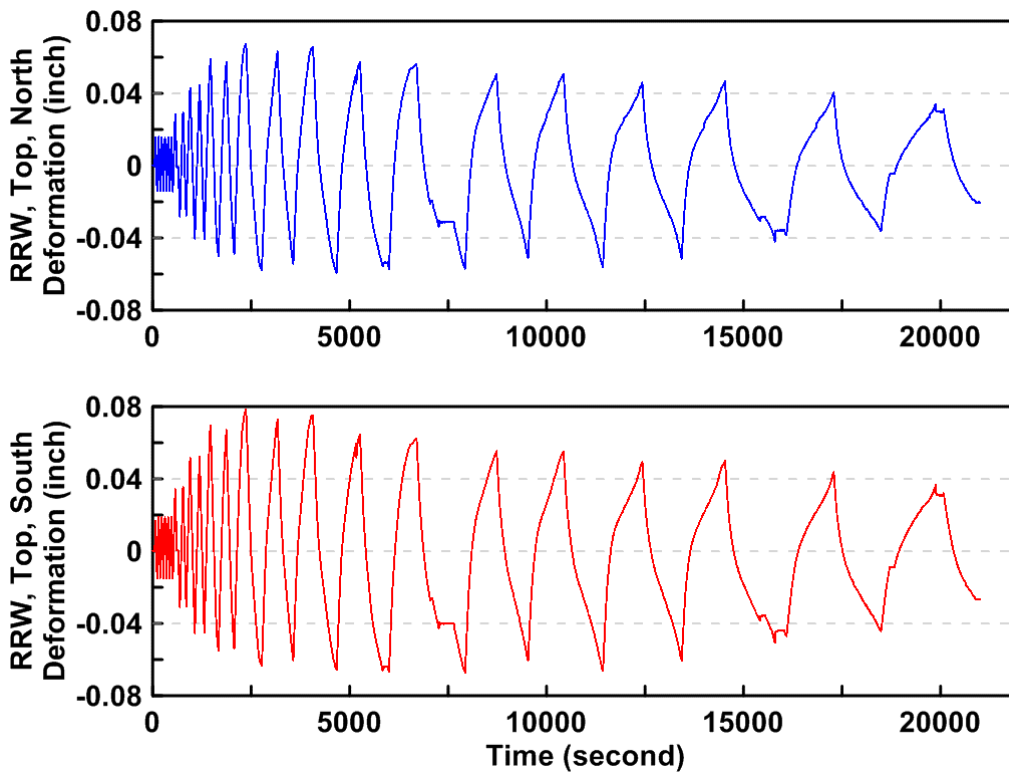


Figure 4.221 Specimen TCBF-B-2: reconfigurable reaction wall tip deformation time histories.

4.1.3 Specimen TCBF-B-3 (Wide Flange Braces)

This specimen was composed of wide flange braces and did not reuse any components from previous tests. The roof beam size and column size remained the same as the previous two specimens. To prevent premature in the column-to-base plate CJP welds, the column base connection detail was modified by adding four 7/8-in.-thick gussets, as shown in Figure 4.222. At the same time, the lower beam to one-piece gusset plate connections were also modified to a pin connection (Figure 4.223). To prevent the early local buckling and fracture of the lower beam where it connected to the gusset plates, a bolted connection was used to attach the beam web to the gusset plate (Figure 4.223). The gain values in the portable data acquisition software were set to be 50 for all data channels; note that all channels in portable DAQ were connected to strain gauges.

The test began at around 11:01 AM on Monday, January 24, 2011. The entire side views of the specimen before and after test are shown in Figure 4.224.



Figure 4.222 Specimen TCBF-B-3: column base connection detail (four 7/8-in. gussets welded to the column flange and base plate).



Figure 4.223 Specimen TCBF-B-3: lower beam to one-piece gusset plate pin connection detail (eastern side of W24 × 68 beam).



(a) before test



(b) after test

Figure 4.224 Specimen TCBF-B-3 before test and after test.

4.1.3.1 Main Observations

Specimen TCBF-B-3 was subjected to the same pre-defined loading protocol shown in Figure 3.28. Each loading stages contained two complete cycles at a given amplitude, except the first stage contained six complete cycles. Detailed information about each of these cycles is described sequentially below. Table 4.3 lists the major observations on the testing protocol with brief descriptions.

$\Delta = 0.5 D_{pe} = 0.2$ in. (Roof Drift $\delta = 0.1\%$), from 11:01 AM to 11:09 AM

Test started at 10:01 AM, after having completed two small cycles performed to check the operation of the data acquisition and control systems. During this low amplitude loading stage, the entire frame remained elastic. No special findings were found during this loading stage.

$\Delta = 1.0 D_{pe} = 0.4$ in. (Roof Drift $\delta = 0.2\%$), from 11:09 AM to 11:14 AM

The entire frame essentially remained elastic; no special findings were found in this loading step.

$\Delta = 1.0$ D_{by} = 0.6 in. (Roof Drift $\delta = 0.3\%$), from 11:14 AM to 11:22 AM

Some local flaking of the whitewash occurred on the brace-to-gusset cover plates and near the brace erection holes at first story (western wide flange brace on the north face, see Figure 4.225). Minor whitewash flaking also occurred on the column web and column flange near the base plates.

$\Delta = 0.5$ D_{bm} = 1.0 in. (Roof Drift $\delta = 0.5\%$), from 11:22 AM to 11:35 AM

At the beginning of the first half-cycle of the loading step (approaching the positive peak displacement), the brace at first-story west side and the brace at second-story east side began out-of-plane global buckling to the north side of the specimen, and the whitewash on the wide flange brace began flaking at the middle of the brace (Figure 4.226). Note that the whitewash flaking on the second-story brace occurred slightly above the brace midpoint. In the same loading cycle when the roof displacement was moving towards the negative peak displacement, the brace at first-story east side and the brace at second-story west side began out-of-plane global buckling to the south and north side of the specimen, respectively. Flaking of the whitewash on the wide flange braces occurred near the middle of the braces. Some local flaking of whitewash occurred on the roof beam web near the beam-to-column connection shear tab and also on the roof beam top flange near the beam-to-column connection CJP welds. Minor flaking also occurred in the panel zone region, as shown in Figure 4.227. Some minor local flaking of whitewash occurred near the lower beam-to-gusset splice plates (Figure 4.228).

$\Delta = 1.0$ D_{bm} = 2.0 in. (Roof Drift $\delta = 0.9\%$), from 11:36 AM to 12:03 PM

Additional flaking of whitewash occurred in the gusset plates and the braces during this loading stage. Additional global buckling of all four braces occurred in the out-of-plane direction (Figure 4.229). Yielding of the 2t folding lines became easily visible in some gusset plates (Figure 4.230). Some yielding of the column flange occurred at both east-side and west-side column bases (Figures 4.231 and 4.232). Note that the yield lines in the column flanges were at about a 45° angle from the column line, indicating that Lüder's bands had developed in the column flanges.

$\Delta = 1.5$ D_{bm} = 3.0 in. (Roof Drift $\delta = 1.4\%$), from 12:03 PM to 12:43 PM

When the roof displacement approached the first positive peak for this stage, the west-side wide flange brace in the ground story experienced localized buckling at the southern-side flanges near the midpoint of the brace (Figure 4.233). Additional flaking of the whitewash in both columns (near the bases), gusset plates, wide flange braces, and beam-to-gusset plate splices occurred at this load stage. Severe local yielding was found in the beam-to-gusset plate splices near the corner short-slotted holes (Figure 4.234). The beam-to-gusset connections also slipped as expected, as shown in Figure 4.235.

$\Delta = 2.0$ D_{bm} = 4.0 in. (Roof Drift $\delta = 1.9\%$), from 12:44 PM to 2:18 PM

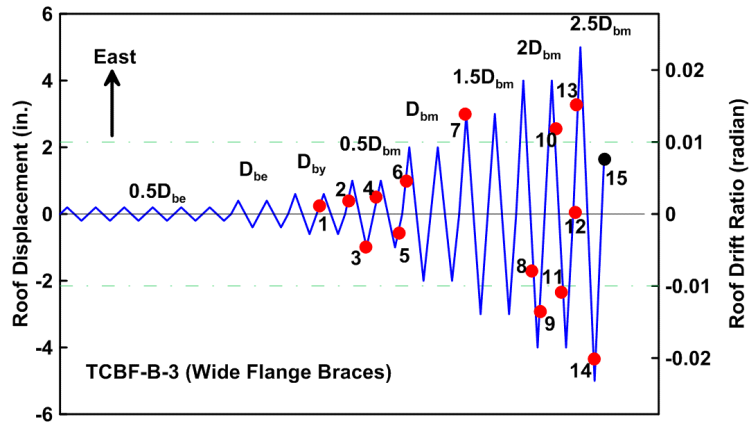
Although loud popping noises were heard at the second excursion of the first load cycle at about 1.7-in. roof displacement to the west (heading to the negative 4 in. peak), no drop in load occurred at this time. The test was manually paused at about five minutes to inspect the specimen

and then restarted. After moving back from the negative peak roof displacement in the first load cycle, the northern face of the east side brace at the second story began to locally buckle (at about -2.6-in. roof displacement). Several loud popping noises were heard at the beginning of the second cycle in this load step. The test was again manually paused for about six minutes to inspect the specimen. No fractures associated with the popping noises were found, and testing resumed. The base shear was small (less than 10 kips) and the roof displacement was about 2.36 in. during the short pause. Again, no significant load drop occurred. When the roof displacement approached negative 2.32 in. during the second half of the second cycle in the loading stage, the east column exterior column flange fractured near the tip of base plate stiffeners (Figures 4.236 and 4.237). The test was paused at about 1:35 PM and was resumed at around 2:05 PM. Partial fracture of the west-side wide flange brace in the first story was noticed during this loading phase (Figures 4.238 and 4.239).

$\Delta = 2.5$ D_{bm} = 5.0 in. (Roof Drift $\delta = 2.3\%$), from 2:19 PM to 2:57 PM

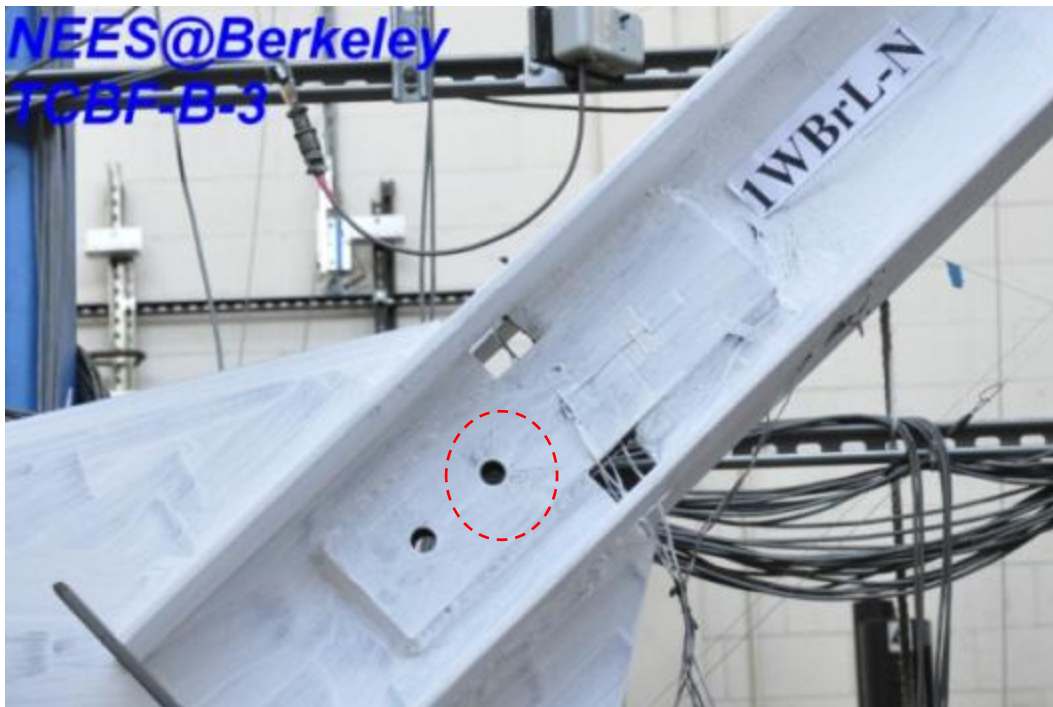
At the first cycle of this load stage when the roof displacement approached 3.5 in., the top flange of the west-side brace in the lower story fractured completely (Figure 4.240). Later, at the negative 4.3-in. roof displacement (approaching to the first negative peak roof displacement in this load stage), the west-side brace in the first story completely fractured (Figure 4.241). In this excursion, the crack tip in the east column web also moved toward the center of the web, and the crack opening became bigger (Figure 4.242). The test was stopped at a roof displacement equal to 1.67 in. after completing the first cycle of this load step. This displacement was estimated to return the structure to a nearly plumb position after unloading. The entire side view of the specimen after test is shown in Figure 4.243.

Table 4.3 Specimen TCBF-B-3: major observations noted during test.

	
Major Observations	
1	Whitewash flaking on the brace-to-gusset cover plates and near the brace erection holes at first story (Figure 4.225).
2	The brace at first story west side and the brace at second story east side began global buckling brace (see Figure 4.226, buckled out-of-plane to the north side).
3	The brace at first story east side and the brace at second story west side began global buckling brace (out-of-plane to the south and north side, respectively).
4	Minor local flaking of whitewash developed near the column base at both east and west side.
5	Minor local flaking of whitewash developed near the corner of lower beam-to-gusset splice plates (Figure 4.228).
6	Additional flaking of whitewash developed in the gusset plates and the braces. The 2t folding lines became visible in some gusset plates (Figure 4.230).
7	The west-side wide flange brace in the first story local buckled at the southern-side flanges near the midpoint of the brace (Figure 4.233).
8	Loud popping noises were heard but no load drop occurred at this time.
9	The northern face of the east side brace at the second story began locally buckled.
10	Test paused about six minutes to inspect the specimen. No significant load drop occurred.
11	The east column exterior column flange fractured near the tip of base plate stiffeners (Figures 4.236 and 4.237). And a partial fracture of the west-side wide flange brace in the first story was noticed (Figures 4.238 and 4.239).
12	The crack in the top flange of the west-side brace continued to propagate to the north side.
13	The top flange of the west-side brace in the first story completely fractured (Figure 4.240).
14	The west-side brace in the first story completely fractured (Figure 4.241). The crack tip in the east column web moved toward the center (Figure 4.242).
15	Test stopped at roof displacement equaled to 1.67 in.



(a)



(b)

Figure 4.225 Specimen TCBF-B-3: flaking of whitewash on brace-to-gusset cover plates.



Figure 4.226 Specimen TCBF-B-3: flaking of whitewash on global buckled braces (west brace at the first story and east brace at the second story).



Figure 4.227 Specimen TCBF-B-3: flaking of whitewash at west-side roof beam-to-column connection.

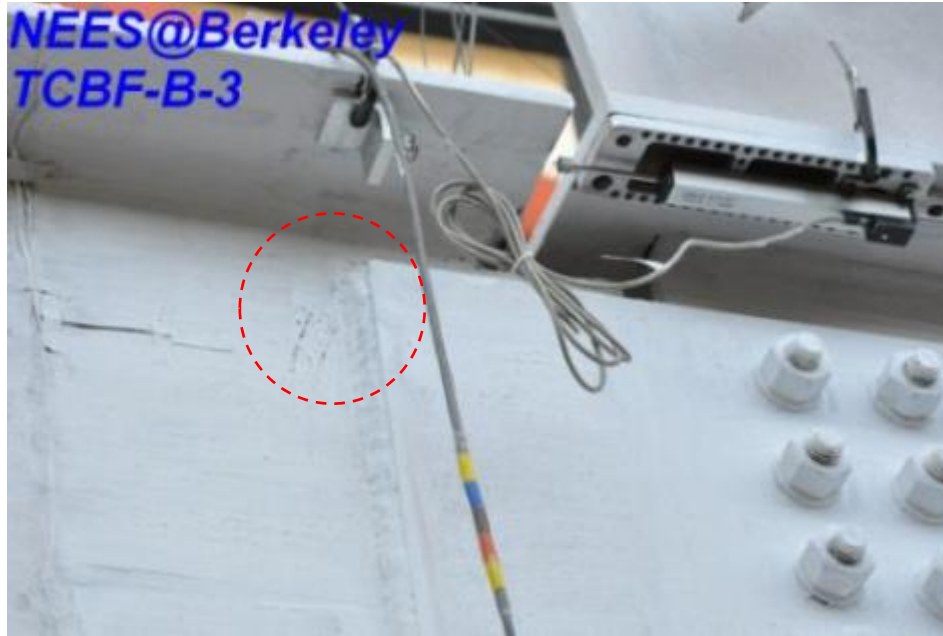


Figure 4.228 Specimen TCBF-B-3: local flaking of whitewash in lower beam web near beam-to-gusset splice plate.



(a)



(b)

Figure 4.229 Specimen TCBF-B-3: buckling shapes of all four wide flange braces: three of them buckled to the north side while only the east-side brace at the first story buckled to the south side.

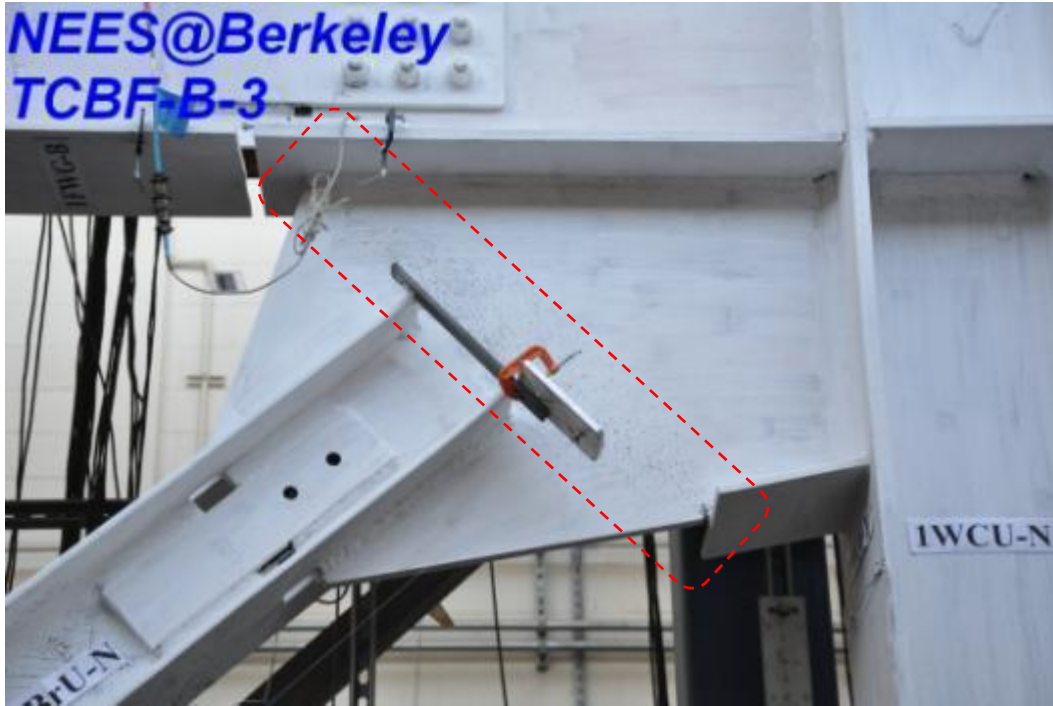
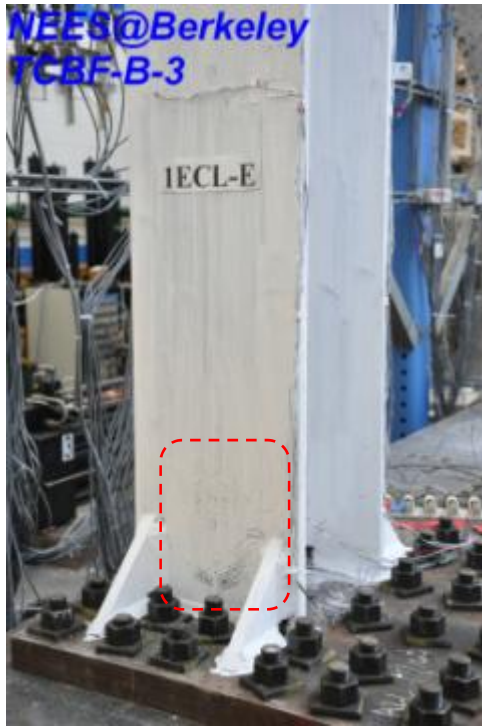


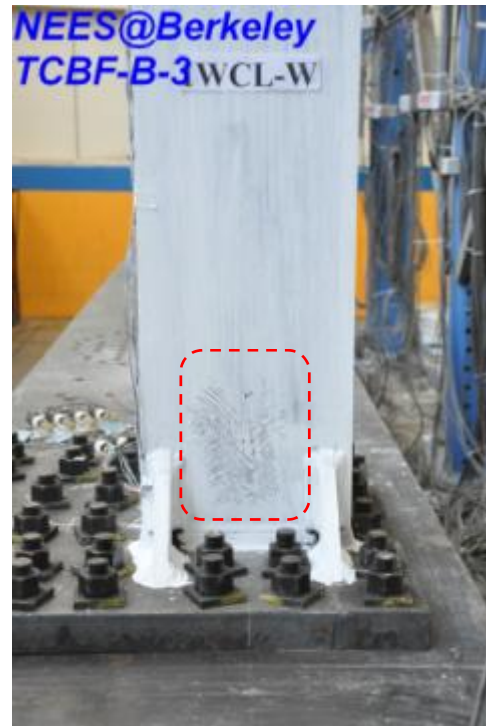
Figure 4.230 Specimen TCBF-B-3: flaking of whitewash at the $2t$ gap region in gusset plate.



Figure 4.231 Specimen TCBF-B-3: whitewash flaking patterns shown on column flanges near the west-side column base plate.



(a) east column base



(b) west column base

Figure 4.232 Specimen TCBF-B-3: whitewash flaking patterns shown on column flanges near column base plate.



Figure 4.233 Specimen TCBF-B-3: close view of local buckling at first-story west-side wide flange brace.

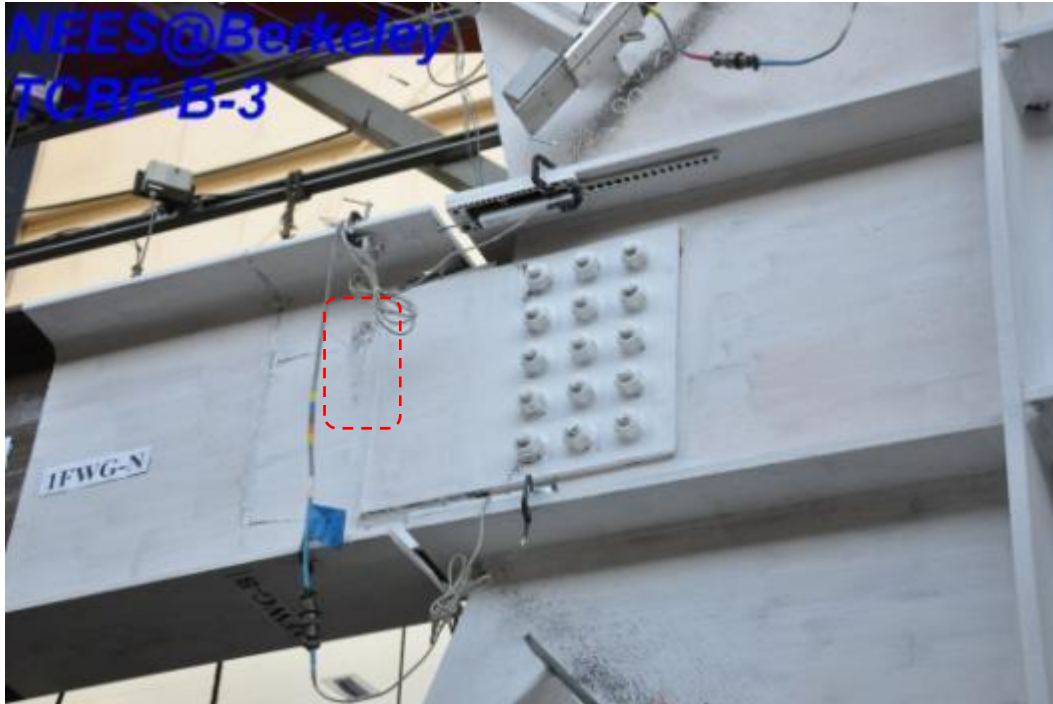


Figure 4.234 Specimen TCBF-B-3: local yielding in the beam-to-gusset plate splices near the short-slotted holes.



Figure 4.235 Specimen TCBF-B-3: evidence of slippage between splice plate and one-piece gusset plate.



Figure 4.236 Specimen TCBF-B-3: east column flange fractured near base plate stiffeners (view from north-west side).



Figure 4.237 Specimen TCBF-B-3: east column flange fractured near base plate stiffeners (view from east side).



Figure 4.238 Specimen TCBF-B-3: west wide flange brace partially fractured near middle of the brace (view from north-west side).



Figure 4.239 Specimen TCBF-B-3: west wide flange brace partially fractured near middle of the brace (view from east side).



Figure 4.240 Specimen TCBF-B-3: top flange of the west wide flange brace completely fractured near the middle of brace (view from north-west side).



Figure 4.241 West wide flange brace completely fractured near the middle of the brace (view from north side) of Specimen TCBF-B-3.



Figure 4.242 Specimen TCBF-B-3: crack tip in the web of east column near column base.



(a) view from north-east side



(b) view from north-west side

Figure 4.243 Specimen TCBF-B-3 after test.

4.1.3.2 Key Response Quantities

The paragraphs below briefly describe the response quantities record in the test and the post-processed response quantities derived from the raw data. Detail discussion of the individual response quantities are described in Chapter 5.

4.1.3.2.1 System Response

Figures 4.244 and 4.245 show the time history of the actuator displacements and actuator load cell force feedbacks for Specimen TCBF-B-3. The base shear versus controlled roof displacement of the specimen is shown in Figure 4.246. The relationship between story shear and story drift for the specimen is shown in Figure 4.247.

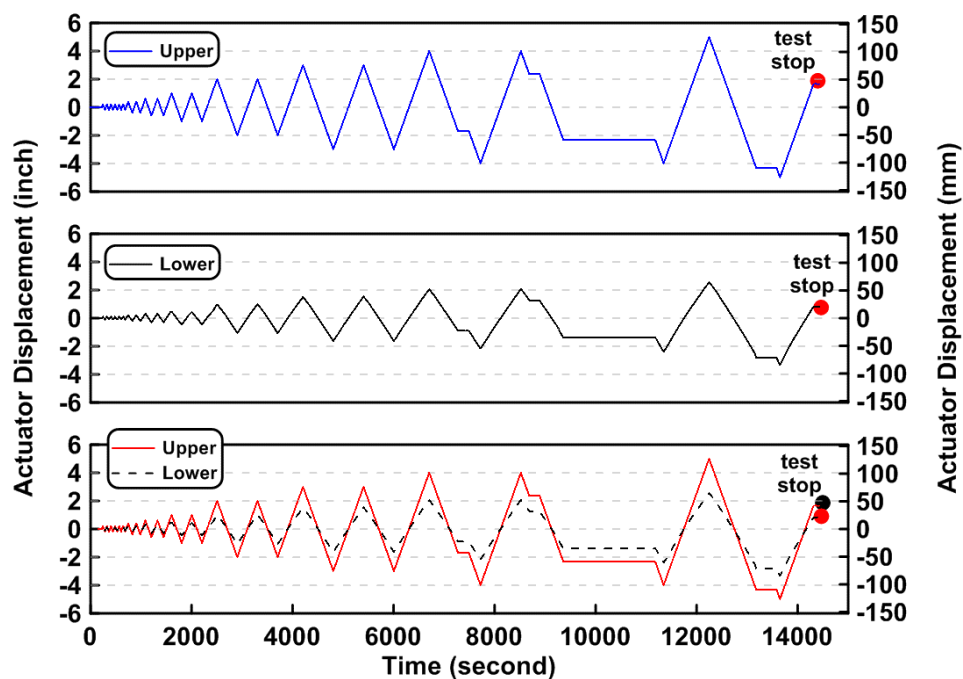


Figure 4.244 Specimen TCBF-B-3: actuator displacement time history.

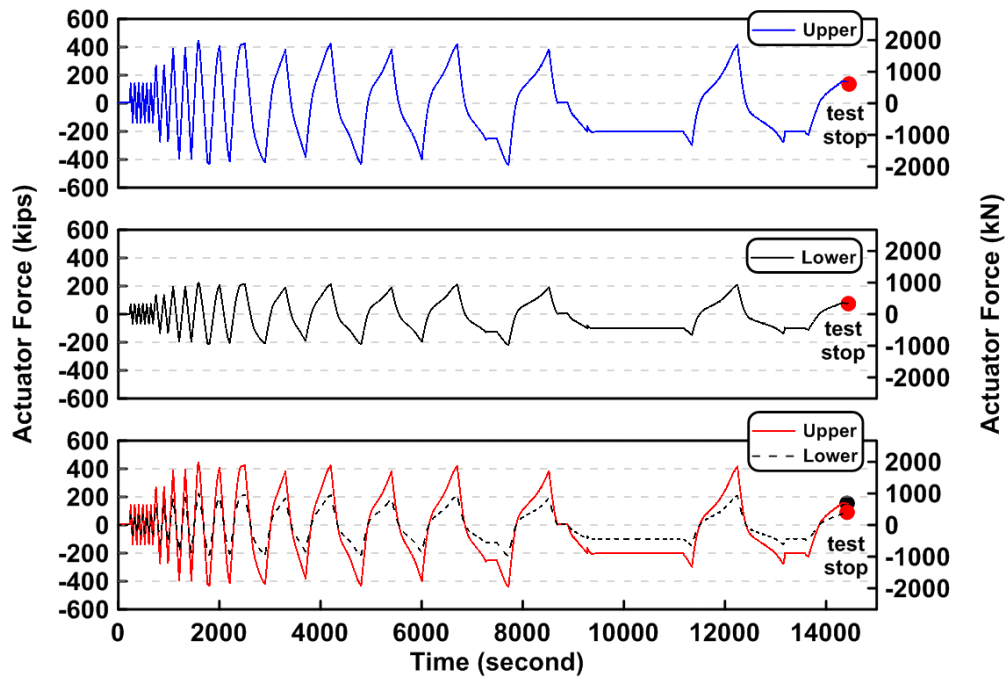


Figure 4.245 Specimen TCBF-B-3: actuator force histories.

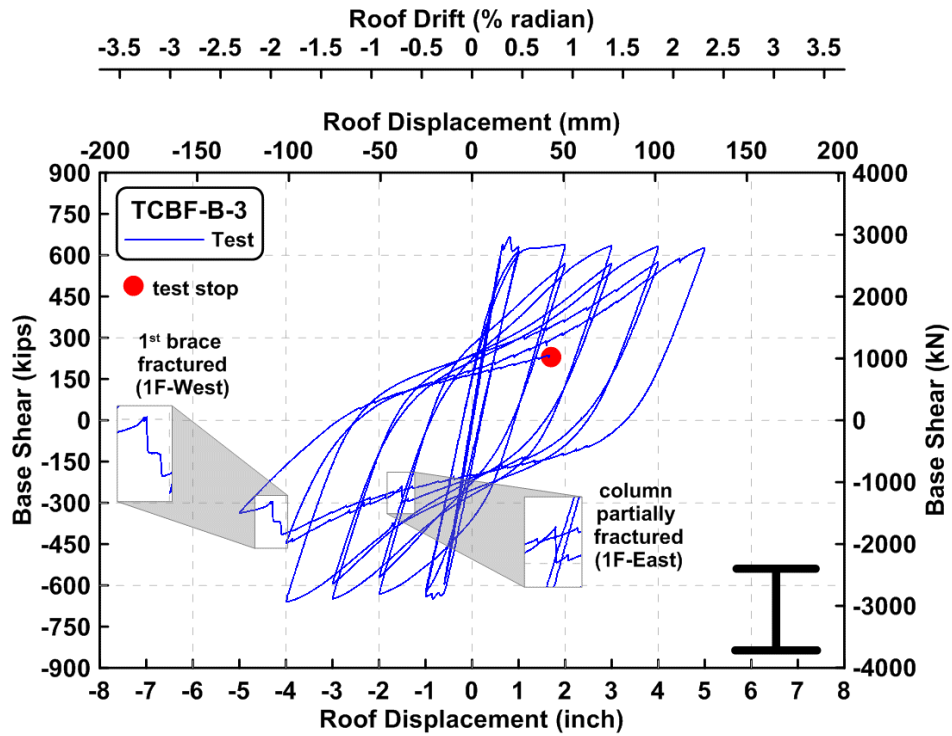


Figure 4.246 Specimen TCBF-B-3: base shear versus roof displacement relationship.

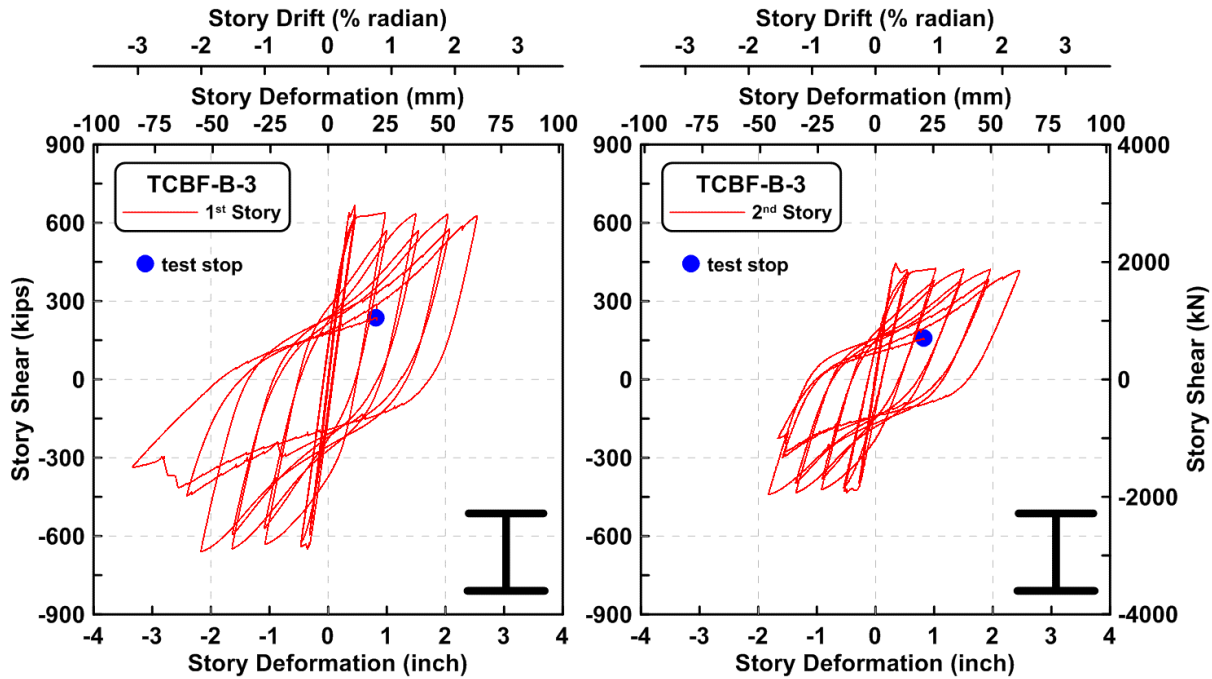


Figure 4.247 Specimen TCBF-B-3: story shear versus story deformation relationship.

4.1.3.2.2 Column Response

The time history of the axial forces in $W12 \times 96$ columns at western and eastern sides of the specimen is plotted in Figure 4.248. The relationship between roof displacements and axial forces at both columns is shown in Figure 4.249. The bending moment time history at the top and bottom ends of the column in each story is shown in Figures 4.250 and 4.251. Derived column shear force time history in both stories are plotted in the Figures 4.252 and 4.253, respectively. Two column shear forces in each floor were added together and are shown in Figure 4.254.

The column web shear stress versus shear strain readings from strain rosettes is plotted in Figure 4.255. The sum of the column shear force components versus the total story shear forces for each story is shown in Figure 4.256. The derived rosette-type strain gauge readings in the column web at each story are shown in Figures 4.257 to 4.260. Normalized maximum and minimum principal stress relationships along with different yield criteria are plotted in Figures 4.261 to 4.264. The normalized P-M and P-V interaction diagrams at column bases and column top ends are shown in Figures 4.265 to 4.268.

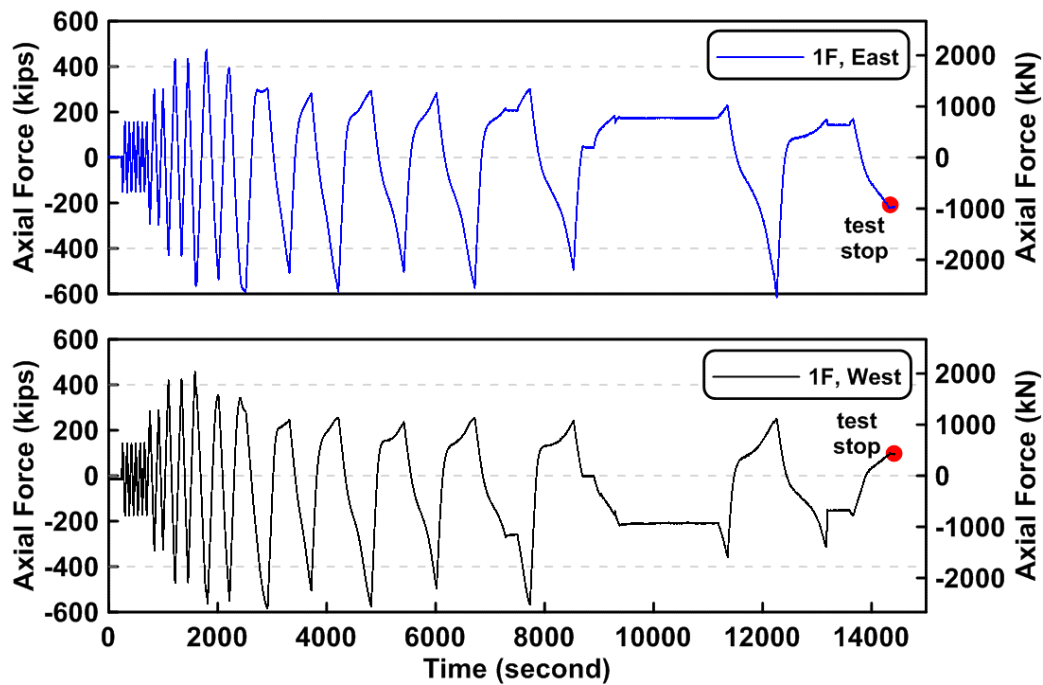


Figure 4.248 Specimen TCBF-B-3: time history of first-story column axial forces (location: 3 ft above column base plate).

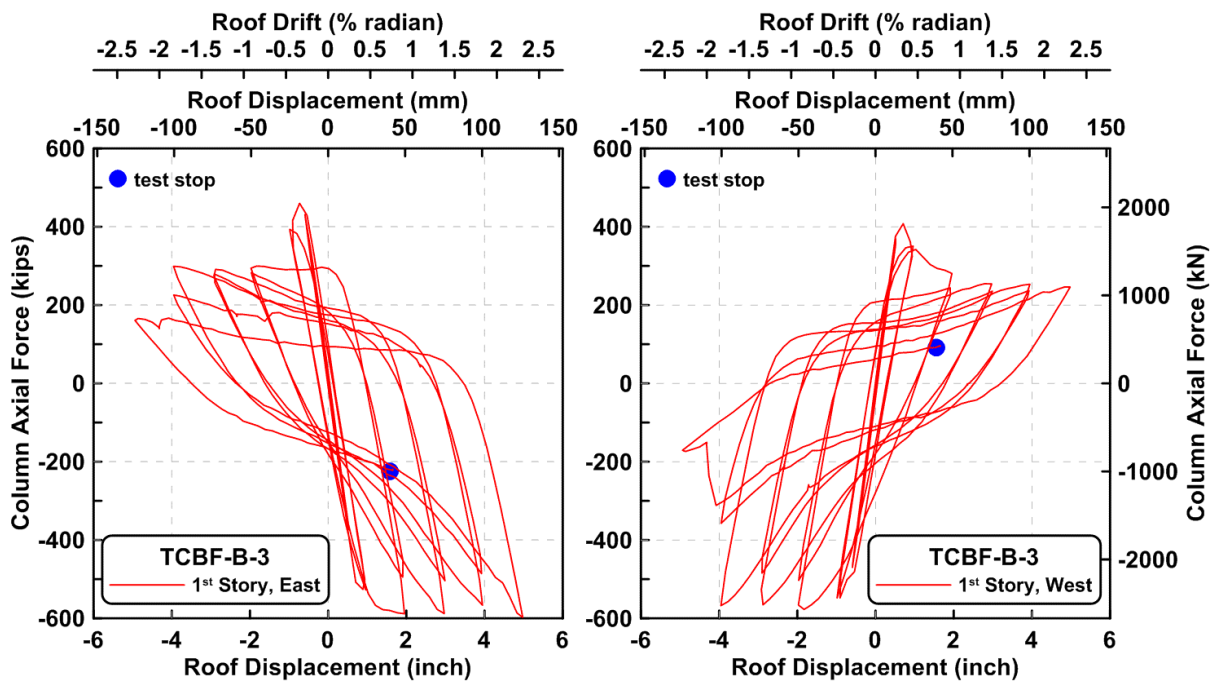


Figure 4.249 Specimen TCBF-B-3: roof displacement versus first-story column axial forces.

$M_y = 7270.5 \text{ kip-in}$, $M_p = 8158.5 \text{ kip-in}$

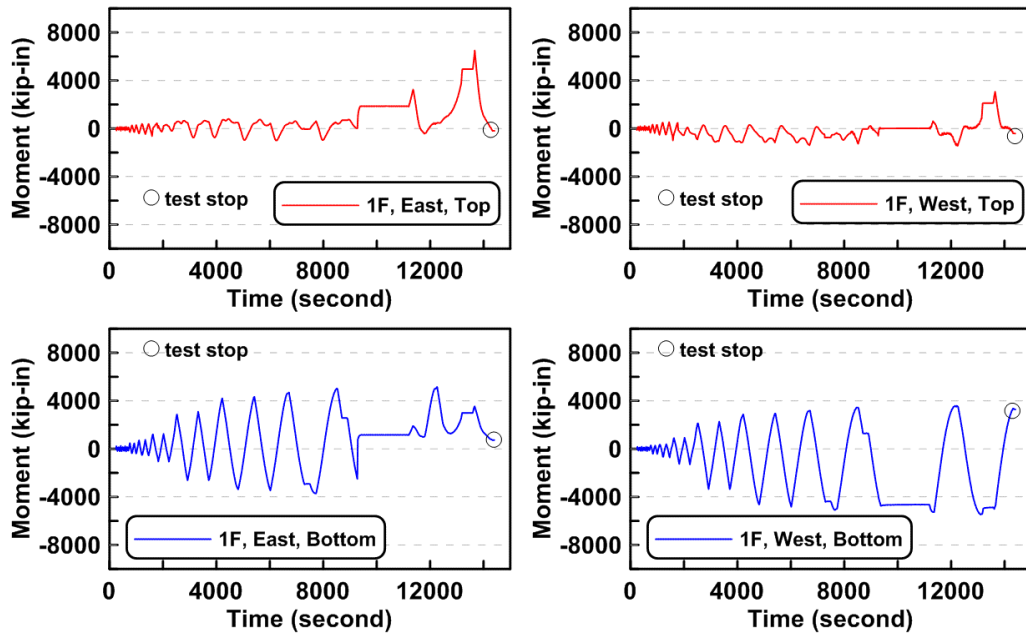


Figure 4.250 Specimen TCBF-B-3: time history of first-story column bending moments (3 ft above column base plate and 3 ft below lower beam centerline).

$M_y = 7270.5 \text{ kip-in}$, $M_p = 8158.5 \text{ kip-in}$

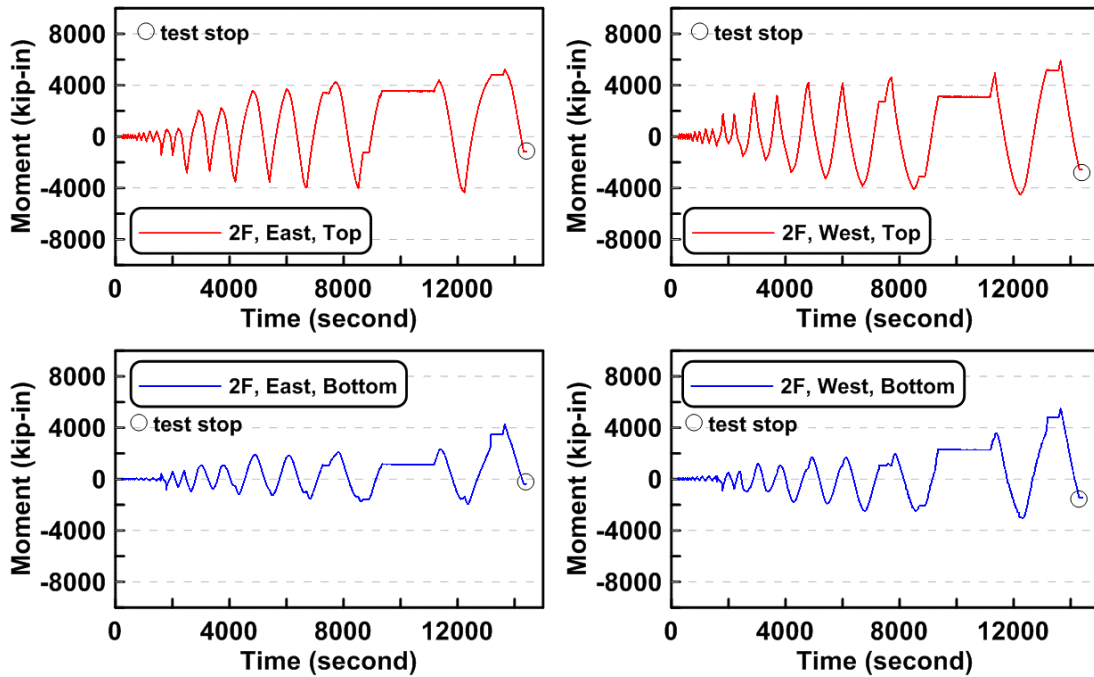


Figure 4.251 Specimen TCBF-B-3: time history of second-story column bending moment (3 ft above lower beam centerline and 3 ft below roof beam centerline).

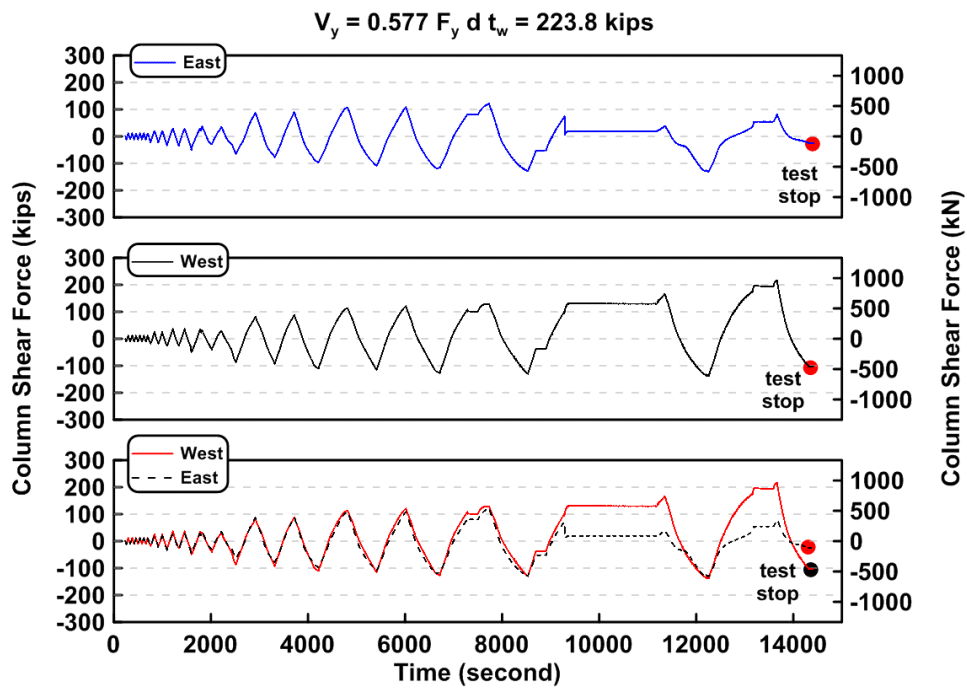


Figure 4.252 Specimen TCBF-B-3: time history of first-story column shear forces.

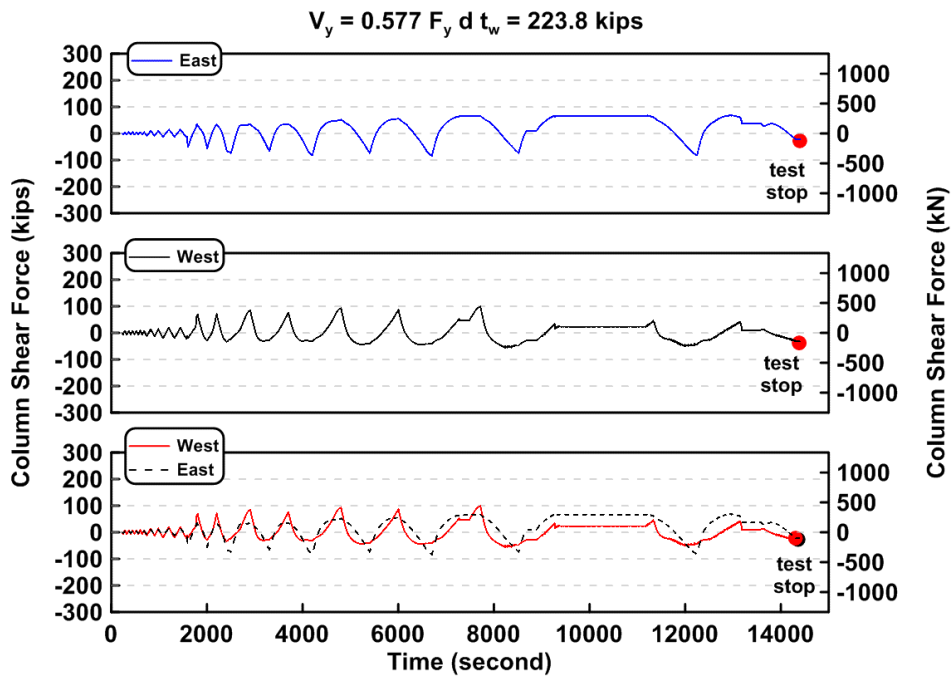


Figure 4.253 Specimen TCBF-B-3: time history of second-story column shear forces.

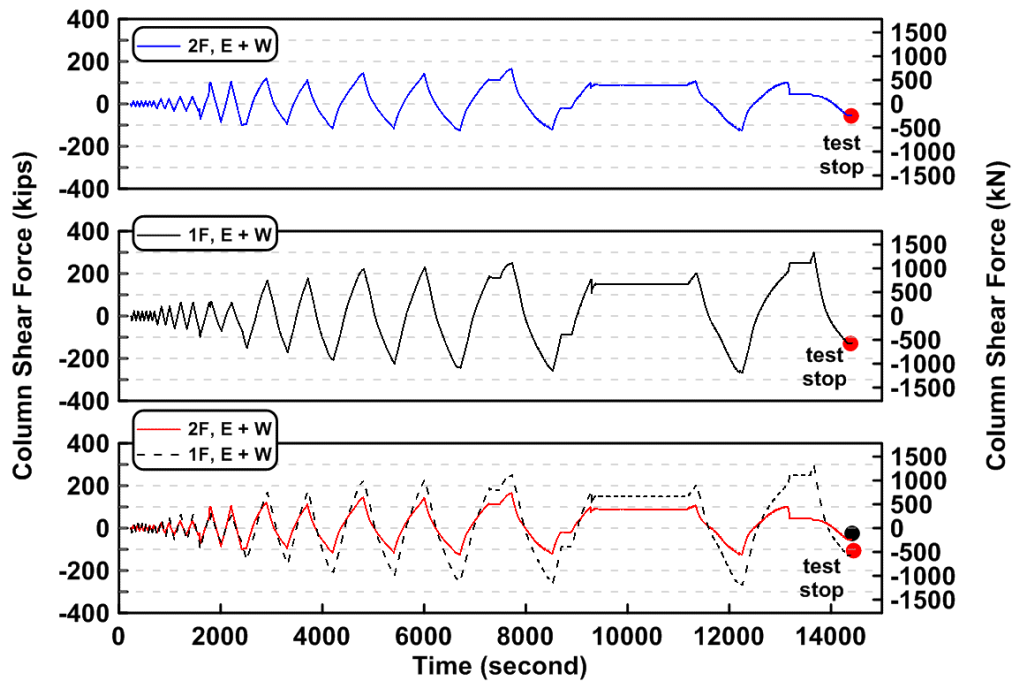


Figure 4.254 Specimen TCBF-B-3: time history of sum of east and west column shear forces for both stories.

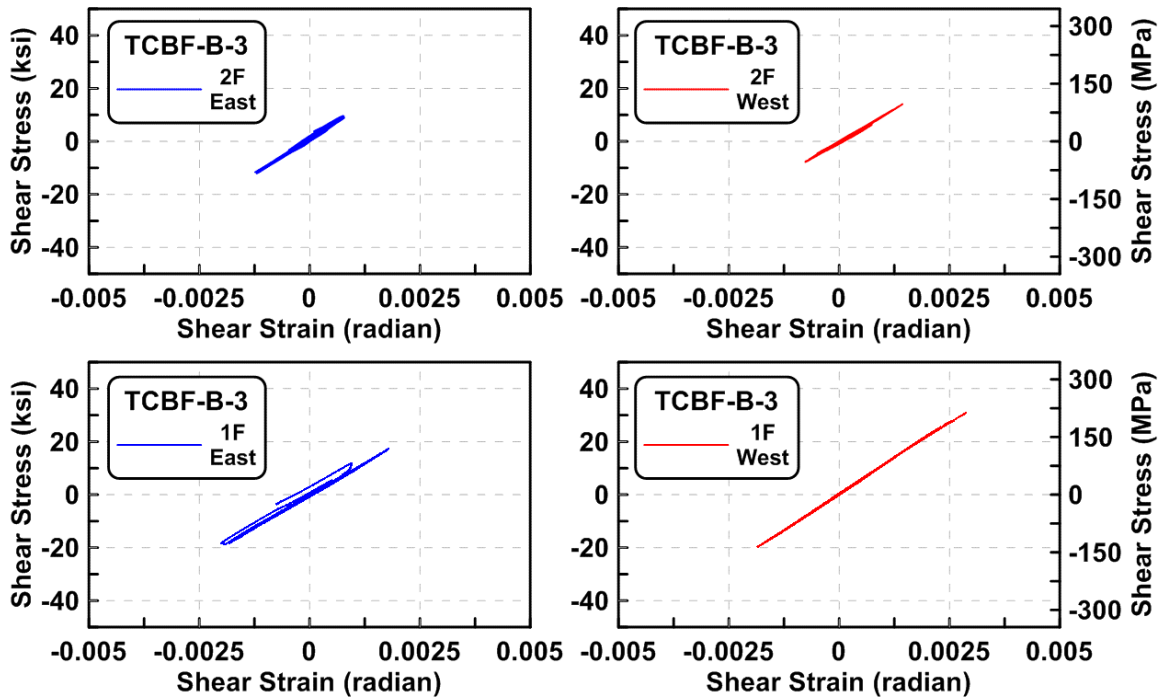


Figure 4.255 Specimen TCBF-B-3: column shear stress versus shear strain relationships (locations: EC1-B-N, EC2-B-N, WC1-B-N, and WC2-B-N).

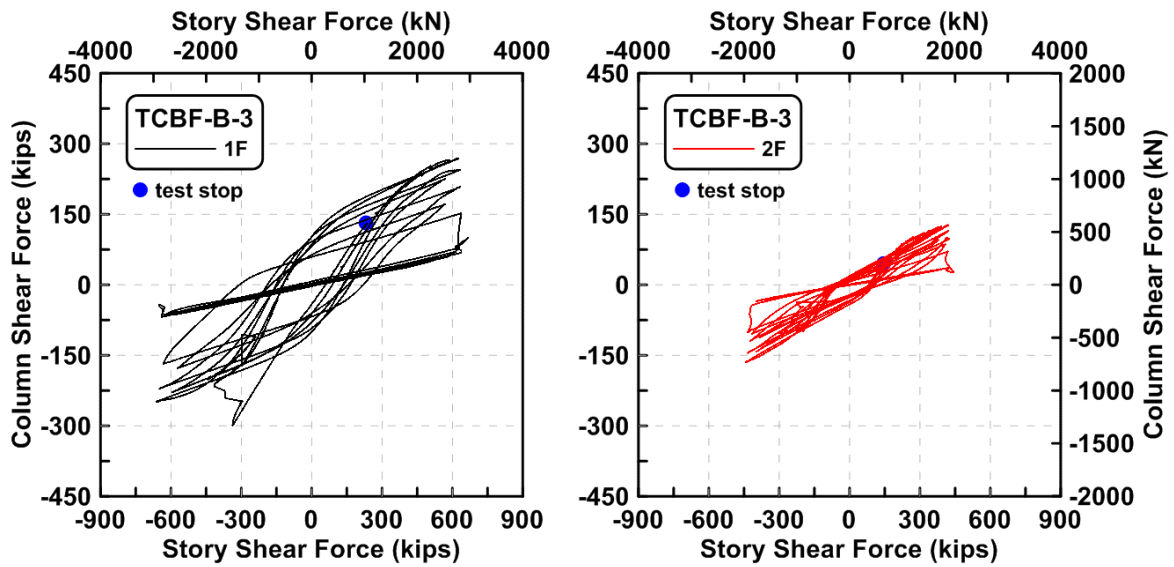


Figure 4.256 Specimen TCBF-B-3: story shear component from columns versus total story shear forces.

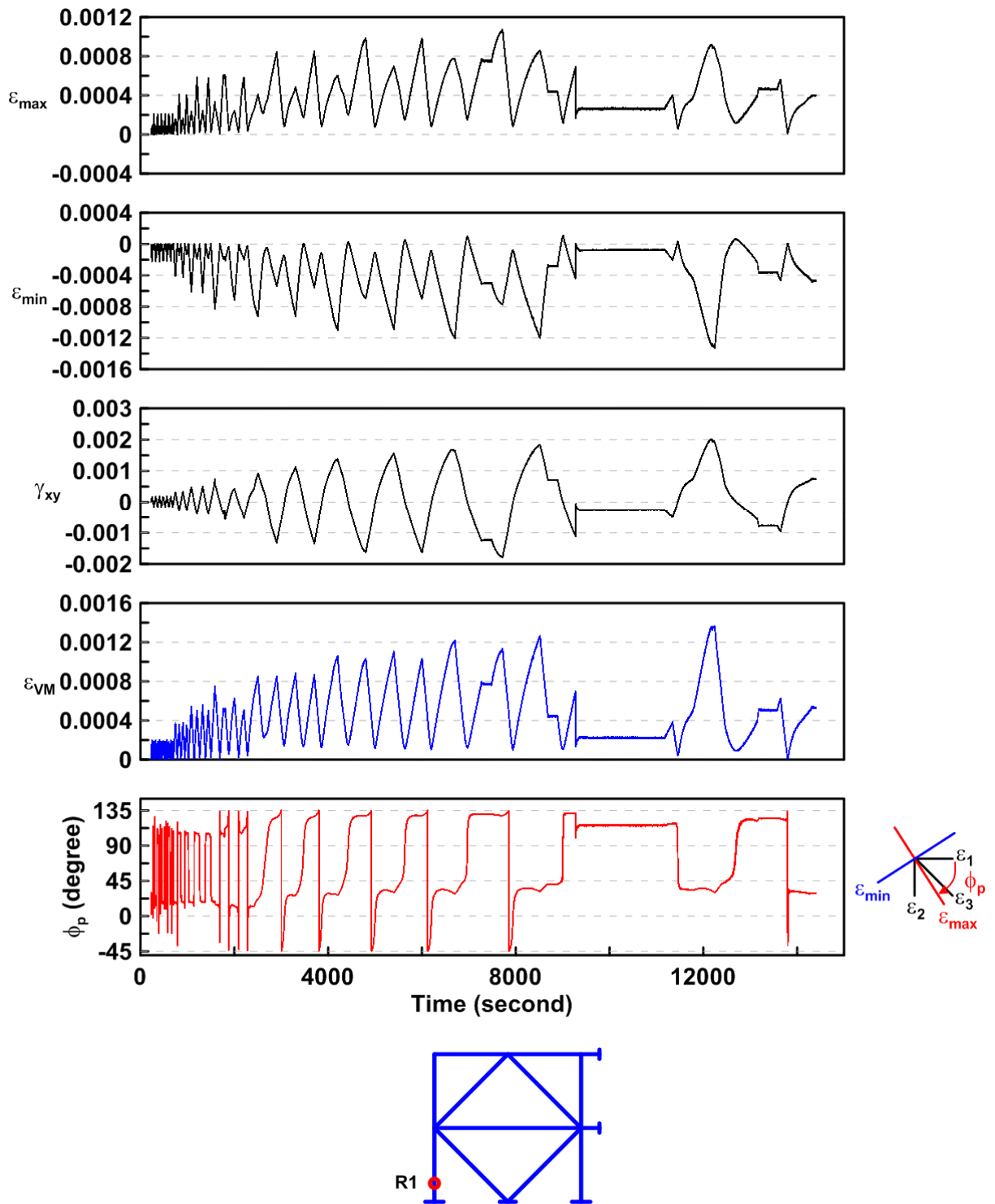


Figure 4.257 Specimen TCBF-B-3: time history of rosette-type strain gauge readings in first-story column web (location: R1).

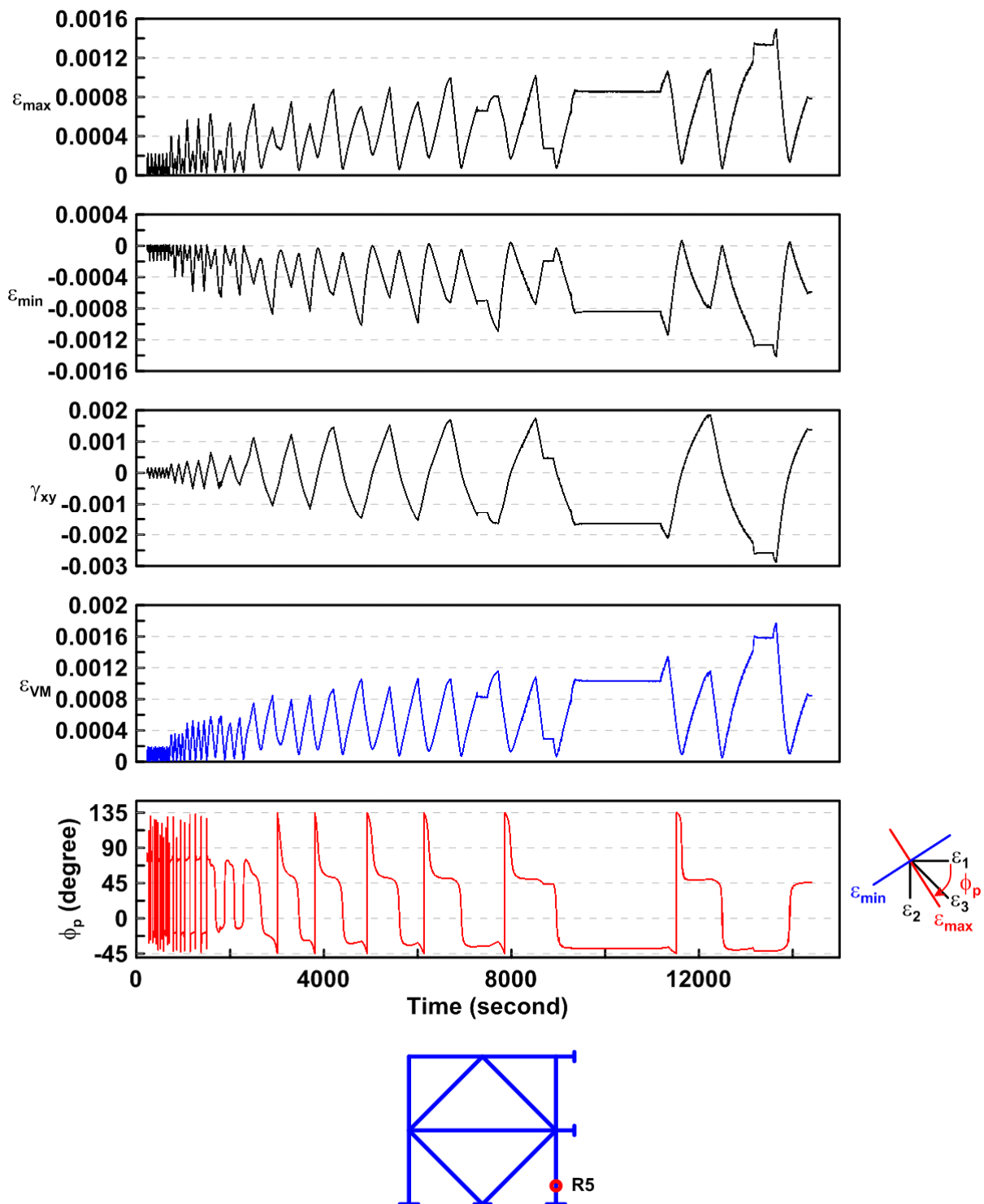


Figure 4.258 Specimen TCBF-B-3: time history of rosette-type strain gauge readings in first-story column web (location: R5).

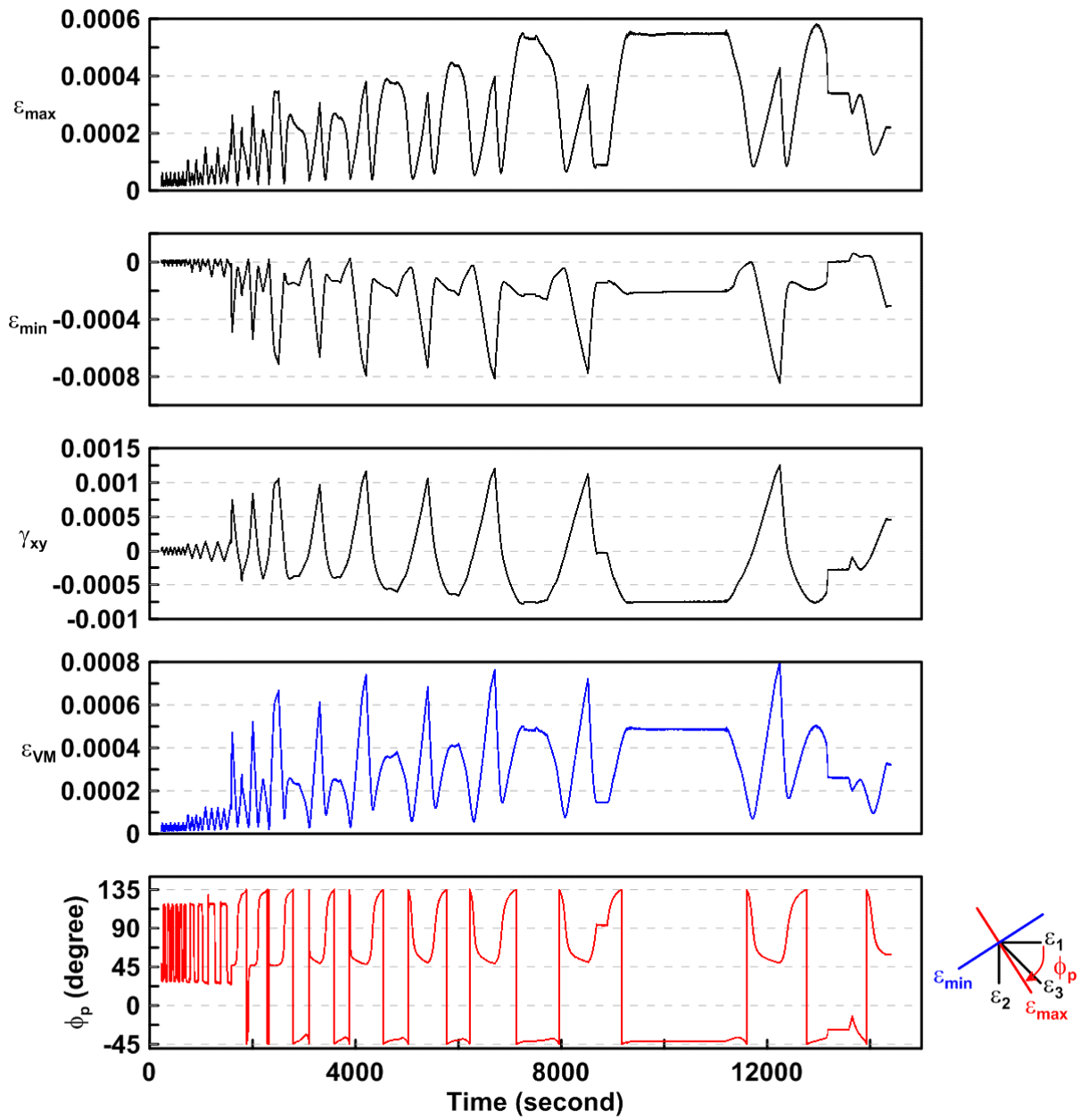


Figure 4.259 Specimen TCBF-B-3: time history of rosette-type strain gauge readings in first-story column web (location: R3).

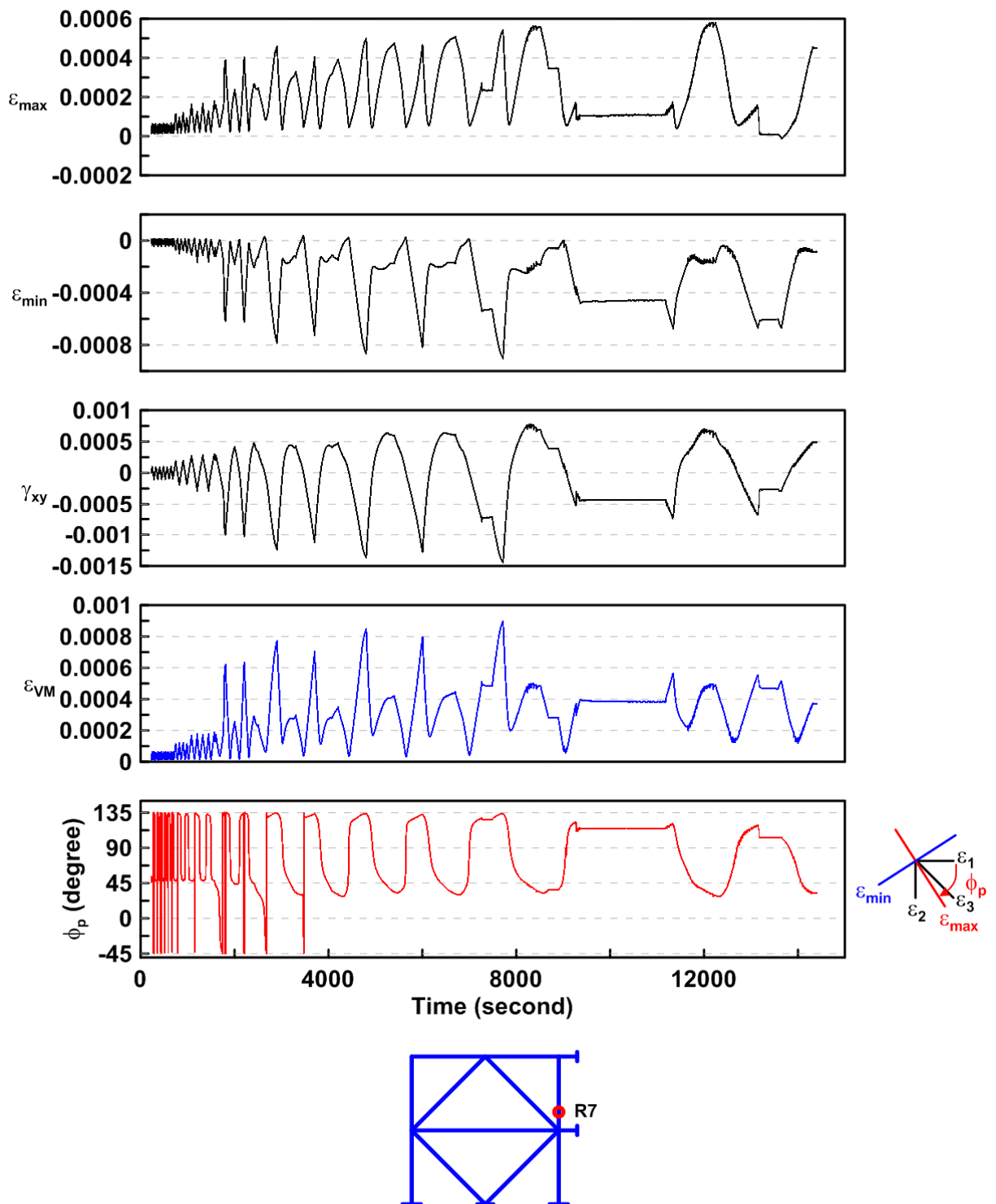


Figure 4.260 Specimen TCBF-B-3: time history of rosette-type strain gauge readings in first-story column web (location: R7).

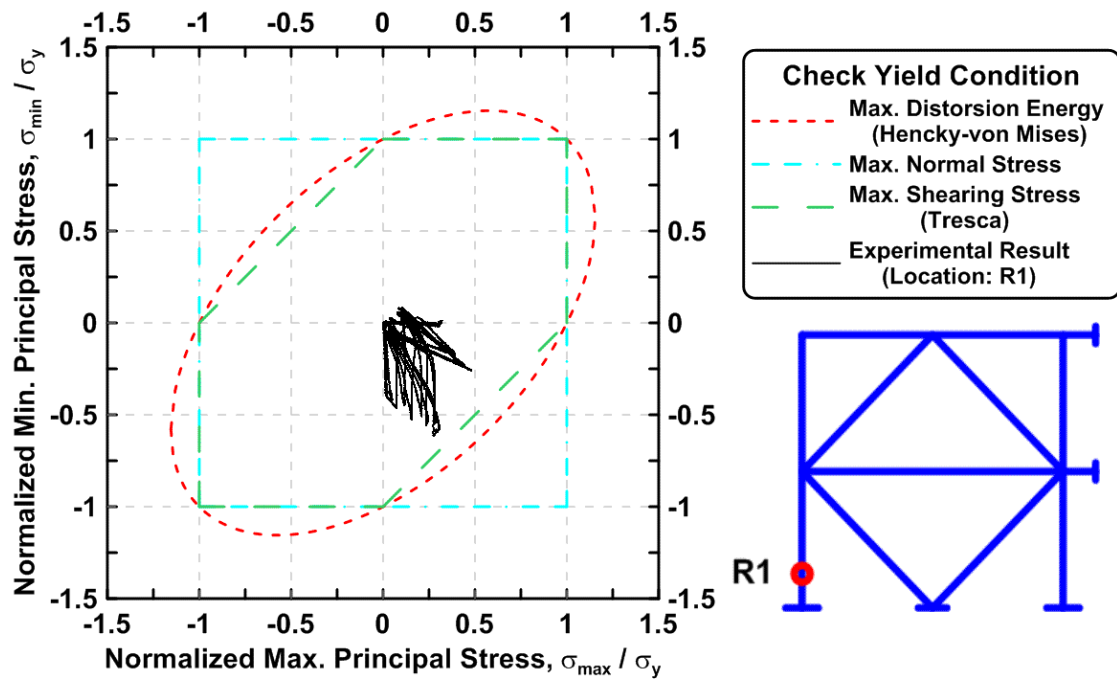


Figure 4.261 Specimen TCBF-B-3: maximum principal stress versus minimum principal stress in first-story column (location: R1).

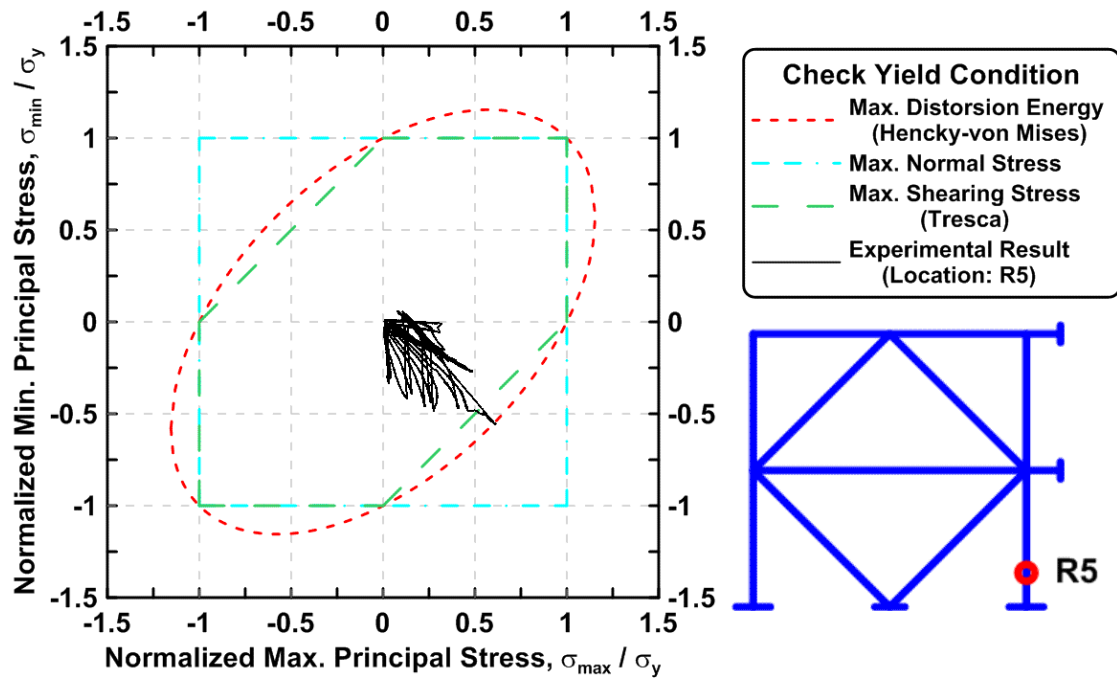


Figure 4.262 Specimen TCBF-B-3: maximum principal stress versus minimum principal stress in first-story column (location: R5).

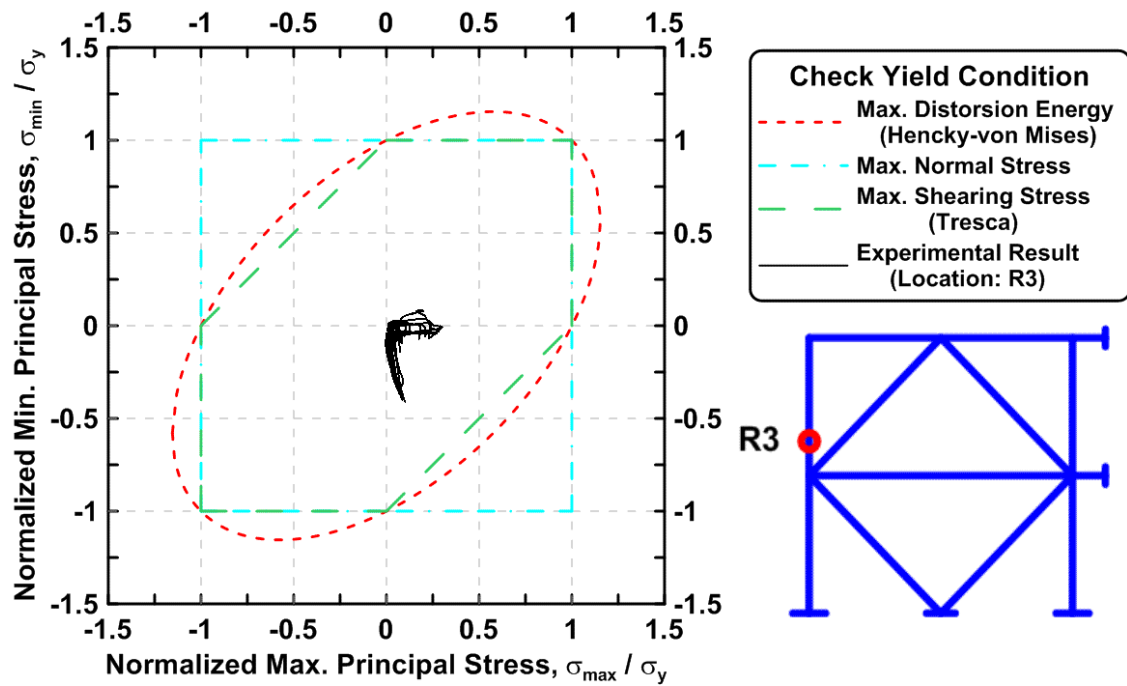


Figure 4.263 Specimen TCBF-B-3: maximum principal stress versus minimum principal stress in first-story column (location: R3).

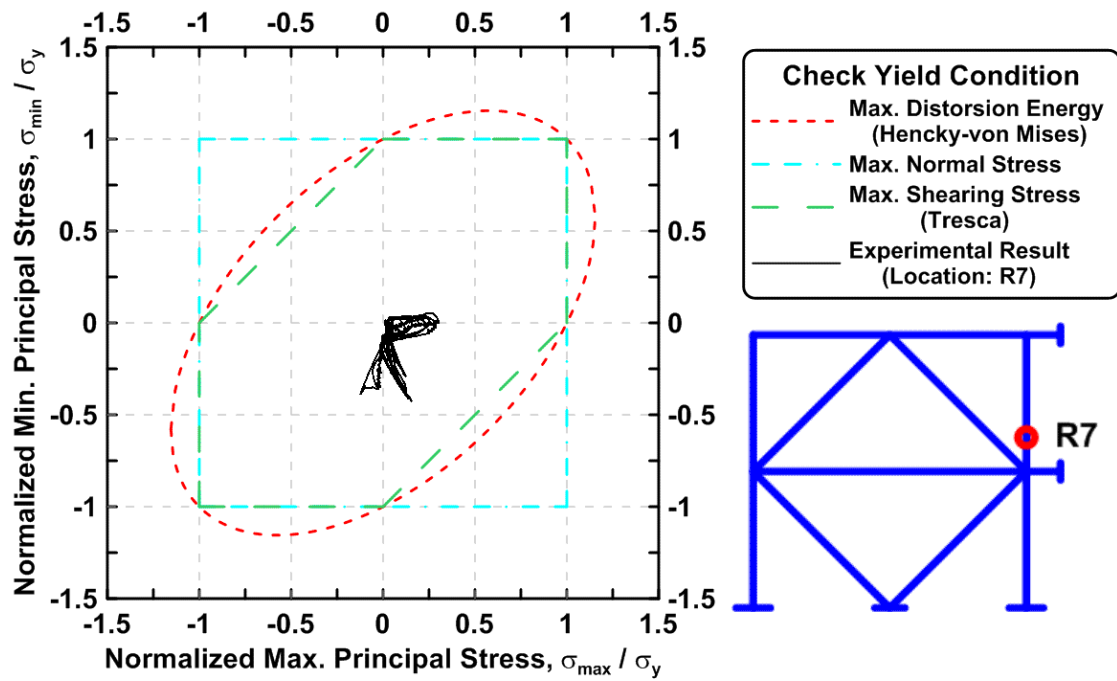


Figure 4.264 Specimen TCBF-B-3: maximum principal stress versus minimum principal stress in first-story column (location: R7).

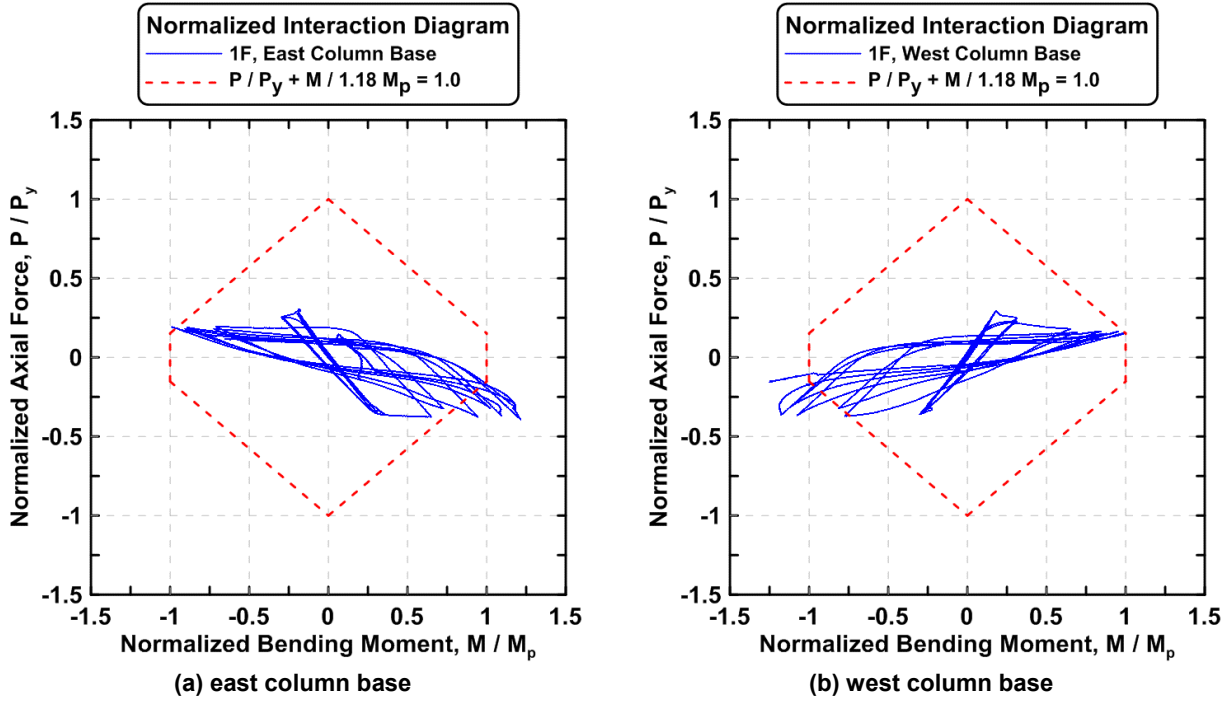


Figure 4.265 Specimen TCBF-B-3: normalized P-M interaction diagrams of first-story columns.

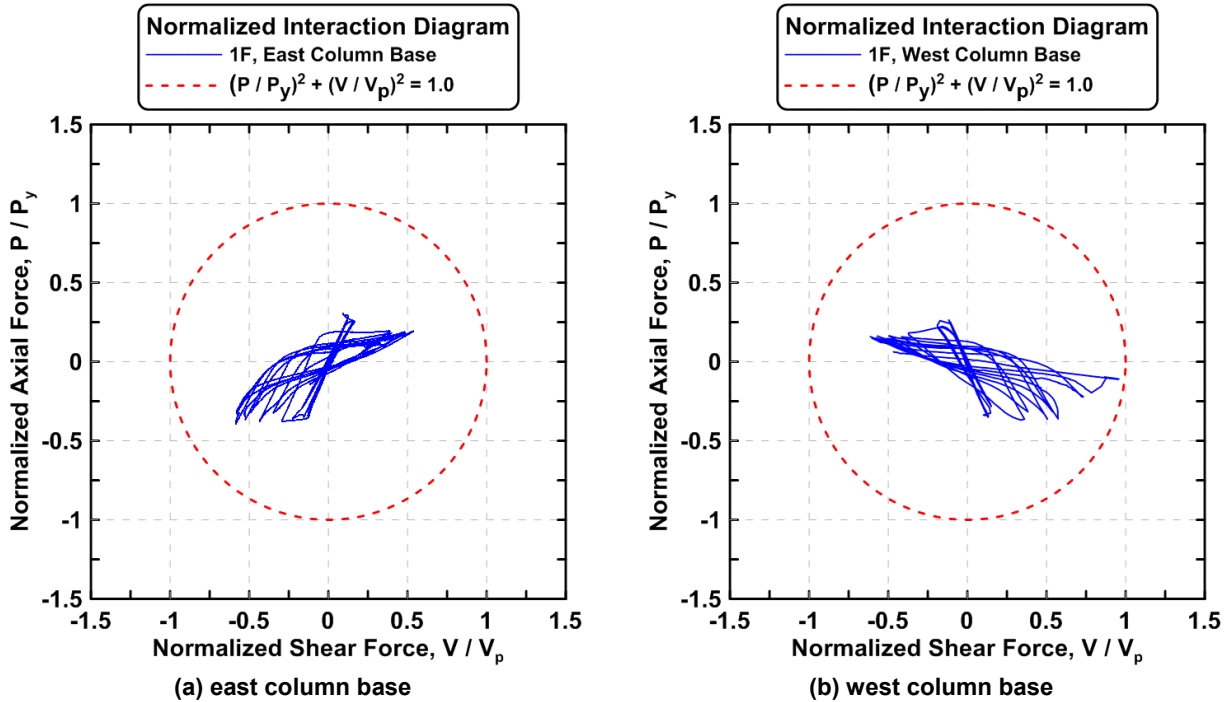


Figure 4.266 Specimen TCBF-B-3: normalized P-V interaction diagrams of first-story columns.

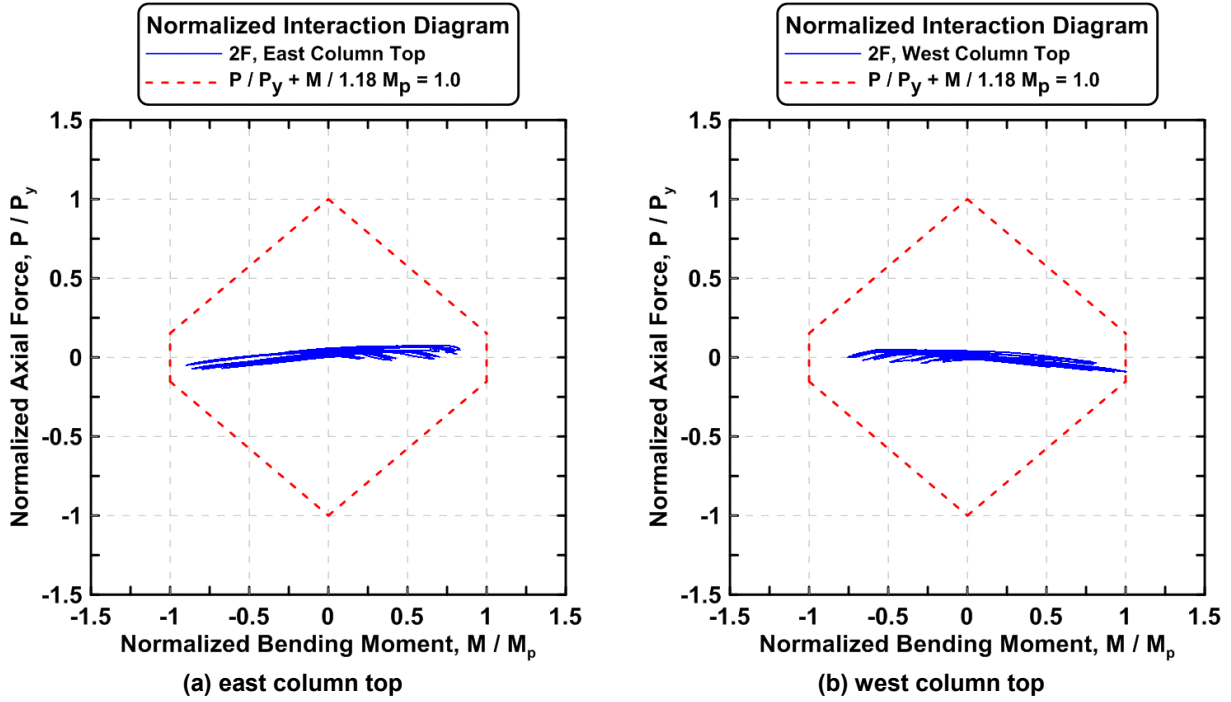


Figure 4.267 Specimen TCBF-B-3: normalized P-M interaction diagrams of second-story columns.

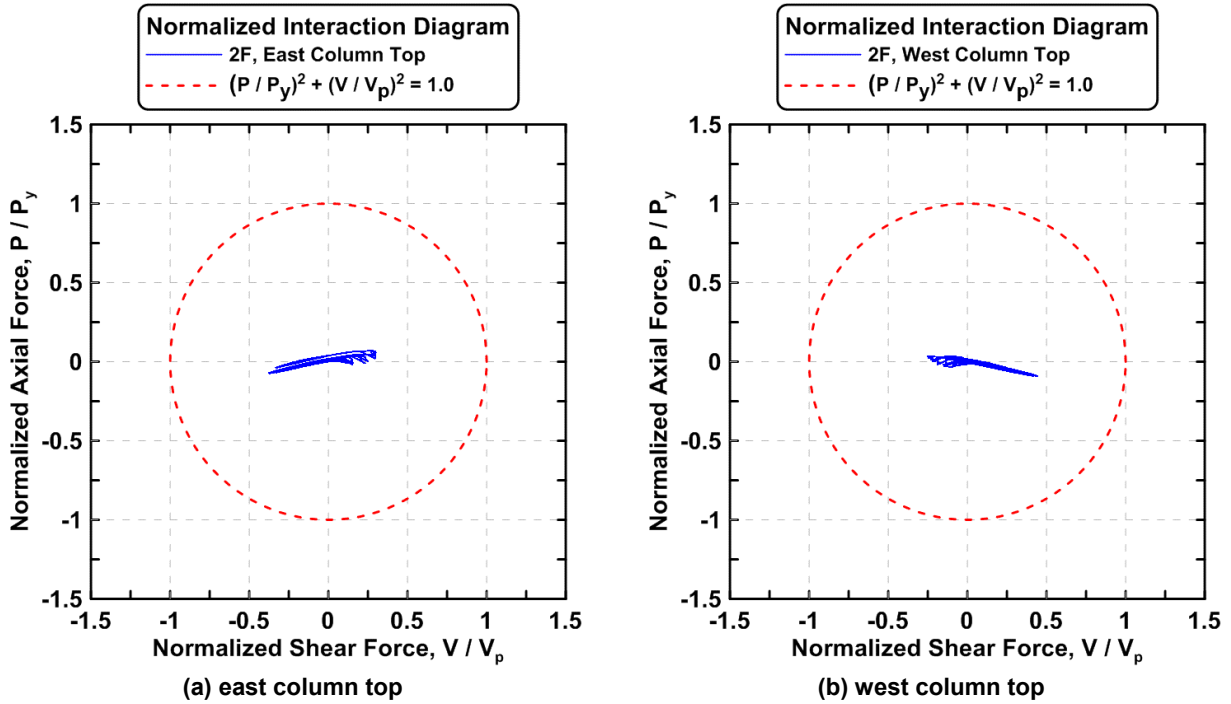


Figure 4.268 Specimen TCBF-B-3: normalized P-V interaction diagrams of second-story columns.

4.1.3.2.3 Beam Response

The vertical deflection time history at the center of W24 × 117 roof beam and W24 × 68 lower beam are plotted in Figure 4.269. The time history of strain readings at both ends of roof beam and lower beam are shown in Figures 4.270 and 4.271, respectively. Both beam axial force time histories derived from linear type strain gauges at different locations of the beams are plotted in Figures 4.272 and 4.273. The bending moment time histories of both beams are shown in Figures 4.274 and 4.275. Estimated beam shear force time histories are illustrated in Figures 4.276 and 4.277. Unbalanced force in the roof beam center is plotted in Figure 4.278.

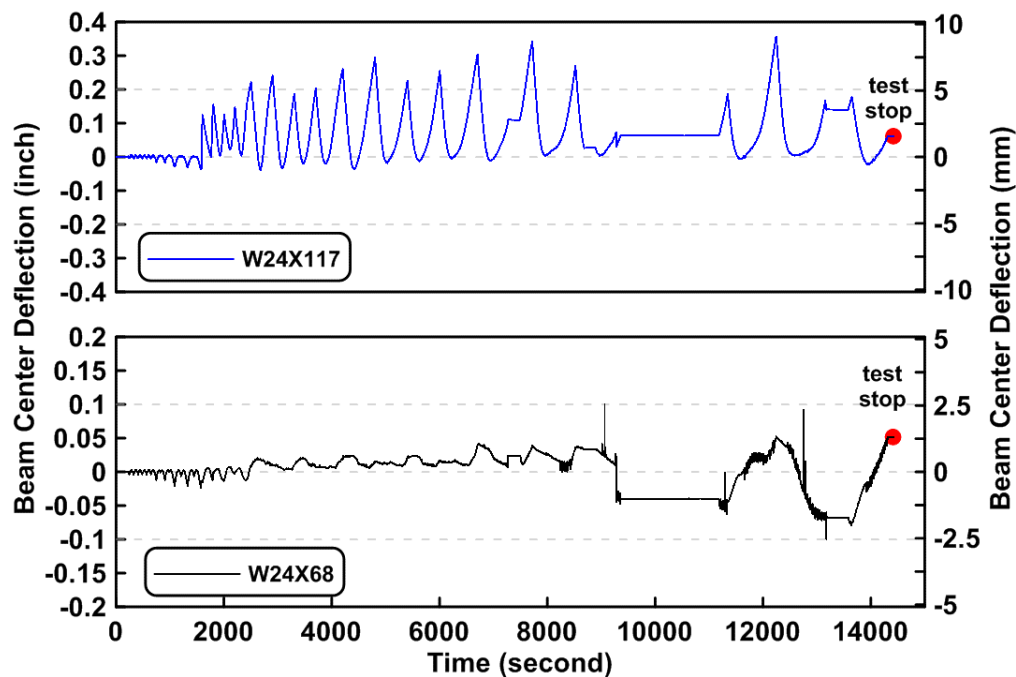


Figure 4.269 Specimen TCBF-B-3: deflection time history at center of beam span (roof beam: W24 × 117, lower beam: W24 × 68).

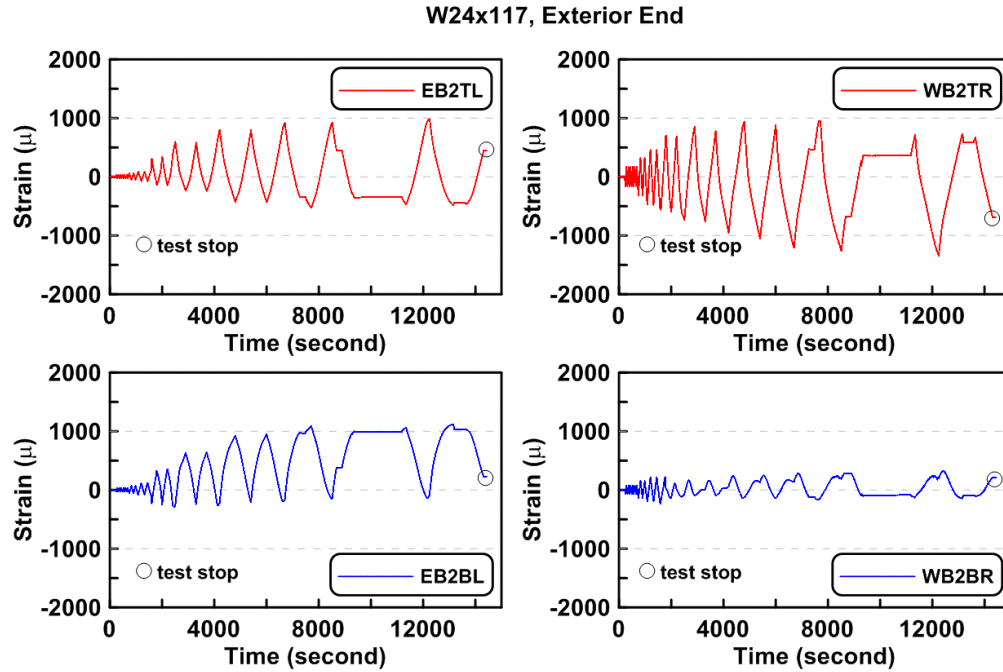


Figure. 4.270 Specimen TCBF-B-3: time history of strain readings at both exterior ends of W24 \times 117 roof beam.

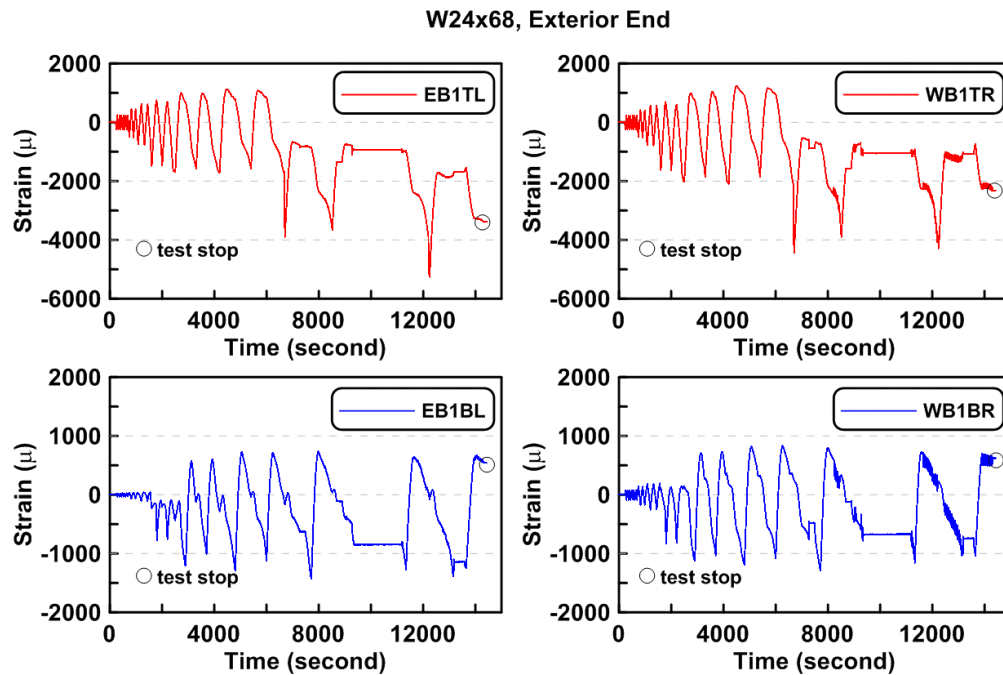


Figure. 4.271 Specimen TCBF-B-3: time history of strain readings at both exterior ends of W24 \times 68 lower beam.

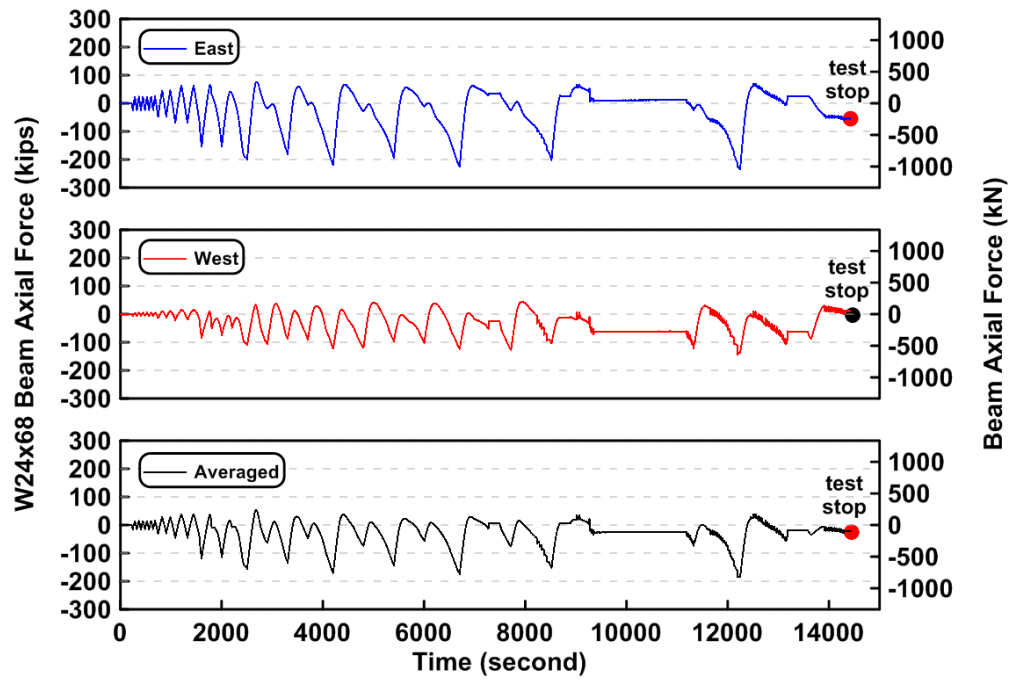


Figure 4.272 Specimen TCBF-B-3: time history of lower beam axial forces.

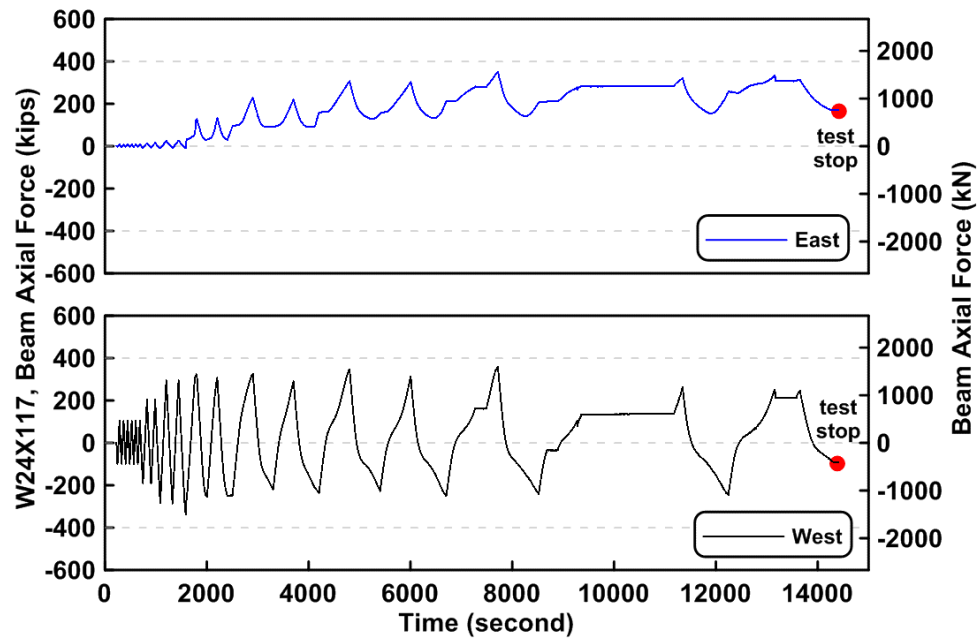


Figure 4.273 Specimen TCBF-B-3: time history of roof beam axial forces.

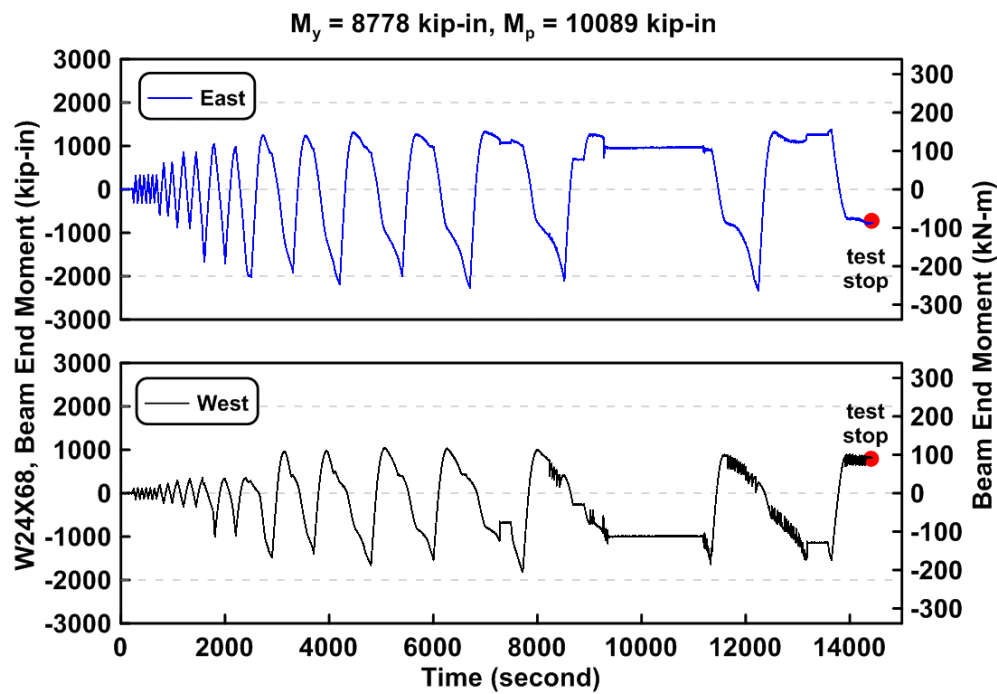


Figure 4.274 Specimen TCBF-B-3: time history of the lower beam end bending moment.

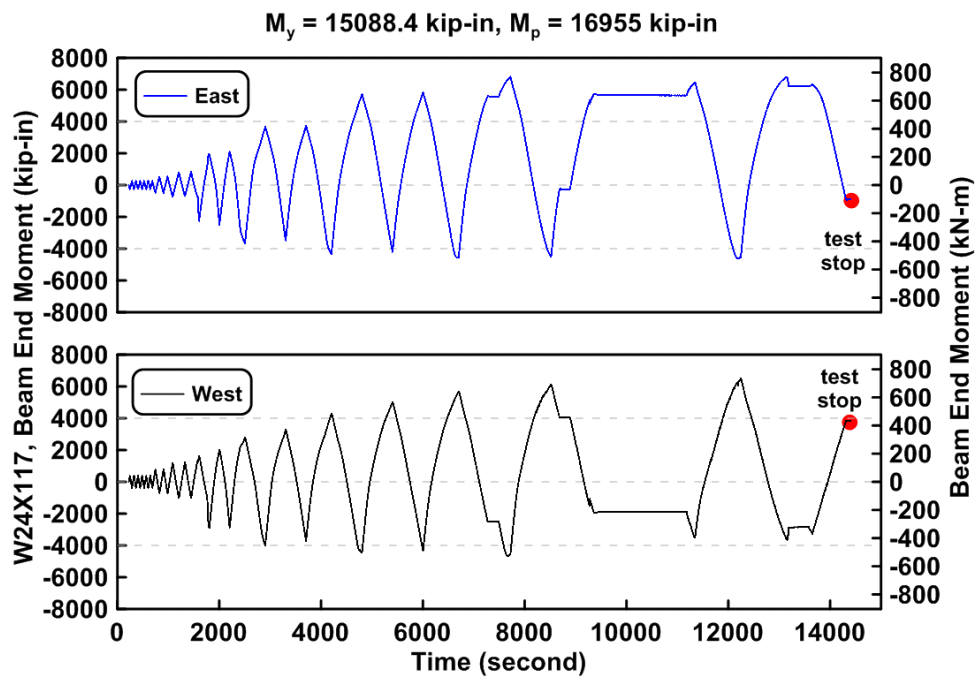


Figure 4.275 Specimen TCBF-B-3: time history of roof beam end bending moment.

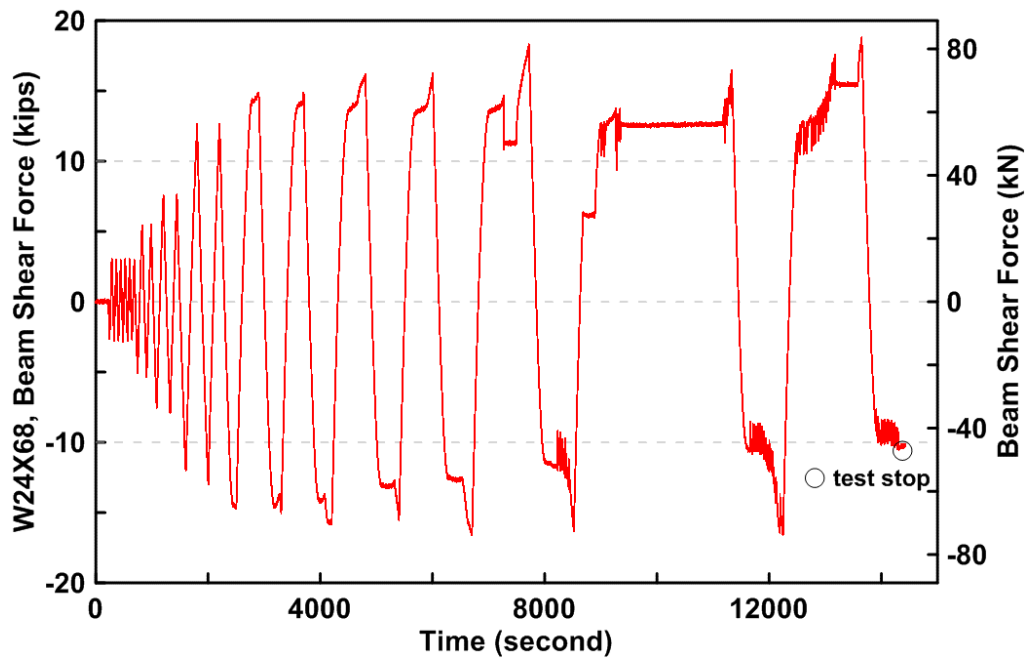


Figure 4.276 Specimen TCBF-B-3: lower beam estimated shear force time history.

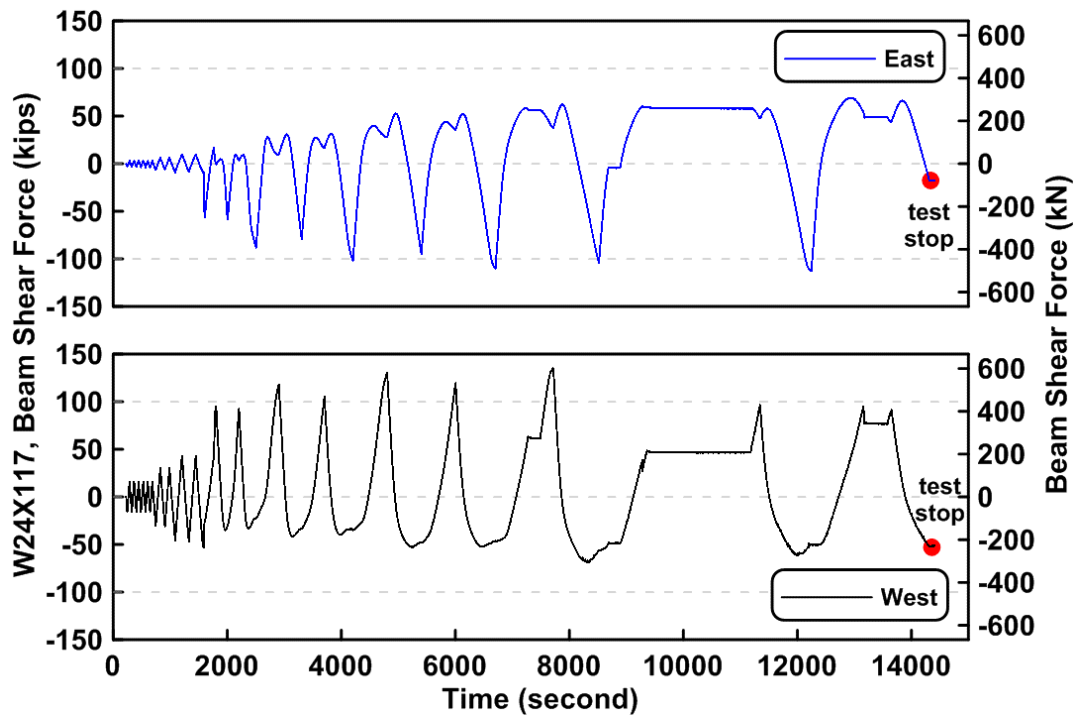


Figure 4.277 Specimen TCBF-B-3: roof beam estimated shear force time history.

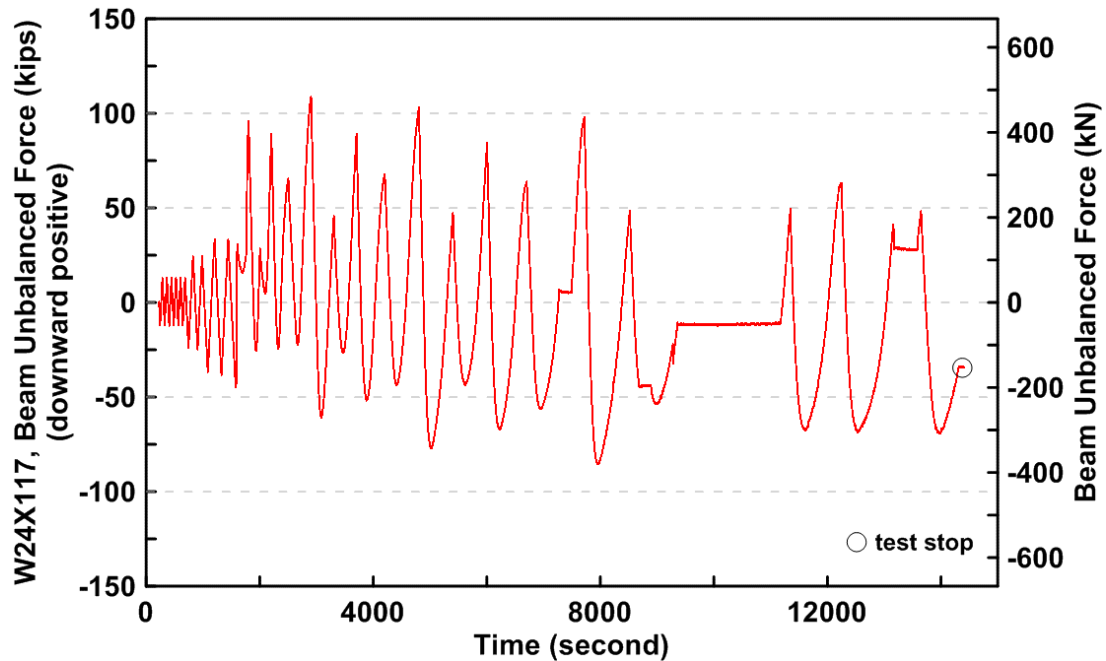


Figure 4.278 Specimen TCBF-B-3: estimated unbalanced force time history of roof beam.

4.1.3.2.4 Brace Response

The estimated brace axial forces versus brace axial deformations for each wide flange braces are shown in Figure 4.279. The estimated brace axial forces versus measured brace out-of-plane displacements at the brace center point for each wide flange brace are shown in Figure 4.280. Combined brace axial force, axial deformation, and out-of-plane displacement relationships are shown in Figure 4.281. The decomposed strain [axial strain, in-plane bending strain, out-of-plane bending strain, and warping strain; definition of strain components are similar to that shown in Figure 4.62(b)] time histories of each brace are plotted in Figures 4.282 to 4.285.

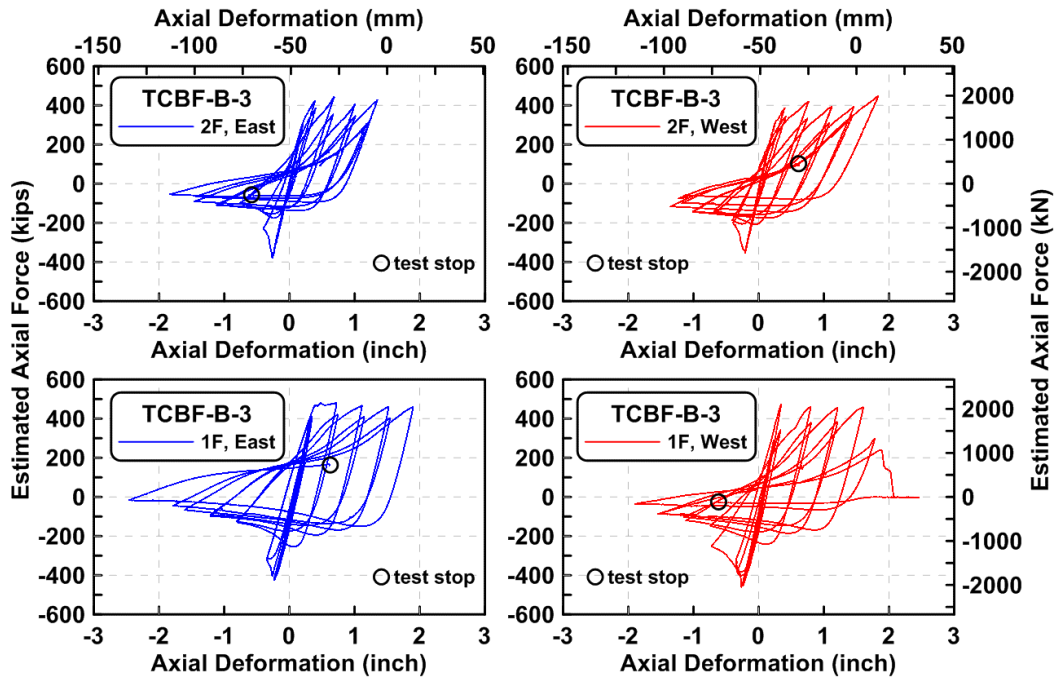


Figure 4.279 Specimen TCBF-B-3: estimated brace axial forces versus brace axial deformations.

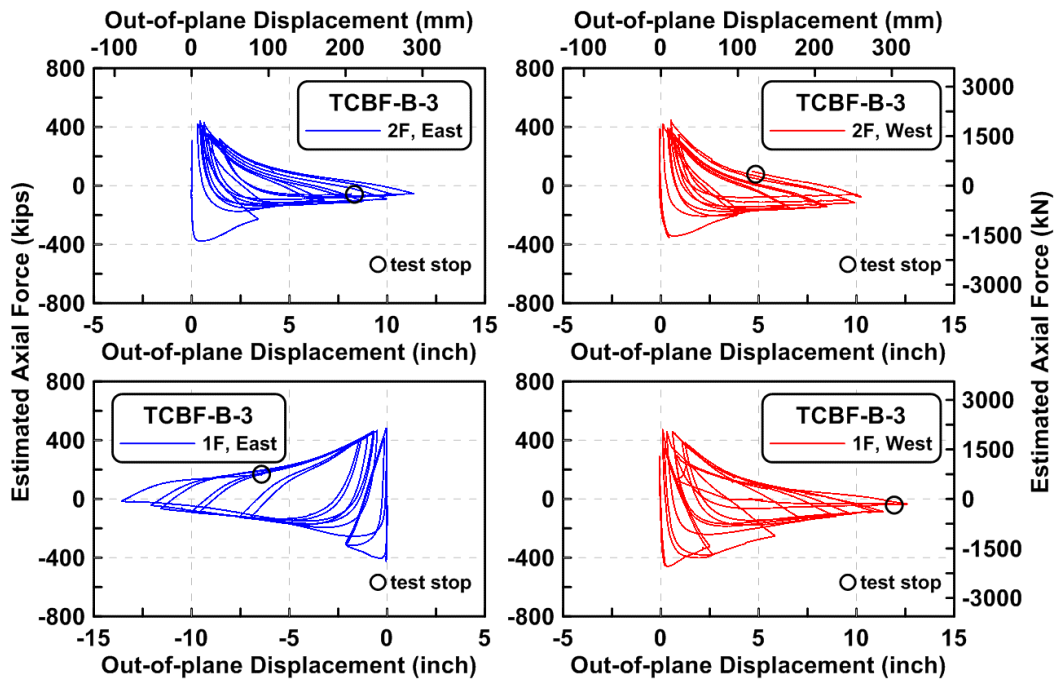


Figure 4.280 Specimen TCBF-B-3: estimated brace axial forces versus measured brace out-of-plane displacements at brace center point of each WF brace.

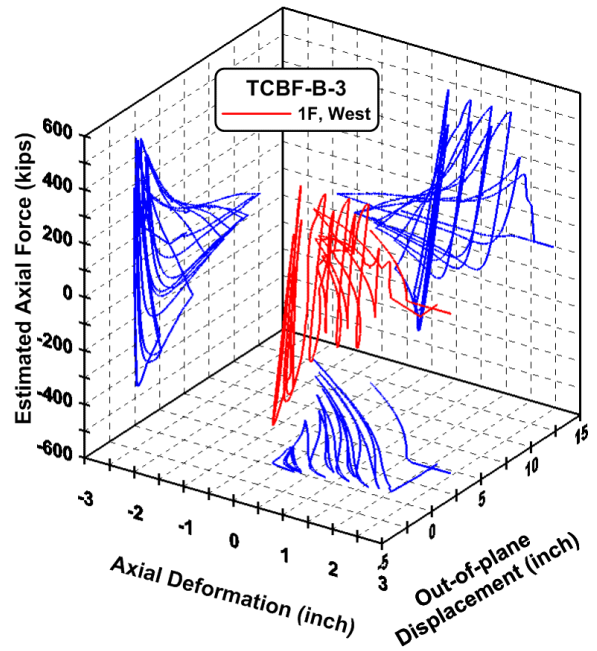
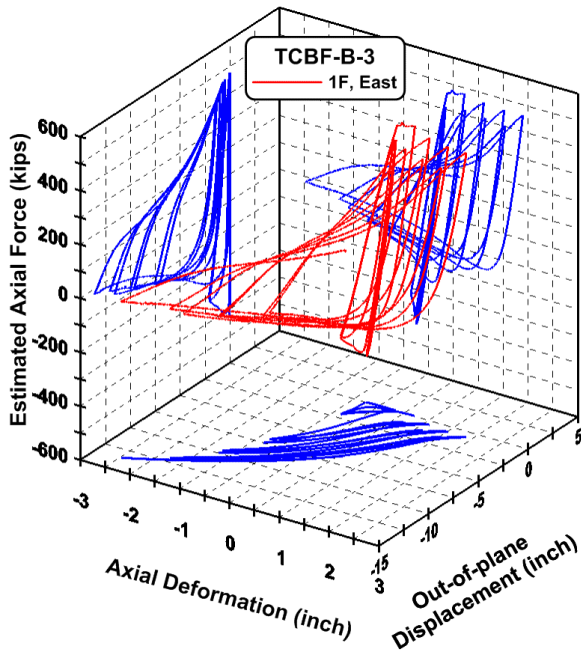
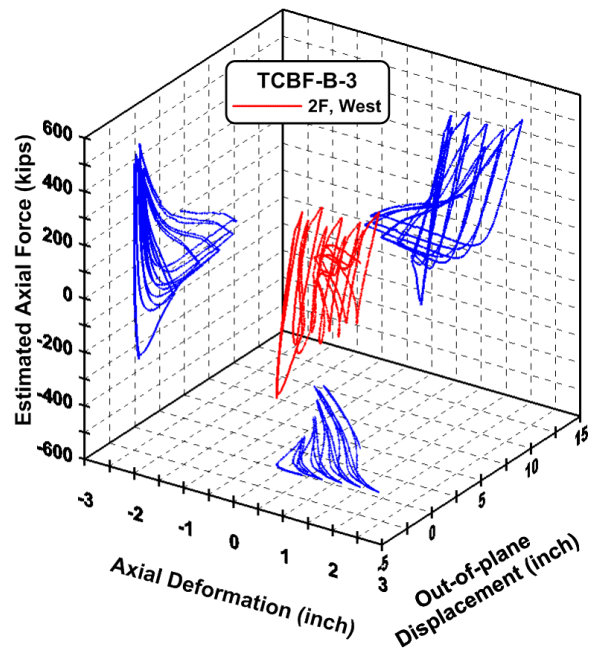
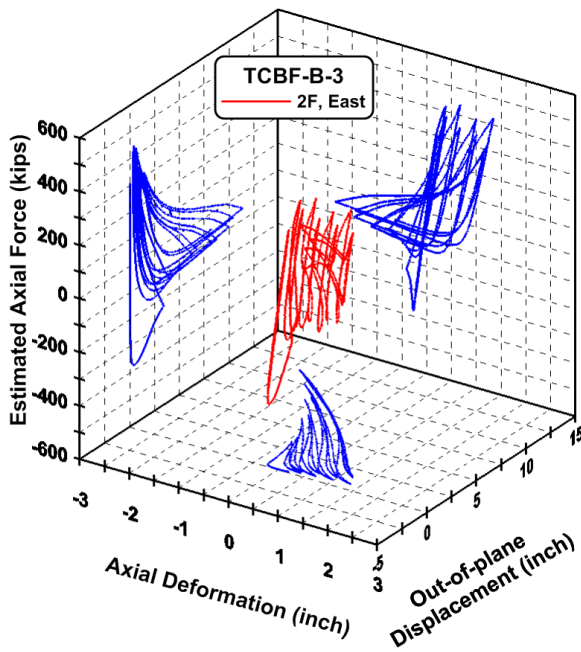


Figure 4.281 Specimen TCBF-B-3: estimated brace axial force, brace axial deformation, and measured brace out-of-plane displacement relationships.

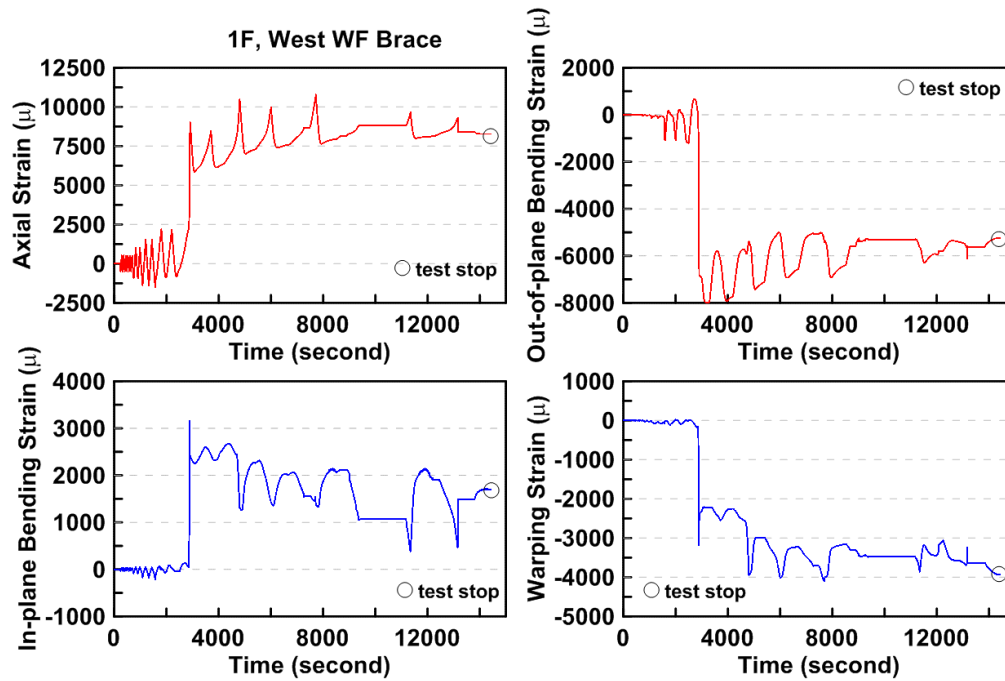


Figure 4.282 Specimen TCBF-B-3: time history of the decomposed strain components of first-story eastern-side wide flange brace.

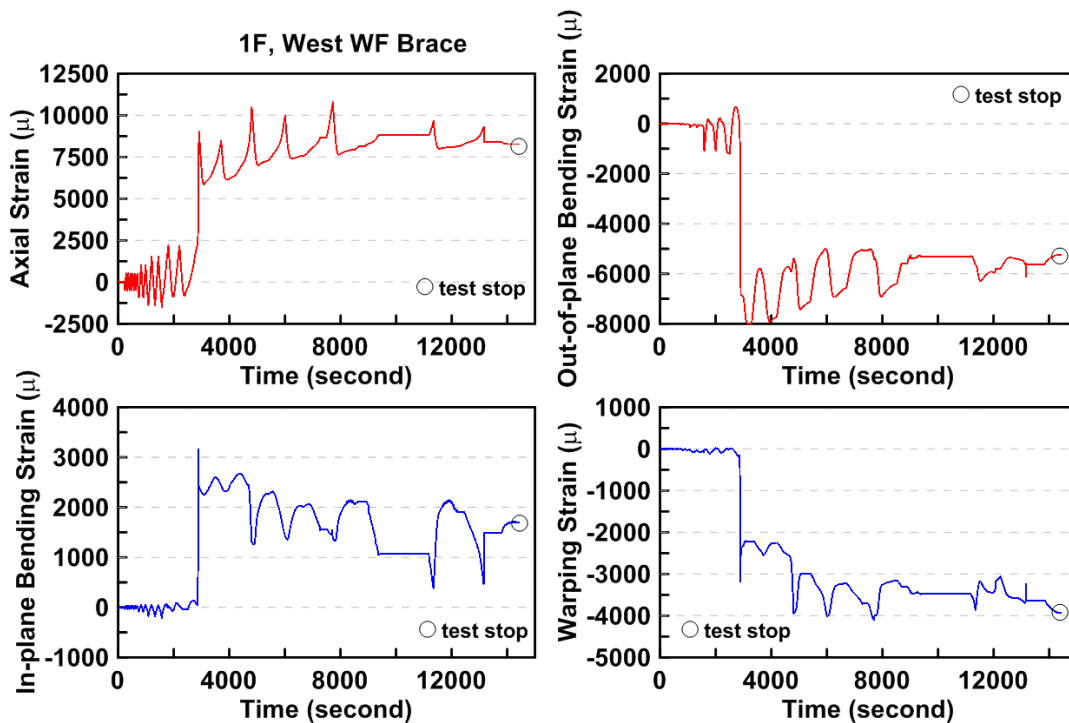


Figure 4.283 Specimen TCBF-B-3: time history of the decomposed strain components of first-story western-side wide flange brace.

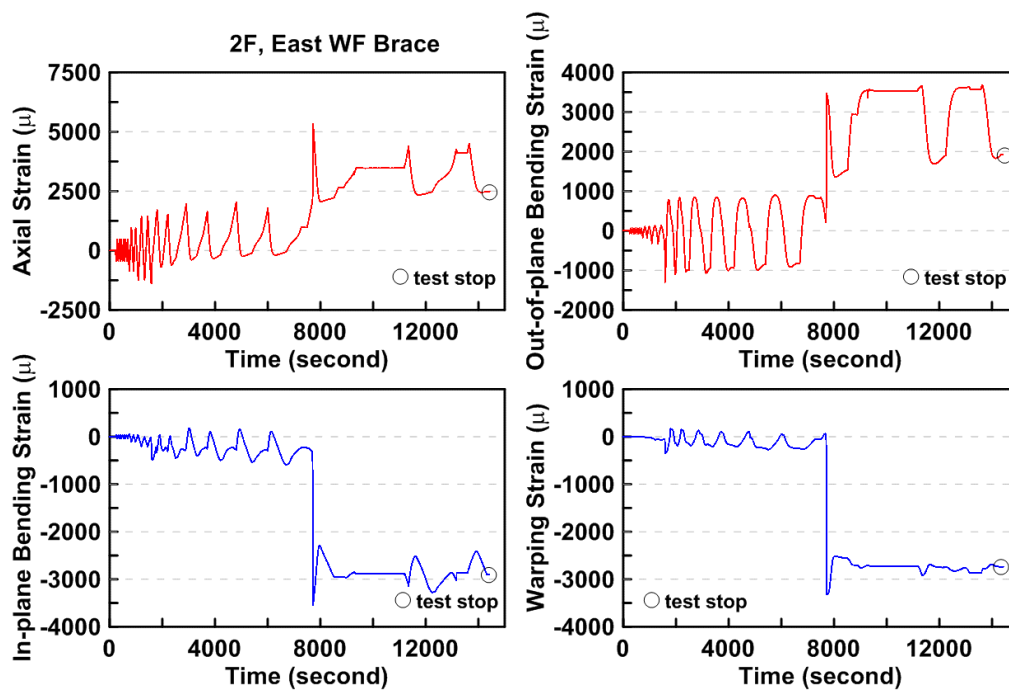


Figure 4.284 Specimen TCBF-B-3: time history of the decomposed strain components of second-story eastern-side wide flange brace.

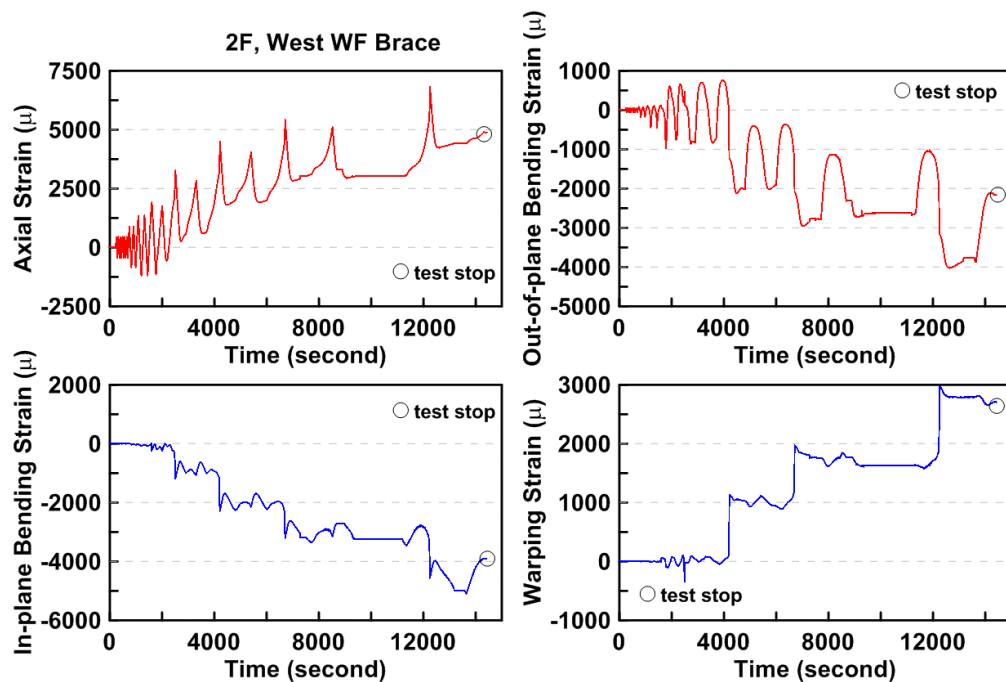


Figure 4.285 Specimen TCBF-B-3: time history of the decomposed strain components of second-story western-side wide flange brace.

4.1.3.2.5 Panel Zone Response

Estimated panel zone shear stress versus measured panel zone shear strain relationship for four locations are plotted in Figure 4.286. The time history of derived rosette-type strain gauge readings in the panel zone area at each story are shown in Figures 4.287 to 4.290. Normalized maximum and minimum principal stress relationships along with different yield criteria for the panel zone regions are plotted in Figures 4.291 to 4.294.

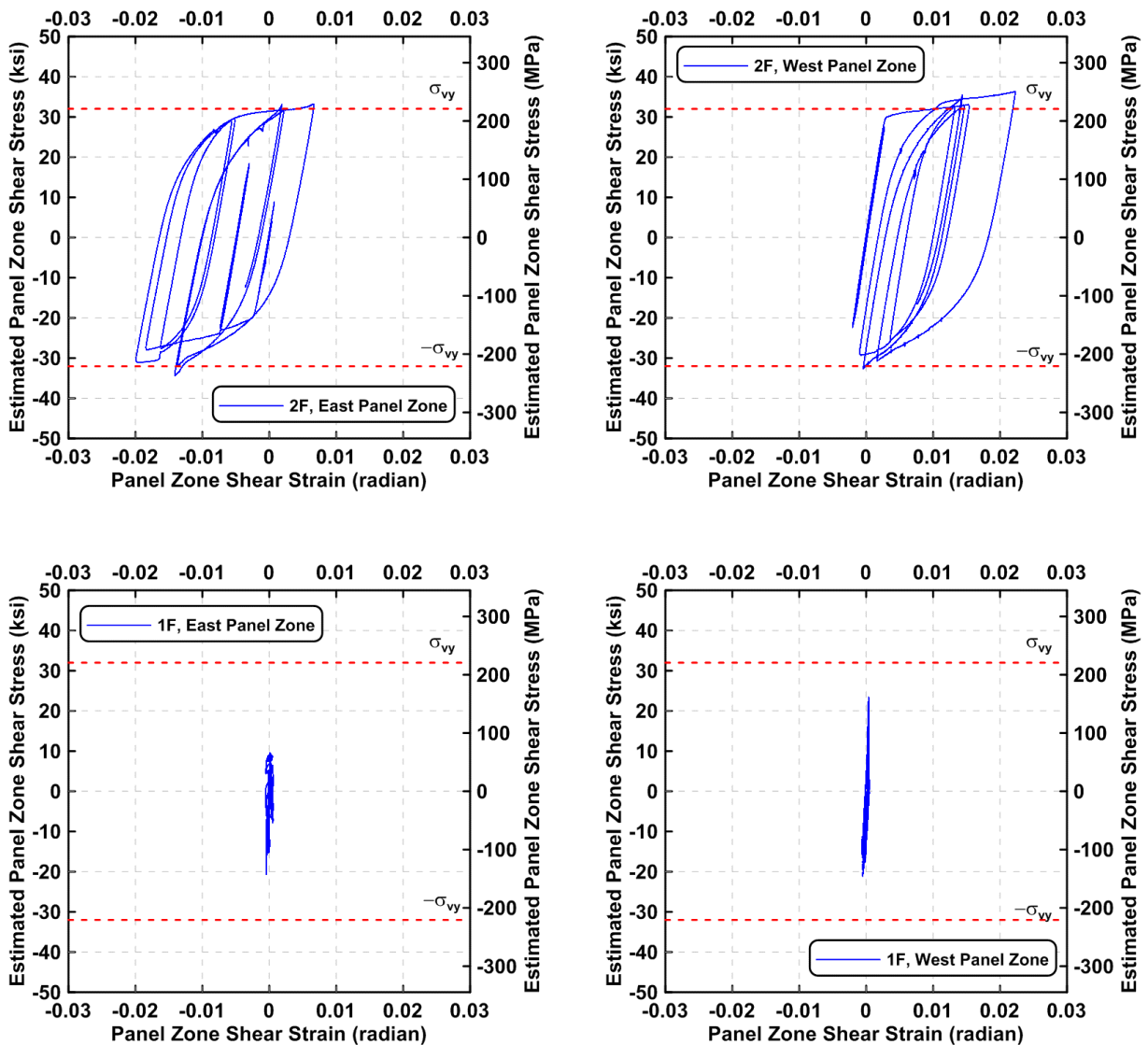


Figure 4.286 Specimen TCBF-B-3: estimated panel zone shear stress versus shear strain relationships.

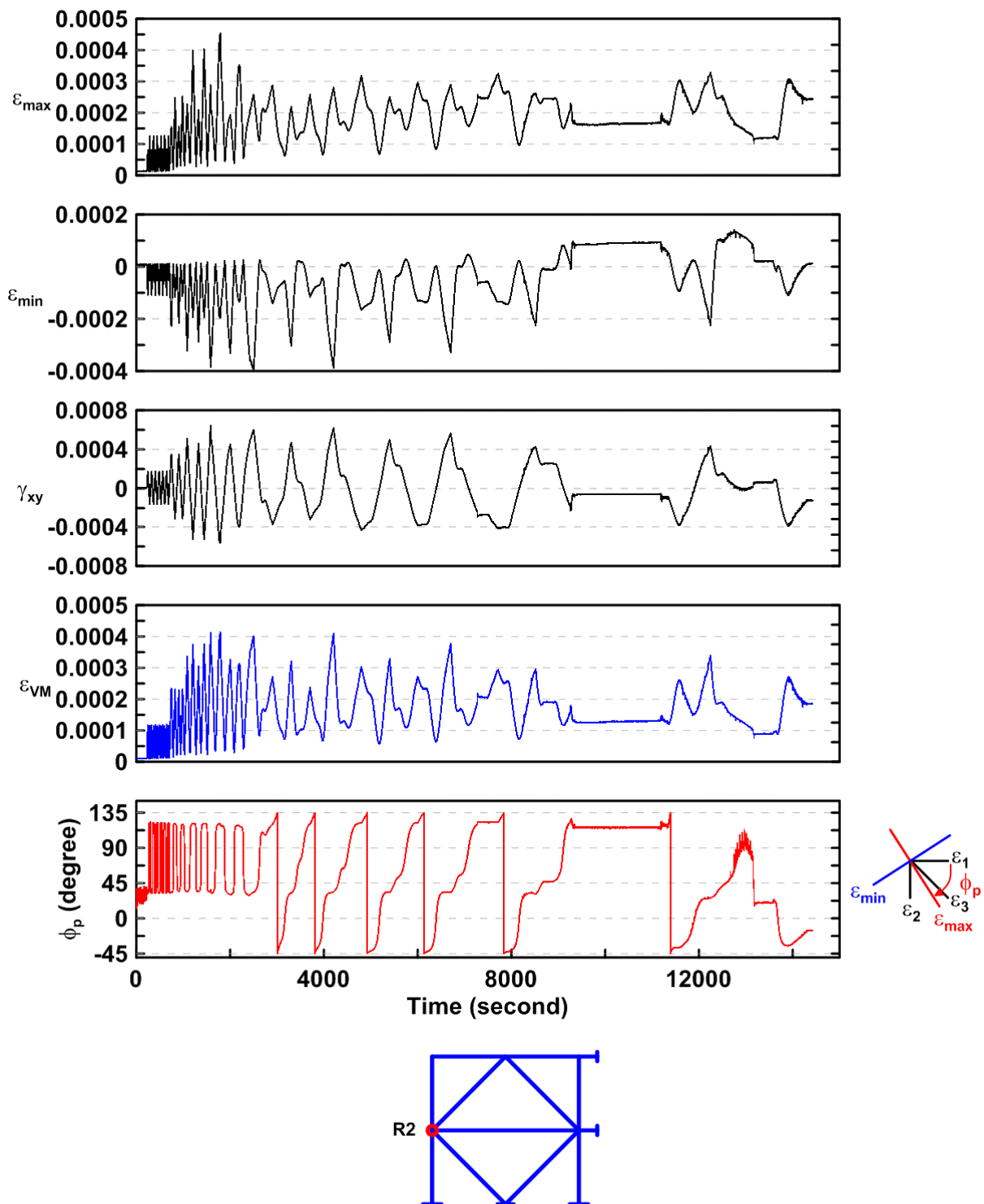


Figure 4.287 Specimen TCBF-B-3, lower panel zone: time history of rosette-type strain gauge readings (location: R2).

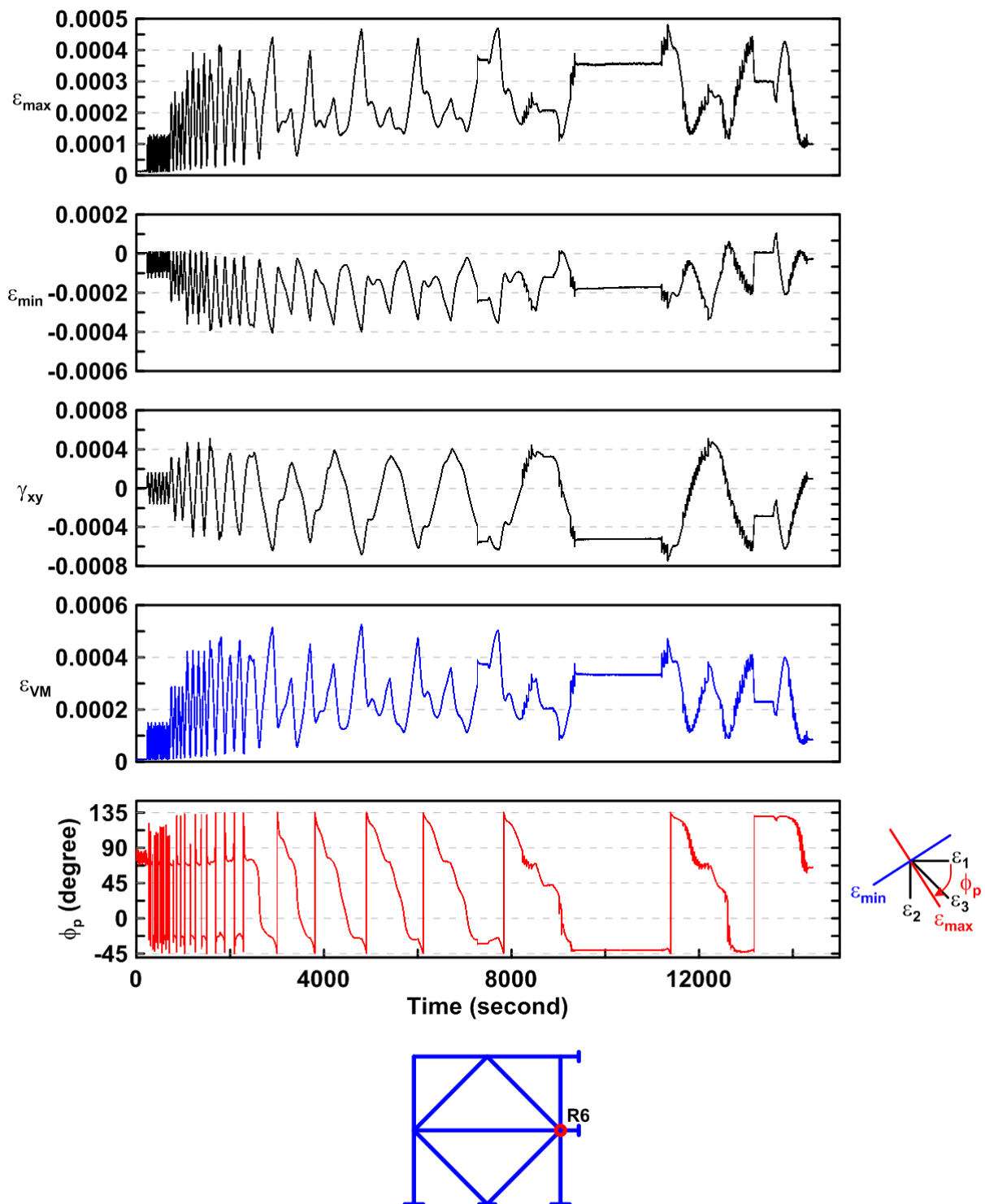


Figure 4.288 Specimen TCBF-B-3, lower panel zone: time history of rosette-type strain gauge readings (location: R6).

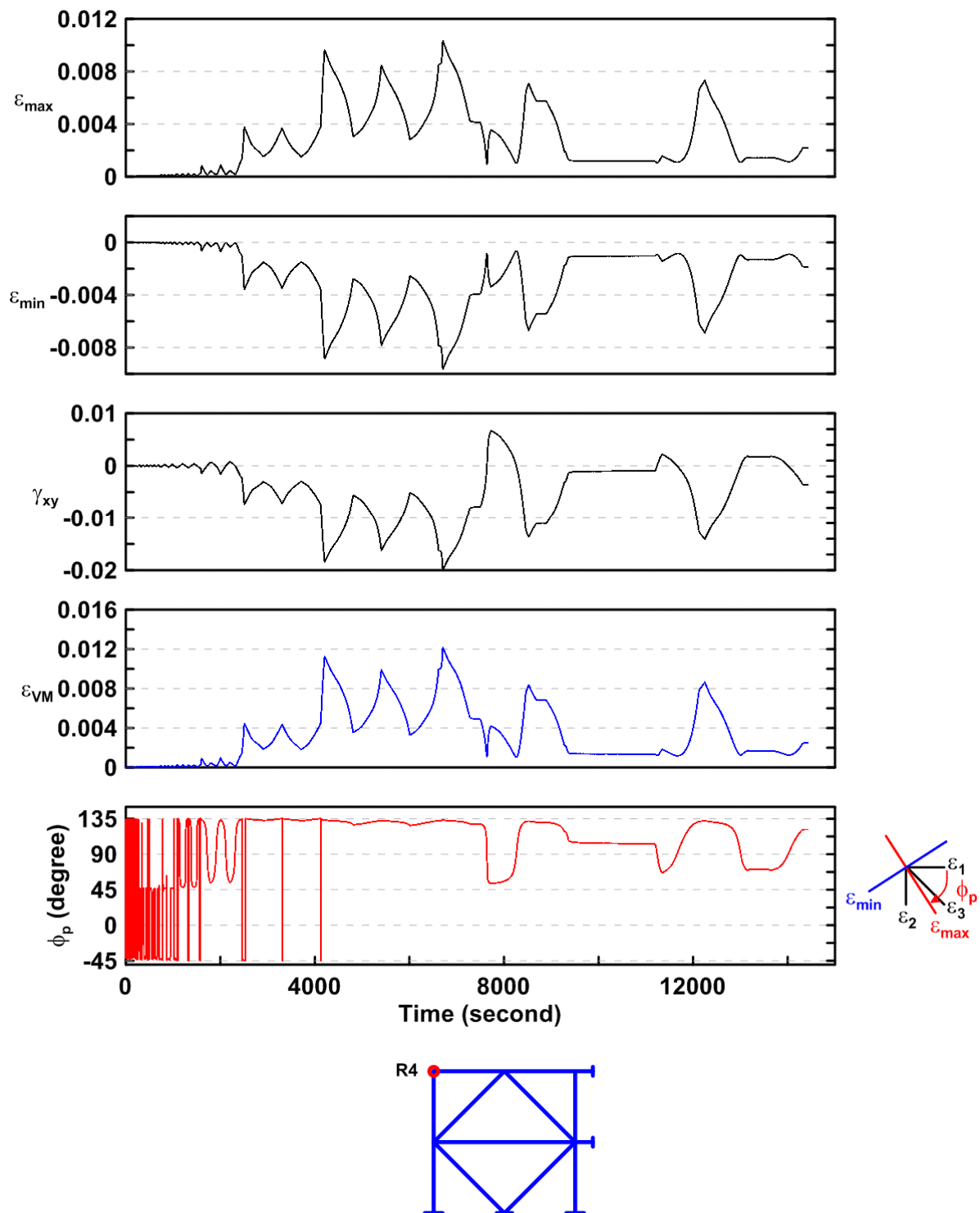


Figure 4.289 Specimen TCBF-B-3, roof panel zone: time history of rosette-type strain gauge readings (location: R4).

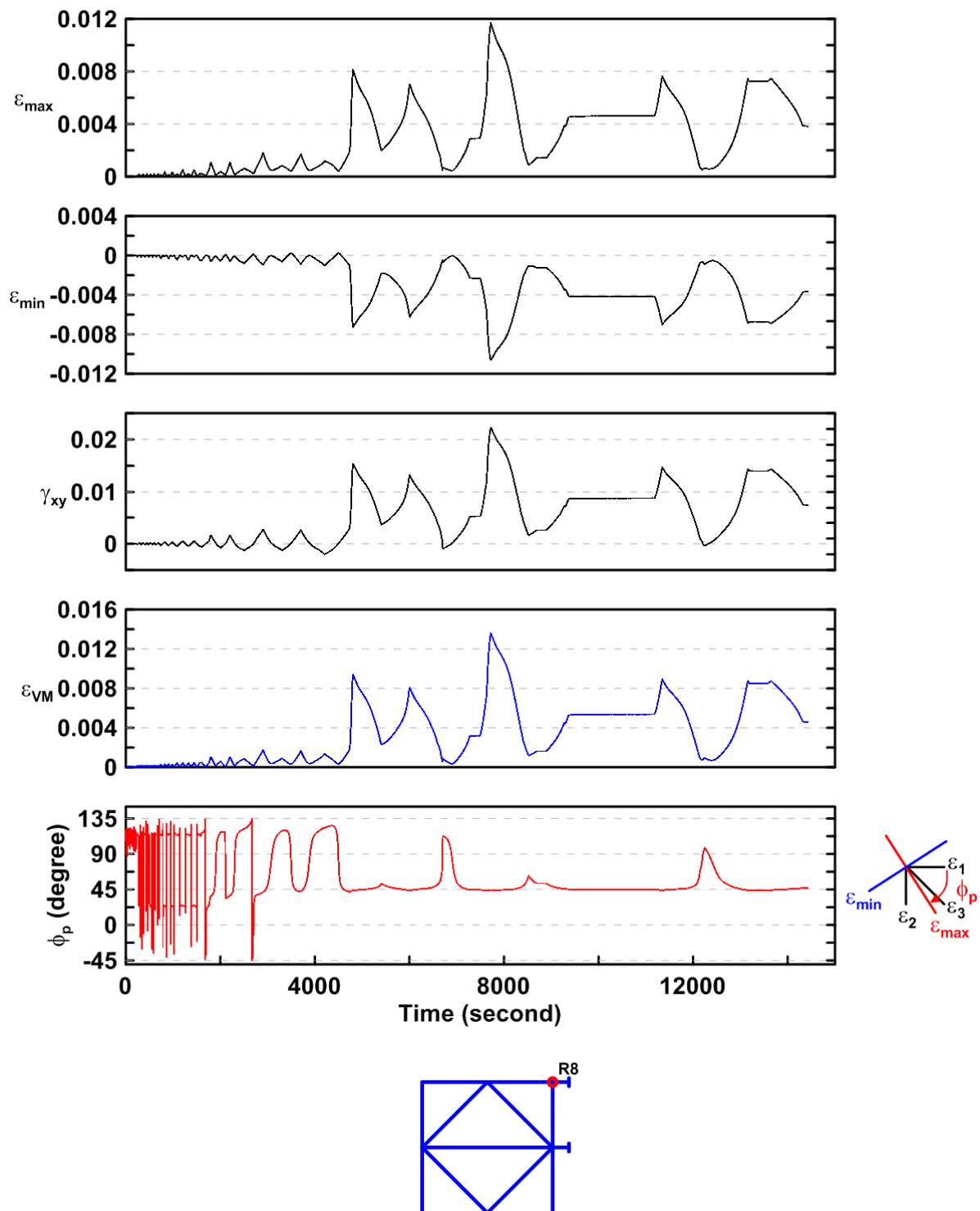


Figure 4.290 Specimen TCBF-B-3, roof panel zone: time history of rosette-type strain gauge readings (location: R8).

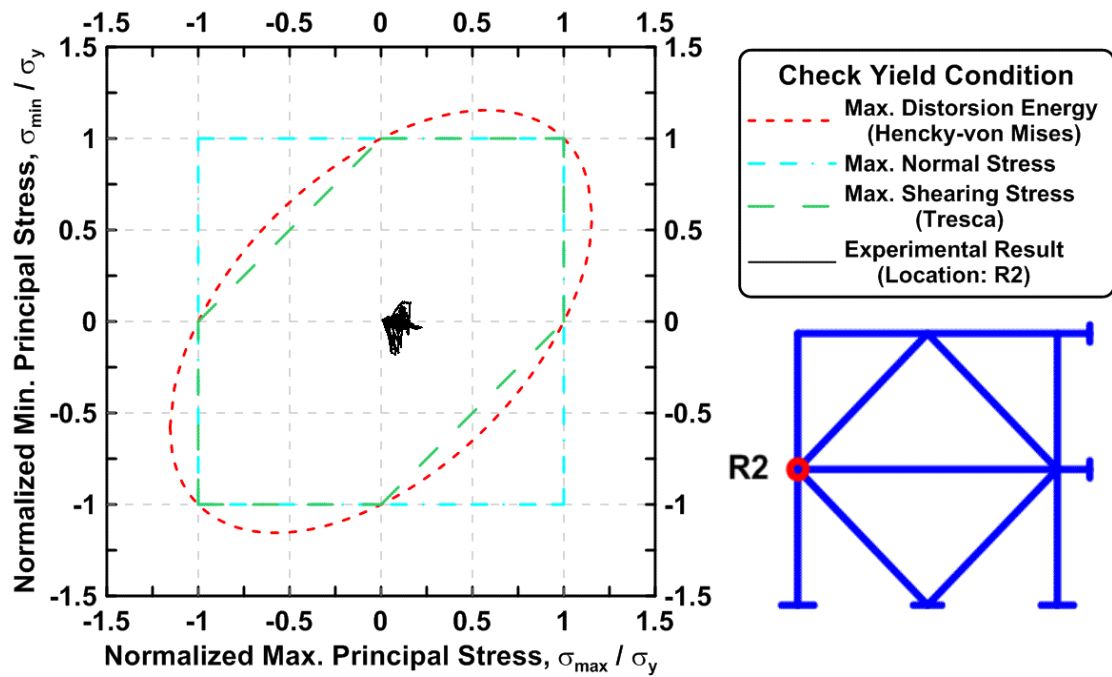


Figure 4.291 Specimen TCBF-B-3, lower panel zone: normalized maximum principal stress versus normalized minimum principal stress (location: R2).

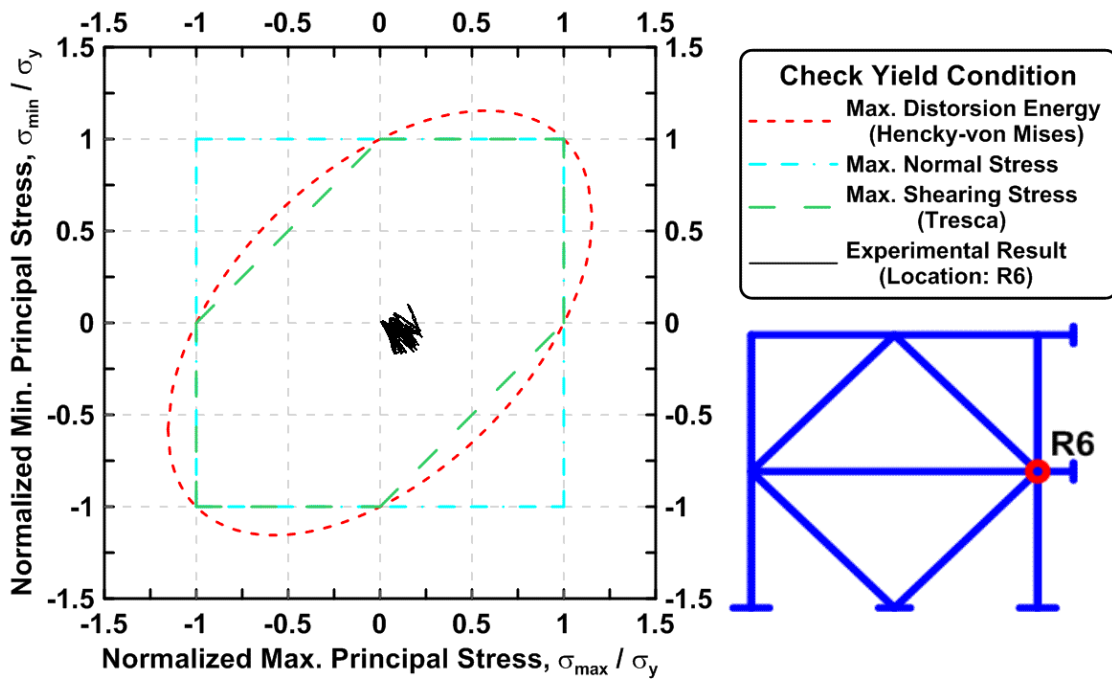


Figure 4.292 Specimen TCBF-B-3, lower panel zone: normalized maximum principal stress versus normalized minimum principal stress (location: R6).

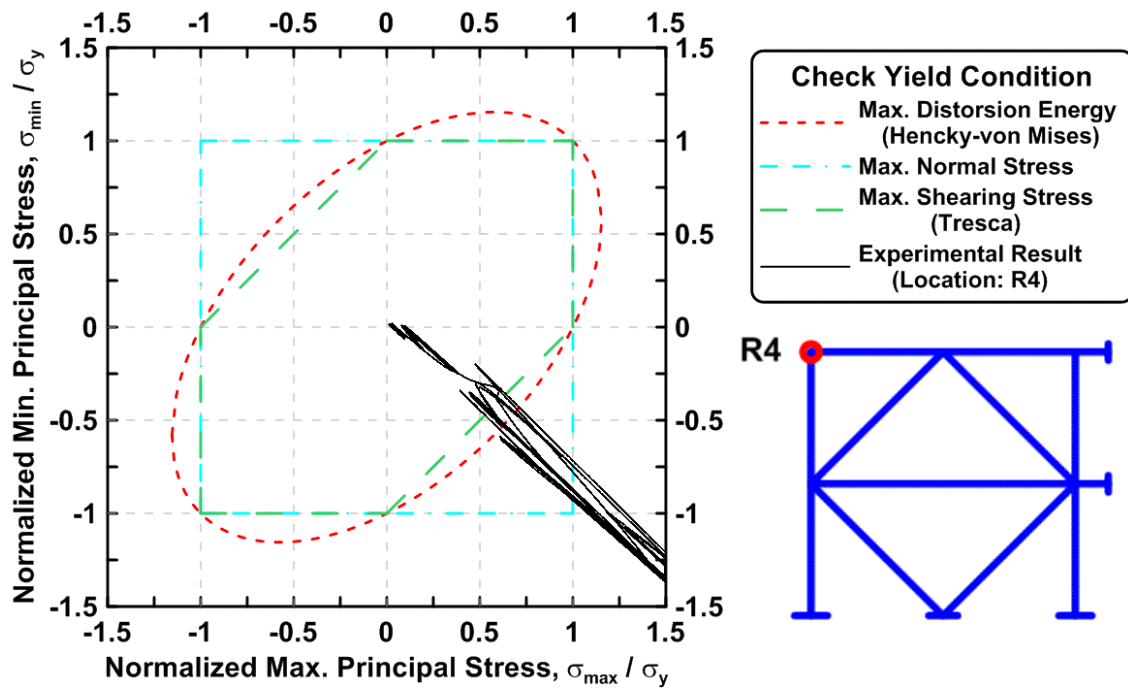


Figure 4.293 Specimen TCBF-B-3, roof panel zone: normalized maximum principal stress versus normalized minimum principal stress (location: R4).

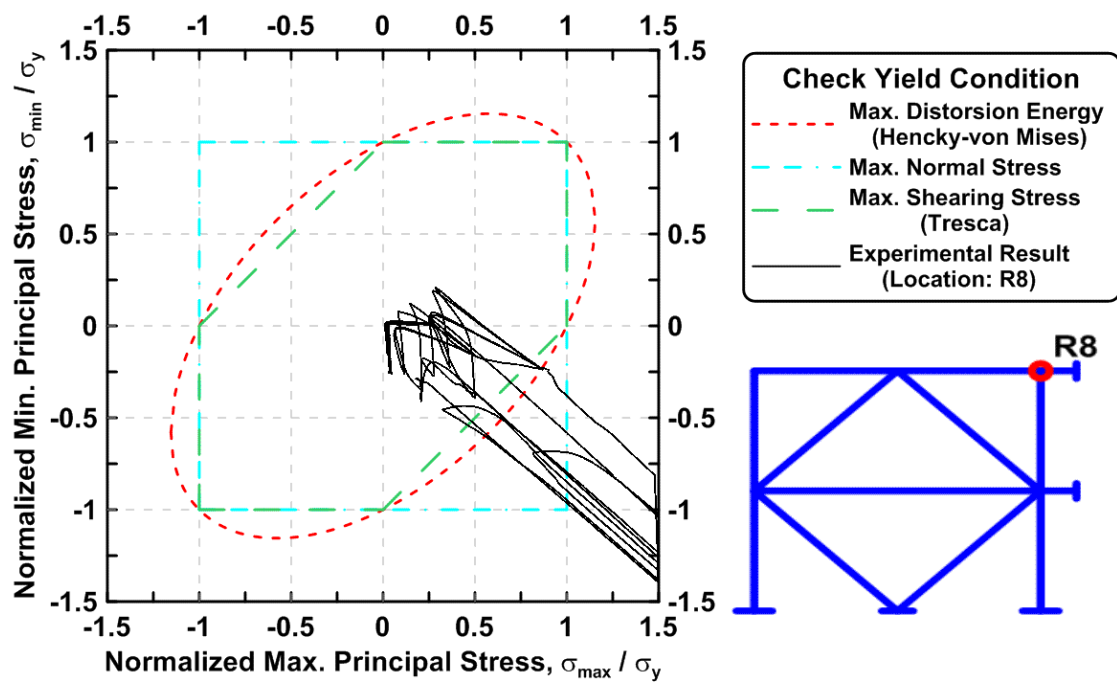


Figure 4.294 Specimen TCBF-B-3, roof panel zone: normalized maximum principal stress versus normalized minimum principal stress (location: R8).

4.1.3.2.6 Gusset Plate Response

The time history of derived rosette-type strain gauge readings in the 3/4-in.-thick one-piece gusset plate is shown in Figures 4.295 to 4.306. Normalized maximum and minimum principal stress relationships along with different yield criteria for the rosettes on the gusset plate are plotted in Figures 4.307 to 4.318. The averaged axial strain and bending strain time history in the tapered gusset plate at eastern side of the specimen are shown in Figures 4.319 and 4.320, respectively.

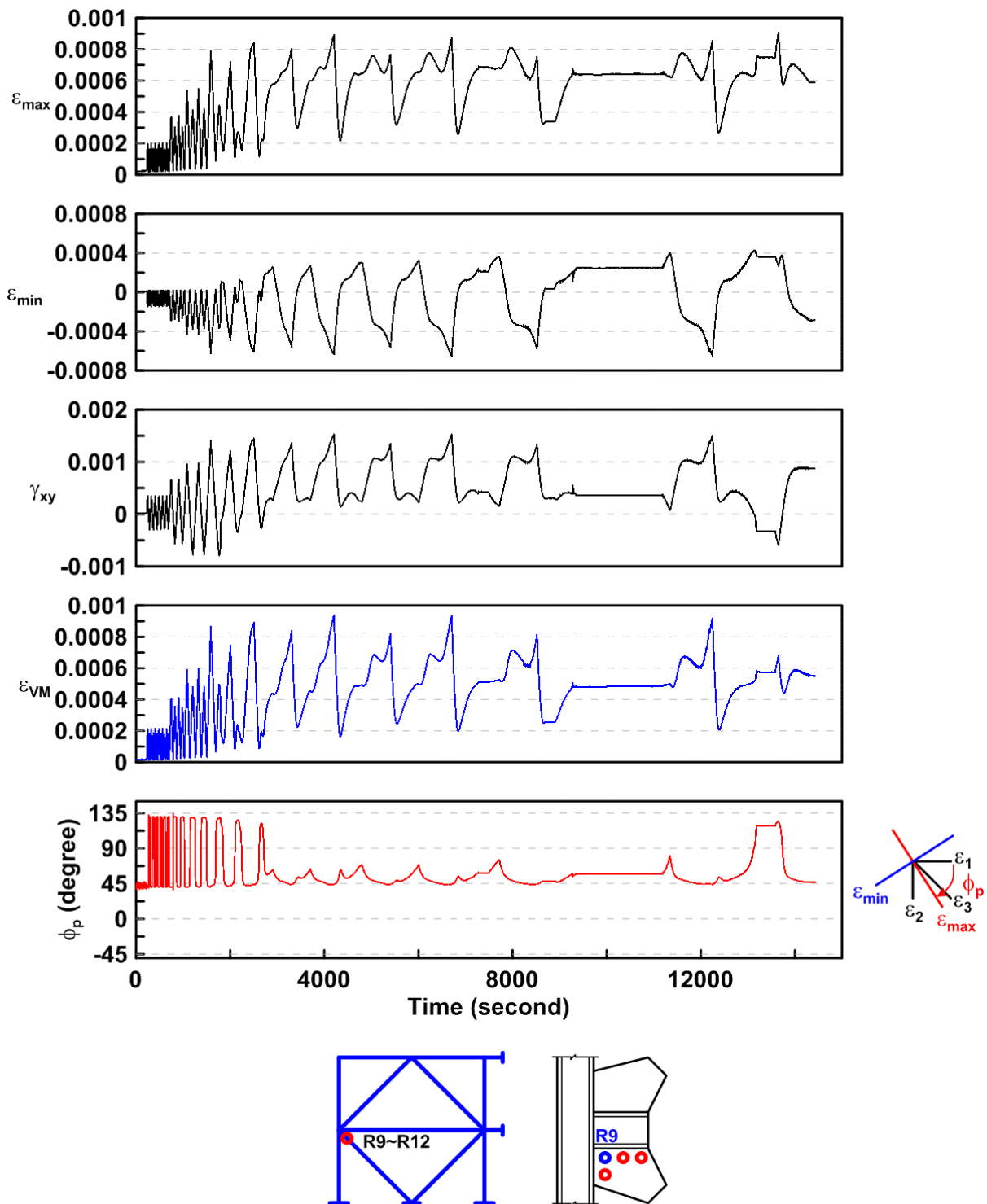


Figure 4.295 Specimen TCBF-B-3: time history of rosette-type strain gauge readings in one-piece gusset plate (location: R9).

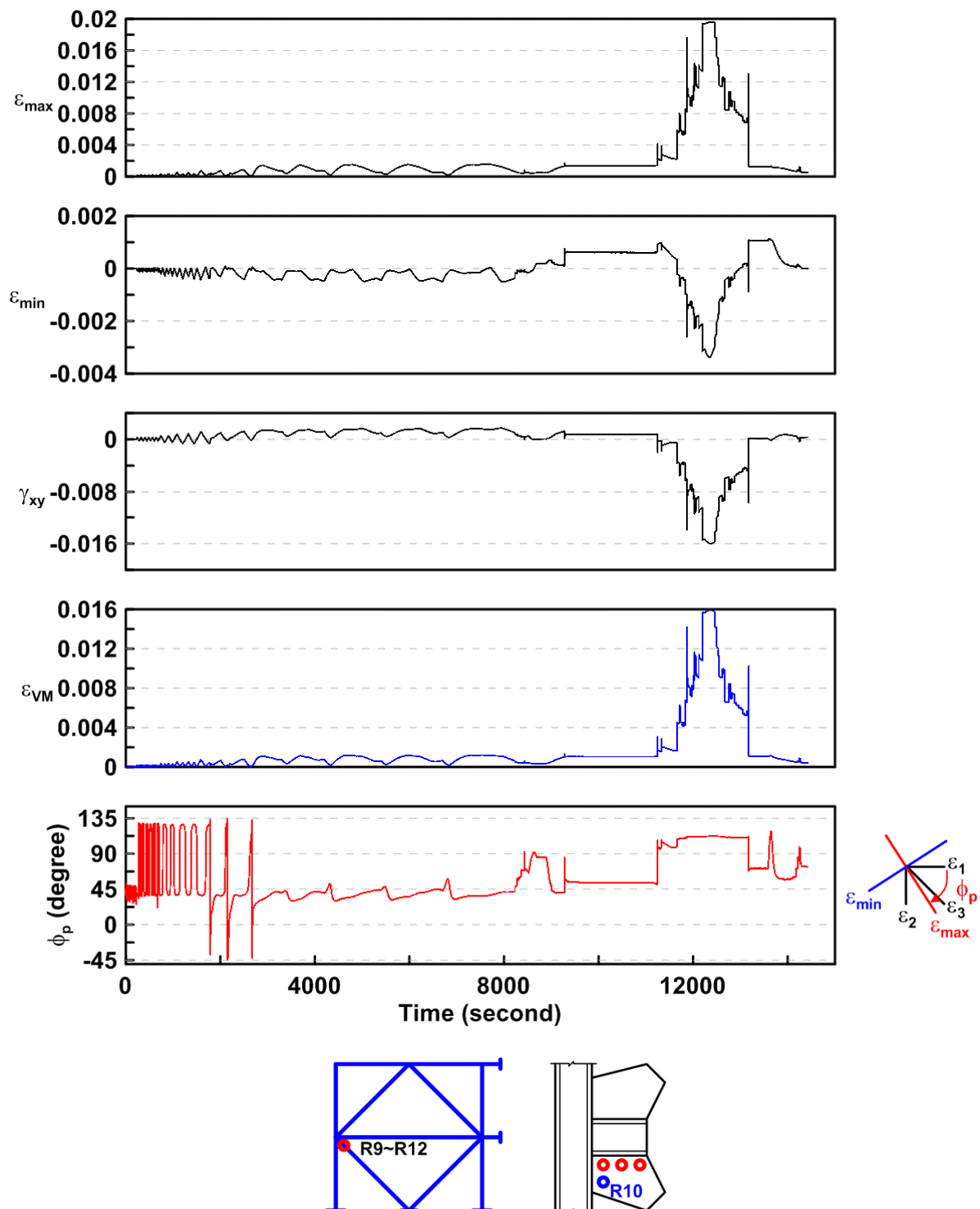


Figure 4.296 Specimen TCBF-B-3: time history of rosette-type strain gauge readings in one-piece gusset plate (location: R10).

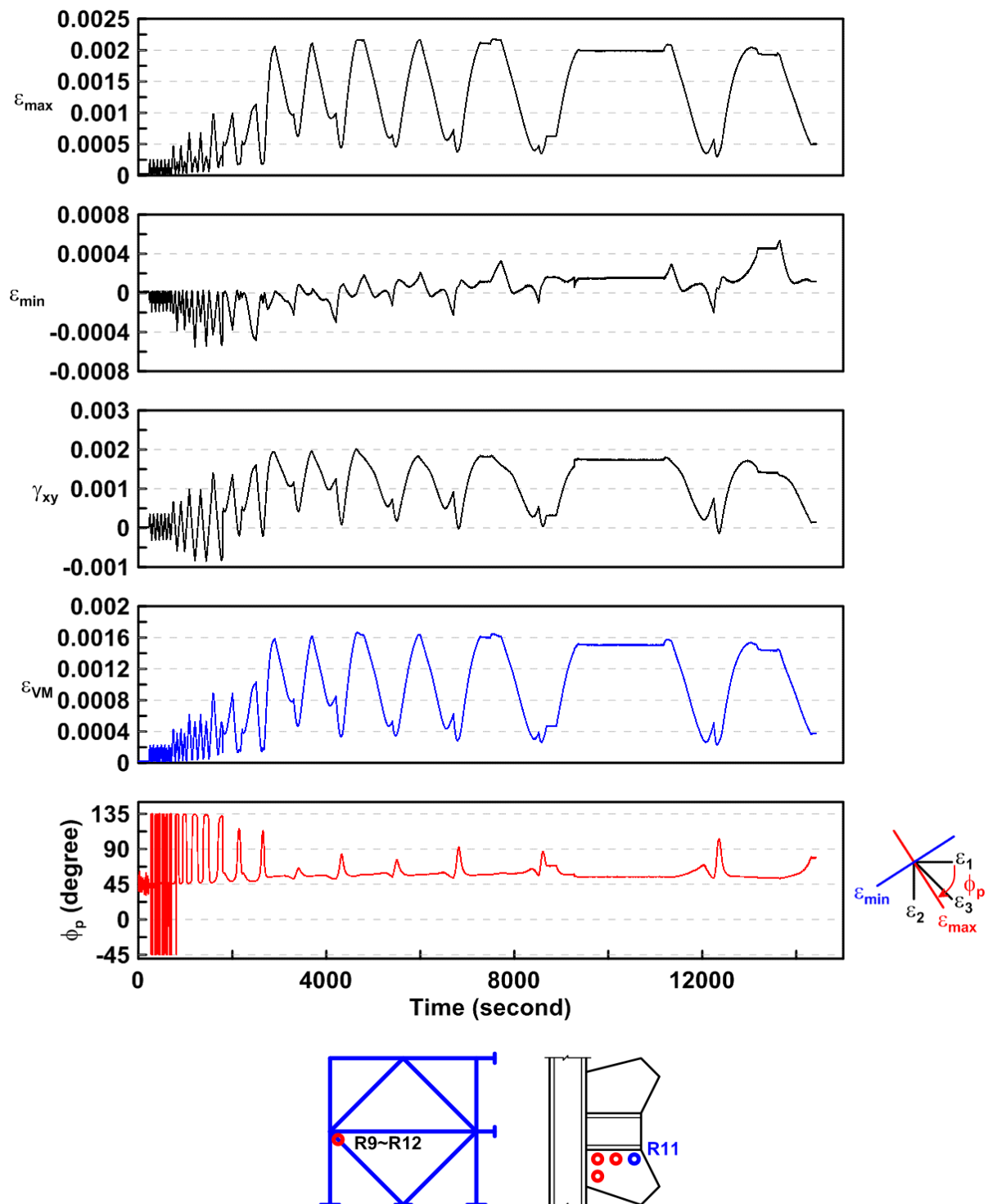


Figure 4.297 Specimen TCBF-B-3: time history of rosette-type strain gauge readings in one-piece gusset plate (location: R11).

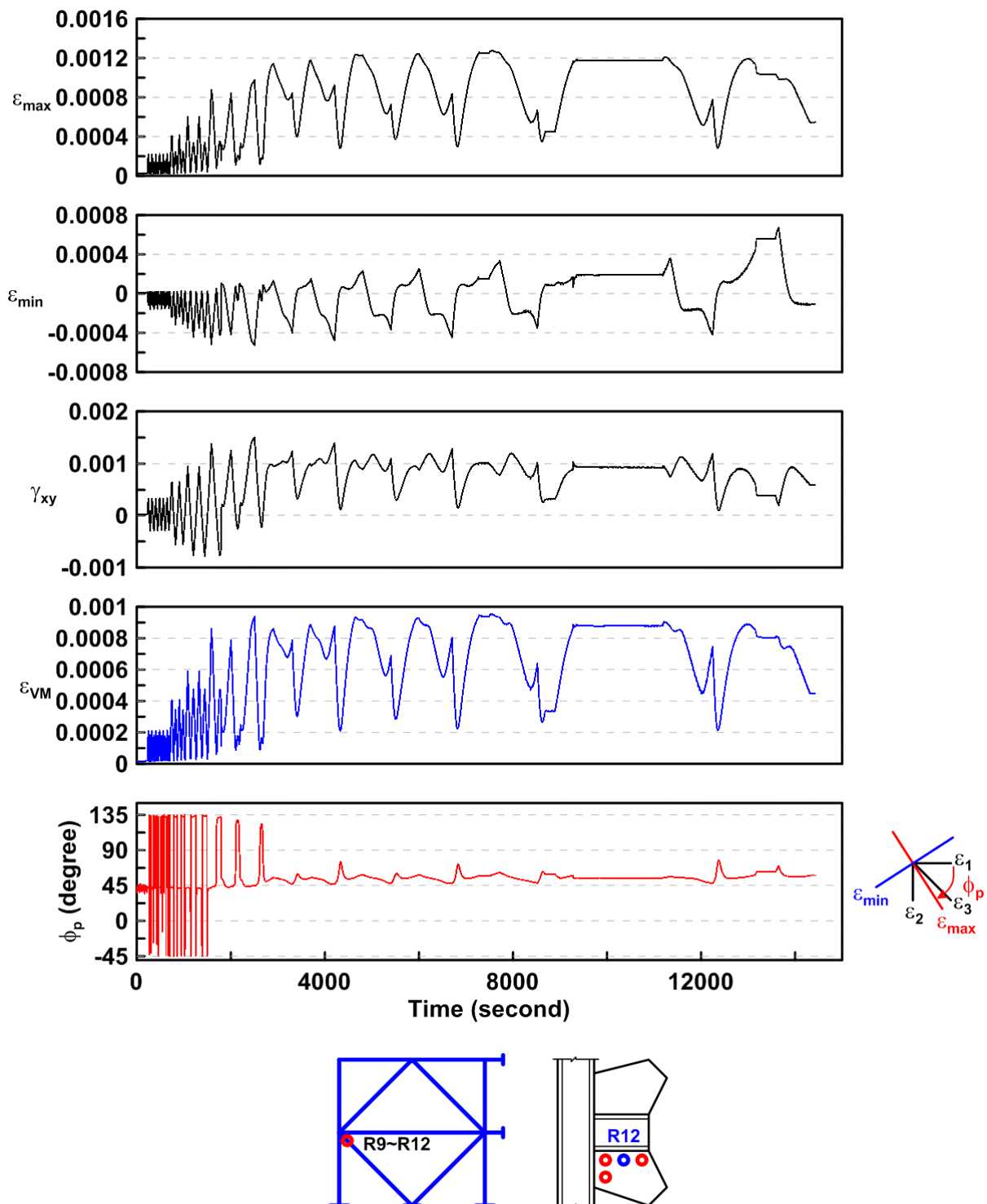


Figure 4.298 Specimen TCBF-B-3: time history of rosette-type strain gauge readings in one-piece gusset plate (location: R12).

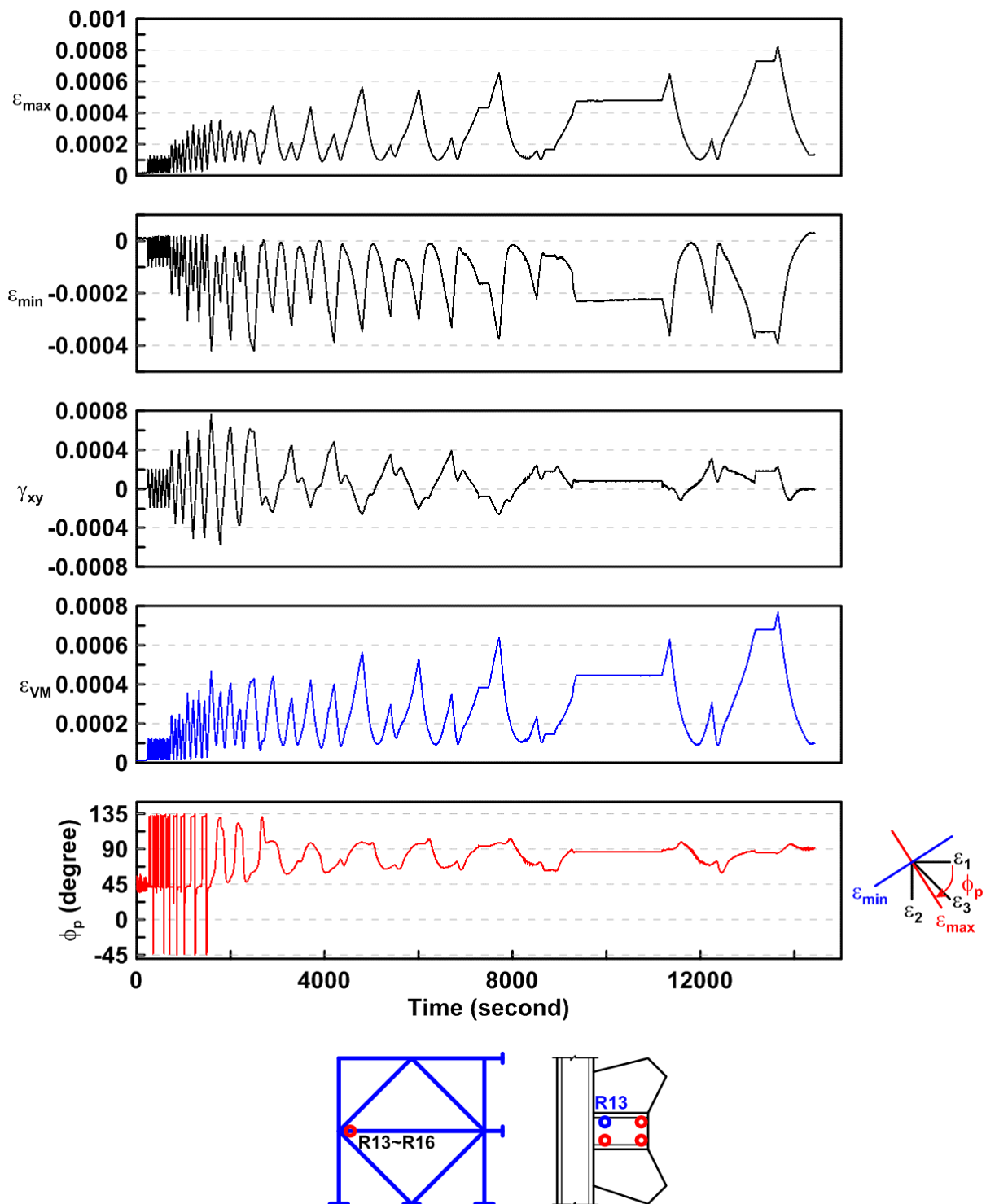


Figure 4.299 Specimen TCBF-B-3: time history of rosette-type strain gauge readings in one-piece gusset plate (location: R13).

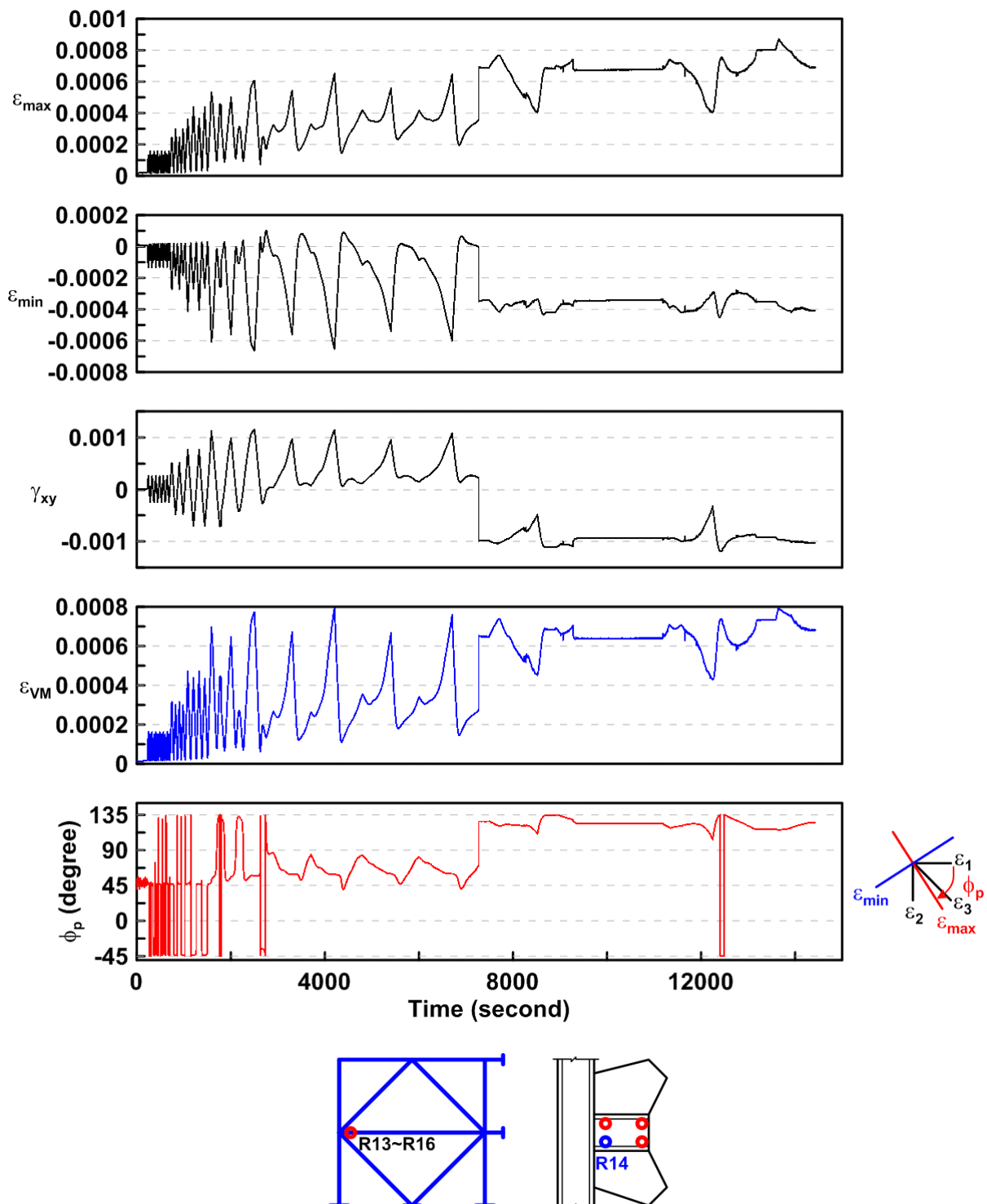


Figure 4.300 Specimen TCBF-B-3: time history of rosette-type strain gauge readings in one-piece gusset plate of (location: R14).

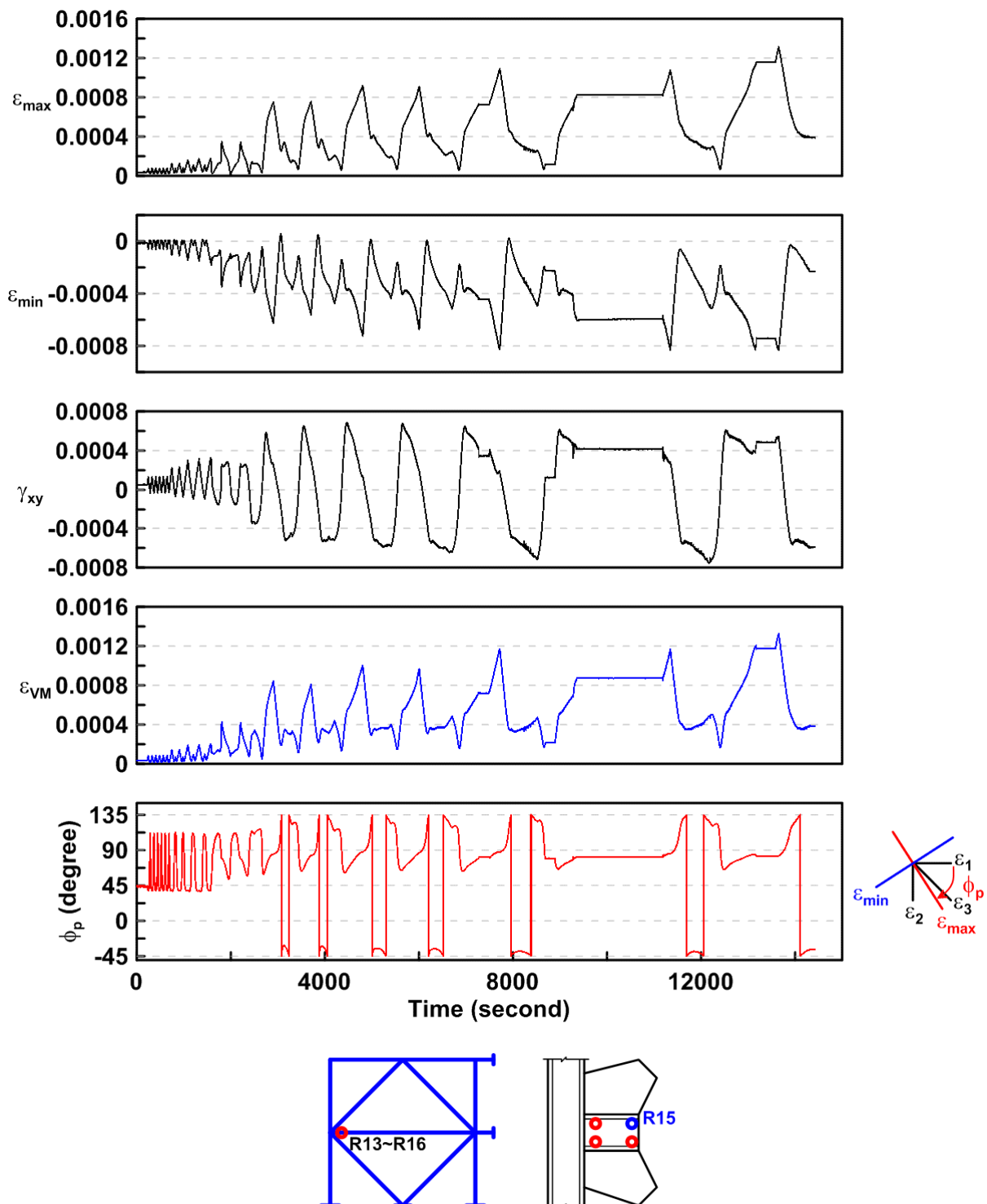


Figure 4.301 Specimen TCBF-B-3: time history of rosette-type strain gauge readings in one-piece gusset plate (location: R15).

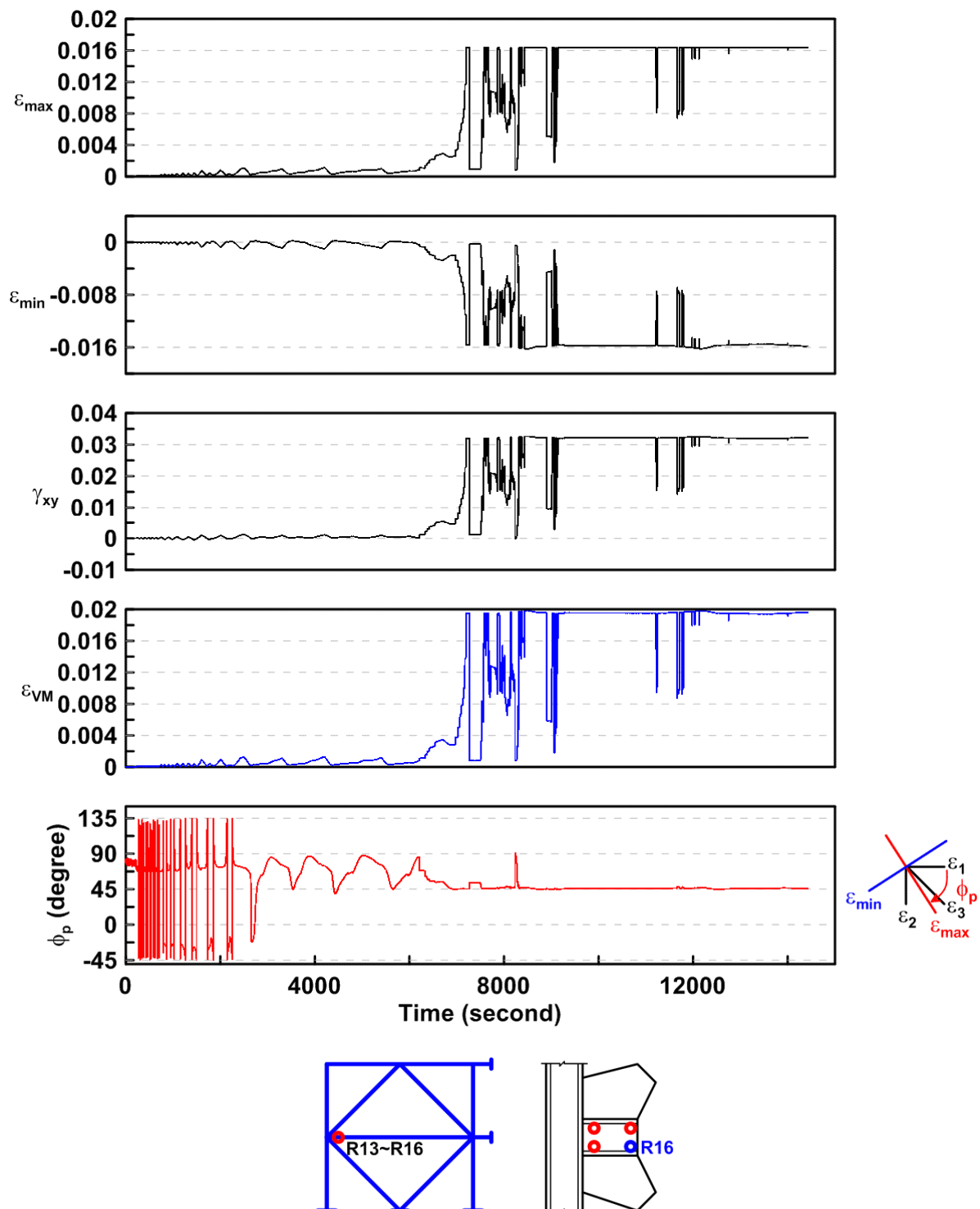


Figure 4.302 Specimen TCBF-B-3: time history of rosette-type strain gauge readings in one-piece gusset plate (location: R16).

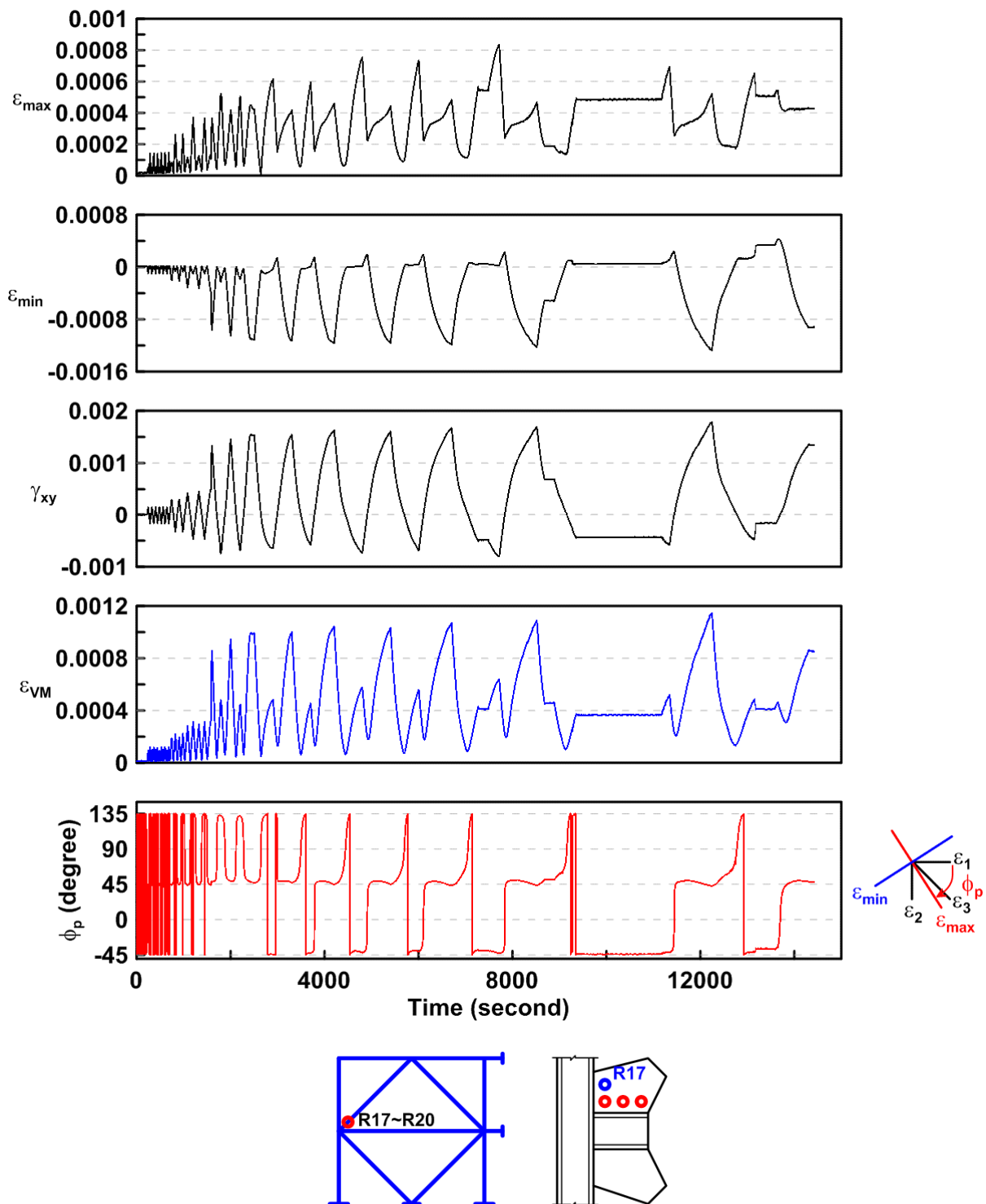


Figure 4.303 Specimen TCBF-B-3: time history of rosette-type strain gauge readings in one-piece gusset plate (location: R17).

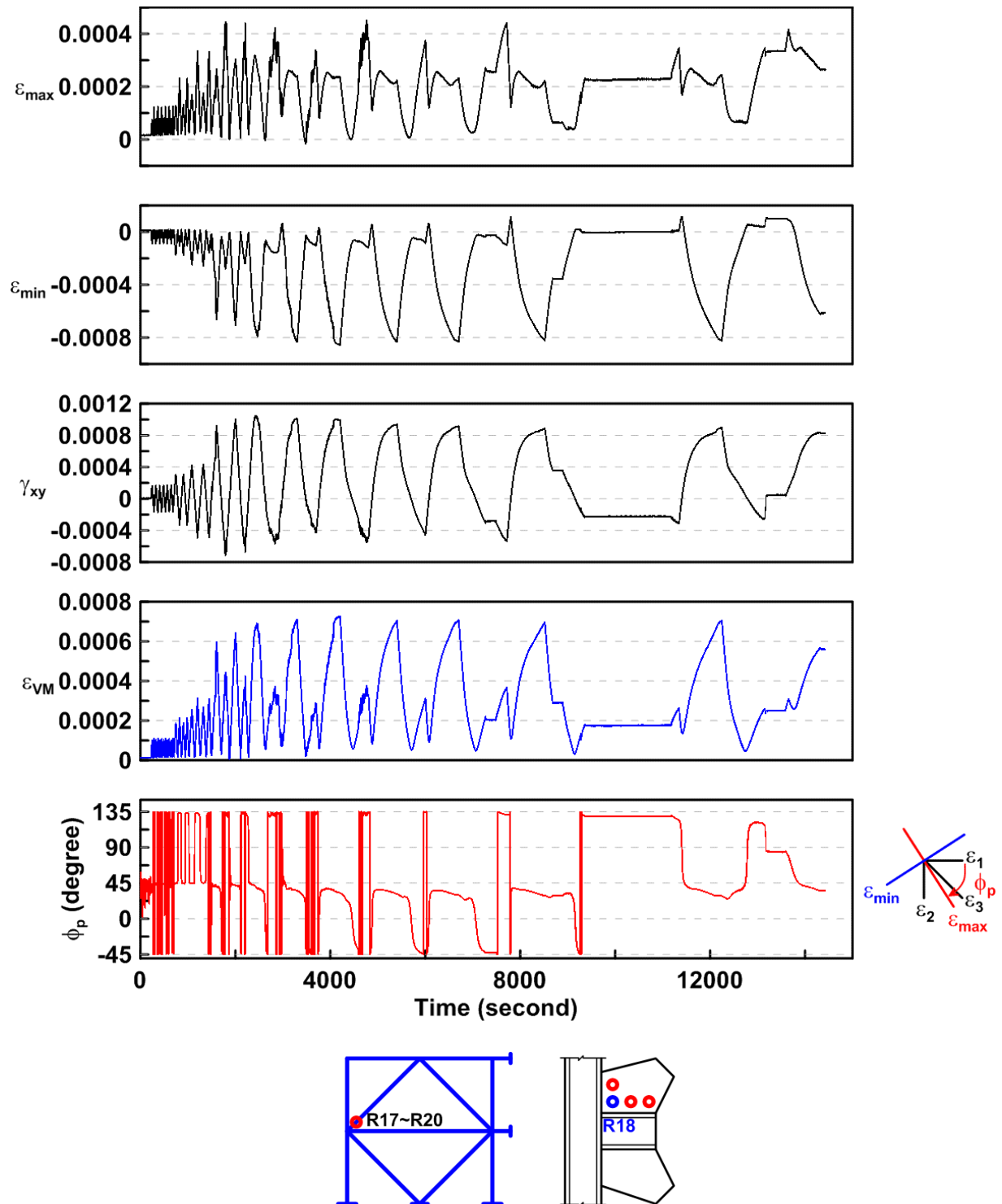


Figure 4.304 Specimen TCBF-B-3: time history of rosette-type strain gauge readings in one-piece gusset plate (location: R18).

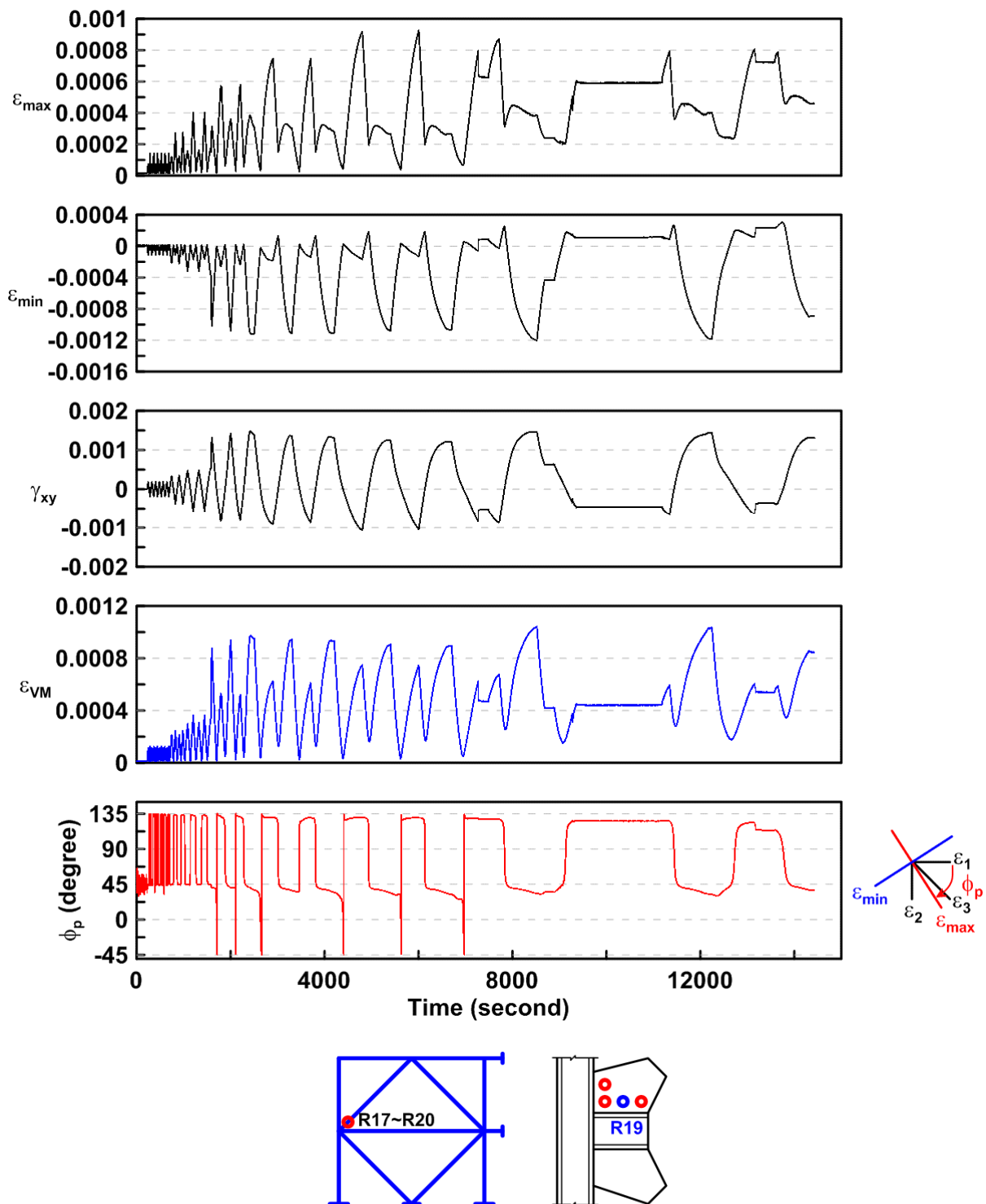


Figure 4.305 Specimen TCBF-B-3: time history of rosette-type strain gauge readings in one-piece gusset plate (location: R19).

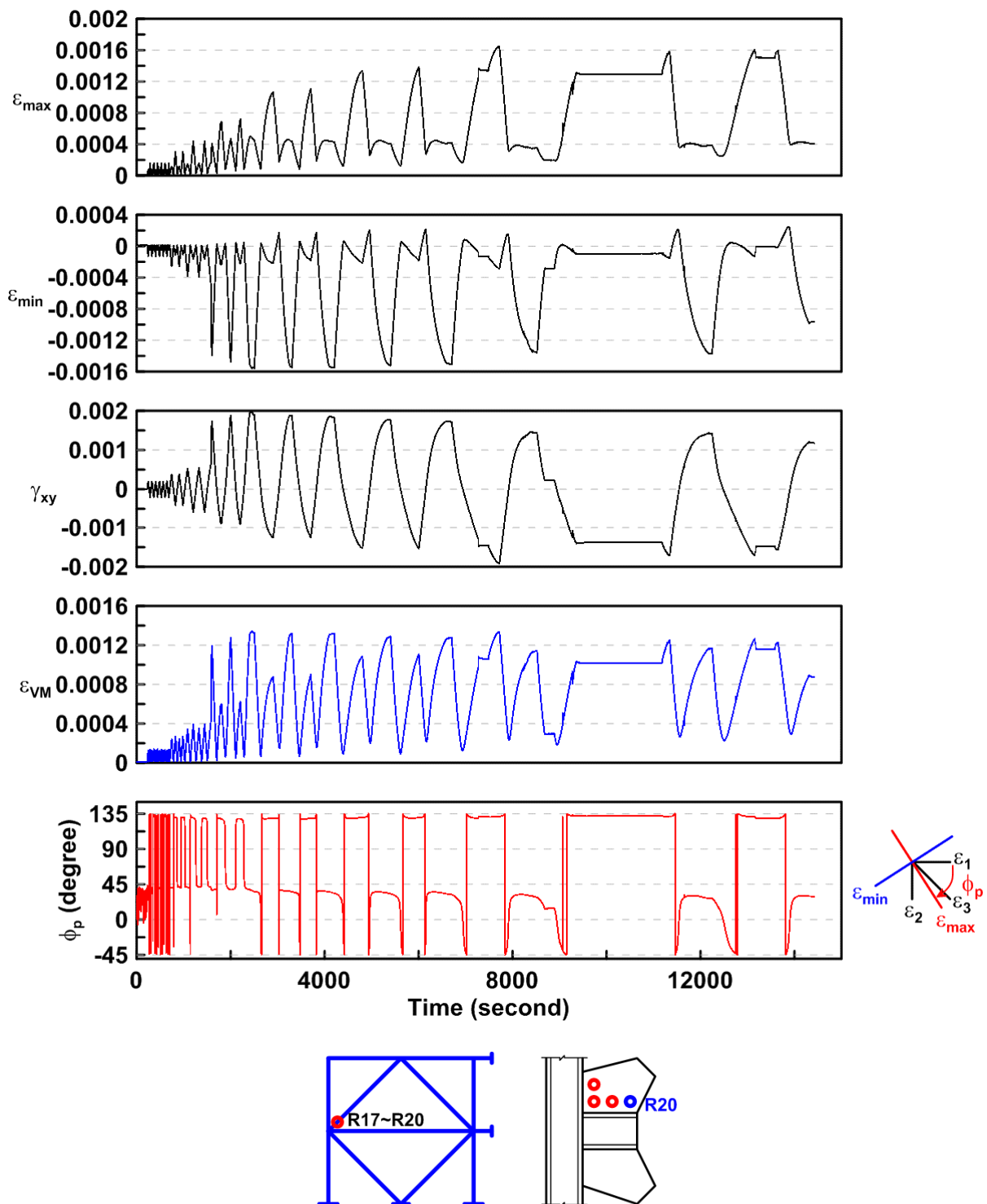


Figure 4.306 Specimen TCBF-B-3: time history of rosette-type strain gauge readings in one-piece gusset plate (location: R20).

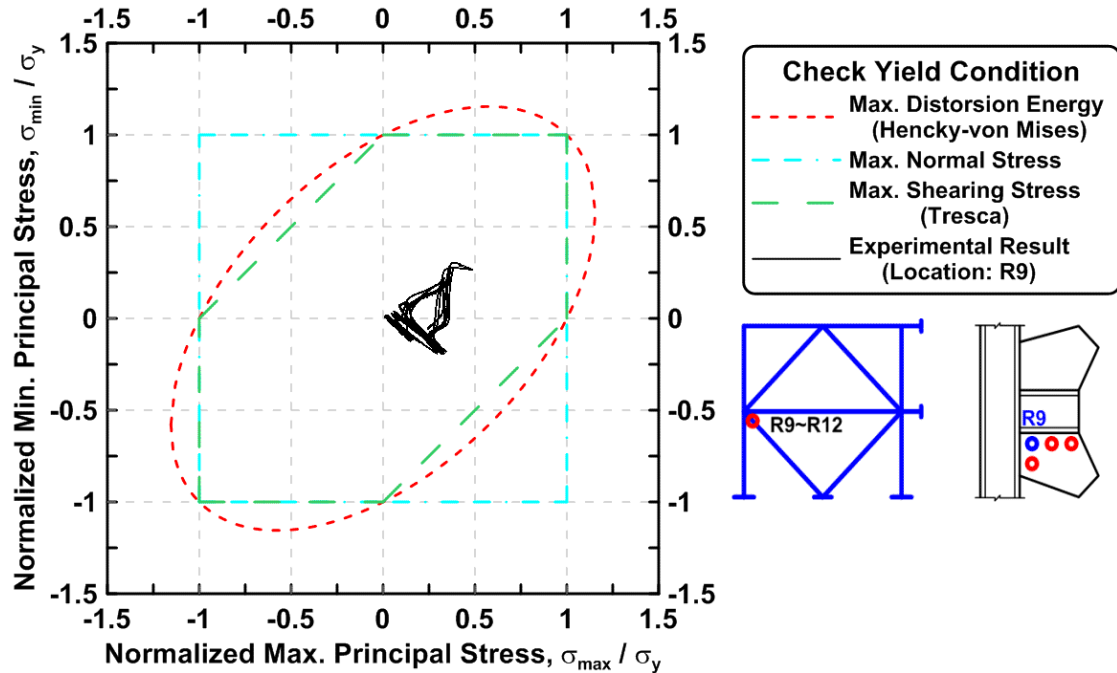


Figure 4.307 Specimen TCBF-B-3: normalized maximum principal stress versus normalized minimum principal stress in one-piece gusset plate (location: R9).

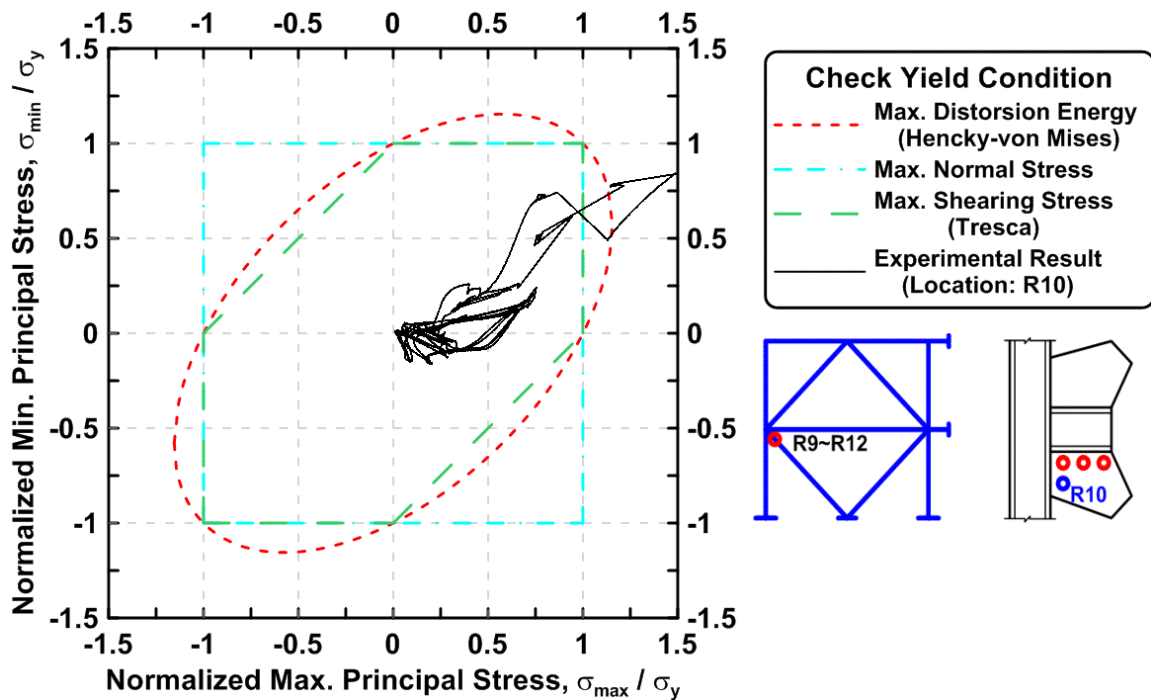


Figure 4.308 Specimen TCBF-B-3: normalized maximum principal stress versus normalized minimum principal stress in one-piece gusset plate (location: R10).

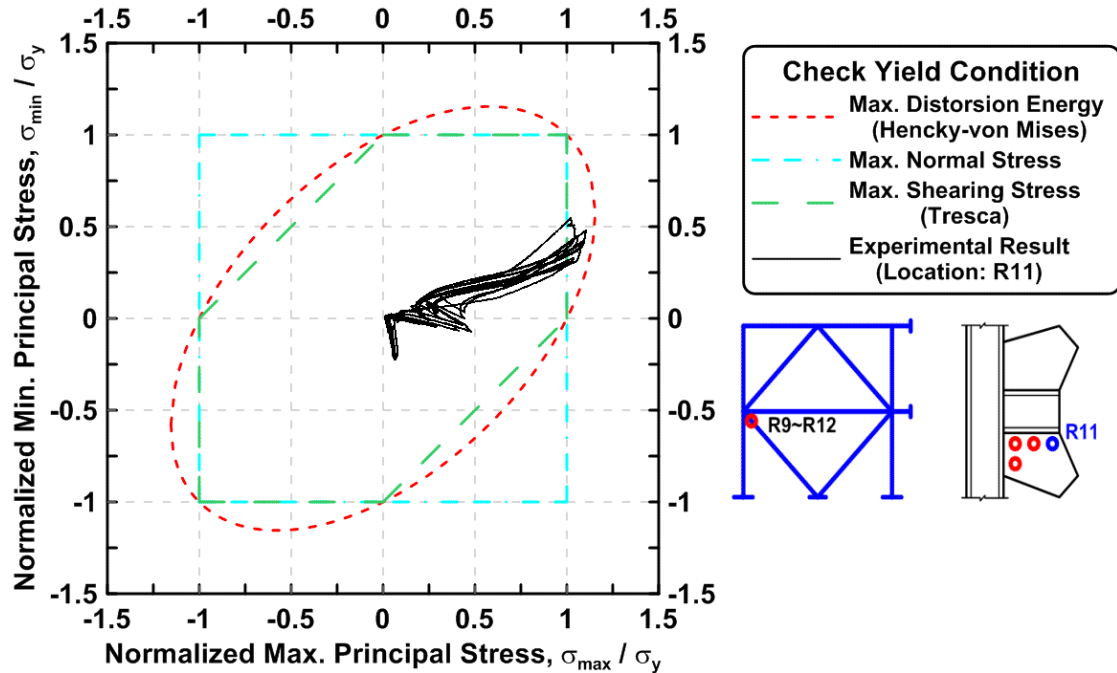


Figure 4.309 Specimen TCBF-B-3: normalized maximum principal stress versus normalized minimum principal stress in one-piece gusset plate (location: R11).

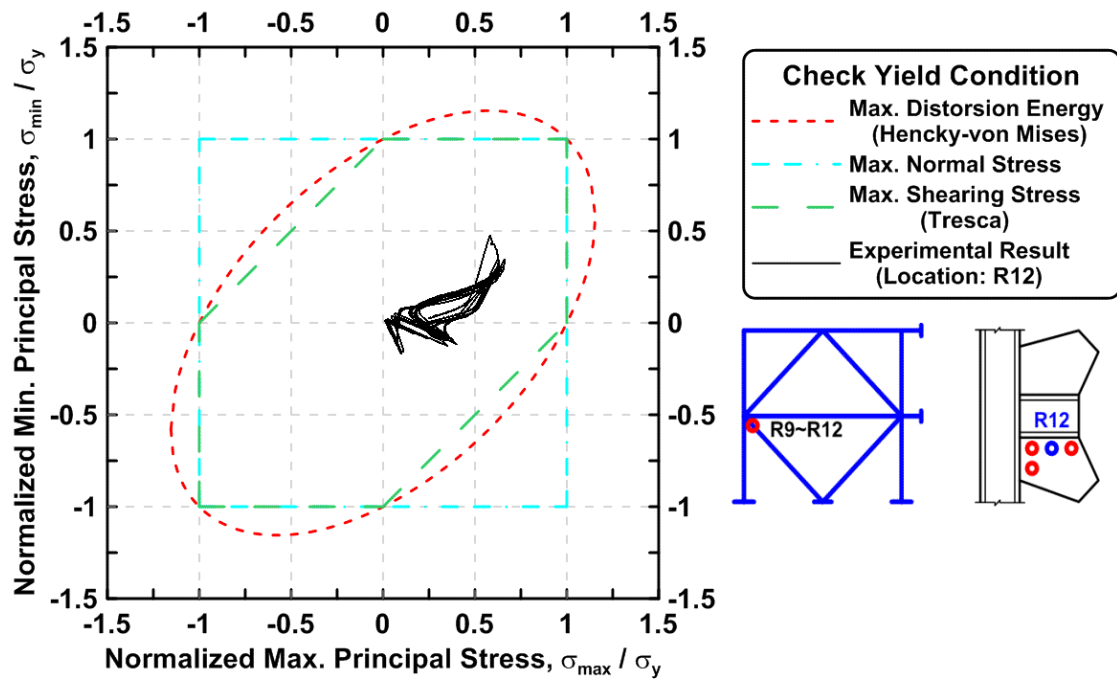


Figure 4.310 Specimen TCBF-B-3: normalized maximum principal stress versus normalized minimum principal stress in one-piece gusset plate (location: R12).

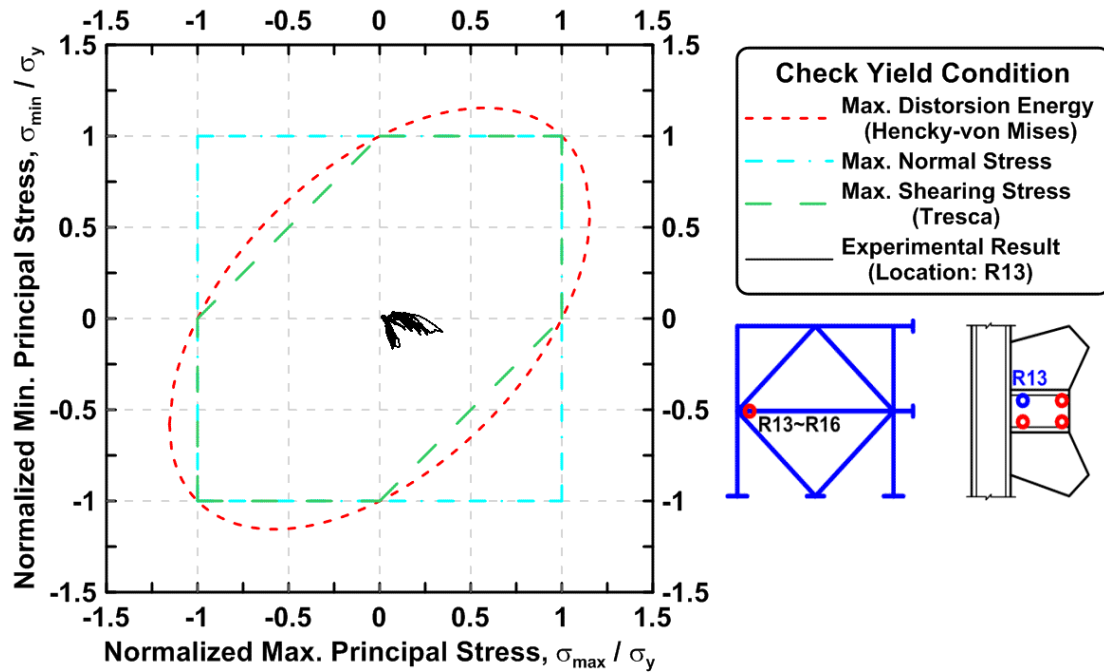


Figure 4.311 Specimen TCBF-B-3: normalized maximum principal stress versus normalized minimum principal stress in one-piece gusset plate (location: R13).

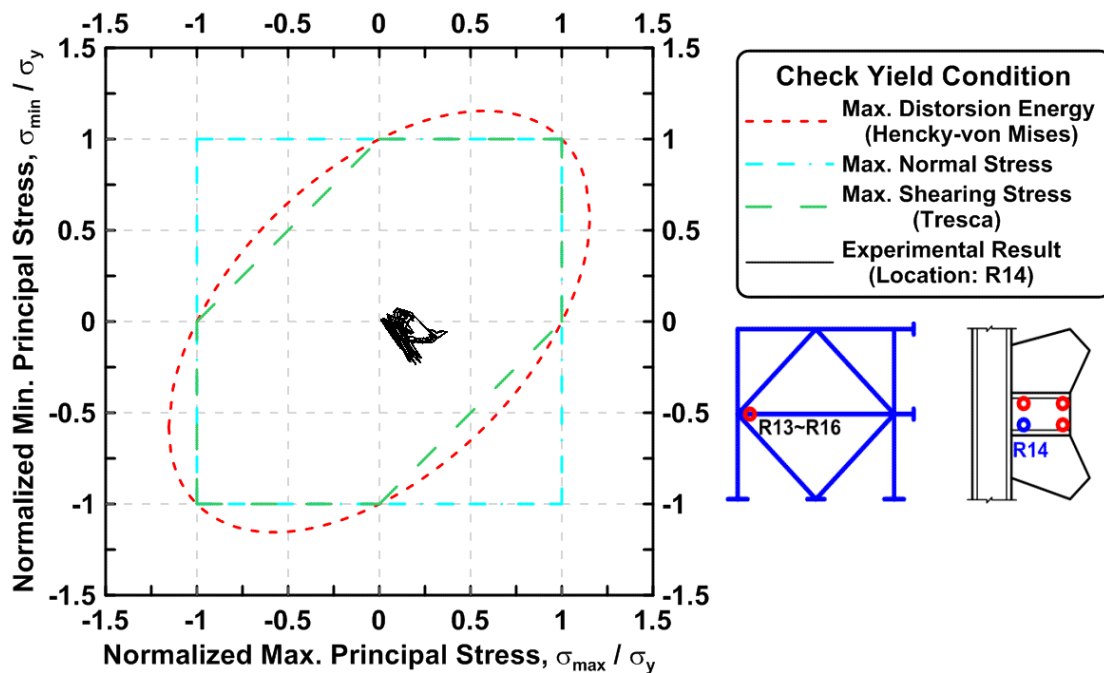


Figure 4.312 Specimen TCBF-B-3: normalized maximum principal stress versus normalized minimum principal stress in one-piece gusset plate (location: R14).

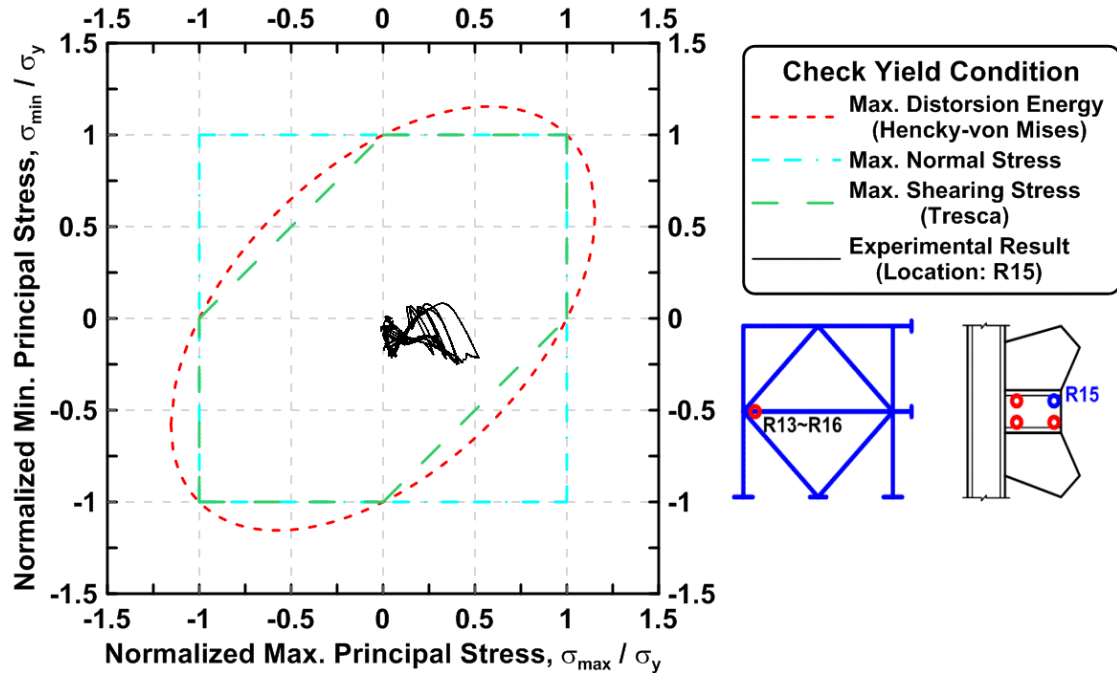


Figure 4.313 Specimen TCBF-B-3: normalized maximum principal stress versus normalized minimum principal stress in one-piece gusset plate (location: R15).

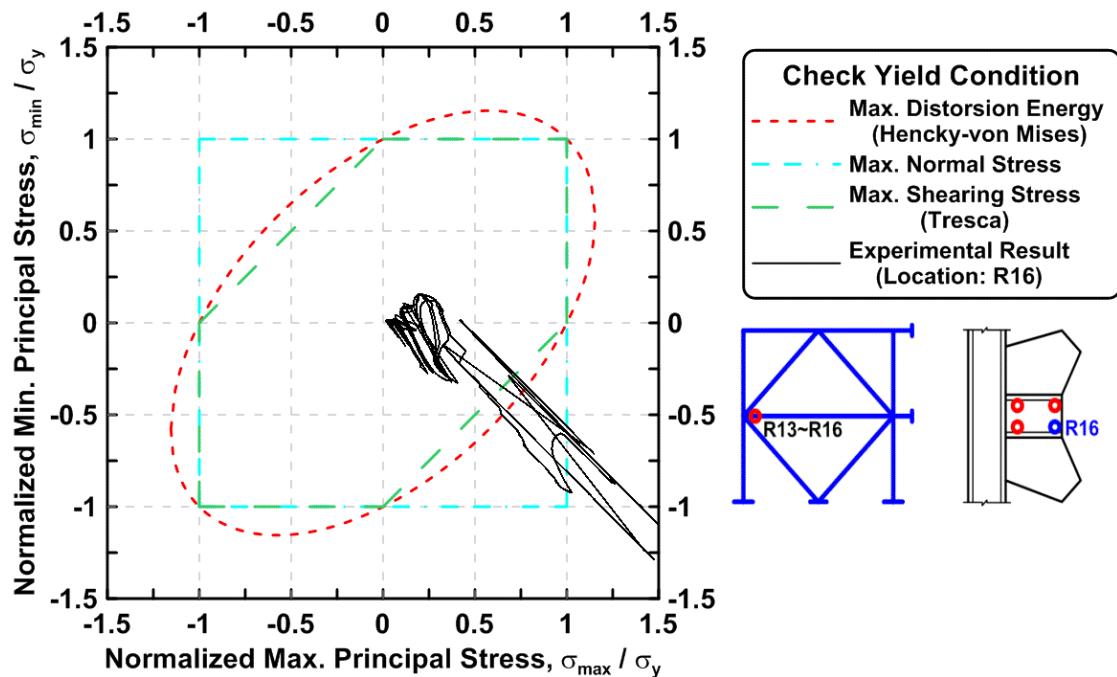


Figure 4.314 Specimen TCBF-B-3: normalized maximum principal stress versus normalized minimum principal stress in one-piece gusset plate (location: R16).

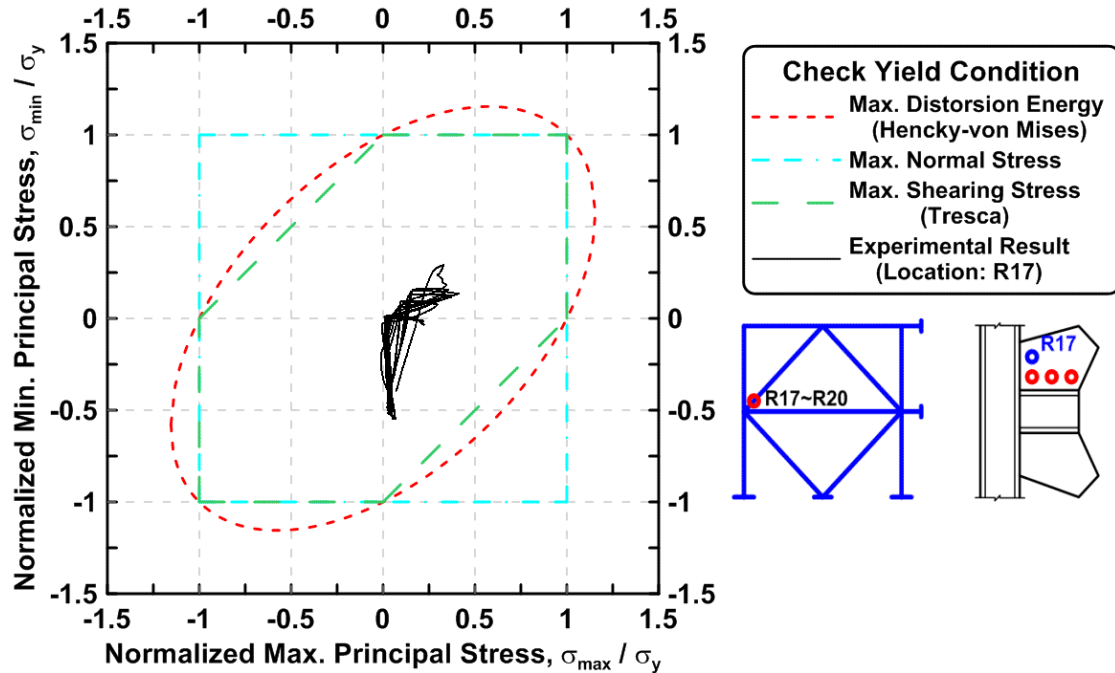


Figure 4.315 Specimen TCBF-B-3: normalized maximum principal stress versus normalized minimum principal stress in one-piece gusset plate (location: R17).

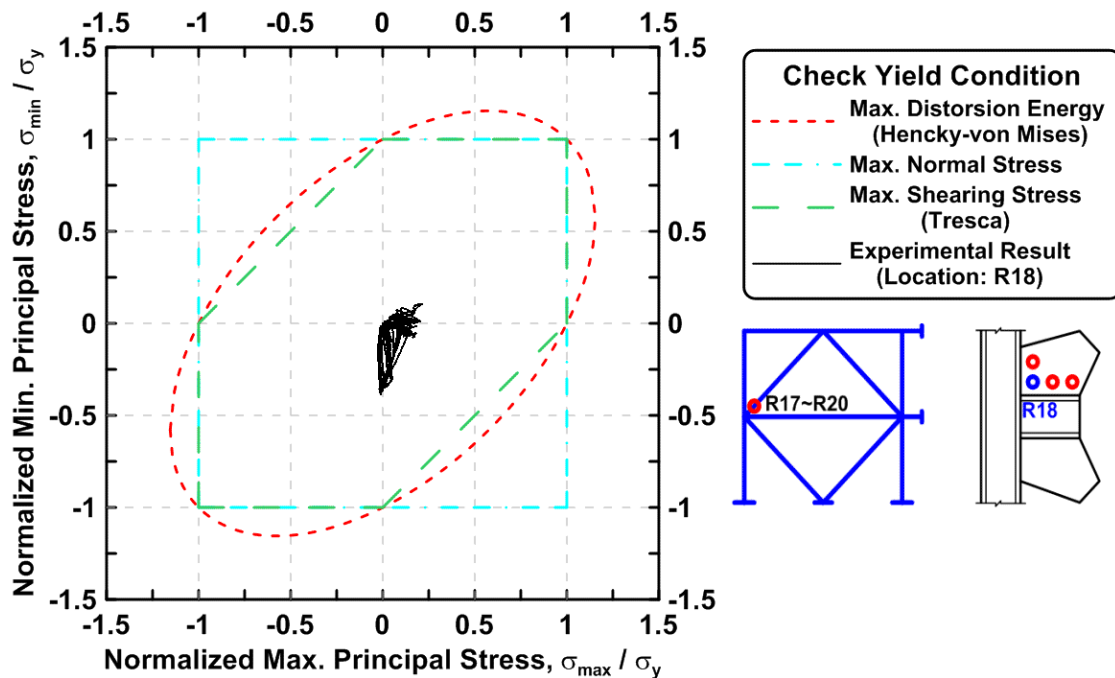


Figure 4.316 Specimen TCBF-B-3: normalized maximum principal stress versus normalized minimum principal stress in one-piece gusset plate (location: R18).

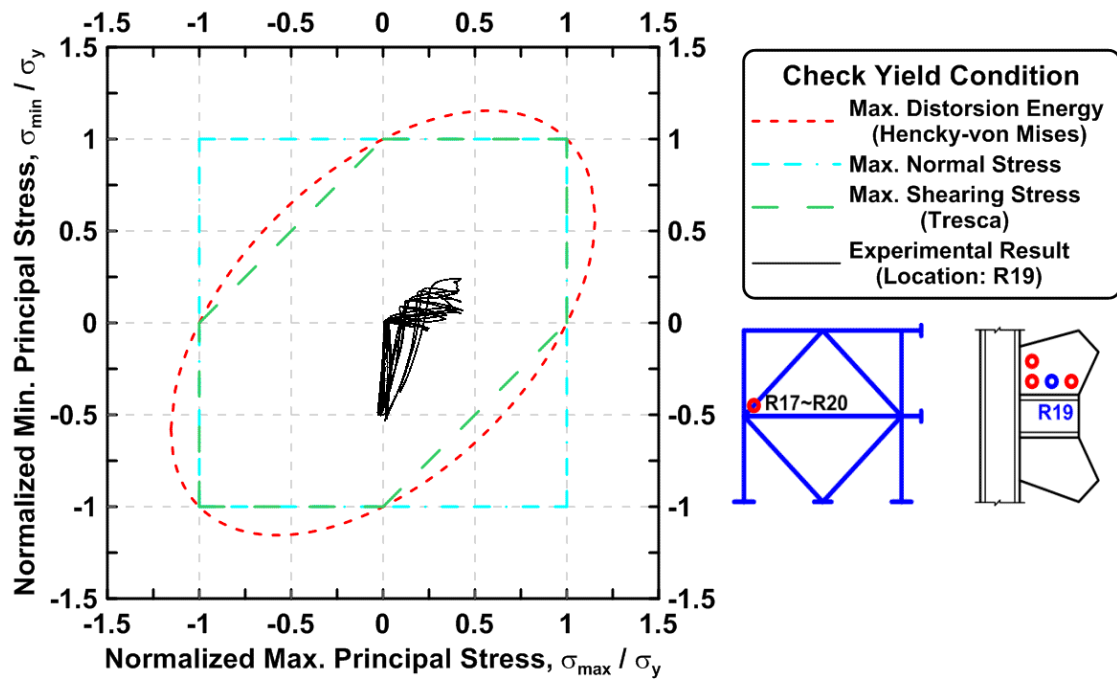


Figure 4.317 Specimen TCBF-B-3: normalized maximum principal stress versus normalized minimum principal stress in one-piece gusset plate (location: R19).

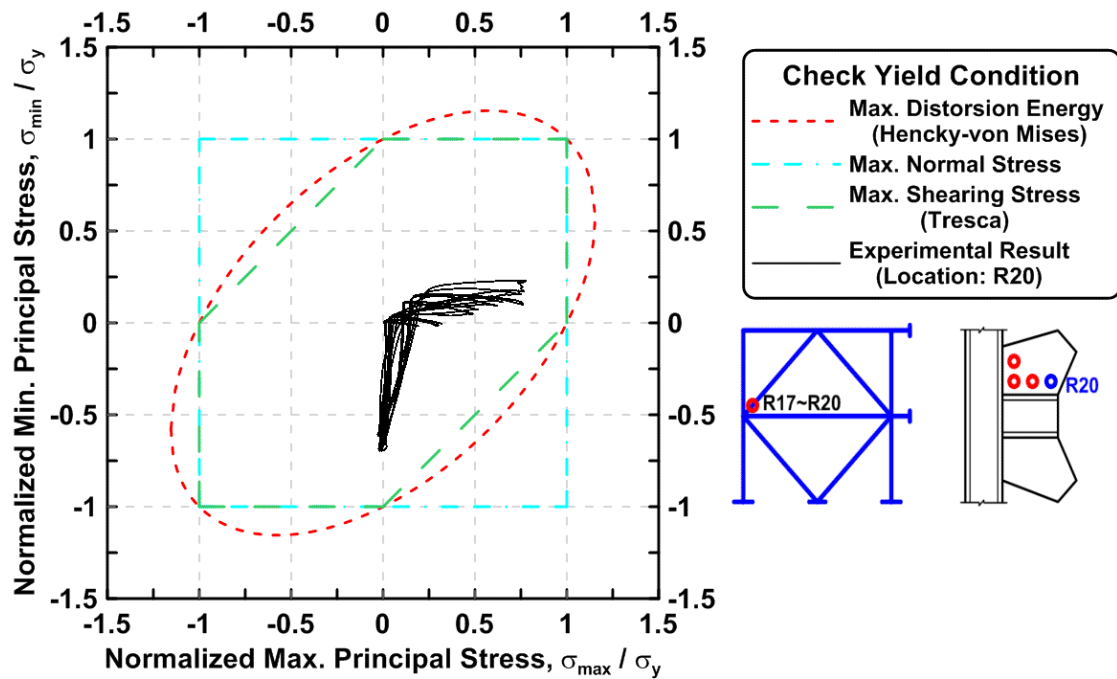


Figure 4.318 Specimen TCBF-B-3: normalized maximum principal stress versus normalized minimum principal stress in one-piece gusset plate (location: R20).

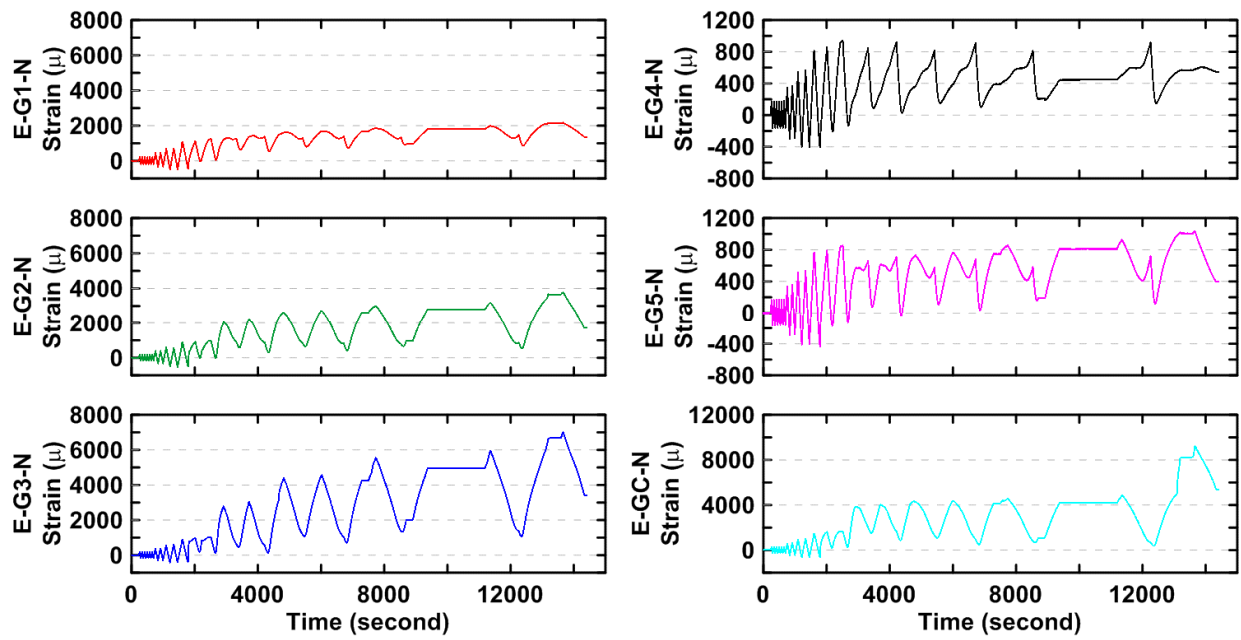


Figure 4.319 Specimen TCBF-B-3: averaged axial strain time history in tapered eastern-side gusset plate.

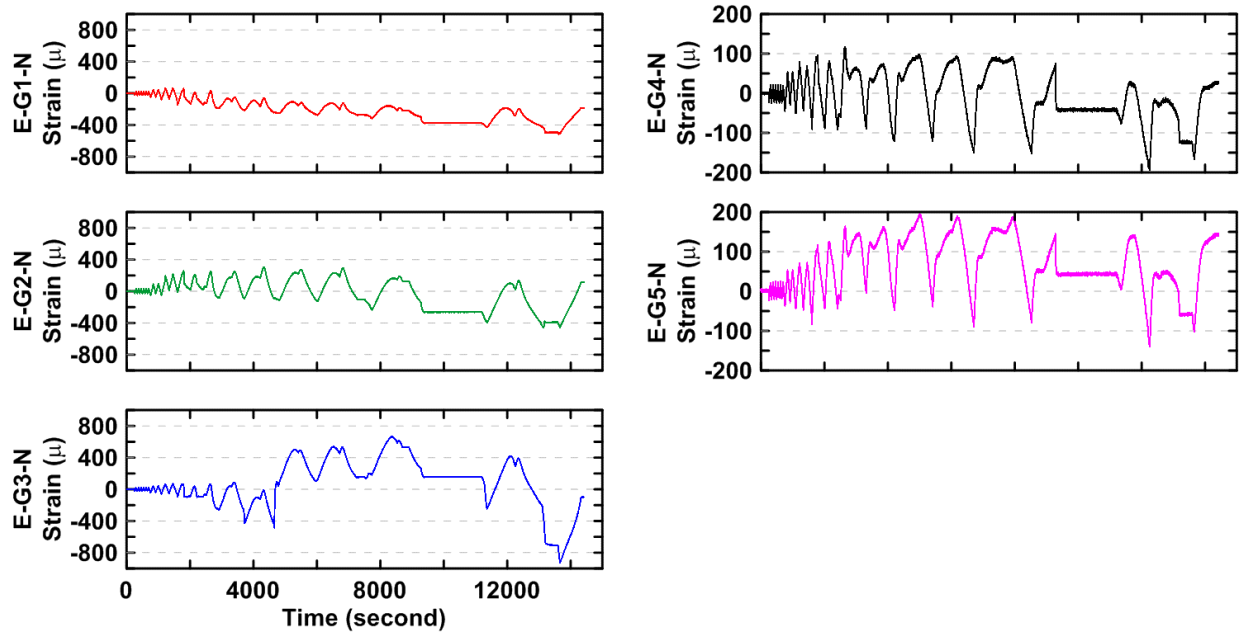


Figure 4.320 Specimen TCBF-B-3: bending strain time history in tapered eastern-side gusset plate.

4.1.3.2.7 Test Set Up Response

The actuator bracket deformations versus actuator forces are plotted in Figure 4.321. The relative displacement time history between base plates of the specimen and the floor beam, relative displacement time history between floor beam and strong floor, and relative displacement time history between integrated reconfigurable reaction wall and strong floor at northern and southern sides are shown in Figure 4.322. The out-of-plane deformation time history of the lateral supporting frame with respect to the wall of the building at different locations is plotted in Figure 4.323. The RRW tip deformation time histories during the test are shown in Figure 4.324.

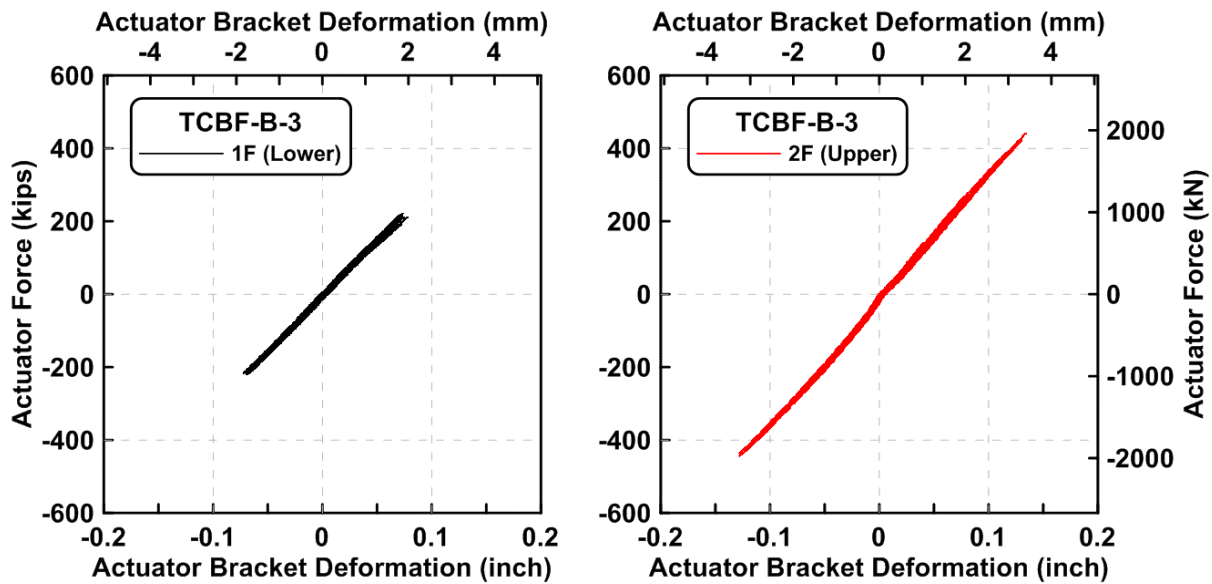


Figure 4.321 Specimen TCBF-B-3: actuator force versus bracket deformation relationship at both floor levels.

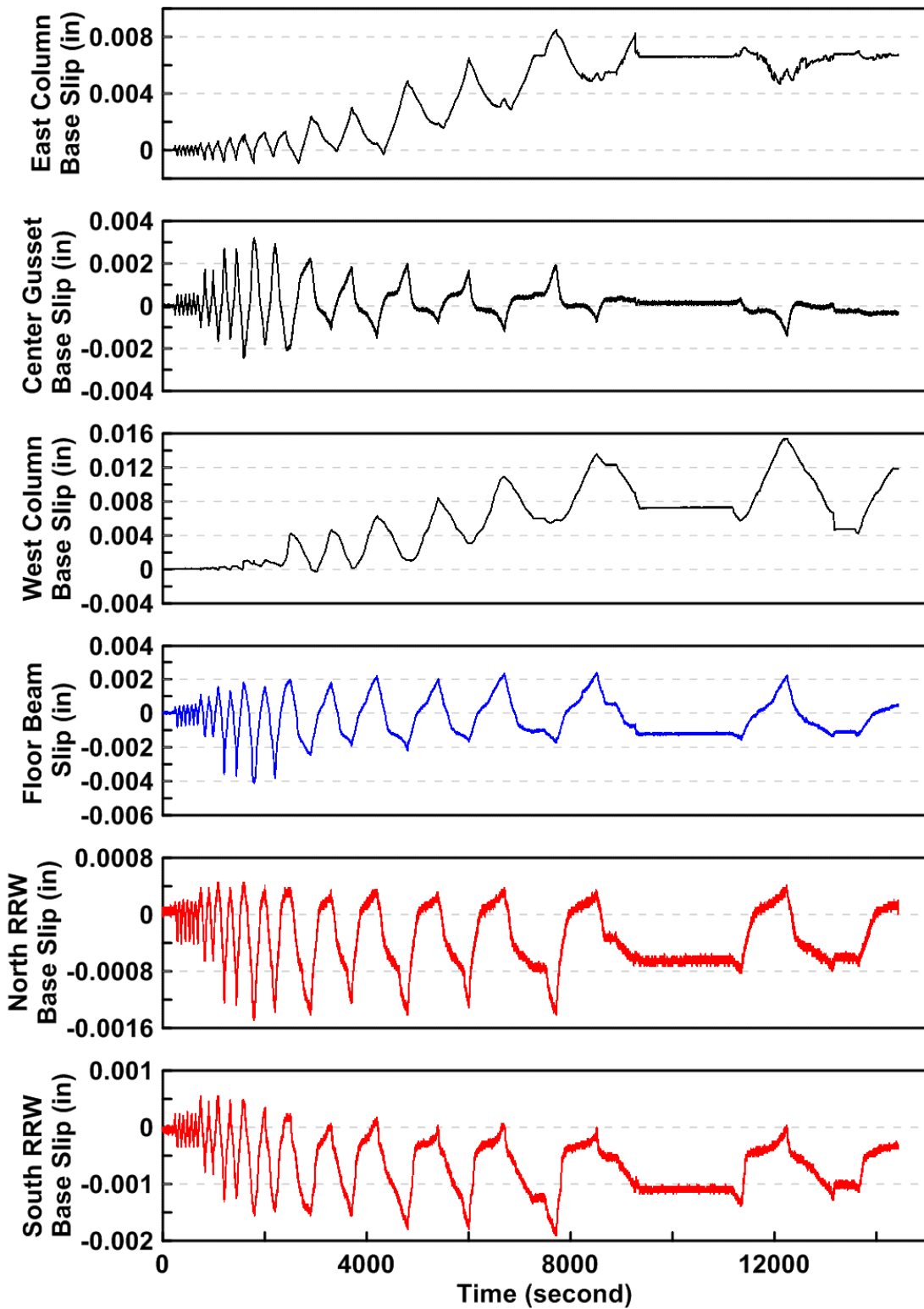


Figure 4.322 Specimen TCBF-B-3: slippage time history between specimen and test set up boundaries.

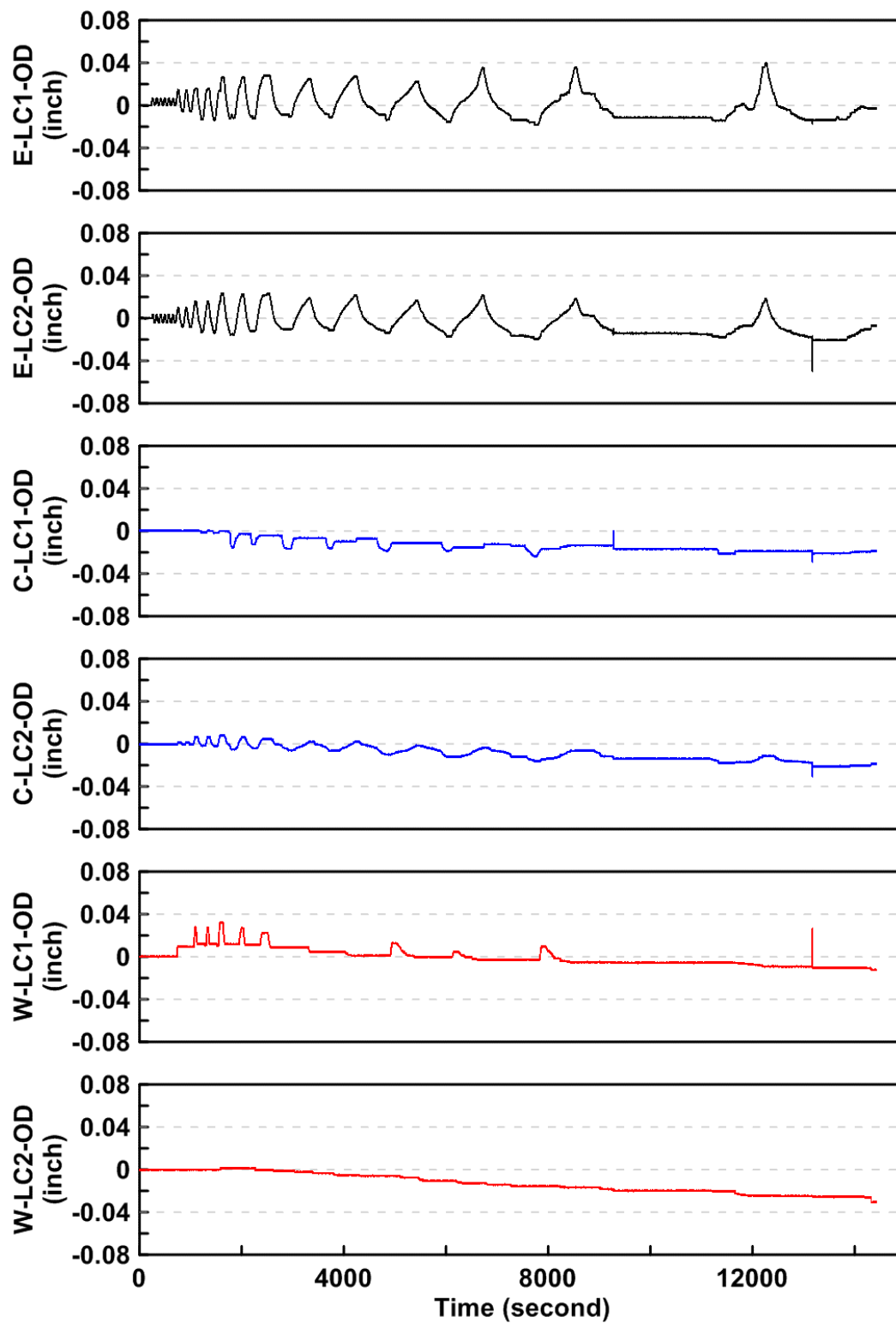


Figure 4.323 Specimen TCBF-B-3: out-of-plane deformation time history of lateral supporting frame at different monitoring points.

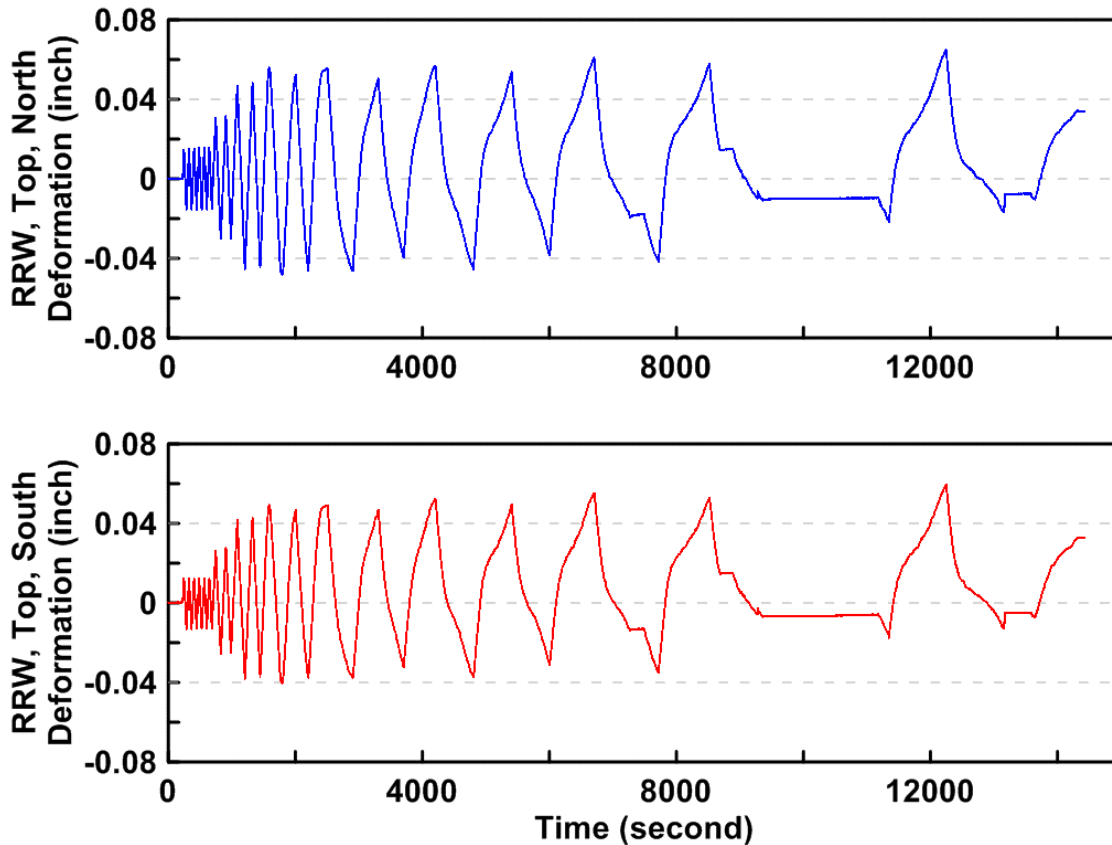


Figure 4.324 Specimen TCBF-B-3: reconfigurable reaction wall tip deformation time histories.

4.2 HYBRID SIMULATION TEST RESULTS OF SPECIMEN TCBF-B-4 (SQUARE HSS BRACES)

This specimen re-used the roof beam, two W12 \times 96 columns, and base plates from Specimen TCBF-B-3. The east-side column flange and web near the column base region were repaired with CJP welds. Stiffener plates and cover plates were also provided in this region, as illustrated in Figures 3.62 and 3.63. As with Specimen TCBF-B-3, pinned connections between the lower beam and the one-piece gusset plates were used in this specimen. The connection detail was the same as shown in Figure 4.223 for Specimen TCBF-B-3.

Before running the design earthquake (DE) level ground motion, two one-tenth amplitude DE level ground motions were executed to check instrumentations, data readings, actuator control algorithms, and to determine the adequate actuator speed. The hybrid test system was used to simulate a low-amplitude free-vibration test to derive the fundamental period and inherent damping of the specimen. Both actuators were displacement controlled, and the actuator speed was selected as 0.002 in./sec; this setting did not change during the entire hybrid simulation.

The test began at 10:54 PM on Saturday, March 26, 2011. The entire side views of the braced frame specimen before and after hybrid simulations are shown in Figure 4.325.



(a) before test



(b) after elastic test



(c) after design earthquake



(d) after maximum credible earthquake

Figure 4.325 Specimen TCBF-B-4 before and after hybrid simulation.

4.2.1 Main Observations

The hybrid test started at 10:54 PM on Saturday, March 26, 2011, after two small elastic range tests were completed and instrument readings were carefully checked. The input ground motions for the hybrid simulation are shown in Figure 3.77. The hybrid test was divided into three major phases: a 20-sec-long DE-level ground motion, a 3-sec silence and followed by a 20-sec MCE-level ground motion. The damage condition of the specimen at the end of the MCE event did not permit assessment of the effects of aftershocks.

Some key observations at specific time steps are briefly described below.

Time step 460 (4.60 sec) at 12:11 AM

Some whitewash flaking (Figure 4.326) occurred at the northern face of column web in the first-story eastern-side column.

Time step 507 (5.07 sec) at 12:45 AM

The east-side HSS brace in the lower story began to buckle out-of-plane towards the south side of the lab (Figure 4.327). The bottom story drift at this time was about 0.79%.

Time step 510 (5.10 sec) at 12:52 AM

The west-side HSS brace in the second story also buckled out-of-plane towards the south side of the lab (Figure 4.328). The top story drift at this time was about 0.85%.

Time step 515 (5.15 sec) at 1:00 AM

Local buckling of the square HSS section near the middle part of entire bracing member was observed at both the eastern-side brace in the bottom story and the western-side brace in the top story (Figures 4.329 and 4.330). The bottom story drift at this time was 1.45%.

Time step 537 (5.37 sec) at 1:19 AM

Minor whitewash flaking occurred at the west bottom side of the lower beam-to-gusset plate splice (Figure 4.331).

Time step 540 (5.40 sec) at 1:26 AM

The west-side HSS brace in the lower story buckled out-of-plane towards the south side of the lab. The bottom story drift at this time was 0.30%.

Time step 541 (5.41 sec) at 1:30 AM

The east-side HSS brace in the second story also buckled out-of-plane to the south side of the lab. The top story drift at this time was 0.42%.

Time step 559 (5.59 sec) at 1:50 AM

Local buckling of the square HSS section near the middle part of entire bracing member was observed at both eastern-side brace in the second story and western-side brace in the first story. Additional flaking of whitewash occurred near the lower beam-to-gusset plate splice at the

western beam end (Figure 4.332). Minor flaking of whitewash also occurred near the west column base in the first story.

Time step 656 (6.56 sec) at 3:04 AM

Several loud popping noises were heard at the time steps equaled to 648, 652, and 656 when the roof actuator displacement corresponding to -2.4 in., -2.5 in. and -2.9 in. At the same time, panel zones (both east and west sides) in the second story began to yield (detected visually via whitewash flaking, see Figure 4.333).

Time step 676 (6.76 sec) at 3:30 AM

Cracks initiated at the corner of the square HSS section in the first-story eastern-side brace (Figure 4.334). The bottom story drift at this time was 0.11%.

Time step 682(6.82 sec) at 3:40 AM

Cracks initiated at the corner of the square HSS section in the second-story western-side brace (Figure 4.335).

Time step 701 (7.01 sec) at 4:00 AM

Cracks propagated from the corner of the square HSS section to the center of cross section in the second-story western-side brace (Figure 4.336).

Time step 726 (7.26 sec) at 4:30 AM

Cracks initiated at the corner of the square HSS section in the first-story western-side brace and the second-story eastern-side brace (Figure 4.337).

Time step 734 (7.34 sec) at 4:47 AM

Cracks propagated from the corner of the square HSS section to the center of the cross section in the second-story east-side brace (Figure 4.338).

Time step 740 (7.40 sec) at 4:57 AM

The top-story eastern-side brace completely fractured when the roof actuator was around -4.2 in. (Figure 4.339). No damage was found in the repaired column base in the first-story east side.

Time step 1019 (10.19 sec) at 7:24 AM

No special findings observed.

Time step 2000 (20.00 sec) at 10:52 AM

The DE-level ground motion for the hybrid simulation finished. At this point, one brace had completely fractured (top story, east side) and the other three braces were partially fractured. No severe column plastic hinging was observed. Figure 4.325(c) shows the entire specimen after DE level ground motion.

The MCE-level ground motion for the hybrid simulation continued at time step 2300 after 3-sec silence of input ground motion. This period of time without input ground motion was sufficient to stop vibration of the test specimen.

Time step 2765 (27.65 sec) at 12:29 PM

The second-story western-side brace completely fractured (Figure 4.340).

Time step 2766 (27.66 sec) at 12:30 PM

The first-story eastern-side brace completely fractured (Figure 4.341).

Time step 2799 (27.99 sec) at 1:42 PM

The first-story western-side brace completely fractured (Figure 4.342).

Time step 3023 (30.23 sec) at 6:27 PM

Both column flanges experienced localized buckling near the first-story column base when the roof actuator displacement was about -10.44 in. (Figure 4.343).

Time step 3124 (31.24 sec) at 9:26 PM

The roof actuator hit the displacement interlock at about -10.5 in. This interlock setting was smaller than the ideal capacity of the actuator (12 in.) because the actuator was not exactly at its mid-position at the beginning of the tests. The simulation terminated automatically.

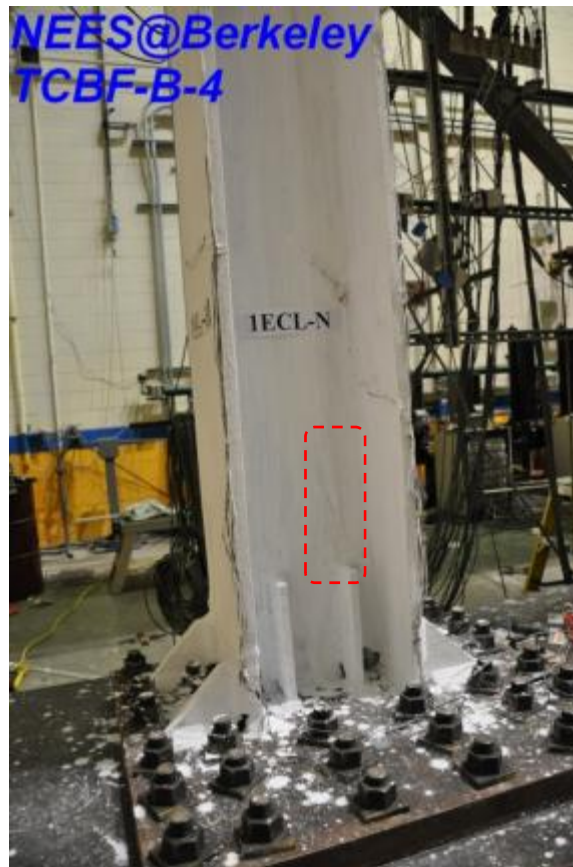


Figure 4.326 Flaking of whitewash near repaired column base.



Figure 4.327 Global buckling of eastern-side brace in the first story.



Figure 4.328 Global buckling of western-side brace in the second story.



Figure 4.329 Local buckling of eastern-side brace in the first story.



Figure 4.330 Local buckling of western-side brace in the second story.



Figure 4.331 Local yielding in beam-to-gusset plate splice.



Figure 4.332 Additional flaking of whitewash near lower beam splice plate.



Figure 4.333 Panel zone yielding in the roof beam to column connection region.



Figure 4.334 Cracks in the first-story eastern-side brace.



Figure 4.335 Cracks in the second-story western-side brace.

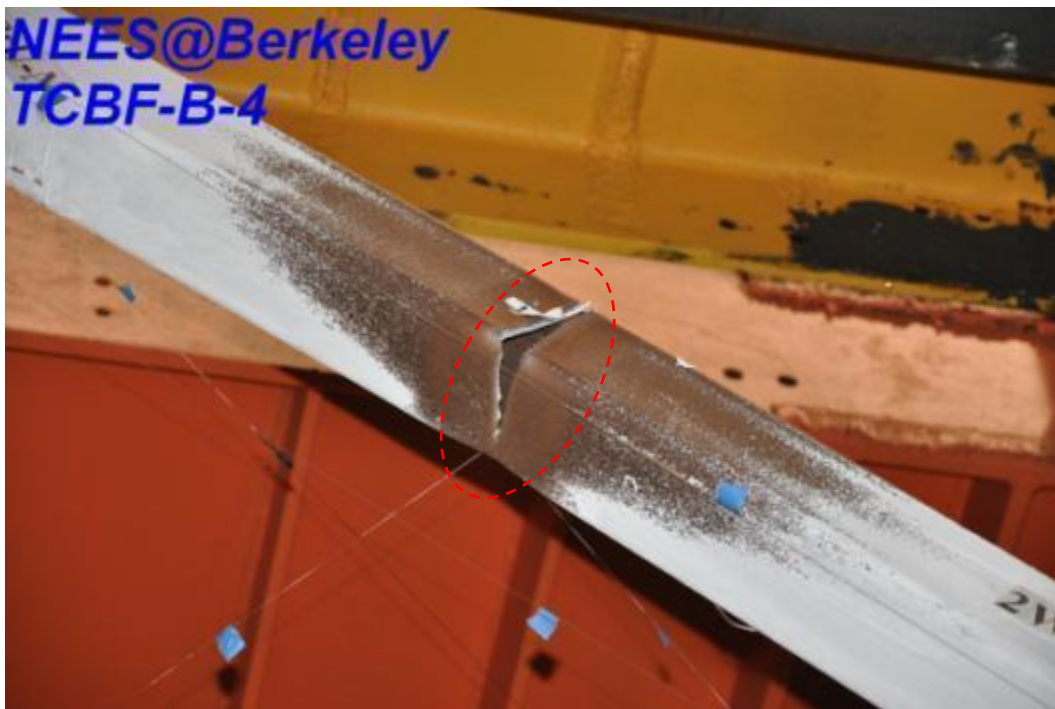


Figure 4.336 Crack propagation in the second-story western-side brace.



Figure 4.337 Cracks in the first-story western-side brace.



Figure 4.338 Cracks opening in the second-story eastern-side brace.



Figure 4.339 Complete fracture of the second-story eastern-side brace.



Figure 4.340 Complete fracture of the second-story western-side brace.



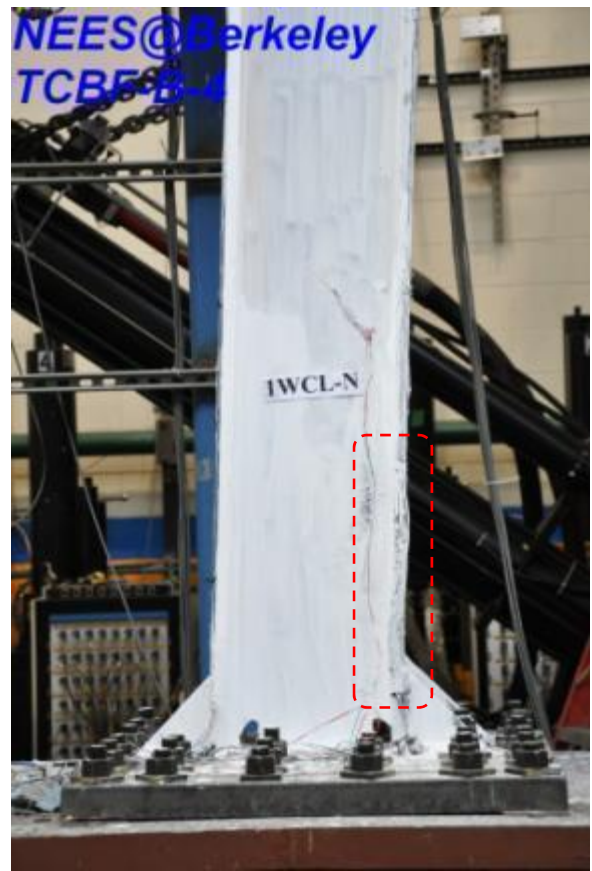
Figure 4.341 Complete fracture of the first-story eastern-side brace.



Figure 4.342 Complete fracture of the first-story western-side brace.



(a) east side



(b) west side

Figure 4.343 Local buckling of column flanges in first-story columns.

4.2.2 Key Response Quantities

The paragraphs below briefly describe the response quantities record in the hybrid simulation and the post-processed response quantities derived from the raw data. Detailed discussion of the individual response quantities are described in Chapter 5.

4.2.2.1 System Response

Figures 4.344 and 4.345 show the time history of the actuator displacements and actuator load cell force feedbacks for Specimen TCBF-B-4. The base shear versus controlled roof displacement of the specimen is shown in Figure 4.346. The relationship between story shear and story drift for the specimen is shown in Figure 4.347. Upper actuator force versus lower actuator force relationship is shown in Figure 4.348. Upper actuator displacement versus lower actuator displacement relationship is shown in Figure 4.349.

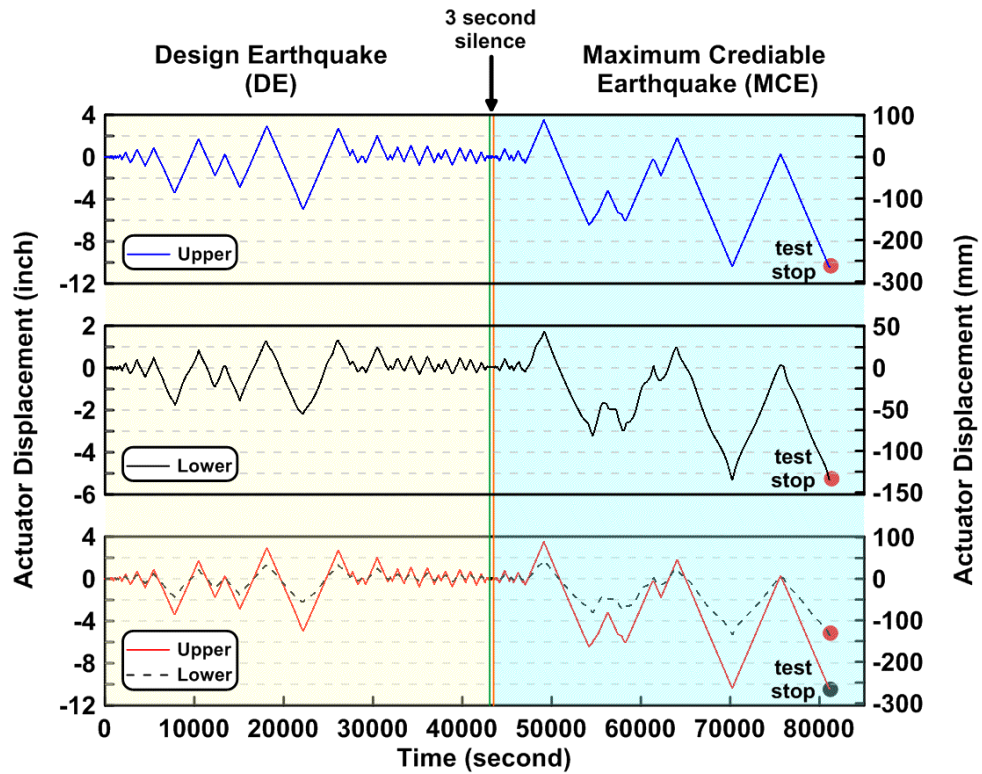


Figure 4.344 Specimen TCBF-B-4: actuator displacement time history.

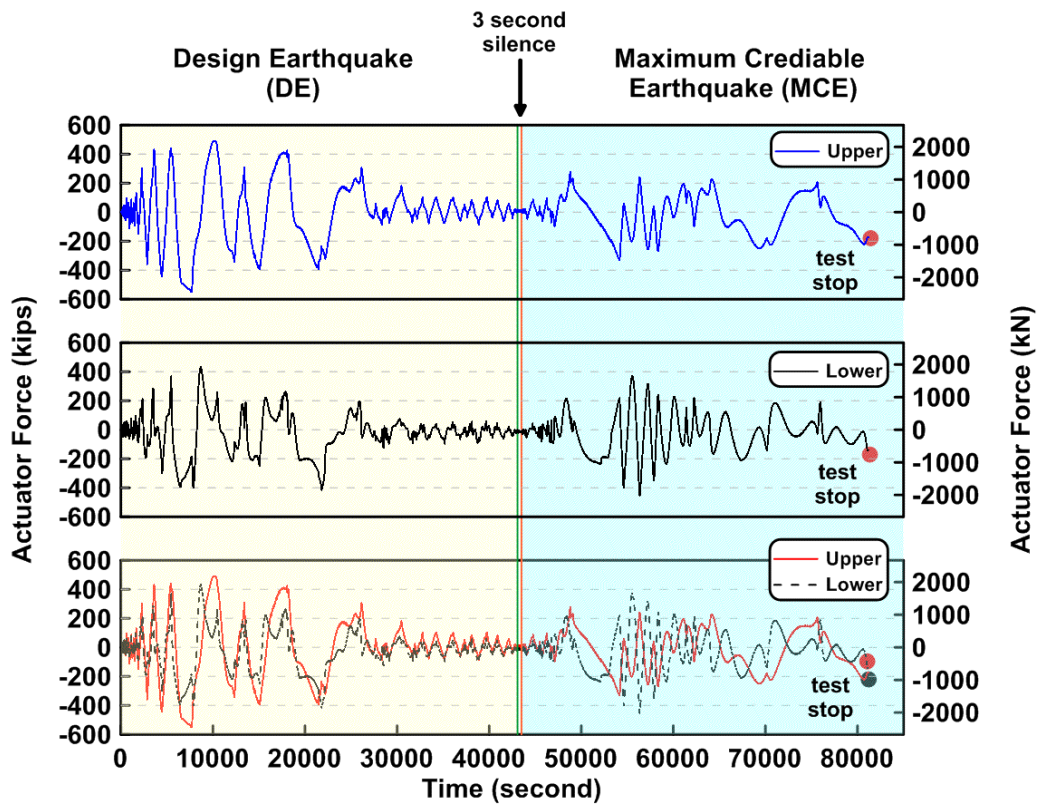


Figure 4.345 Specimen TCBF-B-4: actuator force histories.

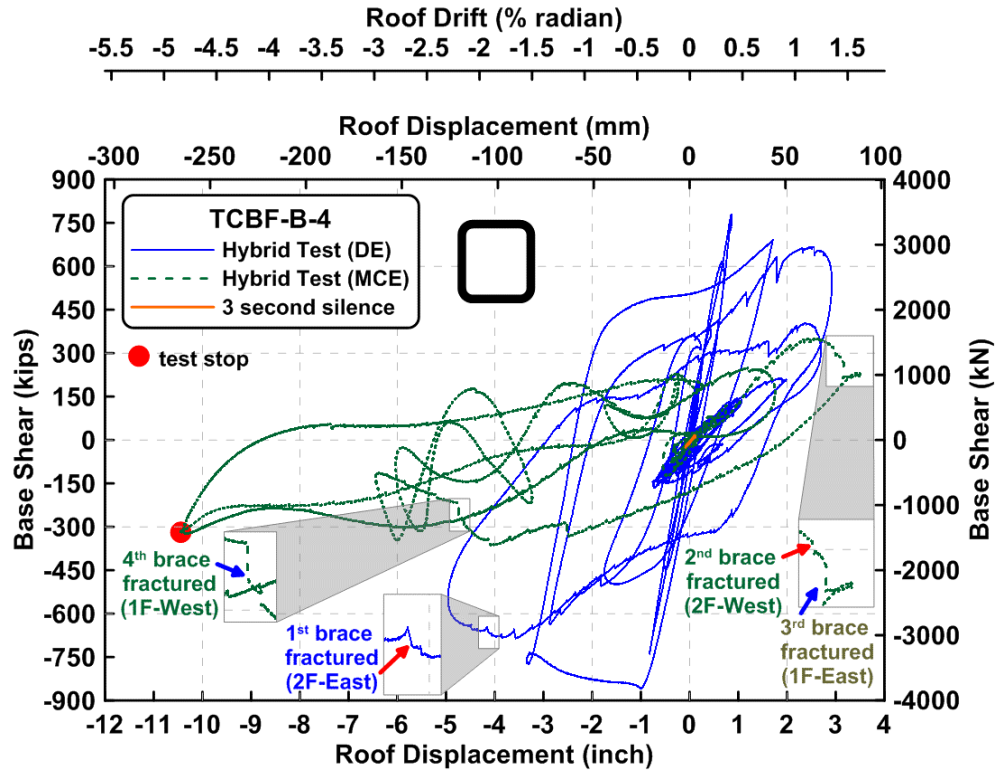


Figure 4.346 Specimen TCBF-B-4: base shear versus roof displacement relationship.

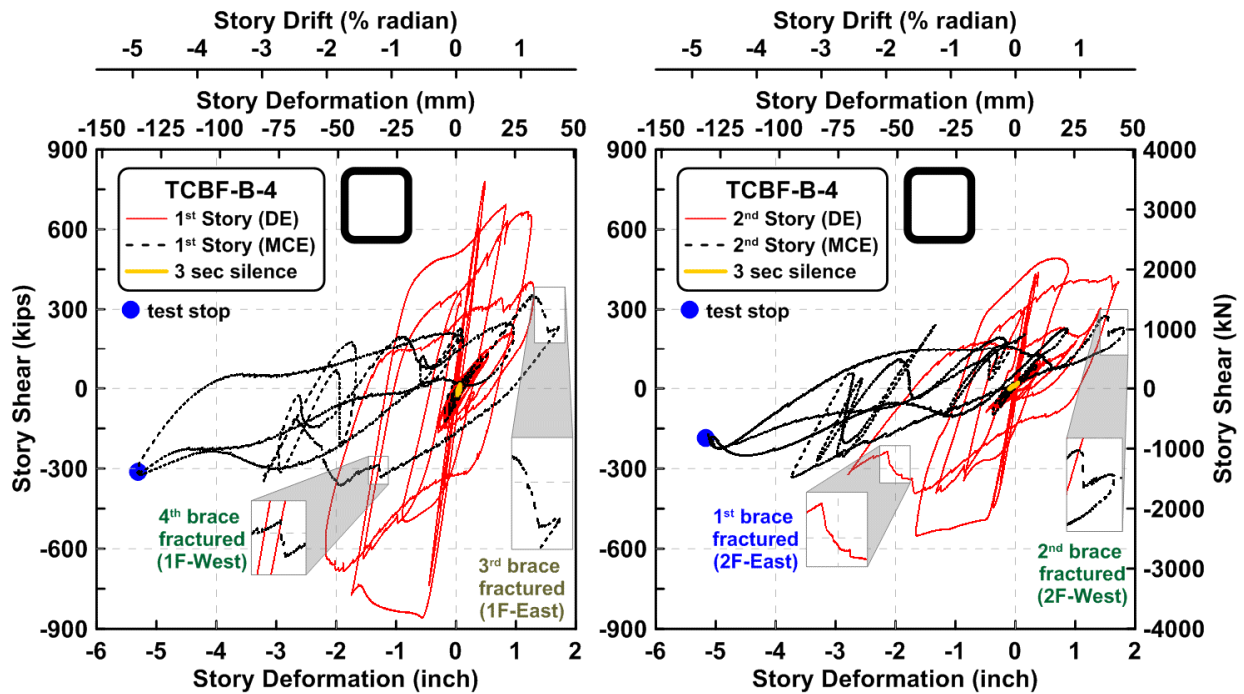


Figure 4.347 Specimen TCBF-B-4: story shear versus story deformation relationship.

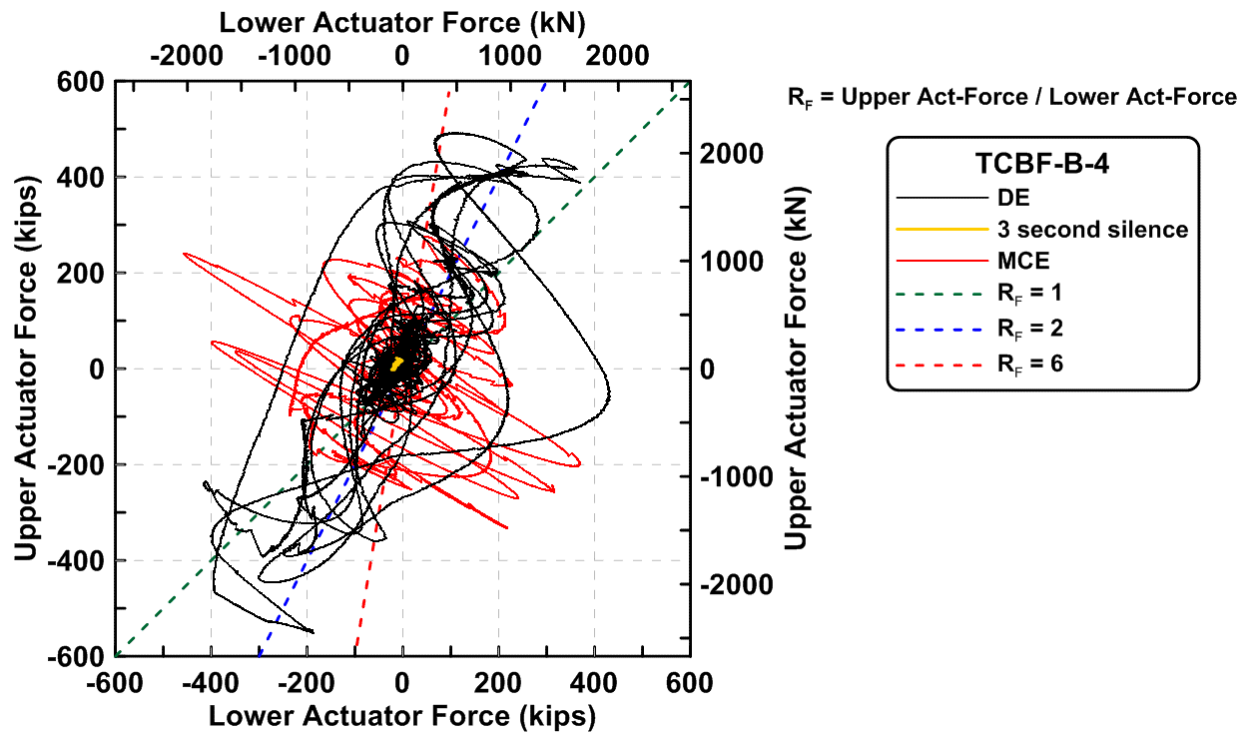


Figure 4.348 Specimen TCBF-B-4: upper actuator force versus lower actuator force relationship.

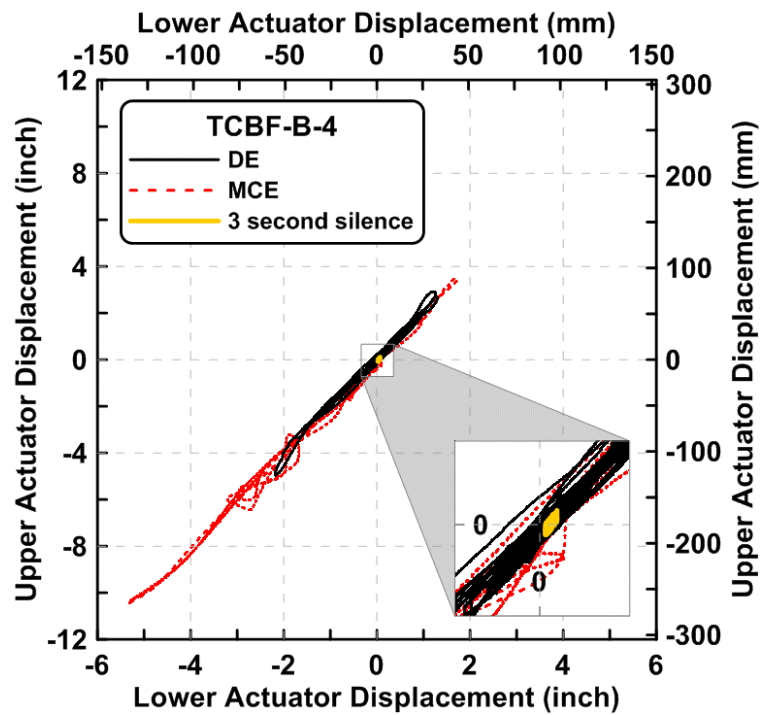


Figure 4.349 Specimen TCBF-B-4: actuator displacement versus lower actuator displacement relationship.

4.2.2.2 Column Response

The time history of the axial forces in $W12 \times 96$ columns at the western and eastern sides of the specimen is plotted in Figure 4.350. The relationship between roof displacements and axial forces at both columns is shown in Figure 4.351. The bending moment time history at the top and bottom ends of the column in each story is shown in Figures 4.352 and 4.353. Derived column shear force time history in both stories are plotted in Figures 4.354 and 4.355, respectively. Two column shear forces in each floor were added together and are shown in Figure 4.356. The column web shear stress versus shear strain readings from strain rosettes is plotted in Figure 4.357. The sum of the column shear force components versus the total story shear forces for each story is shown in Figure 4.358. The derived rosette-type strain gauge readings in the column web at each story are shown from Figures 4.359 to 4.362. Normalized maximum and minimum principal stress relationships along with different yield criteria are plotted in Figures 4.363 to 4.366. The normalized P-M and P-V interaction diagrams at column bases and column top ends are shown in Figures 4.367 to 4.370.

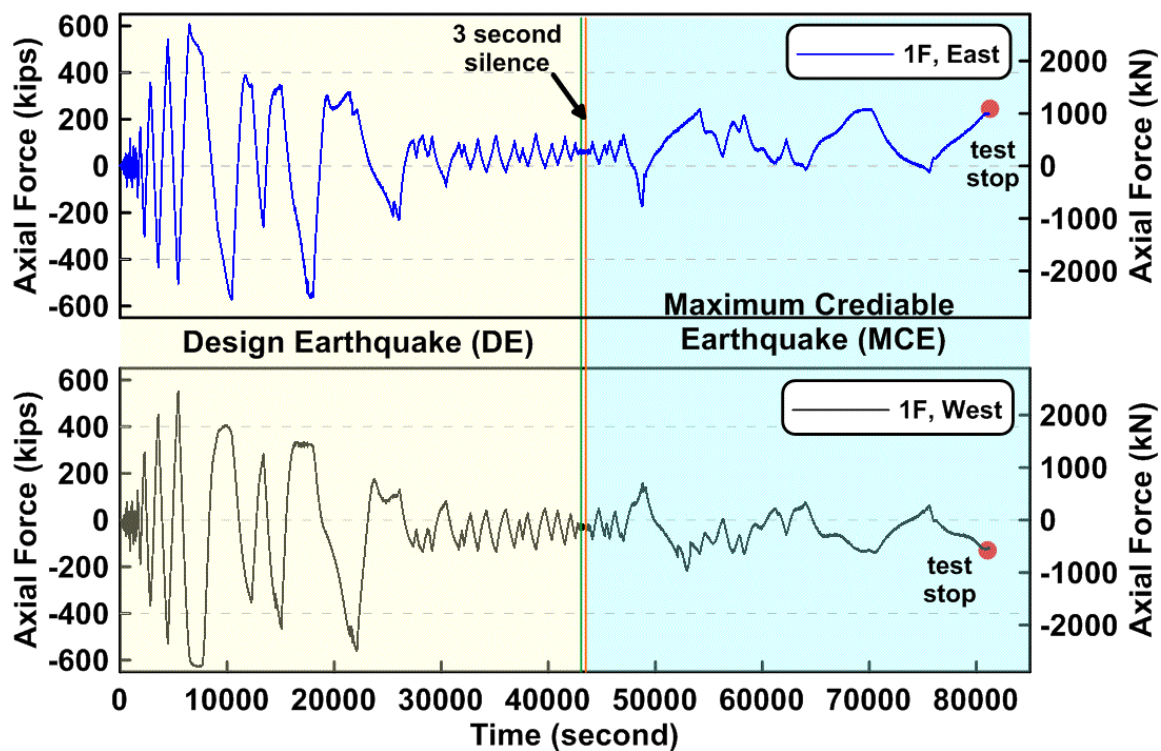


Figure 4.350 Specimen TCBF-B-4: time history of first-story column axial forces (location: 3 ft above column base plate).

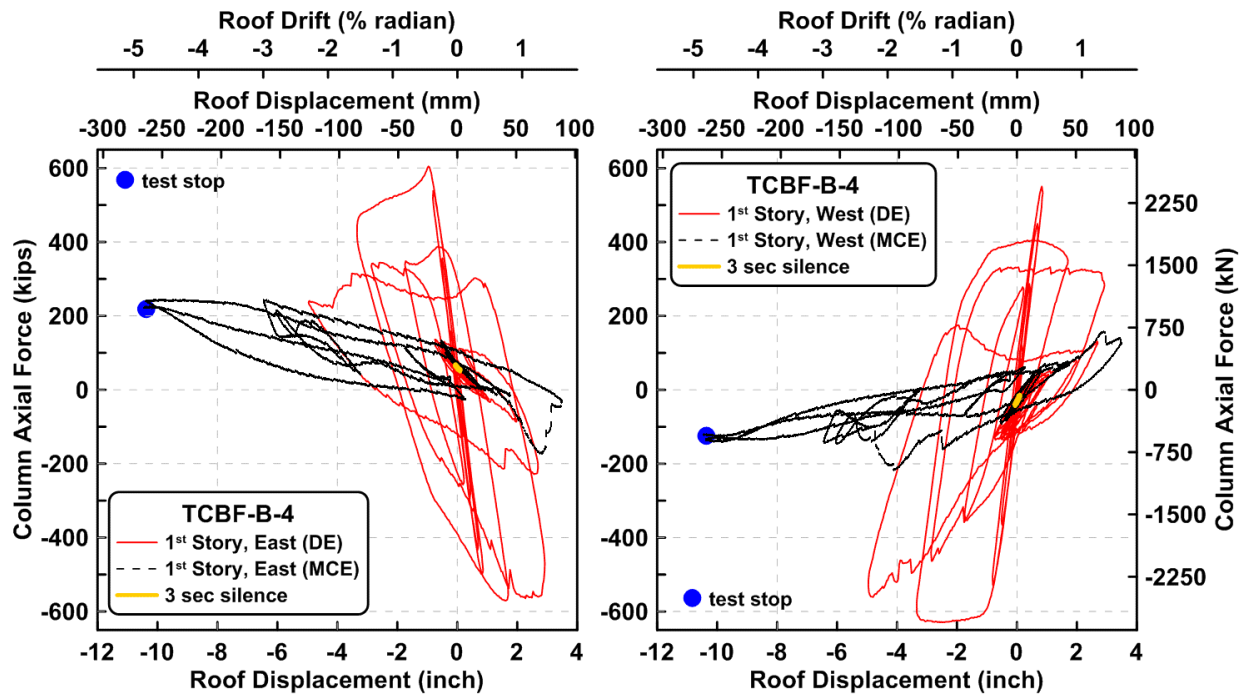


Figure 4.351 Specimen TCBF-B-4: roof displacement versus first-story column axial forces.

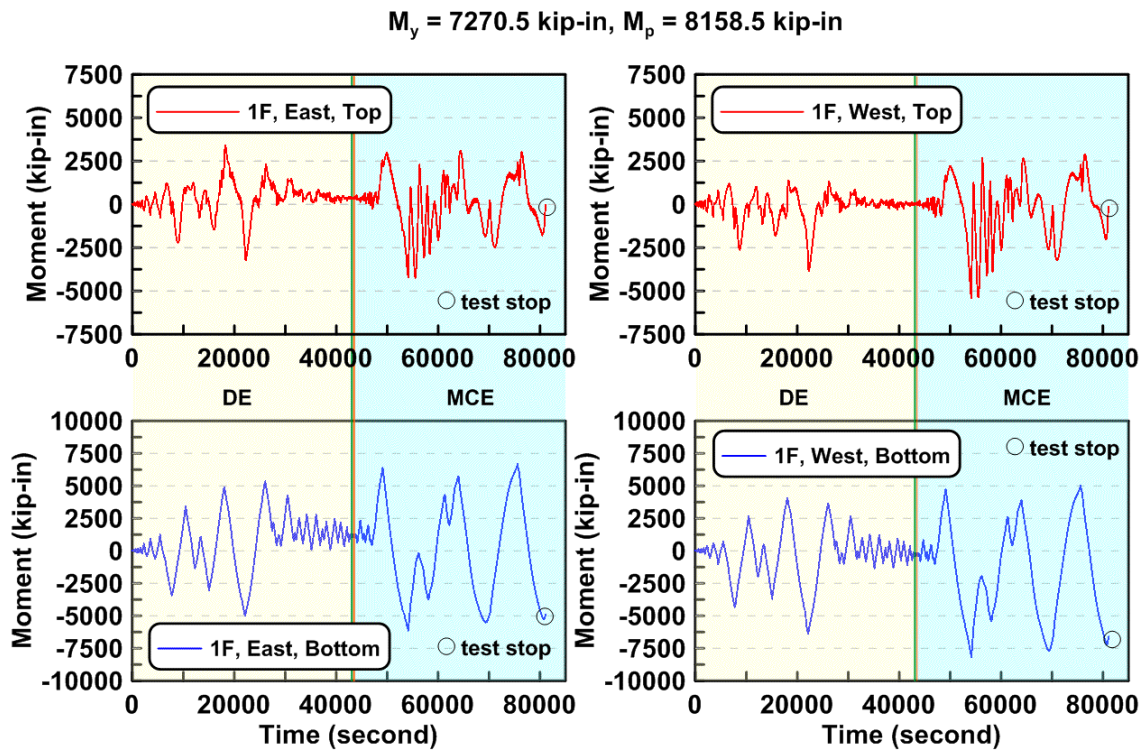


Figure 4.352 Specimen TCBF-B-4: time history of first-story column bending moments (3 ft above column base plate and 3 ft below lower beam centerline).

$$M_y = 7270.5 \text{ kip-in}, M_p = 8158.5 \text{ kip-in}$$

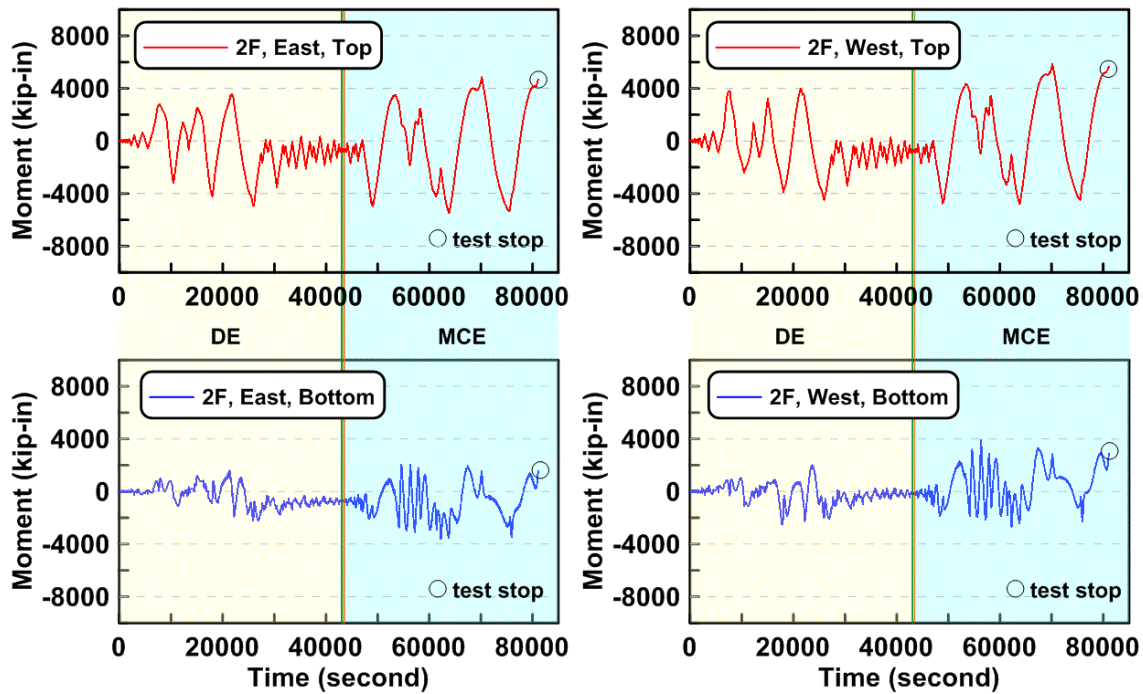


Figure 4.353 Specimen TCBF-B-4: time history of second-story column bending moments (3 ft above lower beam centerline and 3 ft below roof beam centerline).

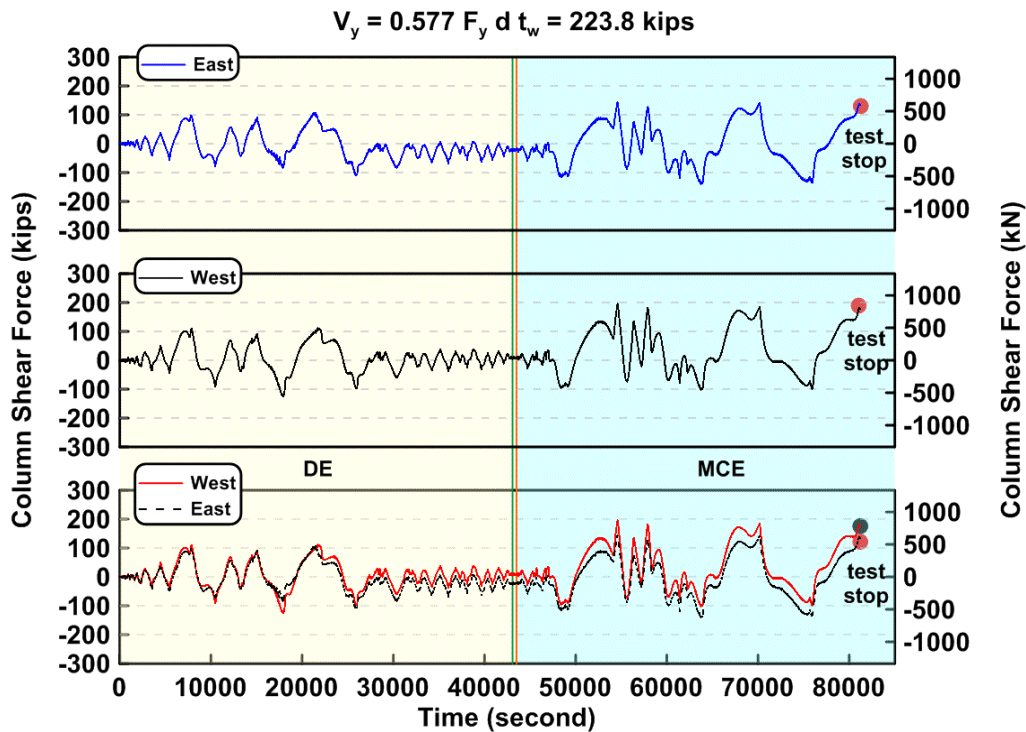


Figure 4.354 Specimen TCBF-B-4: time history of the first-story column shear forces.

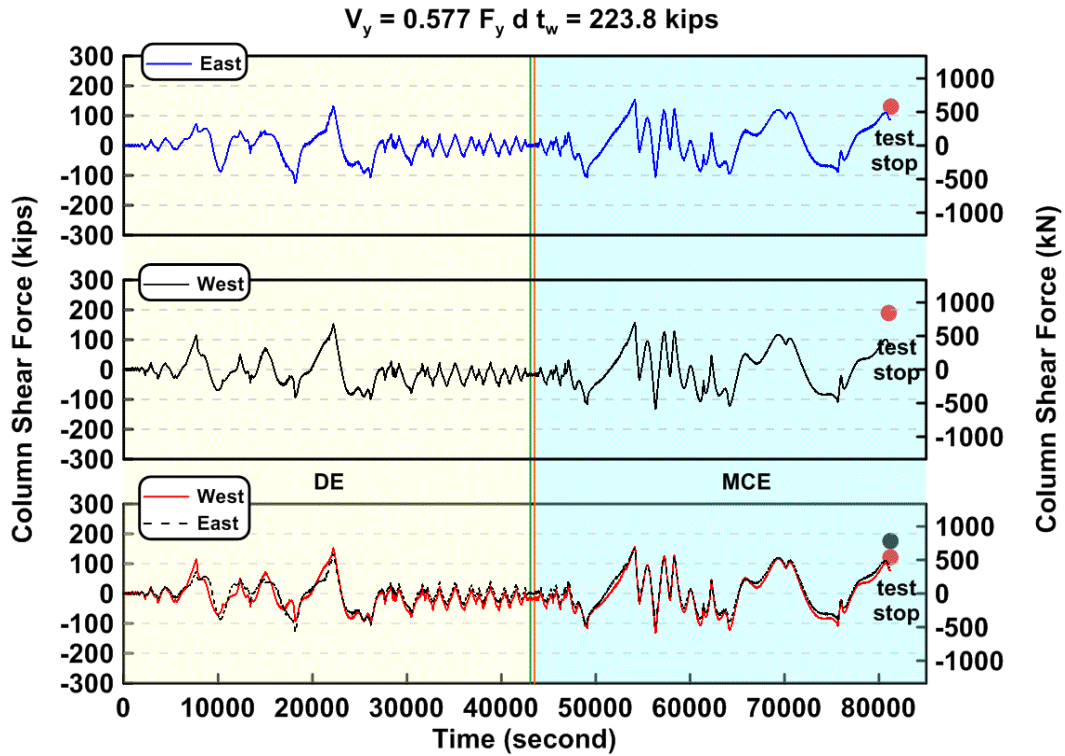


Figure 4.355 Specimen TCBF-B-4: time history of second-story column shear forces.

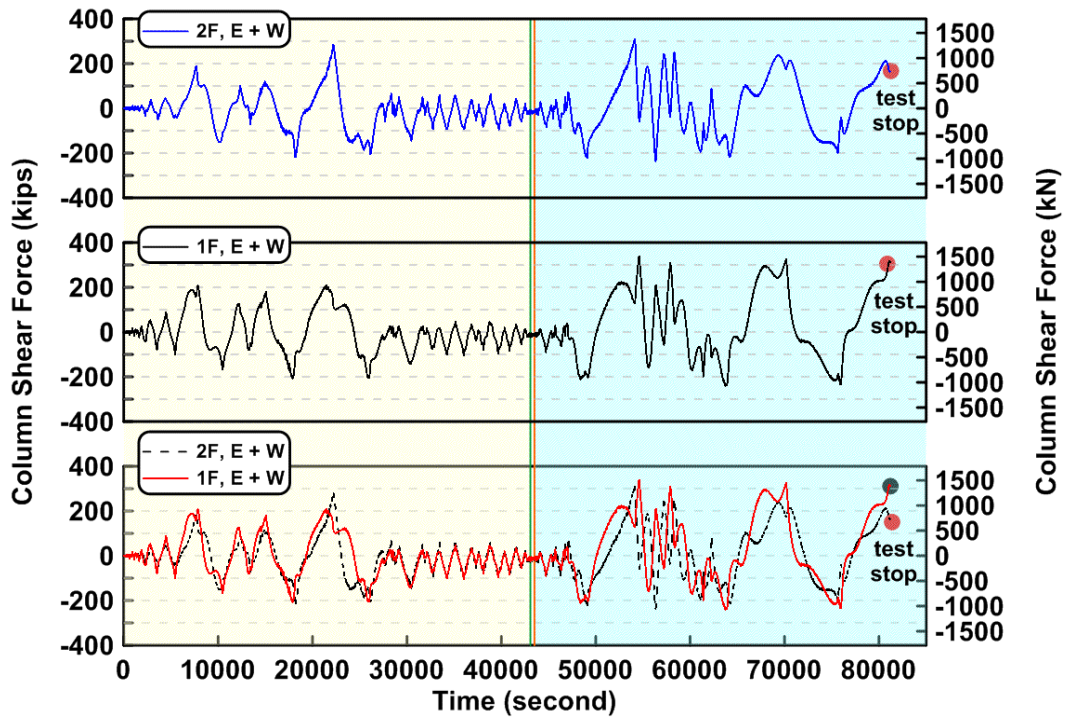


Figure 4.356 Specimen TCBF-B-4: time history of sum of east and west column shear forces for both stories.

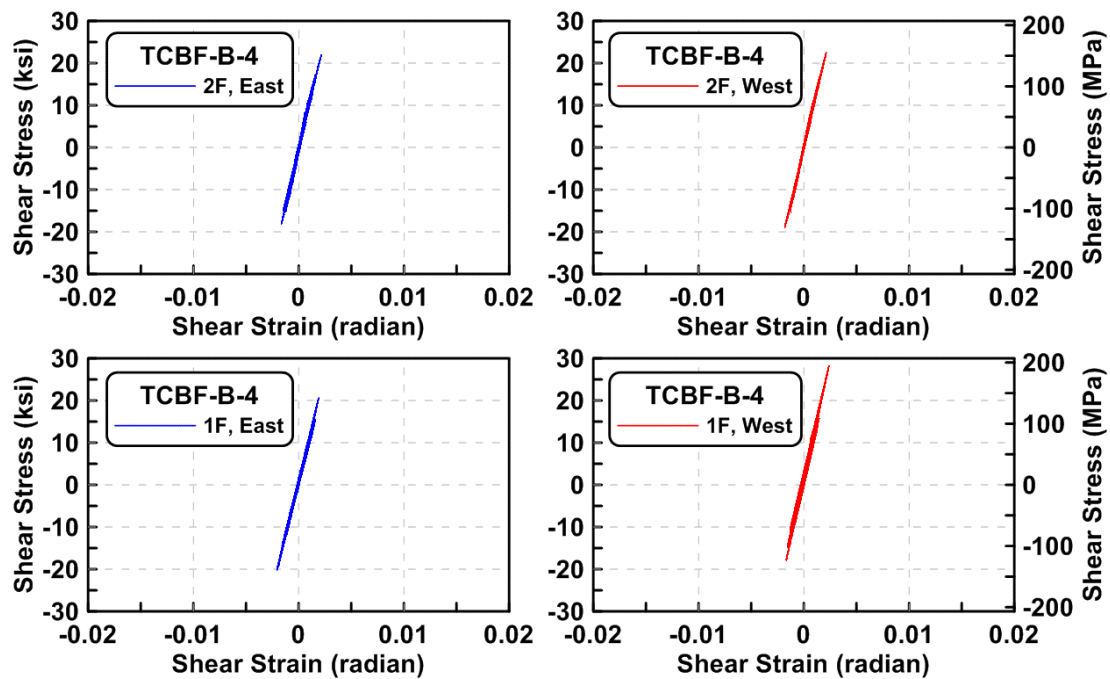


Figure 4.357 Specimen TCBF-B-4: column shear stress versus shear strain relationships (locations: EC1-B-N, EC2-B-N, WC1-B-N and WC2-B-N).

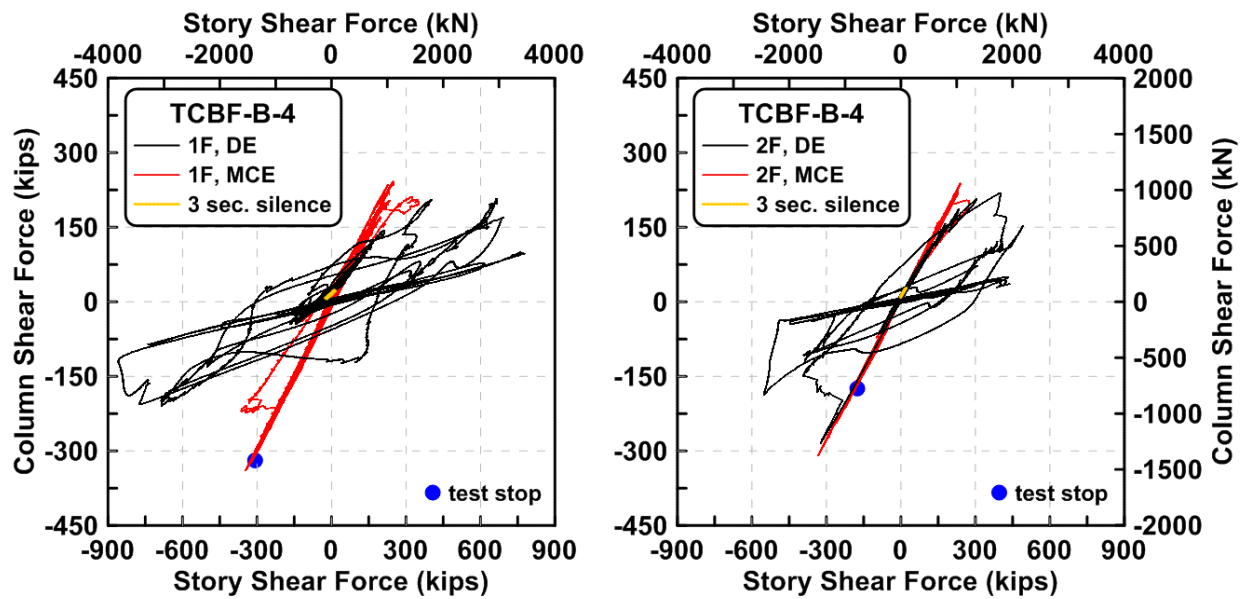


Figure 4.358 Specimen TCBF-B-4: story shear component from columns versus total story shear forces.

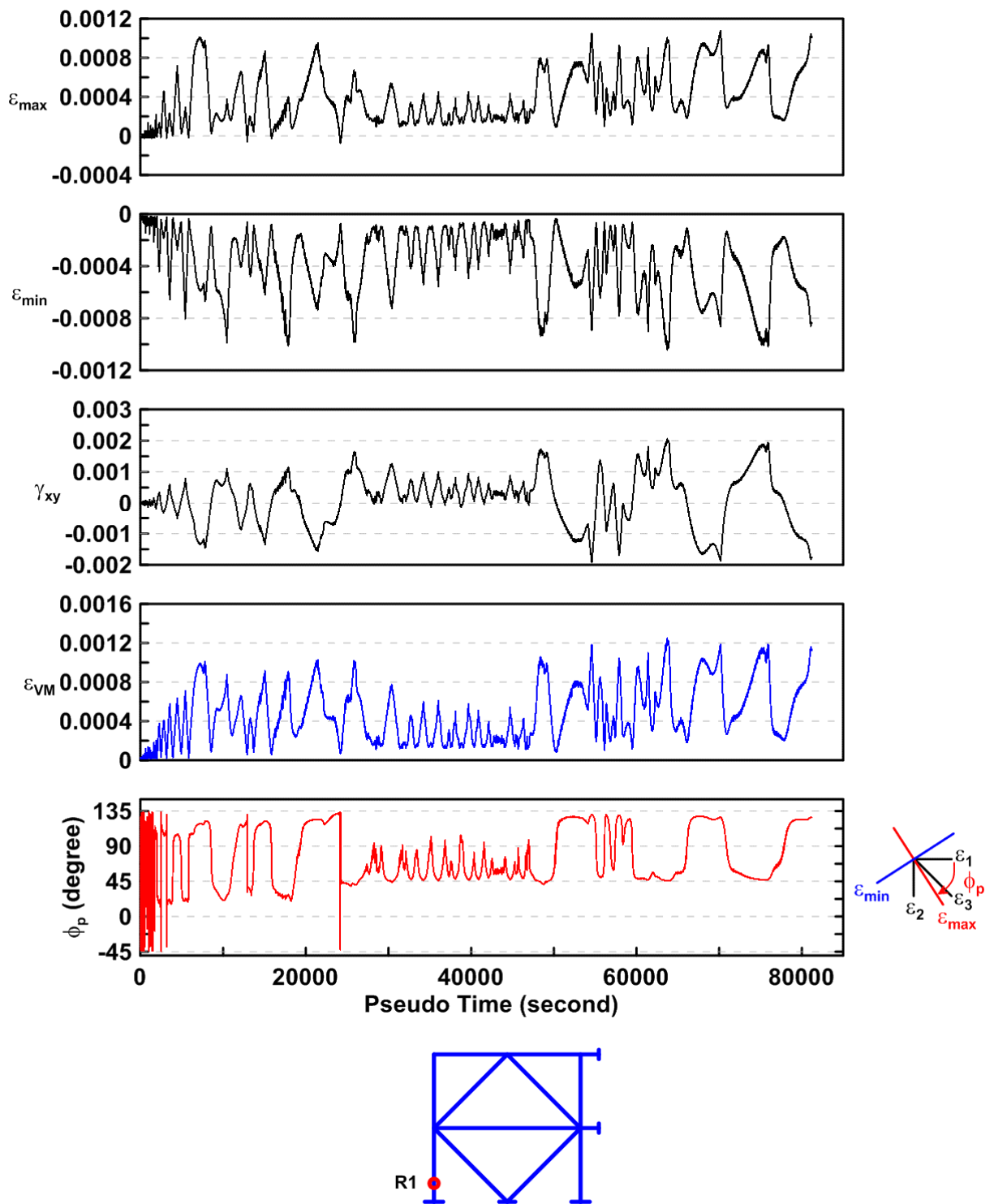


Figure 4.359 Specimen TCBF-B-4: time history of rosette-type strain gauge readings in the first-story column web (location: R1).

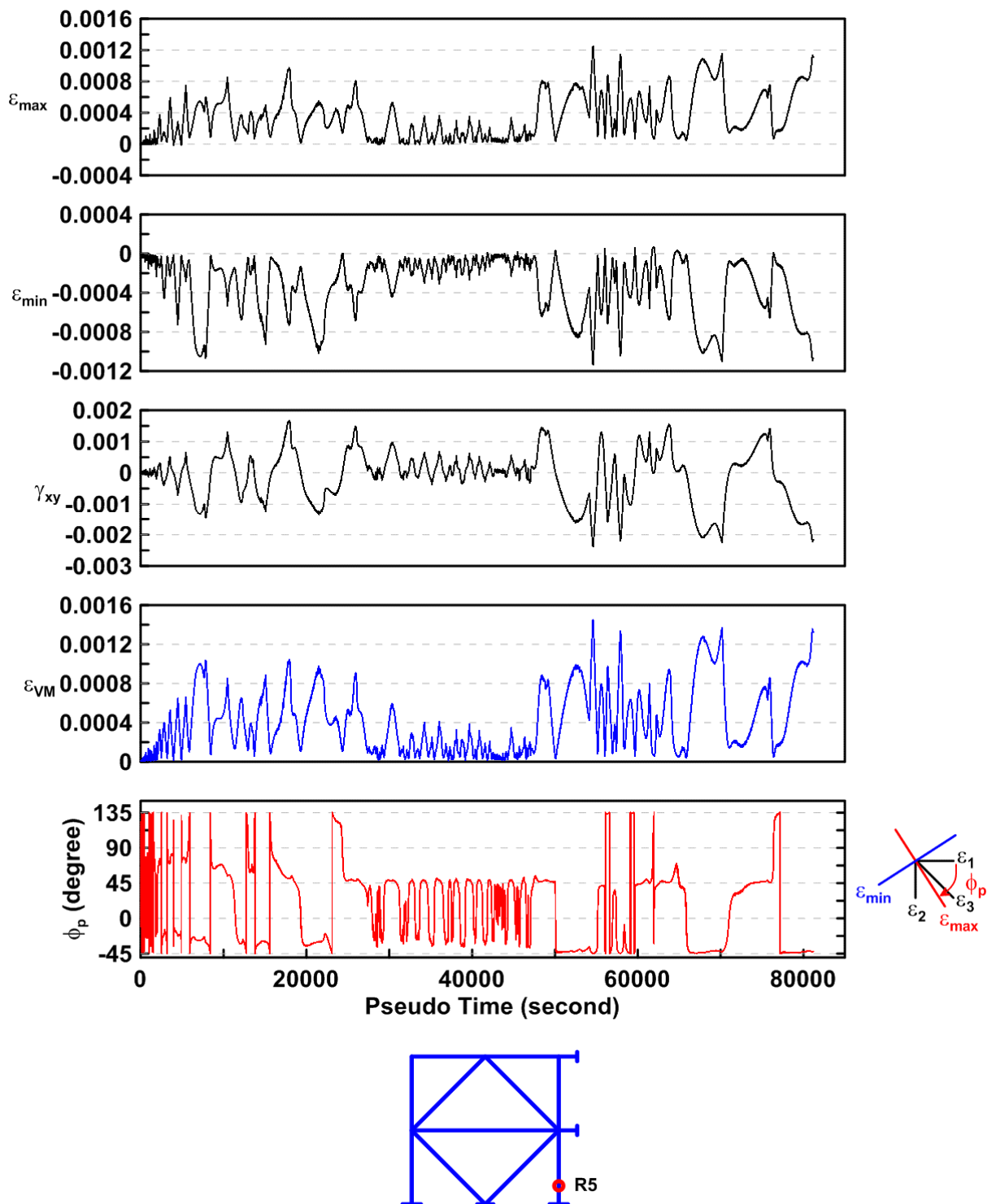


Figure 4.360 Specimen TCBF-B-4: time history of rosette-type strain gauge readings in first-story column web (location: R5).

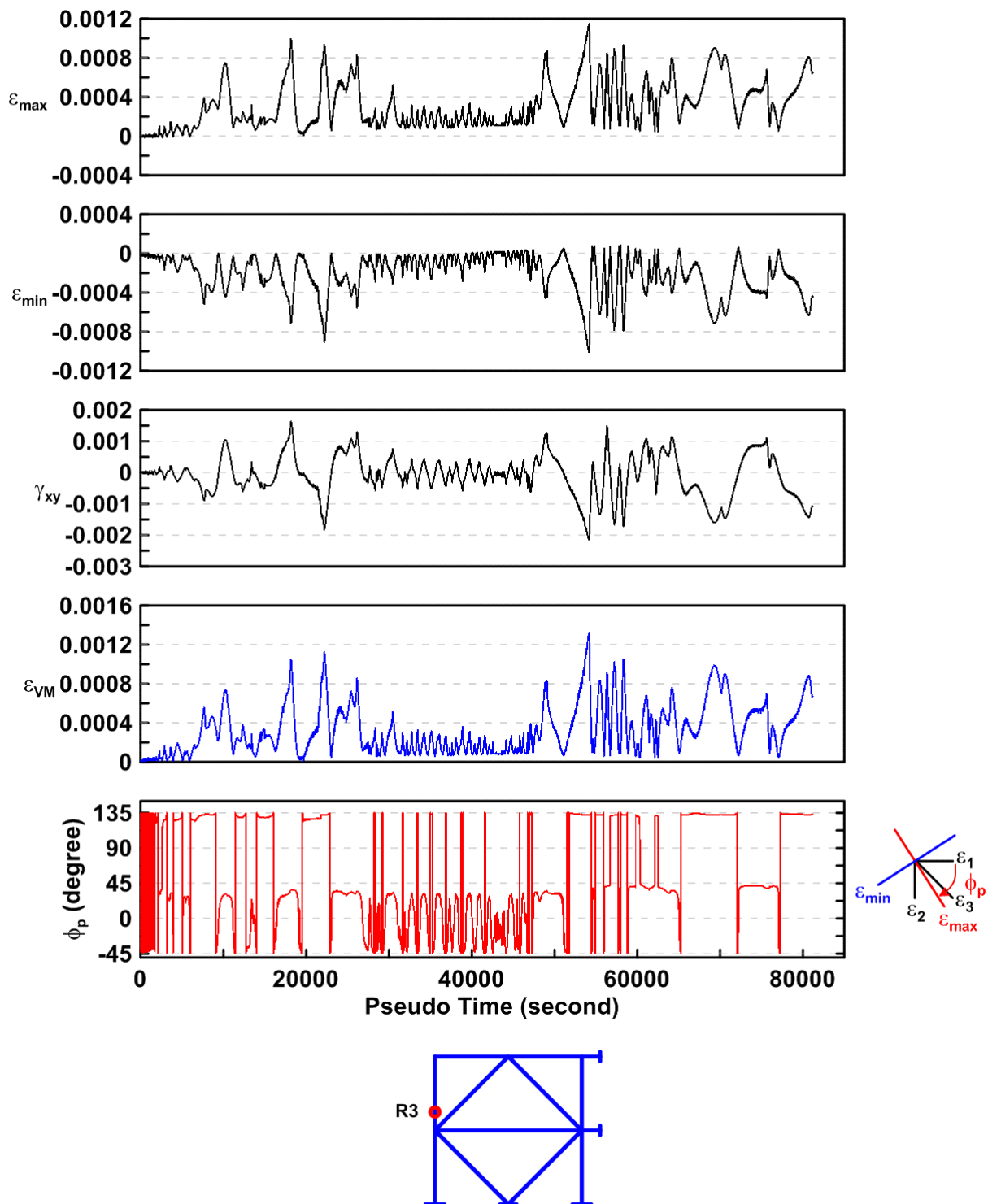


Figure 4.361 Specimen TCBF-B-4: time history of rosette-type strain gauge readings in first-story column web (location: R3).

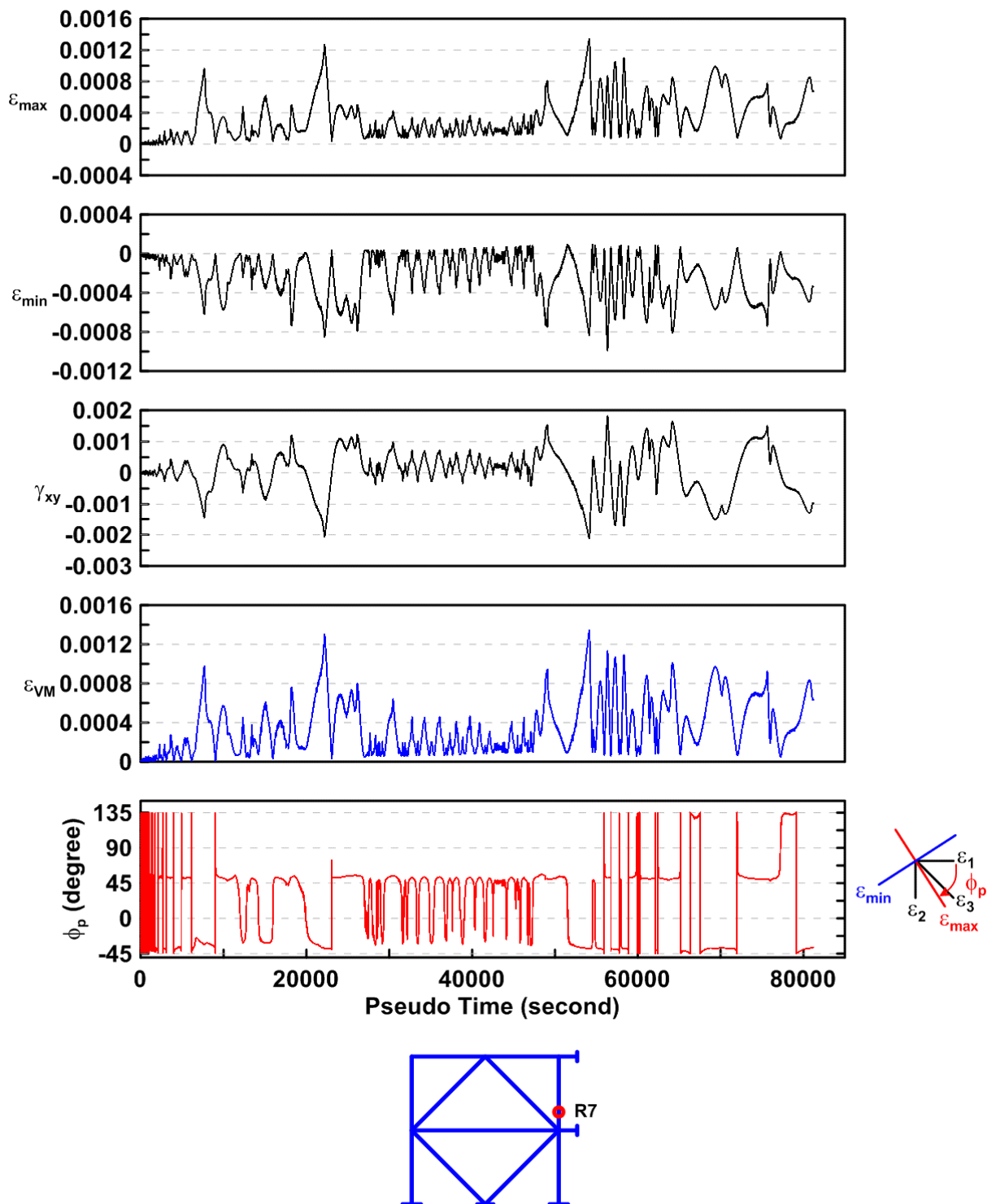


Figure 4.362 Specimen TCBF-B-4: time history of rosette-type strain gauge readings in first-story column web (location: R7).

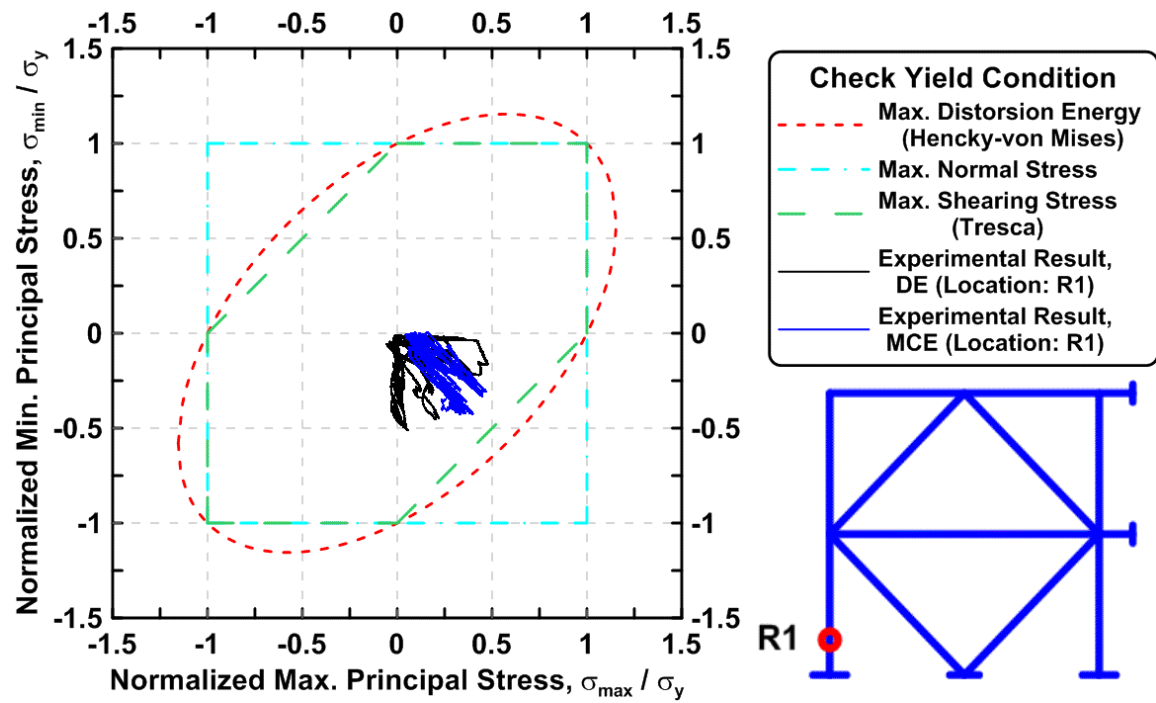


Figure 4.363 Specimen TCBF-B-4: maximum principal stress versus minimum principal stress in the first-story column (location: R1).

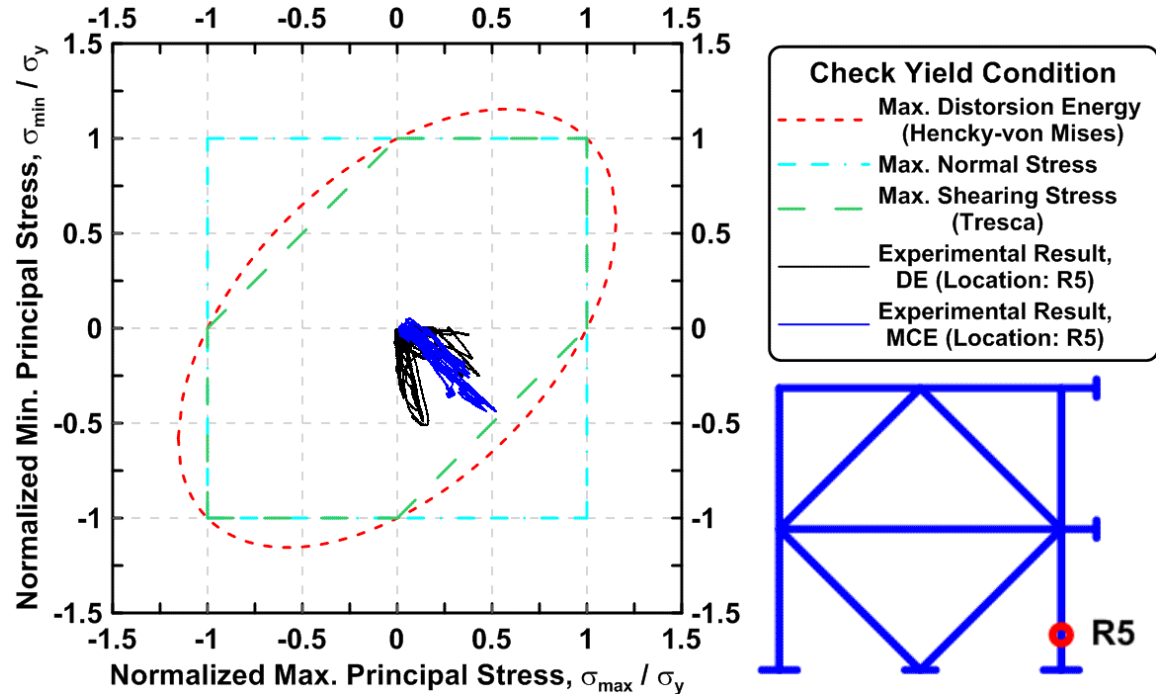


Figure 4.364 Specimen TCBF-B-4: maximum principal stress versus minimum principal stress in the first-story column (location: R5).

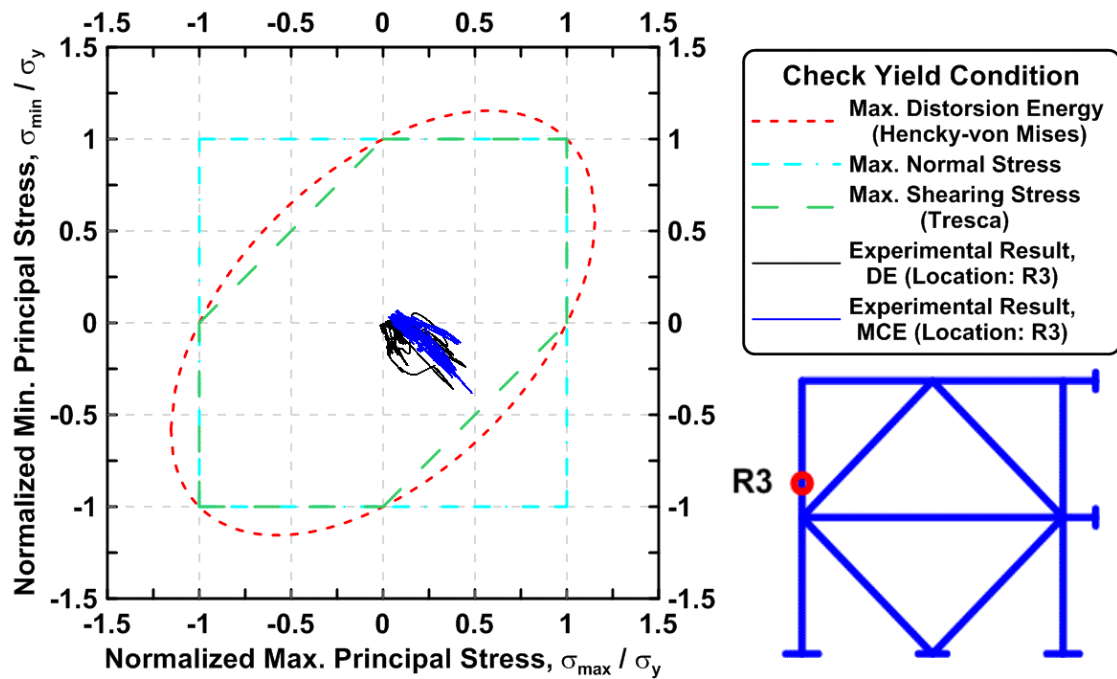


Figure 4.365 Specimen TCBF-B-4: maximum principal stress versus minimum principal stress in first-story column (location: R3).

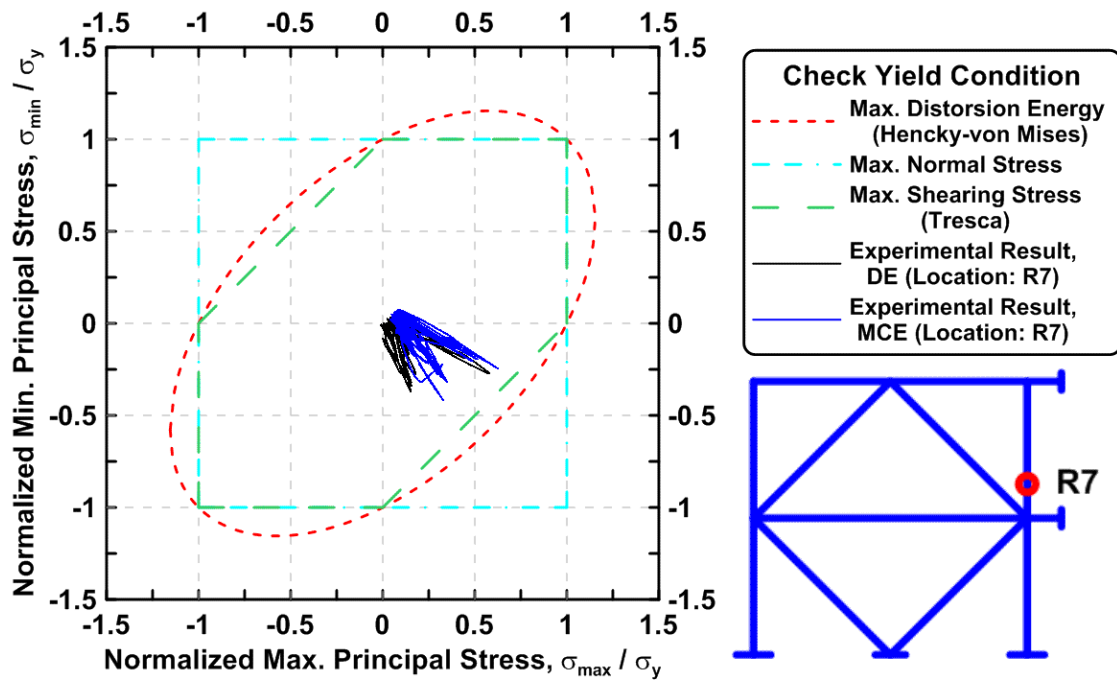


Figure 4.366 Specimen TCBF-B-4: maximum principal stress versus minimum principal stress in first-story column (location: R7).

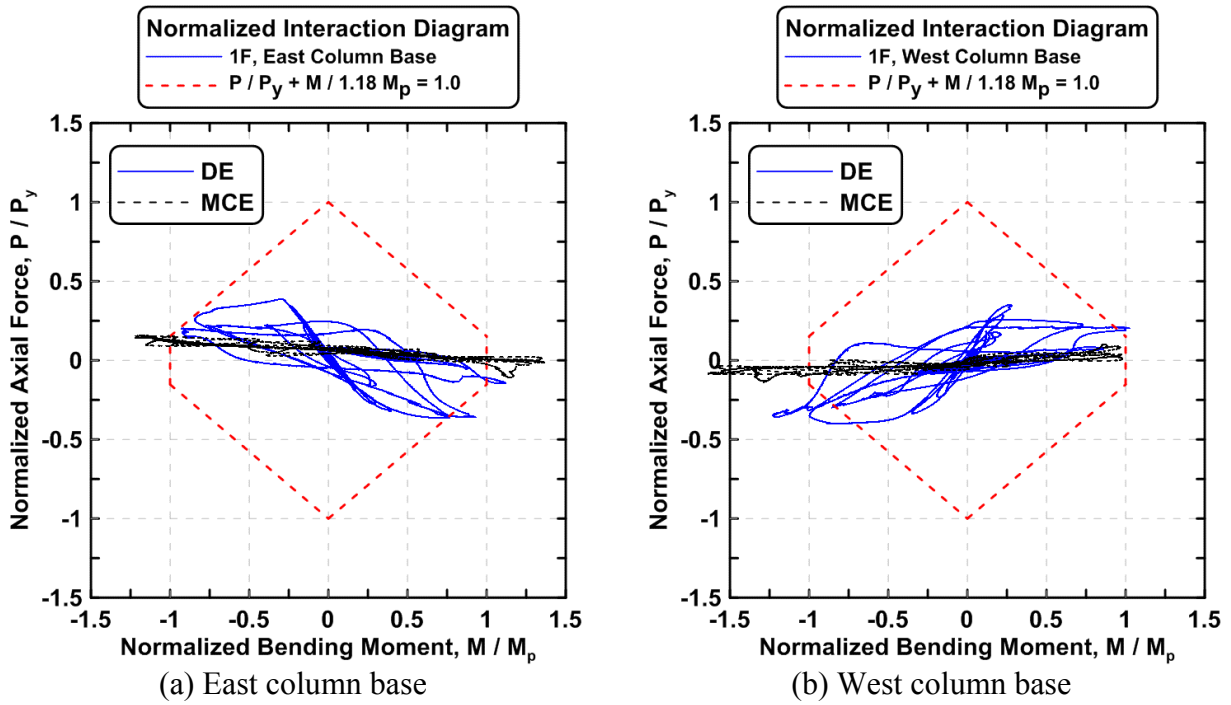


Figure 4.367 Specimen TCBF-B-4: normalized P-M interaction diagrams of first-story columns.

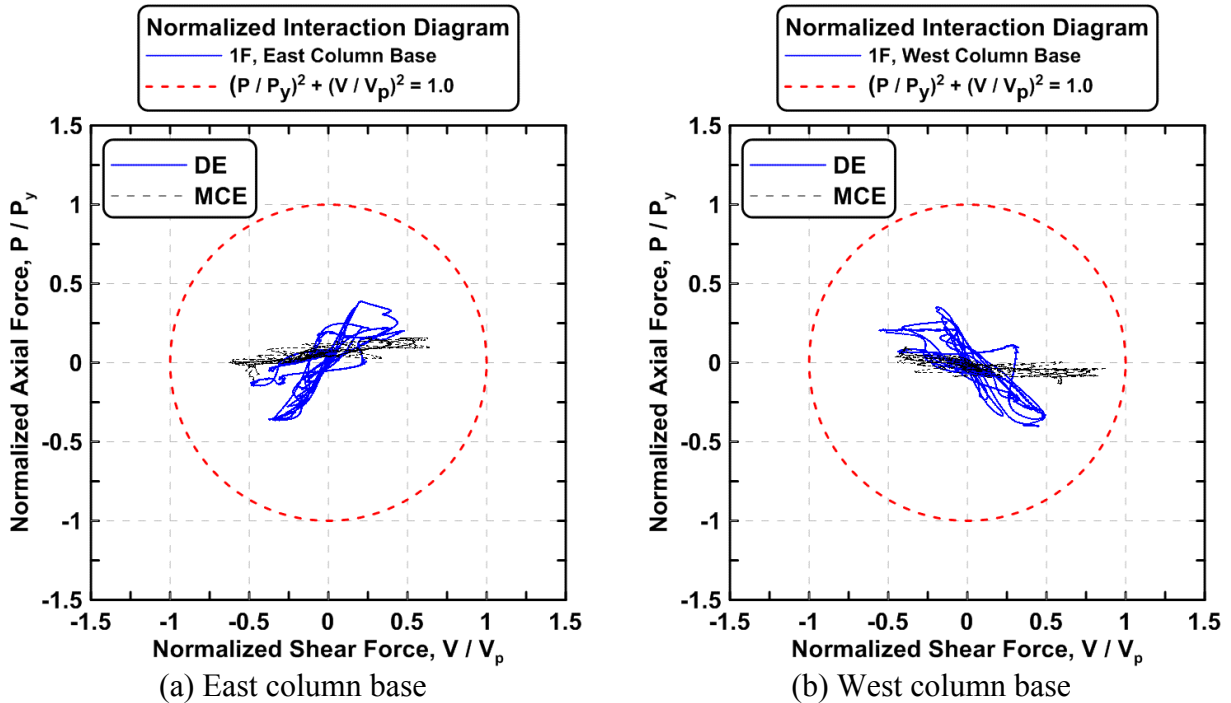
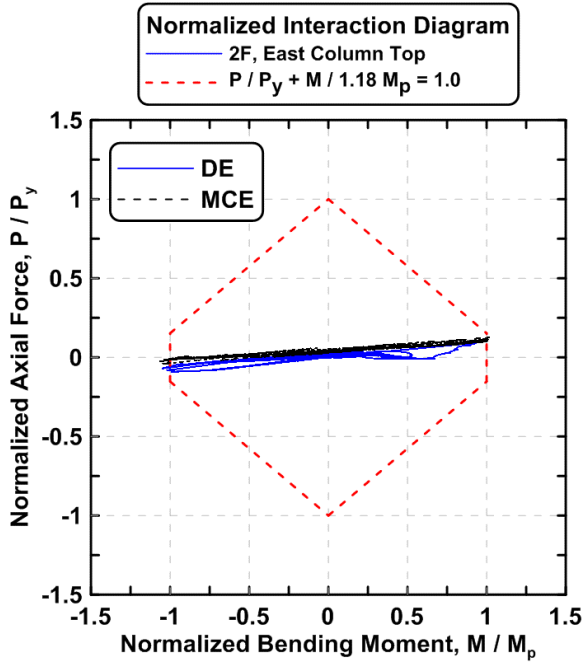
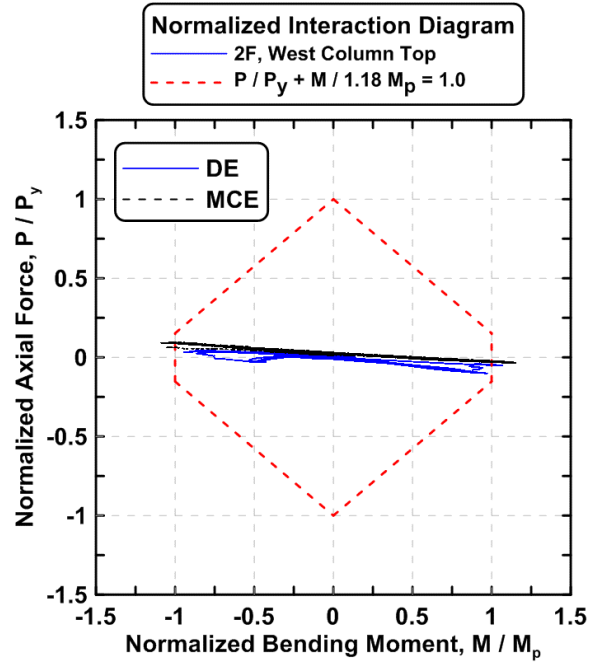


Figure 4.368 Specimen TCBF-B-4: normalized P-V interaction diagrams of first-story columns.

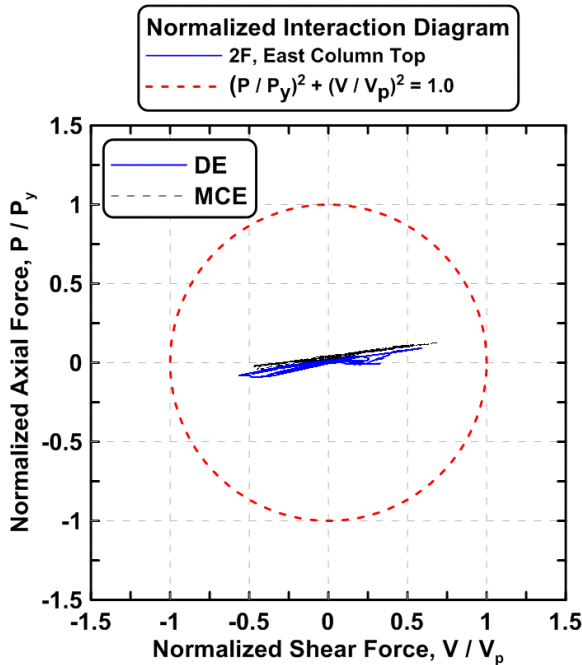


(a) East column top

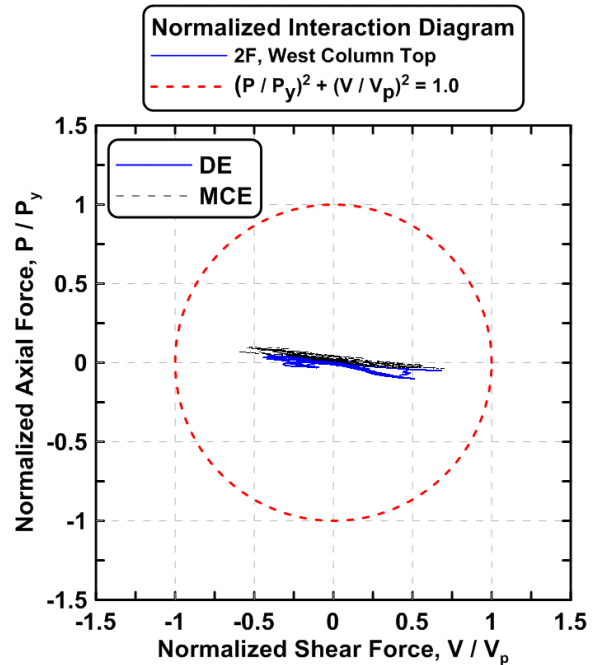


(b) West column top

Figure 4.369 Specimen TCBF-B-4: normalized P-M interaction diagrams of second-story columns.



(a) East column top



(b) West column top

Figure 4.370 Specimen TCBF-B-4: normalized P-V interaction diagrams of second-story columns.

4.2.2.3 Beam Response

The vertical deflection time history at the center of W24 \times 117 roof beam and W24 \times 68 lower beam is plotted in Figure 4.371. The time history of strain readings at both ends of roof beam and lower beam are shown in Figures 4.372 and 4.373, respectively. Both beam axial force time histories derived from linear type strain gauges at different locations of the beams are plotted in Figures 4.374 and 4.375. The bending moment time histories of both beams are shown in Figures 4.376 and 4.377. Estimated beam shear force time histories are illustrated in Figures 4.378 and 4.379. The unbalanced force in the roof beam center is plotted in Figure 4.380.

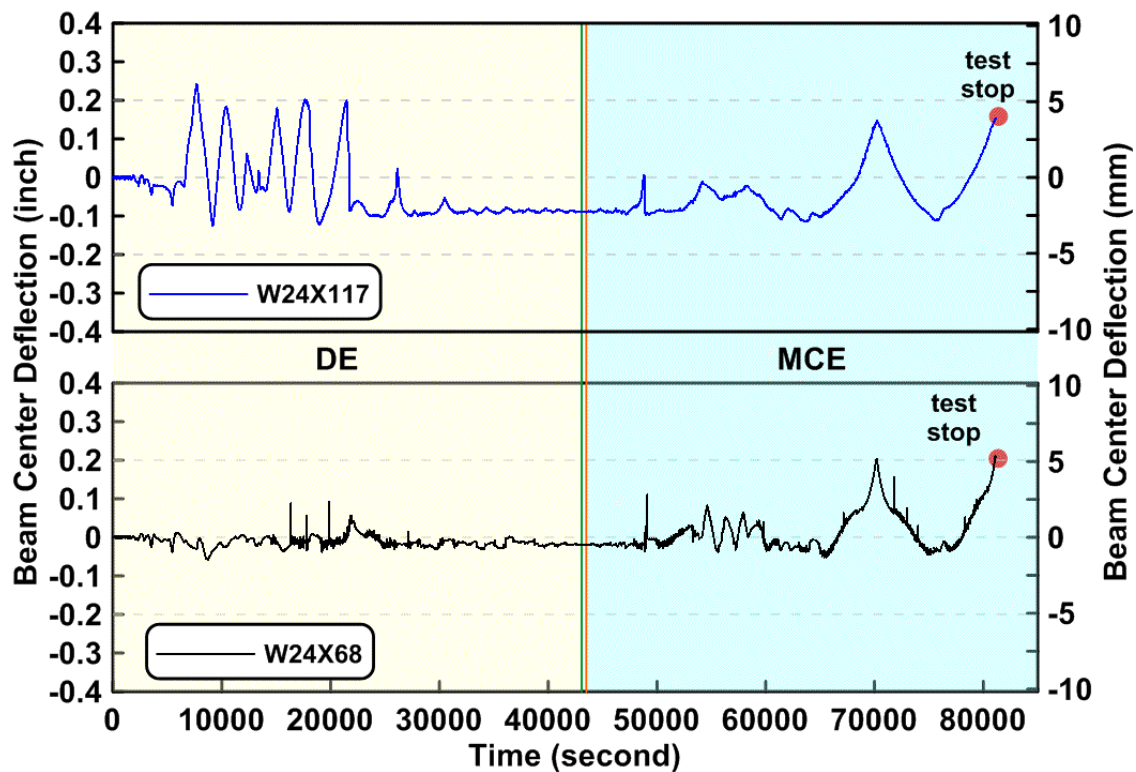


Figure 4.371 Specimen TCBF-B-4: deflection time history at center of beam span (roof beam: W24 \times 117, lower beam: W24 \times 68).

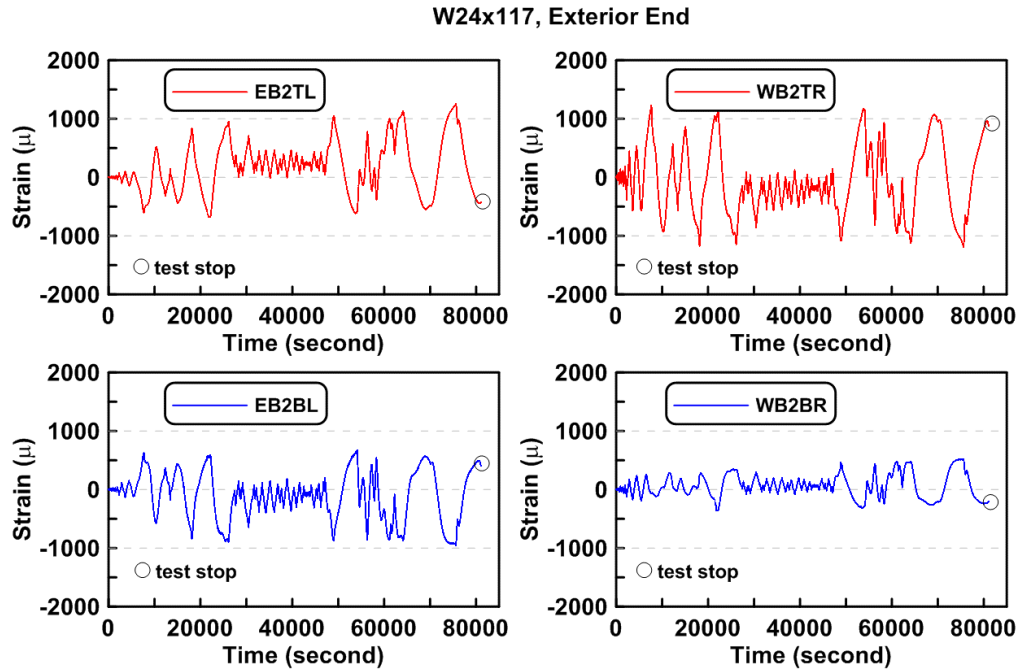


Figure 4.372 Specimen TCBF-B-4: time history of strain readings at both exterior ends of W24 \times 117 roof beam.

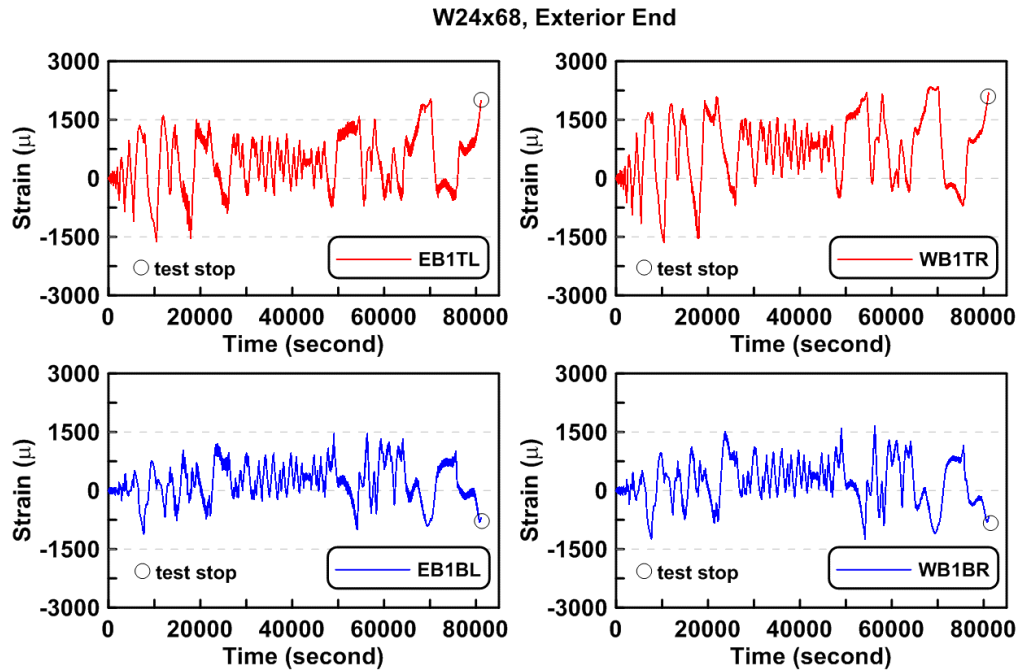


Figure 4.373 Specimen TCBF-B-4: time history of strain readings at both exterior ends of W24 \times 68 lower beam.

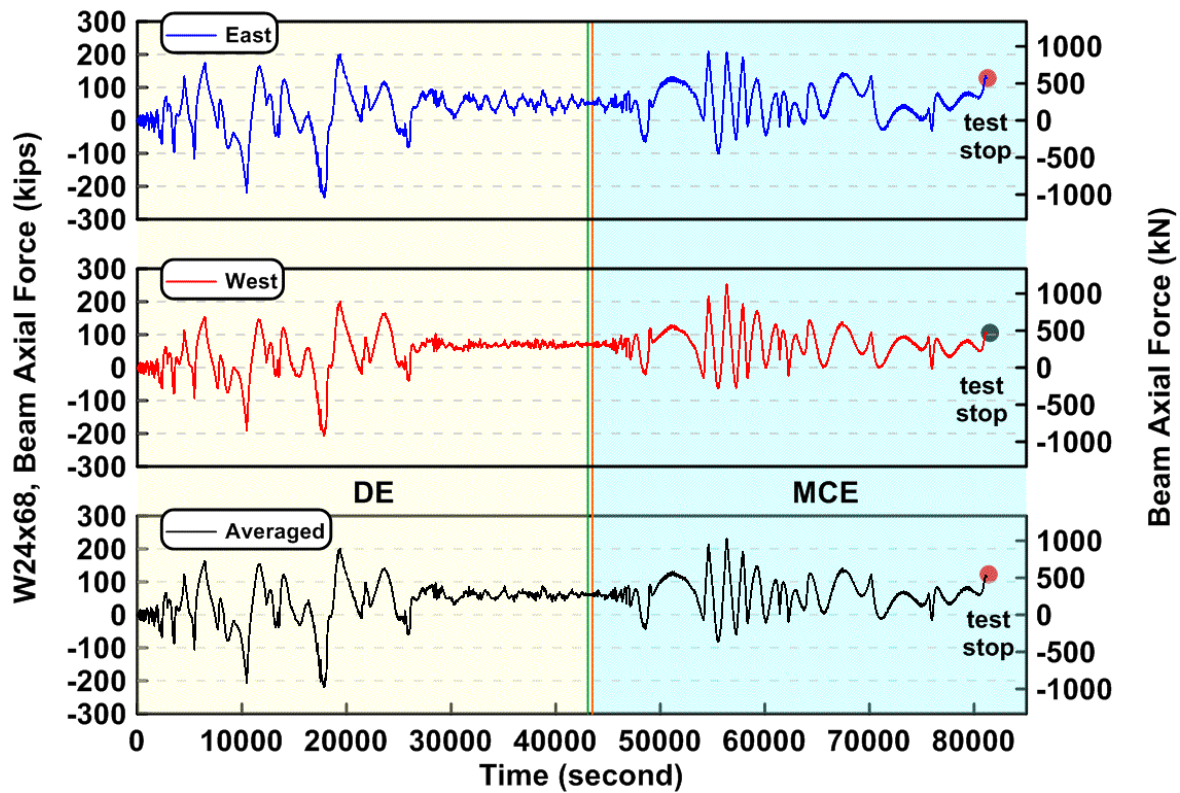


Figure 4.374 Specimen TCBF-B-4: time history of lower beam axial forces.

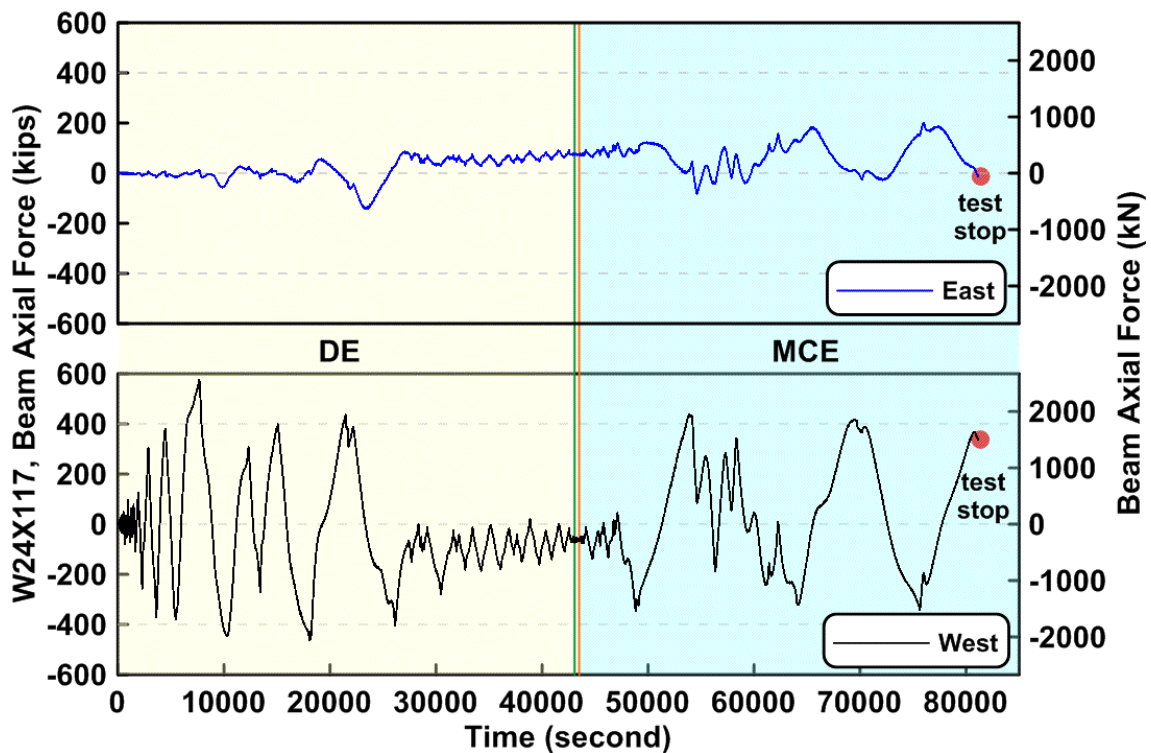


Figure 4.375 Specimen TCBF-B-4: time history of roof beam axial forces.

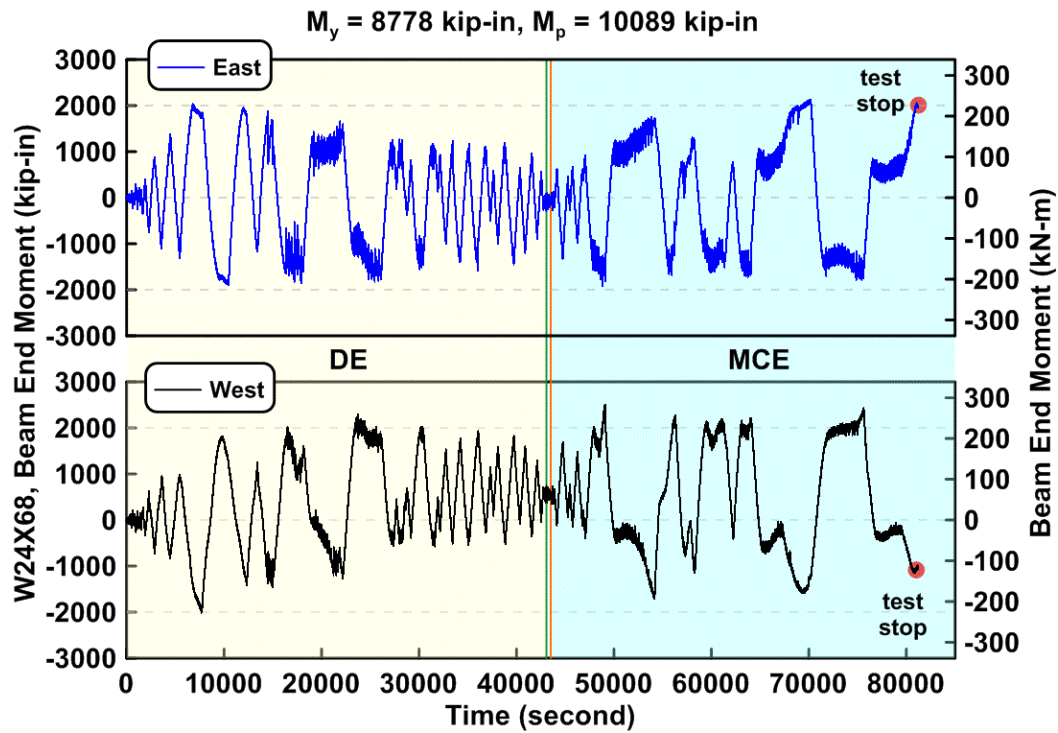


Figure 4.376 Specimen TCBF-B-4: time history of lower beam end bending moment.

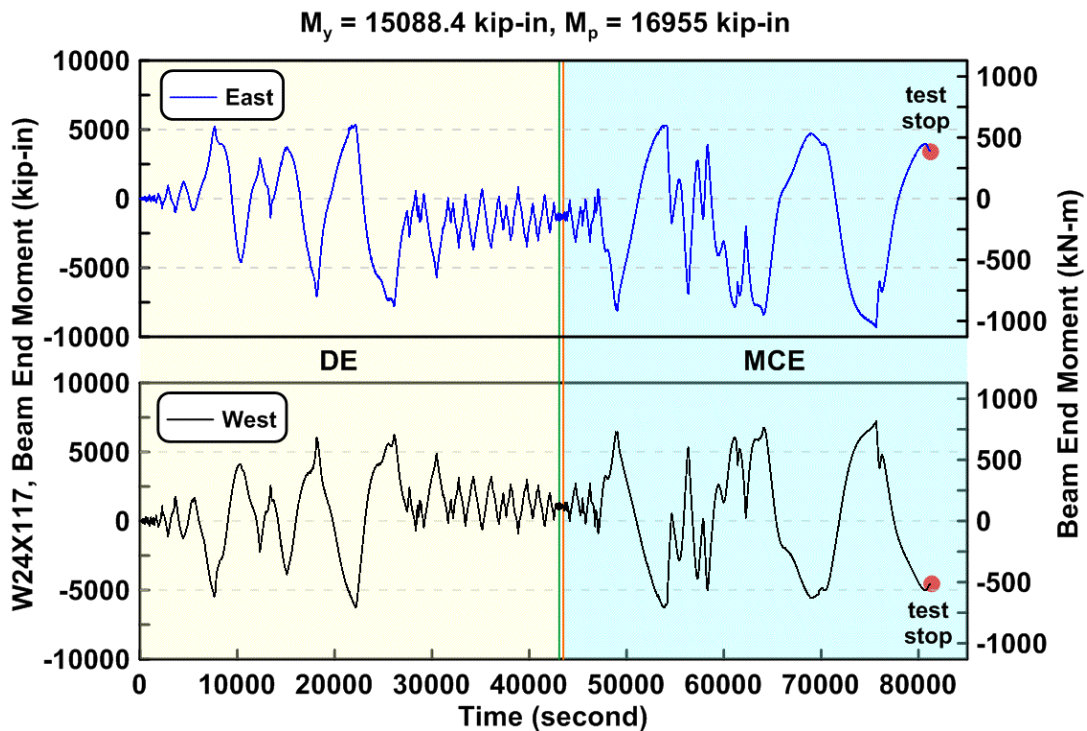


Figure 4.377 Specimen TCBF-B-4: time history of roof beam end bending moment.

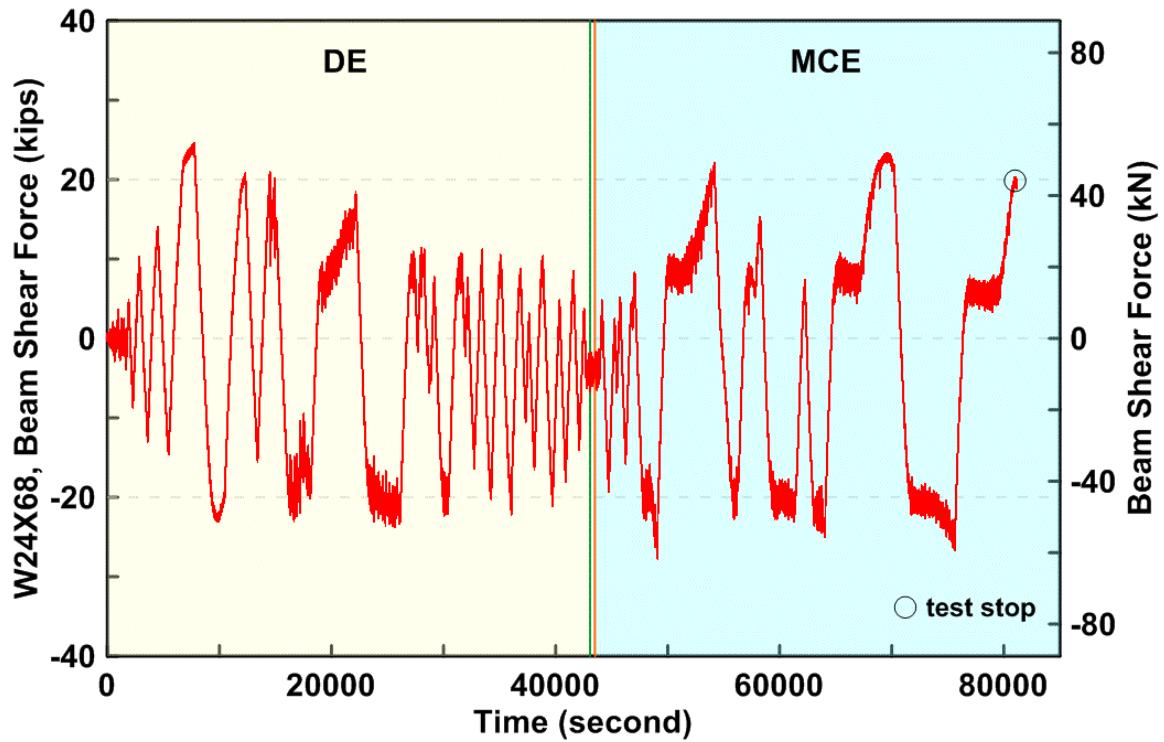


Figure 4.378 Specimen TCBF-B-4: lower beam estimated shear force time history.

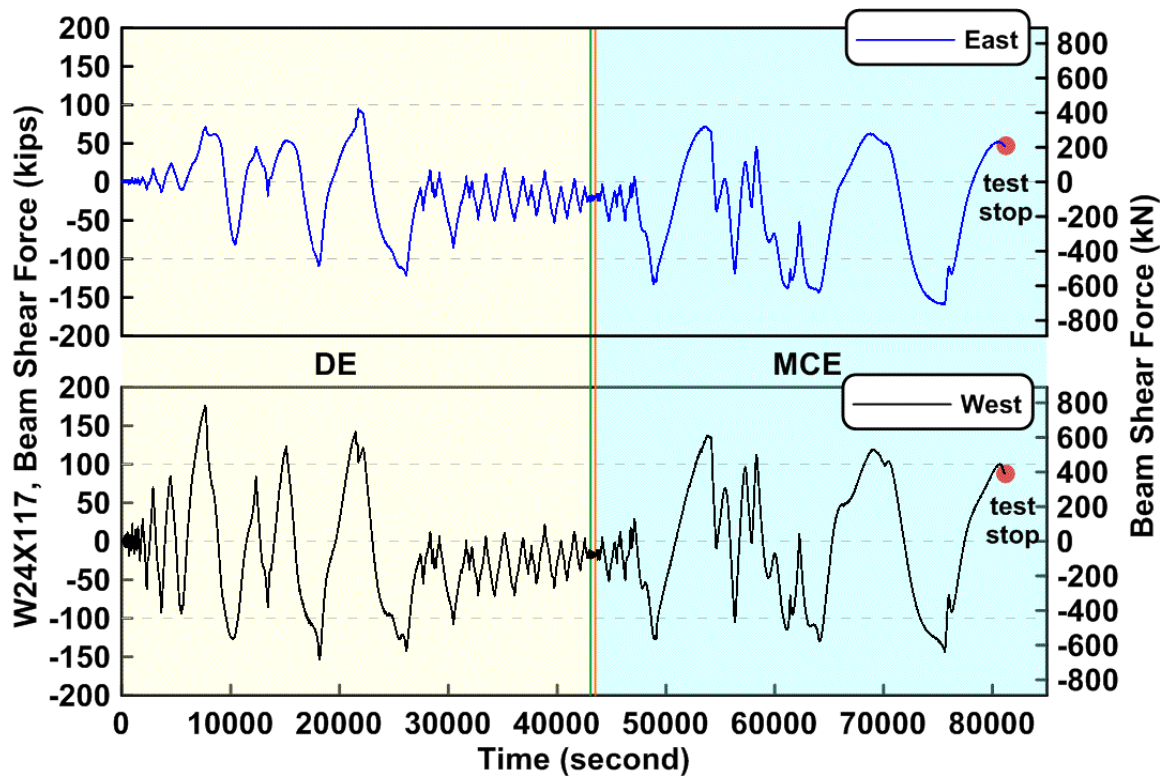


Figure 4.379 Specimen TCBF-B-4: roof beam estimated shear force time history.

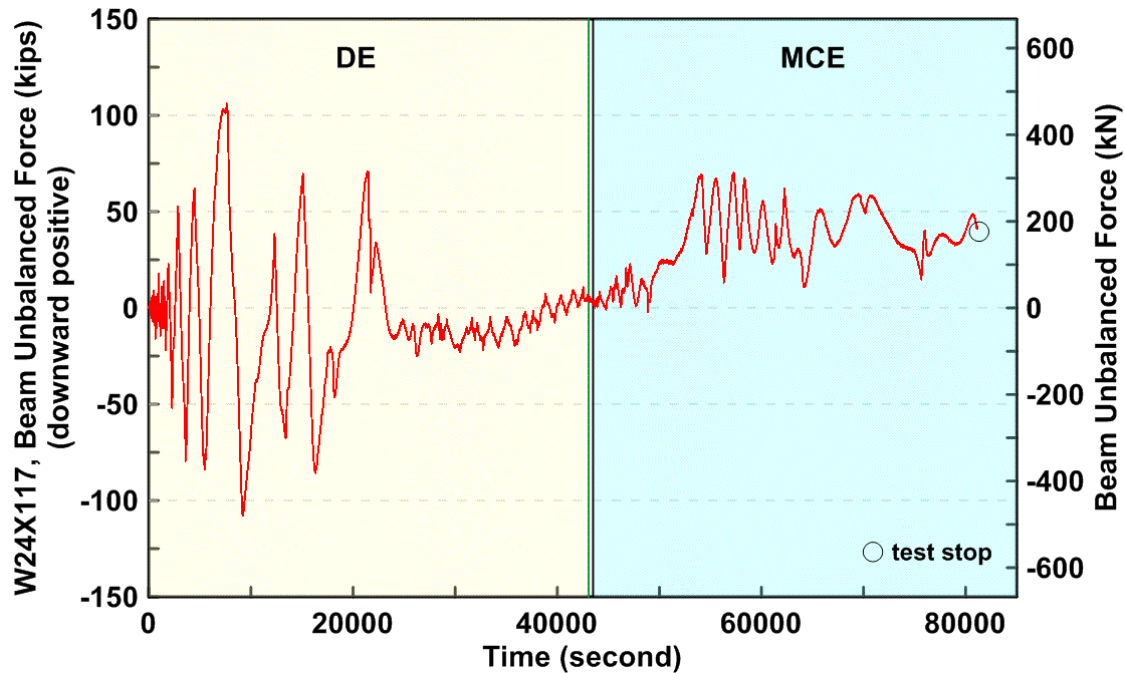


Figure 4.380 Specimen TCBF-B-4: estimated unbalanced force time history of roof beam.

4.2.2.4 Brace Response

The estimated brace axial forces versus brace axial deformations for each square HSS brace are shown in Figure 4.381. The estimated brace axial forces versus measured brace out-of-plane displacements at the brace center point for each square HSS brace are shown in Figure 4.382. Combined brace axial force, axial deformation, and out-of-plane displacement relationships are shown in Figure 4.383. The decomposed strain [axial strain, in-plane bending strain, out-of-plane bending strain, and warping strain; definition of strain components are shown in Figure 4.62(b)] time histories of each brace are plotted in Figures 4.384 to 4.387.

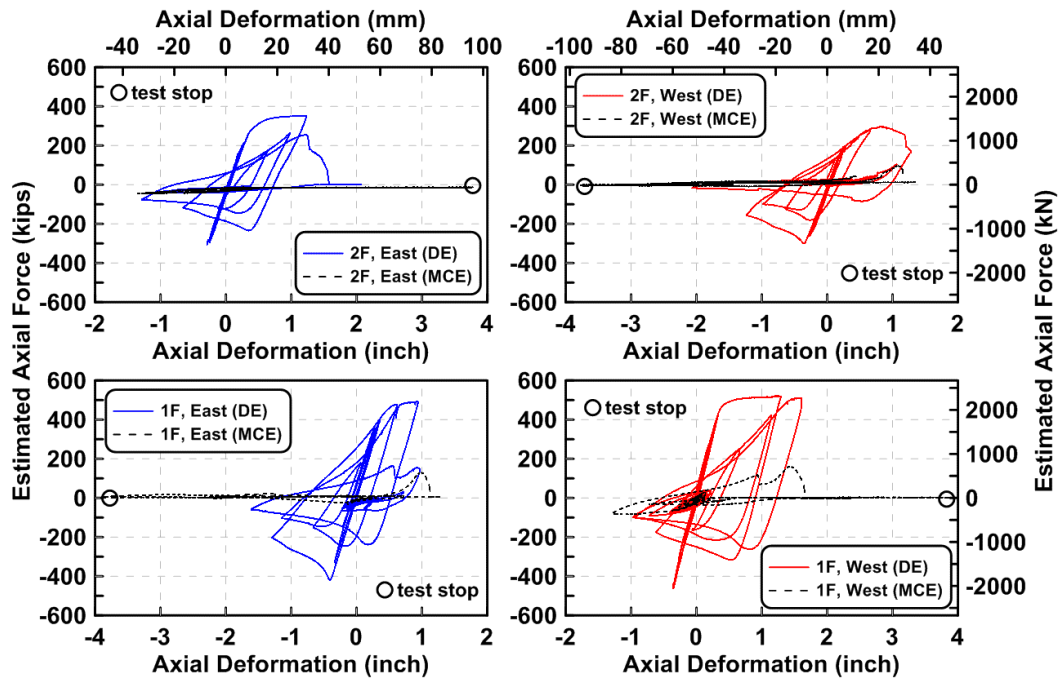


Figure 4.381 Specimen TCBF-B-4: estimated brace axial forces versus brace axial deformations.

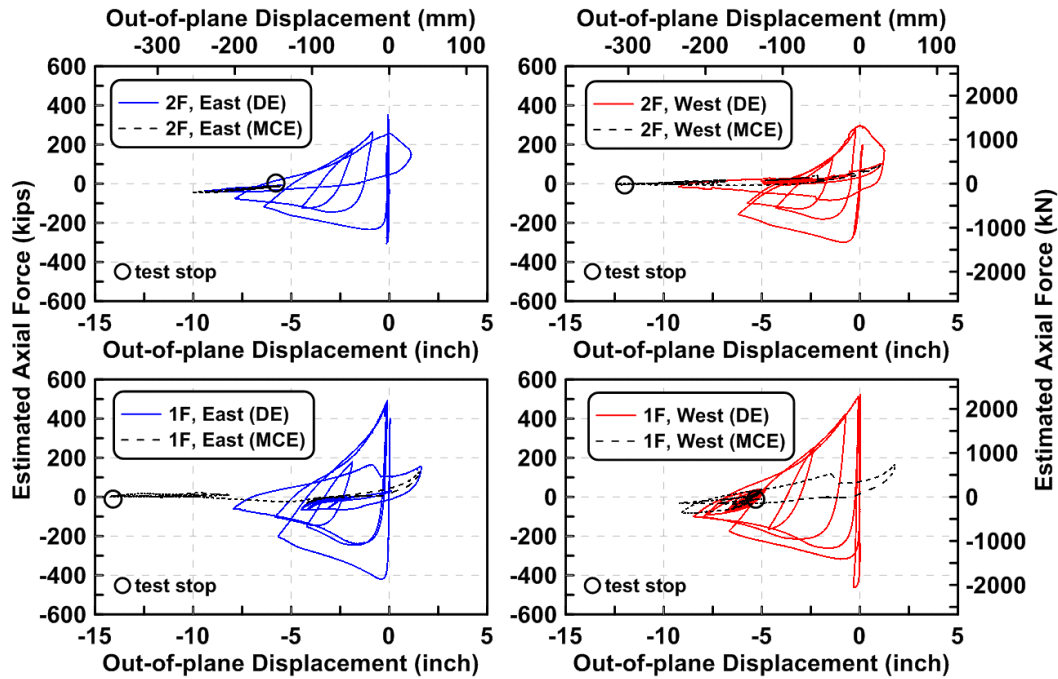


Figure 4.382 Specimen TCBF-B-4: estimated brace axial forces versus measured brace out-of-plane displacements at brace center point of each HSS brace.

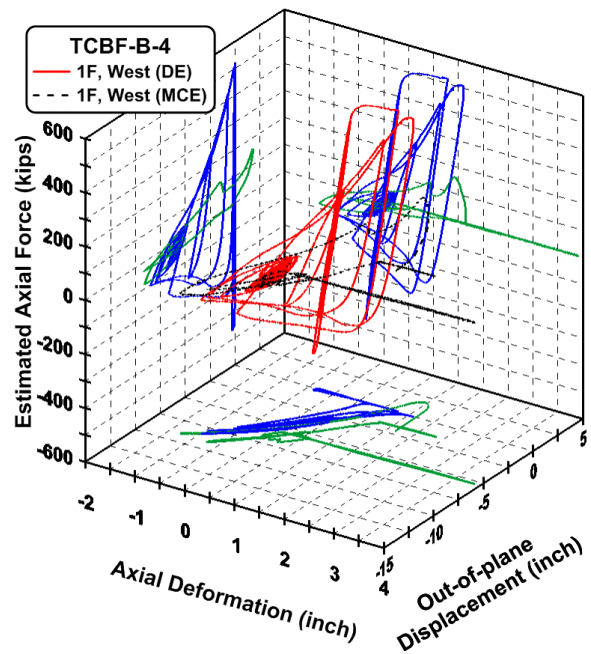
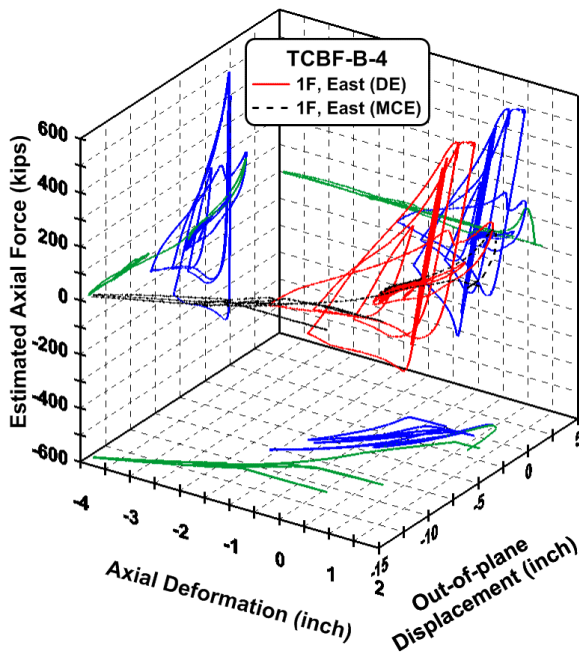
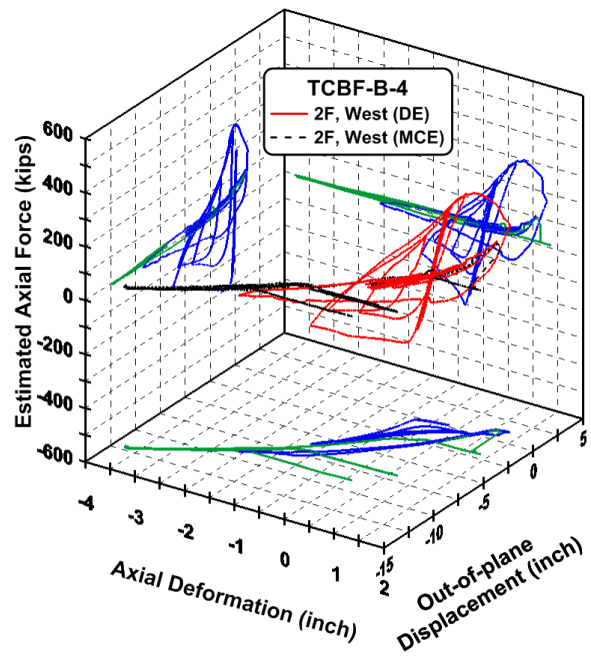
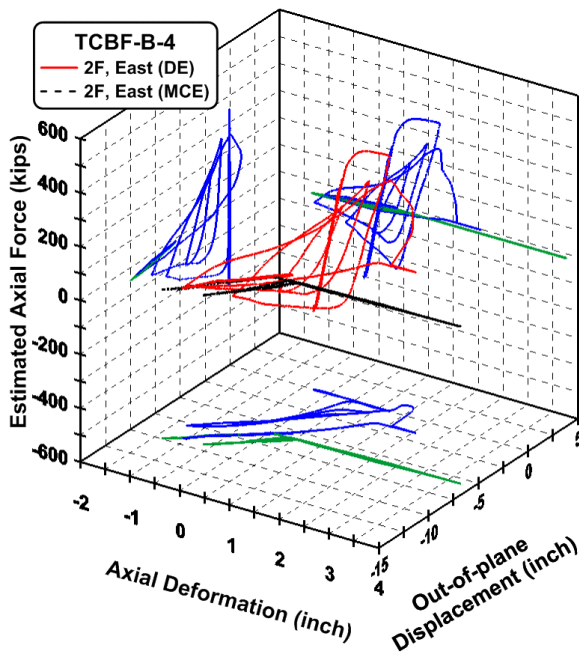


Figure 4.383 Specimen TCBF-B-4: estimated brace axial force, brace axial deformation and measured brace out-of-plane displacement relationships.

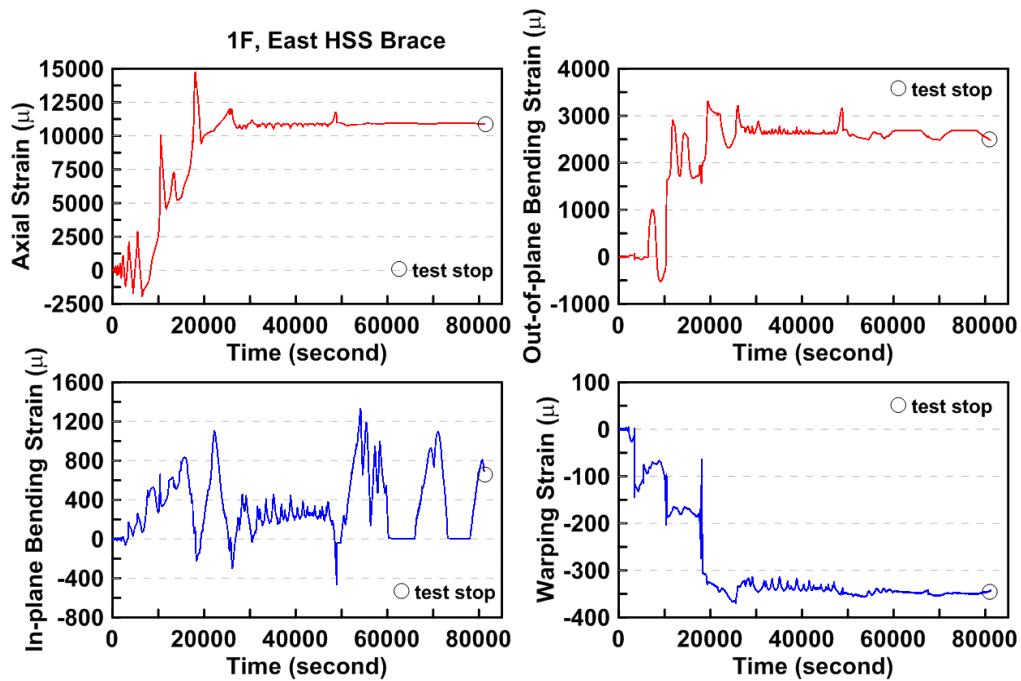


Figure 4.384 Specimen TCBF-B-4: time history of decomposed strain components of first-story eastern-side HSS brace.

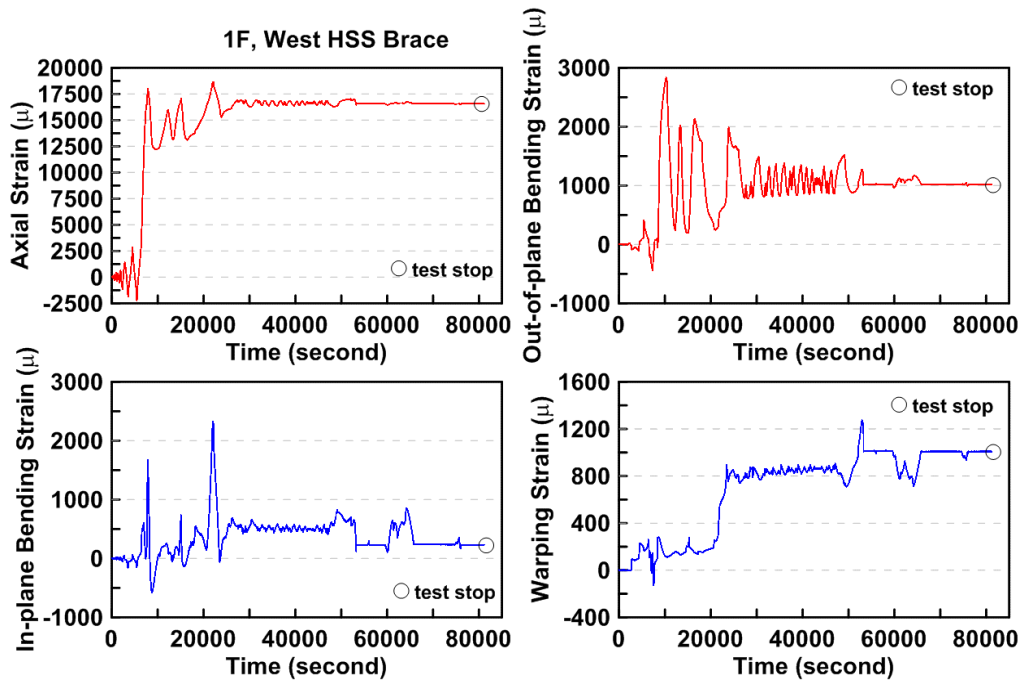


Figure 4.385 Specimen TCBF-B-4: time history of decomposed strain components of first-story western-side HSS brace.

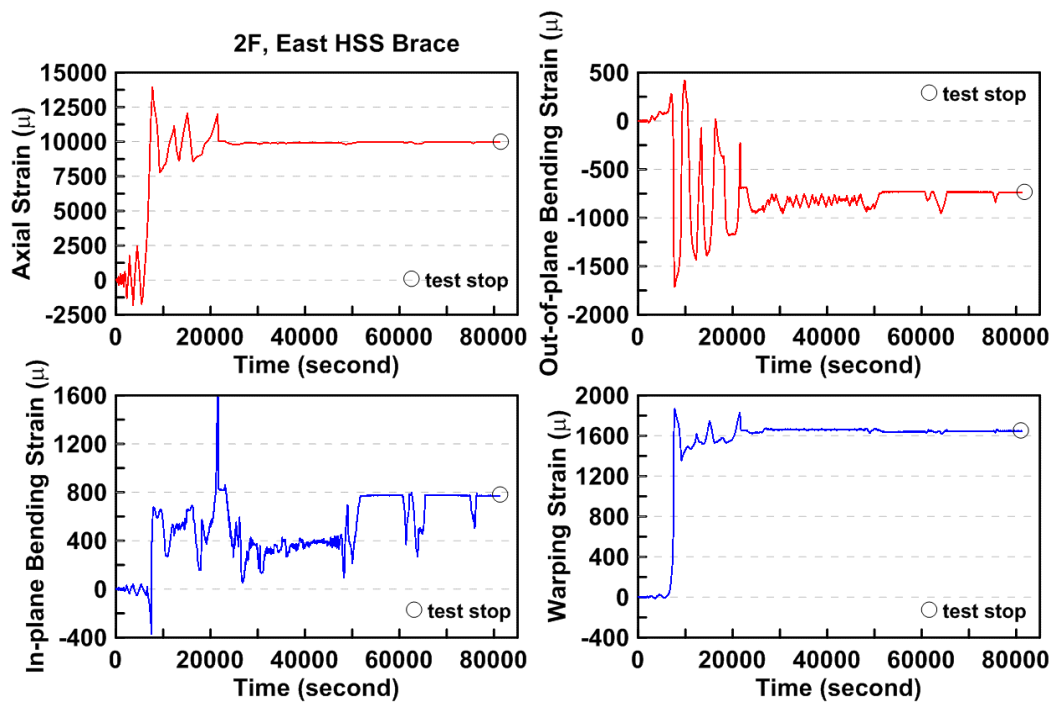


Figure 4.386 Specimen TCBF-B-4: time history of decomposed strain components of second-story eastern-side HSS brace.

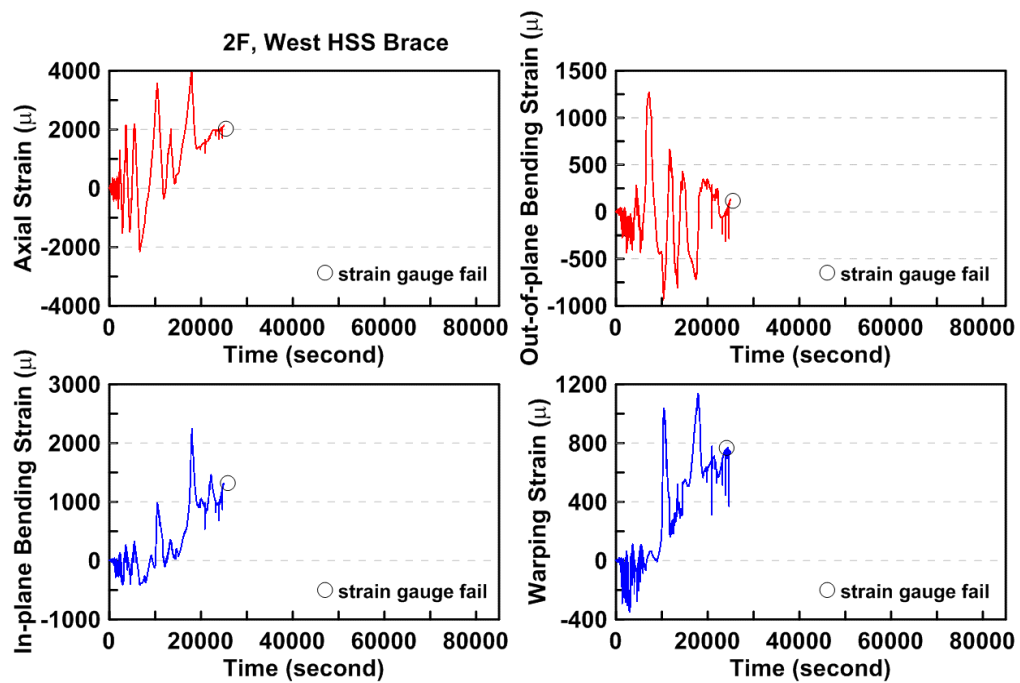


Figure 4.387 Specimen TCBF-B-4: time history of decomposed strain components of second-story western-side HSS brace.

4.2.2.5 Panel Zone Response

Estimated panel zone shear stress versus measured panel zone shear strain relationship for four locations is plotted in Figure 4.388. The time history of derived rosette-type strain gauge readings in the panel zone area at each story is shown in Figures 4.389 to 4.392. Normalized maximum and minimum principal stress relationships along with different yield criteria for the panel zone regions are plotted in Figures 4.393 to 4.396.

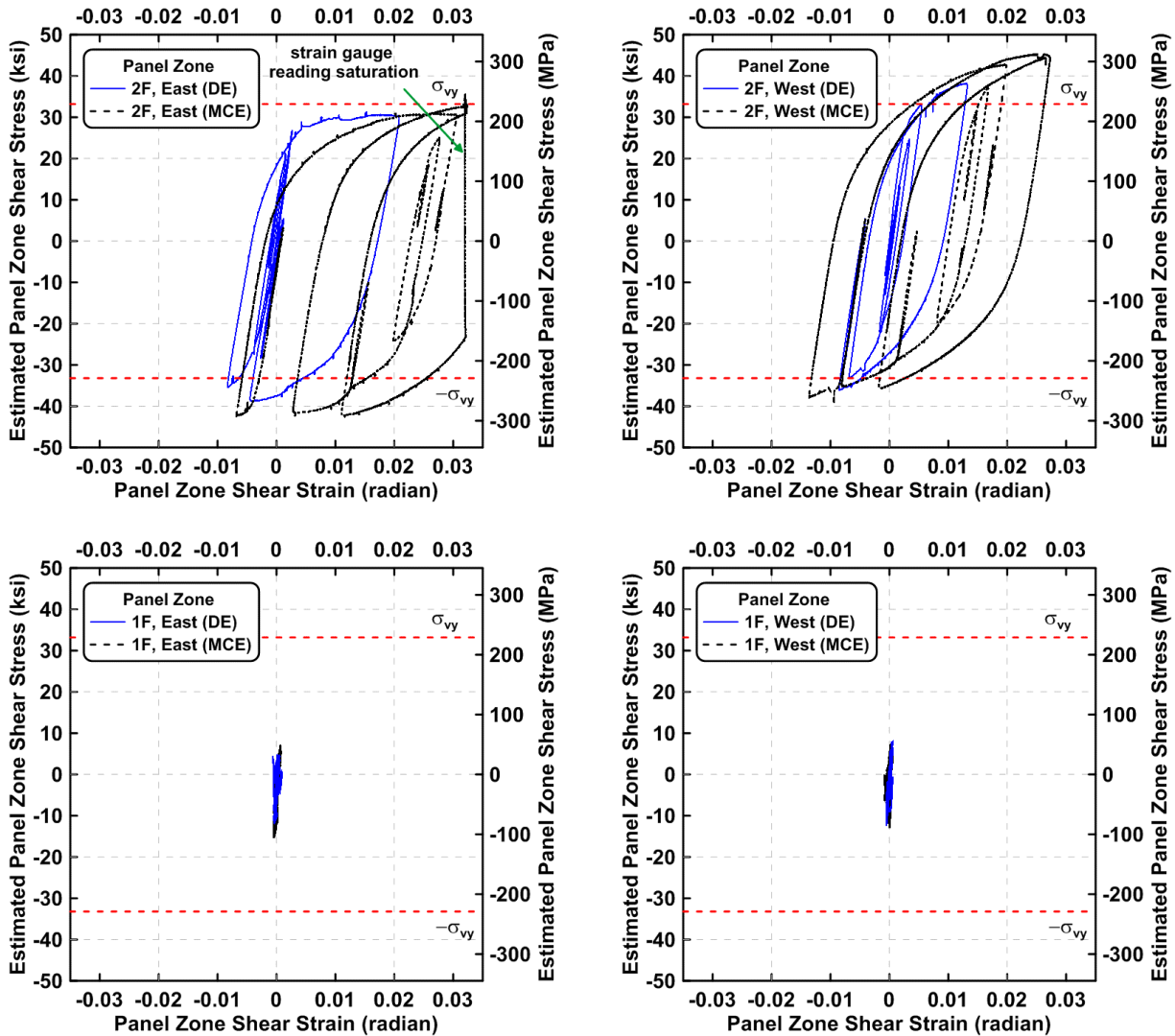


Figure 4.388 Specimen TCBF-B-4: estimated panel zone shear stress versus shear strain relationships.

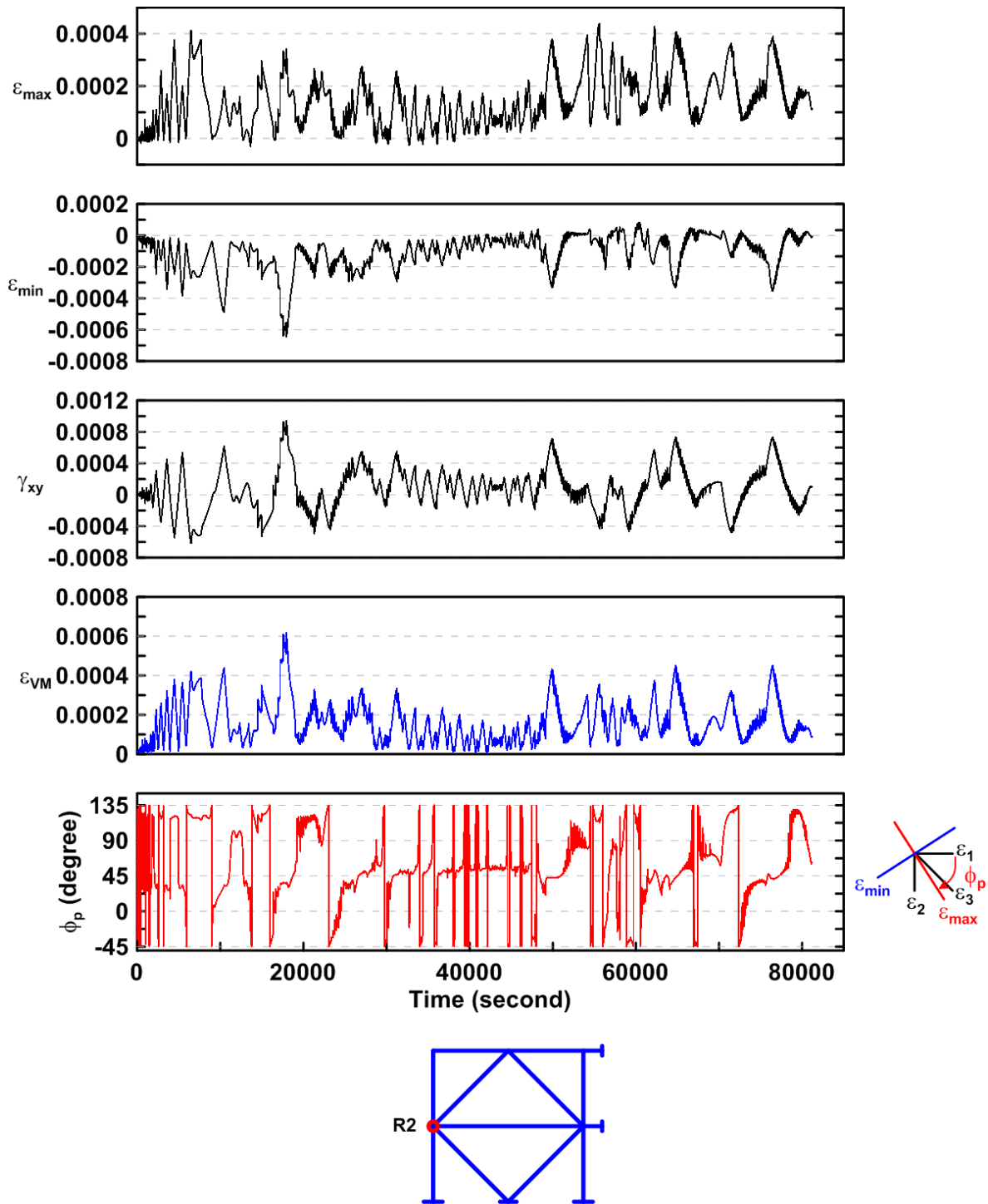


Figure 4.389 Specimen TCBF-B-4, lower panel zone: time history of rosette-type strain gauge readings (location: R2).

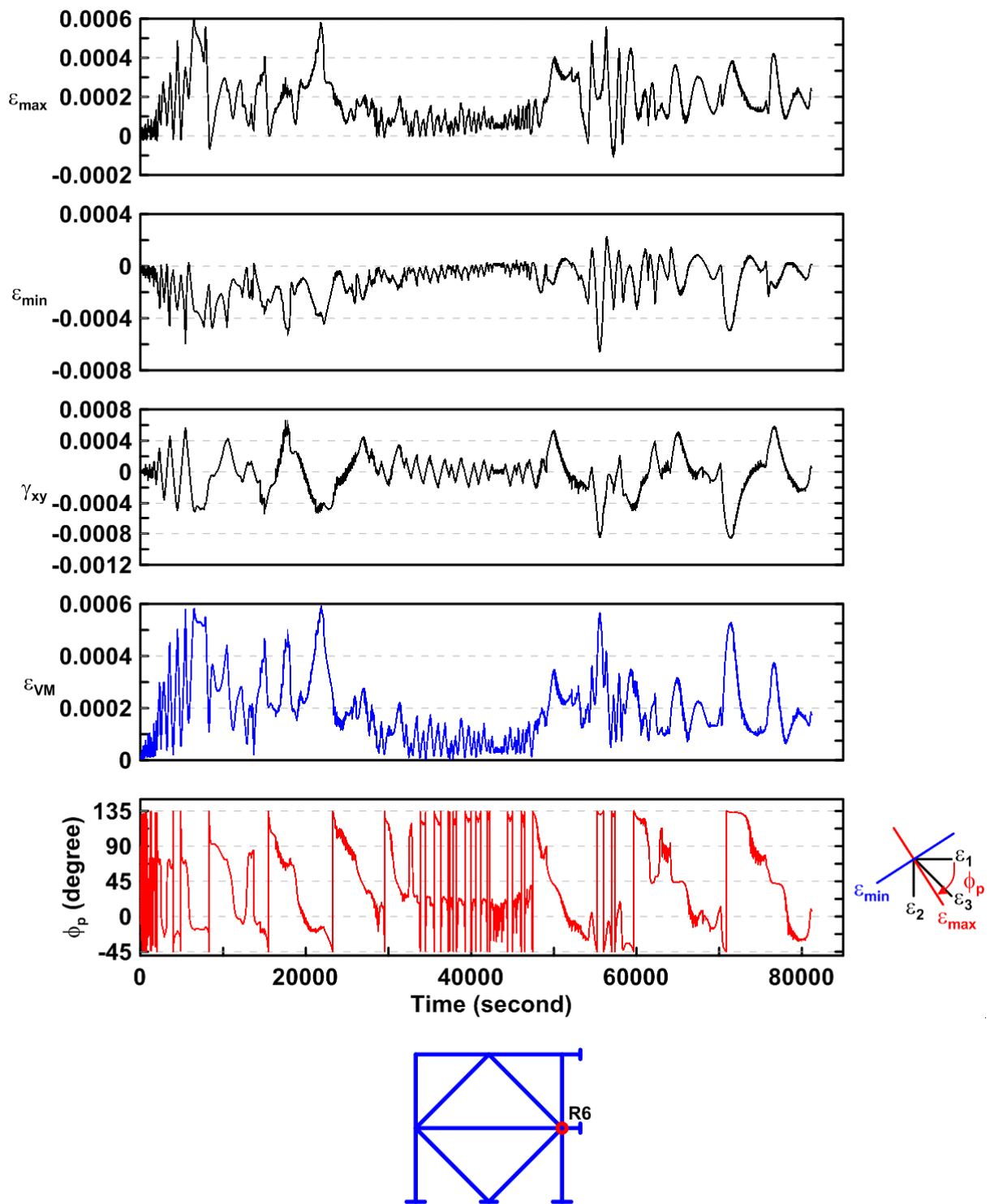


Figure 4.390 Specimen TCBF-B-4, lower panel zone: time history of rosette-type strain gauge readings (location: R6).

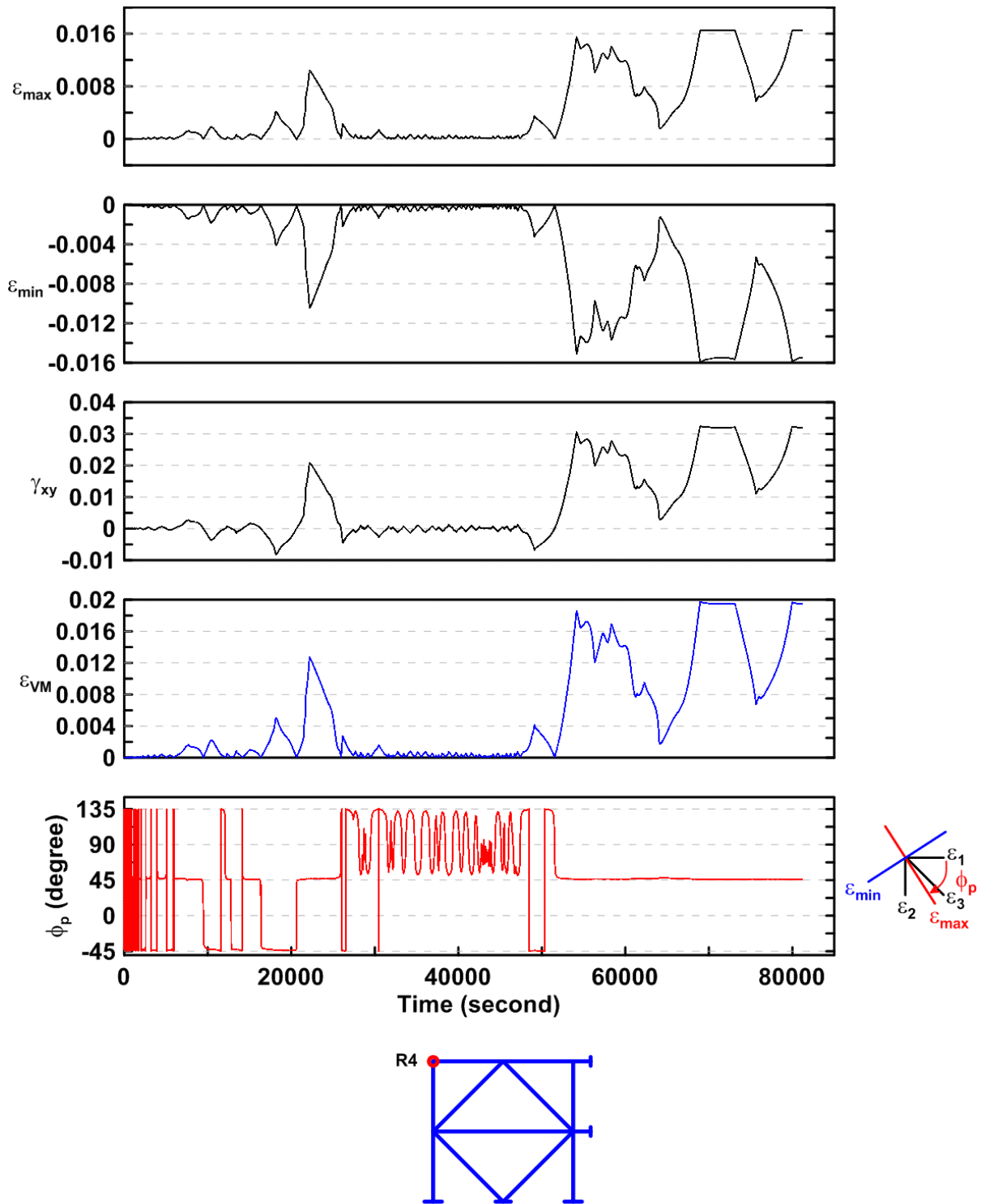


Figure 4.391 Specimen TCBF-B-4, lower panel zone: time history of rosette-type strain gauge readings (location: R4).

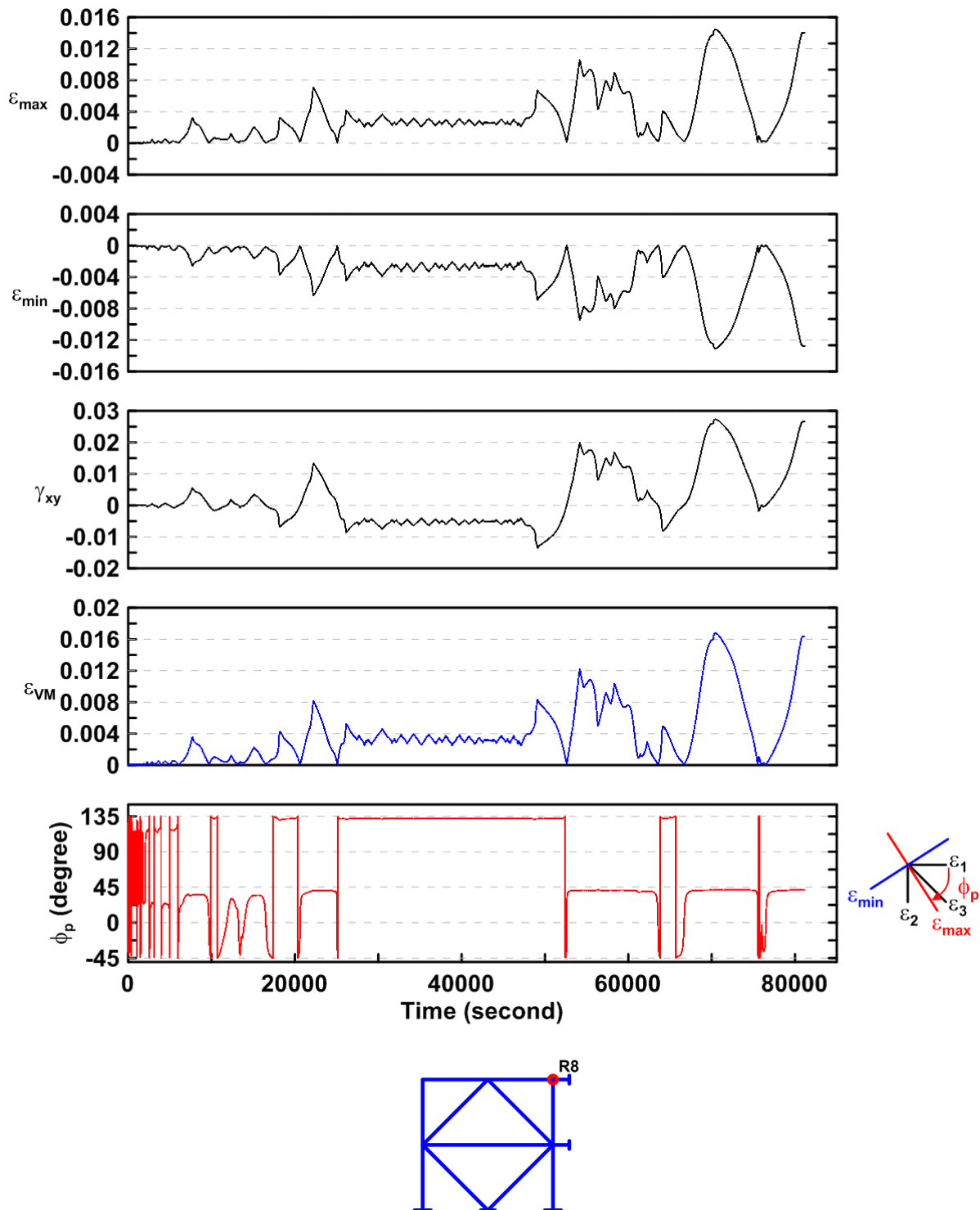


Figure 4.392 Specimen TCBF-B-4, lower panel zone: time history of rosette-type strain gauge readings (location: R8).

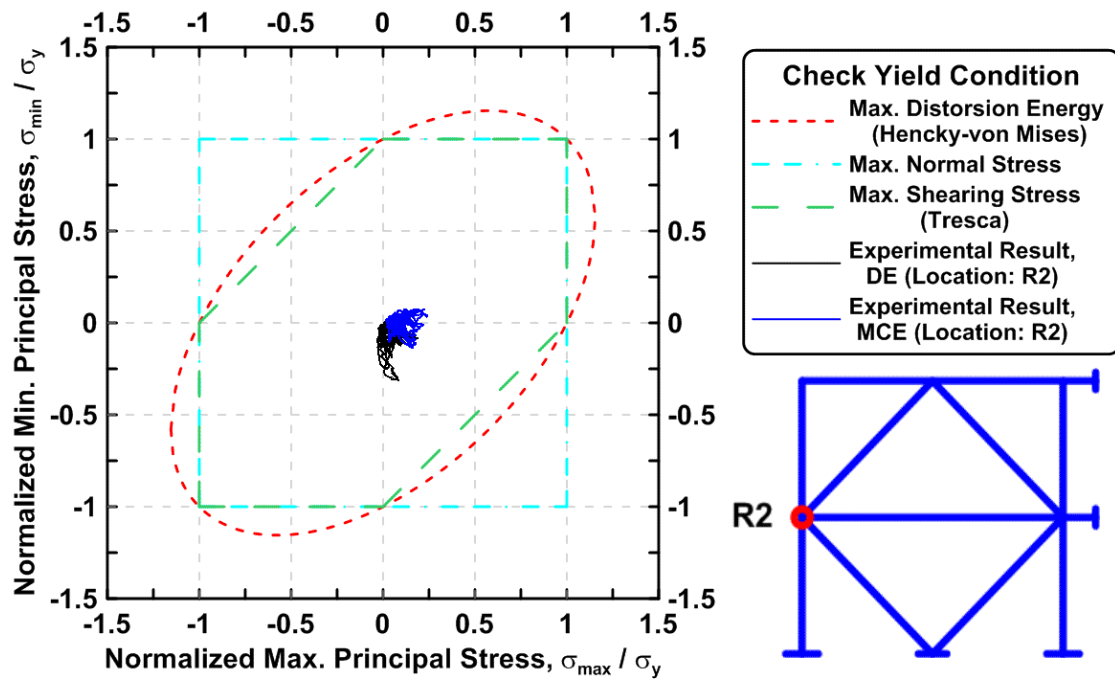


Figure 4.393 Specimen TCBF-B-4, lower panel zone: normalized maximum principal stress versus normalized minimum principal stress (location: R2).

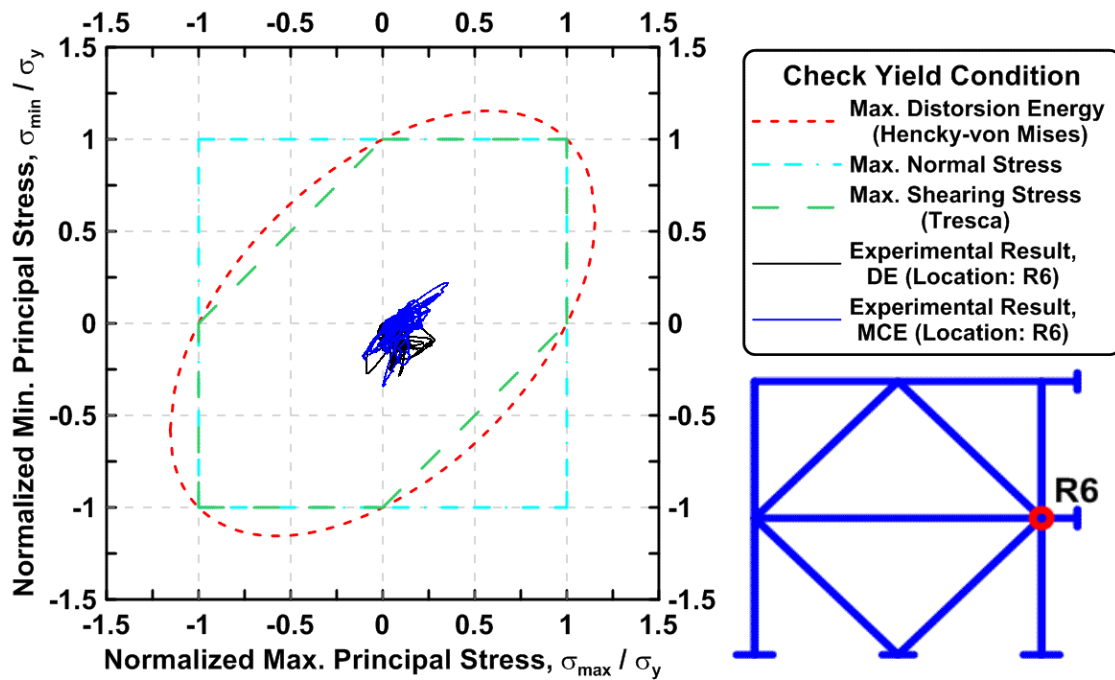


Figure 4.394 Specimen TCBF-B-4, lower panel zone: normalized maximum principal stress versus normalized minimum principal stress (location: R6).

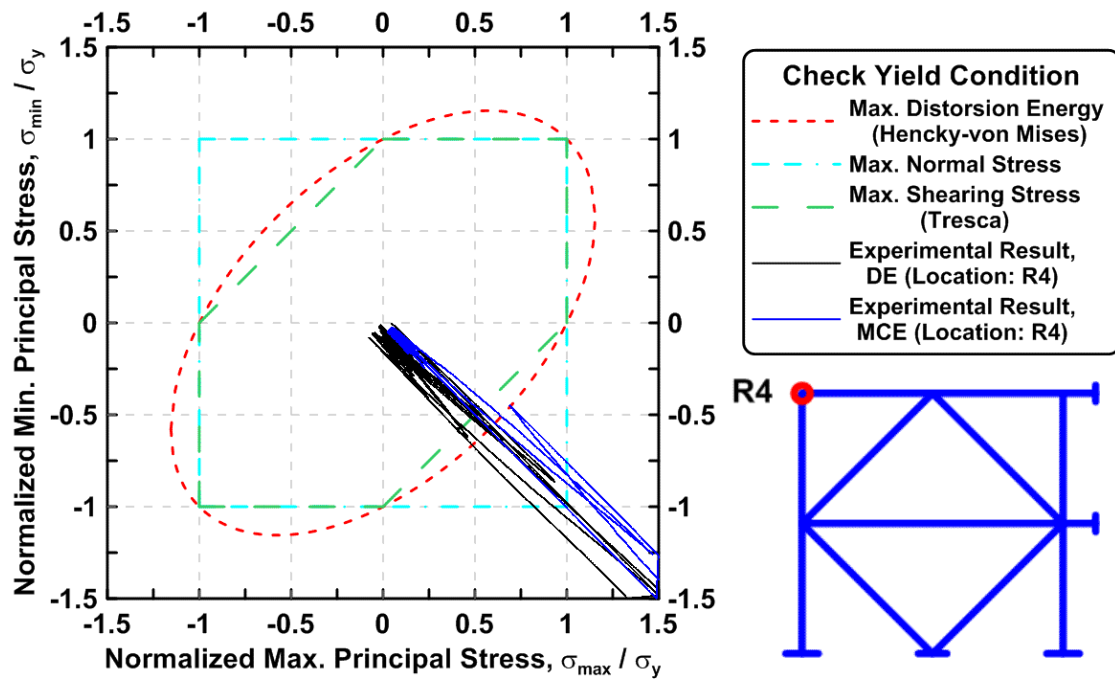


Figure 4.395 Specimen TCBF-B-4, lower panel zone: normalized maximum principal stress versus normalized minimum principal stress (location: R4).

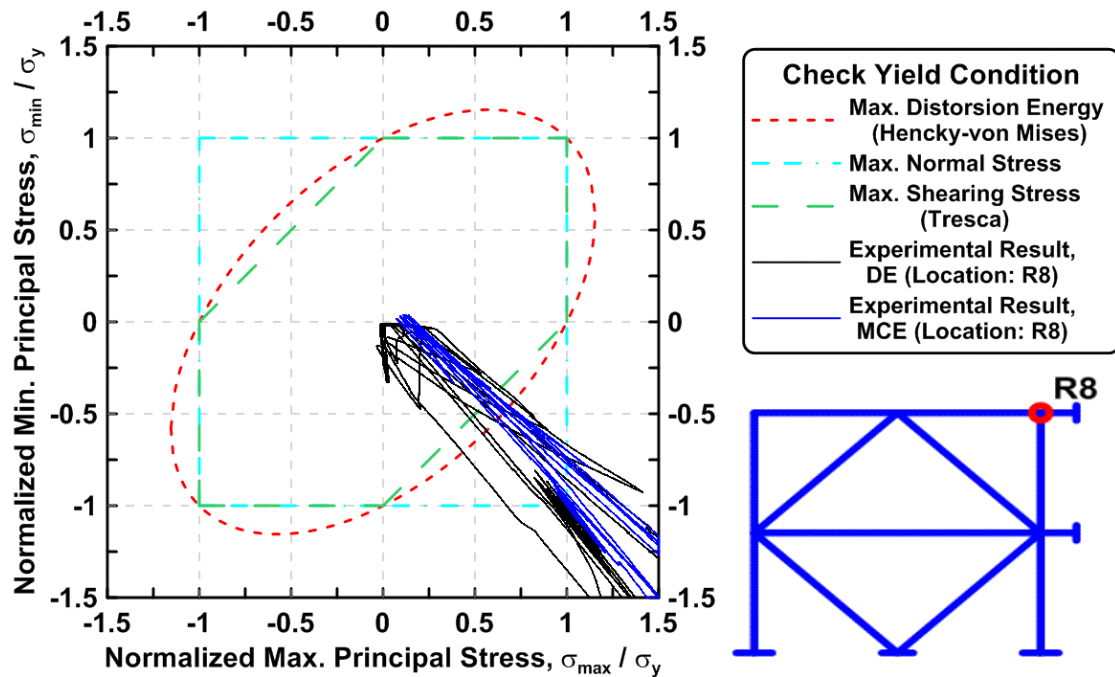


Figure 4.396 Specimen TCBF-B-4, lower panel zone: normalized maximum principal stress versus normalized minimum principal stress (location: R8).

4.2.2.6 Gusset Plate Response

The time history derived from rosette-type strain gauge readings in the 3/4-in.-thick one-piece gusset plate is shown in Figures 4.397 to 4.408. Normalized maximum and minimum principal stress relationships along with different yield criteria for the rosettes on the gusset plate are plotted in Figures 4.409 to 4.420.

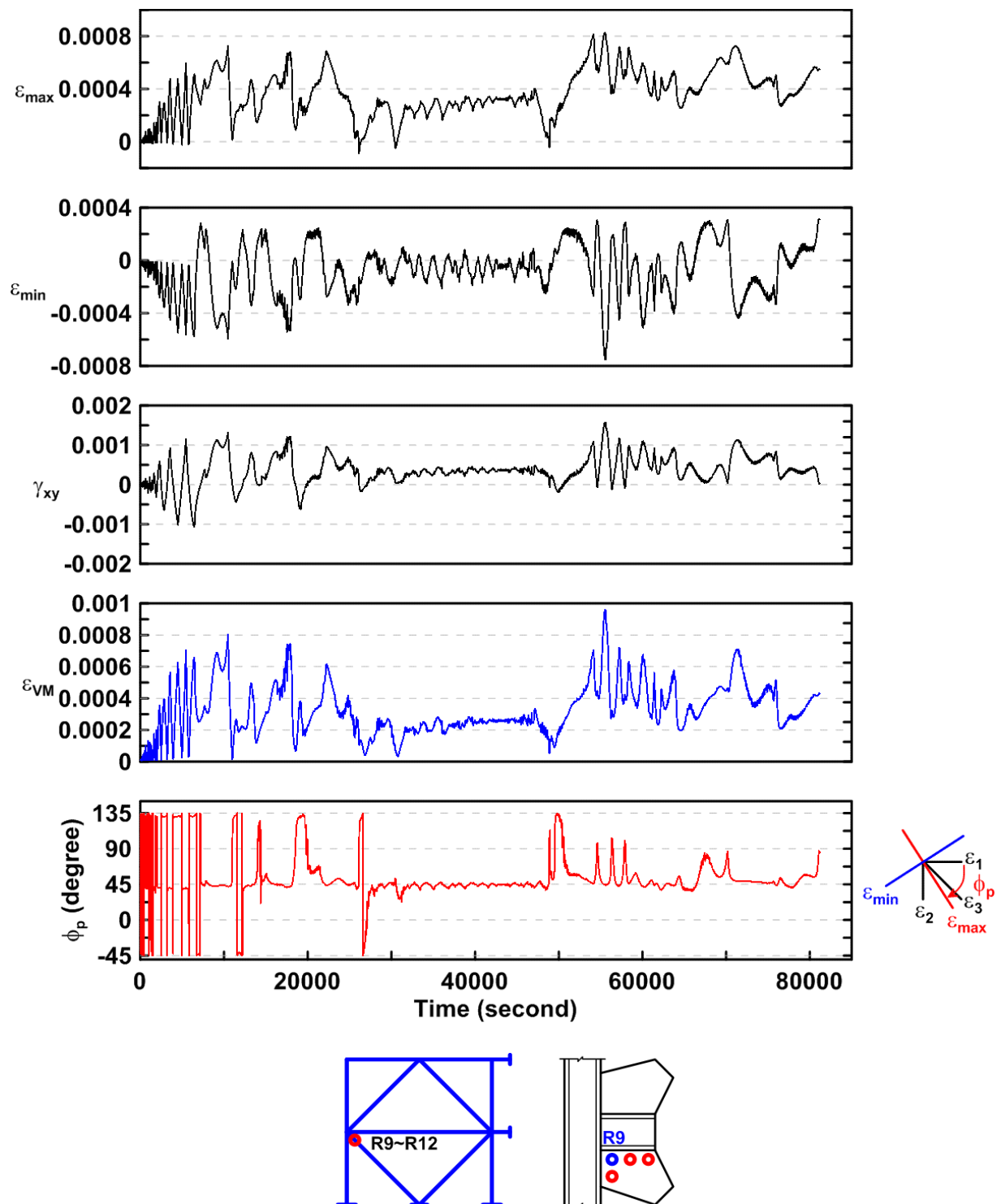


Figure 4.397 Specimen TCBF-B-4: time history of rosette-type strain gauge readings in one-piece gusset plate (location: R9).

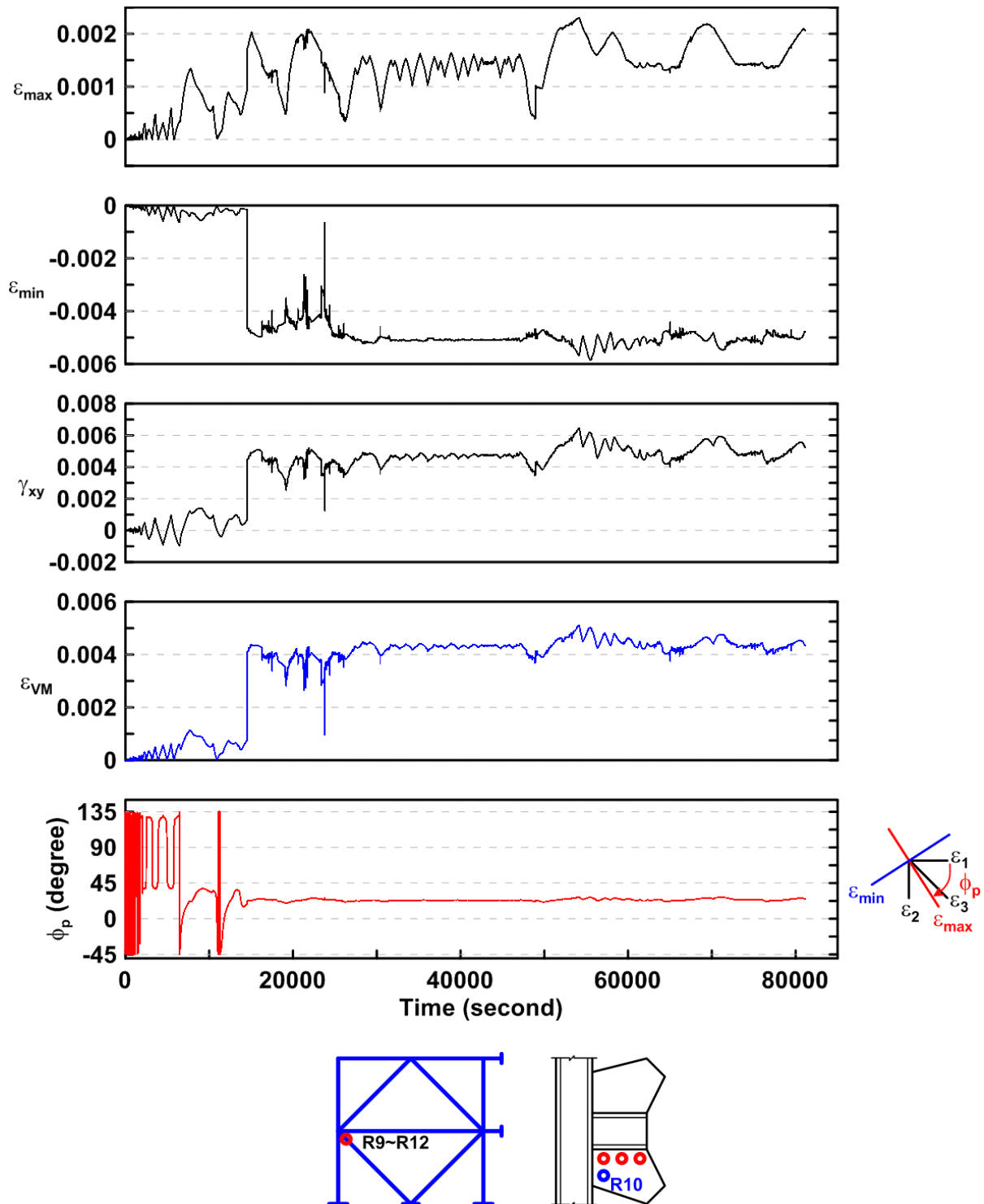


Figure 4.398 Specimen TCBF-B-4: time history of rosette-type strain gauge readings in one-piece gusset plate (location: R10).

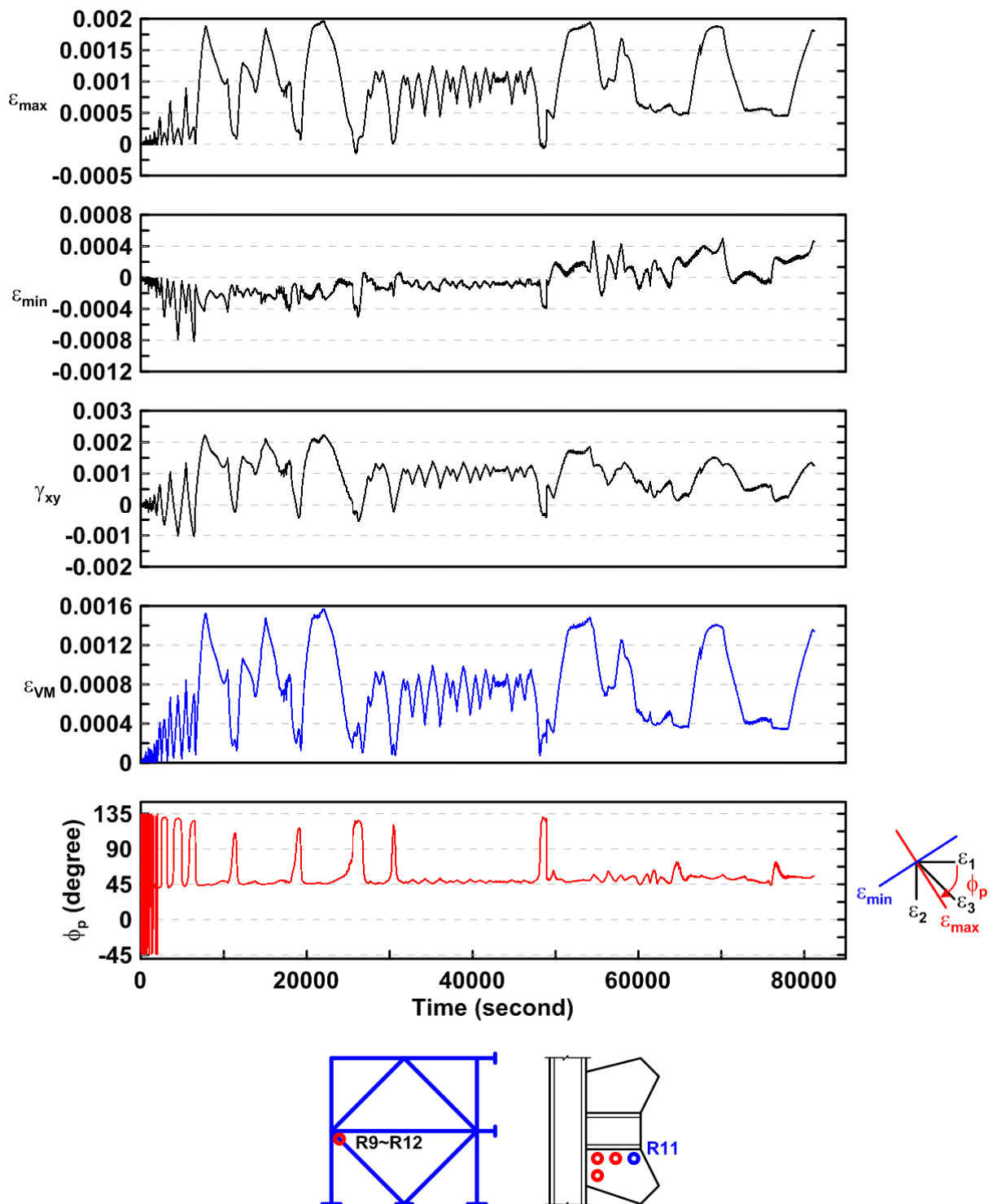


Figure 4.399 Specimen TCBF-B-4: time history of rosette-type strain gauge readings in one-piece gusset plate (location: R11).

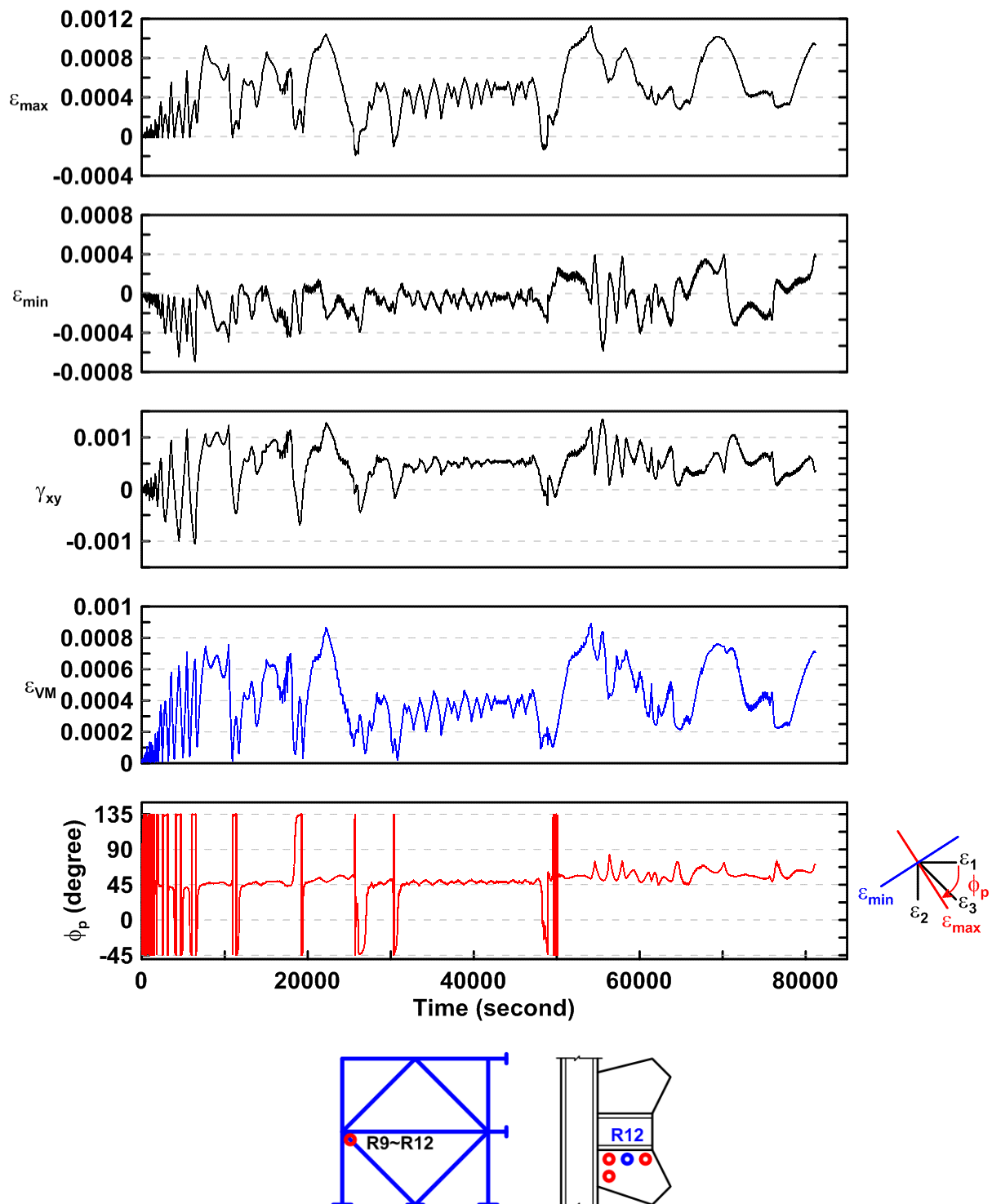


Figure 4.400 Specimen TCBF-B-4: time history of rosette-type strain gauge readings in one-piece gusset plate (location: R12).

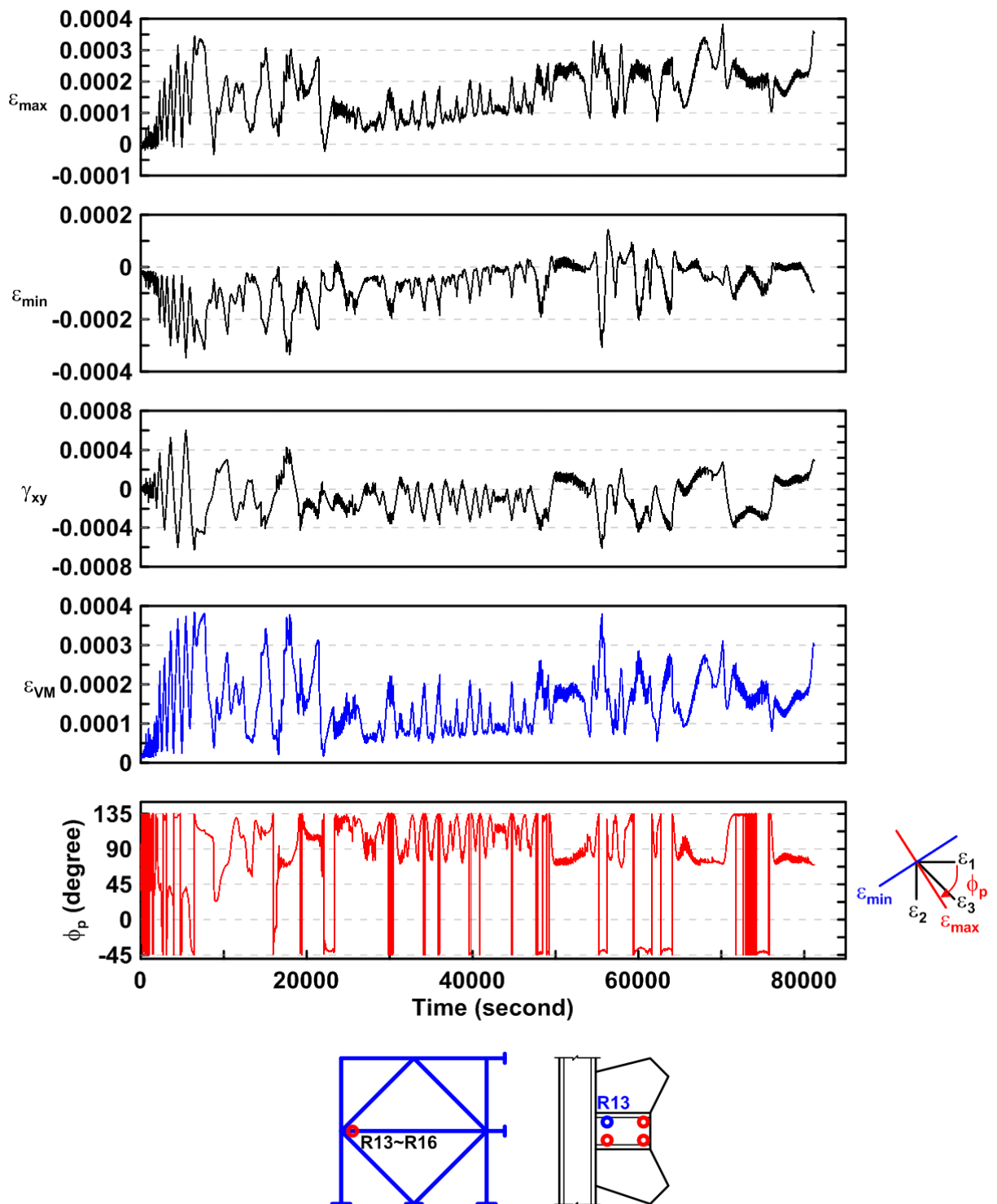


Figure 4.401 Specimen TCBF-B-4: time history of rosette-type strain gauge readings in one-piece gusset plate (location: R13).

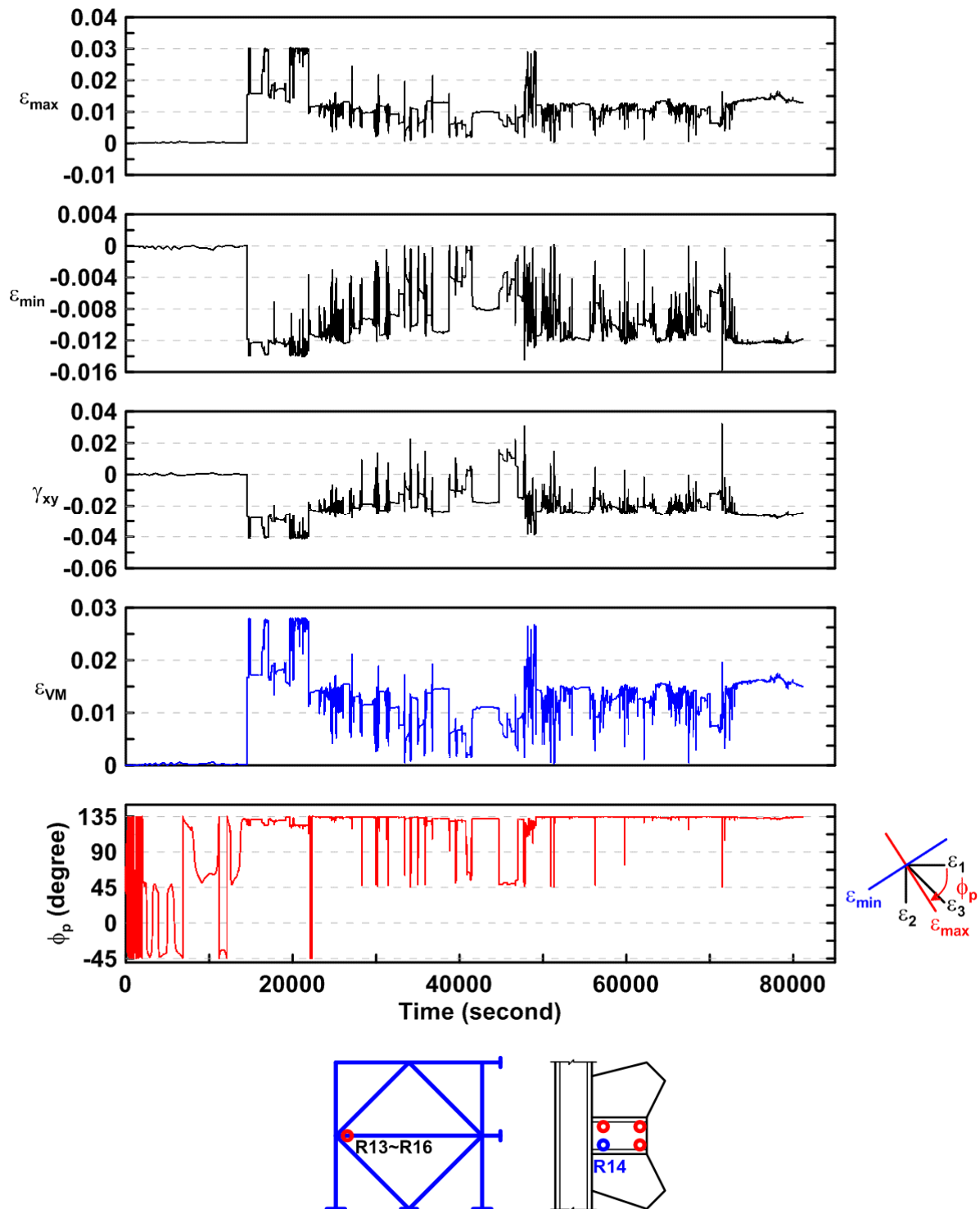


Figure 4.402 Specimen TCBF-B-4: time history of rosette-type strain gauge readings in one-piece gusset plate (location: R14).

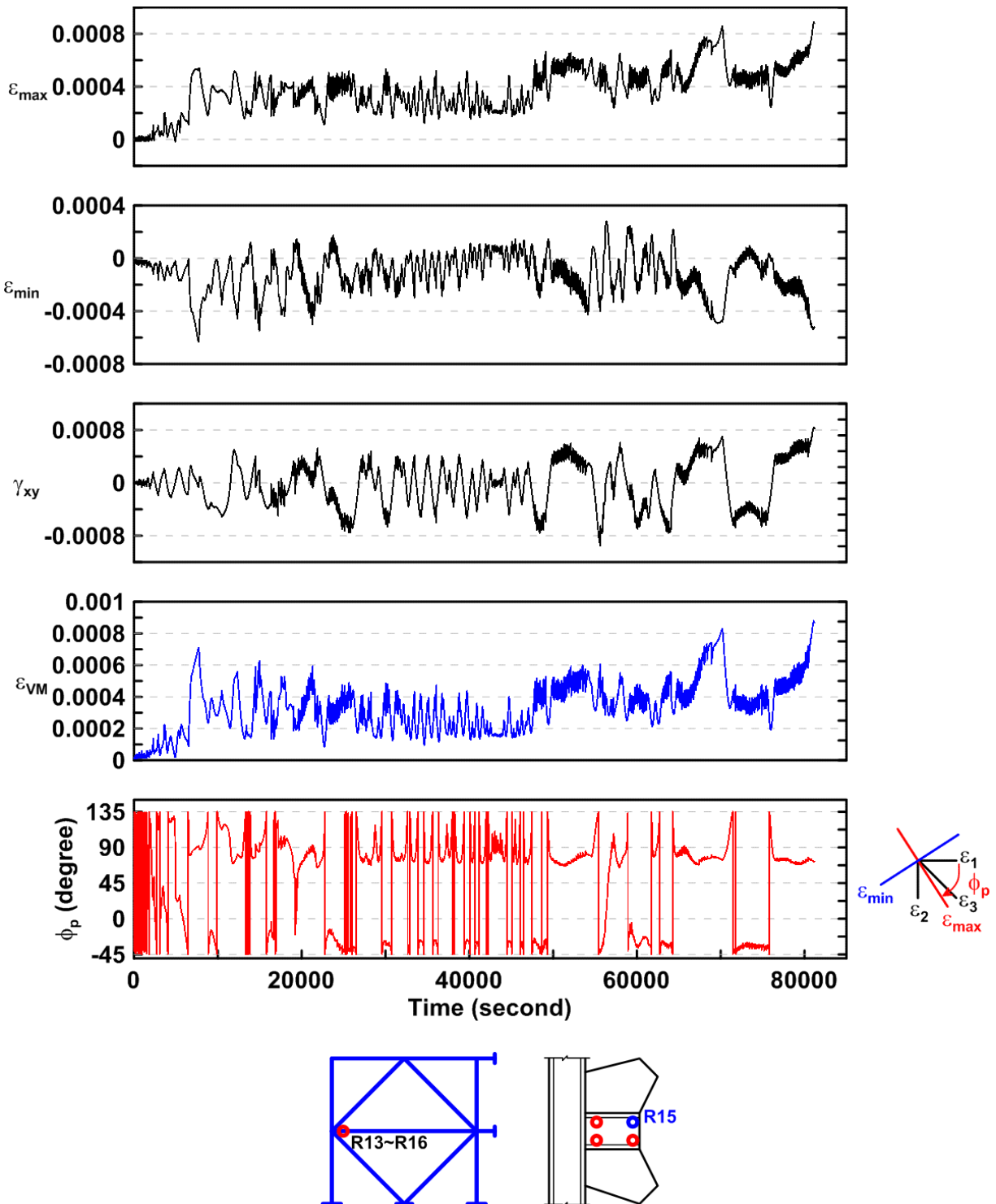


Figure 4.403 Specimen TCBF-B-4: time history of rosette-type strain gauge readings in one-piece gusset plate (location: R15).

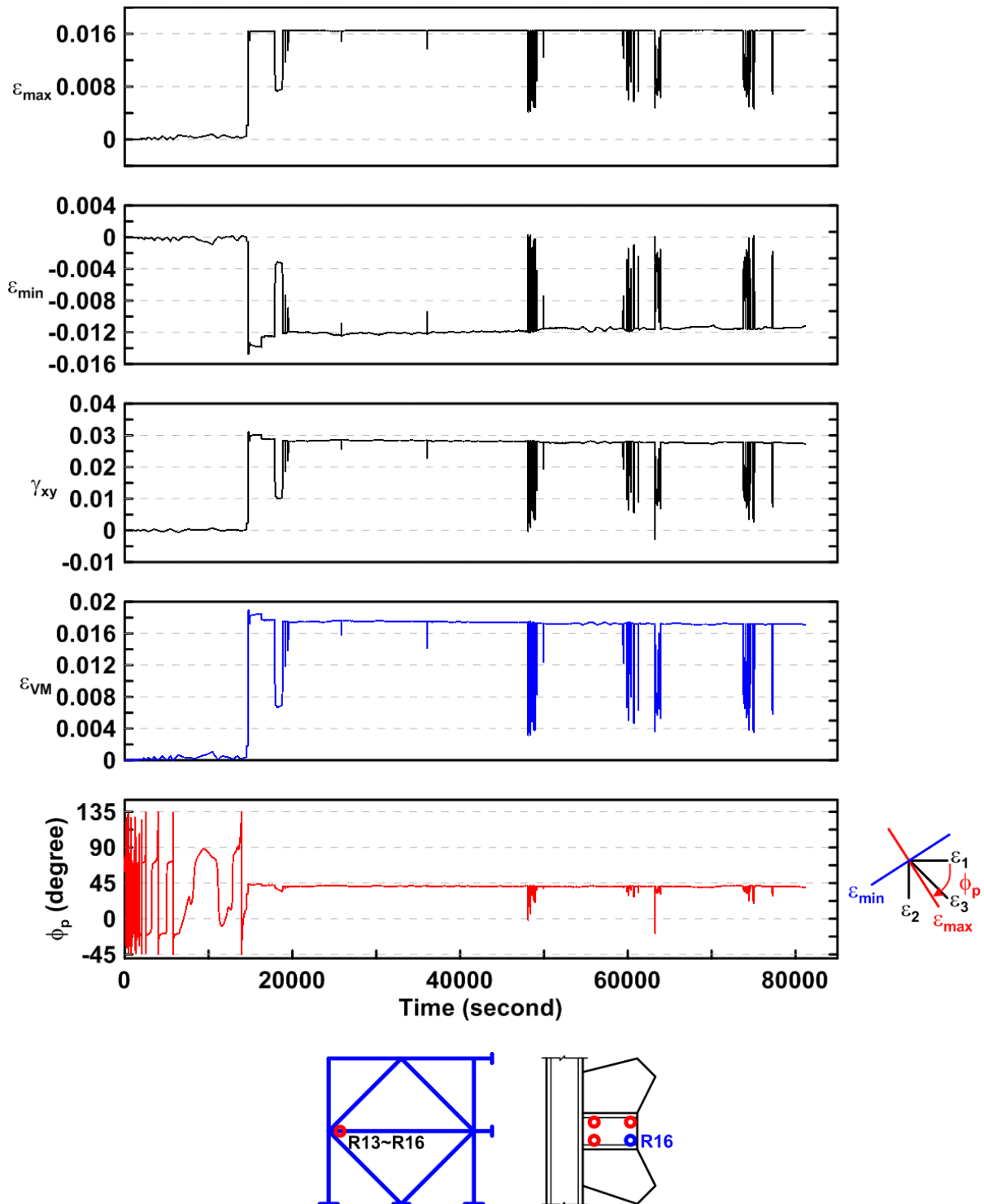


Figure 4.404 Specimen TCBF-B-4: time history of rosette-type strain gauge readings in one-piece gusset plate (location: R16).

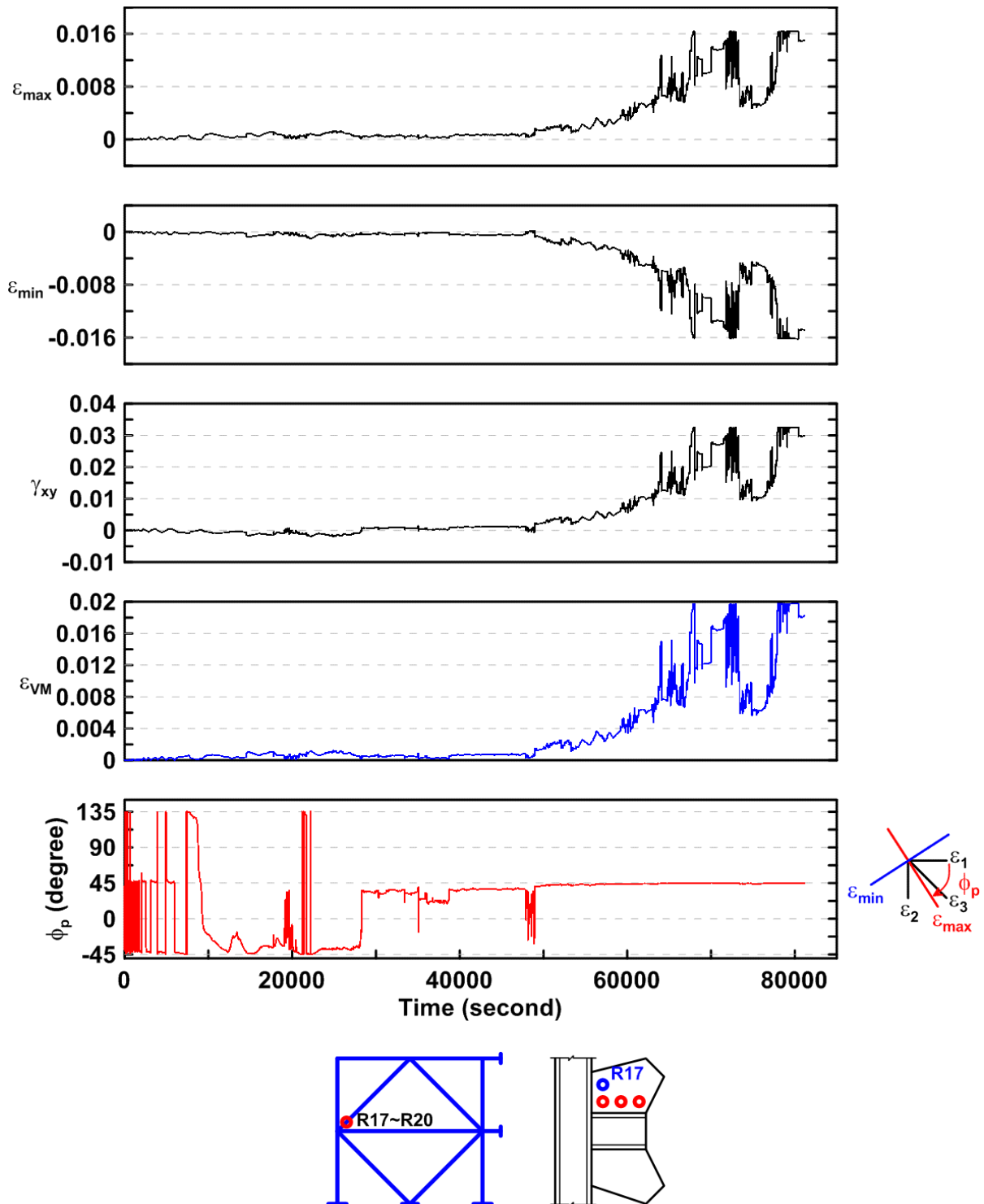


Figure 4.405 Specimen TCBF-B-4: time history of rosette-type strain gauge readings in one-piece gusset plate (location: R17).

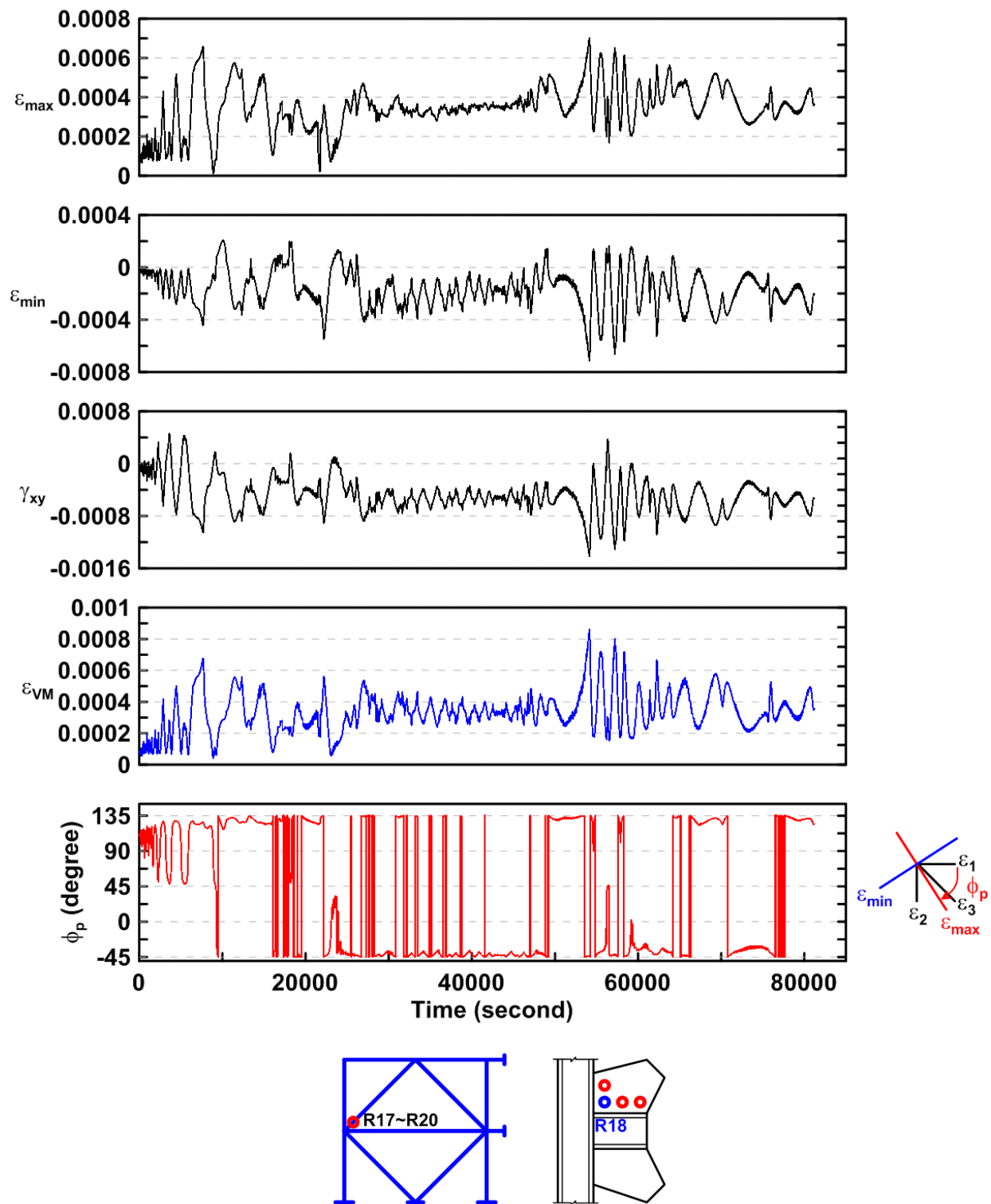


Figure 4.406 Specimen TCBF-B-4: time history of rosette-type strain gauge readings in one-piece gusset plate (location: R18).

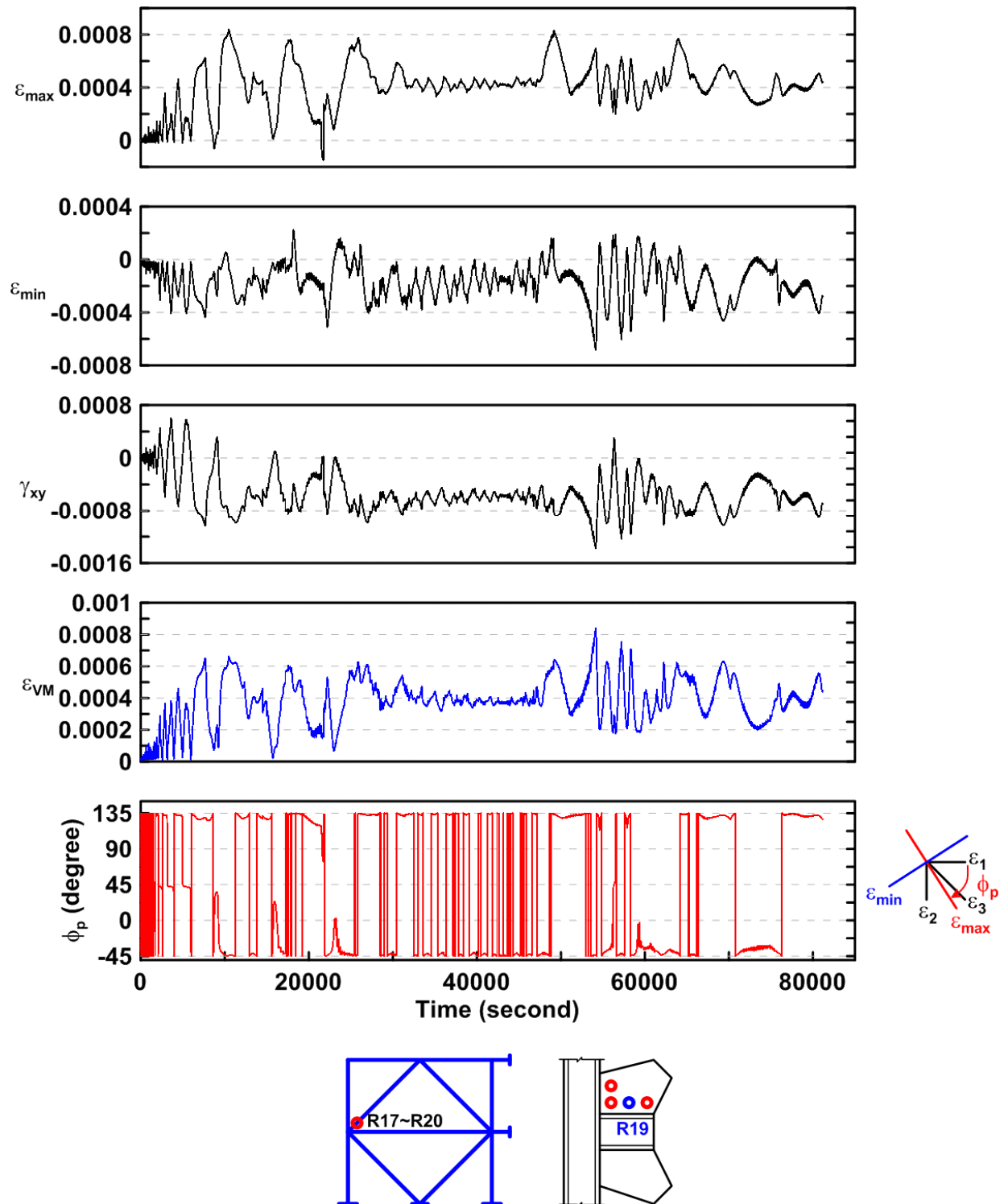


Figure 4.407 Specimen TCBF-B-4: time history of rosette-type strain gauge readings in one-piece gusset plate (location: R19).

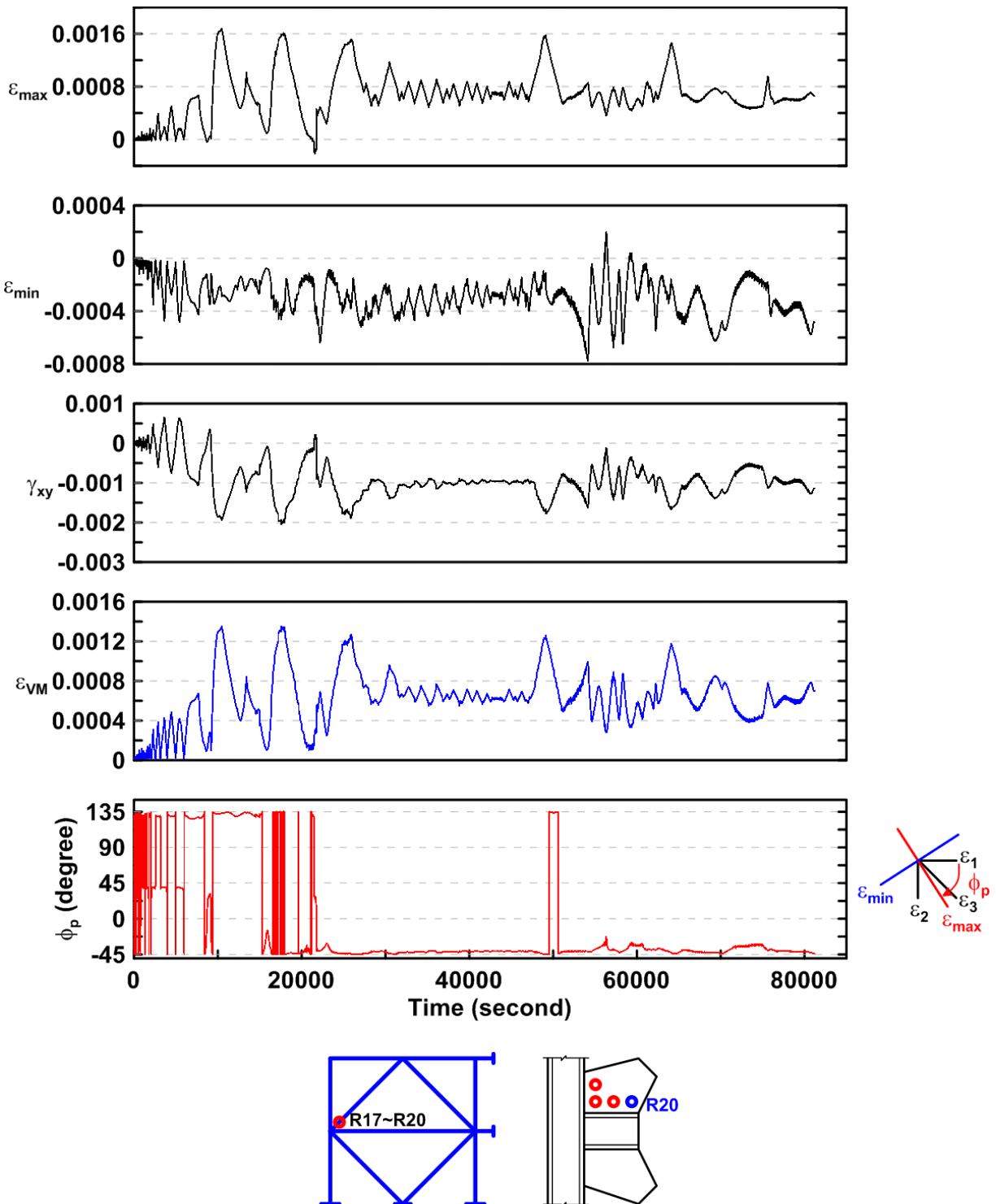


Figure 4.408 Specimen TCBF-B-4: time history of rosette-type strain gauge readings in one-piece gusset plate (location: R20).

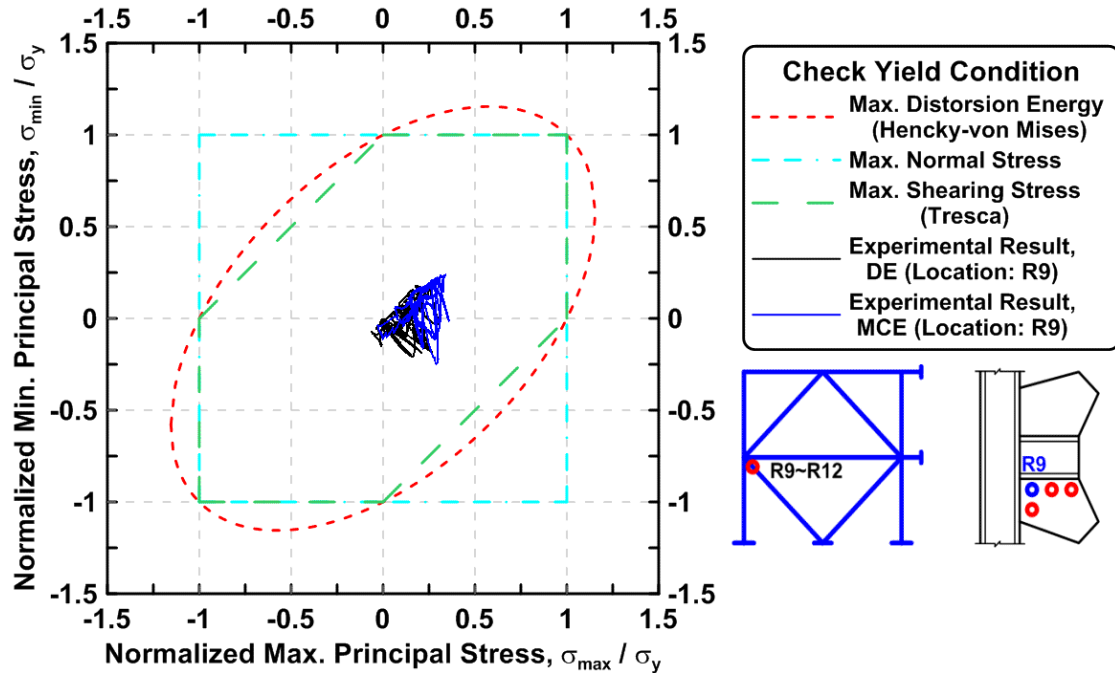


Figure 4.409 Specimen TCBF-B-4: normalized maximum principal stress versus normalized minimum principal stress in one-piece gusset plate (location: R9).

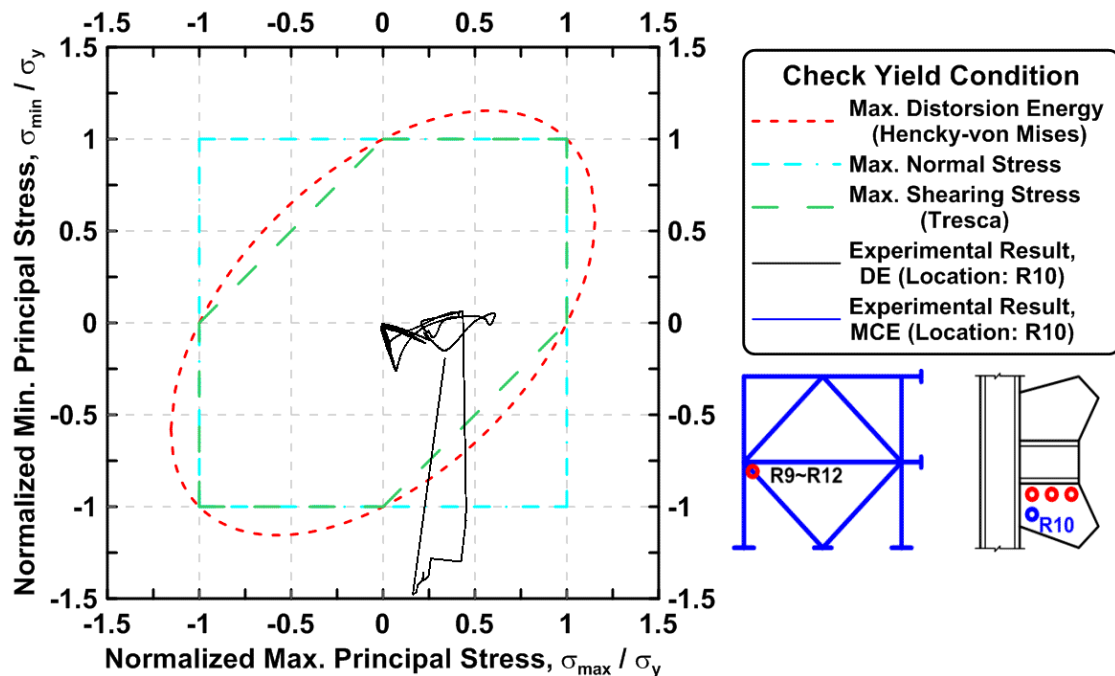


Figure 4.410 Specimen TCBF-B-4: normalized maximum principal stress versus normalized minimum principal stress in one-piece gusset plate (location: R10).

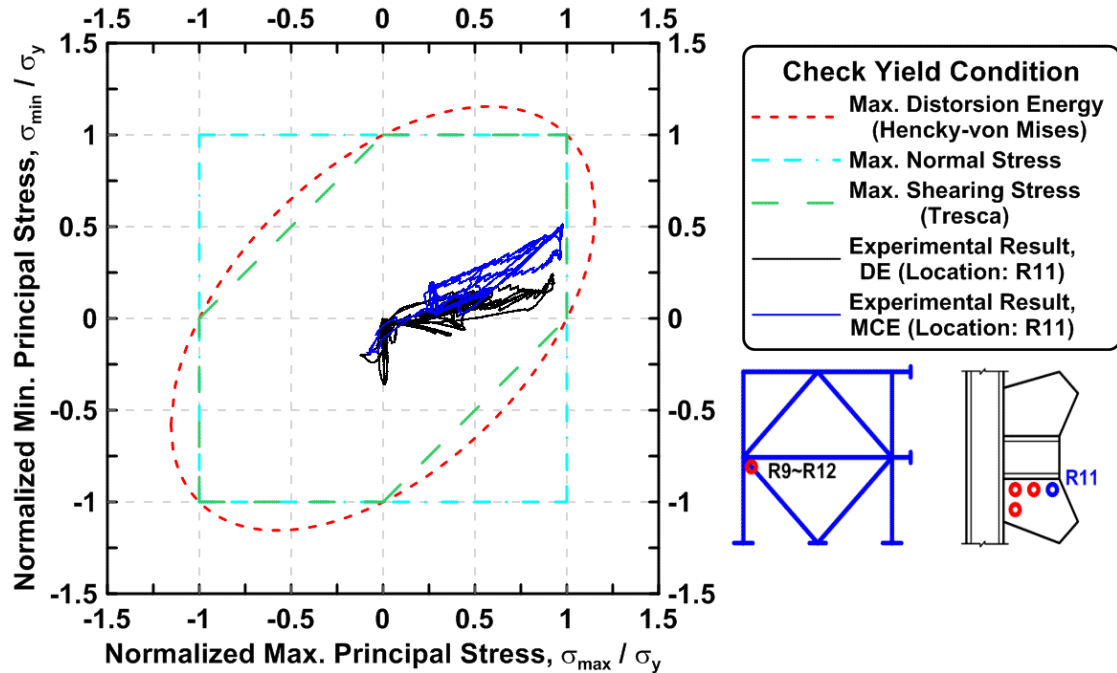


Figure 4.411 Specimen TCBF-B-4: normalized maximum principal stress versus normalized minimum principal stress in one-piece gusset plate (location: R11).

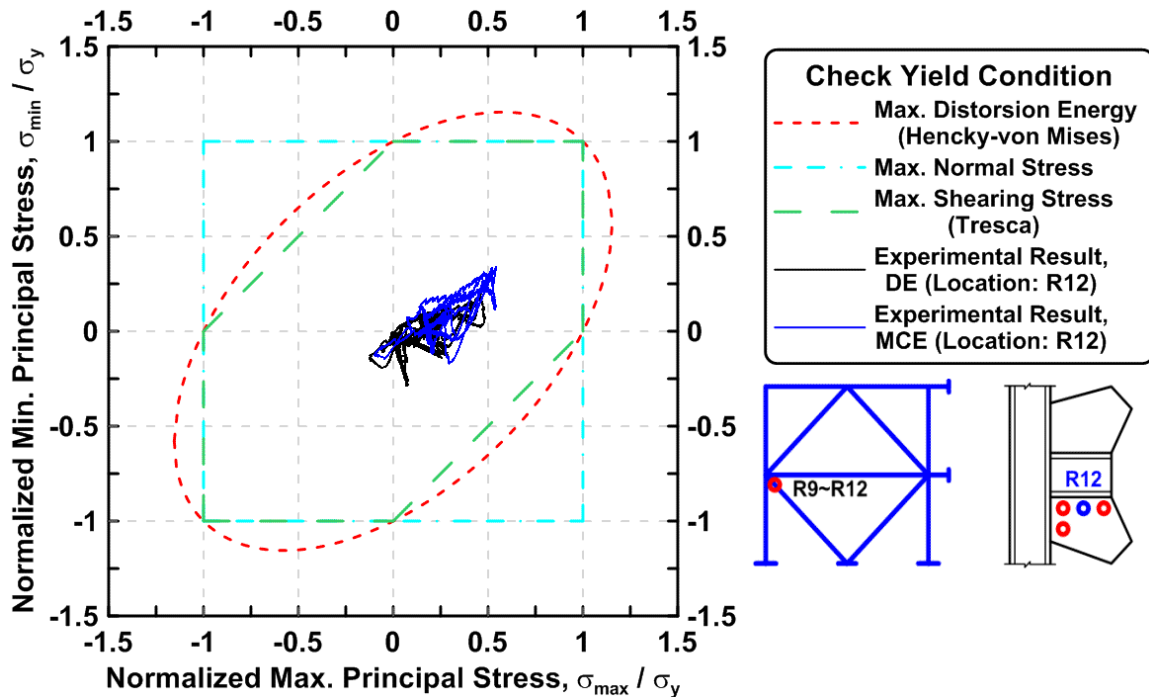


Figure 4.412 Specimen TCBF-B-4: normalized maximum principal stress versus normalized minimum principal stress in one-piece gusset plate (location: R12).

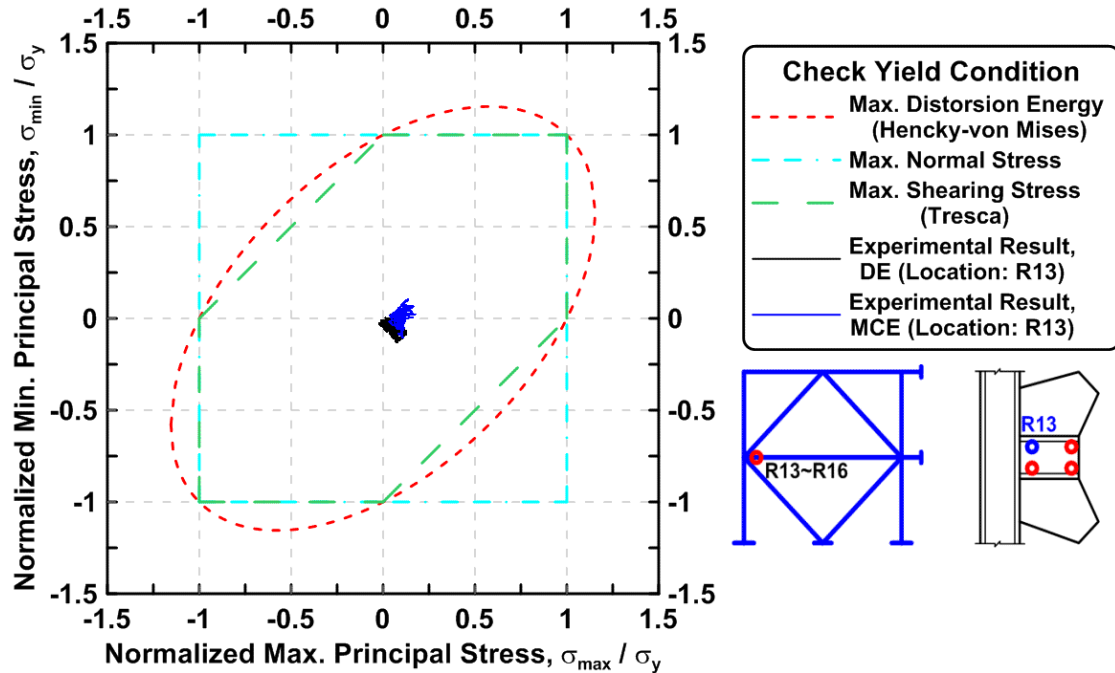


Figure 4.413 Specimen TCBF-B-4: normalized maximum principal stress versus normalized minimum principal stress in one-piece gusset plate (location: R13).

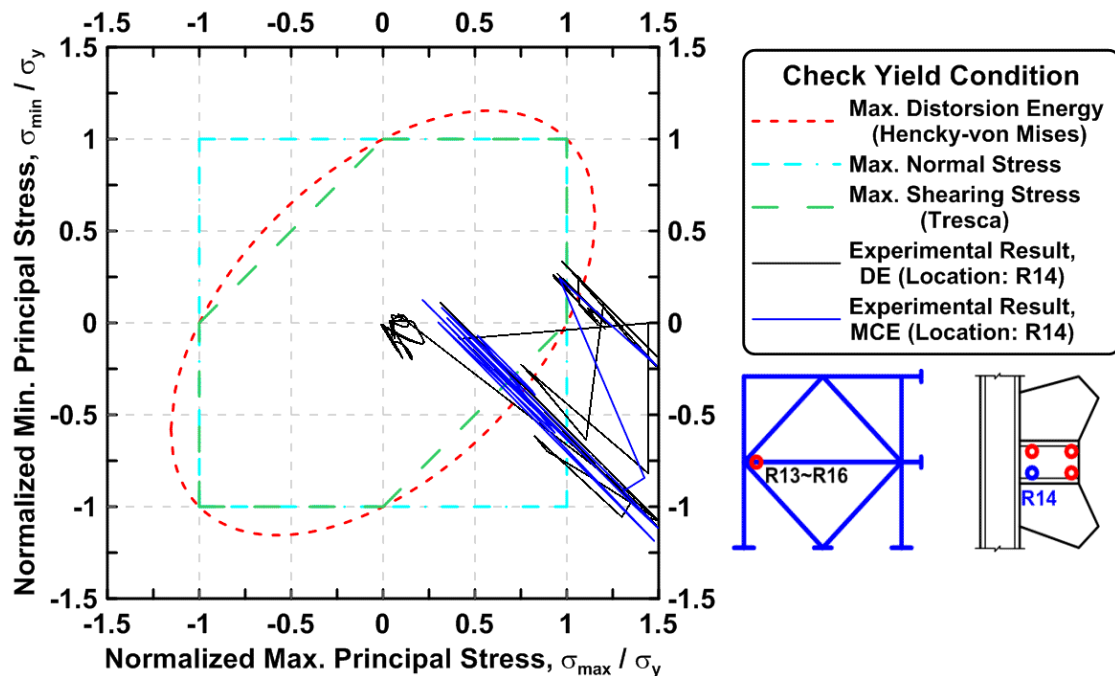


Figure 4.414 Specimen TCBF-B-4: normalized maximum principal stress versus normalized minimum principal stress in one-piece gusset plate (location: R14).

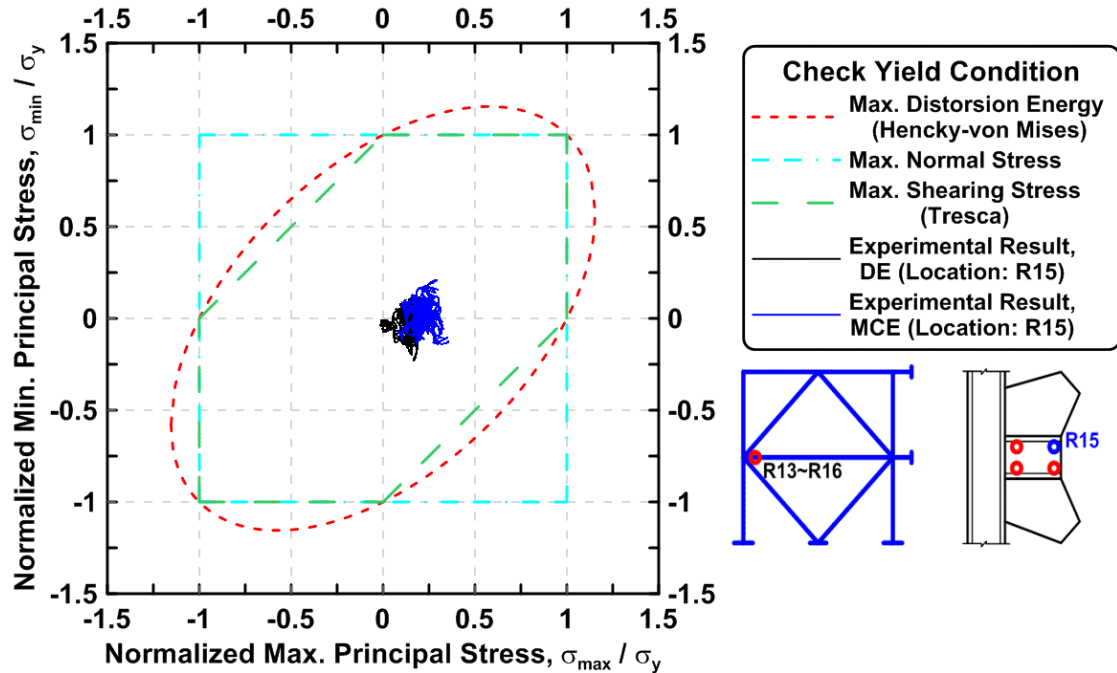


Figure 4.415 Specimen TCBF-B-4: normalized maximum principal stress versus normalized minimum principal stress in one-piece gusset plate (location: R15).

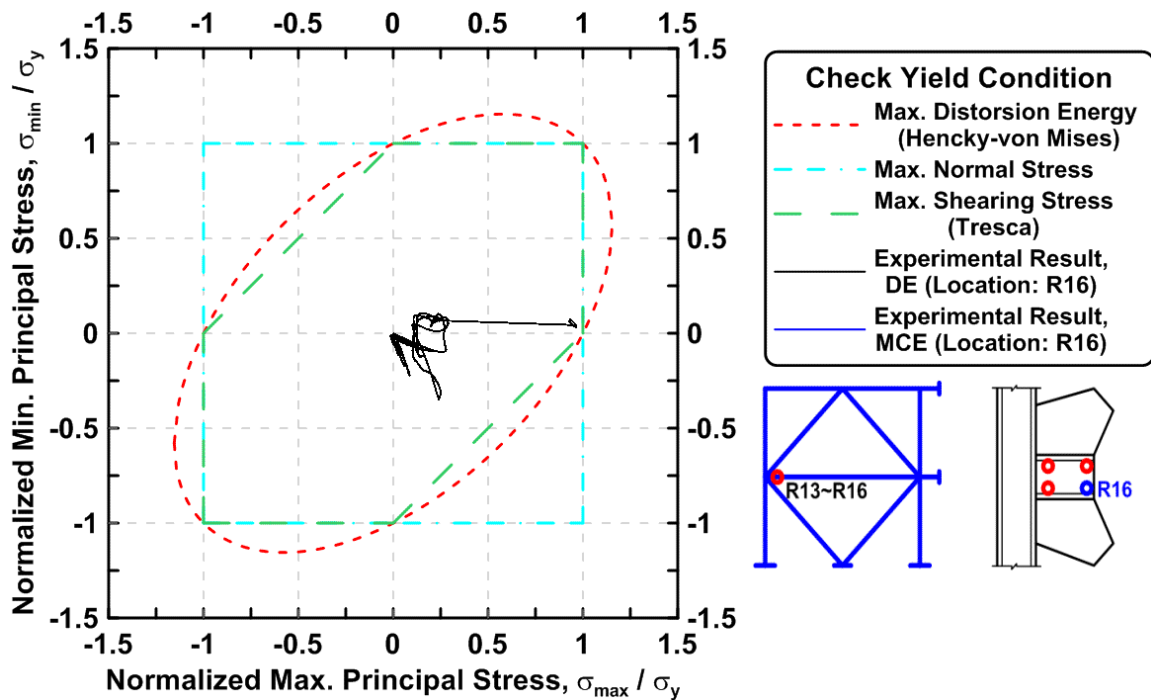


Figure 4.416 Specimen TCBF-B-4: normalized maximum principal stress versus normalized minimum principal stress in one-piece gusset plate (location: R16).

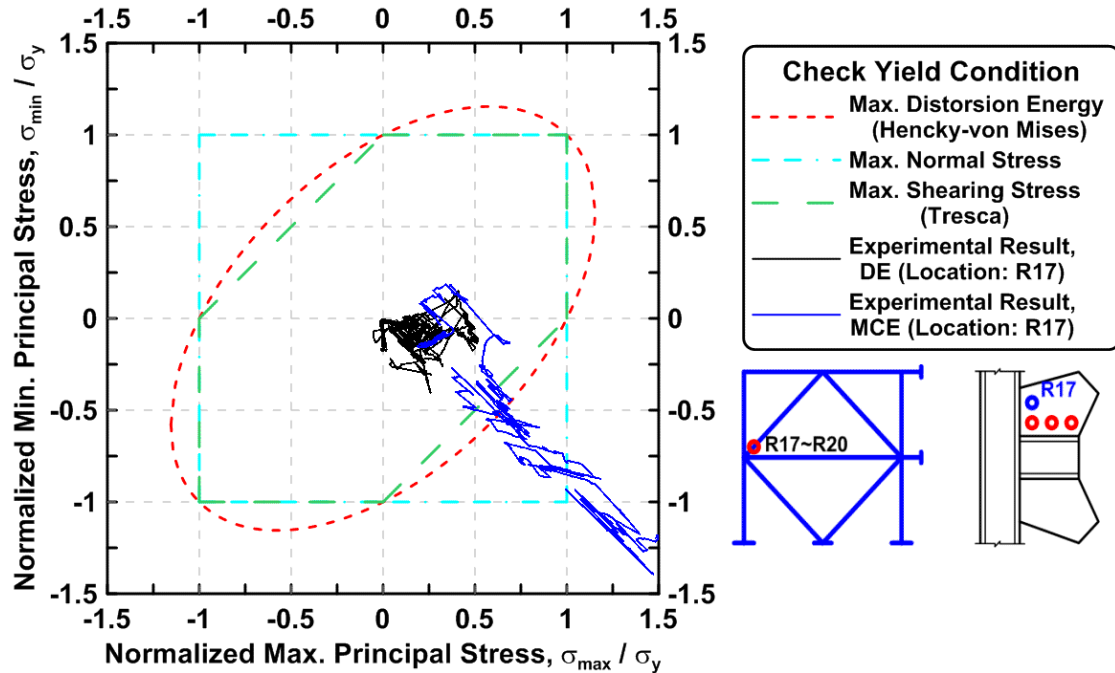


Figure 4.417 Specimen TCBF-B-4: normalized maximum principal stress versus normalized minimum principal stress in one-piece gusset plate (location: R17).

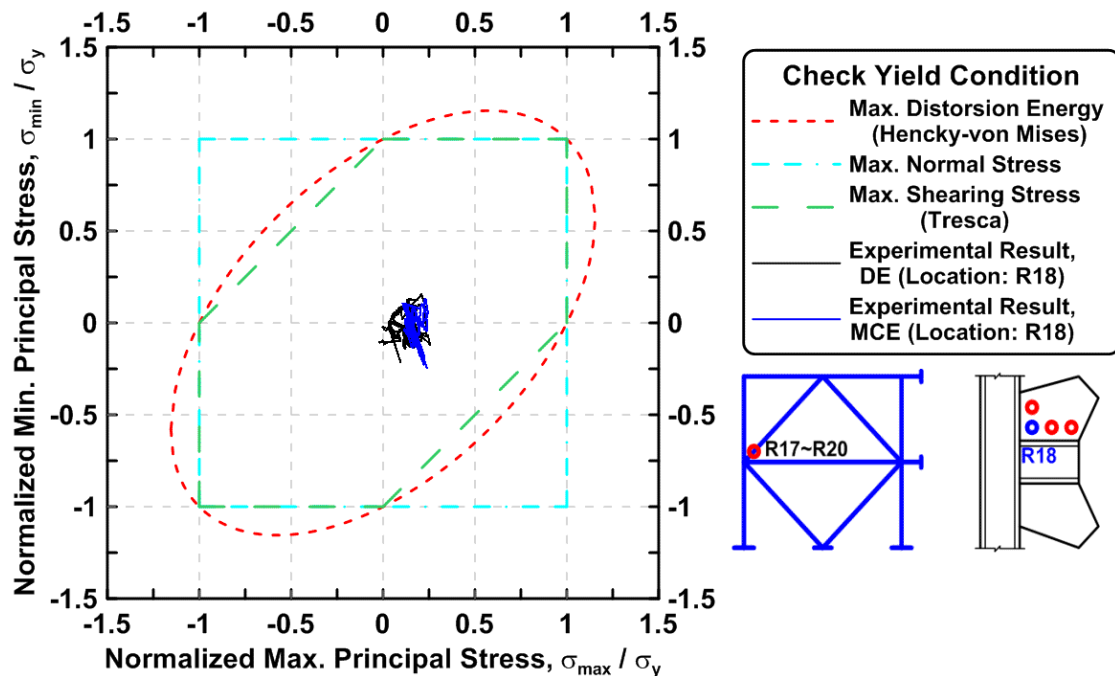


Figure 4.418 Specimen TCBF-B-4: normalized maximum principal stress versus normalized minimum principal stress in one-piece gusset plate (location: R18).

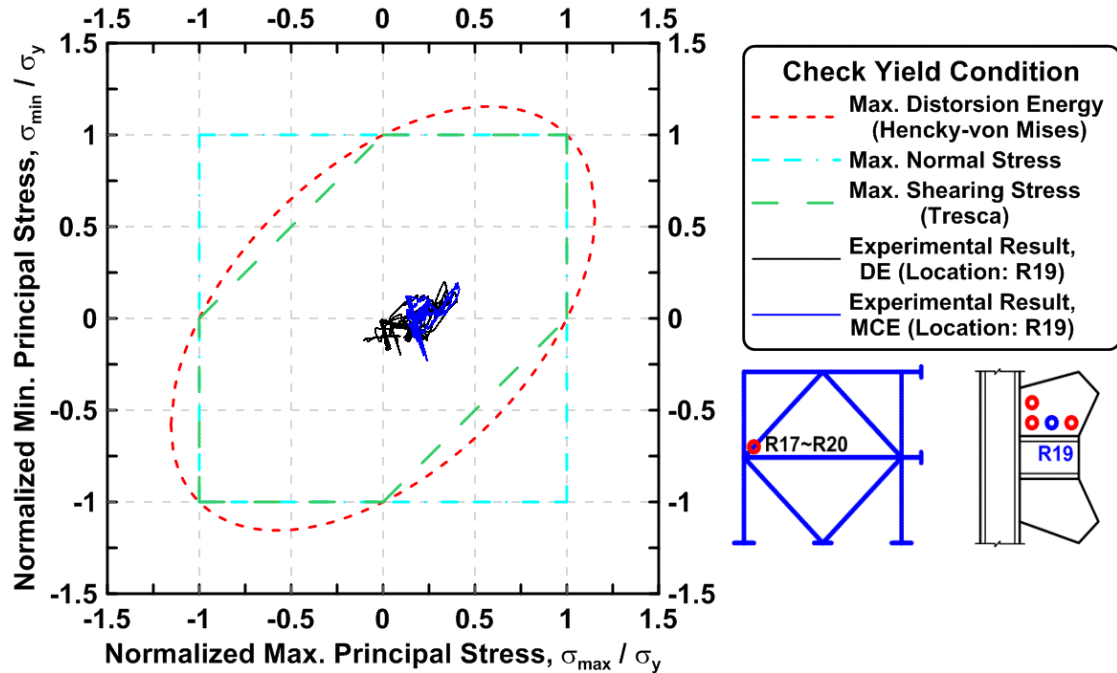


Figure 4.419 Specimen TCBF-B-4: normalized maximum principal stress versus normalized minimum principal stress in one-piece gusset plate (location: R19).

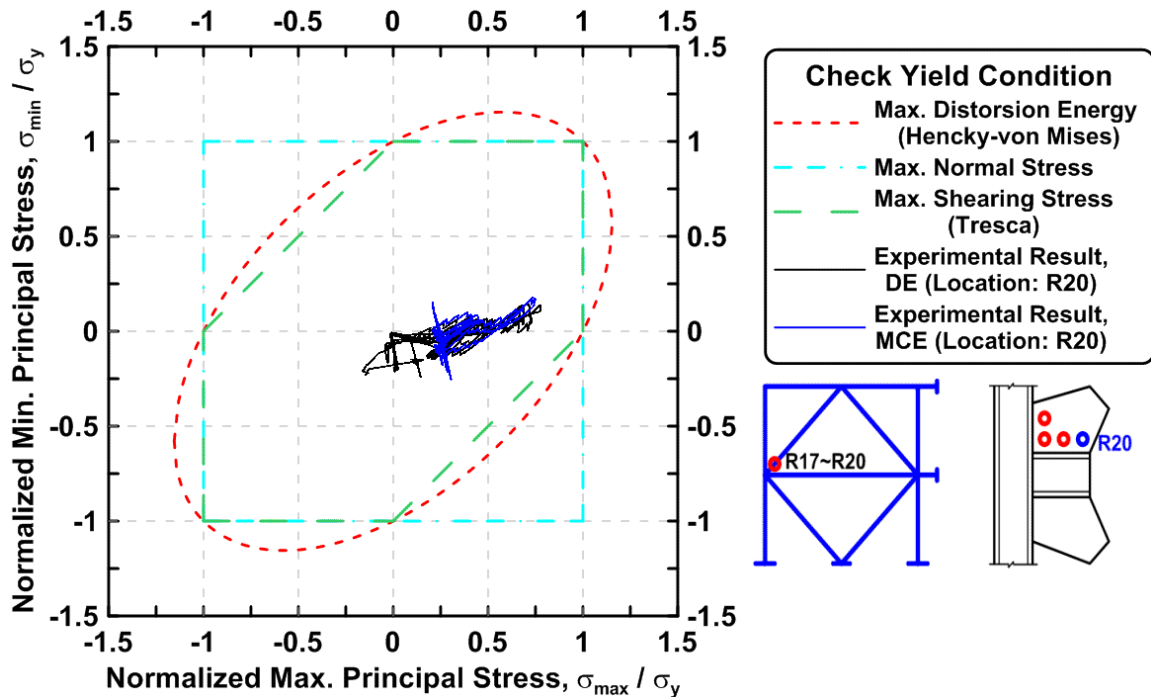


Figure 4.420 Specimen TCBF-B-4: normalized maximum principal stress versus normalized minimum principal stress in one-piece gusset plate (location: R20).

4.2.2.7 Test Set Up Response

The actuator bracket deformations versus actuator forces are plotted in Figure 4.421. The relative displacement time history between the base plates of the specimen and the floor beam, relative displacement time history between floor beam and strong floor, and relative displacement time history between integrated reconfigurable reaction wall and strong floor at the northern and southern sides are shown in Figure 4.422. The out-of-plane deformation time history of the lateral supporting frame with respect to the wall of the building at different locations is plotted in Figure 4.423. The RRW tip deformation time histories during the test are shown in Figure 4.424.

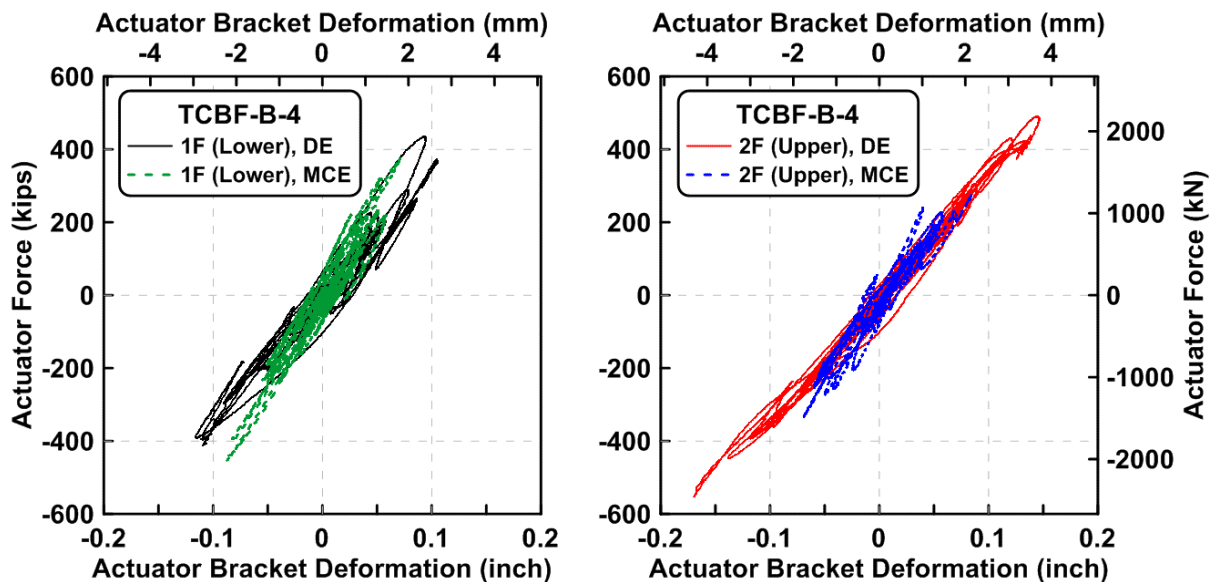


Figure 4.421 Specimen TCBF-B-4: actuator force versus bracket deformation relationship at both floor levels during hybrid simulation.

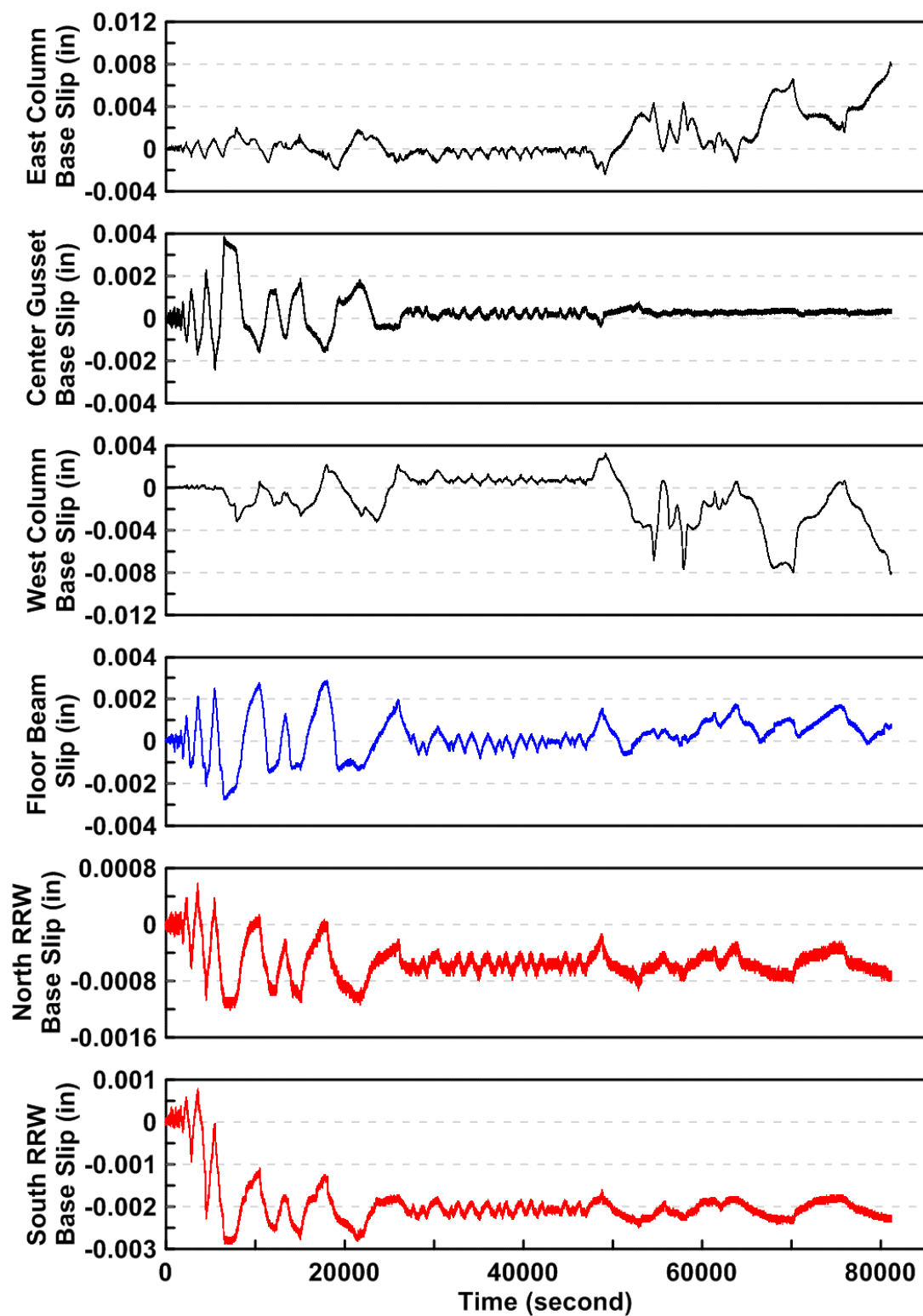


Figure 4.422 Specimen TCBF-B-4: slippage time history between specimen and test set up boundaries during hybrid simulation.

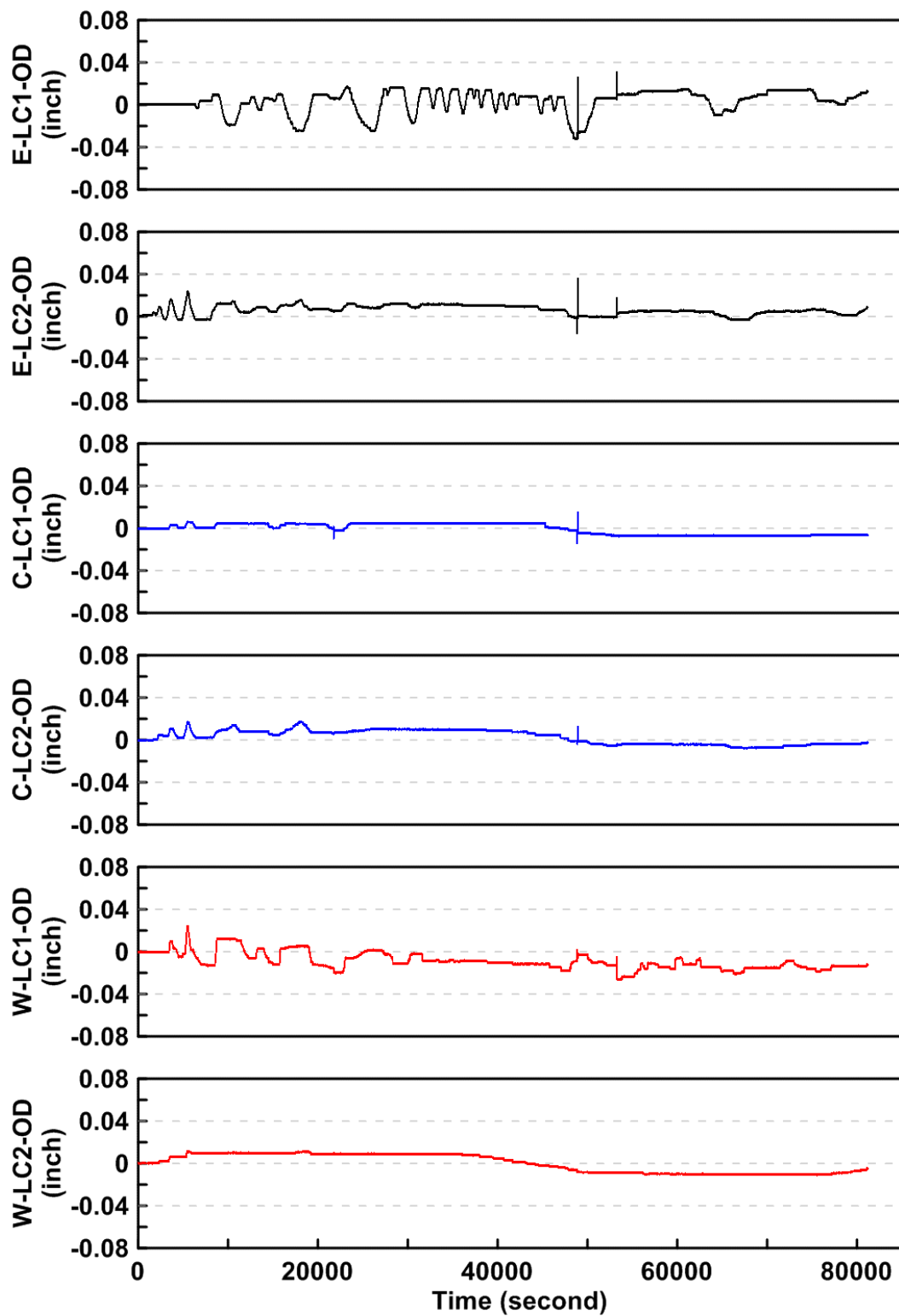


Figure 4.423 Specimen TCBF-B-4: out-of-plane deformation time history of lateral supporting frame at different monitoring points during hybrid simulation.

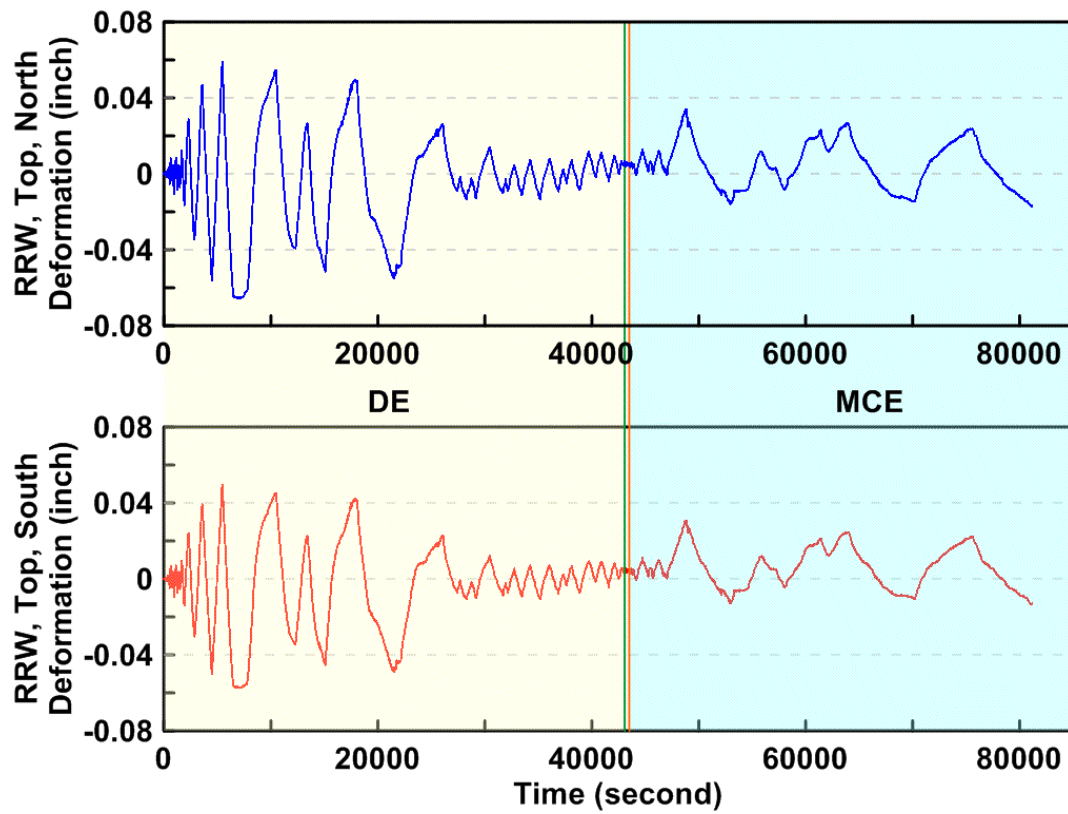


Figure 4.424 Specimen TCBF-B-4: reconfigurable reaction wall tip deformation time histories during hybrid simulation.

5 Discussion of Experimental Results

This chapter examines, compares, and discusses the results from tests on four concentric braced frame specimens having the same basic configuration but with different bracing elements and details. Three of the specimens were tested using the same prescribed cyclic quasi-static displacement history, and one was tested using hybrid simulation. The following sections describe the key response and behavioral characteristics investigated herein. Test results are compared to numerical simulations presented in Chapter 6.

5.1 QUASI-STATIC TEST RESULTS

The three quasi-statically tested braced frame specimens are discussed in this section. To facilitate further discussion, the cyclic loading protocol shown in Figure 3.28 is reformatted in Table 5.1. The loading protocol has been grouped into several stages (having the same displacement amplitude). The minimum number of cycles for each stage (amplitude) is two [FEMA 2007]. The design parameter D_{be} in Table 5.1, defined as elastic story drift, was determined from the elastic analysis of model building under seismic forces given in Table 3.5 without introducing any amplification factors. Elastic structural analysis indicated a 0.46-in. roof displacement under this distribution of seismic forces. A nominal value of D_{be} that equals 0.40 in. was selected. Under the same loading condition, the maximum stress ratio $P/\phi_c P_n = 183/270$ in the braces was about 0.678. By extrapolation, D_{by} , the displacement at which a brace would reach its critical compression strength is estimated as:

$$D_{by} = \frac{D_{be}}{0.678} = 0.59 \quad (5.1)$$

and a nominal value of D_{by} equals to 0.60 in. was selected. The D_{bm} was selected based on the following formula:

$$D_{bm} = C_d \times D_{be} = 5.0 \times 0.4 = 2.0 \quad (5.2)$$

where C_d is the deflection amplification factor as defined in AISC Seismic Provisions [AISC 2005b].

Roof drift ratios are computed as the targeted roof displacement (measured at the centerline of roof beam) divided by roof height $\times 100$, and expressed as percent (%) radians. The

excursion numbers in Table 5.1 are the cycle numbers from the very beginning of cyclic test. Note that the table lists all target roof displacements that are reachable based on the stroke of the actuators. The cyclic tests typically stop before reaching the limit of the actuator stroke.

Table 5.1 Specimens TCBF-B: loading protocol details.

Load Stage Number	Number of Cycles	Target Roof Displacements (in.)	Roof Displacements (design parameters)	Roof Drift Ratio (%)	Excursion Number
1	6	0.2	$0.5 D_{be}$	0.09	1 ~ 6
2	2	0.4	D_{be}	0.19	7 ~ 8
3	2	0.6	D_{by}	0.28	9 ~ 10
4	2	1.0	$0.5 D_{bm}$	0.46	11 ~ 12
5	2	2.0	$1.0 D_{bm}$	0.93	13 ~ 14
6	2	3.0	$1.5 D_{bm}$	1.39	15 ~ 16
7	2	4.0	$2.0 D_{bm}$	1.85	17 ~ 18
8	2	5.0	$2.5 D_{bm}$	2.31	19 ~ 20
9	2	6.0	$3.0 D_{bm}$	2.78	21 ~ 22
10	2	7.0	$3.5 D_{bm}$	3.24	23 ~ 24
11	2	8.0	$4.0 D_{bm}$	3.70	25 ~ 26
12	2	9.0	$4.5 D_{bm}$	4.17	27 ~ 28
13	2	10.0	$5.0 D_{bm}$	4.63	29 ~ 30
14	2	11.0	$5.5 D_{bm}$	5.09	31 ~ 32
15	2	12.0	$6.0 D_{bm}$	5.56	33 ~ 34

(Note: loading is stopped when both braces completely fracture in the first story. Actuator displacement rate is 0.01 in./sec in each load stage)

5.1.1 Specimen Global Behavior

Tables 5.2, 5.3, and 5.4 summarize the base shear and roof displacement data in each excursion for the first three specimens. The excursion number column in the aforementioned tables is the cycle number from the very beginning of each cyclic test; the sign that follows the number indicates the positive or negative roof displacement of the excursion. As defined previously, a positive roof displacement means the specimen is pushed towards the east side of the laboratory, and a negative roof displacement means the specimen is pulled towards the west. Looking at the target roof displacements and the peak roof displacements in each excursion, we can clearly see that the peak roof displacements in each excursion essentially follow the commands with only minor differences. The exception to this is Specimen TCBF-B-2, during which an offset of around 0.15 in. was necessitated after excursion 16⁺ due to shifting of the specimen during the column base repairs.

There are a number of ways to characterize the deformation capacity of a braced frame. The AISC Seismic Provisions for cyclic qualification tests of buckling restrained braces suggests that the capacity be defined at the onset of rupture, brace instability, or connection failures. This definition will be used herein. However, others have recognized the ability of a structural system to deform plastically beyond the first rupture of components. In the case of braced frames, the beams, columns, and remaining braces may continue to provide substantial lateral stiffness and lateral load capacity. As such, some guidelines consider the deformation capacity of the structure to be reached when the strength of the system reduces from its peak value by 20% (or other such criteria).

Using the first complete fracture of a brace as the displacement capacity, the first brace completely fractured in Specimen TCBF-B-1 during excursion number 17⁻ (at a 1.85% roof drift ratio). While in Specimens TCBF-B-2 and TCBF-B-3, the excursion numbers at complete brace fracture corresponded to 21⁻ (2.78% roof drift ratio) and 19⁻ (2.31% roof drift ratio), respectively (see key observations “CF” in Tables 5.2, 5.3, and 5.4). It is clear that the Specimen TCBF-B-2 using round hollow structural section as bracing members had the best system deformation capacity among the three specimens tested. The displacement capacity of the specimen with round HSS braces is about 50% greater than that for the specimen with square HSS braces. This also can be seen from the specimen base shear versus roof displacement relationships for all three quasi-static tested specimens (see Figures 4.23, 4.143, and 4.246).

The maximum base shears during these cyclic loading tests were all less than 900 kips, as intended from the specimen design phase (see the backbone curves in Figure 5.1). Maximum base shears for Specimens TCBF-B-1, TCBF-B-2, and TCBF-B-3 are 789.1 kips (13⁺, 0.93%), -845.6 kips (15⁻, 1.39%), and 666.5 kips (11⁺, 0.46%), respectively, where the values in the parentheses indicates the excursion number, loading direction, and target roof drift ratio.

For Specimens TCBF-B-1 and TCBF-B-2, the peak base shear occurred after the onset of brace global buckling but before local buckling in the braces occurred. During the TCBF-B-3 test, however, the peak base shear occurred in the excursion where a wide flange brace began to buckle globally. While this difference may be associated with the shape of the brace cross section, it is also possible that this difference is due to the lower beam-to-gusset plate connection rigidity. In the first two specimens rigid connections (CJP welds at the top and bottom flanges and also at the beam web) were used at both ends of the W24 × 68 lower beam, while pin connections were used in Specimen TCBF-B-3. The lower beam-end moment connections substantially contributed to the story shear through the frame action once the braces began to buckle in the first two specimens. This behavior is also evident in the specimen base shear versus roof displacement relationships plotted for these specimens in Figures 4.23, 4.143, and 4.246.

The peak base shears in each loading excursion degraded faster once local buckling at the middle length of braces occurred, as can be seen in Tables 5.2, 5.3, and 5.4; where Specimen TCBF-B-3 has the smallest peak shear degradation rate among the three braced frame specimens. By comparing the specimen base shear versus roof displacement relationships for these specimens (Figures 4.23, 4.143, and 4.246) at around a positive 4-in. (excursion 17⁺) roof displacement, we find that the peak base shears in this excursion are about the same for all three

specimens. Based on the test observations, at this point in this excursion the lower beam-to-gusset plate connections for Specimens TCBF-B-1 and TCBF-B-2 are substantially damaged; they are not completely rigid, and in both cases only one beam flange remains connected at both ends of the beam to the gusset plates. Thus, moment connections at the ends of the gusset plates partially fractured and deteriorated to act like “pin connections.” As such, it is not believed that the end fixity of the beam to gusset plate has a significant effect on the displacement capacity. Therefore, it can be inferred that the peak shear degradations between different load stages in Specimens TCBF-B-1 and TCBF-B-2 mainly come from the deterioration of the rigidity of lower beam-to-gusset plate connections, while the peak shear degradations within the same load stage come from the deteriorations of buckled braces.

If we look at the total energy dissipation prior to the complete fracture of the first brace, the three specimens individually dissipated 13,698 kip-in., 30,294 kip-in., and 15,111 kip-in. It is evident that Specimen TCBF-B-2 dissipated the most energy before the first brace fracture, which was more than twice that dissipated by either of the other two specimens. Figure 5.2 compares the cumulative energy dissipation of each specimen, demonstrating that the total energy dissipation for all three specimens increased substantially after excursion number 11⁺, which is the same excursion where brace global buckling is observed. Before the first brace completely fractured in Specimen TCBF-B-1, Specimens TCBF-B-1 and TCBF-B-2 dissipated similar quantities of energy. However, Specimen TCBF-B-3 only dissipated about 80% of the energy dissipated by either of the first two specimens. As examined below, this may mean that about 20% of the system energy dissipation is contributed by the formation of plastic hinges at the lower beam-to-gusset plate moment connections.

Examining the energy dissipation in each load excursion (Figures 5.3, 5.4, and 5.5), note that the energy dissipation typically increases as the excursion number increases (i.e., target displacement increases), but the system energy dissipation per excursion drops after brace fracturing. Also, the energy dissipation decreases in the second cycle of each load stage by comparing the energy dissipation for subsequent pairs of excursions to the same target displacement.

Similar results are found by comparing the cumulative roof plastic deformation (Figure 5.6) or the normalized energy dissipation (Figure 5.7). The cumulative roof plastic deformation and the normalized energy dissipation are defined in the title row of Tables 5.2, 5.3, and 5.4. The P_y value used in these equations for each specimen is averaged from four base shear forces corresponding to roof displacements equal to ± 0.6 in. during the tests. Again, Specimen TCBF-B-2 has the largest cumulative roof plastic deformation (51.4 in.) and cumulative normalized energy dissipation (85.7) among three specimens before the first brace fractures. The specimens TCBF-B-1 and TCBF-B-3 have cumulative roof plastic deformations, 24.6 in. and 25.8 in., respectively, about half the value for Specimen TCBF-B-2. For the normalized energy dissipation, they have 41.0 and 43.1, respectively, also about half the value for Specimen TCBF-B-2.

A key aspect of behavior of interest to engineers and researchers is whether soft-story mechanisms form in the specimens as inelastic displacement amplitudes increase. Story

deformations or story drifts are taken herein as the difference between the lateral displacements at the top and lower beam for the top story, and the lower beam and the base for the ground story. Looking at the story shear versus story deformation relationships shown in Figures 4.24, 4.144, and 4.247, we clearly see that the story deformation in Specimen TCBF-B-1 has a tendency to concentrate at the first story during the test. The ratios of story deformation to total roof displacement at each story are shown in Figures 5.8, 5.9, and 5.10. We see in Figure 5.8 that story drift ratios during early cycles in Specimen TCBF-B-1 for top and bottom story are around 30% and 70% of the total roof displacement, respectively. Note that there is an asymmetry in the data after the first few cycles, with the first story taking a higher percentage of the roof displacement during displacement cycles in the negative direction than when loaded in the positive direction. For Specimens TCBF-B-2 and TCBF-B-3 the displacements were more equally distributed between the two stories during the initial cycles (Figures 5.9 and 5.10).

Worth noting for Specimen TCBF-B-1, the bottom story deformation was measured using the position transducers located at the west side of the specimen (next to the actuators, see Appendix D for details). This was not the true specimen displacement since the position transducers also measure the gaps between clevis pin, actuator rod head, and the specimen end plate; this also resulted in unsymmetrical readings during the test. It is believed that in that test the unsymmetrical readings caused the story deformation ratios to deviate from 50 %. To rule out this effect for the tests of Specimens TCBF-B-2 and TCBF-B-3, an additional position transducer was installed and directly measured the first-story deformation.

For Specimen TCBF-B-2, the first-story contribution to the roof displacements increased once buckling of the braces began. In excursion 17, however, a significant asymmetry of deformations occurred, with the first floor contributing more than half of the roof displacement in cycles with negative displacement and less than 50% for positive displacement excursions. This change in behavior occurred when the lower level beams fractured, suggesting that the asymmetry was associated with the width of the specimen changing during the test. In this case the horizontal displacements were different at the west and east edges of the specimen. The redistribution of axial forces between the braces once buckling occurred, results in axial forces in the beam that will change its length; more significant changes in beam length might be expected with the formation of plastic hinges at the ends of the lower beam and with the formation of local buckles and especially flange fractures. For specimen TCBF-B-3, the displacement ratios (Figure 5.10) are essentially close to 50% throughout the test. This specimen had considerable brace yielding in tension and buckling at both levels; the bolted connections at the face of the gusset plates at the lower floor level prevented the formation of plastic hinges.

The energy dissipation ratios for each story shown in Figures 5.11, 5.12, and 5.13 indicate that for all three specimens, more than 60% of total energy dissipates in the first story.

Table 5.2 Specimen TCBF-B-1: base shear and roof displacement data ($P_y = 556.4$ kips from experiment, corresponding to $D_{by} = 0.6$ in. at roof).

Excursion i^+, i^-	Target Roof Displacement (in.)	Peak Roof Displacement in Excursion (in.)	Base Shear at Peak Roof Displacement (kips)	Max. Base Shear in Excursion (kips)	Cumulative Hysteretic Area (Energy Dissipation) E (kip-in.)	Cumulative Plastic Roof Displacement $E / (P_y)$ (in.)	Normalized Energy Dissipation $E / (P_y \times D_{by})$	Key Observations
1 ⁺	0.2	0.196	194.4	202.3	16	0.0	0.0	
1 ⁻	-0.2	-0.198	-198.3	-215.7	21	0.0	0.1	
2 ⁺	0.2	0.201	203.9	203.9	23	0.0	0.1	
2 ⁻	-0.2	-0.199	-208.7	-215.2	27	0.0	0.1	
3 ⁺	0.2	0.199	183.1	202.9	25	0.0	0.1	
3 ⁻	-0.2	-0.203	-211.4	-217.6	31	0.1	0.1	
4 ⁺	0.2	0.201	183.0	202.2	30	0.1	0.1	
4 ⁻	-0.2	-0.197	-216.4	-216.4	38	0.1	0.1	
5 ⁺	0.2	0.201	193.5	200.3	35	0.1	0.1	
5 ⁻	-0.2	-0.197	-199.8	-216.5	40	0.1	0.1	
6 ⁺	0.2	0.199	182.0	200.7	39	0.1	0.1	
6 ⁻	-0.2	-0.197	-213.0	-218.8	46	0.1	0.1	
7 ⁺	0.4	0.400	359.7	380.2	93	0.2	0.3	
7 ⁻	-0.4	-0.403	-411.4	-418.1	124	0.2	0.4	
8 ⁺	0.4	0.398	366.8	386.4	118	0.2	0.4	
8 ⁻	-0.4	-0.400	-410.8	-415.5	140	0.3	0.4	
9 ⁺	0.6	0.596	532.3	532.3	219	0.4	0.7	
9 ⁻	-0.6	-0.602	-575.5	-580.8	286	0.5	0.9	
10 ⁺	0.6	0.599	542.7	550.0	288	0.5	0.9	
10 ⁻	-0.6	-0.599	-575.1	-579.7	335	0.6	1.0	
11 ⁺	1.0	0.997	723.9	731.4	561	1.0	1.7	GB*
11 ⁻	-1.0	-1.001	-735.7	-736.9	819	1.5	2.5	

Table 5.2—Continued

Excursion \bar{i}^+, \bar{i}^-	Target Roof Displacement (in.)	Peak Roof Displacement in Excursion (in.)	Base Shear at Peak Roof Displacement (kips)	Max. Base Shear in Excursion (kips)	Cumulative Hysteretic Area (Energy Dissipation) E (kip-in.)	Cumulative Plastic Roof Displacement $E / (P_y)$ (in.)	Normalized Energy Dissipation $E / (P_y \times D_{by})$	Key Observations
12 ⁺	1.0	0.997	687.7	709.1	991	1.8	3.0	
12 ⁻	-1.0	-1.001	-691.3	-711.7	1211	2.2	3.6	
13 ⁺	2.0	1.999	779.1	789.1	2057	3.7	6.2	
13 ⁻	-2.0	-1.999	-772.8	-778.9	3062	5.5	9.2	
14 ⁺	2.0	1.998	737.7	755.7	3844	6.9	11.5	
14 ⁻	-2.0	-2.002	-754.3	-760.2	4610	8.3	13.8	
15 ⁺	3.0	2.998	725.4	756.9	5993	10.8	18.0	LB*
15 ⁻	-3.0	-2.999	-750.7	-761.3	7652	13.8	22.9	
16 ⁺	3.0	2.997	656.3	662.4	8964	16.1	26.9	
16 ⁻	-3.0	-2.999	-670.1	-685.6	10215	18.4	30.6	
17 ⁺	4.0	4.000	651.2	667.1	11915	21.4	35.7	CI*
17 ⁻	-4.0	-4.019	-443.6	-560.1	13698	24.6	41.0	PF*, CF*
18 ⁺	4.0	3.998	484.5	497.5	15103	27.1	45.2	
18 ⁻	-4.0	-3.998	-364.6	-375.7	16130	29.0	48.3	BF*
19 ⁺	5.0	4.998	353.5	422.3	17419	31.3	52.2	
19 ⁻	-5.0	-2.232	-258.3	-258.3	17620	31.7	52.8	

*Note: GB (global buckling), LB (local buckling), PF (partial fracture), CF (complete fracture), CI (crack initial), BF (lower beam-to-gusset plate fracture).

Table 5.3 Specimen TCBF-B-2: base shear and roof displacement data ($P_y = 589.0$ kips from experiment, corresponding to $D_{by} = 0.6$ in. at roof).

Excursion i^+, i^-	Target Roof Displacement (in.)	Peak Roof Displacement in Excursion (in.)	Base Shear at Peak Roof Displacement (kips)	Max. Base Shear in Excursion (kips)	Cumulative Hysteretic Area (Energy Dissipation) E (kip-in.)	Cumulative Plastic Roof Displacement $E / (P_y)$ (in.)	Normalized Energy Dissipation $E / (P_y \times D_{by})$	Key Observations
1 ⁺	0.2	0.204	217.6	217.8	19	0.0	0.1	
1 ⁻	-0.2	-0.199	-226.7	-226.9	23	0.0	0.1	
2 ⁺	0.2	0.205	218.4	220.7	25	0.0	0.1	
2 ⁻	-0.2	-0.199	-224.8	-224.8	28	0.0	0.1	
3 ⁺	0.2	0.206	205.6	216.9	29	0.0	0.1	
3 ⁻	-0.2	-0.198	-225.3	-225.9	33	0.1	0.1	
4 ⁺	0.2	0.204	219.1	219.6	34	0.1	0.1	
4 ⁻	-0.2	-0.199	-221.9	-225.5	38	0.1	0.1	
5 ⁺	0.2	0.204	211.0	218.6	40	0.1	0.1	
5 ⁻	-0.2	-0.199	-222.7	-223.7	43	0.1	0.1	
6 ⁺	0.2	0.205	216.9	219.0	45	0.1	0.1	
6 ⁻	-0.2	-0.198	-224.6	-224.8	48	0.1	0.1	
7 ⁺	0.4	0.405	405.4	405.7	104	0.2	0.3	
7 ⁻	-0.4	-0.394	-408.2	-427.5	116	0.2	0.3	
8 ⁺	0.4	0.403	394.1	414.2	122	0.2	0.3	
8 ⁻	-0.4	-0.396	-408.5	-427.6	133	0.2	0.4	
9 ⁺	0.6	0.606	558.7	579.1	220	0.4	0.6	
9 ⁻	-0.6	-0.595	-603.5	-610.3	265	0.4	0.7	
10 ⁺	0.6	0.602	592.9	592.9	286	0.5	0.8	
10 ⁻	-0.6	-0.595	-600.9	-607.9	307	0.5	0.9	
11 ⁺	1.0	1.005	725.7	748.8	577	1.0	1.6	GB*
11 ⁻	-1.0	-0.996	-720.5	-741.1	850	1.4	2.4	
12 ⁺	1.0	1.001	704.9	725.6	1073	1.8	3.0	

Table 5.3—Continued

Excursion \bar{i}^+, \bar{i}^-	Target Roof Displacement (in.)	Peak Roof Displacement in Excursion (in.)	Base Shear at Peak Roof Displacement (kips)	Max. Base Shear in Excursion (kips)	Cumulative Hysteretic Area (Energy Dissipation) E (kip-in.)	Cumulative Plastic Roof Displacement $E / (P_y)$ (in.)	Normalized Energy Dissipation $E / (P_y \times D_{by})$	Key Observations
12 ⁺	-1.0	-0.996	-709.0	-728.5	1293	2.2	3.7	
13 ⁺	2.0	2.004	817.0	828.1	2227	3.8	6.3	
13 ⁻	-2.0	-1.995	-829.8	-839.1	3274	5.6	9.3	
14 ⁺	2.0	2.004	771.4	782.3	4023	6.8	11.4	
14 ⁻	-2.0	-1.997	-774.4	-791.3	4760	8.1	13.5	
15 ⁺	3.0	3.002	777.4	798.7	6111	10.4	17.3	
15 ⁻	-3.0	-2.996	-836.9	-845.6	7796	13.2	22.1	
16 ⁺	3.0	2.842	695.6	695.6	8988	15.3	25.4	
16 ⁻	-3.0	-3.150	-835.3	-845.0	10936	18.6	30.9	
17 ⁺	4.0	3.847	661.9	664.2	12598	21.4	35.6	BF*
17 ⁻	-4.0	-4.152	-834.2	-839.0	14993	25.5	42.4	
18 ⁺	4.0	3.845	587.5	591.8	16338	27.7	46.2	
18 ⁻	-4.0	-4.152	-753.0	-756.9	18143	30.8	51.3	
19 ⁺	5.0	4.843	599.5	604.5	19708	33.5	55.8	LB*
19 ⁻	-5.0	-5.152	-797.5	-811.1	22259	37.8	63.0	
20 ⁺	5.0	4.845	541.6	554.0	23750	40.3	67.2	
20 ⁻	-5.0	-5.148	-727.8	-731.7	25917	44.0	73.3	CI*
21 ⁺	6.0	5.843	572.1	575.5	27675	47.0	78.3	
21 ⁻	-6.0	-6.152	-545.1	-601.3	30294	51.4	85.7	PF*, CF*
22 ⁺	6.0	5.845	506.8	517.1	31790	54.0	90.0	
22 ⁻	-6.0	-6.148	-515.3	-521.5	33953	57.6	96.1	
23 ⁺	7.0	6.843	385.7	445.2	35500	60.3	100.5	
23 ⁻	-7.0	-1.373	-311.8	-311.8	36045	61.2	102.0	

*Note: GB (global buckling), LB (local buckling), PF (partial fracture), CF (complete fracture), CI (crack initial), BF (lower beam-to-gusset plate fracture).

Table 5.4 Specimen TCBF-B-3: base shear and roof displacement data ($P_y = 584.8$ kips from experiment, corresponding to $D_{by} = 0.6$ in. at roof).

Excursion i^+, i^-	Target Roof Displacement (in.)	Peak Roof Displacement in Excursion (in.)	Base Shear at Peak Roof Displacement (kips)	Max. Base Shear in Excursion (kips)	Cumulative Hysteretic Area (Energy Dissipation) E (kip-in.)	Cumulative Plastic Roof Displacement $E / (P_y)$ (in.)	Normalized Energy Dissipation $E / (P_y \times D_{by})$	Key Observations
1 ⁺	0.2	0.202	214.0	214.0	18	0.0	0.1	
1 ⁻	-0.2	-0.198	-201.0	-208.4	16	0.0	0.0	
2 ⁺	0.2	0.203	212.9	215.0	20	0.0	0.1	
2 ⁻	-0.2	-0.197	-200.4	-207.4	18	0.0	0.1	
3 ⁺	0.2	0.206	212.8	214.4	22	0.0	0.1	
3 ⁻	-0.2	-0.199	-204.9	-206.7	20	0.0	0.1	
4 ⁺	0.2	0.203	213.0	215.4	23	0.0	0.1	
4 ⁻	-0.2	-0.195	-199.8	-206.2	20	0.0	0.1	
5 ⁺	0.2	0.202	213.1	215.2	24	0.0	0.1	
5 ⁻	-0.2	-0.199	-203.5	-205.6	23	0.0	0.1	
6 ⁺	0.2	0.204	208.3	215.3	24	0.0	0.1	
6 ⁻	-0.2	-0.196	-204.4	-206.0	24	0.0	0.1	
7 ⁺	0.4	0.404	403.3	404.5	80	0.1	0.2	
7 ⁻	-0.4	-0.401	-408.7	-409.4	83	0.1	0.2	
8 ⁺	0.4	0.401	402.5	409.0	88	0.2	0.3	
8 ⁻	-0.4	-0.399	-407.0	-407.8	90	0.2	0.3	
9 ⁺	0.6	0.602	580.4	582.5	180	0.3	0.5	
9 ⁻	-0.6	-0.595	-587.8	-595.4	196	0.3	0.6	
10 ⁺	0.6	0.603	588.7	590.1	210	0.4	0.6	
10 ⁻	-0.6	-0.592	-582.3	-594.0	211	0.4	0.6	
11 ⁺	1.0	1.006	622.4	666.5	428	0.7	1.2	GB*
11 ⁻	-1.0	-0.996	-636.6	-649.8	635	1.1	1.8	

Table 5.4—Continued

Excursion \bar{i}^+, \bar{i}^-	Target Roof Displacement (in.)	Peak Roof Displacement in Excursion (in.)	Base Shear at Peak Roof Displacement (kips)	Max. Base Shear in Excursion (kips)	Cumulative Hysteretic Area (Energy Dissipation) E (kip-in.)	Cumulative Plastic Roof Displacement $E / (P_y)$ (in.)	Normalized Energy Dissipation $E / (P_y \times D_{by})$	Key Observations
12 ⁺	1.0	1.005	611.4	614.7	794	1.4	2.3	
12 ⁻	-1.0	-0.998	-620.3	-622.8	934	1.6	2.7	
13 ⁺	2.0	2.001	638.4	638.4	1607	2.7	4.6	
13 ⁻	-2.0	-1.993	-625.0	-632.8	2373	4.1	6.8	
14 ⁺	2.0	2.001	567.0	570.0	2930	5.0	8.3	
14 ⁻	-2.0	-1.992	-568.8	-570.8	3450	5.9	9.8	
15 ⁺	3.0	2.998	632.0	634.8	4414	7.5	12.6	LB*
15 ⁻	-3.0	-2.993	-642.4	-649.8	5519	9.4	15.7	
16 ⁺	3.0	2.996	568.1	570.0	6373	10.9	18.2	
16 ⁻	-3.0	-2.993	-588.7	-595.1	7235	12.4	20.6	
17 ⁺	4.0	4.002	630.5	632.8	8488	14.5	24.2	
17 ⁻	-4.0	-3.989	-660.0	-661.0	9984	17.1	28.5	
18 ⁺	4.0	3.997	570.6	575.0	11204	19.2	31.9	
18 ⁻	-4.0	-3.996	-445.0	-448.1	12206	20.9	34.8	CI*, PF*
19 ⁺	5.0	4.998	619.6	627.3	13794	23.6	39.3	
19 ⁻	-5.0	-4.997	-335.4	-414.7	15111	25.8	43.1	CF*
20 ⁺	5.0	1.654	234.8	234.8	15337	26.2	43.7	

*Note: GB (global buckling), LB (local buckling), PF (partial fracture), CF (complete fracture), CI (crack initial).

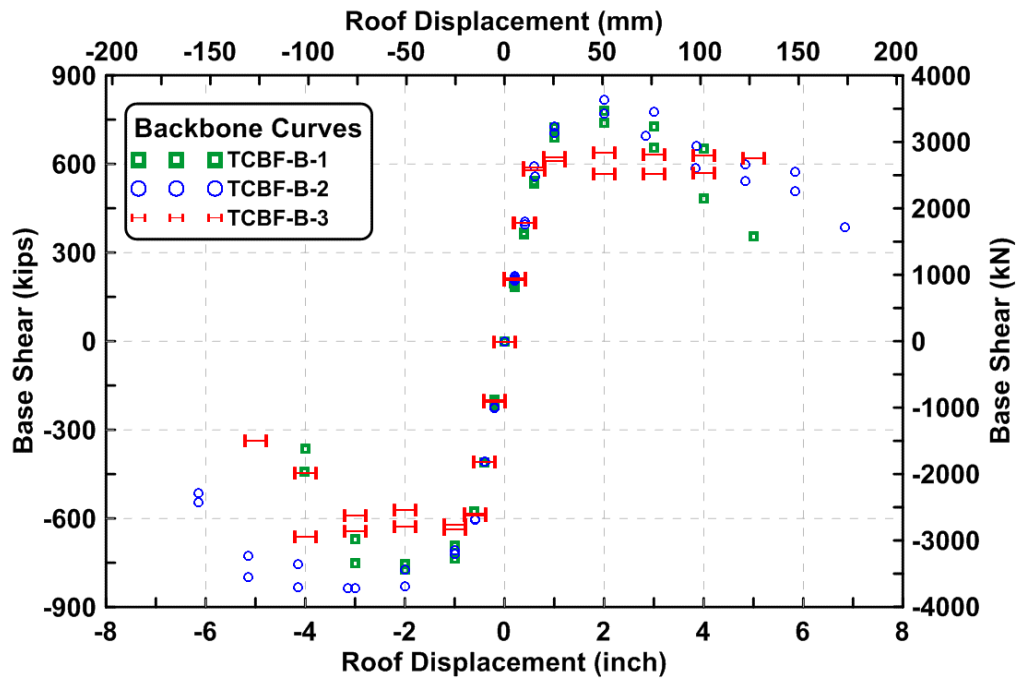


Figure 5.1 Backbone curves of each specimen (both cycle one and cycle two in each load stage).

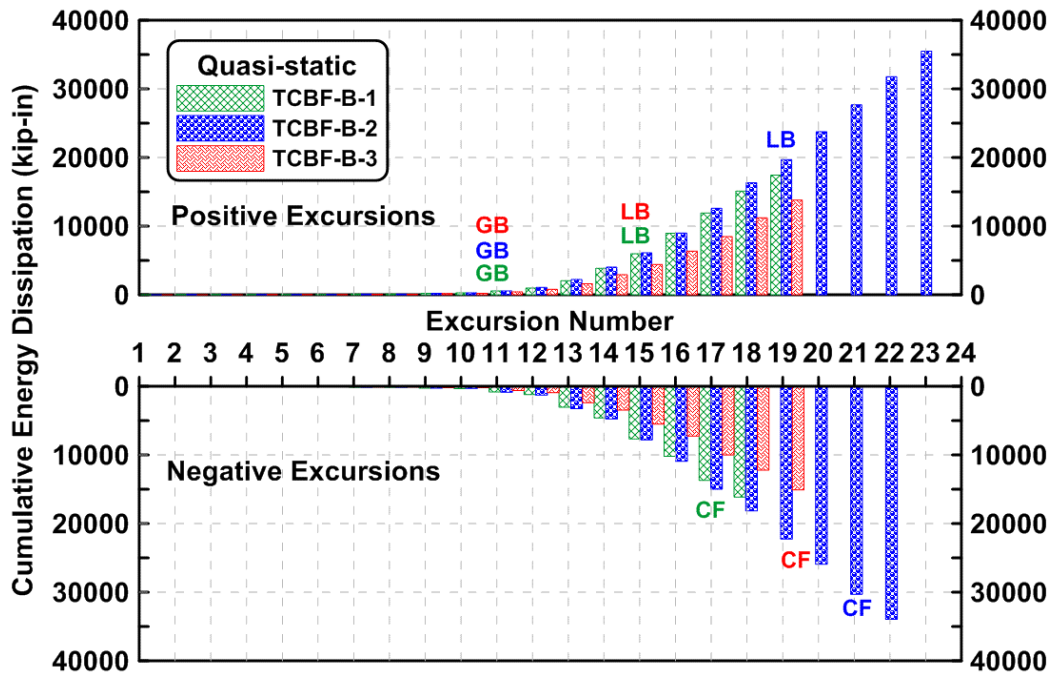


Figure 5.2 Total cumulative energy dissipation of each specimen (GB: global buckling, LB: local buckling, CF: first brace completely fracture).

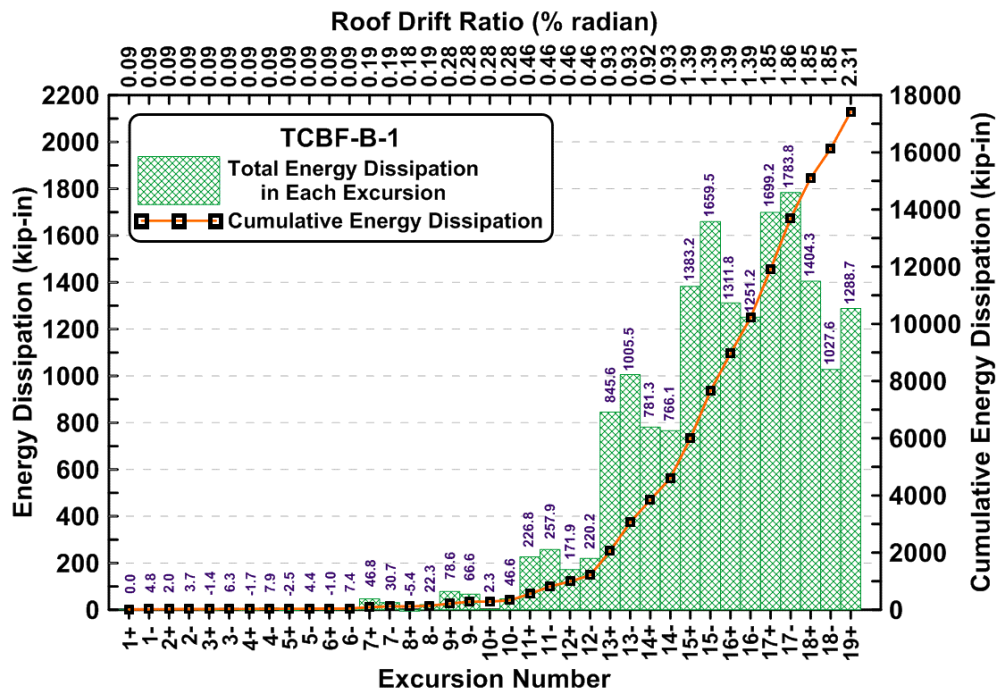


Figure 5.3 Specimen TCBF-B-1: total energy dissipation in each excursion and total cumulative energy dissipation.

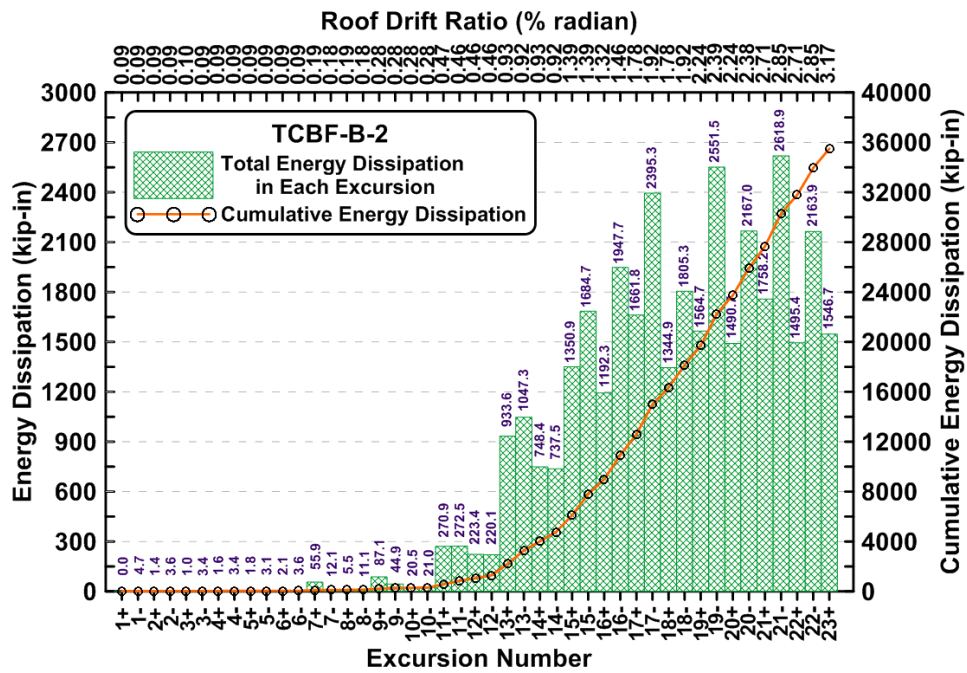


Figure 5.4 Specimen TCBF-B-2: total energy dissipation in each excursion and total cumulative energy dissipation.

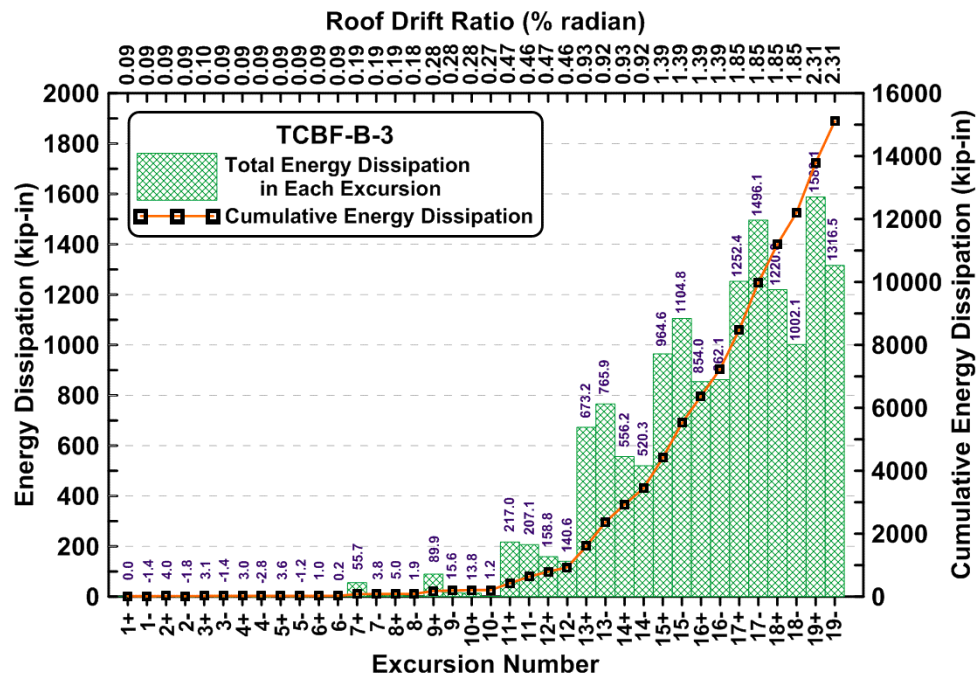


Figure 5.5 Specimen TCBF-B-3: total energy dissipation in each excursion and total cumulative energy dissipation.

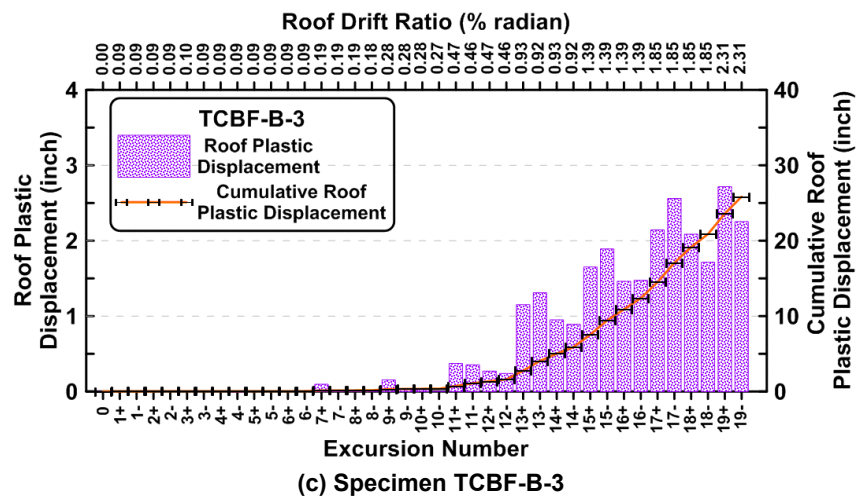
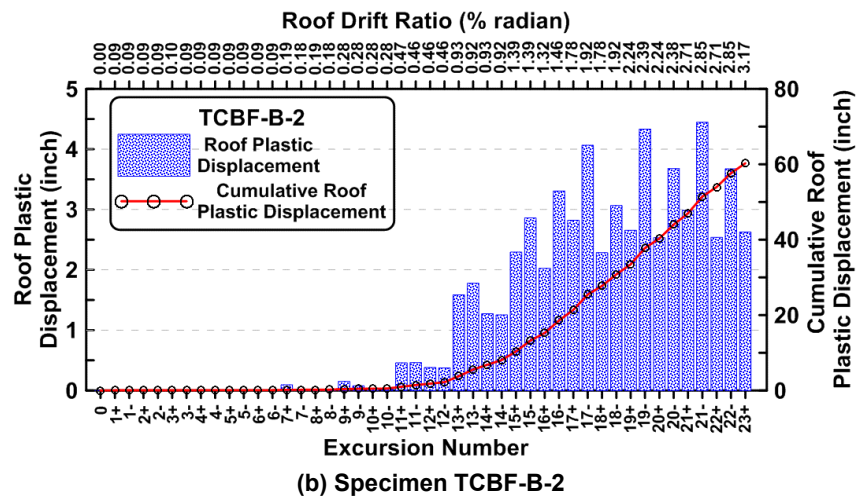
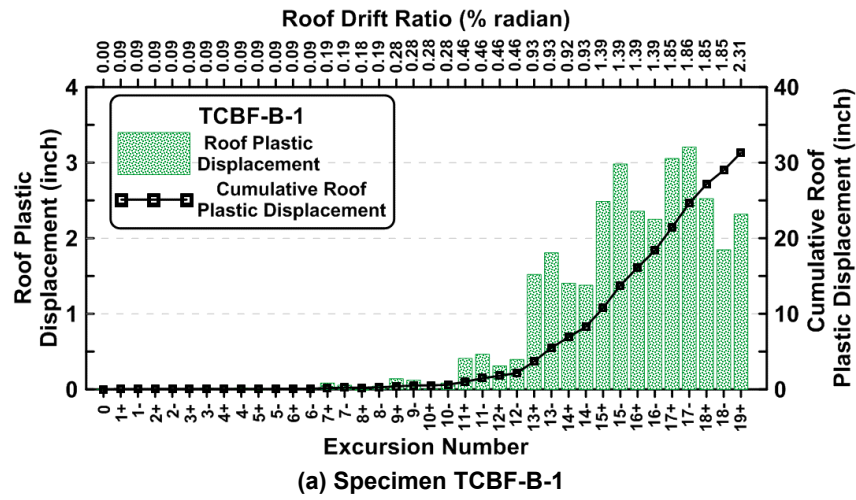


Figure 5.6 Total roof plastic displacement in each excursion and total cumulative roof plastic displacement of three specimens.

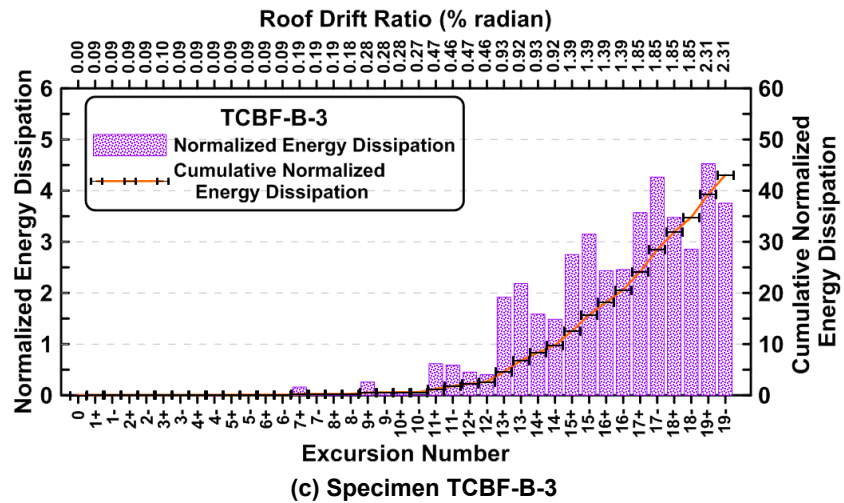
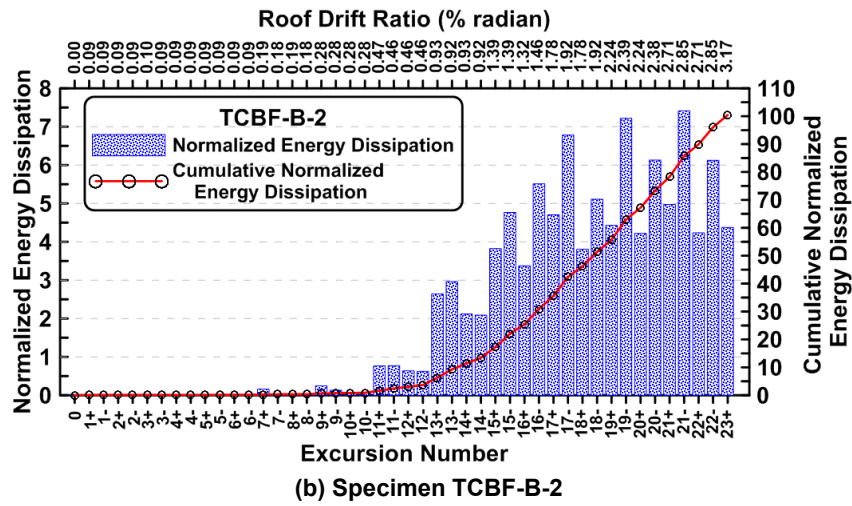
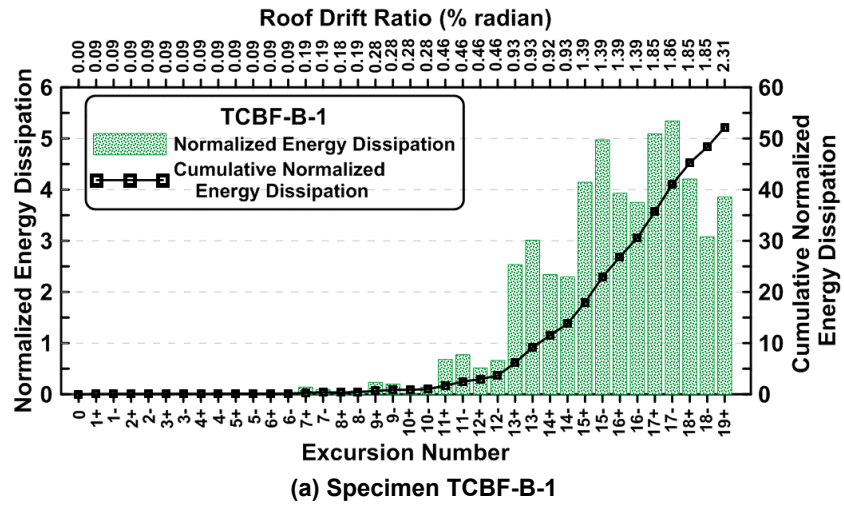


Figure 5.7 Normalized energy dissipation in each excursion and cumulative normalized energy dissipation of three specimens.



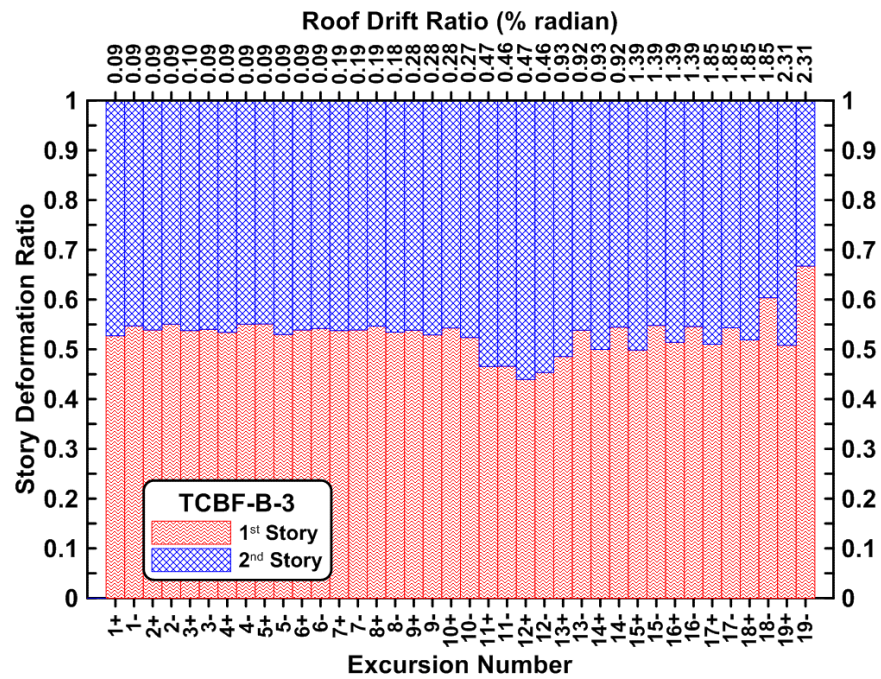


Figure 5.10 Specimen TCBF-B-3: story deformation ratio.

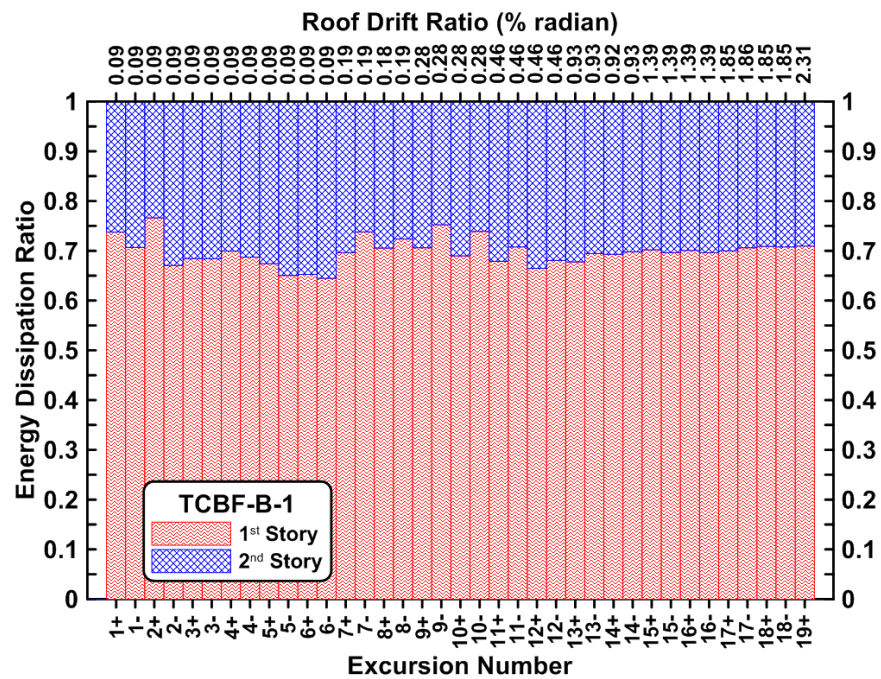


Figure 5.11 Specimen TCBF-B-1: story energy dissipation ratio.

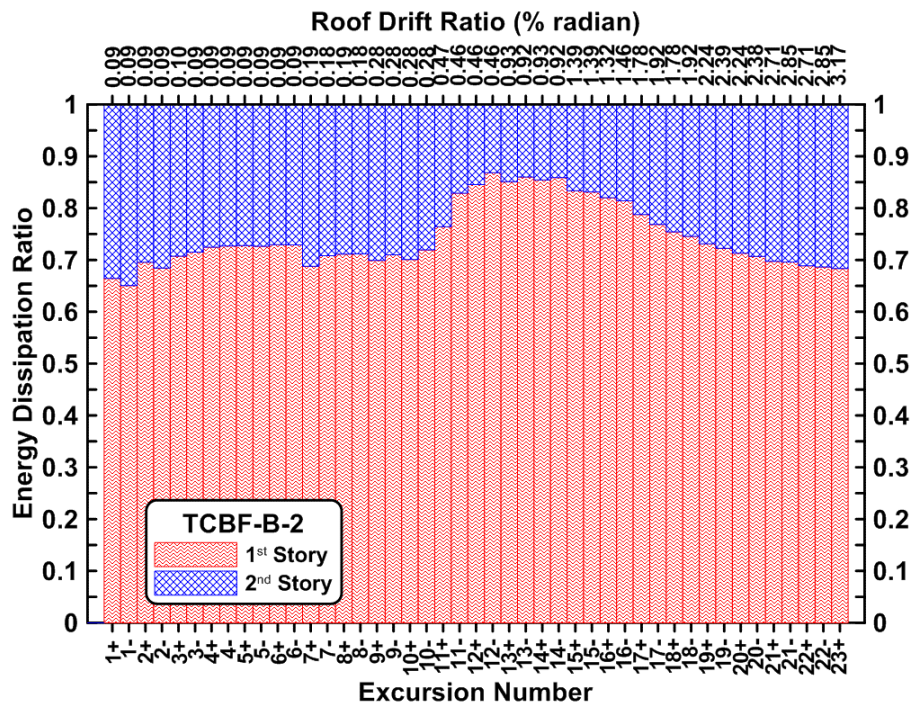


Figure 5.12 Specimen TCBF-B-2: story energy dissipation ratio.

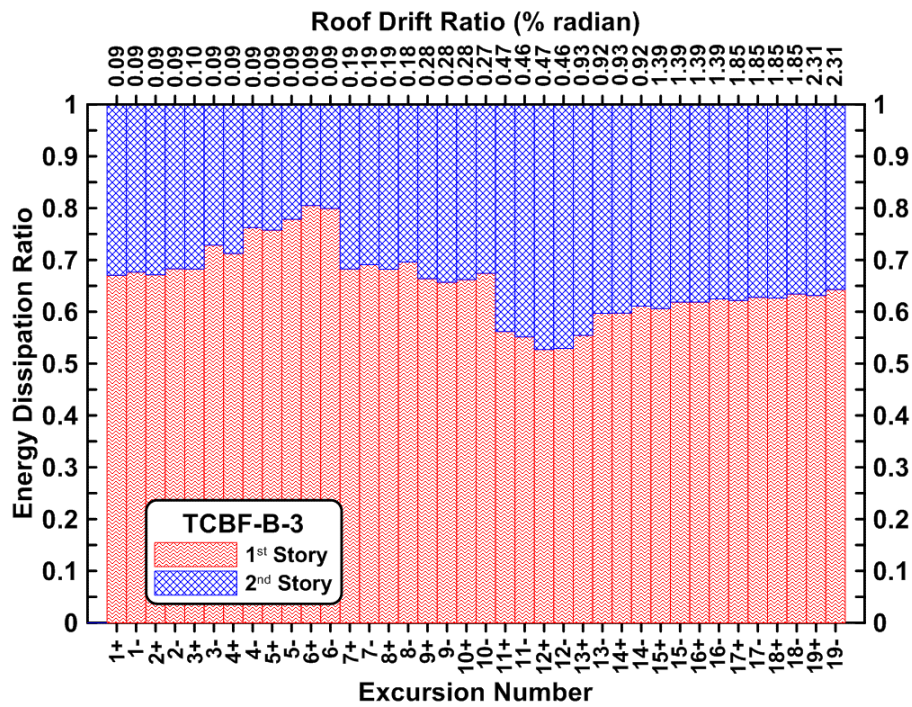


Figure 5.13 Specimen TCBF-B-3: story energy dissipation ratio.

5.1.2 Brace Behavior

As expected from the design, all braces buckled out-of-plane during the quasi-static cyclic loading tests. Measured eccentricities (out-of-plane misalignments at gusset plate to brace connections) of bracing members at both top and bottom brace-to-gusset plate connections are shown in Table 5.5. In a comparison among the specimens of the actual direction of out-of-plane buckling during the tests, note that only the TCBF-B-1 specimen had consistent results. The braces connected to the same one-piece gusset plate tended to buckle in the same direction, as shown in Table 5.5 and in photographs of the tests (see Chapter 4).

From Figures 4.58, 4.178, and 4.281, the out-of-plane displacement at the middle length of braces can be as much as ten times the axial deformation of the braces. The non-structural component around the braced bay such as partition walls, windows, or façade could be severely damaged due to this out-of-plane displacement. Note that the brace out-of-plane displacements tended to change sign (see Figures 4.57 and 4.177) after a crack began to propagate across a cross section of the brace since the neutral axis of the cracked brace shifts toward the uncracked side of the cross section. When the brace was loaded in tension, this eventually created an eccentricity that displaced the center of the brace in the opposite direction from which it buckled. This phenomenon was only observed in the cracked square or round HSS braces (as the cracking pattern was different for the wide flange section [Figure 4.280]).

The brace out-of-plane deformed shapes of each specimen are plotted in Figures 5.14 to 5.25. Once local buckling of bracing members occurred, the out-of-plane deformed shape concentrated plastic deformations at the middle of the braces. This reduced the member curvature outside the mid-span region. This can be seen by comparing the deformed shape in the compression excursions, as shown in the upper part of Figures 5.14 through 5.25. Note that at the initial “elastic range” deformed shapes of braces (see lower part of Figures 5.14 to 5.25), the maximum deflection point was not always at the middle length of brace when the brace deformed elastically.

Strain decomposition plots shown in Chapter 4 illustrate the sources of brace strain readings during the tests. The strain gauges were located at the quarter-length points along the brace close to the gusset plate where two braces meet at the beam side (for more detail on sensor locations, see Appendices D, E, and F). Permanent residual strains typically developed for each component (i.e., axial, out-of-plane, in-plane, and warping strains) by the end of test. Maximum axial strains in the braces ranged from 3 to 7 times the yield strain of steel, and residual tension strains ranged from 2 to 4 times the yield strain (Figures 4.59 to 4.62, 4.179 to 4.182, and 4.282 to 4.285). Axial strains at the monitored locations tended to be tensile because the compression strains during compression phases of a cycle were basically concentrated at the central plastic hinge at the middle of the brace. Spread of strain hardening was observed locally via the spreading of Luder’s bands (or whitewash flakings) along the length of braces, as shown in photographs of the test, especially in the wide flange braces (which experienced larger than 0.01 axial strain). Brace cross-section necking (shrinking of shape or thinning of thickness) was observed before brace fracture. Contact bearing of fractured braces was also observed in these three tests when a fractured brace was shortened due to frame movement.

Most of in-plane bending strain readings are close to or less than the yield strain (between 1600μ to 2350μ in this study), while out-of-plane strains could be as large as 2 to 4 times the yield strain (4000μ to 8000μ). Deviation of out-of-plane bending strain also indicates the buckling direction of the brace. For example, all braces buckled to the north side during the TCBF-B-1 test, which is consistent with the deviation of out-of-plane bending strains as shown in the top-right corner (deviate to negative side) in Figures 4.59, 4.60, 4.61, and 4.62. Note that the sensor locations and sign conventions are different for Specimen TCBF-B-2 compared to Specimens TCBF-B-1 and TCBF-B-3. The effect of frame action on braces is obvious by comparing the sign of axial strain and in-plane bending strain of each brace. For instance, the in-plane bending strains always have the same sign as the axial strains of the first-story braces, while they have opposite sign for the second-story braces. In general, as expected the wide flange braces (opened section) had a larger (roughly 5 times) warping strain compared with square HSS braces (closed section); it was assumed that no warping strains would develop in the round HSS braces.

Brace end-to-end cumulative plastic deformations, cumulative normalized energy dissipation, plastic deformations, and normalized energy dissipation in each excursion of each specimen are shown in Figures 5.26 to 5.31. For all three specimens both the cumulative normalized energy dissipation and cumulative plastic deformations of first-story braces have larger values at the end of tests. In the Specimen TCBF-B-1 test, plastic deformations and ductility ratios of both story braces start to accumulate at about the same excursion, but the first-story braces accumulate plastic deformations more rapidly and consistently than the second-story braces throughout the test. This was not the case for Specimen TCBF-B-2, where plastic deformations and normalized energy dissipation of the first-story braces began to cumulate earlier than in the second story. Later in the test the second-story braces began to accumulate plastic deformations and normalized energy dissipation more rapidly than the first-story braces; but by the end of the test these values were the same. Specimen TCBF-B-3 behaved similarly to Specimen TCBF-B-1, with plastic deformations and normalized energy dissipation of both story braces starting to accumulate at about the same excursion, but with the first-story braces (especially the eastern-side brace) accumulating faster than the second-story braces later in the test.

The components contributing to the total energy dissipation of the three specimens are identified in Figures 5.32, 5.33, and 5.34. Braces in each specimen basically contributed significantly more than 50% of total energy dissipated during the tests until the brace fractured. The braces dissipated more energy when they were in tension, as indicated in the stacked bar charts of each specimen. Energy dissipation by other components, such as beams, columns, and panel zones, increased as the target roof displacement increased.

Table 5.6 summarizes conditions in the specimens at the time the first two braces completely fractured. Note that the cumulative ductility capacities for braces having square HSS, round HSS, and wide flange sectional shapes were all within the range from 42 to 55. Clearly the round HSS braces accumulated more plastic deformations than the other two specimens before brace fracture occurred. Based on the test observations described in Chapter 4 and examining

Table 5.6, it is assumed that the formation of local buckling of braces may have a significant effect on the cumulative plastic deformation capacity under cyclic loading.

Table 5.5 Measured eccentricities of brace before test and buckling direction during test.

Location	1F, East Brace		1F, West Brace		2F, East Brace		2F, West Brace	
Specimen	Top	Bottom	Top	Bottom	Top	Bottom	Top	Bottom
TCBF-B-1	1/16 in. N	1/16 in. N	1/16 in. N	1/8 in. S	1/32 in. S	1/16 in. N	1/16 in. N	1/16 in. N
	N		N		N		N	
TCBF-B-2	1/8 in. S	1/16 in. N	1/16 in. N	1/16 in. S	1/16 in. S	1/16 in. S	1/16 in. N	1/8 in. S
	N		S		N		S	
TCBF-B-3	1/16 in. N	1/16 in. S	1/16 in. S	0	0	1/8 in. N	1/16 in. S	1/8 in. N
	S		N		N		N	

(Note: N stands for north, S stands for south, and the number before indicates the eccentricity from the centerline of gusset plate.)

Table 5.6 Specimen failure characteristics (brace completely fractures).

Specimen Name	TCBF-B-1		TCBF-B-2		TCBF-B-3	
Fracture Sequence	1 st	2 nd	1 st	2 nd	1 st	2 nd
Location	1F-West	1F-East	1F-West	1F-East	1F-West	N.A.
Load Stage Number	7	8	9	10	8	N.A.
Excursion Number	17 ⁻	19 ⁺	21 ⁻	23 ⁺	19 ⁻	N.A.
Roof Displacement at Fracture (in.)	-3.8	4.7	-5.3	7.0	-4.3	N.A.
Roof Drift Ratio at Fracture (% radian)	-1.76	2.16	-2.45	3.24	-1.99	N.A.
Brace Cumulative Plastic Deformation at Fracture (in.)	7.7	9.5	11.5	11.9	7.2	N.A.
Brace Cumulative Ductility Ratio at Fracture	44.4	55.0	46.1	47.7	42.3	N.A.

(Note: in Specimen TCBF-B-3, test is stopped before the second brace fracture.)

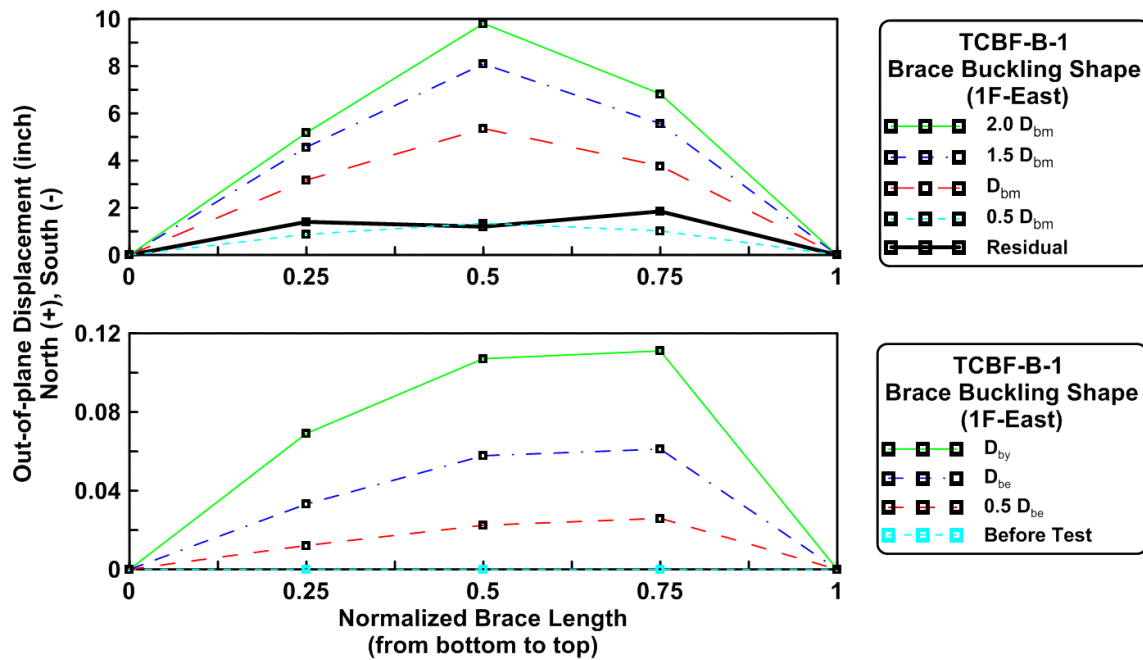


Figure 5.14 Specimen TCBF-B-1: buckling shape of the first-story eastern-side brace in compression excursions.

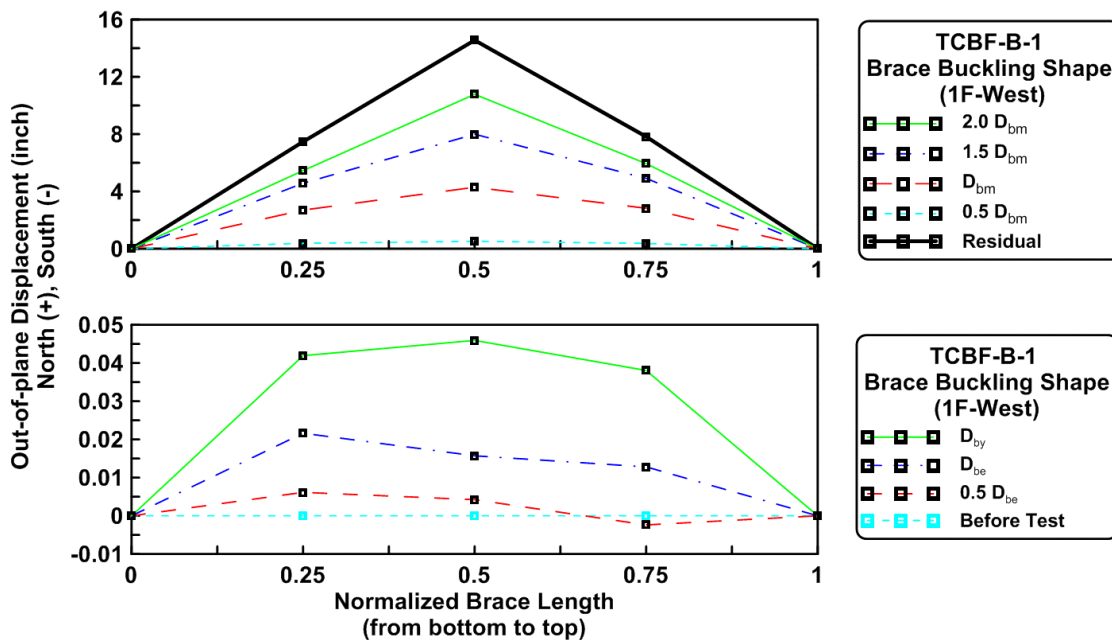


Figure 5.15 Specimen TCBF-B-1: buckling shape of the first-story western-side brace in compression excursions.

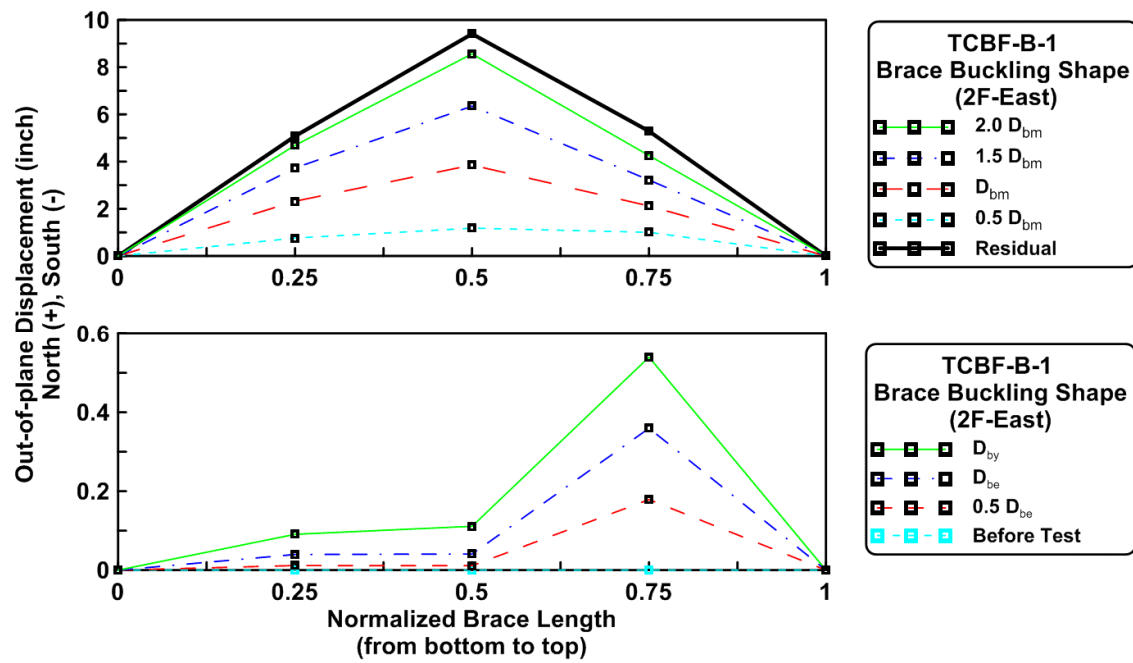


Figure 5.16 Specimen TCBF-B-1: buckling shape of the second-story eastern-side brace in compression excursions.

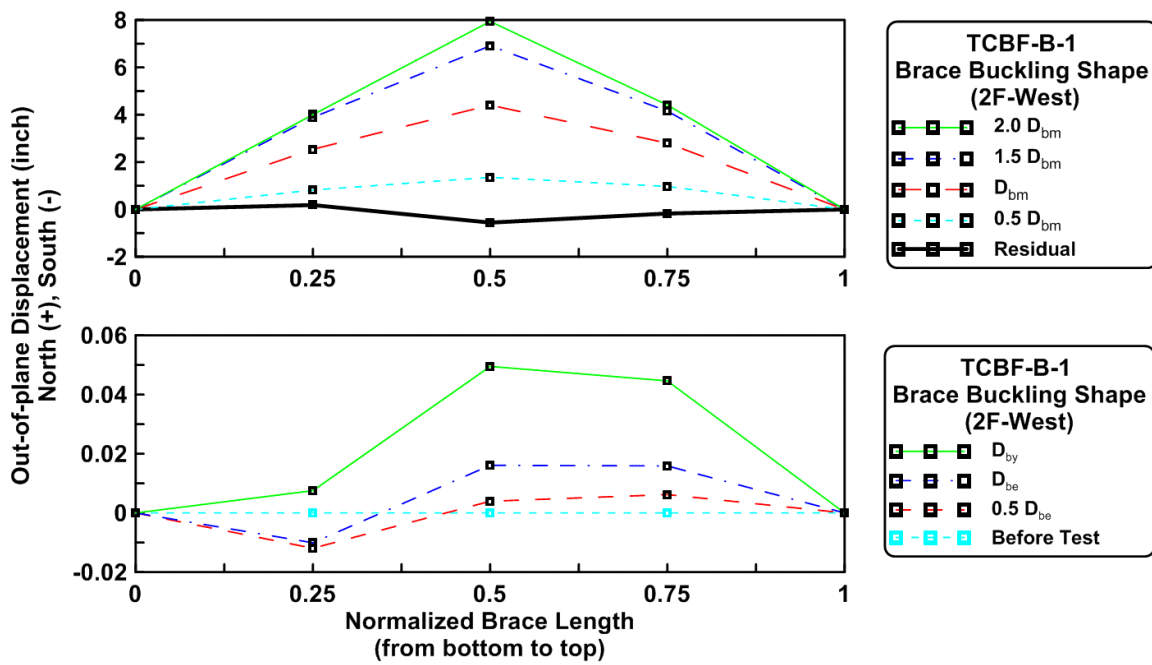


Figure 5.17 Specimen TCBF-B-1: buckling shape of the second-story western-side brace in compression excursions.

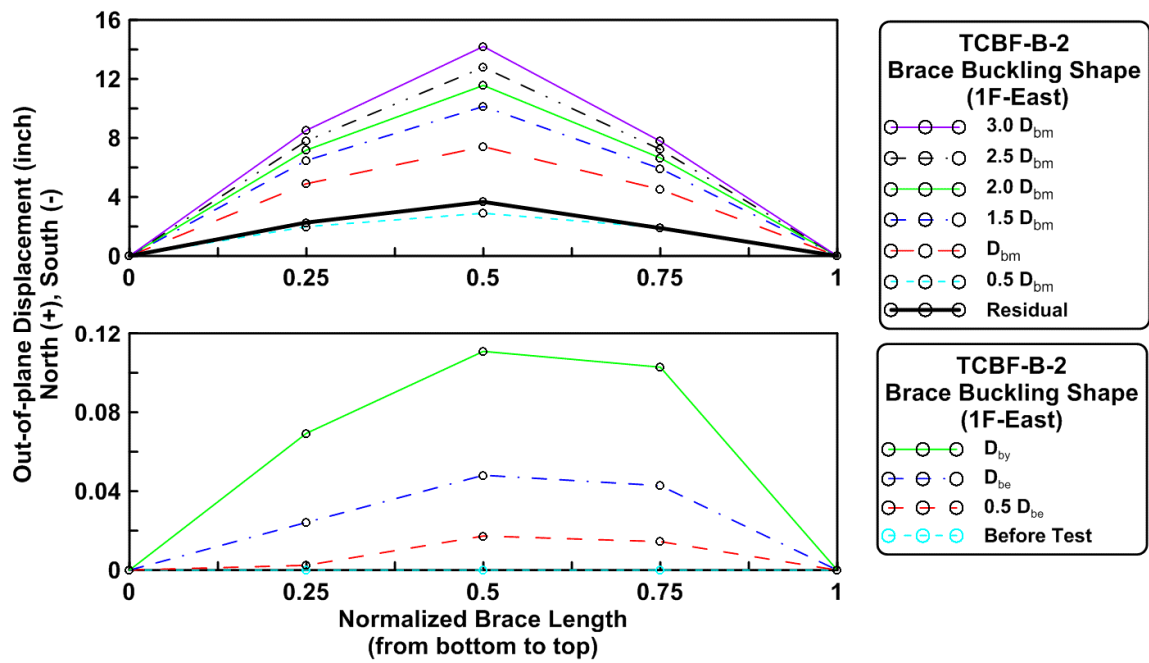


Figure 5.18 Specimen TCBF-B-2: buckling shape of the first-story eastern-side brace in compression excursions.

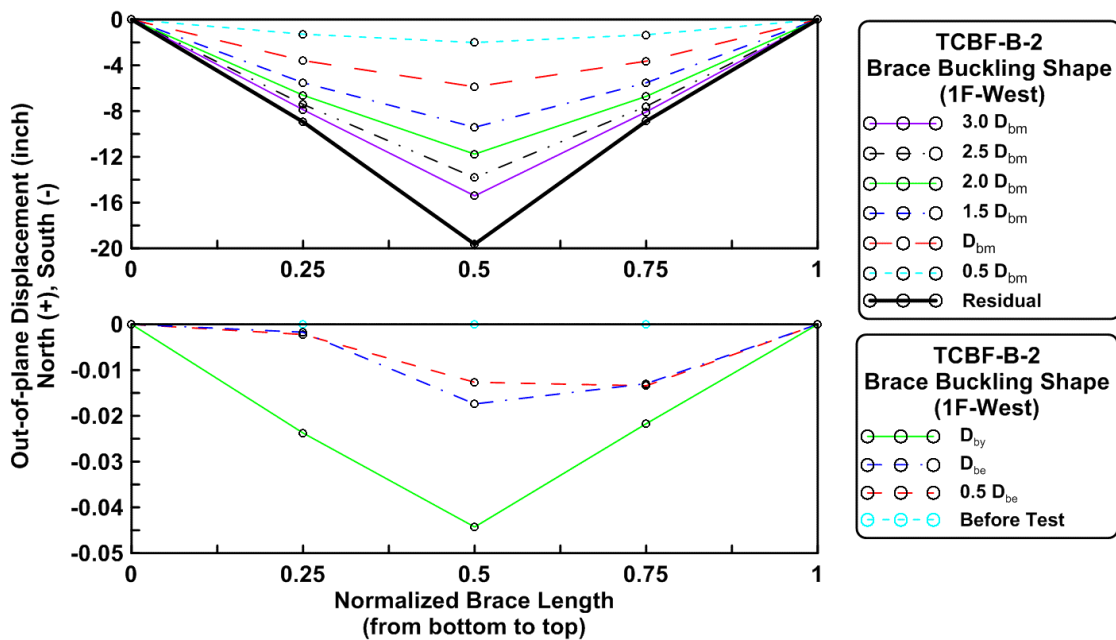


Figure 5.19 Specimen TCBF-B-2: buckling shape of the first-story western-side brace in compression excursions.

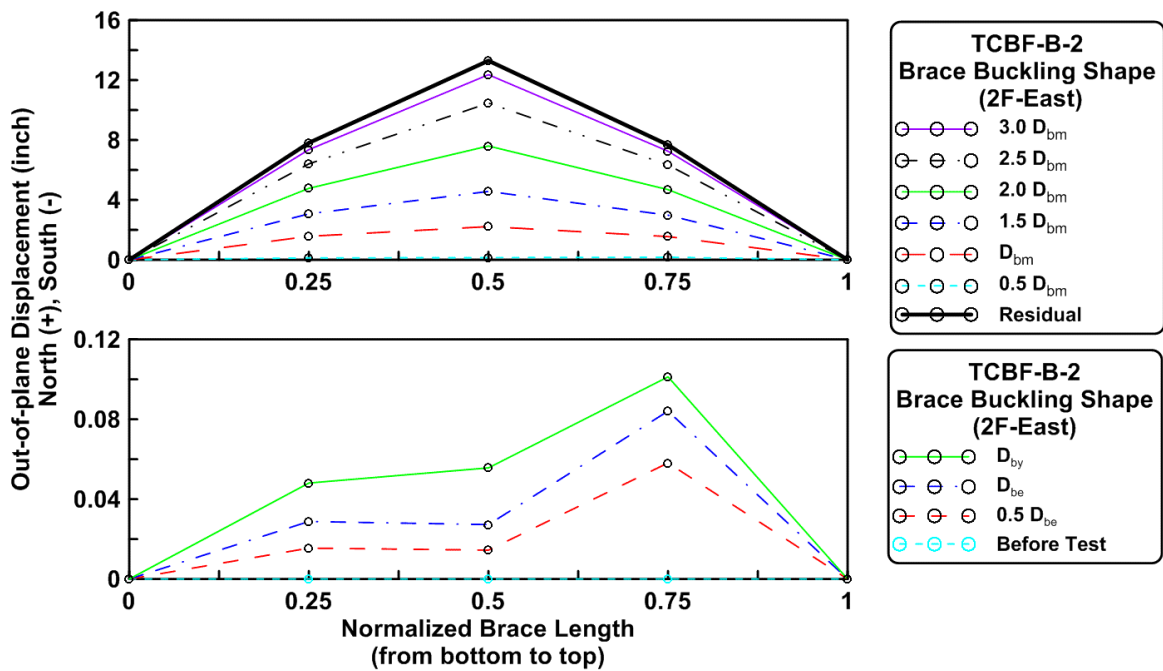


Figure 5.20 Specimen TCBF-B-2: buckling shape of the second-story eastern-side brace in compression excursions.

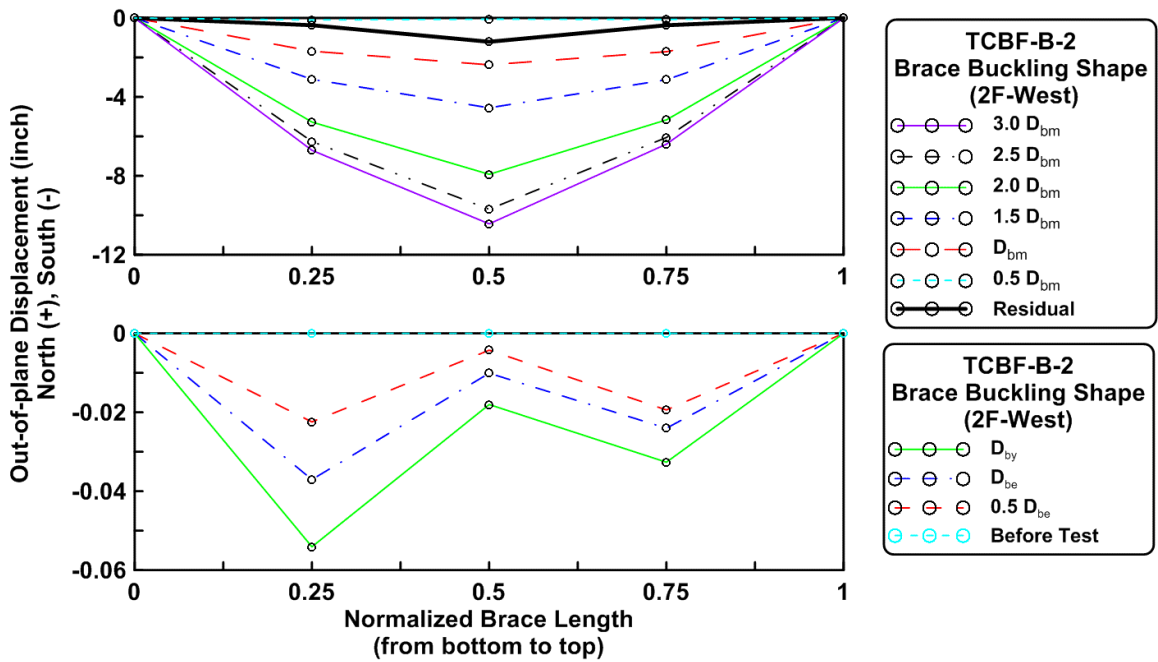


Figure 5.21 Specimen TCBF-B-2: buckling shape of the second-story western-side brace in compression excursions.

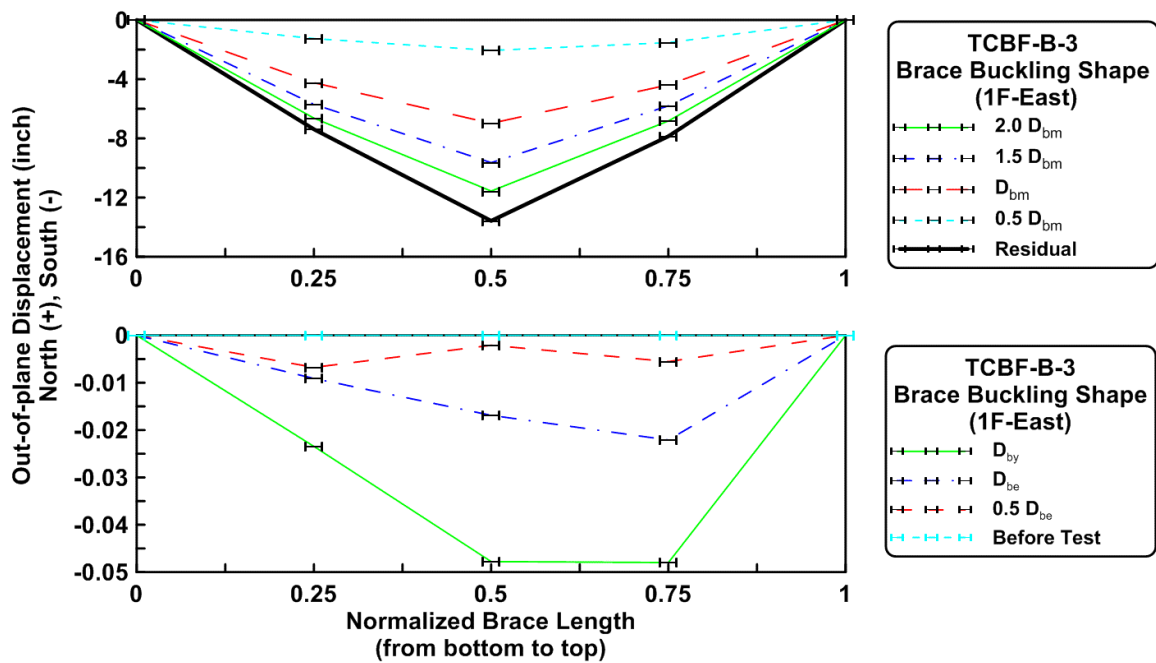


Figure 5.22 Specimen TCBF-B-2: buckling shape of the first-story eastern-side brace in compression excursions.

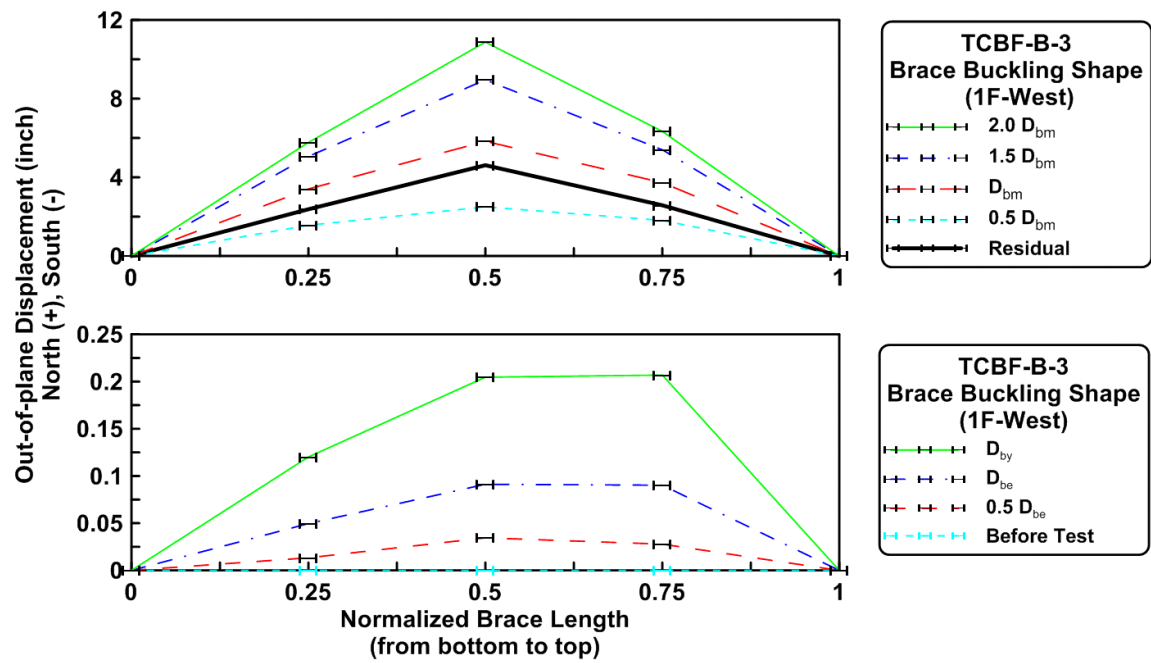


Figure 5.23 Specimen TCBF-B-2: buckling shape of the first-story western-side brace in compression excursions.

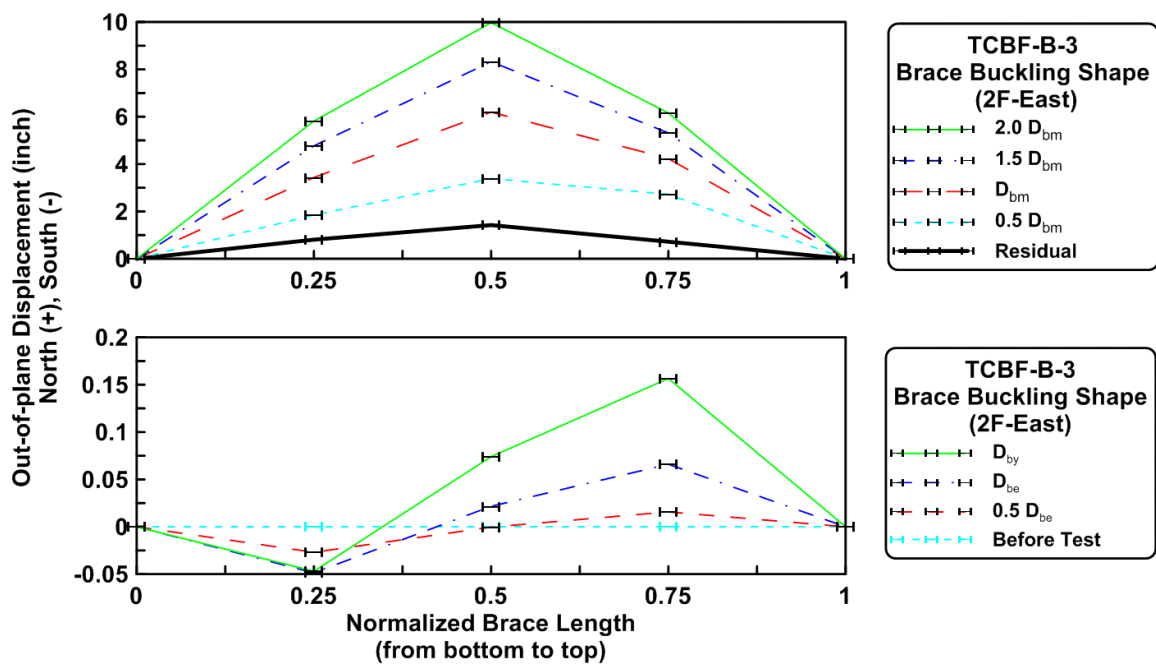


Figure 5.24 Specimen TCBF-B-2: buckling shape of the second-story eastern-side brace in compression excursions.

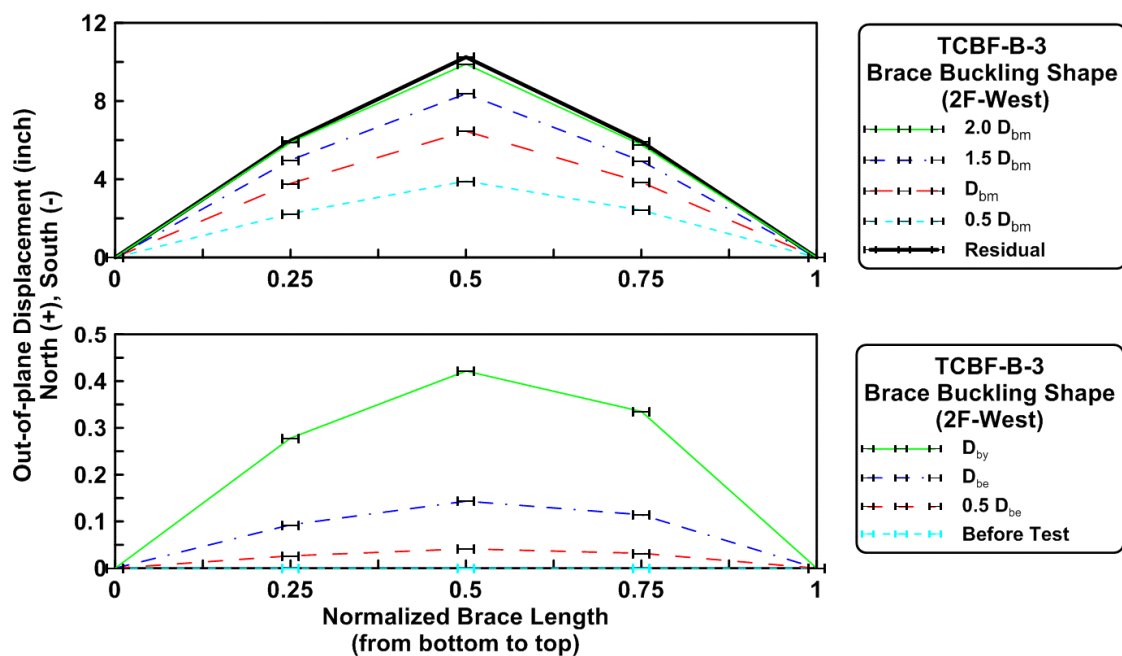


Figure 5.25 Specimen TCBF-B-2: buckling shape of the second-story western-side brace in compression excursions.

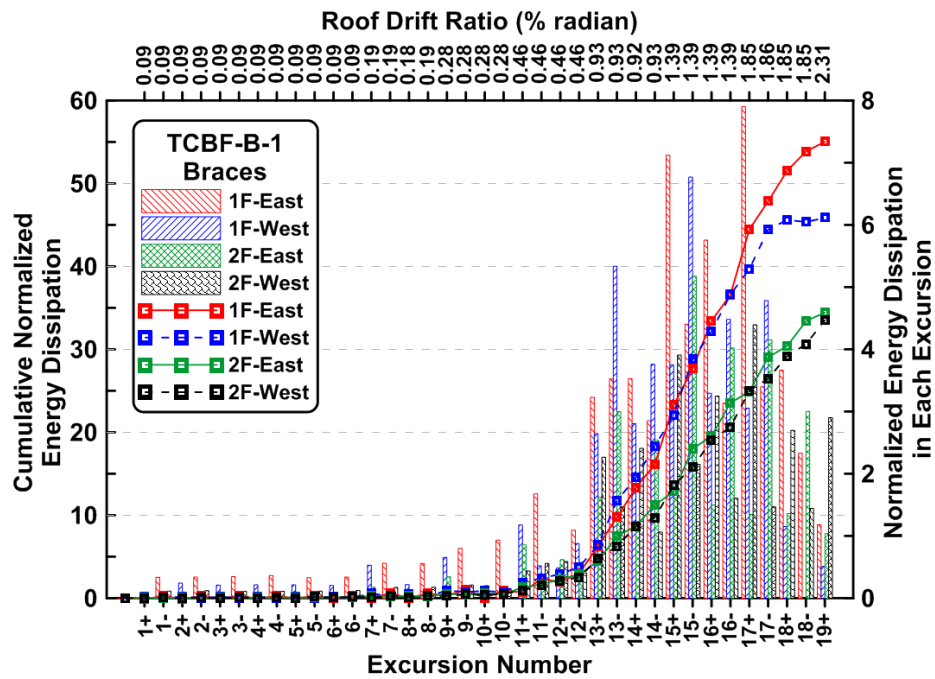


Figure 5.26 Specimen TCBF-B-1: brace cumulative normalized energy dissipation and normalized energy dissipation in each excursion.

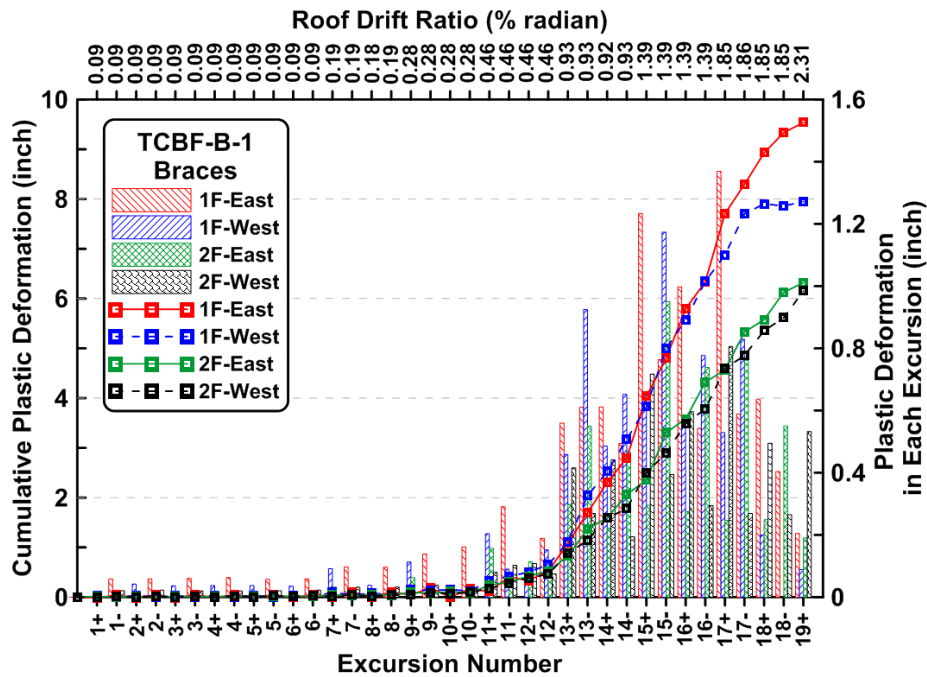


Figure 5.27 Specimen TCBF-B-1: brace cumulative plastic deformations and plastic deformations in each excursion.

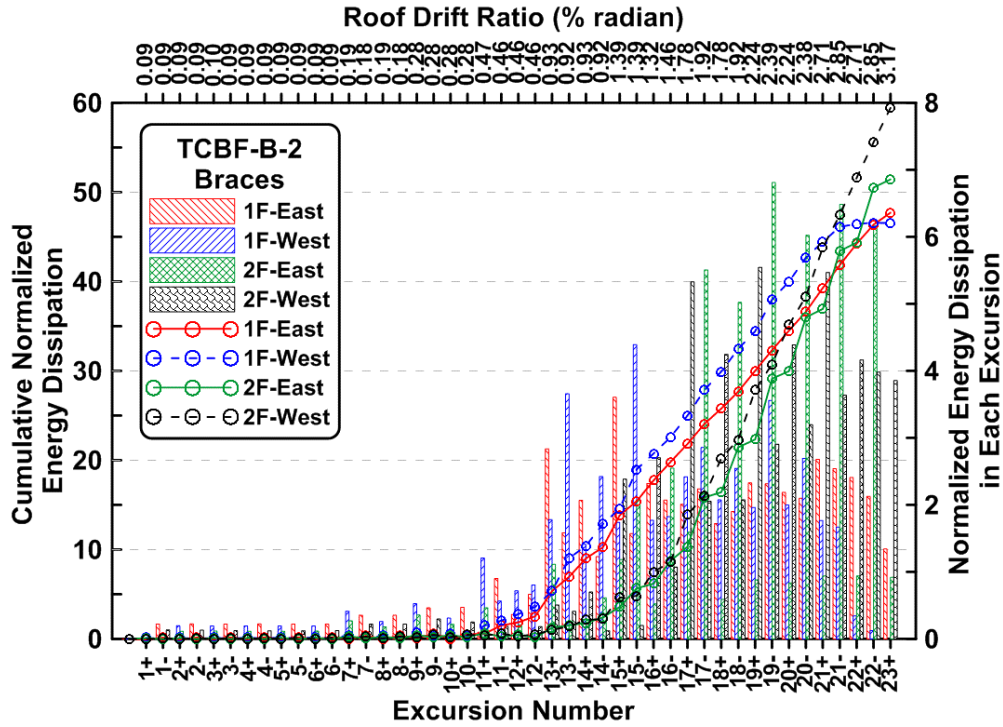


Figure 5.28 Specimen TCBF-B-2: brace cumulative normalized energy dissipation and normalized energy dissipation in each excursion.

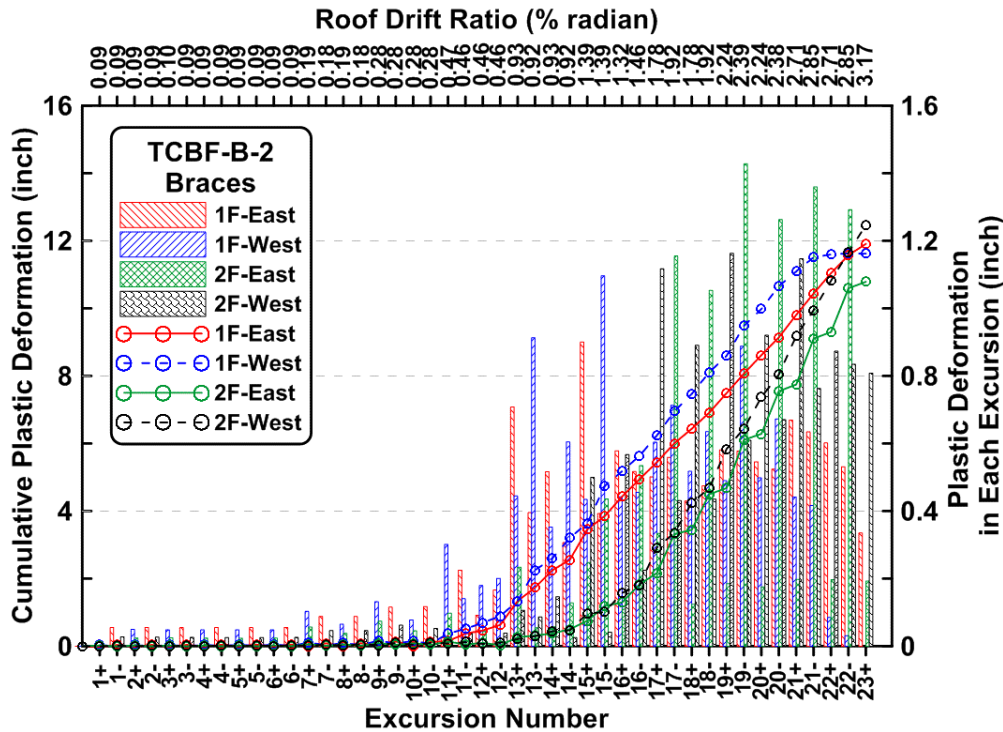


Figure 5.29 Specimen TCBF-B-2: brace cumulative plastic deformations and plastic deformations in each excursion.

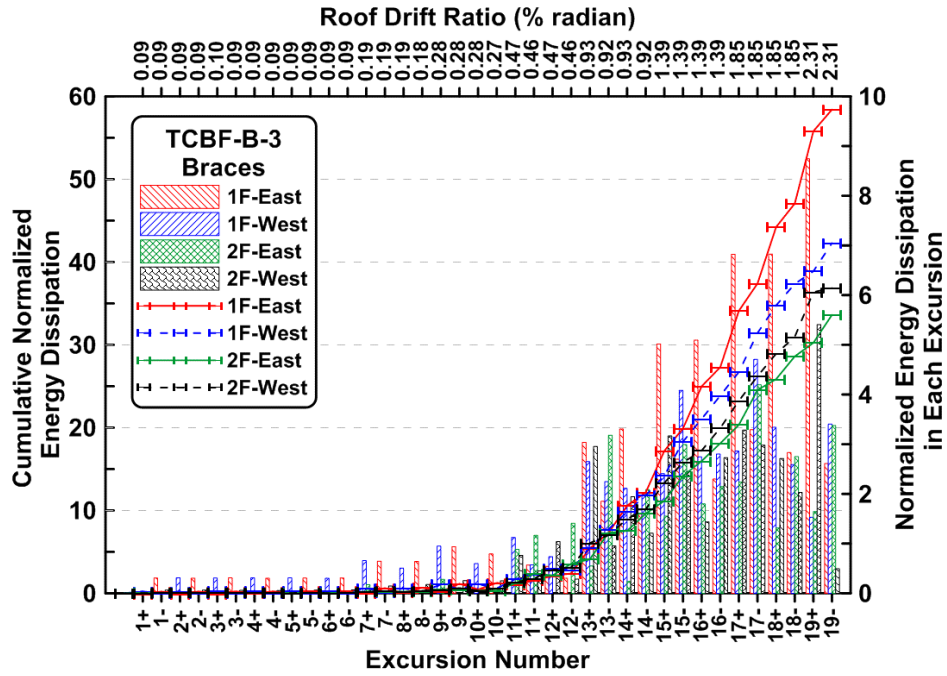


Figure 5.30 Specimen TCBF-B-3: brace cumulative normalized energy dissipation and normalized energy dissipation in each excursion.

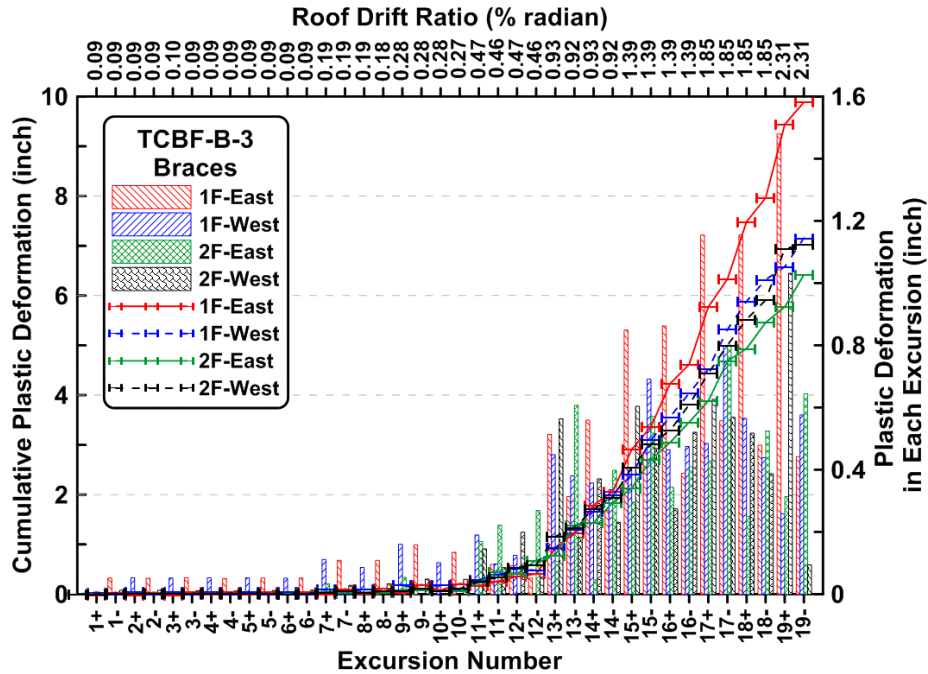


Figure 5.31 Specimen TCBF-B-3: brace cumulative plastic deformations and plastic deformations in each excursion.

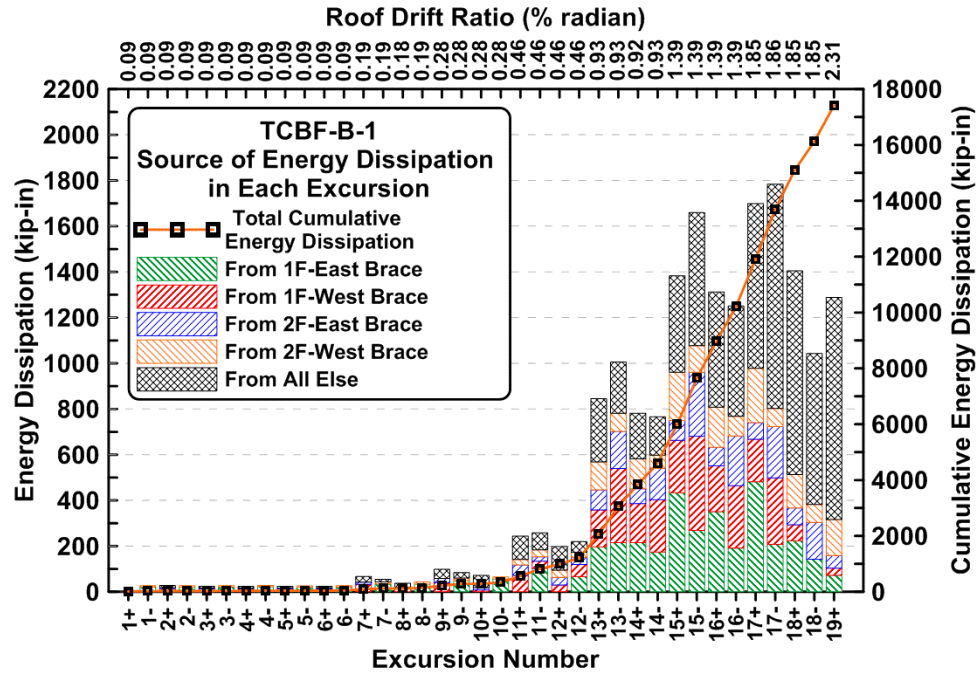


Figure 5.32 Specimen TCBF-B-1: source of total energy dissipation in each excursion and total cumulative energy dissipation.

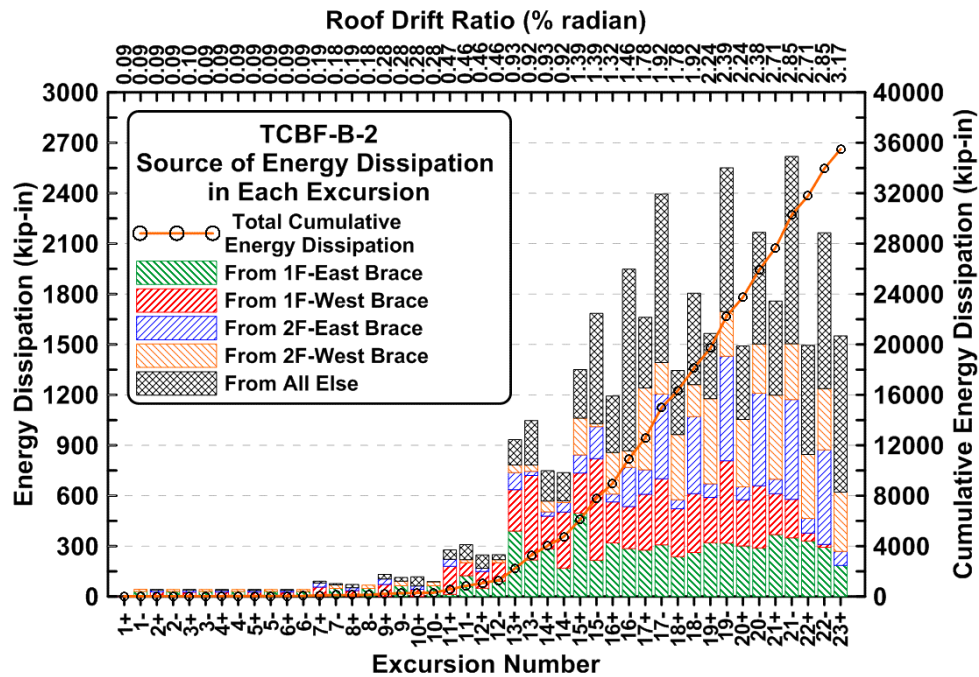


Figure 5.33 Specimen TCBF-B-2: source of total energy dissipation in each excursion and total cumulative energy dissipation.

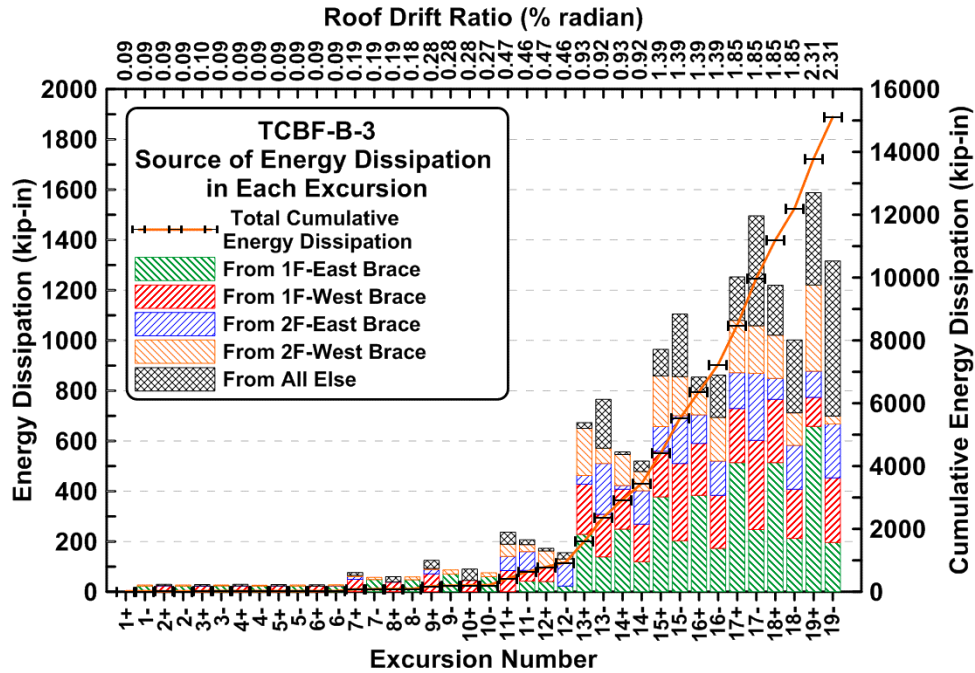


Figure 5.34 Specimen TCBF-B-3: source of total energy dissipation in each excursion and total cumulative energy dissipation.

5.1.3 Column Behavior

For all three tests, the column axial forces typically ranged between 500 kips tension force to 600 kips compression force (see Figures 4.25, 4.145, and 4.248), except for Specimen TCBF-B-2. For Specimen TCBF-B-2, the first-story east-side column axial forces rose up, as shown in Figure 4.146, to 700 kips (tension) in the excursion just before the weld fractured at the western-side of the east column's base plate. The peak axial forces dropped as the target roof displacement increased, and the peak tension force in the column was usually less than the peak compression force in each test, as shown in Figures 4.26, 4.146, and 4.249. The column axial forces also dropped after the fracture of the braces.

Column bending moments away from the probable plastic hinge zones were derived from the strain gauge readings (typically readings from two locations, near the top and bottom of each column) and then extrapolated to find the bending moment at a specific location in the column. Shear forces in the columns were also derived from the column bending moment diagrams. From the column bending moment time history plots shown in Figures 4.27, 4.28, 4.147, 4.148, 4.250, and 4.251, the bending moment values were typically within the elastic range, except in the TCBF-B-2 test, where the column base repair details shifted the probable plastic hinge zones upward during the second trial. Also, larger target roof displacements were imposed on this specimen since the braces fractured at larger lateral displacements.

Derived column web shear time histories, shown in Figures 4.29 4.30, 4.31, 4.149, 4.150, 4.151, 4.252, 4.253, and 4.254, indicate significant column web shear yielding in the first-story columns and the second-story western column of Specimen TCBF-B-2, while the column webs

in Specimens TCBF-B-1 and TCBF-B-3 basically remained elastic. Further examination of the rosette readings on the column webs in Figures 4.32, 4.152, and 4.255 show different column shear behavior for the three specimens. The eastern-side column web in the first story of Specimen TCBF-B-1 had a 2% peak shear strain after the fracture of the braces. Both the west- and east-side column webs in the first story of Specimen TCBF-B-2 had about 3% peak shear strain after the failure of braces. Column webs remained essentially elastic in Specimen TCBF-B-3, as shown in Figure 4.255.

Rosette readings also express the primary behaviors of the columns during cyclic tests. Figures 4.34 to 4.41 show that the column axial forces and shear forces obviously interact in the column webs in the first story of Specimen TCBF-B-1, while shear forces dominated the behavior in the column webs in the second story (detected via the time histories of principal strain directions and the slopes in the normalized maximum principal stress versus normalized minimum principal stress relationships). In Specimen TCBF-B-2 column axial forces and shear forces interacted in the column webs in both stories, as shown in Figures 4.154 to 4.161. In Specimen TCBF-B-3 the column axial forces and shear forces interacted in the column webs in the first story, while interaction occurs in the column webs in the second story, but the axial forces govern the behavior more, as shown in Figures 4.257 to 4.264.

Columns in the first story of each specimen took 10% to 16% of the total story shear at the beginning of tests and eventually took 75% to 100% of the total story shear at the end of the tests (braces fracture in the first story). However, columns in the second story of each specimen took 9% to 16% of total story shear at the beginning of tests and eventually took only 33% to 75% of total story shear at the end of tests. These ratios can be estimated from the slopes of the plots shown in Figures 4.33, 4.153, and 4.256.

Normalized P-M and P-V interaction diagrams at the first-story column bases of each specimen illustrate that plastic hinges formed at the column bases during the cyclic tests (see Figures 4.42, 4.43, 4.162, 4.163, 4.265, and 4.266). Typically, flexural plastic hinges formed at the column bases of the three specimens. In Specimen TCBF-B-2 plastic shear deformations also occurred at the bases. The interaction diagrams at the second-story column top end (the roof beam and column centerlines intersection) of the three specimens (Figures 4.44, 4.45, 4.164, 4.165, 4.267, and 4.268) show that the cross sections were essentially elastic at those locations.

In Specimen TCBF-B-2, fracture of the column-to-base plate welds was observed during the test. Note that these columns were reused after the Specimen TCBF-B-1 test, and repair of welds were performed in some locations where cracks were detected.

Because of the fractures that occurred during the Specimen TCBF-B-2 test, reinforcing plates were added at the column to base plate connection in the entirely new Specimen TCBF-B-3. This detail also suffered unexpected brittle fracture of column flange at the ends of the welds of the stiffeners.

5.1.4 Beam Behavior

The roof beam in each specimen basically remained elastic during the tests. No significant damage or flaking of whitewash was observed near the roof beam-to-column connections at either end of the roof level beam. Moreover, elastic behavior is indicated by the time histories of beam flange strain, beam axial force, shear force, and beam-end bending moment, as shown in Figures 4.48, 4.50, 4.52, 4.54, 4.168, 4.170, 4.172, 4.174, 4.270, 4.273, 4.275, and 4.277.

The corresponding time history plots for the lower level beam (see Figures 4.47, 4.49, 4.51, 4.53, 4.167, 4.169, 4.171, 4.173, 4.271, 4.272, 4.274, and 4.276) indicate that significant inelastic behavior occurred locally. Severe flexural plastic hinges (and fractures in the ensuing local buckles) were observed at both ends of lower beam in the Specimen TCBF-B-1 and TCBF-B-2 tests. The bolted pin connection detail for Specimen TCBF-B-3 avoided this behavior. For Specimen TCBF-B-3, no significant plastic deformations were observed in the lower beam, but small amounts of whitewash flaking was observed in the connection splice plate region.

The maximum average axial forces developed in the lower beam of Specimens TCBF-B-1 and TCBF-B-2 were about 200 kips (in both tension and compression). In the Specimen TCBF-B-3 test, the maximum average axial force in the lower beam was about 200 kips in compression but only about 50 kips in tension. Very small shear forces were estimated for this beam during all three tests.

Due to a geometric amplification effect caused by the stiff gusset plate details at both ends of the lower beam (see Figure 5.35), the lower beam tended to have larger rotational demands than the upper beam (or compared to the overall drift angle). Plastic hinges formed at both ends of lower beam between 1% to 2% roof displacement ratio during tests of Specimens TCBF-B-1 and TCBF-B-2. Based on the equation shown in Figure 5.35, the theoretical amplification factor between beam end plastic rotation and plastic drift of the structure was 1.36 considering the actual dimensions of the specimen. From Figure 5.36, the slope of plots of lower beam-end rotation versus first-story drift responses followed the theoretical prediction for Specimen TCBF-B-3. For this specimen, pin connections at this location made the theoretical equation applicable throughout the entire range of testing. For Specimens TCBF-B-1 and TCBF-B-2, elastic behavior preceded the formation of plastic hinges, and the relation does not initially match the experimental results; however, test results for Specimen TCBF-B-2 show that the slopes increased and approached the theoretical slope until the sensors failed. Unfortunately, the readings from the tilt meters used in Specimen TCBF-B-1 stopped providing accurate readings as soon as the beam yielded. As a result, the reference targets were moved to give better reading in subsequent tests. It is clear that deterioration of the plastic hinge region due to local buckling and rupture may have been exacerbated by the geometric amplification of plastic rotations due to the physical size of the two gusset plates at this level.

From the beam center deflection time histories of each specimen (see Figures 4.46, 4.166, and 4.269), larger deflections were found and expected as the result of unbalanced loads that developed in the roof beam of each specimen. Estimated unbalanced loads were as high as 150

kips, 200 kips, and 100 kips for the roof beam in Specimens TCBF-B-1, TCBF-B-2, and TCBF-B-3, respectively, as shown in Figures 4.55, 4.175, and 4.278.

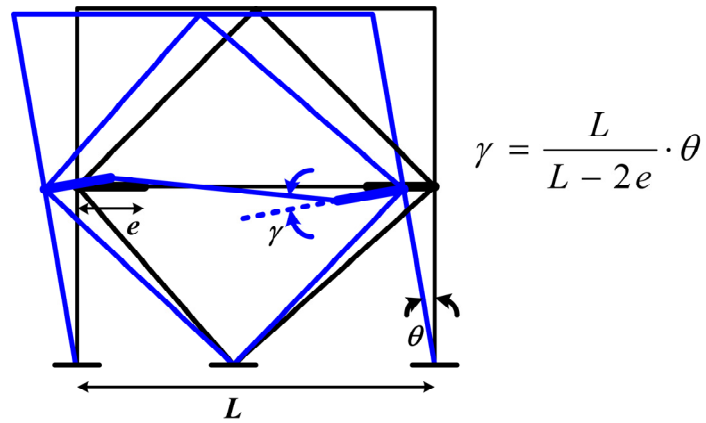


Figure 5.35 Demonstration of geometry amplification effect at the lower beam to gusset plate connections.

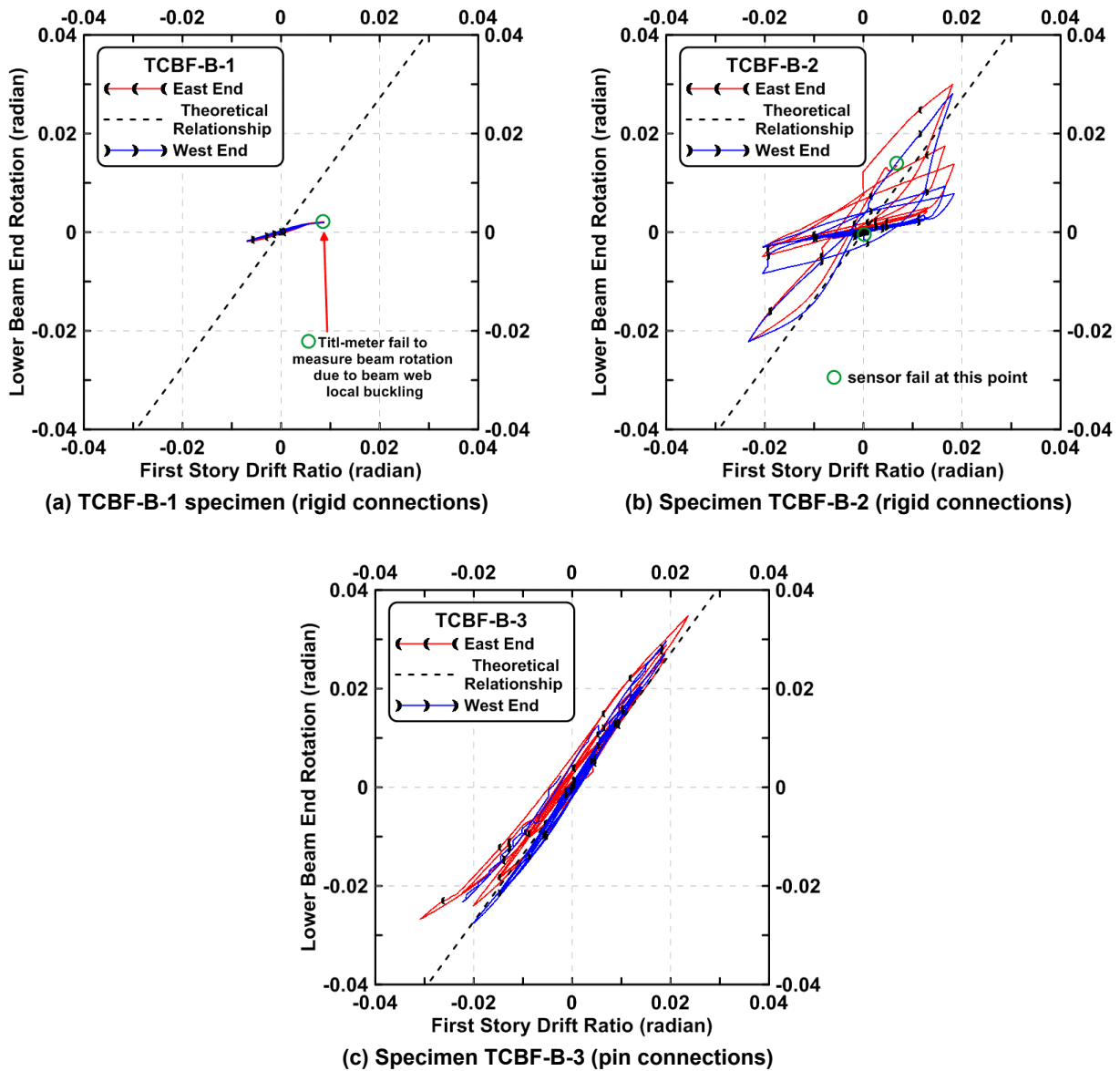


Figure 5.36 The lower beam end rotation versus first-story drift ratio relationships of each specimen.

5.1.5 Panel Zone Behavior

Shear yielding occurred in panel zones adjacent to the roof beam, as shown in Figures 4.63, 4.183, and 4.286. Panel zones next to the one-piece gusset plate remained elastic throughout the test of each specimen. No doubler plates were used in any of the three specimens to reinforce the panel zones.

At the roof level, maximum panel zones shear strains ranged from 1.2% to 2.7%, as shown in the time histories of rosette readings and the normalized principal stress relationships (Figures 4.64 to 4.71, 4.184 to 4.191, and 4.287 to 4.294). From the normalized principal stress relationship plots, it is clear that shear strains were the principal deformations in the panel zones

(inferred from the slopes in the plots), as also shown in the time histories of principal strain directions.

5.1.6 Gusset Plate Behavior

The gusset plate fold lines formed as expected in the $2t$ -gap region for all four specimens. Significant yielding occurred in the fold-line region, detected through flaking of whitewash, time histories of rosette readings, and derived strain time histories, as plotted in Figures 4.72 to 4.75, 4.80 to 4.87, 4.92 to 4.95, 4.192 to 4.195, 4.200 to 4.207, 4.212 to 4.215, 4.295 to 4.298, 4.303 to 4.310, and 4.315 to 4.318. Rosette gauges not located within the fold-line regions remained elastic.

The middle portions of one-piece gusset plates of each specimen that connect to the lower beam essentially remained elastic during the test, as illustrated by the rosette readings (Figures 4.76 to 4.79, 4.88 to 4.91, 4.196 to 4.199, 4.208 to 4.211, 4.299 to 4.302, and 4.311 to 4.314). In Specimen TCBF-B-3, however, local yields of middle portion of one-piece gusset plate near the splice plate edge were detected via the rosette readings shown in Figure 4.314 (location R16).

Additional linear strain gauges are used to monitor the strain distributions on one face of the tapered region of the gusset plate at the upper end of the brace on the east side of the first story in tests of Specimen TCBF-B-2 and TCBF-B-3. Note that both averaged axial strains and in-plane bending strains were higher at sensor locations further from the brace-to-gusset weld lines and higher closer to the fold lines (Figures 4.216, 4.217, 4.319, and 4.320).

5.1.7 Test Set Up Behavior

Actuator brackets deformed elastically during these three tests, as shown in Figures 4.96, 4.218, and 4.321. The derived stiffness of the bracket from those plots was around 3000 kip/in. for both brackets. As shown in Figures 4.97, 4.219, and 4.322, no significant slippage was observed during these three tests. For the lateral stability frame, maximum out-of-plane deformation was less than 0.1 in., and typically the measured locations that were away from the reconfigurable reaction wall had larger deformations, as shown in the time histories in Figures 4.98, 4.220, and 4.323. The maximum deformations (relative to the 4 M-lb universal test machine, east-west direction) at the tip of the RRW were also less than 0.08 in. for tests of Specimens TCBF-B-2 and TCBF-B-3, as illustrated in Figures 4.221 and 4.324. It is assumed that these relatively small reaction wall deformations (less than 2% of the specimen maximum roof displacements) did not significantly affect the experimental control and test results.

5.2 HYBRID SIMULATION RESULTS

Test results for Specimen TCBF-B-4 are discussed in this section. The small level elastic test results used to check the operation of the hybrid simulation are not discussed herein since the behavior was entirely elastic, and observed behavior was similar to that for the cyclically loaded specimens. Thus, results are presented for the 20-sec DE-level ground motion and the 20-sec

MCE-level ground motion. Ground motion parameters for the hybrid simulations are briefly summarized in Table 5.7; detail parameters are listed in Table 3.6 of Chapter 3. The combined ground motion input time history for the hybrid simulation is shown in Figure 5.37. The OpenFresco time step numbers are also shown in the same plot.

Although the dynamic analysis that controlled the hybrid simulation was carried out using a constant time step to integrate the governing equations of motion (see Section 3.10.2), the computed command displacements were imposed by commanding the actuator having the largest incremental displacement for a particular step to move at a constant velocity (0.002 in./sec) until it reached end of the step. The second actuator was commanded to move at an appropriately lower velocity so that it reached its target displacement at the same instant in time as did the faster moving actuator. In this way, the test was completed as quickly as possible. This implementation method for the hybrid simulation can be seen in the actuator displacement time histories shown in Figure 4.344, where the actuators appear to be moving at nearly a constant velocity. Some actuator velocity variations did occur, especially in the lower actuator. The test was conducted very slowly compared to real time. Thus, the distortion of velocities due to this use of a variable time over which the displacements computed for each integration step is not believed to have introduced additional inaccuracies.

The test was continued until the end of the stipulated records or the actuators reaching their displacement limit. Accordingly, the test was stopped at about 11.28 sec into the 20-sec-long MCE motion when the upper actuator reached its stroke limit. As shown in Figure 4.344, both actuator displacements imposed oscillations in the structure with increasingly negative values towards the end of the simulation.

Table 5.7 Input ground motion parameters.

Ground Motion	Scale Factor	PGA (<i>g</i>)
Elastic Earthquake Level	0.13	0.063
Design Earthquake Level	1.30	0.627
Maximum Credible Earthquake Level	1.95	0.940

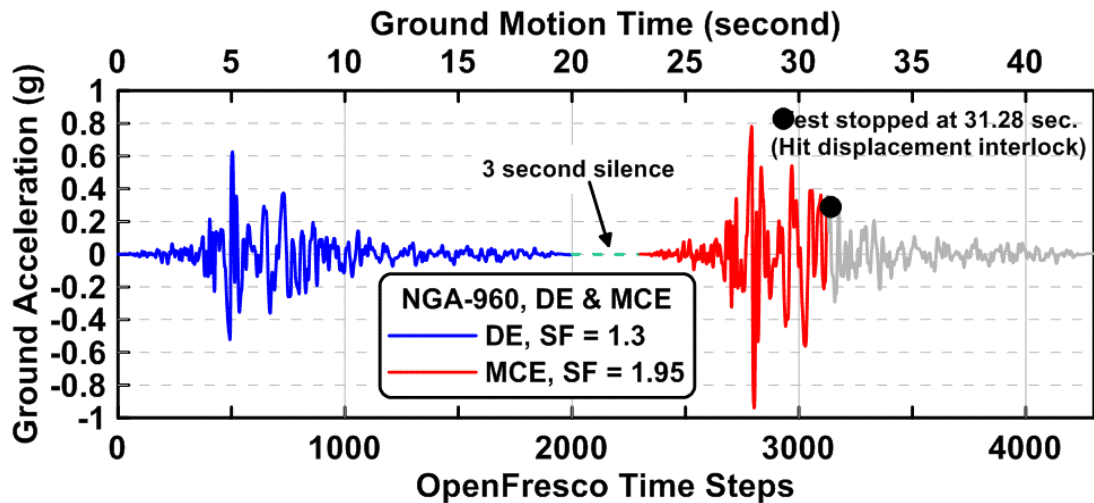


Figure 5.37 Ground motion time history for the hybrid simulation.

5.2.1 Specimen Global Behavior

From the actuator force time histories plotted in Figure 4.345, peak actuator forces for upper and lower actuators were 551 kips and 457 kips, respectively. The peak base shear was 761.1 kips, compared to the maximum value of 789.1 kips for the similar Specimen TCBF-B-1: note the connections of the lower beam to gusset plates and column base conditions differed.

It is notable that the upper actuator force to lower actuator force ratios typically ranged from one to six, and most of the time maintained a ratio of two during the hybrid test, as illustrated in Figure 4.348. From the same plot, we can see that the upper actuator forces and lower actuator forces may have had opposite signs during the hybrid test (especially during MCE-level ground motion; see the red curves in the plot), indicating significant story shear redistribution or higher mode effects in the specimen. The actuator force ratios that were close to a value of two provide strong support that the lateral force distribution assumption in the quasi-static tests is reasonable; however, the observed higher mode effects in the hybrid tests may not be adequately represented in the quasi-static tests.

From the actuator displacement relationships between upper and lower actuators shown Figure 4.349, some instantaneous local concentrations of deformation in the first or second story are illustrated via the slope deviating from the 45° orientation. Significant deviation of actuator displacements during the MCE ground motion are also shown in this plot. Recall that the hybrid simulation numerical model incorporates the gravity-only columns, and these may help avoid soft story tendencies.

Based on observations from the similar Specimen TCBF-B-1, it is surprising that a HSS brace in the second-story fractured near the end of the DE ground motion (see Figure 4.346). After fracturing of this brace at around 2% roof drift ratio, the second story tended to deform more than the first story, as shown in Figure 4.347. While no other fractures occurred after the DE motion, there was considerable lateral and local buckling of all of the other braces [see photo in Figure 4.325(c)] and distributed yielding throughout the structure, as described in Section

4.2.2. The residual displacement of the frame after the DE-level shaking is modest, being about 0.08 in. at the roof and 0.04 in. at the lower level; however, the residual out-of-plane deformations of the braces were significant, ranging from 6.2 in. near the mid-span of the E-2F brace to 3.5 in. near the mid-span of the E-1F brace. The initial stiffness of the entire specimen dropped to about 20% of that for the initial undamaged specimen at the end of the design earthquake (via slopes in Figure 4.346). Story stiffness of both stories had similar reductions after design earthquake (Figure 4.347).

During the subsequent response to the MCE-level ground motion, two braces (2F-West and 1F-East) completely fractured at nearly the same time while in tension at around 1.5% roof drift ratio (Figure 4.346). Note that the peak base shear dropped from around 375 kips to 225 kips after these braces fractured. The last remaining brace fractured at about a roof drift ratio of 3.0%. During the hybrid simulation a total of 36 time points were selected to examine local peak responses. Table 5.8 summarizes the local peak story shear and floor level displacement data obtained from the Specimen TCBF-B-4 at these points during the hybrid simulation.

Time histories of floor level displacement and the story force are plotted in Figures 5.38 and 5.39. The vertical light gray grid lines indicate the 36 time points where the local peak responses were further investigated. In these plots and subsequent discussion, the reference to time is the time in the computations used to carry out the hybrid simulations not the actual time in the laboratory. From Table 5.8, the peak base shear was 761.1 kips before the braces began to buckle globally. Lateral buckling of the first square HSS brace was noted at about 5.22 sec., and local buckling was observed 0.34 sec later. Cracks initiated at the corner of the cross section at about 1.43 sec later. About 0.5 sec (ground motion time) later, the first brace fractured at the second-story eastern side. Thus, about 2.27 sec ($0.34 + 1.43 + 0.5$) transpired from the first lateral buckling until complete fracture of a brace occurred. Thereafter, no other braces fractured during the rest of the DE ground motion. As noted above, no significant floor level residual displacements were observed after 20-sec DE ground motion (see Table 5.8 and Figure 5.38).

Looking at the total energy dissipations until the first brace completely fractured, the specimen dissipated only 7799 kip-in., and at the end of DE ground motion the total energy accumulated to 8832 kip-in. This is only about 60% of energy dissipated in Specimen TCBF-B-1 until the first brace fractured. At the instant where all four braces fractured during the MCE event, the total energy dissipation from the beginning of the test was 10,552 kip-in., which was, again, around 60% of energy dissipated in Specimen TCBF-B-1 until quasi-static test was stopped. It is believed that the characteristic of the input ground motion during the ground motions used for the hybrid tests introduced several large pulse-like cyclic displacement excursions (see Figure 5.38) without developing a series of earlier incremental displacement cycles, which caused the brace behavior deteriorates faster.

The total energy dissipated between each of the 36 key points in the ground motion time history is shown in Figure 5.40. Note that the energy dissipation occurred during a few relatively short portions of the ground motion time histories. Much of the energy was dissipated between time 5 and 8 sec. For example, between the short interval 6.99 to 7.49 sec, more than 20% of the total energy dissipated during the DE ground motion was dissipated. Between these intervals

with major energy dissipation, little significant energy dissipation occurred. Similar observations were found during the MCE ground motion.

Detailed roof plastic deformation and the normalized energy dissipation in each ground motion time segment are plotted and compared in Figures 5.41 and 5.42, and it is not surprising that the results are similar. Note that the cumulative roof plastic deformation and the normalized energy dissipation are defined in the title row of Table 5.8. The P_y value for the specimen in the hybrid test was obtained from the initial base shear-roof displacement plot corresponding to a roof displacement of 0.6 in.

In terms of the story deformation, the ratio of the individual story deformation to total roof displacement at each story is plotted in Figure 5.43. The story deformation ratios for the top and bottom story are around 50% and 50%, respectively, at the beginning of ground motion. As the intensity of ground shaking increased, especially after local buckling was observed in the braces, the second story tended to deform more than the lower story; the upper-story deformation ratio did not exceed 75% most of the time. However, at 20.77 sec and 29.15 sec into the ground motion, the story drifts were of opposite sign, and the drifts were relatively small (the actuator displacements as listed in Table 5.8 are less than 0.25 in.). Deformation concentration at the second story did occur during the hybrid simulation, specifically when the structure deformed to the negative direction (to the west).

The energy dissipation ratios for each story are shown in Figure 5.44. Although the drifts were larger in the second story, more than 60% of total energy dissipation came from the first story, which is similar to observations made from the quasi-static tests.

Table 5.8 Specimen TCBF-B-4: story shear and floor level displacement data ($P_y = 589.3$ kips from hybrid simulation, corresponding to $D_{by} = 0.6$ in. at roof).

Ground Motion Time (sec)	Roof Level Displacement (in.)	Lower Level Displacement (in.)	Base Shear (kips)	Second Story Shear (kips)	Cumulative Hysteretic Area (Energy Dissipation) E (kip-in.)	Cumulative Plastic Roof Displacement $E / (P_y)$ (in.)	Normalized Energy Dissipation $E / (P_y \times D_{by})$	Key Observations
3.93	0.44	0.22	366.3	299.3	86	0.1	0.2	
4.15	-0.52	-0.27	-414.7	-360.1	128	0.2	0.4	
4.34	0.71	0.37	569.2	420.3	232	0.4	0.7	
4.54	-0.82	-0.45	-735.5	-444.4	353	0.6	1.0	
4.94	0.86	0.48	758.4	433.3	434	0.7	1.2	
5.22	-3.35	-1.71	-761.1	-486.1	2162	3.7	6.1	GB*
5.56	1.71	0.83	692.4	434.5	3383	5.7	9.6	LB*
5.91	-1.75	-0.89	-456.5	-344.8	3705	6.3	10.5	
6.22	0.24	0.08	315.4	306.4	3753	6.4	10.6	
6.61	-2.87	-1.55	-637.4	-390.1	4518	7.7	12.8	
6.99	2.92	1.21	524.6	396.8	5930	10.1	16.8	CI*
7.49	-4.96	-2.17	-540.3	-321.7	7799	13.2	22.1	PF*, CF1*
8.07	2.70	1.28	305.5	300.2	8603	14.6	24.3	
8.78	-0.55	-0.20	-133.4	-74.3	8511	14.4	24.1	
10.11	1.99	0.96	207.7	180.9	8704	14.8	24.6	
12.97	-0.75	-0.30	-159.6	-75.0	8730	14.8	24.7	
13.45	1.03	0.53	126.4	100.1	8777	14.9	24.8	
15.49	-0.76	-0.27	-144.4	-88.2	8815	15.0	24.9	
15.98	0.86	0.45	118.3	95.6	8838	15.0	25.0	
17.44	-0.59	-0.21	-123.9	-63.3	8845	15.0	25.0	
20.77	-0.06	0.03	-22.4	1.8	8832	15.0	25.0	DE finished
25.31	-0.39	-0.11	-76.0	-49.9	8844	15.0	25.0	
25.68	0.77	0.41	109.1	83.0	8876	15.1	25.1	

Table 5.8—Continued

Ground Motion Time (sec)	Roof Level Displacement (in.)	Lower Level Displacement (in.)	Base Shear (kips)	Second Story Shear (kips)	Cumulative Hysteretic Area (Energy Dissipation) E (kip-in.)	Cumulative Plastic Roof Displacement $E / (P_y)$ (in.)	Normalized Energy Dissipation $E / (P_y \times D_{by})$	Key Observations
26.63	-0.37	-0.11	-63.8	-50.9	8860	15.0	25.1	
26.84	0.58	0.26	52.7	94.0	8874	15.1	25.1	
27.32	-0.56	-0.19	-83.1	-77.8	8885	15.1	25.1	
27.73	3.50	1.70	226.6	208.0	9453	16.0	26.7	CF2*, CF3*
28.07	-6.45	-2.72	-126.4	-323.5	10552	17.9	29.8	CF4*
28.38	-3.23	-1.87	-201.7	233.2	10520	17.9	29.8	
28.71	-6.04	-2.79	-92.8	-234.9	10707	18.2	30.3	
29.15	-0.22	0.03	189.1	103.0	10884	18.5	30.8	
29.4	-1.75	-0.58	110.4	-95.4	10802	18.3	30.6	
29.67	1.77	0.93	164.3	210.0	11247	19.1	31.8	
30.19	-10.39	-5.29	-305.9	-190.0	12752	21.6	36.1	
30.6	0.28	0.12	182.7	204.9	13291	22.6	37.6	
31.28	-10.44	-5.31	-316.3	-174.7	14216	24.1	40.2	test stop

*Note: GB (global buckling), LB (local buckling), PF (partial fracture), CF1 (first brace complete fracture), CI (initial crack).

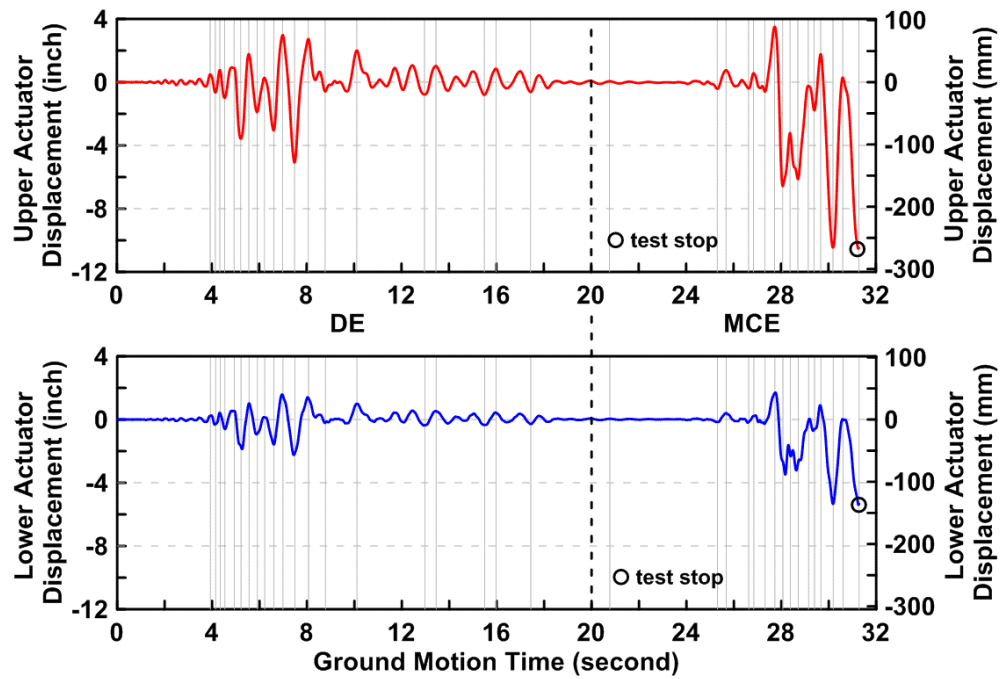


Figure 5.38 Specimen TCBF-B-4: floor level displacement time histories.

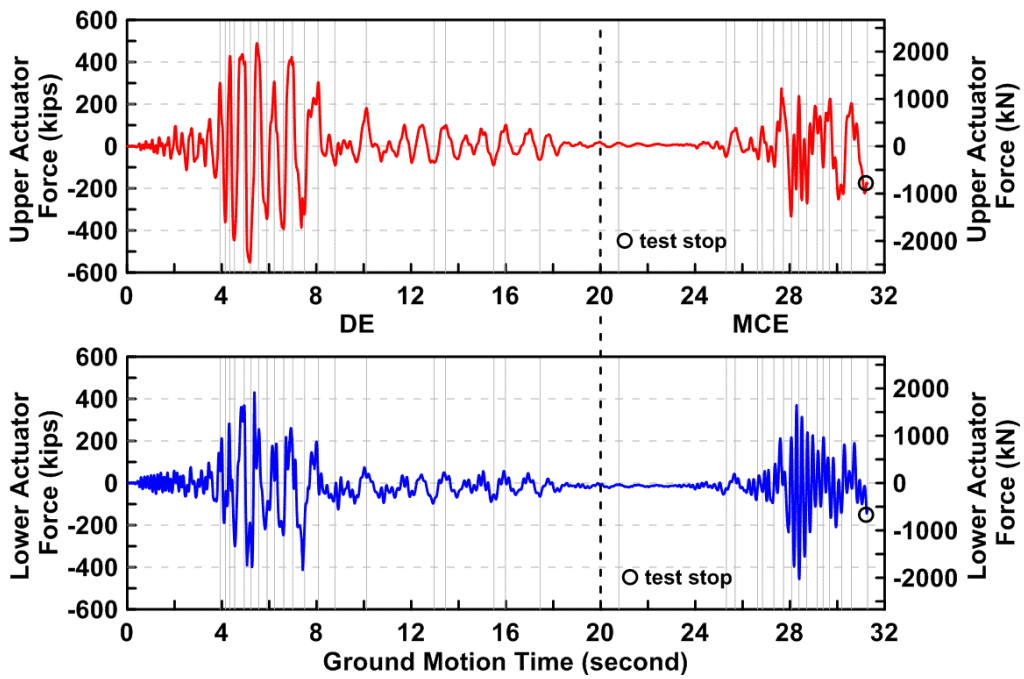


Figure 5.39 Specimen TCBF-B-4: story force time histories.

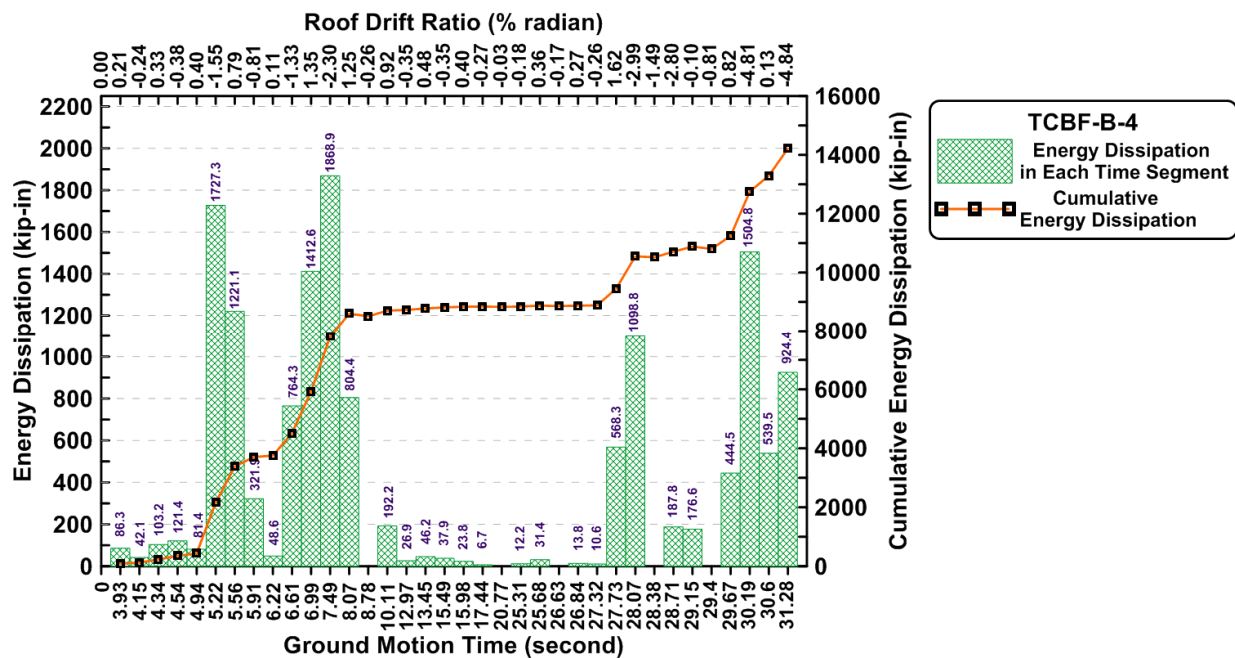


Figure 5.40 Specimen TCBF-B-4: total energy dissipation in each time segment and total cumulative energy dissipation.

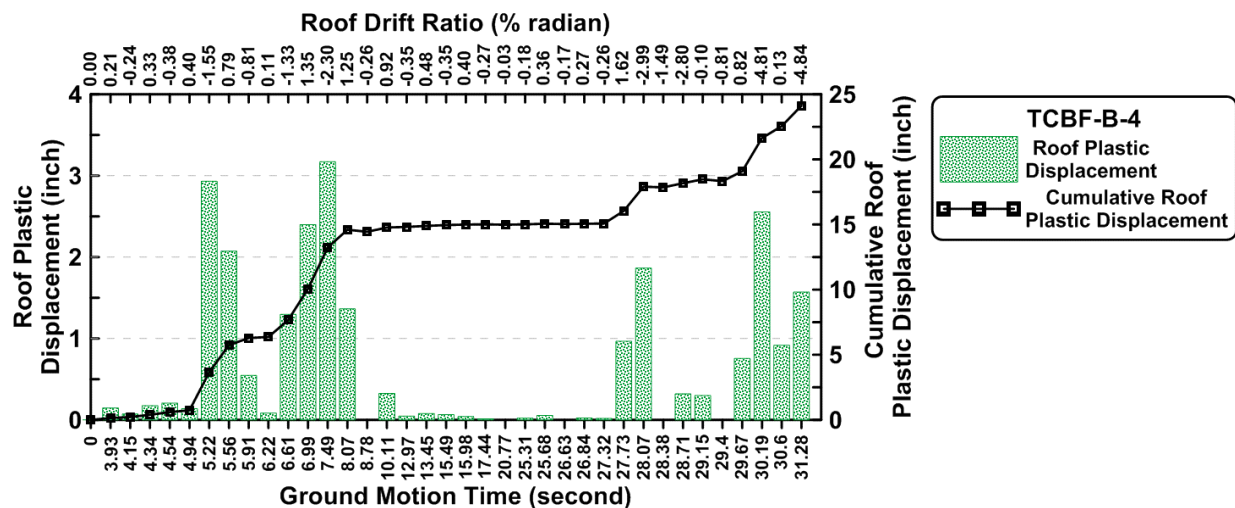


Figure 5.41 Specimen TCBF-B-4: total roof plastic displacement in each time segment and total cumulative roof plastic displacement.

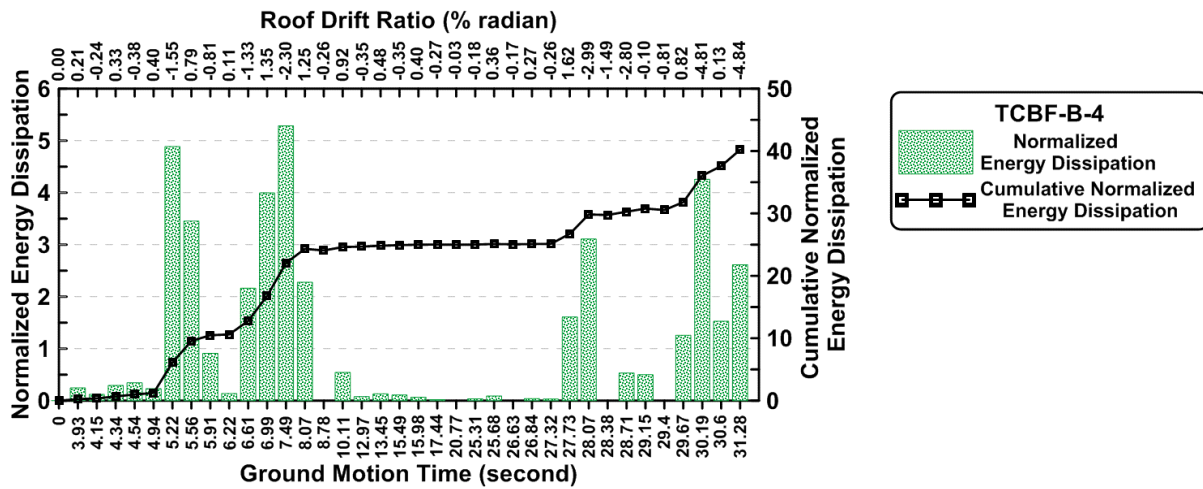


Figure 5.42 Specimen TCBF-B-4: normalized energy dissipation in each time segment and cumulative normalized energy dissipation.

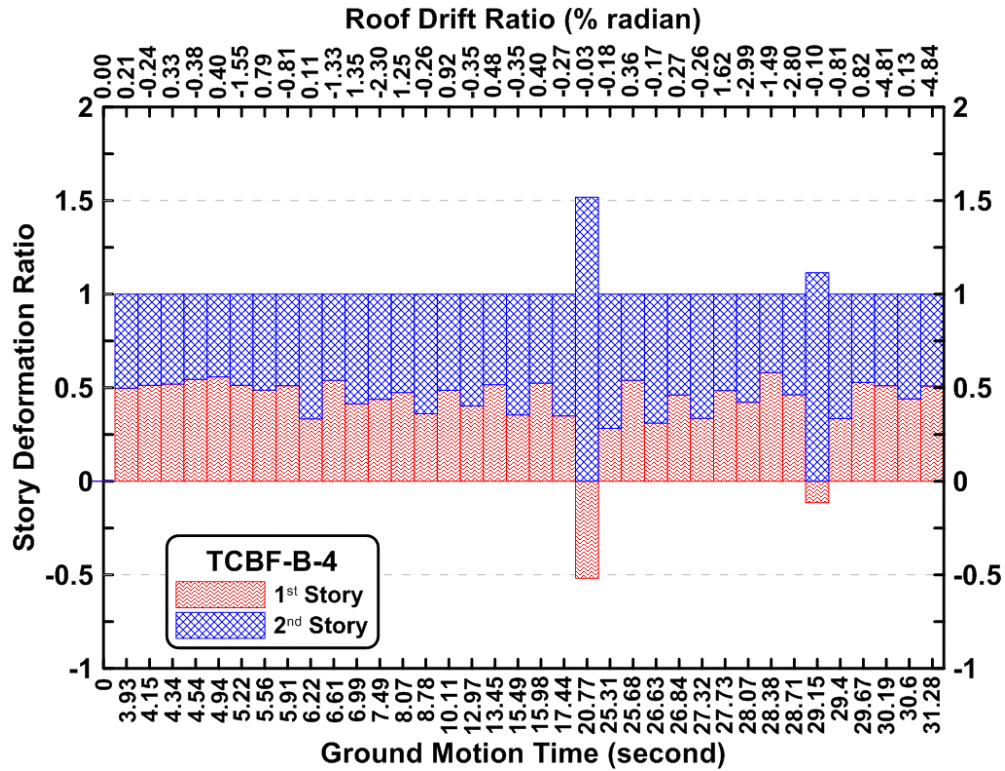


Figure 5.43 Specimen TCBF-B-4: story deformation ratio.

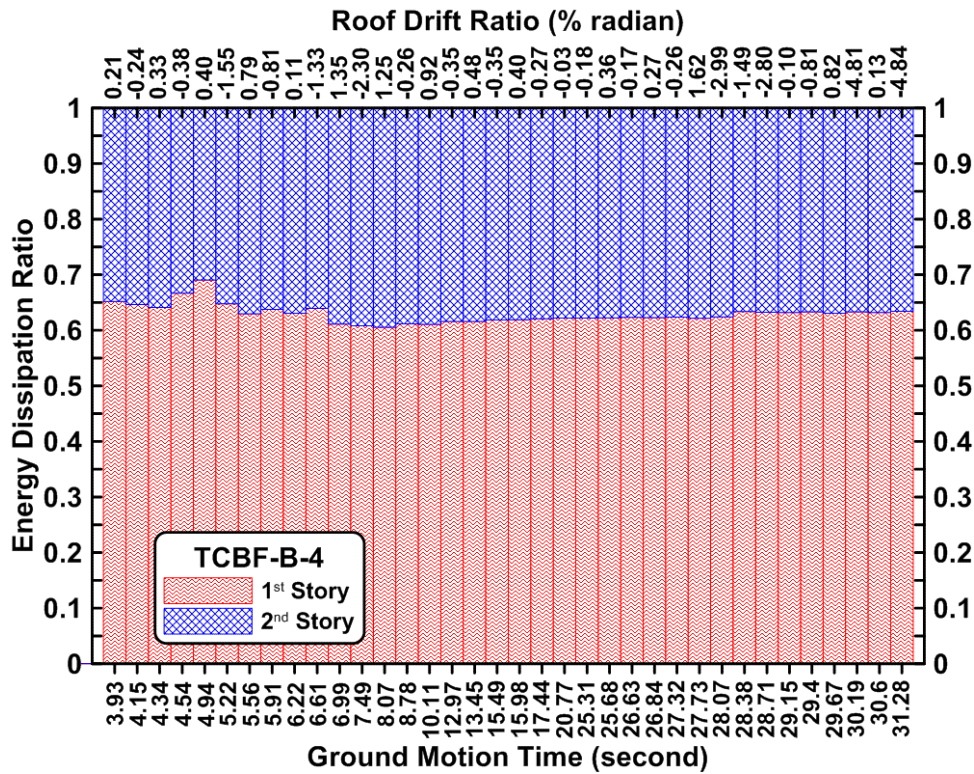


Figure 5.44 Specimen TCBF-B-4: story energy dissipation ratio.

5.2.2 Brace Behavior

All four braces buckled out-of-plane to the southern side during the hybrid simulations. Similar to results obtained in the quasi-static tests, the braces connecting to the same one-piece gusset plate tended to buckle to the same direction, as shown in Figure 4.325.

As shown in Figure 4.383, the out-of-plane displacement at the middle length of braces was as much as ten times the axial deformation of the braces. As with the quasi-static tests, the brace out-of-plane displacements tended to change sign during a cycle (see Figure 4.382) after a crack propagated partially through the cross section (since the neutral axis of the cracked braces shifts toward the un-cracked side of the cross section). As mentioned previously, this eventually creates an eccentricity when the braces reload in tension.

Strain decomposition plots for the braces shown in Figures 4.384 to 4.387 illustrate the sources of strain readings during the hybrid tests. Note that the strain gauge locations are at the quarter length of brace close to the gusset plate where two braces meet at the beam side (see sensor locations in Appendix G for details). Permanent residual strains typically developed for each component by the end of simulation. Maximum axial strains in the braces ranged from 5 to 9 times the yield strain of steel, and residual tension strains ranged from 5 to 8 times the yield strain. Axial strains shifted to the tension side because the compression strains basically concentrated around the middle length of braces under compression.

Most of the brace in-plane bending strain readings were close to or less than the yield strain of steel (between 1200μ to 2200μ), and the maximum out-of-plane bending strains were typically larger than in-plane bending strains, ranging from 1250μ to 3100μ . Deviation of out-of-plane bending strain also indicates the buckling direction of the brace. The effect of frame action on braces can be clearly observed by comparing the sign of axial strain and in-plane bending strain of each brace. The brace cumulative plastic deformations, cumulative normalized energy dissipation, plastic deformations, and normalized energy dissipation in each ground motion time segment are shown in Figures 5.45 and 5.46.

Similar to the quasi-static test results, the cumulative normalized energy dissipation and cumulative plastic deformations of first-story braces typically had larger values at the end of test; however, the normalized energy dissipation and plastic deformations that accumulated during the ground motion time segment show that braces in the second story sometimes accumulated more energy or plastic deformations, as can be seen in Figures 5.45 and 5.46. During the DE-level ground motion, plastic deformations and normalized energy dissipation of both story braces started to accumulate at about the same time, but the first-story west brace and the second-story east brace accumulated faster than the other two remaining braces until the second-story east-brace fractures. A relatively small amount of energy was accumulated by the braces during the MCE ground motion.

The total energy dissipation components during the hybrid test are illustrated in Figure 5.47. Braces basically contributed more than 50% of total energy dissipated during the DE-level ground motion, as shown in the stacked bar charts. The total energy dissipated by other components, such as beams, columns, and panel zones, increased as the displacement demand

increased. A significant amount of energy was dissipated (50% to 100%) by structure members other than braces during the MCE-level ground motion.

Table 5.9 summarizes the specimen failure characteristics related to total brace fracture during the hybrid simulation. Note that the plastic deformation capacities of the first-story braces were about a half of the capacities observed from the TCBF-B-1 quasi-static test results. This is likely due to the different history of deformations associated with the earthquake response simulations.

Table 5.9 Specimen TCBF-B-4 brace failure characteristics (brace completely fractured).

Specimen Name	TCBF-B-4			
	1 st	2 nd	3 rd	4 th
Fracture Sequence				
Location	2F-East	2F-West	1F-East	1F-West
Ground Motion Time (sec.)	7.49	27.72	27.73	28.07
Roof Displacement at Fracture (in.)	-4.96	3.49	3.50	-6.45
Roof Drift Ratio at Fracture (% radian)	-2.30	1.62	1.62	-2.99
Brace Cumulative Plastic Deformation at Fracture (in.)	3.2	3.1	3.7	5.4
Brace Cumulative Normalized Energy Dissipation at Fracture	14.4	15.9	17.1	25.0

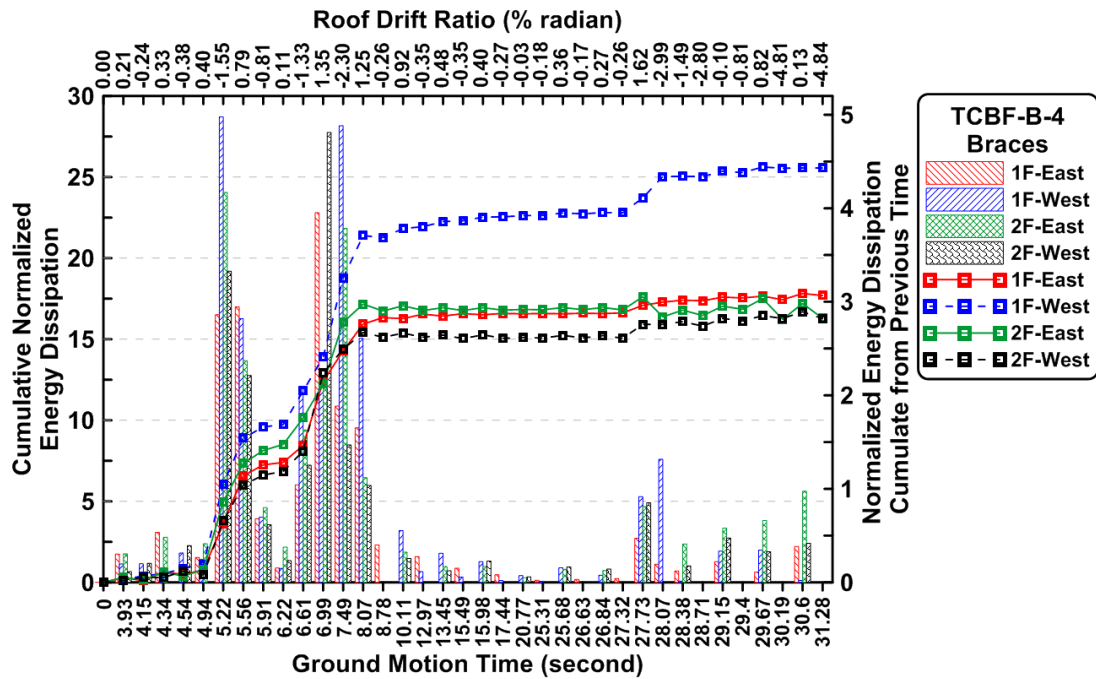


Figure 5.45 Specimen TCBF-B-4: brace cumulative normalized energy dissipation and normalized energy dissipation in each time segment.

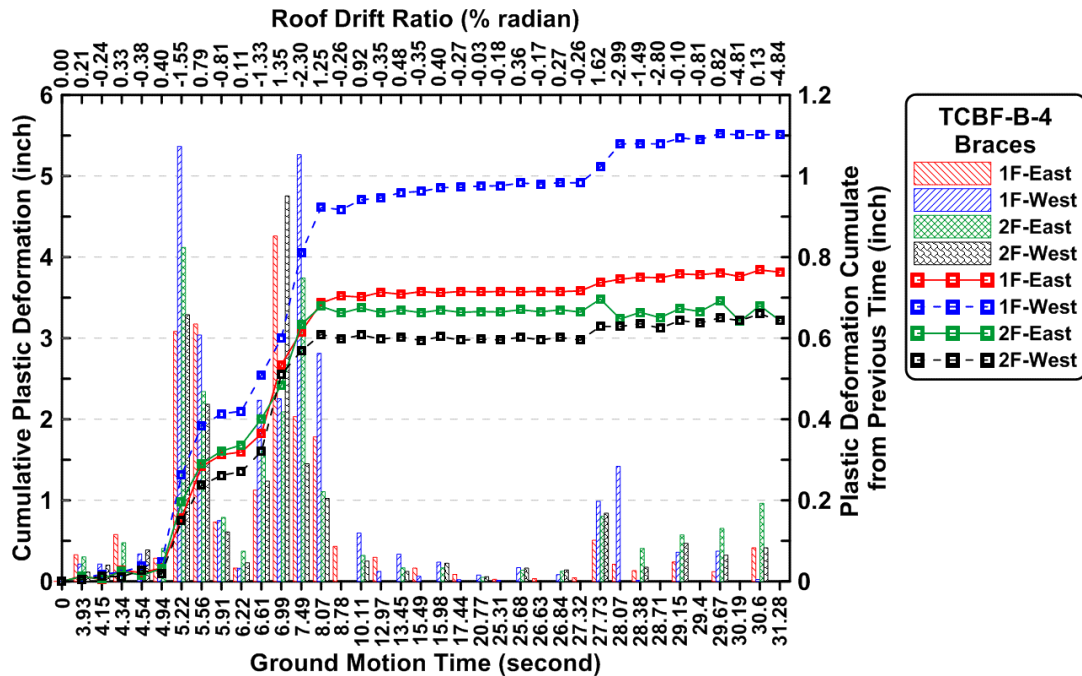


Figure 5.46 Specimen TCBF-B-4: brace cumulative plastic deformations and plastic deformations in each time segment.

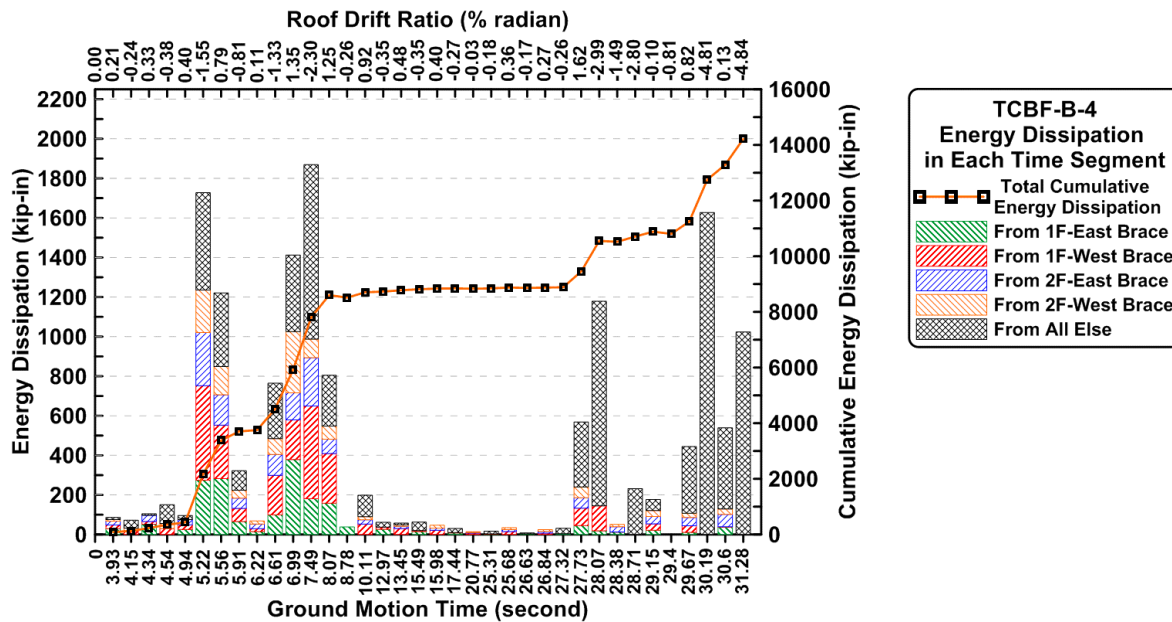


Figure 5.47 Specimen TCBF-B-4: source of energy dissipation in each time segment and total cumulative energy dissipation.

5.2.3 Column Behavior

Column axial forces were significantly reduced as a result of the brace fractures that occurred in the MCE event. During the MCE ground motion, the column force demands were only about 30% or less than those developed during the DE-level ground motion (see Figures 4.350 and 4.351). Bending moments in the $W12 \times 96$ columns at both floor levels typically were less than the yield moment except at the column bases (Figures 4.352 and 4.353). Derived column shear forces in the webs were also less than the yield shear value, as shown in Figures 4.354, 4.355, and 4.356. The column webs essentially remain elastic throughout the hybrid simulations (see Figure 4.357).

From the column shear versus story shear relationships plotted in Figure 4.358, columns withstood about 16% story shear at the beginning of DE ground motion and then gradually contributed more to the story shear during the hybrid simulation. At the end of the DE, the first-story columns resisted about 42% of the total story shear, while the second-story columns resisted the entire story shear in the second story. Eventually the entire story shear force was resisted by the columns after all four braces fracture during the MCE ground motion.

The time histories of rosette readings shown in Figures 4.359 to 4.362 also demonstrate that the column webs remained elastic. It is notable that the normalized principal stress states at the first-story rosette sensor locations were different during DE- (normal stress dominated) and MCE- (shear stress dominated) level ground motions. These are presented in Figures 4.363 and 4.364. Similar to the results from quasi-static tests, column webs stress states were dominated more by shear stresses after failure of the braces. There were no significant changes of stress states in the second-story column webs during the hybrid tests (see Figures 4.365 and 4.366).

Interaction diagrams shown in Figures 4.367 and 4.368 reveal that substantial P-M or P-V interaction at the column bases occurred during the DE ground motion, while in MCE ground motion the flexural behavior essentially governed the column base responses. The interaction diagrams for the second-story column top end (the roof beam and column centerlines intersection) of this specimen (Figures 4.369 and 4.370) indicate that the cross sections remained essentially elastic for the hybrid tests.

5.2.4 Beam Behavior

As with the quasi-static tests, the roof level beam remained elastic during the hybrid tests in spite of the greater distress to the braces in the second story. This behavior can be seen by examining the strain gauge time histories in the beam flanges, axial force time histories, estimated shear force time histories, and beam-end bending moment time histories in Figures 4.372, 4.375, 4.377, and 4.379. No significant local yielding was observed near any of the roof beam to column flange welds.

The response of the $W24 \times 68$ lower beam is shown in Figures 4.373, 4.374, 4.376, and 4.378). Pin connection details were used for TCBF-B-4 rather than the fixed connection used in Specimen TCBF-B-2. As in Specimen TCBF-B-3, no significant plastic deformations were observed in the lower beam, but some local yielding in the connection splice plate was observed via flaking of the whitewash. Maximum average axial forces of about 200 kips (both in tension and compression) developed in the lower beam of this specimen, which was similar to the maximum axial forces observed in the lower beam of Specimen TCBF-B-1 during quasi-static tests. Very small shear forces were recorded during hybrid tests of the beam with pin connections to the gusset plates.

As with the quasi-static tests, similar rotational amplification effects occurred during hybrid simulations in the lower beam ends. The slopes of responses of Specimen TCBF-B-4 essentially follow the theoretical prediction until sensors failed; see Figure 5.48.

From the beam center deflection time histories plotted in Figure 4.371, as expected higher deflections (compared with Specimen TCBF-B-1) were found as a result of unbalanced loads that developed in the roof beam. Estimated peak unbalanced loads was about 100 kips, as shown in Figure 4.380.

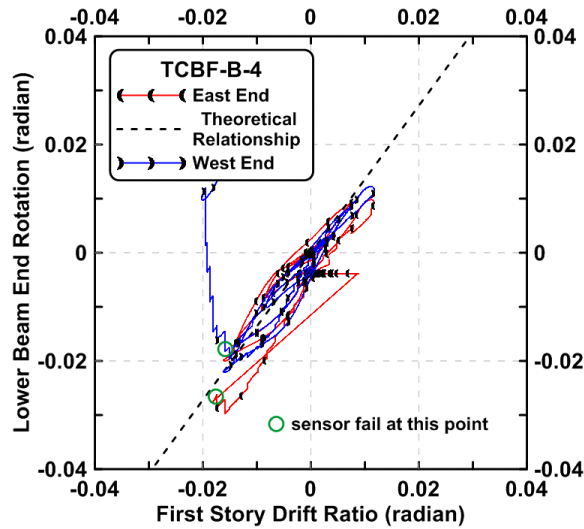


Figure 5.48 Specimen TCBF-B-4: lower beam end rotation versus first-story drift ratio relationships.

5.2.5 Panel Zone Behavior

Shear yielding also occurs in the panel zones that are next to the roof beam during the hybrid simulations, as shown in Figure 4.388. Maximum panel zones shear strains range from 1.2% to 2% during the DE ground motion and are more than 3% during the MCE ground motion, as shown in the time histories of rosette readings and the normalized principal stress relationships in Figures 4.389 to 4.396. Signal saturation occurred in the rosette readings when the shear strains approached 3.2% in the second-story eastern side panel zone. Unlike the upper beam to column connection, the panel zones on the lower floor next to the one-piece gusset plate remained elastic throughout the hybrid tests. From the normalized principal stress relationship plots, it is clear that the shear strains were the principal deformations in the panel zones (via slopes in the plots). This also can be seen from the time histories of principal strain directions.

5.2.6 Gusset Plate Behavior

Similar to quasi-static test results, gusset plate fold lines formed as expected in the $2t$ -gap region for this specimen. Significant yields were found after formation of fold lines through flaking of the whitewash, the time history of rosette readings, and the derived strain time histories, as plotted in Figures 4.397 to 4.400, 4.405 to 4.408, 4.409 to 4.412 and 4.417 to 4.420. Again, rosettes at locations not within the fold line regions remained elastic.

The middle portions of one-piece gusset plates of this specimen that connect to the lower beam essentially remained elastic during the test, as illustrated by the rosette readings (Figures 4.401 to 4.404 and 4.413 to 4.416). But local yields of middle portion of one-piece gusset plate near the splice plate edge were detected via the rosette readings shown in Figures 4.402 and 4.404 (locations R14 and R16).

It is interesting to point out that from the normalized principal stress state plots shown in Figures 4.411, 4.412 and 4.419 (locations R11, R12, and R19 as illustrated in Appendix G), bi-axial tension stresses occurred in the one-piece gusset plate during the hybrid tests (via the trends of plots), especially during the MCE ground motion. Further investigation using finite element models are suggested to examine this phenomenon further.

5.2.7 Test Set Up Behavior

Like in quasi-static tests, actuator brackets deformed elastically during these three tests, as shown in Figure 4.421. The measured stiffness of the bracket was around 3000 kip/in. from both brackets during DE ground motion. Direct measured stiffness was about 30% higher during the MCE ground motion (which was not corrected with the reaction wall deformations). It is believed that the difference might come from the interaction between test set up and the reference frame used to measure the bracket deformations.

No significant slippage of the test set up was observed during hybrid simulations; see Figure 4.422. The maximum deformation for the lateral stability frame was less than 0.04 in. and typically the measured locations that were away from the reconfigurable reaction wall had larger deformations, as shown in the time histories in Figure 4.423. The maximum deformations at the tip of RRW were less than 0.07 in. in hybrid tests (smaller than 0.04 in. during MCE ground motion test), as illustrated in Figure 4.424. The maximum deformation of the reaction wall was less than 0.7% of the maximum deformation of the braced specimen. Note that two position transducers used for external control during the hybrid simulation were mounted on an independent instrument reference frame welded to the laboratory structure. It is assumed that the deformations of the reaction wall, strong floor, and actuator brackets did not affect the hybrid simulation results.

5.2.8 Performance of Servo-Hydraulic Control System

The performance of servo-hydraulic control system can be evaluated through examining the differences between command and feedback of displacement and force. The differences (or errors) also represent the accuracy of the hybrid simulation. From the response histories recorded in the MTS-STC software during the hybrid test, the maximum displacement error for top and bottom actuators was equal to 0.021 in. and 0.0313 in., respectively. These errors corresponded to about 0.2% and 0.58% of the maximum actuator displacement at that floor level, implying that the servo-control system accurately pushed or pulls the specimen to the command displacements.

To identify the source of any errors during the hybrid simulation, synchronization subspace plots [Mercan 2007; Schellenberg et al. 2009] of both actuators are plotted in Figures 5.49 and 5.50. Displacement errors come from actuator lag, actuator lead, actuator undershoot, and actuator overshoot that can be identified if the plot is not a perfect 45° straight line. Note that the top actuator identification number was set to 3 (actID = 3), and the bottom actuator was set to 4 (actID = 4) in the STC software during the hybrid simulation. From the plots shown in Figures 5.49 and 5.50, it is clear that the displacement errors were very small.

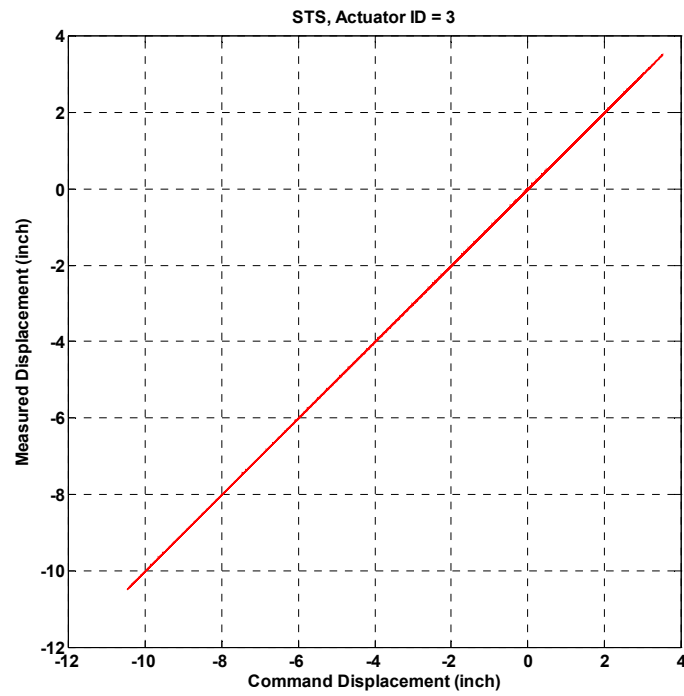


Figure 5.49 Synchronization subspace plot of top actuator during hybrid test.

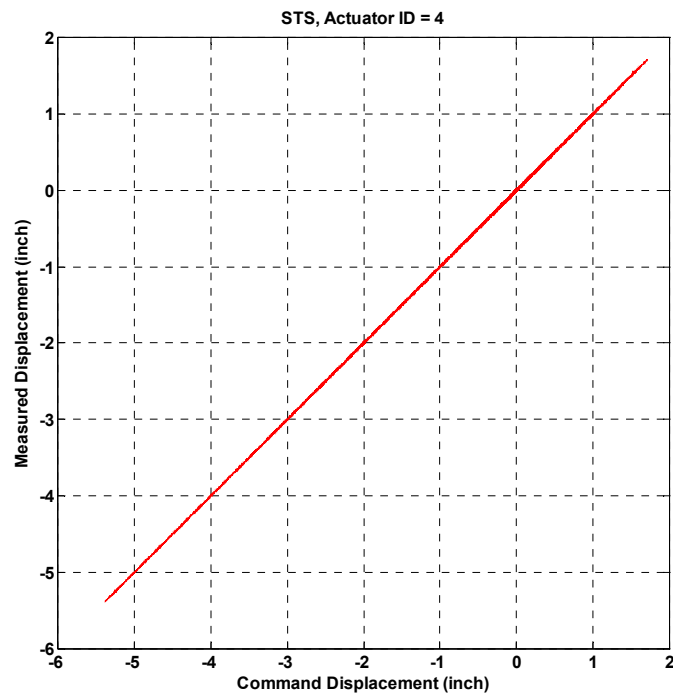


Figure 5.50 Synchronization subspace plot of bottom actuator during hybrid test.

5.3 CONCLUDING REMARKS

From the experimental results discussed, several conclusions can be summarized:

1. Specimen TCBF-B-2 (round HSS braces) had the largest deformation capacity among the three quasi-static test specimens under the same predefined loading protocol. It also experienced the largest total energy dissipated and cumulative roof plastic deformations among the three specimens.
2. Specimen TCBF-B-3 (wide flange braces) had the smallest peak base shear degradation among the three quasi-static test specimens under the same predefined loading protocol.
3. Two braces connecting to the same one-piece gusset plate tended to buckle in the same out-of-plane direction. Without the floor slab (diaphragm) acting as a restraint, the column that is closest to the single-piece gusset plate may be subject to torsion. Further investigation seems warranted on evaluating the demand of the bi-axial bending or torsion in the column induced by out-of-plane buckling of the braces, and how much this affects the behavior of column when severe buckling occurred in the braced frame.
4. Brace deformation tended to concentrate at the middle length of the brace where the local buckling of section wall occurred, and the brace out-of-plane deformation could be as large as ten times the axial deformation under compression. This indicates that significant damage of nonstructural components near the deformed braced frame could occur.
5. Significant fractures initiated near the complete joint penetration welds at the column bases occurred. Brittle failure mode in the column flange near column base stiffeners also observed during the tests, suggesting need for further research on the cyclic behavior of column bases using standard connection details and common weld procedures.
6. Reinforcing details at the brace-to-gusset plate connections for each specimen performed well during both quasi-static tests and hybrid simulation. Adding reinforcing plates at the net section region to develop sufficient effective net section area was successful.
7. The brace and one-piece gusset plate configuration of the braced frame specimen tended to amplify the rotational demand at both ends of lower beam-to-gusset splices, which is similar to the rotational amplification (due to geometry) in the link beam of an eccentrically brace frame (EBF) system. For Specimens TCBF-B-3 and TCBF-B-4, pinned beam-to-gusset details were used to avoid local damage such as flange or web buckling and fracture at these regions. From the observations during these two tests, the pinned connection details effectively avoided any undesired failure mode at beam-to-gusset plate connection regions. However, the entire braced frame lateral capacity was reduced as a result of the moment release at lower beam end connections.
8. During the hybrid simulation, brace fracturing occurred closest to the end of design-level ground motion; the fractured brace was located in the second story not in the ground story, as was expected. Since only one ground motion record was used during the simulation, the braced frame responses may change as input ground motion changes. This result does not represent the general responses of steel braced frames. Further

investigation on the effect of ground motions upon the seismic responses of braced frame systems is suggested before more solid conclusions can be made.

9. Story deformation concentration was observed in the second story, especially after the second-story brace began localized buckling locally during the hybrid simulation. This deformation concentration was easily identified, especially when entire hybrid test specimen moved toward the negative direction (to the west side of the laboratory).
10. Lateral force distribution during the hybrid simulation demonstrated that the distribution varied with time, but most of the time the shape was close to an inverted triangle. This observation supports the force distribution assumption used in quasi-static tests.
11. From the synchronization subspace plots, it is clear that the errors between command displacement and measured displacement were very small during the hybrid simulation. The servo-control system could reach the target displacement accurately mainly because of the testing was running at a very slow rate.

6 Analytical Modeling using OpenSees and LS-DYNA

This chapter focuses on the numerical simulation of the behavior of the four test specimens described in Chapters 3, 4, and 5. Two computer programs were utilized to assess the ability of modern computer software to simulate the observed experimental responses. In the research-oriented program, OpenSees [McKenna 1997] simplified fiber-based line elements were used, while in the commercial software program LS-DYNA [Hallquist 1990; LSTC 2007] more refined finite discretization based on shell elements. Both programs incorporated features to model yielding, lateral buckling, and the deterioration and rupture of members due to low-cycle fatigue. Other modeling capabilities differed as described below.

Modeling efforts initially began by comparing the predicted and measured behavior of with individual struts. This was done to insure that the element, material, and fatigue models used would simulate actual strut behavior with reasonable accuracy. Next, braced frame models were formulated to model the test specimens, incorporating the modeling parameters calibrated from the strut studies. Specimen global responses recorded during the quasi-static tests and hybrid simulations were then compared with responses simulated using OpenSees and LS-DYNA. The following sections describe the responses obtained with the analytical models, which were then compared to the experimental results. Simulated responses are typically plotted over the measured responses for discussion convenience.

6.1 CALIBRATION USING DATA DERIVED FROM PREVIOUS STRUT TESTS

In order to identify optimal material modeling parameters in OpenSees, calibration was done using existing test data. Simple strut tests had been previously conducted in UC Berkeley's Structural Laboratory located in Davis Hall [Yang and Mahin 2005]. A test set-up photo and a specimen shop drawing are shown in Figure 6.1. A total of five square HSS struts and one round HSS strut were subjected to different loading protocols (see Figure 6.2). The test data collected from Specimens #4 and #5 were used herein for calibration since the specimen connection details are most similar to those used for Specimen TCBF-B-1 (with reinforcing plates located on both sides of net section of the brace-to-gusset-plate connections). These two struts were subjected to a near-fault (tension dominated) loading protocol and a symmetrically applied cyclic loading protocol having incrementally increasing displacement amplitudes from cycle to cycle. By using

the same material modeling parameters in the OpenSees, comparison of results for these two different protocols can show how sensitive response is to loading protocol.

Each strut was modeled using a total of four line elements. The number of integration points along each element was set to five. At each integration point the section was represented by a series of fibers. Four fiber layers across and along the walls of the square HSS struts was used; see Figure 6.3. For subsequent analyses a similar discretization was used for wide flange strut models. Four fiber layers were used across the round HSS section, but 16 fibers were used around the perimeter. To help initiate lateral buckling, a small initial offset of the mid-point of the brace was assumed, equal to the 1/1000 of the total length of the strut (see Table 6.1). Each fiber was represented by a Giuffr -Menegotto-Pinto material model (*Steel02* in OpenSees) having the following properties, F_y (yield strength of steel), $E = 29000$ ksi (Young's Modulus of steel), $b = 0.003$ (strain-hardening ratio) and $R_o = 25$. The yield strength of steel is based on the mill certificate report provided by the steel fabricator. The factors b and R_o are obtained based on trial and error.

The low-cycle fatigue wrapper developed by Uriz and Mahin [2008] was also used to simulate rupture of the critical sections. The algorithm uses a modified rain-flow cycle counting method to determine the number and amplitude of individual inelastic deformations occurring in each fiber during an analysis. A Coffin-Manson low-cycle damage model was used to compute the damage inflicted by each cycle, and Miner's rule was used to accumulate the damaging effects of each cycle. The properties of the fiber can be degraded with increasing damage. In this study, individual fibers were removed from the model when the damage model indicated that the low-cycle fatigue limit had been reached. Equation 6.1 represents the Coffin-Manson relationship where ε_i is the strain amplitude, N_f is the number of cycles to failure, and ε_o and m are material parameters determined from experiments. The low-cycle fatigue parameters determined previously [Uriz and Mahin 2008] for these and other specimens were $m = -0.458$ (default value) and $\varepsilon_o = 0.099$. These were found to be adequate for this study.

$$\varepsilon_i = \varepsilon_o (N_f)^m \quad (6.1)$$

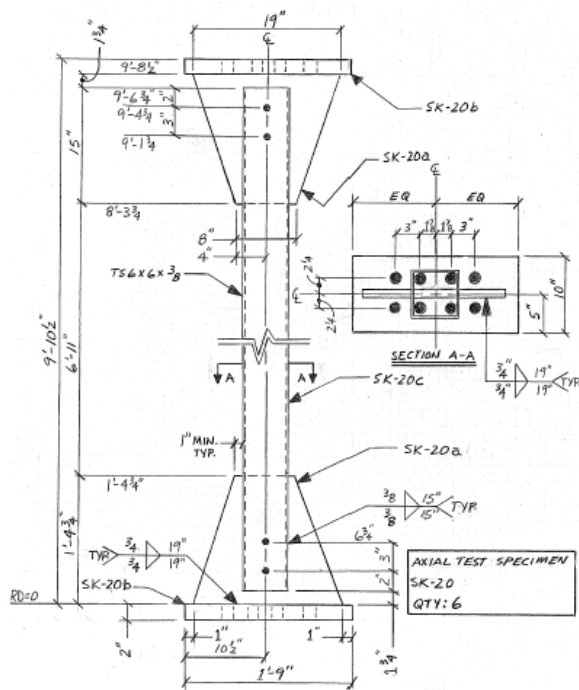
From the plots of axial force versus axial displacement and axial force versus out-of-plane displacement shown in Figures 6.4 to 6.7, it is clear that OpenSees results overall match the actual test results with an acceptable degree of accuracy. Suspicious readings from the experiments are pointed out in the plots. Since the fiber-section models in OpenSees assume a constant cross-sectional geometry and that plane sections before deformations remain plane afterwards, they cannot simulate the local buckling observed for the walls of the HSS section near the mid-point [Uriz 2005]. For example, in Figures 6.4 and 6.6, the OpenSees results tend to over-predict the post buckling strength of the struts in compression. Moreover, the Uriz-Mahin damage model is based solely on low-cycle considerations, and the effects of fracture mechanics once the section begins to rupture are not considered. As such, the numerical results predict total fracture of the brace with reasonable precision, but the nature of the deterioration prior to complete rupture differs for the two specimens. As noted by Uriz [2005], cyclic test results may

differ from analytical results, and the behavior of the same specimen tested under the different loading protocols may differ as well.

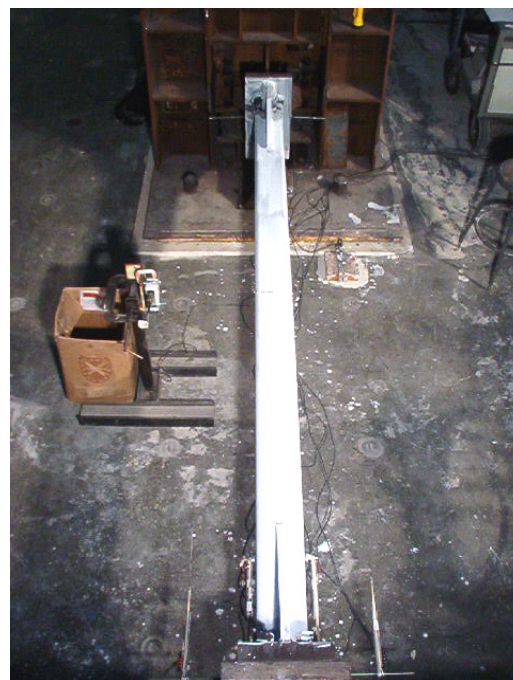
Table 6.1 Input parameter details in OpenSees 2D model.

Specimen	Section Name	F_y (ksi)	Young's Modulus E (ksi)	m	ε_0	No. of Element and Fiber Layers		δ_{ecc} (in.)
#4	HSS 6×6×3/8	60.6	29,000	-0.458	0.099	4	4	0.113
	near-fault loading procol							
#5	HSS 6×6×3/8	60.6	29,000	-0.458	0.099	4	4	0.113
	symmetric-cycle loading procol							

(Note: $\delta_{ecc} = L/1000$, is the assumed initial crookedness at the middle length of the strut model)



(a) Shop drawing



(b) Test set up and specimen overview

Figure 6.1 Simple strut tests at University of California, Berkeley [Yang and Mahin 2005].

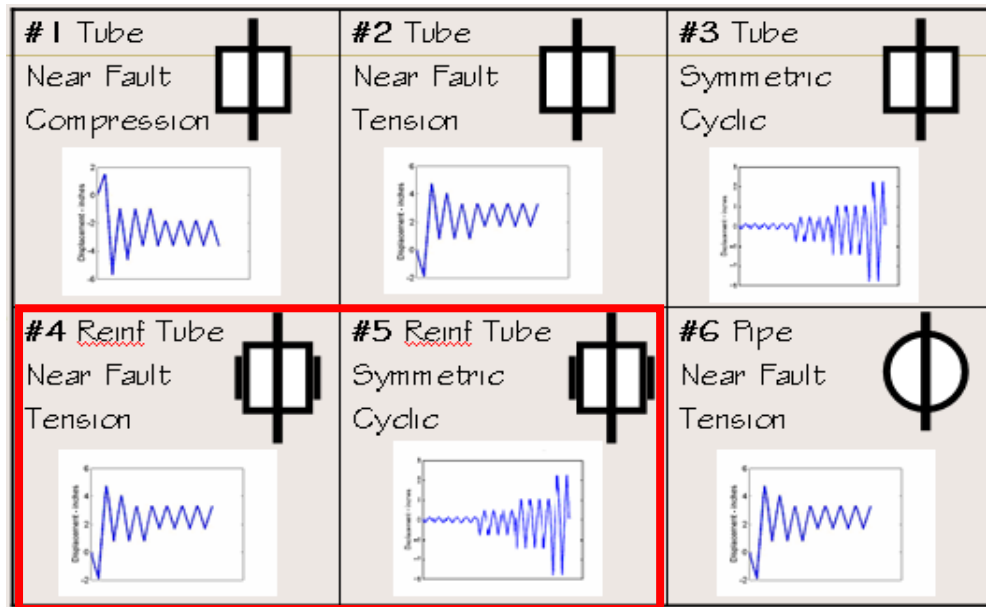


Figure 6.2 Loading protocols of simple strut tests [Yang and Mahin 2005].

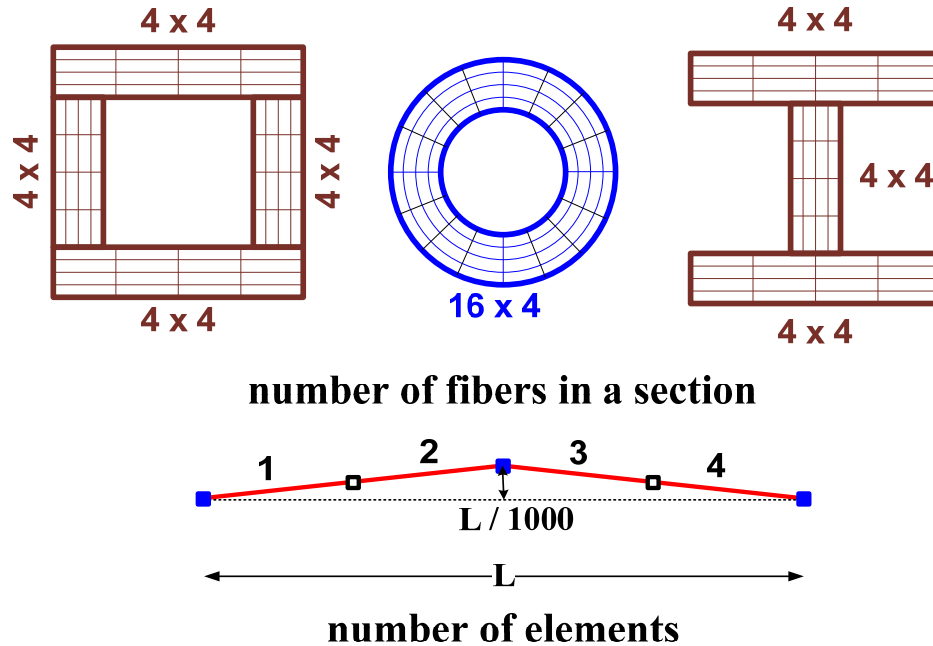


Figure 6.3 Demonstration of the fiber sections and element numbers used in OpenSees strut models.

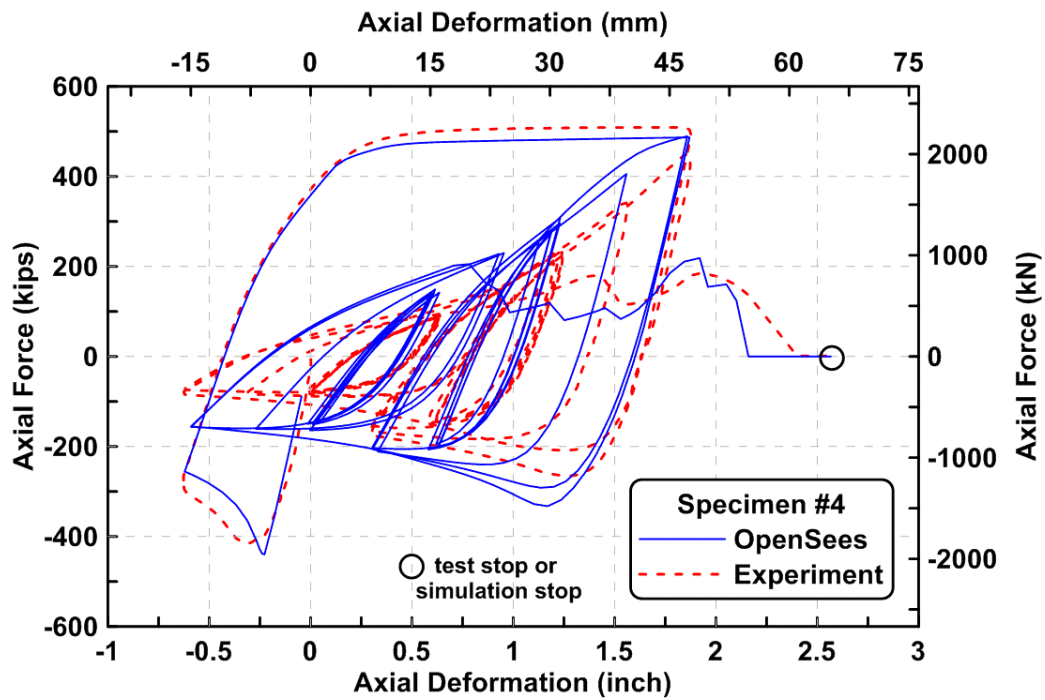


Figure 6.4 Axial force versus axial deformation relationship of Specimen #4 from experiment and OpenSees simulation.

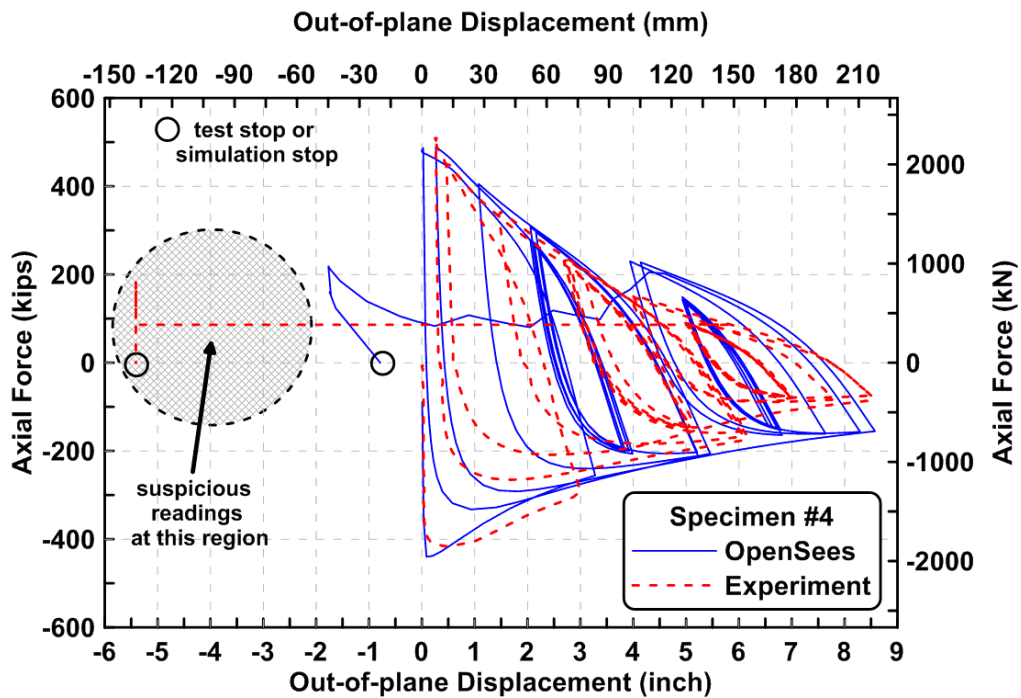


Figure 6.5 Axial force versus out-of-plane displacement relationship of Specimen #4 from experiment and OpenSees simulation.

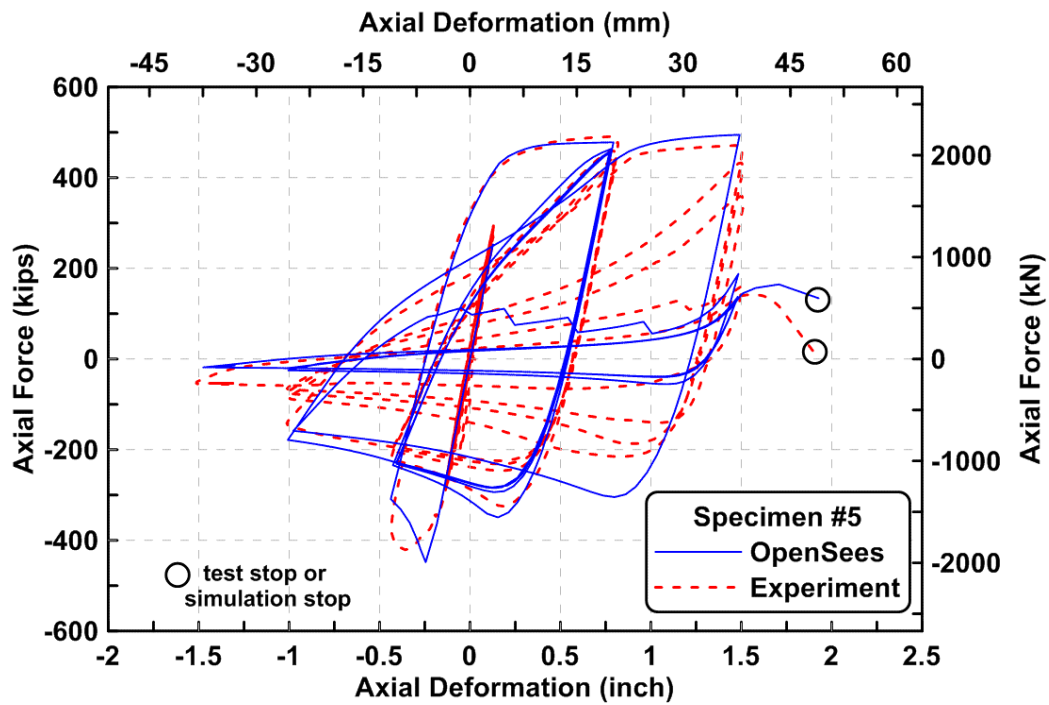


Figure 6.6 Axial force versus axial deformation relationship of Specimen #5 from experiment and OpenSees simulation.

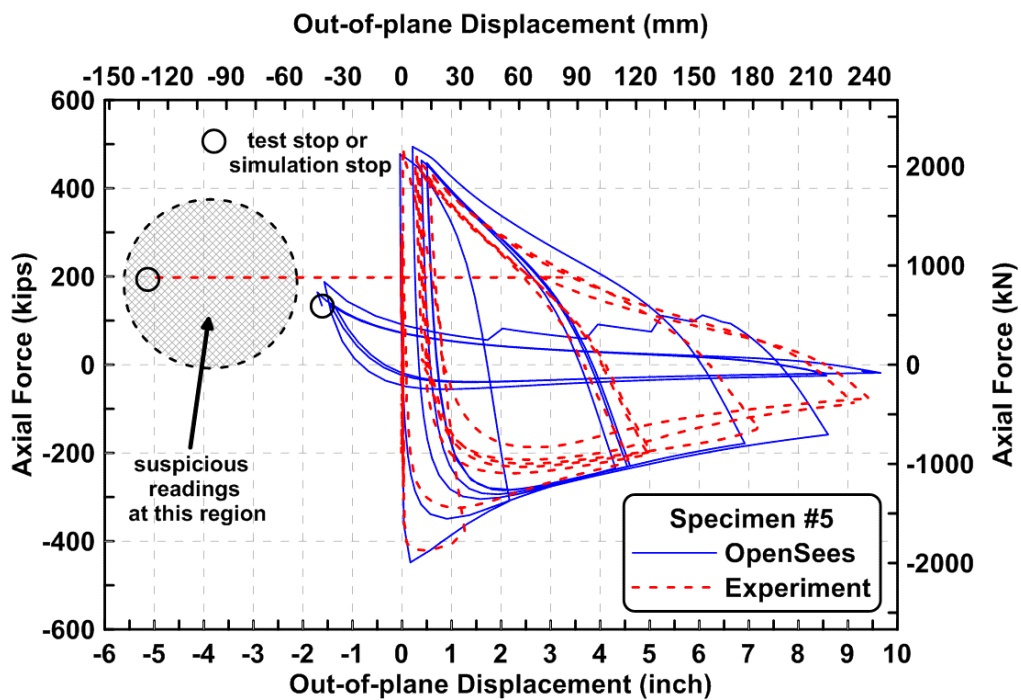


Figure 6.7 Axial force versus out-of-plane displacement relationship of Specimen #5 from experiment and OpenSees simulation.

6.2 PREDICTION OF QUASI-STATIC TEST RESULTS

Two-dimensional models were developed in OpenSees to represent Specimens TCBF-B-1, TCBF-B-2, and TCBF-B-3. Figure 6.8 shows an overview of the nodal distributions, displacement (or load) control nodes, and rigid end zones used for the OpenSees braced frame models. To simplify the model, the braces were assumed to be pin ended at the location of the $2t_g$ fold line in the gusset plate, and buckling in the analytical model was induced in-plane rather than out-of-plane as observed in the test specimens. This was to be found to be a reasonable assumption in earlier tests by Uriz and Mahin [2008]. As with the previously described models of individual struts, a small initial offset was introduced at the center of each brace to initiate lateral buckling. The beam-to-column connections and the gusset plates were assumed to be perfectly rigid. While some deformations are associated with these regions, the effect is believed to be small once brace buckling commences. Material models were similar to those described in the previous tests. Material strengths were based on mill test reports, along with the modulus of elasticity. The low-cycle fatigue damage parameters for fibers were initially set to be the same as used as previously based on past square HSS brace tests.

Cyclic analyses were performed using the same loading protocol as used for the actual specimens. That is, the same lateral displacements were imposed on the top level of the specimen, and a force equal to half of the force needed to impose the specified displacement on the roof was applied to the lower floor level. This was done for the first three specimens that were tested quasi-statically.

From the base shear versus roof displacement relationships shown in Figure 6.9 for Specimen TCBF-B-1, the initial behavior of the specimen is well predicted. The stiffness and ultimate strength are reasonably predicted. However, it is clear that the simulated base shear from the OpenSees fiber model degrades earlier than in the actual tests results. Additional investigation of the simulation results revealed that the braces in the model fracture earlier than in the test, which causes degradation of the base shear capacity to occur sooner. As shown in Figure 6.10, modification of the fatigue material input parameter ϵ_0 from 0.099 to 0.148 and leaving the m value unchanged resulted in a better match. It is clear that modeling of the complete behavior of the braced frame requires accurate modeling of the deterioration and rupture of the individual braces.

A comparison between the individual brace responses for the Trial 2 fatigue model with the actual test data (Figure 6.11) shows that the hysteretic brace axial force-axial deformation characteristics are predicted well overall by the numerical model. However, there are substantial discrepancies between the maximum measured and simulated displacements in individual braces, and the behavior as fracture is approached and the sequence of individual brace fractures is not well predicted. For instance, the brace axial deformations derived from the tests in the first story were larger than those from the OpenSees simulations, while the situation in the second story was reversed. The derived brace axial deformations were calculated from story deformations by geometry. As noted previously, for the test of Specimen TCBF-B-1, the first-story deformation was calculated from the position transducers that were found not to be ideally positioned. This

error in experimental results might explain some of the deviation of peak experimental and numerical axial deformations.

OpenSees results for Specimen TCBF-B-2 are shown in Figures 6.12 and 6.13. To achieve a reasonable match, the low-cycle fatigue parameter ε_0 used for the circular HSS section was again modified, in this case to $\varepsilon_0 = 0.270$. Although the resulting simulation matches the overall system behavior well, the brace fracture sequences and the deterioration of base shear with cycling during larger displacement cycles were not the same as the test results. As can be seen in Figure 6.13, simulated brace peak axial forces were less than the estimated brace peak axial forces obtained from the test. Again, the distribution of axial deformations in the braced during the final few cycles is not well simulated by the fiber based model.

In Specimen TCBF-B-3, the lower beam-to-gusset plate splices were bolted and designed to accommodate significant rotations at the connection. The connections in the numerical model were initially defined as fully pinned connections, but the simulation results did not match the experimental results well. As a result, zero length elements were used instead to simulate semi-rigid connection behavior. More specific information on the method used to model the semi-rigid nature of these connections is provided in Section 6.3. To accommodate the in-plane buckling required using the 2D model implemented in OpenSees, the wide flange braces used in this specimen were pin ended as with the other specimens and rotated 90° about their longitudinal axes to be able to represent weak axis buckling behavior.

Plots of the quasi-static cyclic base shear versus roof displacement results for Specimen TCBF-B-3 are plotted in Figure 6.14. The simulation matches the overall system test behavior quite well until the final cycle. However, as seen in Figure 6.15, the simulated response of individual brace differs significantly from those derived from the test results. In particular, the numerically predicted brace peak tensile axial forces are larger in the lower story than derived from the test results. The opposite is true for the upper story, where the numerically simulated peak brace axial forces are larger in compression and smaller in compression than estimated from test results. The numerically predicted brace fracture sequences were not the same as the test results. For this test, the optimum value of the low-cycle fatigue parameter ε_0 was found by trial and error to be 0.220; this is between the values determined for the square and round HSS braces.

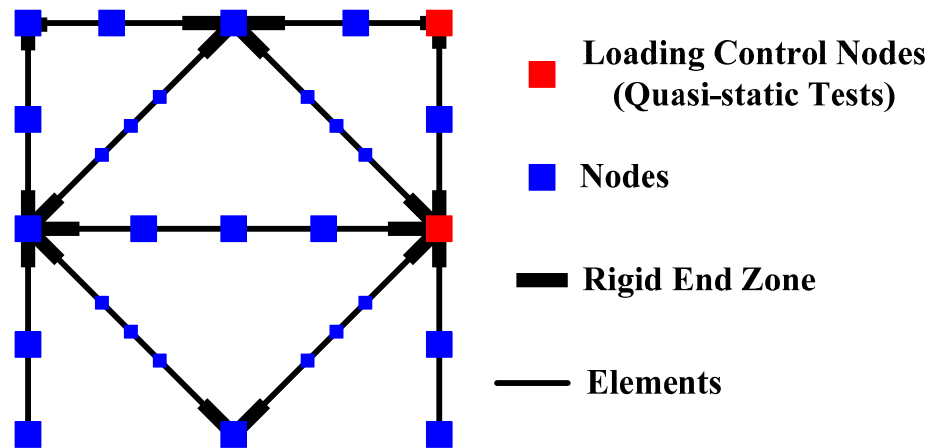


Figure 6.8 Demonstration of a braced frame model in OpenSees.

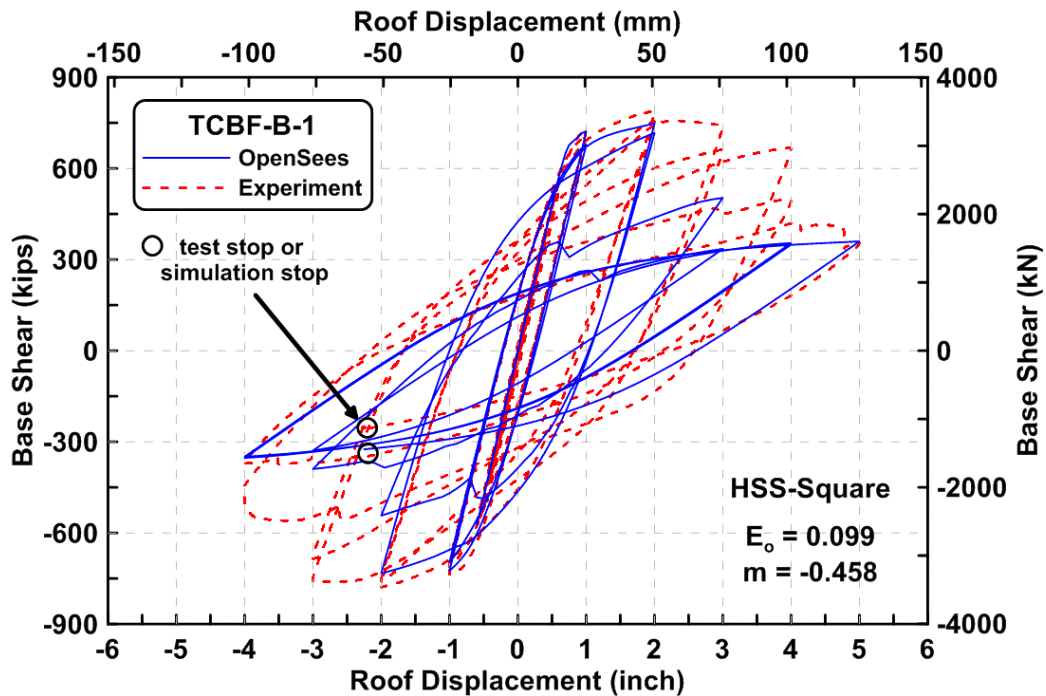


Figure 6.9 Base shear versus roof displacement relationship of Specimen TCBF-B-1 from experimental results and OpenSees simulation (Trial 1).

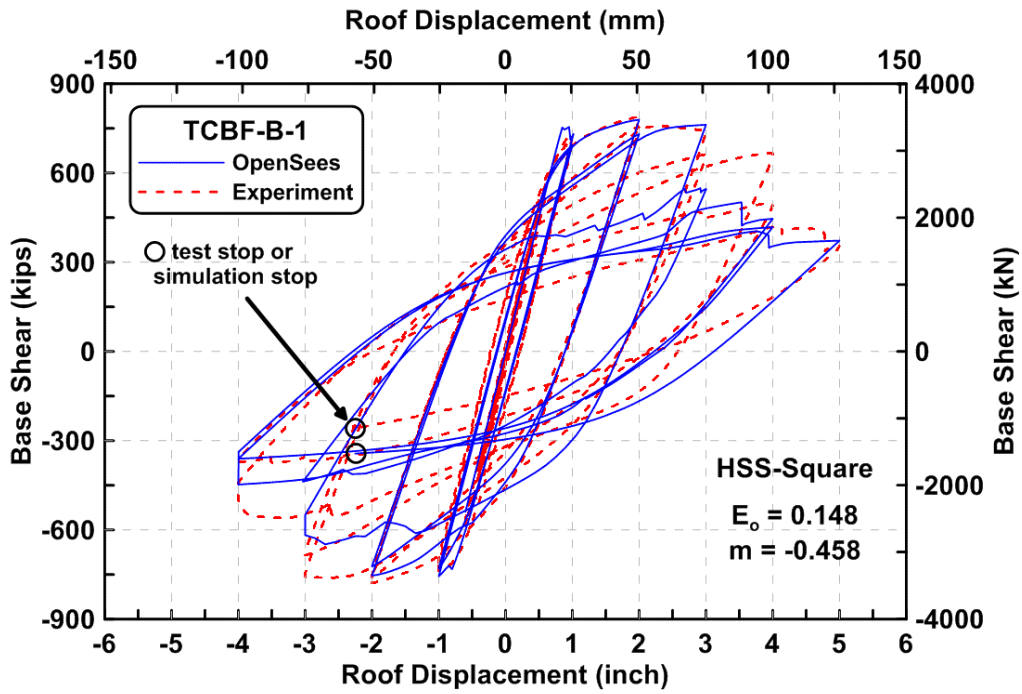


Figure 6.10 Specimen TCBF-B-1: base shear versus roof displacement relationship from experimental results and OpenSees simulation (Trial 2).

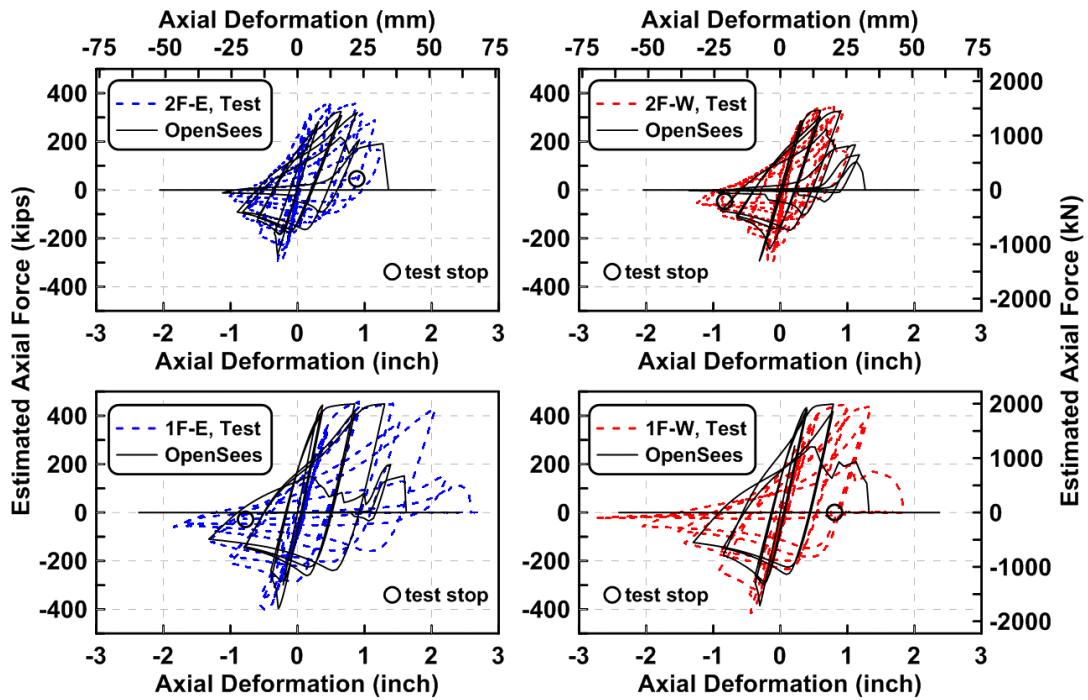


Figure 6.11 Specimen TCBF-B-1: brace axial force versus axial deformation relationships from experiment and OpenSees simulation (Trial 2).

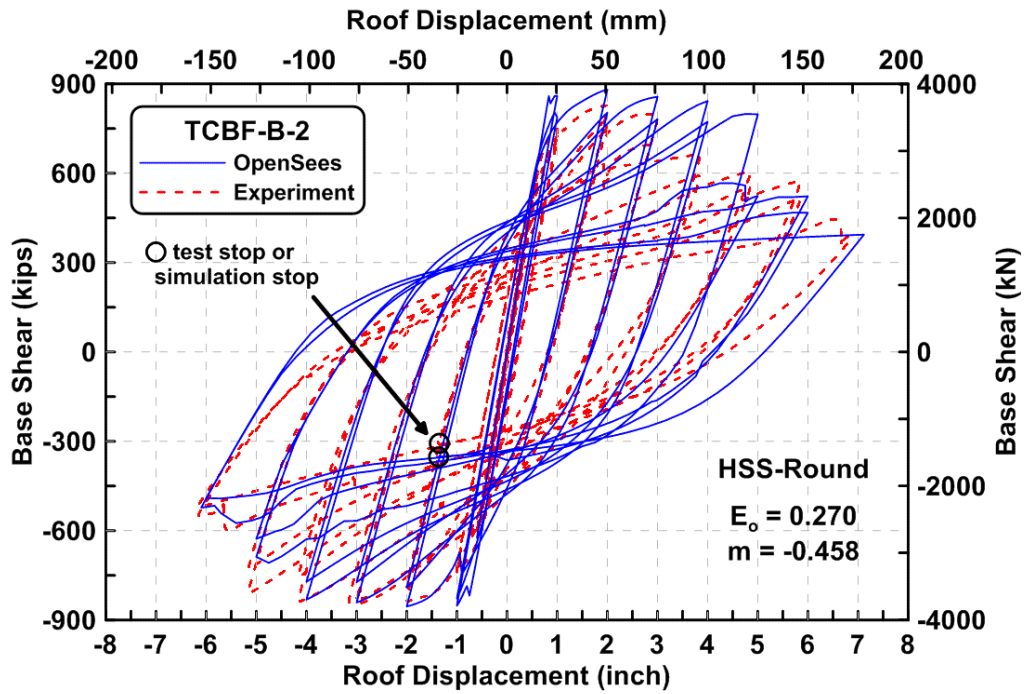


Figure 6.12 Specimen TCBF-B-2: base shear versus roof displacement relationship from experiment and OpenSees simulation.

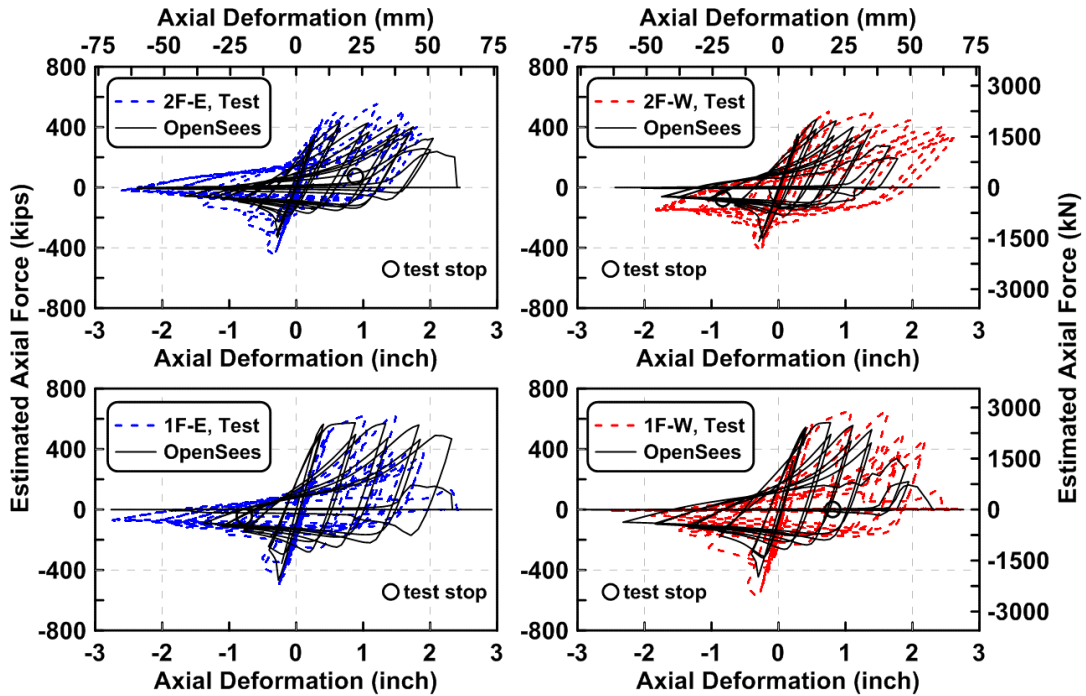


Figure 6.13 Specimen TCBF-B-2: brace axial force versus axial deformation relationships from experimental results and OpenSees simulation.

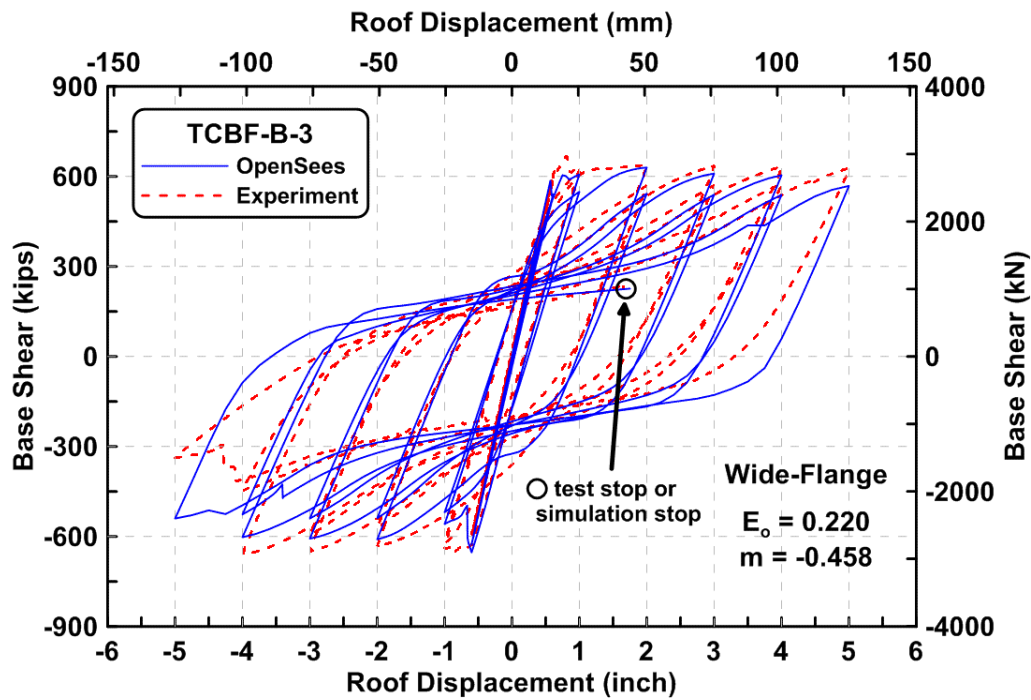


Figure 6.14 Specimen TCBF-B-3: base shear versus roof displacement relationship from experimental results and OpenSees simulation.

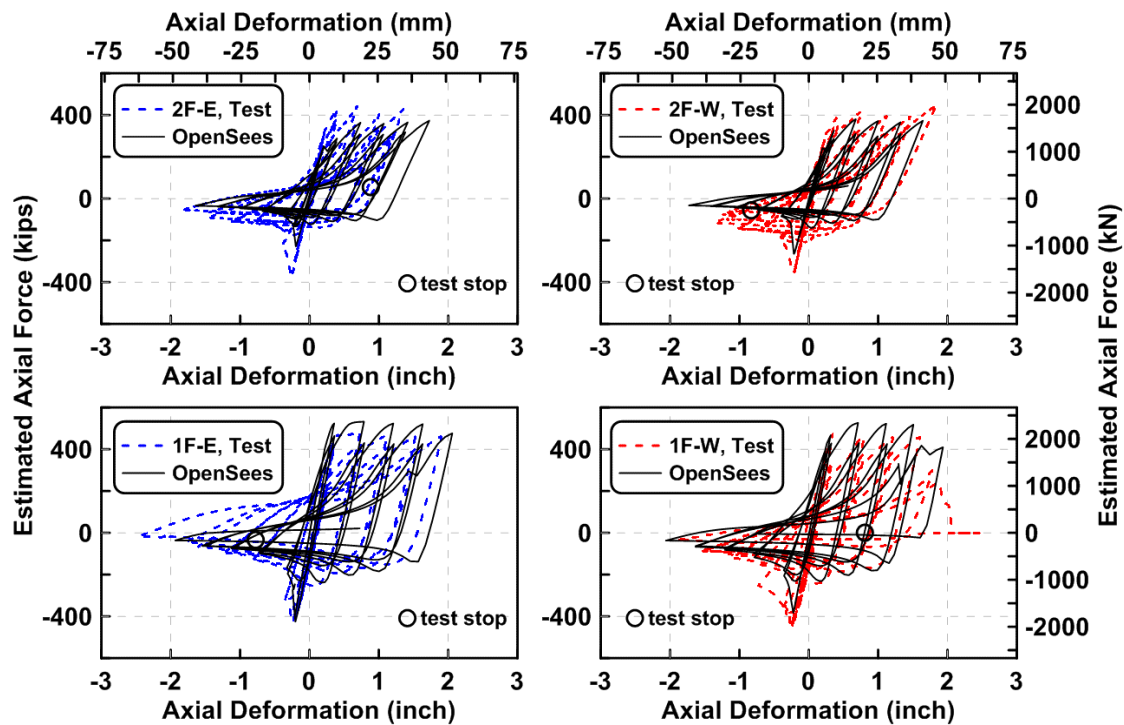


Figure 6.15 Specimen TCBF-B-3: brace axial force versus axial deformation relationships from experimental results and OpenSees simulation.

6.3 PREDICTING THE HYBRID SIMULATION RESULTS

The OpenSees model developed to simulate Specimens TCBF-B-3 and TCBF-B-4 was initially calibrated using the hybrid test results of Specimen TCBF-B-4. Specimen TCBF-B-4 utilized identically sized square HSS bracing members as used in Specimen TCBF-B-1. Thus, the basic model and modeling parameters for Specimen TCBF-B-4 were the same as used in Trial 2 for Specimen TCBF-B-1; in particular, $\varepsilon_0 = 0.148$, $m = -0.458$. However, the lower beam-to-gusset plate connections were bolted (rather than being continuous) and initially modeled as being fully pinned connections. The test results in the elastic range show significant discrepancies between measured and computed frame stiffnesses, however, and for the hybrid test of Specimen TCBF-B-4 in dynamic response. For example, the fundamental period of the specimen from the hybrid simulation and from the OpenSees model do not match when a pin connection is assumed in the numerical model; see Figure 6.16

To simulate the semi-rigid behavior of the connections, zero-length elements were introduced into the model at these locations having elastic-perfectly plastic behavior. An estimated moment capacity (M_y) of the bolted connections was derived from the equation below (see Figure 6.18 for a simplified physical interpretation).

$$M_y = P \times L = 1852.2 \text{ kip} - \text{in.} \quad (6.2)$$
$$L = 9 \text{ in.}$$

$$P = n_s \cdot n_b \cdot \mu_s \cdot N_b = 2 \cdot 6 \cdot 0.35 \cdot 49 = 208.8 \text{ kips} \quad (6.3)$$

where P is the resultant friction resistant force of bolts, L is the moment arm between the resistant forces at the top and bottom side, n_s is the number of friction surface, n_b is the number of bolts used to calculate the friction force, μ_s is the friction coefficient between steel plates, and N_b is the minimum code specified pretention force of the tension controlled bolt.

A calibrated rotation limit (θ_y) was used as the input parameters of the uniaxial material properties; the rotation limit is:

$$\theta_y = 0.003 \text{ radians} \quad (6.4)$$

This adjustment improved the fit between the numerical simulation results and the test results (see Figure 6.17).

A 3-sec-long free vibration test was conducted before the main hybrid simulations to identify the fundamental period of the specimen and the inherent damping characteristics of the specimen and the test set up. To perform the hybrid free vibration test, displacements of 0.1 in. and 0.061 in. were imposed on the upper and lower floor levels, respectively, using the computer electro-hydraulic control system. These displacements are proportional to the computed first mode shape of the specimen. The hybrid test control software then simulated the free vibration

response of the specimen as it was released from this initial condition (initial deformed shape). The numerical model used in the hybrid model included modest amounts of Rayleigh viscous damping (with mass proportional and constant initial stiffness) corresponding to 1.5% and 2.5% for mode one and mode two, respectively. For this free vibration simulation, the leaning column described in Chapter 3 was included. Figure 6.19 shows the floor level displacement time histories during the hybrid free vibration test. The average period for the first four complete cycles of the free vibration were 0.3799 sec and 0.3740 sec from upper and lower floor level displacement time histories. Using a log decrement approach, the viscous damping ratios were estimated to be 2.65% and 4.06%. Thus, it can be seen that the test specimen and test set up introduced additional damping effects.

The fundamental period of the OpenSees model of Specimen TCBF-B-4 was 0.3925 sec when pinned lower beam end connections were included in the model. It is apparent that the model with pinned lower beam ends was too soft. However, when semi-rigid lower beam end conditions were included in the model, the computed fundamental became 0.3798 sec, which is very close to that measured. Rayleigh damping parameters 2% and 3% for mode one and mode two, respectively, were used in both simulated models (pinned and semi-rigid lower beam end models). Note that in the OpenSees model used for hybrid simulation the Rayleigh damping parameters 1% and 2% for mode one and mode two, respectively, were used to simply accommodate the damping effects from the test set up.

The displacement time histories of each floor level under the DE ground motion and MCE ground motion during the hybrid test and the OpenSees simulation are plotted in Figure 6.20. The OpenSees roof displacement predictions were fairly accurate until the first brace fractured (second-story east-side brace) at a ground motion time of around 7.49 sec. After that, the numerically predicted roof displacements deviated to the negative side and ended the DE with a 0.65 in. residual roof displacement. The hybrid test results showed a very small residual roof displacement (less than 0.08 in.) after the DE ground motion.

During the MCE-level excitation, there are greater discrepancies between the numerically simulated and test results. Nonetheless, the same trend in having the structure go through large inelastic excursions can be seen. While the tests were stopped before the end of the record since the lateral displacements exceeded the stroke capacity of the actuators (about 5% roof drift), the OpenSees results indicate that the structure does not completely collapse due to the diminishing of the excitation. However, the frame has a permanent roof drift of about 16 in. (about 6.6% overall drift).

A comparison the base shear (only the base shear of braced frame, not including the leaning column shear forces) versus roof displacement relationships for the hybrid simulation and OpenSees simulation can be seen in Figures 6.21(a), 6.21(b) and 6.21(c). During the DE ground motions, the OpenSees model underestimates the peak base shear, especially in the negative roof displacement direction. It can also be seen that the period of the structure has significantly deteriorated by the end of the test as seen from the slope of the hysteretic loops at the end of the DE portion of the results. However, the OpenSees model is considerably stiffer than observed in the tests.

During the MCE portion of the response, the structure is only able to develop about half of the strength exhibited during the DE phase of the response. The prior damage during the earlier DE portion of the response may have adversely impacted the ability of the frame to withstand subsequent large events (or aftershocks). The OpenSees numerical model is able to develop much greater base shear forces than was seen in the test. The test was stopped due to the stroke capacity of the actuators being reached. The lateral resistance of the frame at the end of the OpenSees simulation was only about 15% of that predicted at first yield.

For the individual brace response, Figure 6.22 shows a comparison of axial force versus axial deformation relationships for the hybrid test and the OpenSees simulation. Although overall brace behavior was captured by the OpenSees simulation model, the prediction of brace fracturing was not accurate.

As noted above, the DE-level event may have adversely affected the ability of the frame to withstand the MCE-level event. Therefore, the OpenSees simulation was repeated, with the sequence of excitations reversed. The ground motion input sequence was altered from DE + 3-second silence + MCE to MCE + 3-sec silence + DE. In this case, the DE event might represent a strong aftershock following a very rare MCE-level seismic event. The predicted response of Specimen TCBF-B-4 for this case is shown in Figure 6.23. The peak roof drift ratio during the MCE portion of the response is about 7 in. (2.9% drift ratio), and the residual roof displacements are in the positive direction. These measure 2.60 in. at roof level and 1.35 in. at the lower level (instead of being in the negative direction, as shown in Figure 6.20). The permanent story drift ratio is about 1.1%, which would likely be difficult and costly to repair. The effect of the DE aftershock is to continue motion of the structure in the positive direction with the peak displacement being about 10 in. and a residual displacement being about 7.5 in. (3.1% drift ratio). This indicates a potential adverse problem with low-rise SCBF systems subjected to strong aftershocks.

Figure 6.24 plots the base shear versus roof displacement relationships for simulated Specimen TCBF-B-4. This shows that when subjected to the MCE-level event all of the braces fractured, resulting in a much more flexible and weaker structure. The response during the DE aftershock is basically that of the moment frame provided by the semi-rigid lower beam connections and the upper beam. Figure 6.25 shows the axial force versus axial deformation relationships of the simulated specimen under different ground motion series.

The effect of leaning columns was also investigated using OpenSees. The simulated gravity columns were removed from the computer model and the simulation was then re-run. Response histories of story shear forces and floor level displacements were compared. From the comparison plots shown in Figure 6.26, it is clear that the presence of leaning columns has significant effects on the overall global behavior of the braced frame models. The effects were prevailed in the nonlinear range, especially after the crack initiation in the braces was observed (see Figure 6.27). In addition, the brace hysteretic loops and rupturing sequences were affected by the presence of the leaning columns; see Figure 6.28. If we compare the range of brace axial deformations at each floor level, note that the leaning columns do somewhat help in preventing deformation concentration in the simulated models; see Figure 6.28.

From the above comparisons between the results obtained from the OpenSees simulation and those from actual test results, it is safe to say that OpenSees simulates the overall global behavior of the braced frame structures with reasonable accuracy. However, the localized brace and other member behavior predicted by OpenSees is less accurately predicted. The elements used to model buckling braces cannot simulate localized buckling and fracture of the braces to a high degree of confidence. This behavior is likely to occur during the response of low-rise braced frames subjected to the DE-level and especially MCE-level excitations. This is one of intrinsic difficulties of the fiber models used herein in the OpenSees simulations. Using a finite element analysis program to simulate localized brace buckling behavior is one way to overcome this drawback.

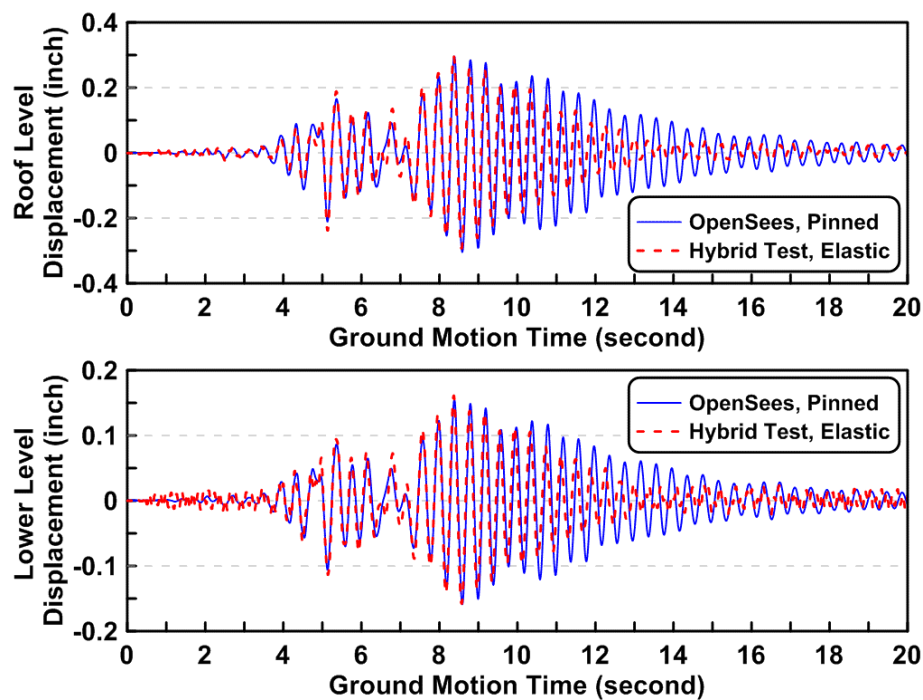


Figure 6.16 Specimen TCBF-B-4: displacement time histories from elastic hybrid test and OpenSees simulation (pinned lower beam ends).

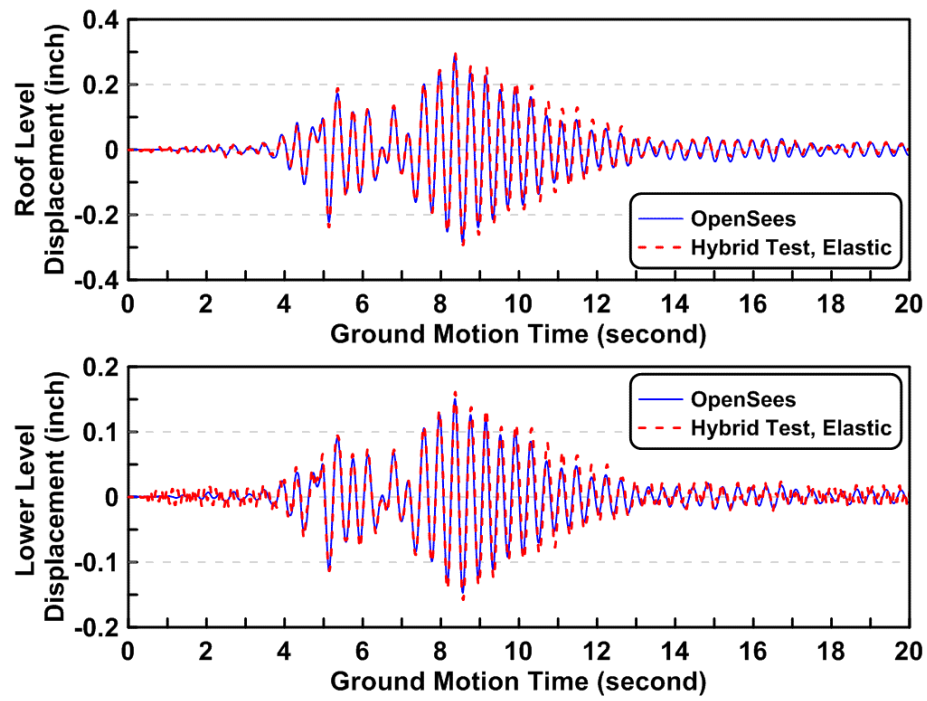


Figure 6.17 Specimen TCBF-B-4: displacement time histories from elastic hybrid test and OpenSees simulation (semi-rigid lower beam ends).

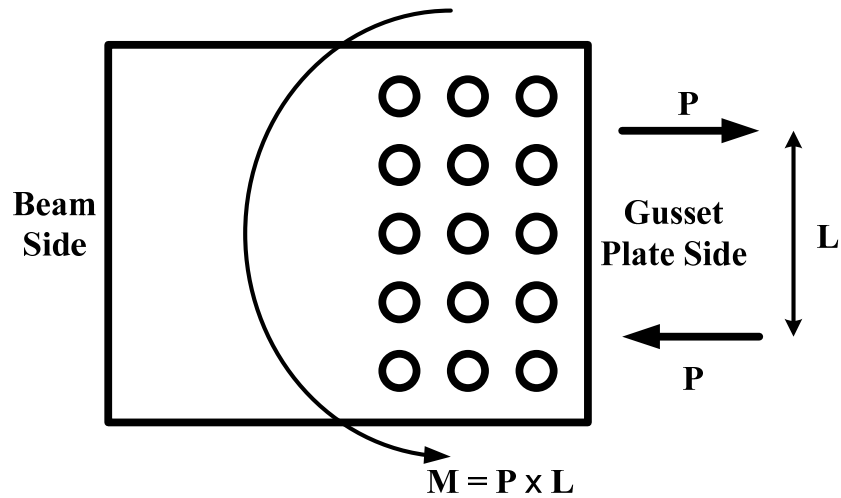


Figure 6.18 Specimen TCBF-B-4: demonstration of semi-rigid lower beam ends.

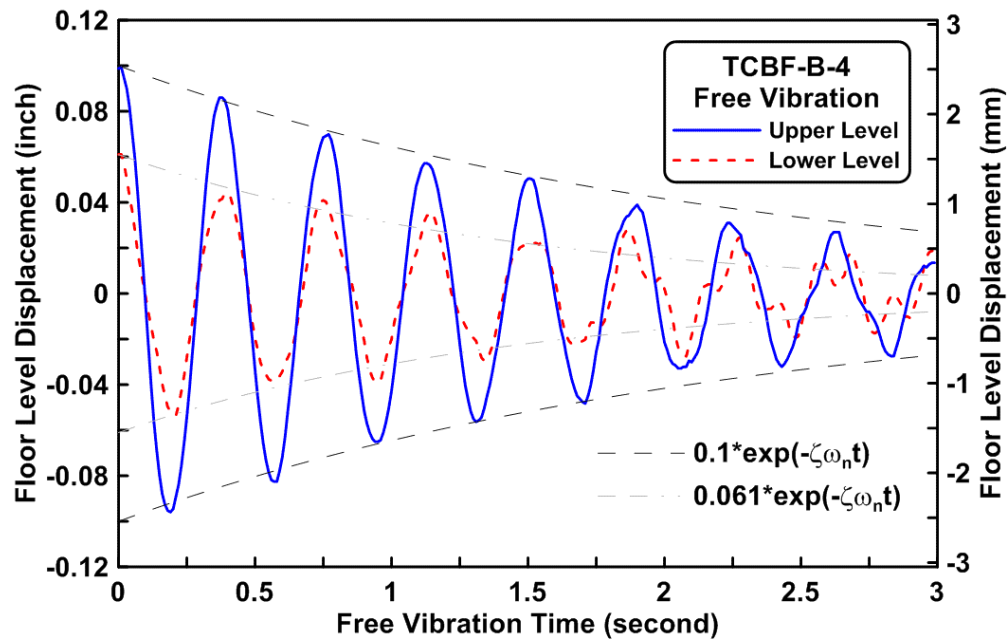


Figure 6.19 Specimen TCBF-B-4: free vibration test results.

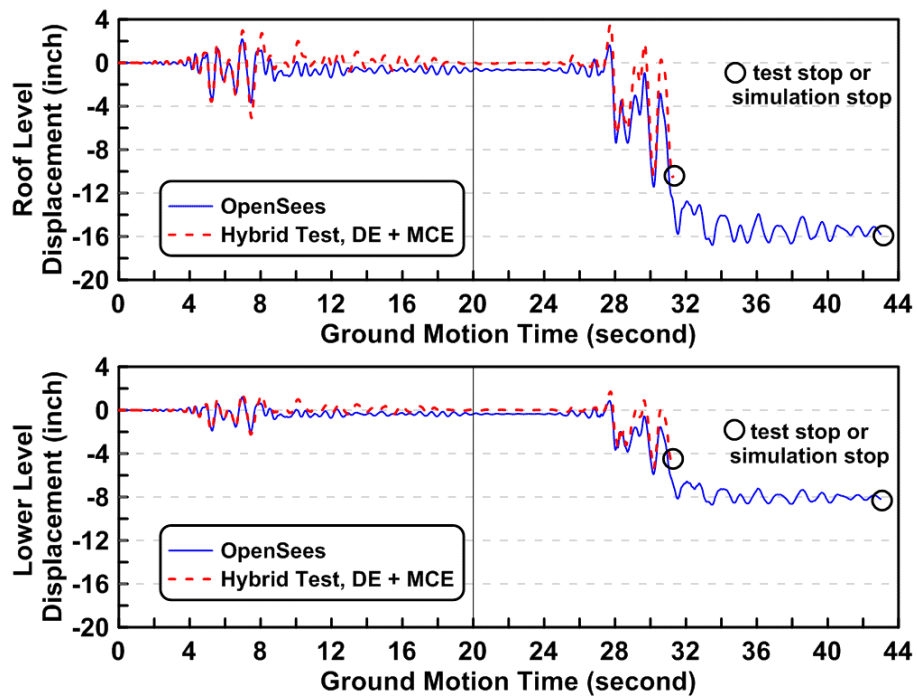


Figure 6.20 Specimen TCBF-B-4: displacement time histories of from DE and MCE hybrid test and OpenSees simulation (semi-rigid lower beam ends).

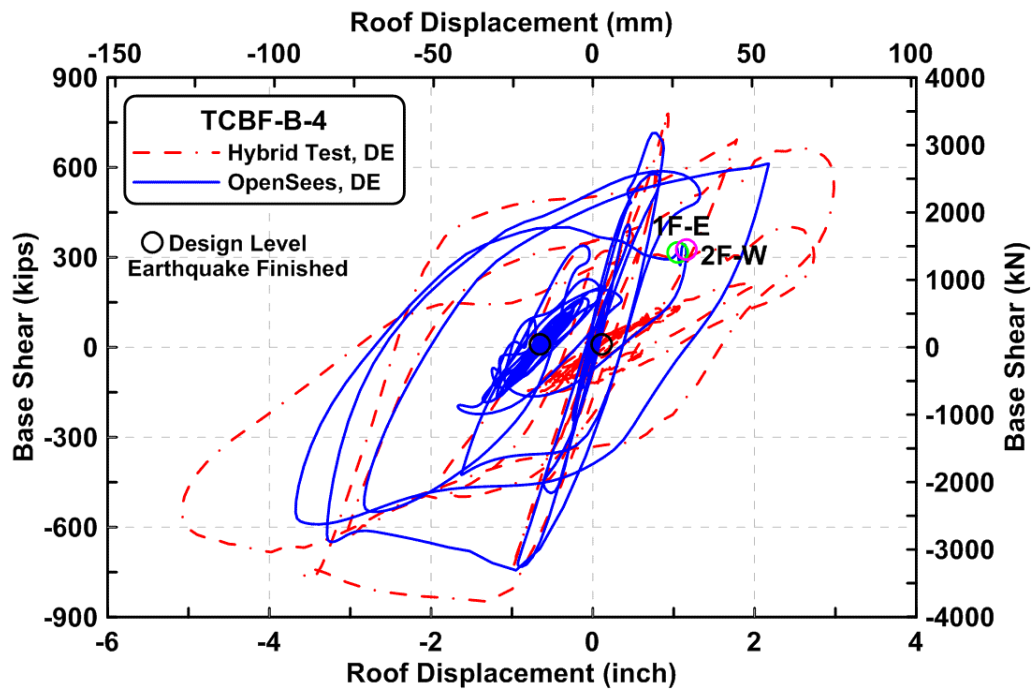


Figure 6.21(a) Specimen TCBF-B-4: base shear versus roof displacement relationships from DE hybrid test and OpenSees simulation (semi-rigid lower beam ends).

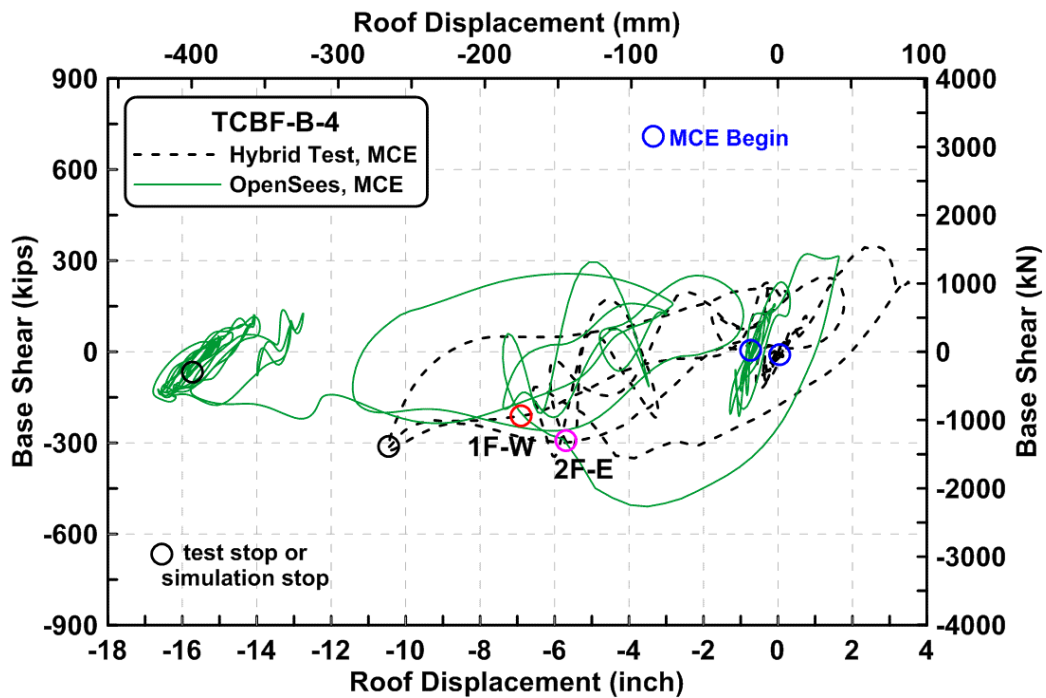


Figure 6.21(b) Specimen TCBF-B-4: base shear versus roof displacement relationships from MCE hybrid test and OpenSees simulation (semi-rigid lower beam ends).

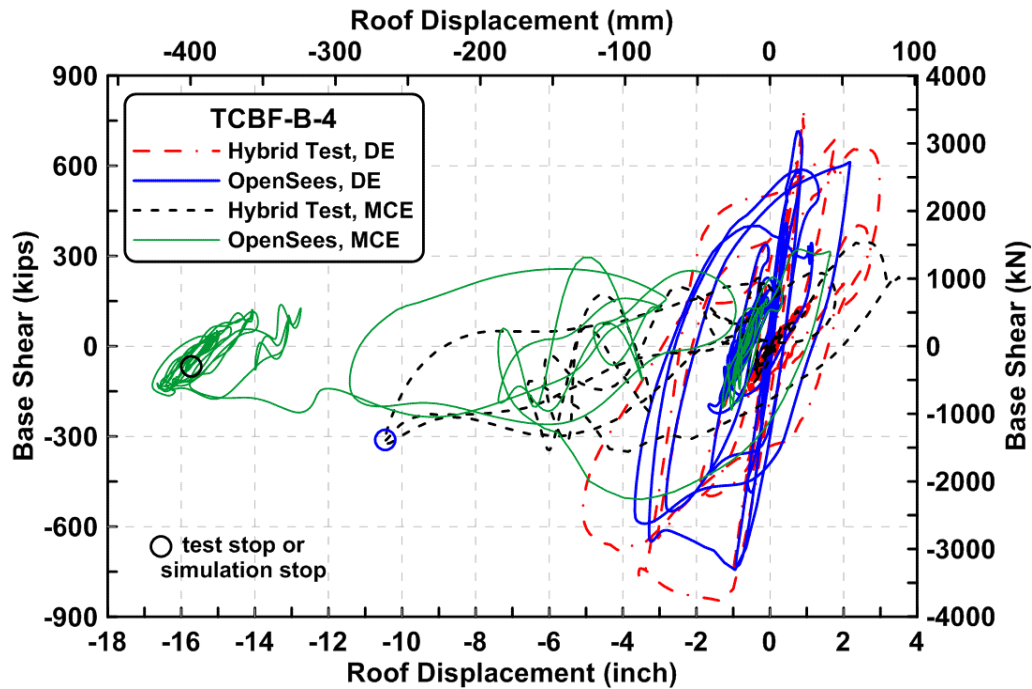


Figure 6.21(c) Specimen TCBF-B-4: base shear versus roof displacement relationships from DE and MCE hybrid test and OpenSees simulation (semi-rigid lower beam ends).

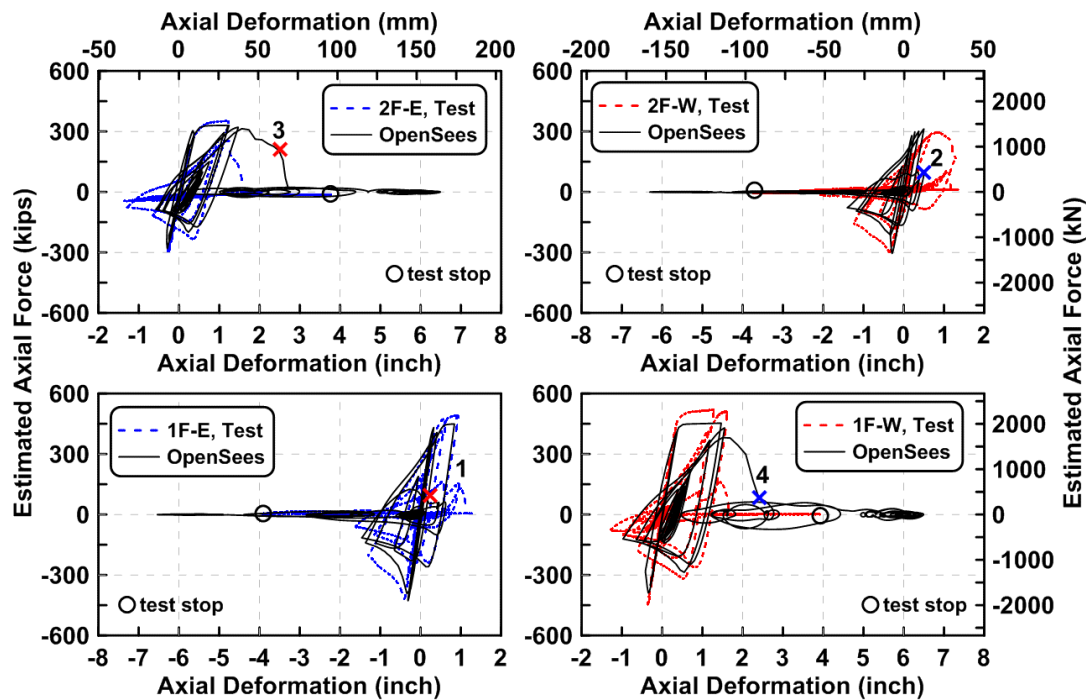


Figure 6.22 Specimen TCBF-B-4: brace axial force versus axial deformation relationships from DE and MCE hybrid test and OpenSees simulation (semi-rigid lower beam ends).

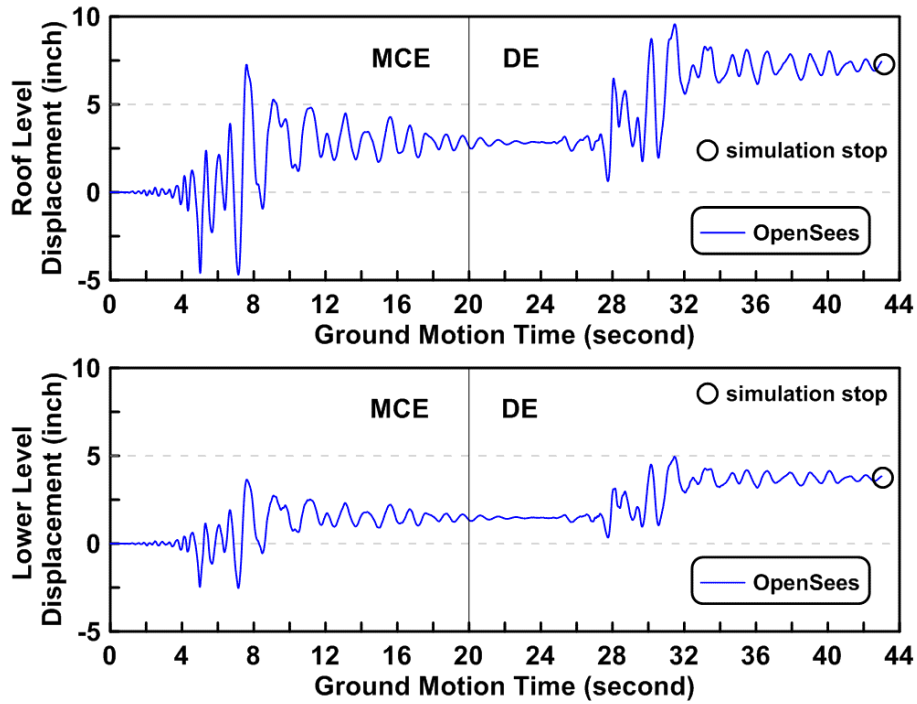


Figure 6.23 Simulated Specimen TCBF-B-4: displacement time histories subjected to MCE ground motion and then DE ground motion (semi-rigid lower beam ends).

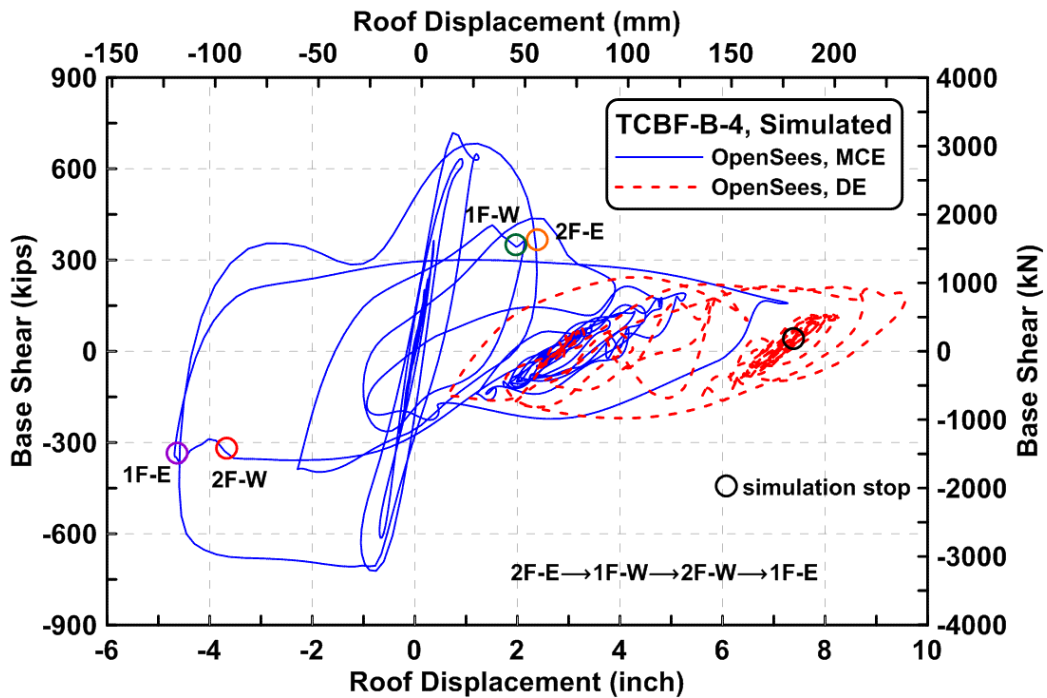


Figure 6.24 Simulated Specimen TCBF-B-4: base shear versus roof displacement relationships subjected to MCE ground motion and then DE ground motion (semi-rigid lower beam ends).

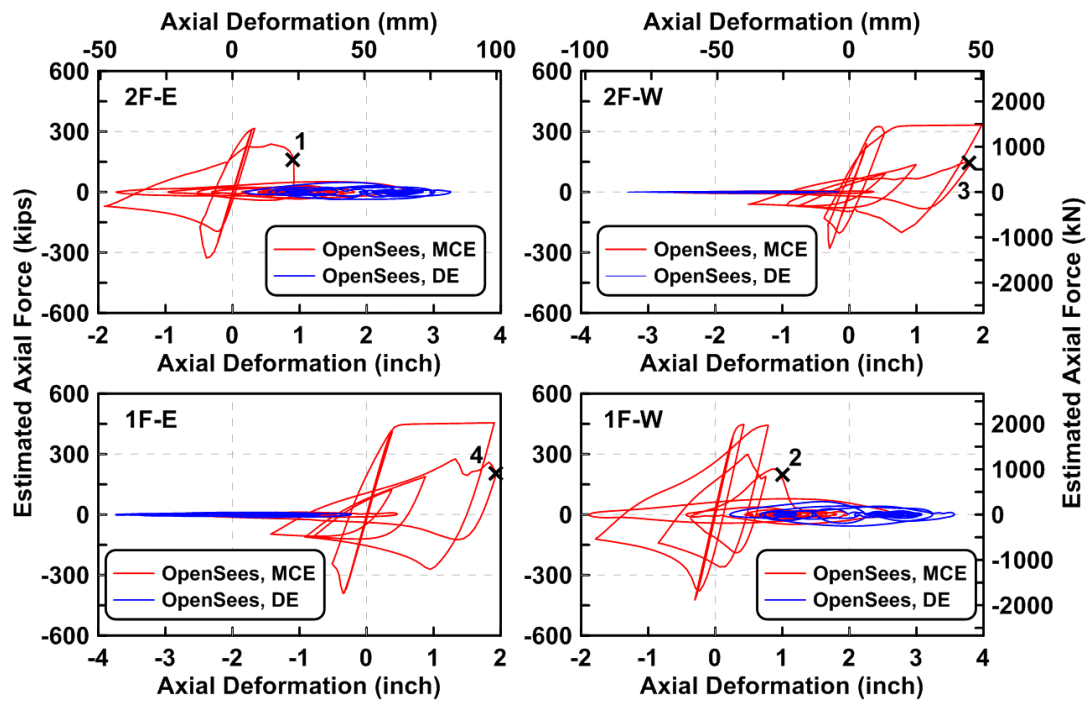


Figure 6.25 Simulated Specimen TCBF-B-4: brace axial force versus axial deformation relationships subjected to MCE ground motion and then DE ground motion (semi-rigid lower beam ends).

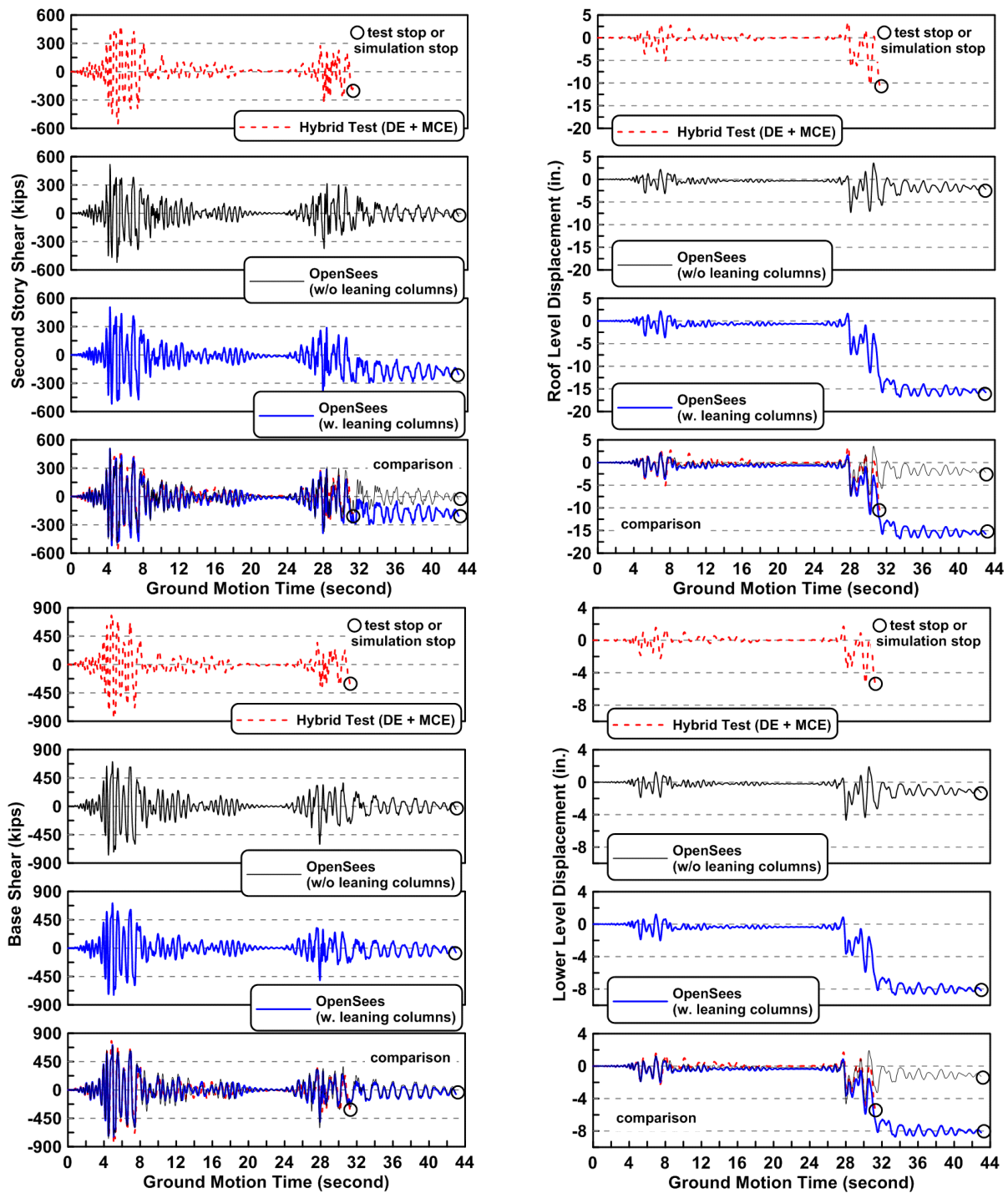


Figure 6.26 Specimen TCBF-B-4: story shear force and story displacement histories subjected to DE ground motion and then MCE ground motion (with versus without leaning columns in the OpenSees models).

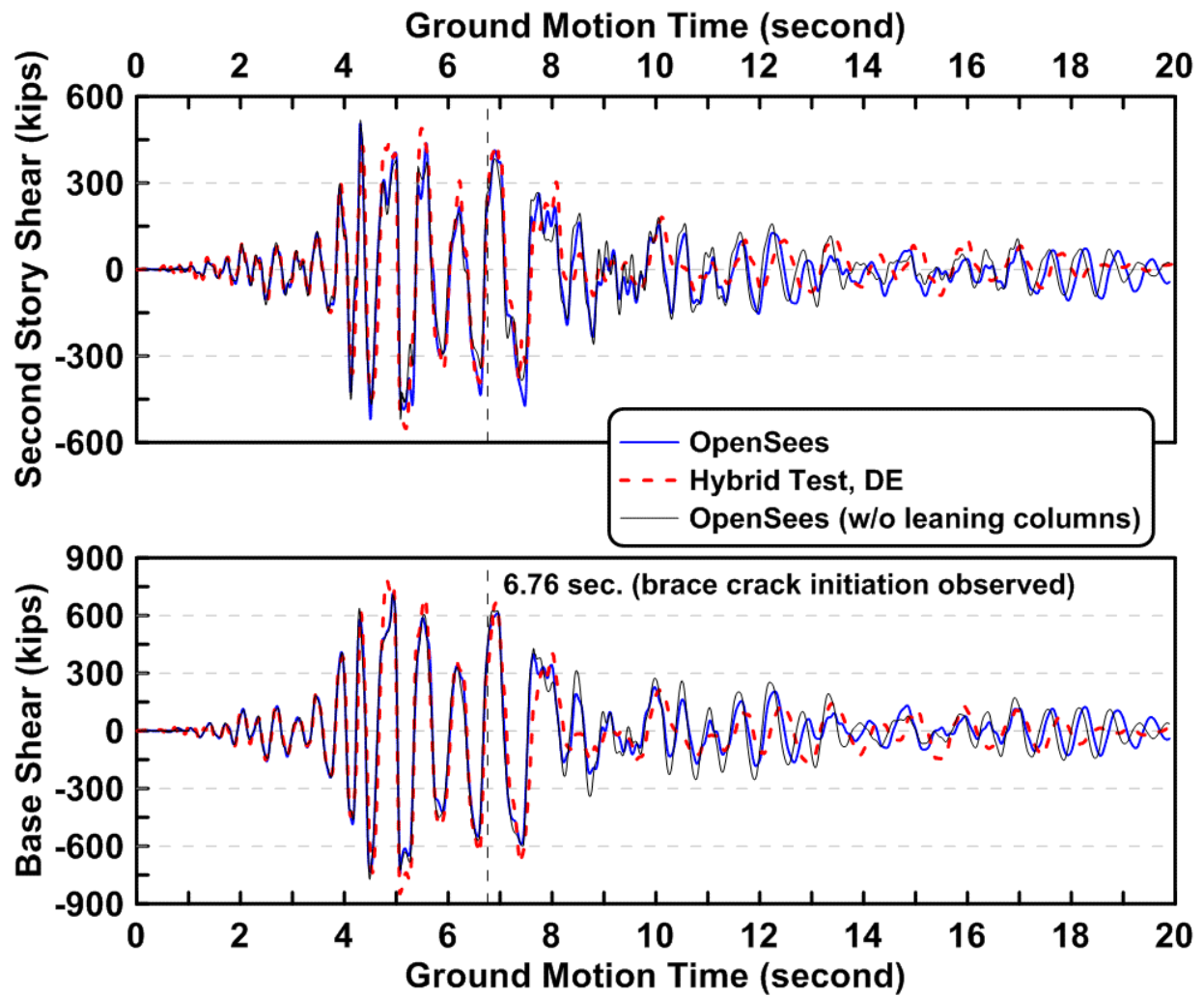


Figure 6.27 Specimen TCBF-B-4: tory shear force histories under the DE ground motion (with versus without leaning columns in the OpenSees models).

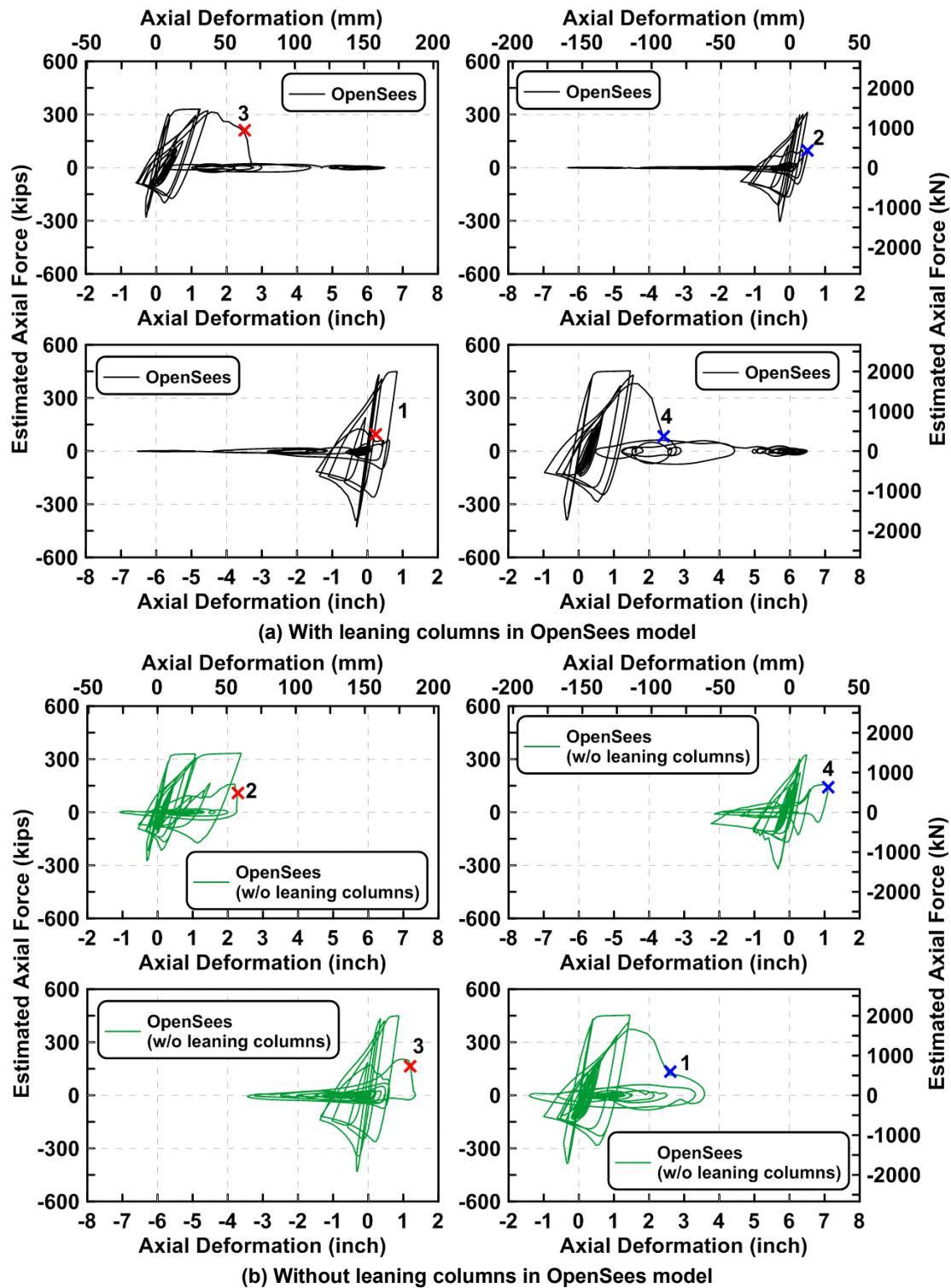


Figure 6.28 Simulated Specimen TCBF-B-4: brace axial force versus axial deformation relationships subjected to DE and MCE ground motions.

6.4 COMPARISON OF SQUARE HSS BRACE CYCLIC BEHAVIORS USING OPENSEES

Square hollow structural sections are the most popular section shape used in braced frame structures. They are structurally efficient, economical, and easy to handle at construction sites. Currently, about 88 available square HSS standard dimensions are listed in the AISC Manual of Steel Construction [AISC 2001]. The width of available sections range from 1-1/4 in. (HSS 1-1/4) to 16 in. (HSS 16); the width-to-wall thickness ratios (b/t) range from 5.58 to 54.5. There are also larger hollow structural sections (from HSS 18 to HSS 24—also called jumbo square HSS) available by special request from HSS manufacturers. For HSS widths larger than 3 in. but smaller than 18 in., there are 61 available sections and only 40 of these are compact sections. The dimensions of these compact sections are listed in Table 6.2.

Because of the expense in conducting tests on full-scale specimens, a simplified investigation of the effect of b/t ratio and kL/r slenderness ratio on brace energy-dissipation capacity under cyclic loadings was conducted using OpenSees. The 40 compact sections in Table 6.2 were modeled in OpenSees using fiber sections. The modeling used for these parametric studies is the similar to that described in Section 6.1. However, the yield strength was set equal to 46 ksi for all of the models. The number of elements along the brace length was increased from 4 to 20. The low-cycle fatigue material parameters recommended by Uriz and Mahin ($\varepsilon_0 = 0.099$, $m = -0.458$) were used for all if the brace models [Uriz and Mahin 2008]. This assumption may not be valid due to the different degree that strain may localize in braces having different kL/r and b/t values. All of the other input parameters, except the cross-section geometries and longitudinal dimensions were the same as previously used. As done previously, net reduced section failures or brace-to-gusset plate connection failures were not considered.

The brace models were subjected to symmetric incremental cyclic loadings. The cross-sectional properties (b/t ratio and radius of gyration) of each section were fixed, and the length of the brace was varied to obtain kL/r ratios of 40, 60, 80, 100, 150, and 200. Note that $kL/r = 200$ is the AISC maximum limit permitted for compression members. Loading protocols were based on the lateral displacement protocol established for the two-story test frames. This is displacement drift protocol is defined in Table 5.1. To convert the protocol from story drifts to brace axial displacements, it was assumed that the braces were installed in a 45° angle configuration, as illustrated in Figure 6.29. The axial deformation protocols were determined using the equation shown in the left-hand corner of Figure 6.29. As a result, there were a total of 240 cyclic analyses conducted, considering 40 different cross sections and six different kL/r ratios. In some cases, unrealistically short or long brace lengths may result by having small braces with small sections and kL/r ratios, or large sections and kL/r ratios. Because of the limitation of OpenSees in predicting local buckling and brace fracture, this investigation was not able to determine the exact fatigue life or energy-dissipation capacity of the selected braces, but helps provide understanding the overall influence of b/t and kL/r on brace cyclic behavior.

Strut axial force versus axial deformation relationship, axial force versus out-of-plane deformation relationship, and cumulative energy dissipation were the main responses of interest. Outputs from the simulations were normalized for easy comparison. For example, axial forces

were normalized by axial tension yield forces (P_y), axial deformations were normalized by yield deformations (δ_y) under tensile loading, brace out-of-plane deformations were also normalized by δ_y , and the cumulative energy dissipations were normalized by $P_y \cdot \delta_y$.

Response plots for two specific HSS braces with different kL/r ratios are shown in Figures 6.30 and 6.31. Plots for all 240 cases are shown in Appendix J. Table 6.3 summarizes the normalized cumulative energy dissipation of selected square hollow structural sections for different kL/r ratios. Figure 6.32 to 6.37 summarize the normalized cumulative energy dissipation ratios for each kL/r ratio in bar chart format, and Figure 6.38 combined those results in a single plot.

In general, the normalized cumulative energy-dissipation ratio is a minimum for sections with kL/r ratios between 60 and 100. The energy-dissipation capacity did not change that much for the square HSS with slenderness ratios equal to 60, 80, or 100. This range is typical for braces used in practice. When the kL/r ratio increased in the range from 80 to 200, the normalized cumulative energy dissipation increased (due to the increasing contribution of tension yielding). Similarly, the normalized cumulative energy-dissipation ratio increased as the kL/r ratio decreased from 60 to 40 (stocky braces with limited deterioration of compression capacity during buckling). In most cases, the normalized cumulative energy dissipation was larger for very stocky braces than for very slender braces (Figure 6.38 and Table 6.3).

The AISC code specifies an upper bound limit on kL/r for the braces used in special concentric braced frames:

$$\frac{kL}{r} \leq 4 \sqrt{\frac{E}{F_y}} = 4 \sqrt{\frac{29000}{46}} = 100.4 \quad (6.5)$$

where E is the Young's modulus of steel, and F_y is the yield strength of the steel. As seen, for the conditions assumed in these analyses, the slenderness ratio limit is equal to 100.4.

Table 6.4 groups the b/t ratios into three ranges to help understand how b/t ratio effects the energy dissipation. Group 1 contains the square HSS sections that satisfy the seismic compactness requirements of the AISC Seismic Provisions [2010a] for structural steel buildings. Group 2 contains the square HSS sections that satisfy the seismic compactness per the 2005 AISC Seismic Provisions, but that do not satisfy the 2010 AISC Seismic Provisions. Group 3 contains sections that are not seismically compact. From Figure 6.39, it appears that b/t ratios have limited impact on normalized energy dissipation. In particular, the 14% reduction of the limit on b/t ratio imposed by the 2010 AISC Seismic Provisions has little effect in these fiber model analyses. There is some difference when b/t exceeds 16.1, but it is not too great. Limit actually does not improve the energy-dissipation capacity of the braces significantly. However, these results related to the effect of b/t ratio should be viewed with skepticism. The fiber models do not account for the effect of section distortion (which reduces brace compression capacity) due to local buckling, and the tremendous effect of local buckling on the fatigue life of materials in critical regions of the brace. Although these results show some interesting dependencies with

respect to kL/r , the inability to account for sensitivity of response to b/t raises some interesting questions about the veracity of fiber-based models, suggesting the need for additional full-scale experiments and numerical analyses using more sophisticated finite element models that can account for local buckling of sections and the initiation and propagation of cracks due to low-cycle fatigue.

Table 6.2 The dimensions of selected square hollow structural sections.

Section Name	r_x (in.)	b/t	A_s (in ²)	Section Name	r_x (in.)	b/t	A_s (in ²)
HSS 16×16×5/8	6.25	24.5	35	HSS 6×6×5/16	2.31	17.6	6.43
HSS 14×14×5/8	5.44	21.1	30.3	HSS 6 ×6×1/4	2.34	22.8	5.24
HSS 14×14×1/2	5.49	27.1	24.6	HSS 5-1/2×5-1/2×3/8	2.08	12.8	6.88
HSS 12×12×5/8	4.62	17.7	25.7	HSS 5-1/2×5-1/2×5/16	2.11	15.9	5.85
HSS 12×12×1/2	4.68	22.8	20.9	HSS 5-1/2 ×5-1/2 ×1/4	2.13	20.6	4.77
HSS 10×10×5/8	3.8	14.2	21	HSS 5×5×1/2	1.82	7.75	7.88
HSS 10×10×1/2	3.86	18.5	17.2	HSS 5×5×3/8	1.87	11.3	6.18
HSS 10×10×3/8	3.92	25.7	13.2	HSS 5×5×5/16	1.9	14.2	5.26
HSS 8×8×5/8	2.99	10.8	16.4	HSS 5×5×1/4	1.93	18.5	4.3
HSS 8×8×1/2	3.04	14.2	13.5	HSS 5×5×3/16	1.96	25.7	3.28
HSS 8×8×3/8	3.1	19.9	10.4	HSS 4-1/2×4-1/2×1/2	1.61	6.68	6.95
HSS 8×8×5/16	3.13	24.5	8.76	HSS 4-1/2×4-1/2×3/8	1.67	9.89	5.48
HSS 7×7×5/8	2.58	9.05	14	HSS 4-1/2×4-1/2×5/16	1.7	12.5	4.68
HSS 7×7×1/2	2.63	12.1	11.6	HSS 4-1/2×4-1/2×1/4	1.73	16.3	3.84
HSS 7×7×3/8	2.69	17.1	8.97	HSS 4-1/2×4-1/2×3/16	1.75	22.9	2.93
HSS 7×7×5/16	2.72	21.1	7.59	HSS 4 ×4×1/2	1.41	5.6	6.02
HSS 7×7×1/4	2.75	27	6.17	HSS 4×4×3/8	1.47	8.46	4.78
HSS 6×6×5/8	2.17	7.33	11.7	HSS 4×4×5/16	1.49	10.7	4.1
HSS 6×6×1/2	2.23	9.9	9.74	HSS 4×4×1/4	1.52	14.2	3.37
HSS 6×6×3/8	2.28	14.2	7.58	HSS 4×4×3/16	1.55	20	2.58

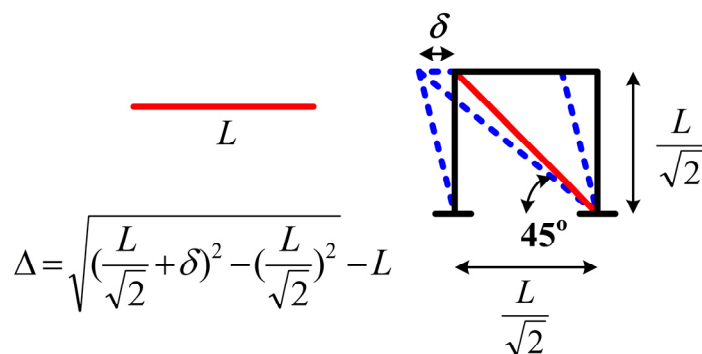


Figure 6.29 Assumed braced bay for the square HSS struts and the relationship between brace axial deformation and story drift.

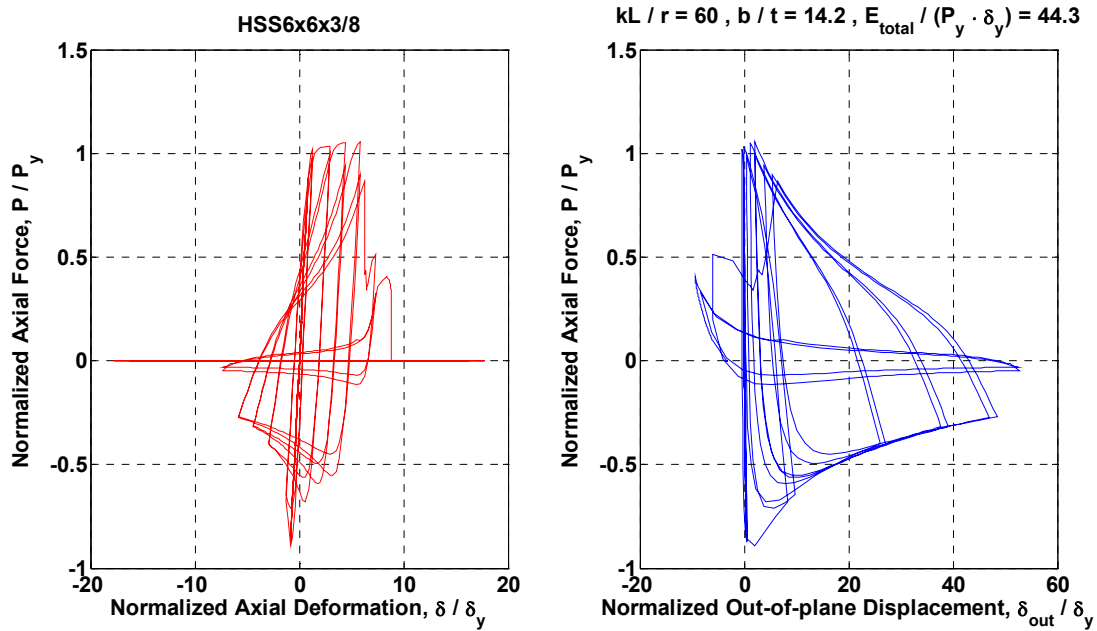


Figure 6.30 Normalized axial force versus normalized axial deformation and normalized out-of-plane deformation relationships of square HSS 6 × 6 × 3/8 with $kL/r = 60$.

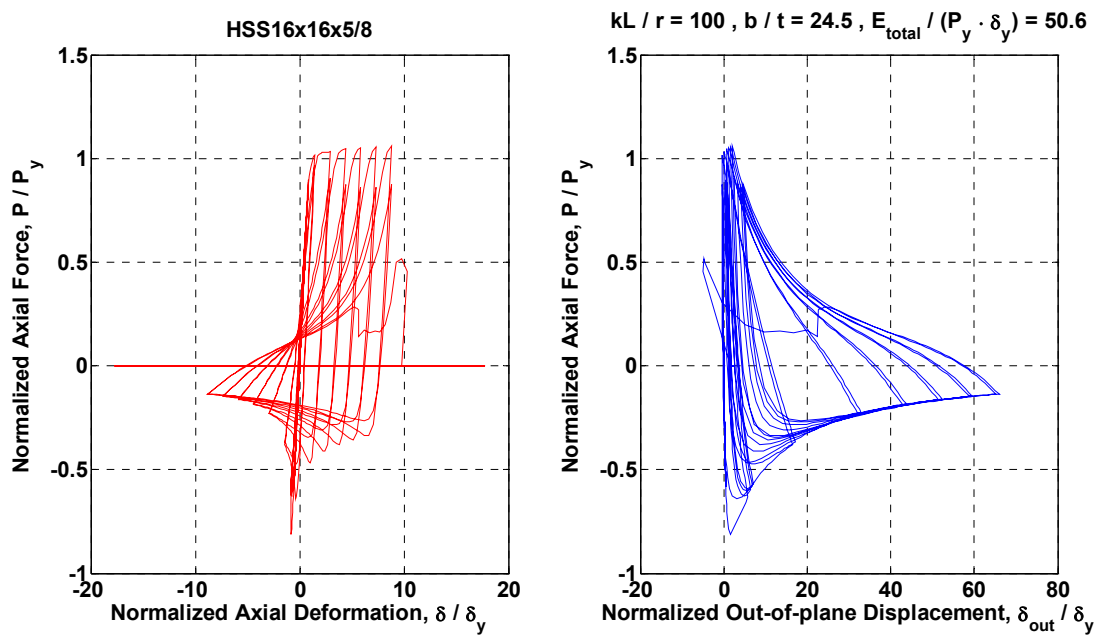


Figure 6.31 Normalized axial force versus normalized axial deformation and normalized out-of-plane deformation relationships of square HSS 16 × 16 × 5/8 with $kL/r = 100$.

Table 6.3 Normalized cumulative energy dissipation of selected square hollow structural sections under different kL/r ratios.

ID	Section Name	b/t	$E_{total} / (P_y \cdot \delta_i)$					
			kL/r					
			40	60	80	100	150	200
1	HSS 16 × 16 × 5/8	24.5	102.0	52.4	48.7	50.6	65.3	76.3
2	HSS 14 × 14 × 5/8	21.1	72.2	52.5	50.2	50.6	62.9	75.3
3	HSS 14 × 14 × 1/2	27.1	58.6	52.4	45.3	49.3	63.3	75.1
4	HSS 12 × 12 × 5/8	17.7	74.5	52.9	50.0	49.9	63.8	76.1
5	HSS 12 × 12 × 1/2	22.8	71.1	53.5	49.6	50.4	64.6	75.2
6	HSS 10 × 10 × 5/8	14.2	74.8	50.3	51.0	49.7	59.4	75.7
7	HSS 10 × 10 × 1/2	18.5	80.2	52.2	49.9	50.6	64.4	75.9
8	HSS 10 × 10 × 3/8	25.7	69.5	52.8	45.5	50.8	63.9	70.8
9	HSS 8 × 8 × 5/8	10.8	94.1	52.6	46.7	51.7	61.0	74.9
10	HSS 8 × 8 × 1/2	14.2	100.3	49.8	48.8	49.4	58.2	73.1
11	HSS 8 × 8 × 3/8	19.9	95.7	46.5	49.9	50.8	62.9	76.3
12	HSS 8 × 8 × 5/16	24.5	71.9	52.0	47.8	51.4	62.8	53.2
13	HSS 7 × 7 × 5/8	9.05	64.6	49.3	46.1	49.9	60.1	73.5
14	HSS 7 × 7 × 1/2	12.1	74.3	49.8	46.2	50.4	60.2	72.8
15	HSS 7 × 7 × 3/8	17.1	76.5	43.6	50.3	47.4	65.2	72.7
16	HSS 7 × 7 × 5/16	21.1	65.8	47.0	48.7	49.5	63.2	74.3
17	HSS 7×7×1/4	27	62.6	49.9	47.9	51.2	63.1	76.7
18	HSS 6×6×5/8	7.33	69.8	48.5	47.9	47.5	59.9	69.3
19	HSS 6×6×1/2	9.9	89.0	51.2	47.7	48.1	59.5	68.8
20	HSS 6×6×3/8	14.2	60.2	44.3	47.0	48.9	62.0	51.9
21	HSS 6×6×5/16	17.6	65.4	47.3	49.8	48.6	63.8	76.4
22	HSS 6×6×1/4	22.8	64.2	46.4	49.3	49.7	64.7	54.7
23	HSS 5-1/2×5-1/2×3/8	12.8	70.1	48.6	44.9	48.8	58.4	72.6
24	HSS 5-1/2×5-1/2×5/16	15.9	65.2	47.6	45.3	47.9	63.6	71.5
25	HSS 5-1/2×5-1/2×1/4	20.6	67.0	46.9	48.8	47.4	63.2	75.0
26	HSS 5×5×1/2	7.75	79.5	51.2	49.4	47.5	54.5	69.5
27	HSS 5×5×3/8	11.3	68.9	50.7	45.5	50.3	59.5	71.6
28	HSS 5×5×5/16	14.2	74.1	49.2	44.9	49.4	58.4	73.4
29	HSS 5×5×1/4	18.5	67.9	47.7	47.0	48.0	63.6	71.4
30	HSS 5×5×3/16	25.7	55.3	48.1	47.5	51.8	59.9	65.7
31	HSS 4-1/2×4-1/2×1/2	6.68	64.0	48.7	46.7	47.6	59.2	68.3
32	HSS 4-1/2×4-1/2×3/8	9.89	76.5	49.2	46.6	51.4	61.2	74.3
33	HSS 4-1/2×4-1/2 ×5/16	12.5	103.7	50.6	46.0	50.9	59.7	74.4
34	HSS 4-1/2×4-1/2×1/4	16.3	61.3	46.6	49.4	51.1	63.7	74.1
35	HSS 4-1/2×4-1/2×3/16	22.9	59.3	41.9	47.7	50.6	61.9	54.2
36	HSS 4×4×1/2	5.6	77.1	49.1	46.1	46.7	53.1	69.0
37	HSS 4×4×3/8	8.46	79.1	49.8	47.7	48.5	60.3	69.5
38	HSS 4×4×5/16	10.7	77.2	52.0	46.9	51.1	61.6	74.6
39	HSS 4×4×1/4	14.2	104.4	51.2	46.2	51.0	59.9	74.8
40	HSS 4×4×3/16	20	58.0	46.4	44.9	52.4	63.3	73.1
-	Mean	16.3	74.1	49.3	47.6	49.7	61.5	71.1
-	Median	16.1	71.5	49.5	47.7	49.9	61.9	73.2
-	Standard Deviation	6.2	13.1	2.7	1.8	1.5	2.73	6.5
-	Maximum	27.1	104.4	53.5	51	52.4	65.3	76.7
-	Minimum	5.6	55.3	41.9	44.9	46.7	53.1	51.9
-	Range	21.5	49.1	11.6	6.1	5.8	12.2	24.8

Table 6.4 Normalized cumulative energy dissipation of selected group of square hollow structural sections under different kL/r ratios.

Group ID	b/t range (no. of sections in the group)	$E_{\text{total}} / (P_y \cdot \delta_y)$						
		Statistical Value	kL/r					
			40	60	80	100	150	200
1	$b/t < 13.8$ (14)	Mean	77.7	50.1	46.7	49.3	59.2	71.6
		Median	76.7	49.8	46.6	49.4	59.8	72.1
		Standard Deviation	11.3	1.3	1.1	1.7	2.4	2.5
		Maximum	103.7	52.6	49.4	51.7	61.6	74.9
		Minimum	64	48.5	44.9	46.7	53.1	68.3
		Range	39.7	4.1	4.5	5.0	8.5	6.7
2	$13.8 \leq b/t \leq 16.1$ (6)	Mean	79.8	48.8	47.2	49.4	60.2	70.0
		Median	74.5	49.5	46.6	49.4	59.7	73.2
		Standard Deviation	18.3	2.5	2.3	1.0	2.1	9.0
		Maximum	104.4	51.3	51	51.0	63.6	75.7
		Minimum	60.2	44.3	44.9	47.9	58.2	51.9
		Range	44.2	6.9	6.1	3.2	5.4	23.8
3	$b/t > 16.1$ (20)	Mean	69.9	48.9	48.4	50.1	63.5	71.1
		Median	67.4	47.9	48.7	50.6	63.5	74.6
		Standard Deviation	11.9	3.4	1.7	1.4	1.2	7.8
		Maximum	102.1	53.4	50.3	52.4	65.3	76.7
		Minimum	55.3	41.8	44.9	47.4	59.9	53.2
		Range	46.7	11.6	5.4	5.1	5.4	23.5

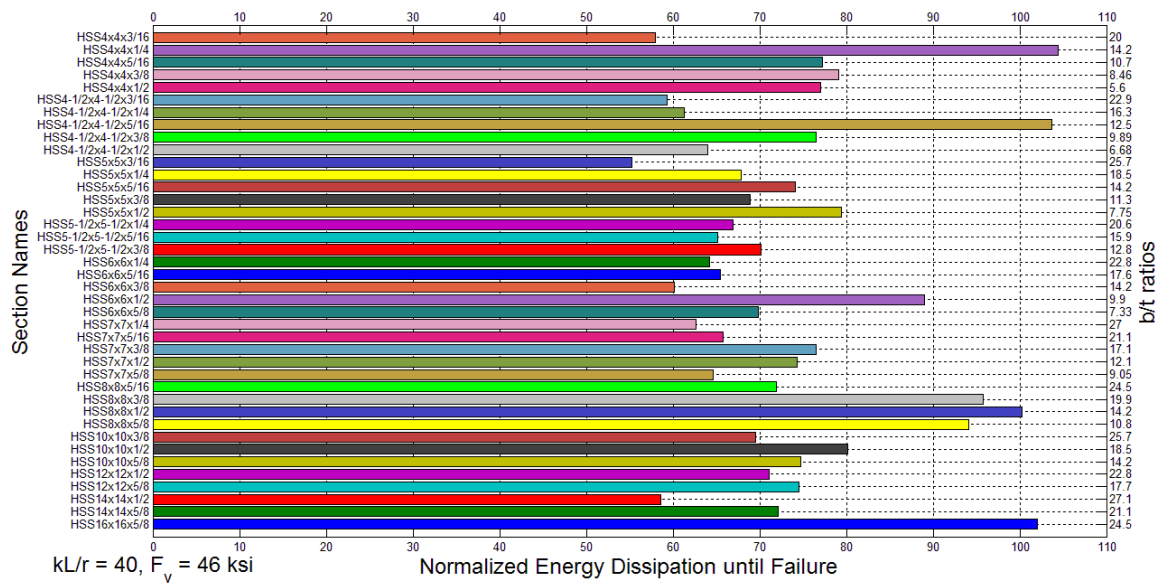


Figure 6.32 Normalized energy dissipation of selected square hollow structural sections until brace failure ($kL/r = 40$).

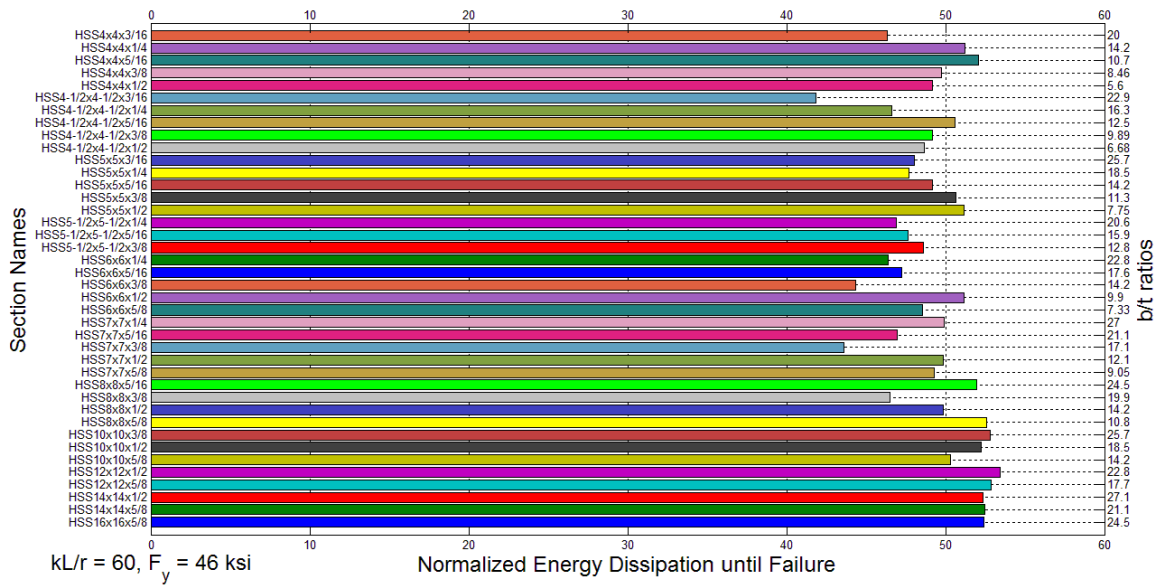


Figure 6.33 Normalized energy dissipation of selected square hollow structural sections until brace failure ($kL/r = 60$).

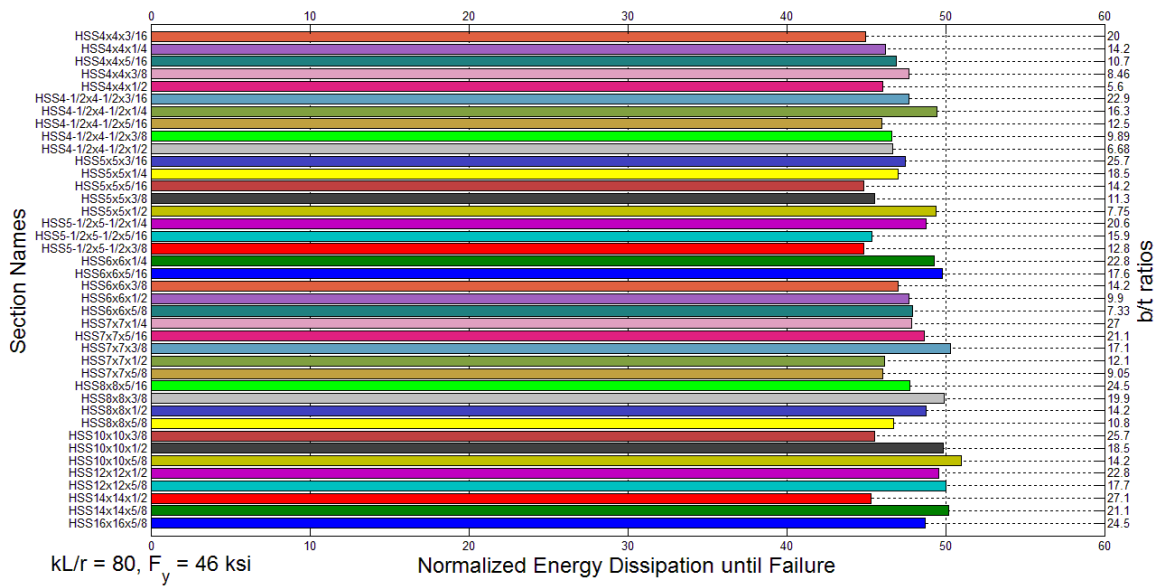


Figure 6.34 Normalized energy dissipation of selected square hollow structural sections until brace failure ($kL/r = 80$).

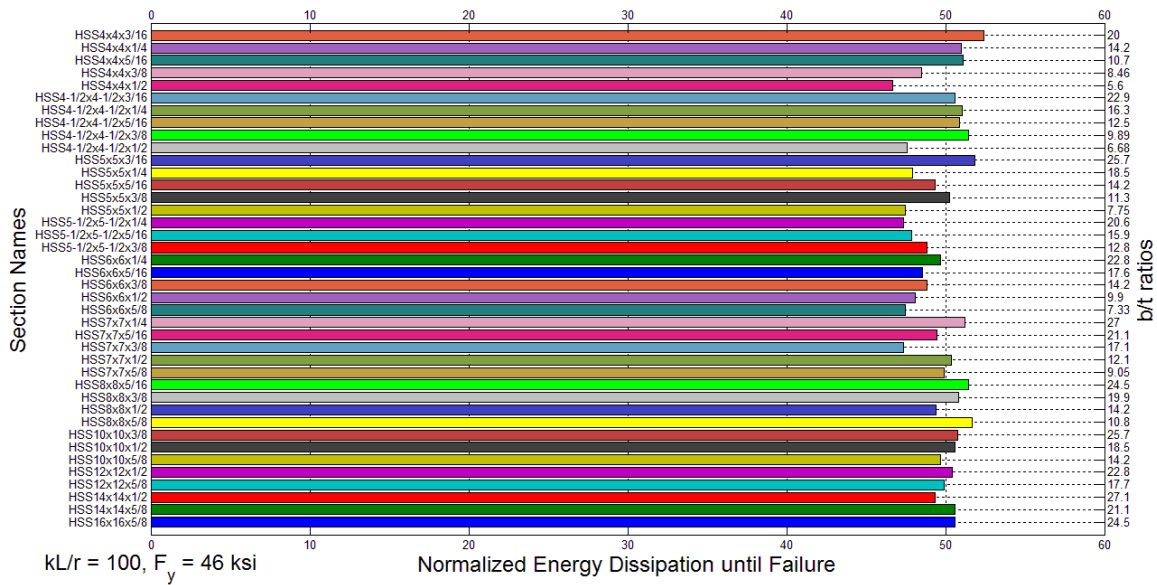


Figure 6.35 Normalized energy dissipation of selected square hollow structural sections until brace failure ($kL/r = 100$).

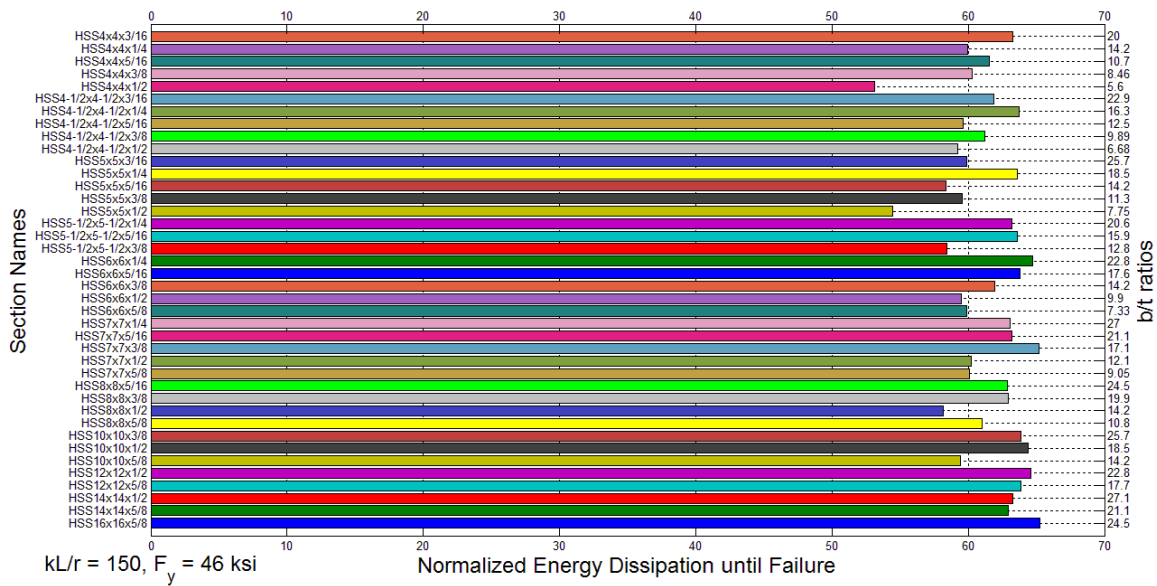


Figure 6.36 Normalized energy dissipation of selected square hollow structural sections until brace failure ($kL/r = 150$).

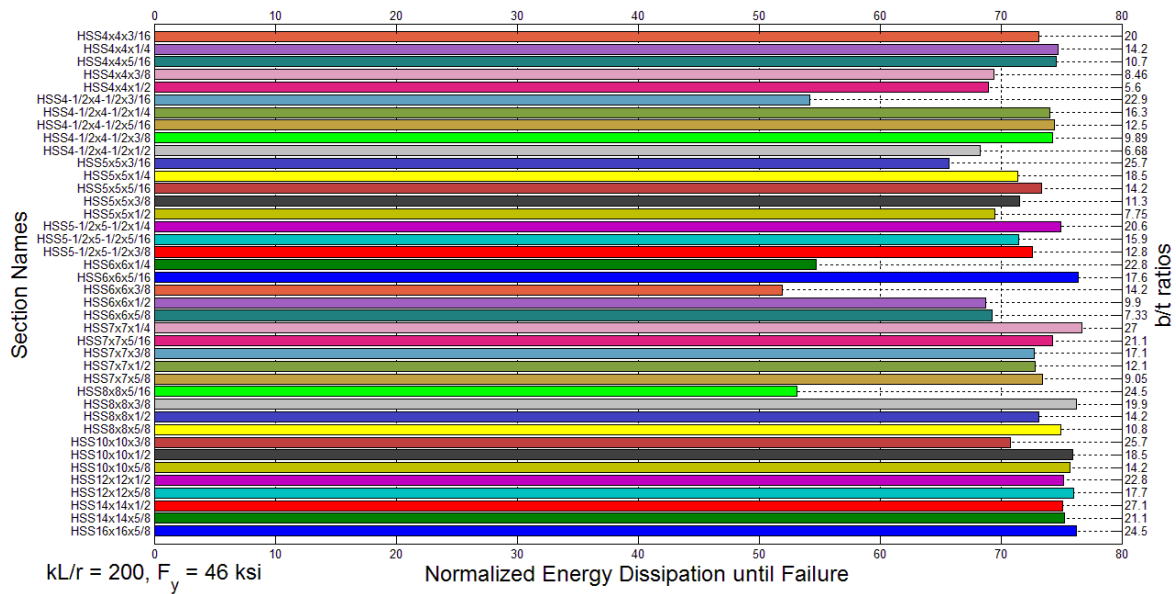


Figure 6.37 Normalized energy dissipation of selected square hollow structural sections until brace failure ($kL/r = 200$),

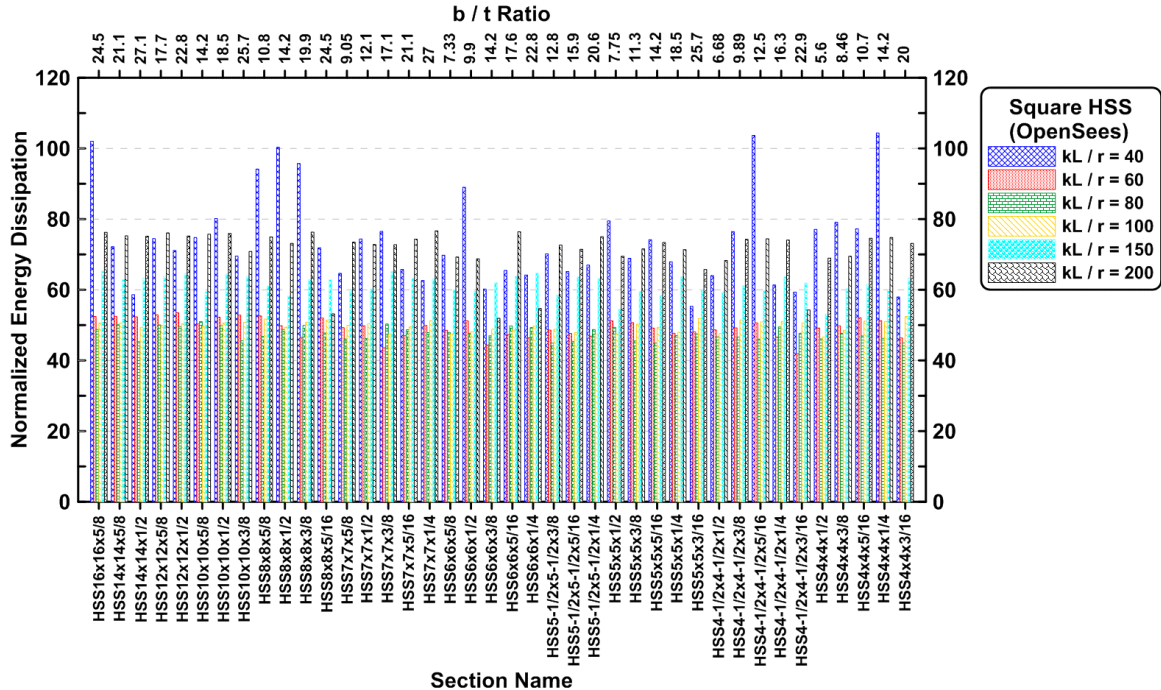


Figure 6.38 Normalized energy dissipation until brace failure of selected square hollow structural sections with different kL/r ratios.

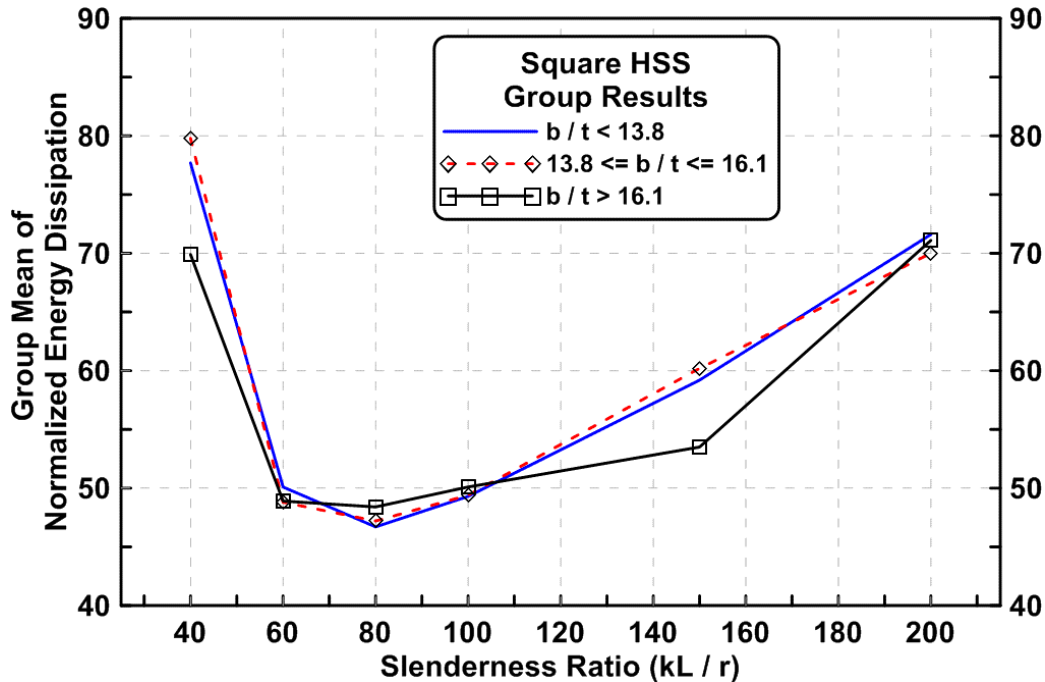


Figure 6.39 Group comparisons of normalized energy dissipation of selected square hollow structural sections with different kL/r ratios.

6.5 PREDICTION OF STRUT AND BRACED FRAME SPECIMEN BEHAVIORS USING LS-DYNA

More detailed 3D finite element models of individual struts and of the braced frame test specimens were developed using shell elements available in the software package LS-DYNA [LSTC 2007]. These models permitted consideration of material yielding, deterioration and rupture of materials due to low-cycle fatigue, local buckling of critical local regions, global buckling of elements and geometric nonlinearities. The models were not formulated to account for issues related to fracture mechanics. Numerous shell elements were used to model elements and connection regions. Material models including plasticity and damage mechanics were utilized.

Shell elements with Belytschko-Tsay formulation were assigned in the model. The material type named Damage_3 (MAT 153) developed by Huang and Mahin [2010] in LS-DYNA was selected to model the low-cycle fatigue deterioration behavior of the steel. This model incorporates a low-cycle fatigue damage index; the member properties can deteriorate (erode) and the local element removed from the model when the low-cycle fatigue life of the material is exceeded. Material properties used here were calibrated from existing cyclic test results extracted from the existing study [Fujimoto et al. 1985] and properly scaled to match the yield strength as reported in the mill certificates for each specimen.

Adaptive meshing [LSTC 2007] with hourglass control was selected in the model to account for local deformation concentration along bracing members (also used in the two-story braced frame simulations) during the simulation. The minimum element size to be adapted was

set equal to the thickness of HSS section wall. Explicit analysis with time scaling was used to simulate the specimens under quasi-static cyclic loading. No initial member imperfections were introduced in the finite element model since the 3D frame models are likely to have in-plane and other deformations to trigger global buckling of the braces, or buckling can be triggered by numerical round-off errors during the analysis.

6.5.1 LS-DYNA Analysis of Individual Struts

The same specimens analyzed in Section 6.1 using OpenSees fiber-based elements are again analyzed using shell elements in LS-DYNA. Figure 6.40 shows the mesh pattern of a simple brace modeled as a complete strut including gusset plates. In LS-DYNA there are several ways to simplify this model and speed execution of the analysis of the strut; see a reduced model and reduced half model shown in Figure 6.41. The experimental results of square HSS simple struts [Yang and Mahin 2005] tested under different loading histories were utilized to compare with the simulation outputs from LS-DYNA. Figure 6.40 shows the mesh pattern of a simple strut model used here (the full model).

Figures 6.42 to 6.50 illustrate the LS-DYNA simulation results compared with the test data and photos taken during the cyclic testing. The analyses were able to match the tests quite well, including the nature and time of brace rupture. The discrepancy of the model is most likely due to the material constitutive model not exactly matching the materials used in the test specimen. Moreover, initial imperfections and residual fabrication stresses were not included in the model. It is clear that localized buckling of HSS section walls can be simulated using shell elements, and that the finite element model properly mimics the brace rupture behavior that occurs due to damage accumulation due to low-cycle fatigue.

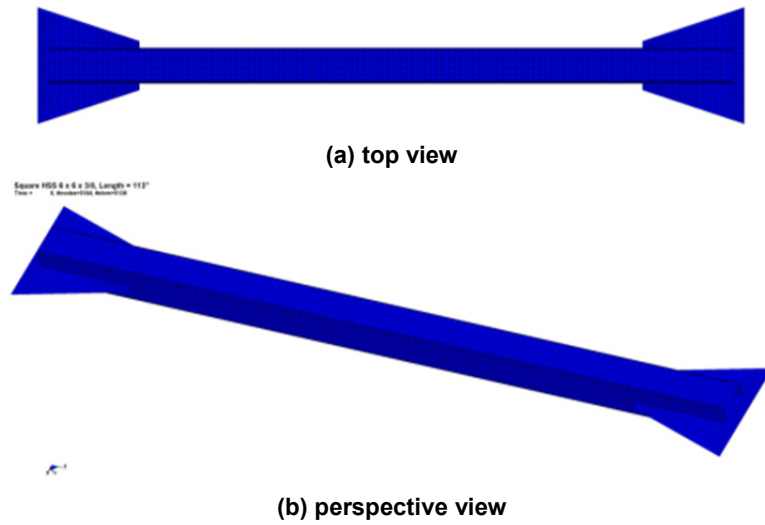


Figure 6.40 Mesh pattern for the simple strut modeling in LS-DYNA.

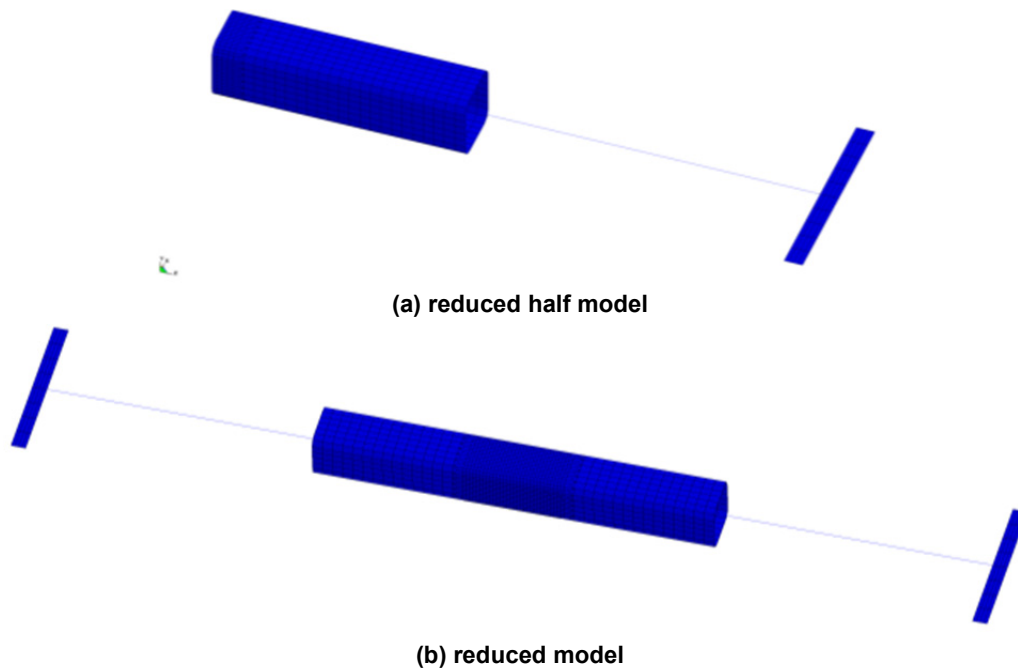


Figure 6.41 Illustration of simplified models for the simple strut modeling in LS-DYNA.

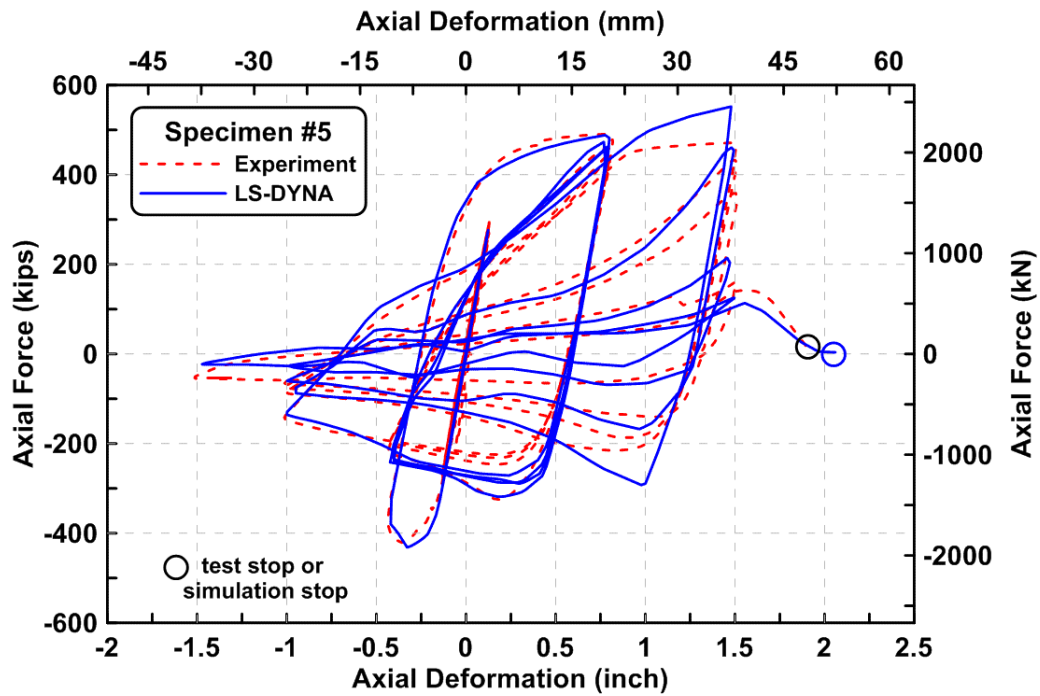


Figure 6.42 Axial force versus axial deformation relationship of Specimen #5 from experiment and LS-DYNA simulation.

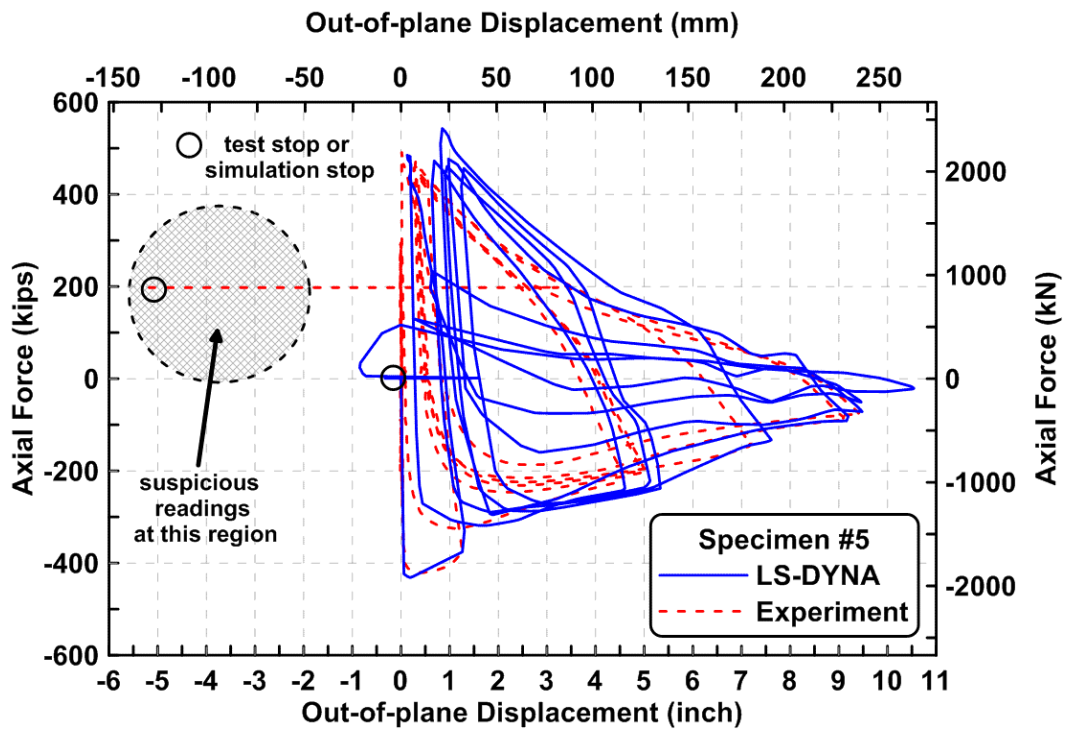
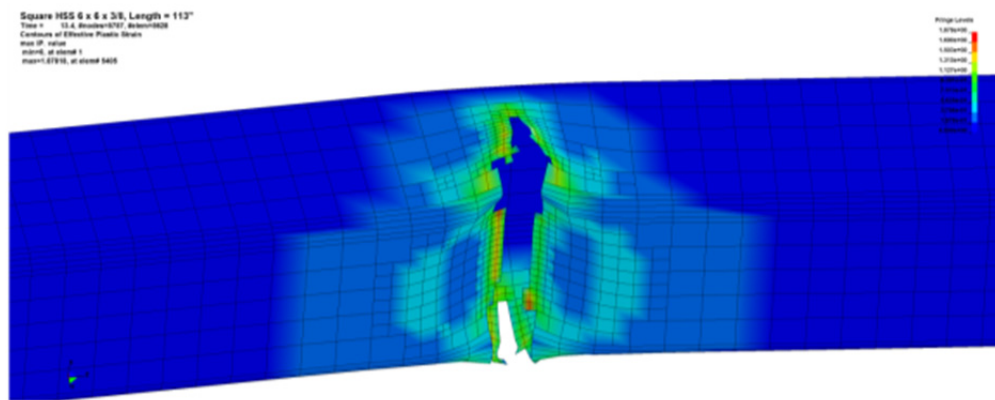
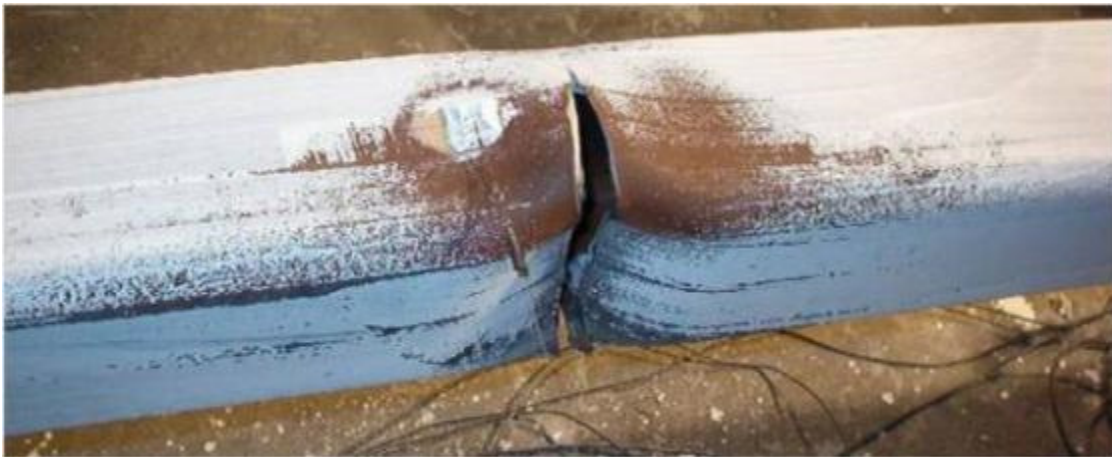


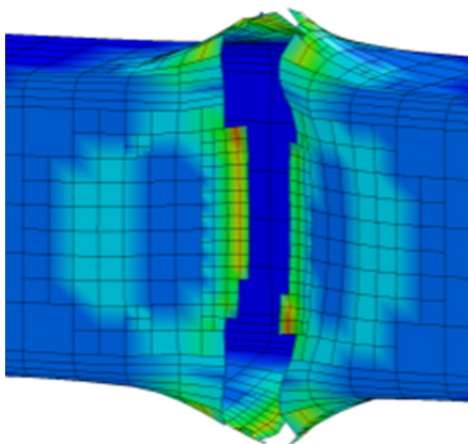
Figure 6.43 Axial force versus out-of-plane displacement relationship of Specimen #5 from experiment and LS-DYNA simulation.



(a) effective plastic strain distribution contour from LS-DYNA simulation



(b) crack propagated at the middle length of brace (extracted from Figure 6 in Yang and Mahin [2005])



(c) effective plastic strain distribution contour from LS-DYNA simulation (closed view)



(d) closed view at middle of brace (extracted from Figure 6 in Yang and Mahin, [2005])

Figure 6.44 Comparison between actual test and LS-DYNA simulation results at the final cycle.

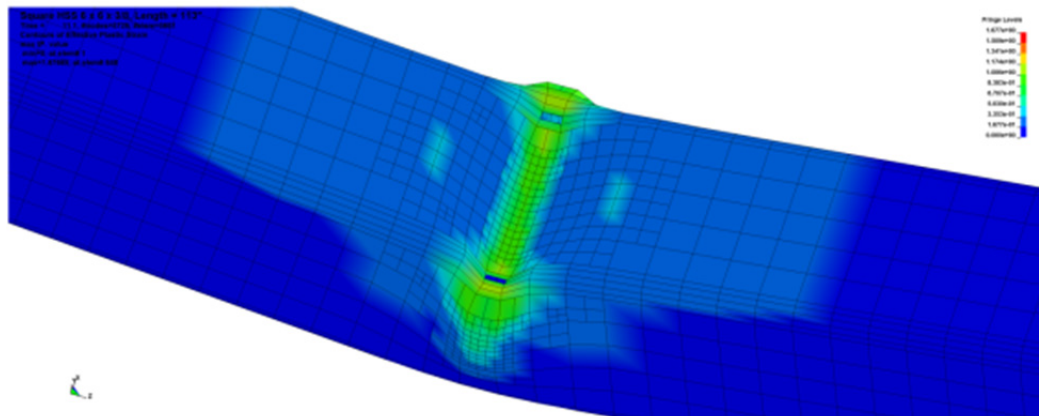
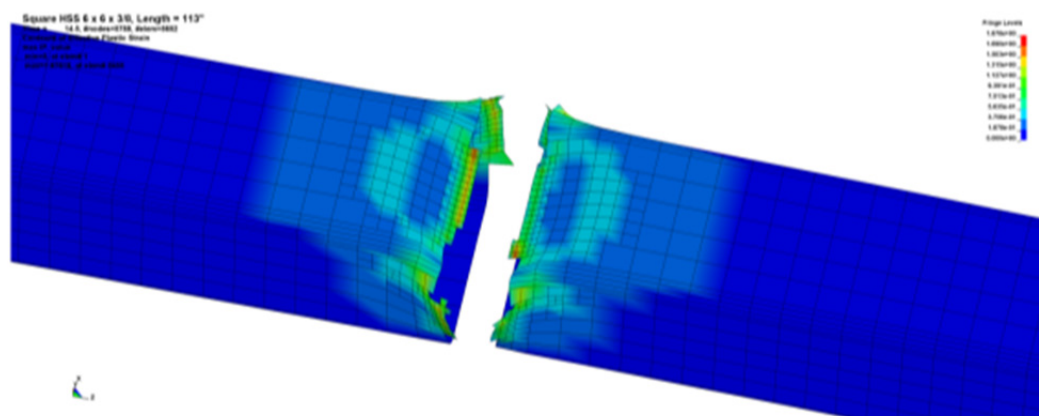
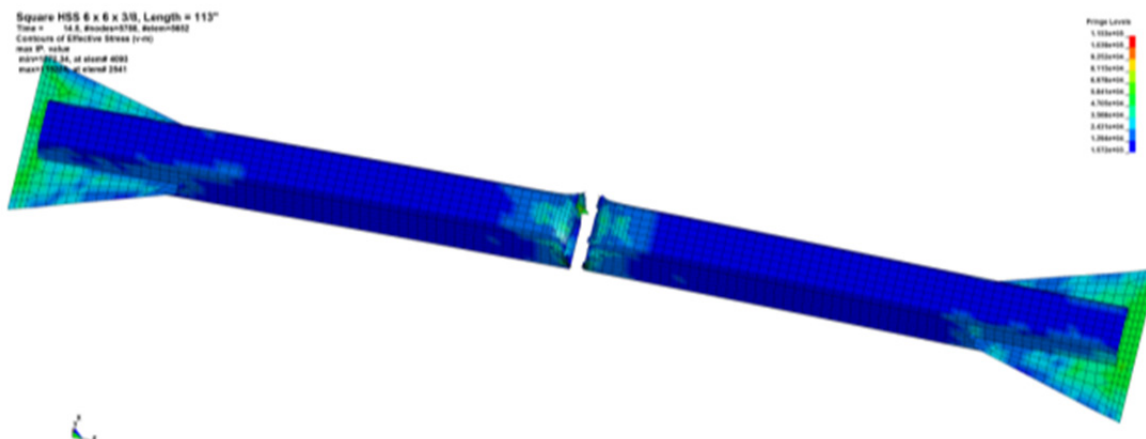


Figure 6.45 Crack initiation in HSS brace section wall simulated by LS-DYNA model.



(a) closed view of the strut after rupture



(b) overview of the strut after rupture

Figure 6.46 Complete fracture in LS-DYNA strut model.

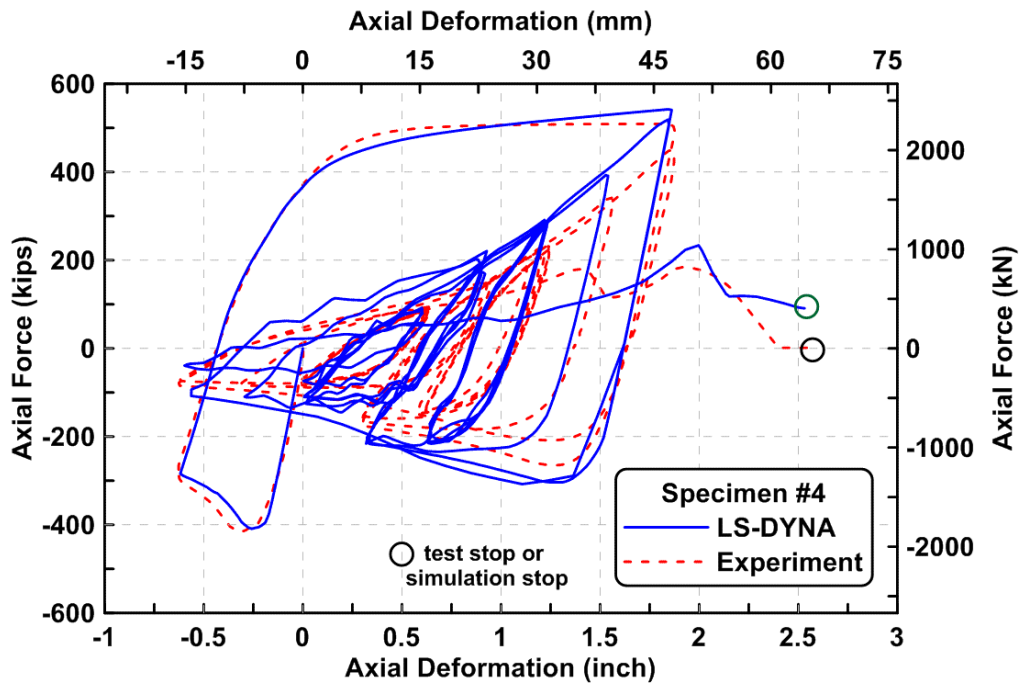


Figure 6.47 Axial force versus axial deformation relationship of Specimen #4 from experiment and LS-DYNA simulation.

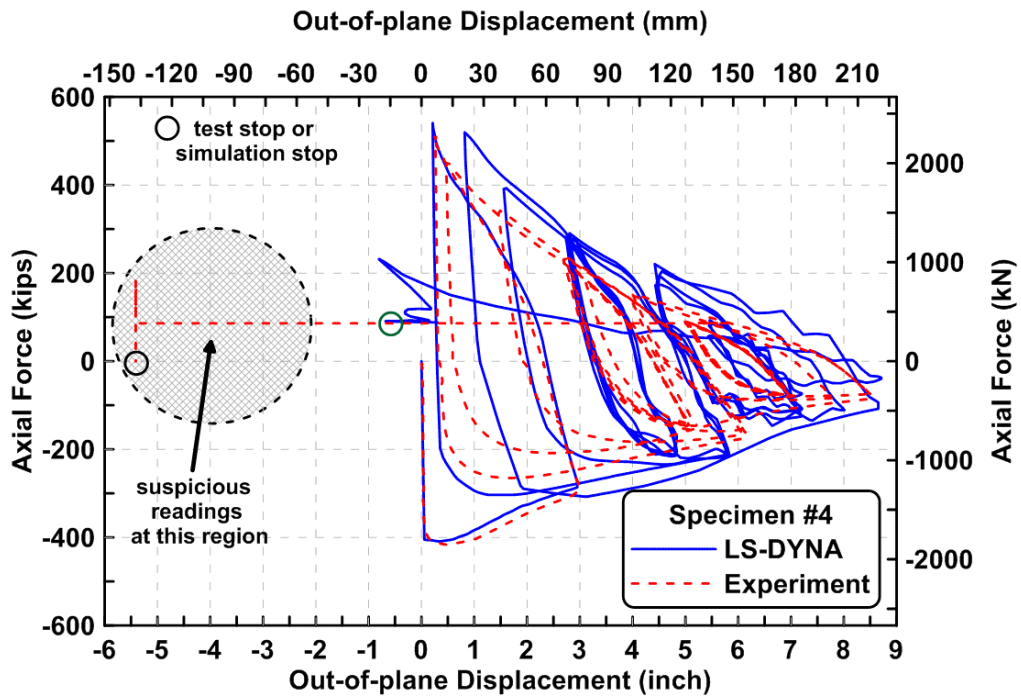
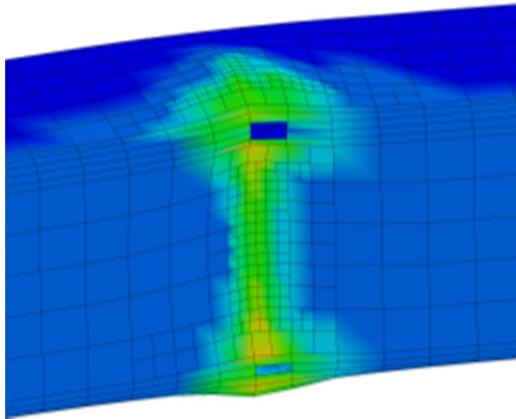
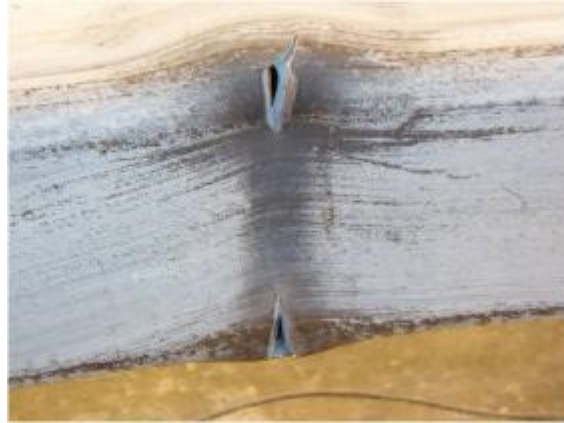


Figure 6.48 Axial force versus out-of-plane displacement relationship of Specimen #4 from experiment and LS-DYNA simulation.

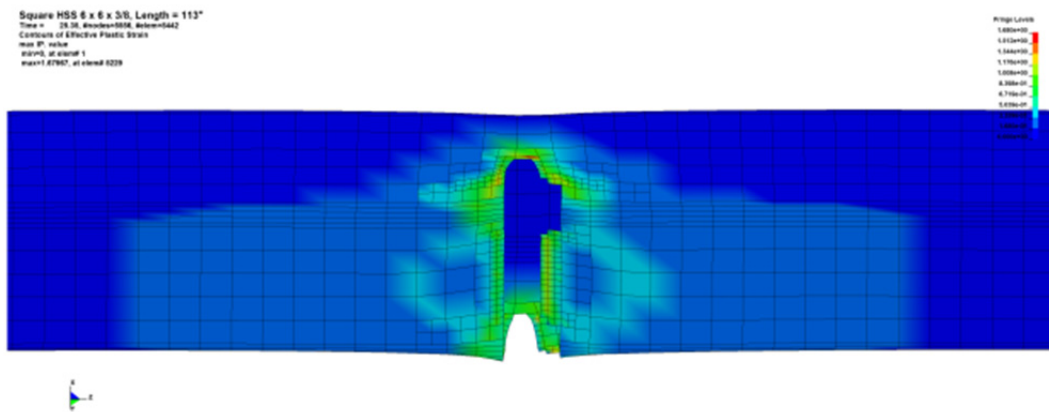


(a) crack initiation in HSS section walls (LS-DYNA model)



(b) crack initiation at center region of brace (extracted from Figure 12 in Yang and Mahin [2005])

Figure 6.49 Comparison between actual test and FE model under near-fault loading protocol.



(a) LS-DYNA model



(b) test photo at middle length of HSS brace (extracted from Figure 12 in Yang and Mahin [2005])

Figure 6.50 Comparison between actual test and finite element model at the final stage of testing.

6.5.2 LS-DYNA Analysis of Quasi-Static TCBF Test Specimens

The two-story quasi-static tests were also simulated using LS-DYNA. Figure 6.51 shows the entire model and the mesh layout for Specimen TCBF-B-1. To save simulation time, prescribed displacement histories for both floor levels were specified based on the measured test results. This is not the same as the method used during the test where half of the force applied at the roof level was imposed at the lower floor level. LS-DYNA does not have load functions that are similar to actual test conditions. However, the whiffletree [Harris and Sabins 1999] concept can be applied in the LS-DYNA model to represent the actual load pattern. Other possible numerical constraint schemes [Huang and Mahin 2010] can also be applied in LS-DYNA (for monotonic quasi-static pushover). This is an area for further investigation.

Figure 6.52 shows the LS-DYNA simulated base shear versus roof displacement relationship superimposed on the actual experimental results obtained from Specimen TCBF-B-1. The simulation results match the quasi-static test results quite well. The hysteretic loops from the finite element simulation show a bit more rapid initial deterioration in the positive direction than the experiment and dissipate more energy than the test specimen in the final few cycles. Localized buckling of brace section walls and beam-to-gusset plate connection regions were simulated (see Figures 6.53 and 6.54). Crack initiation and partial propagation are also shown. For the estimated brace axial forces versus axial deformation relationships (Figure 6.55), the LS-DYNA simulation predicted the peak brace axial forces quite well, and the brace axial deformations were relatively uniform than the actual test results. Similar to the results from OpenSees, the predicted brace-rupturing sequence was not the same as experimental observation during the quasi-static test.

Simulation results of Specimens TCBF-B-2 and TCBF-B-3 are shown in Figure 6.56 to Figure 6.63. The results for Specimen TCBF-B-2, with round HSS braces, were particularly well modeled throughout its response. The initial simulation of Specimen TCBF-B-3 is good but poorer than the other simulations in later cycles. This may be associated with the modeling of the bolted lower beam to gusset plate connections, which were simplified for these analyses. The explicit analysis in LS-DYNA took a significantly greater amount of computer time to finish the quasi-static loading histories than for the simpler fiber-based models in OpenSees.

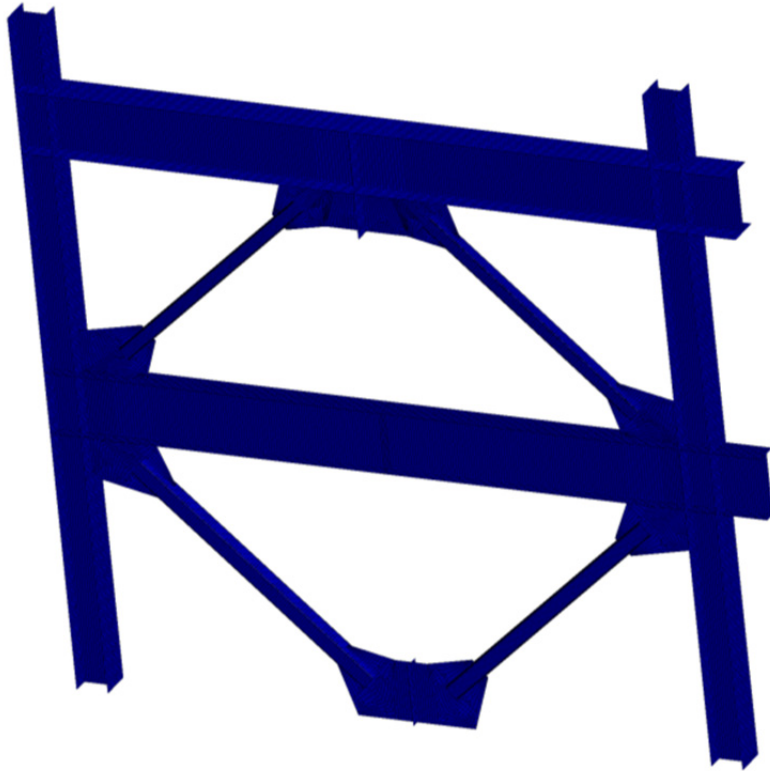


Figure 6.51 Specimen TCBF-B-1: mesh layout in the LS-DYNA simulation.

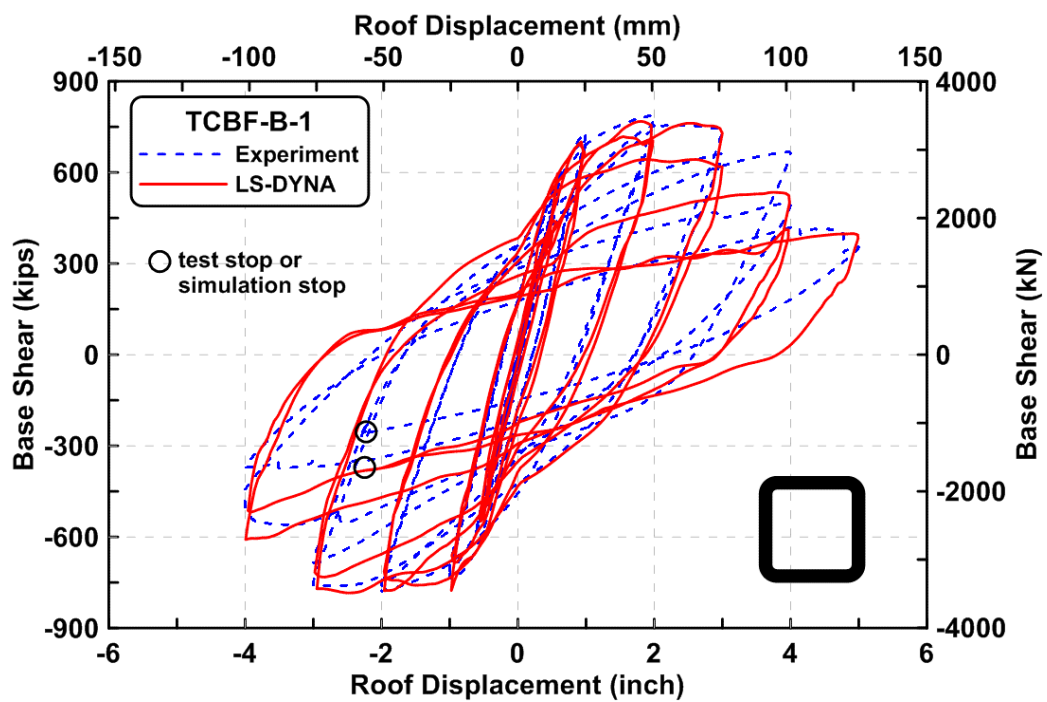


Figure 6.52 Specimen TCBF-B-1: base shear versus roof displacement from LS-DYNA simulation.

TCBF-B-1 Specimen from igs file
 Time = 848, Nodes=77187, Elements=67489
 Contour of Effective Stress (v-m)
 reference shell surface
 min=0.000e+00, at elnode 11280
 max=1.001e+07, at elnode 87164

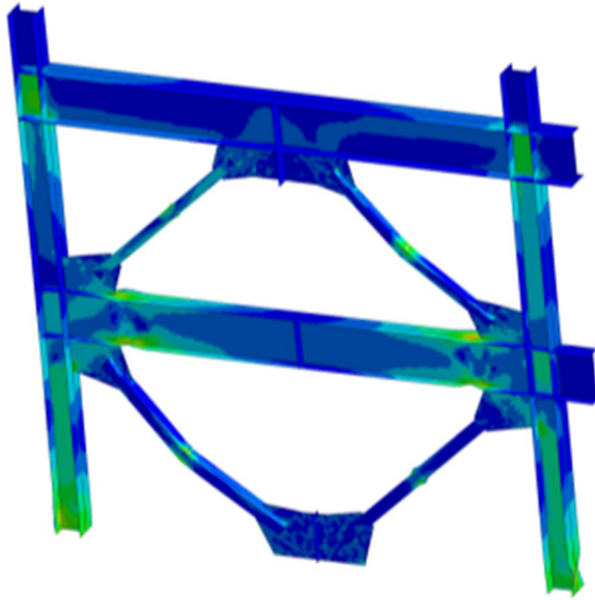
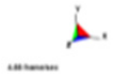
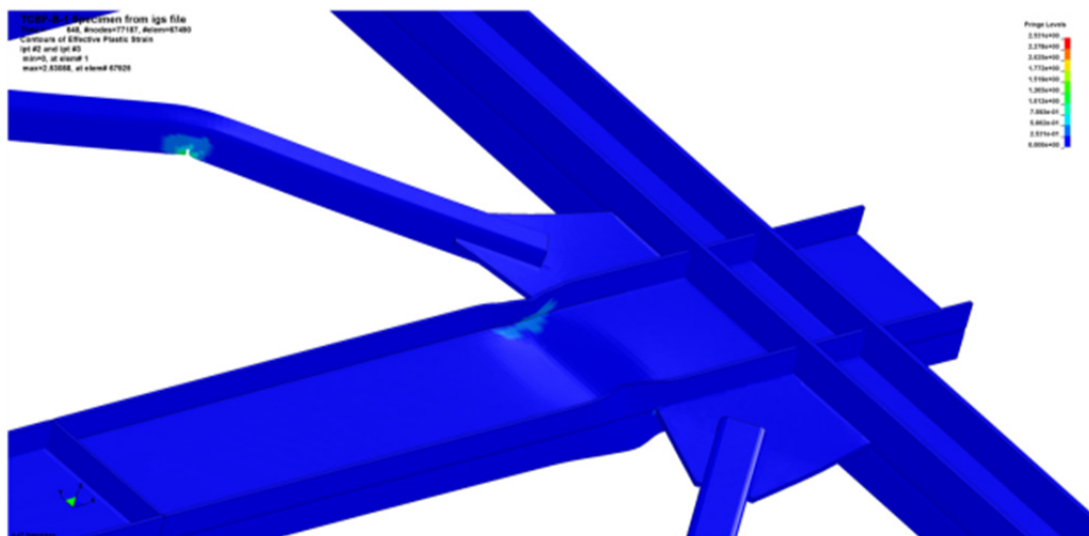
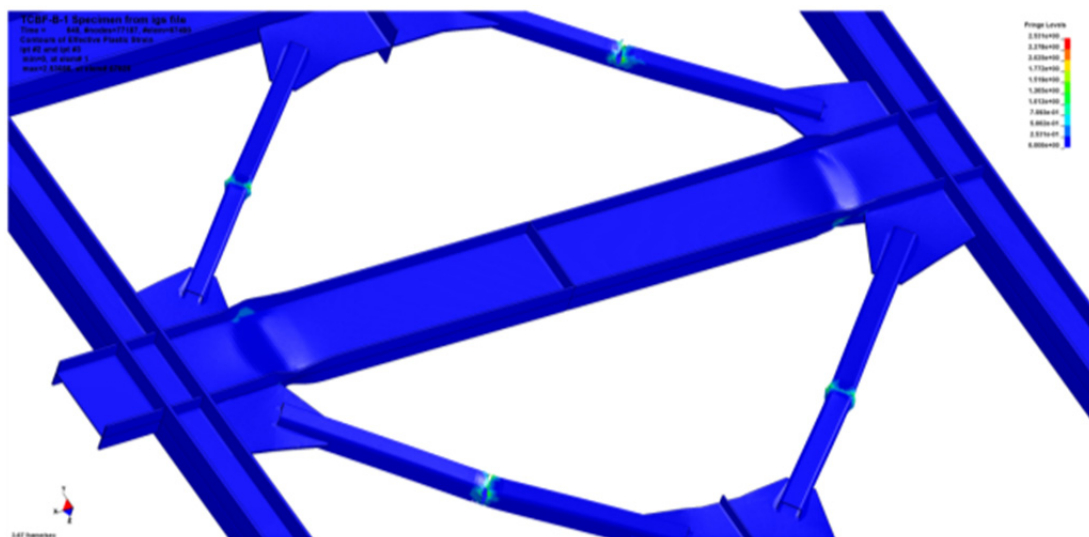


Figure 6.53 Specimen TCBF-B-1: Von Mises stress distribution at the end of LS-DYNA simulation.



(a) western side beam-to-gusset plate connection region (local buckling of beam web, top and bottom flanges)



(b) overview of specimen from south-west side (crack initiated and partially propagated in all four braces, lower beam end plastic hinges are also shown)

Figure 6.54 Specimen TCBF-B-1: plastic strain distribution at the end of LS-DYNA simulation.

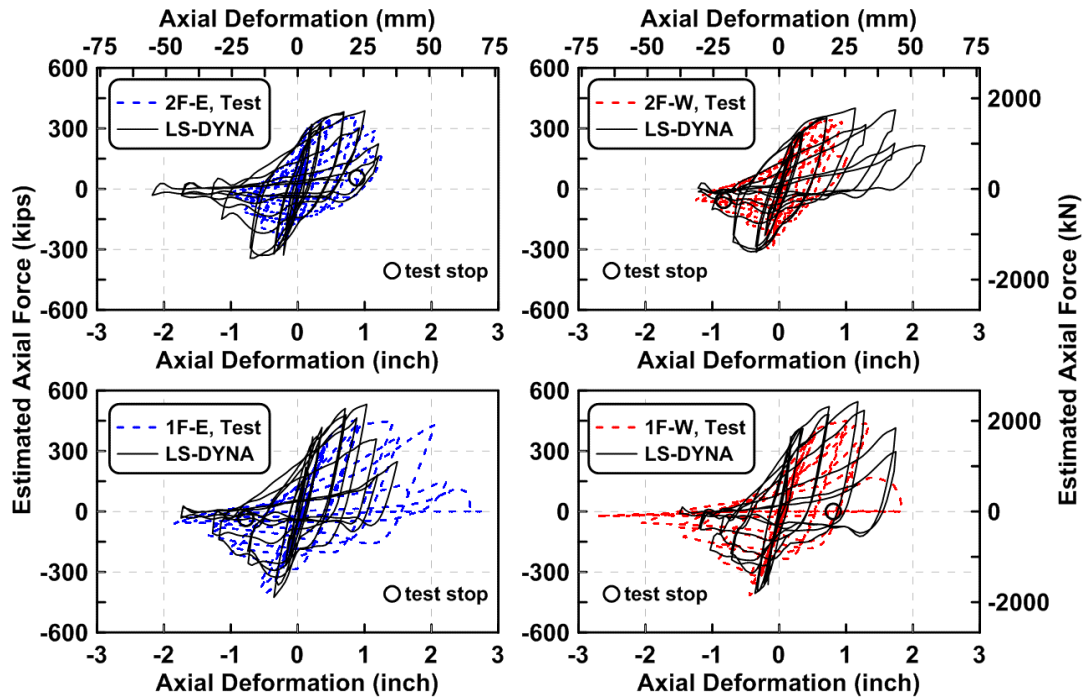


Figure 6.55 Specimen TCBF-B-1: estimated brace axial force versus axial deformation relationships from experimental results and LS-DYNA simulation.

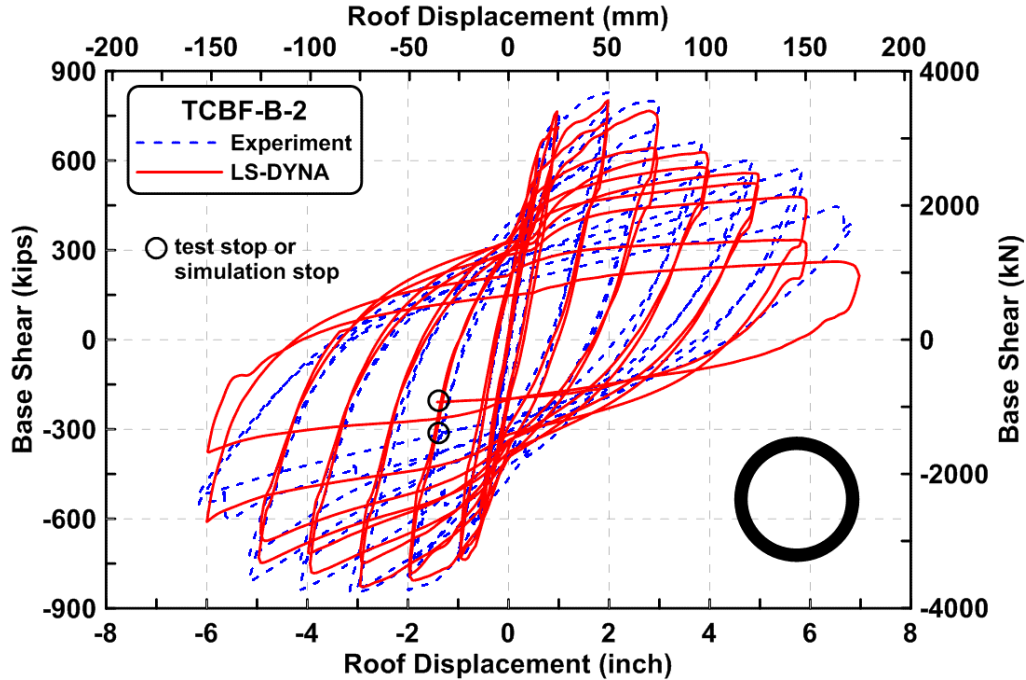


Figure 6.56 Specimen TCBF-B-2: base shear versus roof displacement from LS-DYNA simulation.

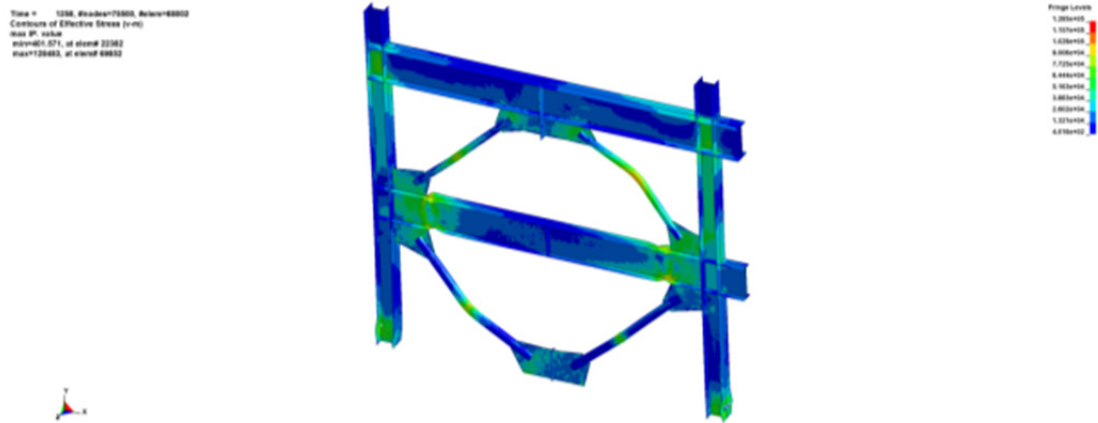
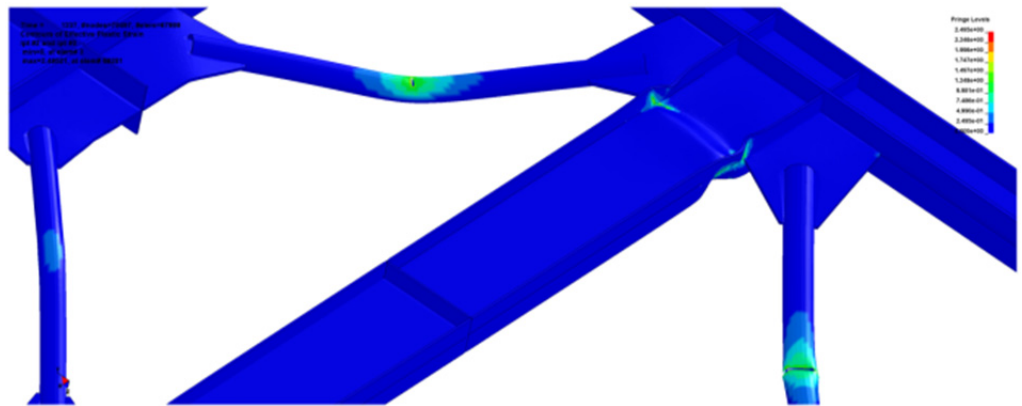
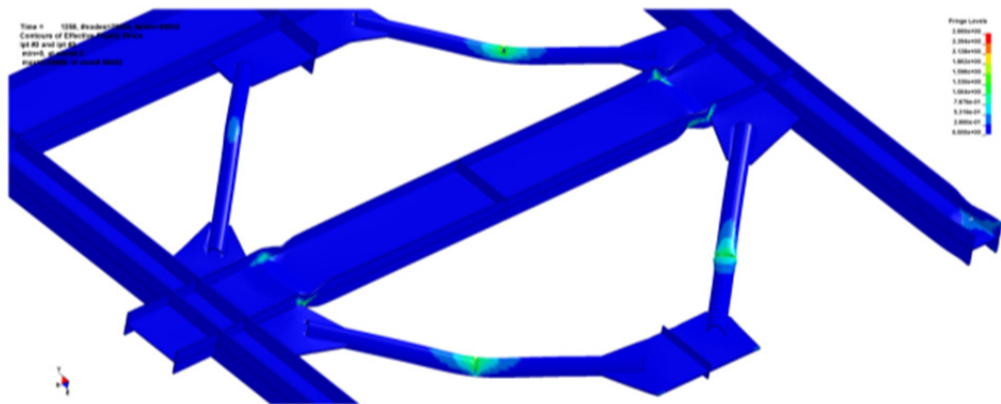


Figure 6.57 Specimen TCBF-B-2: Von Mises stress distribution at the end of LS-DYNA simulation.



(a) eastern side beam-to-gusset plate connection region (local buckling of beam web, top and bottom flanges)



(b) overview of specimen from south-west side (crack initiated and partially propagated in three braces, lower beam end plastic hinges are also shown)

Figure 6.58 Specimen TCBF-B-2: plastic strain distribution at the end of LS-DYNA simulation.

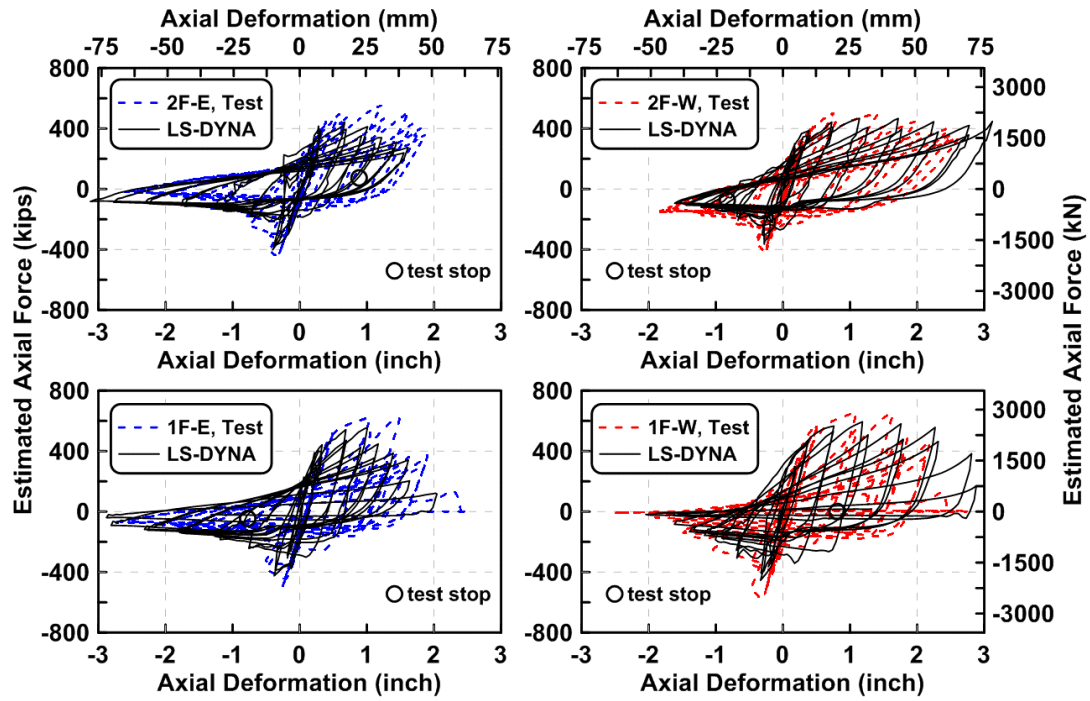


Figure 6.59 Specimen TCBF-B-2: estimated brace axial force versus axial deformation relationships from experimental results and LS-DYNA simulation.

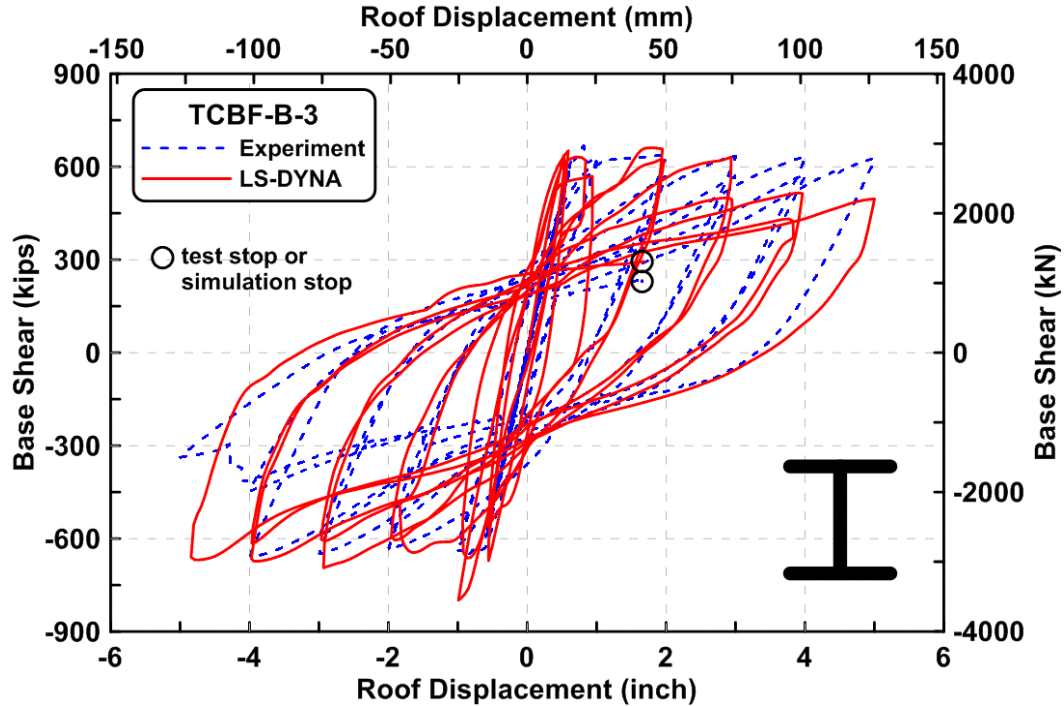


Figure 6.60 Specimen TCBF-B-3: base shear versus roof displacement from LS-DYNA simulation.

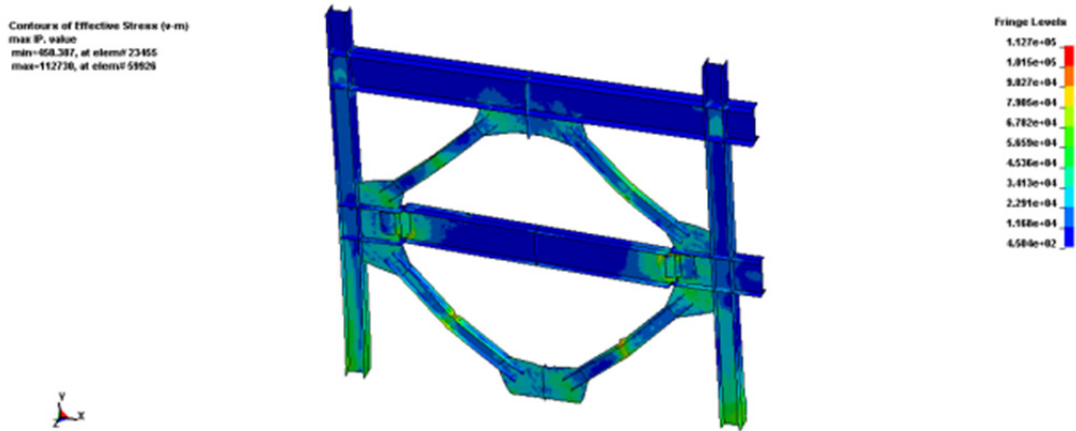
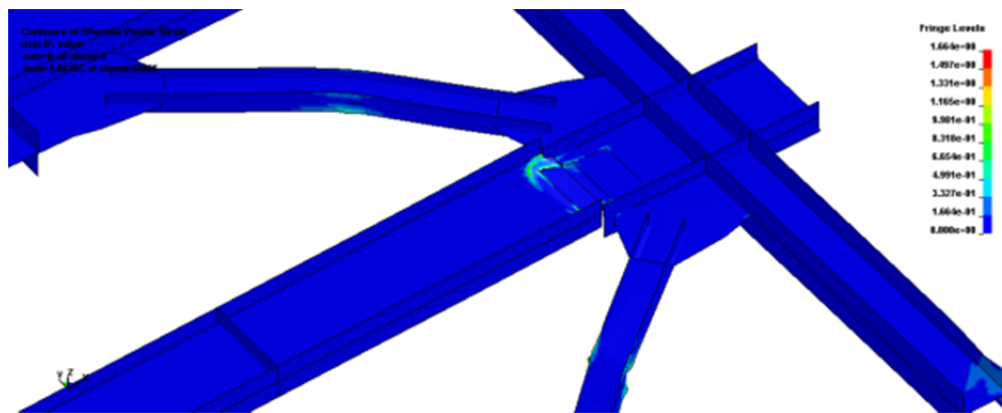
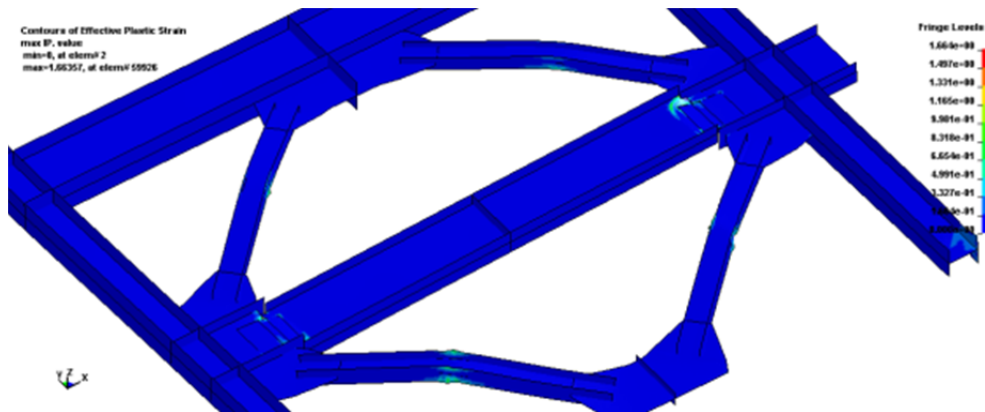


Figure 6.61 Specimen TCBF-B-3: Von Mises stress distribution at the end of LS-DYNA simulation.



(a) eastern side beam-to-gusset plate connection region (twisting of beam web)



(b) overview of specimen from north-east side

Figure 6.62 Specimen TCBF-B-3: plastic strain distribution at the end of LS-DYNA simulation.

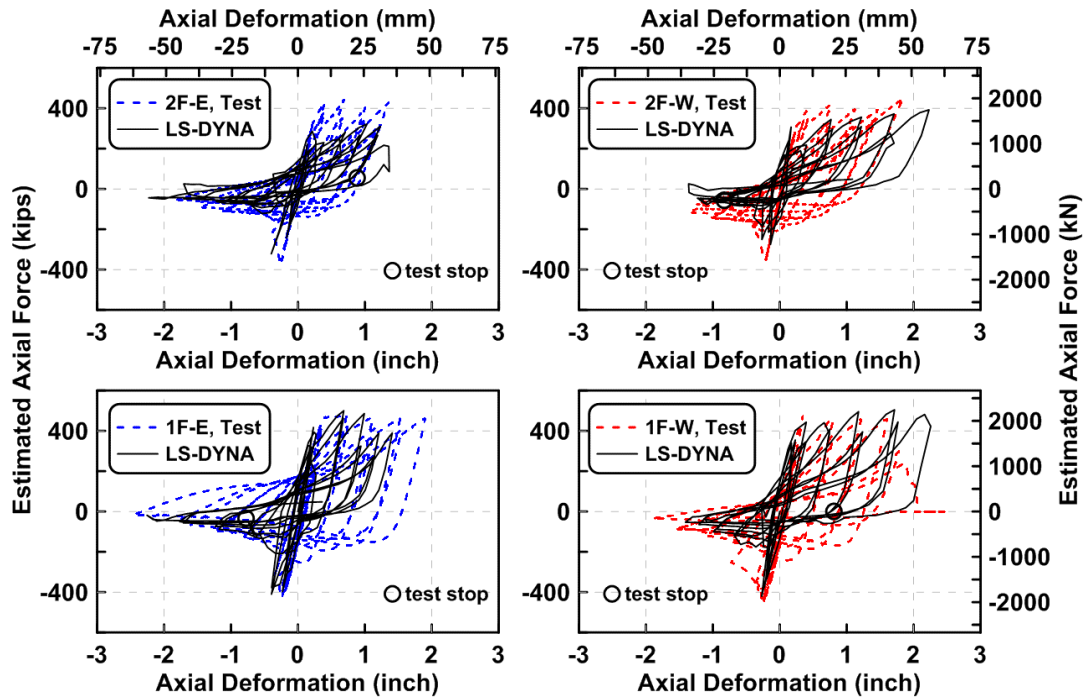


Figure 6.63 Specimen TCBF-B-3: estimated brace axial force versus axial deformation relationships from experimental results and LS-DYNA simulation.

6.6 COMPARISON BETWEEN OPENSEES AND LS-DYNA RESULTS

To compare the analytical results obtained from OpenSees and LS-DYNA, all three quasi-static test models in OpenSees were re-run using the same displacement loading protocol as input in LS-DYNA. As mentioned in Section 6.5.2, prescribed displacement histories for both floor levels were specified in the OpenSees models. The global responses such as roof displacement versus base shear relationships and brace axial force versus axial deformation responses are compared.

Both OpenSees and LS-DYNA results match the actual test results quite well globally (see Figures 6.52, 6.56, 6.60, 6.64, 6.65, and 6.66) but could not precisely predict the damage sequences. The crack initiation in the braces were triggered in both OpenSees and LS-DYNA simulation models, but the corresponding time and sequences were not the same; see Figures 6.67 to 6.72. The simulated damage sequences were not the same as those observed during the quasi-static tests. Furthermore, no brace completely fracture was observed in the simulated models using LS-DYNA.

Table 6.5 summarizes the comparison between OpenSees and LS-DYNA simulation. The simulation time required for the LS-DYNA shell element models is considerably longer than the needed for OpenSees fiber-based element models. Note that proper mass scaling was introduced in the LS-DYNA explicit simulations.

Post-processing with visualization is one of advantages using LS-DYNA models. One can demonstrate the results visually such as brace global buckling (see Figures 6.53, 6.57, and

6.61), local buckling of brace section walls (see Figure 6.54, 6.58, and 6.62), local strain histories (e.g., Figure 6.73), local stresses (e.g., Figure 6.74), and cross-section deformed shapes.

Table 6.5 Comparison between OpenSees and LS-DYNA simulation.

Comparison		OpenSees	LS-DYNA
Analysis CPU Time (2-CPU)	TCBF-B-1	2 hr. 1 min.	23 hr. 36 min.
	TCBF-B-2	5 hr. 47 min.	22 hr. 43 min.
	TCBF-B-3	0 hr. 26 min.	21 hr. 42 min.
Simulate Global Buckling		Yes	Yes
Simulate Local Buckling		No	Yes
Element Type		Fiber-based	Shell
Element Erosion		Yes (Calibrated)	Yes (Calibrated)
Post Processing and Visualization		No	Yes

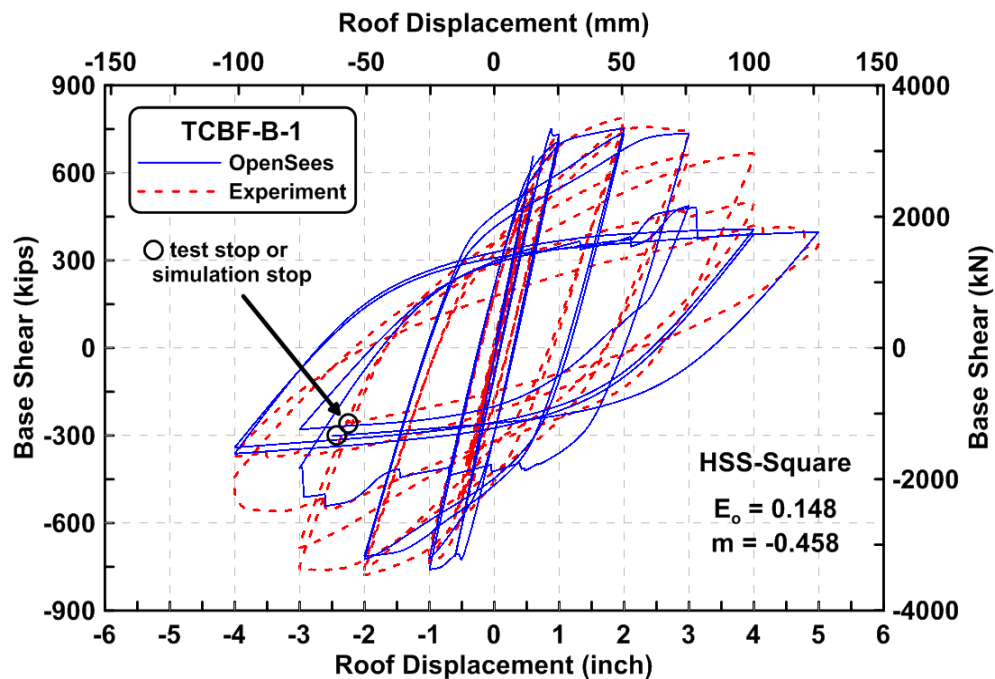


Figure 6.64 Specimen TCBF-B-1 model: base shear versus roof displacement from OpenSees.

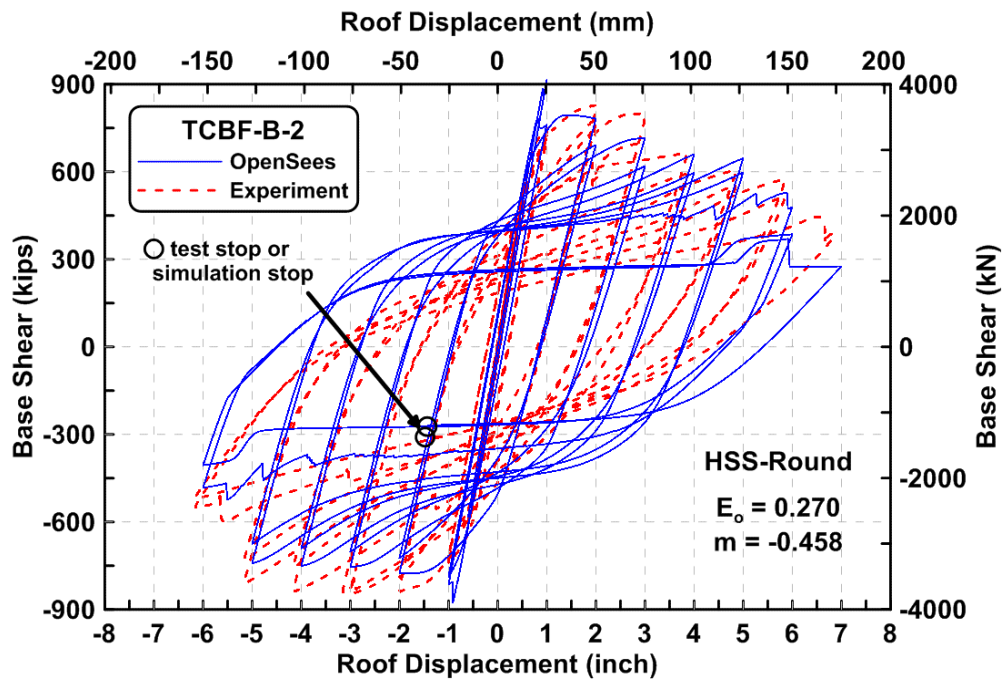


Figure 6.65 SpecimenTCBF-B-2 model: base shear versus roof displacement from OpenSees.

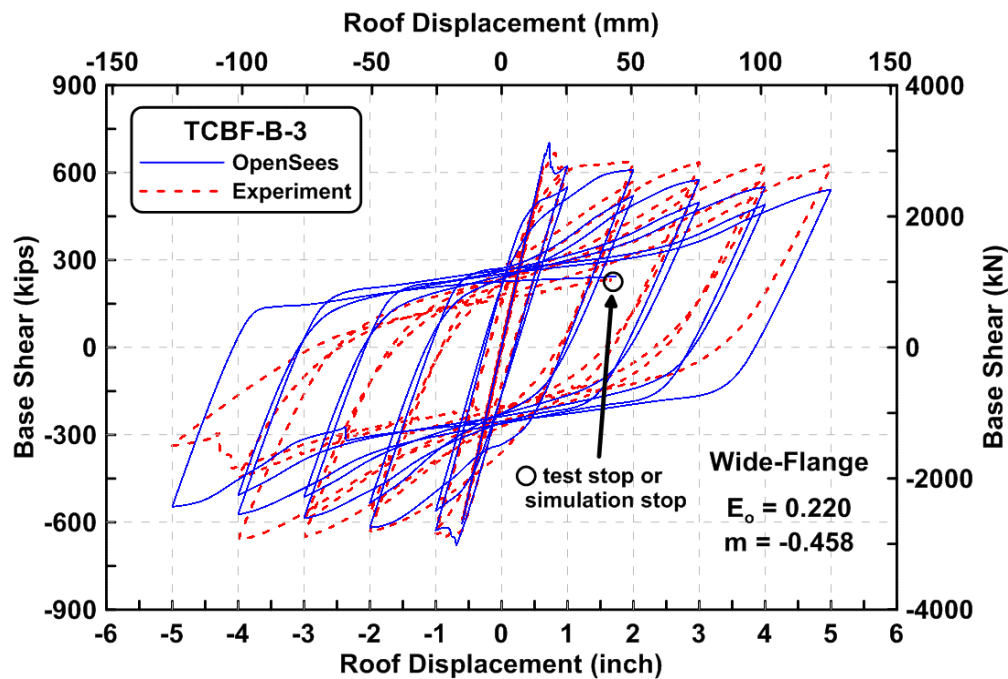


Figure 6.66 SpecimenTCBF-B-3 model: base shear versus roof displacement from OpenSees.

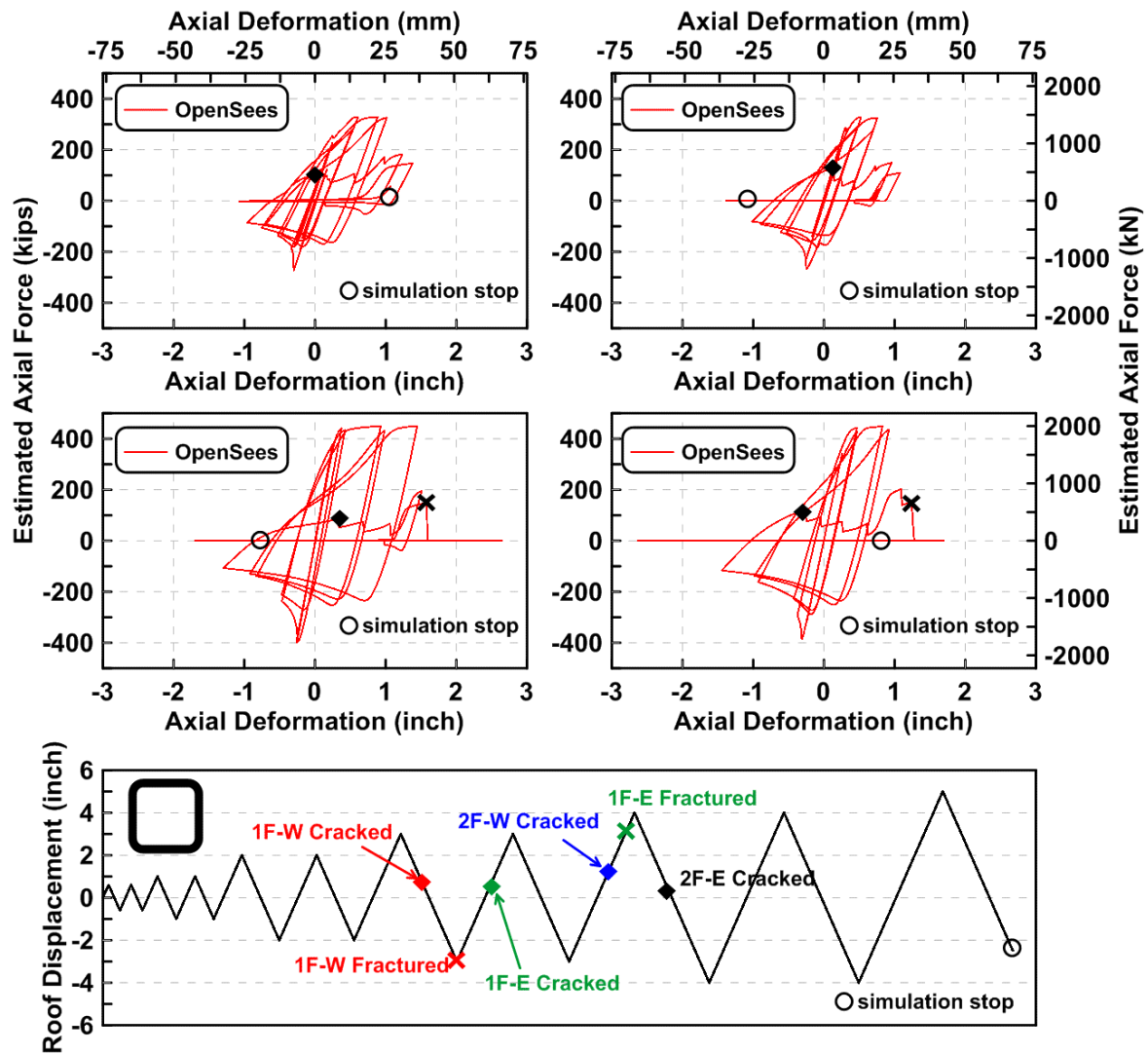


Figure 6.67 SpecimenTCBF-B-1 model: estimated brace axial force versus axial deformation relationships.

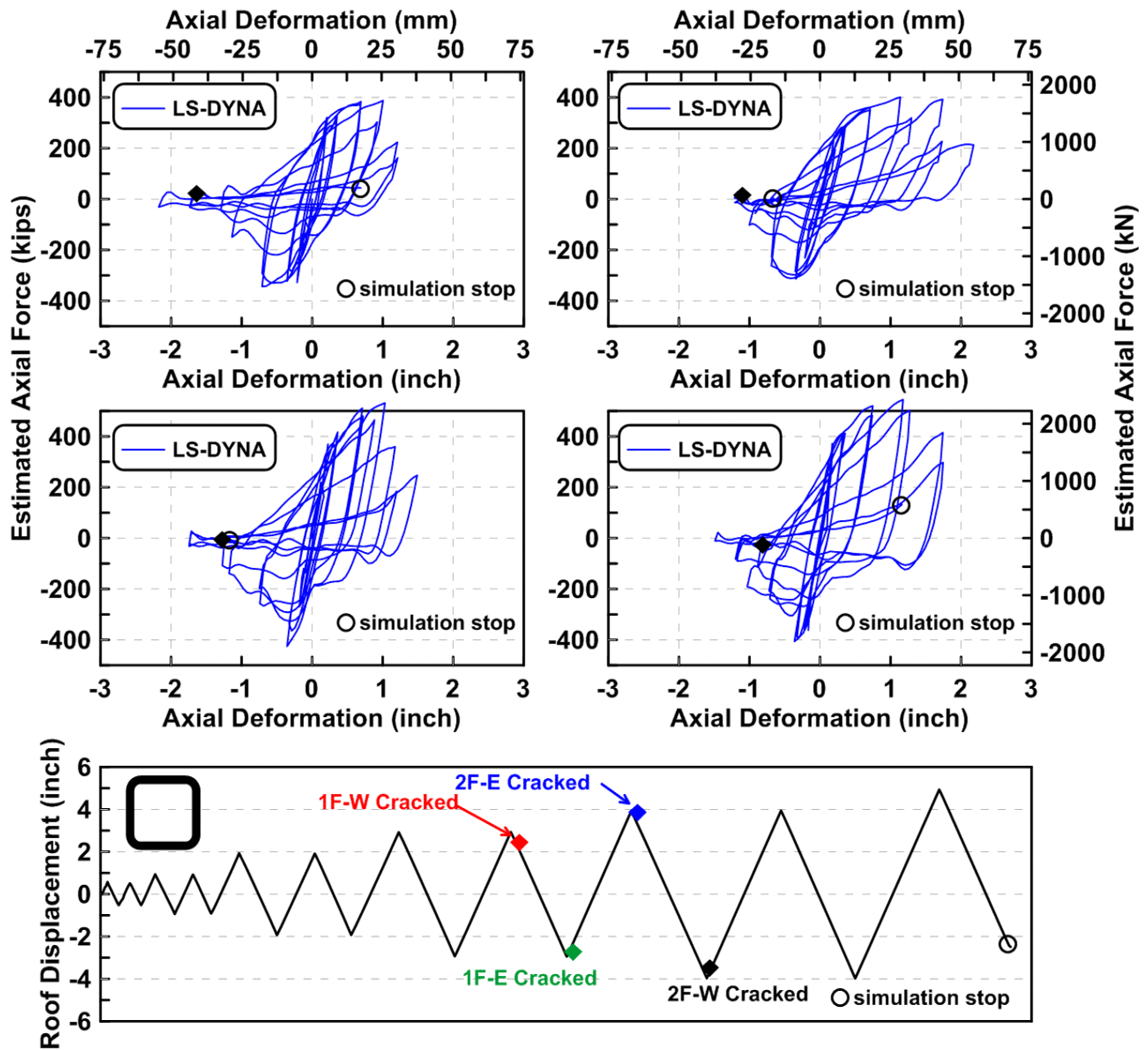


Figure 6.68 SpecimenTCBF-B-1 LS-DYNA model: estimated brace axial force versus axial deformation relationships.

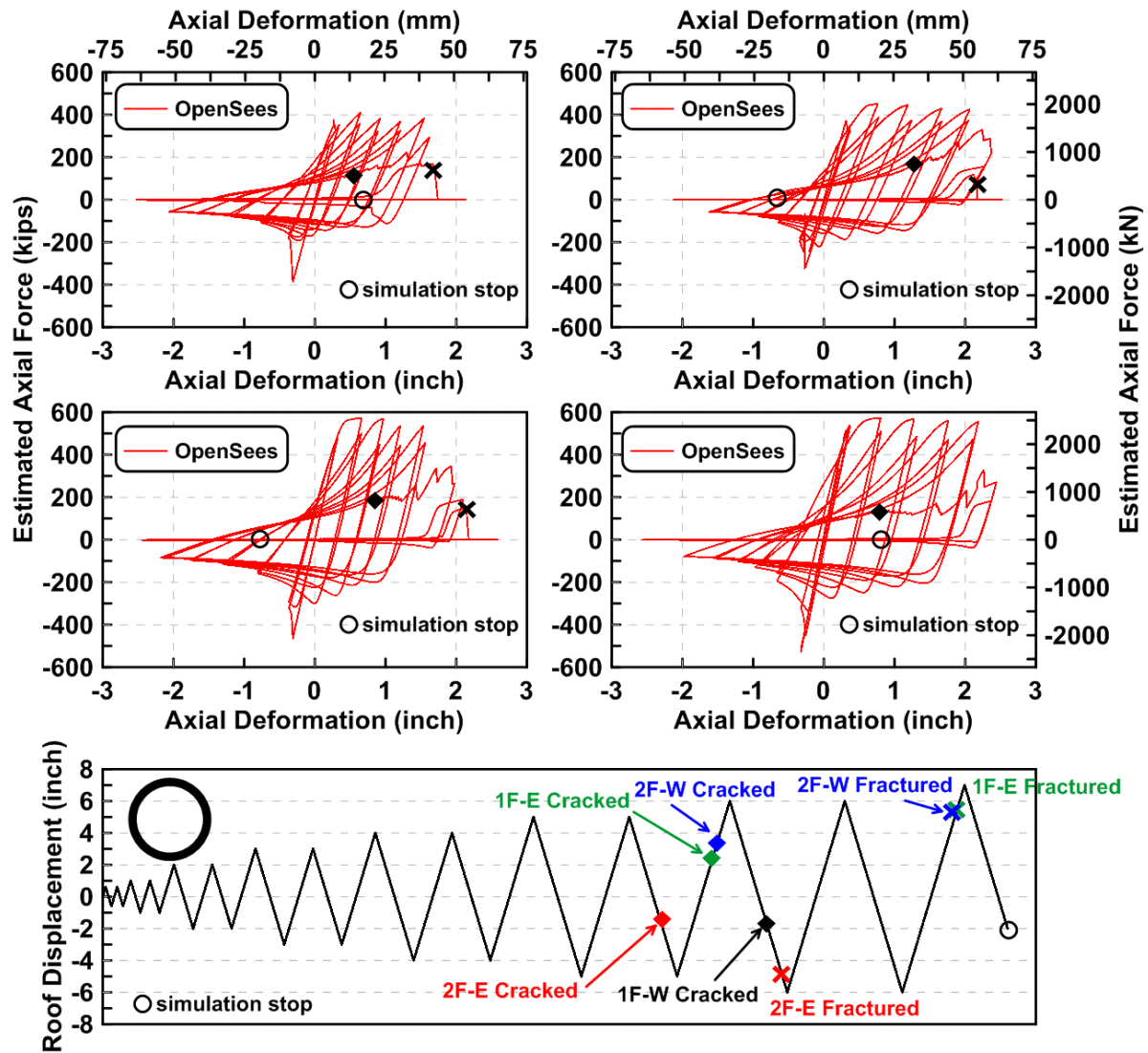


Figure 6.69 SpecimenTCBF-B-2 OpenSees model: estimated brace axial force versus axial deformation relationships.

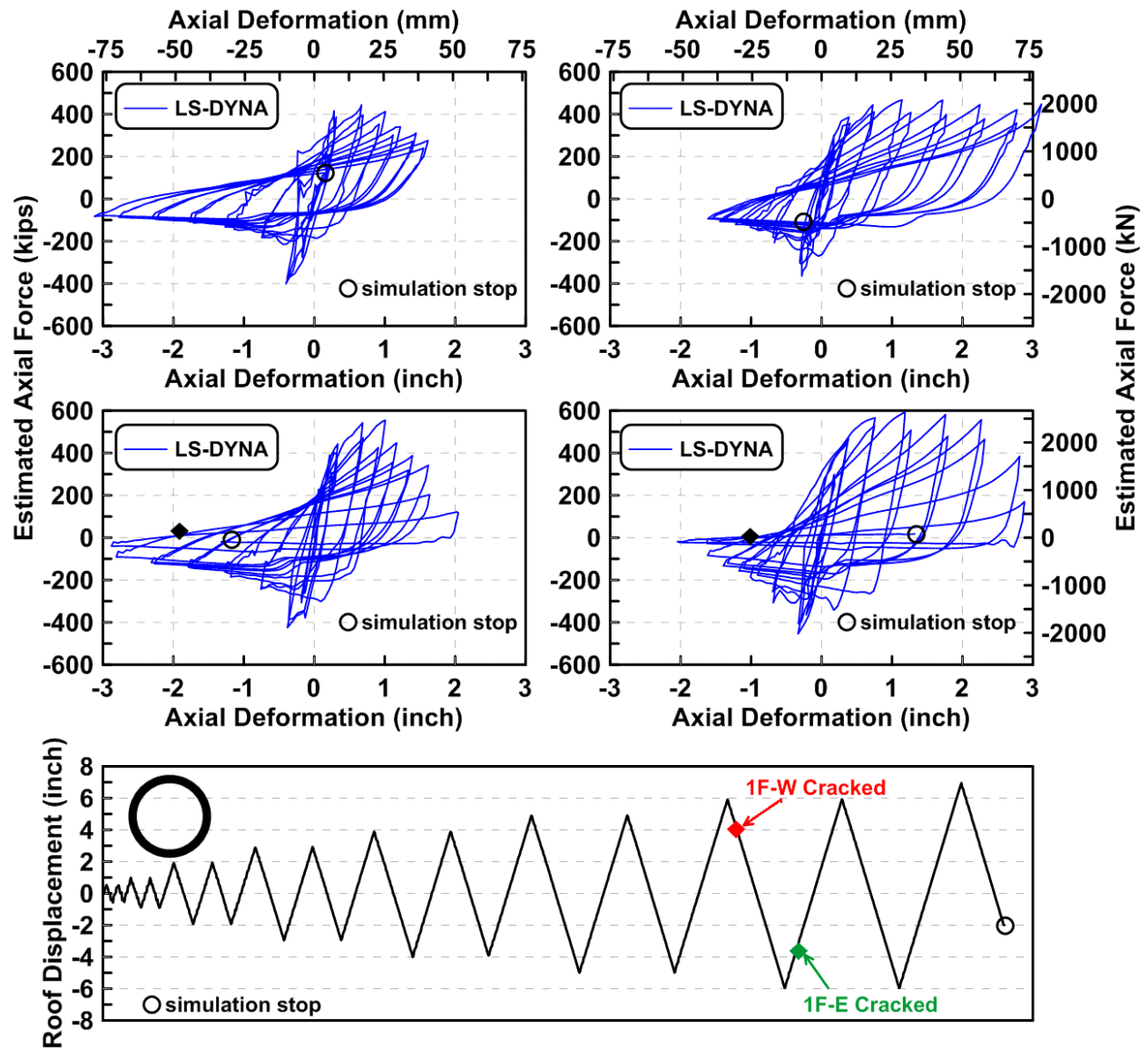


Figure 6.70 SpecimenTCBF-B-2 LS-DYNA model: estimated brace axial force versus axial deformation relationships.

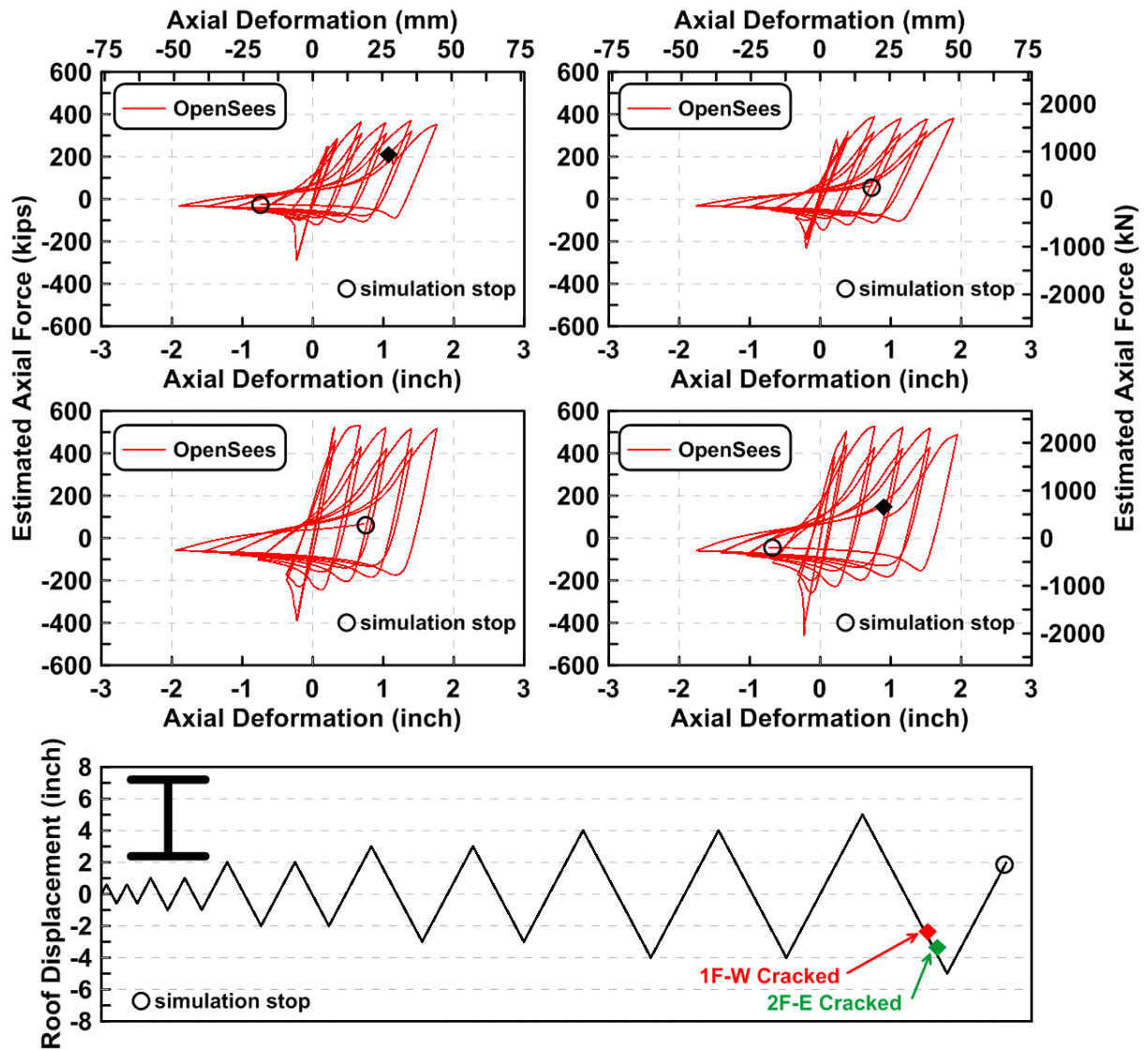


Figure 6.71 Specimen TCBF-B-3 OpenSees model: estimated brace axial force versus axial deformation relationships.

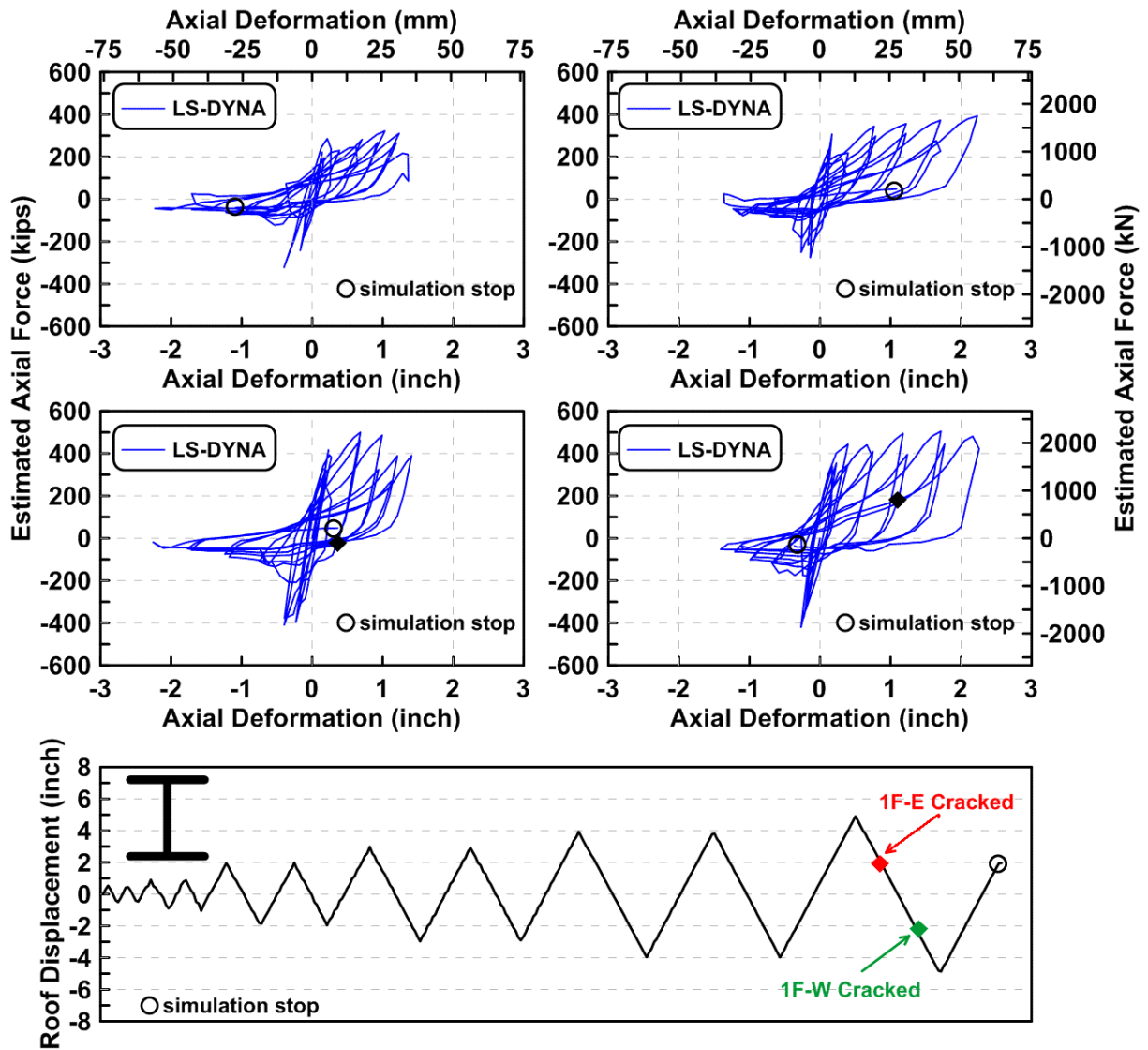


Figure 6.72 Specimen TCBF-B-3 LS-DYNA model: estimated brace axial force versus axial deformation relationships.

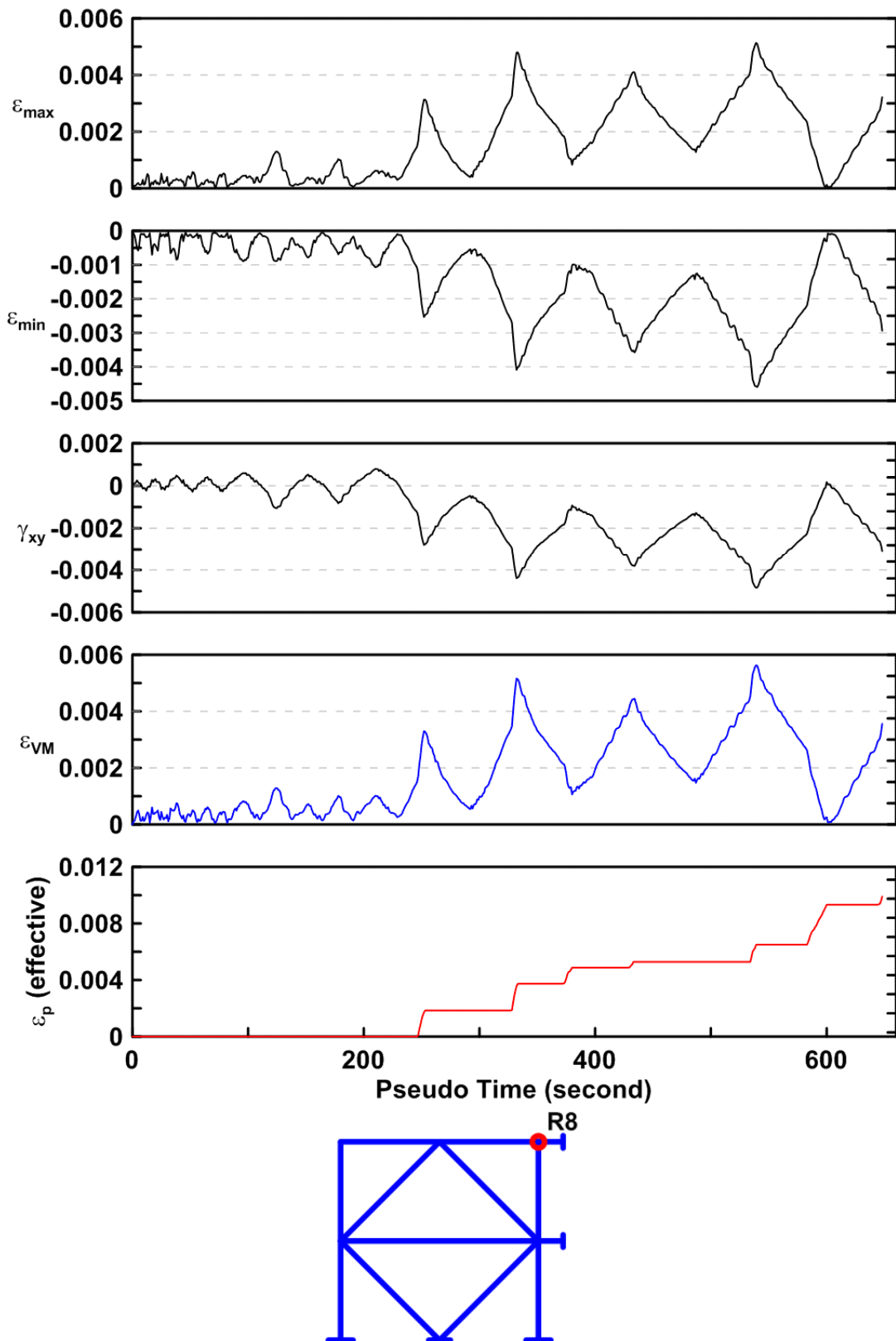


Figure 6.73 SpecimenTCBF-B-1 model from LS-DYNA output: time history of simulated strain at the roof panel zone region (corresponding to location R08).

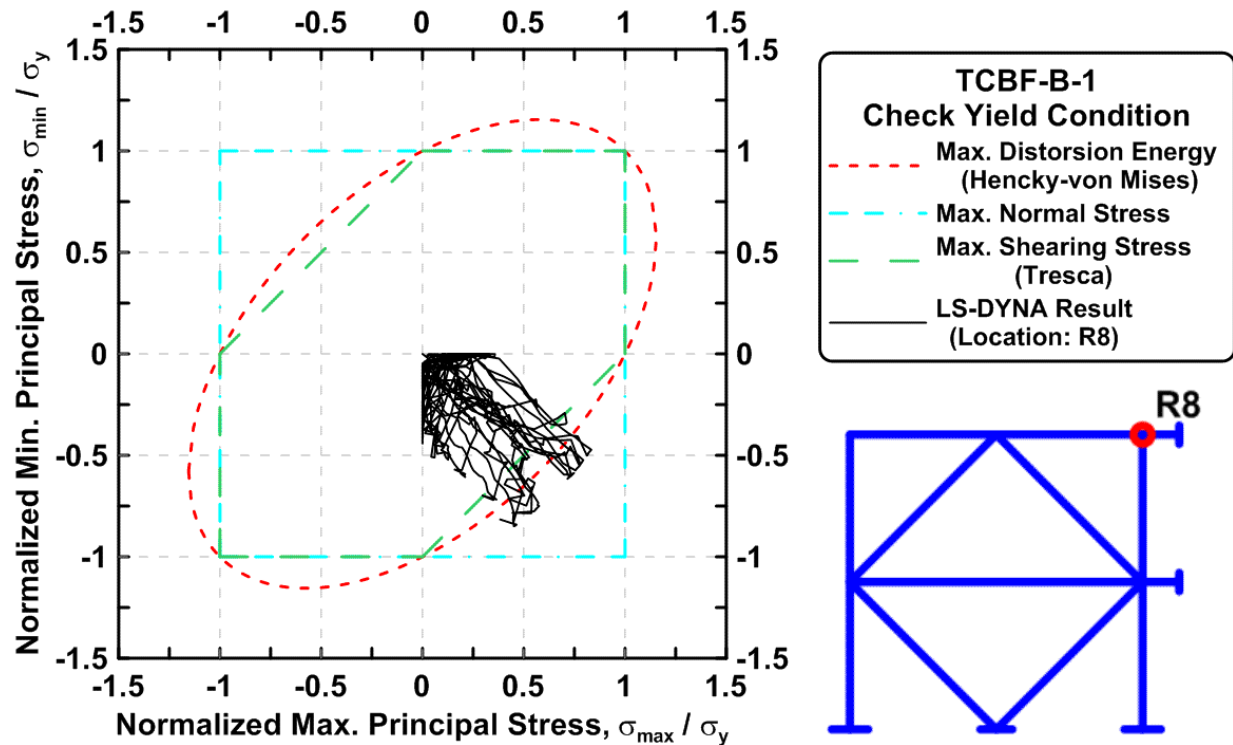


Figure 6.74 SpecimenTCBF-B-1 model from LS-DYNA output: normalized maximum principal stress versus normalized minimum principal stress at the roof panel zone region (corresponding to location R08).

6.7 CONCLUDING REMARKS

From the specimen response comparisons discussed above, it is clear that both OpenSees and LS-DYNA can simulate global test responses with reasonable accuracy. The simulation of deterioration details and local behavior such as local buckling and member rupture is generally far better when shell models are used rather than fiber-based element models. However, in general, the simulation time required for the OpenSees fiber based models is considerably shorter than that needed for the LS-DYNA model. Nonetheless, in practice, the OpenSees model seems to be a more efficient choice for predicting the global response of for large and complicated structures.

7 Hybrid Braced Frames: The Strong-Back System

As discussed in previous chapters, a literature survey and the current test program has identified the tendency of braced frames to form a weak-story mechanism, limiting the overall ability of concentrically braced frames to resist strong ground motion, with their overall safety (or system behavior) being dependent on the most severely damaged story. This chapter examines a newly developed seismic force-resisting system: the Strong-Back System (SBS). This is a hybrid system that combines the features of two types of lateral load resisting systems to achieve improved behavior, features not easily achievable using either system alone. In this case, a traditional braced frame is combined with a rocking or leaning braced frame or mast. The mast acts like a “strong back” that acts to resist the formation of soft- or weak-story mechanisms. Its aim is to promote more or less uniform story drifts over the height of the structure consistent with the stiffness of the mast and dynamic characteristics of the overall structure.

First, the relevant literature is reviewed to show the evolution of this hybrid concept. Next, three prototypes of SBSs (SB6-3, SB6-3B, and SB6-3L) were designed and analyzed considering a variety of earthquake excitations. Computed responses were compared with responses for three other concentric braced frame systems. The systems used for comparison include two conventional symmetric, concentric braced frames (V6 and X6), and a novel asymmetric concentric double-story X braced frame (X6-3) that has similar geometry to the hybrid systems studied. Quasi-static inelastic analyses, both monotonic and cyclic, were initially conducted on these six braced frame systems to enable comparison of the fundamental hysteretic behavior of the systems under simplified loading. A series of nonlinear dynamic time-history analyses were then performed on each system to compare the system’s dynamic responses, both globally and locally.

7.1 INTRODUCTION

It is well-known that during strong earthquake ground shaking, conventional steel concentrically braced frames are prone to form a weak-story mechanism [Khatib et al. 1988]. This concentration of deformations in one or a few stories intensifies damage to braces at these levels, leading to greater nonstructural and structural damage at these levels, and premature rupture of the braces, compared to systems with more uniform distribution of damage over height. Weak

stories are also likely to have significant residual displacements, which can be costly or infeasible to repair.

Over the years, researchers and engineers have explored many ideas in an attempt to improve the behavior of braced frame systems. An obvious example is the development of buckling-restrained braces [Watanabe et al. 1988]. This kind of brace significantly improves the hysteresis behavior and the energy-dissipation capacity at the component level [Watanabe et al. 1988; Kalyanamaran et al. 1998, 2003; Chen et al. 2001; Mahin et al. 2004; Lai and Tsai 2004; Lai et al. 2004]. Although the entire system behavior benefits from the higher brace ductility capacity, the deformation concentration and the system's permanent deformations are not generally ameliorated, and may be even larger than observed in conventional concentric braced frames [Sabelli et al. 2003; Uriz and Mahin 2008; Kiggins and Uang 2006; Chen and Mahin 2010].

Another component-focused strategy is that of engineered self-centering brace elements [Aiken et al. 1992; McCormick et al. 2007; Christopoulos et al. 2008; Tremblay et al. 2008b; Yang et al. 2010]. These devices exhibit “flag pole” shaped hysteretic loops that have significant, but reduced, energy-dissipation capabilities compared to buckling restrained braces with similar strength and deformation capabilities. These pinched hysteretic loops give the braces substantial re-centering characteristics that minimize the permanent deformations in the overall system. When properly designed such devices reduce residual displacements of the structural system within which they are placed; however, the systems are still likely to concentrate structural and nonstructural damage in one or a few stories. Moreover, many current designs for self-centering braces have a limited displacement range over which self-centering is realized, and they may not be able to fully re-center if larger displacements concentrate at one story.

As such, it is desirable to provide concentric braced frames with improved capabilities to avoid the concentration of deformations and damage in a few stories. If a system is able to mitigate soft- or weak-story behavior, the peak deformation demands on individual braces and maximum residual displacements might be reduced. Several approaches have been followed to modify the system behavior of braced frames to develop large deformation capacity, reduce damage concentration, and achieve smaller residual displacement. These systems include: (1) dual systems, where a moment frame is used in addition to the braced frame; (2) zipper or vertical tie-bar systems; (3) rocking/uplifting systems; and (4) mastod or strong-back hybrid systems.

7.2 PREVIOUS STUDY

For many years building codes in the U.S. have encouraged the use of dual systems, where one system with limited ductility is provided with a back-up system. In early design approaches, the primary system and the combined systems were designed to resist 100% of the lateral load required by the code; in addition, the secondary system alone was required to carry 25% of the design seismic lateral load. Such dual systems were allowed to be used in taller structures and in some cases designed to lower overall lateral seismic loads. With the advent of buckling

restrained braces, additional interest in dual systems was raised by the possible benefit of the back-up system helping reduce soft-story behavior and reducing residual displacements. In these cases, independent moment-resisting frames were introduced into structural systems and combined with the existing BRB frames. Often, the moment frame employed was designed so that the columns and beams provided framing for the buckling restrained braced bays. The addition of flexible moment-resisting frames was intended to provide a partial re-centering mechanism to return the entire structure to its original position after strong earthquakes. Studies by Kiggins and Uang [2006] found that using dual BRB/moment frames reduced the ductility demand slightly, and the maximum story drift was reduced about 10% to 12%. Analytical studies demonstrated significant reduction in residual drift when the dual system was used. However, when large interstory drifts occurred and both the BRB and moment frame yielded, the re-centering tendencies expected were significantly reduced.

Previous research on reducing weak story behavior in braced frame systems by Khatib et al. [1988] designed zipper braced frame systems and tie-bar-to-ground braced frame systems to prevent weak-story mechanisms. The responses of these systems were compared with other basic braced frame systems (see Figure 7.1). In the zipper or tie-bar-to-ground systems, the vertical struts at the center of the bays were designed to promote the formation of the same mechanism at each level. In the case of the zipper system, the unbalanced force at the center of a chevron brace pattern would normally tend to displace the beam intersected by the braces in the vertical direction. With the addition of the vertical strut, this vertical movement would be transferred to the floors above and below. In these zipper/tie-bar systems, the braces on both sides of the central strut were expected to yield: one by tensile yielding and the other through buckling. The authors showed that this approach was effective but did not indicate how to size or proportion the vertical struts. In the tie-bar-to-ground system, the unbalanced forces simply accumulated, requiring that the vertical tie bar carry large forces. Its size increased as a result, and it simply became another column in the system. That is, the system became a two-bay frame with a single diagonal brace in each bay. The analytical studies found that both these systems performed better than the chevron braced frame system preferred in practice at that time.

The results of the analytical studies by Khatib et al. [1988] also demonstrated that the steel braced frame behavior was extremely sensitive to the ground motion records selected and the distribution of lateral forces used in design. It was demonstrated that behavior could be improved by using more realistic distributions of lateral force over the height of the structure rather than simplified distributions that are a part of equivalent static lateral force design methods. Further research—such as shaking table tests, pseudo-dynamic tests, and more advanced analytical studies—was suggested to validate the feasibility and the superiority of these two alternative braced frame systems.

Additional zipper frame system studies have been carried out to improve the performance of this system and to develop design recommendations (e.g., Sabelli [2001]; Tirca and Tremblay [2004]; and Yang et al. [2008, 2010]). In most of these studies, it was demonstrated that the vertical struts in zipper braced frames incorporating conventional buckling braces needed to be very large to prevent yielding. While elastic behavior was not a condition for the design of these vertical struts in the original work by Khatib et al. [1988], development of simple and effective

design guidance for cases where these struts yielded proved difficult to formulate. Yielding of the vertical struts and higher mode effects made it difficult to achieve the desired uniform distributed story drifts. Several investigators noted that the zipper frame system might not be suitable for structures located in near-fault seismicity zones and in structures over four stories in height (e.g., Tirca and Tremblay [2004]).

Another approach was suggested by MacRae et al. [2004]. They noted that in most concentric braced frames there were a large number of gravity load-resisting columns. While these columns were often pinned at their base, they were generally spliced in such a way that they might be considered continuous for the height of the structure. Since there were many such columns, their combined stiffness and strength might be effective in minimizing soft- or weak-story effects. They developed equations for two-story and general multistory concentric braced frame buildings to predict moment amplifications in the columns and the increase in displacements relative to a uniform distribution over the height. They found that these elements were indeed able to reduce the soft-story tendency. However, there was significant variability in the response, and in some cases the number and size of columns needed to be large to provide adequate control of the formation of weak stories.

Researchers have studied the effectiveness of allowing concentric braced frames to rock during seismic response [Uriz and Mahin 2008; Midorikawa et al. 2010]. In these cases the braced frame remained essentially elastic, and energy dissipation was provided by impact or energy-dissipation devices installed in the direction of the uplift. These systems were found to be effective in reducing soft-story behavior and re-centering behavior was achieved. Design procedures to proportion members and to select appropriate amounts of supplemental damping are still active areas of research.

Building on the ideas related to the tied eccentrically braced frames [Martini et al. 1990], the continuous leaning columns by MacRae et al. [2004], and uplifting/rocking braced frames, Canadian researchers proposed a modified zipper bracing configuration where a vertical strut was provided along the center of a braced bay; framing in one half of the bay along with the vertical strut remained elastic and inelastic action in conventional braces or buckling restrained braces was permitted in the other half of the bay [Tremblay 2003; Tremblay and Merzouq 2004]. Basically, half of the braced bay remained elastic and deformed like a very strong column or mast. The structural deformation shape looks essentially like a SDOF system that occurs for braced frames that uplift or rock. Incremental dynamic analyses performed by Tremblay on an eight-story building showed that although the hybrid bracing system uniformly distributed the deformation, the elastic bracing member force demands varied from two to at least fifteen times the brace force demands, corresponding to the design level lateral load calculated from elastic analysis. The half of the braced bay that remains essentially elastic acts like a vertical elastic truss or strong back that attempts to achieve a uniform distribution of drifts over the height of the building. Engineers have recently applied this concept in both new constructions and retrofit projects [Mar 2010]. They found that not only do such “trussed mast frames” or strong-back braced frames provided better performance compared to traditional braced frames, they are also cost effective.

In this chapter, the trussed mast frame or SBS is examined in more detail. The SBS concept described herein does not specifically incorporate a self-centering component, but self-centering braces can be used in conjunction with the system by incorporating self-centering braces, various forms of prestress, or providing additional frames that uplift. This simpler approach is pursued here to see if the avoidance of a weak story is sufficient to reduce residual displacements to tolerable levels.

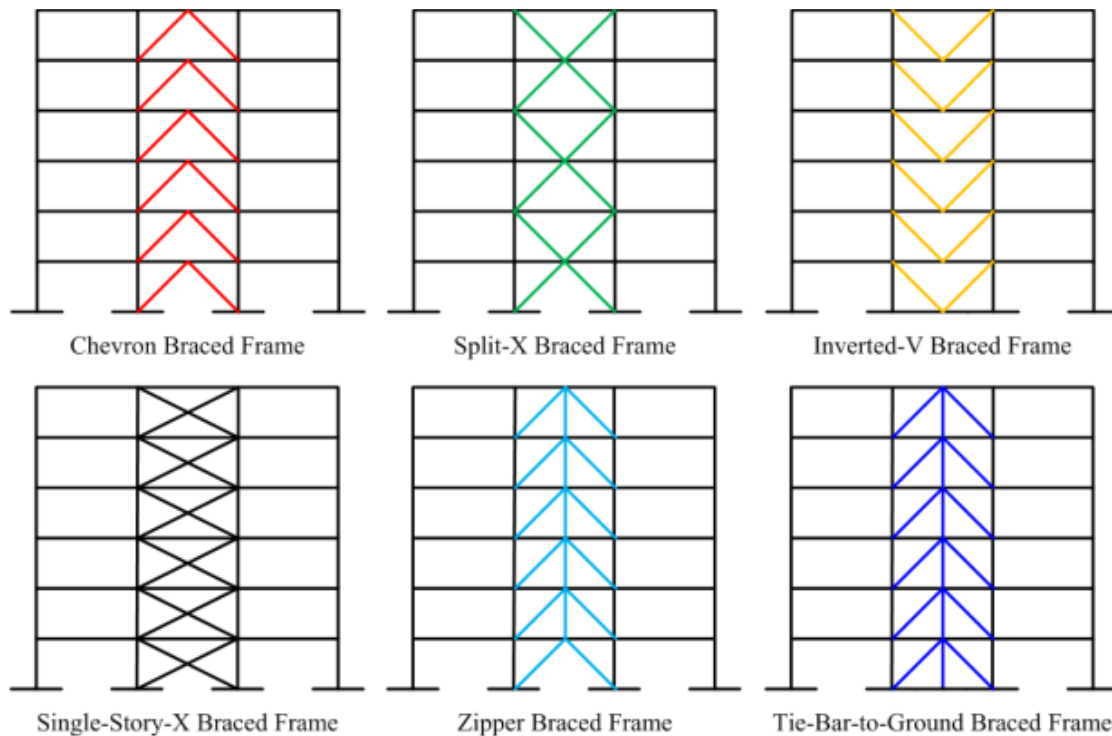


Figure 7.1 Illustration of different braced frame systems [Khatib et al. 1988].

7.3 THE PROPOSED HYBRID BRACED FRAME SYSTEM

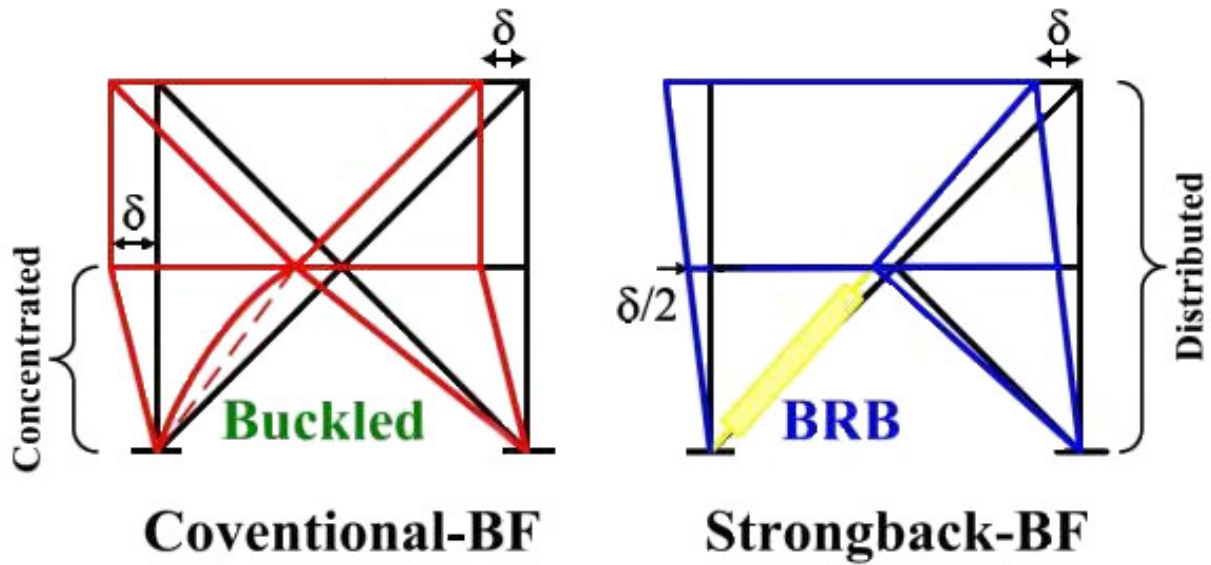
This section extends the concept of a hybrid system based on the strong-back truss system [Mahin and Lai 2008]. The intent is to incorporate a vertical truss that remains elastic within a braced bay or system. The vertical elastic truss provides a strong back or mast that imposes a nearly uniform story deformation over the height of the structures (see Figure 7.2). Other possible bracing configurations and strong-back spines are shown in Figures 7.3 and 7.4. The braces used in the system could be either conventional, buckling restrained, or self-centering braces (see Figures 7.3 and 7.4).

For cases with chevron, inverted V, or dual-story X bracing systems the intersection of the braces at the floor beams can be shifted from the center of the beam. This may help in proportioning the load to the various members in the SBS. In the cases considered herein, the vertical elastic truss portion of the bay is narrower than half the bay width, thereby lengthening the inelastic elements so that they have greater length over which to yield. Although the sizes in

the spine may need to become larger than customary, by reducing the inclination of the inelastic braces they can be smaller to resist the same load. Moreover, for large lateral displacements of the frame, the increased length of the beam in the inelastic portion of the bay will be longer, reducing its shear and the plastic hinge rotations that might form at the ends of the beams.

One case examined below used low-yield strength steel in the buckling restrained bracing members. It has been noted that frames with buckling restrained braces are often larger than those for SCBF systems since the area of steel in the braces is less, resulting in a more flexible (longer period) and weaker system. By using lower strength steel, more steel is required for the same strength, and the flexibility and period are reduced. Depending on the period range, this may increase the amount of steel needed even more. The intent of using the low-strength steel is to increase the stiffness and decrease the displacement of the system without increasing the strength by a large amount. High-strength steel could be considered for portions of the structure not expected to yield. Low-yield strength steel is currently available and usually has lower yield-to-tensile ratio compared with other grades of steel. The lower yield-to-tensile ratio typically implies the material has higher potential to deform between first significant yielding and material tensile failure. This provides a buffer, redistributing the member forces to other members without failure. Members made of low-yield strength steels usually have larger cross-sectional areas compared to those made of normal strength steels (assuming the force demands are similar). This is also an advantage when proportioning member sizes and tuning the stiffness ratios within the structural system.

The following sections assess the SBS's performance by comparing their dynamic responses with several more conventional braced frame systems subjected to different hazard level ground motions. Quasi-static monotonic and cyclic analysis results are also presented.



(a) concentrated drift in conventional braced frame system

(b) more uniform drift in braced frame with strong-back system

Figure 7.2 Comparison of concentrically braced frame drifts with and without strong-back concept.

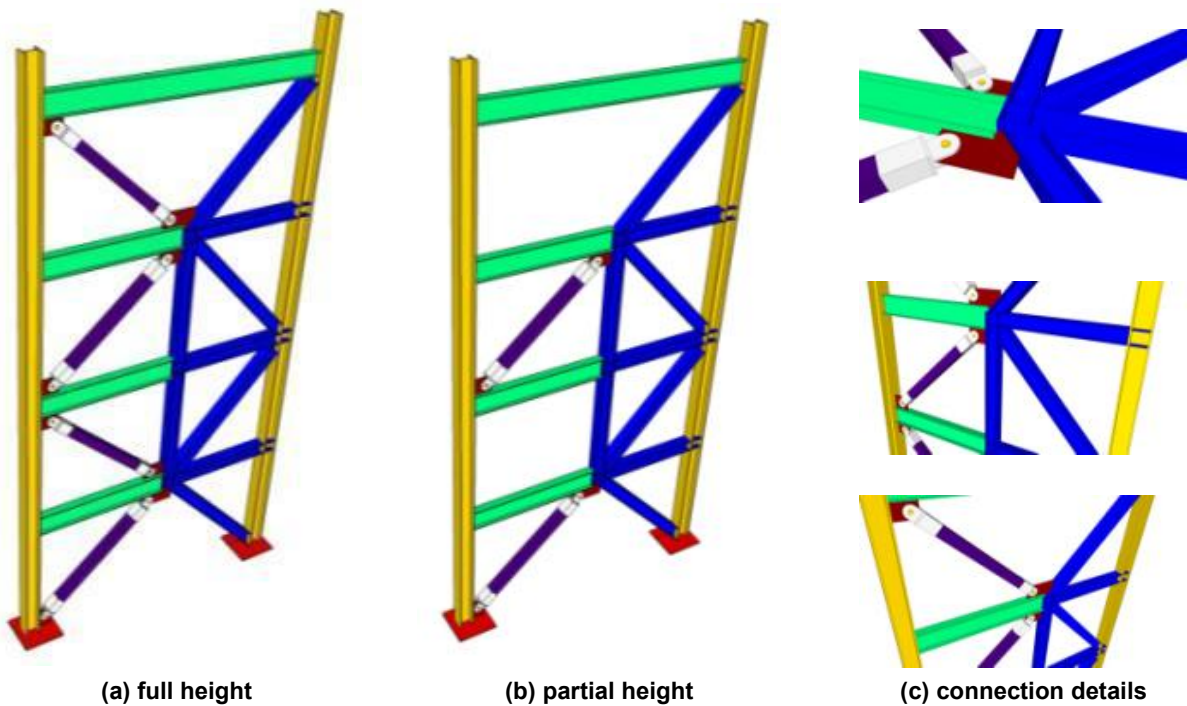
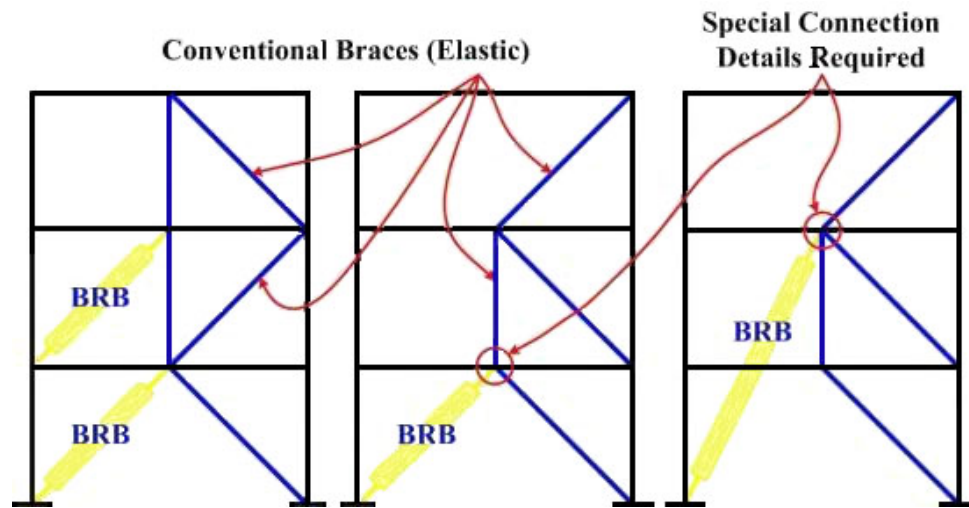
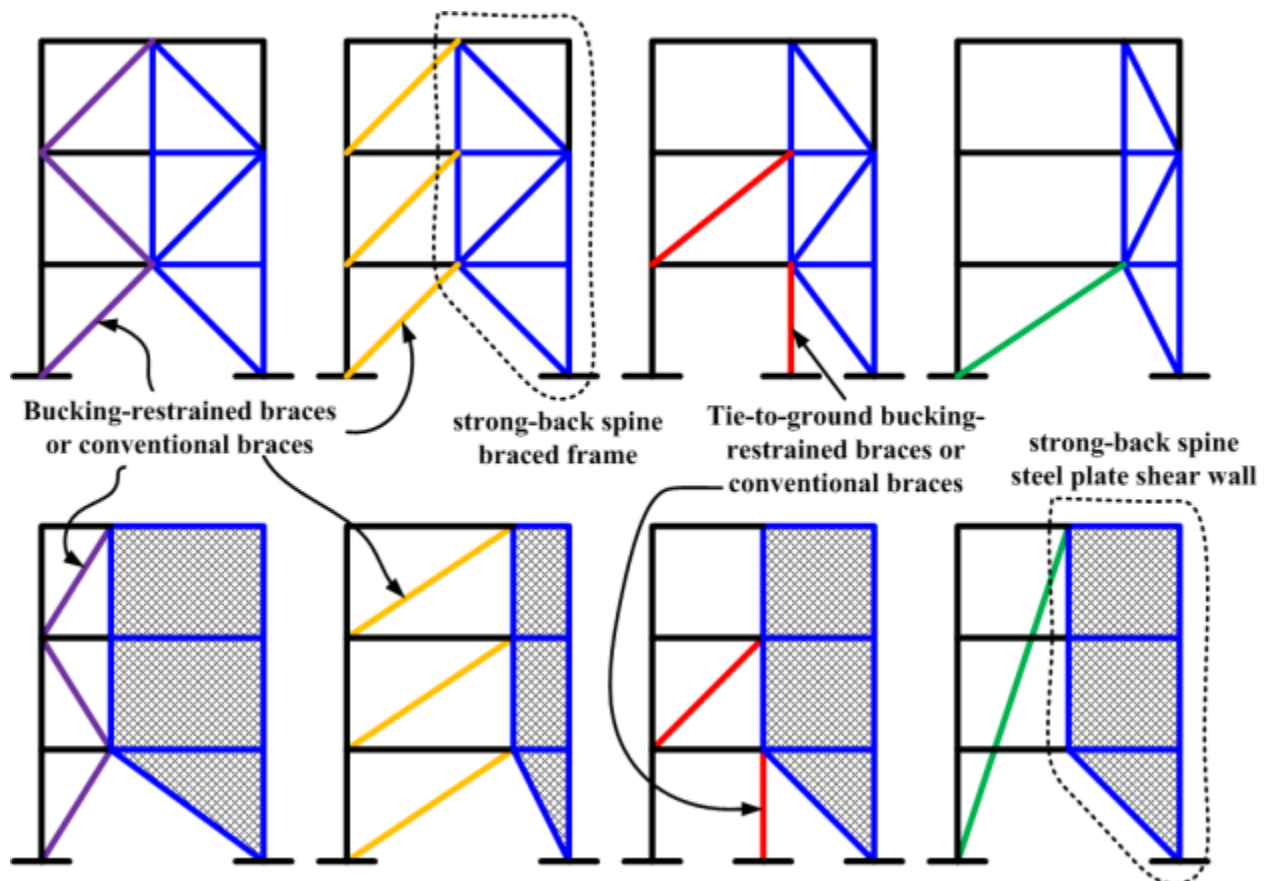


Figure 7.3 Possible strong-back configuration details with buckling-restrained braces along the entire or partial height of the building.



(a) different strong-back system configurations with buckling-restrained braces



(b) different strong-back spine configurations with conventional braces or buckling-restrained braces

Figure 7.4 More possible strong-back configurations with different spine systems.

7.4 ANALYTICAL STUDY OF THE STRONG-BACK SYSTEM

In this section, a comparison is made of the inelastic responses of the proposed hybrid SBS with those for more common braced frame systems. The example building, seismic force-resisting systems, and some basic assumptions will be introduced, the quasi-static monotonic and cyclic analyses results presented, and finally nonlinear response history analyses of each system will be compared for different hazard level ground motions.

7.4.1 Example Building

The six-story model building used in these studies is shown in Figure 7.5. Its seismic force-resisting systems in both directions are indicated. Each direction had five beam spans. Bay widths are equal to 30 ft. Each story is 13 ft high, except the ground story, which is 18 ft high. The same site location and site conditions were used as described in Chapter 3. The following criteria applied:

Governing Code: ASCE-7-2005
Occupancy: Typical Office Building
Location: Downtown Berkeley, zip code 94720
Site Class: D
Floor Height: Ground Story = 18-ft; all other stories = 13 ft
Typical Bay Size: 30-ft by 30-ft
Dead Load: 100 psf
Live Load: 50 psf

The seismic design coefficients are briefly summarized below:

Importance Factor, I : 1.0
Seismic Design Category: D
Site Class: D
Response Modification Factor, R : 6
System Overstrength Factor, Ω_o : 2.0
Deflection Amplification Factor, C_d : 5.0
 S_1 : 0.787
 S_S : 2.014
 F_a : 1.0
 F_v : 1.5
 S_{D1} : 0.787
 S_{DS} : 1.343

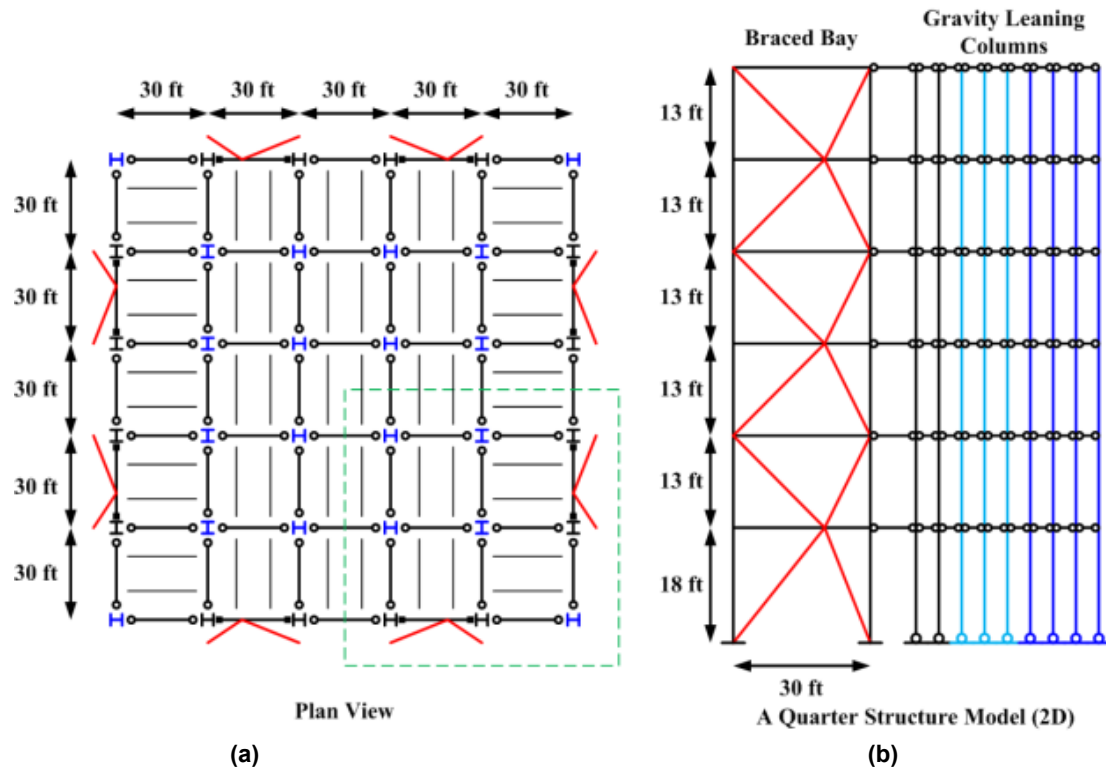


Figure 7.5 Plan view of the example building and the two-dimensional model elevation.

7.4.2 Seismic Force-Resisting Systems and Design Strategies

A total six different configurations of seismic force-resisting systems were selected for this study (see Figure 7.6). Table 7.1 summarizes the braced frame systems considered. The V6 model—a typical stacked chevron bracing configuration—was used as the benchmark. The two-story split-X bracing configuration (Model X6) was selected as representative of another typical configuration. A transformed model (Model X6-3) is basically the same as Model X6, but the meeting points of braces are shifted from the beam middle points to the one-third points. Each direction of the prototype building has four braced bays (two at each perimeter face). To ensure a symmetric lateral force-resisting system, the shifted points are aligned about the centerline of the elevation. That is, if one bay has a yielding/buckling braced inclined to the left, the other bay has the corresponding brace inclined to the right. Design of these three braced frame systems basically follows the ASCE-07 and the AISC Seismic Provisions.

System X6-3 was transformed to SBS SB6-3 by incorporating a vertical tie-column along the height of the braced bay from the second story to the fifth story. This completes the vertical spine. In addition to the basic design requirements stipulated in ASCE-07 and the AISC Seismic Provisions, the members in the vertical elastic truss were designed to remain essentially elastic under the design level seismic forces. The simple concept used here for design is based on the system code specified over-strength factor, which is 2.0 for this case. Member stress checks were

performed in SAP2000 using the load combinations listed in ASCE-07. Stress ratios in members within the vertical spine were specified to be less than 0.5, which is the reciprocal of the system overstrength factor for special concentrically braced frames. All tie-columns were designed based on the maximum expected tension and compression forces that could be developed. Although the vertical spine was designed to essentially remain elastic, it was expected that under severe ground shaking some members in the vertical spine would be subjected to inelastic demands. One of the reasons behind using this simple design strategy is to design a system that achieves the goal of preventing deformation concentration in the system at little increased cost. It is acknowledged that design optimization based on the performance goals is possible, but is not within the scope of this study.

The bracing members in Models V6, X6, X6-3, and SB6-3 were all conventional buckling braces. Hysteresis behaviors of buckling braces are typically non-symmetric and severe degradations of compression strengths are usually observed under cyclic loadings. As mentioned above, BRBs have nearly symmetric hysteresis loops and stable energy dissipation characteristics. As a result, BRBs are used in the SBS outside the vertical spine, as shown in Model SB6-3B of Figure 7.6 ($F_{y, \text{brb}} = 42$ ksi). Model SB6-3L is essentially the same as Model SB6-3B, except the materials used in the steel cores of BRBs were composed of low-yield strength steels ($F_{y, \text{brb}} = 15$ ksi). The design strategy of the vertical spine in these two models was the same as for Model SB6-3. The selection procedures for the steel cores of the BRBs followed the Steel Tips report by Lopez and Sabelli [2004]. Note that the stiffness modification factors were taken as 1.3 for the first-story BRB and 1.4 for all other stories. These were applied in the structural analysis phase to account for the variation in steel core area from the yielding core to the enlarged attachment regions at the brace ends. Tables 7.2 to 7.7 list the member size for each model.

Table 7.1 Six-story model building with different seismic force-resisting systems.

Model No.	Structural System Descriptions	ID	Note
1	six-story Chevron brace configuration	V6	Benchmark
2	six-story double story split-X brace configuration	X6	
3	six-story double story split-X brace configuration meeting at one-third point of beam span	X6-3	
4	six-story strong-back brace configuration meeting at one-third point of beam span	SB6-3	
5	six-story strong-back brace configuration meeting at one-third point of beam span with buckling-restrained braces using normal yield strength steel cores	SB6-3B	$F_{y, \text{brb}} = 42 \text{ ksi}^*$ $F_{u, \text{brb}} = 58 \text{ ksi}$
6	six-story strong-back brace configuration meeting at one-third point of beam span with buckling-restrained braces using low-yield strength steel cores	SB6-3L	$F_{y, \text{brb}} = 15 \text{ ksi}$ $F_{u, \text{brb}} = 38 \text{ ksi}$

(*Note: the $F_{y, \text{brb}} = 42 \text{ ksi}$ is calculated from the average of upper bound and lower bound BRB steel core yield strength typically used in practice, where $38 \text{ ksi} \leq F_{y, \text{brb}} \leq 46 \text{ ksi}$).

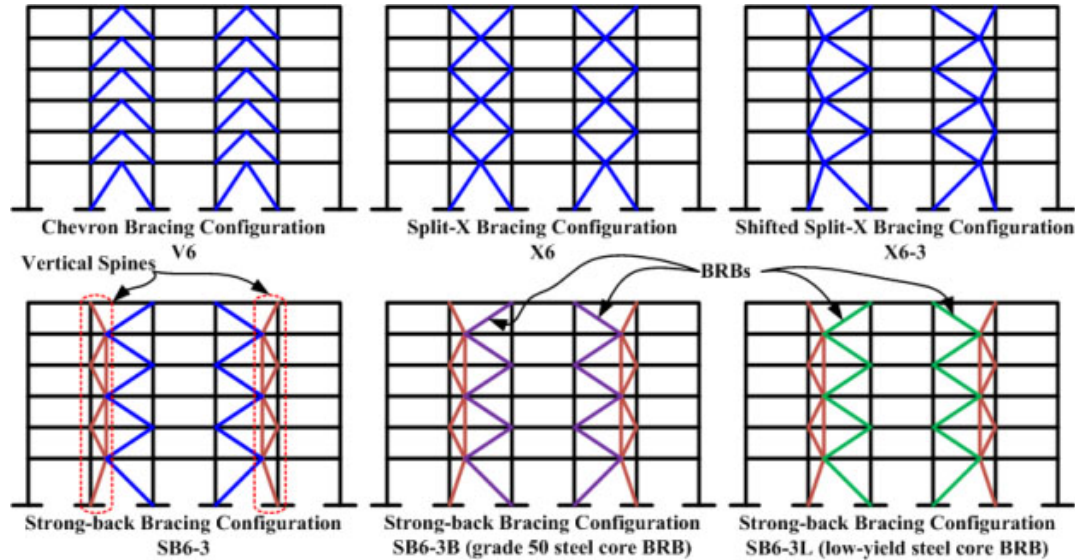


Figure 7.6 Elevation views of six different bracing configurations.

Table 7.2 Model V6 member size information.

Story	Braced Bay Column	Braced Bay Beam	Brace	Gravity Column (corner)	Gravity Column (interior)	Gravity Beam
1	W14x342	W36x282	HSS10x10x5/8	W14x68	W14x132	W18x71
2	W14x342	W30x261	HSS9x9x5/8	W14x68	W14x132	W18x71
3	W14x342	W30x261	HSS8x8x1/2	W14x68	W14x132	W18x71
4	W14x132	W27x217	HSS8x8x1/2	W14x68	W14x132	W18x71
5	W14x132	W27x217	HSS7x7x1/2	W14x68	W14x68	W18x71
6	W14x132	W27x161	HSS6x6x1/2	W14x68	W14x68	W18x71

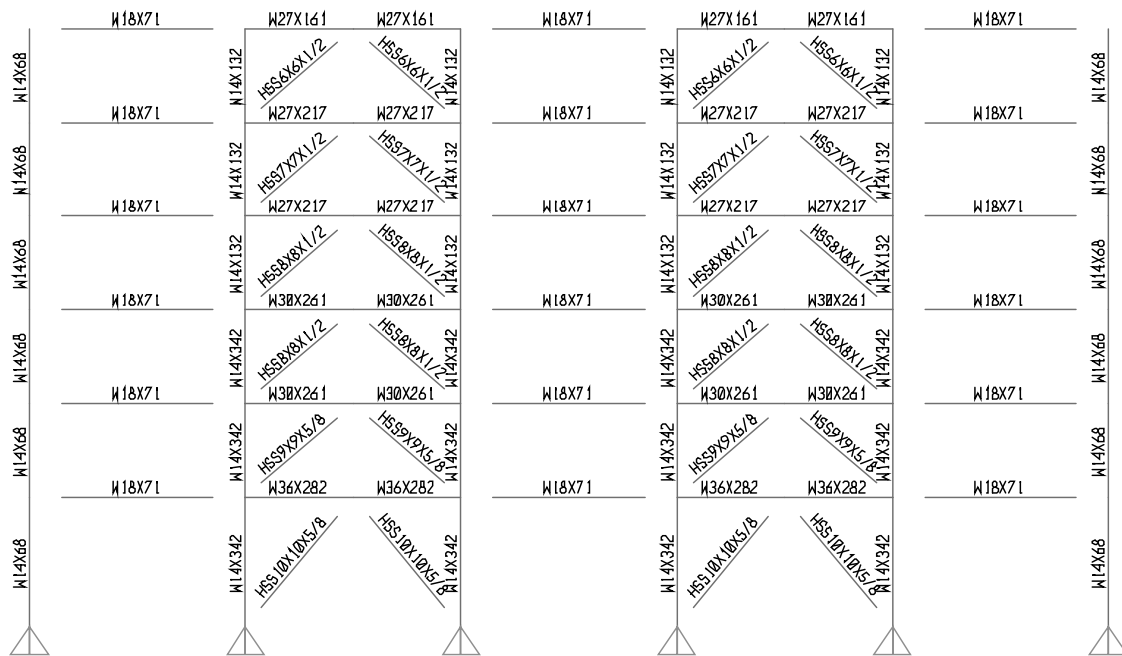


Table 7.3 Model X6 member size information.

Story	Braced Bay Column	Braced Bay Beam	Brace	Gravity Column (corner)	Gravity Column (interior)	Gravity Beam
1	W14x342	W18x86	HSS10x10x5/8	W14x68	W14x132	W18x71
2	W14x342	W18x86	HSS9x9x5/8	W14x68	W14x132	W18x71
3	W14x342	W18x86	HSS8x8x1/2	W14x68	W14x132	W18x71
4	W14x132	W18x86	HSS8x8x1/2	W14x68	W14x132	W18x71
5	W14x132	W18x86	HSS7x7x1/2	W14x68	W14x68	W18x71
6	W14x132	W18x86	HSS6x6x1/2	W14x68	W14x68	W18x71

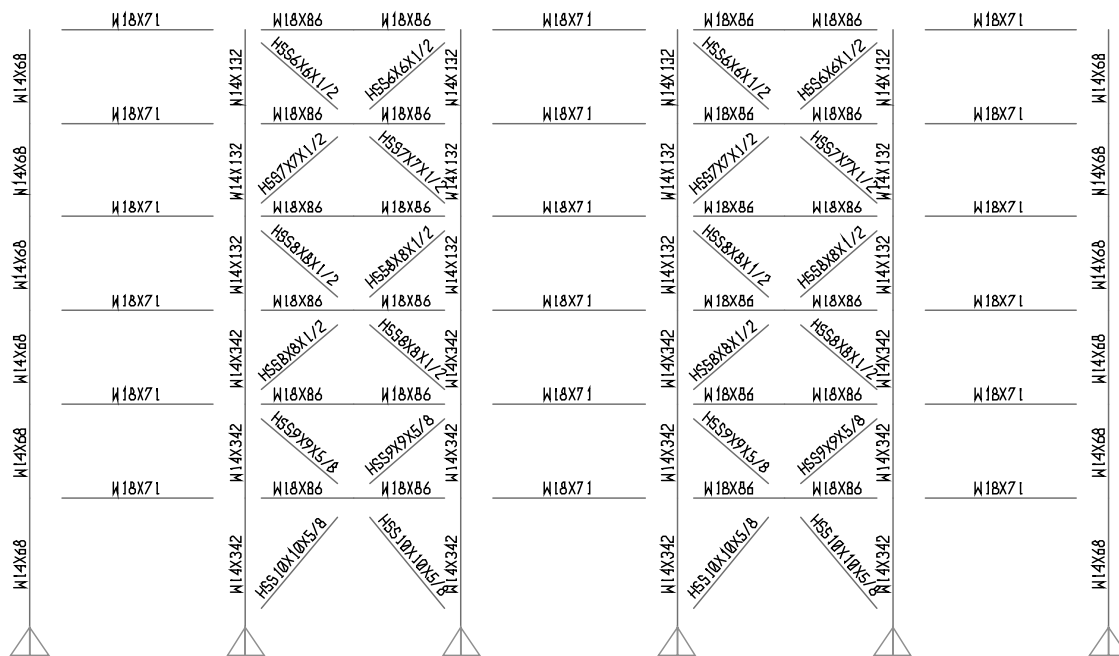


Table 7.5 Model SB6-3 member size information.

Story	Braced Bay Column	Braced Bay Beam	Brace and Tie-Column			Gravity Column (corner)	Gravity Column (interior)	Gravity Beam
1	W14x342	W18x86	HSS 12x12x5/8	-	W14x132	W14x68	W14x132	W18x71
2	W14x342	W18x86	HSS 10x10x5/8	HSS 12x12x5/8	HSS 12x12x5/8	W14x68	W14x132	W18x71
3	W14x342	W18x86	HSS 9x9x5/8	HSS 12x12x5/8	HSS 12x12x5/8	W14x68	W14x132	W18x71
4	W14x132	W18x86	HSS 9x9x5/8	HSS 8x8x1/2	HSS 10x10x1/2	W14x68	W14x132	W18x71
5	W14x132	W18x86	HSS 8x8x1/2	HSS 8x8x1/2	HSS 10x10x1/2	W14x68	W14x68	W18x71
6	W14x132	W18x86	HSS 7x7x1/2	-	HSS 8x8x1/2	W14x68	W14x68	W18x71

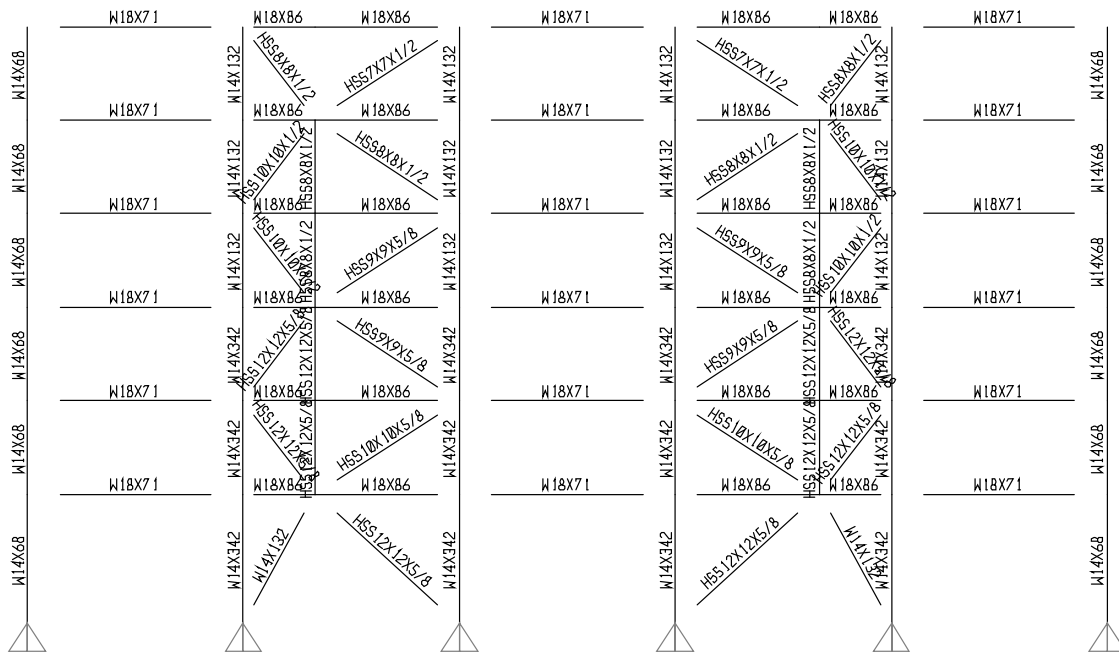


Table 7.6 Model SB6-3B member size information.

Story	Braced Bay Column	Braced Bay Beam	Brace and Tie-Column			Gravity Column (corner)	Gravity Column (interior)	Gravity Beam
1	W14x342	W18x86	BRB 18 in ²	-	W14x132	W14x68	W14x132	W18x71
2	W14x342	W18x86	BRB 16 in ²	HSS 10x10x1/2	HSS 12x12x5/8	W14x68	W14x132	W18x71
3	W14x342	W18x86	BRB 14 in ²	HSS 10x10x1/2	HSS 12x12x5/8	W14x68	W14x132	W18x71
4	W14x132	W18x86	BRB 12 in ²	HSS 8x8x1/2	HSS 10x10x1/2	W14x68	W14x132	W18x71
5	W14x132	W18x86	BRB 8 in ²	HSS 8x8x1/2	HSS 10x10x1/2	W14x68	W14x68	W18x71
6	W14x132	W18x86	BRB 4 in ²	-	HSS 8x8x1/2	W14x68	W14x68	W18x71

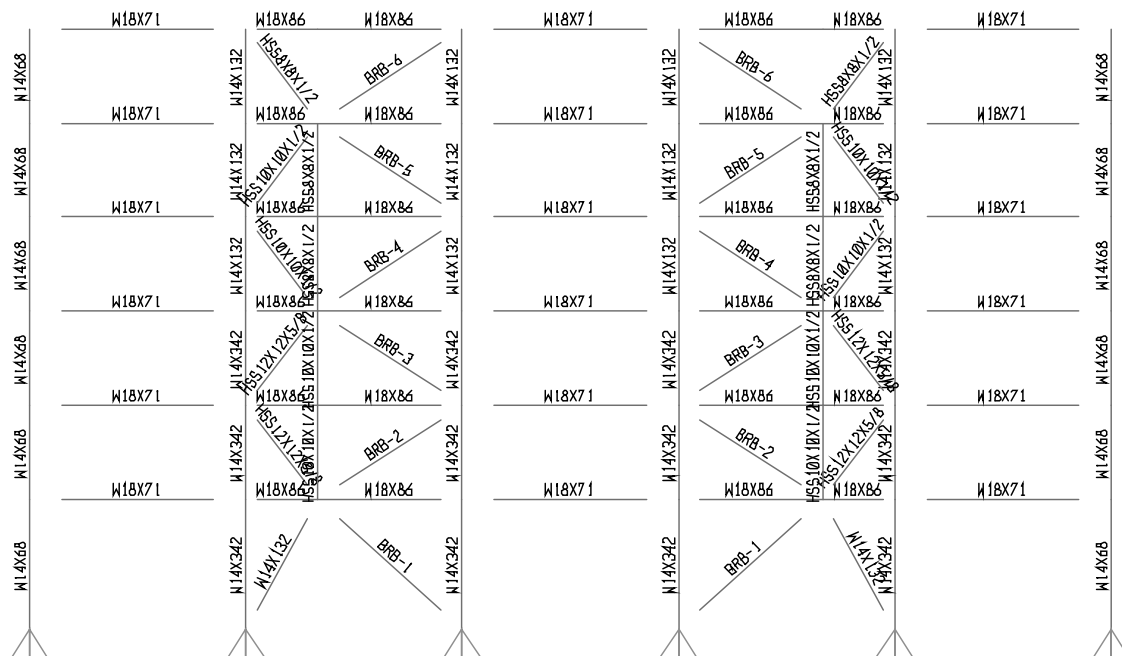
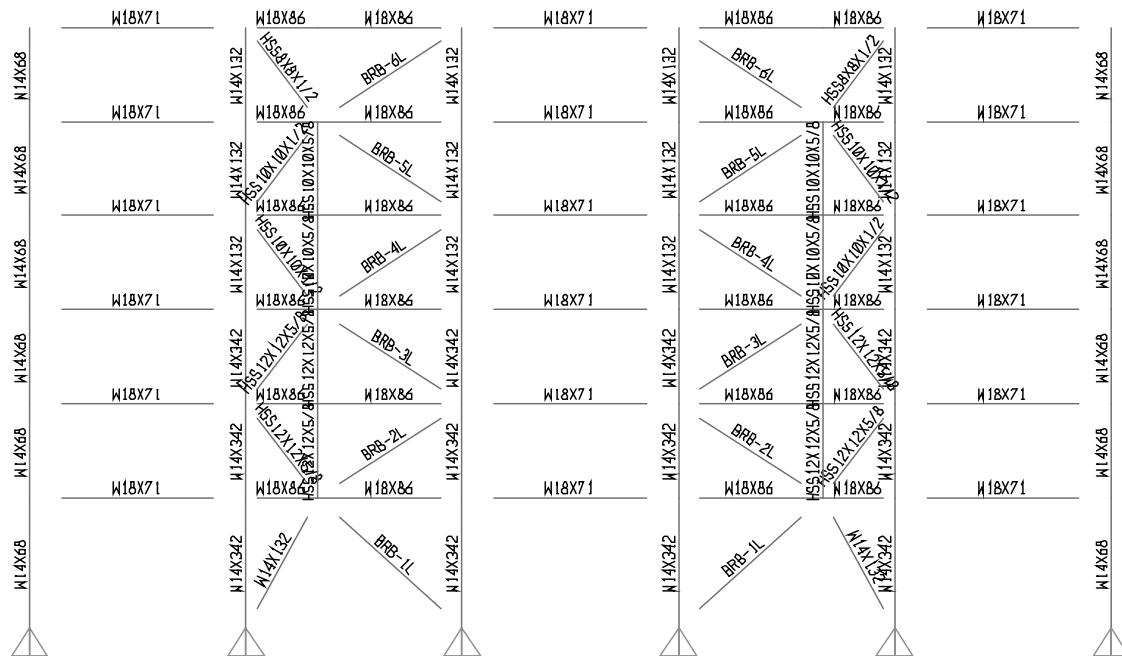


Table 7.7 Model SB6-3L member size information.

Story	Braced Bay Column	Braced Bay Beam	Brace and Tie-Column			Gravity Column (corner)	Gravity Column (interior)	Gravity Beam
1	W14x342	W18x86	BRB-LYS* 70 in ²	-	W14x132	W14x68	W14x132	W18x71
2	W14x342	W18x86	BRB-LYS 62 in ²	HSS 12x12x5/8	HSS 12x12x5/8	W14x68	W14x132	W18x71
3	W14x342	W18x86	BRB-LYS 50 in ²	HSS 12x12x5/8	HSS 12x12x5/8	W14x68	W14x132	W18x71
4	W14x132	W18x86	BRB-LYS 46 in ²	HSS 10x10x5/8	HSS 10x10x1/2	W14x68	W14x132	W18x71
5	W14x132	W18x86	BRB-LYS 30 in ²	HSS 10x10x5/8	HSS 10x10x1/2	W14x68	W14x68	W18x71
6	W14x132	W18x86	BRB-LYS 16 in ²	-	HSS 8x8x1/2	W14x68	W14x68	W18x71



(*Note: LYS stands for low-yield strength steel)

7.4.3 Modeling

Two-dimensional computer models were developed in OpenSees using the same modeling concepts described in Section 6.2. Because of symmetry, only a quarter of the building was included in the analytical model. The braced bay was modeled and the gravity columns modeled as leaning columns aside the braced bay, as illustrated in Figure 7.5(b). The leaning columns were pinned at the base and individually modeled for each gravity column line in OpenSees. All leaning columns were connected at each floor level using rigid links. Tributary gravity forces at each floor level were added for the corresponding nodal points of leaning columns. Monotonic and, cyclic quasi-static analyses, and nonlinear time history analyses were performed for each structural system (Models V6, X6, X6-3, SB6-3, SB6-3B, and SB6-3L). A Rayleigh damping parameter of 2% was used for both first and second mode for all six analyses. Initial imperfections equal to 1/1000 of brace entire length was used in the models for all conventional buckling braces. Rigid end zones were applied at member ends based on the actual member sizes in the models. Pinned connections were assumed at every brace end.

7.4.4 Ground Motions

Ground motions for dynamic analysis were selected from the PEER Ground Motion Database (Beta version, http://peer.berkeley.edu/peer_ground_motion_database/). Two different hazard levels were considered: design level ground motion (10% probability of exceedance in 50 years) and maximum consider level ground motion (2% probability of exceedance in 50 years). Each hazard level contained five pairs of ground motions, representing the fault-normal and fault-parallel components. This results in ten excitations being considered for the 2D model analyzed. Vertical components of ground motions were not included in this study.

Each ground motion pair is selected using the online ground motion database searching tool with predefined record acceptance criteria. The scale factors of the ground motions are limited to be less than three. Table 7.8 summarizes the criteria used in the search engine. Each pair of ground motions is summarized in Table 7.9. Scaled average spectral acceleration of selected ground motion records are plotted in Figure 7.7 with the target spectrum (for design level ground motions). The scale factors for the maximum consider level ground motions are simply 1.5 times the scale factors for the design level ground motions.

Table 7.8 Predefined ground motion search criteria.

Criteria	Magnitude (min.)	Magnitude (max.)	V_{S30} (m/sec)	Fault Type	Weighted Period Range (min. ~ max.)	Scale Factor
Values	5.0	7.5	182 ~ 366	Strike Slip (SS)	0.2T ~ 1.5T	< 3.0

(Note: T is the fundamental period of the structure, $T = 0.6$ sec. is used for six-story structures in this case.)

Table 7.9 Selected ground motion pairs for nonlinear dynamic response history analysis.

NGA No.	Event	Year	Magnitude	Mechanism	V_{S30} (m/sec)	R_{rup} (km)	Scale Factor
160	Imperial Valley-06	1979	6.53	Strike-Slip	223	2.7	0.8848
1119	Kobe- Japan	1995	6.9	Strike-Slip	312	0.3	0.9566
558	Chalfant Valley-02	1986	6.19	Strike-Slip	271.4	7.6	1.2984
1853	Yountville	2000	5.0	Strike-Slip	271.4	11.4*	1.5067
1602	Duzce- Turkey	1999	7.14	Strike-Slip	326	12	1.0469

(Note: R_{rup} with asterisk is estimated value.)

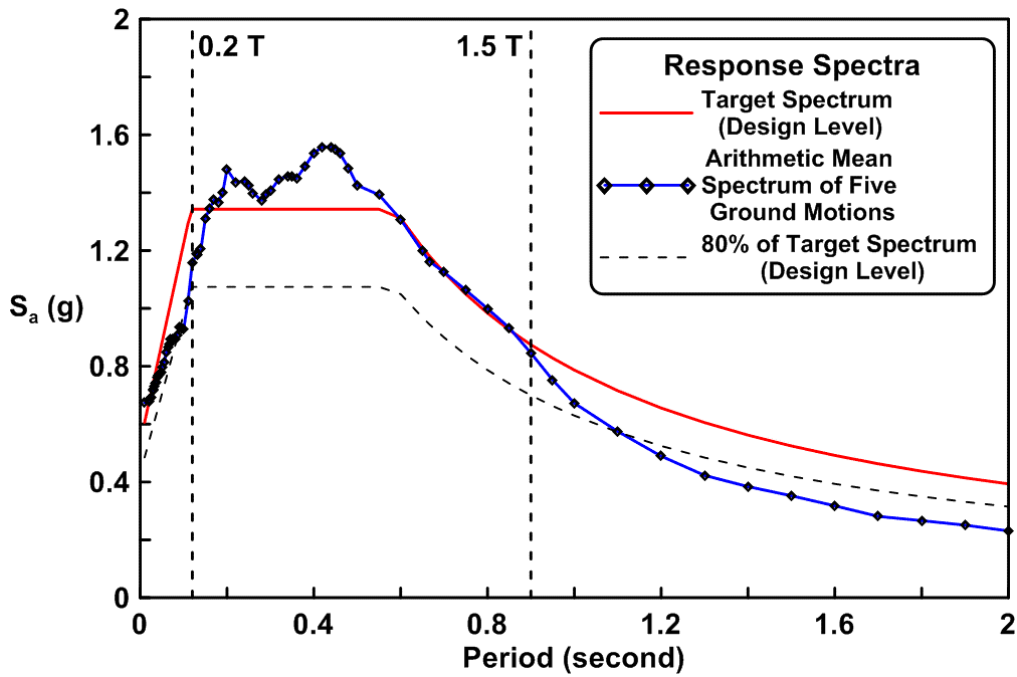


Figure 7.7 Averaged spectrum of selected ground motion records.

7.5 RESPONSE OF HYBRID STRONG-BACK SYSTEM

7.5.1 Monotonic Pushover Results

Static pushover analyses were performed on the six models using OpenSees with a control node at the roof level of the example building. The target displacement was set to be equal to 5% roof drift, which in this case corresponds to 49.8 in. An inverted triangle lateral force distribution was maintained during the pushover analyses. Monotonic pushover curves are shown in Figure 7.8. Note that all models were pushed in the positive direction; gravity forces were included in the analytical models.

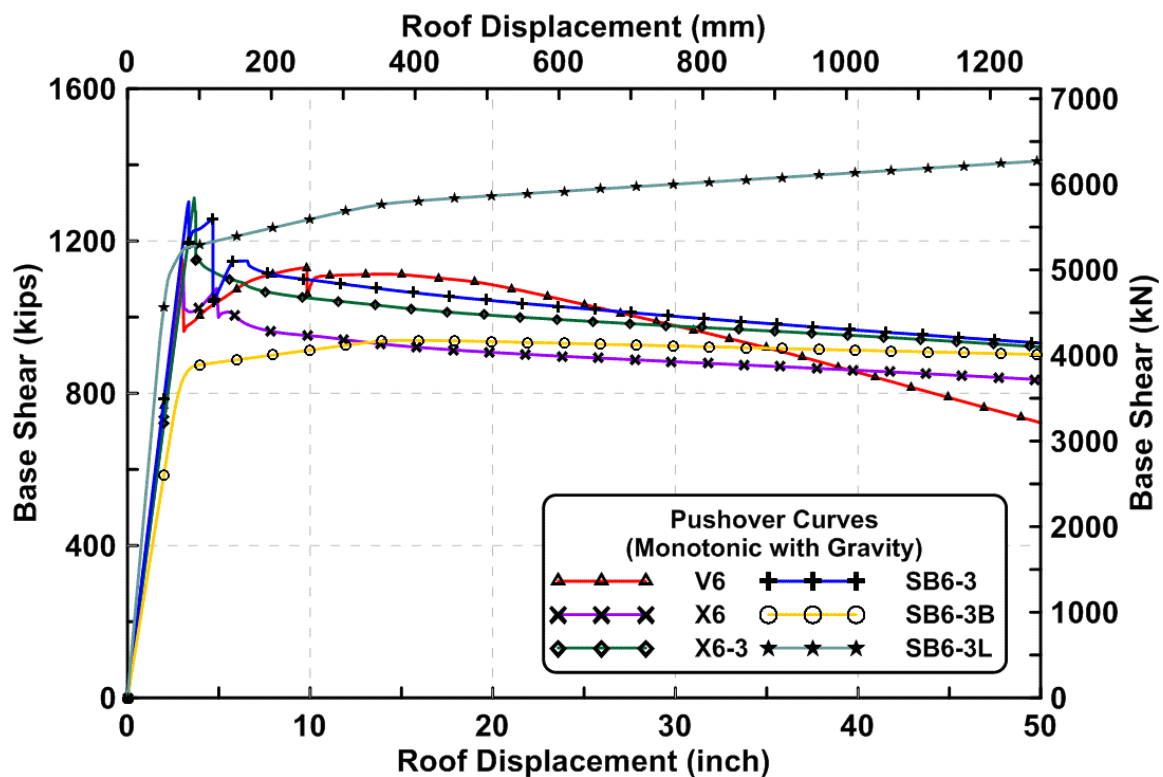


Figure 7.8 Base shear versus roof displacement relationships of six models.

7.5.2 Quasi-Static Cyclic Results

In addition, cyclic analyses were performed in OpenSees for all six models. The pre-defined cyclic target roof displacements are listed in Table 7.10 for all six models. Similar to monotonic pushover analyses, an inverted triangle lateral force distribution was applied during the cyclic loading. Hysteretic curves with including gravity effects are shown in Figure 7.9 for each model.

Table 7.10 Prescribed roof displacements for cyclic pushover analyses.

Sequence Number	Number of Cycle	Target Roof Displacement (in.)	Corresponding Roof Drift Ratio (%)
1	2	±2.99	±0.3
2	2	±4.98	±0.5
3	2	±9.96	±1.0
4	2	±19.92	±2.0
5	2	±29.88	±3.0
6	2	±39.84	±4.0
7	2	±49.8	±5.0

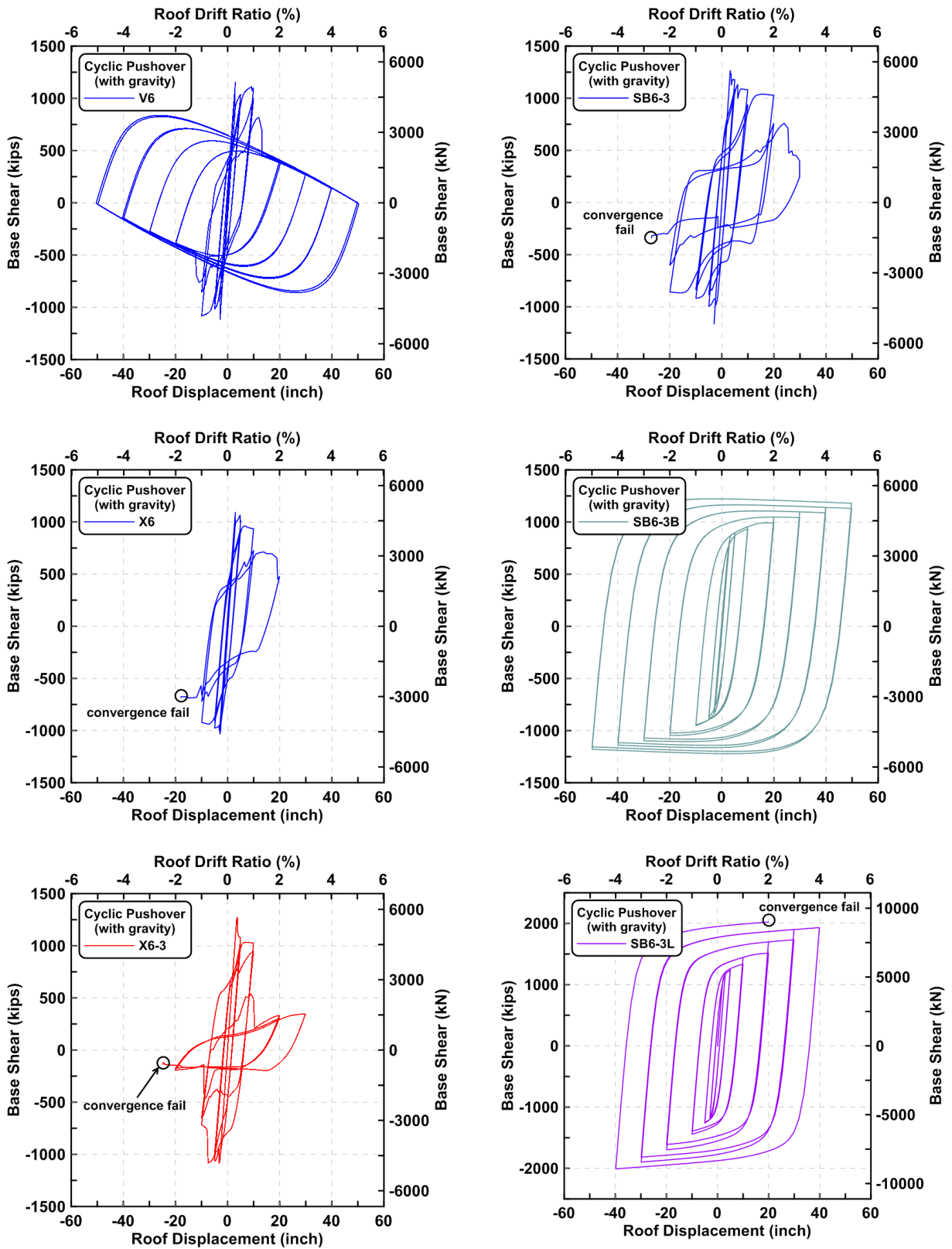


Figure 7.9 Base shear versus roof displacement relationships of each model under cyclic pushover.

7.5.3 Nonlinear Response History Analysis Results

A total of ten ground motions (two components from five records) were used in the dynamic analysis. These were rotated to the fault-normal and fault-parallel directions. As mentioned earlier, ground motions were scaled to match two hazard levels. For simulation convenience, all ground motions were assigned an identification number, as listed in Table 7.11. Several dynamic response quantities were examined and summarized for each model. Table 7.12 shows the first two highest periods for each model. The fundamental period of each model is close to the empirical value of 0.6 sec and larger than the code empirical period of 0.55 sec ($T = 0.02 \times 83^{0.75} = 0.55$). Tables 7.13 to 7.16 list the mean responses of each model under selected ground motion pairs.

Table 7.11 Identification number list for all ground motions.

ID	NGA Number	Component	Scale Factor	Δt (sec)	Duration (sec)
01	NGA-160	fault-normal	0.8848	0.005	37.61
02	NGA-558	fault-normal	1.2984	0.005	39.98
03	NGA-1119	fault-normal	0.9566	0.01	40.96
04	NGA-1602	fault-normal	1.0469	0.01	55.90
05	NGA-1853	fault-normal	1.5067	0.005	72.00
06	NGA-160	fault-parallel	0.8848	0.005	37.61
07	NGA-558	fault-parallel	1.2984	0.005	39.98
08	NGA-1119	fault-parallel	0.9566	0.01	40.96
09	NGA-1602	fault-parallel	1.0469	0.01	55.90
10	NGA-1853	fault-parallel	1.5067	0.005	72.00
11	NGA-160	fault-normal	1.3272	0.005	37.61
12	NGA-558	fault-normal	1.9476	0.005	39.98
13	NGA-1119	fault-normal	1.4349	0.01	40.96
14	NGA-1602	fault-normal	1.5704	0.01	55.90
15	NGA-1853	fault-normal	2.2601	0.005	72.00
16	NGA-160	fault-parallel	1.3272	0.005	37.61
17	NGA-558	fault-parallel	1.9476	0.005	39.98
18	NGA-1119	fault-parallel	1.4349	0.01	40.96
19	NGA-1602	fault-parallel	1.5704	0.01	55.90
20	NGA-1853	fault-parallel	2.2601	0.005	72.00

Table 7.12 Fundamental and second mode periods of each mode.

Model Name	1st Mode (sec)	2nd Mode (sec)
V6	0.688	0.245
X6	0.701	0.244
X6-3	0.701	0.248
SB6-3	0.667	0.234
SB6-3B	0.770	0.282
SB6-3L	0.564	0.192

Table 7.13 Mean responses of each model under selected ground motions (10% probability of exceedance in 50-years events, fault-normal component).

Mean Response	V6	X6	X6-3	SB6-3	SB6-3B	SB6-3L
Max. Base Shear (kips)	1199.7	1272.6	1354.7	1448.3	1067.1	1389.5
Max. Roof Displacement (in.)	5.10	5.14	5.70	5.59	5.98	4.99
Max. 1 st Story Drift Ratio (%)	1.208	0.634	0.658	0.605	0.517	0.324
Max. 2 nd Story Drift Ratio (%)	0.305	0.514	0.662	0.615	0.543	0.383
Max. 3 rd Story Drift Ratio (%)	0.406	0.980	0.852	0.714	0.577	0.489
Max. 4 th Story Drift Ratio (%)	0.565	0.857	0.793	0.760	0.688	0.593
Max. 5 th Story Drift Ratio (%)	0.487	0.540	0.819	0.790	0.909	0.743
Max. 6 th Story Drift Ratio (%)	0.376	0.382	0.444	0.769	0.923	0.730
Residual Roof Displacement (in.)	0.322	0.498	0.286	0.195	0.448	0.702
Residual 1 st Story Drift Ratio (%)	0.092	0.150	0.110	0.052	0.069	0.040
Residual 2 nd Story Drift Ratio (%)	0.010	0.091	0.078	0.030	0.050	0.056
Residual 3 rd Story Drift Ratio (%)	0.029	0.060	0.081	0.032	0.050	0.066
Residual 4 th Story Drift Ratio (%)	0.037	0.080	0.068	0.030	0.048	0.083
Residual 5 th Story Drift Ratio (%)	0.034	0.057	0.049	0.024	0.057	0.090
Residual 6 th Story Drift Ratio (%)	0.006	0.013	0.028	0.032	0.055	0.105
Max. Column Uplift Force, LHS (kips)	2122.7	2022.3	2364.7	2352.9	1493.8	2284.5
Max. Column Uplift Force, RHS (kips)	2104.9	1994.1	2132.2	2274.9	1572.3	2212.3
Max. 2 nd Floor Acceleration (g)	1.17	1.05	1.15	1.20	1.02	1.13
Max. 3 rd Floor Acceleration (g)	1.08	1.10	1.14	1.08	1.01	0.99
Max. 4 th Floor Acceleration (g)	0.98	1.00	1.06	0.94	0.94	0.89
Max. 5 th Floor Acceleration (g)	0.92	0.81	0.90	0.81	0.78	0.68
Max. 6 th Floor Acceleration (g)	0.84	0.66	0.72	0.67	0.58	0.52
Max. Roof Acceleration (g)	1.24	1.30	1.38	1.38	1.20	1.39

(Note: LHS stands for left hand side, RHS stands for right hand side.)

Table 7.14 Mean responses of each model under selected ground motions (10% probability of exceedance in 50-years events, fault-parallel component).

Mean Response	V6	X6	X6-3	SB6-3	SB6-3B	SB6-3L
Max. Base Shear (kips)	1186.3	1237.2	1349.6	1424.4	1038.4	1331.5
Max. Roof Displacement (in.)	6.23	6.52	6.68	6.45	7.65	5.39
Max. 1 st Story Drift Ratio (%)	1.627	0.971	0.994	0.689	0.588	0.366
Max. 2 nd Story Drift Ratio (%)	0.324	0.703	0.720	0.762	0.661	0.442
Max. 3 rd Story Drift Ratio (%)	0.422	1.017	0.865	0.749	0.737	0.537
Max. 4 th Story Drift Ratio (%)	0.620	0.909	0.765	0.858	0.862	0.611
Max. 5 th Story Drift Ratio (%)	0.480	0.548	0.866	0.700	1.013	0.755
Max. 6 th Story Drift Ratio (%)	0.363	0.362	0.400	0.647	1.001	0.738
Residual Roof Displacement (in.)	0.351	0.899	0.588	1.588	1.111	0.880
Residual 1 st Story Drift Ratio (%)	0.103	0.161	0.110	0.175	0.093	0.091
Residual 2 nd Story Drift Ratio (%)	0.012	0.124	0.092	0.227	0.010	0.086
Residual 3 rd Story Drift Ratio (%)	0.022	0.098	0.073	0.153	0.111	0.091
Residual 4 th Story Drift Ratio (%)	0.062	0.085	0.081	0.206	0.121	0.091
Residual 5 th Story Drift Ratio (%)	0.031	0.048	0.115	0.107	0.121	0.087
Residual 6 th Story Drift Ratio (%)	0.008	0.010	0.015	0.098	0.128	0.090
Max. Column Uplift Force, LHS (kips)	2191.2	2106.9	2460.3	2401.6	1596.5	2236.3
Max. Column Uplift Force, RHS (kips)	2155.6	1937.3	2108.1	2216.7	1565.7	2244.6
Max. 2 nd Floor Acceleration (g)	1.08	0.98	0.96	1.00	0.89	1.01
Max. 3 rd Floor Acceleration (g)	0.84	0.91	0.87	0.95	0.79	0.87
Max. 4 th Floor Acceleration (g)	0.83	0.84	0.88	0.83	0.70	0.71
Max. 5 th Floor Acceleration (g)	0.80	0.78	0.70	0.63	0.58	0.50
Max. 6 th Floor Acceleration (g)	0.72	0.56	0.60	0.60	0.44	0.35
Max. Roof Acceleration (g)	1.21	1.17	1.26	1.18	1.17	1.16

(Note: LHS stands for left hand side, RHS stands for right hand side)

Table 7.15 Mean responses of each model under selected ground motions (2% probability of exceedance in 50 years, fault-normal component).

Mean Response	V6	X6	X6-3	SB6-3	SB6-3B	SB6-3L
Max. Base Shear (kips)	1212.6	1288.9	1341.9	1492.7	1143.2	1594.8
Max. Roof Displacement (in.)	7.90	8.12	8.12	8.86	8.76	6.63
Max. 1 st Story Drift Ratio (%)	2.206	1.368	1.725	1.023	0.818	0.624
Max. 2 nd Story Drift Ratio (%)	0.427	0.977	0.971	0.984	0.842	0.659
Max. 3 rd Story Drift Ratio (%)	0.484	1.156	0.923	0.971	0.881	0.702
Max. 4 th Story Drift Ratio (%)	0.727	0.896	0.753	1.142	1.028	0.752
Max. 5 th Story Drift Ratio (%)	0.601	0.627	0.956	1.128	1.240	0.902
Max. 6 th Story Drift Ratio (%)	0.408	0.401	0.428	1.147	1.320	0.902
Residual Roof Displacement (in.)	0.728	1.767	1.583	1.114	1.406	0.748
Residual 1 st Story Drift Ratio (%)	0.202	0.298	0.248	0.107	0.165	0.119
Residual 2 nd Story Drift Ratio (%)	0.048	0.298	0.215	0.114	0.153	0.102
Residual 3 rd Story Drift Ratio (%)	0.050	0.254	0.208	0.099	0.144	0.074
Residual 4 th Story Drift Ratio (%)	0.091	0.129	0.139	0.142	0.134	0.068
Residual 5 th Story Drift Ratio (%)	0.046	0.052	0.101	0.110	0.117	0.082
Residual 6 th Story Drift Ratio (%)	0.022	0.012	0.033	0.108	0.124	0.092
Max. Column Uplift Force, LHS (kips)	2104.1	1984.5	2198.4	2131.7	1547.1	2372.8
Max. Column Uplift Force, RHS (kips)	2232.5	2057.7	2175.2	2284.6	1652.2	2361.4
Max. 2 nd Floor Acceleration (g)	1.58	1.44	1.47	1.73	1.44	1.55
Max. 3 rd Floor Acceleration (g)	1.31	1.37	1.37	1.39	1.40	1.34
Max. 4 th Floor Acceleration (g)	1.29	1.32	1.39	1.28	1.28	1.18
Max. 5 th Floor Acceleration (g)	1.22	1.21	1.18	1.11	1.12	0.97
Max. 6 th Floor Acceleration (g)	1.10	1.04	0.95	0.90	0.84	0.74
Max. Roof Acceleration (g)	1.64	1.56	1.63	1.60	1.59	1.82

(Note: LHS stands for left hand side, RHS stands for right hand side)

Table 7.16 Mean responses of each model under selected ground motions (2% probability of exceedance in 50 years, fault-parallel component).

Mean Response	V6	X6	X6-3	SB6-3	SB6-3B	SB6-3L
Max. Base Shear (kips)	1197.2	1265.0	1344.5	1420.3	1137.9	1498.3
Max. Roof Displacement (in.)	11.19	11.06	11.30	12.78	10.72	8.59
Max. 1 st Story Drift Ratio (%)	3.291	1.862	1.876	1.348	0.890	0.689
Max. 2 nd Story Drift Ratio (%)	0.593	1.426	1.292	1.320	0.935	0.763
Max. 3 rd Story Drift Ratio (%)	0.535	1.530	1.315	1.377	1.042	0.880
Max. 4 th Story Drift Ratio (%)	0.812	1.157	1.387	1.439	1.208	0.955
Max. 5 th Story Drift Ratio (%)	0.662	0.719	1.052	1.431	1.454	1.064
Max. 6 th Story Drift Ratio (%)	0.426	0.414	0.509	1.515	1.475	1.041
Residual Roof Displacement (in.)	2.030	2.607	1.541	2.348	1.633	1.576
Residual 1 st Story Drift Ratio (%)	0.689	0.495	0.342	0.344	0.151	0.161
Residual 2 nd Story Drift Ratio (%)	0.113	0.400	0.227	0.254	0.159	0.162
Residual 3 rd Story Drift Ratio (%)	0.060	0.322	0.173	0.225	0.169	0.161
Residual 4 th Story Drift Ratio (%)	0.071	0.182	0.100	0.201	0.178	0.164
Residual 5 th Story Drift Ratio (%)	0.060	0.074	0.036	0.214	0.173	0.149
Residual 6 th Story Drift Ratio (%)	0.046	0.016	0.040	0.178	0.164	0.150
Max. Column Uplift Force, LHS (kips)	2302.5	1987.4	2326.8	2336.2	1683.1	2361.9
Max. Column Uplift Force, RHS (kips)	2233.2	2076.1	2199.6	2274.4	1604.7	2432.6
Max. 2 nd Floor Acceleration (g)	1.41	1.37	1.38	1.30	1.30	1.32
Max. 3 rd Floor Acceleration (g)	1.14	1.31	1.23	1.34	1.07	1.09
Max. 4 th Floor Acceleration (g)	1.13	1.21	1.12	1.13	0.96	0.96
Max. 5 th Floor Acceleration (g)	1.06	1.00	0.99	0.84	0.81	0.74
Max. 6 th Floor Acceleration (g)	0.95	0.86	0.80	0.79	0.66	0.58
Max. Roof Acceleration (g)	1.53	1.53	1.52	1.66	1.61	1.56

(Note: LHS stands for left hand side, RHS stands for right-hand side.)

7.6 DISCUSSION

7.6.1 Pushover Analysis

The monotonic pushover curves shown in Figure 7.8 show that the first four models (V6, X6, X6-3 and SB6-3) had similar initial stiffnesses. Models V6 and X6 had similar peak base shear capacity. Models X6-3 and SB6-3 had similar peak base shear capacity and were about 10% higher than that found for Models V6 and X6. Once the brace at a certain floor level began to buckle, the base shear began to drop. The base shear of Model V6 dropped after the brace at first

story buckled, but later increased. With continued lateral displacement of Model V6, the unbalanced forces in the first story pulled down the center of the beam and plastic hinges formed in the beam ends (beam-to-column connections were rigid connections). Later, plastic hinges formed in the columns, and the entire model developed a negative tangent stiffness at around 17.5-in. roof displacement. The beam-to-column connections were pinned in Models X6, X6-3, and SB6-3; once the story mechanism formed in these models, the base shear decreased gradually. Note that the negative slopes were smaller than Models X6, X6-3 and SB6-3 for Model V6. The pushover curve of Model SB6-3 had several local peaks, indicating that braces other than first story buckled or yielded.

Pushover curves of Models SB6-3B and SB6-3L both exhibited a tri-linear shape. Model SB6-3L had a higher initial stiffness (due to larger brace steel core areas), while Model SB6-3B had lower initial stiffness compared to the other four models (due to its smaller brace steel core areas). The slope of the pushover curve of Model SB6-3L never became negative. Model SB6-3B did exhibit a slightly negative slope when the roof displacement exceeded 18 in.

Quasi-static cyclic analyses show that the cyclic base shear capacity of Model V6 degraded more rapidly compared to the monotonic pushover analysis; the braces at the first story fractured at about 1.5% roof drift ratio, and the base shear capacity dropped to about zero at roof drift ratio corresponding to 5% (see Figure 7.9). Models X6, X6-3, and SB6-3 failed to complete the entire cyclic analysis protocol due to numerical convergence issues. Brace fracturing in these three models was observed, as can be deduced from Figure 7.9. Substantial cyclic hardening was observed in Models SB6-3B and SB6-3L. Note that the base shear capacity kept increasing in model SB6-3L, while in Model SB6-3B the base shear capacity very gradually decreased at larger roof displacements. Brace fracturing of part of the vertical spine of the six-story conventional brace (Model SB6-3) was observed in the cyclic analyses; see the noticeable small spike Figure 7.9. The material modeling used for buckling-restrained braces did not include low-cycle fatigue features.

Clearly, the SBS with conventional braces or BRBs out-performed the braced frames with traditional bracing configurations. Using low-yield strength BRBs in the strong-back hybrid system had a greater post-yield deformation hardening characteristic than did the conventional BRBF.

7.6.2 Dynamic Analysis

As listed in Tables 7.13 to 7.16, peak base shear forces were all between 1000 kips to 1600 kips. The order of peak base shear forces from dynamic analysis basically followed the order of the fundamental periods of six models: the lower the fundamental period, the higher the peak shear force.

Maximum roof displacements under fault-parallel ground motions were all larger than the maximum roof displacements under fault-normal ground motions. The strong-back system with low-yield strength BRBs tended to have small roof displacements. Because of a larger cross-

section area of steel cores, Model SB6-3L was stiffer and stronger. As such, it tended to have smaller maximum roof displacements.

Figure 7.10 shows that a weak-ground-story formed in Model V6. Under the MCE-level event, this model exhibited a mean drift ratio of more than 3% that was concentrated at the first story. Model X6 tended to form a soft two-story-panel mechanism. It is interesting to note that slightly larger story drift ratios tended to occur in the upper stories of the SBS's. The distribution of story drift ratios of Model SB6-3 was close to a uniform pattern. The story drift ratios of Models SB6-3B and SB6-3L had quite a uniform distribution at the lower stories. All residual story drift ratios were less than 0.7%, as shown in Figure 7.11. The residual story drift ratios under fault-parallel ground motions were all larger than that under fault-normal ground motions.

For the column base force demands, Model SB6-3B had the smallest column uplift forces among all six models for the two hazard levels (about 25% smaller). The other five models had similar column uplift force demands.

Distributions of floor accelerations exhibited a sickle-shaped pattern for all six models, as shown in Figure 7.12. For example, maximum floor acceleration under 2% probability of exceedance in 50 years varied from around 1.5g at the top of the first story to about 1.0g at the top of the fifth story, and then jumped to about 1.5g at roof level. The maximum floor accelerations at each floor level under fault-normal ground motions were all larger than that under fault-parallel ground motions.

Base shear versus roof displacement loop diagrams, story drift ratio histories of each floor level, and axial force-deformation relationships of all twelve braces for each model are shown in Figures 7.13 to 7.60. Only the responses selected from two ground motions, NGA-1119 fault-normal component (GM #03) and NGA-1602 fault-parallel component (GM #19) are shown in this section. Each figure represents one hazard level and one ground motion component, with larger responses out of five ground motions in the analysis group.

From Figures 7.14 to 7.16, it is clear that for Model V6, the deformation concentrated at the first story, as the ground shaking intensity increased, the concentration still occurred at the ground story, as shown in Figures 7.18 to 7.20. Localized concentration of deformation improved slightly in Model X6, but the lower stories tended to have higher story drift ratios (see Figure 7.22 and Figure 7.26). Model X6-3 responded similarly, but with a somewhat reduced the concentration of deformation.

Model SB6-3 successfully prevented localized concentration of story deformation (Figures 7.38 and 7.42). Most of the braces in the vertical spine remained elastic during the dynamic analyses, and all braces outside the spine were triggered to buckle (see Figures 7.39 and 7.40; Figures 7.43, and 7.44).

Similar system responses were observed in Models SB6-3B and SB6-3L. All BRBs deformed into the nonlinear range and exhibited stable hysteresis loops. Significant strain hardening in the BRBs was observed. Most of the bracing members in the vertical spine remained elastic during the ground shakings.

In some ground motion events, the six-story braces in the vertical spine of Models SB6-3, SB6-3B, and SB6-3L exhibited nonlinear demands, as shown in Figures 7.43 7.61, 7.62, and 7.63, respectively. Note that the braces in the upper stories (i.e., 4-story, 5-story, and 6-story) of the vertical spine (Model SB6-3) tended to exhibit inelastic demands in some events (Figures 7.64 and 7.65). The lower three-story braces in the vertical spine all remained elastic during the dynamics analyses. Only in one event (ground motion number 18) did the first-story brace in the vertical spine of Model SB6-3 exhibit nonlinear demands (yielding), as shown in Figure 7.66. Buckling and yielding of tie-columns in the strong-back vertical spine was also observed in some events, as shown in Figures 7.67 and 7.68.

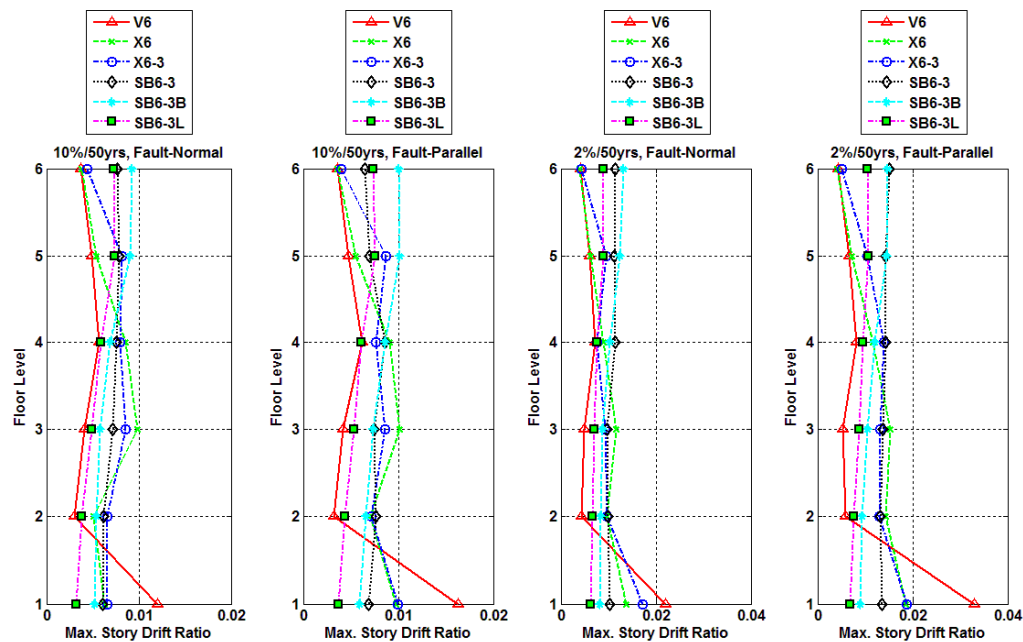


Figure 7.10 Maximum story drift ratios for each model under different hazard level ground motions.

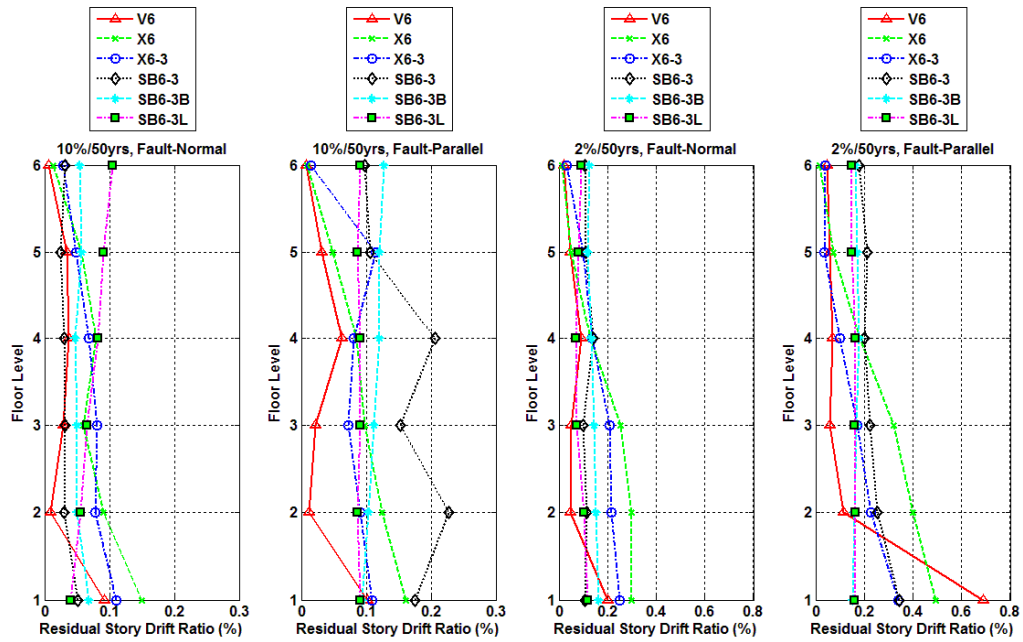


Figure 7.11 Residual story drift ratios for each model after different hazard level ground excitations.

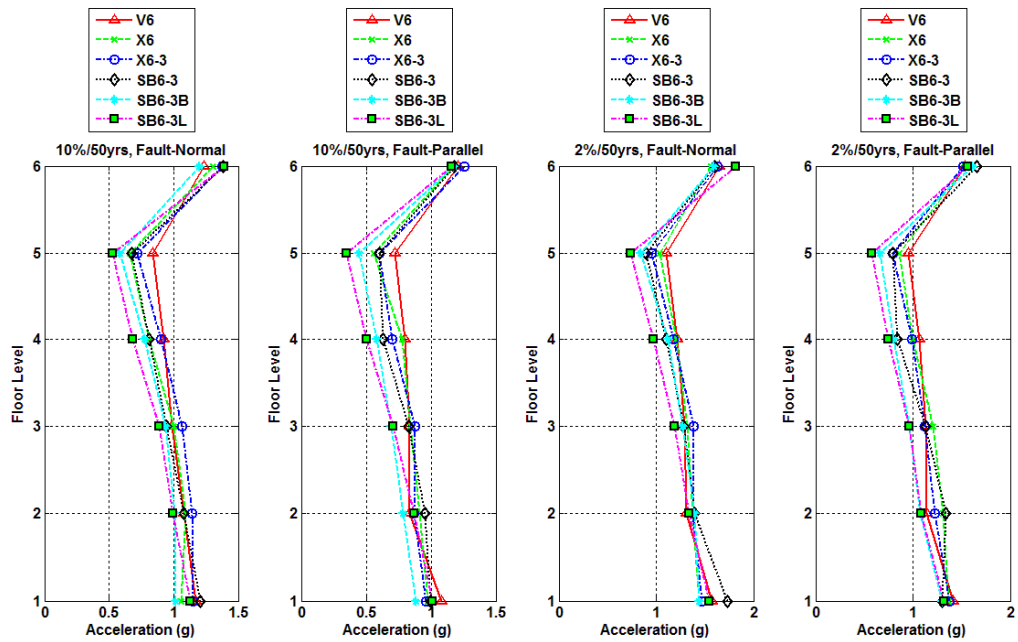


Figure 7.12 Maximum floor level accelerations for each model under different hazard level ground motions.

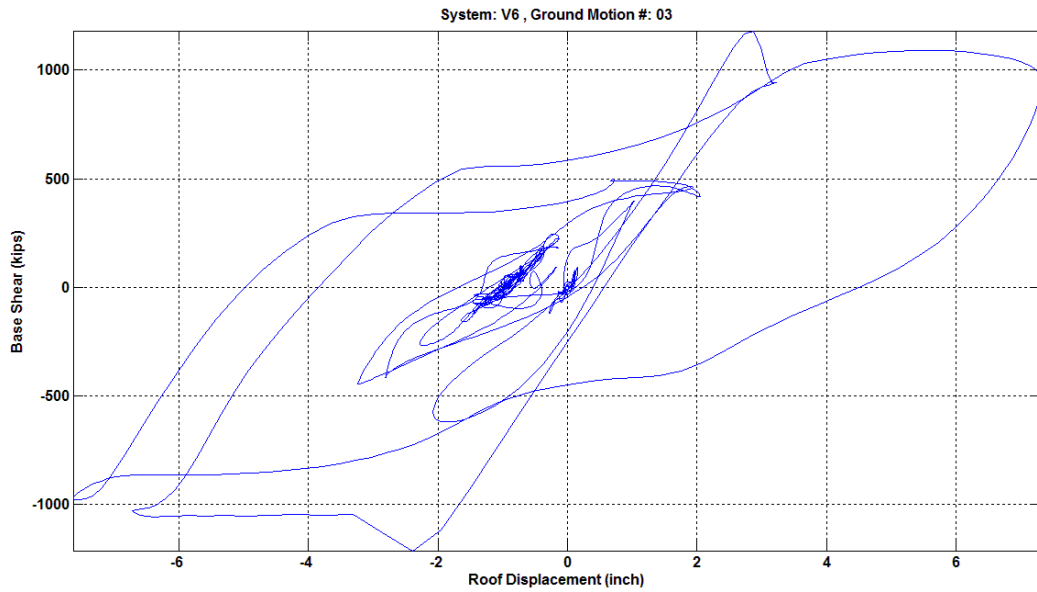


Figure 7.13 Base shear versus roof displacement relationship of Model V6 under NGA 1119 fault-normal component ground motion.

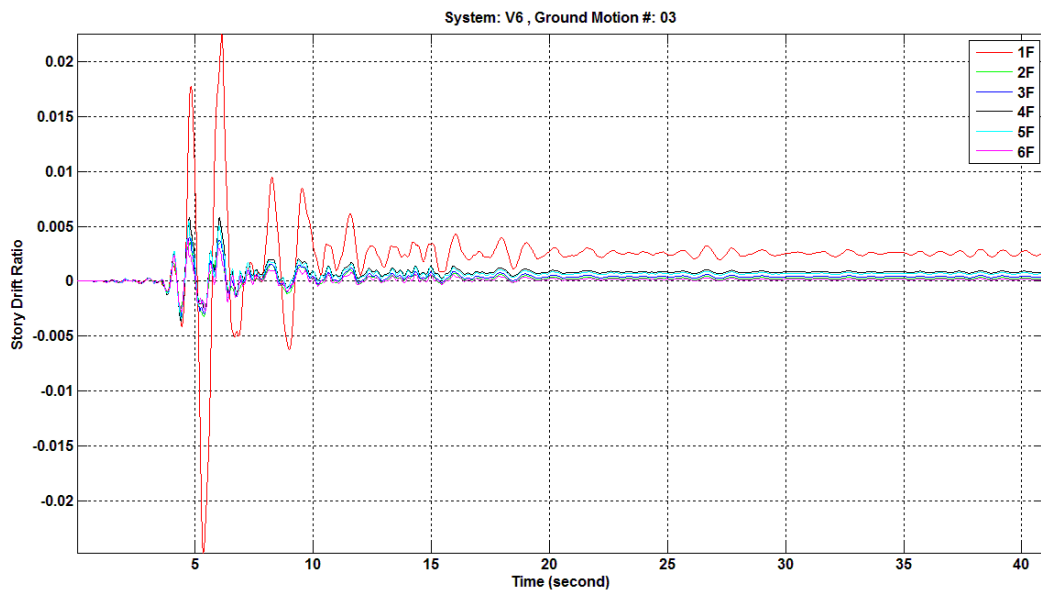


Figure 7.14 Story drift ratio histories of Model V6 under NGA 1119 fault-normal component ground motion.

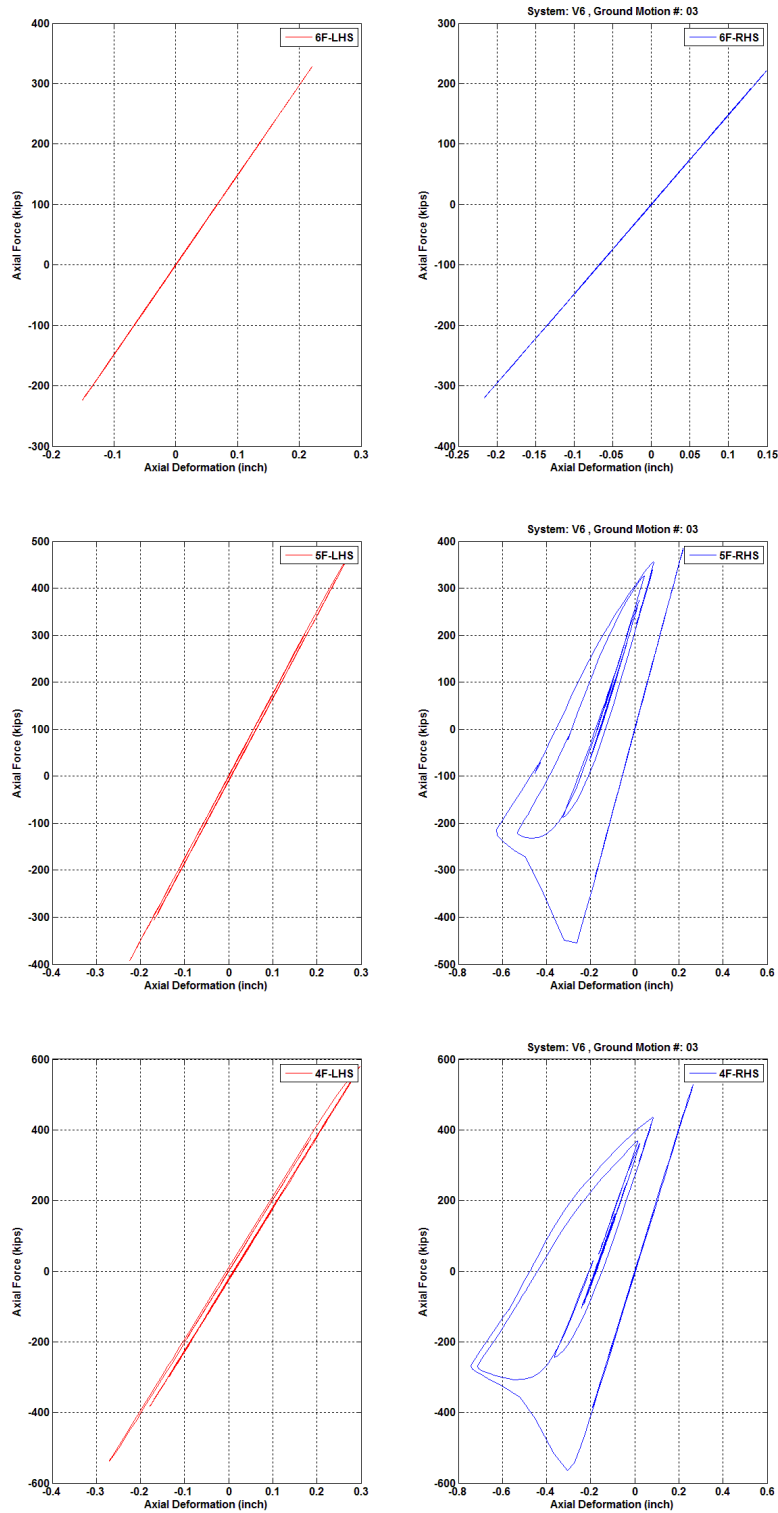


Figure 7.15 Fourth-story to sixth-story brace axial force versus axial deformation relationships of Model V6 under NGA 1119 fault-normal component ground motion.

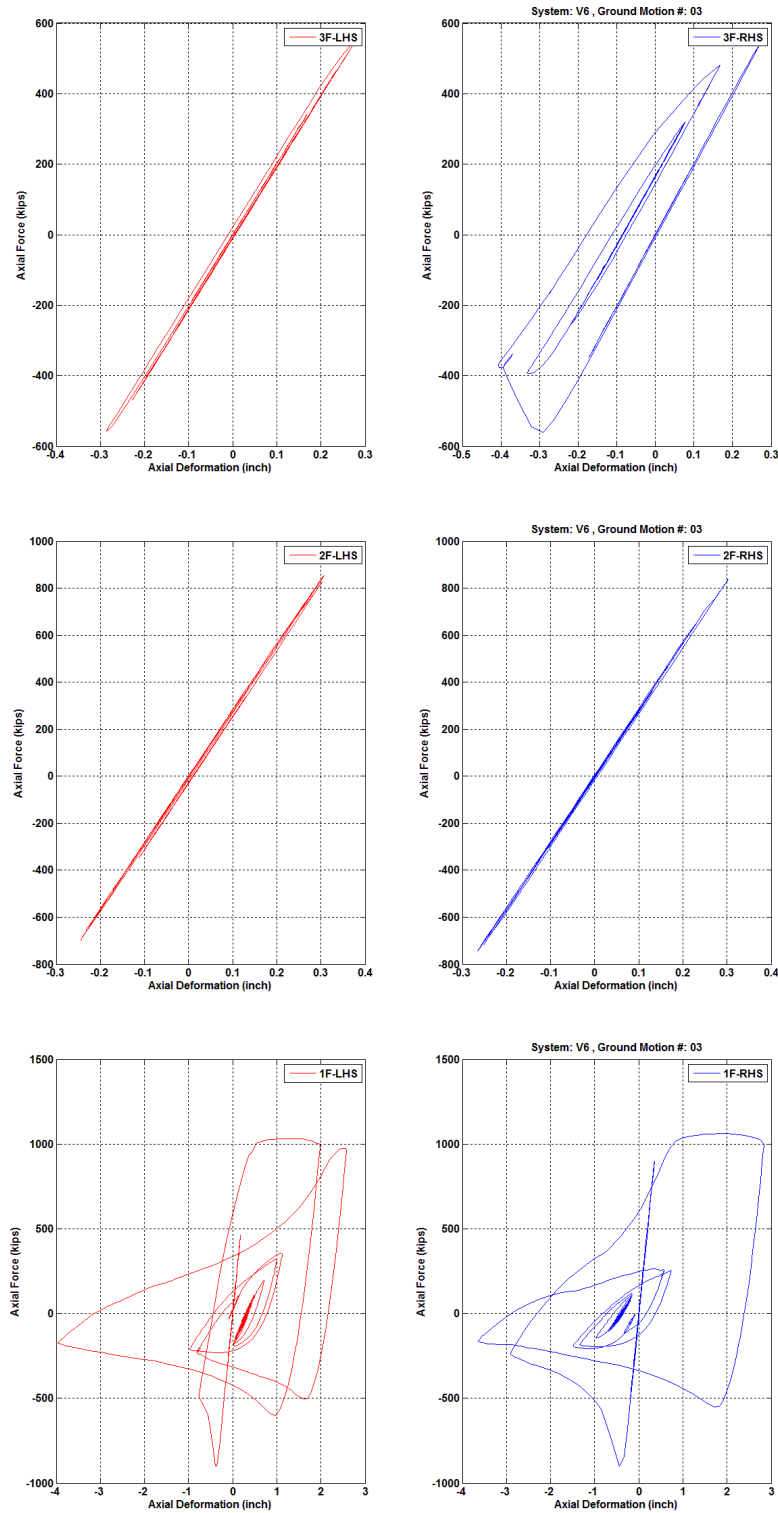


Figure 7.16 First-story to third-story brace axial force versus axial deformation relationships of Model V6 under NGA 1119 fault-normal component ground motion.

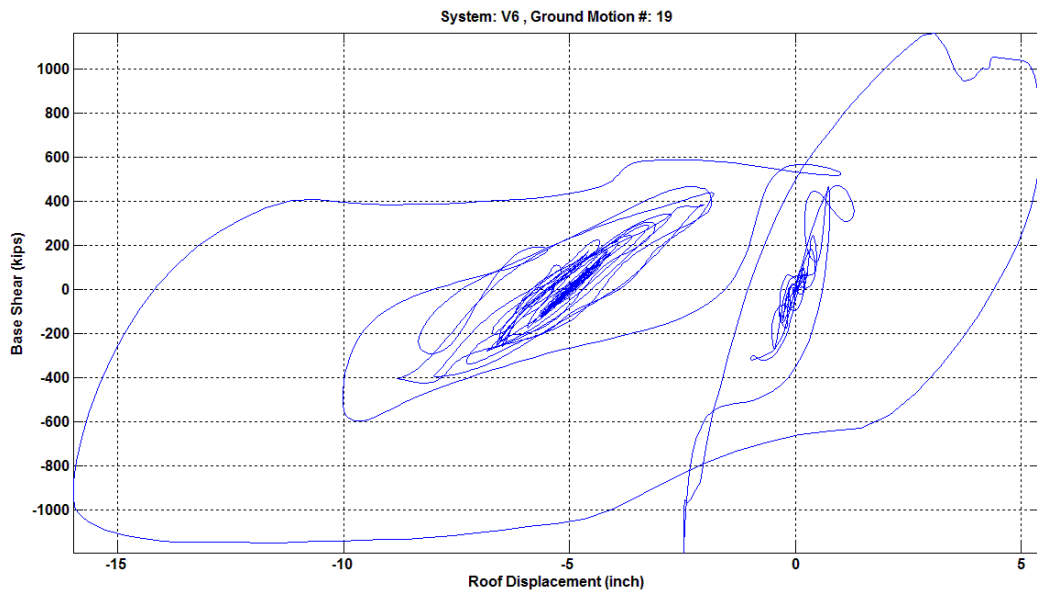


Figure 7.17 Base shear versus roof displacement relationship of Model V6 under NGA 1602 fault-parallel component ground motion.

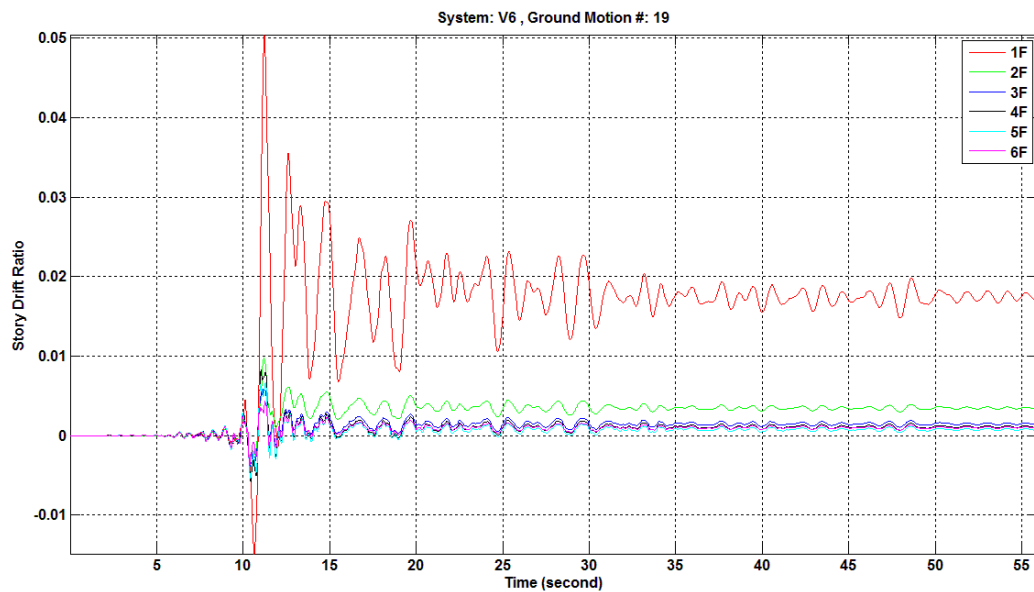


Figure 7.18 Story drift ratio histories of Model V6 under NGA 1602 fault-parallel component ground motion.

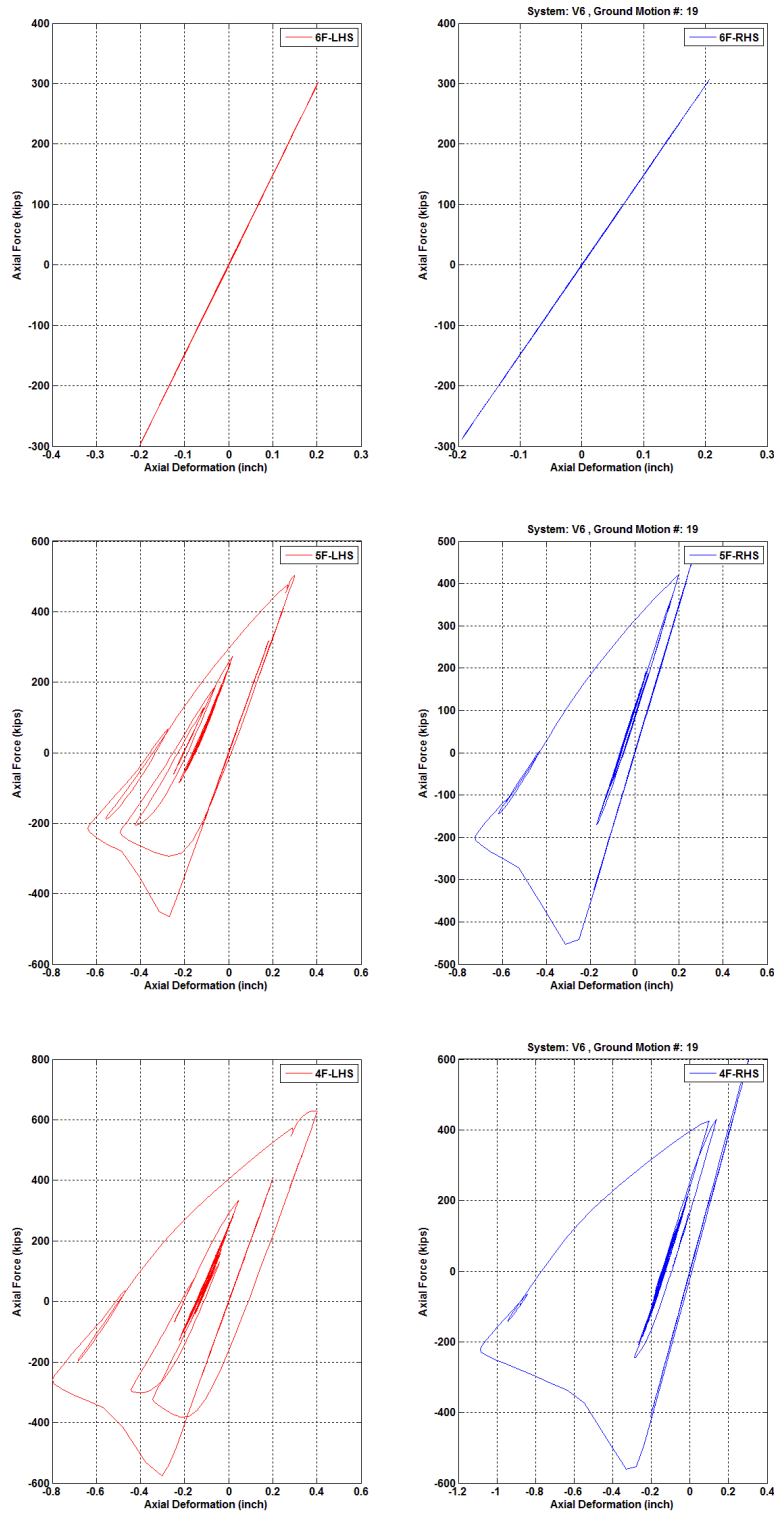


Figure 7.19 Fourth-story to sixth-story brace axial force versus axial deformation relationships of Model V6 under NGA 1602 fault-parallel component ground motion.

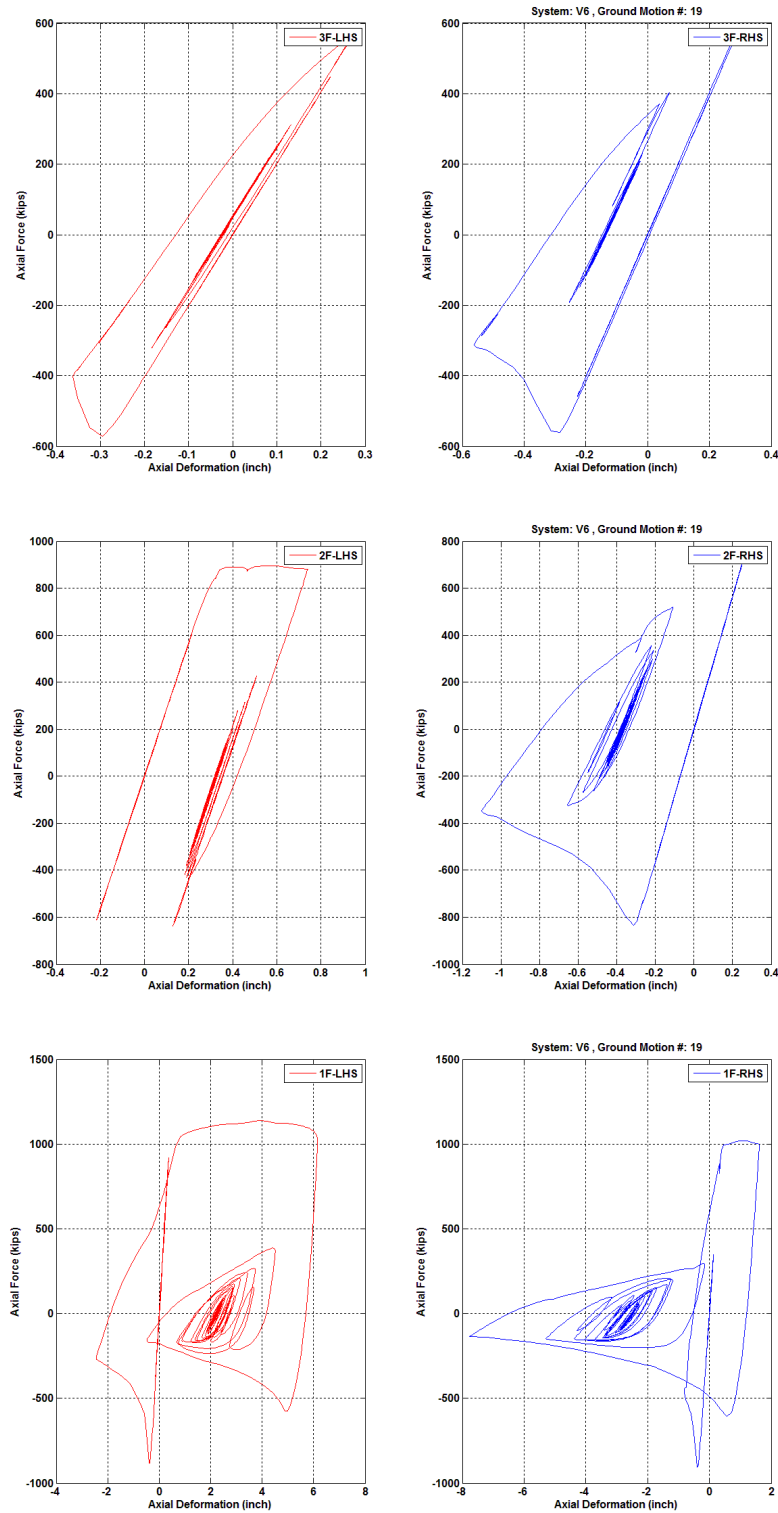


Figure 7.20 First-story to third-story brace axial force versus axial deformation relationships of Model V6 under NGA 1602 fault-parallel component ground motion.

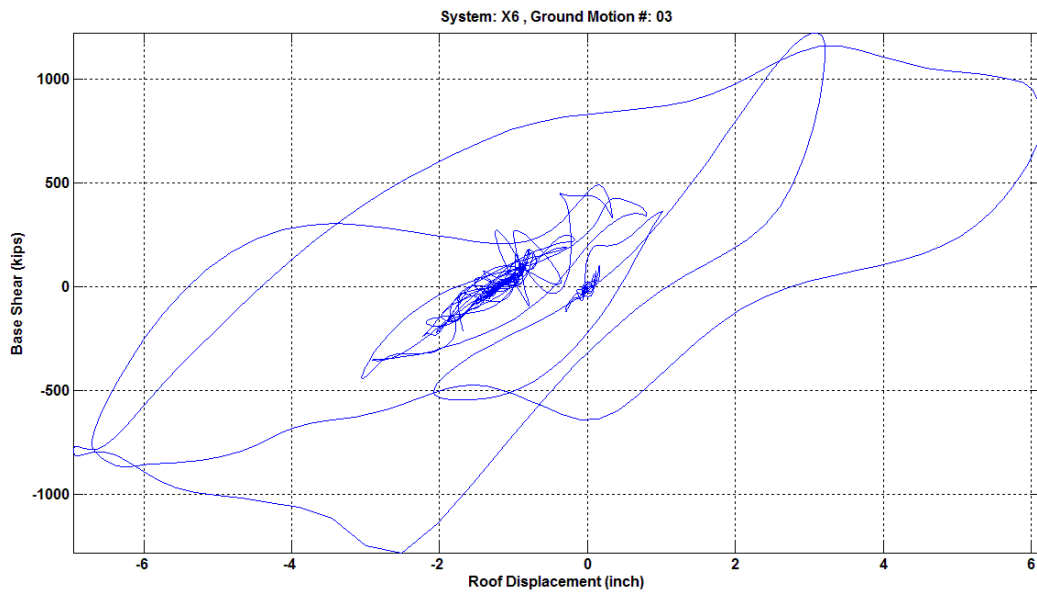


Figure 7.21 Base shear versus roof displacement relationship of Model X6 under NGA 1119 fault-normal component ground motion.

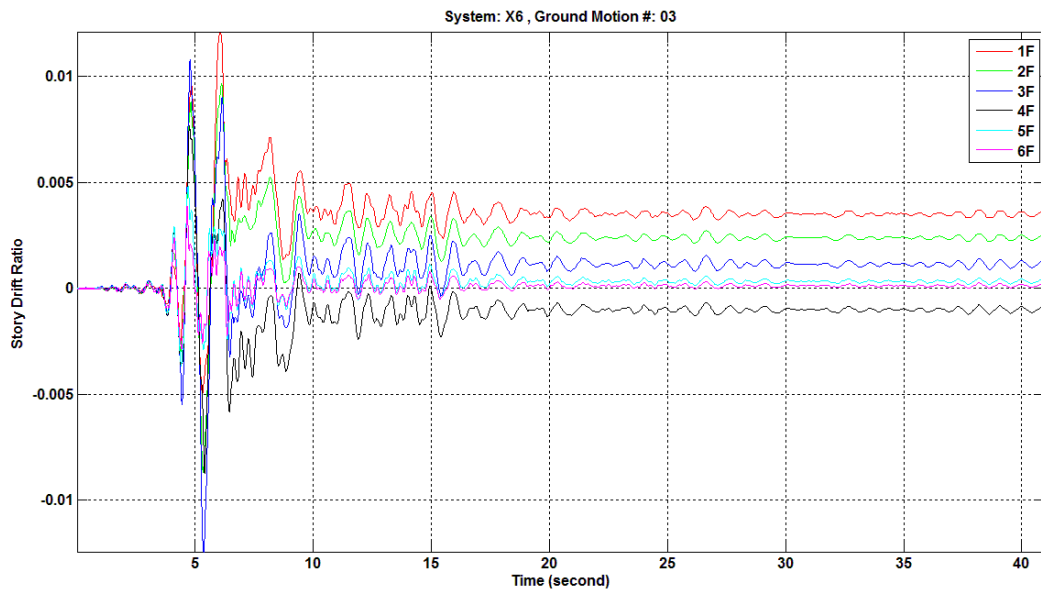


Figure 7.22 Story drift ratio histories of Model X6 under NGA 1119 fault-normal component ground motion.

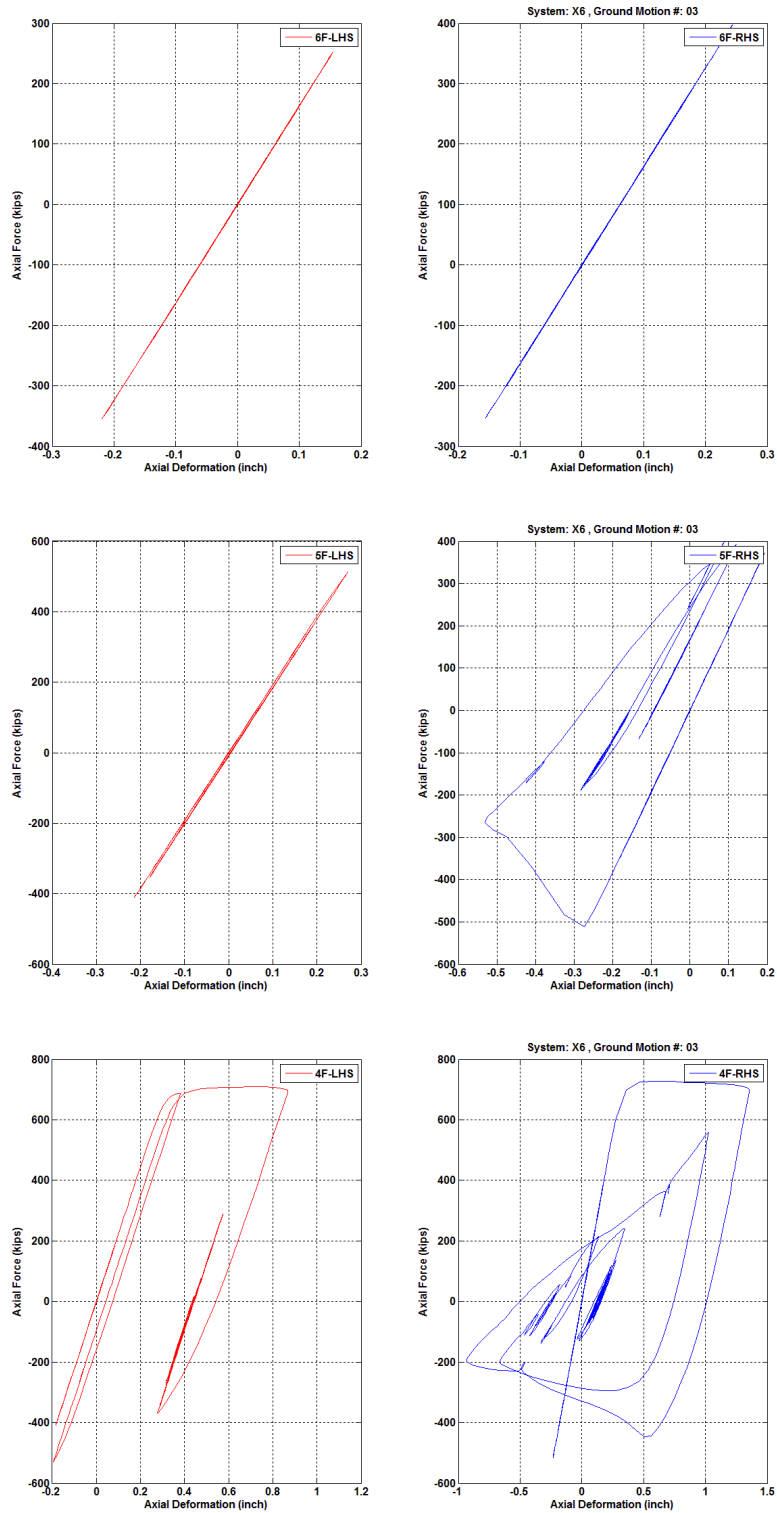


Figure 7.23 Fourth-story to sixth-story brace axial force versus axial deformation relationships of Model X6 under NGA 1119 fault-normal component ground motion.

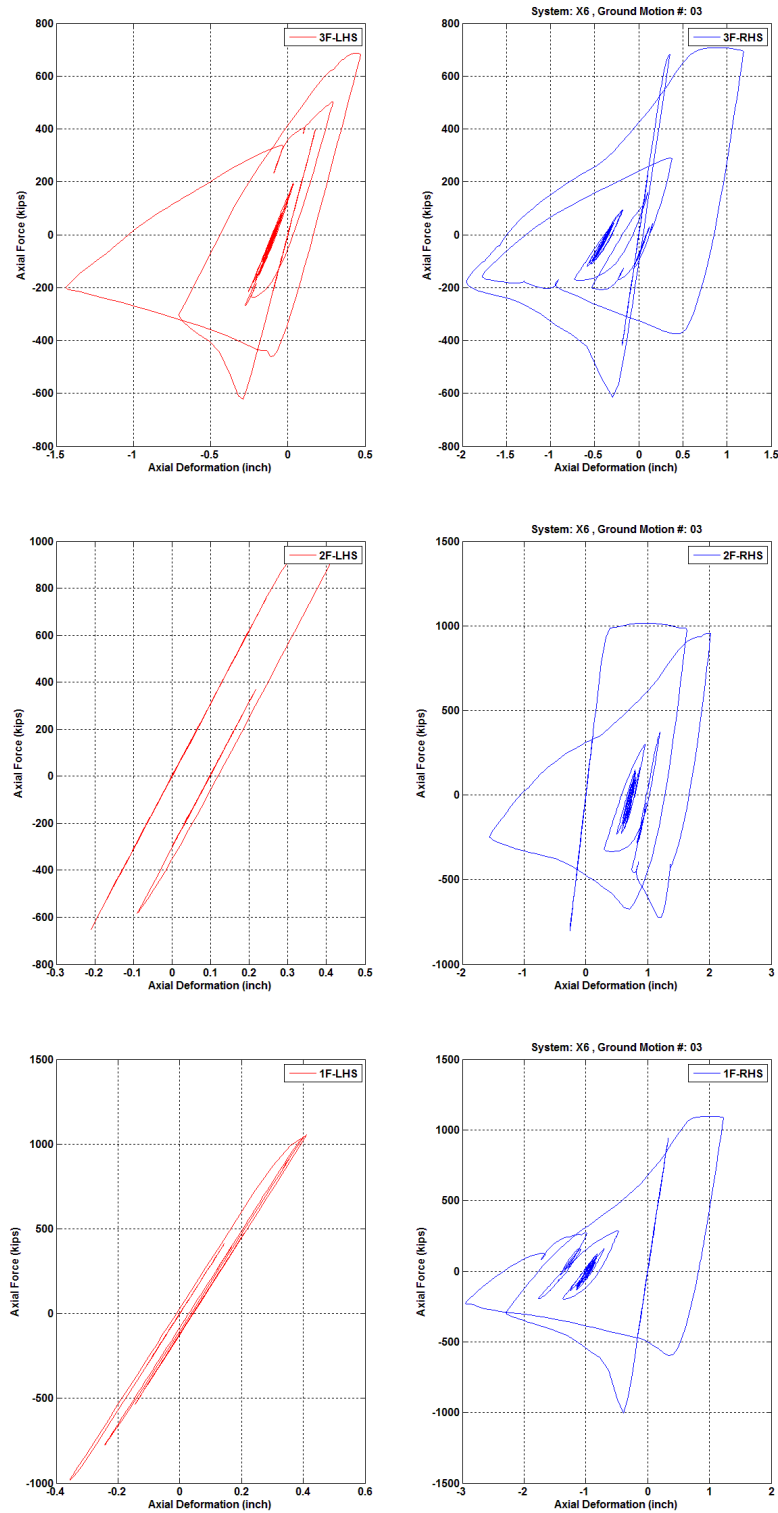


Figure 7.24 First-story to third-story brace axial force versus axial deformation relationships of Model X6 under NGA 1119 fault-normal component ground motion.

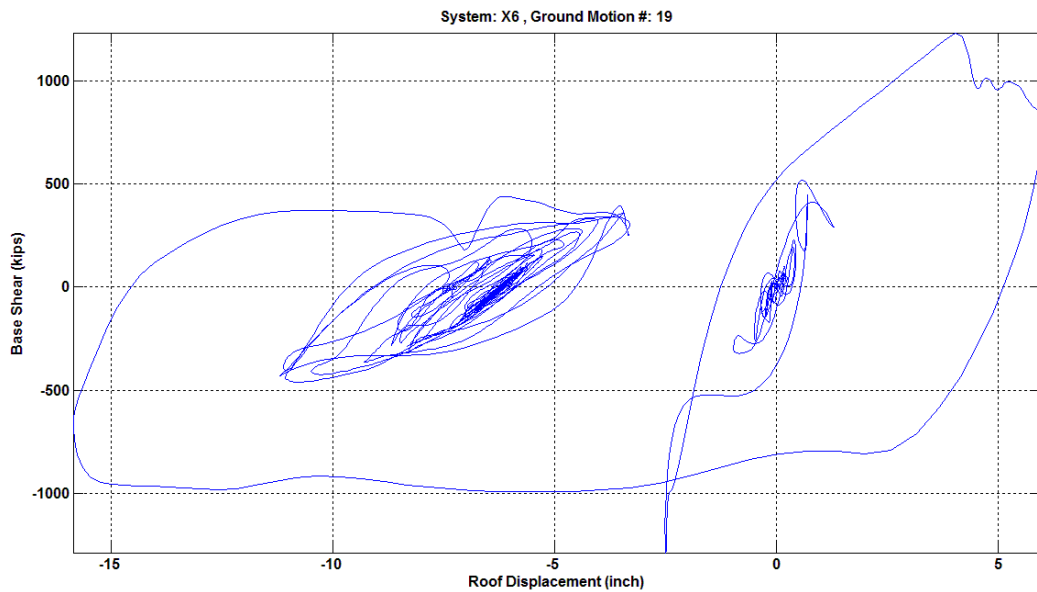


Figure 7.25 Base shear versus roof displacement relationship of Model X6 under NGA 1602 fault-parallel component ground motion.

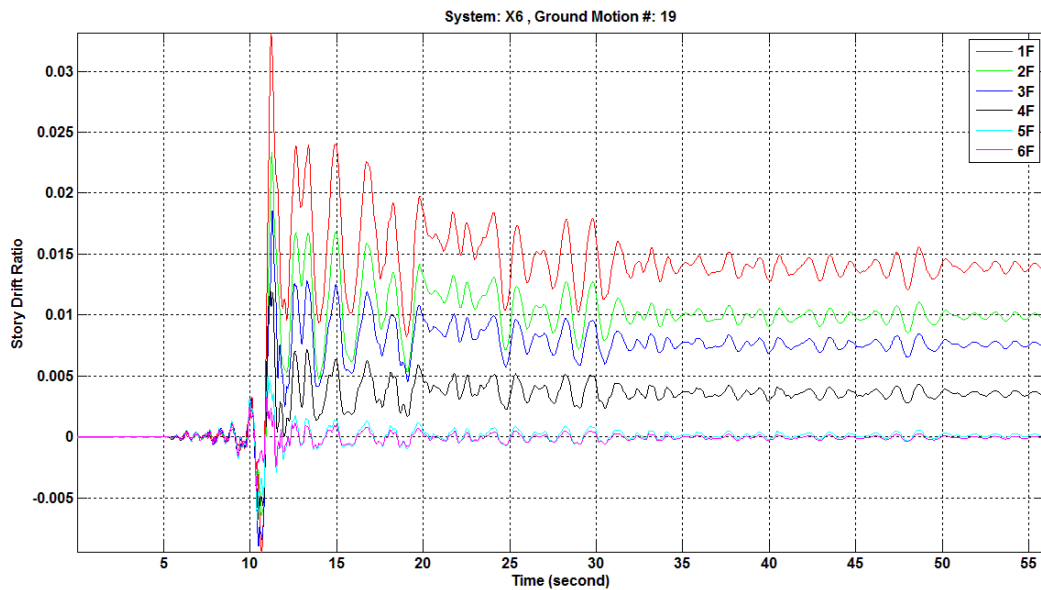


Figure 7.26 Story drift ratio histories of Model X6 under NGA 1602 fault-parallel component ground motion.

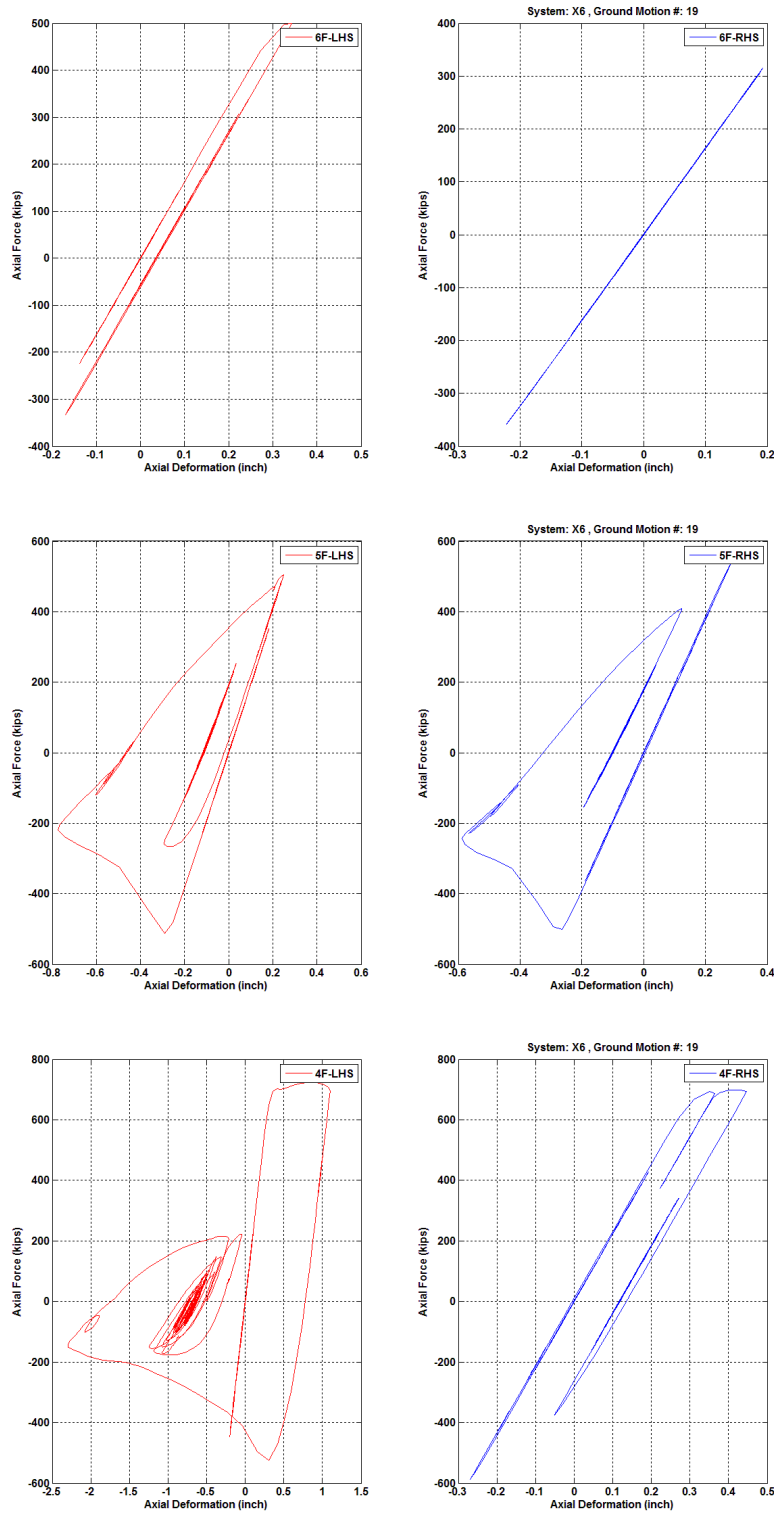


Figure 7.27 Fourth-story to sixth-story brace axial force versus axial deformation relationships of Model X6 under NGA 1602 fault-parallel component ground motion.

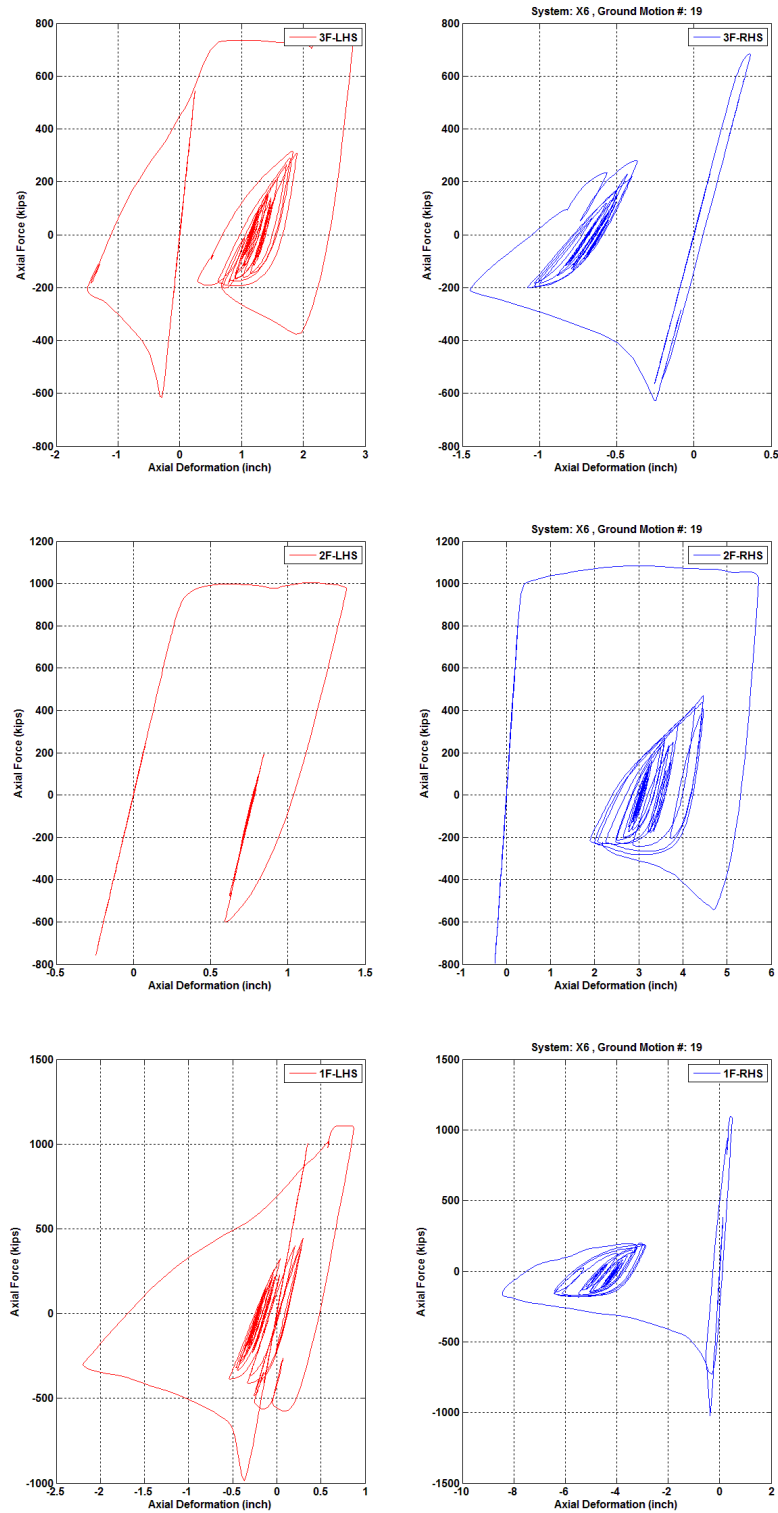


Figure 7.28 First story to third story brace axial force versus axial deformation relationships of Model X6 under NGA 1602 fault-parallel component ground motion.

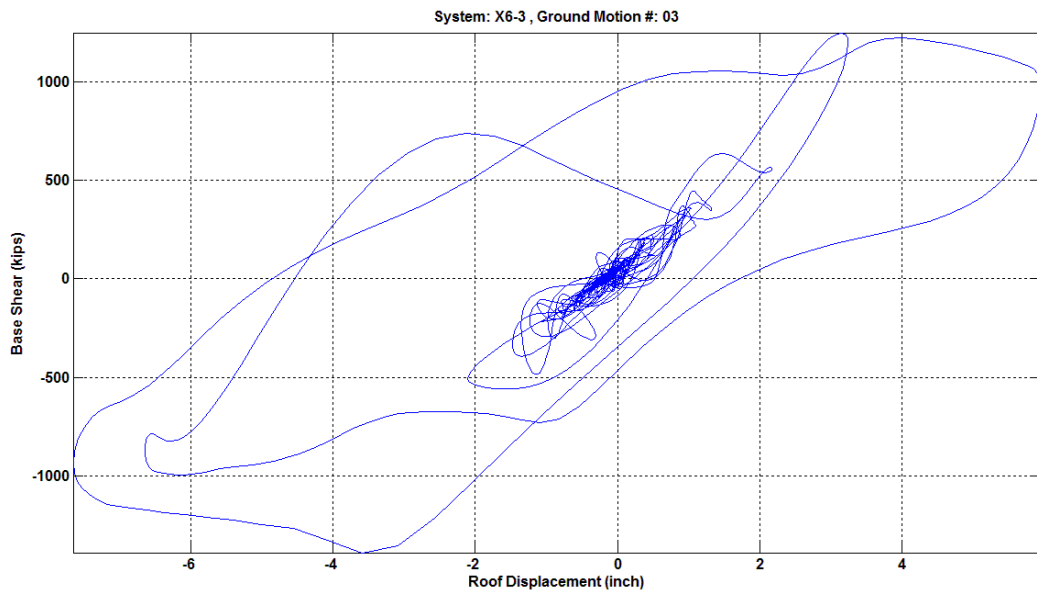


Figure 7.29 Base shear versus roof displacement relationship of Model X6-3 under NGA 1119 fault-normal component ground motion.

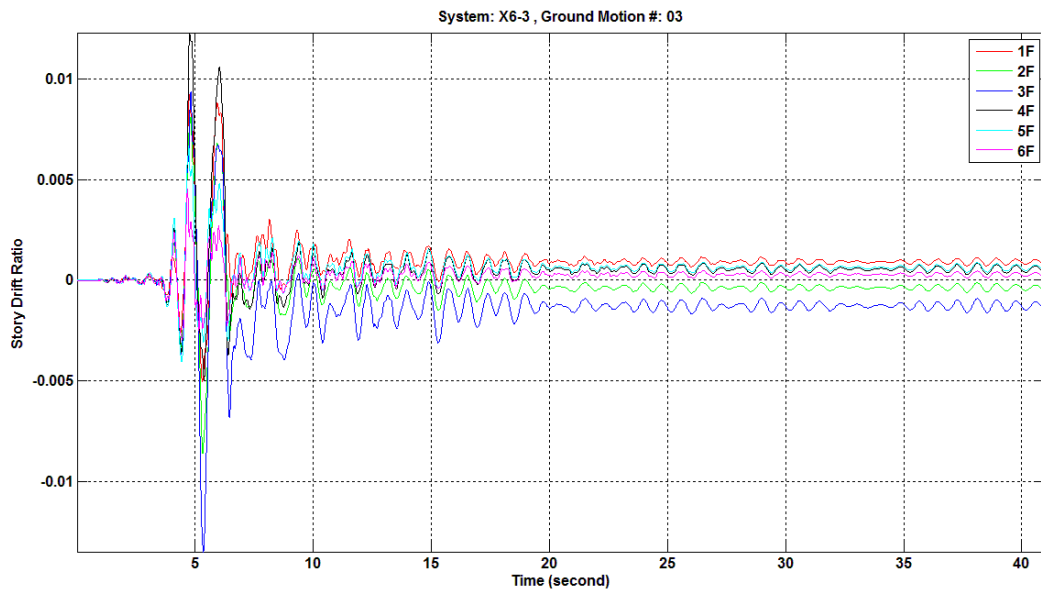


Figure 7.30 Story drift ratio histories of Model X6-3 under NGA 1119 fault-normal component ground motion.

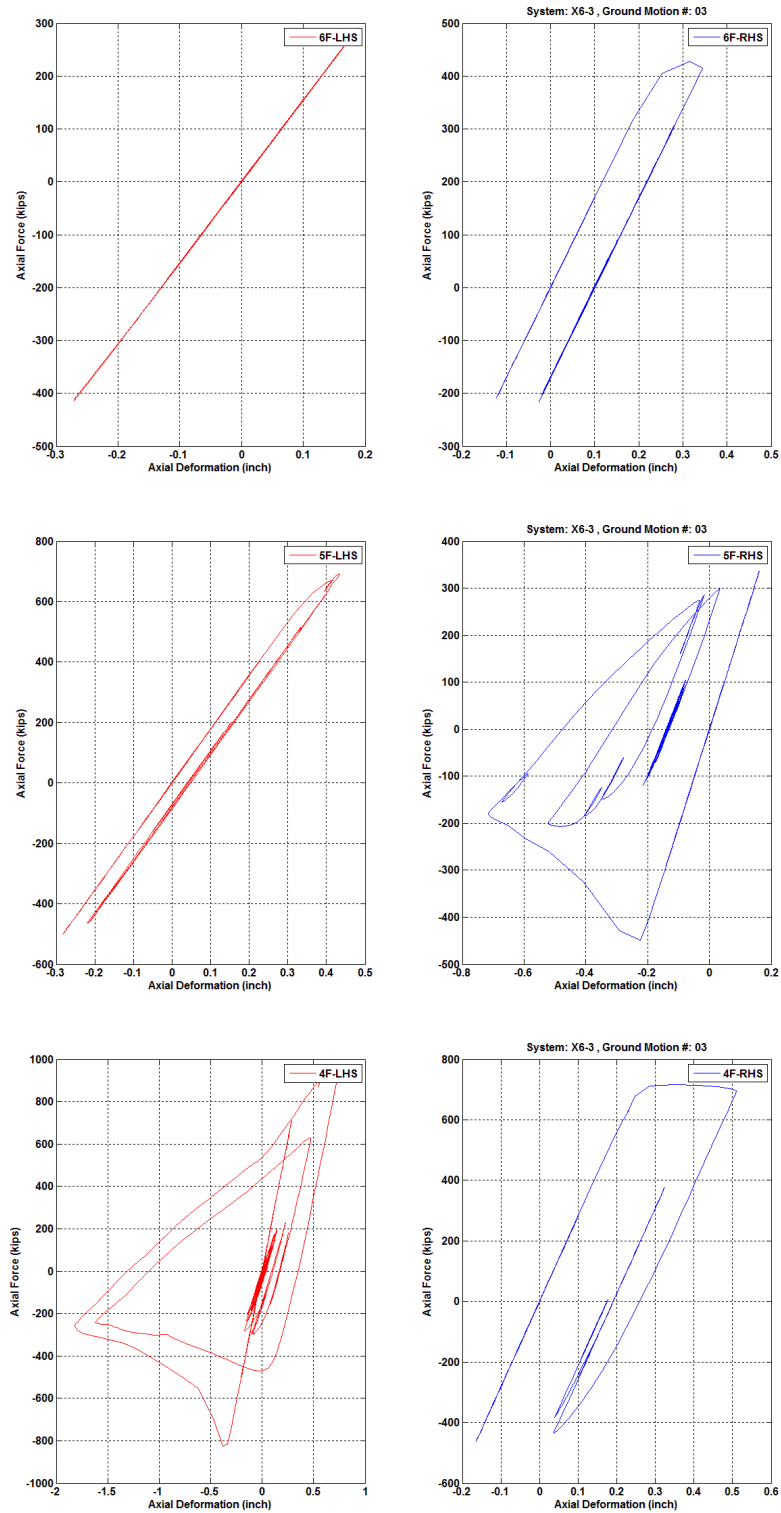


Figure 7.31 Fourth-story to sixth-story brace axial force versus axial deformation relationships of Model X6-3 under NGA 1119 fault-normal component ground motion.

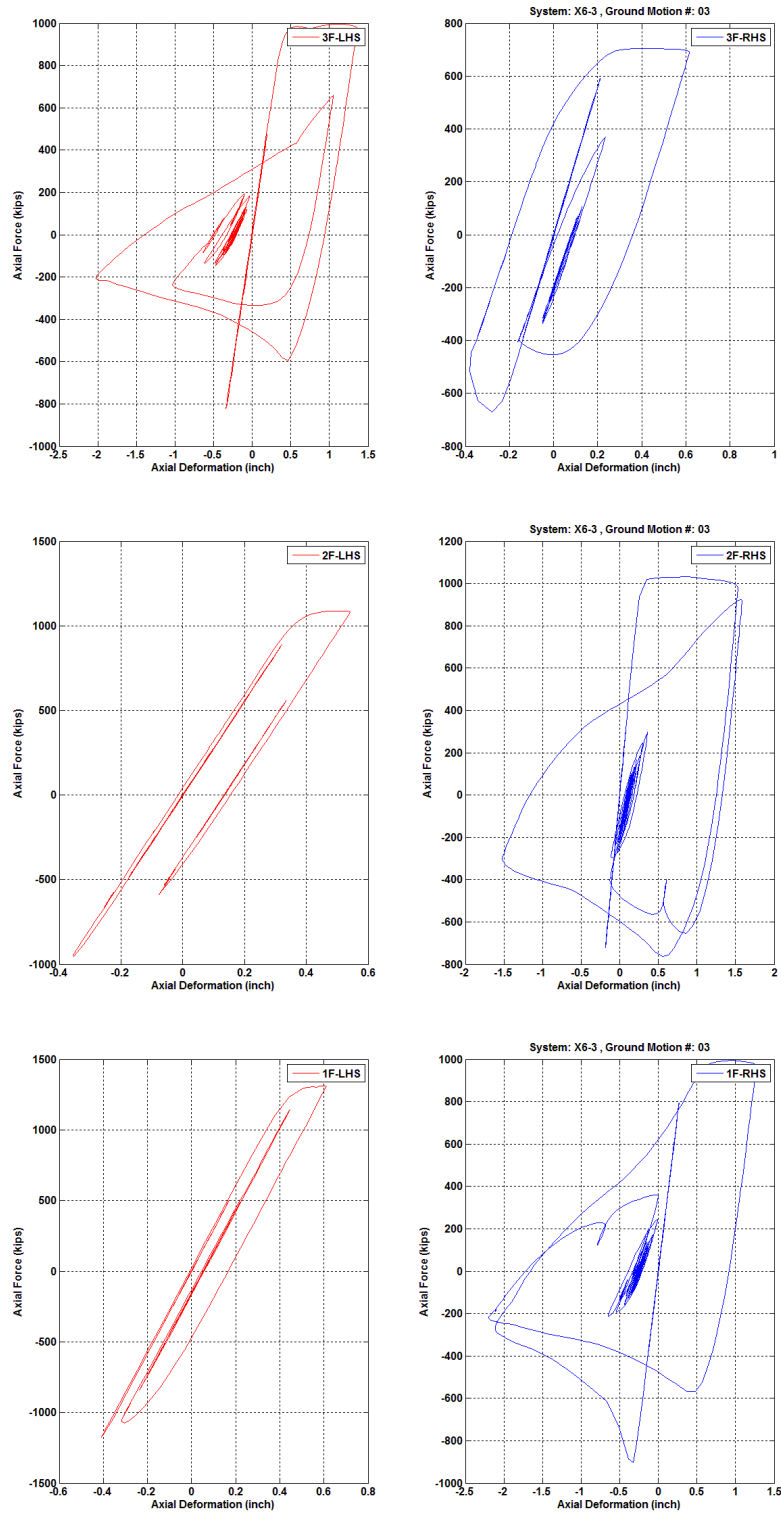


Figure 7.32 First-story to third-story brace axial force versus axial deformation relationships of Model X6-3 under NGA 1119 fault-normal component ground motion.

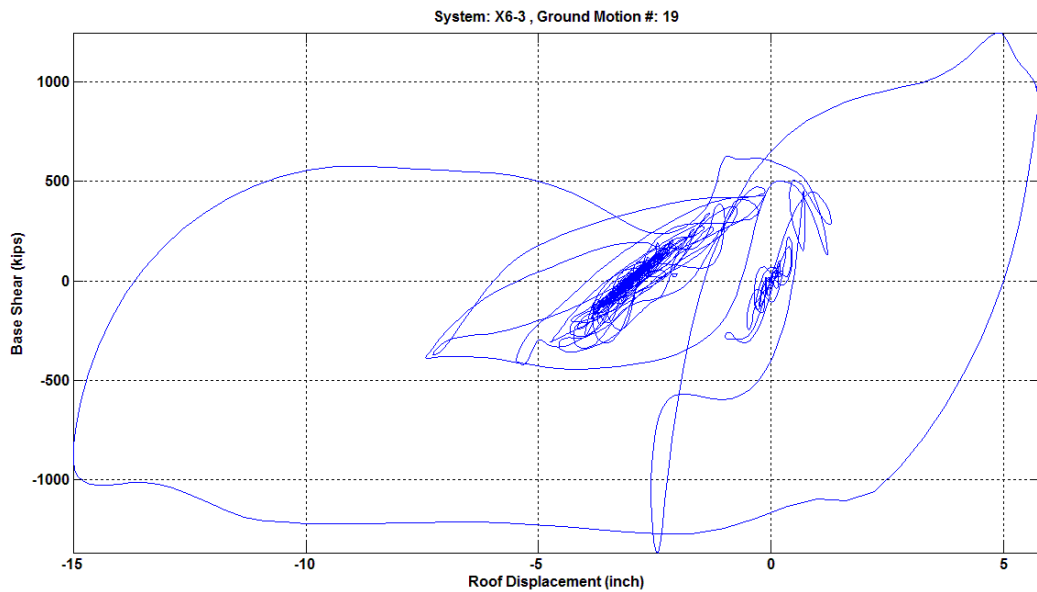


Figure 7.33 Base shear versus roof displacement relationship of Model X6-3 under NGA 1602 fault-parallel component ground motion.

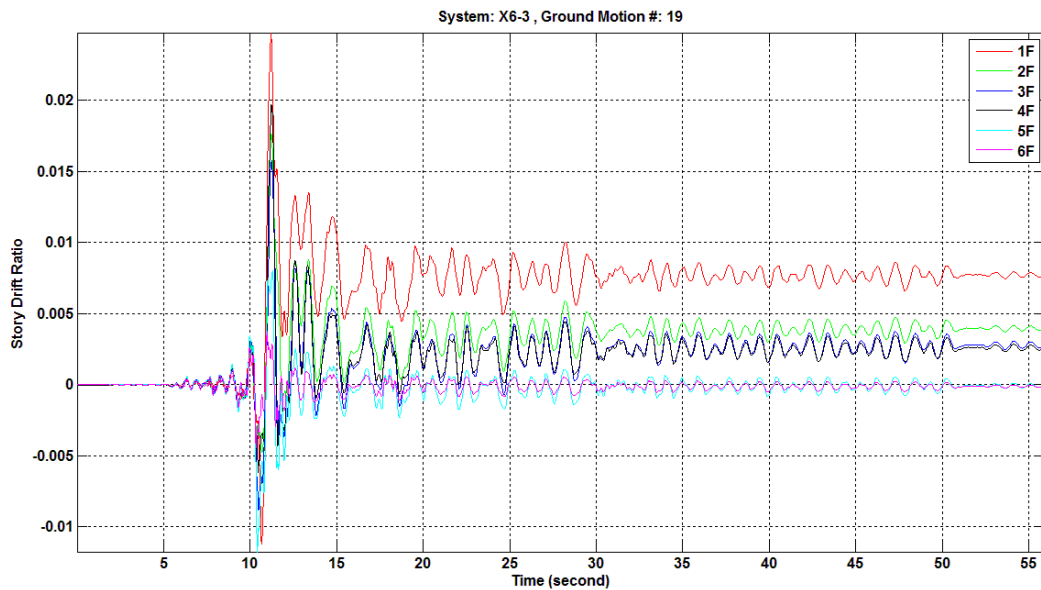


Figure 7.34 Story drift ratio histories of Model X6-3 under NGA 1602 fault-parallel component ground motion.

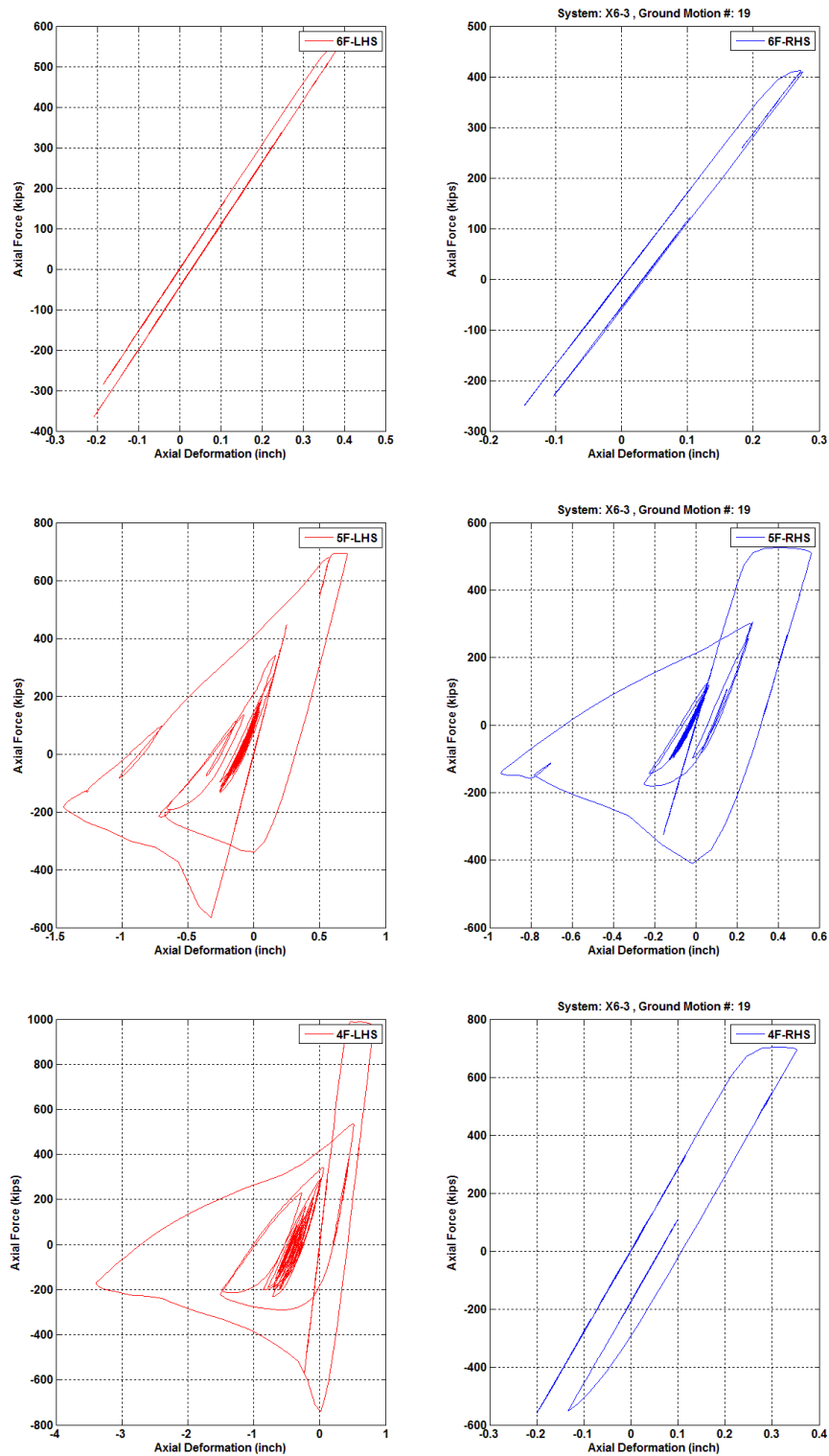


Figure 7.35 Fourth-story to sixth-story brace axial force versus axial deformation relationships of Model X6-3 under NGA 1602 fault-parallel component ground motion.

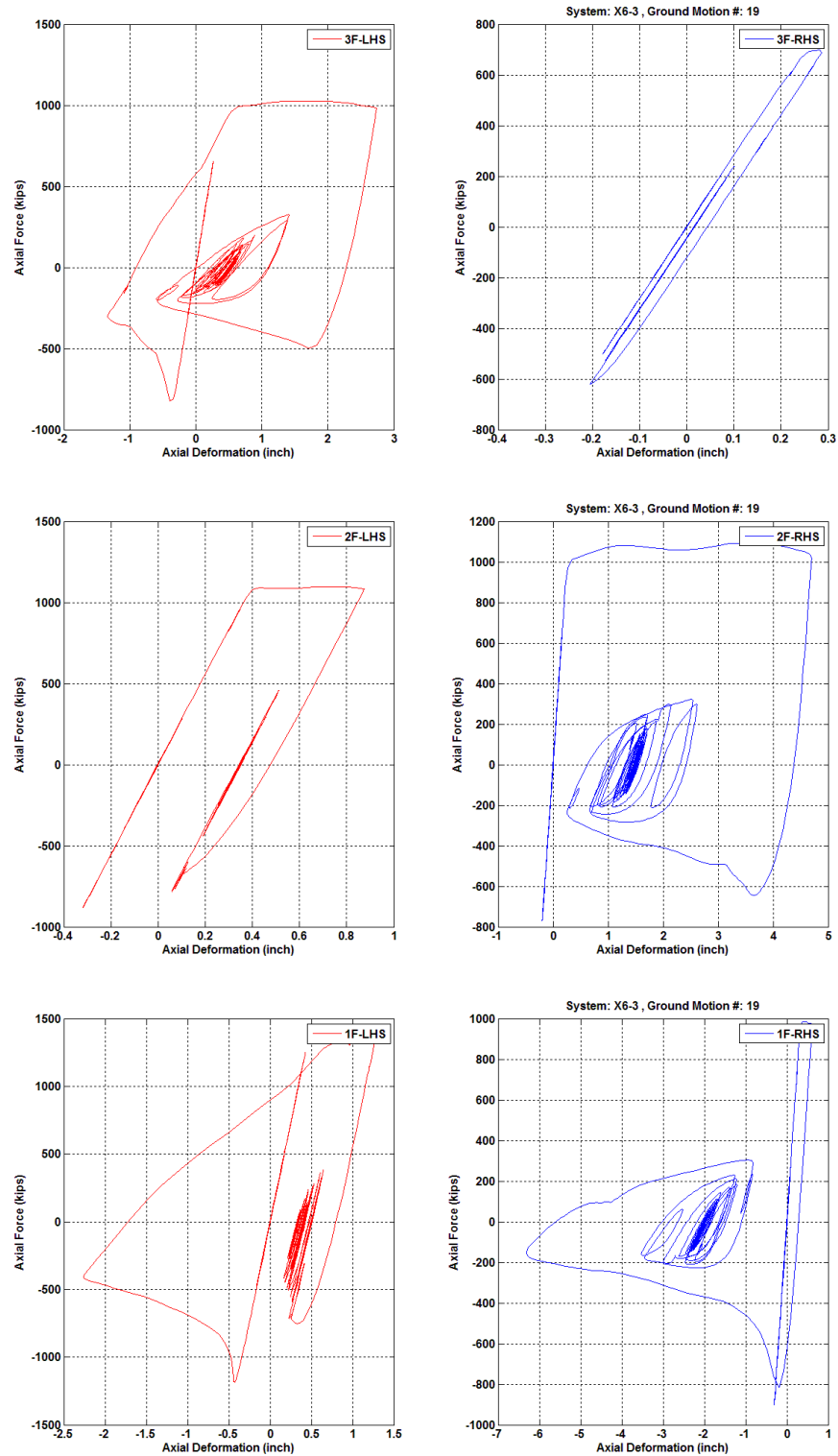


Figure 7.36 First-story to third-story brace axial force versus axial deformation relationships of Model X6-3 under NGA 1602 fault-parallel component ground motion.

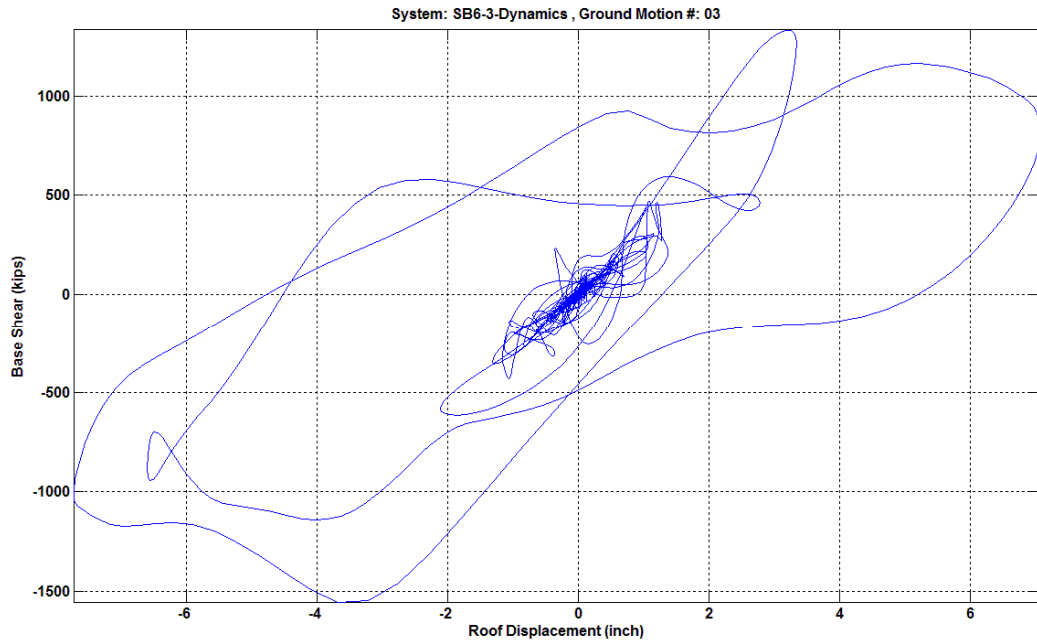


Figure 7.37 Base shear versus roof displacement relationship of Model SB6-3 under NGA 1119 fault-normal component ground motion.

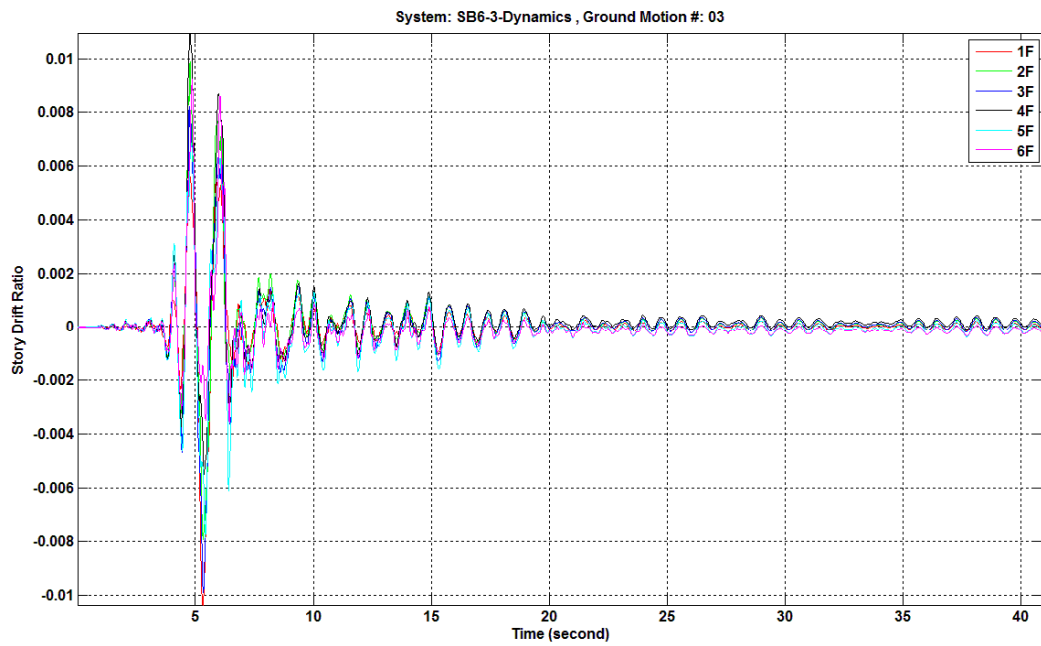


Figure 7.38 Story drift ratio histories of Model SB6-3 under NGA 1119 fault-normal component ground motion.

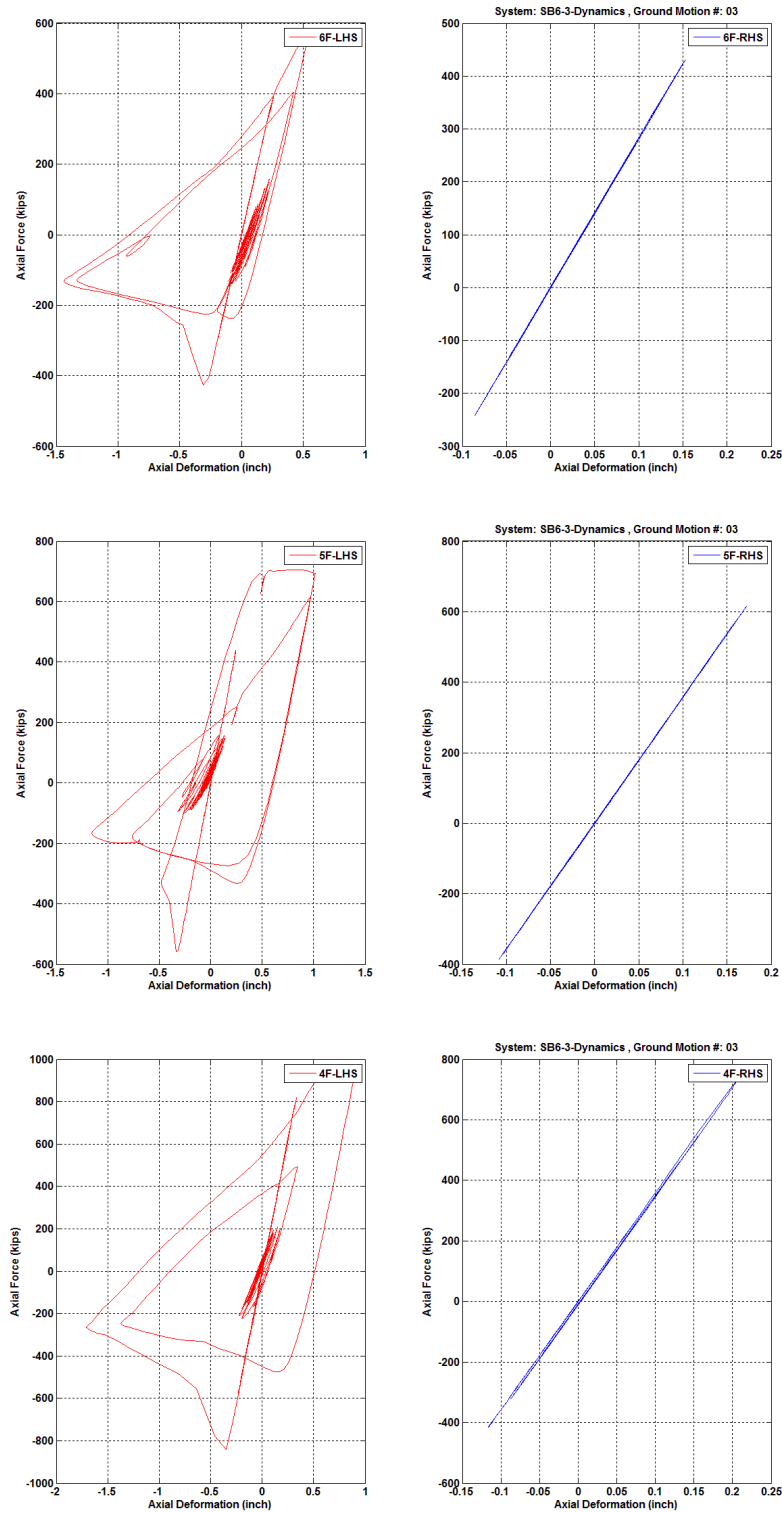


Figure 7.39 Fourth-story to sixth-story brace axial force versus axial deformation relationships of Model SB6-3 under NGA 1119 fault-normal component ground motion.

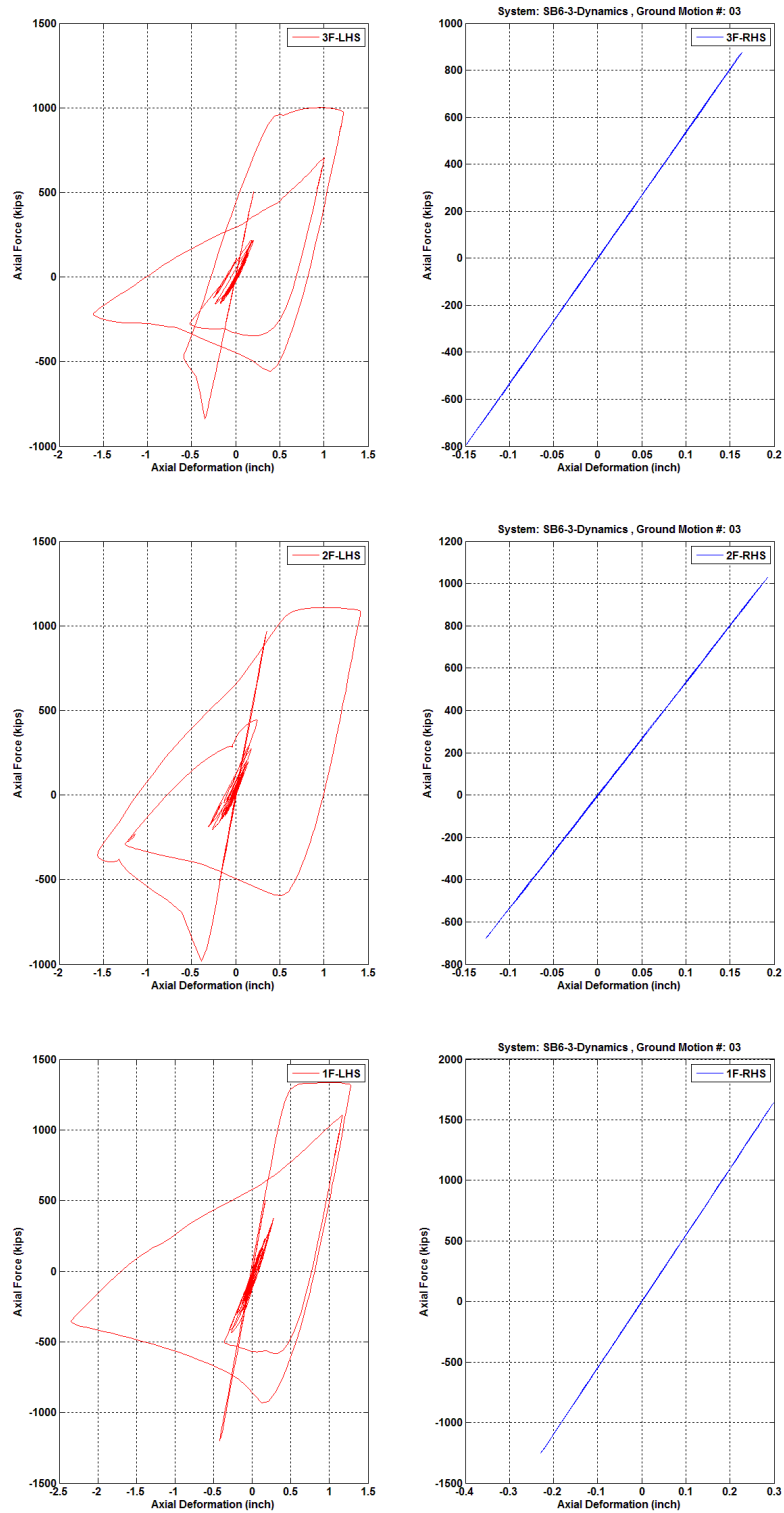


Figure 7.40 First-story to third-story brace axial force versus axial deformation relationships of Model SB6-3 under NGA 1119 fault-normal component ground motion.

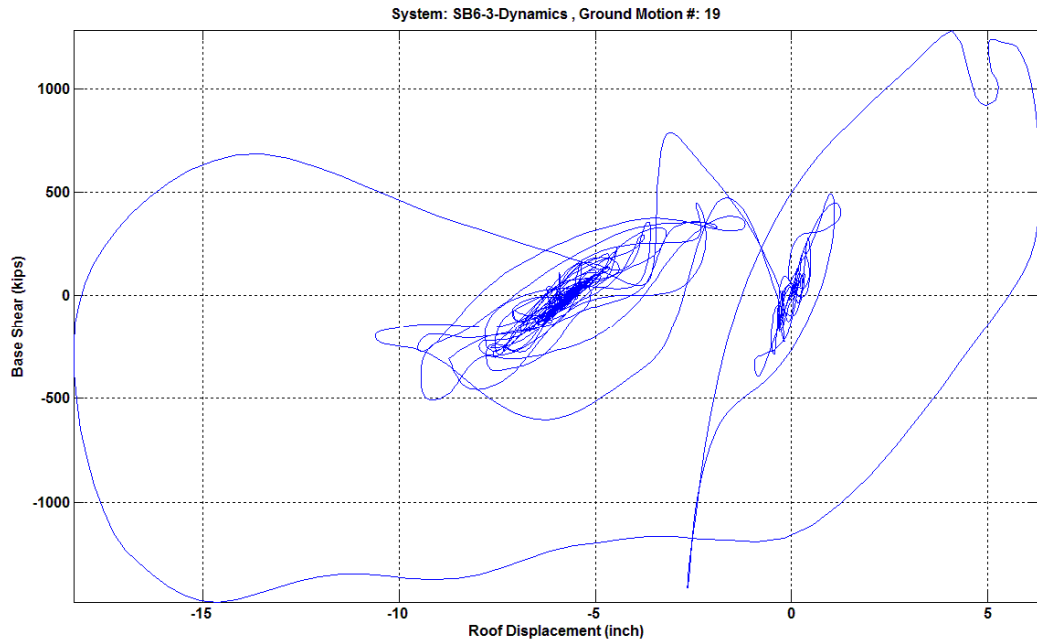


Figure 7.41 Base shear versus roof displacement relationship of Model SB6-3 under NGA 1602 fault-parallel component ground motion.

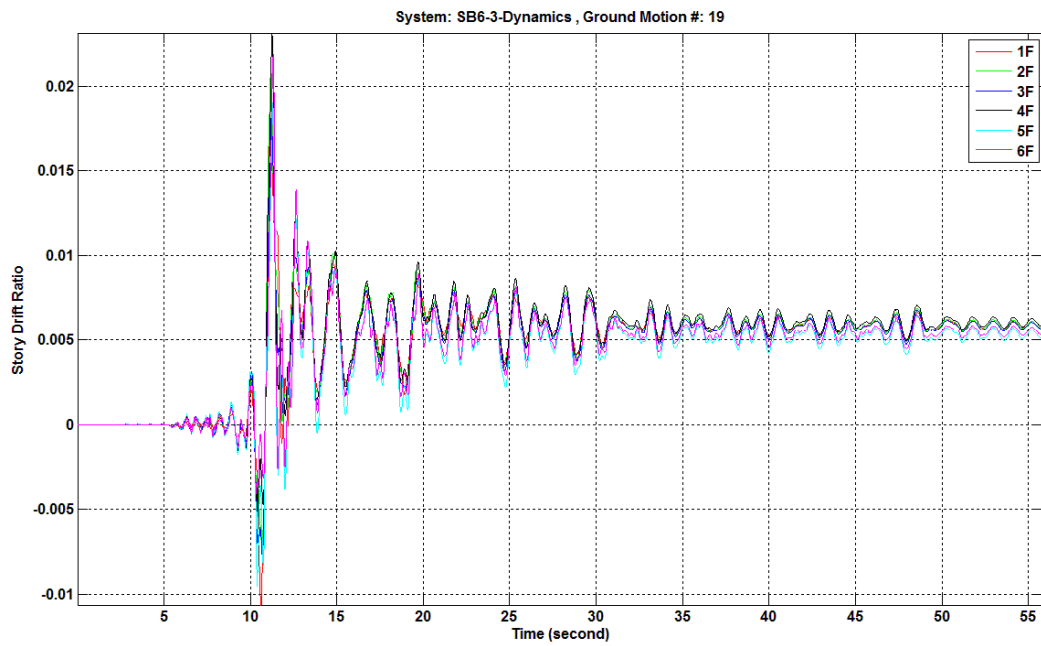


Figure 7.42 Story drift ratio histories of Model SB6-3 under NGA 1602 fault-parallel component ground motion.

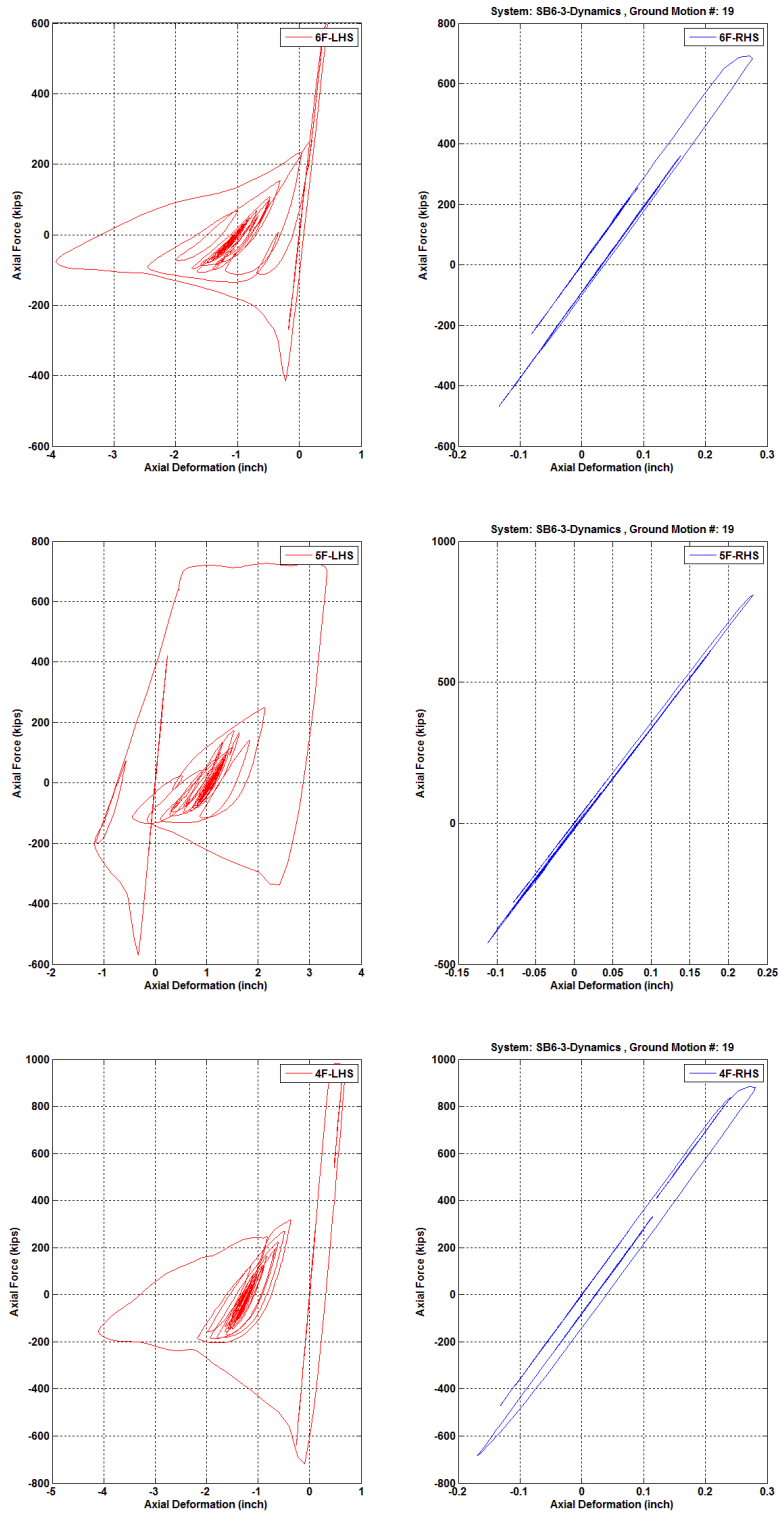


Figure 7.43 Fourth-story to sixth-story brace axial force versus axial deformation relationships of Model SB6-3 under NGA 1602 fault-parallel component ground motion.

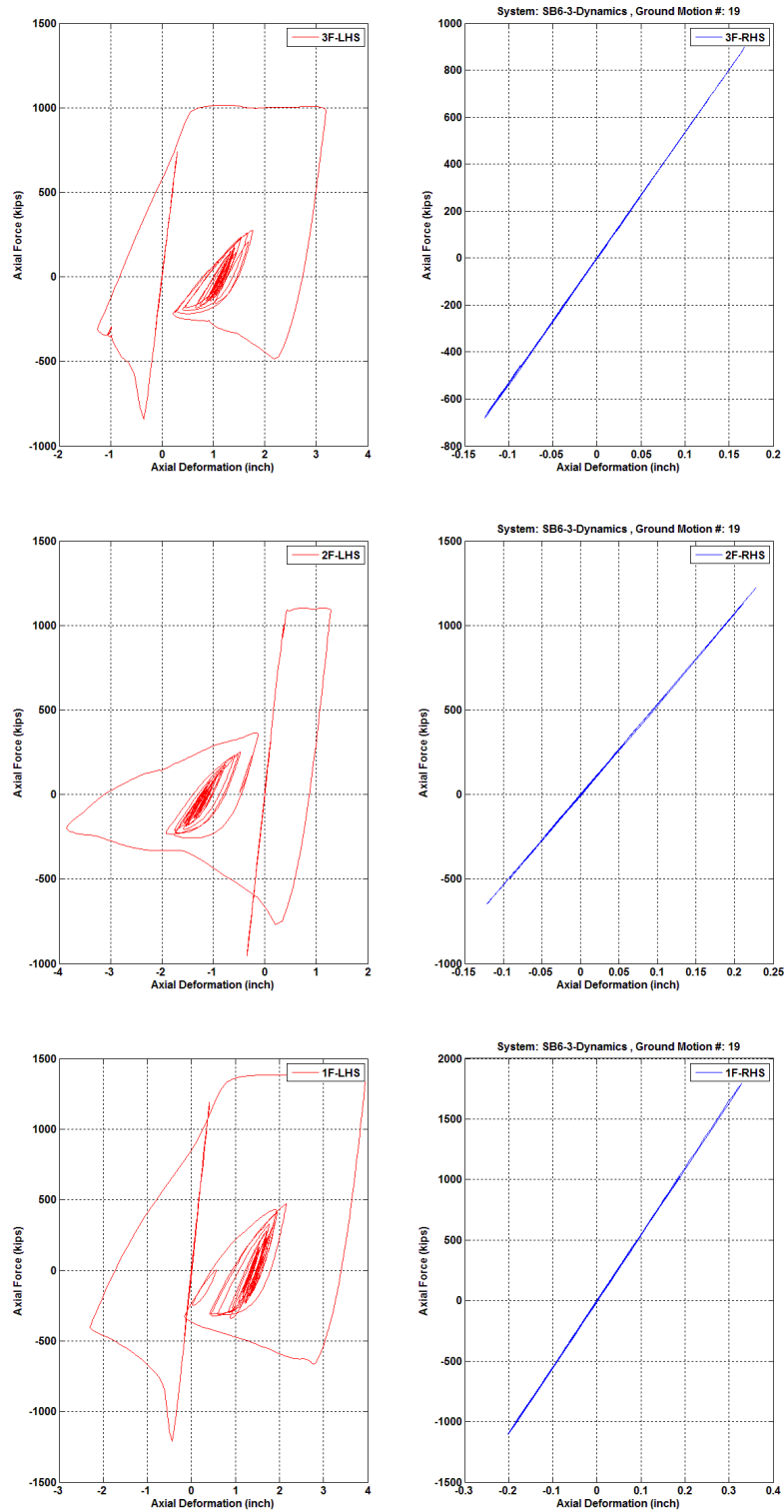


Figure 7.44 First-story to third-story brace axial force versus axial deformation relationships of Model SB6-3 under NGA 1602 fault-parallel component ground motion.

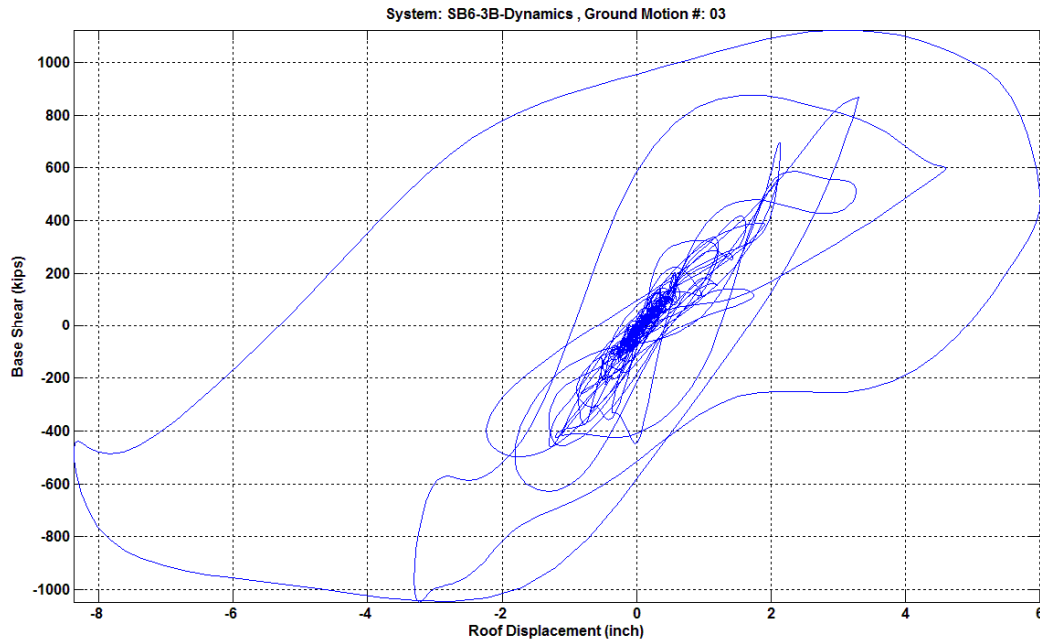


Figure 7.45 Base shear versus roof displacement relationship of Model SB6-3B under NGA 1119 fault-normal component ground motion.

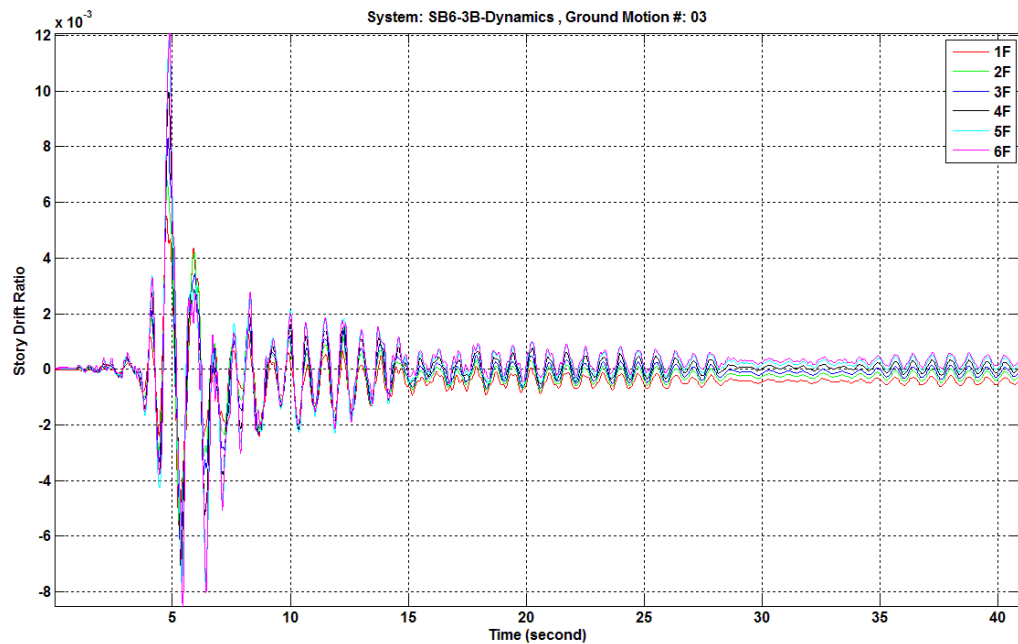


Figure 7.46 Story drift ratio histories of Model SB6-3B under NGA 1119 fault-normal component ground motion.

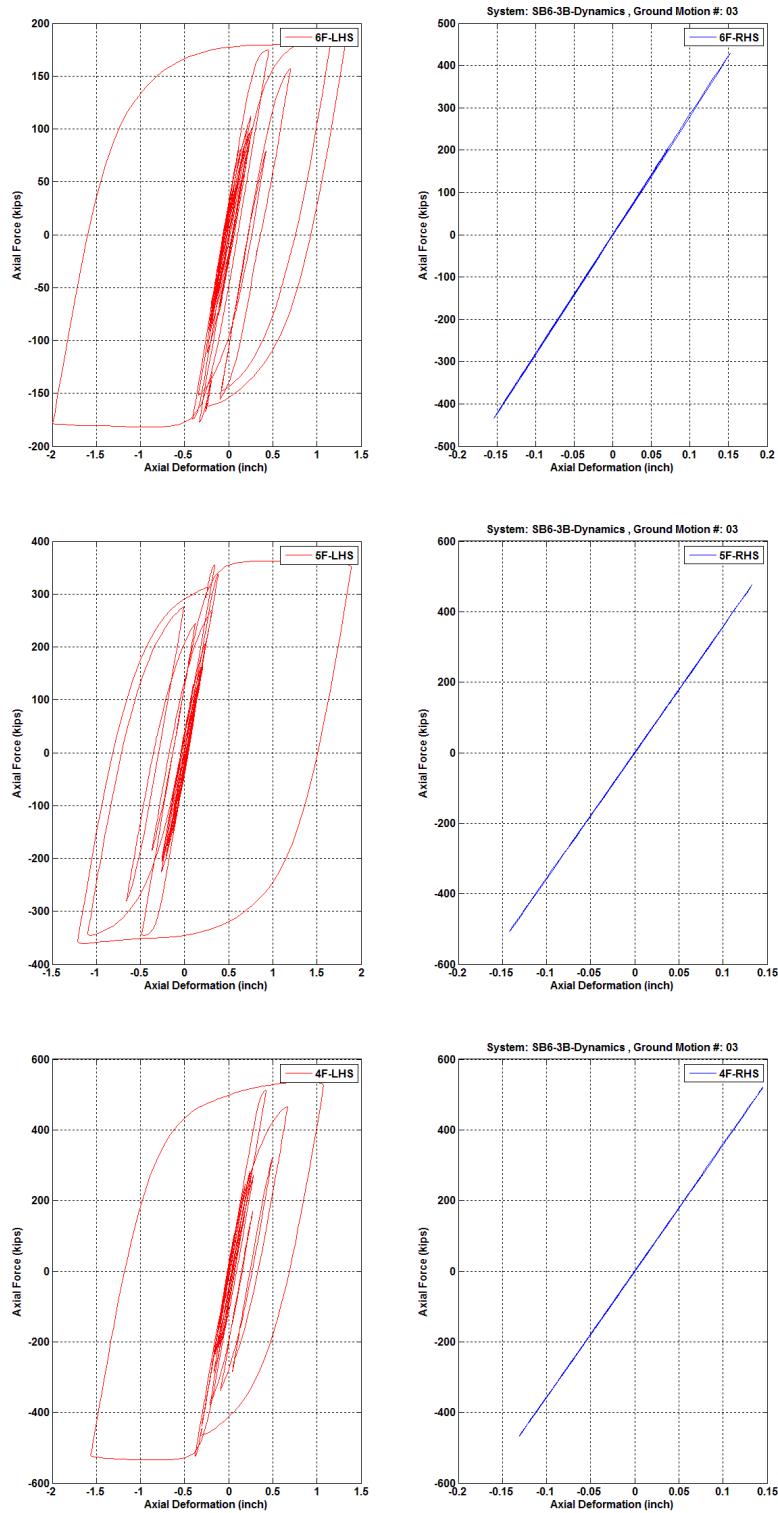


Figure 7.47 Fourth-story to sixth-story brace axial force versus axial deformation relationships of Model SB6-3B under NGA 1119 fault-normal component ground motion.

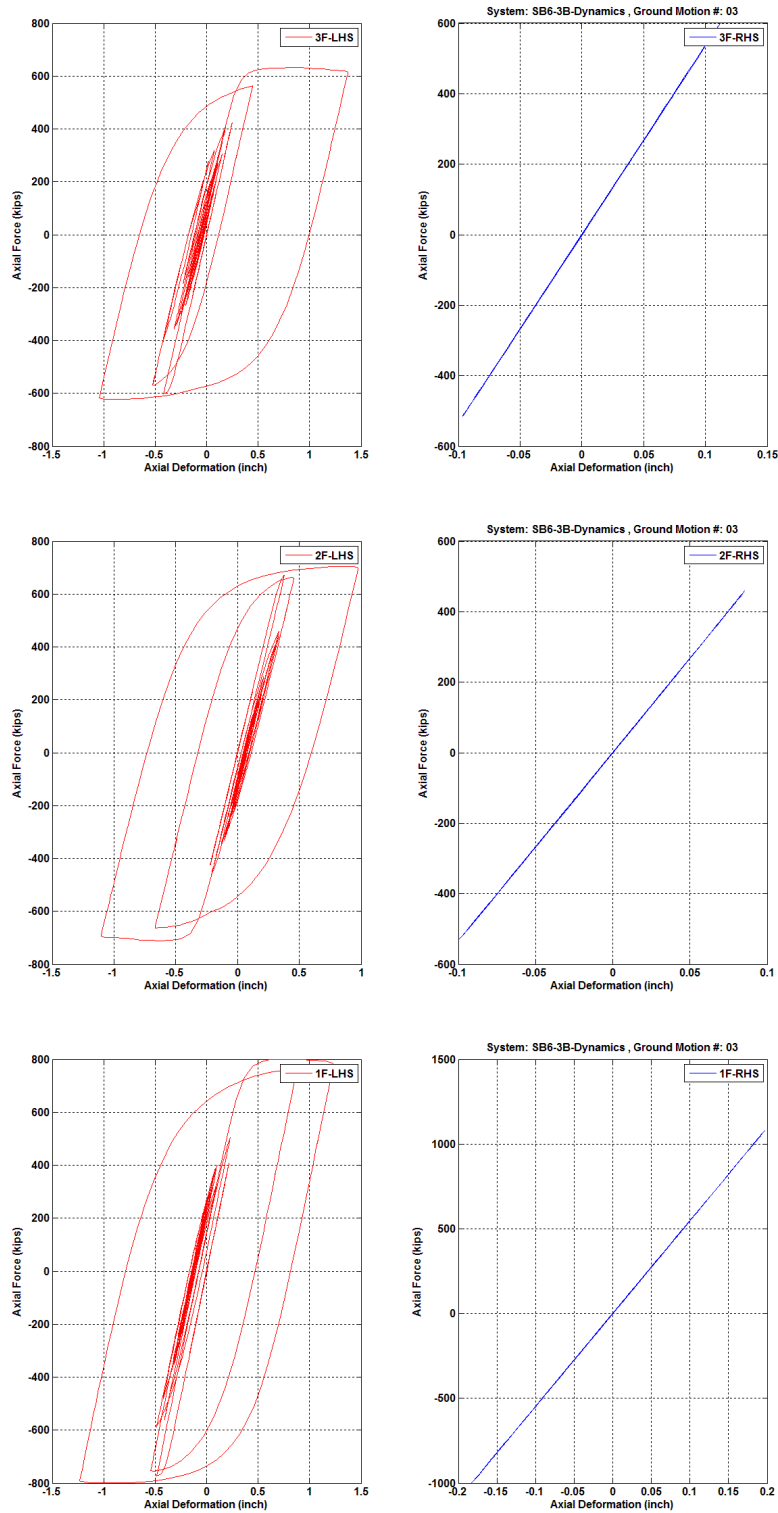


Figure 7.48 First-story to third-story brace axial force versus axial deformation relationships of Model SB6-3B under NGA 1119 fault-normal component ground motion.

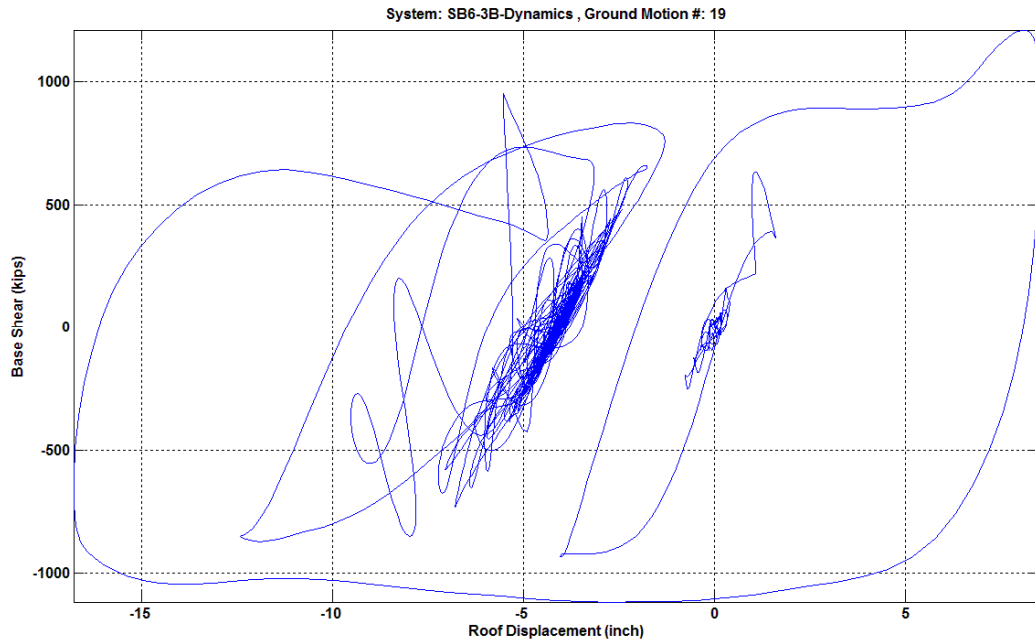


Figure 7.49 Base shear versus roof displacement relationship of Model SB6-3B under NGA 1602 fault-parallel component ground motion.

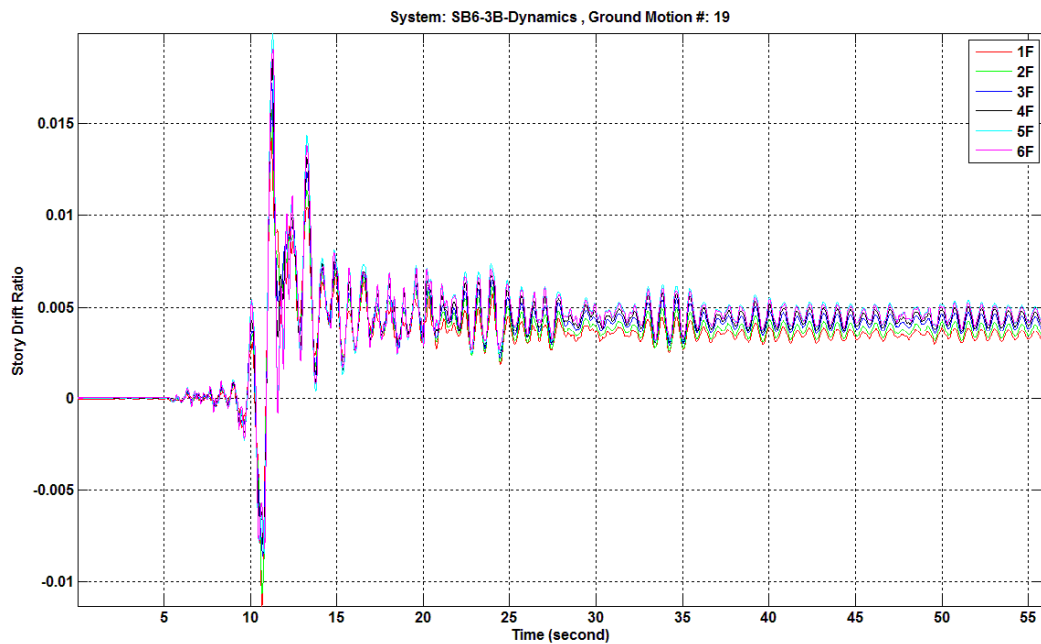


Figure 7.50 Story drift ratio histories of Model SB6-3B under NGA 1602 fault-parallel component ground motion.

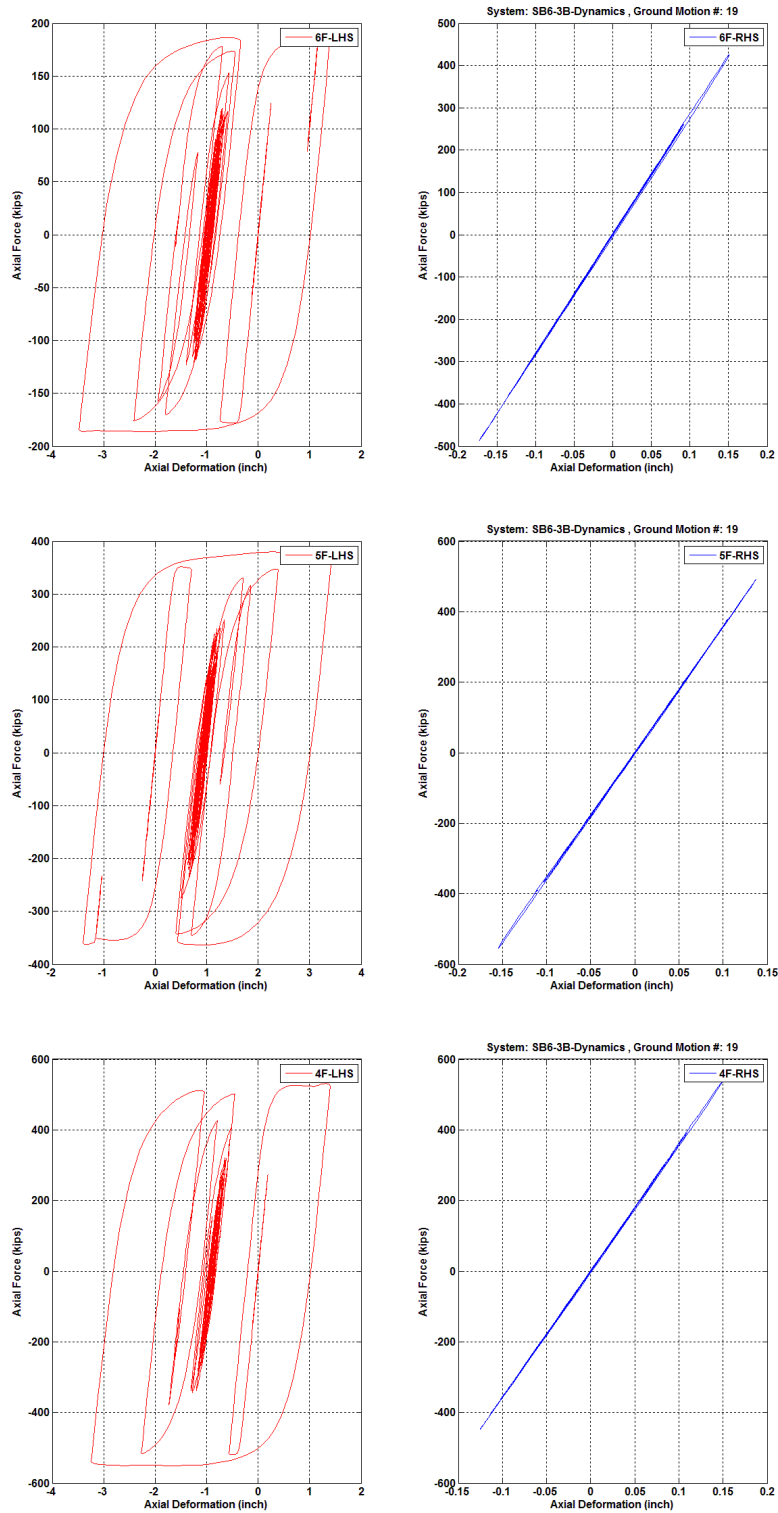


Figure 7.51 Fourth-story to sixth-story brace axial force versus axial deformation relationships of Model SB6-3B under NGA 1602 fault-parallel component ground motion.

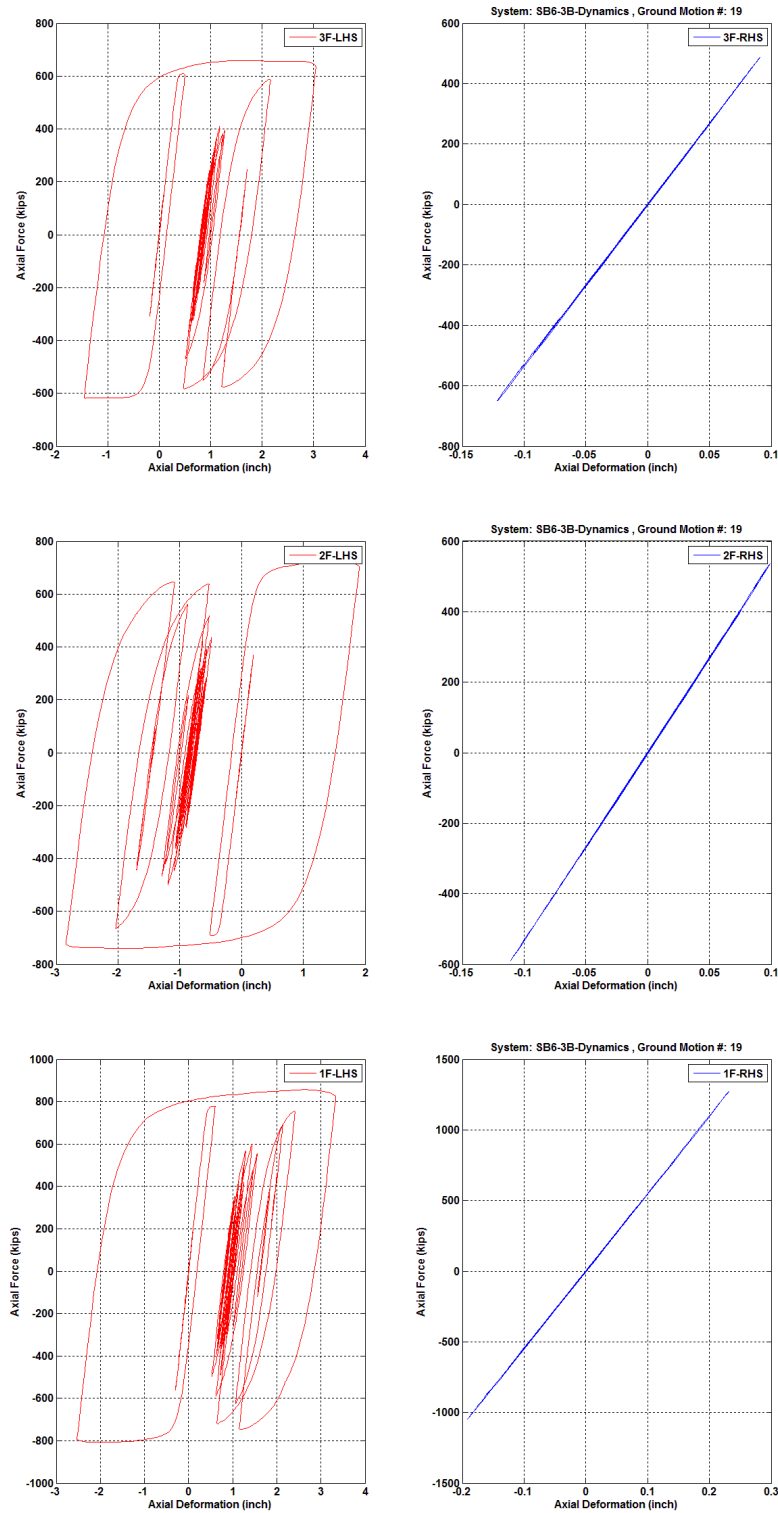


Figure 7.52 First-story to third-story brace axial force versus axial deformation relationships of Model SB6-3B under NGA 1602 fault-parallel component ground motion.

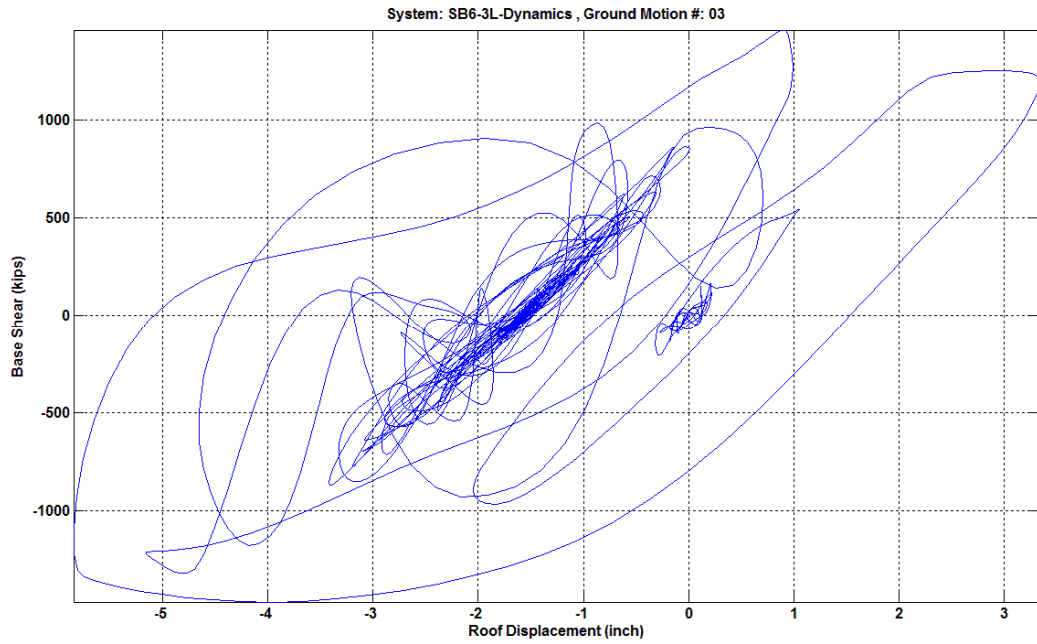


Figure 7.53 Base shear versus roof displacement relationship of Model SB6-3L under NGA 1119 fault-normal component ground motion.

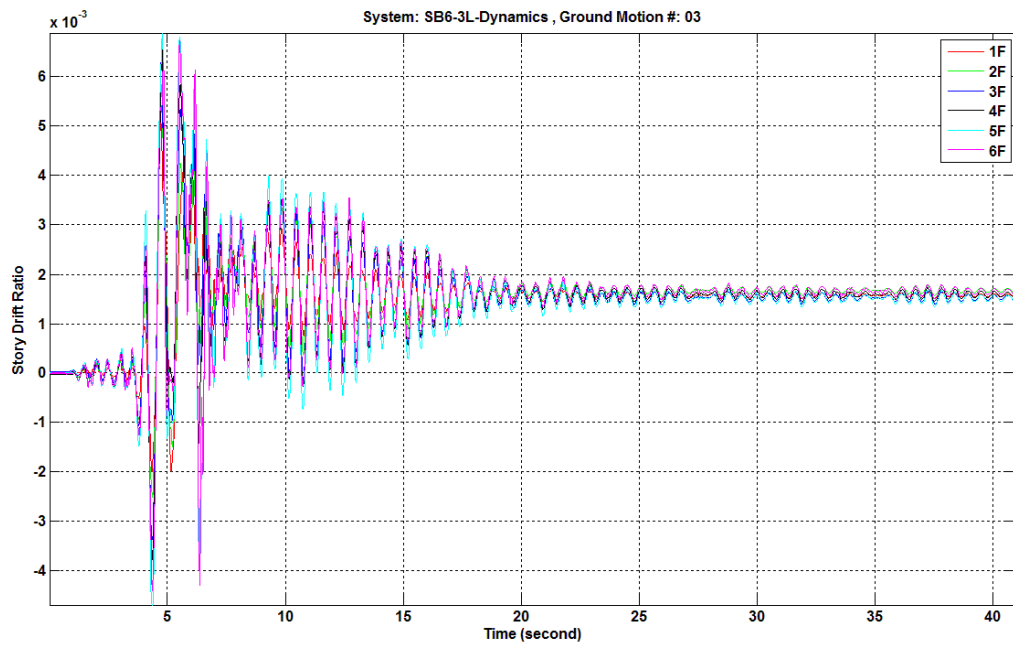


Figure 7.54 Story drift ratio histories of Model SB6-3L under NGA 1119 fault-normal component ground motion.

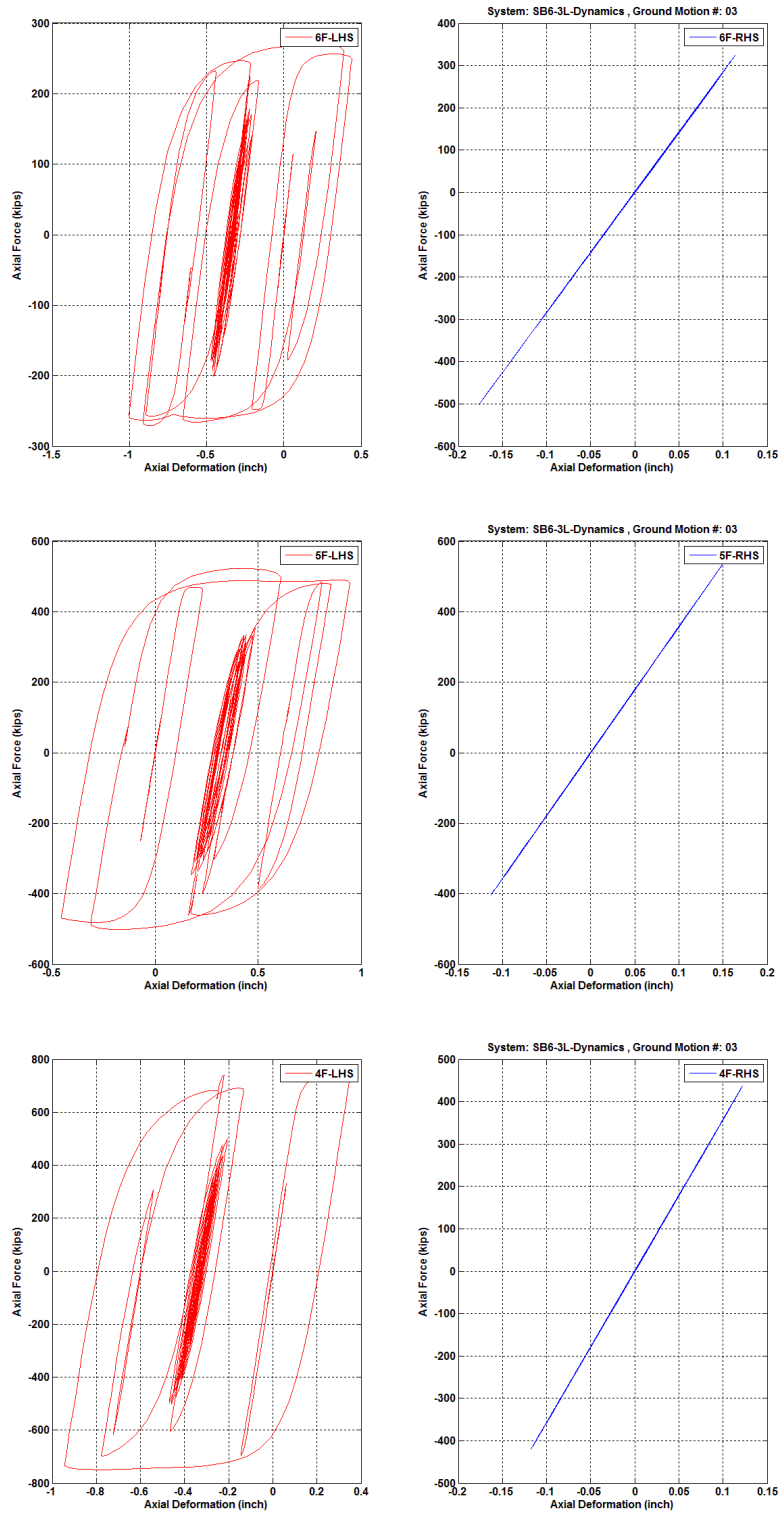


Figure 7.55 Fourth-story to sixth-story brace axial force versus axial deformation relationships of Model SB6-3L under NGA 1119 fault-normal component ground motion.

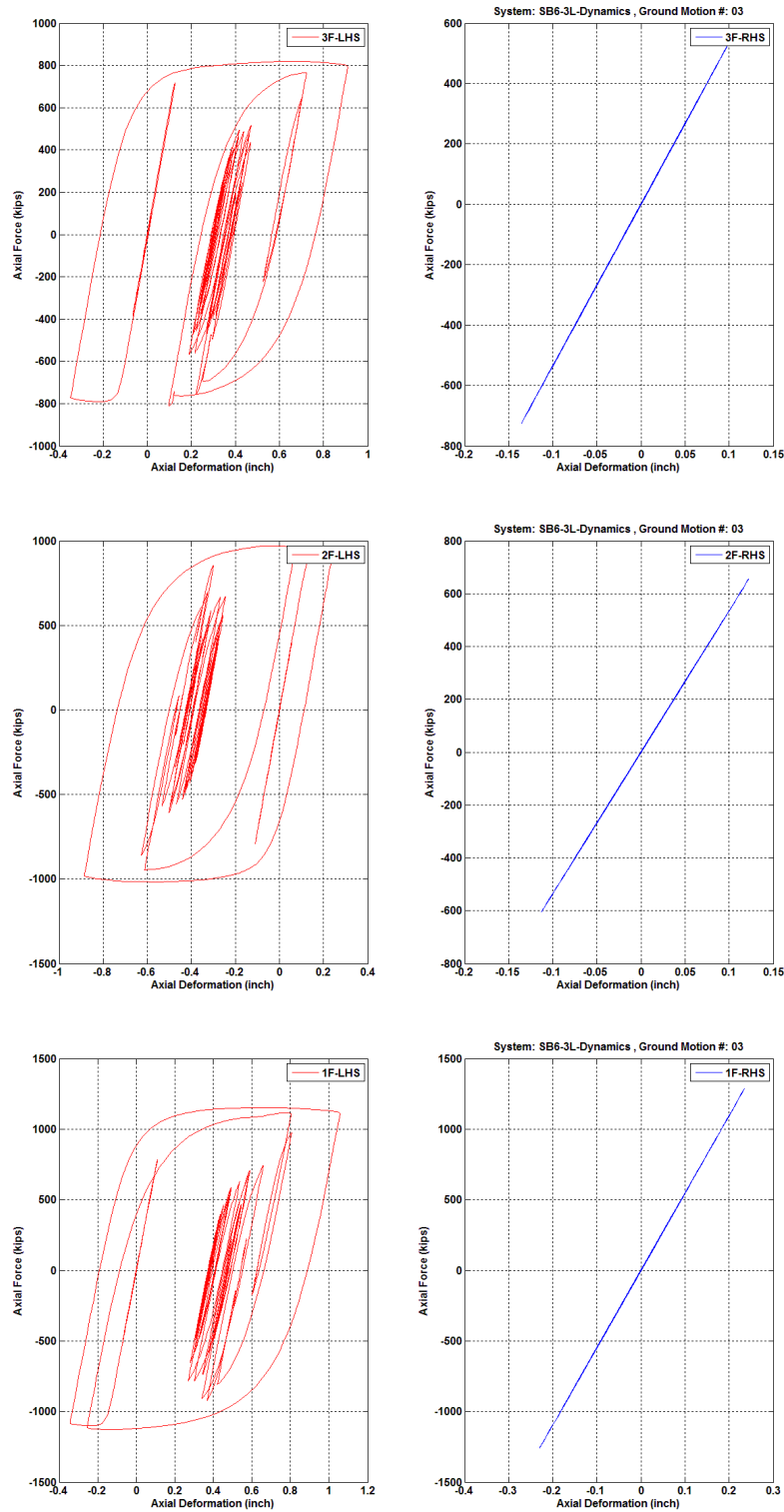


Figure 7.56 First-story to third-story brace axial force versus axial deformation relationships of Model SB6-3L under NGA 1119 fault-normal component ground motion.

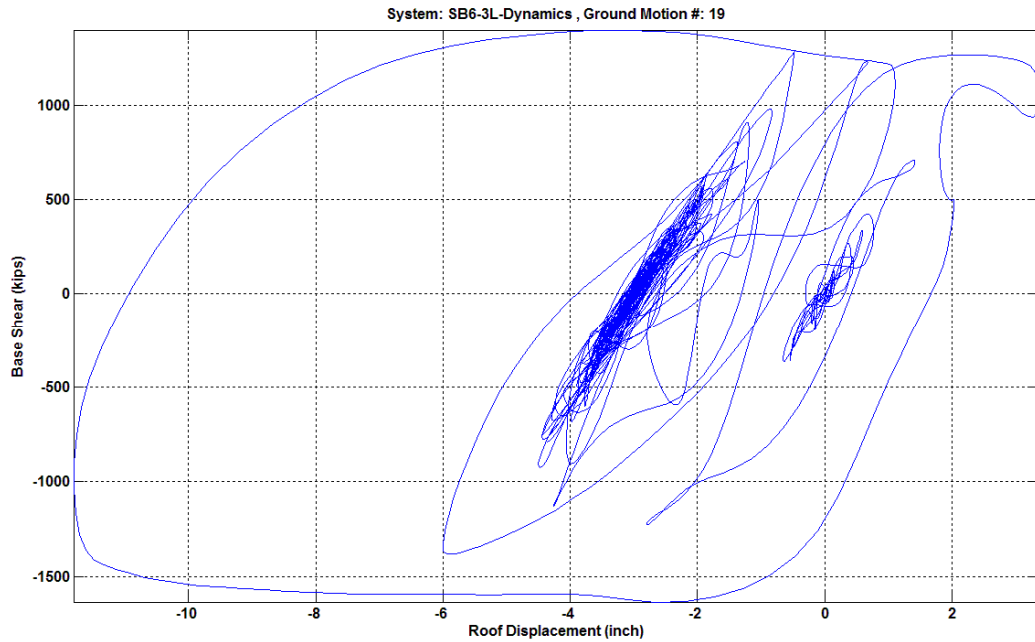


Figure 7.57 Base shear versus roof displacement relationship of Model SB6-3L under NGA 1602 fault-parallel component ground motion.

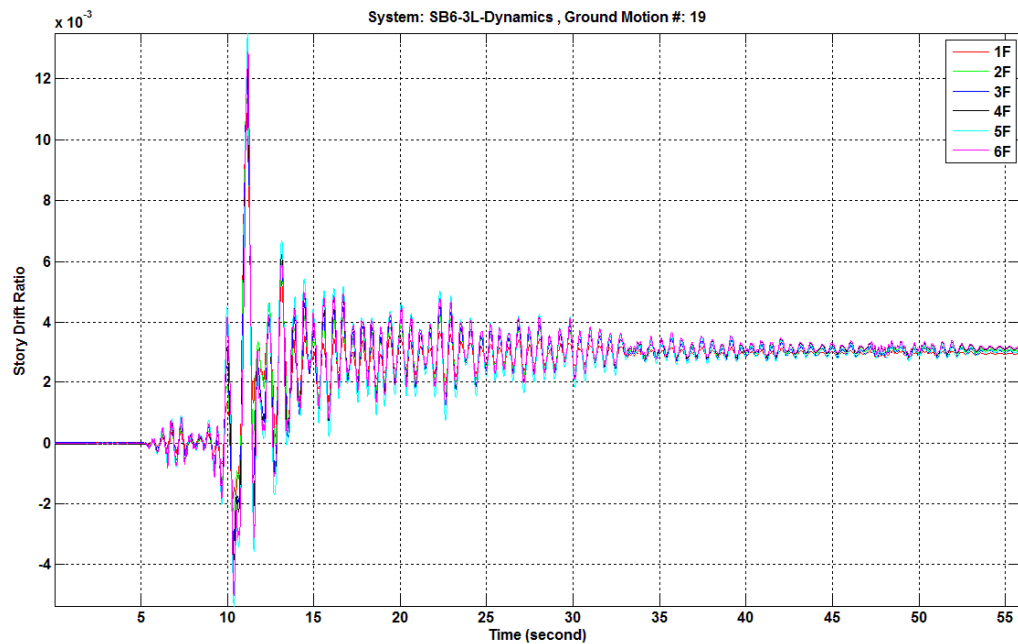


Figure 7.58 Story drift ratio histories of Model SB6-3L under NGA 1602 fault-parallel component ground motion.

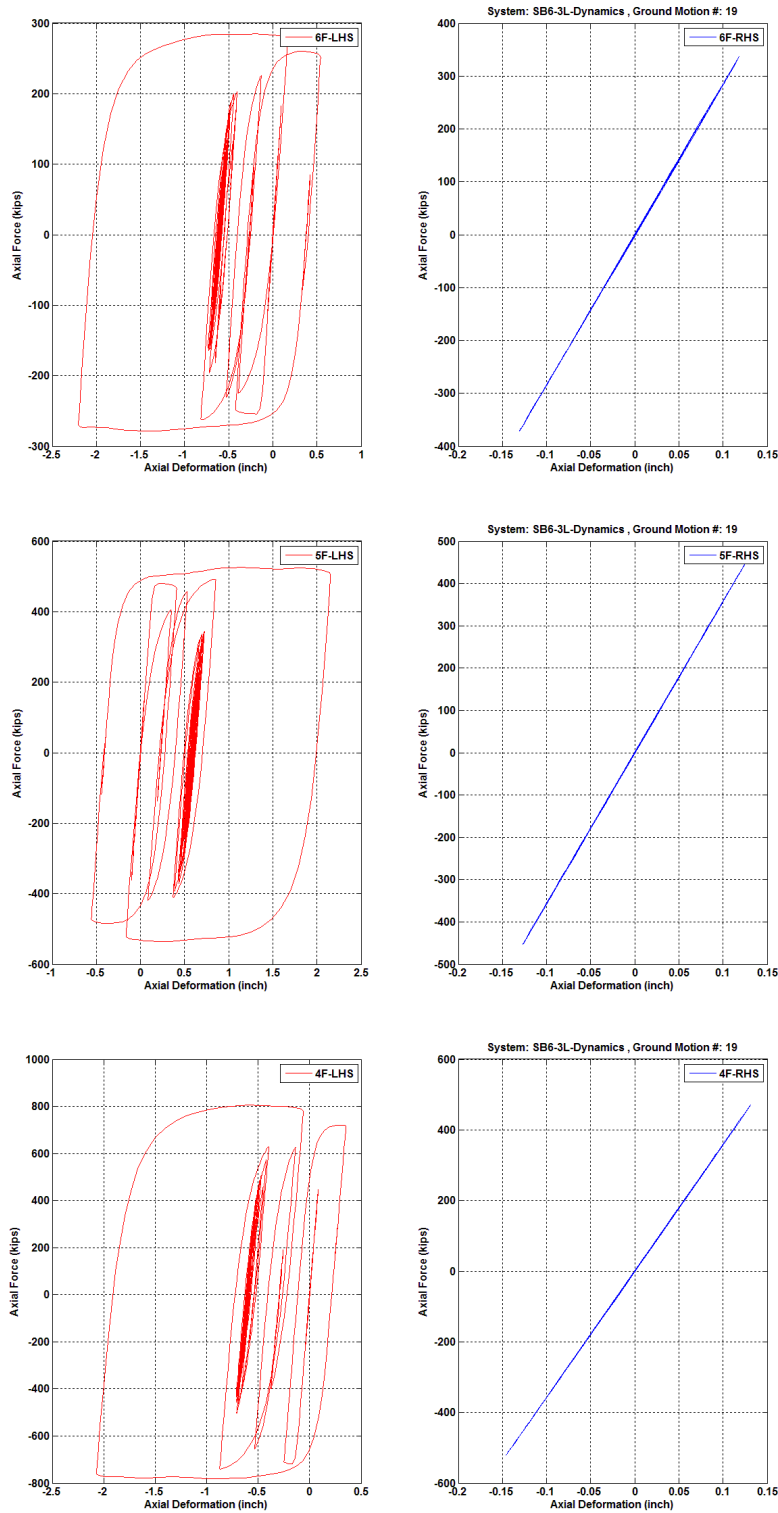


Figure 7.59 Fourth-story to sixth-story brace axial force versus axial deformation relationships of Model SB6-3L under NGA 1602 fault-parallel component ground motion.

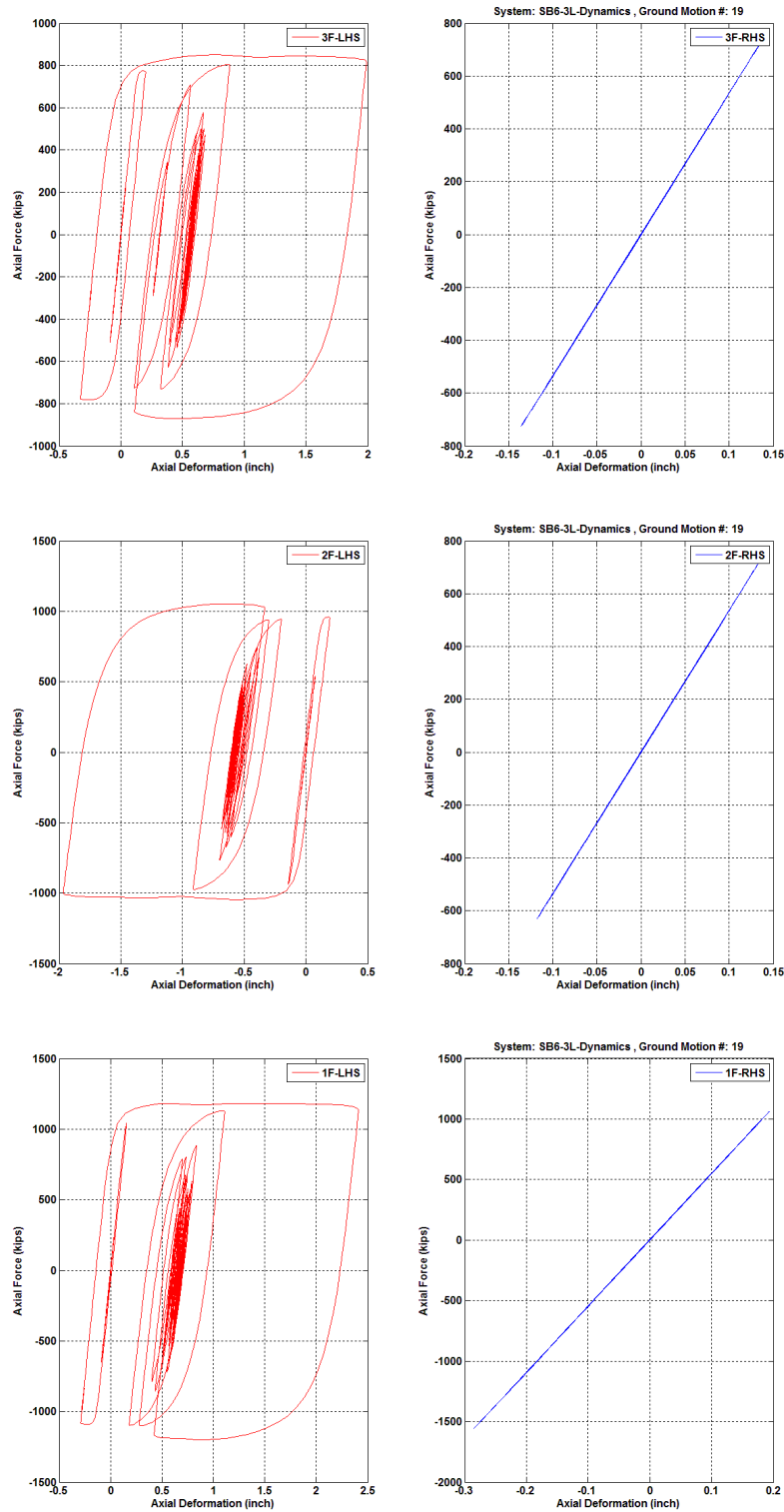


Figure 7.60 First-story to third story brace axial force versus axial deformation relationships of Model SB6-3L under NGA 1602 fault-parallel component ground motion.

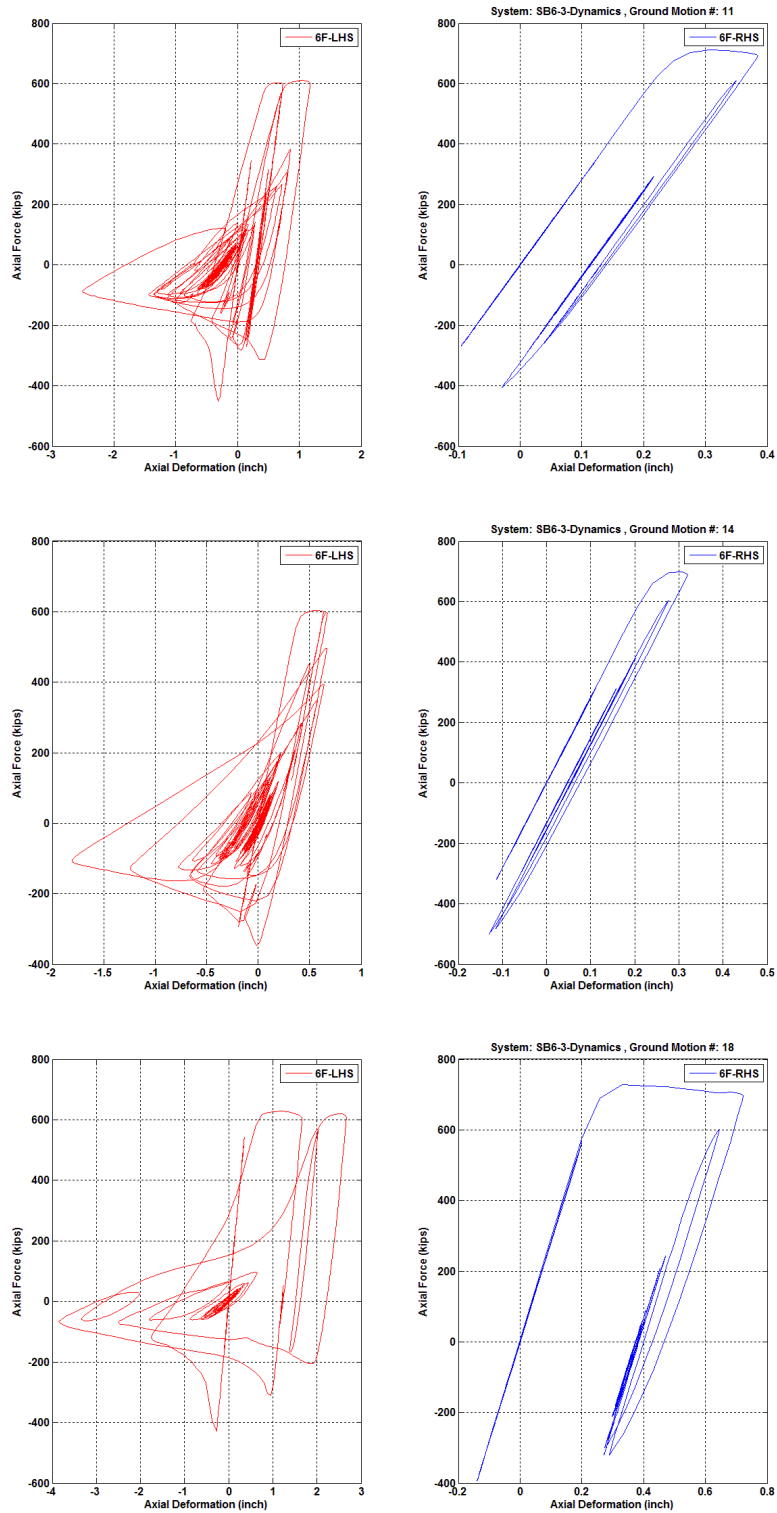


Figure 7.61 Sixth-story brace axial force versus axial deformation relationships of Model SB6-3 under ground motion numbers 11, 14, and 18.

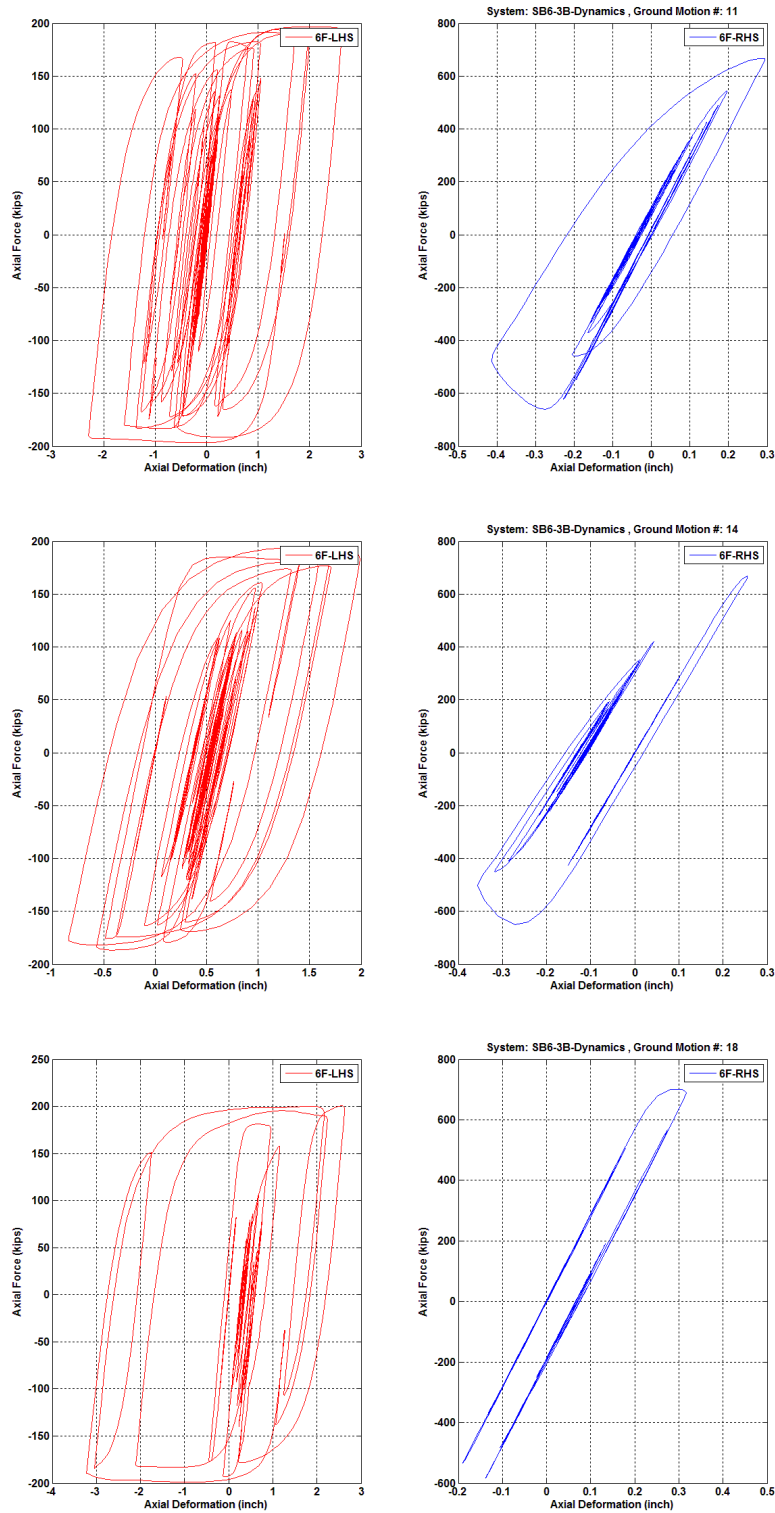


Figure 7.62 Sixth-story brace axial force versus axial deformation relationships of Model SB6-3B under ground motion numbers 11, 14, and 18.

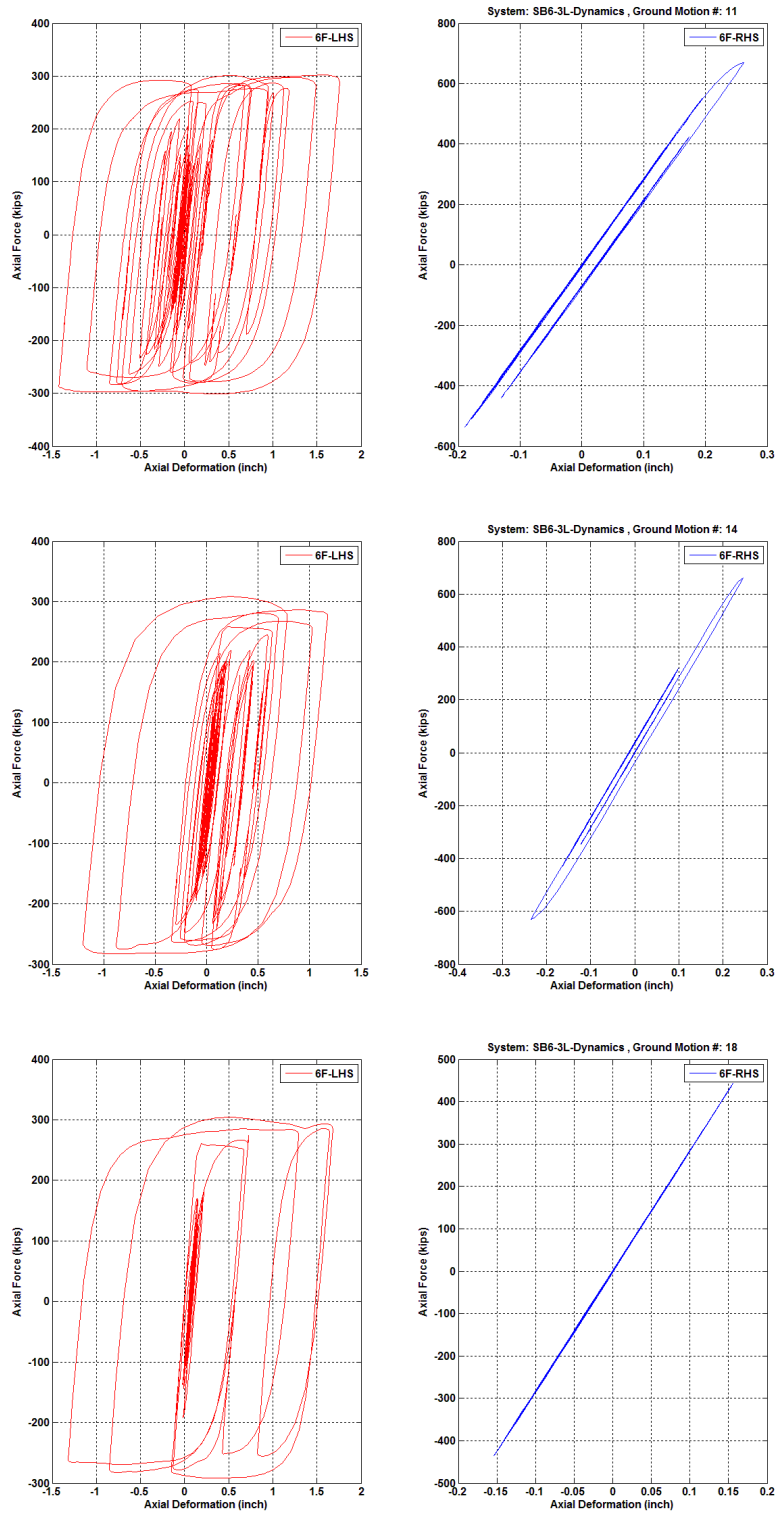


Figure 7.63 Sixth-story brace axial force versus axial deformation relationships of Model SB6-3L under ground motion numbers 11, 14, and 18.

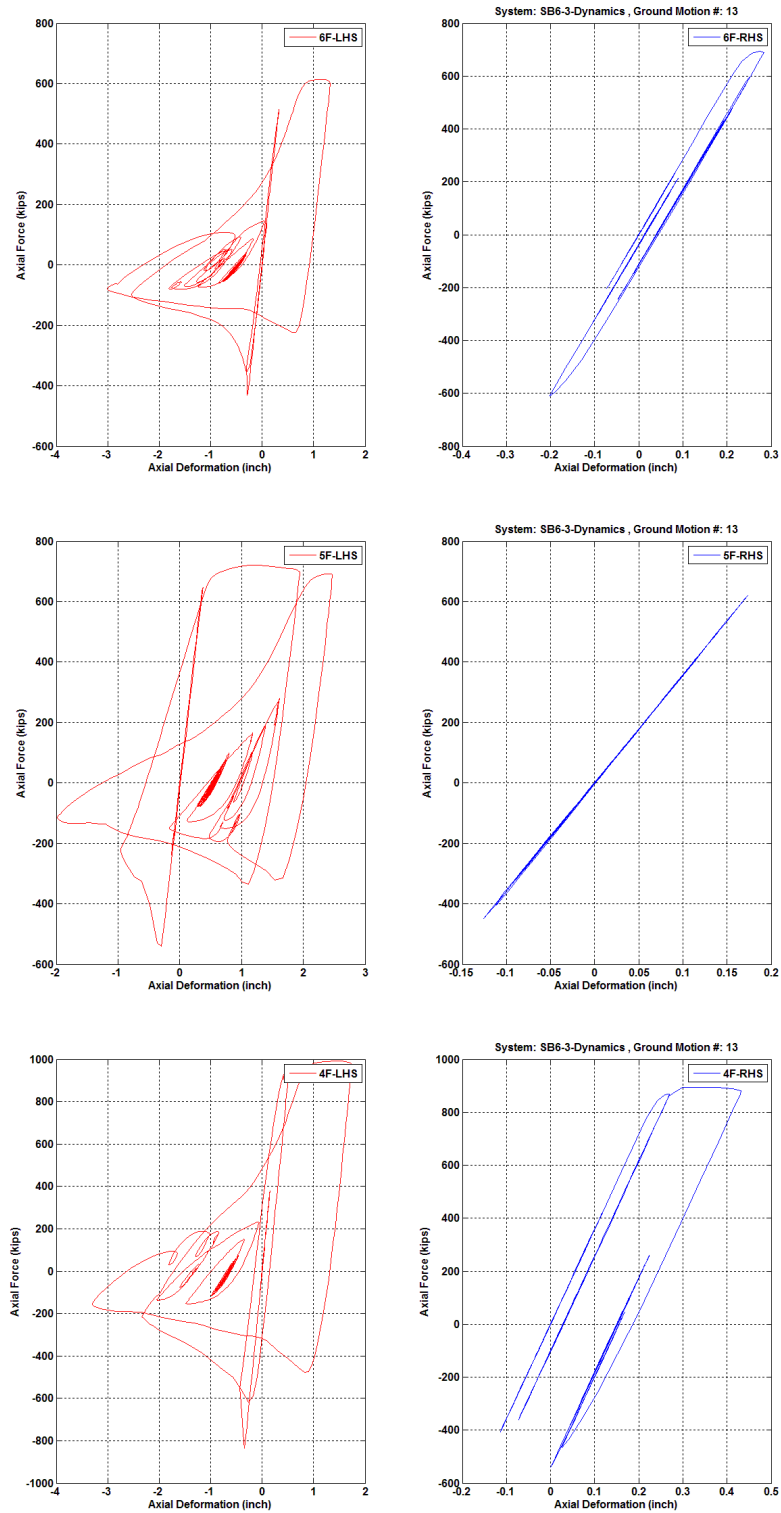


Figure 7.64 Fourth-story to sixth-story brace axial force versus axial deformation relationships of Model SB6-3 under ground motion number 13.

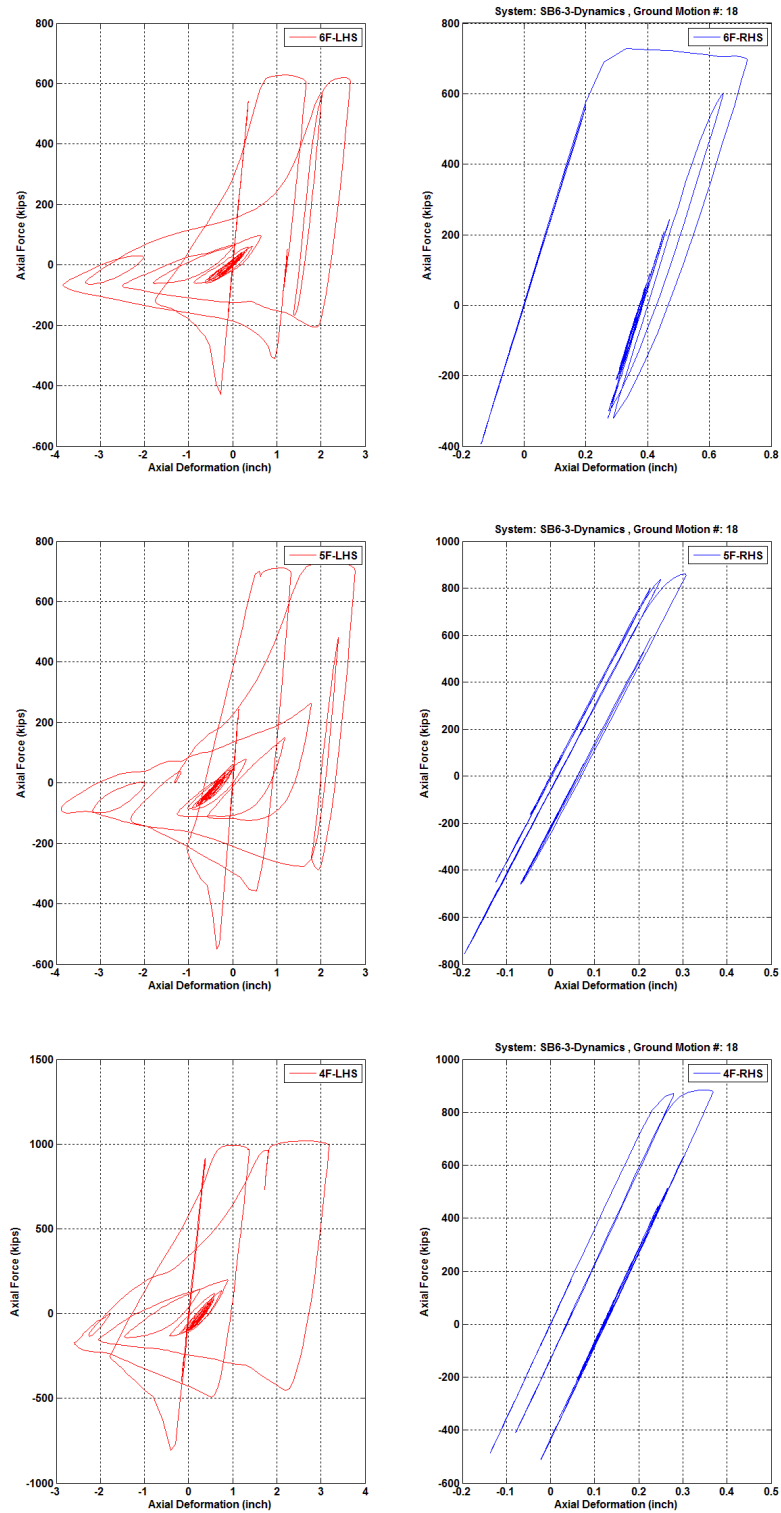


Figure 7.65 Fourth-story to sixth-story brace axial force versus axial deformation relationships of Model SB6-3 under ground motion number 18.

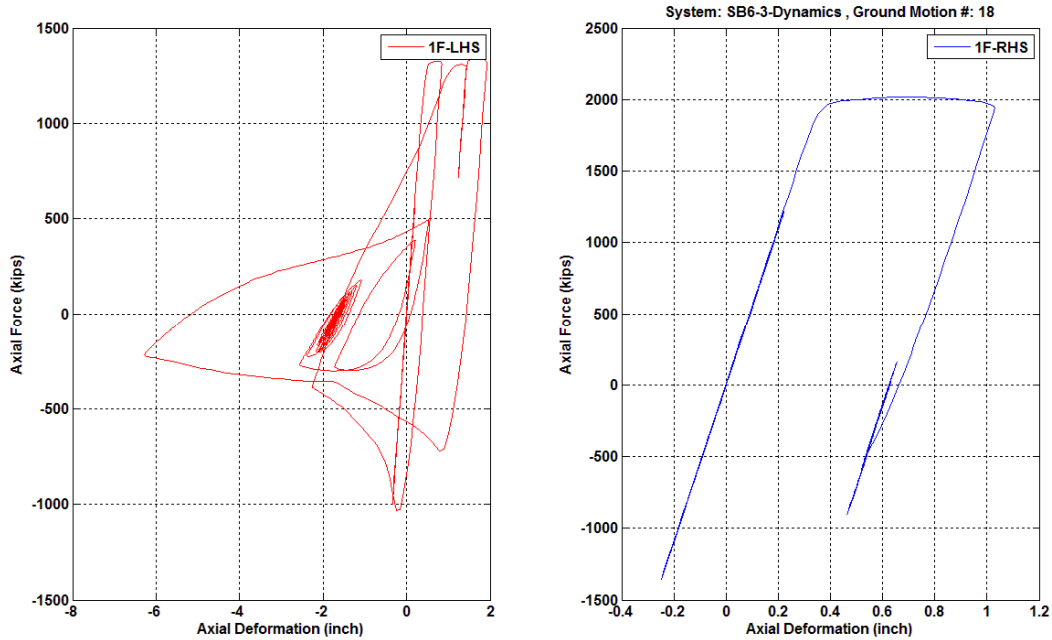


Figure 7.66 First-story brace axial force versus axial deformation relationships of Model SB6-3 under ground motion number 18.

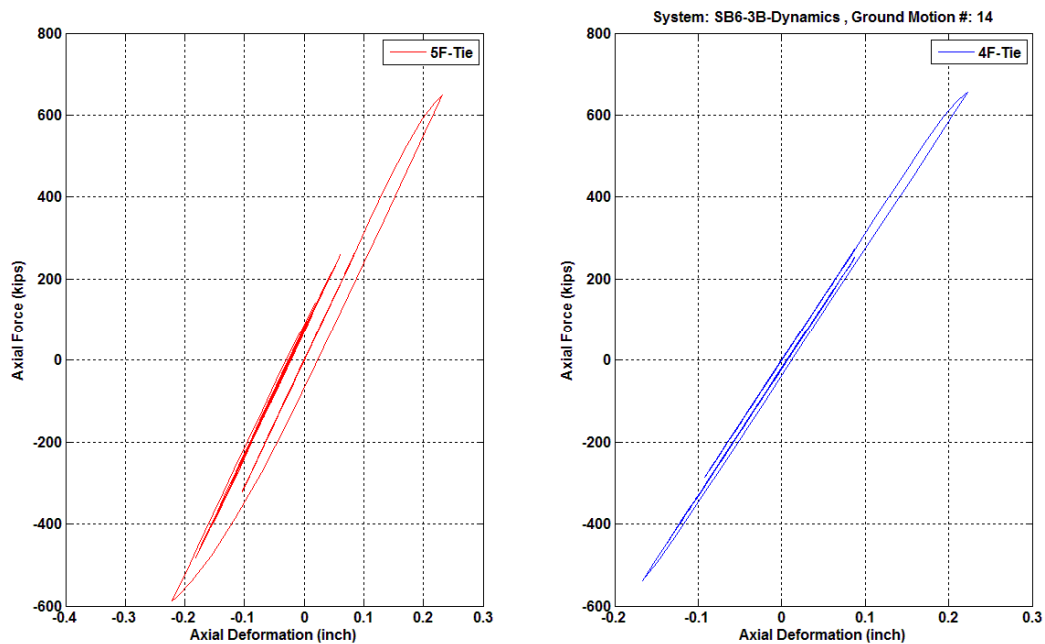


Figure 7.67 Fourth-story and fifth-story tie-column axial force versus axial deformation relationships of Model SB6-3B under ground motion number 14.

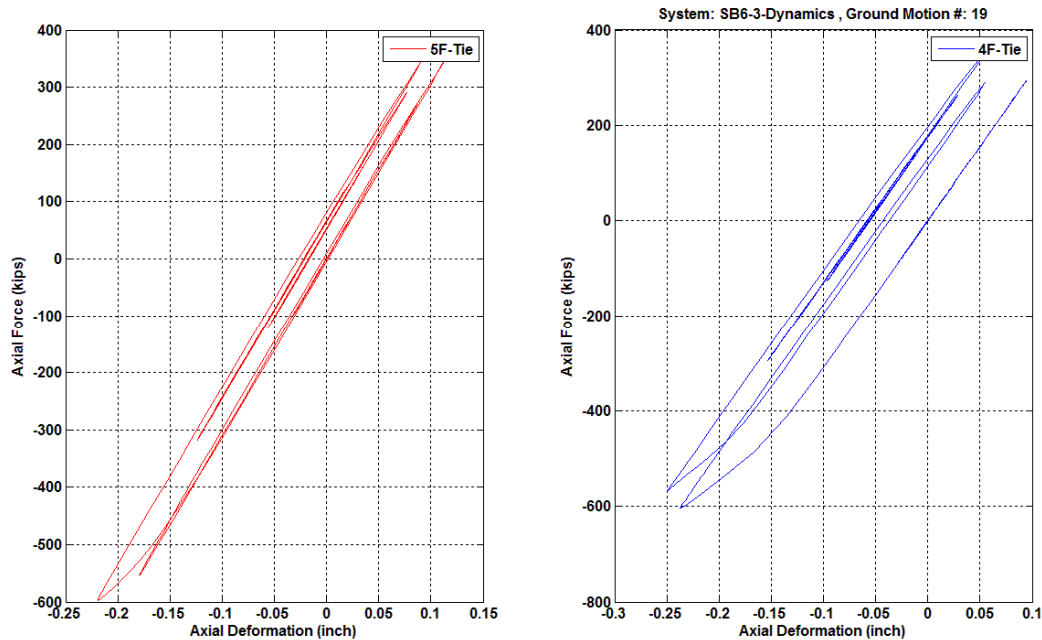


Figure 7.68 Fourth-story and fifth-story tie-column axial force versus axial deformation relationships of Model SB6-3 under ground motion number 19.

7.7 COST COMPARISON

The steel weight of seismic force resisting systems for each model was estimated to examine the increased initial construction costs due to introducing the strong-back vertical spine and buckling-restrained braces into the braced frame systems. The initial fabrication costs per tonnage steel was assumed to be \$3300 US/ton and the costs per BRB for the mid-rise building was assumed to be \$5000 US/brace [DASSE 2009] and \$10,000 US/brace for regular-yield-strength BRBs and low-yield-strength BRBs (including connection costs). The equivalent connection tonnage was assumed as 15% of steel weight (such as columns, beams, conventional braces and tie-columns). Table 7.17 summarizes the weight and costs of each seismic force resisting system. Note that the gravity columns and gravity beams were not included.

From the cost ratios shown in Table 7.17, using strong-back systems instead of chevron configuration braced frame (V6) could reduce the cost of seismic force resisting system up to 18%. Compared with the estimated cost of double-story X-braced frame (X6), the cost of strong-back systems were about 13% to 43% higher.

Table 7.17 Steel weight contributions and estimated initial construction costs for each model (only includes the seismic force resisting system).

Model	V6	X6	X6-3	SB6-3	SB6-3B	SB6-3L
Columns Weight (tons)	80.8	80.8	80.8	80.8	80.8	80.8
Beams Weight (tons)	83.9	31.0	31.0	31.0	31.0	31.0
Braces Weight (tons)	26.4	26.4	29.8	36.7	17.3	17.3
Tie-Columns Weight (tons)	-	-	-	7.4	5.8	5.8
Connections Equivalent Weight (tons) [15%]	28.7	20.7	21.2	23.4	20.2	20.2
Buckling-Restrained Brace (BRB)	-	-	-	-	24	24
BRB Costs (US\$)	-	-	-	-	120,000	240,000
Total Weight without BRB (tons)	219.8	158.9	162.8	179.3	155.1	155.1
Total Costs (US\$)	725,340	524,370	537,240	591,690	631,830	751,830
Cost Ratio	1.00	0.72	0.74	0.82	0.87	1.04

7.8 EFFECT OF GRAVITY LEANING COLUMNS

All leaning columns in the OpenSees models were removed and performed the analyses again to examine the effects of gravity columns. The re-analysis results showed that the fundamental and the second mode periods were essentially the same for all six models with or without leaning columns (see Table 7.12 and Table 7.18).

The mean responses of strong-back models did not have significant changes when the gravity leaning columns were absent (see Tables 7.13, 7.14, 7.15, 7.16, 7.19, 7.20, 7.21, and 7.22) but did have significant changes for the non-strong-back systems (compare Figures 7.10, 7.11, 7.69, and 7.70), especially on the maximum story drift ratio at each floor level. The gravity columns did somewhat help reduce deformation concentrations in the non-strong-back systems (Models V6, X6, and X6-3). The presence of leaning columns in the models had significant effects on the residual story drift ratio at each floor level (see Figures 7.11 and 7.70). The maximum base shear forces, maximum roof displacements, maximum floor accelerations (see Figures 7.12 and 7.71), and maximum column uplift forces were essentially not affected by leaning columns. The peak axial deformations of braces were typically larger if the leaning columns were not modeled, and this phenomenon was more obvious in non-strong-back systems as shown from Figures 7.72 to 7.77.

Table 7.18 **Fundamental and second mode periods of each model (without leaning columns).**

Model Name	1st Mode (sec)	2nd Mode (sec)
V6	0.686	0.245
X6	0.700	0.245
X6-3	0.699	0.249
SB6-3	0.666	0.235
SB6-3B	0.767	0.283
SB6-3L	0.563	0.192

Table 7.19 Mean responses of each model under selected ground motions (10% probability of exceedance in 50-years events, fault-normal, without leaning columns).

Mean Response	V6	X6	X6-3	SB6-3	SB6-3B	SB6-3L
Max. Base Shear (kips)	1200.4	1270.0	1354.5	1445.4	1062.8	1387.3
Max. Roof Displacement (in.)	5.02	5.06	5.68	5.55	5.98	5.00
Max. 1 st Story Drift Ratio (%)	1.202	0.637	0.750	0.595	0.517	0.322
Max. 2 nd Story Drift Ratio (%)	0.294	0.541	0.602	0.617	0.542	0.387
Max. 3 rd Story Drift Ratio (%)	0.410	1.076	0.789	0.713	0.577	0.489
Max. 4 th Story Drift Ratio (%)	0.558	0.799	0.797	0.795	0.690	0.601
Max. 5 th Story Drift Ratio (%)	0.484	0.493	0.860	0.807	0.925	0.745
Max. 6 th Story Drift Ratio (%)	0.373	0.390	0.421	0.782	0.931	0.729
Residual Roof Displacement (in.)	0.441	0.444	0.229	0.169	0.448	0.697
Residual 1 st Story Drift Ratio (%)	0.139	0.152	0.092	0.049	0.070	0.039
Residual 2 nd Story Drift Ratio (%)	0.009	0.057	0.068	0.028	0.051	0.056
Residual 3 rd Story Drift Ratio (%)	0.031	0.049	0.077	0.030	0.051	0.065
Residual 4 th Story Drift Ratio (%)	0.045	0.078	0.068	0.032	0.045	0.083
Residual 5 th Story Drift Ratio (%)	0.038	0.039	0.072	0.029	0.055	0.090
Residual 6 th Story Drift Ratio (%)	0.007	0.014	0.025	0.039	0.052	0.010
Max. Column Uplift Force, LHS (kips)	2102.9	1978.9	2371.5	2348.3	1497.3	2285.8
Max. Column Uplift Force, RHS (kips)	2087.7	1974.7	2126.9	2270.3	1570.1	2212.0
Max. 2 nd Floor Acceleration (g)	1.17	1.08	1.16	1.23	1.02	1.13
Max. 3 rd Floor Acceleration (g)	1.09	1.15	1.14	1.11	1.01	1.01
Max. 4 th Floor Acceleration (g)	0.99	1.07	1.06	0.96	0.93	0.89
Max. 5 th Floor Acceleration (g)	0.93	0.84	0.93	0.84	0.78	0.68
Max. 6 th Floor Acceleration (g)	0.82	0.64	0.67	0.69	0.60	0.52
Max. Roof Acceleration (g)	1.24	1.29	1.41	1.39	1.20	1.39

(Note: LHS stands for left hand side, RHS stands for right hand side)

Table 7.20 Mean responses of each model under selected ground motions (10% probability of exceedance in 50-years events, fault-parallel, without leaning columns).

Mean Response	V6	X6	X6-3	SB6-3	SB6-3B	SB6-3L
Max. Base Shear (kips)	1185.9	1232.7	1345.1	1418.2	1035.1	1328.9
Max. Roof Displacement (in.)	6.19	6.39	6.62	6.48	7.65	5.39
Max. 1 st Story Drift Ratio (%)	1.694	0.885	0.920	0.759	0.586	0.362
Max. 2 nd Story Drift Ratio (%)	0.297	0.663	0.679	0.755	0.659	0.439
Max. 3 rd Story Drift Ratio (%)	0.427	1.135	0.960	0.805	0.736	0.533
Max. 4 th Story Drift Ratio (%)	0.652	0.859	0.715	0.893	0.862	0.615
Max. 5 th Story Drift Ratio (%)	0.453	0.500	0.926	0.742	1.019	0.759
Max. 6 th Story Drift Ratio (%)	0.358	0.361	0.394	0.665	1.001	0.737
Residual Roof Displacement (in.)	0.538	0.720	0.663	0.544	1.050	0.850
Residual 1 st Story Drift Ratio (%)	0.161	0.144	0.095	0.062	0.085	0.089
Residual 2 nd Story Drift Ratio (%)	0.014	0.113	0.111	0.064	0.097	0.083
Residual 3 rd Story Drift Ratio (%)	0.026	0.079	0.096	0.051	0.105	0.087
Residual 4 th Story Drift Ratio (%)	0.078	0.054	0.093	0.065	0.115	0.089
Residual 5 th Story Drift Ratio (%)	0.028	0.045	0.153	0.055	0.116	0.084
Residual 6 th Story Drift Ratio (%)	0.011	0.012	0.017	0.064	0.123	0.086
Max. Column Uplift Force, LHS (kips)	2178.6	2097.5	2444.9	2390.2	1598.1	2235.4
Max. Column Uplift Force, RHS (kips)	2130.2	1919.5	2094.1	2231.0	1566.3	2244.7
Max. 2 nd Floor Acceleration (g)	1.01	0.96	0.96	1.04	0.87	1.01
Max. 3 rd Floor Acceleration (g)	0.88	0.93	0.93	0.98	0.78	0.86
Max. 4 th Floor Acceleration (g)	0.84	0.92	0.85	0.86	0.69	0.72
Max. 5 th Floor Acceleration (g)	0.81	0.80	0.71	0.67	0.58	0.51
Max. 6 th Floor Acceleration (g)	0.73	0.62	0.60	0.62	0.44	0.35
Max. Roof Acceleration (g)	1.20	1.18	1.23	1.23	1.17	1.17

(Note: LHS stands for left hand side, RHS stands for right hand side)

Table 7.21 Mean responses of each model under selected ground motions (2% probability of exceedance in 50-year events, fault-normal, without leaning columns).

Mean Response	V6	X6	X6-3	SB6-3	SB6-3B	SB6-3L
Max. Base Shear (kips)	1213.3	1290.5	1345.7	1495.0	1136.1	1594.1
Max. Roof Displacement (in.)	7.77	8.00	8.24	8.85	8.73	6.53
Max. 1 st Story Drift Ratio (%)	2.314	1.394	1.798	1.021	0.826	0.617
Max. 2 nd Story Drift Ratio (%)	0.310	0.859	0.892	1.000	0.856	0.656
Max. 3 rd Story Drift Ratio (%)	0.467	1.159	0.956	0.971	0.864	0.694
Max. 4 th Story Drift Ratio (%)	0.767	1.012	0.804	1.119	1.018	0.752
Max. 5 th Story Drift Ratio (%)	0.590	0.634	1.054	1.153	1.245	0.898
Max. 6 th Story Drift Ratio (%)	0.392	0.402	0.445	1.169	1.308	0.892
Residual Roof Displacement (in.)	1.027	1.642	1.429	1.043	1.214	0.649
Residual 1 st Story Drift Ratio (%)	0.320	0.294	0.172	0.089	0.156	0.110
Residual 2 nd Story Drift Ratio (%)	0.016	0.243	0.160	0.095	0.136	0.093
Residual 3 rd Story Drift Ratio (%)	0.037	0.210	0.191	0.081	0.125	0.063
Residual 4 th Story Drift Ratio (%)	0.114	0.122	0.170	0.170	0.120	0.068
Residual 5 th Story Drift Ratio (%)	0.049	0.067	0.135	0.126	0.096	0.084
Residual 6 th Story Drift Ratio (%)	0.025	0.016	0.032	0.102	0.104	0.093
Max. Column Uplift Force, LHS (kips)	2053.6	1958.7	2151.2	2126.5	1552.9	2376.3
Max. Column Uplift Force, RHS (kips)	2194.1	2055.7	2168.8	2293.6	1653.6	2358.6
Max. 2 nd Floor Acceleration (g)	1.53	1.38	1.48	1.74	1.42	1.52
Max. 3 rd Floor Acceleration (g)	1.31	1.29	1.41	1.39	1.40	1.37
Max. 4 th Floor Acceleration (g)	1.28	1.40	1.39	1.32	1.32	1.20
Max. 5 th Floor Acceleration (g)	1.20	1.21	1.20	1.15	1.13	0.98
Max. 6 th Floor Acceleration (g)	1.12	1.08	1.02	0.94	0.84	0.75
Max. Roof Acceleration (g)	1.64	1.57	1.63	1.62	1.62	1.83

(Note: LHS stands for left hand side, RHS stands for right hand side)

Table 7.22 Mean responses of each model under selected ground motions (2% probability of exceedance in 50-year events, fault-parallel, without leaning columns).

Mean Response	V6	X6	X6-3	SB6-3	SB6-3B	SB6-3L
Max. Base Shear (kips)	1202.1	1263.7	1320.8	1407.8	1135.6	1493.5
Max. Roof Displacement (in.)	11.12	10.90	11.27	12.67	10.85	8.50
Max. 1 st Story Drift Ratio (%)	3.594	1.806	2.096	1.344	0.897	0.676
Max. 2 nd Story Drift Ratio (%)	0.352	1.376	1.278	1.308	0.946	0.754
Max. 3 rd Story Drift Ratio (%)	0.479	1.618	1.165	1.383	1.049	0.870
Max. 4 th Story Drift Ratio (%)	0.854	1.188	1.206	1.493	1.226	0.951
Max. 5 th Story Drift Ratio (%)	0.652	0.660	1.260	1.448	1.465	1.062
Max. 6 th Story Drift Ratio (%)	0.404	0.415	0.509	1.514	1.482	1.035
Residual Roof Displacement (in.)	2.323	1.759	1.409	1.698	1.493	1.447
Residual 1 st Story Drift Ratio (%)	0.863	0.353	0.340	0.282	0.131	0.147
Residual 2 nd Story Drift Ratio (%)	0.038	0.254	0.223	0.188	0.142	0.149
Residual 3 rd Story Drift Ratio (%)	0.047	0.223	0.173	0.161	0.154	0.148
Residual 4 th Story Drift Ratio (%)	0.110	0.122	0.116	0.212	0.165	0.152
6Residual 5 th Story Drift Ratio (%)	0.064	0.067	0.088	0.182	0.161	0.136
Residual 6 th Story Drift Ratio (%)	0.046	0.014	0.041	0.194	0.154	0.137
Max. Column Uplift Force, LHS (kips)	2269.2	1993.1	2355.5	2344.2	1682.7	2363.3
Max. Column Uplift Force, RHS (kips)	2205.9	2068.5	2173.5	2275.5	1607.5	2432.5
Max. 2 nd Floor Acceleration (g)	1.44	1.40	1.29	1.31	1.28	1.32
Max. 3 rd Floor Acceleration (g)	1.13	1.34	1.26	1.40	1.07	1.10
Max. 4 th Floor Acceleration (g)	1.15	1.11	1.17	1.12	0.97	0.96
Max. 5 th Floor Acceleration (g)	1.07	1.03	0.98	0.89	0.82	0.76
Max. 6 th Floor Acceleration (g)	0.97	0.85	0.79	0.80	0.67	0.60
Max. Roof Acceleration (g)	1.50	1.58	1.57	1.66	1.62	1.56

(Note: LHS stands for left hand side, RHS stands for right hand side)

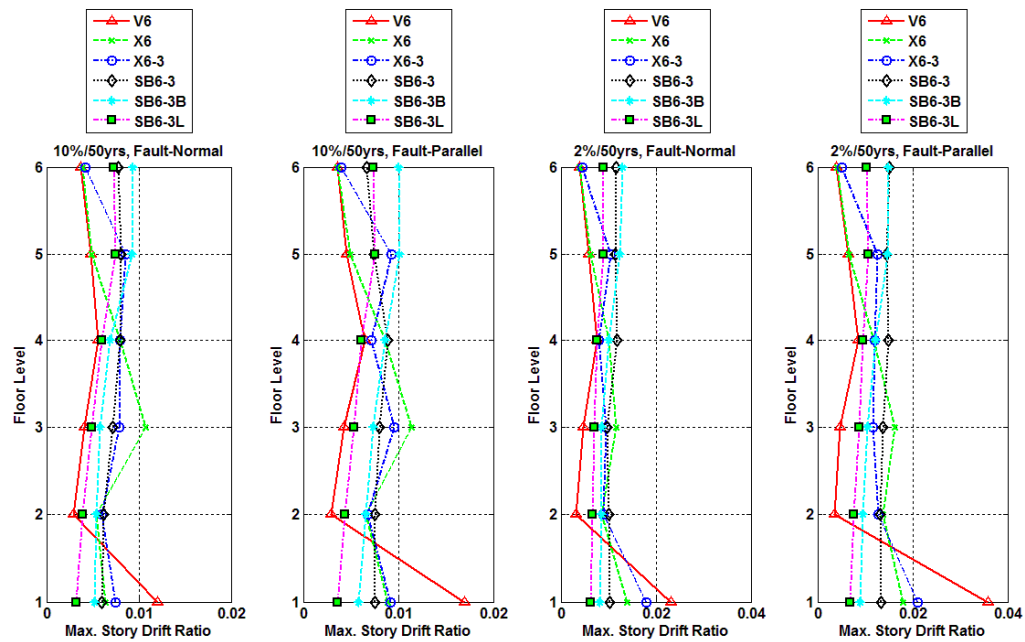


Figure 7.69 Maximum story drift ratios for each model under different hazard level ground motions (without leaning columns).

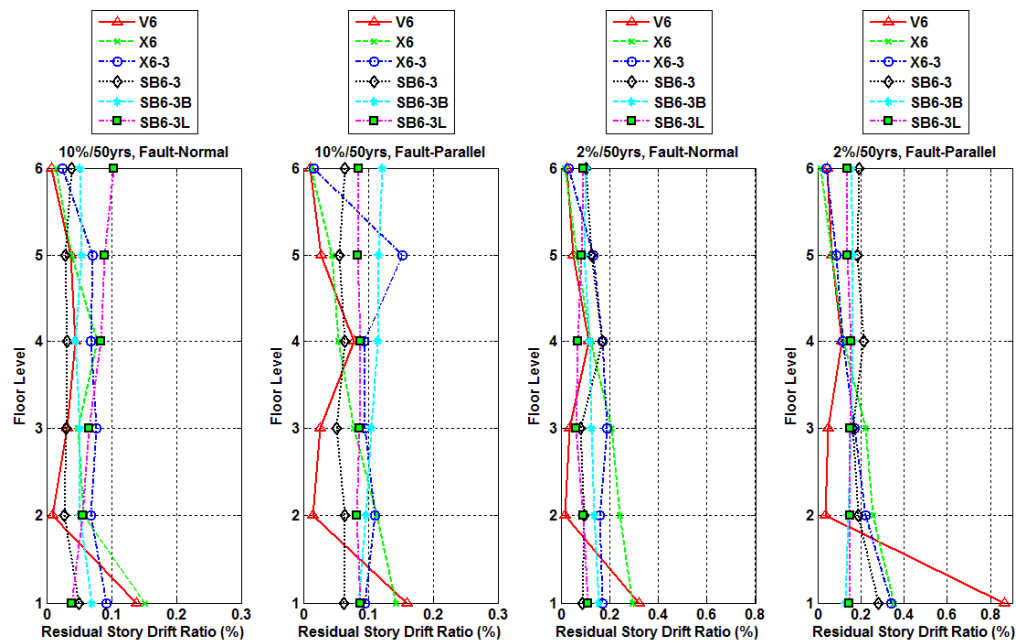


Figure 7.70 Residual story drift ratios for each model after different hazard level ground excitations (without leaning columns).

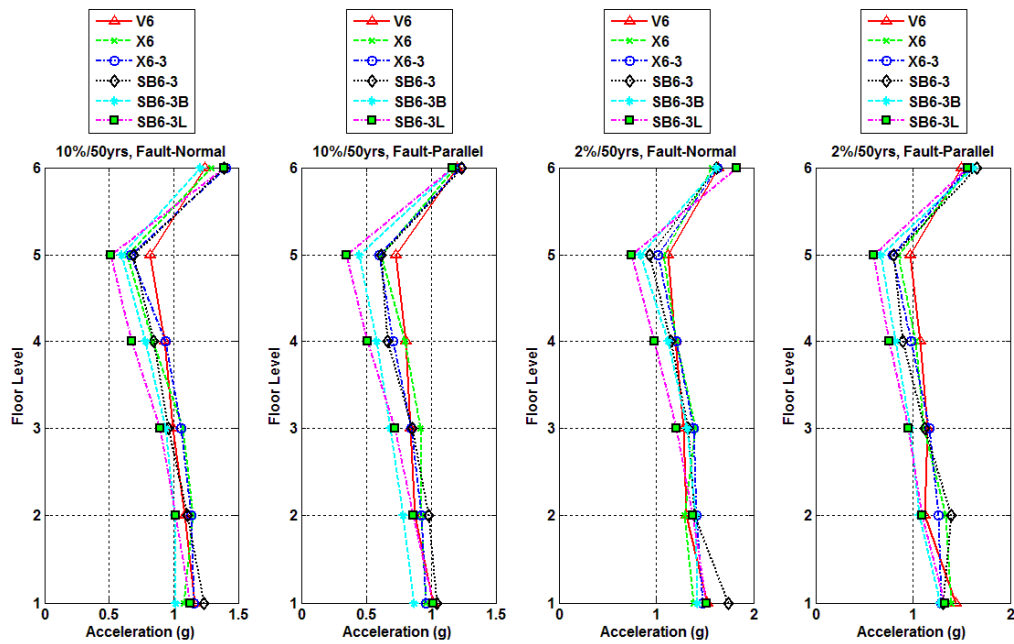


Figure 7.71 Maximum floor level accelerations for each model under different hazard level ground motions (without leaning columns).

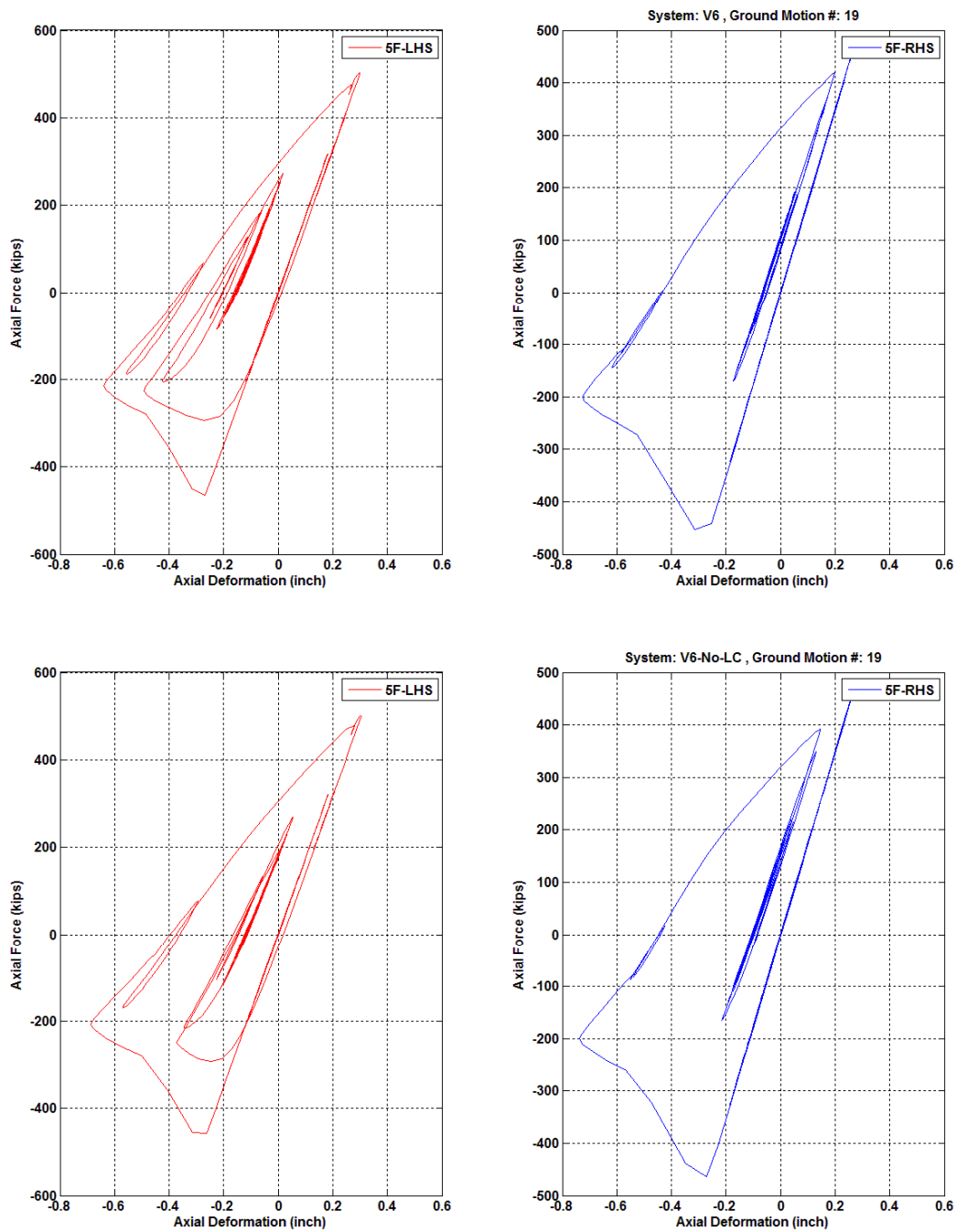


Figure 7.72 Fifty-story brace axial force versus axial deformation relationships of Model V6 under NGA 1602 fault-parallel component ground motion (top: with leaning columns; bottom without leaning columns).

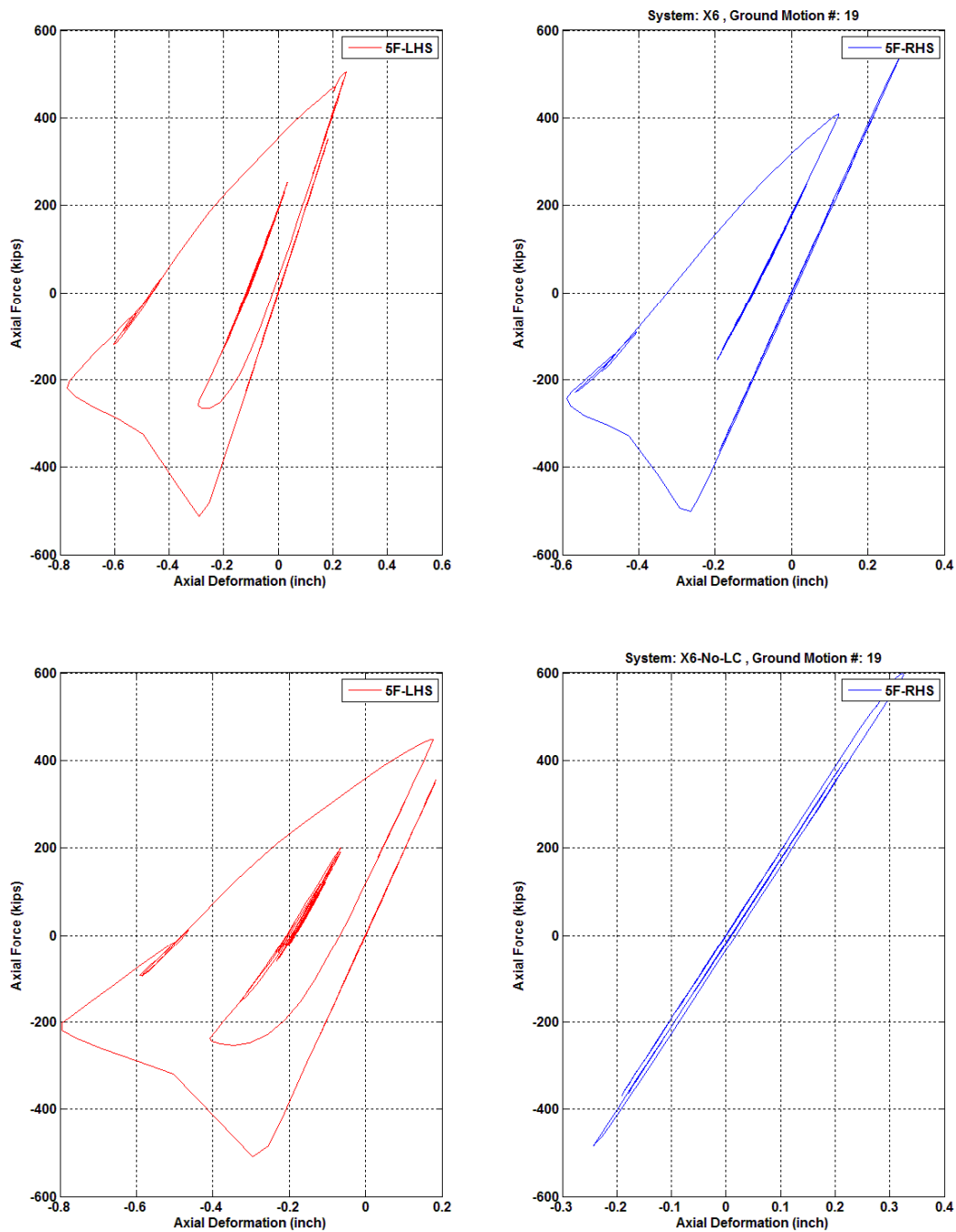


Figure 7.73 Fifty-story brace axial force versus axial deformation relationships of Model X6 under NGA 1602 fault-parallel component ground motion (top: with leaning columns; bottom without leaning columns).

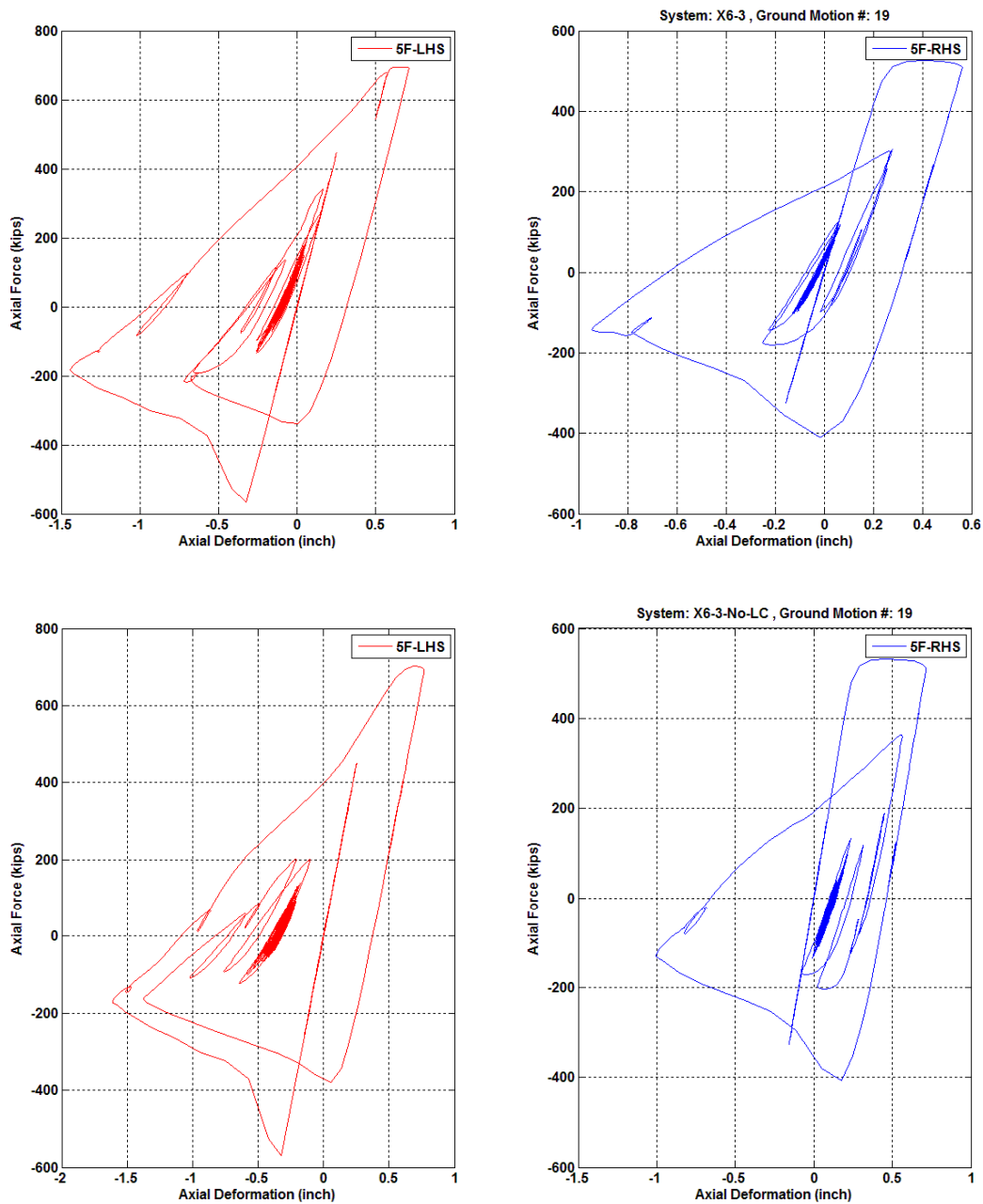


Figure 7.74 Fifty-story brace axial force versus axial deformation relationships of Model X6-3 under NGA 1602 fault-parallel component ground motion (top: with leaning columns; bottom without leaning columns).

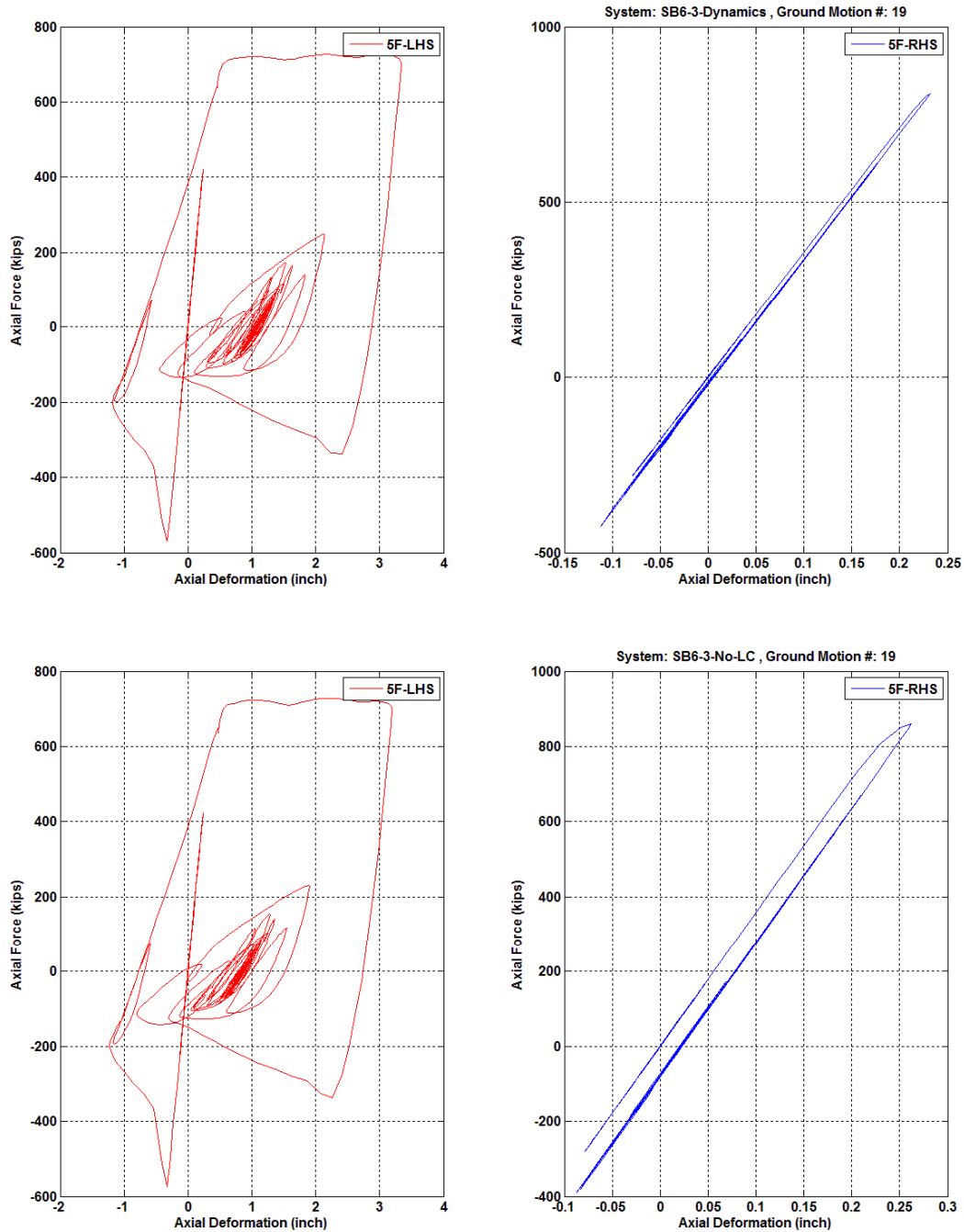


Figure 7.75 Fifty-story brace axial force versus axial deformation relationships of Model SB6-3 under NGA 1602 fault-parallel component ground motion (top: with leaning columns; bottom without leaning columns).

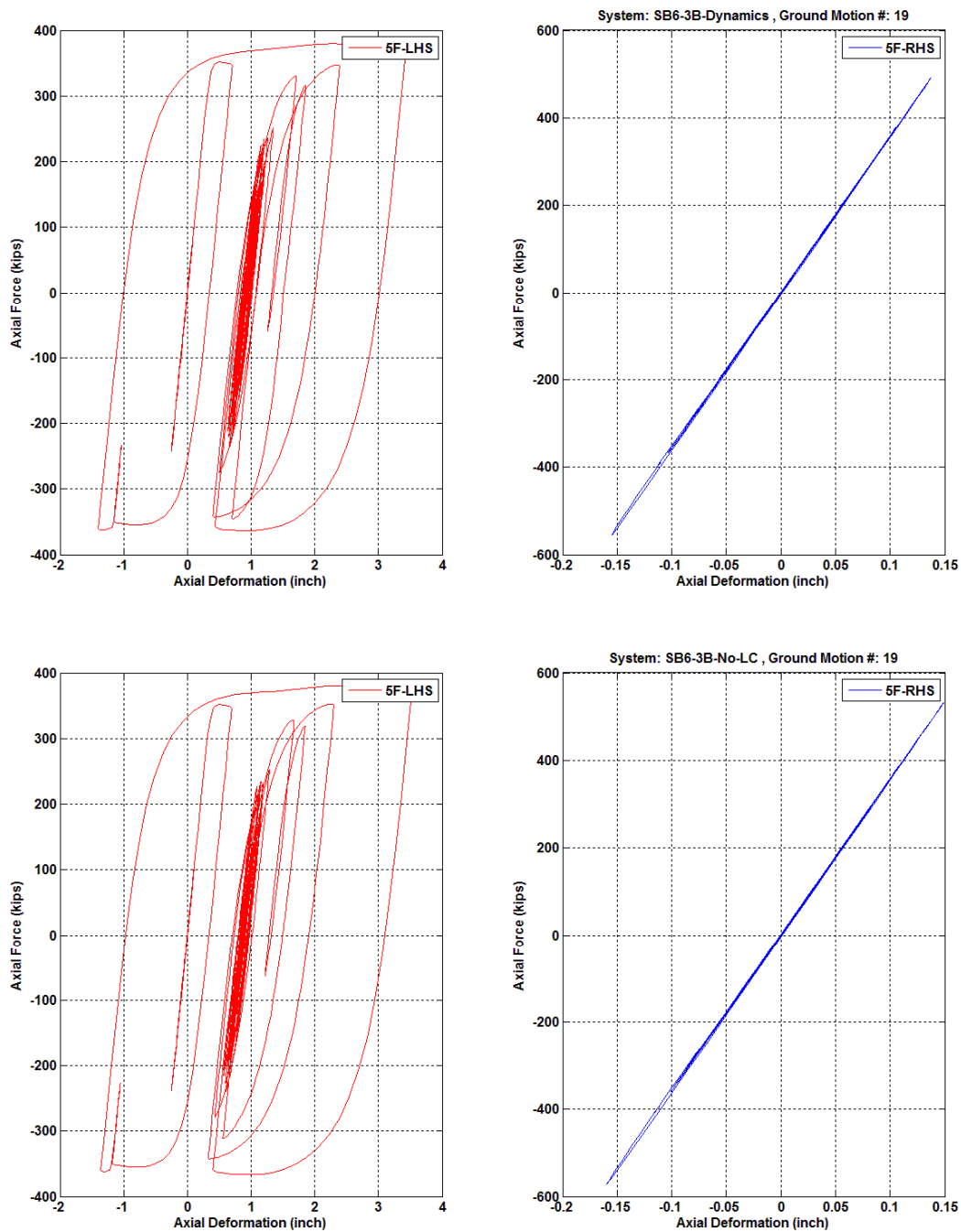


Figure 7.76 Fifty-story brace axial force versus axial deformation relationships of Model SB6-3B under NGA 1602 fault-parallel component ground motion (top: with leaning columns; bottom without leaning columns).

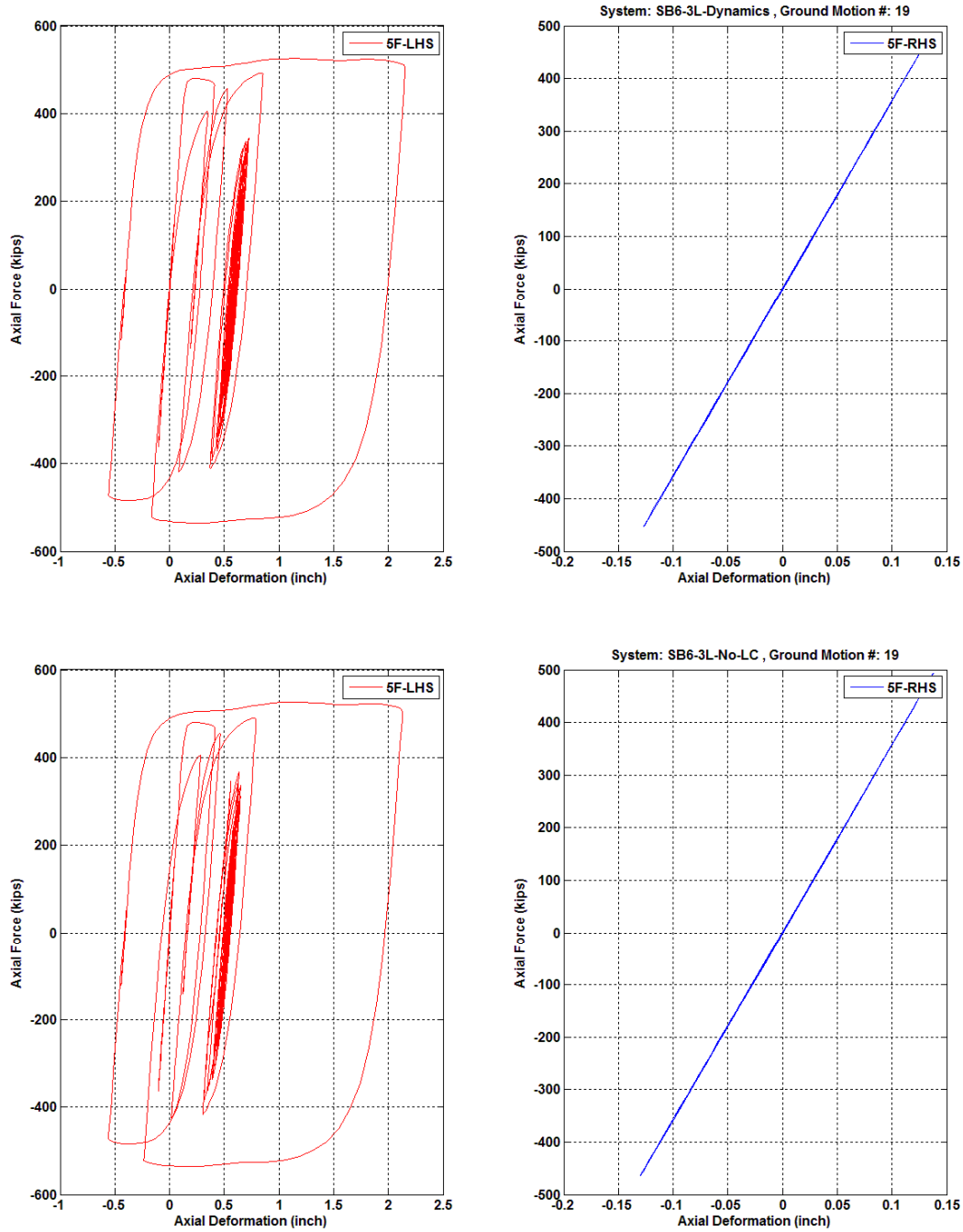


Figure 7.77 Fifty-story brace axial force versus axial deformation relationships of Model SB6-3L under NGA 1602 fault-parallel component ground motion (top: with leaning columns; bottom without leaning columns).

7.9 CONCLUDING REMARKS

Based on the static pushover analysis and nonlinear dynamic response history analysis results, the following conclusions can be drawn:

1. The proposed hybrid strong-back system effectively prevented the soft-story mechanism in the braced frame system.
2. The simplified design strategy that proportioned vertical spine member sizes in the hybrid strong-back system appeared to achieve a key performance goal: uniform story deformation. Design optimization of this simple strategy should be studied further.
3. Compared with the conventional inverted-V braced frame (chevron configuration, V6), the strong-back systems (Models SB6-3 and SB6-3B) not only performed better under selected ground motions but also cost about 13% to 18% less. For the strong-back system using low-yield steel BRBs (SB6-3L), the cost is about 4% more compared with the conventional inverted-V braced frame.
4. The effect of gravity columns on the dynamic responses was obvious in the non-strong-back systems, while there were no significant effects found on the dynamic responses in the strong-back systems.
5. Although using high-performance braces such as BRBs in the strong-back system can further improve the deformation capacity of the entire system, larger residual deformations are expected to occur in such hybrid braced frame systems. Using the devices with self-centering mechanism can further reduce the residual deformation.
6. The current analytical study demonstrated that the shape-tailing concept used in the strong-back system tended to impose higher deformation demands at higher floor levels, especially at the roof floor level. This type of fling effect needs further investigation.

8 Conclusions and Recommendations

This study focused on determining through experimental and analytical means a better understanding of the seismic behavior of concentrically steel braced frame systems, and using that understanding to improve response. A literature review was initially carried out to identify gaps in knowledge and trends in research so that specific high priority experimental and analytical research objectives would be addressed. Relatively few studies of complete concentric braced frame systems had been completed at the beginning of this research, so priority was placed on obtaining experimental data on the behavior of complete large-scale braced frame systems. A total of four full-scale, one-bay, two-story concentrically steel braced frame specimens were tested using both quasi-static and hybrid simulation techniques. These frames a number of details intended to facilitate construction and improve seismic performance. Three different bracing member sectional shapes were considered to be able to relate the behavior of individual braces to system behavior. To examine the sensitivity of observed behavior on test method and loading history, a standard quasi-statically applied test protocol was used as well as a more realistic hybrid test that simulated the response of the frame to an actual earthquake. Various changes in the specimen designs were made during the test program to take advantage of knowledge learned in earlier tests.

Analytical models of the test specimens were developed using line elements with fiber-based section representations (in OpenSees) and using shell elements (in LS-DYNA). In both cases, modeling of the rupture of braces and other key elements was evaluated using available low-cycle fatigue damage models incorporated into the software. The relative benefits and deficiencies of these modeling approaches were identified. The validated numerical modeling approach developed for OpenSees was then used to examine the performance of “vertical truss masted” or “strong-back” braced frame systems with different configurations, and to compare computed responses with those for more the conventional braced frames.

Each chapter presents conclusions and discussions with regard to that phase of this study. The following sections summarize the overall conclusions with some recommendations for future research.

8.1 EXPERIMENTAL PHASE

General behavior of braces

The braces buckles as expected in all specimens, and at relatively low levels of story drift compared to first yielding of moment resisting frames. The tapered gusset plates with $2t_g$ inelastic yield lines performed well in all of the tests. The brace out-of-plane displacement could be as large as ten times the axial displacement under compression. This indicates that significant damage of nearby nonstructural components could occur. Brace inelastic deformations tended to concentrate at the middle length of the braces. Local buckling of section occurred at these locations and braces tended to rupture due to low-cycle fatigue in the region where local buckles occur around 1.9% inter-story drift. The remaining braces and frame are called upon to resist subsequent loading.

Effect of brace cross-sectional shape

From the three experiments having the same quasi-static cyclic loading protocol, it is clear that braced frames using round hollow structural sections as bracing members (i.e., specimen TCBF-B-2) exhibited greater lateral deformation capacity before the onset of significant strength deterioration than specimens using square hollow structural sections (TCBF-B-1) or wide flange sections (TCBF-B-3) for the braces. However, among these three specimens, the peak base shear forces degraded more slowly in Specimen TCBF-B-3 with wide flange braces. Local buckling of the bracing members and large loss of specimen lateral capacity occurred later in Specimen TCBF-B-2. Typically, available round hollow structural sections in the current design manual have width-to-thickness ratios (D/t) that are far below the code limit, whereas square and wide flange members used are often at or near the corresponding code limits. Consequently, round hollow structural sections as brace components will usually be more resistant to local buckling than these other sections, thereby improving the performance of the system. This is consistent with component test results seen in previous studies by others.

Adequacy of reinforcement provided at the net reduced areas regions of brace to gusset plate connections

Reinforcing details at the brace-to-gusset plate connections for each specimen performed well during both quasi-static and pseudo-dynamic tests. The details provided satisfy current AISC Seismic Provisions.

Formation of weak or soft stories

Once buckling initiated, the story drifts at each story in Specimens TCBF-B-2 and TCBF-B-3 tended to be more uniform than in Specimen TCBF-B-1. This may be a result of the more severe deterioration of the hysteretic characteristics of square HSS sections (based on the observations). The three quasi-statically tested specimens were subjected to the same loading protocol where identical roof displacements were imposed and the forces applied to the lower floor were half of the force applied at the roof. For the case where hybrid simulation was used, damage was more uniformly distributed over the height of the structure. Thus, the effects of higher modes, and other characteristics of the response (local deterioration), that would change the distribution of

dynamic loads over the height may be important (and potentially beneficial) effects to consider in future tests.

Frame action

The brace and gusset plate configuration at the lower floor resulted in large, stiff “haunches” at the ends of the beam. During lateral deformation of the frame, the gusset plate geometry tends to amplify the rotational demand at both ends of lower beam-to-gusset splices. This is similar to the rotational amplification (due to geometry) in the link beam of an eccentrically brace frame system. For Specimens TCBF-B-3 and TCBF-B-4, pinned beam-to-gusset details were used to avoid local damage such as flange or web buckling and fracture at these regions. From the observations during these two tests, the pinned connection details effectively avoided any undesired failure mode at beam-to-gusset plate connection regions. However, the entire braced frame lateral capacity was reduced as a result of the moment release at lower beam end connections.

Effectiveness of one-piece gusset plates

No adverse effects were detected with use of one-piece gusset plates rather than two separate gusset plates, one located above and another below a beam where two braces intersect at a column. As noted above, and in other research [Uriz and Mahin 2008], yielding of the beam at the end of the gusset plate can fracture due to stress concentrations in the beam at the end of the gusset plates. These details are complicated especially where the one-piece gusset plate and its stiffeners are welded to the beam to mimic a continuous beam that extends all of the way to the column. The weld access holes and other details at this location may have exacerbated, but not caused the fractures identified in Specimens TCBF-B-1 and TCBF-B-2. The pinned connection used in Specimens TCBF-B-3 and TCBF-B-4 performed as intended. It is not clear that the single-piece gusset plates improve constructability or reduce construction costs.

Effects of brace lateral buckling on frame behavior

Local eccentricities at the both ends of each bracing member measured after the fabrication were not always consistent with the actual direction of out-of-plane buckling; other source of eccentricities at gusset plate-to-beam and gusset plate-to-column interfaces can also affect the buckling direction. For example, two braces connecting to the same one-piece gusset plate tended to buckle in the same out-of-plane direction. Without the floor slab acting as a restraint, the column that is adjacent to the single-piece gusset plate may be subject to torsion due to the eccentricities of the buckled braces. Further investigation seems warranted on evaluating the demand of the bi-axial bending or torsion in the column induced by out-of-plane buckling of the braces, and how much this affects the behavior of column when severe buckling occurred in the braced frame.

Concern for column base plate behavior

In all of the tests, significant fractures initiated in the complete joint penetration welds at the column bases or near the ends of stiffeners provided at this location. Because of the diamond shape configuration of the braces in the specimens tested, gusset plates were not present at the

base of the columns. Thus, these connections resemble situations where thick base plates are provided at the base of columns in moment-resisting frames. This suggests the need for further research on the cyclic inelastic behavior of column bases where high variations of axial load are expected.

Effect of loading protocol

As noted previously, the quasi-static tests tended to form weak or soft stories to varying degrees. For the hybrid simulation, damage at the end of the two earthquake records imposed was more equally distributed between the two stories. During the hybrid simulation one brace fractured near the end of design-level ground motion. The fractured brace was located in the second story not in the ground story, as was expected based on the quasi-static tests. Story deformation concentration was observed in the second story, especially after the second-story brace began localized buckling locally during the hybrid test. This deformation concentration was easily identified, especially when entire hybrid test specimen moved toward the negative direction (to the west side of the lab). No significant residual roof level displacements were found after the 20 sec. at the design-level ground motion.

Since only one ground motion record was used during the simulation, the braced frame responses may change as input ground motion changes. It was also noted in subsequent analysis that the behavior of the braced frame depends on the earthquake histories used. In particular, the hybrid simulation indicated that the specimen would not be able to withstand a design level event followed by a larger MCE level aftershock, but it could withstand the MCE level event had the earlier event not occurred. Thus, this result suggests that behavior is sensitive to the characteristics, intensity, and duration of main shocks and aftershocks. Further investigation on the effect of ground motions upon the seismic responses of braced frame systems is suggested before more solid conclusions can be made. The interested reader is referred to Chen and Mahin [2010].

Lateral force distribution during the hybrid testing demonstrated that the distribution varied with time, but most of the time the shape was close to an inverted triangle. This observation supports the force distribution assumption used in quasi-static tests.

Recommendations for future experiments

The experimental results of four braced framed specimens described in this report focused on a specific bracing configuration, several common braces with different cross-section shapes and typical details in the field. A specific set of geometric parameters were used in the specimen in response to the limitations of the test set up, laboratory space, the laboratory facility, and research funding. A more comprehensive test program covering a wide spectrum of the brace sections—particularly those commonly used in the field—is needed.

8.2 ANALYTICAL PHASE

Adequacy of fiber-based models

The fiber based section models used in conjunction with line elements in OpenSees were able in this study to capture the overall behavior of the braced frame specimens. It was found that due to the early deterioration and fracture of the braces and other elements modeling of the degradation and rupture of elements due to low-cycle fatigue is essential. With the low-cycle fatigue model enabled in OpenSees, the cyclic degradation of bracing and frame members was possible to track approximately. Fatigue material parameters used in OpenSees for three different brace section shapes were slightly different, based on calibration of the numerical model with the actual test results. Although the global behaviors of the braced frame specimens matched the fiber model results within an acceptable range, the match of behaviors of individual brace were not as accurate. As noted previously, the fiber model used in OpenSees cannot simulate local buckling in braces or other elements.

Based on the calibrated fiber models, a parametric analysis was carried out on braces with square hollow structural sections. These braces had different dimensions and lengths and were subjected to the same normalized cyclic deformations (Section 6.4). The group mean of normalized energy dissipation is highly related to the member slenderness ratios and is also affected by the width-to-thickness ratios of the braces. It is noteworthy that the width-to-thickness ratio of the braces has only minor effect on the simulated brace energy dissipation capacity. This is because fiber models as implemented in OpenSees models do not simulate local buckling effects. Because of the limitations of fiber models, more complete data from full-scale experiments or from sophisticated finite element analyses are required before the successful modeling of localized buckling of braces and the propagation of cracks can occur.

Adequacy of shell based models

Finite element models using the shell elements implemented in LS-DYNA were able to simulate yielding, lateral buckling and local buckling as well as deterioration of individual shell elements due to low-cycle fatigue. As a result, they were able to predict braced frame global behavior and member response with higher fidelity than the fiber based models. Existing mechanics-based damage material models with element erosion were able to simulate initiation and propagation of section rupturing due to low-cycle fatigue. Adaptive meshing technique used in the finite element model provides an efficient way to refine the mesh layout only at the regions where the deformations were relatively larger. Input parameters used in LS-DYNA model were also calibrated from the available test data. Additional material testing is suggested to develop a database of material and low-cycle fatigue input parameters for the steel material types that are commonly used in braced frame systems.

Relative advantages of fiber and shell element modeling approaches

Compared to the fiber based elements in OpenSees, the shell element models implemented in LS-DYNA require significantly more execution time. For larger and more complicated structures, it is impractical to run an analysis in LS-DYNA. Thus, a multistep approach may be

needed where refined models of members and/or connections are based on realistic shell elements, and these results are used to calibrate more efficient and simpler fiber based models in programs like OpenSees. Alternatively, different levels of refinement may be used in programs like LS-DYNA, where critical regions are identified and these are modeled in a refined manner, but other regions are modeled using simpler elements.

Improving the behavior of concentric braced frames

As noted previously, concentric braced frames constructed using conventional or buckling restrained braces tend to concentrate damage in one or a few stories. The proposed hybrid vertical elastic truss or strong-back braced frame system was suggested as a method for avoiding weak story behavior. A simplified design method was proposed. This was applied on systems utilizing conventional as well as buckling restrained braces. These systems were quite effective in mitigating the formation of a weak story mechanism. Monotonic and cyclic inelastic analyses demonstrated the benefits of the strong-back system. These systems out perform traditional braced frame systems in terms of system deformation capacity, shape of hysteresis loops, energy dissipation, and story drift distributions. The strong-back systems studied here typically had higher base shear capacities than conventional braced frames since all of the braces over the height of the structure contributed to the lateral load resistance. For, the strong-back system that used conventional buckling restrained braces (SB6-3B) the strength was not as high as some systems with conventional braces because of the overstrength in tension associated with conventional braces. The strong back system with low yield strength steel buckling restrained braces was found to have lower drifts than a similar system with normal strength bracing, since its flexibility and period decreased and its design strength increased accordingly due the larger area of steel provided in the braces.

Dynamic analysis results show that the peak base shear forces were inversely proportional to the fundamental periods of the six models studied: the lower the fundamental period, the higher the peak shear force. Compared with the conventional chevron brace configuration design (i.e., Model V6), the peak story drifts were greater in the strong-back systems, but the story drift distributions were more uniform in the strong-back systems. The tendency for the story drift in the strong-back frames to increase substantially in the upper few stories was noted. Such behavior needs further investigation. Peak floor accelerations at the roof level for all six models were typically higher than the floor levels below roof. Although using high-performance braces such as buckling-restrained braces in the strong-back system can improve the deformation capacity of the entire system, larger residual deformations were predicted for this case. The use of devices with self-centering mechanism may be a topic for future study.

The simplified design strategy for proportioning vertical spine member sizes in the hybrid strong-back system appeared to achieve the performance goal: nearly uniform story deformation. No soft-story mechanisms (neither single- nor multi- story mechanisms) were found in the strong-back systems. The optimization of design strategy needs to be further studied to improve the system performance.

8.3 RECOMMENDATIONS FOR FUTURE RESEARCH

As noted, there were some issues found during this study and many other related topics were not covered here that still need to be further studied including:

1. The cyclic behavior of the column bases using current design details and weld procedures.
2. The demand of the bi-axial bending and torsion in the braced frame columns due to the out-of-plane buckling of the braces.
3. A brace component test program covering a wider range of sizes and shapes especially those commonly used in the field. Standard loading protocol also needs to be developed for the test program.
4. The effect of ground motion characteristics on the response of conventional braced frame systems and also the strong-back systems.
5. A material testing program to develop a database of material and low-cycle fatigue input parameters for the steel materials that are commonly used in the braced frame systems.
6. The use of self-centering devices in the strong-back systems to minimize the residual deformations after earthquake.
7. Optimization of the design strategy for the strong-back system.
8. Quantification of the seismic performance factors (SPFs) of the strong-back systems using the FEMA P-695 (ATC-63) methodology [FEMA 2009].

REFERENCES

- AIJ (1995). *Reconnaissance Report on Damage to Steel Building Structures Observed from the 1995 Hyogoken-Nanbu (Hanshin/Awaji) Earthquake*, Architectural Institute of Japan, Steel Committee of Kinki Branch, Japan.
- Aiken I.D, Nims D.K., Kelly J.M. (1992). Comparative study of four passive energy dissipation systems, *Bull. New Zealand Nat. Soc. Earthq. Eng.*, 25 (3): 175–192.
- AISC (1978). *Specification for the Design, Fabrication and Erection of Structural Steel for Buildings*, American Institute of Steel Construction, Inc. Chicago, IL.
- AISC (1992). *Seismic Provisions for Structural Steel Buildings*, American Institute of Steel Construction, Inc. Chicago, IL.
- AISC (1997). *Seismic Provisions for Structural Steel Buildings*, American Institute of Steel Construction, Inc. Chicago, IL.
- AISC (2001). *Manual of Steel Construction: Load and Resistance Factor Design*, 3rd ed., American Institute of Steel Construction, Inc. Chicago, IL.
- AISC (2002). *Seismic Provisions for Structural Steel Buildings, AISC 341-02*, American Institutes of Steel Construction, Inc. Chicago, IL.
- AISC (2005a). *Steel Construction Manual*, 13th ed., American Institute of Steel Construction, Inc. Chicago, IL.
- AISC (2005b). *Seismic Provisions for Structural Steel Buildings, AISC 341-05*, American Institute of Steel Construction, Inc. Chicago, IL.
- AISC (2010a). *Seismic Provisions for Structural Steel Buildings, AISC 341-10*, American Institute of Steel Construction, Inc. Chicago, IL.
- AISC (2010b). *Specifications for Structural Steel Buildings, AISC 360-10*, American Institute of Steel Construction, Inc. Chicago, IL.
- Aktan A.E., Bertero V.V. (1981). The seismic resistant design of R/C coupled structural walls, *Rept. No. UCB/EERC-81/07*, Earthquake Engineering Research Center, University of California, Berkeley, CA.
- ASCE (2005). *Minimum Design Loads for Buildings and Other Structures, ASCE 7-05*, American Society of Civil Engineers, Reston, VA.
- Astaneh-Asl A. (1982). Cyclic behavior of double angle bracing members with end gusset plates, Ph.D. Dissertation, Department of Civil Engineering, University of Michigan, Ann Arbor, MI.
- Astaneh-Asl A. (1989). Simple methods for design of gusset plates, *Proceedings, ASCE Structures Congress*, pp. 345–354, San Francisco, CA.
- Astaneh-Asl A. (1998). Seismic behavior and design of gusset plates, in: *Steel Tips*, Structural Steel Education Council, Moraga, CA.
- Astaneh-Asl A., Goel S.C., Hanson R.D. (1981). Behavior of steel diagonal bracing, *Proceedings, ASCE Conference*, St. Louis, MO.
- Astaneh-Asl A., Goel S.C., Hanson R.D. (1985). Cyclic out-of-plane buckling of double-angle bracing, *J. Struct. Eng.*, 111(5): 1135–1153.
- Astaneh-Asl A., Goel S.C., Hanson R.D. (1986). Earthquake-resistant design of double angle bracing, *AISC Eng. J.*, 23(4): 133–147, Chicago, IL.
- Ballio G., Perotti, F. (1987). Cyclic behavior of axially loaded members: numerical simulation and experimental verification, *J. Constructional Steel Res.*, 7: 3–41.
- Becker R. (1995). Seismic design of special concentrically braced steel frames, in: *Steel Tips*, Structural Steel Education Council, Moraga, CA.

- Bertero V.V., Uang C.-M., Llopiz C.R., Igarashi K. (1989). Earthquake simulator testing of concentric braced dual system, *ASCE J. Struct. Eng.*, 115(8): 1877–1894.
- Birkemoe P.C. (1966). *Distribution of Stress and Partition of Loads in Gusseted Connections*, PhD Dissertation, Department of Civil Engineering, University of Illinois at Urbana-Champaign, Urbana, IL.
- Black R.G., Wenger W.A., Popov E.P. (1980). Inelastic buckling of steel struts under cyclic load reversals, *Rept. No. UCB/EERC-80/40*, University of California, Berkeley, CA.
- Bonneville D., Bartoletti S. (1996). *Case Study 2.3: Concentric Braced Frame, Lankershim Boulevard, North Hollywood*, 1994 Northridge Earthquake Building Case Studies Project, Proposition 122: Product 3.2, SSC 94-06, Seismic Safety Commission, State of California, Sacramento, CA.
- Brown V.L.S (1988). *Stability of Gusseted Connections in Steel Structures*, PhD Dissertation, Department of Civil and Environmental Engineering, University of Delaware, Newark, DE.
- Chambers J.J., Ernst C.J. (2005). *Brace Frame Gusset Plate Research - Phase I Literature Review, Volumes 1 and 2*, Department of Civil Engineering, University of Utah, Salt Lake City, UT.
- Chambers J.J., Bartley T.C. (2007). Geometric formulas for gusset plate design, *AISC Eng. J.*, 44(3): 255–267.
- Chen C.C., Chen S.Y., Liaw J.J. (2001). Application of low yield strength steel on controlled plasticification ductile concentrically braced frames, *Canadian J. Civil Eng.*, 28(5): 823–836.
- Chen C.H., Mahin S.A. (2010). Seismic collapse performance of concentrically steel braced frames, *Proceedings, National Steel Construction Conference*, American Institute of Steel Construction, Inc., pp. 1265–1274, Orlando, FL.
- Cheng J.J.R., Kulak G.L., Khoo H.A. (1998). Strength of slotted tubular tension members, *Canadian J. Civil Eng.*, 25(6): 982–991.
- Christopoulos C., Tremblay R., Kim H.J., Lacerte M. (2008). Self-centering energy dissipative bracing system for the seismic resistance of structures: development and validation, *J. Struct. Eng.*, 134(1): 96–107.
- Clark K., Powell P., Lehman D., Roeder C., Tsai, K.C. (2008). Experimental performance of multi-story X-braced frame systems, *Proceedings, SEAOC 77th Annual Convention*, Big Island, Hawaii.
- Cochran M.L. (2000). *Design and Detailing of Steel SCBF Connections*, Structural Engineers Association of California SEAOC Seminar Series, Sacramento, CA.
- Cochran M.L. (2003). Seismic design and steel connection detailing, *Proceedings, North American Structural Steel Construction Conference*, Baltimore, MD.
- Computers and Structures, Inc. (2009). *SAP2000, Integrated Software for Structural Analysis and Design*, Version 14.0, Berkeley, CA.
- DASSE (2009). *Cost Advantages of Buckling Restrained Braced Frame Buildings*, DASSE Design Inc., San Francisco, CA.
- Daugherty D., Hanley, J., Rodgers G.P. (2011). *Real-Time Data Viewer 2.2.3*, <http://nees.org/resources/rdv>.
- Ding X., Foutch D., Han S.-W. (2008). Fracture modeling of rectangular hollow section steel braces, *AISC Eng. J.*, 3: 171–186.
- Dowswell B. (2006). Effective length factors for gusset plate buckling, *AISC Eng. J.*, 2: 91–101.
- EERI (1978). *Reconnaissance Report Miyagi-Ken-Oki, Japan Earthquake, June 12, 1978*, Earthquake Engineering Research Institute, Berkeley, CA.
- EERI (1998). *Reducing Earthquake Damage through Quality Construction (CD-ROM)*, Earthquake Engineering Research Institute, Oakland, CA.
- Fell B.V. (2008). *Large-Scale Testing and Simulation of Earthquake-Induced Ultra Low Cycle Fatigue in Bracing Members Subjected to Cyclic Inelastic Buckling*, PhD Dissertation, Department of Civil Engineering, University of California, Davis, CA.
- Fell B.V., Kanvinde A.M. (2010). Tensile forces for seismic design of braced frame connections – experimental results, *J. Constructional Steel Res.*, 66(4): 496–503.

- FEMA (2007). *Interim Testing Protocols for Determining the Seismic Performance Characteristics of Structural and Nonstructural Components*, FEMA 461, Federal Emergency Management Agency, Washington, D.C.
- FEMA (2009). *Quantification of Building Seismic Performance Factors*, FEMA P-695, Federal Emergency Management Agency, Washington, D.C.
- Field C. (2003). Simulation of full-scale seismic-resistant structural frame tests using LS-DYNA 960 implicit solver, *Proceedings, 4th European LS-DYNA Users Conference*, Ulm, Germany.
- Foutch D.A., Goel S.C., Roeder C.W. (1986). *Preliminary Report on Seismic Testing of a Full-Scale Six-Story Steel Building*, University of Illinois at Urbana-Champaign, Urbana, IL.
- Foutch D.A., Goel S.C., Roeder C.W. (1987). Seismic testing on full-scale steel building-part I, ASCE, *J. Struct. Eng.*, 113(11): 2111–2129.
- Fujimoto M., Aoyagi T., Ukai K., Wada A., Saito K. (1972). Structural characteristics of eccentric k-braced frames, *Trans. Arch. Institute Japan*, 195: 39–49.
- Fujimoto M., Hashimoto A., Nakagomi T., Yamada T. (1985). Study on fracture of welded connections in steel structures under cyclic loads based on nonlinear fracture mechanics, *J. Struct. Construct. Eng., Trans. Arch. Institute Japan*, 365: 93–102.
- Fukuta T., Nishiyama I., Yamanouchi H., Kato B. (1989). Seismic performance of steel frames with inverted v braces, ASCE, *J. Struct. Eng.*, 115(8): 2016–2028.
- Ghanaat Y. (1980). Study of X-braced steel frame structures under earthquake simulation, *Rept. No. UCB/EERC-80/08*, Earthquake Engineering Research Center, University of California, Berkeley, CA.
- Ghanaat Y., Clough R.W. (1982). Shaking table tests of a tubular steel frame model, *Rept. No. UCB/EERC-82/02*, Earthquake Engineering Research Center, University of California, Berkeley, CA.
- Goel S.C., Liu Z. (1987). Cyclic behavior of concrete-filled tubes, *Proceedings, ASCE Structures Congress*, pp.427–440, New York, NY.
- Gugerli H., Goel S.C. (1982). Inelastic cyclic behavior of steel bracing members, *UMEE 82R1 Report*, Department of Civil Engineering, University of Michigan, Ann Arbor, MI.
- Hallquist J.O. (1990). *LS-DYNA User's Manual (Nonlinear Dynamic Analysis of Solids in Three Dimensions)*, Report 1007, Livermore Software Technology Corporation, Livermore, CA.
- Han S-W., Kim W.T., Foutch D.A. (2007). Seismic behavior of HSS bracing members according to width-thickness ratio under symmetric cyclic loading, ASCE *J. Struct. Eng.*, 133(2): 264–273.
- Harris H.G., Sabins G.M. (1999). *Structural Modeling and Experimental Techniques*, 2nd ed., CRC Press,
- Higginbotham A.B. (1973). *The Inelastic Cyclic Behavior of Axially-Loaded Steel Members*, PhD Dissertation, Department of Civil Engineering, University of Michigan, Ann Arbor, MI.
- Huang Y., Mahin S.A. (2007). *Simulating the Behavior of Steel Members Subjected to Deterioration*, Kajima-CUREE Joint Research Program Report, University of California, Berkeley, CA.
- Huang Y., Mahin S.A. (2010). Simulating the inelastic seismic behavior of steel braced frames including the effects of low-cycle fatigue, *PEER Report 2010/104*, Pacific Earthquake Engineering Research Center, University of California, Berkeley, CA.
- Ikeda K., Mahin S.A., Dermitzakis S.N. (1984). Phenomenological modeling of steel braces under cyclic loading, *Rept. No. UCB/EERC-84/09*, Earthquake Engineering Research Center, University of California, Berkeley, CA.
- Ikeda K., Mahin S.A. (1984). A refined physical theory model for predicting the seismic behavior of braced steel frames, *Rept. No. UCB/EERC-84/12*, Earthquake Engineering Research Center, University of California, Berkeley, CA.
- Ikeda K., Mahin S.A. (1986). Cyclic response of steel braces, ASCE *J. Struct. Eng.*, 112(2): 342–361.
- Jain A.K., Goel S.C., Hanson R.D. (1977). Static and dynamic hysteresis behavior of steel tubular members with welded gusset plates, *UMEE 77R3 Report*, Department of Civil Engineering, University of Michigan, Ann Arbor, MI.

- Jain A.K., Goel S.C., Hanson R.D. (1978a). Hysteresis behavior of bracing members and seismic response of braced frames with different proportions, *UMEE 78R3 Report*, Department of Civil Engineering, University of Michigan, Ann Arbor, MI.
- Jain A.K., Goel S.C. (1978b). Hysteresis models for steel members subjected to cyclic buckling or cyclic end moments and buckling, *UMEE 78R6 Report*, Department of Civil Engineering, University of Michigan, Ann Arbor, MI.
- Kahn L.F., Hanson R.D. (1976). Inelastic cycles of axially loaded steel members, ASCE, *J. Struct. Div.*, 102(5): 947–959.
- Kalyanaraman V., Mahadevan K., Thairani V. (1998). Core loaded earthquake resistant bracing system, *J. Construct. Steel Res.*, 46(1–3): 437–439.
- Kalyanaraman V., Ramachandran B., Prasad B.K., Sridhara B.N. (2003). Analytical study of ‘sleeved column’ buckling restrained braced system, *Proceedings, SEAOC 72nd Annual Convention*, Squaw Creek, CA.
- Kanaan A.E., Powell G.H. (1973). General purpose computer program for inelastic dynamic response of plane structures, *Rept. No. UCB/EERC-73/6*, Earthquake Engineering Research Center, University of California, Berkeley, CA.
- Kato B., Tanaka A., Yamanouchi H. (1980). A field work investigation of steel building damages due to the 1978 Miyagiken-Oki earthquake, *Proceedings, 7th World Conference on Earthquake Engineering*, Istanbul, Turkey.
- Kelly D.J., Bonneville D., Bartoletti S. (2000). 1994 Northridge earthquake: damage to a four-story steel braced frame building and its subsequent upgrade, *Proceedings, 12th World Conference on Earthquake Engineering*, Auckland, New Zealand.
- Khatib I.F., Mahin S.A., Pister, K.S. (1988). Seismic behavior of concentrically braced frames, *Rept. No. UCB/EERC-88/01*, Earthquake Engineering Research Center, University of California, Berkeley, CA.
- Kiggins S., Uang C.M. (2006). Reducing residual drift of buckling-restrained braced frames as a dual system, *Eng. Struct.*, 28: 1525–1532.
- Korol R.M. (1996). Shear lag in slotted HSS tension members, *Canadian J. Civil Eng.*, 23(6): 1350–1354.
- LSTC (2007). *LS-DYNA Keyword User's Manual*, Livermore Software Technology Corporation, Livermore, CA.
- Lai J.W., Tsai K.C. (2004) Research and application of buckling restrained braces in Taiwan, *Proceedings, ANCER Annual Meeting: Networking of Young Earthquake Engineering Researchers and Professionals*, Honolulu, Hawaii, HI.
- Lai J.W., Tsai K.C., Lin S.L., Hsiao P.C. (2004). Large scale buckling restrained brace research in Taiwan, *Proceedings, 1st Asia Conference on Earthquake Engineering*, Manila, Philippines.
- Lai J.W., Chen C.H., Mahin S.A. (2010). Experimental and analytical performance of concentrically braced steel frames, *Proceedings, National Steel Construction Conference*, American Institute of Steel Construction, Inc. Orlando, FL.
- Lee S., Goel S.C. (1987). Seismic behavior of hollow and concrete-filled square tubular bracing members, *UMCE 87-11 Report*, Department of Civil Engineering, University of Michigan, Ann Arbor, MI.
- Lehman D., Roeder C., Yoo J.H., Johnson S. (2004). Seismic response of braced frame connections, *Proceedings, 13th World Conference on Earthquake Engineering*, Paper No. 1459, Vancouver, B.C., Canada.
- Liu Z., Goel S.C. (1987) Investigation of concrete-filled steel tubes under cyclic bending and buckling, *UMCE 87-3 Report*, Department of Civil Engineering, University of Michigan, Ann Arbor, MI.
- Liu Z., Goel S.C. (1988). Cyclic load behavior of concrete-filled tubular braces, ASCE *J. Struct. Eng.*, 114(7): 1488–1506.
- Lopez W.A., Sabelli R. (2004). Seismic design of buckling-restrained braced frames, in: *Steel Tips*, Structural Steel Education Council. Moraga, CA.

- Lumpkin E., Hsiao P., Roeder C.W., Lehman D.E., Tsai K.C., Lin C.H., Wu A.C., Wei C.Y. (2010). Cyclic response of three-story, full-scale concentrically braced frames, *Proceedings, 9th U.S. National and 10th Canadian Conference on Earthquake Engineering*, Toronto, Canada.
- MacRae G.A., Kimura Y., Roeder C. (2004). Effect of column stiffness on braced frame seismic behavior, *ASCE J. Struct. Eng.*, 130(3) 381–391.
- Mahin S.A., Lai J.W. (2008). *An Innovative Approach to Improving the Seismic Behavior of Steel Concentric Braced Frames*, Proposal for SEAONC Special Projects Initiative.
- Mahin S.A., Shing B.P. (1985). Pseudodynamic method for seismic testing, *ASCE J. Struct. Eng.*, 111(7): 1482–1503.
- Mahin S.A., Uriz P., Aiken I.D., Field C., Ko E. (2004). Seismic performance of buckling restrained braced frame systems, *Proceedings, 13th World Conference on Earthquake Engineering*, Paper No. 1681, Vancouver, B.C., Canada.
- Maison B., Popov E.P. (1980). Cyclic response prediction for braced steel frames, *ASCE J. Struct. Div.*, 106(7): 1401–1416.
- Mangat P.S. (1969). Influence of the slenderness and b/t ratios on the inelastic local buckling of angles, Master of Applied Science Thesis, Department of Civil Engineering, University of Windsor, Ontario, Canada.
- Mar D. (2010). Design examples using mode shaping spines for frame and wall buildings, *Proceedings, 9th U.S. National and 10th Canadian Conference on Earthquake Engineering*, Paper No. 1400, Toronto, Canada.
- Marshall P.W. (1978). Design considerations for offshore structures having nonlinear response to earthquakes, *Proceedings, ASCE Annual Convention and Exposition*, Chicago, IL.
- Martinez-Saucedo G., Packer J.A., Christopoulos C. (2008a). Gusset plate connections to circular hollow section braces under inelastic cyclic loading, *ASCE J. Struct. Eng.*, 134(7): 1252–1258.
- Martinez-Saucedo G., Tremblay R., Packer J.A. (2008b). Seismic response of circular hollow section braces with slotted end connections, *Proceedings, 12th International Symposium on Tubular Structures*, pp. 227–233, Shanghai, China.
- Martini K., Amin N., Lee P., Bonowitz, D. (1990). The potential role of non-linear analysis in the seismic design of building structures, *Proceedings, 4th U.S. National Conference on Earthquake Engineering*, Vol. 2, pp. 67–76, Palm Springs, CA.
- McCormick J., DesRoches R., Fugazza D., Auricchio F. (2007). Seismic assessment of concentrically braced steel frames with shape memory alloy braces, *ASCE J. Struct. Eng.*, 133(6): 862–870.
- McKenna F. (1997). *Object Oriented Finite Element Programming Frameworks for Analysis, Algorithms and Parallel Computing*, PhD Dissertation, Department of Civil and Environmental Engineering, University of California, Berkeley, CA.
- Mercan O. (2007). *Analytical and Experimental Studies on Large-scale, Real-time Pseudodynamic Testing*, Ph.D. Dissertation, Department of Civil and Environmental Engineering, Lehigh University, Bethlehem, PA.
- Midorikawa M., Takeuchi T., Hikino T., Kasai K., Deierlein G., Ohbayashi M., Yamazaki R., Kishiki, S. (2010). “Seismic Performance of Controlled Rocking Frames with Shear Fuse and PT Wire Anchorage- Shaking Table Tests on Controlled Rocking Steel Frames using Multipurpose Inertial Mass System: Part I”, *Journal of Structural and Construction Engineering, Architectural Institute of Japan*, Vol. 75, No. 654, pp.1547–1556 (in Japanese).
- Midorikawa M. (2011). *Seismic and Tsunami Damage on Building Structures Caused by the 2011 Tohoku Japan Earthquake*, IISSE-UNESCO Lecture Notes Archive, <http://iisee.kenken.go.jp>.
- Mitsui Y., Kurobane Y. (1981). Experimental study on tube-to-through-gusset plate joints, *Summaries of Technical Papers of Annual Meeting, Architectural Institute of Japan*, 56: 1829–1830.

- Mitsui Y., Maeda N. (1986). Experimental study on ultimate tensile strength of welded tube-to-through gusset plate joints: examination of methods for repairing and excessive opening at the tip of the gusset plate, *Proceedings, Annual Research Meeting*, Kyushu Chapter, Architectural Institute of Japan, 29: 317–320.
- Muir L.S. (2008). Designing compact gussets with uniform force method, *AISC Eng. J.*, 1: 13–19.
- Naito T. (1926). Damages to the steel frame buildings in Tokyo, *Investigation Report for Earthquake Disaster Prevention Committee*, University of Tokyo, Tokyo, Japan (in Japanese).
- Nast T.E. (1999). *Cyclic Behavior of Stiffened Gusset Plate-Brace Member Assemblies*, Master of Science Thesis, University of Alberta, Canada.
- Nilforoushan R. (1973). Seismic behavior of multi-story k-braced frame structures, *UMEE 73R9 Report*, Department of Civil Engineering, University of Michigan, Ann Arbor, MI.
- Okazaki T., Lignos D.G., Midorikawa M., Ricles J.M., Love J. (2013). Damage to steel buildings observed after the 2011 Tohoku-Oki earthquake, *Earthq. Spectra*, 29(S1): S219–S243.
- Packer J.A. (2006). Tubular brace member connections in braced steel frames, *Proceedings, 11th International Symposium on Tubular Structures*, pp. 3–14, Quebec, Canada.
- Palmer K., Roeder C.W., Okazaki T., Shield, C., Lehman D.E. (2011). Three-dimensional tests of two-story, one-bay by one-bay, steel concentric braced frames, *Proceedings, ASCE Structures Congress*, pp. 3057–3067.
- Phipps M.T., Jirsa J.O., Picado M., Karp R. (1992). Performance of high technology industries in the Loma Prieta earthquake, *Proceedings, 10th World Conference on Earthquake Engineering*, Madrid, Spain.
- Pons H.F. (1997). *Dynamic Behavior of Tubular Bracing Members with Single Plate Concentric Connections*, Master of Applied Science Thesis, University of Toronto, Canada.
- Popov E.P., Takanashi K., Roeder C.W. (1976). Structural steel bracing systems: behavior under cyclic loading, *Rept. No. UCB/EERC-76/17*, Earthquake Engineering Research Center, University of California, Berkeley, CA.
- Powell G.H. (1973). *DRAIN-2D User's Guide*, *Rept. No. UCB/EERC-73/22*, Earthquake Engineering Research Center, University of California, Berkeley, CA.
- Powell J., Clark K., Tsai K-C., Roeder C.W., Lehman D. (2008). Test of a full scale concentrically braced frame with multi-story X-bracing, *Proceedings, ASCE Structures Congress*, Vancouver, B.C., Canada.
- Rabinovitch J.S. (1993). *Cyclic Behavior of Steel Gusset Plate Connections*, Master of Science Thesis, University of Alberta, Canada.
- Roeder C.W., Popov E.P. (1977). Inelastic behavior of eccentrically braced frames under cyclic loading, *Rept. No. UCB/EERC-77/18*, Earthquake Engineering Research Center, University of California, Berkeley, CA.
- Roeder C.W. (1989). Seismic behavior of concentrically braced frame, *ASCE, J. Struct. Eng.*, 115(8): 1837–1856.
- Roeder C.W., Lehman D.E. (2007). SCBF gusset plate connection design, *Proceedings, North American Structural Steel Construction Conference*, pp. 266–282, New Orleans, LA.
- Roeder C.W., Lumpkin E.J., Lehman D.E. (2011a). A balanced design procedure for special concentrically braced frame connections, *J. Construct. Steel Res.*, 67(11): 1760–1772.
- Roeder C.W., Lehman D.E., Clark K., Powell J., Yoo J.H., Tsai K-C., Lin C.H., Wei C.Y. (2011b). Influence of gusset plate connections and braces on the seismic performance of x-braced frames, *Earthq. Eng. Struct. Dyn.*, 40: 355–374.
- Sabelli R., (2001). *Research on Improving the Design and Analysis of Earthquake-Resistant Steel-Braced Frames*, Earthquake Engineering Research Institute, the 2000 NEHRP Professional Fellowship Report, PF2000-9, Oakland, CA.
- Sabelli R., Mahin S.A., Chang, C. (2003). Seismic demands on steel braced frame buildings with buckling restrained braces, *Eng. Struct.*, 25: 655–666.
- Schellenberg A.H., Mahin S.A., Fenves G.L. (2009). Advanced implementation of hybrid simulation, *PEER Report 2009/104*, Pacific Earthquake Engineering Research Center (PEER), University of California, Berkeley, CA.

- SEAOC (1991). *Reflections on the Loma Prieta Earthquake October 17, 1989*, Ad Hoc Earthquake Reconnaissance Committee, Structural Engineers Association of California, Sacramento, CA.
- Shaback J.B. (2001). *Behavior of Square HSS Braces with End Connections under Reversed Cyclic Axial Loading*, Master of Applied Science Thesis, University of Calgary, Canada.
- Shaback J.B., Brown T. (2003). Behavior of square hollow structural steel braces with end connections under reversed cyclic axial loading, *Canadian J. Civil Eng.*, 30(4): 745–753.
- Shibata M., Nakamura T., Yoshida N., Morino S., Nonaka T., Wakabayashi M. (1973). Elastic-plastic behavior of steel braces under repeated axial loading, *Proceedings, 5th World Conference on Earthquake Engineering*, Vol. 1, Paper No. 845, Rome, Italy.
- Singh P. (1977). Seismic behavior of braces and braced steel frames, *UMEE 77R1 Report*, Department of Civil Engineering, University of Michigan, Ann Arbor, MI.
- Skidmore, Owings & Merrill (1963). *Test Slabs Design Calculations for the University of California Richmond Field Station Structural Research Laboratory*, Skidmore, Owings & Merrill LLP, One Maritime Plaza, San Francisco, CA.
- Skidmore, Owings & Merrill (1964). *Test Slab Details for the University of California Richmond Field Station Structural Research Laboratory*, Drawing Number S7 & S7-SUP-1, Skidmore, Owings & Merrill LLP, One Maritime Plaza, San Francisco, CA.
- Steinbrugge K.V., Schader E.E., Bigglestone H.C., Weers C.A. (1971). *San Fernando Earthquake February 9, 1971, Pacific Fire Rating Bureau*, San Francisco, CA.
- Tanaka A., Morita K., Yamanouchi H. (1980) Damage of braced steel frames due to the 1978 Miyagiken-Oki earthquake, *Proceedings, 7th World Conference on Earthquake Engineering*, Istanbul, Turkey.
- Tanabashi R., Kaneta K., Ishiba T. (1973). On the rigidity and ductility of steel bracing assemblage, *Proceedings, 5th World Conference on Earthquake Engineering*, Rome, Italy.
- Tang X., Goel S.C. (1987). Seismic analysis and design considerations of braced steel structures, *UMCE 87-4 Report*, Department of Civil Engineering, University of Michigan, Ann Arbor, MI.
- Thornton W.A. (1984). Bracing connections for heavy construction, *AISC Eng. J.*, 21(3): 139–148.
- Thornton W.A. (1991). On the analysis and design of bracing connections, *Proceedings, National Steel Construction Conference*, American Institute of Steel Construction, Inc. Chicago, IL.
- Thornton W.A. (1992). Designing for cost efficient fabrication, in: *Steel Tips*, Structural Steel Education Council. Moraga, CA.
- Thornton W.A., Muir L.S. (2009). Design of vertical bracing connections for high-seismic drift, *Modern Steel Construction*, March.
- Tirca L., Tremblay R. (2004). Influence of building height and ground motion type on the seismic behavior of zipper concentrically braced steel frames, *Proceedings, 13th World Conference on Earthquake Engineering*, Paper No. 2894, Vancouver, B.C., Canada.
- Tremblay R. (2002). Inelastic seismic response of steel bracing members, *J. Constructional Steel Res.*, 58, pp. 665–701.
- Tremblay R. (2003). Achieving a stable inelastic seismic response for multi-story concentrically braced steel frames, *AISC Eng. J.*, 2: 111–129.
- Tremblay R., Merzouq S. (2004). Dual buckling restrained braced steel frames for enhanced seismic response, *Proceedings, Passive Control Symposium*, Yokohama, Japan.
- Tremblay R., Haddad M., Martinez G., Richard J., Moffatt K. (2008a). Inelastic cyclic testing of large size steel bracing members, *Proceedings, 14th World Conference on Earthquake Engineering*, Beijing, China.
- Tremblay R., Lacerte M., Christopoulos C. (2008b). Seismic response of multistory buildings with self-centering energy dissipative steel braces, *ASCE J. Struct. Eng.*, 134(1): 108–120.

- Tsai K.C., Hsiao P.C., Wang K.J., Weng Y.T., Lin M.L., Lin K.C., Chen C.H., Lai J.W., Lin S.L. (2008). Pseudo-dynamic tests of a full-scale CFT/BRB frame - Part I: specimen design, experiment and analysis, *Earthq. Eng. Struct. Dyn.*, 37: 1081–1098.
- Uang C.M., Bertero V.V. (1986). Earthquake simulation tests and associated studies of a 0.3-scale model of a six-story concentrically braced steel structure, *Rept. No. UCB/EERC-86/10*, Earthquake Engineering Research Center, University of California, Berkeley, CA.
- Uriz P., Mahin S.A. (2004). Seismic performance assessment of concentrically braced steel frames, *Proceedings, 13th World Conference on Earthquake Engineering*, Vancouver, British Columbia, Canada.
- Uriz P. (2005). *Toward Earthquake-Resistant Design of Concentrically Braced Steel-Frame Structures*, PhD Dissertation, Department of Civil and Environmental Engineering, University of California, Berkeley, CA.
- Uriz P., Filippou F.C., Mahin S.A. (2008). Model for cyclic inelastic buckling of steel braces, *ASCE J. Struct. Eng.*, 134(4): 619–628.
- Uriz P., Mahin S.A. (2008). Toward earthquake-resistant design of concentrically braced steel-frame structures, *PEER Report 2008/08*, Pacific Earthquake Engineering Research Center, University of California, Berkeley, CA.
- Wakabayashi M. et al. (1972). Experimental elastic-plastic behavior of steel bars under repeated axial loading, part 1, *Summaries of Technical Papers of Annual Meeting*, Architectural Institute of Japan, 47: 1315–1316 (in Japanese).
- Wakabayashi M. et al. (1973). Experimental elastic-plastic behavior of steel bars under repeated axial loading, part 2, *Summaries of Technical Papers of Annual Meeting*, Architectural Institute of Japan, 48: 971–972 (in Japanese).
- Wakabayashi M. (1973). Experimental elastic-plastic behavior of steel braces under repeated axial loading, *J. Arch. Bldg. Sci.*, Architectural Institute of Japan, 72: 441–443 (in Japanese).
- Wakabayashi M., Matsui C., Minami K., Mitani I. (1974). Inelastic behavior of full-scale steel frames with and without bracings, *Bull. Disaster Prevention Res. Institute*, 24(1): 1–23.
- Wakabayashi M. et al. (1976). Experimental elastic-plastic behavior of end rotational restrained steel members under repeated axial loading, *Summaries of Technical Papers of Annual Meeting*, Architectural Institute of Japan, 51: 1037–1038 (in Japanese).
- Wakabayashi M., Matsui C., Mitani I. (1977). Cyclic behavior of a restrained steel brace under axial loading, *Proceedings, 6th World Conference on Earthquake Engineering*, Vol. 3, Paper No. 3181, New Delhi, India.
- Walbridge S., Grondin G.Y., Cheng J.J.R. (1998). An analysis of the cyclic behaviour of steel gusset plate connections, *Structural Engineering Report No. 225*, University of Alberta, Edmonton, Alberta, Canada.
- Watanabe A., Hitomi Y., Saeki E., Wada A., Fujimoto M. (1988). Properties of brace encased in buckling-restraining concrete and steel tube, *Proceedings, 9th World Conference on Earthquake Engineering*, , Paper No. 6-7-4, pp. 719–724, Tokyo-Kyoto, Japan.
- Whitmore R.E. (1952). Experimental investigation of stresses in gusset plates, *Bulletin No. 16*, Engineering Experiment Station, University of Tennessee, Knoxville, TN.
- Willibald S., Packer J.A., Martinez-Saucedo G. (2006). Behavior of gusset plate connections to ends of round and elliptical hollow structural section members, *Canadian J. Civil Eng.*, 33(4): 373–383.
- Wyss T. (1923). *Beitrag zur Spannungsuntersuchung an Knotenblechen eiserner Fachwerke*, PhD Dissertation (in German), Swiss Federal Institute of Technology Zurich, Switzerland.
- Yam M.C.H. (1994). *Compressive Behavior and Strength of Steel Gusset Plate Connections*, PhD Dissertation, Department of Civil Engineering, University of Alberta, Edmonton, Alberta, Canada.
- Yam M.C.H., Cheng J.J.R. (2002). Behavior and design of gusset plate connections in compression, *J. Construct. Steel Res.*, 58(5–8): 1143–1159.

- Yamanouchi H., Midorikawa M., Nishiyama I., Watabe M. (1989). Seismic behavior of full-scale concentrically braced steel building structure, *ASCE J. Struct. Eng.*, 115(8): 1917–1929.
- Yang C.S., DesRoches R., Leon R.T. (2010). Design and analysis of braced frames with shape memory alloy and energy-absorbing hybrid devices, *Eng. Struct.*, 32: 498–507.
- Yang C.S., Leon R.T., DesRoches R. (2008). Pushover response of a braced frame with suspended zipper struts, *ASCE, J. Struct. Eng.*, 134(10): 1619–1626.
- Yang C.S., Leon R.T., DesRoches R. (2010). Cyclic behavior of zipper-braced frames, *Earthq. Spectra*, 26(2): 561–582.
- Yang F., Mahin S.A. (2005). Limiting net section fracture in slotted tube braces, in: *Steel Tips*, Structural Steel Education Council. Moraga, CA.
- Yoo J.H. (2006) Analytical investigation on the seismic performance of special concentrically braced frames, PhD Dissertation, Department of Civil Engineering, University of Washington, Seattle, WA.
- Yoo J.H., Lehman D.E., Roeder C.W. (2008). Influence of connection design parameters on the seismic performance of braced frames, *J. Construct. Steel Res.*, 64(6): 607–623.
- Yoo J.H., Roeder C.W., Lehman D.E. (2009). Simulated behavior of multi-story x-braced frames, *Eng. Struct.*, 31: 182–197.
- Zayas V.A., Popov E.P., Mahin S.A. (1980a). Cyclic inelastic buckling of tubular steel braces, *Rept. No. UCB/EERC-80/16*, Earthquake Engineering Research Center, University of California, Berkeley, CA.
- Zayas V.A., Mahin S.A., Popov, E.P. (1980b). Cyclic inelastic behavior of steel offshore structures, *Rept. No. UCB/EERC-80/27*, Earthquake Engineering Research Center, University of California, Berkeley, CA.
- Zayas V.A., Shing B.P., Mahin S.A., Popov E.P. (1981). Inelastic structural modeling of braced offshore platforms for seismic loading, *Rept. No. UCB/EERC-81/04*, Earthquake Engineering Research Center, University of California, Berkeley, CA.

PEER REPORTS

PEER reports are available as a free PDF download from http://peer.berkeley.edu/publications/peer_reports_complete.html. Printed hard copies of PEER reports can be ordered directly from our printer by following the instructions at http://peer.berkeley.edu/publications/peer_reports.html. For other related questions about the PEER Report Series, contact the Pacific Earthquake Engineering Research Center, 325 Davis Hall mail code 1792, Berkeley, CA 94720. Tel.: (510) 642-3437; Fax: (510) 665-1655; Email: peer_editor@berkeley.edu

- PEER 2013/20** *Experimental and Analytical Studies on the Seismic Behavior of Conventional and Hybrid Braced Frames.* Jiun-Wei Lai and Stephen A. Mahin. September 2013.
- PEER 2013/19** *Toward Resilient Communities: A Performance-Based Engineering Framework for Design and Evaluation of the Built Environment.* Michael William Mieler, Bozidar Stojadinovic, Robert J. Budnitz, Stephen A. Mahin and Mary C. Comerio. September 2013.
- PEER 2013/18** *Identification of Site Parameters that Improve Predictions of Site Amplification.* Ellen M. Rathje and Sara Navidi. July 2013.
- PEER 2013/17** *Response Spectrum Analysis of Concrete Gravity Dams Including Dam-Water-Foundation Interaction.* Arnkjell Løkke and Anil K. Chopra. July 2013.
- PEER 2013/16** *Effect of hoop reinforcement spacing on the cyclic response of large reinforced concrete special moment frame beams.* Marios Panagiotou, Tea Visnjic, Grigorios Antonellis, Panagiotis Galanis, and Jack P. Moehle. June 2013.
- PEER 2013/15** *publication pending*
- PEER 2013/14** *publication pending*
- PEER 2013/13** *publication pending*
- PEER 2013/12** *Nonlinear Horizontal Site Response for the NGA-West2 Project.* Ronnie Kamai, Norman A. Abramson, Walter J. Silva. May 2013.
- PEER 2013/11** *Epistemic Uncertainty for NGA-West2 Models.* Linda Al Atik and Robert R. Youngs. May 2013.
- PEER 2013/10** *NGA-West 2 Models for Ground-Motion Directionality.* Shrey K. Shahi and Jack W. Baker. May 2013.
- PEER 2013/09** *Final Report of the NGA-West2 Directivity Working Group.* Paul Spudich, Jeffrey R. Bayless, Jack W. Baker, Brian S.J. Chiou, Badie Rowshandel, Shrey Shahi, and Paul Somerville. May 2013.
- PEER 2013/08** *NGA-West2 Model for Estimating Average Horizontal Values of Pseudo-Absolute Spectral Accelerations Generated by Crustal Earthquakes.* I. M. Idriss. May 2013.
- PEER 2013/07** *Update of the Chiou and Youngs NGA Ground Motion Model for Average Horizontal Component of Peak Ground Motion and Response Spectra.* Brian Chiou and Robert Youngs. May 2013.
- PEER 2013/06** *NGA-West2 Campbell-Bozorgnia Ground Motion Model for the Horizontal Components of PGA, PGV, and 5%-Damped Elastic Pseudo-Acceleration Response Spectra for Periods Ranging from 0.01 to 10 sec.* Kenneth W. Campbell and Yousef Bozorgnia. May 2013.
- PEER 2013/05** *NGA-West 2 Equations for Predicting Response Spectral Accelerations for Shallow Crustal Earthquakes.* David M. Boore, Jonathan P. Stewart, Emel Seyhan, Gail M. Atkinson. May 2013.
- PEER 2013/04** *Update of the AS08 Ground-Motion Prediction Equations Based on the NGA-West2 Data Set.* Norman Abrahamson, Walter Silva, and Ronnie Kamai. May 2013.
- PEER 2013/03** *PEER NGA-West2 Database.* Timothy D. Ancheta, Robert B. Darragh, Jonathan P. Stewart, Emel Seyhan, Walter J. Silva, Brian S.J. Chiou, Katie E. Wooddell, Robert W. Graves, Albert R. Kottke, David M. Boore, Tadahihiro Kishida, and Jennifer L. Donahue. May 2013.
- PEER 2013/02** *Hybrid Simulation of the Seismic Response of Squat Reinforced Concrete Shear Walls.* Catherine A. Whyte and Bozidar Stojadinovic. May 2013.
- PEER 2013/01** *Housing Recovery in Chile: A Qualitative Mid-program Review.* Mary C. Comerio. February 2013.
- PEER 2012/08** *Guidelines for Estimation of Shear Wave Velocity.* Bernard R. Wair, Jason T. DeJong, and Thomas Shantz. December 2012.
- PEER 2012/07** *Earthquake Engineering for Resilient Communities: 2012 PEER Internship Program Research Report Collection.* Heidi Tremayne (Editor), Stephen A. Mahin (Editor), Collin Anderson, Dustin Cook, Michael Erceg, Carlos

Esparza, Jose Jimenez, Dorian Krausz, Andrew Lo, Stephanie Lopez, Nicole McCurdy, Paul Shipman, Alexander Strum, Eduardo Vega. December 2012.

- PEER 2012/06** *Fragilities for Precarious Rocks at Yucca Mountain.* Matthew D. Purvance, Rasool Anooshehpour, and James N. Brune. December 2012.
- PEER 2012/05** *Development of Simplified Analysis Procedure for Piles in Laterally Spreading Layered Soils.* Christopher R. McGann, Pedro Arduino, and Peter Mackenzie-Helnwein. December 2012.
- PEER 2012/04** *Unbonded Pre-Tensioned Columns for Bridges in Seismic Regions.* Phillip M. Davis, Todd M. Janes, Marc O. Eberhard, and John F. Stanton. December 2012.
- PEER 2012/03** *Experimental and Analytical Studies on Reinforced Concrete Buildings with Seismically Vulnerable Beam-Column Joints.* Sangjoon Park and Khalid M. Mosalam. October 2012.
- PEER 2012/02** *Seismic Performance of Reinforced Concrete Bridges Allowed to Uplift during Multi-Directional Excitation.* Andres Oscar Espinoza and Stephen A. Mahin. July 2012.
- PEER 2012/01** *Spectral Damping Scaling Factors for Shallow Crustal Earthquakes in Active Tectonic Regions.* Sanaz Rezaeian, Yousef Bozorgnia, I. M. Idriss, Kenneth Campbell, Norman Abrahamson, and Walter Silva. July 2012.
- PEER 2011/10** *Earthquake Engineering for Resilient Communities: 2011 PEER Internship Program Research Report Collection.* Eds. Heidi Faison and Stephen A. Mahin. December 2011.
- PEER 2011/09** *Calibration of Semi-Stochastic Procedure for Simulating High-Frequency Ground Motions.* Jonathan P. Stewart, Emel Seyhan, and Robert W. Graves. December 2011.
- PEER 2011/08** *Water Supply in regard to Fire Following Earthquake.* Charles Scawthorn. November 2011.
- PEER 2011/07** *Seismic Risk Management in Urban Areas. Proceedings of a U.S.-Iran-Turkey Seismic Workshop.* September 2011.
- PEER 2011/06** *The Use of Base Isolation Systems to Achieve Complex Seismic Performance Objectives.* Troy A. Morgan and Stephen A. Mahin. July 2011.
- PEER 2011/05** *Case Studies of the Seismic Performance of Tall Buildings Designed by Alternative Means.* Task 12 Report for the Tall Buildings Initiative. Jack Moehle, Yousef Bozorgnia, Nirmal Jayaram, Pierson Jones, Mohsen Rahnama, Nilesh Shome, Zeynep Tuna, John Wallace, Tony Yang, and Farzin Zareian. July 2011.
- PEER 2011/04** *Recommended Design Practice for Pile Foundations in Laterally Spreading Ground.* Scott A. Ashford, Ross W. Boulanger, and Scott J. Brandenburg. June 2011.
- PEER 2011/03** *New Ground Motion Selection Procedures and Selected Motions for the PEER Transportation Research Program.* Jack W. Baker, Ting Lin, Shrey K. Shahi, and Nirmal Jayaram. March 2011.
- PEER 2011/02** *A Bayesian Network Methodology for Infrastructure Seismic Risk Assessment and Decision Support.* Michelle T. Bensi, Armen Der Kiureghian, and Daniel Straub. March 2011.
- PEER 2011/01** *Demand Fragility Surfaces for Bridges in Liquefied and Laterally Spreading Ground.* Scott J. Brandenburg, Jian Zhang, Pirooz Kashighandi, Yili Huo, and Minxing Zhao. March 2011.
- PEER 2010/05** *Guidelines for Performance-Based Seismic Design of Tall Buildings.* Developed by the Tall Buildings Initiative. November 2010.
- PEER 2010/04** *Application Guide for the Design of Flexible and Rigid Bus Connections between Substation Equipment Subjected to Earthquakes.* Jean-Bernard Dastous and Armen Der Kiureghian. September 2010.
- PEER 2010/03** *Shear Wave Velocity as a Statistical Function of Standard Penetration Test Resistance and Vertical Effective Stress at Caltrans Bridge Sites.* Scott J. Brandenburg, Naresh Bellana, and Thomas Shantz. June 2010.
- PEER 2010/02** *Stochastic Modeling and Simulation of Ground Motions for Performance-Based Earthquake Engineering.* Sanaz Rezaeian and Armen Der Kiureghian. June 2010.
- PEER 2010/01** *Structural Response and Cost Characterization of Bridge Construction Using Seismic Performance Enhancement Strategies.* Ady Aviram, Božidar Stojadinović, Gustavo J. Parra-Montesinos, and Kevin R. Mackie. March 2010.
- PEER 2009/03** *The Integration of Experimental and Simulation Data in the Study of Reinforced Concrete Bridge Systems Including Soil-Foundation-Structure Interaction.* Matthew Dryden and Gregory L. Fenves. November 2009.
- PEER 2009/02** *Improving Earthquake Mitigation through Innovations and Applications in Seismic Science, Engineering, Communication, and Response. Proceedings of a U.S.-Iran Seismic Workshop.* October 2009.
- PEER 2009/01** *Evaluation of Ground Motion Selection and Modification Methods: Predicting Median Interstory Drift Response of Buildings.* Curt B. Haselton, Ed. June 2009.
- PEER 2008/10** *Technical Manual for Strata.* Albert R. Kottke and Ellen M. Rathje. February 2009.

- PEER 2008/09** *NGA Model for Average Horizontal Component of Peak Ground Motion and Response Spectra.* Brian S.-J. Chiou and Robert R. Youngs. November 2008.
- PEER 2008/08** *Toward Earthquake-Resistant Design of Concentrically Braced Steel Structures.* Patxi Uriz and Stephen A. Mahin. November 2008.
- PEER 2008/07** *Using OpenSees for Performance-Based Evaluation of Bridges on Liquefiable Soils.* Stephen L. Kramer, Pedro Arduino, and HyungSuk Shin. November 2008.
- PEER 2008/06** *Shaking Table Tests and Numerical Investigation of Self-Centering Reinforced Concrete Bridge Columns.* Hyung IL Jeong, Junichi Sakai, and Stephen A. Mahin. September 2008.
- PEER 2008/05** *Performance-Based Earthquake Engineering Design Evaluation Procedure for Bridge Foundations Undergoing Liquefaction-Induced Lateral Ground Displacement.* Christian A. Ledezma and Jonathan D. Bray. August 2008.
- PEER 2008/04** *Benchmarking of Nonlinear Geotechnical Ground Response Analysis Procedures.* Jonathan P. Stewart, Annie On-Lei Kwok, Youssef M. A. Hashash, Neven Matasovic, Robert Pyke, Zhiliang Wang, and Zhaohui Yang. August 2008.
- PEER 2008/03** *Guidelines for Nonlinear Analysis of Bridge Structures in California.* Ady Aviram, Kevin R. Mackie, and Božidar Stojadinović. August 2008.
- PEER 2008/02** *Treatment of Uncertainties in Seismic-Risk Analysis of Transportation Systems.* Evangelos Stergiou and Anne S. Kiremidjian. July 2008.
- PEER 2008/01** *Seismic Performance Objectives for Tall Buildings.* William T. Holmes, Charles Kircher, William Petak, and Nabih Youssef. August 2008.
- PEER 2007/12** *An Assessment to Benchmark the Seismic Performance of a Code-Conforming Reinforced Concrete Moment-Frame Building.* Curt Haselton, Christine A. Goulet, Judith Mitrani-Reiser, James L. Beck, Gregory G. Deierlein, Keith A. Porter, Jonathan P. Stewart, and Ertugrul Taciroglu. August 2008.
- PEER 2007/11** *Bar Buckling in Reinforced Concrete Bridge Columns.* Wayne A. Brown, Dawn E. Lehman, and John F. Stanton. February 2008.
- PEER 2007/10** *Computational Modeling of Progressive Collapse in Reinforced Concrete Frame Structures.* Mohamed M. Talaat and Khalid M. Mosalam. May 2008.
- PEER 2007/09** *Integrated Probabilistic Performance-Based Evaluation of Benchmark Reinforced Concrete Bridges.* Kevin R. Mackie, John-Michael Wong, and Božidar Stojadinović. January 2008.
- PEER 2007/08** *Assessing Seismic Collapse Safety of Modern Reinforced Concrete Moment-Frame Buildings.* Curt B. Haselton and Gregory G. Deierlein. February 2008.
- PEER 2007/07** *Performance Modeling Strategies for Modern Reinforced Concrete Bridge Columns.* Michael P. Berry and Marc O. Eberhard. April 2008.
- PEER 2007/06** *Development of Improved Procedures for Seismic Design of Buried and Partially Buried Structures.* Linda Al Atik and Nicholas Sitar. June 2007.
- PEER 2007/05** *Uncertainty and Correlation in Seismic Risk Assessment of Transportation Systems.* Renee G. Lee and Anne S. Kiremidjian. July 2007.
- PEER 2007/04** *Numerical Models for Analysis and Performance-Based Design of Shallow Foundations Subjected to Seismic Loading.* Sivapalan Gajan, Tara C. Hutchinson, Bruce L. Kutter, Prishati Raychowdhury, José A. Ugalde, and Jonathan P. Stewart. May 2008.
- PEER 2007/03** *Beam-Column Element Model Calibrated for Predicting Flexural Response Leading to Global Collapse of RC Frame Buildings.* Curt B. Haselton, Abbie B. Liel, Sarah Taylor Lange, and Gregory G. Deierlein. May 2008.
- PEER 2007/02** *Campbell-Bozorgnia NGA Ground Motion Relations for the Geometric Mean Horizontal Component of Peak and Spectral Ground Motion Parameters.* Kenneth W. Campbell and Yousef Bozorgnia. May 2007.
- PEER 2007/01** *Boore-Atkinson NGA Ground Motion Relations for the Geometric Mean Horizontal Component of Peak and Spectral Ground Motion Parameters.* David M. Boore and Gail M. Atkinson. May 2007.
- PEER 2006/12** *Societal Implications of Performance-Based Earthquake Engineering.* Peter J. May. May 2007.
- PEER 2006/11** *Probabilistic Seismic Demand Analysis Using Advanced Ground Motion Intensity Measures, Attenuation Relationships, and Near-Fault Effects.* Polsak Tothong and C. Allin Cornell. March 2007.
- PEER 2006/10** *Application of the PEER PBEE Methodology to the I-880 Viaduct.* Sashi Kunnath. February 2007.
- PEER 2006/09** *Quantifying Economic Losses from Travel Forgone Following a Large Metropolitan Earthquake.* James Moore, Sungbin Cho, Yue Yue Fan, and Stuart Werner. November 2006.

- PEER 2006/08** *Vector-Valued Ground Motion Intensity Measures for Probabilistic Seismic Demand Analysis.* Jack W. Baker and C. Allin Cornell. October 2006.
- PEER 2006/07** *Analytical Modeling of Reinforced Concrete Walls for Predicting Flexural and Coupled–Shear–Flexural Responses.* Kutay Orakcal, Leonardo M. Massone, and John W. Wallace. October 2006.
- PEER 2006/06** *Nonlinear Analysis of a Soil-Drilled Pier System under Static and Dynamic Axial Loading.* Gang Wang and Nicholas Sitar. November 2006.
- PEER 2006/05** *Advanced Seismic Assessment Guidelines.* Paolo Bazzurro, C. Allin Cornell, Charles Menun, Maziar Motahari, and Nicolas Luco. September 2006.
- PEER 2006/04** *Probabilistic Seismic Evaluation of Reinforced Concrete Structural Components and Systems.* Tae Hyung Lee and Khalid M. Mosalam. August 2006.
- PEER 2006/03** *Performance of Lifelines Subjected to Lateral Spreading.* Scott A. Ashford and Teerawut Juirnarongrit. July 2006.
- PEER 2006/02** *Pacific Earthquake Engineering Research Center Highway Demonstration Project.* Anne Kiremidjian, James Moore, Yue Yue Fan, Nesrin Basoz, Ozgur Yazali, and Meredith Williams. April 2006.
- PEER 2006/01** *Bracing Berkeley. A Guide to Seismic Safety on the UC Berkeley Campus.* Mary C. Comerio, Stephen Tobriner, and Ariane Fehrenkamp. January 2006.
- PEER 2005/16** *Seismic Response and Reliability of Electrical Substation Equipment and Systems.* Junho Song, Armen Der Kiureghian, and Jerome L. Sackman. April 2006.
- PEER 2005/15** *CPT-Based Probabilistic Assessment of Seismic Soil Liquefaction Initiation.* R. E. S. Moss, R. B. Seed, R. E. Kayen, J. P. Stewart, and A. Der Kiureghian. April 2006.
- PEER 2005/14** *Workshop on Modeling of Nonlinear Cyclic Load-Deformation Behavior of Shallow Foundations.* Bruce L. Kutter, Geoffrey Martin, Tara Hutchinson, Chad Harden, Sivapalan Gajan, and Justin Phalen. March 2006.
- PEER 2005/13** *Stochastic Characterization and Decision Bases under Time-Dependent Aftershock Risk in Performance-Based Earthquake Engineering.* Gee Liek Yeo and C. Allin Cornell. July 2005.
- PEER 2005/12** *PEER Testbed Study on a Laboratory Building: Exercising Seismic Performance Assessment.* Mary C. Comerio, editor. November 2005.
- PEER 2005/11** *Van Nuys Hotel Building Testbed Report: Exercising Seismic Performance Assessment.* Helmut Krawinkler, editor. October 2005.
- PEER 2005/10** *First NEES/E-Defense Workshop on Collapse Simulation of Reinforced Concrete Building Structures.* September 2005.
- PEER 2005/09** *Test Applications of Advanced Seismic Assessment Guidelines.* Joe Maffei, Karl Telleen, Danya Mohr, William Holmes, and Yuki Nakayama. August 2006.
- PEER 2005/08** *Damage Accumulation in Lightly Confined Reinforced Concrete Bridge Columns.* R. Tyler Ranf, Jared M. Nelson, Zach Price, Marc O. Eberhard, and John F. Stanton. April 2006.
- PEER 2005/07** *Experimental and Analytical Studies on the Seismic Response of Freestanding and Anchored Laboratory Equipment.* Dimitrios Konstantinidis and Nicos Makris. January 2005.
- PEER 2005/06** *Global Collapse of Frame Structures under Seismic Excitations.* Luis F. Ibarra and Helmut Krawinkler. September 2005.
- PEER 2005/05** *Performance Characterization of Bench- and Shelf-Mounted Equipment.* Samit Ray Chaudhuri and Tara C. Hutchinson. May 2006.
- PEER 2005/04** *Numerical Modeling of the Nonlinear Cyclic Response of Shallow Foundations.* Chad Harden, Tara Hutchinson, Geoffrey R. Martin, and Bruce L. Kutter. August 2005.
- PEER 2005/03** *A Taxonomy of Building Components for Performance-Based Earthquake Engineering.* Keith A. Porter. September 2005.
- PEER 2005/02** *Fragility Basis for California Highway Overpass Bridge Seismic Decision Making.* Kevin R. Mackie and Božidar Stojadinović. June 2005.
- PEER 2005/01** *Empirical Characterization of Site Conditions on Strong Ground Motion.* Jonathan P. Stewart, Yoojoong Choi, and Robert W. Graves. June 2005.
- PEER 2004/09** *Electrical Substation Equipment Interaction: Experimental Rigid Conductor Studies.* Christopher Stearns and André Filiatrault. February 2005.
- PEER 2004/08** *Seismic Qualification and Fragility Testing of Line Break 550-kV Disconnect Switches.* Shakhzod M. Takhirov, Gregory L. Fenves, and Eric Fujisaki. January 2005.

- PEER 2004/07** *Ground Motions for Earthquake Simulator Qualification of Electrical Substation Equipment.* Shakhzod M. Takhirov, Gregory L. Fenves, Eric Fujisaki, and Don Clyde. January 2005.
- PEER 2004/06** *Performance-Based Regulation and Regulatory Regimes.* Peter J. May and Chris Koski. September 2004.
- PEER 2004/05** *Performance-Based Seismic Design Concepts and Implementation: Proceedings of an International Workshop.* Peter Fajfar and Helmut Krawinkler, editors. September 2004.
- PEER 2004/04** *Seismic Performance of an Instrumented Tilt-up Wall Building.* James C. Anderson and Vitelmo V. Bertero. July 2004.
- PEER 2004/03** *Evaluation and Application of Concrete Tilt-up Assessment Methodologies.* Timothy Graf and James O. Malley. October 2004.
- PEER 2004/02** *Analytical Investigations of New Methods for Reducing Residual Displacements of Reinforced Concrete Bridge Columns.* Junichi Sakai and Stephen A. Mahin. August 2004.
- PEER 2004/01** *Seismic Performance of Masonry Buildings and Design Implications.* Kerri Anne Taeko Tokoro, James C. Anderson, and Vitelmo V. Bertero. February 2004.
- PEER 2003/18** *Performance Models for Flexural Damage in Reinforced Concrete Columns.* Michael Berry and Marc Eberhard. August 2003.
- PEER 2003/17** *Predicting Earthquake Damage in Older Reinforced Concrete Beam-Column Joints.* Catherine Pagni and Laura Lowes. October 2004.
- PEER 2003/16** *Seismic Demands for Performance-Based Design of Bridges.* Kevin Mackie and Božidar Stojadinović. August 2003.
- PEER 2003/15** *Seismic Demands for Nondeteriorating Frame Structures and Their Dependence on Ground Motions.* Ricardo Antonio Medina and Helmut Krawinkler. May 2004.
- PEER 2003/14** *Finite Element Reliability and Sensitivity Methods for Performance-Based Earthquake Engineering.* Terje Haukaas and Armen Der Kiureghian. April 2004.
- PEER 2003/13** *Effects of Connection Hysteretic Degradation on the Seismic Behavior of Steel Moment-Resisting Frames.* Janise E. Rodgers and Stephen A. Mahin. March 2004.
- PEER 2003/12** *Implementation Manual for the Seismic Protection of Laboratory Contents: Format and Case Studies.* William T. Holmes and Mary C. Comerio. October 2003.
- PEER 2003/11** *Fifth U.S.-Japan Workshop on Performance-Based Earthquake Engineering Methodology for Reinforced Concrete Building Structures.* February 2004.
- PEER 2003/10** *A Beam-Column Joint Model for Simulating the Earthquake Response of Reinforced Concrete Frames.* Laura N. Lowes, Nilanjan Mitra, and Arash Altoontash. February 2004.
- PEER 2003/09** *Sequencing Repairs after an Earthquake: An Economic Approach.* Marco Casari and Simon J. Wilkie. April 2004.
- PEER 2003/08** *A Technical Framework for Probability-Based Demand and Capacity Factor Design (DCFD) Seismic Formats.* Fatemeh Jalayer and C. Allin Cornell. November 2003.
- PEER 2003/07** *Uncertainty Specification and Propagation for Loss Estimation Using FOSM Methods.* Jack W. Baker and C. Allin Cornell. September 2003.
- PEER 2003/06** *Performance of Circular Reinforced Concrete Bridge Columns under Bidirectional Earthquake Loading.* Mahmoud M. Hachem, Stephen A. Mahin, and Jack P. Moehle. February 2003.
- PEER 2003/05** *Response Assessment for Building-Specific Loss Estimation.* Eduardo Miranda and Shahram Taghavi. September 2003.
- PEER 2003/04** *Experimental Assessment of Columns with Short Lap Splices Subjected to Cyclic Loads.* Murat Melek, John W. Wallace, and Joel Conte. April 2003.
- PEER 2003/03** *Probabilistic Response Assessment for Building-Specific Loss Estimation.* Eduardo Miranda and Hesameddin Aslani. September 2003.
- PEER 2003/02** *Software Framework for Collaborative Development of Nonlinear Dynamic Analysis Program.* Jun Peng and Kincho H. Law. September 2003.
- PEER 2003/01** *Shake Table Tests and Analytical Studies on the Gravity Load Collapse of Reinforced Concrete Frames.* Kenneth John Elwood and Jack P. Moehle. November 2003.
- PEER 2002/24** *Performance of Beam to Column Bridge Joints Subjected to a Large Velocity Pulse.* Natalie Gibson, André Filiatrault, and Scott A. Ashford. April 2002.

- PEER 2002/23** *Effects of Large Velocity Pulses on Reinforced Concrete Bridge Columns.* Greg L. Orozco and Scott A. Ashford. April 2002.
- PEER 2002/22** *Characterization of Large Velocity Pulses for Laboratory Testing.* Kenneth E. Cox and Scott A. Ashford. April 2002.
- PEER 2002/21** *Fourth U.S.-Japan Workshop on Performance-Based Earthquake Engineering Methodology for Reinforced Concrete Building Structures.* December 2002.
- PEER 2002/20** *Barriers to Adoption and Implementation of PBEE Innovations.* Peter J. May. August 2002.
- PEER 2002/19** *Economic-Engineered Integrated Models for Earthquakes: Socioeconomic Impacts.* Peter Gordon, James E. Moore II, and Harry W. Richardson. July 2002.
- PEER 2002/18** *Assessment of Reinforced Concrete Building Exterior Joints with Substandard Details.* Chris P. Pantelides, Jon Hansen, Justin Nadauld, and Lawrence D. Reaveley. May 2002.
- PEER 2002/17** *Structural Characterization and Seismic Response Analysis of a Highway Overcrossing Equipped with Elastomeric Bearings and Fluid Dampers: A Case Study.* Nicos Makris and Jian Zhang. November 2002.
- PEER 2002/16** *Estimation of Uncertainty in Geotechnical Properties for Performance-Based Earthquake Engineering.* Allen L. Jones, Steven L. Kramer, and Pedro Arduino. December 2002.
- PEER 2002/15** *Seismic Behavior of Bridge Columns Subjected to Various Loading Patterns.* Asadollah Esmaeili-Gh. and Yan Xiao. December 2002.
- PEER 2002/14** *Inelastic Seismic Response of Extended Pile Shaft Supported Bridge Structures.* T.C. Hutchinson, R.W. Boulanger, Y.H. Chai, and I.M. Idriss. December 2002.
- PEER 2002/13** *Probabilistic Models and Fragility Estimates for Bridge Components and Systems.* Paolo Gardoni, Armen Der Kiureghian, and Khalid M. Mosalam. June 2002.
- PEER 2002/12** *Effects of Fault Dip and Slip Rake on Near-Source Ground Motions: Why Chi-Chi Was a Relatively Mild M7.6 Earthquake.* Brad T. Aagaard, John F. Hall, and Thomas H. Heaton. December 2002.
- PEER 2002/11** *Analytical and Experimental Study of Fiber-Reinforced Strip Isolators.* James M. Kelly and Shakhzod M. Takhirov. September 2002.
- PEER 2002/10** *Centrifuge Modeling of Settlement and Lateral Spreading with Comparisons to Numerical Analyses.* Sivapalan Gajan and Bruce L. Kutter. January 2003.
- PEER 2002/09** *Documentation and Analysis of Field Case Histories of Seismic Compression during the 1994 Northridge, California, Earthquake.* Jonathan P. Stewart, Patrick M. Smith, Daniel H. Whang, and Jonathan D. Bray. October 2002.
- PEER 2002/08** *Component Testing, Stability Analysis and Characterization of Buckling-Restrained Unbonded BracesTM.* Cameron Black, Nicos Makris, and Ian Aiken. September 2002.
- PEER 2002/07** *Seismic Performance of Pile-Wharf Connections.* Charles W. Roeder, Robert Graff, Jennifer Soderstrom, and Jun Han Yoo. December 2001.
- PEER 2002/06** *The Use of Benefit-Cost Analysis for Evaluation of Performance-Based Earthquake Engineering Decisions.* Richard O. Zerbe and Anthony Falit-Baiamonte. September 2001.
- PEER 2002/05** *Guidelines, Specifications, and Seismic Performance Characterization of Nonstructural Building Components and Equipment.* André Filiatrault, Constantin Christopoulos, and Christopher Stearns. September 2001.
- PEER 2002/04** *Consortium of Organizations for Strong-Motion Observation Systems and the Pacific Earthquake Engineering Research Center Lifelines Program: Invited Workshop on Archiving and Web Dissemination of Geotechnical Data, 4–5 October 2001.* September 2002.
- PEER 2002/03** *Investigation of Sensitivity of Building Loss Estimates to Major Uncertain Variables for the Van Nuys Testbed.* Keith A. Porter, James L. Beck, and Rustem V. Shaikhutdinov. August 2002.
- PEER 2002/02** *The Third U.S.-Japan Workshop on Performance-Based Earthquake Engineering Methodology for Reinforced Concrete Building Structures.* July 2002.
- PEER 2002/01** *Nonstructural Loss Estimation: The UC Berkeley Case Study.* Mary C. Comerio and John C. Stallmeyer. December 2001.
- PEER 2001/16** *Statistics of SDF-System Estimate of Roof Displacement for Pushover Analysis of Buildings.* Anil K. Chopra, Rakesh K. Goel, and Chatpan Chintanapakdee. December 2001.
- PEER 2001/15** *Damage to Bridges during the 2001 Nisqually Earthquake.* R. Tyler Ranf, Marc O. Eberhard, and Michael P. Berry. November 2001.

- PEER 2001/14** *Rocking Response of Equipment Anchored to a Base Foundation.* Nicos Makris and Cameron J. Black. September 2001.
- PEER 2001/13** *Modeling Soil Liquefaction Hazards for Performance-Based Earthquake Engineering.* Steven L. Kramer and Ahmed-W. Elgamal. February 2001.
- PEER 2001/12** *Development of Geotechnical Capabilities in OpenSees.* Boris Jeremić. September 2001.
- PEER 2001/11** *Analytical and Experimental Study of Fiber-Reinforced Elastomeric Isolators.* James M. Kelly and Shakhzod M. Takhirov. September 2001.
- PEER 2001/10** *Amplification Factors for Spectral Acceleration in Active Regions.* Jonathan P. Stewart, Andrew H. Liu, Yoojoong Choi, and Mehmet B. Baturay. December 2001.
- PEER 2001/09** *Ground Motion Evaluation Procedures for Performance-Based Design.* Jonathan P. Stewart, Shyh-Jeng Chiou, Jonathan D. Bray, Robert W. Graves, Paul G. Somerville, and Norman A. Abrahamson. September 2001.
- PEER 2001/08** *Experimental and Computational Evaluation of Reinforced Concrete Bridge Beam-Column Connections for Seismic Performance.* Clay J. Naito, Jack P. Moehle, and Khalid M. Mosalam. November 2001.
- PEER 2001/07** *The Rocking Spectrum and the Shortcomings of Design Guidelines.* Nicos Makris and Dimitrios Konstantinidis. August 2001.
- PEER 2001/06** *Development of an Electrical Substation Equipment Performance Database for Evaluation of Equipment Fragilities.* Thalia Agnanos. April 1999.
- PEER 2001/05** *Stiffness Analysis of Fiber-Reinforced Elastomeric Isolators.* Hsiang-Chuan Tsai and James M. Kelly. May 2001.
- PEER 2001/04** *Organizational and Societal Considerations for Performance-Based Earthquake Engineering.* Peter J. May. April 2001.
- PEER 2001/03** *A Modal Pushover Analysis Procedure to Estimate Seismic Demands for Buildings: Theory and Preliminary Evaluation.* Anil K. Chopra and Rakesh K. Goel. January 2001.
- PEER 2001/02** *Seismic Response Analysis of Highway Overcrossings Including Soil-Structure Interaction.* Jian Zhang and Nicos Makris. March 2001.
- PEER 2001/01** *Experimental Study of Large Seismic Steel Beam-to-Column Connections.* Egor P. Popov and Shakhzod M. Takhirov. November 2000.
- PEER 2000/10** *The Second U.S.-Japan Workshop on Performance-Based Earthquake Engineering Methodology for Reinforced Concrete Building Structures.* March 2000.
- PEER 2000/09** *Structural Engineering Reconnaissance of the August 17, 1999 Earthquake: Kocaeli (Izmit), Turkey.* Halil Sezen, Kenneth J. Elwood, Andrew S. Whittaker, Khalid Mosalam, John J. Wallace, and John F. Stanton. December 2000.
- PEER 2000/08** *Behavior of Reinforced Concrete Bridge Columns Having Varying Aspect Ratios and Varying Lengths of Confinement.* Anthony J. Calderone, Dawn E. Lehman, and Jack P. Moehle. January 2001.
- PEER 2000/07** *Cover-Plate and Flange-Plate Reinforced Steel Moment-Resisting Connections.* Taejin Kim, Andrew S. Whittaker, Amir S. Gilani, Vitelmo V. Bertero, and Shakhzod M. Takhirov. September 2000.
- PEER 2000/06** *Seismic Evaluation and Analysis of 230-kV Disconnect Switches.* Amir S. J. Gilani, Andrew S. Whittaker, Gregory L. Fenves, Chun-Hao Chen, Henry Ho, and Eric Fujisaki. July 2000.
- PEER 2000/05** *Performance-Based Evaluation of Exterior Reinforced Concrete Building Joints for Seismic Excitation.* Chandra Clyde, Chris P. Pantelides, and Lawrence D. Reaveley. July 2000.
- PEER 2000/04** *An Evaluation of Seismic Energy Demand: An Attenuation Approach.* Chung-Che Chou and Chia-Ming Uang. July 1999.
- PEER 2000/03** *Framing Earthquake Retrofitting Decisions: The Case of Hillside Homes in Los Angeles.* Detlof von Winterfeldt, Nels Roselund, and Alicia Kitsuse. March 2000.
- PEER 2000/02** *U.S.-Japan Workshop on the Effects of Near-Field Earthquake Shaking.* Andrew Whittaker, ed. July 2000.
- PEER 2000/01** *Further Studies on Seismic Interaction in Interconnected Electrical Substation Equipment.* Armen Der Kiureghian, Kee-Jeung Hong, and Jerome L. Sackman. November 1999.
- PEER 1999/14** *Seismic Evaluation and Retrofit of 230-kV Porcelain Transformer Bushings.* Amir S. Gilani, Andrew S. Whittaker, Gregory L. Fenves, and Eric Fujisaki. December 1999.
- PEER 1999/13** *Building Vulnerability Studies: Modeling and Evaluation of Tilt-up and Steel Reinforced Concrete Buildings.* John W. Wallace, Jonathan P. Stewart, and Andrew S. Whittaker, editors. December 1999.

- PEER 1999/12** *Rehabilitation of Nonductile RC Frame Building Using Encasement Plates and Energy-Dissipating Devices.* Mehrdad Sasaki, Vitelmo V. Bertero, James C. Anderson. December 1999.
- PEER 1999/11** *Performance Evaluation Database for Concrete Bridge Components and Systems under Simulated Seismic Loads.* Yael D. Hose and Frieder Seible. November 1999.
- PEER 1999/10** *U.S.-Japan Workshop on Performance-Based Earthquake Engineering Methodology for Reinforced Concrete Building Structures.* December 1999.
- PEER 1999/09** *Performance Improvement of Long Period Building Structures Subjected to Severe Pulse-Type Ground Motions.* James C. Anderson, Vitelmo V. Bertero, and Raul Bertero. October 1999.
- PEER 1999/08** *Envelopes for Seismic Response Vectors.* Charles Menun and Armen Der Kiureghian. July 1999.
- PEER 1999/07** *Documentation of Strengths and Weaknesses of Current Computer Analysis Methods for Seismic Performance of Reinforced Concrete Members.* William F. Cofer. November 1999.
- PEER 1999/06** *Rocking Response and Overturning of Anchored Equipment under Seismic Excitations.* Nicos Makris and Jian Zhang. November 1999.
- PEER 1999/05** *Seismic Evaluation of 550 kV Porcelain Transformer Bushings.* Amir S. Gilani, Andrew S. Whittaker, Gregory L. Fennes, and Eric Fujisaki. October 1999.
- PEER 1999/04** *Adoption and Enforcement of Earthquake Risk-Reduction Measures.* Peter J. May, Raymond J. Burby, T. Jens Feeley, and Robert Wood.
- PEER 1999/03** *Task 3 Characterization of Site Response General Site Categories.* Adrian Rodriguez-Marek, Jonathan D. Bray, and Norman Abrahamson. February 1999.
- PEER 1999/02** *Capacity-Demand-Diagram Methods for Estimating Seismic Deformation of Inelastic Structures: SDF Systems.* Anil K. Chopra and Rakesh Goel. April 1999.
- PEER 1999/01** *Interaction in Interconnected Electrical Substation Equipment Subjected to Earthquake Ground Motions.* Armen Der Kiureghian, Jerome L. Sackman, and Kee-Jeung Hong. February 1999.
- PEER 1998/08** *Behavior and Failure Analysis of a Multiple-Frame Highway Bridge in the 1994 Northridge Earthquake.* Gregory L. Fennes and Michael Ellery. December 1998.
- PEER 1998/07** *Empirical Evaluation of Inertial Soil-Structure Interaction Effects.* Jonathan P. Stewart, Raymond B. Seed, and Gregory L. Fennes. November 1998.
- PEER 1998/06** *Effect of Damping Mechanisms on the Response of Seismic Isolated Structures.* Nicos Makris and Shih-Po Chang. November 1998.
- PEER 1998/05** *Rocking Response and Overturning of Equipment under Horizontal Pulse-Type Motions.* Nicos Makris and Yiannis Roussos. October 1998.
- PEER 1998/04** *Pacific Earthquake Engineering Research Invitational Workshop Proceedings, May 14–15, 1998: Defining the Links between Planning, Policy Analysis, Economics and Earthquake Engineering.* Mary Comerio and Peter Gordon. September 1998.
- PEER 1998/03** *Repair/Upgrade Procedures for Welded Beam to Column Connections.* James C. Anderson and Xiaojing Duan. May 1998.
- PEER 1998/02** *Seismic Evaluation of 196 kV Porcelain Transformer Bushings.* Amir S. Gilani, Juan W. Chavez, Gregory L. Fennes, and Andrew S. Whittaker. May 1998.
- PEER 1998/01** *Seismic Performance of Well-Confined Concrete Bridge Columns.* Dawn E. Lehman and Jack P. Moehle. December 2000.

ONLINE PEER REPORTS

The following PEER reports are available by Internet only at http://peer.berkeley.edu/publications/peer_reports_complete.html.

- PEER 2012/103** *Performance-Based Seismic Demand Assessment of Concentrically Braced Steel Frame Buildings*. Chui-Hsin Chen and Stephen A. Mahin. December 2012.
- PEER 2012/102** *Procedure to Restart an Interrupted Hybrid Simulation: Addendum to PEER Report 2010/103*. Vesna Terzic and Božidar Stojadinovic. October 2012.
- PEER 2012/101** *Mechanics of Fiber Reinforced Bearings*. James M. Kelly and Andrea Calabrese. February 2012.
- PEER 2011/107** *Nonlinear Site Response and Seismic Compression at Vertical Array Strongly Shaken by 2007 Niigata-ken Chuetsu-oki Earthquake*. Eric Yee, Jonathan P. Stewart, and Kohji Tokimatsu. December 2011.
- PEER 2011/106** *Self Compacting Hybrid Fiber Reinforced Concrete Composites for Bridge Columns*. Pardeep Kumar, Gabriel Jen, William Trono, Marios Panagiotou, and Claudia Ostertag. September 2011.
- PEER 2011/105** *Stochastic Dynamic Analysis of Bridges Subjected to Spatially Varying Ground Motions*. Katerina Konakli and Armen Der Kiureghian. August 2011.
- PEER 2011/104** *Design and Instrumentation of the 2010 E-Defense Four-Story Reinforced Concrete and Post-Tensioned Concrete Buildings*. Takuya Nagae, Kenichi Tahara, Taizo Matsumori, Hitoshi Shiohara, Toshimi Kabeyasawa, Susumu Kono, Minehiro Nishiyama (Japanese Research Team) and John Wallace, Wassim Ghannoum, Jack Moehle, Richard Sause, Wesley Keller, Zeynep Tuna (U.S. Research Team). June 2011.
- PEER 2011/103** *In-Situ Monitoring of the Force Output of Fluid Dampers: Experimental Investigation*. Dimitrios Konstantinidis, James M. Kelly, and Nicos Makris. April 2011.
- PEER 2011/102** *Ground-motion prediction equations 1964 - 2010*. John Douglas. April 2011.
- PEER 2011/101** *Report of the Eighth Planning Meeting of NEES/E-Defense Collaborative Research on Earthquake Engineering*. Convened by the Hyogo Earthquake Engineering Research Center (NIED), NEES Consortium, Inc. February 2011.
- PEER 2010/111** *Modeling and Acceptance Criteria for Seismic Design and Analysis of Tall Buildings*. Task 7 Report for the Tall Buildings Initiative - Published jointly by the Applied Technology Council. October 2010.
- PEER 2010/110** *Seismic Performance Assessment and Probabilistic Repair Cost Analysis of Precast Concrete Cladding Systems for Multistory Buildings*. Jeffrey P. Hunt and Božidar Stojadinovic. November 2010.
- PEER 2010/109** *Report of the Seventh Joint Planning Meeting of NEES/E-Defense Collaboration on Earthquake Engineering. Held at the E-Defense, Miki, and Shin-Kobe, Japan, September 18–19, 2009*. August 2010.
- PEER 2010/108** *Probabilistic Tsunami Hazard in California*. Hong Kie Thio, Paul Somerville, and Jascha Polet, preparers. October 2010.
- PEER 2010/107** *Performance and Reliability of Exposed Column Base Plate Connections for Steel Moment-Resisting Frames*. Ady Aviram, Božidar Stojadinovic, and Armen Der Kiureghian. August 2010.
- PEER 2010/106** *Verification of Probabilistic Seismic Hazard Analysis Computer Programs*. Patricia Thomas, Ivan Wong, and Norman Abrahamson. May 2010.
- PEER 2010/105** *Structural Engineering Reconnaissance of the April 6, 2009, Abruzzo, Italy, Earthquake, and Lessons Learned*. M. Selim Güney and Khalid M. Mosalam. April 2010.
- PEER 2010/104** *Simulating the Inelastic Seismic Behavior of Steel Braced Frames, Including the Effects of Low-Cycle Fatigue*. Yuli Huang and Stephen A. Mahin. April 2010.
- PEER 2010/103** *Post-Earthquake Traffic Capacity of Modern Bridges in California*. Vesna Terzic and Božidar Stojadinović. March 2010.
- PEER 2010/102** *Analysis of Cumulative Absolute Velocity (CAV) and JMA Instrumental Seismic Intensity (I_{JMA}) Using the PEER–NGA Strong Motion Database*. Kenneth W. Campbell and Yousef Bozorgnia. February 2010.
- PEER 2010/101** *Rocking Response of Bridges on Shallow Foundations*. Jose A. Ugalde, Bruce L. Kutter, and Boris Jeremic. April 2010.
- PEER 2009/109** *Simulation and Performance-Based Earthquake Engineering Assessment of Self-Centering Post-Tensioned Concrete Bridge Systems*. Won K. Lee and Sarah L. Billington. December 2009.
- PEER 2009/108** *PEER Lifelines Geotechnical Virtual Data Center*. J. Carl Stepp, Daniel J. Ponti, Loren L. Turner, Jennifer N. Swift, Sean Devlin, Yang Zhu, Jean Benoit, and John Bobbitt. September 2009.
- PEER 2009/107** *Experimental and Computational Evaluation of Current and Innovative In-Span Hinge Details in Reinforced Concrete Box-Girder Bridges: Part 2: Post-Test Analysis and Design Recommendations*. Matias A. Hube and Khalid M. Mosalam. December 2009.

- PEER 2009/106** *Shear Strength Models of Exterior Beam-Column Joints without Transverse Reinforcement.* Sangjoon Park and Khalid M. Mosalam. November 2009.
- PEER 2009/105** *Reduced Uncertainty of Ground Motion Prediction Equations through Bayesian Variance Analysis.* Robb Eric S. Moss. November 2009.
- PEER 2009/104** *Advanced Implementation of Hybrid Simulation.* Andreas H. Schellenberg, Stephen A. Mahin, Gregory L. Fenves. November 2009.
- PEER 2009/103** *Performance Evaluation of Innovative Steel Braced Frames.* T. Y. Yang, Jack P. Moehle, and Božidar Stojadinovic. August 2009.
- PEER 2009/102** *Reinvestigation of Liquefaction and Nonliquefaction Case Histories from the 1976 Tangshan Earthquake.* Robb Eric Moss, Robert E. Kayen, Liyuan Tong, Songyu Liu, Guojun Cai, and Jiaer Wu. August 2009.
- PEER 2009/101** *Report of the First Joint Planning Meeting for the Second Phase of NEES/E-Defense Collaborative Research on Earthquake Engineering.* Stephen A. Mahin et al. July 2009.
- PEER 2008/104** *Experimental and Analytical Study of the Seismic Performance of Retaining Structures.* Linda Al Atik and Nicholas Sitar. January 2009.
- PEER 2008/103** *Experimental and Computational Evaluation of Current and Innovative In-Span Hinge Details in Reinforced Concrete Box-Girder Bridges. Part 1: Experimental Findings and Pre-Test Analysis.* Matias A. Hube and Khalid M. Mosalam. January 2009.
- PEER 2008/102** *Modeling of Unreinforced Masonry Infill Walls Considering In-Plane and Out-of-Plane Interaction.* Stephen Kadsiewiczski and Khalid M. Mosalam. January 2009.
- PEER 2008/101** *Seismic Performance Objectives for Tall Buildings.* William T. Holmes, Charles Kircher, William Petak, and Nabih Youssef. August 2008.
- PEER 2007/101** *Generalized Hybrid Simulation Framework for Structural Systems Subjected to Seismic Loading.* Tarek Elkhoraibi and Khalid M. Mosalam. July 2007.
- PEER 2007/100** *Seismic Evaluation of Reinforced Concrete Buildings Including Effects of Masonry Infill Walls.* Alidad Hashemi and Khalid M. Mosalam. July 2007.

The Pacific Earthquake Engineering Research Center (PEER) is a multi-institutional research and education center with headquarters at the University of California, Berkeley. Investigators from over 20 universities, several consulting companies, and researchers at various state and federal government agencies contribute to research programs focused on performance-based earthquake engineering.

These research programs aim to identify and reduce the risks from major earthquakes to life safety and to the economy by including research in a wide variety of disciplines including structural and geotechnical engineering, geology/seismology, lifelines, transportation, architecture, economics, risk management, and public policy.

PEER is supported by federal, state, local, and regional agencies, together with industry partners.



PEER Core Institutions:

University of California, Berkeley (Lead Institution)
California Institute of Technology
Oregon State University
Stanford University
University of California, Davis
University of California, Irvine
University of California, Los Angeles
University of California, San Diego
University of Southern California
University of Washington

PEER reports can be ordered at http://peer.berkeley.edu/publications/peer_reports.html or by contacting

Pacific Earthquake Engineering Research Center
University of California, Berkeley
325 Davis Hall, mail code 1792
Berkeley, CA 94720-1792
Tel: 510-642-3437
Fax: 510-642-1655
Email: peer_editor@berkeley.edu

ISSN 1547-0587X